AD-A257 974

AGARD-CP-498

AGARD

ADVISORY GROUP FOR AEROSPACE RESEARCH & DEVELOPMENT
7 RUE ANCELLE 92200 NEUILLY SUR SEINE FRANCE

DTIC
ELECTE
NOV 2 3 1992
S C D

AGARD CONFERENCE PROCEEDINGS 498

Aerodynamic Engine / Airframe Integration for High Performance Aircraft and Missiles

(L'Intégration Aérodynamique des Moteurs et des Cellules dans les Avions et les Missiles à Hautes Performances)

Papers presented and discussions held at the Fluid Dynamics Panel Symposium held in Fort Worth, Texas, United States, 7th—10th October 1991.

NORTH ATLANTIC TREATY ORGANIZATION

DISTRIBUTION STATEMENT A
Approved for public release;
Distribution Unlimited

Published September 1992

Distribution and Availability on Back Cover

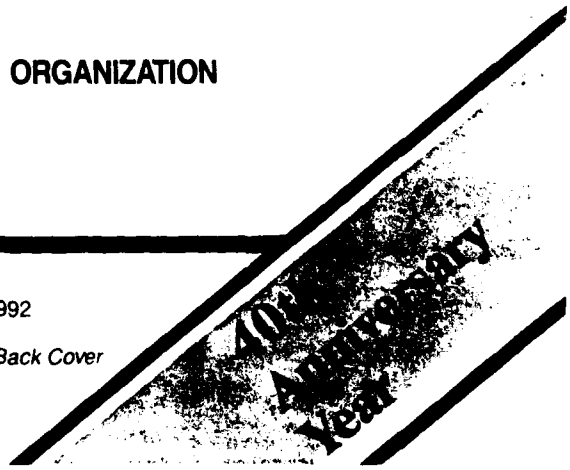

DISCLAIMER NOTICE

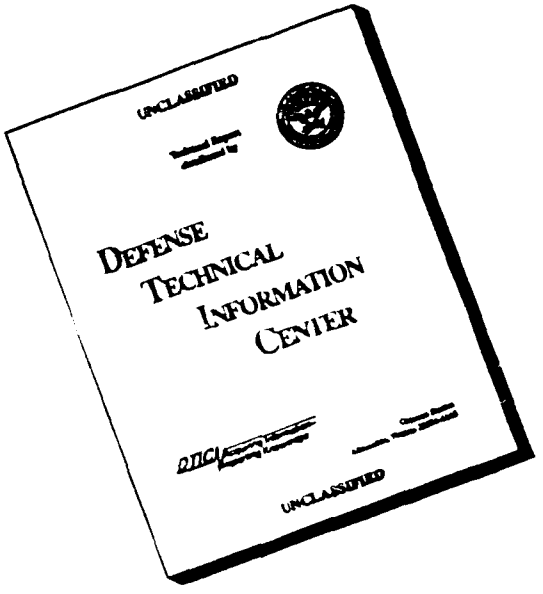

THIS DOCUMENT IS BEST QUALITY AVAILABLE. THE COPY FURNISHED TO DTIC CONTAINED A SIGNIFICANT NUMBER OF PAGES WHICH DO NOT REPRODUCE LEGIBLY.

AGARD

ADVISORY GROUP FOR AEROSPACE RESEARCH & DEVELOPMENT

7 RUE ANCELLE 92200 NEUILLY SUR SEINE FRANCE

DTIC

AGARD CONFERENCE PROCEEDINGS 498

Aerodynamic Engine/Airframe Integration for High Performance Aircraft and Missiles

(L'Intégration Aérodynamique des Moteurs et des Cellules dans les Avions et les Missiles à Hautes Performances)

Accession For
NTIS GRA&I
DTIC TAB
Unannounced
Justification
By
Distribution/
Availability Codes
Dist Avail and/or Special
A-1

Papers presented and discussions held at the Fluid Dynamics Panel Symposium held in Fort Worth, Texas, United States, 7th—10th October 1991.

North Atlantic Treaty Organization
Organisation du Traité de l'Atlantique Nord

92-30015

The Mission of AGARD

According to its Charter, the mission of AGARD is to bring together the leading personalities of the NATO nations in the fields of science and technology relating to aerospace for the following purposes:

- Recommending effective ways for the member nations to use their research and development capabilities for the common benefit of the NATO community;
- Providing scientific and technical advice and assistance to the Military Committee in the field of aerospace research and development (with particular regard to its military application);
- Continuously stimulating advances in the aerospace sciences relevant to strengthening the common defence posture;
- Improving the co-operation among member nations in aerospace research and development;
- Exchange of scientific and technical information;
- Providing assistance to member nations for the purpose of increasing their scientific and technical potential;
- Rendering scientific and technical assistance, as requested, to other NATO bodies and to member nations in connection with research and development problems in the aerospace field.

The highest authority within AGARD is the National Delegates Board consisting of officially appointed senior representatives from each member nation. The mission of AGARD is carried out through the Panels which are composed of experts appointed by the National Delegates, the Consultant and Exchange Programme and the Aerospace Applications Studies Programme. The results of AGARD work are reported to the member nations and the NATO Authorities through the AGARD series of publications of which this is one.

Participation in AGARD activities is by invitation only and is normally limited to citizens of the NATO nations.

The content of this publication has been reproduced
directly from material supplied by AGARD or the authors.

Published September 1992

Copyright © AGARD 1992
All Rights Reserved

ISBN 92-835-0672-3

Printed by Specialised Printing Services Limited
40 Chigwell Lane, Loughton, Essex IG10 3TZ

Recent Publications of the Fluid Dynamics Panel

AGARDOGRAPHS (AG)

Design and Testing of High-Performance Parachutes
AGARD AG-319, November 1991

Experimental Techniques in the Field of Low Density Aerodynamics
AGARD AG-318 (E), April 1991

Techniques Expérimentales Liées à l'Aérodynamique à Basse Densité
AGARD AG-318 (FR), April 1990

A Survey of Measurements and Measuring Techniques in Rapidly Distorted Compressible Turbulent Boundary Layers
AGARD AG-315, May 1989

Reynolds Number Effects in Transonic Flows
AGARD AG-303, December 1988

REPORTS (R)

Unstructured Grid Methods for Advection Dominated Flows
AGARD R-787, Special Course Notes, May 1992

Skin Friction Drag Reduction
AGARD R-786, Special Course Notes, March 1992

Engineering Methods in Aerodynamic Analysis and Design of Aircraft
AGARD R-783, Special Course Notes, January 1992

Aircraft Dynamics at High Angles of Attack: Experiments and Modelling
AGARD R-776 Special Course Notes, March 1991

Inverse Methods in Airfoil Design for Aeronautical and Turbomachinery Applications
AGARD R-780, Special Course Notes, November 1990

ADVISORY REPORTS (AR)

Air Intakes for High Speed Vehicles
AGARD AR-270, Report of WG 13, September 1991

Appraisal of the Suitability of Turbulence Models in Flow Calculations
AGARD AR-291, Technical Status Review, July 1991

Rotary-Balance Testing for Aircraft Dynamics
AGARD AR-265, Report of WG 11, December 1990

Calculation of 3D Separated Turbulent Flows in Boundary Layer Limit
AGARD AR-255, Report of WG10, May 1990

Adaptive Wind Tunnel Walls: Technology and Applications
AGARD AR-269, Report of WG12, April 1990

CONFERENCE PROCEEDINGS (CP)

Effects of Adverse Weather on Aerodynamics
AGARD CP-496, December 1991

Manoeuvring Aerodynamics
AGARD CP-497, November 1991

Vortex Flow Aerodynamics
AGARD CP-494, July 1991

Missile Aerodynamics
AGARD CP-493, October 1990

Aerodynamics of Combat Aircraft Controls and of Ground Effects
AGARD CP-465, April 1990

Computational Methods for Aerodynamic Design (Inverse) and Optimization
AGARD-CP-463, March 1990

Applications of Mesh Generation to Complex 3-D Configurations
AGARD CP-464, March 1990

Fluid Dynamics of Three-Dimensional Turbulent Shear Flows and Transition
AGARD CP-438, April 1989

Validation of Computational Fluid Dynamics
AGARD CP-437, December 1988

Aerodynamic Data Accuracy and Quality: Requirements and Capabilities in Wind Tunnel Testing
AGARD CP-429, July 1988

Aerodynamics of Hypersonic Lifting Vehicles
AGARD CP-428, November 1987

Aerodynamic and Related Hydrodynamic Studies Using Water Facilities
AGARD CP-413, June 1987

Applications of Computational Fluid Dynamics in Aeronautics
AGARD CP-412, November 1986

Store Airframe Aerodynamics
AGARD CP-389, August 1986

Unsteady Aerodynamics — Fundamentals and Applications to Aircraft Dynamics
AGARD CP-386, November 1985

Aerodynamics and Acoustics of Propellers
AGARD CP-366, February 1985

Improvement of Aerodynamic Performance through Boundary Layer Control and High Lift Systems
AGARD CP-365, August 1984

Wind Tunnels and Testing Techniques
AGARD CP-348, February 1984

Aerodynamics of Vortical Type Flows in Three Dimensions
AGARD CP-342, July 1983

Missile Aerodynamics
AGARD CP-336, February 1983

Prediction of Aerodynamic Loads on Rotorcraft
AGARD CP-334, September 1982

Wall Interference in Wind Tunnels
AGARD CP-335, September 1982

Fluid Dynamics of Jets with Applications to V/STOL
AGARD CP-308, January 1982

Aerodynamics of Power Plant Installation
AGARD CP-301, September 1981

Computation of Viscous-Inviscid Interactions
AGARD CP-291, February 1981

Subsonic/Transonic Configuration Aerodynamics
AGARD CP-285, September 1980

Turbulent Boundary Layers Experiments, Theory and Modelling
AGARD CP-271, January 1980

Aerodynamic Characteristics of Controls
AGARD CP-262, September 1979

High Angle of Attack Aerodynamics
AGARD CP-247, January 1979

Foreword

This is the second FDP symposium on the subject of aerodynamic engine/airframe integration. The previous one was organized together with the AGARD Propulsion and Energetics Panel (PEP) in May 1981. Given the overall positive response to the first symposium, and in light of the tremendous progress achieved in related technical areas, and because of the need for increasingly integrated design of civil and military aircraft and missiles, this second symposium seemed to be timely after 10 years.

The aerodynamic engine/airframe integration of aircraft and missiles involves complex flows, highly influenced by viscous effects and, in most cases, by aerodynamic interactions between the airframe and the populsion system. This engineering task is considered to be a "Key Problem" during the design phase of most new flight vehicles. The continuing demand for the highest efficiency in civil transport aircraft and for increased performance and maneuverability of both missiles and fighter aircraft has led to an extensive increase in experimental and especially CFD-related design efforts.

It was the aim of the symposium to review the state-of-the-art in aerodynamic engine/airframe integration techniques and to report on the progress which has been made during engineering project work in recent years. Because aerodynamic engine/airframe integration has become an interdisciplinary challenge, both experimentalists and theoreticians were invited to contribute to the meeting.

This symposium is technically associated with several other activities within the AGARD community: FDP WG 13 (1987–1990) on "Air Intakes for High Speed Vehicles" [AGARD-AR-270] and PEP WG 18 (1985–1988) on "Test Cases for Computation of Internal Flows in Aero Engine Components" [AGARD-AR-275]. More recently, the PEP conducted a symposium in May 1991 on "CFD Techniques in Propulsion Applications" [AGARD-CP-510]. It was decided to include at least technical overviews of these activities in the programme of the present symposium. Therefore, the PEP was invited to organize an "Invited Session" on "Engine Related Integration Problems" (Session II). The Programme Committee gratefully acknowledges the efforts of the PEP and specifically the support given by Professor Leonard Fottner of the University of Neubiberg, Germany, who organized and chaired this session.

Statistics: Papers No. 2, 8 and 29 from the original schedule of 33 papers were withdrawn at a late date. Fortunately, two replacement papers were developed to replace Nos. 2 and 29, and Paper No. 9 was extended to use the time slot for No.8. Therefore, a total of 32 papers were delivered. Contributors to the papers – including authors and co-authors – came from *Belgium* (1), *France* (7), *Germany* (10), Italy (2), The Netherlands (2), the United Kingdom (9), and the United States (9).

On behalf of the Programme Committee, I would like to express my appreciation for the commitments made by J. Leynaert, ONERA, FR; W. Burgsmüller, Deutsche Airbus GE; and R. Rudnik, A. Ronzheimer, C.-C. Rossow, and H. Hoheisel, DLR, GE for preparing replacement papers and presentations in such a short time.

The symposium was structured in six sessions:

(I) Engine Integration for Civil Transport (9 papers)
(II) Engine Related Integration Problems (4 papers)
(III) Experimental Techniques Used in Aerodynamic Engine/Airframe Integration (6 papers)
(IV) Aerodynamic Inlet/Airframe Integration (5 papers)
(V) Aerodynamic Nozzle/Airframe Integration (5 papers)
(VI) Aerodynamic Engine/Airframe Integration for Hypersonic Speed Vehicles (3 papers)

The Technical Evaluation Report (TER) aimed at assessing the relevance and success of the symposium in meeting the technical needs of the aerospace community was prepared by Wolfgang Schmidt, MBB, GE. In addition to the 32 papers from the symposium, the TER and the transcript of the Round Table Discussion held at the end of the meeting are included in these proceedings.

P.W. Sacher
Chairman, Programme Committee

Avant-Propos

Cette réunion est le deuxième symposium organisé par le FDP sur le thème de l'intégration aérodynamique des propulseurs cellules, le premier ayant été tenu au mois de mai 1981 en collaboration avec le Panel PEP de l'AGARD. Vu la réaction globalement favorable à ce premier symposium, vu les progrès considerables qui ont été réalisés dans les domaines techniques connexes, et en raison de la demande croissante de conception intégrée pour les aéronefs civils et militaires et les missiles, le Panel a jugé opportun d'organiser, après un intervalle de dix ans, ce deuxième symposium.

L'intégration aérodynamique des propulseurs/cellules des aéronefs et des missiles met en jeu des écoulements complexes, qui sont fortement influencés par des effets visqueux et, dans la plupart des cas, par les interactions aérodynamiques entre la cellule et le propulseur. Cette opération est considérée comme un "problème clé" pendant la phase d'étude de la majorité des nouveaux véhicules aériens. Les exigences en ce qui concerne le maintien de la plus grande efficacité des avions de transport civils et l'amélioration des performances et de la manoeuvrabilité des missiles et des avions de combat ont eu pour résultat l'amplification des programmes d'études expérimentales, en particulier lorsqu'ils font appel à aérodynamique numérique.

Le symposium a eu pour object de revoir l'état de l'art dans le domaine des techniques d'intégration aérodynamique des propulseurs/cellules et de rendre compte des progrès réalisés par le biais des projects d'ingéniérie ces dernières années. Puisque l'intégration aerodynamique des propulseurs/cellules est actuellement considérée comme un défi interdisciplinaire, les expérimentateurs ont été invités à participer à la réunion au même titre que les théoriciens.

Le symposium est associé techniquement à un certain nombre d'autres activités entreprises au sein de la communauté de l'AGARD: FDP WG13 (1987-1990) "Entrées d'air pour véhicules aériens à grande vitesse" (AGARD AR 270) et PEP WG18 (1985-1988) "Cas d'essai pour le calcul des flux internes dans les organes des moteurs d'avion" (AGARD AR 275). Récemment, le PEP a organisé un symposium, au mois de mai 1991, sur "Les techniques de l'aérodynamique numérique (CFD) pour des applications dans le domaine de la propulsion" (AGARD CP 510). Il a été décidé d'inclure au moins des résumés techniques de ces activités au programme de ce symposium. Ainsi, il a été proposé au PEP d'organiser une "Session par invitation" sur "Les problèmes d'intégration liés aux moteurs" (Session II). Le comité du programme tient à exprimer sa reconnaissance envers le PEP pour les efforts qui y ont été consacrés et, en particulier pour le soutien fourni par le Professeur Leonard FOTTNER de l'Université de Neubiberg, en Allemagne, qui a organisé et présidé cette session.

Quelques chiffres: Les communications Nos. 2, 8, et 29 qui figuraient sur la liste initiale de 33 communications ont été retirées peu avant le symposium. Heuresement, deux autres communications ont pu être proposées en remplacement des Nos. 2 et 29, et la communication No. 9 a été amplifiée afin de profiter du temps programme créé par l'absence du No. 8. Trente deux communications ont donc été présentées au total. Les contributions des auteurs et co-auteurs des différentes communications s'établissent comme suit: la Belgique (1), la France (7), l'Allemagne (10), l'Italie (2), les Pays-Bas (2), le Royaume-Uni (9) et les Etats-Unis (9).

Au nom du comité du programme, je tiens à remercier J. Leynaert de l'ONERA FR; W. Burgsmüller, Deutsche Airbus, GE; et R. Rudnik, A. Ronzheimer, C.C. Rossow et H. Hoheisel, DLR GE pour avoir bien voulu accepter de préparer des presentations de remplacement avec si peu de préavis.

Le symposium a été organisé en six sessions:

(I) L'intégration des moteurs dans les aéronefs civils
(9 communications)
(II) Les problèmes d'intégration liés aux moteurs
(4 communications)
(III) Les techniques experimentales mises en oeuvre pour l'intégration aérodynamique des propulseurs/cellules
(6 communications)
(IV) L'intégration aerodynamique des entrées d'air/cellules
(5 communications)
(V) L'intégration aérodynamique des tuyères/cellules
(5 communications)
(VI) L'integration aérodynamique des propulseurs/cellules pour véhicules hypersoniques
(3 communications)

Le rapport d'évaluation technique (TER), qui a pour object d'évaluer la pertinence du symposium et la mesure dans laquelle il a répondu aux attentes de la communauté aérospatiale, a été rédigé par Wolfgang Schmidt, MBB, GE. Ce compte-rendu comprend, en plus des 32 communications figurant au programme du symposium, le TER et la transcription des discussions qui ont eu lieu lors de la table ronde.

P.W. Sacher
Président, Comité du Programme

Fluid Dynamics Panel

Chairman: Dr W.J. McCroskey
Senior Staff Scientist
US Army Aeroflightdynamics Directorate
Mail Stop N258-1
NASA Ames Research Center
Moffett Field, CA 94035-1099
United States

Deputy Chairman: Professor Ir J.W. Slooff
National Aerospace Laboratory NLR
Anthony Fokkerweg 2
1059 CM Amsterdam
The Netherlands

PROGRAMME COMMITTEE

Dipl. Ing. P.W. Sacher (Chairman)
Messerschmitt-Bolkow-Blohm-GmbH
FE13
Postfach 80 11 60
8000 München 80
Germany

Prof. R. Decuypere
Ecole Royale Militaire
Chaire de Mécanique Appliquée
Avenue de la Renaissance 30
B-1040 Brussels
Belgium

Dr L. Chan
High Speed Aerodyn. Lab. — U66
Institute for Aerospace Research
National Research Council
Montreal Road
Ottawa, Ontario K1A 0R6
Canada

M.J. Leynaert
Directeur Adjoint Grands Moyens d'Essais
ONERA
BP 72
92322 Châtillon Cedex
France

Dr Ing. H. Korner
Direktor
Institut fur Entwurfsaerodynamik der DLR
Flughafen
3300 Braunschweig
Germany

Dr Ing. G. Bucciantini
ALENIA
Aeritalia & Selenia S.p.A.
Settore Aeronautica
Gruppo Aerei Difesa
C.P. 432
10100 Torino
Italy

Ir A. Elsenaar
National Aerospace Laboratory NLR
Anthony Fokkerweg 2
1059 CM Amsterdam
The Netherlands

Dr J. Simon
CASA — Project Division
Aerodynamic Department
Avda. John Lennon s/n
Getafe
28065 Madrid
Spain

Mr P.R. Bignell
BAe PLC, Sowerby Research Centre
FPC 266, P.O. Box 5
Filton
Bristol BS12 7QW
United Kingdom

Mr D.L. Bowers
Flight Dynamics Laboratory
WL/FIMM
Wright-Patterson AFB
Ohio 45433-6553
United States

Dr R.G. Bradley, Jr
Director, Flight Sciences Dept.
Mail Zone 2888
General Dynamics
Fort Worth Div.
P.O. Box 748
Fort Worth, TX 76101-748
United States

Prof. Dr Ing. L. Fottner — PEP Representative
Institut für Strahlantriebe
Universität der Bundeswehr München
Werner Heisenberg Weg 39
D-8014 Neubiberg
Germany

PANEL EXECUTIVE

Dr W. Goodrich

Mail from Europe:
AGARD—OTAN
Attn: FDP Executive
7, rue Ancelle
92200 Neuilly-sur-Seine
France

Mail from US and Canada:
AGARD—NATO
Attn: FDP Executive
Unit 21551
APO AE 09777

Tel: 33 (1) 47 38 57 75
Telex: 610176 (France)
Telefax: 33 (1) 47 38 57 99

Contents

	Page
Recent Publications of the Fluid Dynamics Panel	iii
Foreword	v
Avant-Propos	vi
Fluid Dynamics Panel	vii
	Reference
Technical Evaluation Report by W.Schmidt	T

SESSION I – ENGINE INTEGRATION FOR CIVIL TRANSPORT
Chairmen: R. Bignell and A. Elsenaar

Test Techniques for Engine/Airframe Integration by A.F.Harris	1
Essais de Maquettes Motorisées Equipées de Simulateurs de Réacteurs dans la Soufflerie Basse Vitesse Pressurisée F1, de l'ONERA (Tests of Models Equipped with TPS in Low Speed ONERA F1 Pressurized Wind Tunnel) par J.Leynaert	2
Simulation Numérique de l'Ecoulement Aérodynamique autour des Nacelles par J.J. Lecordix, J.G.Fratello et J.M.Gippet	3
Analyse Détaillée de l'Interaction Voilure-Nacelle d'un Avion de Transport Civil par J.L.Godard, O.-P.Jacquotte et D.Gisquet	4
Investigation of Interference Phenomena of Modern Wing-Mounted High-Bypass-Ratio Engines by the Solution of the Euler-Equations by C.-C.Rossow and A.Ronzheimer	5
Aerodynamic Analysis of Slipstream/Wing/Nacelle Interference for Preliminary Design of Aircraft Configurations by C.M.van Beek, W.J.Piers and B.Oskam	6
Euler Analysis of Turbofan/Superfan Integration for a Transport Aircraft by D.A.Naik, H.C.Chen, T.Y.Su and T.J.Kao	7
Paper 8 withdrawn	
Recent Developments in Low-Speed TPS-Testing for Engine Integration Drag and Installed Thrust Reverser Simulation by W.Burgsmuller, C.Castan, J.W.Kooi and J.P.Bécle	9
Aerodynamic Integration of Thrust Reversers on the Fokker 100 by J.van Hengst	10

Reference

SESSION II -- ENGINE RELATED INTEGRATION PROBLEMS*
Chairman: L. Fottner

Overview on Test Cases for Computation of Internal Flows in Turbomachines 11
by L. Fottner

The PEP Symposium on "CFD Techniques for Propulsion Applications" 12
by Ch. Hirsch

The Influence of Intake Swirl Distortion on the Steady-State Performance of a Low Bypass, Twin-Spool Engine 13
by W. Meyer, W. Pazur and L. Fottner

Analyse en Vol de la Compatibilité Entrée d'Air-Moteur 14
par H. Joubert et H. Eyraud

SESSION III – EXPERIMENTAL TECHNIQUES USED IN AERODYNAMIC ENGINE/AIRFRAME INTEGRATION
Chairman: J. Leynaert

ASTOVL Model Engine Simulators for Wind Tunnel Research 15
by A.F. Harris, G.L. Wilde, V.J. Smith, A.R.G. Mundell and D.P. Davidson

Mass Flow Effects on the Low Speed Cha acteristics of an Advanced Combat Aircraft 16
by F. Barbantini, A. Ferretti and A. Gatti

A Novel High-Performance System for Recording and Analysing Instantaneous Total Pressure Distortion in Air Intakes 17
by K.W. Cotter and R.D. Scherbaum

Water Tunnel Studies of Inlet/Airframe Interference Phenomena 18
by R. Maggio

Experimental Studies of the Flowfields and their Effects Due to a Pair of Lift Jets Discharging in the Ground Effect Region 19
by E.J. Hope and E.C.P. Ransom

The Jet Behaviour of an Actual High-Bypass Engine as Determined by LDA-Measurements in Ground Tests 20
by H. Hohersel et al

SESSION IV – AERODYNAMIC INLET/AIRFRAME INTEGRATION
Chairman: R.G. Bradley

Some Aspects of Intake Design, Performance & Integration with the Airframe 21
by E.L. Goldsmith

AGARD WG13 "Aerodynamics of High Speed Air Intakes": Assessment of CFD Results 22
by M.C. Bissinger, T.J. Benson and R.J. Bradley, Jr

Comparative Performance Tests of a Pitot-Inlet in Several European Wind-Tunnels at Subsonic and Supersonic Speeds 23
by P.-A. Mackrodt et al

Etudes Aérodynamiques de Prises d'Air Supersoniques 24
(Aerodynamic Studies of Supersonic Air Intakes)
par P. Garnero et R.G. Lacau

Application of Subsonic First-Order Panel Methods for Prediction of Inlet & Nozzle Aerodynamic Interactions with Airframe 25
by R.K. Nangia and M.E. Palmer

* Session Organized by the Propulsion and Energetics Panel

Reference

SESSION V – AERODYNAMIC NOZZLE/AIRFRAME INTEGRATION
Chairman: D. Bowers

Survey on Techniques Used in Aerodynamic Nozzle/Airframe Integration 26
by F. T. Bowers and J.A. Laughrey

Calibration of 2D Unstructured Grid Methods on Propulsive Flowfields 27
by S.E. Karman, Jr and G.S. Spragle

CFD Calibration for Three-Dimensional Nozzle/Afterbody Configurations 28
by C.L. Reed and A. Muyshondt

Investigation of the Flowfield around an Isolated Bypass Engine with Fan and Core Jet 29
by R. Rudnik, A. Ronzheimer, C.-C. Rossow and H. Hoheisel

Propulsion Integration Results of the STOL and Maneuver Technology Demonstrator 30
by J.A. Laughrey and D.J. Moorhouse

SESSION VI – AERODYNAMIC ENGINE/AIRFRAME INTEGRATION FOR HYPERSONIC SPEED VEHICLES
Chairman: J. Muylaert

Hypersonic Propulsion System Force Accounting 31
by K. Numbers

Integration of Turbo-Ramjet Engines for Hypersonic Aircraft 32
by O. Herrmann

Prises d'Air a Section de Captation Variable Application aux Lanceurs Aérobies 33
par F. Falempin et Ph. Duveau

Round Table Discussion RTD

Technical Evaluation Report

Wolfgang Schmidt

Messerschmitt-Bölkow-Blohm AG.
DASA - Military Aircraft Division
P.O. Box 80 11 60
D-8000 Munich 80

Abstract

The Fluid Dynamics Panel of AGARD arranged a Symposium on "Aerodynamic Engine/Airframe Integration for High Performance Aircraft and Missiles" during October 7-10, 1991 in Fort Worth/Texas, USA. The purpose of the Symposium was to provide an assessment of the status of CFD, design tools, and testing techniques for aerodynamic engine/airframe integration.

The meeting was structured in six sessions, one of them having been organized and chaired in form of an invited session by PEP contributions. Each session will be reviewed separately in this paper and conclusions (in some case recommendations for future AGARD activities) are made based on the major outcome of the sessions including contributions and comments from the auditorium after the presentations or from the closing Round-Table-Discussion at the end of the meeting.

It has been clearly demonstrated, that the subject of the symposium is a highly interdisciplinary effort, which overlaps the terms of reference of both AGARD Panels, FDP and PEP to a large extend. This is specifically true for major components of the propulsion system like the air intake and the nozzle. Both, experimental and computational techniques for analysis and design being used during engine/airframe integration for all kinds of flight vehicles have been reported.

Introduction

This was the second FDP meeting focussed on the subject of aerodynamic engine/airframe integration. The preceding one was organized together with the AGARD Propulsion and Energetics Panel in May, 1981. Due to the overall positive response to the first symposium, realizing the tremendous progress in the related technical area, and due to the raising need for more and more integrated design of civil and military aircraft and missiles in recent applications, this second symposium after 10 years was very timely.

The aerodynamic engine/airframe integration of aircraft and missiles involves complex flows, highly influenced by viscous effects and, in most cases, by aerodynamic interactions between the airframe and the propulsion system. This engineering task is considered to be a "Key-Problem" during the design phase of new flight vehicles of any kind. The continuing demand for highest efficiency in civil transport aircraft and the increase in performance and maneuverability for both, missile and fighter aircraft development, have led to extensive increase of experimental and specifically C' D-related design efforts.

It was the aim of the symposium to review the state of the art in aerodynamic engine/airframe integration techniques reached at present and to report on the progress which has been achieved during engineering project work in the past. Because of the fact that engine/airframe integration has become a highly interdisciplinary challenge, both experimentalists and theoreticians were invited to contribute to the success of the meeting.

The conference was technically associated with several other activities within the AGARD community. So the AGARD FDP has organized in 1987-1990 WG13 on "Air Intakes for High Speed Vehicles", (AGARD-AR-270) and in 1985-1988 PEP WG18 on "Test Cases for Computation of Internal Flows in Aero Engine Components", (AGARD-AR-275). More recently PEP has arranged a symposium in May 1991 on "CFD Techniques in Propulsion Applications", (AGARD CP 510). It was decided to include at least the technical evaluations of this AGARD activities in the programme of this symposium. So PEP was invited to organize an "Invited Session" on "Engine Related Integration Problems", (Session II). The Programme Commitee gratefully acknowledged the efforts of PEP and specifically the support given by Prof. Leonhard Fottner, University of Neubiberg, GE, who organized and chaired this session.

Statistics:
33 Papers (including three invited papers and four papers in an invited session) have been presented. Contributions to the meeting came from Belgium (1), France (7), Germany (10), Italy (2). The Netherlands (2), The United Kingdom (9) and USA (9).

The symposium was structured in six sessions:

(I) Engine Integration for Civil Transport (10 papers)
(II) Engine Related Integration Problems (4 papers)
(III) Experimental Techniques used in Aerodynamic Engine/Airframe Integration (6 Papers)
(IV) Aerodynamic Inlet/Airframe Integration (5 papers)
(V) Aerodynamic Nozzle/Airframe Integration (5 papers)
(VI) Aerodynamic Engine/Airframe Integration for Hypersonic Speed vehicles (3 papers)

Each session will be reviewed separately in this paper and conclusions (in some cases recommendations for future AGARD activities) are made based on the major outcome of the sessions including contributions and comments from the auditorium after the presentations or from the closing Round-Table-Discussion at the end of the meeting.

As outlined in Fig. 1, there is some logic in the structure of the programme given by more and more complex applications.

The contributions specifically mentioned in this review

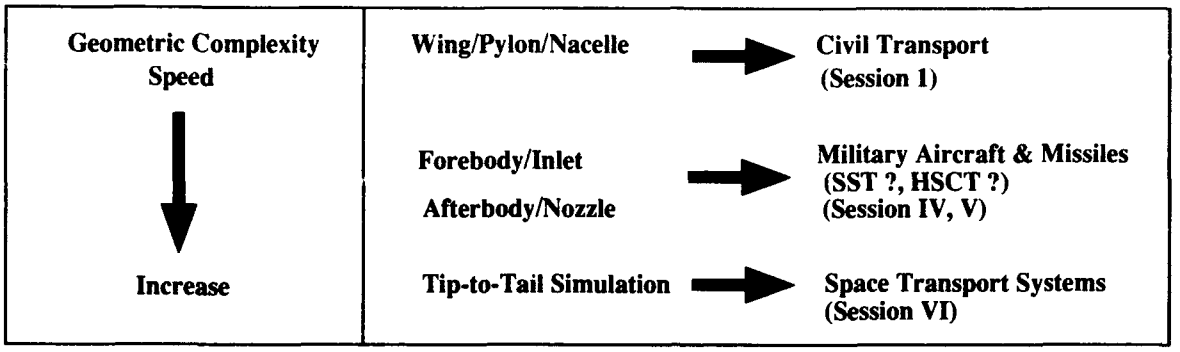

Fig. 1 Logic of the Programme of the Symposium on Aerodynamic Engine/Airframe Integration

will be referenced by the paper number, as to be found in the conference proceedings (AGARD CP 498).

SESSION I: ENGINE/INTEGRATION FOR CIVIL AIRCRAFT

The main objectives of this session can be summarized as follows:

1. Survey of experimental test techniques for engine/nacelle/wing integration [1]
2. Survey of numerical prediction methods for engine/nacelle/wing intereference effects, [3], [4], [5], [6], [7], [8]
3. Integration effects of installed thrust reverser, [9], [10]

This was a quite well balanced session. Both, experimental investigations and theoretical work have been reported. The invited introductory paper, given by A. E. Harris [1], was an extremely detailed description of all major aerodynamic interference effects due to propulsion systems integration for civil and military aircraft at all speeds (see paper [1], Figs. 2, 9 and 18 for a summary). The use of CFD for engine/airframe integration was reported in several papers and for different classes of flow models. In Figs. 11 and 15 in paper [6] results obtained by van Beek/Piers/Oskam demonstrate the usefulness of linearized potential flow codes ("Panel Methods") and Figs. 23 and 24 of paper [4] presents engine installation effects on the wing planform by Godard/Jaquotte/Gisquet predicted by a solution of the full potential flow equations.

As highest level of 3D CFD, solutions of the Euler equations, were demonstrated by Rossow/Ronzheimer, GE [5], see Figs. 5 and 9, Gippet/Fratello/Lecordix from France [3] and Naik/Chen/Su/Kao from US [7]. Two papers [9] and [10], were dealing with the important aspects for civil transport aircraft of thrust reversing in flight and in ground effect.

In conclusion the session may be charcterized as follows:

1. Civil transport aircraft are dominated by economic requirements. Airframe/engine integration is important for
   - second segment climb
   - cruise
   - thrust reverser interference
2. In Europe well established testing techniques exist using TPS for Turbo-Fan and Turbo-Prop simulation in WT's, (TPS is facility equipment). US industry prefers powered nacelles using pressurized air.
3. CFD applications still rather limited for cruise conditions
   - No N.S. solutions
   - Euler analysis [3], [8], [5], [7]
   - Still work using Panel [6] and full potential [4] methods
4. CFD limited not only due to computing cost - to a large degree due to mantime cost (e.g. for grid generation)
5. Many engineering efforts restricted to simply adding pylon/nacelle/engine to clean wing design
6. Wing design procedures taking into acount the effects of propulsion systems installation are required.

SESSION II: ENGINE-RELATED INTEGRATION PROBLEMS (INVITED PEP-SESSION)

The Session was chaired by L. Fottner from the PEP and all contributions came from this panel. The objectives of the session can be summarized as follows:

1. Survey on PEP WG 18, "Test Cases for Internal Flows in Turbomachines" [11]
2. Survey on PEP symposium "CFD Techniques for Propulsion Applications" [12]
3. Intake-engine compatibility [13], [14]

The WG18 had compiled an extensive experimental database on various test cases as L. Fottner [11] showed. The impression remains that a follow-on activity is needed and the question comes up whether the experimental data being available are sufficient for code validation or not.

The review from Ch. Hirsch [12] reported on the outcome of the PEP symposium Spring 1991 in San Antonio, US, on the subject of "CFD Techniques in Propulsion Applications".

Rather than adding own comments, I would like to refer to the recommendations of the Technical Evaluator of this PEP conference, Dr. L. Povinelli, since they are most certainly of general validity also for the FDP community.

- More emphasis should be given to validation and to a strong interaction between experimentalists and CFD specialists.
- Efforts should be expanded on turbulence and transition modelling, including compressibility effects, higher order closures, pdf modelling, direct numerical simulations (DNS) of turbulence.

- Three-dimensional Navier-Stokes simulations are essential for propulsion system simulations, having already led to significant progress. Fine grids are needed, since coarse computations will normally not be sufficient.
- Future activities, such as Symposia, should be encouraged within the AGARD Panels, in the field of Validation of Propulsion CFD.

The remaining two papers dealt with the important effects of intake/engine compatibility. In Fig. 8 the test apparatus and test instrumentation arrangement for the assessment of the flow field at the engine entry cross sections is shown by Meyer/Pazur/Fottner [13]. Swirl distortion is generated by a "Vortex-Generating" Delta Wing planform.

Steady and unsteady distortion of total pressures obtained in ground and flight testing were compared by Joubert/Eyraud in [14] and typical results are shown in Figs. 2 and 13 of [14].

Conclusions for session II:

1. PEP WG18 compiled an extensive experimental data base but follow-on activities are needed.
2. Experiment needs new quality to satisfy requirements for accuracy and details to be datum solutions for validation of CFD, therefore: CFD validation extremely difficult since nothing to validate against in real 3-D flow (only calibration?)
3. Air intake distortions require extensive experimental efforts. So far very limited CFD work (if not none), therefore: Communication airframe/engine manufacturer mandatory.
4. Session indicates many common areas of interest in PEP and FDP activities therfore: coordination, communication and more joined efforts strongly recommended.

SESSION III: EXPERIMENTAL TECHNIQUES USED IN AERODYNAMIC ENGINE/AIRFRAME INTEGRATION

Again the main objectives of the session will be described first:

1. Engine simulators for wind tunnel research of engine integration effects, [15]
2. Intake flow field data acquisition systems used for investigation of Intake/airframe interaction [16], [17], [18]
3. Test technique used for investigation of jets in the ground effect region [19], [20].

Wind tunnel, see Harris/Wilde/Smith/Mundell/Davidson [15], Figs. 4 and 8 water tunnels, see Maggio [18], Figs. 5 and 12 and ground-, see Hoheisel / Bütefisch / Lehmann / Henke/ Roscher/ Seelhorst [20], Figs. 2, 3, 12 and 13 and flight testing were reported extensively. Each of this engineering techniques is heavily in use during investigations of engine/airframe installation effects and during the configuration optimization process during design of a new aircraft. TPS Technique begins also to be used for military fighter aircraft design. In addition complex data reduction and data acquisition systems on a mobile basis are available and laser doppler anemometrie starts to be used for full scale flow analysis allowing validation of experimental tools like TPS in addition to CFD tools. There is a remarkable increased effort on the airframe manufacturer side to understand complex flow physics due to engine integration effects and the question arises whether there is also the same kind of parallel effort on the engine manufacturers side.

Conclusions for session III:

1. Wind tunnel, water tunnel, ground and flight test used for investigations to understand interference effects due to engine/airframe integration.
2. TPS is standard in Europe, tools owned by test facilities therefore reasonable ROI because being used in many programmes.
3. TPS starts to move in military A/C development, problem with hot gas (afterburner) simulation.
4. LDA techniques start to be used for full scale flow analysis [20] allowing for validation of TPS and CFD work.
5. Extensive data reduction and data acquisition systems on a mobile basis available. Question: What can the engine manufacturer do with large amount of flow details obtained?
6. Increased effort on airframe side to understand complex flowfields due to engine integration

SESSION IV: AERODYNAMIC INLET/AIRFRAME INTEGRATION

Five papers were presented in this session. They focussed on the following subjects

1. Techniques used for aerodynamic inlet/airframe integration, [21].
2. CFD applications to inlet airframe integration [24], [25] and the survey on FDP WG13 activities: "Aerodynamics of High Speed Air Intakes" [22].
3. Experimental investigations of pitot type air intakes in several European WT's [23]

An introductory invited paper was given by L. Goldsmith [21] on the techniques used for aerodynamic inlet/airframe integration. A huge variety of geometrical arrangements of intakes exists in different aircraft and missile designs. There was no tendency to find an optimum of the inlet position, because this is dependent on mission profile and geometric shape. The individual results may be an answer to high angle-of-attack or speed requirements and it is completely different for aircraft and missiles. What was missing is a general philosophy on how to find the optimum position of the inlet in each different application. Ganero/Lacau have addressed this question in Figs. 1, 2 and 3 in paper [24].

The results of the FDP WG13 have been quite impressive, see Bissinger/Benson/Bradley [22]. The compilation of test cases and contributions for CFD application is shown in Tables 1 and 2 of paper [22]. A huge amount of data has been produced but the main conclusion from this exercise is, that for code validation "specific designed experiments" are needed. But CFD results show also differences for the same class of equations having been solved. The mesh refinement plays obviously a most important role for the quality of any solution.

Another observation is the need for highly experienced, trained-on-the-job engineers, because these CFD codes are really not any more black boxes which may be used by anyone.

Also experimental investigations on intakes of the same

geometry in different wind tunnels show differences as Mac-Knight/Goldsmith/McGregor/Leynaert/Garcon/Brill report in [23]. This is another remarkable international effort which has been performed in true cooperation. Figs. 1, 14 and 17 of paper [23] shows one of the comparisons of data obtained in three different windtunnels as an representative example.

In summary, the following conclusion might be drawn from the session on inlet/airframe integration problems:

1. Huge variety of geometrical arrangements of intakes for different A/C and missile designs [21], [24].
2. Optimum of intake position dependent on mission profile, vehicle design, AOA- and speed range.
3. Outcome of WG13, [22]:
   - impressive collection of data.
   - CFD needs specifically designed experiments.
   - CFD results differ even for the same class of physical model.
   - Grid resolution plays an important role.
   - Need for highly experienced (trained-on-the-job) engineers - Results from internal flow test cases even more confusing than for external flow.
4. Experimental (Pitot-Type) inlet test case [23], shows significant deviations for DC60 in three different WT's and comparison with CFD is missing.
5. Remarkable effort dedicated to HSCT (2<M<5), CFD-Tools have been applied to 3D external and internal flow simulation A (GV, AST, Missiles...) [24].
6. FDP WG13-Report considered as "State-of-the-Art" notebook for designers and guide for CFD and testing techniques.
7. As already stated new quality of experiments is needed for validation of EFD and CFD.
8. More approaches needed to set up a design concept philosophy for engine/airframe integration [24] using data base, CFD and EFD.
9. CFD community should not only share success but also bad luck (to get "lessons learned").

SESSION V: AERODYNAMIC NOZZLE/AIRFRAME INTEGRATION

The main emphasis was given to the following objectives:

1. Survey on progress made since WG08 (1984) with respect to experimental and numerical techniques [26].
2. Calibration of 2D full N.S. solutions for complex highly integrated propulsive exhaust systems [27], [28].
3. Propulsion integration results of the STOL and Maneuver Technology Demonstrator Programme (S/MTD) [30].

The survey on exhaust system design requirements given by Bowers/Laughrey in [26] is characterized in Figs. 1 and 3 of paper [26]. The increasing requirements on the overall performance of nozzle designs lead to the conclusion that "Exhaust Nozzles Aren't Round Anymore"! More and More of advanced technology has to be implemented in modern military aircraft design. This has led to technology demonstrator vehicles like Laughrey/Moorhouse describe in Figs. 1 and 2 of paper [30]. Typical representative data fom N.S. CFD simulations in comparison with experimental results are shown in Figs. 6, 7, 12, 16, 17 and 18 of paper [28] reported by Reed/Muyshoundt.

The major findings of this session can be summarized as follows:

1. No major break-through since WG08 (1986) in experimental techniques. Interesting Question: "Will the "State-of-the-Art" of tomorrow be as good as today"? (D. Bowers)
2. Major findings from CFD applications:
   - only the highest level (full Navier-Stokes) promising to simulate the complex viscous flow regime
   - again strong requirements for test cases "designed" for CFD validation.
   - Progress in 2D NS Solvers but turbulence modelling still unsatisfactory.
   - Geometric restrictions due to lack of 3D N.S. codes - strong requirement for "User-Friendlyness" of CFD codes.
   - "Magic Triangle":

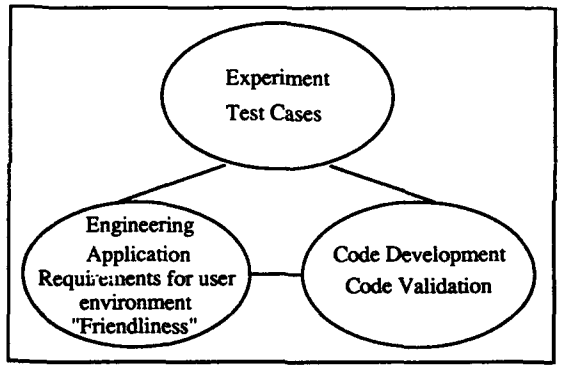

AGARD WG17 starts in 1992!

SESSION VI: AERODYNAMIC ENGINE/AIRFRAME INTEGRATION FOR HYPERSONIC SPEED VEHICLES

The last session was quite short. Only three papers have been submitted, but it concentrates on the highest degree of engine/airframe integration.

Objectives:

1. Force accounting systems for hypersonic propulsion system integration.
2. Integration of turbo-ramjet engines for hypersonic aircraft.
3. Variable-capture-area intakes for hypersonc vehicles

The integration of the airbreathing propulsion system for hypersonic flight vehicles is not yet engineering routine today and therefore it can be explained that the highest identification with the national programmes has to be accepted. This

leads to the conclusion that most of the data but even more the procedures used during systems design are "Company Confidential". But nevertheless the contributions given to this session have been impressive. So O. Herrmann reviews the problems of the integration of turbo-ramjet engines for hypersonic aircraft intensively in paper [32] and Fig. 1.1 of this paper gives some impression of the complexity of the engineering task. Again CFD is extensively used and typical representative results obtained by 2D Euler solutions for the nozzle aftbody integration are shown in Fig. 3.3. The force accounting system for hypersonic flight vehicles was addressed by K. E. Numbers in paper [31], Fig. 4. Nearly each airframe and engine manufacturer has introduced his own version of creating the "engine/airframe-interface". A specific problem for vehicles flying with airbreathing propulsion over an extended Mach number range is treated by Falempin/Duveau in [33]. Three concepts for variable capture area intakes to compromise diverging requirements for massflow and drag at low and high speed are presented according to Figs. 11, 12, 14, 15 and 17 in paper [33].

Conclusions from session IV:

1. Only three papers submitted but highly qualified and impressive presentations given.
2. Highest degree of engine/airframe integration needed - not yet "Routine Engineering Procedure" therefore:)
3. Highest identification with programme/project status
   - NASP
   - HOTEL
   - SÄNGER - Results classified!
   - STAR-H
   - Subject for future AGARD activities (e.g. FDP WG18)

CONCLUSIONS

Some general observations may be as follows:

1. Objectives of the meeting (according to the call for papers) have been reached to a large degree.
2. Successful attempt to "integrate people" working in different engineering areas:
   - experimentalists/theoreticians
   - civil/military/space transport applications
   - external/internal flow specialists
   - FDP/PEP AGARD community
3. Active and stimulating discussions have taken place:
   - all papers being available in written form at the meeting
   - excellent professional presentations
   - perfect organization, optimal local arrangements and
   - outstanding hospitality

The technical evaluation of the outcome of the meeting comes to the following conclusions:

1. Propulsive flowfields involve more and more complex geometry and complex physics.
2. Successful engine/airframe integration relies to a large degree on extensive WT-testing using engine simulation tools (TPS).
3. Optimization of civil and military configurations need complementary support from CFD.
4. Need for viscous flow representation in CFD, but still limitatons for practical ("engineering") work exisit.
5. CFD even more important (and complex) for internal flow.
6. Future trend to even higher integrated designs therefore requirements for "Tip-to-Tail" numerical simulation.

TEST TECHNIQUES FOR ENGINE/AIRFRAME INTEGRATION

A E Harris
Aircraft Research Association Ltd
Manton Lane, Bedford MK41 7PF, England

SUMMARY

The paper traces a path through modern experimental techniques in use for the study of installation performance in the context of military and civil engine/airframe integration studies.

For military and civil transport designs it is shown that separate treatment of air intake and exhaust regions is generally undertaken in contemporary methods. An early entry into the aerodynamics of the complete engine/airframe is emphasised in order to avoid costly integration difficulties.

Using examples largely drawn from direct experience gained during the period 1960 to 1990 the author presents a set of 'most preferred methods' for use in high speed configuration development model tests. It is noted that current trends in civil and military designs require increased attention to be paid to off-axis thrust/drag/lift variations in the engine/airframe integration process.

Methods of flow visualisation are briefly reviewed and the emerging laser methods are also identified.

The paper closes with a conceptual configuration for a year 2000 totally integrated engine/airframe to meet 21st century civil transport mass transit requirements.

LIST OF SYMBOLS AND ABBREVIATIONS

Aannulus	RDS annular compensating cell area
Adisc	RDS disc area
AF, NF	Axial Force, Normal Force
ASTOVL	Advanced Short Take-Off, Vertical Landing
BLC	Boundary Layer Control
BPR	By Pass Ratio
CFD	Computational Fluid Dynamics
C_L	Lift coefficient
CMAPS	Compact Multi-Mission Aircraft Powered Simulator
DBTFN, TFN	Double Body, Through Flow Nacelle
FPR	Fan Pressure Ratio
H	Test cell or TWT stagnation total pressure
HGR	Hot Gas Reingestion
M_l, M_{∞}, M	Local, freestream Mach number
MFR	Mass Flow Ratio
MOD	Ministry of Defence
MST	Mach Simulation Tank
η	Spanwise station
NPR	Nozzle Pressure Ratio
PS	Calibration tank or freestream static pressure
RAE	Royal Aerospace Establishment
S/G	Strain Gauge
S & C	Stability and Control
SFC	Specific Fuel Consumption
TPS	Turbine Powered Simulator
TWT	Transonic Wind Tunnel
UHBPR	Ultra High By Pass Ratio
VHBPR	Very High By Pass Ratio

1 INTRODUCTION

The demands for high quality high accuracy engine/airframe integration testing have progressed steadily in the last 30 years. This paper will focus attention on testing techniques for engine installation aerodynamics arising out of experience gained in the period 1960 to 1990.

In order to avoid a travelogue approach a path is traced to embrace the 'preferred methodology' rather than to review candidate or optional techniques. The main concerns of the paper relate to the studies necessary for combat and transport aircraft types; no reference is made specifically to techniques for studies of missiles, weapons, unmanned aircraft or spacecraft.

With the events of the early 90s close to our collective consciousness, it is clear that a substantial set of re-appraisals of future military and civil requirements is at hand. An increasing emphasis on quality assurance and overall certainty of the methodologies is a natural outfall of the changing priorities. In particular, it now appears that future combat aircraft will be developed to even higher levels of overall refinement and will undoubtedly be produced in more sparing numbers than has hitherto been the case. The 'quantity' cold war is over, quality will become the valid and necessary substitute. Effectiveness above all things will be the key in the drive for stealthy and ASTOVL designs. As a result, the current and future high performance combat/strike aircraft will present increased levels of technical challenge for the engine/airframe integration specialist. Use of the most effective testing techniques giving assured quality accurate simulations will remain the leading requirement; exploitation of the strengths of CFD both in design and for test support will receive increased emphasis.

For civil transports the cycle of events which suggested a more widespread use of open rotors has receded and it now becomes clear that we will see turbofan by-pass ratios move from around 2 to 6 to cover the scale 2 to 15. It is clear that the cycle selection will be firmly based on experimentally determined performance analyses allied to related structural/acoustic/aeroelastic design considerations. The cycle selection is also likely to be made with increased regard to fuel economy, environmental noise and first cost; the expanded use of composities and service life for high performance will play significant parts in the trade studies. The advent of very high performance gas generators will clearly lead to higher by-pass ratio turbofans; it is noted that a natural limit arises due to shaft speed to fan tip speed matching where the step to a geared fan is required. As a result it is likely that installations in the 90s will fall near to BPR = 9 and some much larger (15?) values for geared options. In overall terms it is preferred to call all of these variants VHBPR turbofans to distinguish the UHB or UHBPR open rotor parlance.
Current VHBPR research activities have yet to reach the point where trade studies can be carried out with full powered model interference data in support; however, much has been, and is being achieved in the pursuit of understanding the various features of interference aerodynamics which arise with the step from conventional to VHBPR installations. High accuracy

methods will be in even greater demand for these VHBPR installations as a result of the low specific thrust with very much increased airflow levels. Some advances in methodologies in response to these greater demands are outlined in this paper. Since the first cost of new installations represents a major part of the overall airline system costs it is clear that these new VHBPR and variants of existing turbofans will require yet higher levels of engine/airframe integration test quality assurance and accuracy definition.

2 HISTORICAL PERSPECTIVE

In November 1927 Mr Rex Pierson, the Chief Designer at Vickers Aviation, Weybridge, read a prophetic paper[1] to the Royal Aeronautical Society entitled 'The Use of the Wind Channel for Performance Prediction'. In his paper Pierson made a set of very telling observations. He noted that difficulties of aircraft performance prediction will arise for a completely new design 'owing to our inability to make correct allowances for the effect on lift and drag of various interferences'.

'All these factors', he went on, 'can be taken into account by wind-channel tests on the complete model of the proposed machine in the presence of the propeller delivering the correct thrust'... Pierson also noted that 'if we can obtain from these wind-channel tests accurate predictions by testing with various arrangements, we can find the most efficient combination which will fulfil the specification requirements' and to round off he advised 'The usefulness of the predictions depends entirely on the accuracy of agreement with full-scale tests in all cases'.

Today, despite the length of the intervening period since those prophetic words, extensive efforts are still expended both to match specification requirements and later to show that good agreement between wind-tunnel and full-scale (flight) tests has been achieved in all cases!!

A full 30 years later Mr L F Nicholson, of the Royal Aircraft Establishment at Farnborough, read a benchmark paper,[2] again to the Royal Aeronautical Society in London, his title was simply, Engine-Airframe Integration. In the quite prolonged discussion after his paper the debate focussed on what is meant by the words 'engine/airframe integration'. It is perhaps worth an attempt here to give an answer as the definition was somewhat masked in the 1957 debate.

Let us define 'Engine/Airframe Integration' as that process which is used whenever 'the performance of the integrated engine/airframe, when operated in a designed combination, is significantly different from the sum of the individual engine and airframe performances', that is, for given values of flight Mach number, angle of attack and power setting.

Nicholson's argument, which holds totally today, was that 'the aircraft cannot be conceived first and the propulsive units (be) considered afterwards'.

To a very large degree it can be argued that the engine airframe integration process is at the very heart of the overall design process - certainly this has been noted before. The focus in design of an aircraft must not rest too long on the individual components or the integration process will be entered too late and then things can get to be very costly in time, very costly in manpower, and even very costly in lack of performance achievement. There has certainly been ample evidence to support this viewpoint in the past decade.

In his 1976 paper[3] Mr A B Haines argued the case for 'Computers and Wind Tunnels' using the subtitle 'Complementary Aids to Aircraft Design'. It is as well, today, to reflect on the past decade to draw out those lessons which are evident in this regard, namely, the interplay of computers and wind tunnels in the engine/airframe integration process.

On the one hand, we are regularly assured that 'in 10 years we will no longer need testing in the design process, it will all be done using CFD'; on the other hand, this does seem to have been the stated case for the last 10 years. So where do we really believe we are, being careful to avoid the perception being distorted due to the point from which the subject is viewed. Today it is clear that the wind tunnels and computers co-exist comfortably just as it was argued by Barry Haines in 1976. The isolated performance of many of the separate elements of many engine installations can be relatively well predicted using a combination of CFD and semi-empirical data bases and CFD/experiment matching points. The full CFD three-dimensional viscous treatments have been applied to relatively few complete integrated engine/airframes, to study the external flow fields and, in some cases, to study internal flow fields. Many thousands of hours of wind tunnel time are still being used, each year or project, in pursuit of performance verification for complex overall configuration designs, at all points of the planned operating envelope.

The engine/airframe integration process is thus clear, it is as follows:

Stage 1 — Design based on prior experience; data base from flight and wind tunnel; variations and broad characteristics assessed using CFD;

Stage 2 — Define selected configurations for experiment at model Reynolds numbers based on Stage 1 baseline design plus variants;

Stage 3 — Conduct testing including wind tunnel work at high and low speed with maximum set of performance data, pressures and flow field data covering first:

a) simplest low cost models/tests, then
b) more costly, more refined model hardware;

Stage 4 — Consolidate understanding of design, CFD and test data using CFD modelling of model scale experiments (including tunnel walls, stings etc);

Stage 5 — Refine design as in 2 above.

Stage 6 — Conduct definitive (contract demonstration) testing on the refined design;

Stage 7 — Run CFD computations to strengthen test/CFD correlated data base; and to extrapolate model data to obtain flight prediction;

Stage 8 — Conduct flight tests and define overall performance;

Stage 9 — Consolidate flight to test/CFD data base covering integrated engine/airframe performance for the full operating envelope.

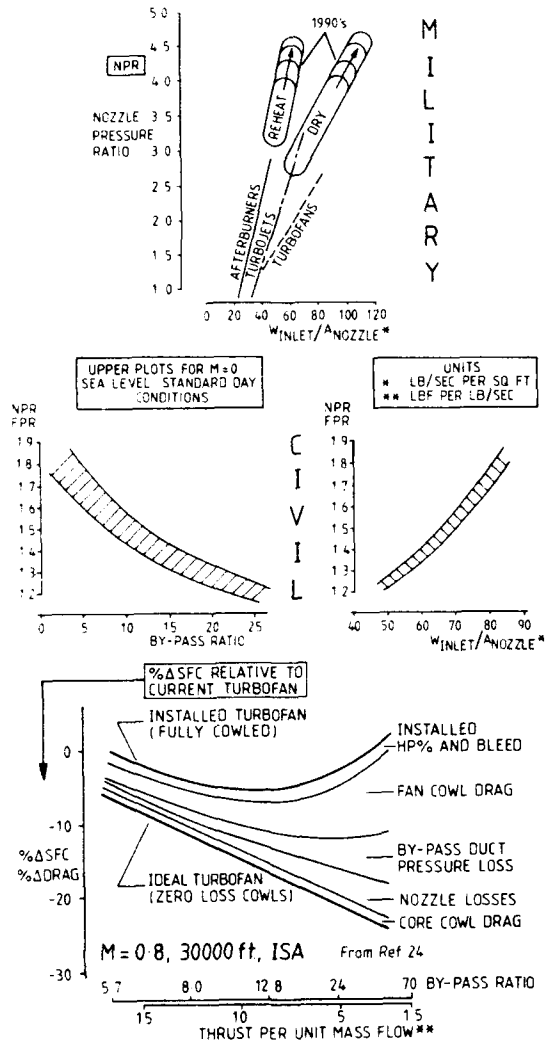

Fig 1 TRENDS IN MILITARY AND CIVIL ENGINES

To return specifically to the testing aspect we must note that much has been published covering modern methods for engine airframe integration at conferences in the period since Haines's astute 1976 guidance. At the May 81 Toulouse AGARD gathering[4] the topic was 'Aerodynamics of Power Plant Installation'; whilst the subject of Aerodynamics and Acoustics of Propellers was well addressed[5] at the Toronto October 1984 meeting; in addition a number of essentially test technique topics have been reported in our May 1984 AIAA paper on turbofan techniques as well as the September 1990 contribution to ICAS on wind tunnel testing techniques for contra-rotating propellers.

This paper will be divided into two main sections dealing with 'preferred methods' appropriate firstly to high speed combat/strike type aircraft and secondly the civil/transport end of the spectrum. In Figure 1 the overall characteristics of contemporary military and civil engines are given in terms of nozzle pressure ratio and inlet specific airflow based on nozzle area; the emerging trends are also indicated. For military installations it is clear that higher specific thrust levels will arise out of the coupling of high performance compact compressors with the new levels of core performance; even at sea level standard day conditions the nozzle pressure ratios are shown to enter the region of 4 to 5; thus more powerful but smaller jet plumes can be anticipated in new designs, at least close to the nozzles. For the emerging civil engines higher fuel efficiencies allied to use of advanced core units will lead to larger airflows and, in some cases, significantly higher BPR with attendant lower specific thrust levels, as shown. The trends for civil transports clearly point to larger nacelles handling larger airflows, a trend offering significant scope for careful design as indicated by large ΔSFC versus BPR trade-off in Figure 1.

3 EXAMPLES OF MILITARY ENGINE/AIRFRAME INTEGRATION

3.1 Special VTOL Problems

In Fig 2 the full range of engine/airframe interactions for a typical VTOL combat aircraft operating in ground proximity are illustrated, clearly the problems are extensive and varied,

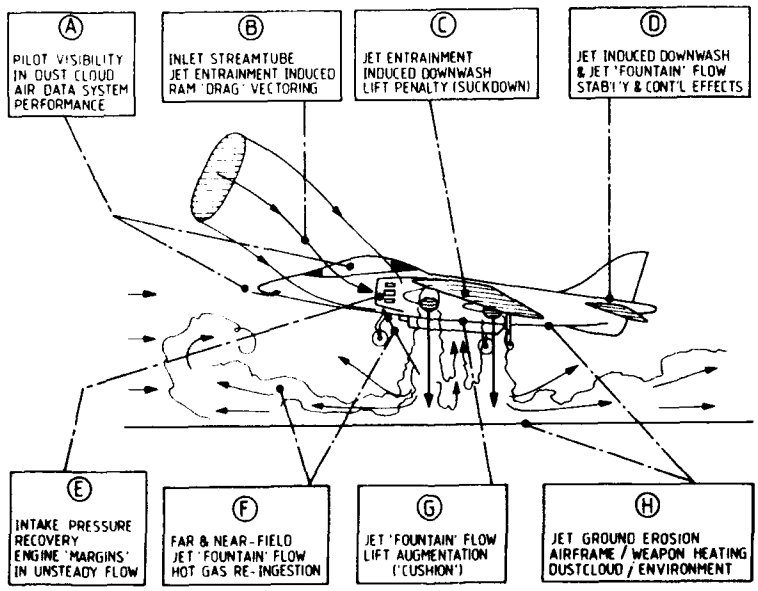

Fig 2 VTOL ENGINE/AIRFRAME INTERACTIONS

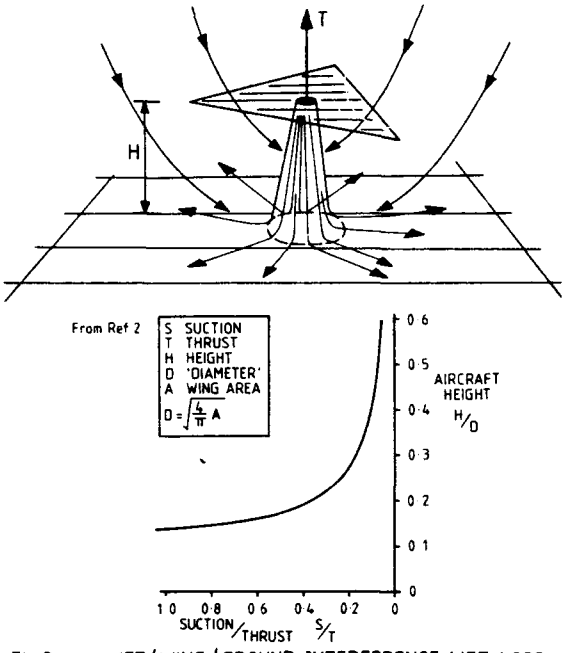

Fig 3 JET/WING/GROUND INTERFERENCE LIFT LOSS

but we need to break this set down for more detailed discussion of the physics of the situation.

In 1957 it was well known that lift losses can arise when a jet is operated from the centre of some surface, due to the jet entrainment induced downwash, as shown in Fig 3, and that if the jets emerge at the perimeter of the surface some substantial lift gains can be realised when close to the ground, due to the ground cushion effect. Fig 3 shows Nicholson's lift loss curve, and we can note that, close to the ground, losses of installed jet thrust of the order of 20% can be expected; for this single jet layout the interactions of engine, airframe and ground effect are dominant. However, apart from the suck-down due to jet mixing (or entrainment) we can show that, for twin vertical jets we have a lift enhancing fountain flow, Fig 4. This fountain arises from the interaction line between the wall jets. These

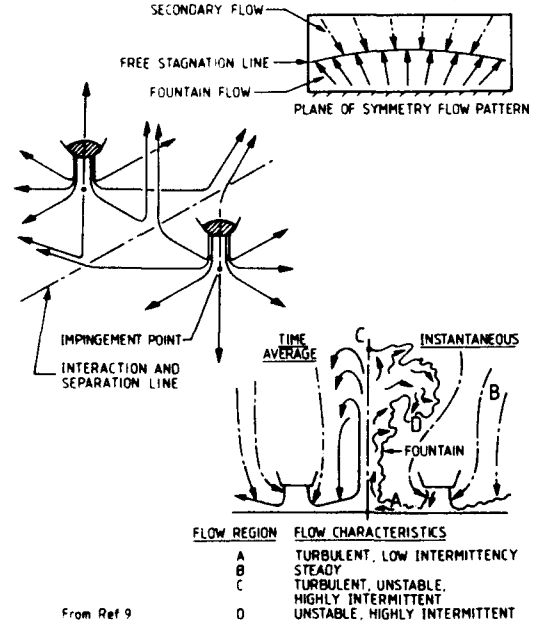

Fig 4 TWIN-JET/GROUND FOUNTAIN FLOW

Fig 5 HARRIER T Mk.2 MAKING ROLLING VERTICAL LANDING

two flow field features along with hot gas re-ingestion and the general unsteadiness associated with the powerful turbulent jet flows make an interesting area for study.

A small anecdote is perhaps worthwhile here: in the period 1953 to 1966 the author was lucky enough to serve Hawker Aircraft Limited at Kingston upon Thames, the home of the Hurricane, the Hunter and the Harrier (Fig 5); and, in particular, to have as task masters the father of the P1127, Mr Ralph Hooper, and Mr John Fozard the father of the Harrier.

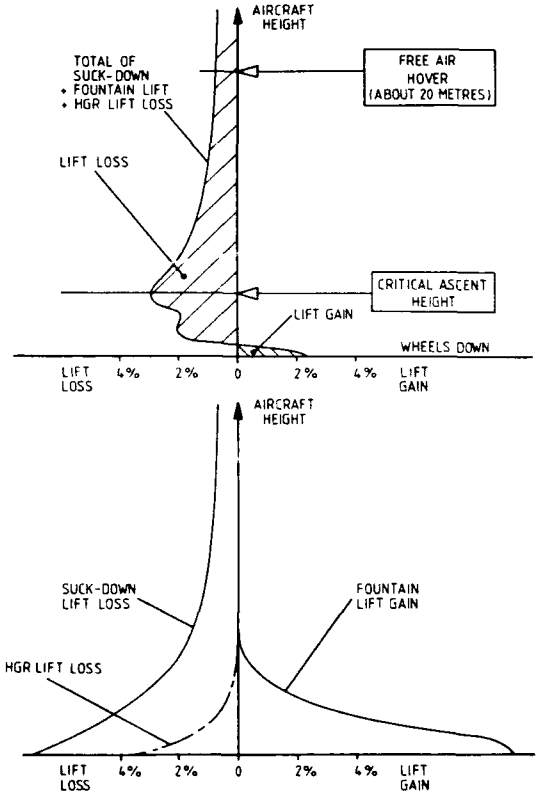

Fig 6 INTERFERENCE LIFT VARIATIONS WITH AIRCRAFT HEIGHT

Now much attention was centred on model testing these feared VTOL ground effects and spread over to the flight test side where Mr Bill Bedford our Chief Test Pilot could not understand why at times the aircraft could not ascend above an altitude of 4 or 5 feet. We now know that Bedford's uncertainties were due to the complex interactions of the jet induced suckdown and ground jet fountain flows, Figure 4, and to some extent, due to variations of Hot Gas Reingestion.

Fig 6 shows the individual lift interference contributions, these being suckdown, fountain lift and HGR; it is apparent that the resulting overall interference lift behaviour is very non-linear.

For the P1127, or Harrier, making a vertical take-off at a weight close to maximum thrust it was found that a critical ascent height needed to be cleared before the freedom of free air hover could be enjoyed; there were many take-offs, which Bill Bedford has recently described, in which the P1127 would simply refuse to break through this critical ascent barrier; on a later attempt with less fuel load the aircraft could get up and away and pass through the barrier without perceptible hesitation.

A further comment concerns the origin of the strakes on the Harrier lower fuselage. These are used to enhance fountain lift by revectoring the largely two-dimensional jet fountain flow which impinges on the lower fuselage when close to the ground; the first strakes on the Hawker P1127 were 10" long pieces of bent aluminium angle fitted to a 1/16th scale P1127 model; at ½" by ½" it seems they were very nearly right first time and they owed much to detailed flow visualisations and flow surveys.

At a recent joint RAeS, AIAA and ASME specialist ASTOVL gathering in London, Knott and Milford (Ref 6), amongst others, provided lucid papers on these flow fields; but we should pay particular attention to the fundamental twin jet work of Abbott[7] at Pyestock and to that of Smith, Ing and Bailey[8] at Kingston. Abbott has examined the fountain flows for a pair of quite high pressure ratio impinging jets and has found that the fountain flow is sensibly similar through a wide range of nozzle pressure ratios. Even when the post exit shock structure interacts with the ground plane, the rates of decay and fountain spread are uninfluenced by NPR in the range 1.1 to 4. In the light of current engine developments this is an important new result. In the Kingston work Smith, Ing and Bailey have demonstrated the physics of the interaction of twin-jet fountain flows with strake-like lift improvement devices (LIDS) using a very simple rig indeed. The results demonstrate both the expected jet fountain impingement pressures and, unexpectedly, a pair of strong vortices which sit in the strake/fuselage corner when the ground clearance is typical of VTOL conditions. It has been shown that this pair of vortices can eliminate the fountain lift under certain circumstances; Figure 7 gives an indication of some of the important flow-field relationships.

CRITICAL POINT IN FLOW FIELD	PARAMETERS INFLUENCING LOCATION OF POINT
WALL JET FAR FIELD SEPARATION POINT POINT Ⓐ	DYNAMIC PRESSURES BUOYANCY PRESSURE WIND STRENGTH (IF ANY)
WALL JET NEAR FIELD SEPARATION POINT (FOUNTAIN LOCATION) POINT Ⓑ	DEPTH AND DYNAMIC PRESSURES OF INTERACTING WALL JETS
FREE STAGNATION POINT AT TOP OF FOUNTAIN POINT Ⓒ	INDUCED FLOW DYNAMIC PRESSURE FOUNTAIN FLOW DYNAMIC & BUOYANCY PRESSURE

From Ref 9

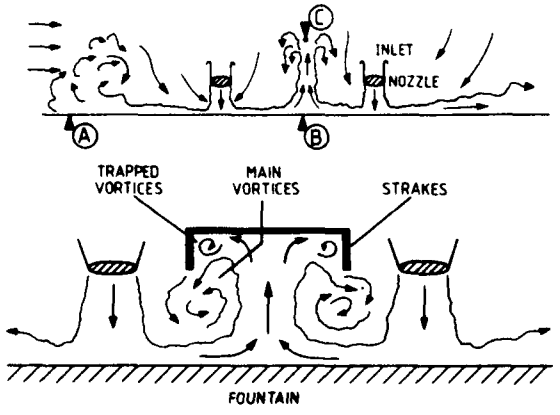

Fig 7 FLOW-FIELD PARAMETERS FOR HGR AND LIFT INTERFERENCE

This use of quite simple jet rigs and the somewhat more sophisticated 'vertical' mode rigs for study of lift interference and Hot Gas Re-ingestion has changed little since the late '50s and early '60s, Figure 8 is an example from the mid-60s.[9]

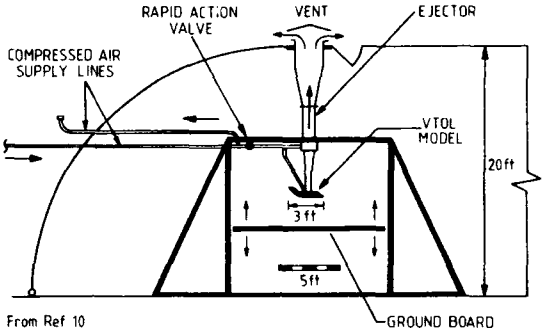

From Ref 10

Fig 8 TYPICAL RIG FOR VTO STUDIES

Certainly, the instrumentation schemes today are well advanced but the fact remains that carefully conducted experiments using simple low-cost rigs can reveal much, if not all, that needs to be known of the complex transient characteristics of VTOL aerodynamics. Care must be, and generally is, exercised in the understanding of scaling laws, whether they relate to timescales, model instrumentation response, gas cloud contamination or temperature scaling. There is no doubting that this fully turbulent unsteady flow field is really quite complex and that an understanding derived from fundamental experiments can provide secure cornerstones in the overall integration process. Further references in this field of research include work relating to pilot visibility,[10] ground erosion,[11] hot gas re-ingestion[12] and particularly to engine response considerations, as described recently by Darryl Williams of Rolls-Royce.[13]

3.2 High Speed and Lower Speed Military Problems

At speeds above those of the vertical take-off manoeuvres we can identify a range of engine/airframe problems which will be significant not only for Harrier/AV8B or ASTOVL aircraft but also for such relatively conventional aircraft like EFA or F22; Fig 9 shows in brief form a range of these flow-field related integration aspects. The detailed aspect concerning thrust vectoring, as illustrated, does not change the general interference considerations.

In the case of the aircraft with nozzles near to the centre of the airframe and with thrust vectoring, it is easy to recognise that the whole of the aerodynamics is 'close-coupled'. The phrase, 'close-coupled' indicates that throttle dependent effects arising due to interference of inlet or nozzle flows on other major airframe elements cannot be linearly superimposed; with 'close-coupled' aerodynamics it is necessary to provide simultaneous simulation of the inlet flow, at appropriate MFR, and of the nozzle flow, at appropriate NPR.

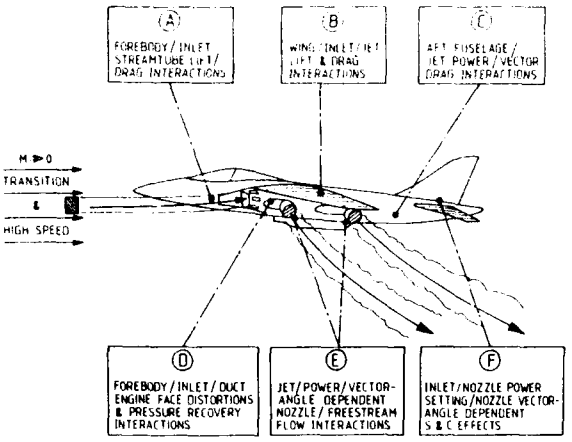

Fig 9 AERODYNAMIC ENGINE/AIRFRAME INTERFERENCES FOR MILITARY AIRCRAFT

The full complexities of 'close-coupling' are highlighted when a vectored thrust aircraft operates at high angle of attack during transition. The flow fields arising even without vectored thrust and even in the case of aft mounted nozzles can still display quite marked 'coupling' of the flow elements.

In certain respects this is not at all surprising as we are, after all, dealing with subsonic flow and, in most if not all cases, the control surfaces and nozzles are downstream of the air intakes. There is evidence both from wind tunnel data and from CFD (Ref 14) that, for a generic aircraft layout with a foreplane (canard), the air intake MFR sets up a significant forward influence; conversely, of course, the foreplane can, and does, disturb the pre-entry streamtube and thus, too, the performance of the air intake.

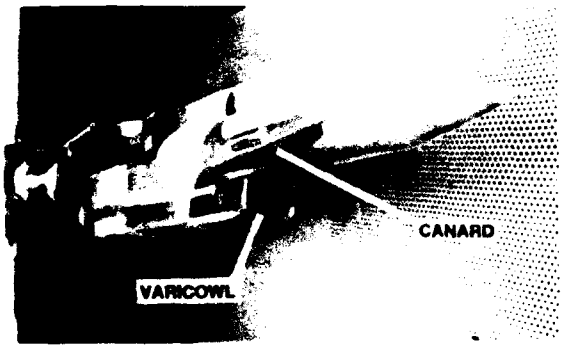

Fig 10 GENERIC FIGHTER INTAKE MODEL FOR INTERNAL & EXTERNAL PERFORMANCE EXPERIMENTS IN TWT

In some recent experiments using a specialist air intake research rig, Fig 10, the tests included examination of engine face pressure recovery, and swirl, as well as steady state and dynamic distortions covering a wide range of model angle of attack, foreplane angle, simulated mass flow ratio variation, sideslip, and freestream Mach number plus study of the influence of foreplane angle on intake performance.

It is probably unnecessary here to show more than a few details of the rakes (Fig 11) and mass flow cells in this type of rig but, very clearly, a massive quantity of data does arise from such tests and some powerful 'number crunching' machines have to be put in place to guide these sophisticated model studies; Laurie Goldsmith and others will restore the balance of detail here (in this conference), when the AGARD FDP WG13 work is reviewed.

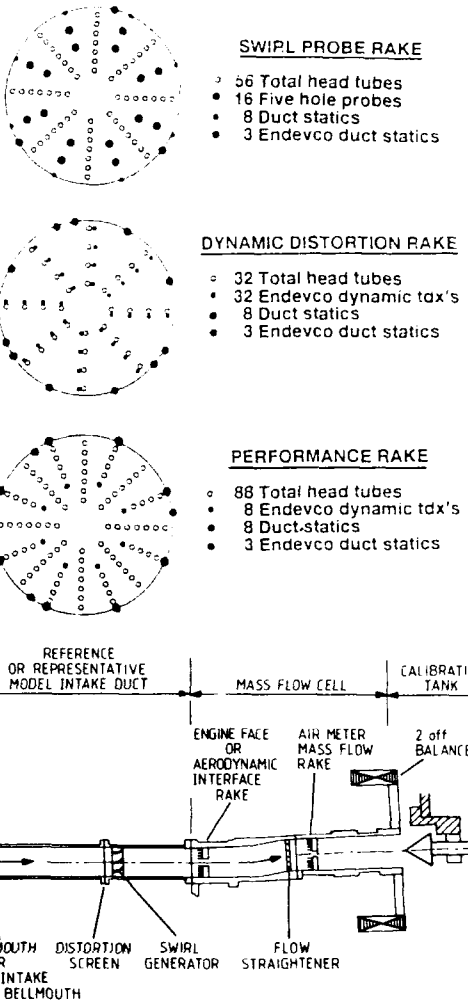

Fig 11 EXAMPLES OF MODULAR INTAKE MODEL, STEADY STATE, DYNAMIC AND SWIRL RAKES

Before leaving this front end topic, we note two things: One is that this conference will also include papers on low speed intake/airframe aerodynamics which are to be discussed by Signor Barbantini of Alenia in Paper No 16 and Herr Lotter and Herr Scherbaum of MBB who will report on the special aspects of time-variant total-pressure distortions in Paper No 17. Secondly we note that this type of test is generally run for both internal performance and external drag performance purposes. This external drag work is, of course, linked to a complete aircraft model (Fig 12) by a suitably rigorous and well defined forces and moments accounting system - only in this way can the predicted flight behaviour including power effects be included in the flight simulator computer data bank.

Fig 12 FULL SPAN AERO-REFERENCE WIND TUNNEL MODEL

A small diversion here to note that television viewers in the UK have been fortunate enough to see a superb series of documentary television programmes entitled 'Reaching for the Skies'. In the course of many totally absorbing hours of viewing a specific remark made by the great US test pilot Chuck Yeager was noted. To quote Yeager, when talking of early test flying of X aircraft, he advised that 'in the early days (of Bell X-1 through to X-15) test pilots flew by the seat of their pants and did not really know what to expect next'. 'Today though', he went on 'the pilot gets in for his first flight and he is already an old hand on account of his (extensive) flying of the flight simulator'.

Certainly, everything that Yeager said is true, of course; however, there are just two riders that we should add - firstly - the flight simulator will only be as good as the aerodynamicists' predictions can make it - based, very largely, on wind-tunnel test data and secondly, and equally importantly - the simulator can only represent pre-planned aircraft manoeuvres and responses. These must include all conceivable engine/airframe flight conditions otherwise the 'unpredicted' case will inevitably arise; it is regrettable that today we do still witness 'unpredicted' events; even today in these days of the supercomputer and these days of sophisticated wind tunnel techniques, we must keep trying.

We will next consider the aerodynamics of the aft regions[15] of a conventional high speed fighter-type aircraft, Fig 13. It is now widely accepted that when a pair of jet nozzles are arranged together at the aft end of a fuselage or twin engine nacelle, there is a potential for serious and adverse dynamic interactions between the jets and freestream flows; moreover, there is the possibility of an aft end separated 'base cavity' associated with the difficulty of closing the aft end internozzle region, at least when the jet centreline spacings are less than 3 or 4 nozzle diameters. This aft end flow field can develop into complex twin jet shock cell interactions with jet screech and cavity resonance problems; this eventually results in a loss of nozzle shroud components due to high powered acoustic fatigue damage.

In Ref 16, John Seiner et al of NASA Langley have discussed a study on the B1-B twin engine nacelle nozzle system; in this 1991 paper Seiner has provided a clear review of published 1980s test data including descriptions of research into the unsteady flow phenomena. The broad outfall of this research is that for closely spaced jet nozzles the dynamic phenomena will depend upon the specific nozzle geometries, upon the nozzle spacing, and upon the upstream flow history. The principal mechanisms appear to be toroidal or helical shed vorticity at the nozzle perimeter, shock-cell resonance, and resonance of these phenomena with the separated base region; Seiner has also very painstakingly traced aft cavity disturbances to flow features such as vortices shed from upstream aircraft locations; in fact, from far upstream of the subject afterbody/nozzle region.

In a recent MoD (UK) funded programme to develop an afterbody/nozzle research rig, Fig 14, early decisions were taken to represent the flow field at as large a scale as practical, to build the rig to permit tests across a significant range of Reynolds number, to put a representative wing/fuselage on the fully metric rig so as to maximise the value of the research findings, and to minimise 'part body forces integration' worries which can arise when part metric, part non-metric rigs are used.

In recent testing this new fully metric rig has been shown to be well suited to the determination of throttle dependent drag

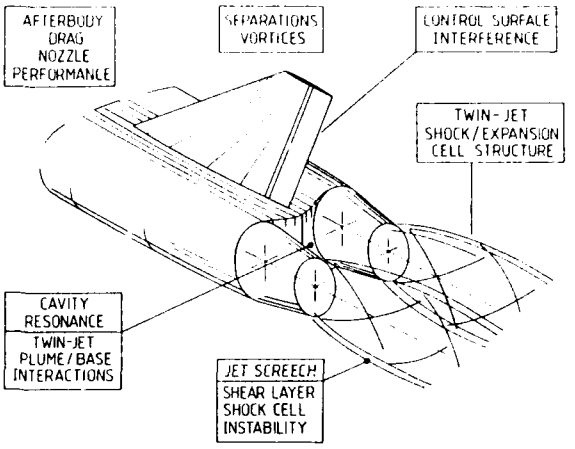

Fig 13 TWIN-NOZZLE/AFTERBODY PERFORMANCE AND FLOW-FIELD PROBLEMS

increments and to the study of the various dynamic phenomena. In a manner similar to that for dynamic intake test data, the testing again requires the use of substantial numbers of dynamic and static pressure measurements with powerful computers so as to yield, at the test site, analysis of the frequency spectra, phase relationships and the necessary cross correlations and fast Fourier transforms to describe the behaviour of the dynamic pressure disturbances. In all studies of this type it is vital that the quality of the upstream freestream and nozzle flows is established and that any unsteady and non-uniform features in these flows are both small and well understood.

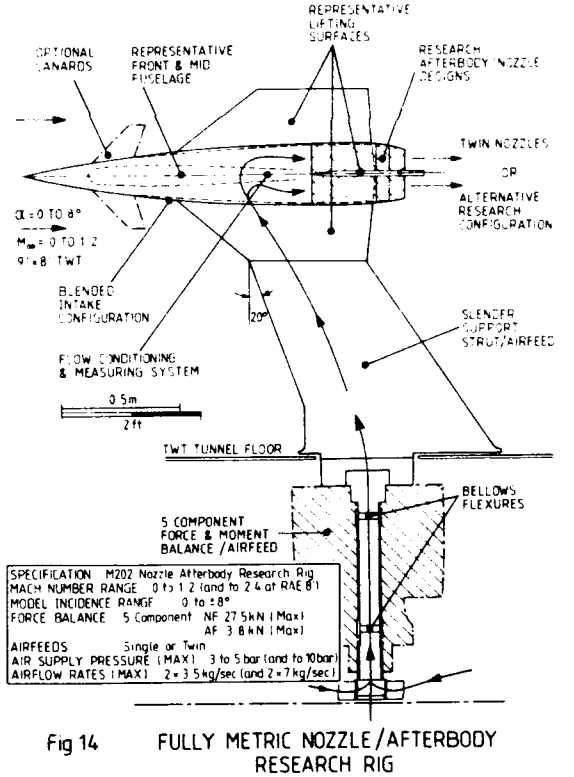

Fig 14 FULLY METRIC NOZZLE/AFTERBODY RESEARCH RIG

The rig discrimination for afterbody drag performance has been established in two series of research tests covering a wide range of NPR, con-di nozzle configuration (dry power, reheat power setting etc), and freestream Mach number; it is not appropriate to go beyond this brief description at this juncture,

but the data will undoubtedly prove to be both of value and interest when it becomes more appropriate to publish the results.

Before leaving this new rig we should note that it provides the means, when suitably equipped, for high speed aft end ASTOVL or for stealthy nozzle systems research. Further, the rig has been specifically tailored for use across a wide range of freestream Mach number and Reynolds number[17] using the ARA 9' x 8' transonic and the RAE 8' high speed variable pressure wind tunnel facilities. Also, the practicality of using shadowgraph, oil flow and liquid crystal flow visualisations have all been demonstrated using video recording methods, Fig 15.

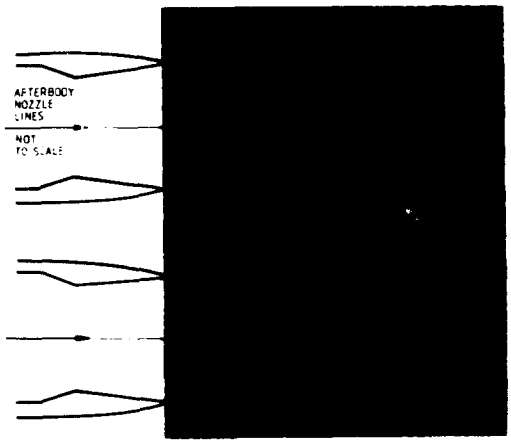

Fig 15 EXAMPLE OF SHADOWGRAPH FROM TWIN-NOZZLE RESEARCH RIG

3.3 Towards More Advanced Simulations of Military Aircraft

For a substantial number of years the development in the USA of the CMAPS military simulator unit and the use of civil TPS units for turbofan installation studies has shown the way ahead for more complete simulations in the engine/airframe integration process.

At this stage it is appropriate only to preface Paper number 15 at this symposium with one or two observations drawn from experience to date; Fig 16 shows a generic ASTOVL aircraft layout in a high-speed, unpowered model test.

Fig 16 UNPOWERED GENERIC ASTOVL RESEARCH MODEL IN HIGH SPEED WIND TUNNEL

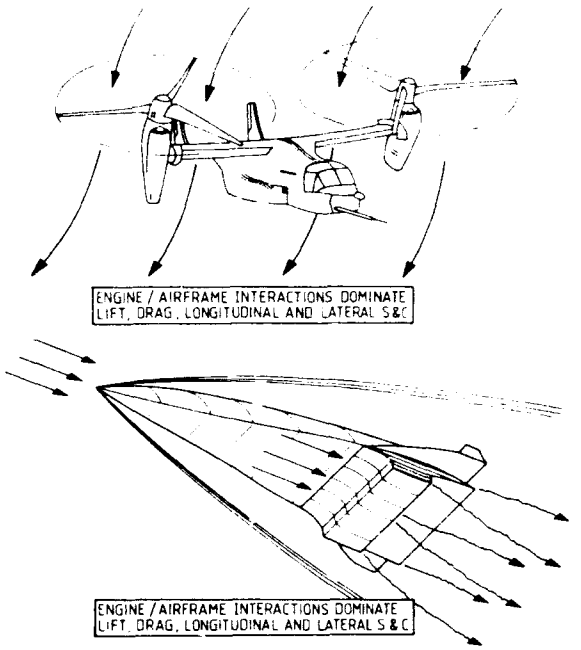

Fig 17 EXAMPLES OF ENGINE/AIRFRAME LAYOUTS WHICH REQUIRE FULLY POWERED SIMULATION

For full development of a new vehicle, the supporting experimental model research testing should leave few technical risks for the full scale aircraft testing stage. This is especially true in regard to those aspects in which flight safety is involved. Thus, it is clear that for the vehicles shown in Figures 16 and 17; use of powered simulation providing total airflow representations must be used to provide both performance and S&C data.

On the other hand though, it can be argued that, provided the layout falls into the category of 'conventional' then the most suitable plan would be to use only the conventional separate intake, nozzle and overall airframe force and pressures modelling approach.

The fluid motion question which is raised here is, at what stage is it reasonable to infer that 3-dimensional subsonic flow fields do not communicate and at what level of communication from upstream flow to downstream flow and vice versa does it become important. It is, well established that engineering designers are most comfortable using established tools but, in light of the present day very large overall programme costs to develop say an EFA or an F22, is it not reasonable to suggest that live intake, powered nozzle arrangements should become commonplace in the armoury for engine/airframe integration testing?

Everything considered, it is very clear that the full power-dependent 'thrust' vector must be established for all installations and that experimental methods must be developed to provide high levels of certainty in these determinations.

4 EXAMPLES OF CIVIL (TRANSPORT) ENGINE/ AIRFRAME INTEGRATION STUDIES

In some respects the civil simulation situation for engine/ airframe integration is now very well established and has been reported extensively in the literature, Refs 18,19. However, today we are faced with the need to adapt methods to cover the requirements of even higher turbofan by-pass ratios and, in recent years revival of propeller technology has emerged.

As noted above a number of specific references should be made, particularly AGARD Toulouse 1981, AGARD Propeller Conference October 1984, AGARD Engineering Methods travelling Lecture Series 1991; also, our May 1984 paper[20] on turbofan techniques; and in our September 1990 ICAS paper[21] on contraprop model testing methods the test approach from a high speed viewpoint was outlined.

To set the scene it is appropriate to briefly note just a few of the important interferences which do arise at high subsonic speeds when we install a large turbofan under a modern, highly tuned transport wing, Fig 18.

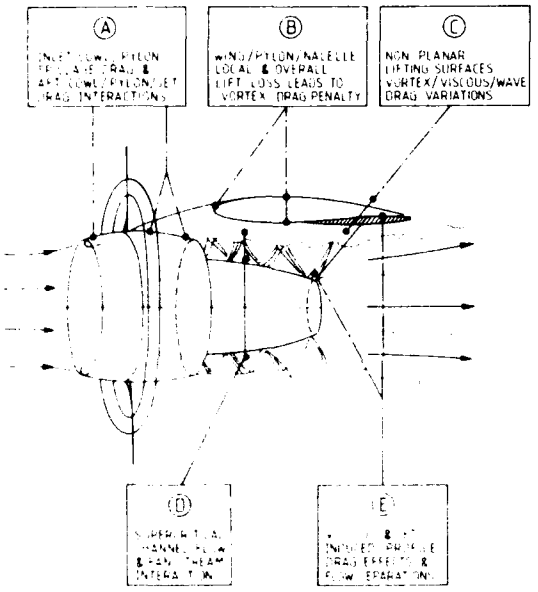

Fig 18 HIGH SPEED INTEGRATION PROBLEMS FOR A VHBPR TURBOFAN

As shown, a number of significant features totally envelop the engine installation. For an optimised engine installation today the industrial leaders in this field set out to select the preferred design features at a level of discrimination at around 1/5 to 1/3 of one percent of aircraft drag. To achieve this level of discrimination in powered experiments serious difficulties are encountered and the need arises for quite rigorous methods of approach to the research. Furthermore, it becomes necessary to adopt a clear, statistical rationale with respect to repeatability, bias, precision, certainty and discrimination of the experiments.

In Fig 18 we have illustrated a flow field in which the fan and core jets behave very well and flow tidily off the aft end of the installation. In practice, considerable attention to detail is required to produce this result at conventional levels of BPR. The advent of larger nacelles mounted in more close coupled installations will only aggravate the problems which can arise when turbulent jets run parallel to the lower wing surface.

In Fig 19 the results of two oil flows obtained a few years ago[22] are shown at off-design conditions for a close-coupled long-cowl powered installation research model and at comparable conditions, for a powered short-cowled turbofan installation. The evidence in this case is that for the long cowl the flow in the gulley between the wing/pylon and nacelle encounters a shock induced separation which then trails downstream as a vortex front; to fulfil continuity needs the flow near the pylon trailing edge is fully reversed and flows forward in a cavity behind the vortex, in spite of the free stream Mach number of 0.8. For the short cowl a similar shock trips the corner flow resulting in a reversed flow/vortex interaction of similarly serious consequence to drag performance; it is emphasised that these two flow visualisations were at conditions well away from the cruise flight envelope.

a) Close coupled, long cowl, off design M and C_L

b) Close coupled, short cowl, off design M and C_L

Fig 19 EXAMPLES OF SURFACE OIL FLOW VISUALISATIONS ON WING/PYLON CLOSE TO NACELLE

These oil flow pictures are just a small example of hundreds of coloured oil flows which are generally recorded using strategically placed video cameras; in this way the flow field developments can usually be traced from off-design, where a great deal of disturbed flow is frequently evident, to on-design where fine tuning of any residual adverse flow features often becomes necessary; as to how the configurations are fine tuned is another story.

There have been many recent high-speed and low-speed advances leading to quite sophisticated powered model representations; we now address some of these developments, with particular reference to the high speed aspects; in particular we consider those rigs and methods necessary to evaluate a typical installed high or very high by-pass ratio turbofan and confine the attention mostly to those aspects not already published in the referenced literature.

In a similar way to the strategy adopted to evaluate candidate military designs so the civil engine nacelle is divided into intake plus cowl and cowl plus nozzle/afterbody.

Figure 20 shows a specialist intake rig (known as Z30 at the ARA); there are similar rigs at many facilities. The rig is equipped with a set of 5 rotatable rakes for the purposes of external drag traverses using the method of wake traverse and momentum integration, and it also has six internal rakes to provide for internal performance assessments. Testing is

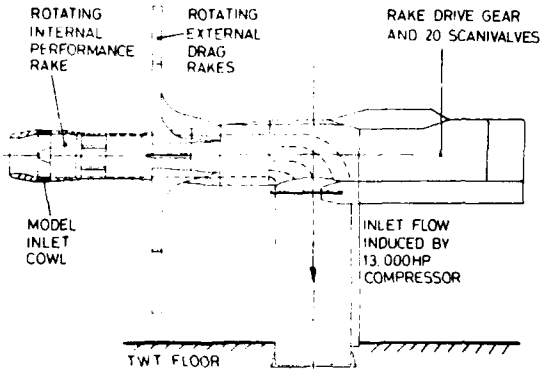

SPECIFICATION :	Z30 Isolated Inlet Rig
MACH NUMBER RANGE :	0·2 to 0·9
MODEL INCIDENCE RANGE :	Low Speed -10° to +25°
	High Speed 0° to 6°
AIRFEED :	Suction using BB Comp'r
AIR SUPPLY :	Suction to 0·3 bar
AIRFLOW RATE (MAX) :	8 kg/sec Suction

Fig 20 AIR INTAKE RESEARCH RIG (Z30) WITH ROTATABLE RAKES

normally conducted over a wide range of Mach number (0 to 0.9) and with angles of attack of up to 21° for incidence performance and cowl external lip separation studies; at all conditions a range of mass flow ratio is used to identify the influence of spillage, or effectively, throttle setting. In recent work the rig has been used for studies of representative pylon features (Fig 21) so as to identify the potentially important influences of the pylon on lip separations, cowl drag rise, or spillage drag variations. Although there is still some further research required in this area the rig does offer the opportunity for very local studies of pylon to cowl interferences at a good scale, using a finely spaced/traversed survey rake. The rig is generally used to evaluate a set of cowls evolved using CFD and empirically derived designs.

In a recent set of refinements the rake blockage of this intake rig was reduced by a factor of 2 and rig-on-cowl and rig-in-

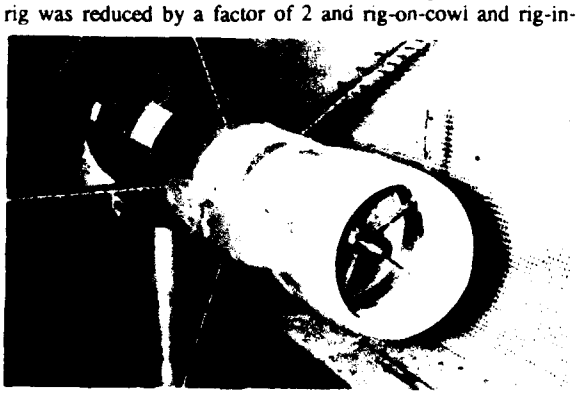

Fig 21 AIR INTAKE MODEL ON Z30 WITH REPRESENTATIVE PYLON

wind-tunnel interferences have been studied using both computational and reference experiments. To date it has proved possible to gain confidence in rig blockage corrections to quite fine levels of Mach number resolution; incremental values of less than 0.002 at M = 0.820 being the order of the blockage corrected Mach number uncertainty.

Fig 22 shows a specialist nozzle rig which is used at ARA to study turbofan static, low speed, and high speed nozzle/afterbody performance. The rig provides for two airstreams, for provision of a representative pylon, and is strut mounted in the high-speed tunnel; a special high accuracy single component Task balance is used for the measurement of nozzle thrust performance. This rig has been extensively used for inter-company compliance demonstration purposes in respect of the influence of free-stream airspeed on nozzle discharge coefficients. The rig has exhibited benchmark levels of overall repeatability and an example, Fig 23, illustrates the fact that discrimination of performance increments has been shown to approach the 0.1% level. At the level of thrust and discharge coefficients repeatability shown here, and regularly demonstrated in successive test campaigns, it becomes a matter of firmly addressing the statistics of the work to establish the levels of confidence in the derived best fit curves. In principal, at least, we can say that if we add a factor of 4 to the number of test data samples we can obtain a twofold reduction (improvement) in the incremental discrimination achievable.

As with all precision rigs, much time and effort must be expended with prior calibrations of load cells, rig seals, and pressure and temperature transducers; clearly the technique must be resilient to avoid bias errors both before the wind tunnel series and during the test entry; clean, steady airflows are also mandatory and high speed servo systems are used to control the compressed airfeeds to the rig to fine levels of flow stability (order ±0.1% maximum variation).

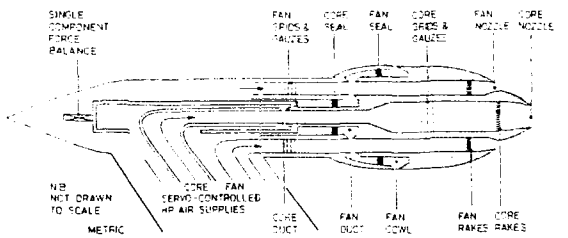

SPECIFICATION :	B20 Isolated Afterbody Nozzle Rig
MACH NUMBER RANGE :	0 to 0·9
MODEL INCIDENCE RANGE :	Preset Rig/Model (0°, 4°, 8°)
FORCE BALANCE :	2·7kN Axial (Max)
AIRFEEDS :	10 bar supply to Fan & Core Streams
AIR SUPPLY PRESSURE (MAX) :	7 bar
AIRFLOW RATES (MAX) :	Fan 4·5 kg/sec
	Core 2·2 kg/sec

Fig 22 TWO STREAM NOZZLE/PYLON RESEARCH RIG (B20)

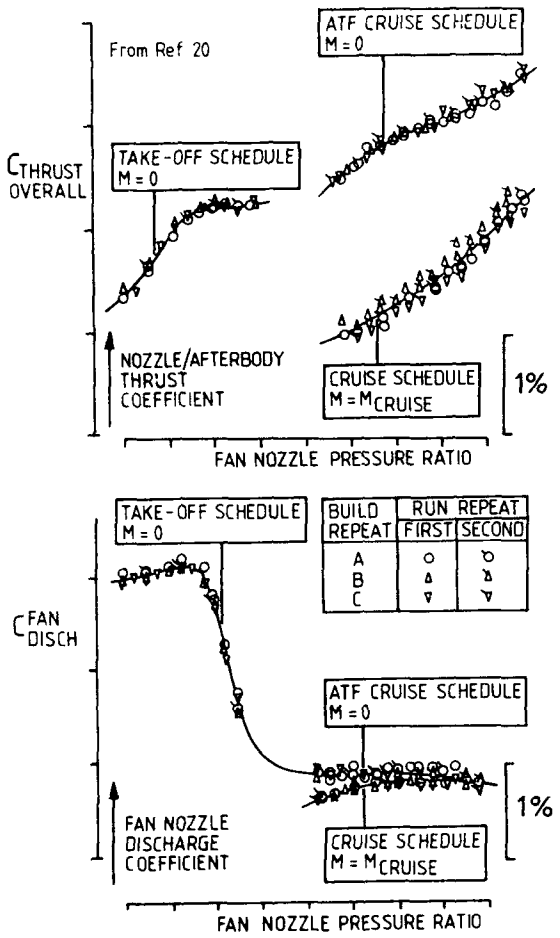

Fig 23 EXAMPLE OF NOZZLE COEFFICIENTS DATA

With the move to even higher levels of by-pass ratio, whether it is to BPR = 9 or 12 or 15 for the new ducted designs, we will face a change to where 0.1% of nozzle gross thrust coefficient reaches the elusive 1/3% of cruise drag; or even greater leverage. Quite clearly, the ram drag of low specific thrust engines inevitably rises since it is proportionate to the inverse of specific thrust or airflow. Thus, we must make the next step in thrust coefficient discrimination to measure up to the target level of discrimination of 1/3% of drag; it may become necessary to apply statistical leverage using much larger numbers of test points.

So far we have addressed the rigs necessary to study isolated intakes and isolated nozzle systems and we have noted that both rigs can evaluate the influences of the addition of pylons to these nacelle components. The next part of this paper addresses complete isolated and installed nacelles.

To study complete through flow, unpowered or powered nacelles, Fig 24, it is practical to use a rig equipped with a 6 component force balance housed in a long, slender, low aerodynamic interference mounting tube. The rig is mounted in a wind tunnel using a conventional sting. Attached to this aerodynamically fine tube is a swept strut onto which is mounted the complete nacelle/pylon.

The rig can provide full incidence traverses giving isolated lift and drag performance polars for the complete nacelle/pylon. In this way, the effects of intake mass flow ratio, angle of attack and Mach number on overall nacelle/pylon performance can all be evaluated for comparison with CFD and prior data bases.

With the advent of the bigger cowls and higher airflow rates we must now account for nacelle and pylon thrust, drag and lift; this rig, giving off-axis data, is thus a key part of the modern accounting process. As with all of these rigs it is vital that the model nacelle/pylon accounting system is run parallel to, and compatible with, the full scale methodologies.

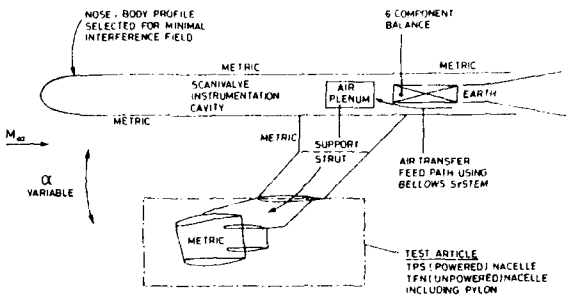

SPECIFICATION :	Z61 Isolated Nacelle / Pylon Rig
MACH NUMBER RANGE :	0·2 to 0·9
MODEL INCIDENCE RANGE :	-6° to +15°
FORCE BALANCE :	6 Component NF 1·56 kN (Max)
	AF 0·75 kN (Max)
AIRFEEDS :	Single or Twin
AIR SUPPLY PRESSURE (MAX) :	45 bar
AIRFLOW RATES (MAX) :	2 × 2·7 kg / sec

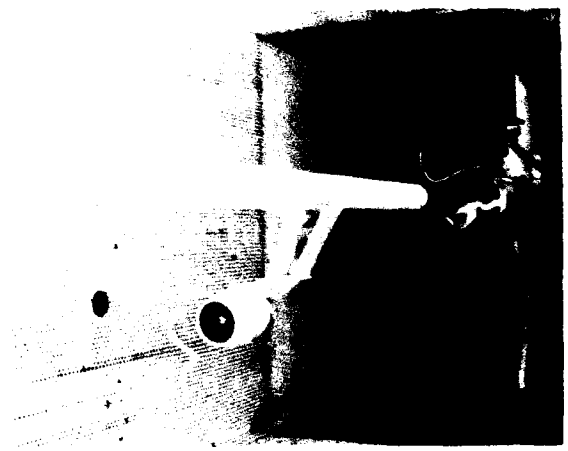

Fig 24 ISOLATED COMPLETE NACELLE/PYLON RIG IN TWT

The off-axis force vectors need to be very carefully addressed for both through flow nacelles and for powered nacelles; also the unpowered and powered methods must be mutually compatible, and must be accounted similarly on the aero-reference full span model which is generally used as the basis of the aircraft drag calculations (base de calcul). In order to provide for off-axis thrust vector accounting the utility of the two Mach Simulation Tanks at ARA have been extended, Fig 25; today both MST1 at about 3 metres diameter and MST2, at about 1½ metres diameter, are equipped with an off-axis precision forces measurement capability. This facility has been made feasible using the well established annular rolling diaphragm seal system, as illustrated; this RDS system creates low, linear forces residuals as well as offering small off-axis seal constraints; as a result it is practical to determine the complete vector of the nozzle system exhaust plume, under quiescent conditions. Using the resolved thrust vector it is then

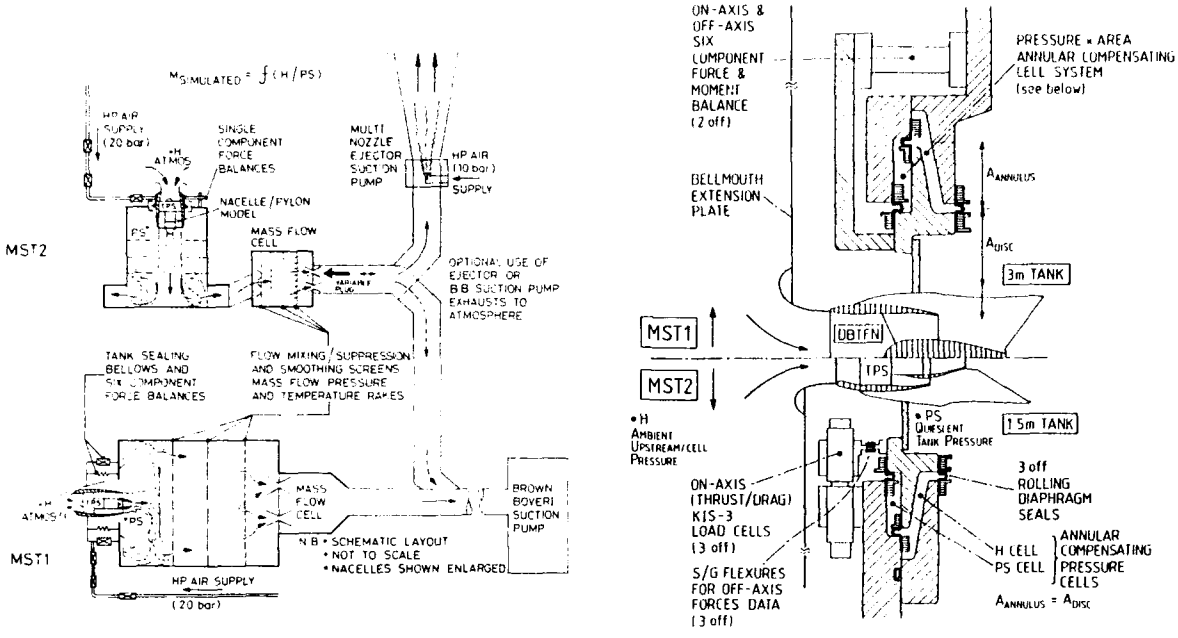

a) Overall MST schematic layout

b) Details of off-axis forces and RDS system

FIG 25 MACH SIMULATION TANKS FOR NACELLE CALIBRATIONS WITH ON & OFF AXIS FORCES AND RDS SEALS

SPECIFICATION : Installed (TPS) Half Models
MACH NUMBER RANGE : 0 to 0·9
MODEL INCIDENCE RANGE : −5° to +10°
FORCE BALANCE : 5 Component NF 11·2 kN (Max)
AF 1·3 kN (Max)
AIRFEEDS : Single or Twin
AIR SUPPLY PRESSURE (MAX) : 45 bar
AIRFLOW RATES (MAX) : 2 x 2·7 kg/sec

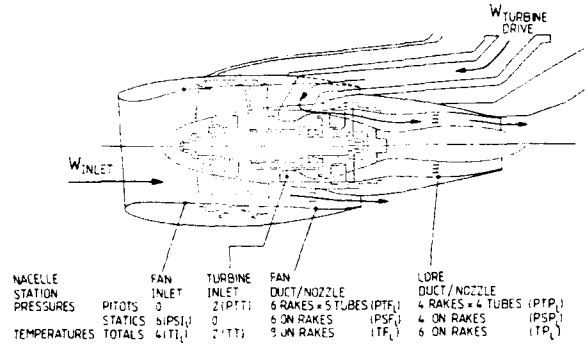

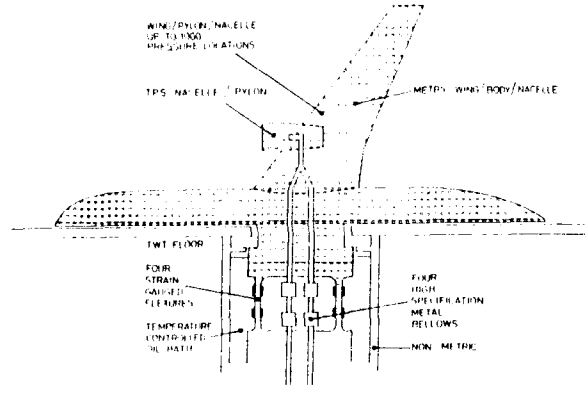

FIG 26 SEMI-SPAN RIG/MODEL FOR HIGH SPEED INSTALLATION STUDIES

possible, using the Z61 rig, to separate the nacelle and pylon lift from the (quiescent) thrust vector contributions; in all, this represents a significant element in the build up to installed studies.

One or two further details of the MST facilities should be noted. To measure tank airflow rates sets of critical venturi meters are used; the design of these venturis has recently been established as an International Standard. It is now established that a bias error of less than one quarter of one per cent can be subscribed to the use of such venturis. In the high pressure airfeeds this ISO design of critical venturi meters is also used so that all flow determinations are traceable to International Standards.

In a recent exercise of the calibration facilities, the UK National Engineering Laboratory calibrated three of the high pressure venturis for use as a 'secondary standard'; it was pleasing to find that, when subsequently exercised against (direct connect) the low pressure venturis (multiple venturi sets) the data all fell sensibly within a plus and minus 0.15% band of the sought after 1 to 1 correlation. This comparison was achieved at pressures in the high pressure system of 1000 psi and of 10 psi in the low pressure (tank) system; a factor of 100 in pressure level: this is, of course, a very satisfactory correlation on airflow measurements.

At this point we have established the calibration of the through flow nacelle and powered nacelle internal flow including the thrust vectors; further, the isolated performance thrust, lift and drag for both powered and through flow nacelle/pylon assemblies is also determined; we can now move on to the installed cases - always using fully compatible thrust and airflow accounting methods.

For many years in Europe and the USA, Fig 26, the semi-span or half model TPS technique has represented a cornerstone of many aircraft development programmes and significant benefits have accrued from the use of compatible and stable methodologies; the half-model technique has been in virtually constant use in one or other of the three leading high-speed facilities in Europe, namely those at NLR in the Netherlands, ONERA Modane in France and at ARA Bedford in the UK. In practice, using the established TPS approach, in which both through flow nacelles, giving variable mass flow ratio using plug nozzles, and powered nacelles giving variable mass flow, by means of power variation, it has proven possible to identify the various contributions to the interference elements shown in Fig 18; the approach makes use of extensively pressure plotted wing, pylon and nacelle components.

For example, provided that a comprehensive set of test configurations are examined, it has been shown that the influences of intake mass flow ratio and exhaust system power level can be identified in the overall aerodymamic interference situation.

In a parallel development a powered full span (Fig 27) rig was created to provide for examination of engine installations where the half model technique might be considered flawed on account of the proximity of the nacelle to the fuselage or to the tunnel floorplane (wall). The fact that this rig has not been extensively used at high-speed mainly reflects the fact that, in general, the budget associated with 2 nacelles, 2 wings and 2 pylons is inevitably larger than that for the half model equivalent; also, the expected push to aft mounted noise shielded installation designs did not materialise as was expected in the early '80s; furthermore, the half model offers higher

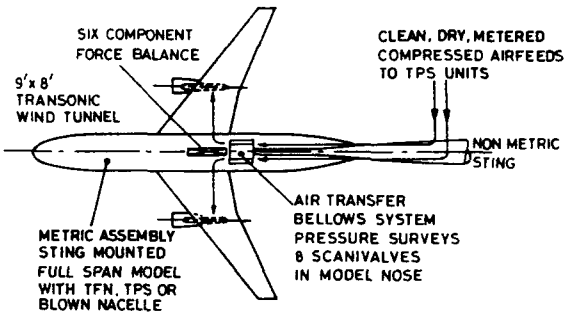

SPECIFICATION :	INSTALLED FULL SPAN
MACH NUMBER RANGE :	0 to 0·88
MODEL INCIDENCE RANGE :	-3° to +6°
FORCE BALANCE : 6 Component	NF 7·1kN (Max)
(Internal)	AF 0·7kN (Max)
AIRFEEDS :	Twin
AIR SUPPLY PRESSURE (MAX) :	35 bar
AIRFLOW RATES (MAX) :	2 × 2 kg/sec

Fig 27 FULL-SPAN RIG/MODEL FOR HIGH SPEED INSTALLATION STUDIES

Reynolds numbers than a . ll span model (at a fixed tunnel blockage). Later in this conference, Herr Burgsmüller will describe the use of a similar powered full-span model in the study of low speed installed drag and thrust reverser performance.

As an example of the value of the TPS testing techniques, we show here two examples taken from an illuminating text[22] presented by Frank Ogilvie of BAe to the Royal Aeronautical Society in 1989, Figs 28 and 29. In Fig 28 Ogilvie has shown that using a rigorous approach to identifying the relevant interference features it is possible to go about 90% of the way to explaining all of the sources and magnitudes of the interference results. The incremental component variations are all shown here plotted against model overall lift coefficient; all components diminish with increasing lift coefficient.

In the second example (Fig 29) Ogilvie illustrated the results of a brief development series in which a close-coupled research

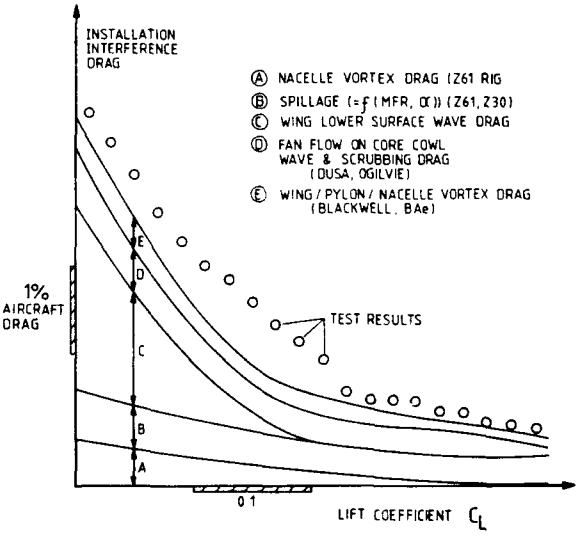

Fig 28 EXAMPLE OF TURBOFAN INSTALLATION DRAG INCREMENTS (FROM REF 22)

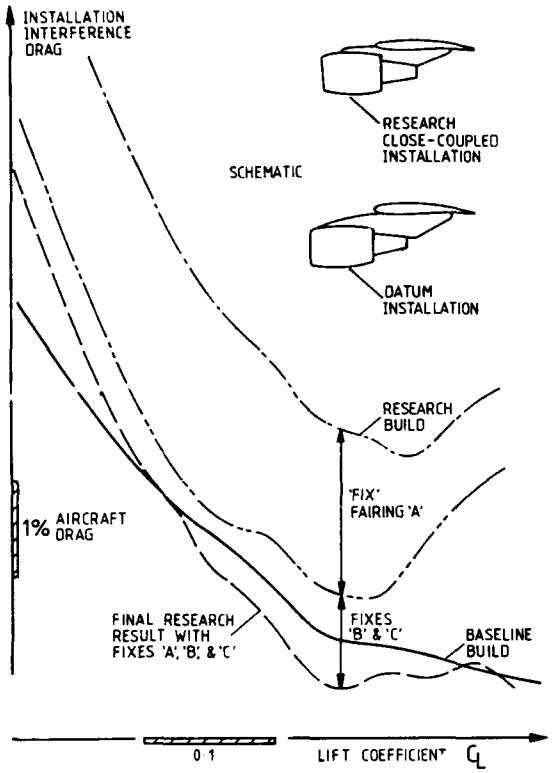

Fig 29 DATA FROM GENERIC CLOSE COUPLED INSTALLATION RESEARCH DRAG IMPROVEMENT STUDY

installation showed adverse drag increments of about 3% of aircraft drag. Using a small group of interference drag fixes (geometry modifications) it was shown that all of the adverse flow could be removed, leaving drag increments very close to the baseline, conventional nacelle installation results.

This positive, favourable drag result was achieved using all of the advantages of oil flow surveys and wing pressures as guides to the fixes necessary; as noted above, the outcome was also based on an in-depth understanding of the flow mechanics and of the variations in the relevant incremental drag contributions.

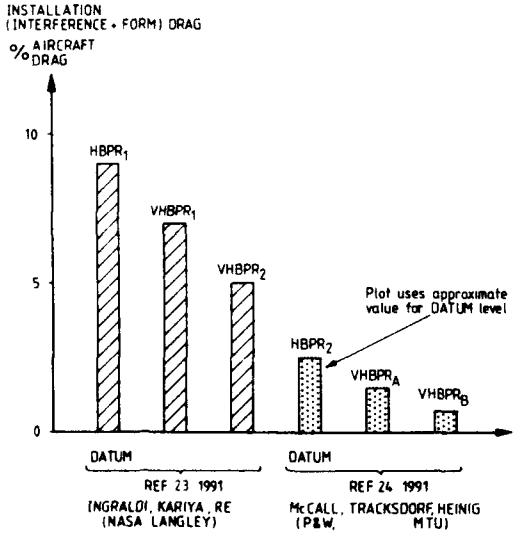

Fig 30 INSTALLATION DRAG DATA FROM TWO SEPARATE HIGH SPEED STUDIES

It is interesting to relate the above work to that published very recently in two ASME papers, Fig 30. The June 1991 papers[23,24] describe the influences on the aerodynamics, including drag, of changing from current turbofan installation designs to very high by-pass designs, as evaluated in two separate test series.

In the NASA Langley contribution (Ingraldi et al Ref 23) we can observe interference plus form drag levels of between 5% and 10% (of aircraft drag) of adverse installation drag; this result is at a cruise-like C_L and Mach number; the results being somewhat in favour of larger nacelles, as compared with the conventional design. It would appear that the conventional design carries an undue level of adverse installation drag and the case for large VHBPR nacelles is clouded by this factor.

In the second example from June '91 (Fig 30) a joint P&W and MTU contribution quotes much lower levels of adverse installation drag; the P&W and MTU results were obtained in the rigorous calibration, isolated and installed approach described above. Although the results again favour VHBPR nacelles all interferences plus form increments fall within the range 1 to 3% of aircraft drag.

The important things to note overall here are that, on the one hand, none of the 1991 installed work discussed here was powered and that, probably on account of very different wing interference contributions or some other more significant difference, the results do illustrate very marked drag differences. In a sense, this highlights a long standing rule in respect of turbofan installation interference - it is clearly not possible to generalise; further we also note that any attempts to generalise should be undertaken with the utmost caution; in consequence the plot of Fig 30 can only be relevant to those having full knowledge of the geometric variations (including baseline designs) and the aerodynamics of the work.

The need for powered experiments in such comparisons cannot be overstated; on the other hand research using through flow nacelles, as described above, can help to build the essential overall aerodynamic understanding and data base. Substantial levels of interference are still to be found and the major companies are still employing the best path to safe results, namely, CFD plus full experimental study leading to good installation performance levels.

The October 1984 AGARD conference provided a major contribution to the technology of advanced propeller aerodynamics and acoustics. Subsequent work at various establishments including technique developments and research results has been reported in Refs 18 and 21. In essence the test techniques for single or contra-rotating propellers run parallel to those used for turbofans. In overview, we should note that the following stages are usually used in a full development programme:

A Isolated tests at M = 0 and wind-on using an axisymmetric aft nacelle on a special isolated rig; large scale and/or small scale experiments to determine propeller aerodynamic (and acoustic) performance; with or without air intake representation;

B Nozzle system calibrations using a Mach Simulation Tank; tests may include presence of (locked) air motor;

C Installed tests using half model plus air turbine motor and rotors from isolated tests; model on underfloor forces and moments balance.

In A and C above the rotor/s are equipped with rotating shaft mounted propeller thrust and torque balances to evaluate performance in isolated and installed modes of operation. Figs 31 and 32 are extracted from Ref 21 where a full description of the techniques described above can be found. As for the work with turbofans,it is vital that accounting procedures and diagnostic data (pressures, flow visualisations, flow field traverses) are coordinated through the test phases. The broad outfall from this research should be: well understood isolated and installed performance data, at least at model scale, plus a substantial set of acoustic data for assessment of overall full scale characteristics.

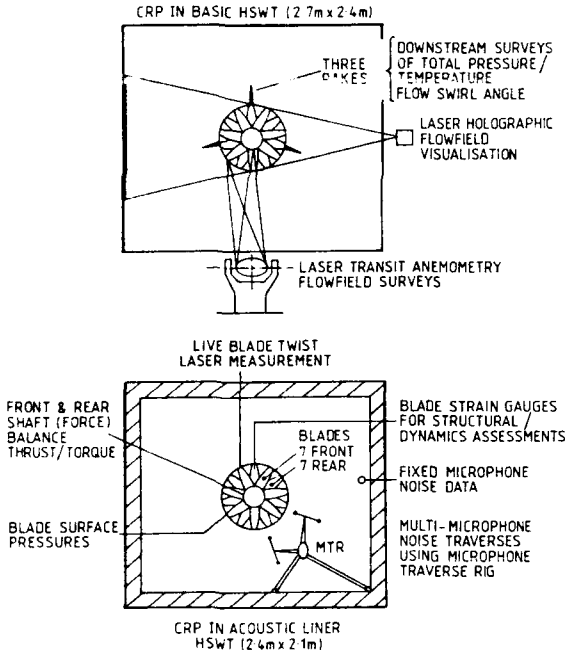

Fig 31 LARGE CONTRA-PROP RIG IN TWT WITH ACOUSTIC LINER

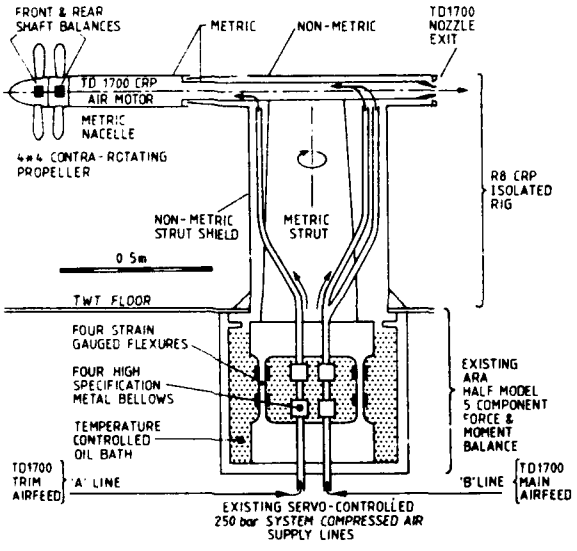

Fig 32 SMALL SCALE ISOLATED ROTOR PERFORMANCE RIG (R8)

For the last few years the state-of-the-art in the use of lasers for 3-dimensional flow field understanding has been actively addressed, Refs 25,26 and 27.

This UK DTI and SERC supported work involved three particular facets which have been studied in the relatively hostile (optical) confines of the ARA 9' x 8' transonic tunnel; the facets are:

1 Laser Holography to visualise installed TPS interference flow fields; whole flow field visualisations;
2 Laser Light Sheet to slice up vapour in transit through these flows; traversable two-dimensional sections;
3 Particle Image Velocimetry to determine the velocities of 1 micron particles of vapour travelling through these flow fields at about 250 metres/second: this PIV work used a 'throw' of 2 metres from the 1 micron particle to the camera (videotelescope); movable, traversable 3" square flow patches;

In the interests of space here it suffices to refer to this recent literature and to note that valuable results have been obtained with all 3 techniques in the period 1990 & 91; the techniques are, as yet, new and have yet to be regularly exploited,; however, early results do give considerable promise for use to enhance the conventional diagnostics tools. In Fig 33 we show one example.

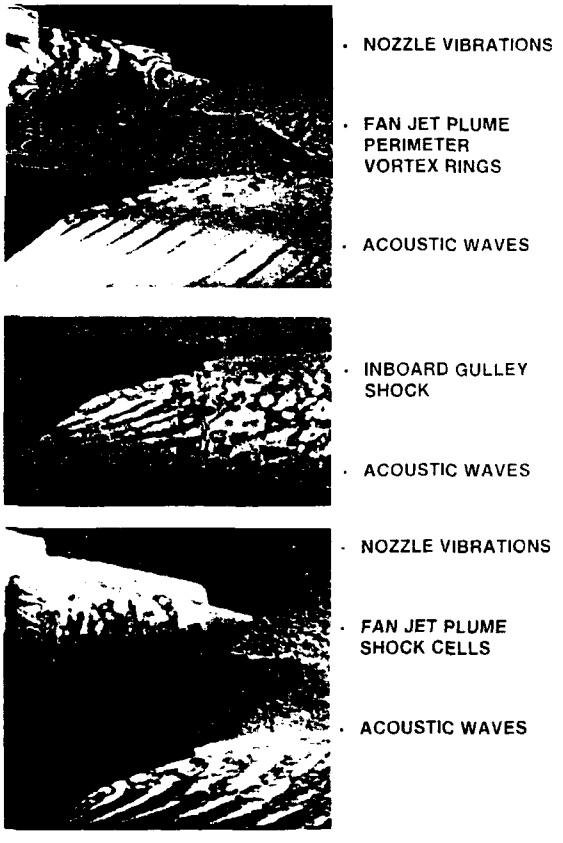

Fig 33 PRINTS FROM HOLOGRAM RECONSTRUCTIONS SHOWING INSTALLED TURBOFAN FLOW FEATURES

In Figure 34 an aircraft layout featuring a fully integrated engine/airframe arrangement suitable for high subsonic speed 21st century mass transit is shown. A few of the design features are:

a) Hybrid BLC using suck or blow or both;
b) Trailing edge windmill BLC power units (Patent applied for);
c) Advanced '2-D' inlet with S ducts to 3, 4 or 5 engines;
d) VHBPR fuel efficient turbofans;
e) Refined L/E, T/E 'adaptive' cruise drag reducing features;
f) S & C using combined winglet/L.E/T.E control system.

The design illustrated gives some indication of possible trends in next generation engine/airframe integration and maybe used to guide future testing requirements.

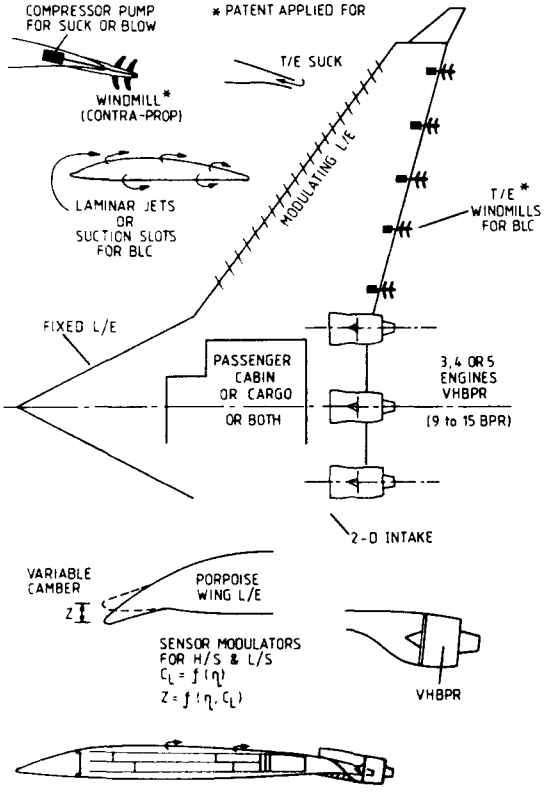

Fig 34 FULLY INTEGRATED ENGINE/AIRFRAME FOR AIR TRANSPORT

5 CONCLUDING REMARKS

1 The demands for high quality engine/airframe integration testing remain substantial as powerplant installations reach new levels of installed specific thrust and fuel efficiency.

2 The majority of the required testing techniques are in place for military and civil studies and these have been reviewed; the uses of CFD for configuration identification and in support of advanced testing techniques have been noted.

3 A need exists for powered simulations to give representative inlet and exhaust airstreams for emerging advanced military (ASTOVL, stealthy, vectored thrust) and civil (VHBPR) installation studies.

4 Significant steps forward have been achieved in respect of more refined installation aspects such as off-axis thrust vector accounting and total aerodynamics diagnostics covering the complete integrated engine/airframe using recent technique advances.

5 The use of powerful laser whole-flow-field visualisation and measurement (survey) techniques has been evaluated at a research level; major contributions to engine/airframe integration technology can be expected to arise when these methods are consolidated in the overall methodology.

6 The needs for extensive and costly large scale and flight test experiments continue to be eroded by the advancement of sophisticated small scale experiments.

7 Total quality engineering testing techniques allied to a variety of CFD methods can give both facets an assured place in future engine/airframe integration studies.

Acknowledgements

The author wishes to express appreciation for support, encouragement and contributions from BAe (Military, Airlines and Airbus Divisions), Rolls-Royce (Bristol and Derby Divisions), GE (Aircraft Engine Business Group), the UK MOD(PE) and from ARA Ltd.

All views expressed are those of the author and do not necessarily represent those of any of the above companies.

The unerring support in preparation of this paper and hitherto in general of my Propulsion Division colleagues and particularly Pearl Farr and Alison Ellum is gratefully acknowledged.

REFERENCES

1 Pierson R, "The use of the wind channel for performance prediction", RAeS Lecture, November 1927

2 Nicholson L F, "Engine-airframe integration", RAeS Lecture, April 1957 (published in RAeS Journal Vol 61 Nov 1957)

3 Haines A B, "Computers and wind tunnels; Complementary aids to aircraft design", RAeS Lecture 1976

4 AGARD FDP, "Aerodynamics of powerplant installation", AGARD FDP symposium Toulouse, France, May 1981

5 AGARD FDP, "Aerodynamics and Acoustics of Propellers", AGARD FDP symposium Toronto, Canada, October 1984

6 Knott P G, Milford C M, "Configuration effects on the ingestion of hot gas into the engine intake". Paper III.2 RAeS/AIAA/SAE International Powered Lift Conference, London, August 1990

7 Abbott W A, White D R, "The effect of nozzle pressure ratio on the fountain formed between two impinging jets", RAE Tech Memo P1166, May 1989

8 Smith A G, Ing D N, Bailey P J, "The experimental and computational study of jet impingement flowfields with reference to VSTOL aircraft performance". Paper III.13 RAeS/AIAA/SAE, International Powered Lift Conference, August 1990

9 Harris A E, Marbert JA , Tatom J W, "VTOL transport hot gas reingestion studies", 7th Annual National conference on Environmental Effects on Aircraft and Propulsion Systems, Princeton, New Jersey, September 1967

10 Tatom J W, Hinson B L, Harris A E, "VTOL transport dust cloud/pilot visibility study", 7th Annual National Conference on Environmental Effects on Aircraft and Propulsion Systems, Princeton, New Jersey, September 1967

11 Wake A J, Hill C J, Angel R G A, "Ground surface erosion - British Aerospace test facility and experimental studies", paper III.11 RAeS/AIAA/SAE International Powered Lift Conference, London, August 1990

12 Johns A L, Neiner G H, Beucic T J, Flood J D, Annuedo K C, Strock T W, Williams B R, "Hot gas ingestion characteristics and flow visualisation of a vectored thrust STOVL concept", paper III.4 RAeS/AIAA/SAE International Powered Lift Conference, London, August 1990

13 Williams D D, "Hot gas reingestion - engine response consideration" paper III.5 RAeS/AIAA/SAE International Powered Lift Conference, London, August 1990

14 Shaw J A, Georgala J M, Weatherill N P, "The construction of component adaptive grids for aerodynamic geometries", Second International Conference on Numerical Grid Generation in Computational Fluid Dynamics, Miami Beach, Florida, December 1988

15 Bowers D L, Laughrey J A, "Integration of advanced exhaust nozzles" paper 11 AGARD FDP symposium "Aerodynamics of Power Plant Installation", Toulouse, France, May 1981

16 Seiner J M, Manning J C, Capone F J, Pendergraft O C Jnr, "Study of external dynamic flap loads on a 6 percent B-1B model", ASME paper 91-GT-236, Orlando, Florida, June 1991

17 Pozniak O M, "A review of the effect of Reynolds number on afterbody drag", paper 16 AGARD FDP symposium "Aerodynamics of Power Plant Installation", Toulouse, France, May 1981

18 Metzger F B, "Prop-fan design and test experience", RAeS International Conference on Advanced Propellers and their Installation on Aircraft, Cranfield, England, August 1988

19 Burgsmuller W, Szodruck J, "Benefits and costs of powered engine simulation at low speeds", AIAA paper 85-0381, 1985

20 Harris A E, Paliwal K C "Civil turbofan propulsion system integration studies using powered testing techniques at ARA Bedford", AIAA paper 84-0593,1984

21 Harris A E, Render P M, Pozniak O M, Wood M E, "Recent wind tunnel testing experience of contra-rotating propellers", 17th ICAS conference, Stockholm, Sweden, September 1990

22 Ogilvie, F B, "Civil turbofan installation aerodynamics as seen by an aircraft designer", Lecture to RAeS, London, November 1989

23 Ingraldi A M, Kariya T T, Re RJ, "Interference effects of very high by-pass ratio nacelle installations on a low-wing transport", ASME paper 91-GT-241, IGTI meeting Orlando, Florida, June 1991

24 McCall J E, Tracksdorf P, Heinig K, "Advanced ducted engines nacelle aerodynamics and integration testing", ASME paper 91-GT-136, IGTI meeting Orlando, Florida, June 1991

25 Bryanston-Cross P J, "The application of submicron particle visualisation for PIV at transonic speeds", Progress in Aerospace Science, volume 27, p237-265 Pergamon Press, 1990

26 Parker R J, "Practical developments in holographic interferometry", Aeronautical Journal of the RAES, p 91-98, London, March 1990

27 Towers C E, Towers D P, Judge T R, Bryanston-Cross P J, "A laser light sheet investigation into transonic external aerodynamics" SPIE Conference paper/92, High Speed Photography and Photonics, Cambridge, England, September 1990

Further Essential Reading

Covert E at al	'Thrust and Drag: Its Prediction and Verification'. Progress in Astronautics and Aeronautics, Volume 98, Published by AIAA 1985.
Abernethy RB et al	'In-Flight Thrust Measurement SAE Study Committee E-33 circa 1988. Includes Error Propagation and Statistical Techniques.
MIDAP Study Group	'Guide to In-Flight Thrust Measurements'AGARDOGRAPH AG-237, January 1979.
Ferri, A	'Airframe-Engine Integration' AGARD Lecture Series LS-53, 1972.

ESSAIS DE MAQUETTES MOTORISEES EQUIPEES DE SIMULATEURS DE REACTEURS DANS LA SOUFFLERIE BASSE VITESSE PRESSURISEE F1, DE L'ONERA

(Tests of Models Equipped with TPS in Low Speed ONERA F1 Pressurized Wind Tunnel)

par

J. Leynaert
Office National d'Etudes et de Recherches Aérospatiales
ONERA
B.P. 72
92322 Châtillon
France

RESUME

Les conditions particulières des essais de maquettes équipées de simulateurs de réacteurs (SDR) à des nombres de Reynolds élevés dans la soufflerie F1 de l'ONERA sont présentées.

L'équipement de la soufflerie en air haute pression pour l'alimentation des SDR, l'aménagement de la balance avec traversée d'air comprimé et son tarage, la méthode de tarage de la poussée de la nacelle motorisée, et le contrôle de ce tarage en soufflerie, sont successivement décrits.

ABSTRACT

The special conditions of the tests of models equipped with TPS (Turbofan Powered Simulator) at high Reynolds numbers in the F1 pressurized ONERA wind tunnel are presented.

The high pressure air supply system of the wind tunnel, the equipment of the balance with the high pressure traversing flow and its calibration, the thrust calibration technique of the TPS and its check in the wind tunnel, are successively detailed.

1 - CONTEXTE GENERAL DES ESSAIS DE MAQUETTES EQUIPEES DE SDR (Simulateurs de réacteurs) DANS LES SOUFFLERIES DE L'ONERA

Une expérience de plus de dix années d'essais de maquettes équipées de SDR est aujourd'hui acquise. Les premiers essais à l'ONERA, en 1980, ont été réalisés sur des demi-maquettes montées à la paroi de la veine transsonique de la soufflerie S2MA, de 1,75 x 1,77 m2 de section (1). De tels essais sont encore aujourd'hui couramment programmés, mais les plus grandes dimensions de la soufflerie S1MA, qui peut atteindre Mach 1, et dont la veine s'inscrit dans un diamètre de 8 m, ont été également retenues depuis, pour effectuer des essais de maquettes motorisées de tailles plus importantes.

La figure 1 présente une demi-maquette de l'Airbus A340 récemment passée dans cette soufflerie, pour étudier la traînée d'installation des moteurs, jusqu'à un nombre de Mach de 0,9. Les deux SDR qui l'équipent ont un diamètre de 14 cm (5,6 pouces).

La figure 2 montre une autre maquette de grande taille essayée cette fois à basse vitesse, dans la même soufflerie. Il s'agit de l'Airbus A320 à l'échelle 1/7,6 , de 4,5 m d'envergure, équipé de deux SDR de 23 cm (9 pouces).

Les essais portaient sur l'intéraction nacelle-voilure, et sur l'effet de sol, avec moteurs en réverse, notamment (2). Des essais de même type effectués dans la soufflerie DNW avec tarage des nacelles au banc de tarage de l'ONERA à Modane font l'objet d'une présentation conjointe de l'Aérospatiale, Deutsche Airbus, DNW et l'ONERA à ce même congrès (3).

Ces essais, conduits à une pression génératrice de soufflerie égale à la pression atmosphérique, peuvent toutefois ne pas rendre compte d'effets tributaires du nombre de Reynolds. Pour s'assurer de ceux-ci, notamment sur la portance maximale en configuration hypersustentée, un montage d'essai pour maquettes motorisées a été réalisé et mis en oeuvre dans la soufflerie basse vitesse, pressurisée à 4 bar, F1, du centre du Fauga Mauzac de l'ONERA. Des essais de fonctionnement de l'installation avec un SDR de "9 pouces" à 3 bar de pression génératrice avaient été effectués en 1985. Récemment, (juin 1991) un programme d'essai complet sur la même demi-maquette de l'Airbus A340 qu'à S1MA, version hypersustentée, a été réalisé. Les conditions et les caractéristiques de cet essai sont décrites ci-après.

2 - LA SOUFFLERIE F1 ET SON EQUIPEMENT POUR L'ALIMENTATION ET LE CONTROLE DES SIMULATEURS DE REACTEURS

La figure 3 présente la demi-maquette réalisée par l'Aérospatiale, de l'Airbus A340 à l'échelle 1/17,5 équipée de ses deux simulateurs de réacteurs "Technofan" dans la soufflerie F1. Les dimensions de veine de la soufflerie sont 4,5 m de largeur, 3,5 m de hauteur et 11 m de longueur. La pression génératrice maximale d'utilisation est 3,85 bar. Des portes permettent d'isoler la veine du reste du circuit pour réduire le temps d'accès à la maquette en limitant la depressurisation à la portion utile de la veine lorsque l'ensemble du circuit est pressurisé.

Cette soufflerie possède un équipement d'essai très performant, basé sur quatre palettes interchangeables formant plancher de la veine d'essai, chaque palette étant munie d'une chaine de mesure complète. Cette disposition permet la préparation simultanée de trois essais dans des halls de préparation individualisés, tandis que la quatrième palette est en essai dans la veine. La description de la soufflerie fait l'objet de la réf. (4).

La figure 4 précise le nombre de Reynolds nominal de la soufflerie, comparé aux souffleries DNW, RAE 5 m, et S1MA de l'ONERA.

La figure 5 décrit les caractéristiques de l'installation d'air comprimé, dont la partie haute pression a été spécialement développée pour les essais avec simulateurs de réacteurs.

Le réseau basse pression (11 bar) est alimenté, soit par le compresseur centrifuge BP1 (débit 5 Kg/s), soit par les compresseurs BP1 et BP2 (3 Kg/s) travaillant en parallèle. Le réservoir à partir duquel s'effectue la pressurisation de la soufflerie F1 a un volume de 300 m3.

L'air haute pression (270 bar) est fourni par un compresseur à piston (3 Kg/s) fonctionnant en série avec le compresseur BP2. Le réservoir de stockage a un volume de 40 m3. Pour son utilisation, l'air est d'abord détendu à une pression règlable entre 60 et 120 bar, et un réchauffeur primaire maintient sa température à 20°C. Une régulation du débit est assurée jusqu'à 20 Kg/s. Un réchauffeur secondaire permet un ajustement de la température jusqu'à 80°C. Un filtre protège le SDR de toute érosion.

Une console de pilotage des SDR permet, par asservissement du débit, de régler le régime, et d'assurer diverses fonctions de sécurité de la machine.

3 - BALANCE DE PAROI ET TARAGE

Le principe d'aménagement de la balance de paroi avec traversée d'air comprimé est présenté figure 6.

La balance constituée de deux plateaux reliés par les éléments de découplage et les dynamomètres comporte un large évidement central. L'air comprimé traverse la balance par un long tube placé dans cet évidement avec un système de rotule et joint torique à chaque extrémité pour minimiser les interactions en efforts transversaux sur la balance. L'effet de fond est entièrement supporté par la balance, mais cet effort qui est un effort transversal pour la demi-maquette montée sur la balance, n'est pas critique pour les mesures, et il fait, de toutes façons, l'objet d'un tarage.

Un tube isolant joue le rôle d'écran thermique entre le tube d'amenée d'air comprimé et la balance, pour éviter tout risque de dérive thermique des dynamomètres.

Le débit se partage en deux au sommet de la balance, par une culotte de distribution qui alimente deux circuits munis chacun d'un règlage de débit par obturateur motorisé, et d'un débitmètre. Le tarage de ce débitmètre est assuré en alimentant successivement chaque conduit, et en se référant au débitmètre standard placé dans le circuit amont d'air comprimé. Les deux circuits sont destinés aux deux turbines du SDR qui équipent la demi-maquette.

L'ensemble de pesée fait l'objet d'un tarage dans une alvéole spécialement aménagée pour recevoir les palettes de la soufflerie, et pour appliquer des efforts calibrés, à une potence fixée sur la balance de la même façon que la maquette.

La conduite d'air comprimé est fermée au niveau de la maquette, et la pression est appliquée par des bouteilles d'air comprimé.

La gamme de pression interne à couvrir est de 120 bar, et celle des efforts de 3000 N.

Sur le pont de traînée, l'effet de la pression se traduit par une légère diminution de la sensibilité de la balance, qui conduit à une correction du coefficient de l'ordre de 3.10-4.

Une faible dérive linéaire est également constatée, qui atteint 20 N à 120 bar.

Après correction, et contrôle par répétition de cycles efforts-pressions, les résidus d'écarts sont inférieurs à 3N.

Le comportement de l'ensemble étant ainsi vérifié en pression, mais sans écoulement interne, un contrôle de la balance avec débit est réalisé en veine, maquette en place, mais débits déviés sur deux tuyères de référence fixées sur un support provisoire, comme représenté figure 7.

Les coefficients de débit et de poussée de ces tuyères sont établis par mesure sur un banc de tarage spécialisé. L'essai en veine permet à la fois le contrôle de la débitmétrie, et le contrôle de la balance dans les conditions réelles d'utilisation.

Les résultats montrent des différences en coefficient de poussée de 0,2% au maximum, avec une fidélité meilleure que 0,1%.

4 - TARAGE DES SDR EN DEBIT ET POUSSEE

Ce tarage s'effectue en plusieurs phases :

- des essais en alimentation contrôlée de l'entrée d'air, sur le banc S4b de Modane où la tuyère débouche dans une ambiance à pression réduite ajustable, afin de simuler au banc le taux de détente de l'essai en soufflerie à différents nombres de Mach. la pression maximale ambiante dans le caisson est limitée à 1 bar.

- des essais en atmosphère libre, type point fixe, au même banc, avec nacelle munie d'un pavillon d'entrée, pour vérifier le tarage du débit et de la poussée aux conditions du point fixe.

- des essais identiques effectués sans vent, dans la soufflerie, à plusieurs niveaux de pressurisation de la veine, pour établir des corrections éventuelles d'effets du niveau de pression sur les coefficients de poussée.

4.1 - Essai en caisson

Deux montages, qui peuvent être alternativement installés dans le même caisson, "S4B" du centre de Modane sont utilisés àl'ONERA pour ces essais, l'un pour les SDR de diamètre au plus égal à "5,6 pouces", l'autre pour les SDR pouvant atteindre "16 pouces".

Ces deux montages sont décrits réf.(5). Une utilisation particulière du second montage pour des essais de reverse est présentée au présent congrès (3).

Une particularité d'utilisation de ce second montage est que l'ajustement de la pression du caisson se fait par règlage d'un effet trompe utilisant le jet propre du SDR. Les caractéristiques de ce système sont analysées dans la référence (5).

Les deux montages eux-mêmes sont de même principe, et le schéma du premier est rappelé figure 8.

La balance est traversée par deux alimentations munies d'un système de découplage. La première débouche dans une chambre qui alimente la prise d'air de la nacelle du SDR, prise d'air équipée à l'amont d'un pavillon permettant de restituer au plan d'entrée de la soufflante un écoulement comparable à celui de l'essai en soufflerie. La seconde entraîne la turbine du SDR.

Les débits sont mesurés au niveau des alimentations à l'amont de la balance.

Les paramètres essentiels sont la vitesse réduite de la machine et le taux de détente de la soufflante, repéré par le rapport de la pression génératrice amont à la pression statique de sortie, pression ambiante du caisson. Le coefficient de débit en est tributaire, mais il peut être également repéré par le rapport d'une pression locale interne d'entrée d'air à la pression génératrice amont.

L'extraction du débit et le règlage de la pression du caisson se font, pour ce montage, par contrôle d'une évacuation sur une sphère à vide de grande capacité.

Le contrôle des mesures s'effectue en mixant les deux débits traversant la balance dans la même chambre de tranquillisation et en remplaçant le SDR par une tuyère standard type ASME, de débit et poussée connus.

4.2 - Essai de la nacelle au point fixe avec pavillon, au même banc

La figure 9 représente l'essai en atmosphère libre de la nacelle munie de son pavillon. Cet essai a pour but de vérifier que la poussée mesurée au point fixe a bien la même valeur que celle mesurée dans l'essai précédent en alimentation forcée, à la même pression ambiante.

Un ajustement des repères de débit avec pavillon peut éventuellement en être déduit.

4.3 - Essai de la nacelle au point fixe avec pavillon, en soufflerie

Comme déjà mentionné, ces essais ont pour objet de vérifier en soufflerie les tarages de poussée effectués au caisson d'étalonnage et de contrôler l'effet de l'élévation du niveau moyen de pression par pressurisation de la soufflerie sur le coefficient de poussée du SDR.

Pour ceci, la nacelle avec pavillon est montée sur la même balance paroi que celle recevant ensuite la maquette motorisée.

Des vues en veine de ce montage sont présentées figures 10 et 11.

Les résultats obtenus jusqu'à présent montrent que les caractéristiques de l'écoulement de la soufflante ne sont pratiquement pas modifiées par le niveau de pression, mais que le débit générateur peut devoir être légèrement réajusté. La plage de pression génératrice couverte par ces essais a été limitée à 3 bar, le SDR n'ayant pas été conçu pour un niveau plus élevé.

Des essais analogues ont été réalisés lors de l'étude, plus récente, faite sur la demi-maquette de l'A340 au 1/17,5, mais, pour des raisons de commodité, la maquette elle-même a servi de support à la nacelle munie de son pavillon de point fixe. Afin toutefois d'éviter, au point fixe, toute interaction du débit du SDR avec la maquette elle-même, ce qui aurait faussé la mesure de la poussée, un mât spécial d'attache de la nacelle à l'aile a été réalisé, de hauteur suffisante pour écarter largement le SDR de la maquette.

Le schéma de cette installation est présenté figure 12, et la vue en veine figure 13. On notera sur cette figure, par comparaison avec la figure 3, que les hypersustentateurs ont été ôtés, pour éviter l'interaction des jets. Les essais, dans un premier temps, ont été limités à une pression génératrice de 2,5 bar, pour un problème de rigidité du mât, qui pourra être résolu. La fidélité des résultats a confirmé celle identifiée pour la balance au paragraphe 3.

5 - CONCLUSIONS

Les moyens et les principes d'essai des maquettes équipés de simulateurs de moteur dans la soufflerie basse vitesse pressurisée F1 de l'ONERA ont été présentés. Les diverses opérations de tarage et de contrôle de la balance avec traversée d'air comprimé d'une part, et des paramètres de débit et de poussée du SDR d'autre part, permettent d'effectuer ces essais dans des conditions satisfaisantes de fidélité et de précision.

REFERENCES

(1) J.P. BECLE et R. PERIN -
Essais en soufflerie de maquettes motorisées - Comparaison de deux méthodes de simulation des jets des réacteurs -
AGARD CP 301 (1981)

(2) A. CONDAMINAS - J.P. BECLE -
Détermination de l'effet de sol sur les caractéristiques de l'avion A320
AGARD CP 465 (1989)

(3) W. BURGSMULLER - C. CASTAN - J.W KOOI- J.P.BECLE -
Recent developments in low speed TPS testing for engine integra tion drag and installed thrust reverse simulation
69th AGARD Symposium - Fort Worth - Oct. 1991

(4) J.M. CARRARA - A. MASSON
Three years of operation of the ONERA pressurized subsonic wind tunnel
12th Congress of ICAS (1980) - ONERA TP 1980 - 29

(5) J.P. BECLE - J. COSTE - J. LEYNAERT
Nouveau banc d'étalonnage de nacelles équipées de turbines pour soufflantes (TPS), et essais d'éjecteurs - AGARD CP 348 (1983)

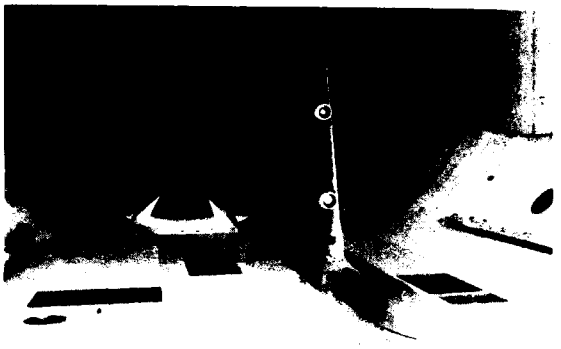

Fig. 1 - Demi-maquette motorisée Airbus A340 dans la soufflerie S1MA de l'ONERA.

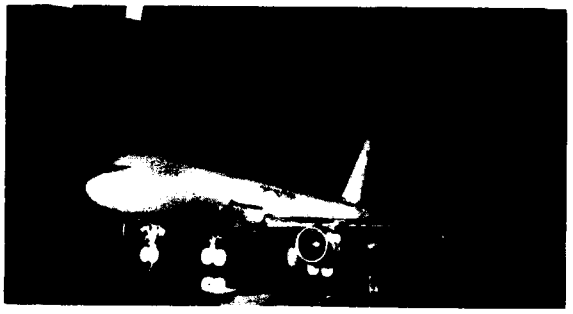

Fig. 2 - Maquette motorisée Airbus A320 échelle 1/7,6 dans la soufflerie S1MA.

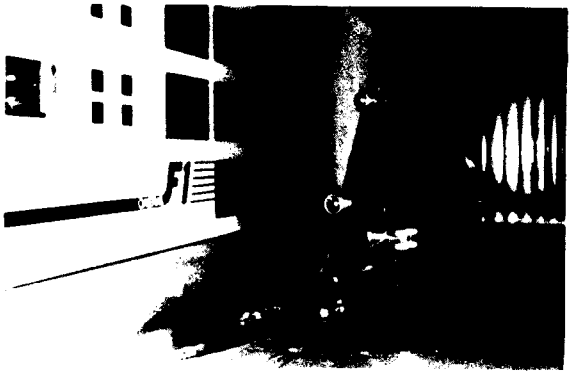

Fig. 3 - Demi-maquette motorisée (Aérospatiale) Airbus A340, échelle 1/17,5 dans la soufflerie pressurisée F1 de l'ONERA.

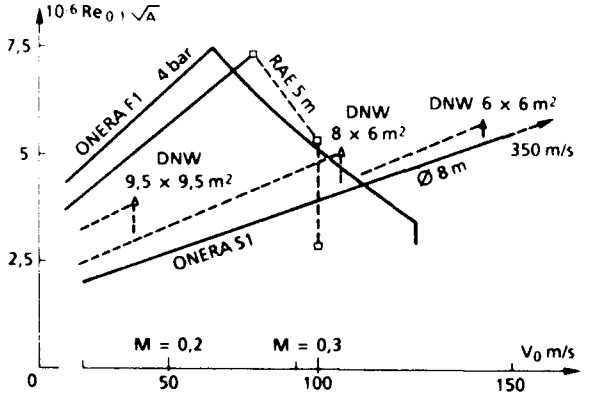

Fig. 4 - Diagramme de nombre de Reynolds de diverses souffleries.

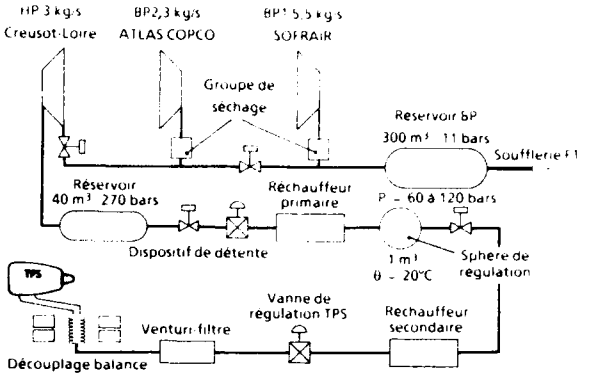

Fig. 5 - Installation d'air comprimé de la soufflerie F1.

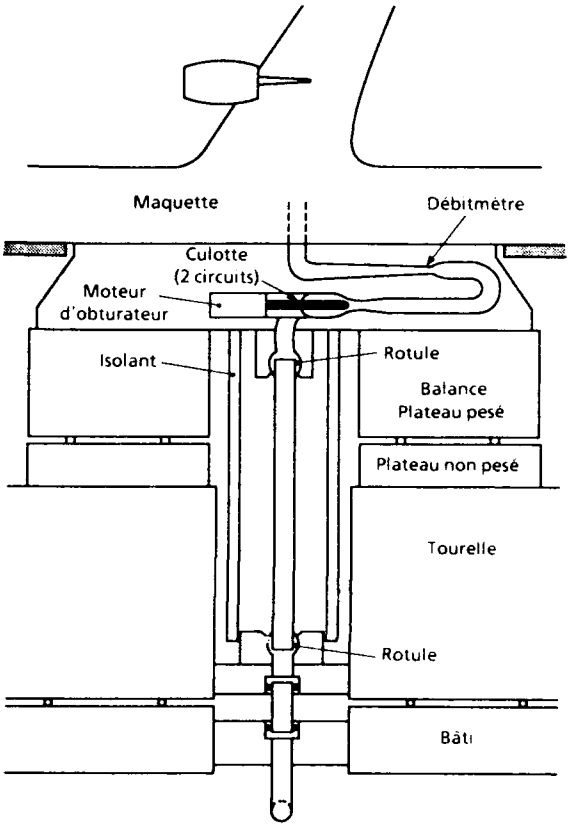

Fig. 6 - Balance de paroi de la soufflerie F1 avec traversée d'air comprimé.

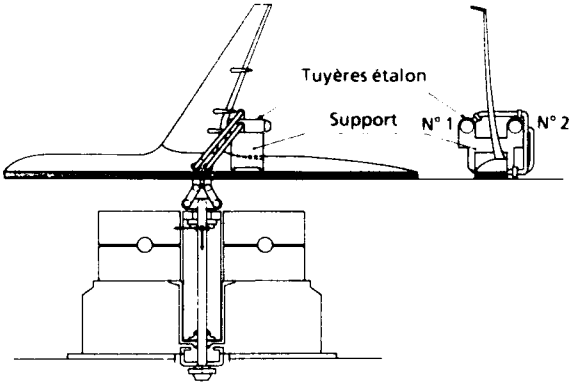

Fig. 7 - Contrôle du tarage en poussée de la balance par des tuyères de référence.

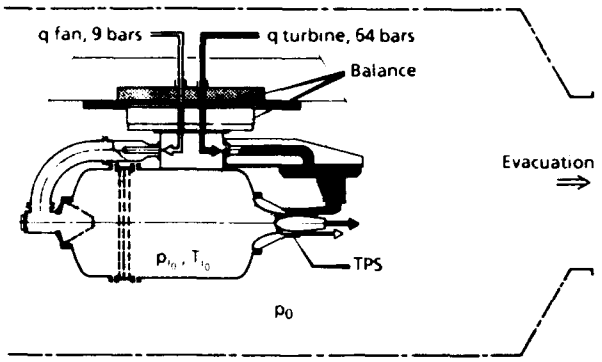

Fig. 8 Schéma de principe des bancs de tarage des simulateurs de réacteurs (SDR) au caisson S4B de l'ONERA Modane.

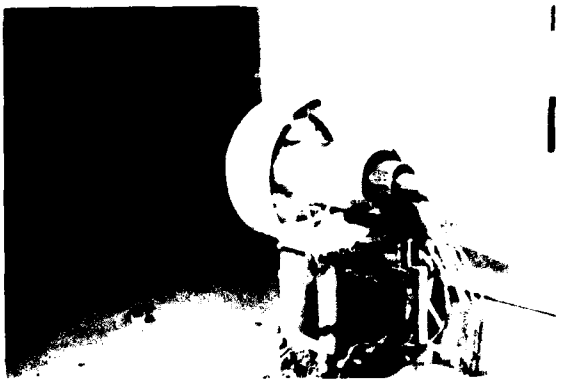

Fig. 11 Montage de tarage au point fixe, vu de l'arrière

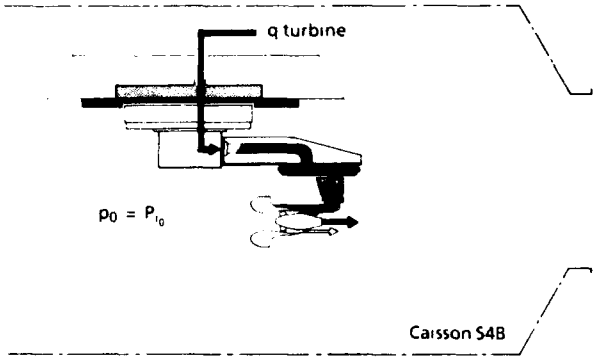

Fig. 9 Contrôle du tarage des SDR au caisson S4B en configuration d'essai au point fixe avec pavillon

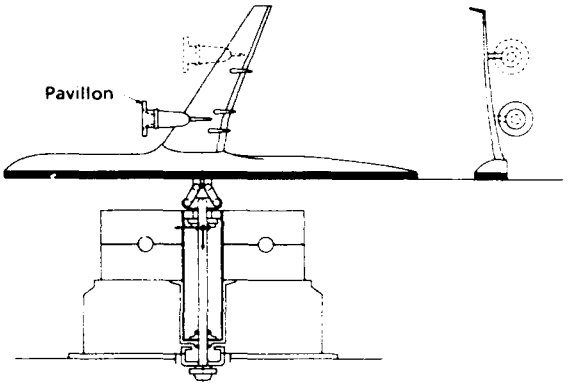

Fig. 12 Schéma du montage de tarage au point fixe du SDR sur demi maquette A340 dans la soufflerie F1

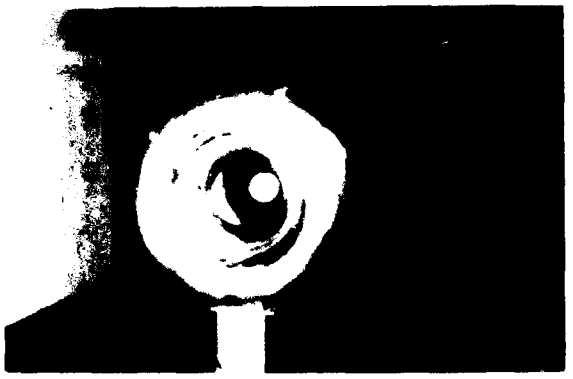

Fig. 10 Contrôle au point fixe, à différentes pressions, des paramètres de tarage du SDR, dans la soufflerie F1.

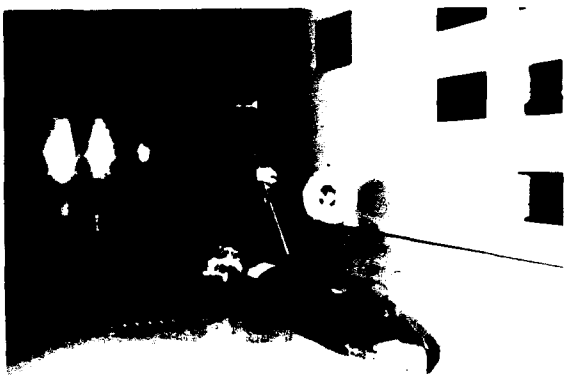

Fig. 13 Vue en veine de la demi maquette A340 avec SDR en configuration de tarage dans la soufflerie F1.

SIMULATION NUMERIQUE DE L'ECOULEMENT AERODYNAMIQUE AUTOUR DES NACELLES

par

J.L. Lecordix, J.G. Fratello et J.M.Gippet
SNECMA
Centre de Villaroche
77550 Moissy Cramayel
France

RESUME

Dans le but de réduire le nombre et le coût de ses essais, la SNECMA s'est dotée d'un code Euler tridimensionnel. Celui-ci résout les équations d'Euler compressibles mises sous leur forme conservative, et à convergence est capable de prédire les écoulements aérodynamiques autour de géométries multidomaines complexes. Le schéma numérique est de type volumes finis et est d'ordre 2 en temps avec une approche prédicteur-correcteur à 2 pas.
D'autre part, il utilise un pas de temps local et une viscosité artificielle de type TURKEL-JAMESON.
Cette méthode a été validée par des calculs sur des nacelles isolées et les résultats numériques obtenus recoupent de manière satisfaisante ceux issus des essais.
Ce code a été industrialisé et permet aujourd'hui la critique des lignes aérodynamiques des nacelles.

INTRODUCTION.

Dans le but de réduire le nombre et le coût de ses essais, la SNECMA s'est dotée d'une chaîne numérique lui permettant de calculer les champs d'écoulement autour de géométries complexes. Pour se faire, elle s'appuie sur un code Euler tridimensionnel développé par l'ONERA.
Dans un premier temps, ce code a été adapté aux calculs de nacelles isolées et aujourd'hui,grâce à lui, la SNECMA peut valider ses nacelles en s'en servant comme outil de conception.
Après une description du code utilisé et des techniques de maillage employées, il sera présenté des calculs sur la nacelle d'un turboréacteur à hélices rapides, qui ont permis sa validation par comparaison avec les essais effectués sur cette nacelle.
On présentera également des résultats de traînée obtenus à l'aide d'un calcul de couche limite basé sur une méthode intégrale. Il sera également présenté une comparaison calcul/expérience.
Ensuite, une application à la prédiction de l'écoulement établi autour et au travers d'une nacelle avec corps central sera exposée.

1. PRESENTATION DU CODE DE CALCUL.

1.1. GENERALITES.

Le code utilisé pour la prédiction des écoulements tridimensionnels et compressibles de fluide parfait en intégration aérodynamique a la SNECMA, a été développé à l'ONERA. Il a pour nom SESAME (Simulation d'Ecoulements Stationnaires avec Approche Multidomaine Euler) [1]
C'est un code de type industriel de par sa facilité d'utilisation pour des applications variées, et la modularité de ses éléments.
Il est capable de simuler des écoulements internes (grilles d'aubes, entrées d'air) et externes (missiles, voilures, nacelles) par résolution instationnaire des équations d'Euler compressibles tridimensionnelles.
Son domaine d'application validé va du fortement subsonique (Mach = 0.15) au supersonique faible (Mach = 3). En écoulement externe, il peut prendre en compte de fortes incidences (jusqu'à 30 degrés). Ce code a été vectorisé pour un rendement optimal sur CRAY.

1.2. CARACTERISTIQUES.

Sésame est un code multidomaine (domaines pouvant se recouvrir ou non) dont l'exécution se fait entièrement en mémoire centrale.
A convergence, il donne les champs stationnaires $(\rho,\rho u,\rho v,\rho w,\rho e)$ d'un problème aérodynamique par résolution des équations d'Euler insta-

tionnaires.
IL utilise des maillages structurés "I,J,K" par bloc et les variables de calcul sont données aux noeuds "sommet".
La discrétisation des équations est effectuée au moyen d'un schéma "volumes finis" et explicite du type LAX-WENDROFF-NI à deux pas en temps.
La stabilité du schéma est assurée par un terme de viscosité artificielle de type TURKEL-JAMESON.
La convergence de la solution peut être accélérée à l'aide d'une méthode multigrille de type NI.
Le traitement des conditions aux limites et de raccord entre sous-domaines est basé sur la méthode des relations de compatibilité.
[2] et [3].

1.3. VARIABLES ET SYSTEME D'EQUATIONS.

Le code résout le système des équations d'Euler complètes qui s'écrit sous forme conservative :

$$\frac{\partial \rho}{\partial t} + \mathrm{div}(\rho \bar{V}) = 0$$

$$\frac{\partial \rho \bar{V}}{\partial t} + \mathrm{div}(\rho \bar{V} \otimes \bar{V} + p \bar{\bar{I}}) = \bar{0}$$

$$\frac{\partial \rho E}{\partial t} + \mathrm{div}(\rho E \bar{V} + p \bar{V}) = 0$$

soit sous forme compacte :

$$(1)\quad \frac{\partial f}{\partial t} + \mathrm{div} F = 0$$

où f représente les variables conservatives

$$(\rho, \rho u, \rho v, \rho w, \rho e)$$

et F les densités de flux.

1.4. SCHEMA NUMERIQUE.

Le schéma numérique utilisé dans Sésame est un schéma explicite d'ordre 2 en espace et en temps du type LAX-WENDROFF-NI [4]

1.4.1. DISCRETISATION EN TEMPS.

La discrétisation en temps est effectuée à l'aide d'un schéma prédicteur-correcteur à 2 pas. Le prédicteur donne les valeurs des variables conservatives à l'instant

$$t^{n+\frac{1}{2}} = t^n + \frac{1}{2}\Delta t$$

soit :

$$(2)\quad f^{n+\frac{1}{2}} = f^n - \frac{\Delta t}{2}\,\mathrm{div} F^n$$

Le correcteur donne la solution à l'instant $t^{n+1} = t^n + \Delta t$ soit :

$$f^{n+1} = f^n + \Delta t \left(\frac{\partial f}{\partial t}\right)^{n+\frac{1}{2}}$$

$$(3)\quad f^{n+1} = f^n - \Delta t\,\mathrm{div} F^{n+\frac{1}{2}}$$

$$\text{où}\quad F^{n+\frac{1}{2}} = F\left(f^{n+\frac{1}{2}}\right)$$

1.4.2. DISCRETISATION EN ESPACE.

Le schéma utilise une approximation du type volumes finis. Il est basé sur l'utilisation de formules de distribution qui permettent de distribuer vers les huit sommets d'une cellule, les variations de la solution calculée en son centre. En particulier, le terme

$$A = -\frac{\Delta t}{2}\,\mathrm{div} F^n$$

du prédicteur est calculé au barycentre de chaque cellule du maillage à l'aide de la formule de la moyenne :

$$A = -\frac{\Delta t}{2v(\Omega)} \int_\Omega \mathrm{div} F^n \, dv$$

$$(4)\quad A = -\frac{\Delta t}{2v(\Omega)} \int_{\partial\Omega} F^n \bar{n} \, ds$$

où Ω représente la cellule et $\partial\Omega$ son enveloppe.
Les flux F^n étant connus aux noeuds du maillage, l'intégrale de contour est calculée en supposant qu'ils sont constants sur chacune des six faces de la cellule et ont pour valeur la moyenne arithmétique des valeurs aux quatre sommets de la face.

Le terme f^n du prédicteur est la moyenne arithmétique des valeurs de f^n aux huit sommets de la cellule. En ce qui concerne le prédicteur, le terme

$$B = -\Delta t\,\mathrm{div} F^{n+\frac{1}{2}}$$

est évalué en chaque point du maillage par une formule de la moyenne analogue à (4), où le volume de contrôle est la cellule générée par les barycentres des huit cellules qui entourent ce point.

Les valeurs f^{n+1} aux points "frontière" sont obtenues par extrapolation.

REMARQUE :

Etant donné l'approximation choisie, la régularité et l'orthogonalité du maillage améliorent la qualité des résultats.

1.5. PAS DE TEMPS LOCAL.

Le schéma utilise un pas de temps local qui est déterminé à partir d'un critère CFL du type :

$$\Delta t = \eta \frac{h}{V+a}$$

où h est une longueur caractéristique du domaine de dépendance numérique, V le module de la vitesse du fluide et a, la célérité du son. η est un coefficient de sécurité compris entre 0 et 1, introduit en raison du caractère approché du critère.

1.6. ADIMENSIONNEMENT.

Les variables aérodynamiques sont adimensionnées par les valeurs à l'infini amont. En particulier, les masses volumiques sont adimensionnées par la masse volumique d'arrêt et les vitesses par la célérité du son d'arrêt. L'adimensionnement de tout autre grandeur s'en déduit.

2. TECHNIQUES DE MAILLAGE.

2.1. GENERALITES.

L'approche multidomaine du code Sésame s'avère extrêmement pratique. Dans le cas de géométries complexes, elle permet une décomposition du domaine de calcul en plusieurs zones topologiquement et numériquement indépendantes. Dans le calcul global, ces zones sont reliées les unes aux autres par des conditions aux limites de raccord basées sur la méthode des relations de compatibilité. Le code Sésame peut traiter des frontières entre deux zones sans qu'il y ait correspondance des noeuds, les deux zones pouvant même se chevaucher.
Les maillages utilisés pour les études de nacelles isolées sont générés en BATCH à l'aide de logiciels dédiés. Ce sont des maillages 3D cylindriques constitués d'une suite de maillages 2D plans coaxiaux.

2.2. MAILLAGE 2D DE REFERENCE.

Des maillages de type C sont utilisés pour discrétiser les domaines de calcul proches des profils. Ceux-ci permettent une bonne définition de la géométrie, tout particulièrement dans les zones de fortes courbures ainsi qu'une discrétisation fine de la zone entourant le bord d'attaque. Ceci, afin d'optimiser le calcul des champs d'écoulement dans cette zone à forts gradients et plus particulièrement la prise en compte des phénomènes sur l'extrados des profils (poches supersoniques). Pour générer de tels maillages, chacun des sous-domaines "support" est divisé en une suite de blocs topologiquement dépendants afin de bien prendre en compte les variations de courbure (Cf. planche 1). Ensuite, chacune des frontières de ces blocs est discrétisée à l'aide de répartitions uniformes ou en utilisant des progressions géométriques simples ou doubles. Dans la mesure du possible, la continuité des tailles de maille est assurée au passage des frontières entre blocs tout comme au passage des frontières de raccord entre zones.
Des maillages de type H à l'amont, au-dessus, voire en aval des zones des profils, permettent de discrétiser le reste du domaine de calcul, en étendant celui-ci de manière à approcher les conditions du fluide à l'infini aux frontières externes de ce domaine. La planche 2 donne une représentation d'un maillage 2D de référence.

2.3. MAILLAGE 3D.

Dans le cas de nacelles axisymétriques, le maillage 3D est obtenu par rotation du maillage 2D de référence.
Dans le cas d'une nacelle non-axisymétrique, celle-ci est découpée en une suite de profils de base, obtenus par intersection avec des plans radiaux qui s'appuient sur l'axe de la nacelle. Ensuite, un maillage 2D est généré autour de chaque profil en prenant pour support le plan radial ayant servi à sa création.
La planche 3 donne une représentation de la discrétisation angulaire du domaine de calcul. Théoriquement, cette discrétisation ne devrait pas dépasser 5° par secteur angulaire, mais une discrétisation uniforme avec des secteurs de 18° donne des résultats corrects avec un nombre de points de maillage pas trop élevé.
La planche 4 donne une représentation du maillage de la nacelle, du jet ainsi que du plan d'entrée compresseur.

3.CONFRONTATION CALCUL/EXPERIENCE.

3.1. GENERALITES.

Une confrontation calcul/expérience a été menée sur la nacelle axisymétrique du turboréacteur à hélices rapides (THR). Ce système propulsif est équipé de deux hélices transsoniques contrarotatives (Propfan). Ces hélices sont elles-mêmes entraînées par deux turbines contrarotatives lentes. Ce moteur a été déve-

loppé par les sociétés General Electric et SNECMA dans le cadre d'un projet de réduction des consommations en carburant. La nacelle entourant le générateur de gaz a fait l'objet de notre étude.
Les caractéristiques de l'écoulement établi autour de cette nacelle ont été obtenues par l'utilisation du code Sésame dans différentes conditions de vol. Afin de rendre compte de la validité du modèle numérique et d'évaluer ses limites, une confrontation calcul/expérience a été réalisée à partir des résultats d'essais obtenus sur cette nacelle au cours de la campagne de janvier 1988 dans la soufflerie S1MA de l'ONERA [5]. Cette confrontation a été effectuée pour des conditions d'écoulement variant selon le Mach amont, le débit dans l'entrée d'air et l'incidence géométrique de la nacelle.
Dans un premier temps, le comportement aérodynamique de cette nacelle soumise à une incidence de 3° sera déterminé pour un écoulement amont uniforme de Mach Mo = 0.82.
D'autre part, des résultats obtenus à incidence nulle seront présentés dans deux conditions de vol définies par les couples (Mo = 0.78 ; W2 = 47.58 kg/s) et (Mo = 0.82 ; W2 = 65.78 kg/s).

3.2. PRESENTATION DES ESSAIS.

3.2.1. GENERALITES.

La nacelle du THR a été étudiée à haute vitesse dans la soufflerie S1 de l'ONERA qui fonctionne jusqu'en subsonique élevé à une pression génératrice égale à la pression atmosphérique. Les conditions de croisière ont été simulées et le rendement de l'entrée d'air ainsi que la traînée de la nacelle ont pu être mesurés.

3.2.2. MONTAGE D'ESSAI.

Un tripode fixé à l'amont du diffuseur de la soufflerie supporte de l'aval vers l'amont :

- un obturateur à volets qui permet de régler le débit à l'intérieur de l'entrée d'air,
- un venturi de mesure du débit de 195mm de diamètre au col,
- un peigne de sondage de l'écoulement externe,
- la maquette du THR équipée d'un peigne interne de mesures stationnaires.

La mise en incidence et en dérapage de cet ensemble est réalisée par un dispositif placé dans la pointe avant du tripode.
L'écoulement interne se fait par aspiration naturelle.

3.2.3. DESCRIPTION DE LA MAQUETTE.

La maquette représente un moteur gauche et son mât support à l'arrière d'un fuselage d'avion de transport bimoteur (Cf. planche 14). La forme externe de la maquette représente la nacelle du moteur jusqu'au plan des hélices ; en aval une forme de transition permet le raccordement au diamètre externe de la virole amont des peignes externes. Le conduit interne porte les peignes de mesure des pressions d'arrêt internes et le diffuseur aval supporte un corps central.

3.2.3.1. EQUIPEMENT DE MESURE DES PRESSIONS INTERNES ET SUR LES LEVRES.

La maquette est équipée de prises de pression pariétales sur le mât et sur la nacelle. Toutes ces pressions sont mesurées par des multiplicateurs P.S.I. de + 200000 pascals (+ 30 P.S.I.) de capacité. La contrepression des capteurs est la pression de consigne d'un réservoir ajustée en fonction de la pression génératrice de la soufflerie.
Le rendement de la prise d'air est déterminé à l'aide des mesures des pressions d'arrêt dans le plan compresseur, effectuées à l'aide d'un peigne interne. Ces pressions sont également relevées sur des multiplicateurs P.S.I.

3.2.3.2. EQUIPEMENT DE MESURE DES PRESSIONS EXTERNES DANS LE SILLAGE.

La mesure des pressions statiques et d'arrêt de l'écoulement externe à l'aval de la nacelle et du mât est effectuée par un peigne tournant

3.2.4. METHODOLOGIE D'ESSAI.

Les pressions ainsi que les conditions d'essai sont mesurées à chacun des points constituant le lot d'enregistrement. Ces lots d'enregistrement sont de deux types

a) Lot de type "continu" : ensemble de points de mesure acquis lors d'une variation d'un paramètre d'essai (incidence, dérapage, débit, déplacement du peigne de sillage) à la cadence fixée par le calculateur et l'unité d'acquisition de mesures et égale à :
   - un point toutes les 4 secondes lors des mesures avec le peigne interne,
   - 4 points par seconde lors des mesures avec le peigne externe.

b) Lot de type "condition stabilisée" : ensemble de 30 points de mesure acquis à la cadence d'un point par seconde, sans variation d'autre paramètre que le temps.

3.2.5. MESURE DE LA TRAINEE.

L'application du théorème des quantités de mouvement à la maquette

du THR permet de calculer la traînée de l'ensemble nacelle + pylône en n'utilisant que les mesures de pression totale et statique du peigne externe.
Ce calcul correspond à une analyse du sillage développé par Betz. Elle est élaborée en écrivant le théorème de la dynalpie sur un tube de courant entourant la nacelle d'une section amont Ao (Mo, Po, Pio) à une section aval A" (M",Po). Le plan de mesure situé dans le sillage de la nacelle est représenté par la section A' (M', P', Pi'). La traînée totale externe de la nacelle est obtenue par l'intégration sur la section A' des valeurs caractéristiques du champ aérodynamique, soit:

$$X = \gamma P_o \int \left(M_o^2 \frac{P_i'}{P_{io}} \frac{\Sigma(M_o)}{\Sigma(M')} - M''^2 \frac{\Sigma(M'')}{\Sigma(M')} \right) dA$$

$$\text{où } \Sigma(M) = \frac{1}{M} \left(\frac{1+0.2M^2}{1.2} \right)^3$$

La méthode expérimentale consiste à réaliser une mesure de pression statique et d'arrêt de l'écoulement autour de la nacelle à l'aide du peigne rotatif. A partir de ces mesures, le champ de Mach est reconstitué dans les sections A' et A". La traînée totale est alors calculée à partir de l'expression ci-dessus. On note que l'introduction de la section théorique A' où l'écoulement a retrouvé la pression statique amont permet de ne faire aucune hypothèse quant à la position du plan de mesure A' dans le sillage.

Remarque : La nacelle étant symétrique par rapport au plan vertical, et le pylône désaxé, une intégration des mesures sur un secteur de 180° permet d'avoir la traînée nacelle seule.

3.3. DESCRIPTION DU MAILLAGE.

La nacelle étant axisymétrique, le maillage utilisé a été obtenu par rotation autour de l'axe de la nacelle, d'un maillage 2D radial de référence. Il est constitué de 21 plans radiaux équi-répartis en angle. Ce maillage est celui qui a servi d'exemple dans le chapitre sur les maillages (Cf. planches 1 à 4).
Le maillage 2D de référence comporte 2015 noeuds et le maillage 3D complet en contient 42315.
Les confrontations calcul/expérience réalisées sur les répartitions de Mach et de pression sur la nacelle ont mis en évidence l'importance du dimensionnement de la zone de maillage située au-dessus de la nacelle. Ainsi, il est nécessaire de surdimensionner cette zone, en particulier lorsque la nacelle est soumise à une incidence importante. Une série de tests nous a amenés à retenir un maillage dont la hauteur de cette zone est 15 fois supérieure à celle du maître-couple de la nacelle.
La partie du maillage qui prolonge la nacelle du bord de fuite à la frontière "aval" est cylindrique et simule le jet issu du moteur.

3.4. CONDITIONS LIMITES.

Le traitement des conditions limites est basé sur la méthode des relations de compatibilité.
Sur la nacelle et le jet, sont appliquées des conditions de glissement.
Sur la frontière "amont" subsonique, sont imposées la pression et la température d'arrêt ainsi que la direction de l'écoulement.
Sur la frontière "aval" subsonique et sur la frontière entrée compresseur, sont imposées respectivement la pression statique de l'écoulement à l'infini, et la pression statique d'entrée compresseur, cette dernière étant calculée à partir du débit voulu et répartie uniformément sur toute la surface d'entrée.

Sur la frontière externe du domaine qui symbolise l'infini, est appliquée une condition de non-réflexion. Cette condition conserve partiellement des informations issues du champ initial qui doit donc être défini avec soin et tout particulièrement sur ces frontières.
Sur les frontières internes entre les différentes zones du maillage, sont appliquées des conditions limites de raccord, fonction de la direction de l'écoulement et de sa vitesse.
Sur l'axe de la nacelle, est appliquée une moyenne prenant en compte les mailles dégénérées qui l'entourent.
La planche 5 représente l'application des conditions limites sur le plan radial 2D de référence.

3.5. INITIALISATION.

L'initialisation du calcul se fait en deux parties. Dans la partie (1) (Cf. planche 5) ou domaine d'écoulement externe, le calcul est initialisé par les caracteristiques du fluide à l'infini amont. Dans la partie (2) ou domaine d'écoulement interne, l'initialisation est effectuée à partir d'une interpolation linéaire entre les caractéristiques du fluide à l'infini amont et celles à l'entrée compresseur.

3.6. CALCUL à 3° D'INCIDENCE.

Le champ aérodynamique de la nacelle à $\alpha = 3°$ est représenté sur les planches 6, 7 et 8 (profils supérieur, inférieur et latéraux) pour un Mach amont Mo = 0.83 et un débit de 47.9kg/s à l'entrée compresseur. L'écoulement au-dessus de la nacelle est caractérisé par une importante

zone où le Mach est compris entre 0.9 et 1, et une poche supersonique de Mach inférieur à 1.1 (Cf. planche 6).
Au-dessus de la nacelle et sur les côtés, l'écoulement reste subsonique avec une zone où le Mach est compris entre 0.9 et 1 qui demeure relativement importante (Cf. planches 7 et 8).
En particulier, on constate une bonne continuité des lignes iso-Mach au passage d'une zone à l'autre.
Les résultats du calcul de Mach et de pression recoupent de façon satisfaisante les mesures, les écarts calcul/expérience pour les profils inférieur et latéraux restant inférieurs à 3% (Cf. planches 9 et 10). En revanche, sur le profil supérieur, l'écart calcul/expérience atteint 5% dans la zone de Mach supersonique (Cf. planche 11). En effet, le calcul a tendance à sous-estimer l'étendue de cette zone sur le profil.
Par contre, sur la lèvre interne du profil et quel que soit le plan considéré, la confrontation calcul/expérience sur les répartitions de Mach et de pression demeure satisfaisante avec des écarts de l'ordre du pour cent.
D'une manière générale, la variation de pression d'arrêt sur le profil est inférieure à 1%, traduisant une bonne représentation numérique des phénomènes aérodynamiques.

3.7. CALCUL à INCIDENCE NULLE.

Les résultats obtenus sur la nacelle du THR à incidence nulle et pour les deux cas de vol étudiés (Mo = 0.78 ; W2 = 47.5 kg/s et Mo = 0.8 ; W2 = 65.78 kg/s), indiquent une bonne corrélation calcul/expérience (Cf. planches 12 et 13).
Les écarts calcul/expérience sont de l'ordre du pour cent sauf dans une zone située entre 5 et 10% de la corde du profil à partir du bord d'attaque, où les résultats du calcul sont légèrement supérieurs aux mesures (Cf. planche 13).

3.8. CALCUL DE LA TRAINEE.

La traînée externe de la nacelle est déterminée à partir d'un calcul de couche limite. Un premier calcul, basé sur la même technique d'analyse de sillage de la nacelle que celle utilisée au cours des essais, permet d'obtenir le cx de forme à partir des résultats du code Euler SESAME. Ce code basé sur l'hypothèse d'un fluide parfait, permet d'obtenir les efforts de traînée dus aux variations de pression, en particulier dans des régions d'écoulement affectées par des chocs.
Toutefois, afin de s'affranchir des pertes de pression totale engendrées par le code numérique, on suppose l'écoulement isentropique dans les régions non affectées par des chocs, les pertes de pression engendrées par les chocs étant déterminées à l'aide des relations de RANKINE-HUGONIOT. Ensuite, au Cx de forme obtenu, un Cx de frottement est ajouté,
provenant d'un calcul de couche limite 2D développé sur chaque section du profil. Ce calcul de la traînée de frottement est basé sur la détermination de l'épaisseur de quantité de mouvement à partir des distributions de Mach obtenues avec le code SESAME. Le Cx de frottement est ensuite calculé avec la formule :

$$C_x = \frac{2}{S_{ref}} \int_0^{\pi} ((R+\delta_2)^2 - R^2)\, d\theta$$

Cette méthode donne de bons résultats dans des cas où les chocs et les décollements ne sont pas trop importants. Dans le cas de la nacelle du THR où il n'y a pas de choc, l'écart avec les résultats d'essais est de l'ordre de 5%. (Cf. planche 15). Dans la gamme de nombre de Mach auquel a été essayée la nacelle du THR, aucune divergence de traînée n'apparaît du fait de l'absence de choc sur la nacelle.
Afin de montrer la capacité de la méthode à prédire un nombre de Mach de divergence, la même technique a été appliquée à un profil de nacelle de turboréacteur conventionnel. Au-delà de Mach 0.82 la courbe de traînée tend à diverger du fait de l'apparition de chocs sur la nacelle (Cf. planche 16).

4. APPLICATION A UNE NACELLE AVEC CORPS CENTRAL.

4.1. GENERALITES.

SESAME a été appliqué à une nacelle non axisymétrique avec un corps central axisymétrique dans le cadre d'une étude purement aérodynamique (l'écoulement traverse librement la nacelle et est perturbé uniquement par la géométrie des enveloppes).
Un calcul sera présenté pour un écoulement à l'infini amont de Mach Mo = 0.89 et une incidence de 3°.

4.2. MAILLAGE

Le maillage utilisé est constitué de 21 maillages 2D radiaux équi-répartis en angle. La planche 17 qui montre le maillage de la géométrie, donne une représentation de cette discrétisation en angle.
Chacun des maillages 2D radiaux est constitué de 4 zones (Cf. planche 18). Deux maillages de type C enveloppent chacun des profils (Cf. planche 18 bis) et deux maillages en H étendent le domaine de calcul en amont et en hauteur. Chaque

maillage 2D radial comporte 5976 noeuds et le maillage 3D complet, 125496 noeuds.

4.3. CONDITIONS LIMITES.

Les conditions limites appliquées sont les mêmes que pour la nacelle précédente mis à part le fait que l'écoulement étant libre de traverser la nacelle, on n'applique plus de condition de pression à l'entrée compresseur, mais seulement une condition de pression sur la frontière infinie "aval".

Remarque : on initialise le calcul sur tout le domaine par les caractéristiques du fluide à l'infini amont.

4.4. RESULTATS DE CALCUL.

Le calcul effectué avec un Mach amont Mo = 0.82 et α = 3° demande 6000 itérations pour converger de manière satisfaisante.
Les planches 19 à 21 montrent les champs de Mach obtenus autour des profils supérieur, inférieur et latéraux, et notamment les poches supersoniques qui se développent sur la partie externe de la nacelle.
Les planches 22 à 24 donnent les répartitions de Mach isentropique sur les profils supérieur, inférieur et latéraux de la nacelle.

CONCLUSION

Aujourd'hui, grâce au code SESAME, la SNECMA est capable de critiquer l'aérodynamique des nacelles et s'appuie sur celui-ci comme outil de conception.

Elle utilise un code Euler 3D pour calculer l'écoulement de fluide parfait et un code de couche limite 2D pour estimer la traînée et le Mach de divergence.
Ces codes ont été validés sur la nacelle du projet de turboréacteur à hélices rapides, pour laquelle la SNECMA dispose de nombreux résultats d'essai, et appliqués à d'autres cas d'étude.
A l'avenir, elle compte étendre ses moyens de calcul pour critiquer des installations motrices complètes (fuselage, voilure, mât et nacelle) et s'en servira comme aide à l'installation dans une optique de réduction des coûts d'essais.

REMERCIEMENTS

Cet article et les études présentées ont pu être réalisés grâce au programme SESAME développé par l'ONERA. Le service intégration aérodynamique de la SNECMA tient à remercier toute l'équipe de M. VEUILLOT pour ce code et pour leur assistance dans l'utilisation de ce code.
Les auteurs remercient la direction technique de la SNECMA qui leur a donné les moyens de réaliser ces études et a permis leur diffusion.

REFERENCES

[1] V. COUAILLIER
Application du code SESAME aux calculs d'écoulements tridimensionnels de fluide parfait.
Discussion technique du 26 Juin 1990, ONERA

[2] J.P. VEUILLOT, G. MEAUZE
A 3D Euler Method for Internal Transonic Flows computation with Multi-Domain Approach in AGARD - LS - 140.

[3] L. CAMBIER, F.DUSSON et J.P. VEUILLOT
Méthode multi-domaines pour les équations d'Euler.
Appplications pour des sous-domaines avec recouvrement.
La Recherche Aérospatiale, Année 1985, n°3 (Mai-Juin) p. 181 à 188.

[4] R. PEYRET
Résolution numérique des systèmes hypersoniques. Application à la dynamique des gaz.
Publication ONERA 1977-5

[5] Essais de l'entrée d'air GE36 à l'échelle 0.29480 dans la soufflerie S1MA.
Déc. 1987 - jan. 1988, ONERA

[6] H. JOUBERT et P. FESSOU, J.C. RAYNAL et F. GARCON
Essai en soufflerie de l'entrée d'air d'un turboréacteur à hélices rapides.
AAAF - 25ème colloque d'aérodynamique appliquée
Talence 12-13-14 Octobre 1988

ETUDE THR
DECOUPAGE EN BLOCS ET
MAILLAGE DE LA ZONE PROFIL

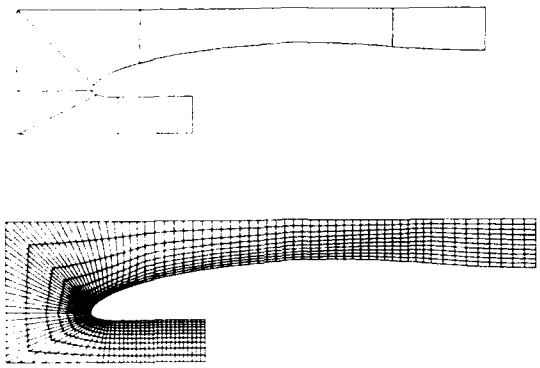

PLANCHE 1

ETUDE THR

MAILLAGE RADIAL 2D DE REFERENCE

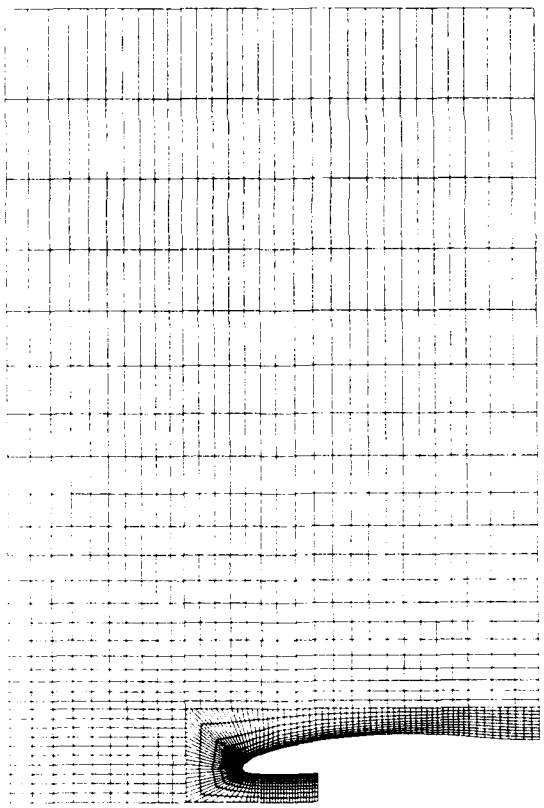

PLANCHE 2

ETUDE THR

MAILLAGE PLAN D'ENTREE COMPRESSEUR

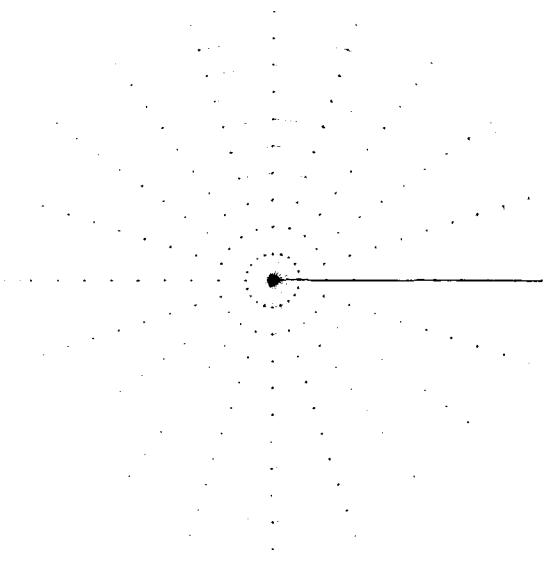

PLANCHE 3

ETUDE THR

ENVELOPPE DISCRETISEE DE LA NACELLE

ET SIMULATION DU JET

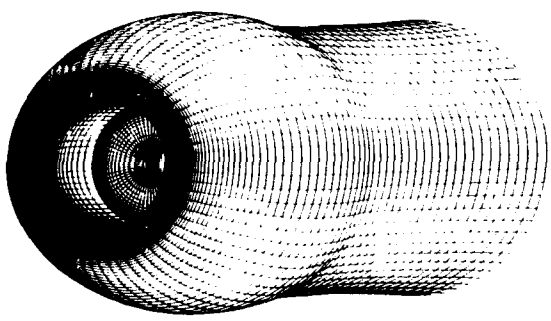

PLANCHE 4

ETUDE THR

CONDITIONS LIMITES ET INITIALISATION

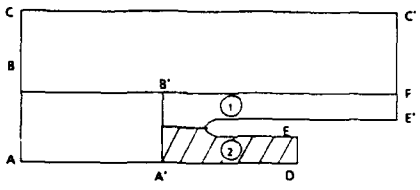

CONDITIONS LIMITES :

AC : condition d'injection
BF-A'B' : condition de coupure
CC' : condition de non-réflexion
DE-EC' : condition de pression statique
EE' : condition de glissement
AA'-A'D : condition d'axe

INITIALISATION :

PARTIE BLANCHE (1)

Ecoulement externe initialisé par les caractéristiques du fluide à l'infini amont

PARTIE HACHUREE (2) :

Ecoulement interne initialisé par une interpolation linéaire entre les conditions amont et celles à l'entrée compresseur

PLANCHE 5

ETUDE THR

PROFIL SUPERIEUR

CHAMP DE MACH

M0 = 0.83
ALPHA = 3
DM = 0.04

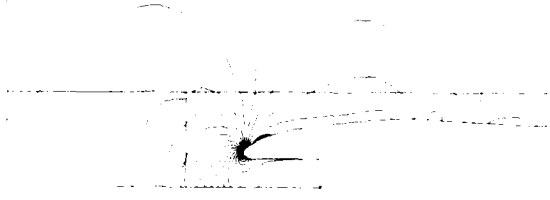

PLANCHE 6

ETUDE THR

PROFIL INFERIEUR

CHAMP DE MACH

M0 = 0.83
ALPHA = 3
DM = 0.04

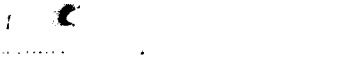

PLANCHE 7

ETUDE THR

PROFIL LATERAL

CHAMP DE MACH

M0 = 0.83
ALPHA = 3
DM = 0.04

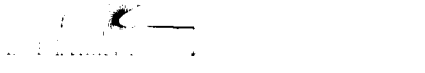

PLANCHE 8

ETUDE THR
EVOLUTION DU MACH ISENTROPIQUE
SUR LE PROFIL INFERIEUR
COMPARAISON AVEC L'EXPERIENCE

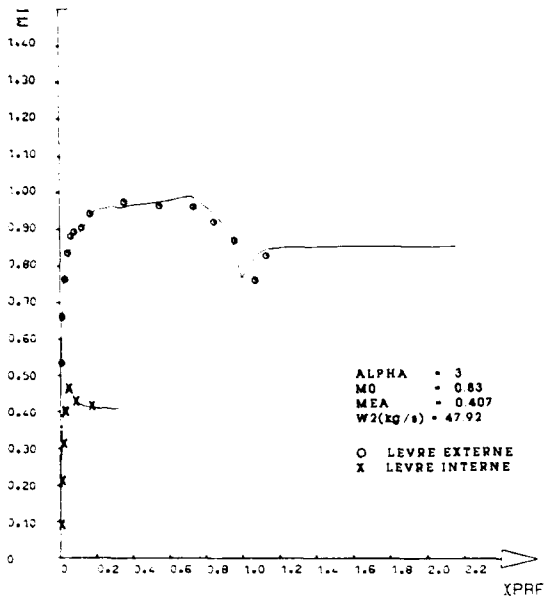

PLANCHE 9

ETUDE THR
EVOLUTION DU MACH ISENTROPIQUE
SUR LE PROFIL LATERAL
COMPARAISON AVEC L'EXPERIENCE

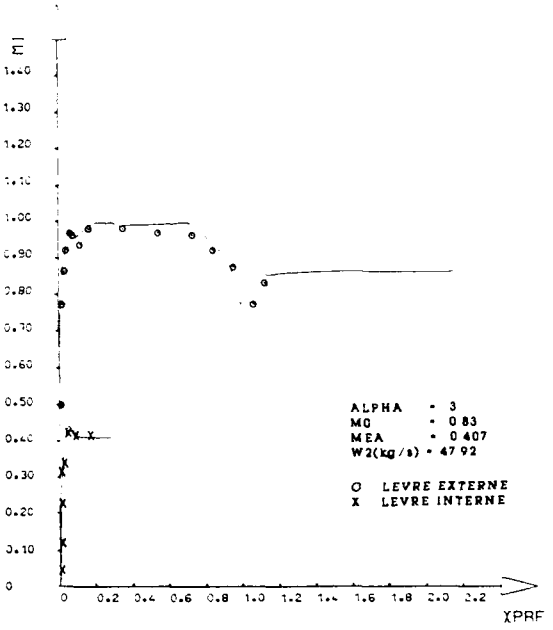

PLANCHE 10

ETUDE THR
EVOLUTION DU MACH ISENTROPIQUE
SUR LE PROFIL SUPERIEUR
COMPARAISON AVEC L'EXPERIENCE

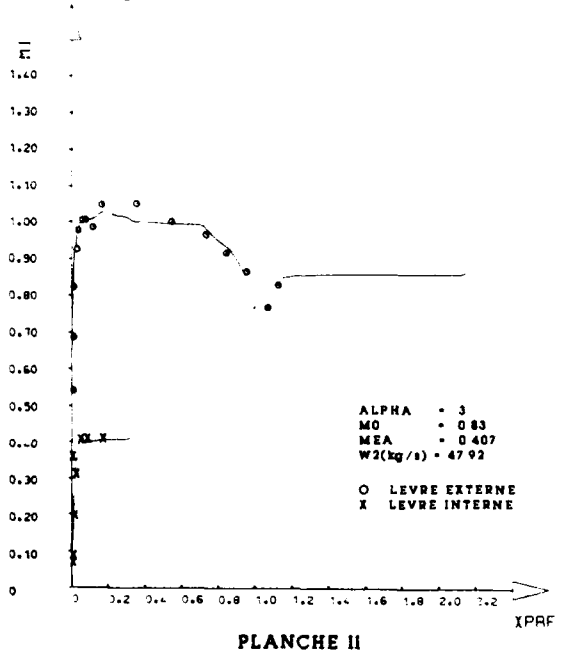

PLANCHE 11

ETUDE THR
EVOLUTION DU MACH ISENTROPIQUE
SUR LE PROFIL SUPERIEUR
COMPARAISON AVEC L'EXPERIENCE

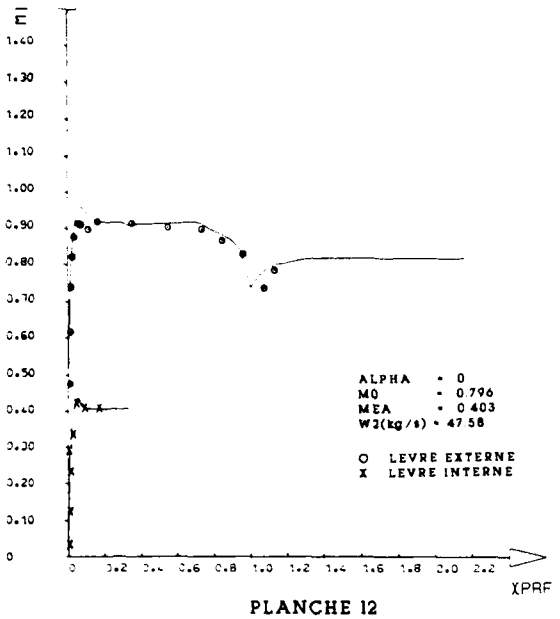

PLANCHE 12

ETUDE THR
EVOLUTION DU MACH ISENTROPIQUE
SUR LE PROFIL SUPERIEUR
COMPARAISON AVEC L'EXPERIENCE

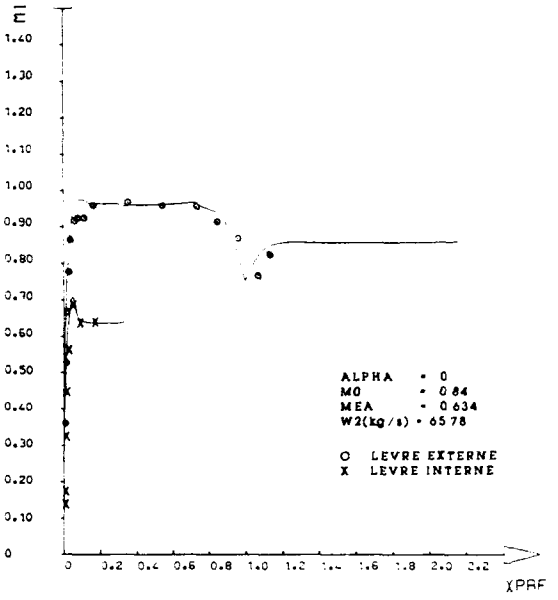

PLANCHE 13

ETUDE THR
ESSAIS HAUTE VITESSE
MODANE S1 (1987)

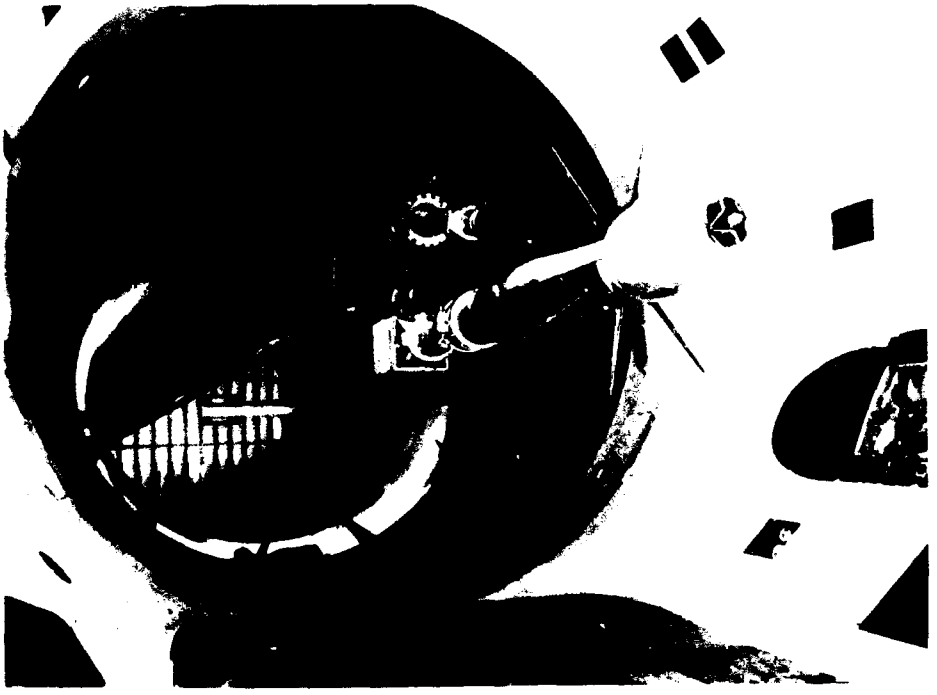

PLANCHE 14

TRAINEE DE LA NACELLE DU THR
comparaison calcul/experience

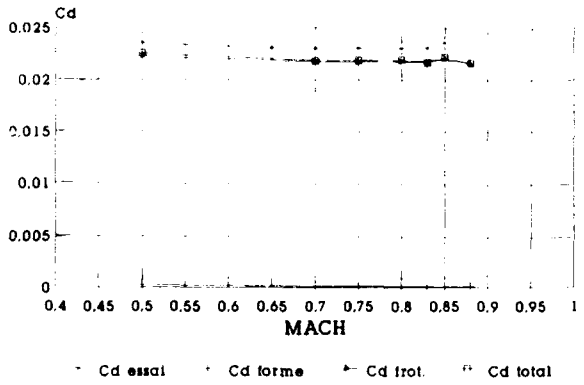

PLANCHE 15

TRAINEE D'UNE NACELLE CONVENTIONNELLE

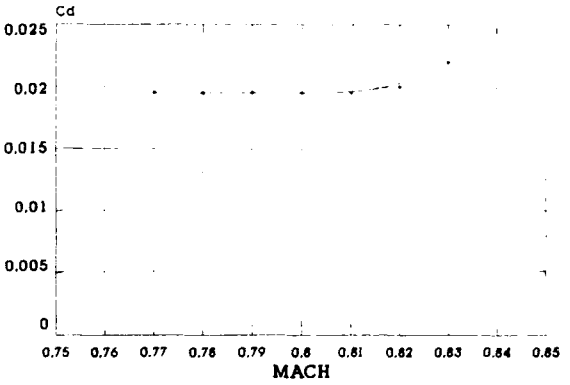

PLANCHE 16

NACELLE AVEC CORPS CENTRAL
MAILLAGE DE LA GEOMETRIE

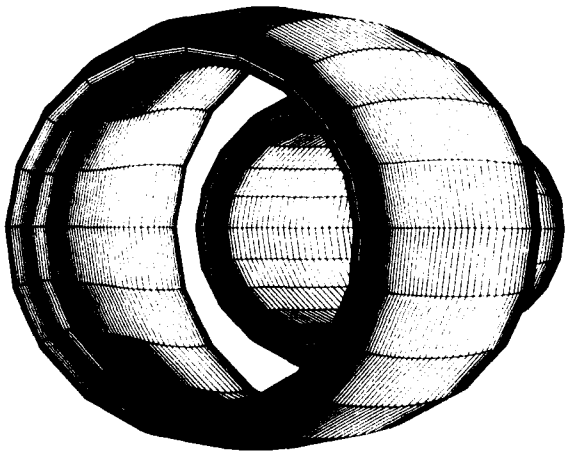

PLANCHE 17

ETUDE NACELLE AVEC CORPS CENTRAL
MAILLAGE 2D RADIAL
PROFIL SUPERIEUR

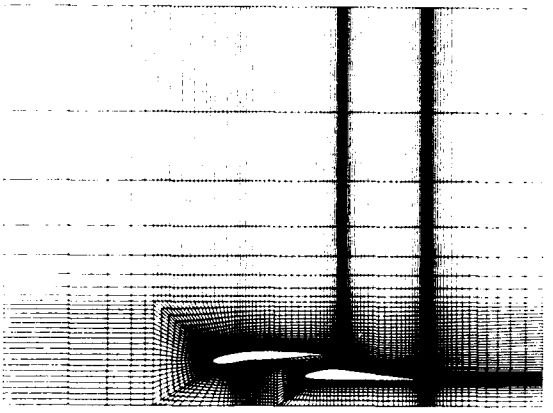

PLANCHE 18

ETUDE NACELLE AVEC CORPS CENTRAL
DETAIL MAILLAGE 2D RADIAL
PROFIL SUPERIEUR

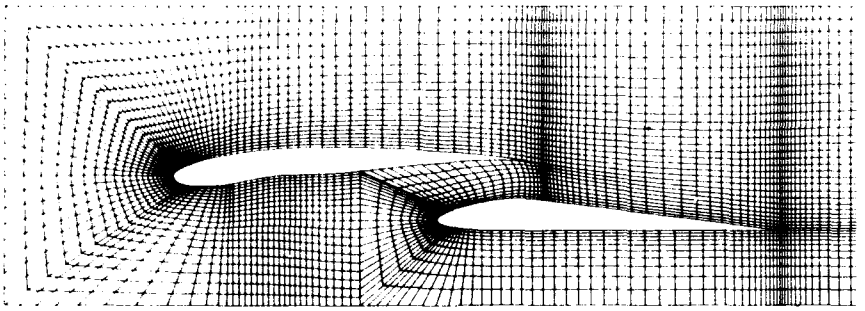

PLANCHE 18 bis

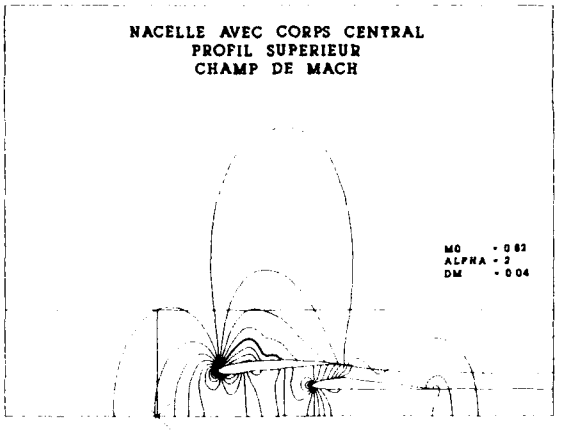

PLANCHE 19

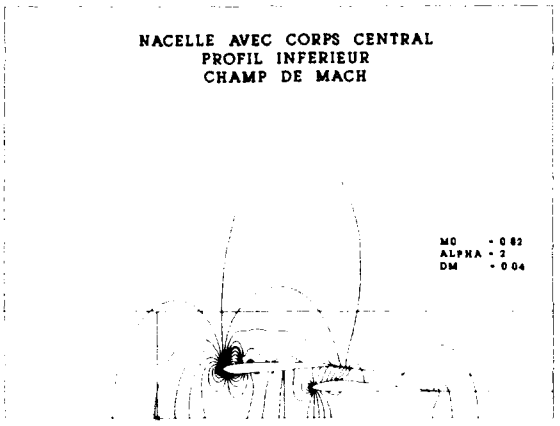

PLANCHE 20

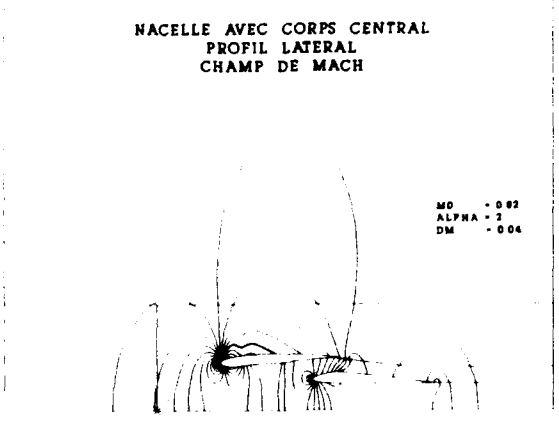

PLANCHE 21

NACELLE AVEC CORPS CENTRAL
EVOLUTION DU MACH ISENTROPIQUE
SUR LE PROFIL SUPERIEUR

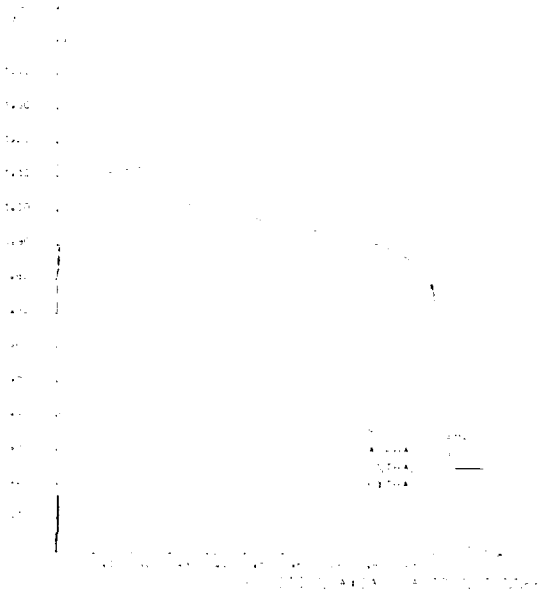

PLANCHE 22

NACELLE AVEC CORPS CENTRAL
EVOLUTION DU MACH ISENTROPIQUE
SUR LE PROFIL INFERIEUR

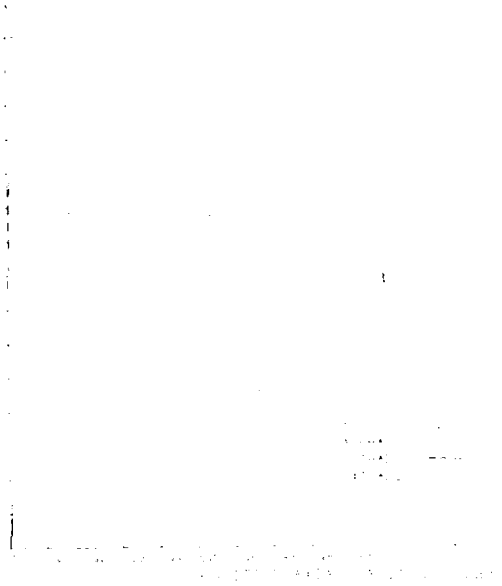

PLANCHE 23

NACELLE AVEC CORPS CENTRAL
EVOLUTION DU MACH ISENTROPIQUE
SUR LE PROFIL LATERAL

PLANCHE 24

ANALYSE DETAILLEE DE L'INTERACTION VOILURE-NACELLE D'UN AVION DE TRANSPORT CIVIL

J L. GODARD
O. P. JACQUOTTE
Office National d'Etudes et de Recherches Aerospatiales (ONERA)
92322 Chatillon Cedex - FRANCE
D. GISQUET
AEROSPATIALE Toulouse
31060 Toulouse Cedex 03 - FRANCE

Résumé :

Un montage expérimental a été développé à l'ONERA pour l'étude détaillée de l'interaction nacelle-voilure d'avions de transport civils en transsonique. La maquette est un tronçon d'aile fortement instrumenté en prises de pression, défini et fabriqué par l'AEROSPATIALE. Ce montage permet la mesure des efforts globaux, des répartitions de pression sur la maquette, et des vitesses dans le champ par vélocimétrie laser. La complémentarité de ces différents types de mesure assure une description complète et détaillée des phénomènes aérodynamiques qui sont analysés dans le papier. Cette analyse permet une meilleure compréhension de l'interaction nacelle-voilure et fournit les meilleurs éléments de comparaison pour une modélisation par le calcul.

1 INTRODUCTION

L'implantation des réacteurs sur une voilure d'avion de transport civil transsonique pose des problèmes difficiles du fait de la complexité des formes et des écoulements à traiter, et du fait des délais souvent limités pour résoudre les problèmes rencontrés [1] [2].

En effet, l'optimisation de cette installation des nacelles doit, pour être pleinement réussie, pouvoir agir à la fois sur la conception des formes de la voilure, de la nacelle et du mât support lui-même. En pratique, les composants précédents intègrent des pièces à long cycle de fabrication et les définitions nécessaires doivent être disponibles très rapidement après le lancement du programme.

L'aérodynamicien utilise pour ces définitions des codes de calcul plus ou moins sophistiqués. Ces codes doivent être performants et fiables afin de sélectionner dans les meilleurs délais un nombre restreint de géométries qui seront ensuite évaluées en soufflerie industrielle pour un choix final des formes retenues. Ces essais ont généralement pour but l'évaluation des performances, en particulier la traînée, et ne permettent pas une analyse fine des phénomènes locaux. Dans ce contexte, il a semblé utile de développer un moyen d'essais de recherche, complémentaire des essais de type industriel, permettant une analyse détaillée de l'écoulement dans les zones où se manifestent essentiellement les interactions installation motrice/voilure, dans le but de mieux comprendre les phénomènes et de développer et valider les codes de calcul appropriés pour les représenter au mieux.

C'est avec cet objectif que l'ONERA a mis en oeuvre un nouveau montage expérimental permettant d'effectuer ce type d'essais. Une bonne compréhension des phénomènes nécessite des informations en grand nombre et diverses: ce montage permet de mesurer les efforts globaux s'exerçant sur la maquette ; un équipement important en prises de pression permet une analyse locale et détaillée de l'écoulement; enfin le champ de vitesses dans l'espace est mesuré par vélocimétrie laser et constitue une information précieuse pour compléter cette analyse.

Ce papier décrira d'abord le montage expérimental, puis dans les conditions de croisière on présentera à titre d'exemple l'ensemble des informations recueillies sur une maquette définie et fabriquée par l'AEROSPATIALE. Ces données seront commentées et le phénomène d'interaction sera analysé en détail. La dernière partie du papier présentera quelques calculs effectués avec une méthode potentielle multidomaine et qui permettent de compléter l'analyse des résultats expérimentaux.

2 MONTAGE EXPERIMENTAL

2.1 Géométrie et équipement de la maquette

Pour cette étude de détail une maquette de grande échelle a été réalisée, qui est représentative de l'installation motrice externe d'un quadriréacteur long-courrier. Cette maquette est une portion d'aile qui traverse la veine d'essais dans toute sa largeur (Fig.1). Les extrémités ont été adaptées, compte tenu de la présence des parois latérales, pour assurer dans la zone centrale un écoulement semblable à celui de la partie externe de l'aile complète du quadriréacteur. Les principales caractéristiques géométriques de cette maquette sont:

Corde de référence Cr=0,4407 m

Envergure Br=0,800 m

Surface conventionnelle Sr=0,22138 m^2

La nacelle est une nacelle longue de grande échelle et de géométrie proche de celles de nacelles existantes (Fig.1). Cette nacelle est perméable, sa partie interne a été dessinée pour avoir un débit représentatif de celui d'un réacteur au point de croisière.

Le pylône a un volume classique vis à vis des contraintes d'avionabilité mais n'est pas adapté aérodynamiquement (squelette plan, Fig.1).

Le tronçon d'aile est équipé de 220 prises de pression fournissant une description assez détaillée du champ de pression pariétal (Fig.2). La position des prises a été adaptée à l'analyse du phénomène d'interaction nacelle-voilure, c'est à dire offrant un plus grand nombre de prises à l'intrados qu'à l'extrados, et un nombre plus important du côté interne de l'axe nacelle. Des prises de pression sont aussi implantées sur le pylône (10 prises) et sur la nacelle (21 prises), en majorité du côté interne de l'installation (Fig.3).

2.2 Montage en veine

Les essais ont lieu dans la soufflerie à circuit fermé S3Ch de l'ONERA-Chalais. Cette soufflerie transsonique permet une variation du nombre de Mach de 0,3 à 1,2 . La veine d'essais est de taille moyenne, de section 0,8x0,8 m. Elle fonctionne à pression atmosphérique ce qui impose le nombre de Reynolds par mètre pour un nombre de Mach donné.

Le montage retenu est très particulier et caractérisé par les points suivants (Fig.4):

- Le tronçon d'aile traverse la veine d'essais dans toute sa largeur.
- La nacelle est généralement fixée sous l'aile par un pylône, mais pendant les sondages par vélocimétrie laser en l'absence de pylône elle est soutenue par un dard aval.
- La balance mesurant les efforts globaux s'exerçant sur la maquette est constituée de deux éléments séparés. Ils sont placés sur chaque paroi latérale de la veine, sont liés à la structure de la soufflerie, et soutiennent le tronçon à chaque extrémité. Chaque demi-balance comporte 3 dynamomètres et

l'ensemble permet la mesure des 6 composantes de forces et moments globaux.

- Un système d'étanchéité constitué de chicanes est implanté sur les parois latérales à la traversée du tronçon d'aile. Il permet la mesure des efforts en évitant tout contact entre la maquette et les parois, tout en empêchant un écoulement entre la veine d'essais et le caisson de la soufflerie.

- Compte tenu de l'occupation de la maquette dans la veine, des formes de parois haute et basse ont été définies de façon théorique pour minimiser l'influence de ces parois au point de croisière (Fig.5). Ces parois s'appuient sur des lignes de courant calculées et ont des formes très tridimensionnelles. Pendant l'essai quelques répartitions de pression sont mesurées sur celles-ci afin de déterminer les corrections résiduelles s'appliquant aux efforts globaux.

- Pour les sondages par vélocimétrie laser, des hublots de dimensions 0,75x0,25 m sont implantés sur chaque paroi latérale de la veine d'essais.

Des sondages d'écoulement par vélocimétrie laser sont effectués dans la région comprise entre le tronçon d'aile et la nacelle où l'interaction est la plus forte, et en l'absence de pylône (Fig.6). Cette absence permet une mesure laser par diffusion avant qui simplifie le montage et assure une bonne qualité de la mesure. Le banc émetteur et le banc récepteur sont donc situés de part et d'autre de la veine d'essais. On détermine les 3 composantes de la vitesse à l'aide de 3 faisceaux laser de différentes couleurs et fréquences émis en direction du point de mesure, le banc récepteur supportant 3 cellules orientées vers ce même point. Les angles minima nécessaires entre les faisceaux émetteurs pour avoir une bonne qualité de mesure et la taille des hublots limitent la région pouvant être sondée et qui est représentée sur la Figure 6.

3 ETUDE EXPERIMENTALE DE L'INTERACTION NACELLE-VOILURE

3.1 Conditions d'essais

Ce papier se limite à une étude de l'interaction nacelle-voilure au point de croisière de l'aile dans les conditions:

Mach=0,82 et Incidence=1,60°

La soufflerie fonctionnant à pression atmosphérique, le nombre de Reynolds formé avec la corde de référence est de 5,2 millions.

Les efforts globaux et les répartitions de pression seront analysés pour les 3 configurations: tronçon d'aile isolé, tronçon d'aile et nacelle, puis tronçon d'aile et pylône et nacelle.

Les sondages d'écoulement par vélocimétrie laser concernent uniquement le tronçon d'aile et la nacelle en l'absence de pylône. Ils fournissent en chaque point de sondage les 3 composantes de la vitesse locale. Ces points de sondage se situent dans 7 plans verticaux symétriques par rapport à l'axe nacelle, et principalement dans la région comprise entre le tronçon d'aile et la nacelle (Fig.7). Les positions de ces plans et des points ont été adaptées au phénomène à étudier, et environ 1200 points ont été sondés.

3.2 Analyse des efforts globaux et repartitions de pression

Les efforts globaux pesés par la balance pour les différentes configurations sont:

	Tronçon d'aile	*Tronçon + nacelle*	*Tronçon + pylône + nacelle*
CZ	0,544	0,514	0,476
DCZ	0	0,030	0,068
CX 10^4	159		196
DCX 10^4	0		+ 37

La présence de la nacelle modifie le champ de pression sur le tronçon de voilure, entraînant une perte de portance de 5,5%. En présence du pylône et de la nacelle, cette perte atteint 12,5%, l'effet du mât est donc à cet égard supérieur à celui de la nacelle. Cette analyse sous-entend que seul le tronçon d'aile participe à la portance.

La traînée de la seconde configuration n'est pas présentée car seule l'aile est pesée. La géométrie complète voit le CX augmenter de 23%, pour une incidence identique et non à portance donnée. Il est habituel de décomposer cet écart en différents termes:

DCX= CX nacelle isolée + CX pylône + CX interaction

Les traînées de la nacelle et du mât ont été évaluées par calcul (CX de frottement) et par étalonnage (CX interne nacelle). Le CX d'interaction est alors de 12 10^{-4}, ce qui représente environ la moitié de la traînée propre du pylône et de la nacelle et 7,5% de celle du tronçon de voilure isolé. Ce terme est encore plus important si l'on se place à iso-portance.

Les portances locales sur le tronçon de voilure sont évaluées à partir des répartitions de pression mesurées (Fig.8). La nacelle seule provoque une perte de CZ local variant peu suivant l'envergure, un peu plus élevée du côté interne, l'écart maximal se situant à 40% de l'envergure du tronçon d'aile. En présence du pylône et de la nacelle, les écarts s'accroissent considérablement. Le pylône introduit une dissymétrie, l'effet étant plus marqué du côté interne. Les écarts par rapport au tronçon d'aile isolé évoluent aussi davantage en fonction de l'envergure, diminuant vers les extrémités à partir d'un maximum situé au droit du pylône.

Les répartitions de pression donnent des indications locales sur l'interaction. Les phénomènes observés sont les suivants:

- Influence de la nacelle seule (Fig.9,10):

  A l'intrados du tronçon d'aile, on note une accélération importante, maximale dans le canal entre aile et la nacelle (Fig.9). Cette zone accélérée se termine à une abscisse x qui évolue peu suivant l'envergure et semble liée à la position du bord de fuite de la nacelle (Fig.10). Du fait de la flèche du tronçon, cet effet concerne une portion importante des profils du côté interne de l'aile et semble s'étendre jusqu'à l'emplanture de la maquette. Cette zone se rétrécit lorsque l'on se déplace vers l'extrémité et ne concerne plus que le bord d'attaque dans les sections externes, au delà de 60% de l'envergure de la maquette. Au voisinage du bord de fuite de la nacelle, l'écoulement sur l'aile est légèrement ralenti dans une zone symétrique par rapport à l'axe nacelle, son extension en envergure est de l'ordre de grandeur du diamètre de la nacelle (Fig.10).

  A l'extrados du tronçon, les survitesses de bord d'attaque sont plus faibles au droit de la nacelle et du côté externe, du fait du déplacement de la ligne de partage à l'intrados (Fig.9). Ce ralentissement affecte une partie du plateau supersonique jusqu'à 25% de la corde et entraîne une avancée de l'onde de choc d'environ 3% de corde sur toute l'envergure de la maquette, suivie par une légère accélération liée à ce déplacement.

  On notera que la perte de portance locale par rapport au tronçon de voilure seul évolue peu en envergure mais est due à des phénomènes locaux très différents selon la section considérée.

- Influence de la nacelle et du pylône; rôle du pylône (Fig.9,11,12):

  Les effets relevés sur la configuration précédente sont accentués par la présence du pylône.

  A l'intrados du côté interne, on retrouve l'accélération provoquée par la nacelle. Près du pylône, celui-ci provoque une survitesse très brutale près du bord d'attaque, l'écoulement devient supersonique et une onde de choc apparaît (Fig.9). Cet effet est toutefois beaucoup moins étendu en envergure que l'effet de la nacelle (Fig.12 et 10). Du côté externe intrados, une légère accélération est présente dans la zone centrale (Fig.12): le pylône introduit une dissymétrie marquée entre les régions interne et externe de la maquette, et ce phénomène se retrouve sur les répartitions de pression du pylône. Toujours à l'intrados de l'aile en dehors de la région centrale, l'écoulement est accéléré par le pylône, cet effet est de faible intensité mais étendu en envergure (Fig.9). Ceci conduit, entre autres, à une quasi disparition de la zone ralentie en aval de la nacelle, observée pour la géométrie précédente. De plus, dans la région externe, il subsiste un écart entre tronçon+pylône+nacelle et le tronçon de voilure seul.

  A l'extrados, les survitesses de bord d'attaque du côté externe de l'axe nacelle décroissent encore en présence du pylône et entraînent une baisse du niveau du plateau supersonique (Fig.9). L'onde de choc avance de 1% de la corde et ce déplacement se répercute sur toute l'envergure.

  Les écarts entre les configurations 'tronçon+pylône+nacelle' et 'tronçon+nacelle' donnent une idée de l'influence du pylône s'il pouvait être isolé (Fig.12). L'accélération intrados est brutale du côté interne du mât et s'étend sur 20% d'envergure. Du côté externe elle est plus faible, plus reculée, et s'étend sur 15% d'envergure. Une accélération très faible semble s'étendre sur toute l'envergure du tronçon dans la région centrale de la voilure (Fig.9).

3.3 Exploitation des mesures de vitesse dans l'espace

L'intérêt des sondages par vélocimétrie laser est de fournir des informations détaillées dans le champ, notamment le module et la direction de la vitesse, grandeurs qui sont généralement inaccessibles lors d'essais dans des souffleries industrielles.

Le tracé des vecteurs vitesse visualise les déflections de l'écoulement dans la région comprise entre aile et nacelle (Fig.13). Dans les plans verticaux y=cte, le fluide s'oriente suivant la forme des profils: en amont du tronçon d'aile il n'est quasiment pas dévié, puis s'incline fortement dans le canal entre aile et nacelle, et en aval de la nacelle les déviations sont surtout liées à la cambrure arrière du profil supercritique de l'aile.

Les lignes iso-Mach dans ces mêmes plans mettent en évidence les gradients longitudinaux au droit de la nacelle, qui s'atténuent à mesure que l'on se déplace vers les sections les plus externes (Fig.14); dans la dernière section y/b=0.56, on ne voit plus de gradient suivant x sous l'aile. Ceci est en accord avec les répartitions de pression sur la surface du tronçon d'aile (Fig.9): la nacelle provoque à l'intrados du tronçon une accélération puis une décélération, cet effet contribue à augmenter les gradients de pression dans la région centrale des profils pour les sections du côté interne de la nacelle et à les diminuer dans les sections du côté externe. Les courbes iso-Mach portent aussi l'empreinte de la ligne de partage au bord d'attaque du tronçon et de la charge arrière.

Les tracés dans les plans horizontaux z=cte, compris entre le tronçon et la nacelle, donnent des indications sur les effets transversaux qui sont très marqués pour ce type de géométrie, et qui peuvent intervenir de façon déterminante dans le dessin du pylône (Fig.15,16). Aux orientations habituellement rencontrées au voisinage d'une aile supercritique en flèche isolée, se superposent des déviations dues à la nacelle qui par sa présence modifie le champ de pressions dans l'espace, et du fait du rétreint provoque des déviations de l'écoulement vers l'extérieur du tronçon dans la région du côté interne et des déviations vers l'intérieur du côté externe de la nacelle.

Compte tenu de ces remarques, les phénomènes observés sont les suivants:

-En amont du tronçon de voilure, la flèche induit une déviation transversale vers l'extrémité de la maquette,d'autant plus marquée que l'on s'approche de l'aile (Fig.15); ceci est lié au ralentissement de l'écoulement qu'illustrent les lignes iso-Mach (Fig.16). La composante latérale de la vitesse est accentuée du côté interne car l'obstruction de la nacelle croît à mesure que le fluide se déplace latéralement jusqu'à l'axe nacelle. Du côté externe, la forme de la nacelle et son obstruction qui décroît latéralement induisent un ralentissement de l'écoulement, s'opposant ainsi à l'effet de flèche du tronçon: la déviation transversale globale devient quasiment nulle pour les sections les plus externes, et ceci correspond à des lignes iso-Mach perpendiculaires à l'écoulement infini amont.

- Du bord d'attaque du tronçon de voilure au bord de fuite de la nacelle se trouve la région où l'interaction est la plus forte car un canal est crée entre le tronçon et la nacelle dans lequel l'écoulement est très évolutif. La vue de dessus de la géométrie montre que le recouvrement entre la nacelle et le tronçon de voilure est beaucoup plus important du côté interne de l'axe nacelle que du côté externe, du fait de la flèche. Aussi il n'est pas étonnant de constater une zone accélérée, donc à faible pression, décalée vers l'emplanture de la maquette (Fig.16). En outre, compte tenu du rétreint de la nacelle et de la position du bord d'attaque du tronçon, l'écoulement est fortement accéléré au voisinage du bord d'attaque puis il est ralenti.

En ce qui concerne les vecteurs vitesse dans la section au droit de l'axe nacelle, les composantes transversales sont importantes et orientées vers l'extrémité de la maquette au voisinage du bord d'attaque de celle-ci (Fig.15); puis ces composantes décroissent car l'écoulement est accéléré et le fluide se dirige vers l'emplanture c'est à dire vers les zones de basse pression; dans la zone ralentie qui suit la tendance s'inverse.

Dans les sections de part et d'autre de l'axe nacelle aux orientations précédentes s'ajoutent les déviations supplémentaires, évoquées au début de cette analyse, causées par la forme de la nacelle. Finalement dans les sections les plus internes l'écoulement est toujours dévié vers l'extrémité de la maquette mais la déviation importante au droit du bord d'attaque de l'aile décroit compte tenu de l'accérération qui suit (Fig.15). Dans les sections externes la déviation transversale est faible au droit du bord d'attaque et augmente en direction de l'emplanture jusqu'au bord de fuite de la nacelle.

- En aval du bord de fuite de la nacelle, les lignes iso-Mach sont quasiment parallèles à la flèche du tronçon et on ne note presque plus d'effet tridimensionnel provoqué par la nacelle (Fig.16). Le fluide prend alors des orientations semblables à celles observées dans le cas d'une aile isolée. L'écoulement étant ralenti et le tronçon ayant de la flèche le fluide dévie de plus en plus vers l'extrémité de la maquette, à partir de son orientation au droit du bord de fuite nacelle (Fig.15). Près du bord de fuite de l'aile une légère accélération, liée à la charge arrière, réduit ces déviations transversales.

Les remarques concernant l'écoulement dans les plans horizontaux entre aile et nacelle s'appliquent à tous ces plans, les phénomènes évoluant peu, qualitativement, suivant z. En particulier, les lignes iso-Mach issues des sondages par vélocimétrie laser ont des allures proches de celles obtenues à l'intrados du tronçon de voilure à partir des mesures de pression (Fig.16).

La connaissance du champ de vitesses locales permet le calcul des lignes de courant dans la région comprise entre le tronçon d'aile et la nacelle. Ces lignes ont des formes très tridimensionnelles qui illustrent et complètent l'analyse précédente sur les vitesses (Fig.17):

- les lignes de courant dans la section la plus interne sont constamment déviées latéralement vers l'extrémité, et verticalement elles suivent approximativement la forme des profils de la voilure.
- les lignes dans la section la plus externe se dirigent vers la région interne de la maquette puis s'infléchissent vers l'extrémité à l'arrière du tronçon de voilure. Ces déplacements suivant y combinés aux évolutions en z donnent des formes inhabituelles: vues de face ces lignes semblent s'enrouler sur elles-mêmes.
- dans la section centrale, la forme des lignes est intermédiaire entre les formes précédentes et les surfaces de courant sont donc très gauches.
- dans une section donnée, les allures des différentes lignes sont peu évolutives et dépendent peu de l'altitude.

Ces lignes de courant peuvent être utilisées pour la définition d'un pylône 'adapté'.

4 COMPARAISON ENTRE ESSAIS ET CALCULS

Une méthode de calcul d'écoulements transsoniques autour de géométries complexes est en cours de développement à l'ONERA [3]. Elle est ici appliquée aux calculs des configurations tronçon et tronçon+nacelle qui ont fait l'objet des essais qui viennent d'être décrits. Toutefois on ne cherchera qu'une comparaison qualitative avec les résultats expérimentaux car le code de calcul ne prend pas encore en compte les effets visqueux.

4.1 Généralités sur le maillage et sur la méthode de résolution

La géométrie du tronçon avec nacelle étant très tridimensionnelle, il est impossible de créer un maillage de qualité qui soit globalement structuré, c'est à dire dont l'ensemble des noeuds puisse être numéroté en I, J et K. L'option retenue à l'ONERA consiste à découper l'espace en domaines de calcul dans lesquels le maillage est structuré, puis chaque domaine est découpé en blocs de maillage. Un nombre important de blocs permet de contrôler avec une grande souplesse la position des noeuds et leur répartition. Les blocs ne sont utilisés que lors de la construction du maillage alors que les domaines interviennent lors de la résolution. La donnée des blocs et des domaines constitue la topologie.

Pour la géométrie étudiée, 4 domaines ont été définis (au dessus du tronçon, entre le tronçon et la nacelle, sous le tronçon, et un domaine entrant dans la nacelle), et 62 blocs de maillage ont été choisis pour obtenir les répartitions de points désirées (Fig.18). Le maillage de surface de l'objet est créé séparément à l'aide d'outils de CAO. Il comporte environ 1800 points sur le tronçon d'aile et 1000 points sur la nacelle (Fig.19). Le code ONERA-MESH3D génère alors le maillage d'espace en positionnant les points sur chaque arête de bloc puis sur les faces et enfin à l'intérieur des blocs.

Le maillage d'espace comporte environ 120000 points, c'est un maillage en H autour des bords d'attaque de l'aile et de la nacelle (Fig.20).

Un second maillage a été crée autour du tronçon d'aile isolé, en vue d'une évaluation théorique de l'effet de la nacelle. Le maillage de surface est identique. L'espace est découpé en 2 domaines et 8 blocs et ce maillage comporte environ 80000 points.

Les calculs aérodynamiques sont effectués à l'aide d'un code multidomaine résolvant l'équation complète du potentiel sous la forme conservative avec une formulation en éléments finis. Cette méthode peut traiter des écoulements faiblement supersoniques (Mach local normal<1.4), et la formulation est bien adaptée aux géométries complexes car elle tolère des maillages irréguliers et peu orthogonaux.

Dans les calculs, la nappe tourbillonnaire issue de l'aile a une position figée sur une ligne de maillage. La nacelle est traitée comme une entrée d'air dont on impose le coefficient de débit. La nappe issue de la nacelle est traitée comme une surface de glissement et le jet n'est pas calculé.

4.2 Résultats

Le code résolvant l'équation du potentiel sous forme conservative, les intensités des ondes de choc sont surestimées et ont une position reculée par rapport aux essais, bien que les calculs aient été effectués à une incidence plus faible que les essais (Mach=0.82, Incidence=1.10 degrés). L'absence de traitement des effets visqueux conduit aussi à une surestimation des portances globales:

Cz tronçon = 0.709 et Cz tronçon+nacelle=0.625

La perte de portance occasionnée par la nacelle est aussi plus élevée que ce que prévoit l'expérience. L'examen des efforts locaux confirme cette constatation (Fig.21 et 8). D'autre part, les écarts sur ces efforts calculés sont plus importants du côté externe de la nacelle, ce qui n'est pas en accord avec les essais.

Les répartitions de pression par section ainsi que les lignes iso-Kp d'écarts entre tronçon d'aile et tronçon+nacelle fournissent des indications plus détaillées (Fig.22,23). On constate tout d'abord que malgré les écarts au niveau des coefficients globaux le calcul rend compte des principaux phénomènes provoqués par la nacelle:

- zone accélérée à l'intrados du tronçon d'aile en amont du bord de fuite de la nacelle, s'étendant jusqu'à l'emplanture du tronçon, et limitée à la région du bord d'attaque du côté externe de la nacelle.
- région ralentie centrée sur l'axe nacelle et peu étendue en envergure, localisée juste en aval de la zone précédente.
- ralentissement au bord d'attaque extrados au droit de la nacelle et dans les sections plus externes.
- cette perte de survitesse est suivie d'une baisse du niveau du plateau supersonique, plus marquée du côté externe de la nacelle, et conduit à un déplacement du choc vers l'amont sur toute l'envergure de l'aile.

Les répartitions de Kp sur le tronçon en présence de la nacelle ont même allure que les courbes expérimentales (Fig.22 et 9). Il en est de même pour les iso-écarts entre tronçon d'aile+nacelle et tronçon isolé (Fig.23 et 10). Seule la différence de la position du choc est notable.

Par contre l'intensité des effets n'est pas correctement prédite par le calcul. L'analyse des répartitions de pression section par section et des courbes des écarts entre tronçon d'aile et tronçon+nacelle montre que (Fig.22,24):

- A l'extrados, le déplacement du choc est surestimé par le calcul. Ceci est dû à sa position très reculée car on résout en fluide parfait l'équation du potentiel conservative, donc la zone supersonique est très étendue et dans cette zone l'écoulement est très sensible à toute perturbation.
- La variation du niveau du plateau supersonique en présence de la nacelle est plus importante pour le calcul. Les causes sont les mêmes que pour la position du choc.
-A l'intrados, les courbes des écarts évalués par le calcul ou expérimentaux dans quelques sections ont la même allure et sont quasiment parallèles, mais les écarts calculés sont un peu plus faibles. Les lignes iso-Mach d'écarts ont aussi des allures très proches. Les différences peuvent être dues à la présence de la couche limite qui réduit entre autre la taille du canal entre le tronçon et la nacelle.

Il faut cependant noter que l'écoulement autour de ce tronçon entre parois avec une zone supersonique étendue sur toute son envergure est un cas particulièrement sévère pour les méthodes numériques.

Les lignes iso-Mach théoriques ont été déterminées dans le plan vertical passant par l'axe nacelle. La comparaison avec les mêmes courbes issues des sondages par vélocimétrie laser est satisfaisante bien que le jet ne soit pas calculé (Fig.25 et 14).

5 CONCLUSIONS

Le nouveau montage expérimental réalisé dans la soufflerie S3Ch de l'ONERA à Chalais-Meudon permet une étude détaillée de l'écoulement local entre nacelle et tronçon de voilure. Les pesées globales par balance, l'équipement important de la maquette en prises de pression, le vélocimètre laser pour des sondages d'écoulement dans l'espace permettent d'obtenir un ensemble d'informations complet et détaillé. L'ensemble des informations ainsi recueillies a permis une analyse fine des phénomènes aérodynamiques d'interaction grâce, notamment, à la complémentarité des différents types de mesure. Ce moyen d'essais sera un outil important pour la validation de méthodes de calcul appliquées à ce problème.

6 REMERCIEMENTS

Les auteurs tiennent à remercier le personnel de la soufflerie ONERA-S3Ch qui a contribué au succès de cette campagne d'essais, ainsi que les spécialistes de la vélocimétrie laser à l'ONERA.

7 REFERENCES

[1] J.J. MIRAT , R. PERIN , C. CASTAN
Engine installation design for subsonic transport aircraft.
ICAS Congress
Stockholm, Sweden, 9–14 September, 1990

[2] B. EWALD , R. SMYTH
The role and implementation of different nacelle/engine simulation concepts for wind–tunnel testing in research and development work on transport aircraft.
AGARD CP 301, Aerodynamics of power–plant installation
Toulouse, France, 11–14 May 1981

[3] O.–P. JACQUOTTE
Multidomain topology management and solution algorithm for potential flow computations around complex configurations.
Computer methods in applied mechanics and engineering ,
à paraître.

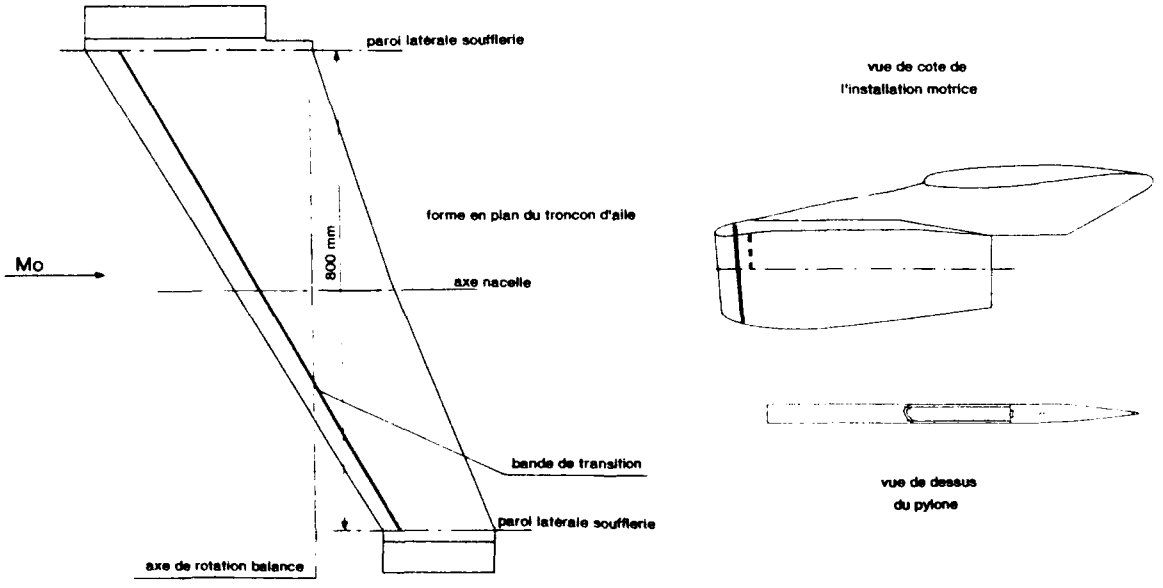

Fig. 1: Maquette pour étude de l'interaction nacelle-voilure

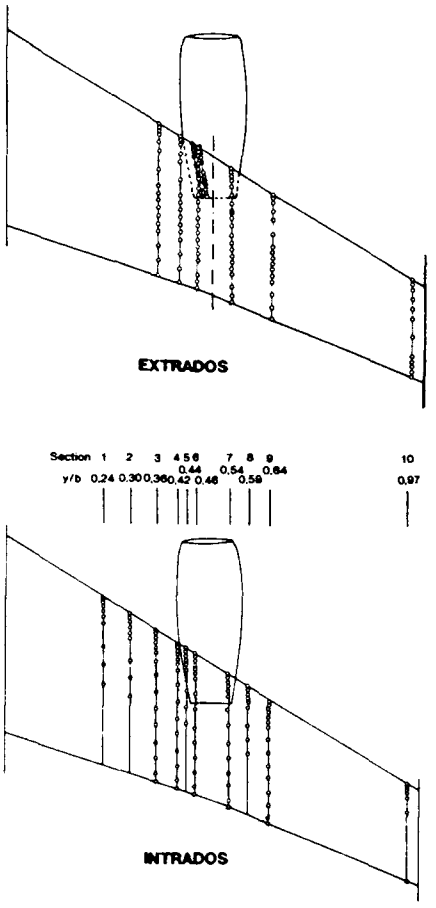

Fig. 2: Equipement en prises de pression du tronçon de voilure

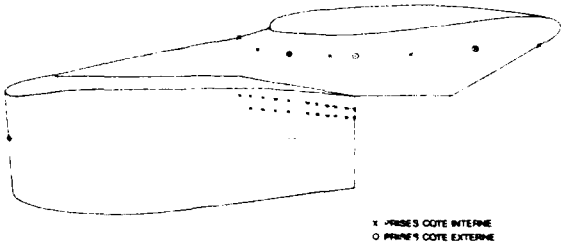

Fig. 3: Equipement en prises de pression du mât et de la nacelle

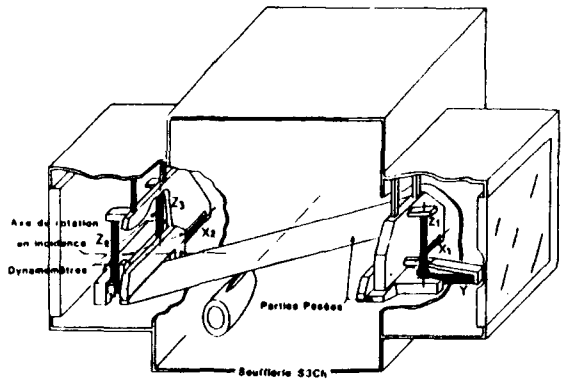

Fig. 4: Schema du montage en soufflerie

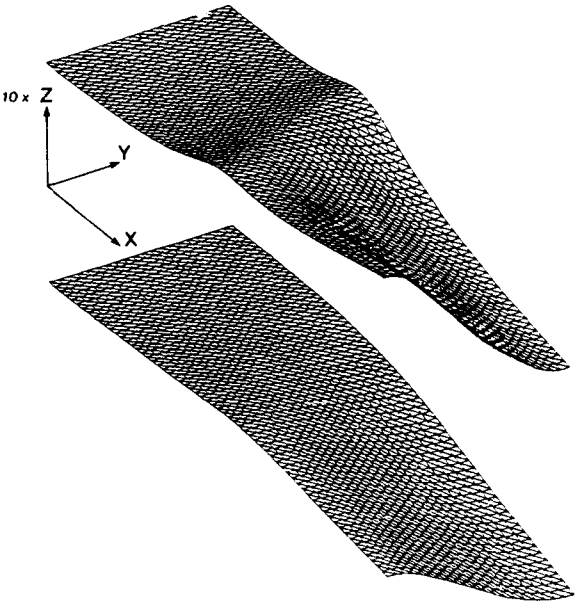

Fig. 5: Parois haute et basse de la soufflerie

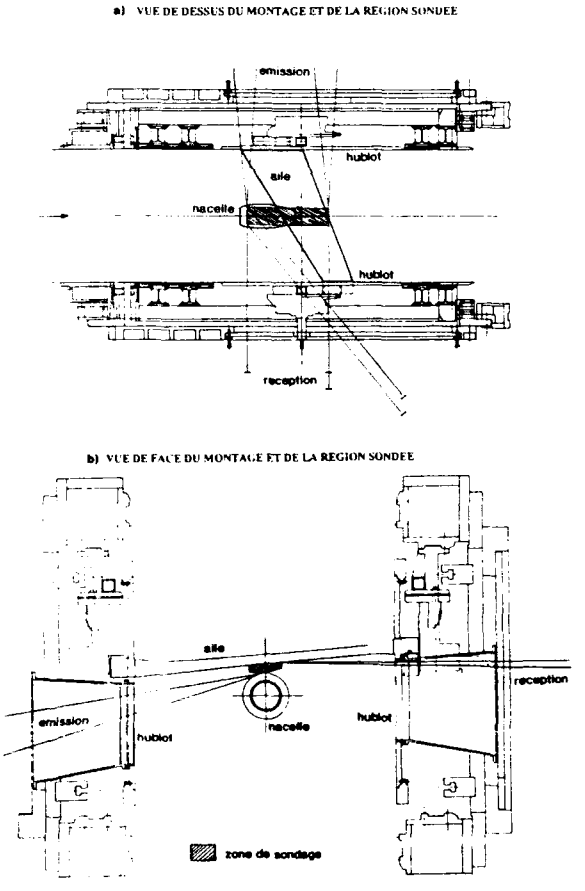

Fig.6: Montage pour vélocimétrie laser

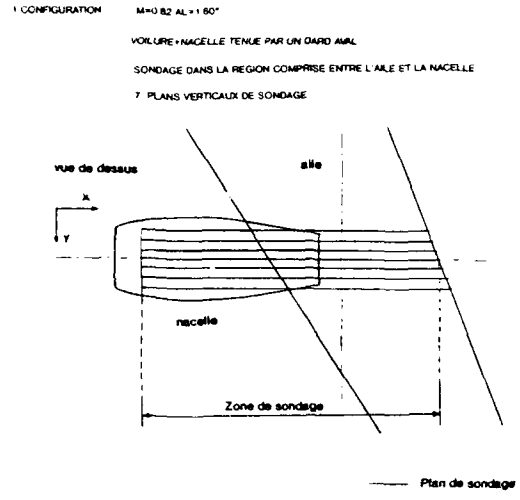

Fig. 7: Sondages d'écoulement par vélocimétrie laser

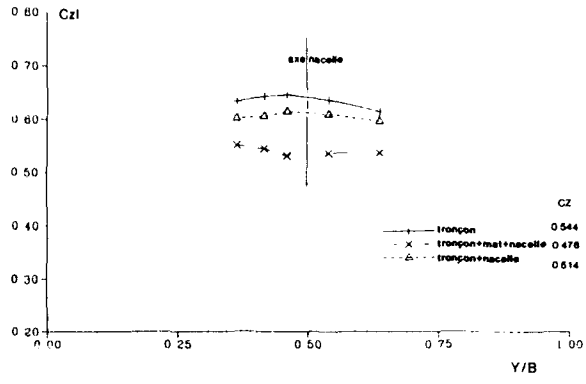

Fig. 8: Répartitions de portances locales expérimentales
Mach=0.82 Incidence=1.60°

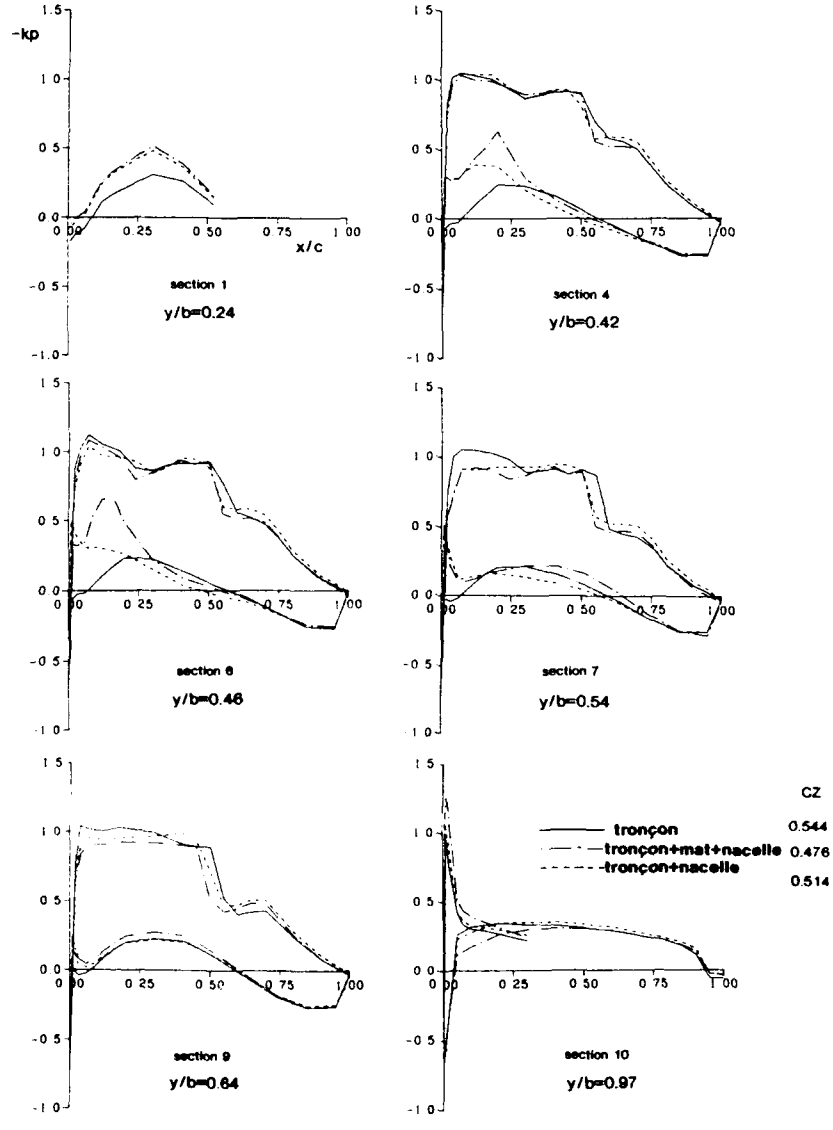

Fig. 9: Répartitions de pression sur tronçon d'aile
Mach=0.82 Incidence=1.60°

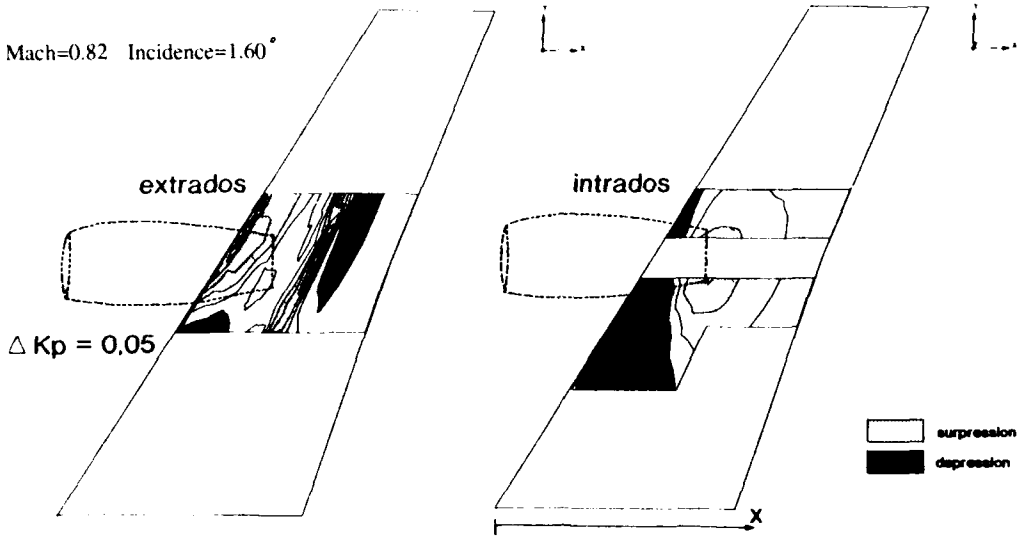

Fig.10: Lignes isobares expérimentales
Ecarts (aile+nacelle)-(aile lisse)

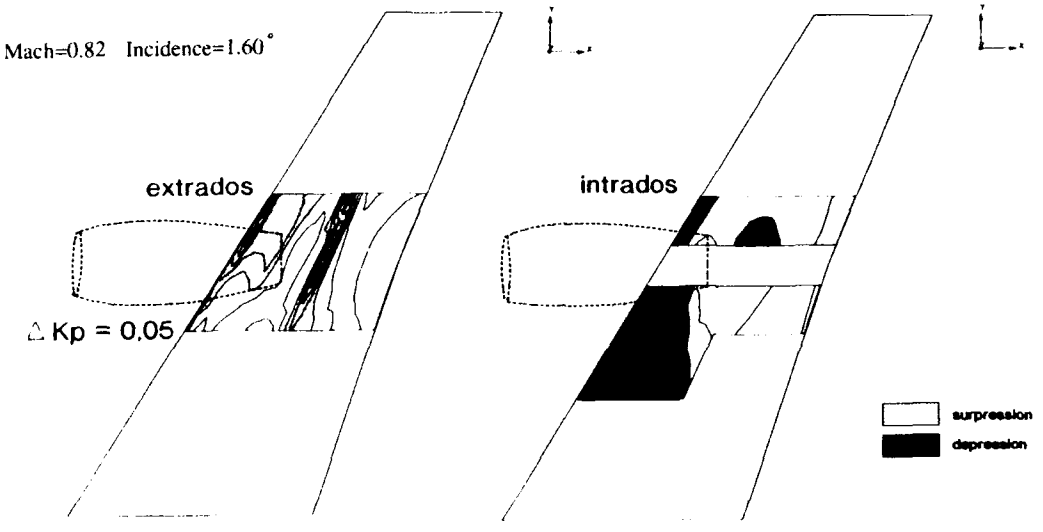

Fig.11: Lignes isobares expérimentales
Ecarts (aile+mât+nacelle)-(aile lisse)

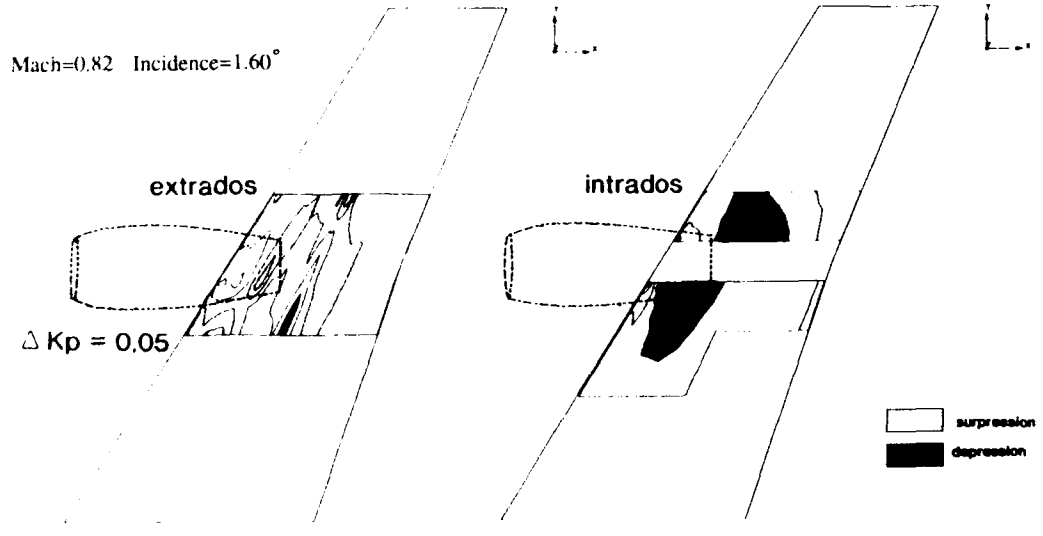

Fig.12: Lignes isobares expérimentales
Ecarts (aile+mât+nacelle)-(aile+nacelle)

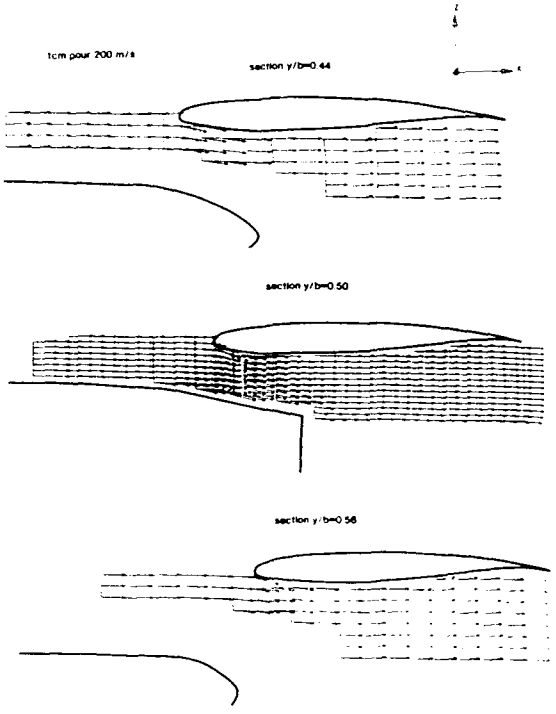

Fig.13: Vecteurs vitesse expérimentaux
Mach=0.82 Incidence=1.60°

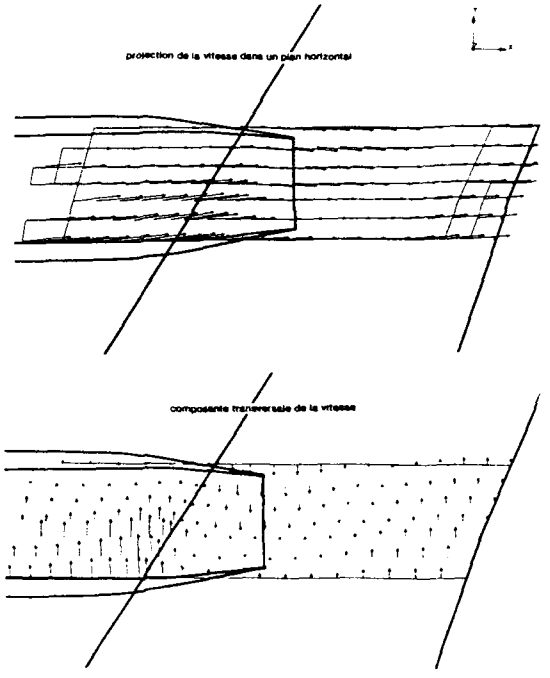

Fig.15: Vecteurs vitesse expérimentaux
Mach=0.82 Incidence=1.60°

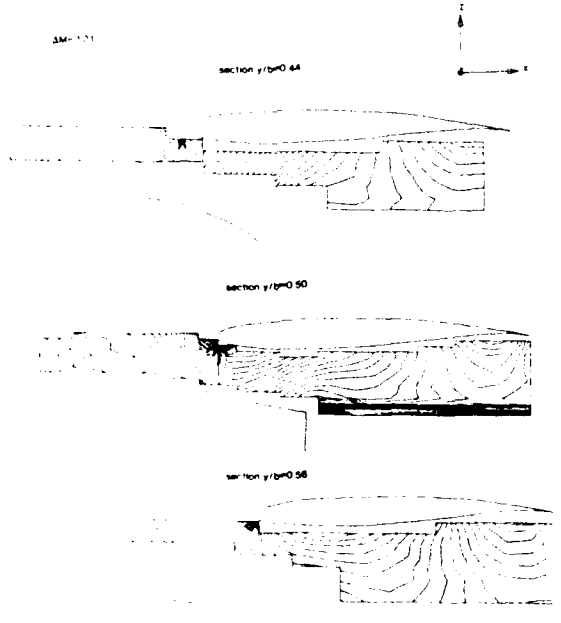

Fig.14: Lignes iso-Mach expérimentales
Mach=0.82 Incidence=1.60°

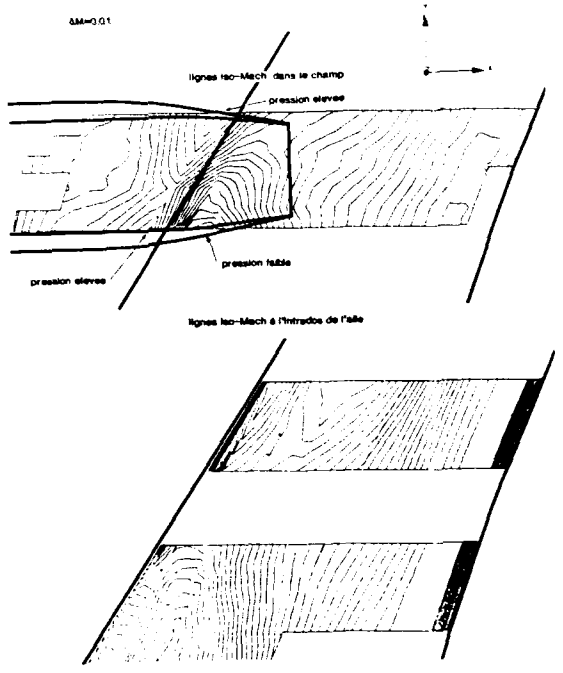

Fig.16: Lignes iso-Mach expérimentales
Mach=0.82 Incidence=1.60°

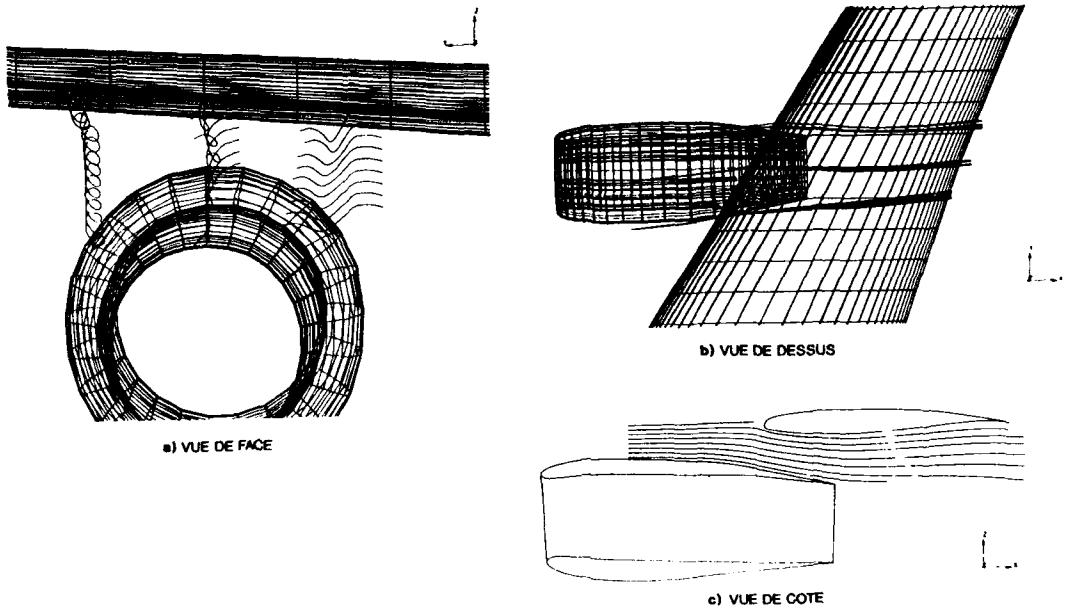

Fig.17: Lignes de courant entre aile et nacelle

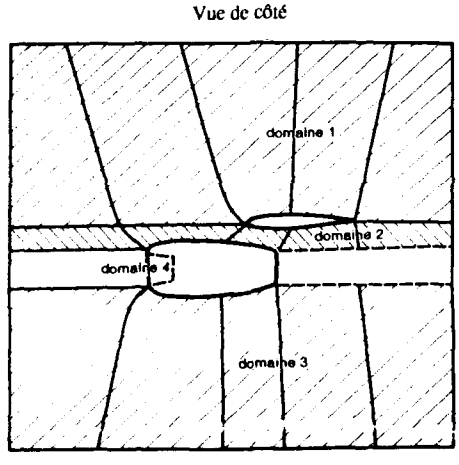

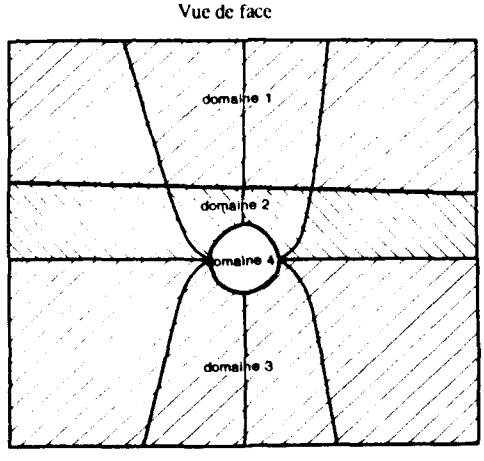

Fig.18: Schema de la topologie de maillage pour tronçon + nacelle

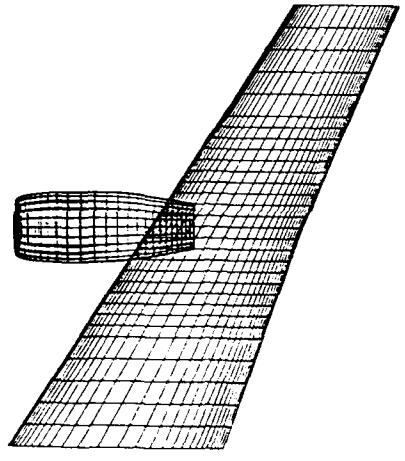

Fig.19: Vue de dessus du maillage de surface

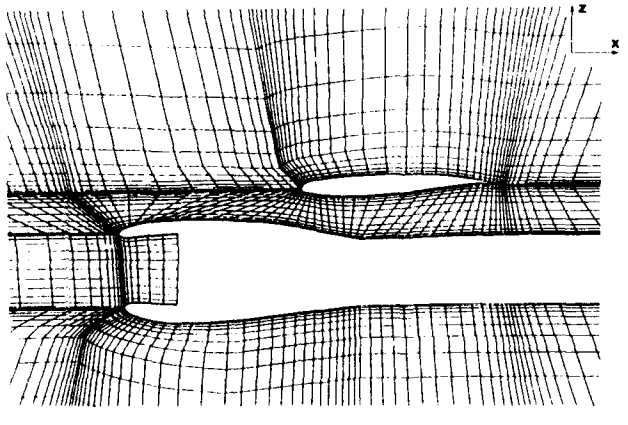

Fig.20: Maillage multibloc tridimensionnel pour tronçon et nacelle

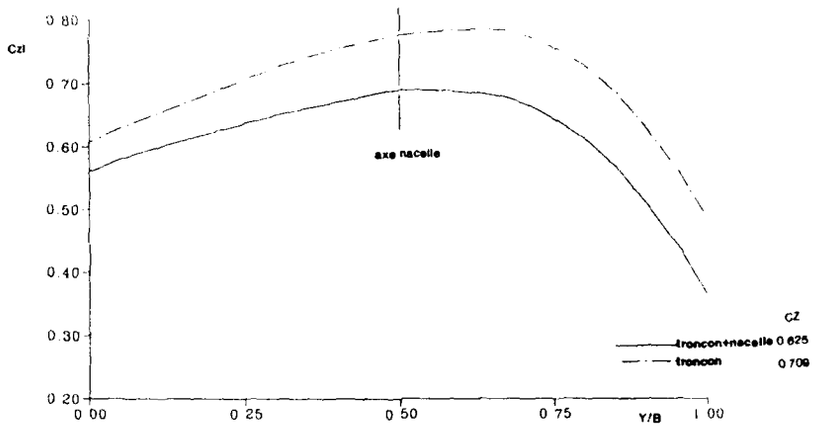

Fig.21: Répartitions de portances locales théoriques
Mach=0.82 Incidence=1.10°

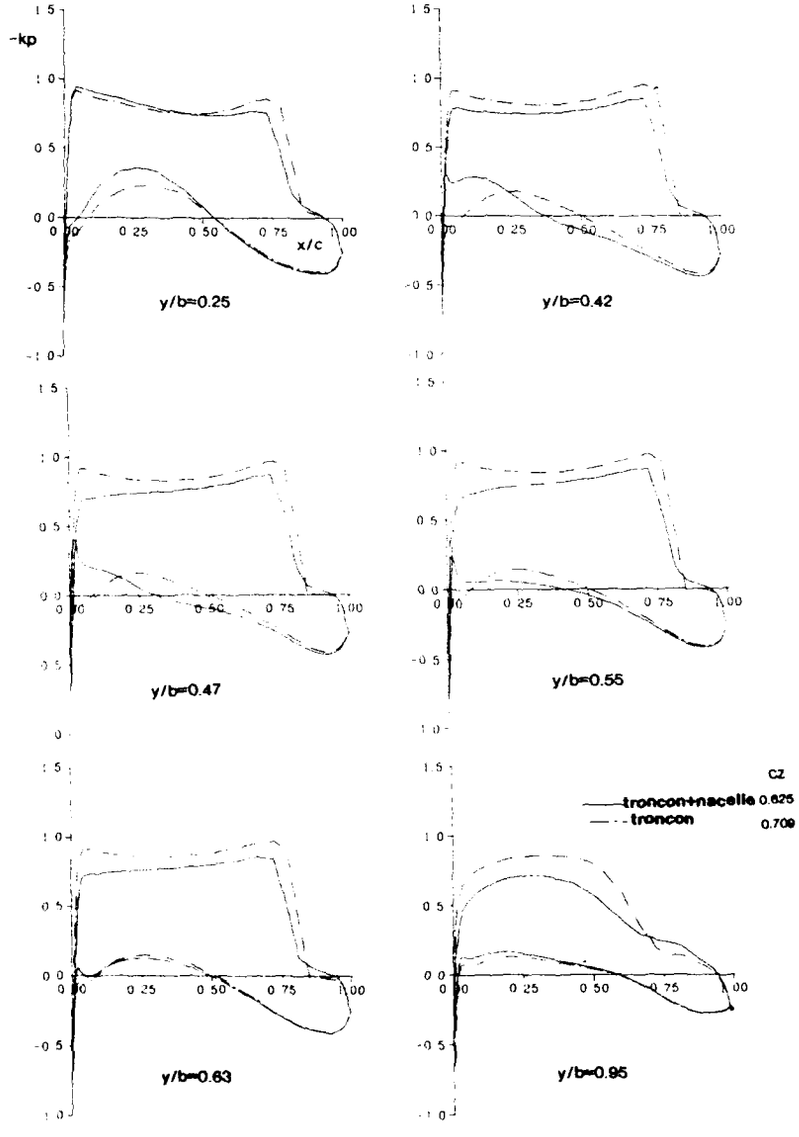

Fig.22: Répartitions de pression théoriques sur tronçon d'aile
Mach=0.82 Incidence=1.10°

Mach=0.82 Incidence=1.10°

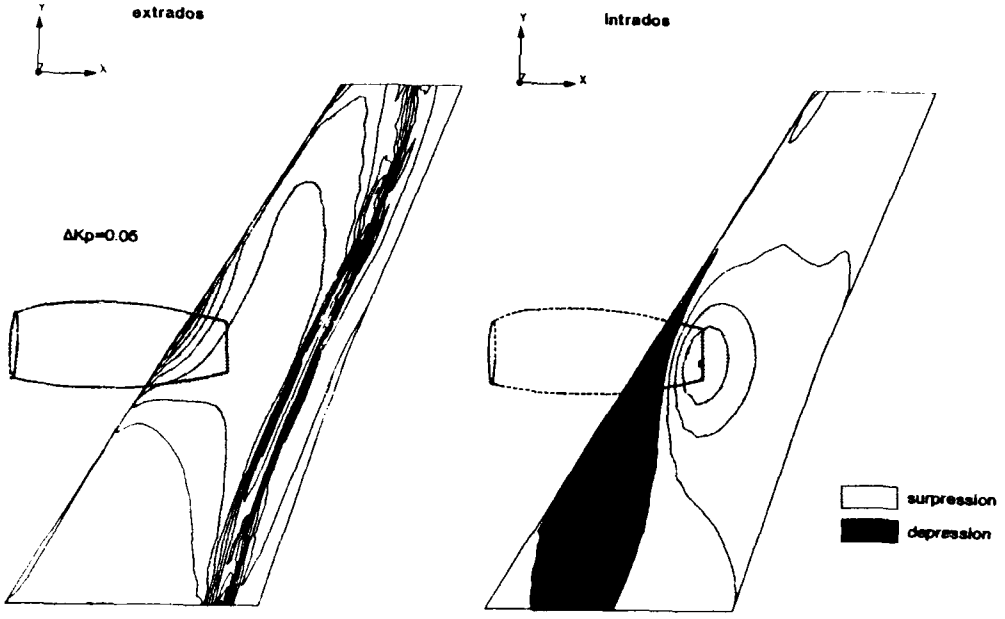

Fig.23: Lignes isobares théoriques
Ecarts Kp(aile+nacelle)-Kp(aile)

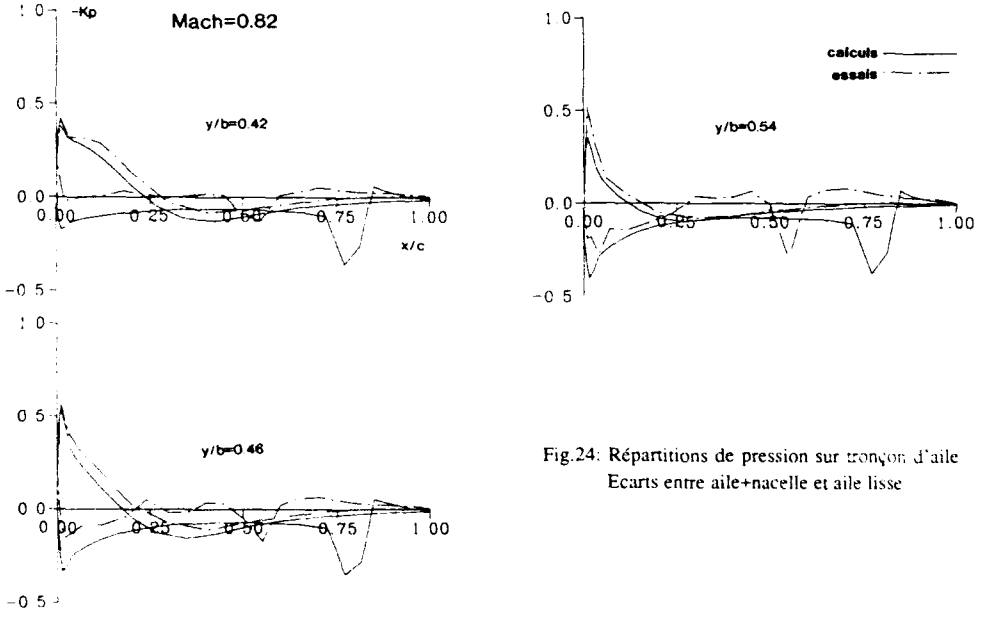

Fig.24: Répartitions de pression sur tronçon d'aile
Ecarts entre aile+nacelle et aile lisse

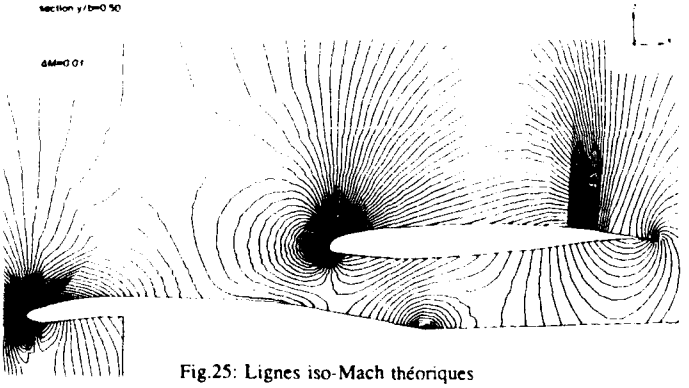

Fig.25: Lignes iso-Mach théoriques
Mach=0.82 Incidence=1.10°

Investigation of Interference Phenomena of Modern Wing-Mounted High-Bypass-Ratio Engines by the Solution of the Euler-Equations

C.-C. Rossow, A. Ronzheimer

DLR Institut für Entwurfsaerodynamik
Flughafen, D-3300 Braunschweig, Germany

SUMMARY

With the development of Ultra-High Bypass (UHB) engines the aerodynamic interference between airframe and engine becomes increasingly important. In this study the solution of the Euler equations is used to simulate the flow field around the DLR-ALVAST wing-body combination with different wing-mounted engines. For a CFM-56 engine, which is taken here to represent a conventional engine, the contributions of single components like engine, pylon, and jet to the aerodynamic interference were investigated. The comparison with the flow field around the wing-body combination without engine showed that the presence of the engine alone lead to a forward movement of the shock on the complete upper surface of the wing. The pylon mainly influenced the lower surface and caused an additional loss of lift which is of the same order of magnitude as the loss due to the engine. The simulation of an inviscid jet showed no significant influence for the conventional engine. A further comparison of the interference effects of the CFM-56 engine and a UHB engine was made. The geometry of the UHB engine corresponds to the DLR-CRUF simulator for Ultra-High Bypass engines. Due to the closer installation to the wing and the larger dimensions, the UHB engine caused a local flow acceleration on the lower surface of the wing. This lead to a significant loss of lift at the engine position, compared to the conventional engine. Simulation with and without jet revealed that the jet was mainly responsible for this behaviour. In case of the UHB engine the jet passed very closely under the wing and the displacement effect of the jet caused a strong flow acceleration.

1. INTRODUCTION

The interaction between the propulsion system and the airframe can have a significant impact on the performance of an aircraft. It is evident that an optimal integration of the propulsion system into the airframe will result in an enhanced performance of the whole aircraft. This task is called propulsion/airframe integration (PAI). PAI becomes the more important the greater the amount of fuel prices as part of the Direct Operating Costs (DOC) becomes. The higher this amount is the more effort has to be made in PAI to reduce the amount of fuel costs. But even when fuel prices are low the development of oil prices poses great uncertainties on the strategic planning of airline companies, and a successful integration of the propulsion system may reduce that dependency.

With the development of Very-High- and Ultra-High-Bypass engines (VHB/UHB) for transonic transport aircraft a substantial increase in economical advantage as well as in environmental compatibility is expected. However, these engines build larger than conventional engines and may cause stronger aerodynamic interference. As a consequence, further efforts in PAI are required for the time the Very-High/Ultra-High-Bypass engines will be installed into an airframe: If the lower specific fuel consumption of these engines should result in higher economical advantage, care must be taken that the benefits from the lower fuel consumption are not compensated (or even overcompensated) by higher drag of the complete aircraft caused by stronger interference. The efforts of PAI are especially relevant for configurations with wing-mounted engines, since here the propulsion system directly influences the flow around the wing. Furthermore, future UHB engines will be mounted closer to the wing due to their larger diameters and the restrictions placed on the available length of the landing gear.

In order to get a better understanding of the elements playing a role in the interference process and to realize an improved installation of the propulsion system, substantial efforts have been made to simulate jet and interference phenomena. Experimentally this is performed by investigating isolated and integrated model engines driven by compressed air (Turbine Powered Simulators) [1], [2]. Wind tunnel investigations are however rather complex and expensive. Therefore numerical methods are increasingly gaining attention. For the numerical simulation of the flow around installed engines panel methods [3], methods solving the full potential equation [4], and more recently methods for the solution of the Euler equations [5], [6], [7], [8] have been used. In the contribution presented here the solution of the Euler equations will be used to predict the interference phenomena between aircraft and engine. One advantage of the solution of the Euler equations with respect to the potential flow model is that the former is exact for inviscid flows, i.e. mass, momentum, and energy are conserved. Secondly, in case of solving the Euler equations, the vortex sheet behind a lifting wing needs not

to be specified. Furthermore, the geometry of an inviscid jet comes out as part of the solution, and no assumptions are a priori necessary. On the other hand, compared to the solution of the Navier-Stokes equations, the effort for the generation of computational grids and the computer time required for the calculation of inviscid flow fields tend to be an order of magnitude smaller, and essential interference phenomena may already be observed in inviscid flow.

The special configuration considered here is a twin engine Airbus-type aircraft.The geometry of the wing-body combination corresponds to the DLR-ALVAST wind tunnel model. Experimental and theoretical investigations for this wing-body combination equipped with a Turbine Powered Simulator were carried out in [6] for low subsonic speeds. Comparison of experimental and theoretical results showed reasonable agreement despite the fact that in the numerical simulation the pylon was neglected.

In this study the numerical simulation of the transonic flow field will be performed for the ALVAST wing-body combination with two different engines installed on a pylon. The first engine is a CFM-56 engine. With this conventional engine the elements playing a role in the interaction between propulsion system and airframe will be analyzed. The other propulsion unit to be investigated is an engine with Ultra-High-Bypass Ratio. The geometry of this engine corresponds to the DLR-CRUF simulator (Counter Rotating Ultra-high-bypass Fan), which shall be used for experimental investigations in the future [9]. The interference effects of the UHB engine will be compared with those of the conventional engine to estimate the problems occurring with the installation of such large future propulsion systems.

2. GOVERNING EQUATIONS

The three-dimensional Euler equations for unsteady compressible inviscid flows may be written in integral form using a cartesian reference frame as

$$\iiint_V \frac{\partial}{\partial t} \vec{W} dV = \iint_{\partial V} \bar{\bar{F}} \cdot \vec{n}\, dS \quad , \qquad (1)$$

where

$$\vec{W} = \begin{bmatrix} \rho \\ \rho u \\ \rho v \\ \rho w \\ \rho E \end{bmatrix} \quad , \quad \bar{\bar{F}} = \begin{bmatrix} \rho \vec{q} \\ \rho u \vec{q} + p \vec{i}_x \\ \rho v \vec{q} + p \vec{i}_y \\ \rho w \vec{q} + p \vec{i}_z \\ \rho H \vec{q} \end{bmatrix} .$$

In equation (1), p, ρ, u, v, w, E, and H are the pressure, density, cartesian velocity components, total energy, and total enthalpy, respectively. V denotes an arbitrary control volume fixed in time and space and ∂V is the closed boundary of the volume V. $\bar{\bar{F}}$ represents the tensor of flux density and $\vec{n}$ is the outward facing normal along ∂V. The unit vectors of the cartesian coordinate system are given by i_x, i_y, i_z, and the velocity vector is hence

$$\vec{q} = u\vec{i}_x + v\vec{i}_y + w\vec{i}_z \quad . \qquad (2)$$

Applying the integral mean value theorem, equation (1) can be converted to

$$\overline{\left(\frac{\partial}{\partial t} \vec{W}\right)} = - \frac{\iint_{\partial V} \bar{\bar{F}} \cdot \vec{n}\, dS}{\iiint_V dV} \quad . \qquad (3)$$

The term on the left-hand side of equation (3) represents the integral mean value of the rate of change of W in the control volume V, and the right-hand side is the flux per volume of mass, momentum, and energy through the surface of V. Together with the equation of state

$$p = \rho R T \quad , \qquad (4)$$

which relates the pressure to the components of W, equation (4) forms a system of five equations for the unknowns ρ, u, v, w, E .

3. NUMERICAL METHOD

3.1 Solution Scheme

The discretization of equation (4) follows the method of lines, i.e. the discretization in space and time is done separately. The physical domain around the aerodynamic body is supposed to be divided into hexahedral cells. The discrete values of the flow quantities are located at the vertices of the mesh cells [10]. The numerical analogue of the integral equation (4) then reads:

$$\left(\frac{d}{dt} \vec{W}\right)_{i,j,k} = - \frac{1}{V_{i,j,k}} \left(\vec{Q}_{i,j,k} - \vec{D}_{i,j,k}\right) \qquad (5)$$

where i,j,k are the indices of a certain grid point in the computational domain, $Q_{i,j,k}$ denotes the convective flux given by an approximation of the surface integral in equation (4), and $D_{i,j,k}$ is a dissipative operator.

The approximation of the convective flux at a vertex i,j,k is accomplished by first evaluating the fluxes through the surfaces of all cells surrounding node i,j,k. On regular grids a vertex has eight neighboring cells in common, as sketched in **Figure 1**. Then the fluxes of all cells having node i,j,k in common are summed up to yield $Q_{i,j,k}$. Using

this cell vertex discretization rather than the common cell centered schemes offers the advantage of higher accuracy on non-smooth meshes, since it can be shown that a cell vertex discretization for the Euler equations is at least first order accurate on arbitrary meshes [10]. In the context of solving the Euler equations for complex configurations on meshes with highly-skewed cells, singular points, and singular lines this is considered to be a distinct advantage.

Since this discretization scheme leads to central difference approximations for the governing equations, additional artificial dissipative terms are necessary to damp out high frequency oscillations. Following [11], a blend of second and fourth differences of the flow variables is used to provide the dissipative operator $D_{i,j,k}$.

The spatial discretization results in a system of ordinary differential equations in time which is solved by an explicit 5-stage Runge-Kutta time stepping scheme. Since here interest is focussed on steady flow fields only, various techniques, like local time stepping, implicit residual averaging, enthalpy damping [11], [12], and multigrid [13] are used to accelerate convergence towards steady state.

In order to define the problem under consideration the specification of appropriate boundary conditions is necessary. At solid surfaces a flow tangency condition is enforced by projecting the local velocity vector at a surface point onto the surface. Far field boundaries are implemented using the concept of characteristic variables as described in [14]. Furthermore, boundary conditions for the simulation of engine flow have to be applied. At fan inflow faces the flow velocity, pressure, and density are calculated as functions of a specified mass flow $\dot{m}_{in}$. The mass flow can be prescribed by specifying the streamtube area ratio $\varepsilon = A_\infty / A_{FAN}$. Corresponding to **Figure 2**, A_{Fan} denotes the area of the fan face and A_∞ is the corresponding streamtube area at infinity. With this ratio and the free stream conditions the massflow $\dot{m}_{in}$ may be calculated:

$$\varepsilon_F = \frac{A_\infty}{A_F} = \frac{\dot{m}_{in}}{A_F \cdot Ma_\infty \cdot \sqrt{\kappa \cdot p_\infty \cdot \rho_\infty}} \quad (6)$$

At engine outflow faces the jet is characterized by the ratio of jet total pressure to freestream static pressure p_{t_j}/p_∞, and the ratio of total jet temperature and total temperature of the ambient flow T_{t_j}/T_{t_∞}. Using the freestream Mach number the jet mass flow may then be calculated.

With these boundary conditions realistic operating conditions can be simulated by prescribing parameters obtained from the engine manufacturers. Note that boundary conditions at in- and outflow faces may be applied independently from each other, so mass is not necessarily conserved, depending on the conditions prescribed. For example, in the following certain calculations will be shown where the correct mass inflow is specified, however, at the outflow faces an isentropic pressure ratio is prescribed. This implies that total pressure of jet and free stream are the same, and therefore in these cases no jet is simulated. As a consequence, mass is not conserved any more.

The algorithms are implemented in the DLR code CEVCATS. This code is written in a block-structured form and allows an arbitrary application of boundary conditions on the block faces. The code is designed as an out-of-core version where only one block at a time is loaded into the main memory of the machine. This enables the handling of problems even larger than the size of the main memory, since the complete domain may be split into appropriate blocks which fit separately into the memory. Details of the multi-block structure and the implementation of the multigrid acceleration technique into the multi-block framework may be found in [15], [16].

3.2 Grid Generation

In this work a method for the generation of body-fitted, block-structured meshes is employed. In the block-structured approach the domain of interest is first decomposed into different appropriate regions, and then subgrids are generated separately in each region. This approach offers a high flexibility since now different surfaces of the configuration under investigation may be represented by different coordinate surfaces of the subgrids.

The first step in the multi-block approach for complex configurations is to decide about a global grid topology which allows the embedding of necessary subgrids around the different components. In this study an H-type structure in streamwise direction and an O-type structure in spanwise direction is chosen for the wing-body combination, as sketched in **Figure 3**. Engine and pylon can be integrated into this topology by introducing a sub-block containing these components. For this purpose a specified region has to be cut out of the global grid to allow the substitution of the subgrid with the propulsion components. The topology for the subgrid around engine and pylon exhibits also an H-type structure in streamwise direction, as shown in **Figure 4a**. In circumferential direction a polar grid topology is applied with respect to the engine. The outer boundary of the polar subgrid is adapted to the boundaries of the cut-out region of the global grid. **Figure 4b** gives a schematic sketch of the resulting topology.

Note that using this topology the global H-O grid around the wing body configuration may be left

unchanged when introducing different subgrids for different engine types.

In order to achieve an efficient process a mesh generation system was designed especially for the generation of grids around transport aircraft with wing-mounted engines. A mesh generator designed for a special task does not provide the flexibility as general mesh generation tools, but on the other hand it may be optimized for the special configurations to be investigated. Furthermore, in case an appropriate grid topology is chosen, different components like wing, body, pylon, and engine may relatively easy be changed as well as their corresponding position. Details of the grid generation procedure and the techniques employed may be found in [17]. A three-dimensional view of a field grid obtained with the grid generation system used here is shown in **Figure 5**. Note that C^1 continuity of the grid lines has not been enforced at the block boundaries. Dropping C^1 continuity leads to a much higher flexibility in the grid generation process, but imposes certain constraints on the accuracy of the solution method used in the flow solver. The cell-vertex scheme used in this study provides a consistent discretization for these cases.

Figure 6 shows a view of the surface mesh around the DLR-ALVAST wing-body combination with CFM-56 engine. Note the H-type structure of the surface mesh on the fuselage at the leading edge of the root-section. The control of grid properties was achieved by elliptic grid generation. The surface mesh on the wing consists of 40 cells in spanwise direction, and cells are concentrated at the pylon location. 144 cells are used around an airfoil section. For the engine 64 cells have been employed in circumferential direction. The complete field grid consists of 11 computational blocks with approximately 600,000 mesh cells.

In **Figure 7** the ALVAST wing-body combination with the DLR-CRUF simulator is displayed. The surface mesh of the wing-body combination is identical with that of the previous configuration. Comparing both figures one realizes the larger dimensions of the UHB engine with respect to the CFM-56 engine. Note the shape of the core engine. Since the turbines for the simulator required a certain space, it was not possible to contract the core engine in the way of the CFM-56 engine. Since mesh topologies are the same, this grid consists also of 11 computational blocks. The number of mesh cells is insignificantly higher than in the case of the CFM-56 engine.

Figure 8 gives a view of a cross-section of the field grid with CFM-56 engine at the pylon location. Note the high skewness of the grid lines. Control of grid properties has been achieved by elliptic grid generation. Note that C^1 continuity has not been enforced at block boundaries in this section either.

4. RESULTS

In the following results computed for the two configurations will be shown. The free stream conditions are always chosen to $M_\infty = 0.75$ and $\alpha = 0.84°$ in order to represent typical cruise conditions. The temperature ratio was always specified as unity, i.e. only cold jets are simulated. Furthermore, no attempt has been made to simulate the correct bypass ratio. Instead, at fan and core outflow faces always identical boundary conditions are applied.

The presentation of results is split into two parts: First, the influence of single components on the interference effects will be investigated for a conventional engine (CFM-56). A comparison of the flow field around the wing-body combination (wb) and the wing-body-engine-pylon configuration (wbep) will be made, and the interference caused by single components like engine, pylon, and jet will be discussed. Second, the interference effects of a conventional engine and a UHB engine will be compared and the reasons for the differences in aerodynamic interference will be analyzed.

4.1 Influence of Single Components

Figure 9 shows the surface pressure distribution of the ALVAST wing-body combination with CFM-56 engine. On the upper surface of the wing a shock is clearly visible by the concentration of isolines. Note the smooth slope of the isolines even on the pylon surface, where the grid lines exhibit a slope discontinuity at the block boundaries. Due to the consistent discretization with the cell vertex scheme the non-smoothness of the grid causes no difficulties.

4.1.1 Assessment of Interference Effects

First, the interference effects of the complete propulsion system will be assessed to analyze the aerodynamic correlations. In **Figure 10** pressure distributions at four different spanwise sections are given. The results of the wing-body (wb) and the wing-body-engine-pylon (wbep) configuration are denoted by dashed-dotted and solid lines, respectively. The four spanwise stations D2, D3, D4, and D5 are given in the sketch of the figure, and the 2nd and 3rd distribution are just inboard and outboard of the pylon. The pressure ratio at the outflow faces of the engine is chosen to be isentropic in this case, so no jet is simulated. Comparing the results of the wb and wbep configuration one observes that the presence of the propulsion system has a significant influence on the flow field:

Lower Wing Surface

On the lower surface inboard of the pylon, the flow is accelerated in a region from the leading edge to about 35% chordlength. The acceleration is the strongest close to the pylon. Further inboard the effect decays somewhat but is still present. Just outboard of the pylon, acceleration takes place only in the leading edge region. From 10% chordlength further downstream the flow is decelerated, and from about 45% up to the trailing edge the pressure distributions are almost identical. Further outboard, the influence of the propulsion system on the lower wing surface has almost vanished, in contrast to the inboard lower part of the wing.

The difference between the pressure distributions in- and outboard of the pylon is caused by the sweep of the wing. Since on a swept wing the streamlines of inviscid flow are not straight lines but curved, the propulsion system distorts the streamline pattern in a certain way. Inboard of the pylon the streamlines are compressed and thus the flow is accelerated. Furthermore, propulsion system and fuselage cause a channel effect, and thus flow acceleration occurs not only closely to the pylon but also further inboard towards the fuselage. Outboard of the pylon the streamlines are widened and the velocity is reduced. This was already observed in [18]. Only very close to the leading edge the displacement effect of the engine causes an acceleration on the outboard side, too. Further outboard, the influence of the propulsion system on the lower surface has decayed almost completely, as can be seen in the fourth section. This behaviour is different from the inboard side, since there the channel effect caused a broader influence of engine and pylon.

Upper Wing Surface

In contrast to the more local effects on the lower side, one observes in Figure 10 that on the upper surface of the wing the shock has been shifted upstream at all four sections.

The upstream shift of the shock becomes clearly visible in a comparison of displays of lines of constant Mach number. In **Figure 11** the Mach number distribution on the upper wing surface is shown for the wb configuration and the wbep configuration. Note that the complete upper surface is influenced by the presence of the propulsion system. This may be explained by the following. The presence of the engine leads to a local reduction in incidence and thus to a forward movement of the shock. The flow on most of the upper surface is supersonic, and therefore this local disturbance is propagated along characteristics. Since the sweep of the wing is 27.1°, which corresponds to the angle of characteristics at $M_\infty = 1.12$, the local disturbance may be propagated over the upper surface from the engine location up to the wing tip. Thus the shock moves upstream in this whole region. Due to the channel effect the change in incidence occurs over the range from fuselage to pylon, and the shock position is also influenced in that region. Together with the effect discussed before, the shock is moved forward on the complete upper surface.

4.1.2 Influence of the Pylon

In order to account for the interference caused by the pylon, in **Figure 12** different pressure distributions of a wing-body, a wing-body-engine-pylon, and a wing-body-engine configuration are compared. The dashed dotted lines represent the wb configuration, the solid lines the wbep configuration, and the dashed lines give the pressure distributions of the configuration with engine but without pylon (wbe). Differences between the results for the wbe and the wbep configuration can now directly be attributed to the presence of the pylon. The pressure distributions are given at the same spanwise stations as in the previous figure. One observes that the pylon has a relatively small influence on the upper surface of the wing. The pressure distributions of both configurations show only small deviations on the upper surface. This suggests that the presence of the engine alone is responsible for the shift in incidence and thus for the shock movement.

On the lower surface, the pressure distributions of the wbe and wbep configuration are qualitatively similar, but the pressures obtained with pylon are almost always lower than without pylon. The qualitative correspondence shows that already the engine alone causes a similar deviation of streamlines and a channel effect as discussed before. The displacement effect of the pylon causes further acceleration of the flow and thus lower pressures. Furthermore, the channel effect between propulsion system and fuselage becomes more severe by the addition of the pylon, which leads to a significant acceleration inboard of the pylon.

The influence of the different components on the lift distribution is shown in **Figure 13**. Again solid, dashed, and dashed-dotted lines represent wbep, wbe, and wb configuration, respectively. Due to the presence of the propulsion system lift is considerably decreased, and it can be seen that the decrease due to the pylon is of the same order of magnitude as the decrease caused by the engine alone.

4.1.3 Influence of the Jet

In order to account for the influence of the inviscid jet for this configuration, **Figure 14** shows a comparison of pressure distributions for calculations with (dashed lines) and without jet (solid lines). The pressure ratio for the simulation of the jet was chosen to $p_{t_j}/p_\infty = 2.0$. There is almost no influence visible on the upper surface. On the lower surface at the region inboard of the pylon

the flow is somewhat accelerated, because the displacement of the jet increases the channel effect between fuselage and propulsion system. Outboard of the pylon only small differences occur.

The small influence of the jet can be explained by the shape of the core engine. In **Figure 15** lines of constant Mach number in a cross section through wing and engine are shown. The isolines at the pylon location correspond to the Mach number distribution on the outboard side of the pylon. The jet is clearly visible by the concentration of isolines at the jet boundaries forming a kind of numerical shear layer. This shear layer is caused by the numerical dissipation, since in true inviscid flow the jet boundaries should be given by perfect discontinuities. As can be seen from the figure, the core engine is contracted in downstream direction. The streamlines of the jet follow this contraction and the jet is bend away from the wing, thus reducing a possible interference between wing and jet.

4.2 Interference Effects of UHB Engine

Figure 16 and **Figure 17** give perspective views of the surface pressure distribution for the wing-body configuration with the UHB engine on the upper and lower wing, respectively. Similar to the results for the CFM-56 engine, all isolines show smooth slopes. Note that even at the block boundaries on the lower wing surface, where the block containing the propulsion system components is adapted to the global mesh, no irregularities of the isolines occur.

4.2.1 Comparison of UHB and Conventional Engine

For the installation of future propulsion systems with significantly larger dimensions it is important to assess their aerodynamic interference with respect to conventional engines. **Figure 18** shows a comparison of pressure distributions of the ALVAST wing-body configuration with the CFM-56 engine and with the CRUF simulator. Solid lines represent the data of the conventional engine, and dashed lines correspond to the pressure distributions of the UHB engine. The pressure distributions are taken at the same spanwise locations as in the previous section. The pressure ratio of the CFM-56 engine is chosen to $p_t/p_\infty = 2.0$, and the ratio of the UHB engine is 1.71. It can be observed from the figure that on the upper wing surface the differences in the pressure distributions of both engines are negligible. However, on the lower side large differences occur, especially at the inboard region of the pylon. The CFM-56 engine leads to a somewhat higher acceleration at the nose region of the wing, but at midchord the UHB engine causes pressures which are considerably lower than for the CFM-56 engine. This effect is also present at the region outboard from the pylon, but not that strong. At the outermost section the differences between the two engines have almost vanished.

The differences in the pressure distributions also show up in the corresponding lift distributions. As can be seen in **Figure 19**, for the UHB engine a considerable loss of lift occurs in the region around the engine location.

4.2.2 Influence of the Jet

The main reason for these large differences can be found by analyzing the jet influence for the UHB engine. In **Figure 20** pressure distributions for the UHB-configuration with and without jet are compared. Especially inboard of the pylon the displacement of the jet causes a considerable acceleration of the flow, and due to the channel effect that acceleration takes place in the whole region between fuselage and pylon. Outboard of the pylon the flow is also more accelerated, but this effect decays further outboard since there no channel effect exists.

The jet influence becomes clearly visible by a comparison of Mach number distributions on the lower wing surface for a case with and without jet. **Figure 21** shows the corresponding lines of constant Mach number for these cases. For the case with jet a supersonic region is generated at the inboard side of the pylon due to the additional displacement effect of the jet.

In order to explain the reason for the strong jet influence, **Figure 22** displays a cross section through wing and pylon. As for the conventional engine, the Mach number distribution at the pylon location corresponds to the outboard pylon surface. The simulated jet is clearly visible by the concentration of Mach lines at the jet boundaries. The strong influence of the jet for the UHB engine is caused by the fact that the core engine could not be contracted for the wind tunnel model. Therefore the streamlines of the jet are not bend away from the wing. Together with the closer position of the engine to the wing, the jet appears to be very close to the wing. Thus the displacement effect of the jet can cause the strong interference.

5. CONCLUSION

This investigation showed several results obtained by numerical simulation of interference effects: The presence of the engine alone moved the shock upstream and influenced the complete upper surface of the wing. On the lower side of the wing the engine created a channel effect between fuselage and engine and influenced the special streamline pattern of a swept wing. These effects are aggravated by the displacement of the pylon, and the flow is substantially accelerated by the addition of the pylon. Roughly half of the loss in lift due to the propulsion system can be

attributed to the presence of the pylon. The inviscid jet increased the interference effects by its displacement,but for the conventional engine the jet influence was small due to the contraction of the core engine.

The comparison of the conventional engine (CFM-56) and the UHB engine lead to the following results: The differences on the upper wing surface are negligible. On the lower surface the closer position and the larger geometry of the UHB engine caused a stronger interference with a considerable loss of lift with respect to the conventional engine. Furthermore, in case of the UHB engine the displacement effect of the jet had a more severe influence. On the lower surface of the wing a supersonic region was generated.

These investigations show that the propulsion system has a clear 3-D influence on the flow field around the wing. The interference caused by the propulsion system leads to a considerable change for the design point of supercritical wings, and the interference becomes especially relevant if a laminar wing is to be designed with wing-mounted engines.

Acknowledgement

Parts of this work were conducted during a one year tenure of the first author at NASA Langley Research Center. He is indepted to Mr. Manuel Salas for his role in the exchange program between DLR and NASA, and to the many NASA colleagues who provided support throughout the year. Both authors like to thank Dr.-Ing. H. Körner for his fruitful contributions to the discussion of interference effects. This work was in part funded by the BRITE/EURAM program of the EC.

6. References

[1] Eckert, D., Burgsmüller, W. *Simulation und Messung von Triebwerkseinflüssen an einem zweistrahligen Flugzeumodell mit Hilfe von Modelltriebwerken*. DGLR 85-92, 1985.

[2] Henderson, W.P. *Propulsion-Airframe Integration for Commercial and Military Aircraft*. SAE-872411, 1987.

[3] Haberland, C., Sauer, G. *On the Computation of Wing Lift Interferences Caused by High Bypass Engines*. ICAS-86-3.9.1, 1986.

[4] Hebert, L.J., Ponsonby, R.E. *Applications of CFD Technology to the Design of Aircraft Propulsion Systems*. ICAS-90-5.4.1, 1990.

[5] Ecer, A., Spyropoulos, J.T. *Block-Structured Solution of Transonic Flows Around Wing/Body/Pylon/Nacelle Configurations*. AIAA 89-2940, 1989.

[6] Hoheisel, H., Kiock, R., Rossow, C.-C., Ronzheimer, A., Baumert, W., Capdevila, H. *Aspects of Theoretical and Experimental Investigations on Airframe/Engine Integration Problems*. ICAS-90-2.7.3, 1990.

[7] Ronzheimer, A., Rossow, C.-C., Pflug, M. *Untersuchungen zum Interferenzeinfluß von modernen Hochbypass - Antriebskonzepten an einer Flügel-Rumpf Kombination durch Lösung der Eulergleichungen*. DGLR, 1990.

[8] Rill, S., Becker, K. *Simulation of Transonic Inviscid Flow over a Twin Jet Transport Aircraft*. AIAA 91-0025, 1981.

[9] Hoheisel, H. *Zelle-Triebwerk Integration - Aufgabe zukünftiger Verkehrsflugzeugentwicklungen*. DLR Nachrichten, Heft 61, 1990.

[10] Rossow, C.-C. *Berechnung von Strömungsfeldern durch Lösung der Euler-Gleichungen mit einer erweiterten Finite-Volumen Diskretisierungsmethode* DLR FB 89/18, 1989.

[11] Jameson, A., Schmidt, W., Turkel, E. *Numerical Solution of the Euler Equations by Finite Volume Methods Using Runge-Kutta Time Stepping Schemes*. AIAA 81-1259, 1981.

[12] Jameson, A., Baker, T.J. *Solution of the Euler Equations for Complex Configurations*. AIAA Paper 83-1929, 1983.

[13] Jameson, A. *Multigrid Algorithms for Compressible Flow Calculations*. Mechanical and Aerospace Engineering Rept. 1743, Princeton Univ., NJ, text of lecture given at 2nd European Conference on Multigrid Methods, Cologne, FRG, 1985.

[14] Whitfield, D.L., Janus, J.M. *Three-Dimensional Unsteady Euler Equations Solution Using Flux Vector Splitting*. AIAA 84-1552, 1984.

[15] Atkins, H.L. *A Multi-Block Multigrid Method for the Euler and Navier-Stokes Equations for Three-Dimensional Flows*. AIAA 91-101, 1991.

[16] Rossow, C.-C. *Efficient Computation of Inviscid Flows Around Complex Configurations Using a Multi-Block Multigrid Method*. Proceedings of 5th Copper Mountain Conference on Multigrid Methods, Copper Mountain, CO, 1991.

[17] Rossow, C.-C., Ronzheimer, A. *Multi-Block Grid Generation Around Wing-Body-Engine-Pylon Configurations*. Proceedings of 3rd International Conference on Numerical Grid Generation in Computational Fluid Dynamics and related Fields, Barcelona, Spain, 1991.

[18] Küchemann, D., Weber, J. *Aerodynamics of Propulsion*. McGraw-Hill Book Company, Inc., New York, Toronto, London, 1953.

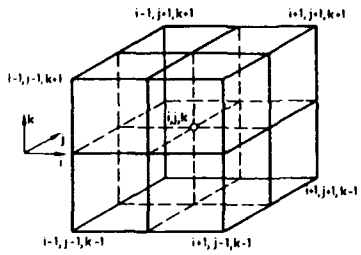

Figure 1: Control volume

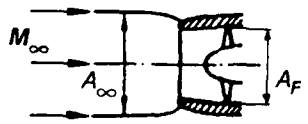

Figure 2: Incoming streamtube

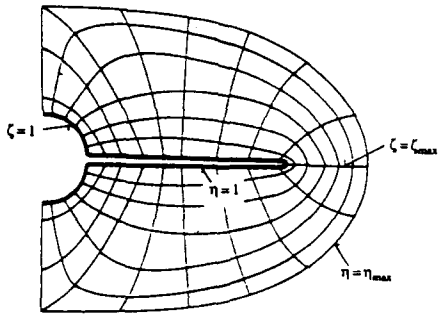

Figure 3: Mesh topology for wing-body combination

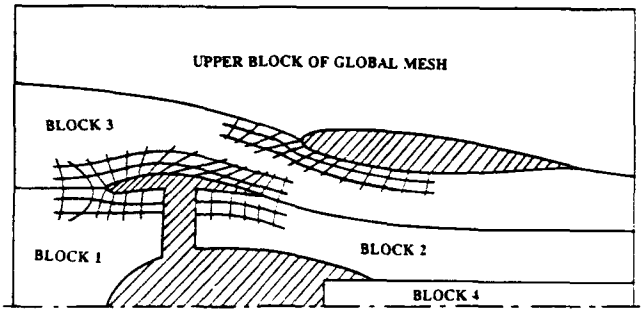

Figure 4a: Streamwise Mesh topology for engine subgrid

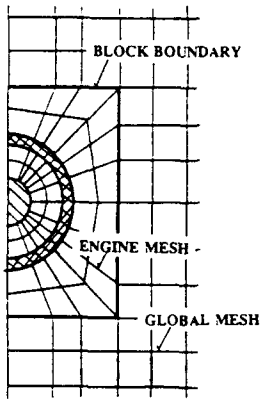

Figure 4b: Topology of embedded subgrid

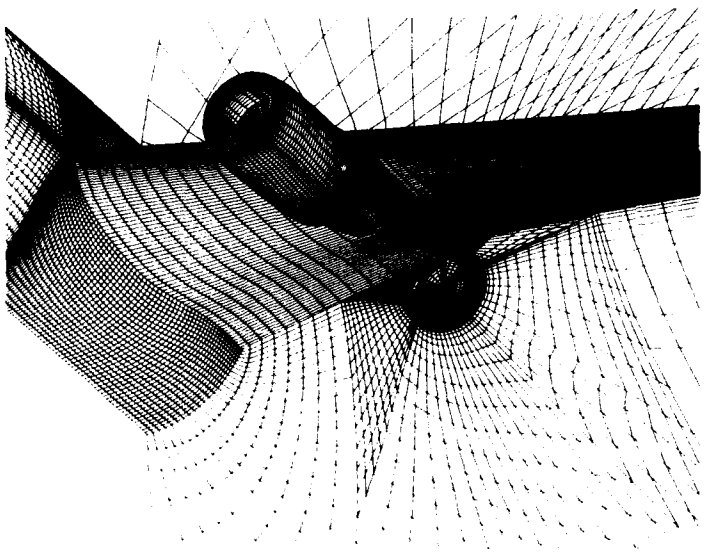

Figure 5: Global grid with embedded subgrid

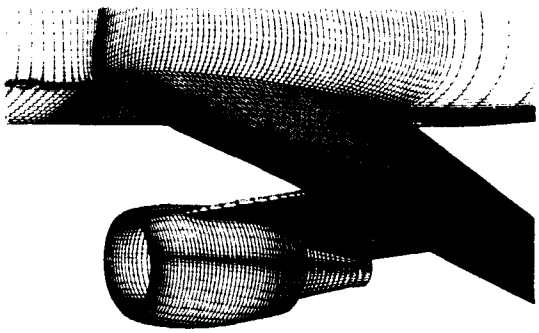

Figure 6: Surface grid with CFM-56 engine

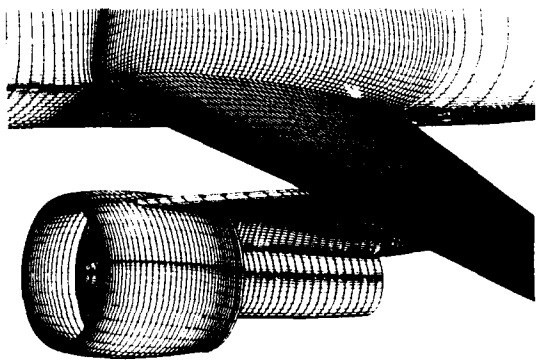

Figure 7: Surface grid with UHB engine

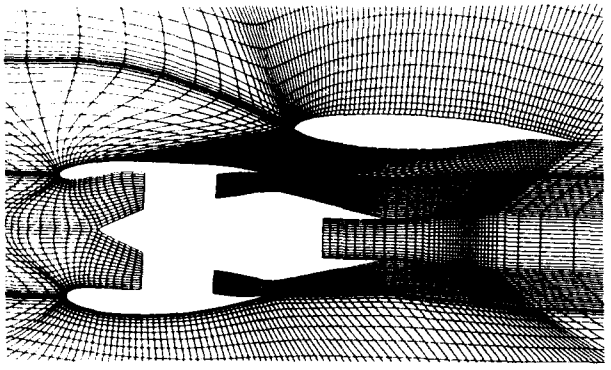

Figure 8: Cross-section of grid with CFM-56 engine

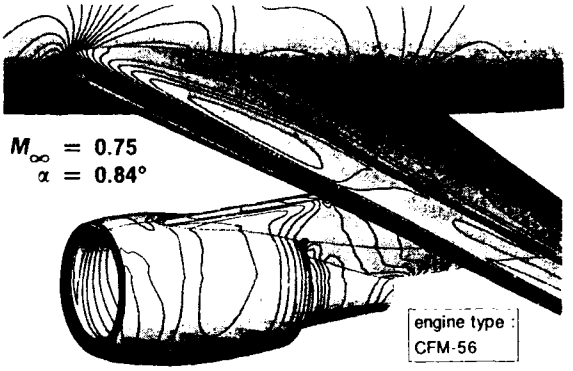

Figure 9: Surface pressure distribution ($\Delta cp = 0.1$)

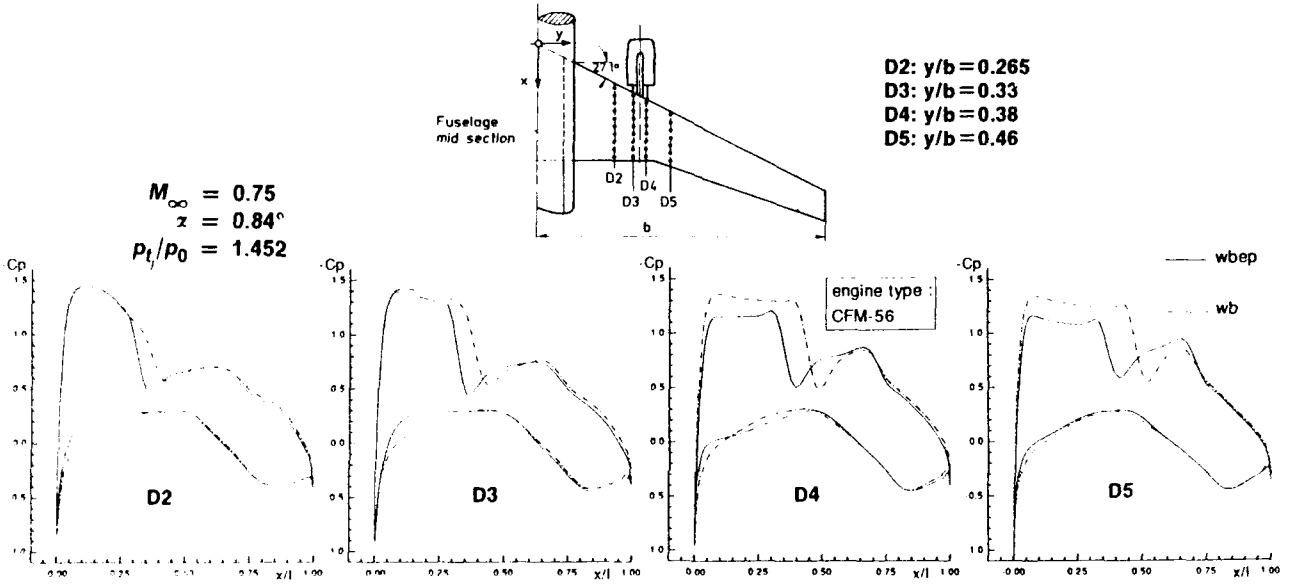

Figure 10: Pressure distributions for wing-body combination with and without CFM-56 engine (Isentropic pressure ratio)

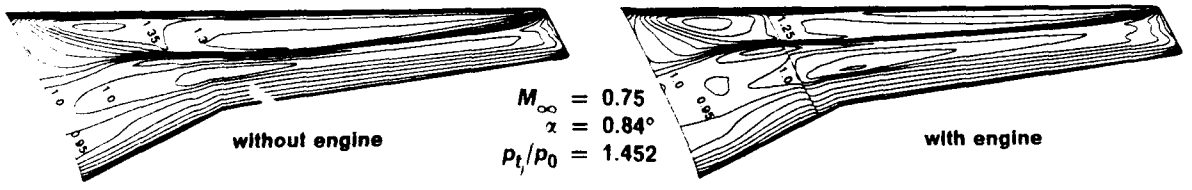

Figure 11: Mach number distribution on upper wing surface with and without CFM-56 engine (Isentropic pressure ratio)

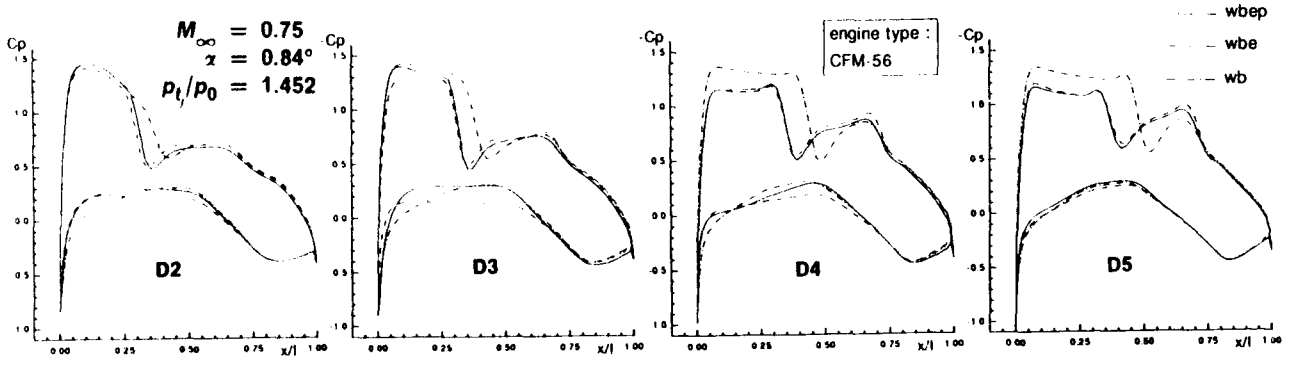

Figure 12: Pylon influence on pressure distribution (Isentropic pressure ratio)

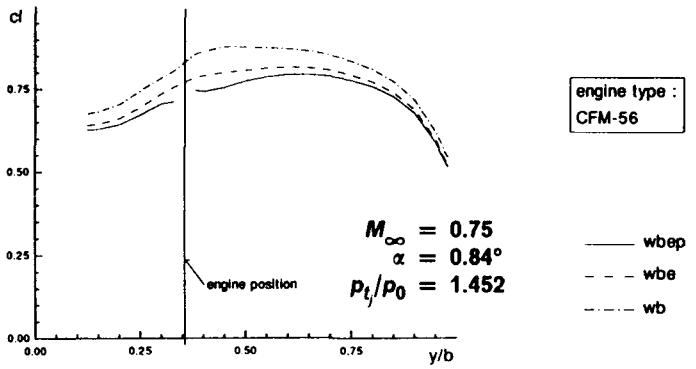

Figure 13: Influence of propulsion system components on lift distribution (Isentropic pressure ratio)

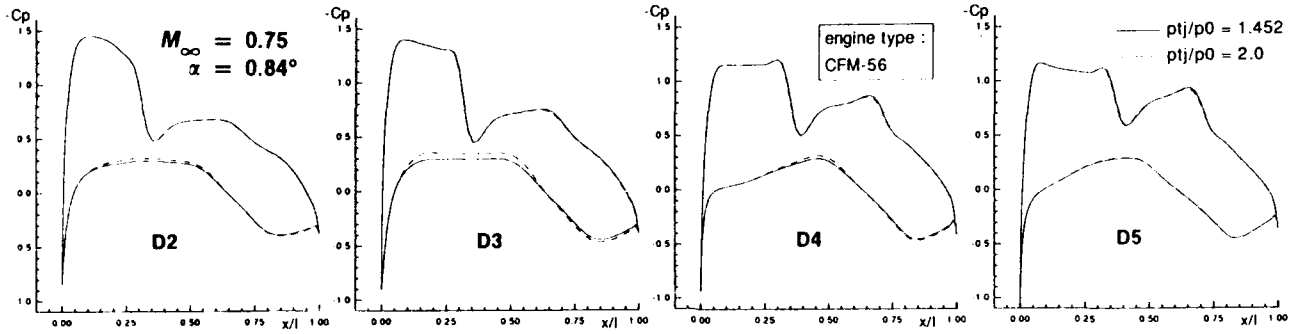

Figure 14: Jet influence on pressure distribution for CFM-56 engine

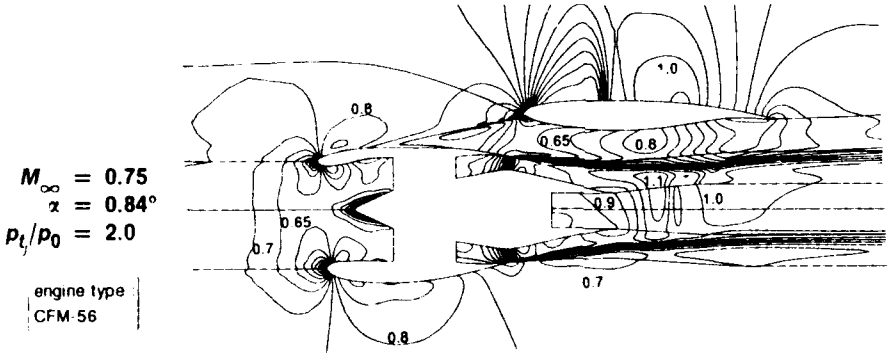

Figure 15: Mach number distribution at pylon location for CFM-56 engine ($\Delta Ma = 0.05$)

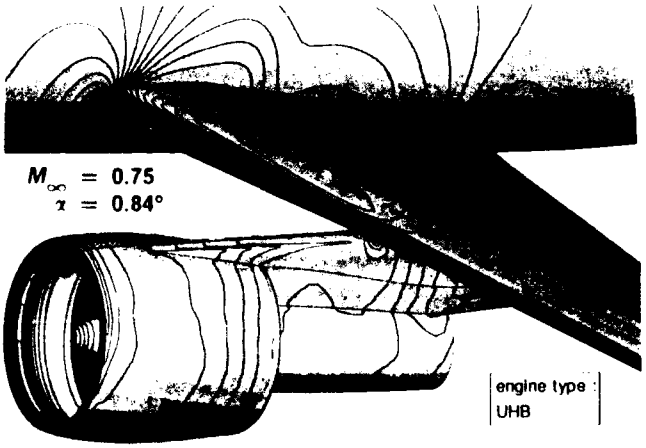

Figure 16: Upper view of surface pressure distribution for UHB engine ($\Delta cp = 0.1$)

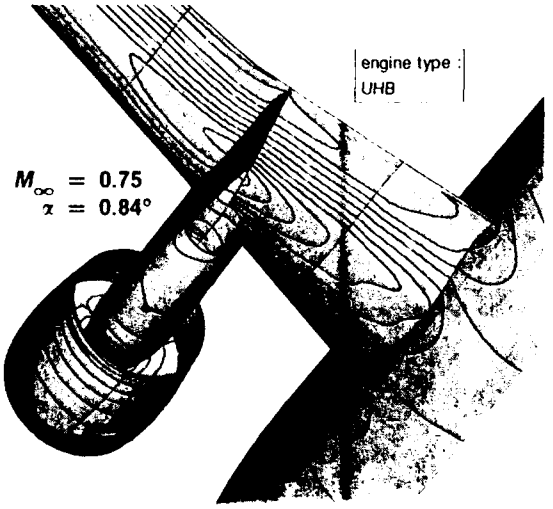

Figure 17: Lower view of surface pressure distribution for UHB engine ($\Delta cp = 0.1$)

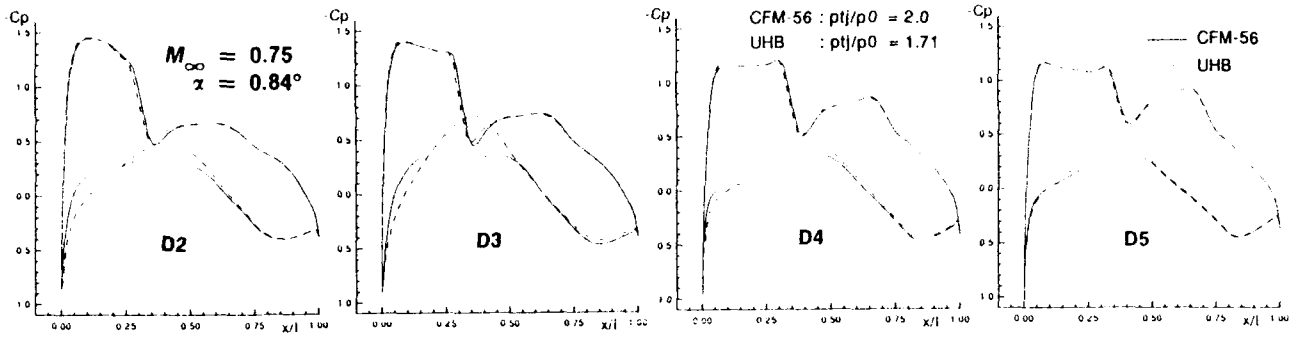

Figure 18: Comparison of pressure distributions for CFM-56 and UHB engine

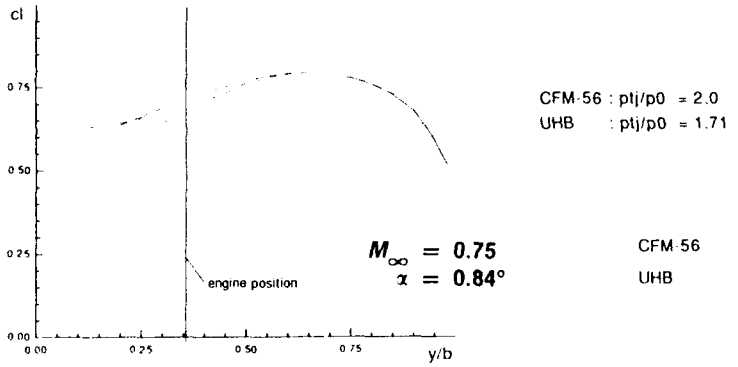

Figure 19: Comparison of lift distributions for CFM-56 and UHB engine

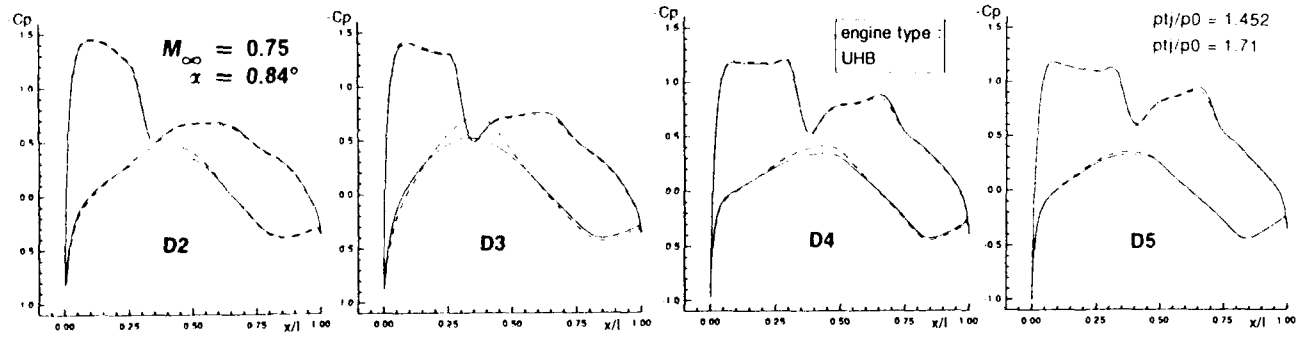

Figure 20: Jet influence on pressure distribution for UHB engine

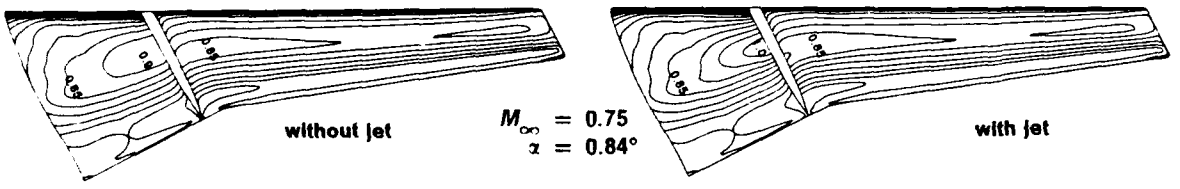

Figure 21: Jet influence on Mach number distribution on lower wing surface for UHB engine ($\Delta Ma = 0.05$)

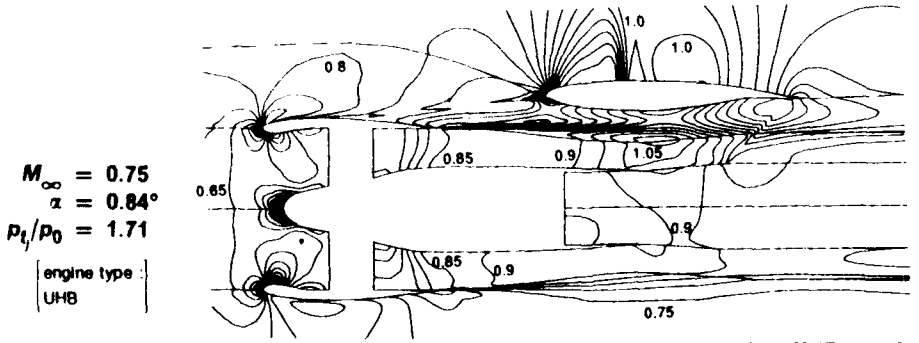

Figure 22: Mach number distribution at pylon location for UHB engine ($\Delta Ma = 0.05$)

AERODYNAMIC ANALYSIS OF SLIPSTREAM/WING/NACELLE INTERFERENCE FOR PRELIMINARY DESIGN OF AIRCRAFT CONFIGURATIONS*

by

C.M. van Beek, W.J. Piers and **B. Oskam**
National Aerospace Laboratory NLR
PO Box 90502
1006 BM Amsterdam
The Netherlands

SUMMARY

A panel method based model for the computation of the time-averaged influence of a propeller slipstream on the aerodynamic characteristics of an aircraft configuration is described.
The slipstream model is based on the simplifications that the single-rotating propeller is replaced by an actuator disk and that all the vorticity of the slipstream is represented on a cylindrical sheet of fixed geometry which envelops the slipstream in combination with a discrete vortex at the axis of the slipstream. Appropriate jump conditions across the actuator disk and boundary conditions on the cylindrical sheet, solved simultaneously with the boundary conditions on the aircraft configuration, yield the mutual influence of the propeller and the slipstream on the aerodynamic characteristics of the aircraft configuration.
This slipstream model is incorporated in a three-dimensional panel method.
Computed lift increments due to the slipstream are presented for a realistic wing/nacelle/fuselage-configuration and compared with wind-tunnel data for several thrust coefficients and angles of attack of the aircraft.

1. INTRODUCTION

The prediction of the influence of the propeller slipstream on the flow around an aircraft is important in all phases of the design of a propeller-driven aircraft, because those parts of the configuration which are affected by the slipstream experience forces and moments quite different from those in the absence of the propeller slipstream. These differences on part of and thus also on the entire configuration for instance directly influence main design criteria, such as the performance and control of the aircraft.
In the preliminary design phase the aerodynamic designer is interested in assessing the influence of the main design parameters, amongst others the location of the propulsion system, on his design in order to fix these parameters for one or a few promising configurations for the next design phase. In the preliminary design phase (semi-) empirical methods and relatively simple numerical methods are at his disposal. Typical results of interest of these methods are forces and moments on parts of and on the entire configuration, the lift distribution on lifting surfaces, etc. rather than detailed information on the flow around the configuration. Panel methods, which area of application is gradually shifting from the detailed to the preliminary design phase, are an important tool in this preliminary design phase. Because of the simplified physics contained in such methods and the associated modest user requirements (no complicated spatial grid required, but only a configuration surface grid), the vast amount of accessible experience gained with panel methods and the relatively modest computer requirements due to the nowadays available and still ever increasing computer power, panel methods are the most widely used numerical aerodynamical techniques throughout the world.
In the detailed design phase the aerodynamic designer is apart from global flow characteristics also interested in detailed flow phenomena, e.g. surface pressure distributions, of the flow around the one or the few configurations which have been proposed during the preliminary design. Apart from experimental techniques (wind-tunnel testing) numerical tools are also available to fulfil the needs of the designer in the detailed design phase.
At NLR an Euler code is available which is used for the analysis of propeller slipstream effects on the aerodynamic characteristics of arbitrary aircraft configurations (Ref.1). This numerical tool consists of :

- block decomposition method to divide the flow domain,
- multi-block grid generator based on algebraic techniques,
- flow solver based on Euler equations.

The time-averaged effect of the propeller is represented as an actuator disk in the flow domain, with continuity of mass flow, but jumps in axial and tangential momentum and a corresponding jump in total enthalpy across the disk. This approach based on Euler equations is validated against test data originating from in-flight pressure measurements on a Fokker-50 turboprop aircraft (see Fig.1 and Ref.2). In general this Euler approach is complementary to the panel method technology presented in this paper.

A slipstream modelling capability in a panel method will thus strongly enhance the preliminary design capability of propeller-driven aircraft. It may be assumed that a time-averaged capability is sufficient to satisfy the needs in this design phase. In the past the first attempts in this direction were made by adding the time-averaged perturbation flow-field resulting from the isolated propeller to the uniform onset flow and considering the resulting flow as the onset flow for the aircraft. The time-averaged perturbation flow-field (if available at all!) was usually derived from wind-tunnel measurements on the isolated propeller or generated by a calculational procedure on the isolated propeller at corresponding conditions (thrust, total pressure increments, etc.). In this most simple model it is assumed that the configuration has a negligible effect on the flow about the propeller and on its slipstream.
This method often yields reasonable results at conditions where no strong interference between

* This investigation has been carried out under contract with the Netherlands Agency for Aerospace Programs (NIVR).

propeller slipstream and configuration is present. However, the results become unsatisfactory in cases of strong interference, e.g. in case of a wing-mounted tractor propeller at higher angle of attack and/or high thrust coefficients. For these cases often the calculated lift force increments due to the slipstream interference were excessively over-estimated. Thus, also at NLR and Fokker, a need arose for a better slipstream capability in the panel method technology. Especially the capability should be able to handle wing/nacelle/slipstream interference problems, because this presents the major interference problem for commercial propeller-driven transport aircraft. Such an improved slipstream capability is the subject of this paper.

In the last decade several researchers reported on work on panel methods for propeller slipstream/aircraft interference. For instance Chandrasekaran and Bartlett (Ref.3) use a set of vortex rings to simulate the slipstream effect on the aircraft configuration, but no mutual influence of the configuration on the propeller and slipstream has been taken into account. The approach of Kirrmann, Rousseau and Yermia (Ref.4) follows the same lines. Clark (Ref.5) describes the slipstream modelling capability in the VSAERO-panel program where mutual influences between propeller slipstream and aircraft configuration are taken into account. The most important aspect of the method is the spatial relaxation procedure for wake and slipstream vortex lines. Smith (Ref.6) shows comparisons of results obtained with the VSAERO-model (and also of an Euler code) with wind-tunnel results for a wing/nacelle/propeller configuration. Valarezo and Hess (Ref.7) report on their panel method for isolated propellers and the time-averaged installation effects of a slipstream on an aircraft. In Ref.8 Valarezo addresses the extension of this method to multiple rotor propellers and in Ref.9 he shows the application of the method to axi-symmetric, shrouded propelier flows. In Ref.10 Clark and Valarezo show results obtained with this panel method for the NASA Langley propeller/wing configuration and a complicated tilt-propeller VSTOL transport configuration. Lötstedt (Ref.11) uses surface vorticity distributions on cylindrical surfaces approximating the spatial vorticity distribution in the slipstream. These vorticity distributions generate the influence of the slipstream at the flow-field around a propeller/nacelle configuration. In Ref.12 he applies his method to two wing/propeller/nacelle configurations.

In the present paper a panel method slipstream model is described which has been incorporated in a panel method for the solution of the subsonic, linearized (Prandtl-Glauert) potential equation. At present the model is restricted to slipstreams of single-rotating propellers, but extension to multiple (counter)-rotating propellers poses no fundamental difficulties. The time-averaged slipstream flow is generated by an actuator disk carrying a radial distribution of vortex lines. The slipstream is enveloped by a surface of more or less cylindrical shape carrying the helically shaped distribution of vortex lines to downstream infinity. The model is completed by a discrete vortex line running from the centre of the actuator disk to downstream infinity. The strengths of the singularity distributions are calculated by applying an appropriate jump condition across the disk and boundary conditions at the cylindrical envelope. The shape and position of the envelope is a priori fixed and thus is to be specified by the user and forms no part of the solution. The parameters defining the operating condition of the propeller are only the mean total pressure jump across the propeller disk and the advance ratio of the propeller. There are no restrictions to the values of the total pressure jump and the advance ratio. Because the singularity strengths on the actuator disk and the envelope are calculated simultaneously with the singularity strengths on the surface and wakes of the aircraft configuration, the mutual interference between propeller, slipstream and aircraft configuration is accounted for.

The first realistic example of application considered with this slipstream model concerns calculations on a Fokker 50 configuration. Calculated results for the lift and the lift increment due to the slipstream are compared with wind-tunnel data for a range of thrust coefficients and angles of attack.

In the next section the background of the mathematical slipstream model is presented. Mathematical aspects are described in section 3, some numerical and user aspects in section 4. The calculated results are presented in section 5. Finally concluding remarks are made in section 6.

2. DESCRIPTION OF THE SLIPSTREAM MODEL

In this section the general idea behind the slipstream model is presented. Firstly a short outline is presented of the panel method in which the slipstream model has been incorporated. Then the relevant results are summarized of a two-dimensional study on lifting surface/slipstream jet interference which provided guidelines for the development of the three-dimensional slipstream model. Afterwards attention is focussed at this three-dimensional slipstream model itself.

2.1 The panel method

The panel method in which the slipstream model is incorporated is a general purpose method for the calculation of subsonic, linearized (Prandtl-Glauert) potential flow about general three-dimensional lifting and non-lifting configurations. For use as a preliminary design tool where the prime interest is in (the distribution of) forces and moments on parts and on the entire configuration rather than in detailed flow phenomena, the lifting surface approximation is used for the lifting components. The linearized boundary condition of zero normal velocity is imposed at a reference surface, e.g. the camber surface, of the lifting components (see Fig.2). Lifting surfaces carry a panelwise quadratic doublet distribution. The wake trailing from a lifting surface can have any user-specified and thus fixed position and shape in space. By choice the doublet distribution on a wake can simply be continued as a constant, equal to the value at the trailing edge, from the trailing edge to downstream infinity (far wake attached to the trailing edge), or can be calculated on the near wake part of the wake by imposing the zero-pressure jump condition across the near wake, i.e. the doublet distribution is relaxed inside a plane of prescribed position and shape allowing the vortex lines to take a force-free location. In that case an approximation to the streamsurface condition on the wake is additionally imposed on the near wake (accompanied by a panelwise linear source distribution). The far wake is now attached to the downstream edge of the near wake.
Bodies can either be modelled by a panelwise constant source distribution or by a quadratic doublet distribution, both on the body surface.

In the former case the normal velocity boundary condition is directly imposed at the external side of the body (Neumann boundary condition), in the latter case in an indirect manner, by setting the perturbation potential equal to zero in the interior of the body (Dirichlet boundary condition). In case of an intersection of a Neumann body with a lifting surface, so-called "lift carry-over" will be applied from the intersection to the body centreline.
No explicit measures have been taken to assure continuity of doublet strength across panel edges, edges of intersecting or abutting lifting surface and body Dirichlet segments.
In a compressible case the doublet distribution on lifting surfaces, its wakes and bodies is accompanied by an associated linear source distribution in order to compensate for the jump in normal velocity across a compressible doublet distribution.

2.2 Results from the two-dimensional study

Prior to the development of the three-dimensional slipstream model some two-dimensional research into the interference effects between a lifting surface and a "two-dimensional" slipstream, i.e. the jet effect, has been carried out. The incompressible problem under consideration consists of a wing, represented by a single bound vortex, located in an initially uniform and thus irrotational jet with twice the velocity ($-U_p$) of the outer flow ($-U_\infty$) (see Fig.3).
The aim of this investigation was to obtain a consistent linearization of the boundary conditions approximating the fully non-linear boundary conditions, i.e. a solution procedure based on surface singularity distributions which uses linearized boundary conditions, on fixed surfaces in order to avoid difficult, spatial relaxation procedures. Because in this two-dimensional study one is interested in the lifting surface/jet interference mechanism, rather than in the actual values of the forces on a real wing, one can approximate its influence by a discrete vortex. The criterion to assess the capabilities of the different proposed solution procedures is the lift increment due to the interference, because this is one of the important issues in the design of propeller-driven aircraft.
In the basic solution the lift force on the lifting surface results from the assumption that the lifting surface is placed in an unbounded uniform flow with velocity U_p ("perturbation flow-field" approach).
In the non-linear (NL) situation the flow-field is calculated by using a vorticity distribution at the two boundaries of the jet in order to generate the velocity in the jet. The position of the jet boundaries and the strength of the vorticity distribution are calculated by applying the condition that the jet boundaries are force-free and form streamlines, i.e. applying the non-linear zero-pressure jump condition across the boundaries, and the zero-normal velocity condition at the boundaries.
In the first linearized (LN1) situation only the linearized zero-pressure jump condition is applied at the fixed, straight jet boundaries in order to calculate the vorticity distribution.
In the second linearized (LN2) situation both the linearized zero-pressure jump and a linearized, composite form of the zero-normal velocity conditions at both sides of the jet boundaries are applied at the fixed, straight jet boundaries. The latter condition implies the parallelism of the velocity vector inside and outside the jet (see Fig.3). A source distribution at the jet boundaries is added to the vorticity distribution in order to satisfy both boundary conditions.

The lift increments of the basic model and the LN1-, LN2- and NL-model are compared in Fig. 4, as a function of the thrust coefficient T_c. The basic model predicts a lift increment which is 200 percent higher than the lift increment of the NL-model for a representative test case as shown in Fig. 4. The LN2-model overpredicts the lift increment by approximately 40 percent. Further analysis has shown that the LN2-model is a consistent approximation of the NL-model for small lift coefficients (first order in the lift). It has therefore been concluded that both boundary conditions, as in the LN2-model, are required in order to obtain a consistent approximation to the solution of the slipstream/lift interference. For 3D slipstream/lift interference problems the results of the 3D implementation of the LN2-model are expected to be substantially more accurate than the results of the 2D model shown in Fig. 4.

2.3 The slipstream model

Main differences between propeller/slipstream flow and "ordinary" flow around an aircraft configuration as handled by panel method technology are the inherent unsteady nature of propeller flow and the vortical type of flow inside the slipstream. Because the interest is in time-averaged interference effects between slipstream and aircraft configuration, the first point is simply circumvented by considering only these time-averaged effects. The classical propeller/slipstream model (Ref.13) then replaces the finite number of propeller blades by an infinite number of blades (actuator disk model, see Fig.5). This implies that also the slipstream consists of an infinite number of helical vortex wakes, i.e. the entire space in the slipstream is filled with vorticity. This would imply a continuous field distribution of vorticity. Although this is in principle possible in (field) panel method technology, this is not appropriate for the preliminary design purpose of the model. Therefore it is assumed that the "wake" rolls up immediately downstream of the propeller blades and it is allowed to concentrate the vorticity of the slipstream in an infinitesimal thin layer (vortex sheet) enveloping the slipstream (see Fig.5). The sheet is attached to the tip edge of the actuator disk and extends to downstream infinity. A physical argument to justify the thin sheet model for a slipstream is that in reality at relatively short distance behind the propeller most of the vorticity inside the slipstream is indeed concentrated near the outer edge region of the slipstream. Actually, the enveloping sheet can be thought of as a wake of a wing, but of cylindrical shape and closed in itself and enclosing a region with a different level of the energy of the flow.
The representation of the position and the shape of the envelope is fixed (by the user of the program), no relaxation with relation to its position will take place in order to obtain the force-free, streamsurface position of the envelope.

In the present model the actuator disk has to generate the jump in circumferential velocity and, only in the compressible case, in axial velocity across the disk. The radial velocity is assumed to be continuous across the disk. In panel method technology these jump characteristics will be generated by a vorticity distribution for the circumferential jump (vortex lines directed in radial direction) and a source distribution for the axial jump (see Fig.5). Use of such a vorticity model implies that this vorticity distribution has to be extended to downstream infinity at both the tip side and at the axis side. Therefore the vorticity distribution

is continued across the tip edge onto the cylindrical enveloping sheet and at the axis side the distributed vorticity is concentrated in a discrete line vortex extending also to downstream infinity (see Fig.5). The location of the line vortex is not strictly defined, because in the present model the line vortex is not subjected to any boundary condition, but should of course be at or near the centreline of the slipstream and in such a way that undesirable interference with parts of the configuration inside the slipstream, e.g. a nacelle or a lifting surface, is avoided.
The present method employs associated surface doublet distributions rather than the surface vorticity distributions, because of the advantage of automatically satisfying Helmholtz vortex theorem. This implies that a sheet of constant doublet strength (no distributed vorticity, only discrete vortices at the edges) is required to avoid discrete vortices at physically undesirable locations on actuator disk and envelope. This sheet connects the envelope to the axis vortex and runs from actuator disk to downstream infinity (see Fig.5), thereby "removing" discrete vortices along the intersection with the actuator disk and the envelope. In this way it resembles the "lift carry-over" concept for wing/(Neumann) body configurations. It is actually the same "membrane" as used in the VSAERO-propeller model (Refs. 5 and 6).
The vorticity at the envelope and the axis vortex have to generate the characteristic slipstream flow-field, i.e. both the axially oriented jet effect and the circumferentially oriented swirl effect. This renders the vorticity distribution at the envelope its characteristic helical shape (see Fig.5).

Conform the conclusion concerning the required boundary conditions at the slipstream boundary drawn in the previous section both the conditions for a force-free streamsurface, i.e the zero-pressure jump condition and a combined form of the zero-normal velocity conditions are applied at the envelope in order to calculate the doublet and source distribution on the sheet. So the relaxation of the distributed vortex lines within a fixed surface is accounted for

At a certain (user-specified) distance behind the propeller, wherefrom the influence of the precise details of the slipstream is assumed to be of little importance for the flow-field around the configuration, the enveloping sheet is continued to downstream infinity as a cylindrical envelope (see Fig.5). No boundary conditions are imposed on this far wake slipstream, the vortex lines are spiralling downstream at a constant helix angle and the source strength is constant in downstream direction.

An important aspect concerns the interference between the slipstream and the aircraft configuration, i.e the wing/nacelle/slipstream interference for propeller-driven transport aircraft. Usually the nacelle will be located entirely inside the slipstream and thus poses no special problem. The nacelle is modelled as a "Neumann"-body using a source distribution on its surface. The discrete vortex at the slipstream axis is then placed inside the nacelle to obtain the best results in analogy with the so-called "lift carry-over" modelling for wing/Neumann-body configurations (see Fig.6).
For the lifting surface/slipstream intersection the division of the lifting surface and envelope in different segments has to reflect the load distribution on the lifting surface. The typical load distribution is sketched in Fig.6. Discontinuities in the slope occur at both lifting surface/envelope intersections and a very strong gradient occurs near the axis of the slipstream. The latter is dependent on the distance d of the discrete vortex to the lifting surface; this distance may even be zero in which case the largest gradient occurs. The load (doublet) distribution is assumed to be continuous and smoothly (panelwise quadratically) varying over a segment. Thus a discontinuity in the slope can only occur at a segment edge and also a large gradient can not be properly handled by the present doublet distribution on a segment. Therefore the lifting surface is accordingly subdivided into different segments. Also the actuator disk/enveloping sheet is appropriately subdivided into different segments in circumferential direction in order to account for discontinuities in the derivative in circumferential direction of the doublet distribution on the sheet.

Because the combined aircraft configuration/propeller slipstream flow problem is solved simultaneously, interference effects are automatically and consistently taken into account.
Once the singularity distributions on aircraft configuration and propeller/slipstream envelope have been calculated, velocity and pressure distribution can be computed and also the forces and moments on the configuration by integration of the pressure over the configuration.

3. MATHEMATICAL ASPECTS OF THE SLIPSTREAM MODEL

In this section the mathematical expressions underlying the key features which are specific for the slipstream model are presented.
The flow equation to be solved is the Prandtl-Glauert equation for the linearized potential flow (perturbation velocities are small of $O(\varepsilon)$). In a Cartesian coordinate system with the x-axis close to the direction of the free-stream velocity $\vec{U}_\infty$ this equation reads:

$$(1-M_\infty^2)\,\varphi_{xx} + \varphi_{yy} + \varphi_{zz} = 0 \qquad (1)$$

where M_∞ is the free-stream Mach number and φ the perturbation velocity potential. In case of incompressible flow (M_∞=o) the equation reduces to the Laplace equation; in this case no assumption is required with relation to the magnitude of the perturbation velocities.
The equation for the conservation of total enthalpy along streamlines reads:

$$\frac{\gamma}{\gamma-1}\,\frac{p}{\rho} + \frac{1}{2}\,\vec{v}.\vec{v} = \text{constant} + \Delta H \qquad (2)$$

where γ is the ratio of the specific heats, p the pressure, ρ the density and $\vec{v}$ the total velocity vector. The total enthalpy increment ΔH applies only to the flow-field inside the slipstream; its meaning is the energy increment of a flow particle added by the propeller at the time the flow particle is passing through the disk. Eq.(2) may also be applied in the coordinate system co-rotating with the propeller. Because of the constant angular velocity Ω of the propeller blades, pressure and density are invariant under this coordinate transformation and the total enthalpy increment ΔH is zero, because in the co-rotating coordinate system the propeller does not perform work. Combining the energy equations in both coordinate systems results in the following expression for the total enthalpy increment:

$$\Delta H(\theta,r) = \Omega\, r\, (v_{t_2}(\theta,r) - v_{t_1}(\theta,r)) \qquad (3)$$

where r is the radial distance from the propeller

axis (see Fig.7) and v_{t_1} and v_{t_2} are the circumferential velocity components just in front of and behind the disk respectively.
Applying the equation of conservation of mass just in front of and behind the actuator disk together with the conservation of mass through the disk yields as non-singular solution for the doublet strength μ at the actuator disk:

$$\mu(\theta, r) = \text{constant} * \theta \qquad (4)$$

where θ is the circumferential angle starting and ending at the intersection with the membrane (see Fig.7). Comparing the circumferential velocity jump resulting from Eqs.(3) and (4) yields:

$$\mu = \frac{\Delta H}{\Omega}\,\theta \qquad (5)$$

In terms of the associated vorticity distribution this yields the desired distribution of radially running distributed vortex lines of constant strength. Another implication is that the total enthalpy increase has to be constant over the entire actuator disk in order to obtain the non-singular solution for the doublet strength. Also the (unrealistic) radial loading distribution is fixed by this type of doublet distribution. The propeller operation is now completely fixed by the mean total enthalpy (total pressure) jump across the actuator disk and the angular velocity of the propeller blades (i.e. the advance ratio) which are the only two parameters to be specified by the user.
The strength of the discrete vortex at the axis of the slipstream is thus:

$$\Gamma_{axis} = 2\pi\,\frac{\Delta H}{\Omega} \qquad (6)$$

Accordingly the doublet strength on the membrane is also given by Eq.(6).

The two boundary conditions on the slipstream envelope are the zero-pressure jump condition and an approximate form of the streamsurface condition.
Equating the pressure at the inside and outside of the envelope yields as first condition to be applied at the cylindrical envelope (the incompressible equation is presented for shortness' sake):

$$(\vec{U}_\infty + \vec{u}_m^P)\ .\ (\vec{\nabla}\mu - q\vec{e}_n) = \Delta H \qquad (7)$$

where $\vec{u}_m^P$ is the mean (Cauchy Principal) velocity induced at the envelope by all singularities on the configuration and propeller/slipstream, $\vec{\nabla}\mu$ the gradient of the doublet strength at the envelope, q the source strength at the envelope and $\vec{e}_n$ the normal vector at the envelope (see Fig.8).
Because no restrictions are imposed on the magnitude of the perturbation velocity in the incompressible case, the corresponding boundary condition has not been linearized and has consequently to be solved for in an iterative manner.
If q is taken zero in Eq.(7) the driving force behind the slipstream becomes clear. It states namely that the vorticity lines on the slipstream envelope are not parallel to the mean total velocity tangential to the envelope, as would be the case at the wake of a wing, but there is a difference in direction. The angle between vorticity lines and velocity is defined by the total enthalpy increment ΔH. This renders the vorticity distribution its helical shape.

The streamsurface condition implies zero-normal velocity at both sides of the envelope. In order to exactly satisfy these two normal velocity equations one has to relax the position and shape of the geometry of the envelope. To avoid this difficult and computer time consuming task, both conditions are replaced by a combined one and this condition is applied at the fixed geometry of the enveloping sheet. Conform to the condition of parallelism of the velocity vectors at the inner and outer side of the slipstream boundary in the two-dimensional study (section 2.2), also in the three-dimensional case a parallelism condition has been postulated. It states that the components of the velocity vectors at the inner and outer side of the envelope, which are the projections onto a plane normal to the envelope, are parallel (see Fig.8). This plane normal to the envelope is constituted by the vector normal to the sheet $\vec{e}_n$ and the vector in the far wake direction of the sheet $\vec{e}_w$, usually the direction of the x-axis. So the non-linear boundary condition reads:

$$\frac{V_{r_i}}{V_{a_i}} = \frac{V_{r_o}}{V_{a_o}} \qquad (8)$$

where the indices r and a refer to the radial and axial directions respectively and the indices i and o to the inner and outer side of the envelope. Eq.(8) results in the following, non-linear expression for the doublet and source distribution (again the incompressible equation is presented):

$$\left[\,(\vec{U}_\infty + \vec{u}_m^P) \times (\vec{\nabla}\mu - q\vec{e}_n)\,\right].\vec{e}_t = 0 \qquad (9)$$

where $\vec{e}_t$ is the vector normal to $\vec{e}_n$ and $\vec{e}_w$.
The Eqs.(7) and (9) are also the two boundary conditions on the wake of a wing which are applied if one chooses to relax the doublet distribution within the fixed geometry of the wake. Only the total enthalpy increment ΔH equals zero in Eq.(7) in that case, because the total enthalpy level is equal at both sides of the wake of a wing, clearly if the wake is located outside a propeller slipstream, but also if the wake is inside the slipstream where the total enthaipy level is different from outside, but constant throughout the slipstream.

4. NUMERICAL AND USER ASPECTS OF THE SLIPSTREAM MODEL

In this section some numerical and associated user aspects concerning specific slipstream features will be discussed.
The geometric input of the slipstream for the panel method is virtually equal to the input for a lifting surface segment, see Fig.9. The actuator disk/envelope consists of one segment or, in case intersections with lifting surfaces are present, it is divided in circumferential direction in two or more segments. In the latter case the lifting surface should also be split into different segments at the slipstream/lifting surface intersection, as described in section 2.3.
The actuator disk is defined by radially oriented contours, running from axis or spinner surface to the tip edge of the disk, each consisting of a number of discrete points (like the chordwise definition of a lifting surface). Each contourline is continued onto the enveloping sheet in streamwise direction for some, user-specified, extent; this constitutes the near wake part of

the cylindrical envelope. A far wake is automatically attached to the near wake.
The discrete axis vortex is usually located at the centreline of the slipstream. In case of the presence of a nacelle the position of the vortex is kept at the centreline of the slipstream, inside the nacelle, conform to the "lift carry-over" modelling concept for wing/fuselage configurations (see section 2.3). In case of intersection with a lifting surface one has to take care that the lifting surface is split into two segments near the slipstream centreline, if the distance between surface and vortex is small, or even zero (i.e. vortex on the lifting surface), in order to be able to approximate the resulting load distribution on the lifting surface near the centreline. In case of a larger distance the entire part of the lifting surface inside the slipstream may be represented by one segment.
A "membrane" has to be specified between envelope and axis vortex. It may be attached to the envelope at any circumferential position. In the method a "membrane" segment is treated like a "lift carry-over" segment.
As is usual in panel methods at intersecting geometry parts, the panel distributions on lifting surface, its wake, slipstream envelope and "membrane" should be adapted to each other, especially in chordwise direction, in order to obtain regular panel distributions and optimal results.
The geometrical representation of the cylindrical envelope has to be defined a priori by the user and it puts the same type of problem to the user as for example the specification of the wake of a wing. Points of concern are the position and shape of the envelope, contraction of the slipstream, intersection with a lifting surface and its wake.
As parameters for the specification of the propeller operation the total enthalpy increase across the disk and the advance ratio have to be specified. The first parameter is also required for those aircraft configuration components which are located inside the slipstream (nacelle, part of the lifting surface concerned). As total enthalpy increase the single value obtained by averaging over the entire circular actuator disk surface is used, see also section 3. The distribution of the total enthalpy increase across the real propeller usually results from wind-tunnel measurements or propeller performance calculations on the isolated propeller.

5. CALCULATED RESULTS

As the first application of the slipstream model in order to investigate the capability of the method to predict aircraft/propeller slipstream interference effects an effort has been started to perform calculations on the Fokker 50 aircraft and to compare the results with available wind-tunnel data. This experiment has been chosen for validation of the method, because it concerns a complex, three-dimensional configuration and, apart from an obvious interest in this aircraft, it has been performed at a low Mach number which makes it amenable to the panel method calculations. Further the geometry, flow conditions and some results were easily accessible to the authors.
The main objective of the present calculations is the influence of the interference on the entire configuration, i.e. the difference in performance of the aircraft between the propeller-on and -off cases.

In the design phase of the Fokker 50 aircraft extensive wind-tunnel measurements have been performed on different configuration layouts in the German Dutch wind-tunnel DNW. The configuration for which the calculations have been performed is a wing/fuselage/nacelle configuration with two installed co-rotating model propellers, right-turning as seen in the upstream direction. No horizontal and vertical tail surfaces were present. The model was supported by three vertical struts which were mounted on the wind-tunnel floor and supported the model underneath both wings and the aft part of the fuselage respectively (see Fig.10). The aft strut was able to move vertically in order to adjust the angle of attack of the model.
In all measurements considered the wing flaps were not deflected, the angle of side-slip was zero degrees and the free-stream Mach number ranged from 0.11 to 0.21. The measurements of interest have been performed at a full matrix of angle of attack, ranging from -4 to 16 degrees, and thrust coefficients, ranging from 0.0 to 2.5. The thrust coefficient T_C is defined in the experiment as:

$$T_C = \frac{T}{\frac{1}{2}\rho_\infty U_\infty^2 \pi R_{tip}^2} \qquad (10)$$

where T refers to the thrust, ρ_∞ and U_∞ to the free-stream values of density and velocity, and R_{tip} to the tip radius of the propeller. This corresponds to a total (free-stream U_∞ plus slipstream induced) mean axial velocity in the slipstream far downstream of the propeller of approximately $v_{ax} = 1.23*U_\infty$ at $T_C = 0.5$ and $v_{ax} = 1.90*U_\infty$ at $T_C = 2.5$. The no-thrust case $T_C=0$ is the situation with installed propellers which generate no thrust.
The results of the experiments consisted of total forces and moments on the entire configuration including propellers. Here we will consider the lift force data only. These data have been corrected for wind tunnel wall interference and support interference in order to obtain interference-free data. These interference effects are known to be large in this experiment. A main source of interference were the supporting struts which turned out to be not optimally shaped (occurrence of flow separation). For these reasons there is some uncertainty about the quality of the corrected wind-tunnel data.

The calculations have been performed for the interference-free situation, i.e. wind-tunnel walls and support have not been taken into account. Also starboard/port-side symmetry has been assumed in the calculations which implies contra-rotating instead of co-rotating propellers.
A set of discrete points has been generated at the surface of the starboard configuration as geometrical input for the panel method. These points constitute the panel network used in the calculations on the lifting surface/fuselage/nacelle/propeller configuration, see Fig.11 for a top view of the configuration. The fuselage and nacelle are modelled as body Neumann configuration parts. Because slipstream/aircraft lift force interference is mainly restricted to the wing, the panel distribution on the wing (lifting surface) and the slipstream envelope will be of prime importance in the prediction of the interference effects. The starboard lifting surface has been divided in 21 spanwise strips of almost equal width and in 36 chordwise panels according to a cosine distribution with a refined panel distribution near the leading edge. Especially the chordwise distribution is rather coarse. A limited convergence study for the lifting surface alone indicated that in chordwise direction a far

more dense distribution is required to obtain converged results in terms of lift and drag. But above all, the present panel distribution means that only four strips, two on both sides of the wing/nacelle intersection, are located inside the slipstream. The near wake of the lifting surface, on which the zero-pressure jump and approximate streamsurface condition are imposed, extends from the trailing edge, fuselage and nacelle conforming, along straight horizontal lines downstream to the axial station just downstream of the endpoint of the fuselage.
The starboard, right-turning as seen in the upstream direction, propeller/slipstream consists in circumferential direction of 14 strips (see Fig.12). The actuator disk is located in the plane of the propeller at the exact downward and outward angle and with the radius equal to the tip radius of the actual propeller. The streamwise panel distribution on the envelope is adapted to the lifting surface and wake panel distribution and extends to the trailing edge of the near wake. The shape of the envelope is slightly and linearly contracting between the actuator disk and the leading edge of the lifting surface. It continues as a straight circular cylinder with a diameter which is estimated from the T_C=0.5 condition and with its axis being a straight horizontal line. Because the lifting surface is intersecting the slipstream almost through its centreline, the axis vortex of the slipstream is located on the lifting surface and its wake, see Fig.12. The sheet of constant doublet strength (membrane) connecting the axis vortex to the envelope is attached to the upper side of the envelope.
The calculations for all angles of attack and thrust coefficients have been performed with one and the same position and shape of the wake of the lifting surface and the slipstream envelope. No attempts have been made to adapt the position and shape to each individual flow condition.
The total number of panels on half the configuration, including actuator disk, lifting surface near wake and slipstream envelope amounts to 2900. Taking into account both the unknown doublet and source distribution on the wake and slipstream envelope, the number of unknown singularity parameters to be solved for amounts to 3978 on half the configuration.
Because sufficient data were available from the wind-tunnel experiment it is possible to derive an analytical expression for the mean total enthalpy (total pressure) jump required for the present computational model. Assuming incompressible flow through an isolated actuator disk with the free-stream velocity normal to the propeller disk, it follows from integrating Eq.(2) over the actuator disk and using Eqs.(3) and (10):

$$\frac{\Delta H}{U_\infty^2} = \pi \frac{S_{prop} - \sqrt{S_{prop}^2 - 2\,T_C\,J^2\,R_{tip}^4 \ln \frac{R_{tip}}{R_{sp}}}}{2\,J^2\,R_{tip}^2 \ln \frac{R_{tip}}{R_{sp}}} \qquad (11)$$

where $S_{prop} = \pi(R_{tip}^2 - R_{sp}^2)$ is the area of the actuator disk, see Fig.12, and the advance ratio J is defined as:

$$J = \frac{U_\infty}{2\,n\,R_{tip}} \qquad (12)$$

where n is the rotational speed of the propeller (rotations per second). The values of J for all values of T_C have been obtained by wind-tunnel experiments on the isolated propeller, at the same values of U_∞ as used at the wind-tunnel tests on the Fokker 50 configuration. The associated values for ΔH then follow from Eq.(11).
The no-thrust case T_C=0 in the calculations refers to the configuration without actuator disk/slipstream envelope segments.
The calculations have been performed at the NEC SX-3 supercomputer of NLR.

In Fig.13 the calculated spanwise lift distribution is shown at a constant value of the thrust coefficient T_C=1.0 and for a range of angles of attack.
The lift on the segment of the lifting surface between fuselage and propeller slipstream is increased for all angles of attack compared to the no-thrust situation. This can be attributed by some kind of "tunnel" effect: like the fuselage, the slipstream envelope acts like a solid surface for the flow between fuselage and envelope, because of its approximate streamsurface condition; this displacement effect results in higher velocities of the flow in this region.
On the upwash flow side of the slipstream the lift on the lifting surface is strongly increased with regard to the prop-off case. This is due to the increased total upwash at the lifting surface caused by the slipstream upwash flowfield and because of the increased magnitude of the local oncoming flow vector. The latter can mainly be attributed to the axial jet effect.
On the downwash flow side of the slipstream the lift force on the lifting surface is decreased compared to the prop-off case at the lower angles of attack, but increased at the higher angles of attack. This is due to the now opposite effects of the downwash induced by the slipstream and the increased flow vector magnitude resulting from the jet effect. At an angle of attack of approximately 7 degrees both effects compensate each other, at lower angles of attack the slipstream induced decrease of angle of attack is relatively important compared to the configuration angle of attack and exceeds the axial jet effect, at higher angles of attack it is relatively less important and it is exceeded by the jet effect.
The lift force distribution on the outer part of the lifting surface outside the slipstream is, especially at the higher angles of attack, hardly affected. Mainly at the lower angles of attack there is some difference, because the approximate streamsurface condition on the slipstream envelope changes the flow about the part of the lifting surface outside and near the slipstream.

In Fig.14 the calculated spanwise lift distribution is shown for a constant angle of attack of 4 degrees and at varying thrust coefficient.
The amplifying effects of increasing local angle of attack and increasing axial jet effect with increasing T_C result in the strongly increasing lift distribution on the upwash side of the slipstream.
On the downwash side the opposite effects of decreased local angle of attack and jet effect almost compensate each other for all thrust coefficients.

In Fig.15 the lift on the entire configuration, including the component of the force in lift direction on the propellers, is presented as a function of the angle of attack and for a number of thrust coefficients. Shown are both the calculated and the experimental results obtained from the DNW-measurements, which have been corrected for wind-tunnel wall and support interference. At T_C=1.75 no corrected experimental data are available. For clearness' sake the curves for the propeller-on situation have been shifted upwards over the respective increment as indicated in the figure. To get an impression of the magnitude of

the corrections applied to the experimental data, the uncorrected data at T_c=0 have also been presented.
For the T_c=0 situation agreement between calculated and experimental results is reasonable at the lower angles of attack, but the experimental results show a slightly smaller slope of the lift curve compared to the calculated results. Because the thin lifting surface theory used in the calculations is known to usually provide correct lift slopes due to the cancelling effects of viscosity and wing thickness, the discrepancy in lift slope might be a result of insufficient correction of the experimental data as is suggested by the still smaller slope of the uncorrected data.
Also for the prop-on conditions the calculated lift slopes are larger than the corrected experimental ones. For increasing thrust coefficient the calculated lift coefficients tend to increasingly overpredict the experimental values.

This tendency can also be observed in Fig.16. Here the increment in lift force due to the propeller/slipstream is presented as a function of the thrust coefficient for a number of angles of attack for the same corrected experiments and calculations as of Fig.15. The increment is defined as the lift force on the entire configuration, including the propellers, minus the lift force at T_c=0 for the same angle of attack.
Comparison of results shows that at T_c=0.5 the calculated lift increments are more closely situated than the experimental values. At α=-4° the calculated lift increment is larger than the experimental one, at α=0° almost equal and at increasing angle of attack the calculated lift increments are increasingly smaller than the experimental increments. All calculated curves feature a larger slope compared to the slope of the experimental curves. This results in an overrating of the calculated lift increments compared to the experimental ones at T_c=2.5 for all angles of attack.

At this moment the following conclusions on the calculated lift force results can be drawn.
For the experimental results the accuracy of the corrections which have been applied for wind-tunnel wall and support interference is questionable, because it is known that these interference effects are large. Alternatively it should be possible to perform the calculations on the configuration including the walls and support in order to make a direct and consistent comparison between experimental and computational results. The inherent more complex configuration poses no problem to the panel method which requires only surface panel networks.
In the calculations starboard/port-side symmetry has been assumed which effectively implies contra-rotating instead of the co-rotating propellers which are present in reality and in the experiments. Co-rotating propellers will severely affect the symmetry of the flow-field. Also the panel distribution on the configuration is not adequate to accurate calculations. Particularly the spanwise panel distribution at the part of the lifting surface which is affected by the slipstream is far too coarse and also the chordwise distribution should be refined on the entire lifting surface.

Finally it has been investigated which parts of the configuration are responsible for the lift force increase shown in Fig.16. The build-up of this increase has been determined for an angle of attack of 4 deg and it is presented in Fig.17 as a function of the thrust coefficient. The figure presents the accumulated contributions of the different parts of the configuration to the slipstream induced lift increment. The upper line is thus the contribution of the entire configuration which is already shown in Fig.16.
Clearly all parts of the configuration, fuselage, nacelle, lifting surface and actuator disk add a positive increment to the total. As remarked earlier on the spanwise lift force distribution on the lifting surface, the presence of the propeller and slipstream also influences the flowfield outside the slipstream. The contribution of the entire lifting surface amounts to approximately 47% of the total lift force increment for all values of T_c, the part of it affected by the slipstream approximately 39%. The contribution of the lifting surface has been split into the contributions from both parts located outside the slipstream and the upwash and downwash part inside the slipstream. The largest contribution is due to the upwash part of the lifting surface inside the slipstream, as already can be seen in the spanwise lift force distribution shown in Fig.14. The part between fuselage and slipstream adds also a positive contribution, while the downwash part inside the slipstream and the outer part outside the slipstream both add a small, negative increment at this angle of attack (shaded areas in Fig.17). This is also in agreement with the lift distribution in Fig.14. The actuator disk adds a positive increment which is in fact the component of the thrust force in lift direction.

6. CONCLUDING REMARKS

A computational model for propeller slipstream/aircraft configuration interference has been described which fits into the framework of panel method technology. The use of the method is aimed at the preliminary design phase of propeller-driven aircraft. It is based on surface singularity techniques and has been implemented in a panel method. The main components of the slipstream model are : 1) an actuator disk which simulates the operation of the propeller, 2) an infinitesimal thin sheet of cylindrical shape which represents the envelope of the slipstream and extends from the tip edge of the actuator disk to downstream infinity and 3) a discrete vortex at the axis of the slipstream which also extends from the actuator disk to downstream infinity. The vorticity distribution on these components and the discrete vortex generate the characteristic axial and circumferential features of the flow inside a slipstream. Appropriate jump conditions across the actuator disk and boundary conditions at the envelope define the vorticity distribution. Because these conditions are simultaneously solved with the boundary conditions at the aircraft configuration, aircraft/propeller slipstream interference effects are automatically taken into account.
In order to assess the capabilities of the slipstream model calculations have been started on the Fokker 50 configuration. Calculated lift force results have been compared with available wind-tunnel results. The preliminary calculations show the correct trends, but comparison of calculated and experimental results is hampered by uncertainties in both results.
Apart from the lift force it would be also of great interest to investigate the capabilities of the method to predict the changes in induced drag and pitching and yawing moment on the configuration due to the presence of a slipstream. All these performance characteristics play an important role already in the preliminary design phase

of a new aircraft. The present method should be able to accomplish these tasks.

REFERENCES

1. Amendola, A., Tognaccini, R., Boerstoel, J.W., Kassies, A.: Validation of a Multi-Block Euler Flow Solver with Propeller Slipstream Flows. AGARD Conference Proceeding, Lisbon, Portugal, pp. P1-1 to P1-15 (1988).

2. Kuijvenhoven, J.L.: Validation of Propeller Slipstream Calculations Using a Multi-Block Euler Code. AIAA Paper 90-3035 (1990).

3. Chandrasekaran, B., Bartlett, G.: Method for Calculating Effects of a Propfan on Aircraft Aerodynamics at Subsonic Speeds. AIAA Paper 83-1216 (1983).

4. Kirrmann, C., Rousseau, A., Yermia, M.: Calcul du souffle moyen d'une hélice et de son influence sur les performance d'un avion. L'Aeronautique et L'Astronautique, No. 104-1984-1, pp. 45-61 (1984).

5. Clark, D.R.: The Use of Panel Methods in the Calculation of Flows around General Configurations Including the Coupled Effects of Rotors and Propellers. Computational Fluid Dynamics in Aerospace Design Workshop, University of Tennessee Space Institute, Tullahoma, Tennessee, June 1985.

6. Smith, B.A.W.: The Flow over a Wing/Nacelle Combination in the Presence of a Propeller Slipstream. First Canadian Symposium on Aerodynamics, Ottawa, Ontario, December 4-5, 1989.

7. Valarezo, W.O., Hess, J.L.: Time-Averaged Subsonic Propeller Flowfield Calculations. AIAA Paper 86-1807 (1986).

8. Valarezo, W.O.: Calculation of Isolated and Installed Multiple Rotor Flows Using a Surface Panel Method. AIAA Paper 89-2214 (1989).

9. Valarezo, W.O.: Calculation of Subsonic Shrouded Propeller Flows. AIAA Paper 90-0029 (1990).

10. Clark, R.W., Valarezo, W.O.: Subsonic Calculation of Propeller/Wing Interference. AIAA Paper 90-0031 (1990).

11. Lötstedt, P.: A propeller slipstream model in subsonic linearized potential flow - Preliminary results. Report L-0-1 R114, Saab-Scania (1987).

12. Lötstedt, P.: A propeller slipstream model in subsonic linearized potential flow. ICAS Paper 90-5.4.4 (1990).

13. Glauert, H.: Airplane Propellers. In Aerodynamic Theory, Vol. IV, ed. W.F. Durand, Dover Publications, New York (1963).

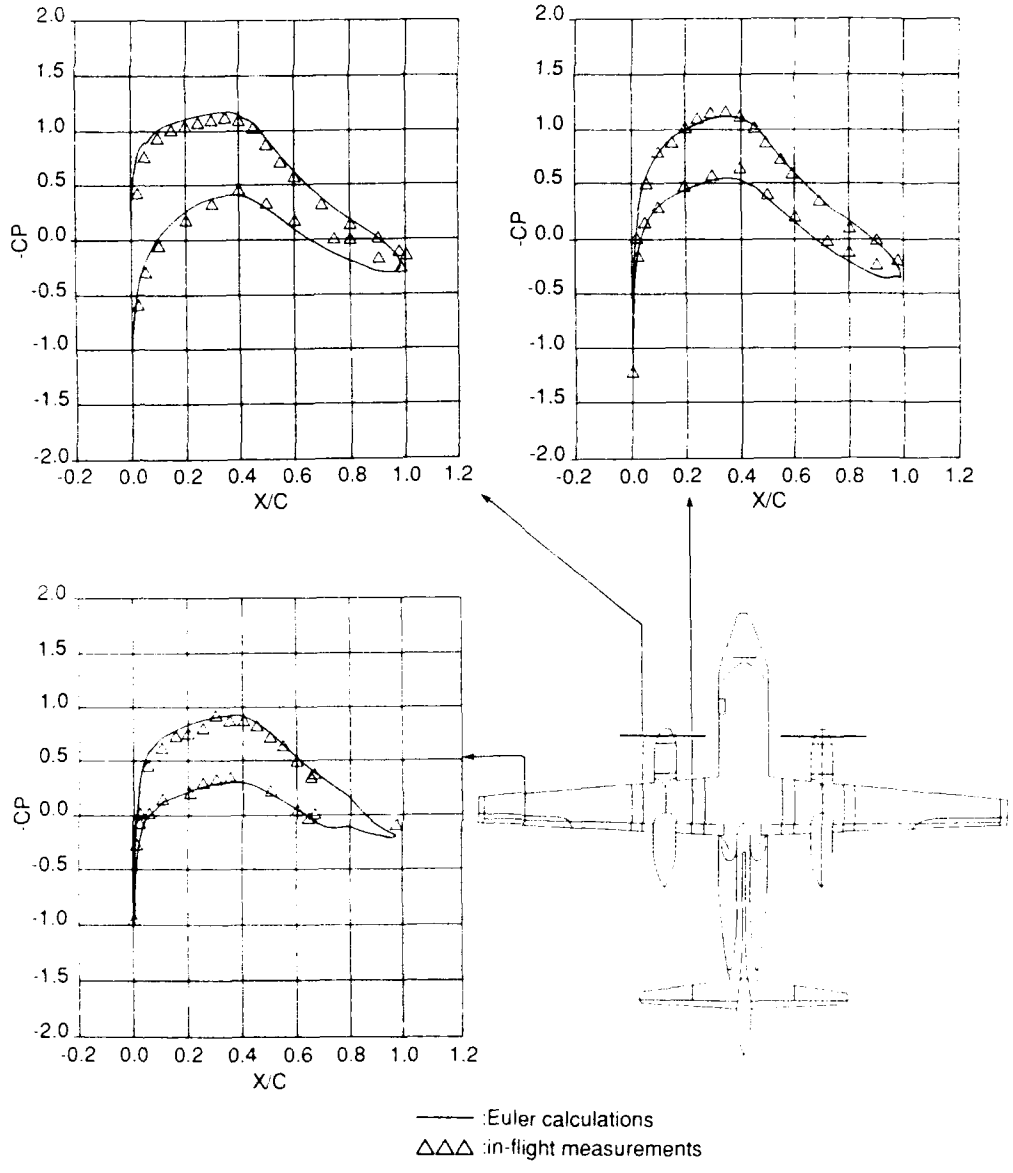

Fig. 1 Pressure distributions on the wing of the Fokker 50

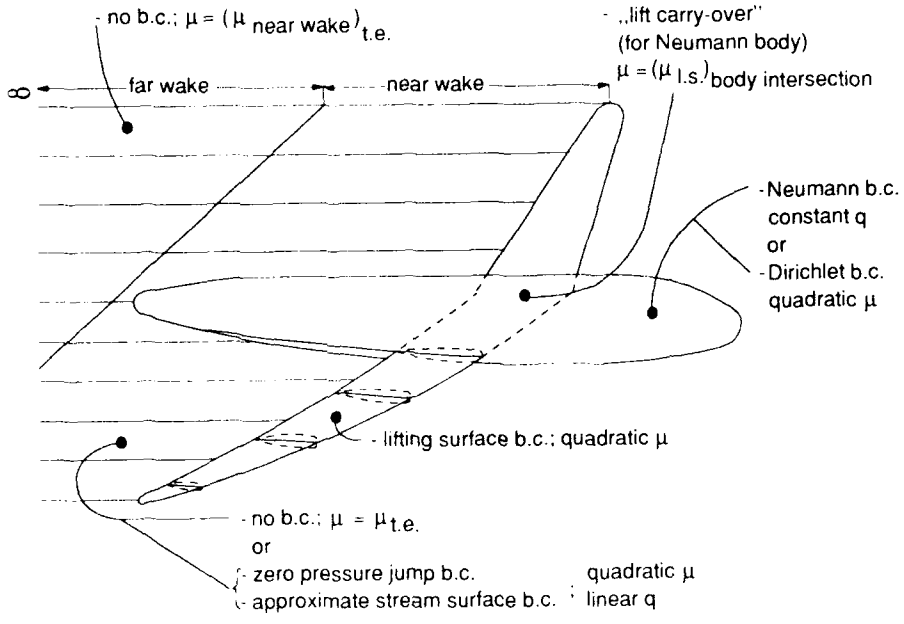

Fig. 2 Main features of the panel method

models:

basic	unbounded flow U_p		
non-linear (NL)	relaxed jet geometry.	γ.	$p_i = p_o$. $V_{n_i} - V_{n_o} = 0$
linear (LN1)	fixed jet geometry.	γ.	$p_i = p_o$
linear (LN2)	fixed jet geometry.	γ. q.	$p_i = p_o$. $V_i \parallel V_o$

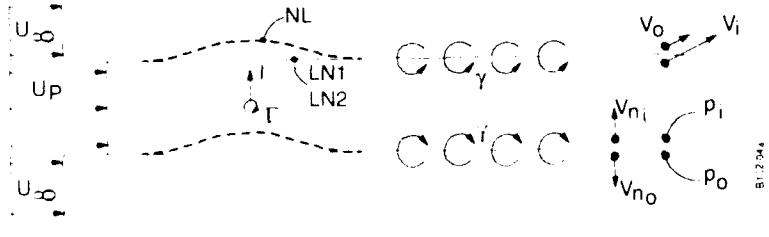

Fig 3 The two-dimensional study

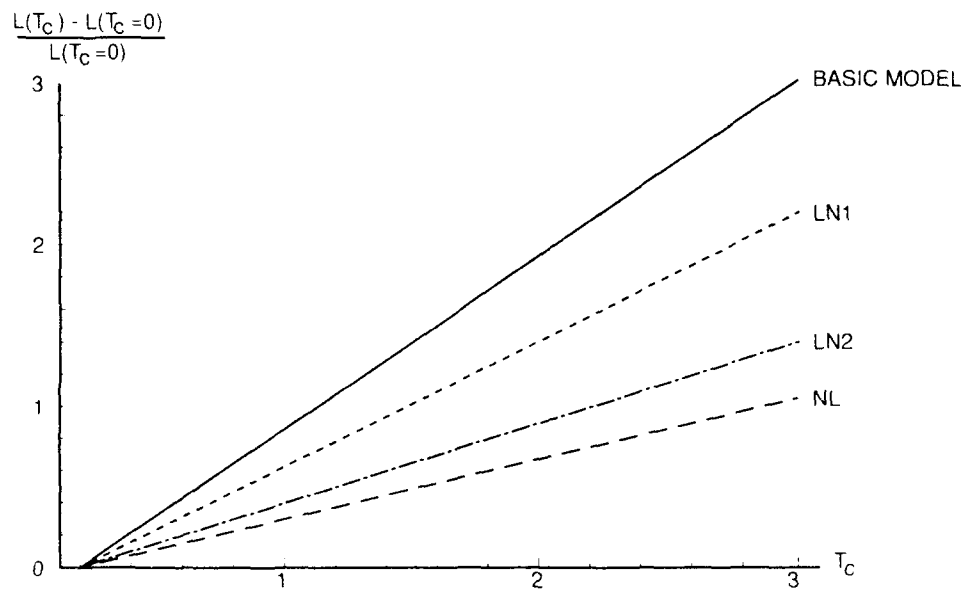

Fig. 4 Lift-increase as function of thrust coefficient for representative 2D test case

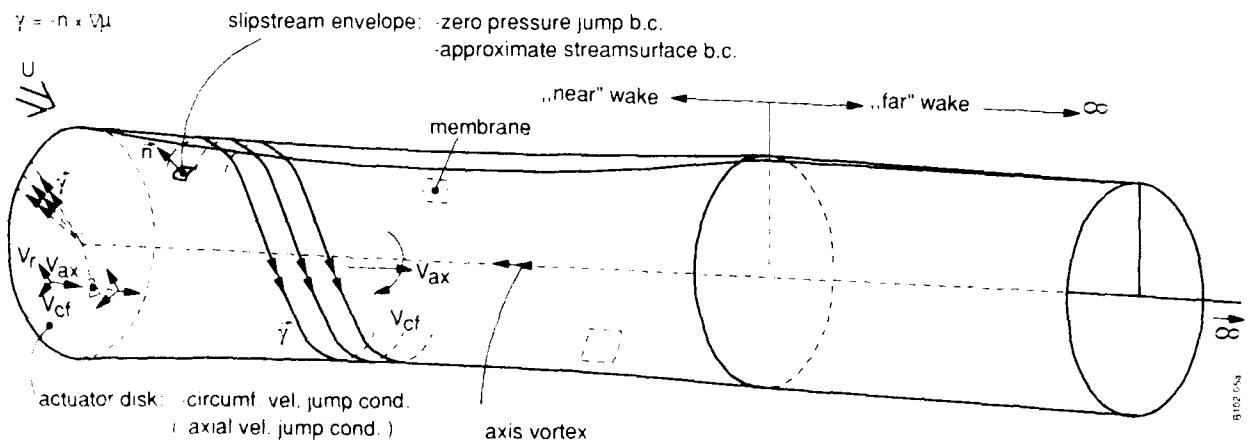

Fig. 5 The slipstream model

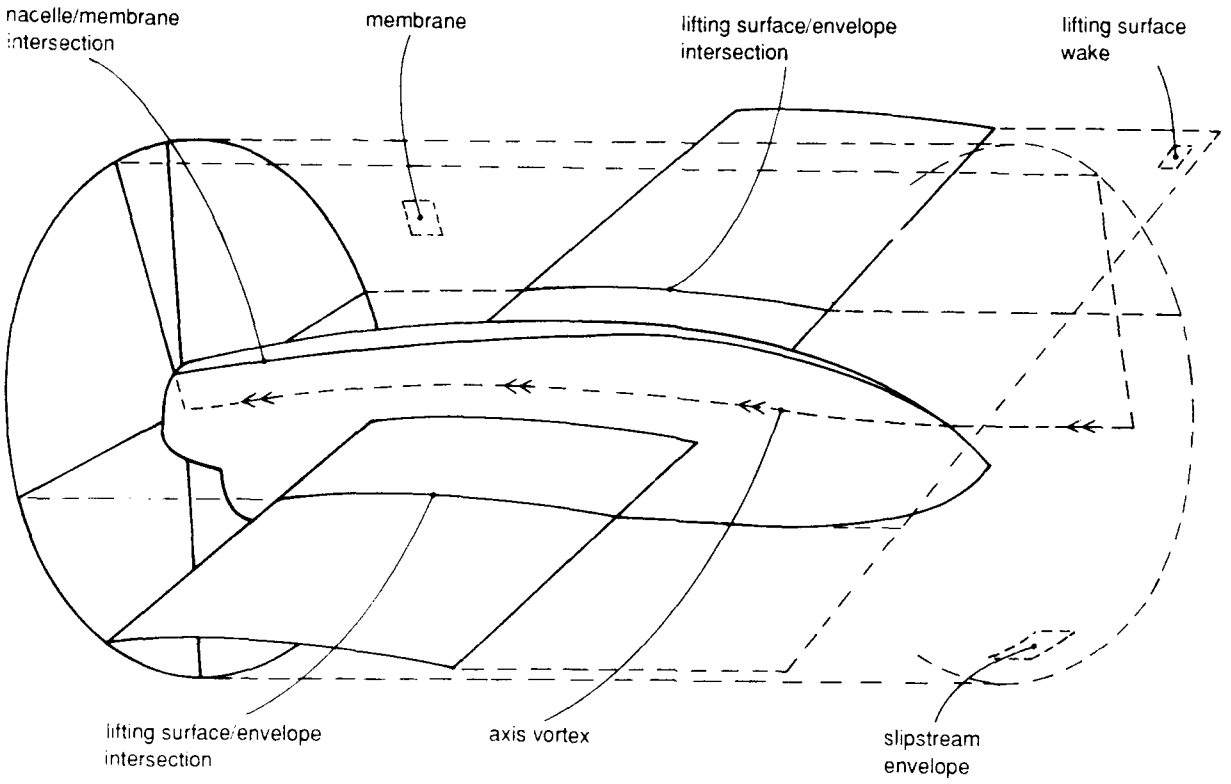

The lifting surface/nacelle/slipstream envelope intersections

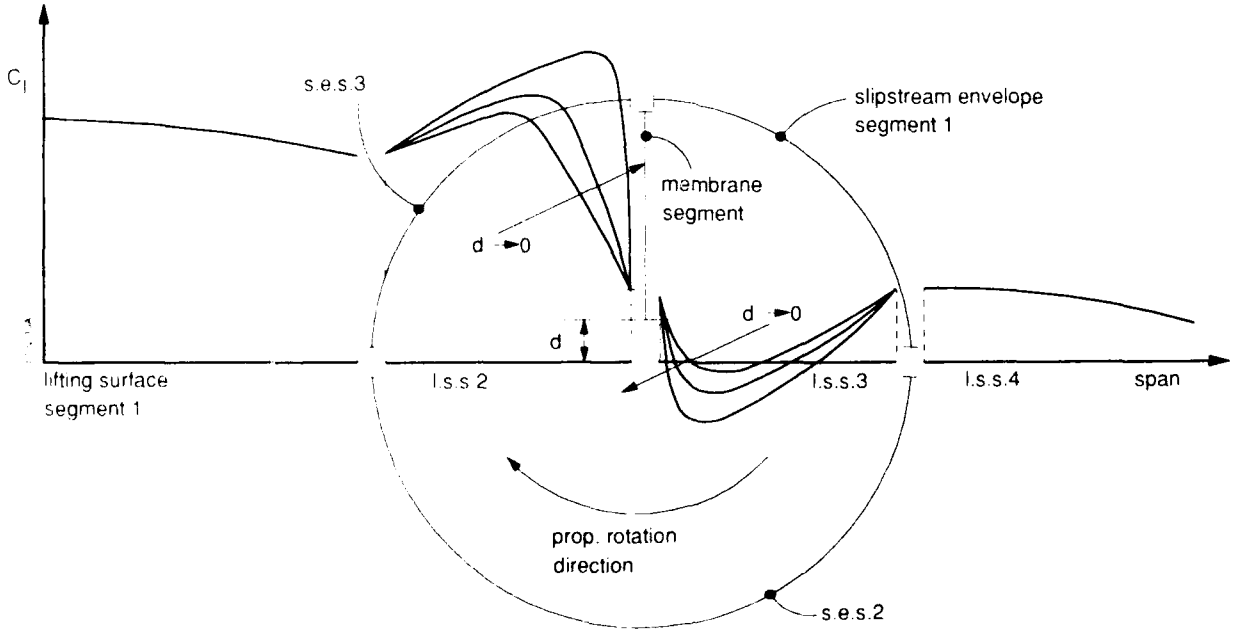

The spanwise load distribution on the lifting surface (no nacelle present)

Fig 6 The lifting surface/propeller slipstream interference

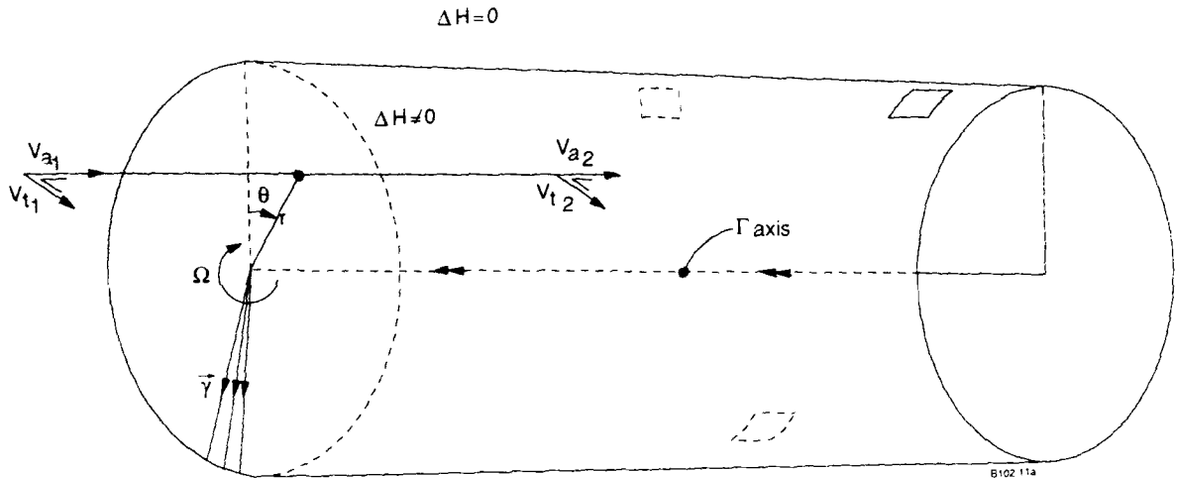

actuator disk:

$$\mu = \frac{\Delta H}{\Omega}\theta$$

axis vortex:

$$\Gamma = 2\Pi\frac{\Delta H}{\Omega}$$

Fig. 7 The jump conditions across the actuator disk

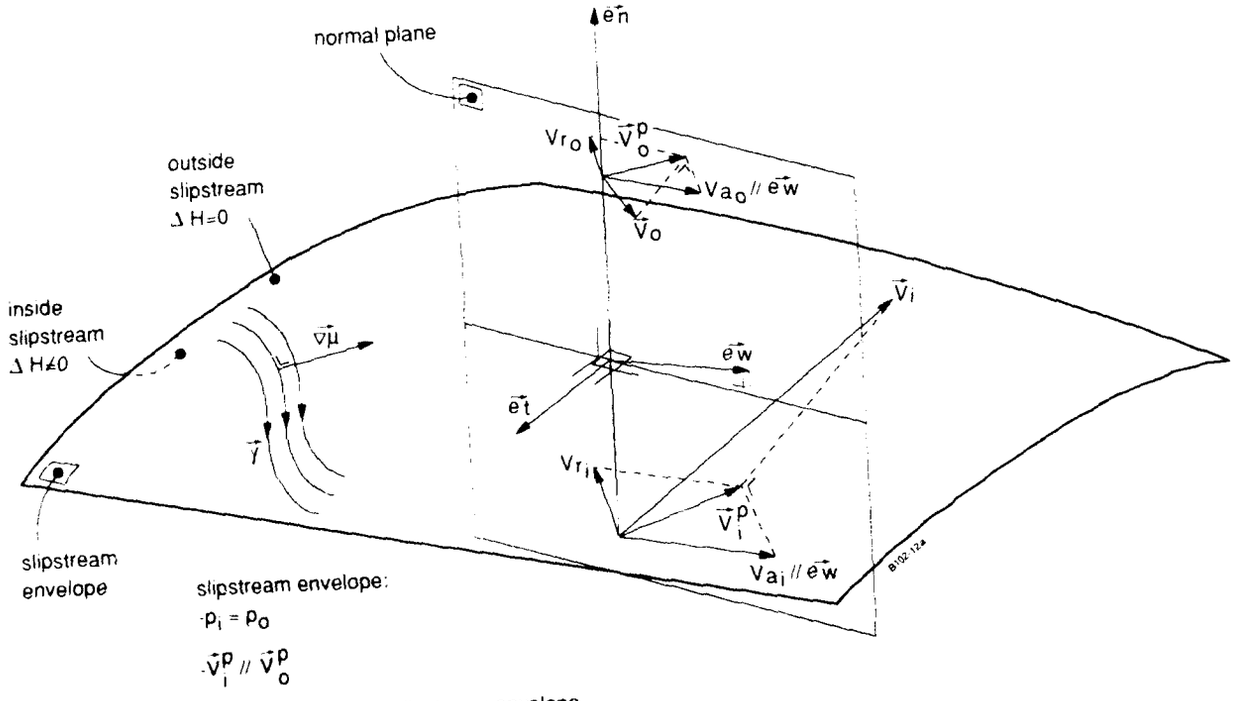

slipstream envelope:

$p_i = p_o$

$\vec{V}^p_i // \vec{V}^p_o$

Fig. 8 The boundary conditions on the slipstream envelope

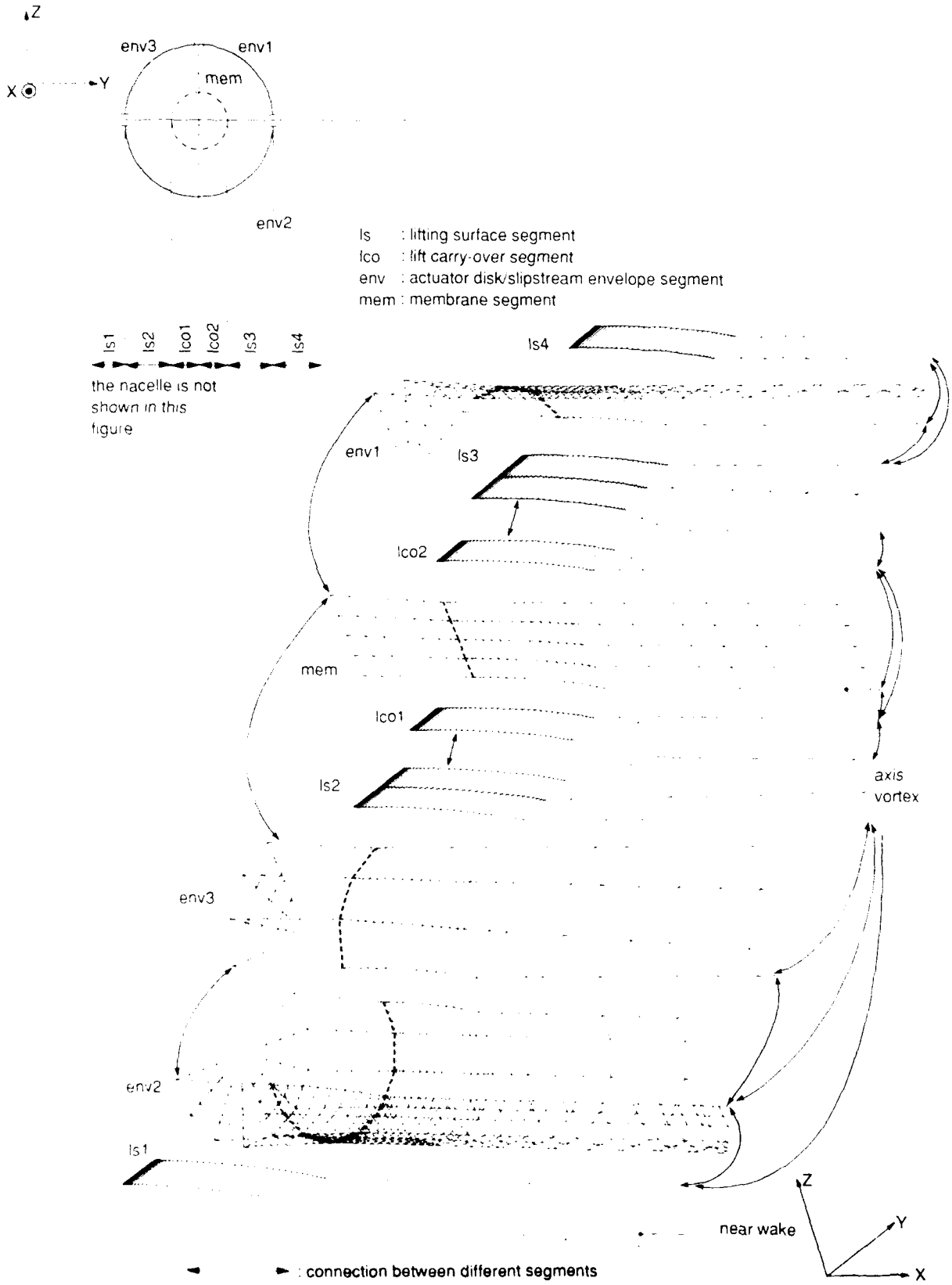

Fig. 9 Exploded view of the lifting surface, actuator disk and slipstream envelope paneling

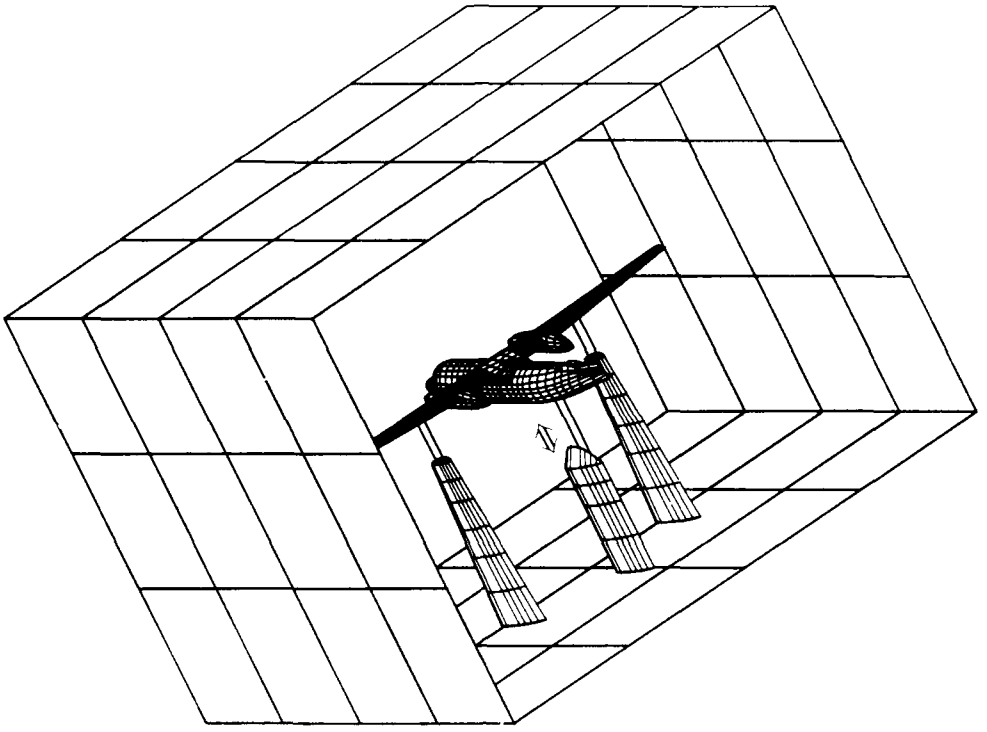

Fig. 10 The Fokker 50 configuration with the support in the DNW test-section

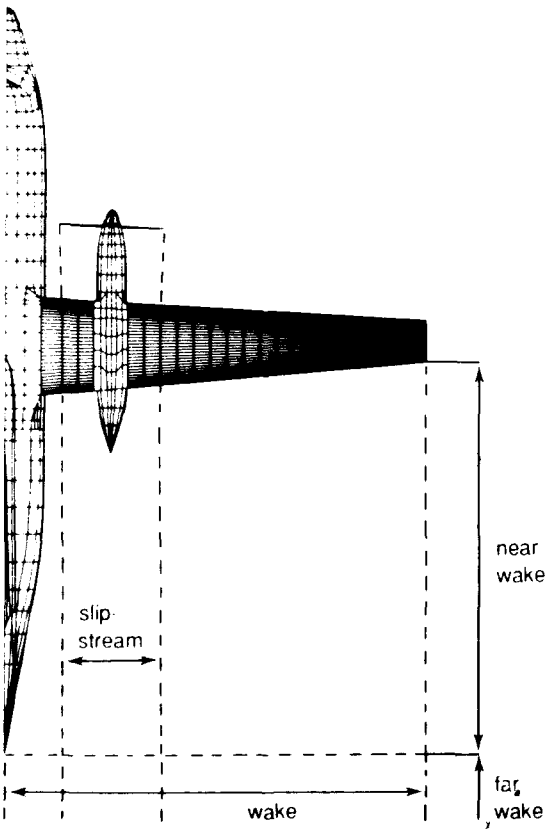

Fig. 11 Top view of the Fokker 50 configuration

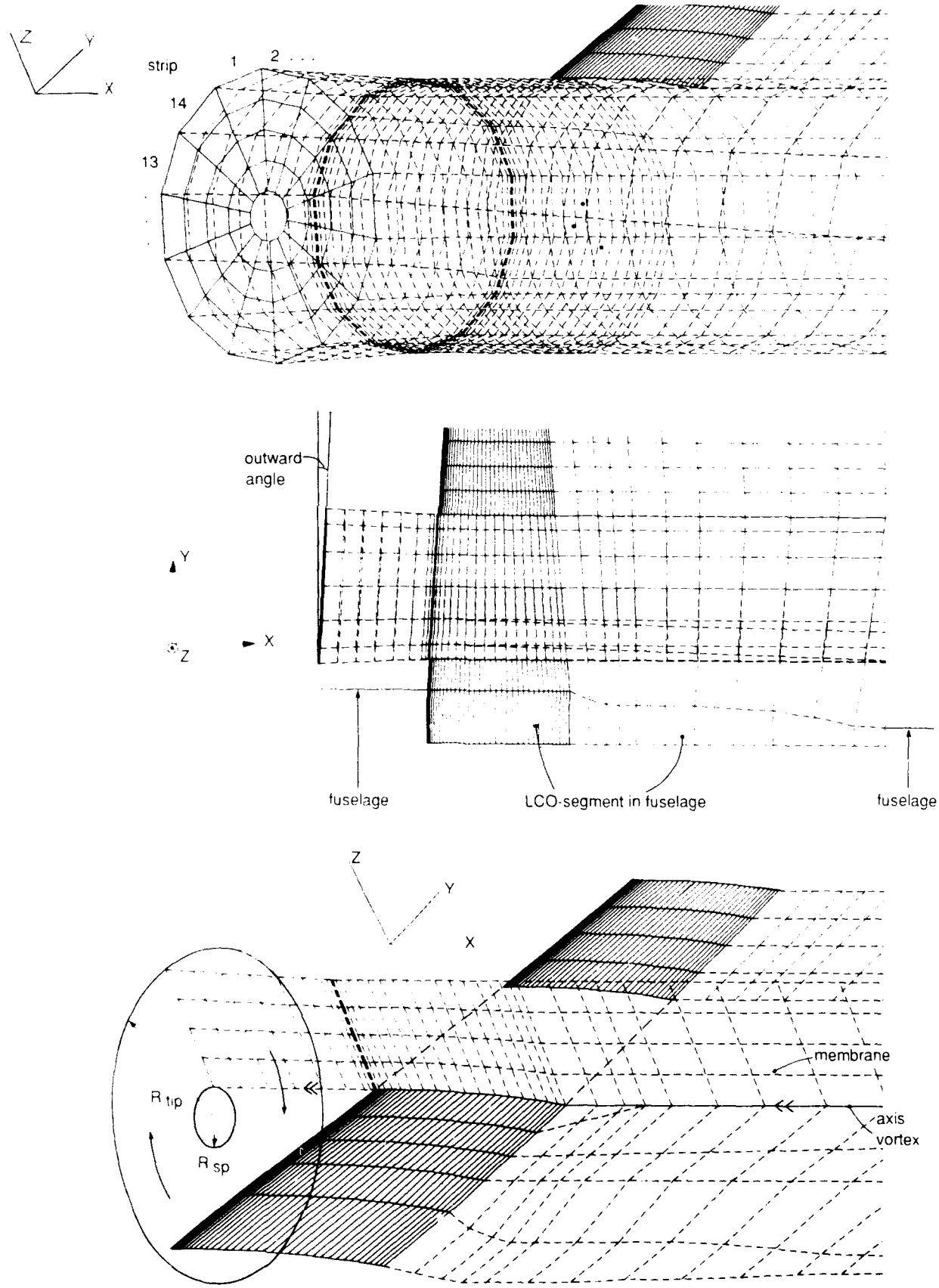

Fig. 12 The actuator disk and slipstream envelope panieling of the Fokker 50 configuration

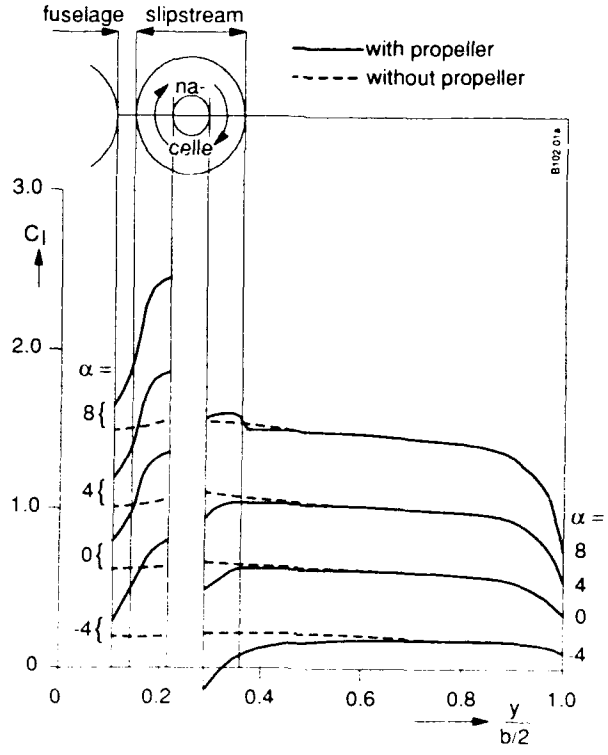

Fig. 13 The spanwise lift distributions at $T_c = 1.0$

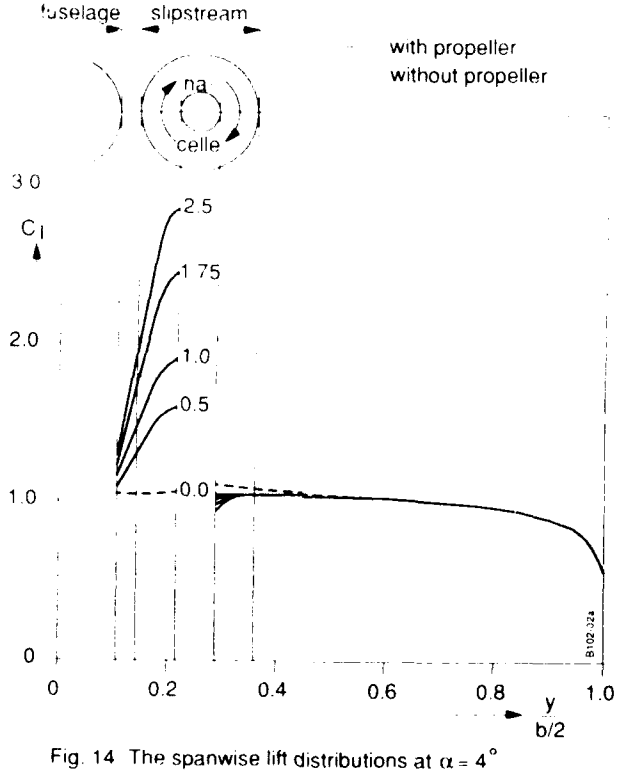

Fig. 14 The spanwise lift distributions at $\alpha = 4°$

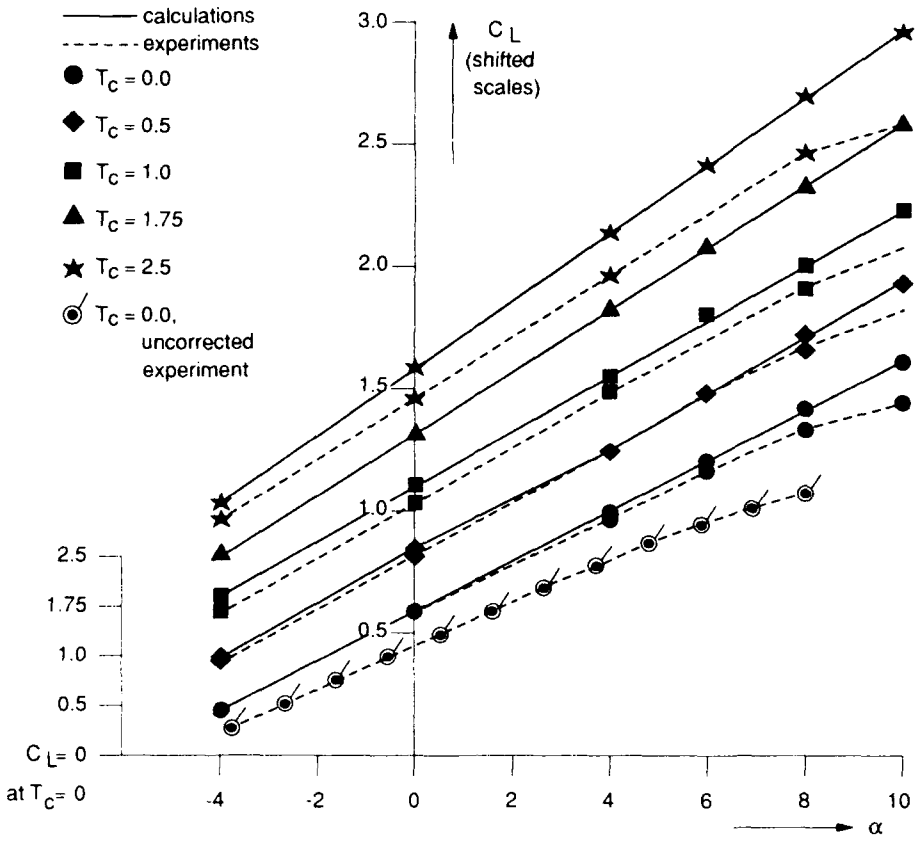

Fig. 15 The lift coefficient as function of the angle of attack for various thrust coefficients for the Fokker 50

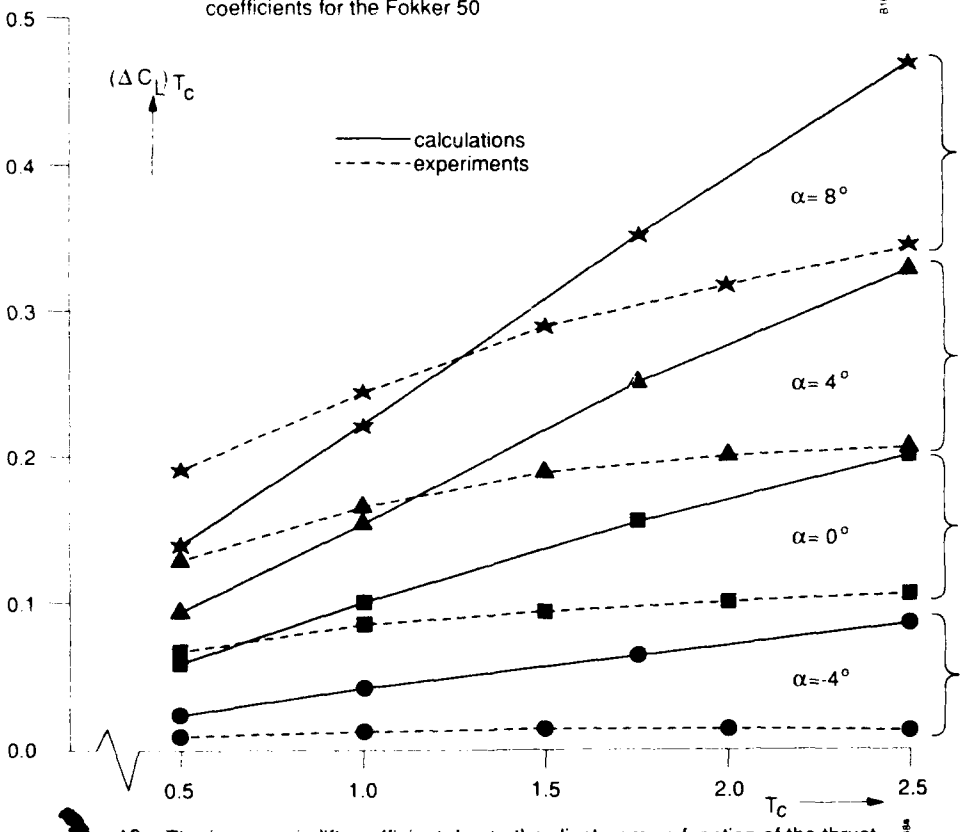

Fig. 16 The increase in lift coefficient due to the slipstream as function of the thrust coefficient for various angles of attack for the Fokker 50

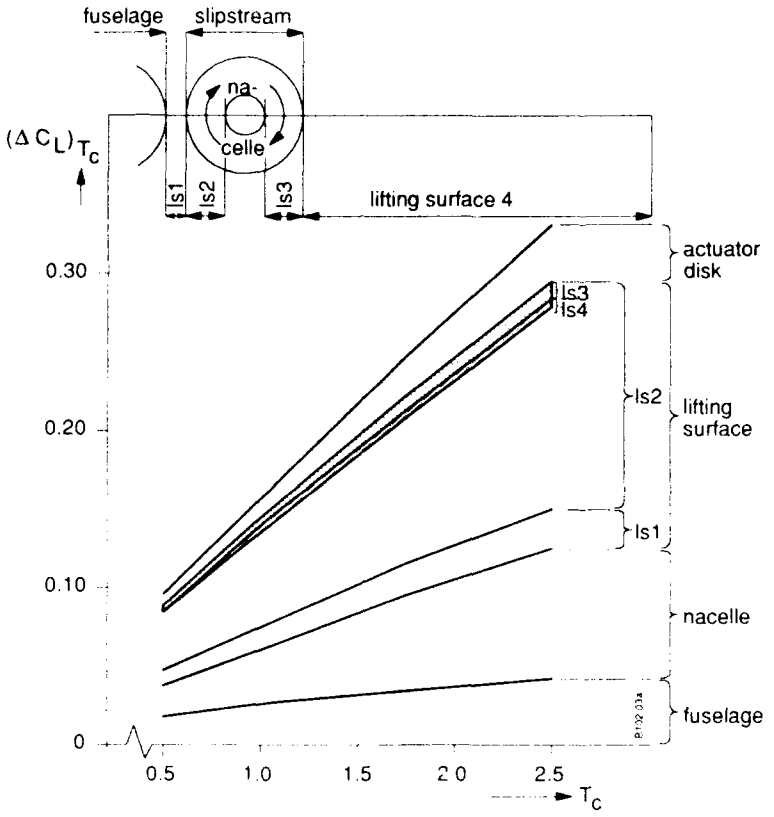

Fig. 17 The build-up of the increase in lift coefficient due to the slipstream as function of the thrust coefficient at $\alpha = 4\,^{\circ}$ for the Fokker 50

Euler Analysis of Turbofan/Superfan Integration for a Transport Aircraft

D. A. Naik
ViGYAN, Inc., 30 Research Drive, Hampton, VA 23666-1325, USA
H. C. Chen
T.Y. Su
T.J. Kao
The Boeing Company, Seattle, WA 98124-2207, USA

1. SUMMARY

A three-dimensional general multi-block Euler solver (GMBE) has been developed to analyze the propulsion integration effects of turbofan/superfan installations. Either flow-through or powered nacelles can be modelled. The code is demonstrated on a generic NASA low wing transport model with an advanced turbofan flow-through nacelle. The results compare favourably with experimental data obtained in the NASA Langley 16-Foot (4.88 m) Transonic Tunnel. The computed pressure distributions are used to identify, in terms of pressure coefficient peaks (maximum negative values) and gradients, undesirable flow regions in the vicinity of the pylon and nacelle. The results suggest that a change in toe angle and pylon trailing edge closure geometry will improve the propulsion integration.

2. NOMENCLATURE

b	wing span
c	wing reference chord
C_L	lift coefficient, lift/qS
C_p	static pressure coefficient, $(p - p_\infty)/q_\infty$
M	Mach number
p	static pressure
q	dynamic pressure
S	wing reference area
x	streamwise coordinate; origin at airplane nose
y	spanwise ordinate w.r.t. fuselage centreline
α	angle of attack
η	non-dimensional spanwise wing station, 2y/b
ϕ	meridian angle about nacelle centreline (clockwise from crown-line looking upstream)

Subscripts

∞	freestream conditions

3. INTRODUCTION

The increases in fuel cost over the last two decades has spurred the development of fuel efficient advanced turbofans and high bypass ratio superfans for transport aircraft with supercritical wings. The work presented in this paper is part of an ongoing effort, supported by NASA Langley Research Center, on propulsion integration for transport aircraft operating in the high-subsonic Mach number regime.

The nacelle-pylon assembly introduces installation drag which is composed of skin friction drag (from the wetted portions of the pylon and nacelle) and "induced [illegible] drag. There are various causes for the latter. [illegible] the thickest portion of the [illegible] low pressure region acting on the [illegible] surface, resulting in lift loss and possibly wave drag from regions of supersonic flow. This could be compounded if the wing maximum thickness occurs in the vicinity of the pylon maximum thickness; which would be particularly true for supercritical airfoil sections. Additionally, an adverse pressure gradient arising from the pylon trailing edge closure could encourage flow separation on the lower wing surface resulting in form drag. Flow separation could also be present at the nacelle-pylon junction, as could regions of supersonic flow, if the nacelle is not properly contoured or aligned with the local flow direction.

Computational fluid dynamics (CFD) modelling of the propulsion integration problem must therefore address several complex issues: complicated geometry; regions of transonic flow; rotational flow; non-uniformity in total temperature and pressure; and, viscous effects on the configuration surfaces.

The Euler analysis code used here does not address the viscous flow problem; skin-friction is not modelled and flow separation is tackled indirectly in terms of pressure coefficient peaks (maximum negative values) and adverse pressure gradients.

4. COMPUTATIONAL METHOD

The flow code is a generalized version of the Euler analysis code that was successfully used to address the problem of wing-mounted and aft-mounted propfan engine-airframe integration for a generic NASA low wing turboprop transport configuration (Refs. 1 and 2). The flow solver is derived from Jameson's cell-centered finite-volume approach.

The flow field around a complicated geometry is divided into a number of topologically simple blocks, so that surface fitted grids and an efficient flow solution algorithm can be easily applied within each block (Ref. 3). The computational grid within each block can be generated using a combination of elliptic and algebraic methods. Typically, either GRIDGEN (Ref. 4) or EAGLE (Ref. 5) are used to generate the surface and volume grids from a given surface definition. The block relationships and face boundary conditions may be specified manually. As this can be quite labourious, a grid-generation/flow-solver interface program was developed to facilitate the process. This block relationship and boundary condition code, BCON, is a menu driven graphics interface program (Ref. 6).

Each block is allowed an arbitrary number of neighbours and each face is allowed an arbitrary combination of boundary conditions. Typical boundary conditions are: solid surface; far field (subsonic or supersonic inflow or

outflow); nacelle inlet (mass flux, velocity, or pressure distributions); and nacelle exhaust (swirl, total pressure and temperature distributions; or, force and work distributions). The boundary condition implementation is described in Ref. 3. The flow solver inputs are described in Ref. 7.

GMBE includes special treatment of the convective and dissipative flux terms for highly skewed cells, including zero-volume cells. A multiblock version of multigrid is used to speed up convergence. The code applies a V-cycle multigrid only to those blocks with even cell distributions. This approach is necessary because it is difficult to ensure that every block of a complex multiblock system contains an even number of cells in each computational direction. In order for the strategy to be computationally effective, non-multigrid blocks should be small in number and size.

For super-computer systems with central memory limitations, a pre-processor is used to adjust the central memory requirement to each block. This ensures that the grid and flowfield information for each block is moved to the working area in a block by block manner with the updates returned to the block storage area. More details are available in Ref. 3.

5. GENERIC TURBOFAN TRANSPORT

The GMBE analysis was performed in conjunction with an experimental study on a generic NASA twin-engine transport model. The experiments (Refs. 8,9 and 10) were conducted with flow-through turbofan (bypass ratio $\approx$ 6) and superfan (bypass ratio $\approx$ 18) nacelles. Force, moment, surface pressure, and flow visualization data were taken for the airplane in an un-yawed condition for a Mach number range of 0.5 to 0.8, and for an angle of attack range of -4^{o} to $+8^{o}$. Several combinations of nacelle/pylon toe and incidence angles were investigated at two span locations; η = 0.34 and η = 0.40. This paper concentrates on the installation at η = 0.34.

The airplane is designed for a cruise lift coefficient of 0.55 at a Mach number of 0.77 with twin, under-wing, advanced turbofan nacelles located at η = 0.34. The surface grid and symmetry plane for this configuration is shown in Fig. 1. The volume grid contained approximately 1.2 million grid points and was composed of 26 to 32 blocks, depending on the nacelle simulation. A typical solution took 4 hours on a Cray YMP super-computer. The convergence criterion for the Euler runs was a three order of magnitude decrease in the incremental maximum density.

The entire flow-through nacelle configuration (with pylon, wing, and fuselage) is modelled with 32 blocks. Fifteen of these blocks are used for the flow-through core and fan cowls, Fig. 2 (a). Three blocks form a cylinder from the fan entrance through the core cowl to the core cowl exit. The forward portion of this cylinder is surrounded by an annulus, formed of three blocks, from the fan inlet face to the fan exit. The cylinder from the core exit face to the downstream far field is composed of three blocks. Another annulus, also composed of three blocks, extends from the fan exit, around the outer core cowl and core exhaust cylinder, to the downstream farfield. Three blocks form a cylinder from the upstream far farfield to the fan inlet face. The remaining 17 blocks wrap around the external geometry.

Variations of this block structure are permissible. For example, for the powered nacelle case, the blocks inside the propulsive unit may be eliminated; with boundary conditions specified at the fan inlet, the fan exhaust, and the core exhaust. The resulting structure consists of 26-blocks. A close-up of the surface grid near the inboard side of the installation is shown in Fig. 2 (b). This is for a three degree incidence angle with no toe.

The overall model dimensions are given in Table 1.

Table 1. Model Dimensions (Ref. 8)

S	587.96 sq.in	0.3793 m^2
Aspect ratio	10.795	
Taper ratio	0.275	
1/4-chord sweep	21^{o}	
1/4-chord dihedral	5.78^{o}	
c	8.176 in	0.2077 m
Airfoil	Supercritical	

A sketch of the wing orifice locations is given in Fig. 3. Note that there is an extra row of lower surface pressure orifices on each side of η = 0.34. The nacelle and pylon external surface pressure orifices are sketched in Fig. 4. The x-coordinate ranges for these orifices are given in Table 2.

Table 2. Pressure orifice locations (Ref. 10)

	x-min	x-max
Pylon upper row	31.275 in	39.032 in
	0.7944 m	0.9914 m
Pylon lower row	39.430 in	43.81. in
	1.0015 m	1.1128 m
Fan cowl	28.923 in	36.660 in
	0.7346 m	0.9317 m
Core cowl	36.718 in	39.243 in
	0.9326 m	0.9968 m

6. RESULTS

6.1 Flow-through Nacelles at Cruise Condition, M_∞ = 0.77, $C_L \approx$ 0.55

6.1.1 Computational results

Static pressure coefficient contours are shown in Figs. 5 (a) through (e) for different elements of the airplane. This dismembered approach is necessary for clarity and for the ease of dissemination of this information in a black and white format. The contours range from 1.0 to -1.5 in increments of 0.1. The dotted lines correspond to freestream pressure.

The fuselage, Fig. 5 (a), has a gradual variation from near freestream pressure, except at the wing junction where the closeness of the contours represents the effects of the wing upper surface. The contours continue on to the root region of the wing upper surface, Fig. 5 (b). The 0.05c to 0.5c region on the wing upper surface has the typical gradual variation in local supersonic flow that is expected of supercritical airfoils. A weak shock occurs near 0.7c, after which the flow compresses to freestream near the trailing edge as indicated by the dotted contour. The lower surface contours, Fig. 5 (c), are locally modified by the propulsion installation. The contours show a return to freestream pressure at roughly 0.6c. This is characteristic of supercritical airfoils (Ref. 11) and is followed by additional compression from the substantial aft-camber.

Near η = 0.34, the lower surface wing Cp contours continue on to the inboard, Fig. 5 (d), and outboard, Fig. 5 (e), sides of the pylon. The flow on the aft portion of the pylon compresses because of the pylon trailing edge closure. This compression introduces substantial adverse pressure gradients which are communicated to the wing surface and could encourage flow separation there. Ahead of this compression, the flow is nearly sonic ($0.97 < M < 1$) on the inboard side of the pylon and at roughly 0.4c on the wing. This high negative-Cp on the wing lower surface causes a loss in lift.

Regions of high negative-Cp are present at the junction of the pylon tip with the outboard fan cowl, and on the forward portion of the outboard fan cowl. By comparison, the inboard sides of the forward portion of the pylon and nacelle have lower negative-Cp. This asymmetry in the pressure distribution on the fan cowl could be alleviated by toeing in the propulsion assembly. The experimental data (Ref. 10) showed that the pylon-nacelle assembly with a 1^{o} toe-in resulted in lower drag than the 0^{o} toe configuration studied here.

6.1.2 Comparison with Experiment

Figs. 6 (a) through (f) show the comparison between experimental and calculated (GMBE) wing Cp. The code seems to slightly under predict inboard upper surface peaks, Figs. 6 (a) and (b), while it over predicts the outboard peaks, Figs. 6 (e) and (f). This discrepancy could possibly arise because of aeroelastic twist. As is typical of inviscid solutions, the computed shock is farther aft than the experimental shock, Fig. 6 (e).

On the lower surface the comparison is fairly good up to 0.7c. Particular attention is drawn to the vicinity of the propulsion installation, Figs. 6 (c) and (d). The inboard Cp peaks and the consequent adverse pressure gradients, from roughly 0.4c to 0.7c, could be crucial from the standpoint of propulsion installation drag. Both the experimental data and the Euler calculations indicate that the effect is stronger on the inboard side of the installation.

There is remarkable similarity between the experimental and computed pressure distributions on the fan cowl, Figs. 7(a) through (e). It is unfortunate that there are no experimental pressure orifices coincident with the primary Cp peaks predicted by GMBE. However, the available experimental pressures do confirm the asymmetry in the fan cowl pressures that was predicted by the GMBE solution in Fig. 5.

Although the experimental data available for the core cowl is sparse, Figs. 8 (a) through (e) show that the pressures computed on the cowl are not unreasonable. The x-axis scale is deliberately set to be consistent with Figs. 7 and 9.

Figs. 9 (a) through (d), show the comparison of the pylon surface pressures. Figs. 9 (a) and (b) are for the upper row of orifices. Figs. 9 (c) and (d) are for the lower row. Along the upper rows, the computed pressures are consistent with the experimental data; except for the first experimental data point in Fig. 9 (b). The computed results predict high flow velocities near the forward portion of the outboard pylon, but there is no experimental data available to corroborate this. The plots for the lower row, which extends to the pylon trailing edge closure, also suffer from a paucity of experimental pressure data, although the two orifices in Fig. 9 (a) do show the same trend as the GMBE solution. Beyond this, the computed results predict high flow velocities, particularly on the inboard side, and show the aft compression gradients, which are transmitted to the wing lower surface and might be steep enough to result in the flow separation shown in the flow visualization photograph, Fig. 10. The outer limits of this separation region on the wing lower surface are reflected in the experimental pressures, Figs. 6 (c) and (d), which did show a tendency to flatten out over the last 20 percent of the chord.

Separation of this scale could drastically alter the aerodynamic integrity of the engine-airframe integration. Euler code predictions of Cp peaks and gradients, although an indirect means of addressing flow separation, have had some success in improving pylon design (Refs. 12 and 13).

In summary, the Euler calculations indicate that there is room for improving the propulsion integration in two ways: (1) the fan cowl should be toed in; and, (2) the aft portion of the pylon should be redesigned, for lower Cp peaks and gentler pressure gradients, in order to minimize flow separation.

6.2 Flow-through Nacelles at Off-Design Condition, M_∞ = 0.80, C_L ≈ 0.55

At this higher freestream Mach number, the regions of high flow velocity that were seen at M_∞ = 0.77 on the pylon-nacelle junction, the outboard fan cowl, and the inboard aft portion of the pylon all contain pockets of supersonic flow. The asymmetry in the fan cowl pressure distribution is also evident at this Mach number, Fig. 11.

A small supersonic region is present on the outboard aft portion of the pylon. This is followed by an adverse pressure gradient on the pylon trailing edge closure region. The change, due to Mach Number, in the aft pylon pressure distribution is also reflected in the sparse experimental data that is superimposed on Figs. 12 (a) and (b).

6.3 Powered Nacelles at Cruise Condition, $M_\infty = 0.77$, $C_L \approx 0.55$

The power-on condition was simulated by specifying total pressure ratios of 1.6 at the fan exit, and 1.92 at the core exit (Ref. 3). The result is shown in Fig. 13. This particular power-on condition affects the flow over the core cowl, Fig. 14 (a), and the flow downstream of the core exit, but the effects are local enough to not significantly affect the adverse pressure gradients on the aft portion of the pylon, Fig 14 (b), or on the wing lower surface, Fig. 13 (c). This is not surprising as the fan exhaust contributes a far smaller static pressure effect than the core exhaust which itself is well below the wing lower surface. Thus, this powered condition would have minimal effect on the pylon-wing junction.

7. CONCLUDING REMARKS

A three-dimensional general multi-block Euler solver (GMBE) has been developed to analyze the propulsion integration effects of turbofan/superfan installations. Both flow through and powered nacelles are modelled. The code is demonstrated on a generic NASA low wing transport model with an advanced turbofan nacelle. The results are compared with experimental surface pressure and flow visualization data obtained in the NASA Langley 16-Foot (4.88 m) Transonic Tunnel.

The computed pressure distributions are in general agreement with the available experimental pressure data for the airplane at cruise conditions. The computed pressures also provide insight into the propulsion integration problem. Regions of high flow velocity are present on the pylon-nacelle junction, the outboard fan cowl, and the aft portion of the pylon. These regions contain supersonic pockets at a Mach number higher than cruise. The pylon pressure gradients caused by flow compression at the pylon trailing edge closure could be severe enough, even at power-on conditions, to cause flow separation on the wing lower surface. The pressure distributions indicate that this particular propulsion integration may be improved by a toe-in of the fan cowl and a redesign of the pylon trailing edge closure geometry.

While further maturity in three-dimensional viscous and adaptive grid technology, unstructured methods, turbulence models, 3-D Navier-Stokes codes, and computer storage hardware is awaited for the proper modelling of separated junction flows, the Euler analysis of propulsion integration seems efficacious from an applied CFD standpoint.

8. ACKNOWLEDGEMENTS

This research is funded by the National Aeronautics and Space Administration, Langley Research Center, Applied Aerodynamics Division, Propulsion Aerodynamics Branch, under NASA Contract Nos. NAS1-17919 and NAS1-18703. Supercomputer resources for this project were provided by the National Aerodynamic Simulator complex at NASA Ames Research Center. CFD graphics were created with P. Buning's PLOT3D program from NASA Ames. The postscript version was provided by D. Yip of NASA Ames. The authors would like to thank O.C. Pendergraft, Jr., R. J. Re, A.M. Ingraldi and T.T. Kariya for providing the experimental pressure data.

9. REFERENCES

1. Samant, S. S., and Yu, N.J., "Flow Prediction for Propfan Engine Installation Effects on Transport Aircraft at Transonic Speeds", NASA CR 3954, January 1986.

2. Naik, D. A., "3-D Euler Calculations for Aft-Propfan Integration", AIAA 90-2147, July 1990.

3. Chen, H. C., Su, T. Y., and Kao, T. J., "A General Multiblock Euler Code for Propulsion Integration, Volume I: Theory Document", NASA CR 187484, May 1991.

4. Steinbrenner, J. P., Chawner, J.R., and Fouts, C. L., "The GRIDGEN 3D Multiple Block Grid Generation System", WRDC-TR-90-3022, July 1990.

5. Lijewski, E., and Cipolla, J., "Program EAGLE User's Manual", AFATL-TR-88-117, September 1988.

6. Su, T. Y., Appleby, R. A., and Chen, H. C., "A General Multiblock Euler Code for Propulsion Integration, Volume II: User Guide for BCON, Pre-Processor for Grid Generation and GMBE", NASA CR 187484, May 1991.

7. Chen, H. C., "A General Multiblock Euler Code for Propulsion Integration, Volume III: User Guide for the Euler Code", NASA CR 187484, May 1991.

8. Pendergraft, Jr., O.C., Ingraldi, A.M., Re, R. J., and Kariya, T. T., "Nacelle/Pylon Interference Study on a 1/17th-Scale, Twin-Engine, Low-Wing Transport Model", AIAA-89-2480.

9. Ingraldi, A.M., Kariya, T. T., Re, R. J., and Pendergraft, Jr., O.C., "Interference Effects of Very High Bypass Ratio Nacelle Installations on a Low-Wing Transport", ASME-91-GT-241, June 1991.

10. Pendergraft, Jr., O.C., Ingraldi, A.M., Re, R. J., and Kariya, T. T., "Installation Effects of Wing-Mounted Turbofan Nacelle/Pylons on a 1/17th-Scale, Twin-Engine, Low-Wing Transport Model", NASA TP 3168, 1992.

11. Harris, C.D., "NASA Supercritical Airfoils: A Matrix of Family-Related Airfoils," NASA TP 2969, 1990.

12. Naik, D. A., "Innovative Pylon Concepts for Engine-Airframe Integration for Transonic Transports," AIAA-89-1819, June 1989.

13. Naik, D. A., Ingraldi, A. M., Pendergraft, Jr., O. C., "Experimental Analysis of Pylon Geometries for Propulsion Integration of Transport Aircraft", 30th AIAA Aerospace Sciences Meeting, Reno, Nevada, Jan 6th - 9th, 1992.

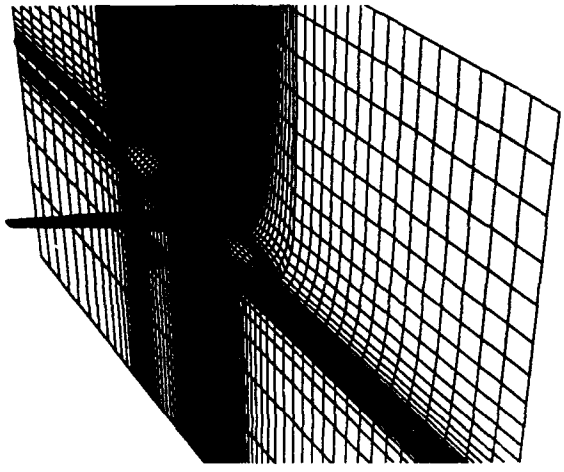

Fig. 1 Euler surface grid with symmetry plane.

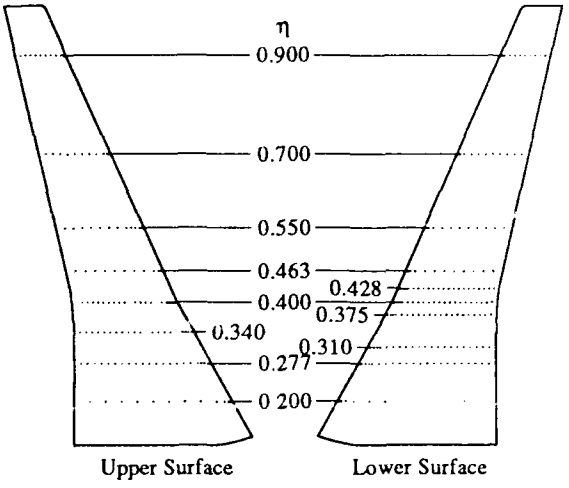

Fig. 3 Wing surface pressure orifices (Ref. 9).

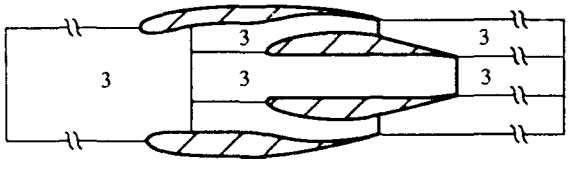

Fig. 2 (a) Schematic of block structure for fan and core cowls.

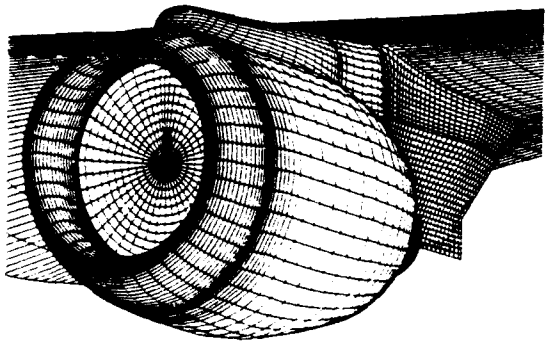

Fig. 2 (b) Close-up of powered nacelle showing surface grid detail.

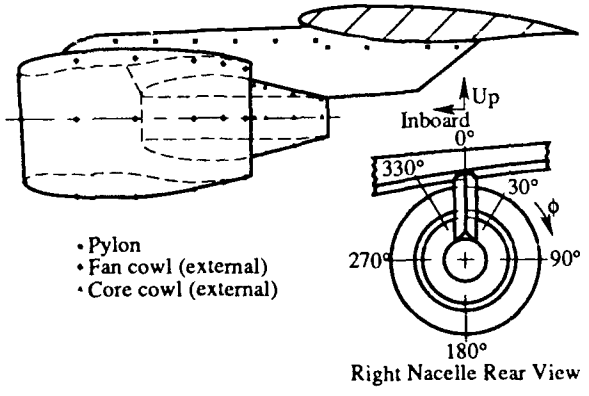

Fig. 4 Fan cowl, core cowl, and pylon surface pressure orifices (Ref. 10).

(a) Fuselage

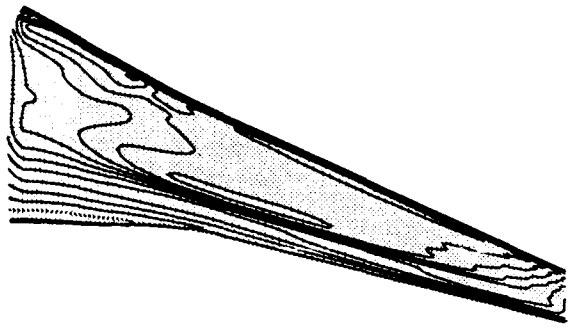

(b) Wing upper surface

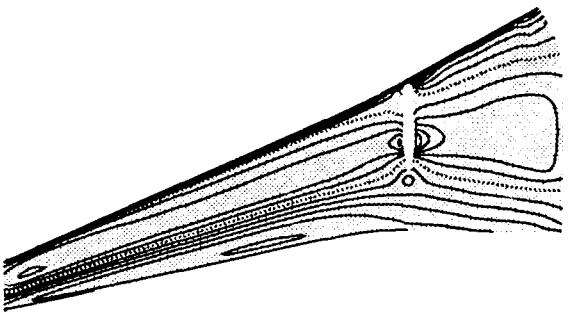

(c) Wing lower surface

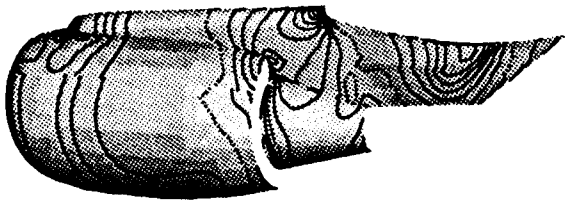

(d) Inboard side of nacelle

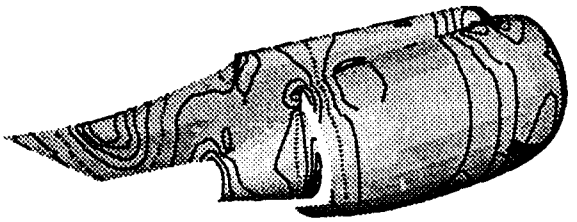

(e) Outboard side of nacelle

Fig. 5 C_p contours for low-wing aircraft with flow-through nacelle at $\eta = 0.34$. $M_\infty = 0.77$, $C_L \approx 0.55$. The contour range is from 1.0 to -1.5 in increments of 0.1. The dotted lines denote freestream pressure.

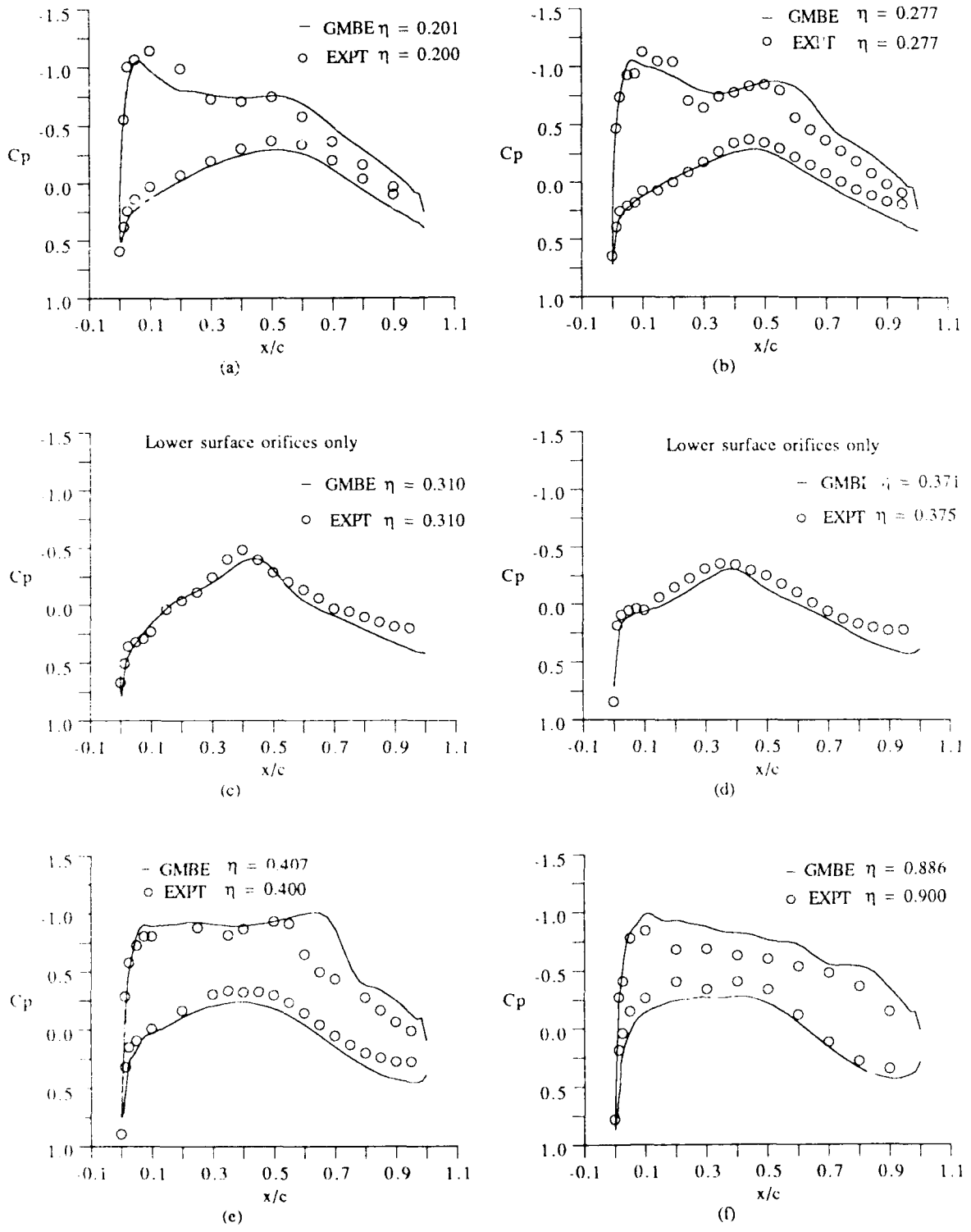

Fig. 6 Comparison of GMBE computed wing C_p with wind-tunnel data. Low-wing aircraft with nacelle installed at $\eta = 0.34$. $M_\infty = 0.77$, $C_L = 0.55$.

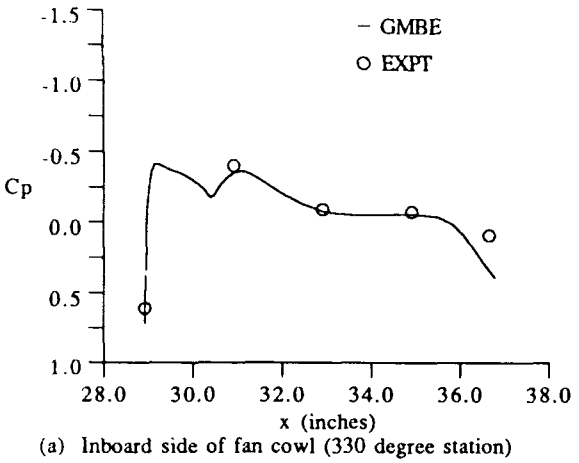

(a) Inboard side of fan cowl (330 degree station)

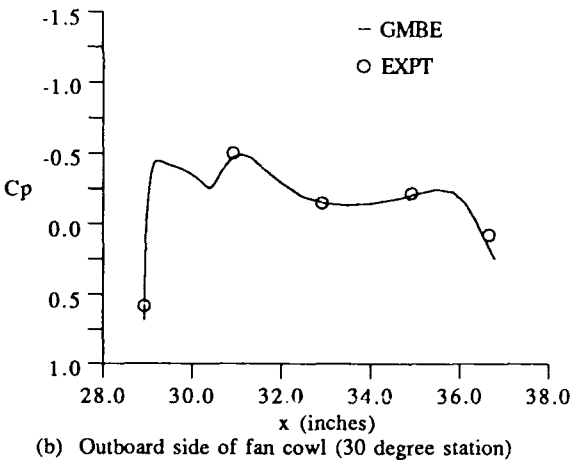

(b) Outboard side of fan cowl (30 degree station)

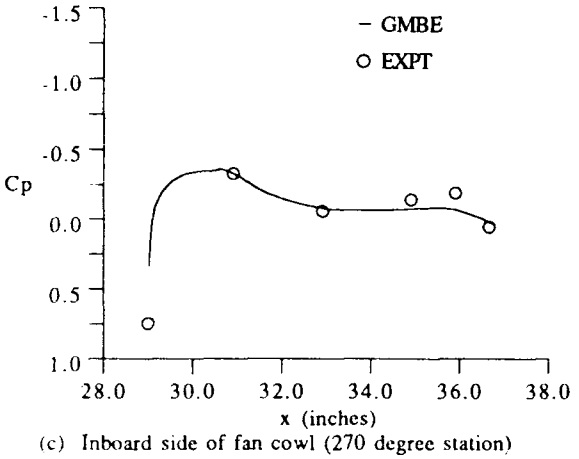

(c) Inboard side of fan cowl (270 degree station)

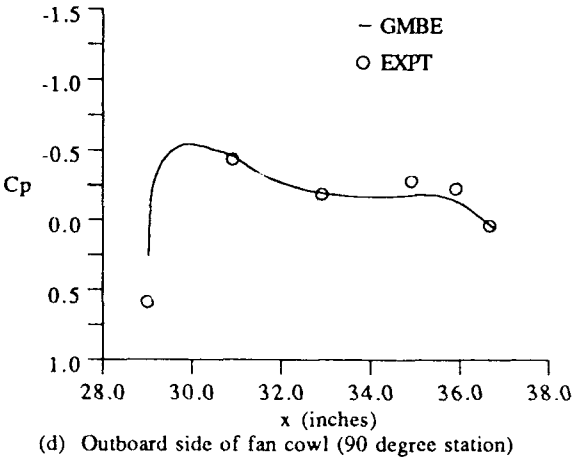

(d) Outboard side of fan cowl (90 degree station)

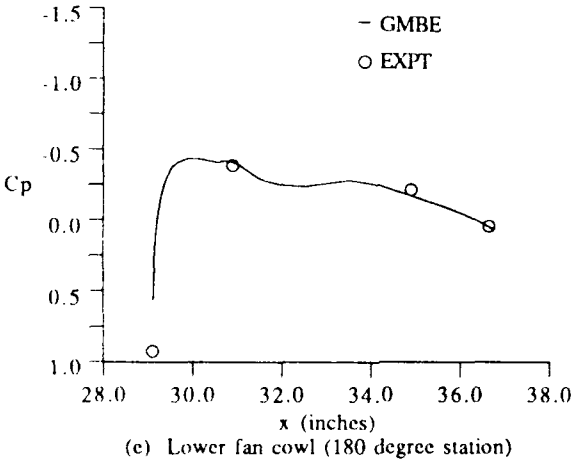

(e) Lower fan cowl (180 degree station)

Fig. 7 Comparison of GMBE computed fan cowl C_p with wind-tunnel data. Low-wing aircraft with nacelle installed at $\eta = 0.34$. $M_\infty = 0.77$, $C_L = 0.55$.

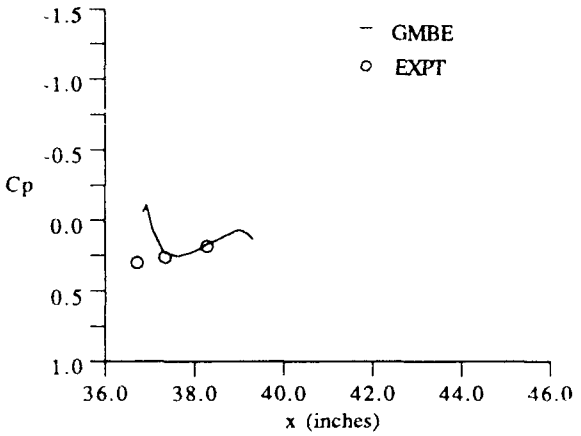

(a) Inboard side of core cowl (330 degree station)

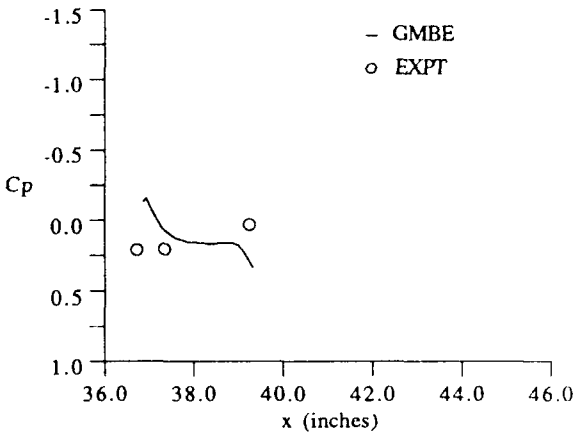

(b) Outboard side of core cowl (30 degree station)

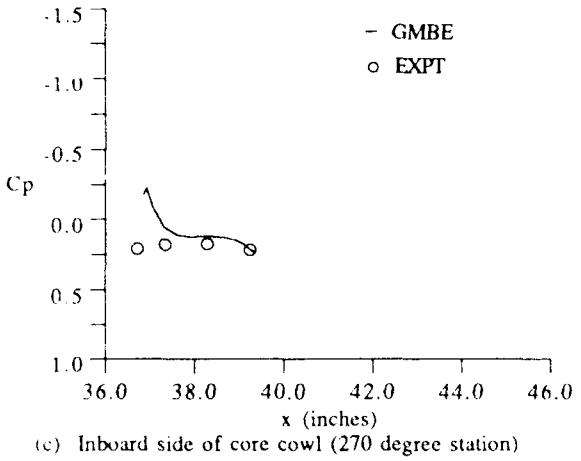

(c) Inboard side of core cowl (270 degree station)

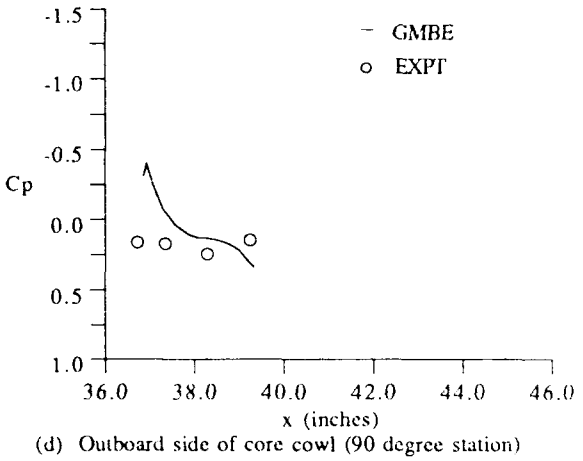

(d) Outboard side of core cowl (90 degree station)

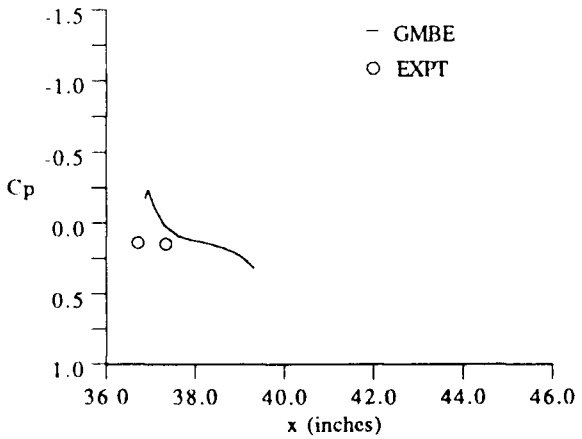

(e) Lo ·er core cowl (180 degree station)

Fig. 8 Comparison of GMBE computed core cowl C_p with wind-tunnel data. Low-wing aircraft with nacelle installed at $\eta = 0.34$. $M_\infty = 0.77$, $C_L \approx 0.55$ (Note: Axis scales are set to be consistent with Figs. 7 and 9).

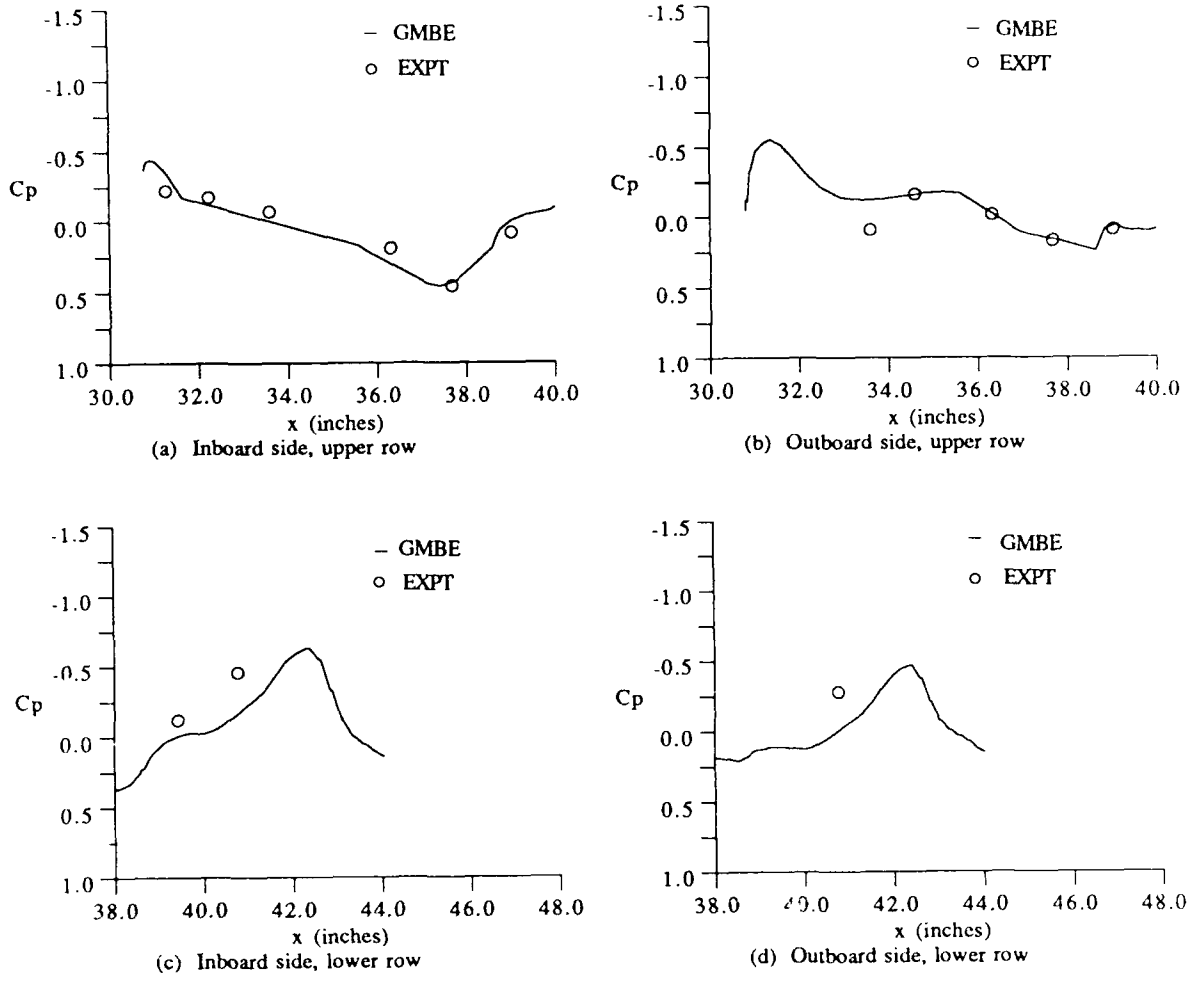

Fig. 9 Comparison of GMBE computed pylon C_p with wind-tunnel data. Low-wing aircraft with nacelle installed at $\eta = 0.34$. $M_\infty = 0.77$, $C_L \approx 0.55$.

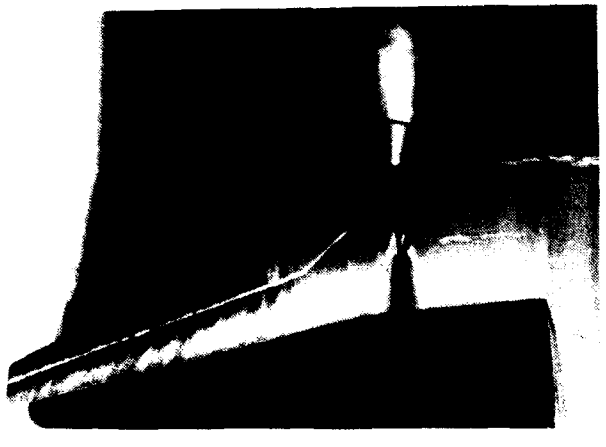

Fig. 10 Wing lower surface oil flow visualization photograph for low-wing aircraft with nacelle installed at $\eta = 0.34$. $M_\infty = 0.77$, $C_L \approx 0.55$.

(a) Inboard side of nacelle

(b) Outboard side of nacelle

Fig. 11 C_p contours for low wing aircraft with flow-through nacelle at η = 0.34, M_∞ = 0.80 (off-design), C_L = 0.55. The contour range is from 1.0 to -1.5 in increments of 0.1. The dotted lines denote freestream pressure.

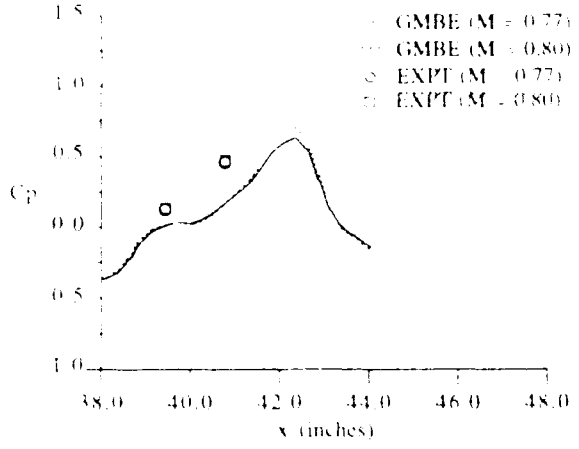

(a) Inboard side, lower row

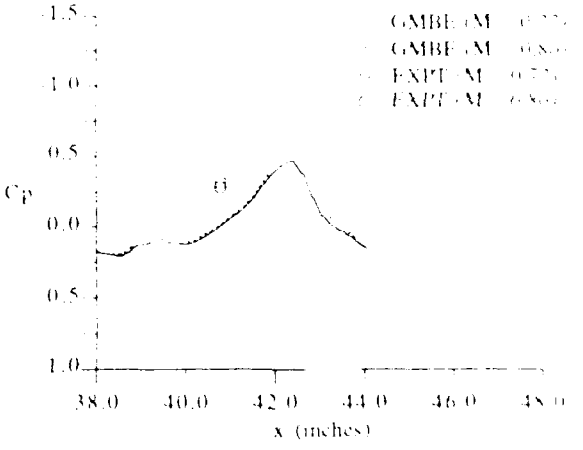

(b) Outboard side, lower row

Fig. 12 C_p distribution on the aft portion of the pylon for low-wing aircraft with flow-through nacelle at η = 0.34. Comparison of M_∞ = 0.77, C_L = 0.55 with M_∞ = 0.80 (off-design), C_L = 0.55. Wind tunnel data is also superimposed.

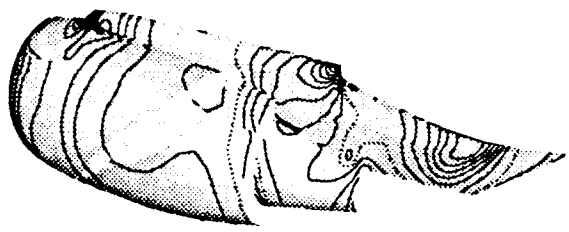

(a) Inboard side of nacelle

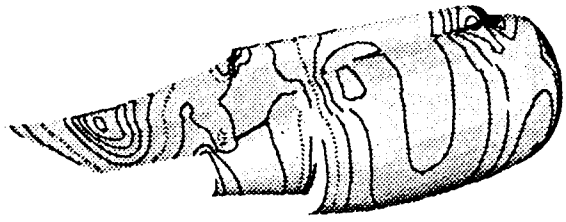

(b) Outboard side of nacelle

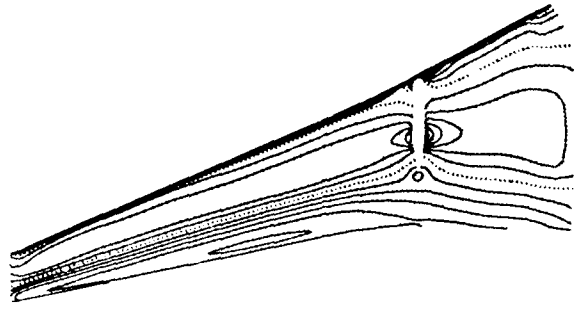

(c) Wing lower surface

Fig. 13 C_p contours for low wing aircraft with powered nacelle at $\eta = 0.34$, $M_\infty = 0.77$, $C_L \approx 0.55$. The contour range is from 1.0 to -1.5 in increments of 0.1. The dotted lines denote freestream pressure.

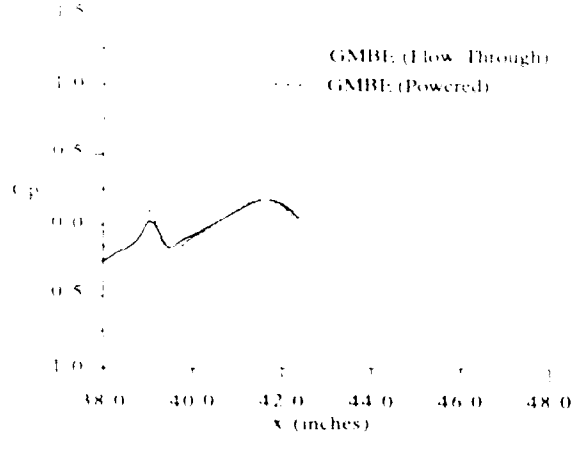

(a) Inboard side, fan exhaust above core cowl

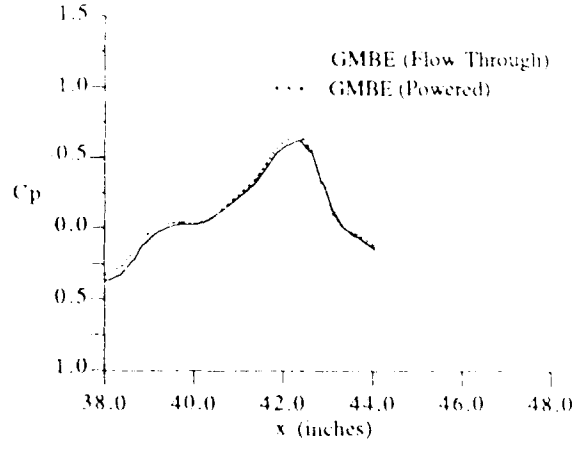

(b) Inboard side, lower row

Fig. 14 C_p distribution on the pylon for low-wing aircraft with powered nacelle at $\eta = 0.34$, $M_\infty = 0.77$, $C_L \approx 0.55$.

Recent Developments in Low-Speed TPS-Testing for Engine Integration Drag and Installed Thrust Reverser Simulation

W. Burgsmüller
Deutsche Airbus
Hünefeldstrasse 1-5, 2800 Bremen, Germany
C. Castan
Aerospatiale, Aircraft Division
316 route de Bayonne, 31060 Toulouse Cedex 03, France
J.W. Kooi
DNW
Postbus 175, 8300 AD Emmeloord, The Netherlands
J.P. Bècle
ONERA, Centre de Modane-Avrieux
BP 72, 92322 Châtillon, France

Summary

In accordance with the steady increase in bypass ratio and hence fan nacelle diameter of engines for modern transport aircraft, also the investigation of engine airframe interference effects is of increasing importance. This covers not only the interferences between the wing and nacelle/pylon bodies, but also the effects due to the presence of the engine jet flow field.

In the low speed range of an aircraft, i.e. take off, second segment climb, landing and roll out with thrust reversing, the jet interference investigations require wind tunnels with special high quality equipment, highly instrumented models with engine simulators and test setups outside the tunnel for special investigations. Concerning the different possibilities for engine simulation, the use of turbine-powered simulators (TPS) has proven as the best and most flexible instrument. The paper presented here describes the technical progress made in the last years in testing technique, based on close cooperation between Deutsche Airbus, Aerospatiale, DNW and ONERA.

Furtheron, a survey about the possible applications for low speed jet interference testing is given, mainly based on the Airbus A340 development programme. Finally, some of these recent test results concerning performances and understanding of the aerodynamic and thermodynamic phenomena, especially concerning second segment climb jet interference, thrust reverser efficiency and plume reingestion effects are shown and discussed.

It can be summarized, that a high level of technical test standard has been achieved and this together with a better understanding of the flow phenomena gives a reliable basis for the integration of the coming generations of aircraft and engines.

List of symbols

CD	drag coefficient
CDa	basic aircraft drag
CDab	air brakes drag with reverser interaction
CDr	reverser plume effect on aircraft drag
Cis	TPS isentropic core thrust (N)
CL	lift coefficient
CLa	basic aircraft lift
CLab	air brakes lift with reverser interaction
CLr	reverser plume effect on aircraft lift
C.L.	center-line
D	drag (N)
F	thrust (N)
Fe	effective thrust
Fis	TPS isentropic fan thrust (N)
HFD	horizontal fuselage datum line
L	lift (N)
Po	static tunnel pressure
PTF	fan total pressure
Qo	tunnel dynamic pressure
S	model reference area
T	engine reversed thrust from the deck (N)
TF	fan total temperature
TG	core total temperature
Tin	inlet average temperature
Tto	tunnel total temperature
Tmax	inlet maximum temperature
v_o	tunnel or flight velocity (m/s)
W	weight (kg)
WF	actual fan mass flow
WG	actual core mass flow
X	balance thrust measurement
Xrev	TPS total measured reverse thrust (N)
A/D	fan nozzle diameters
α	incidence (°)
β	sideslip (°)
Δ	delta coefficient
γ	angle between main thrust vector and engine center-line (°)
μ	runway friction coefficient

Indices

a	aircraft
ab	air brake
aerod.	aerodynamic
D	drag component
L	lift component
in	inlet
is	isentropic
j	jet
MTO	max. take-off condition
o	ambient
r	reversed
TFN	through-flow nacelle condition

1. Introduction

Optimized engine integration is of high importance for the overall economy of every modern aircraft. In the low-speed flight regime this covers jet interference drag during the climb phase, ground effects during take-off and landing, and the impact of thrust reverser deployment. In the future, the experimental investigation of engine integration will become even more important as the engine diameter increase. This holds in particular for new types of engines such as the ducted propfan. Their large diameters lead to a close coupling between engine and wing flow field.

For a wide range of aircraft development testing in wind tunnels, the engines can be represented by through flow nacelles. However, jet simulation is required to measure the jet interference drag during take-off and landing. The same holds for measuring thrust reverser efficiency and as-

sessing the impact of failures and reingestion. Out of the existing simulation techniques (see ref. 1) the so called Turbo Powered Simulators (TPS) have proven as the most appropriate technique (Fig.1). A TPS consists of a fan which is driven by a turbine. This turbine is powered by compressed air, supplied by the wind tunnel compressor plant.

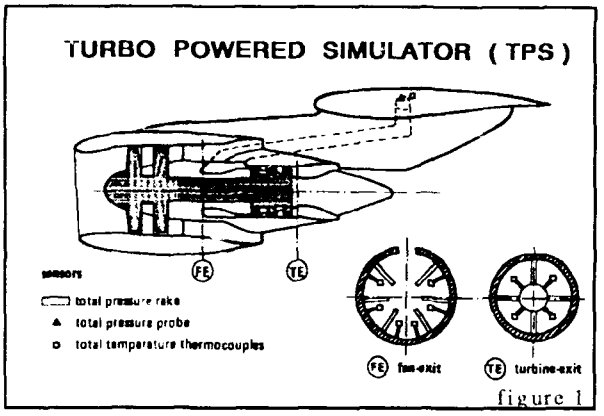

figure 1

The first low-speed wind tunnel tests in Europe using TPS were done in 1980 in the low speed wind tunnel LSWT at VFW-Bremen (now Deutsche Airbus, see ref. 2).The aim of the tests was to study the interference between the engine and the wing high lift devices deflected for second segment climb. The size of the wind tunnel , 2.1x2.1 m, forced to use half models for these tests. Based on the experience gained, the TPS technique was next installed in the German-Dutch Wind tunnel (8x6m) enabling to test complete models. For the necessary calibrations of the simulators, NLR built close to the DNW an Engine Calibration Facility. The first tests with a model equipped with two simulators were performed in 1982. Again, the goal was to study the second segment climb jet interference drag. Later on, the ground effect on the longitudinal stability was included (ref. 11). Since, in close cooperation between DNW, NLR and Deutsche Airbus the testing technique was steadily improved (see ref. 3 to 6). The major latest developments were connected with a series of tests led by Deutsche Airbus, on an Airbus A340 complete powered model in the DNW.

Another application of the TPS technique was pioneered by Aerospatiale. Besides forward thrust simulation (ref. 1), Aerospatiale since 1978 used the TPS technique for thrust reverser development. Through an extensive wind tunnel simulation, the aerodynamic integration of the thrust reverser system was carried out, up to the certification process. In 1986, Aerospatiale completed in this way successfully a test campaign for the Airbus A320 in the large ONERA S1 transonic wind tunnel (ref. 7 and 8). Although rather complex, this methodology reduces the costs to spend in full scale aircraft development program. Aerospatiale's long standing experience in both forward as well as in reversed mode engine simulation (ref. 1, 7 to 9) and the close and fruitful cooperation with Deutsche Airbus, Hispano-Suiza, ONERA and DNW made it possible to complete successfully a series of installed thrust reverser performance tests on a complete powered Airbus A340 model in the DNW low speed wind tunnel. The model used was the same as for the second segment climb jet interference drag test mentioned above.

The purpose of the tests was firstly to measure the braking capacity and secondly the extra reverser limitations such as reingestion, parasitic loads and aircraft handling qualities. Before the wind tunnel test the reverser system was calibrated at the specially modified ONERA Modane S4b calibration facility. The wind tunnel test program included also the handling quality of the aircraft in case of reverser inadvertent opening in flight. These low speed data together with the results of a planned transonic test in the ONERA S1 will be used in aircraft certification process.

From all types of tests with jet simulation the drag interference for the second segment climb require the highest accuracy and repeatability. To achieve this goal, a constant improvement of test equipment and procedures is necessary. The improvements made during the last years are described below. All these tests were done for performance prediction of the new A340 aircraft as well as for a better understanding of the physical flow phenomena. Some of the recent results will be shown and discussed in detail.

2. Recent Developments in Low-Speed TPS-Testing for Engine Integration Drag

2.1 Test objectives

The integration of airframe covers two major shares of aerodynamic effects, i.e. (fig. 2) :

- the incremental forces and moments due to the addition of engine-nacelle and pylon-bodies to the airframe,
- the interferences due to the engine jet flow-field

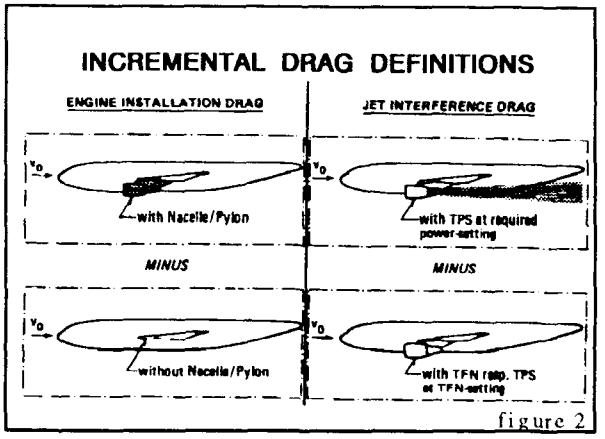

figure 2

For the first item, through-flow nacelles can be used, while the jet interference effects are investigated by the use of TPS-equipped nacelles, running at different power-settings. The main objectives for test with jet-simulation described in this chapter of the paper were :

- performance prediction for a new aircraft, concerning second segment climb jet interference drag and jet effects on tailplane efficiency during take-off and landing,
- to improve the understanding of the physical flow phenomena

For these purposes, force- and pressure-distribution-measurements as well as wake flow measurements and flow visualizations were made.

2.2 Improvements in testing technique

2.2.1 Wind tunnel equipment

The German-Dutch Wind Tunnel (DNW) is an atmospheric single return wind tunnel with two exchangeable test sections, of which the smallest one has convertible cross section. Of these two test sections, the largest one has a cross section of 9.5x9.5 m and the convertible either 8x6 or 6x6 m. All test sections have a length of 20 m and are equipped at the downstream end with breathers. The purpose of these breathers is to equalize the static pressure inside the test section to the ambient pressure. The maximum speed in the largest test section is 62 m/s, in the medium seized one 117 m/s and in the smallest one 153 m/s. For the test described in this paper, the medium-seized test section was used.

To measure the loads, the Airbus A340 model had an internal six-components balance. The balance maximum axial load is 20000 N, the maximum normal force is 50000 N and maximum side force 6250 N. The resolution of the balance in axial direction is 1.6 N and in normal direction 3.6 N. To suspend the model on a dorsal sting was selected. The sting was connected to the support mechanism which has an angle of attack range of ±45° and a yaw range of ±30°. Although continuous variation of the angle of attack is possible, the A340 test was executed in the step by step mode.

The model's angle of attack and roll angle were measured with a system mounted inside the model and consisting of three Q-Flex accelerometers. The Q-Flex is a completely self-contained unit which is very suitable to be used for accurate angle measurements. It has a seismic element which is held at constant horizontal position through the built-in servo electronics. The resolution of the system is 0.01 degree. For the yaw angle measurement, the sting mounted sensors were used. The resolution of these sensors is also 0.01 degree.

The compressed air to drive the simulators was delivered by the DNW Air Distribution System. Two compressor units form the hart of this system. Each unit has a maximum mass rate of 3 kg/s at 280 bars. This capacity is large enough to run three 7.1" fan diameter simulators continuously even at maximum rpm. Because the air delivered by the compressors is hot and too wet, it is cooled down and dried. For accurate TPS measurement a low residual humidity is important. If the humidity is too high, ice forms at the simulator core nozzle exit and changes the exhaust area and thereby the generated thrust. Experience has shown that a dewpoint of at least -70°C (at ambient pressure) is necessary.

The single supply line from the two compressor units split up in two lines. Each line has a heat exchanger and a computer controlled regulating valve. The computer can be programmed to keep the pressure constant at any downstream point, or alternatively to keep the TPS rpm constant. In this test the pressure in the supply line inside the model was held constant at 40 bars.

To measure the thrust vector of an isolated TPS, with or without flow, DNW has build a special test stand. This test stand is in effect a fuselage center section which can house one of the DNW's standard balances together with the airline bridges. Attached to the metric part of the center cross section is a vertical strut which points downward. The TPS to be measured is mounted to this strut. In front of the strut and the balance, a plate is installed for mounting instrumentation. The center section, the plate and the strut are surrounded by a non-metric shell. the nose shape of the shell is designed in such a way that the TPS-intake is in a uniform flow field.

2.2.2 Model hardware

The mounting of the engines to the model makes it necessary to subtract the thrust from the balance measurements in order to get the pure aerodynamic loads. The measuring rakes in the engine, installed for this purpose, were steadily improved to get a fail safe and very accurate system. In this context e g. the simple open thermocouples were replaced by the more accurate PT100 thermo-sensors.

Due to the low temperatures in the turbine region, water condensation occurs in the TPS nozzle after stopping the tunnel. This water, in combination with lubrication oil, can affect all electric connectors in this area. This necessitate a proper sealing of all wirings and avoidance of connectors wherever possible.

Another critical area is the sealing between the TPS-body itself and the cowlings and pylon. Leakages of compressed air from core to fan and from fan to pylon influence the accuracy of thrust calculation. Due to the unfavorable ratio between thrust and aerodynamic forces in the low-speed regime (thrust is about 2 to 4 times higher than drag) even small inaccuracies in thrust calculation heavily endanger the quality of test results. To avoid these problems, a special equipment has been built, by which inlet and nozzle exits can be closed. Then, after pressurizing the engine via the drive air connection on the pylon, all leakages can be detected and sealed afterwards.

To control the engine power setting and measure the drive air mass-flow, a remotely controlled valve plus a critical venturi nozzle system were usually located outside the model on the mounting sting or even further upstream. This system had the general disadvantage, that the response time was quite long. Additionally, the time delay between the actual turbine inlet mass-flow and the readings from the venturi nozzle measuring system causes inaccuracies in the thrust calculation. To improve this system, a model internal control and measuring unit was developed and build by Deutsche Airbus (fig. 3).

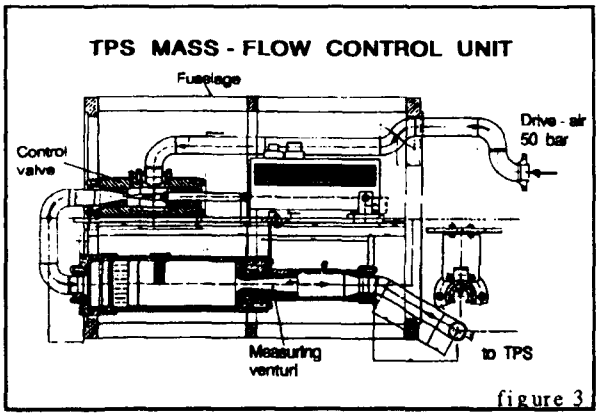

figure 3

Each unit consists of a needle-valve, remotely controlled and driven by a linear motor, plus a critical venturi nozzle for drive air measurement. This equipment was used for the Airbus A340

tests in DNW (Fig. 4). The model had a span of about 5.5 meters and a scale of 1/10.6. The weight of the complete model including all instrumentation used in this test was about 1.6 tons.

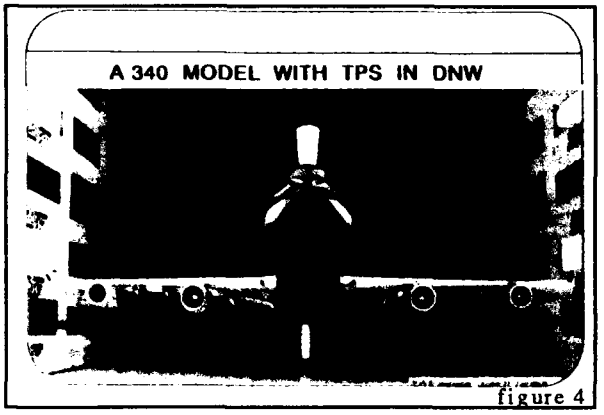

figure 4

Due to the fact, that the performance used for certification of the second segment climb flight is always with one engine failed and the others at maximum take-off power, one of the Airbus A340 engines was simulated by conventional through flow nacelle. So, three mass-flow control units were installed in the model fuselage ahead of the balance (Fig. 5) to control the three TPS units, designed and manufactured by Deutsche Airbus. The TPS-diameter was 7.1" and the units were equipped with cowlings representing CFM56-5C2 nacelles.

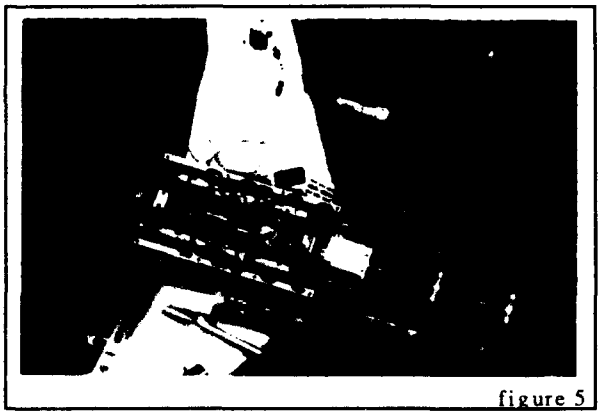
figure 5

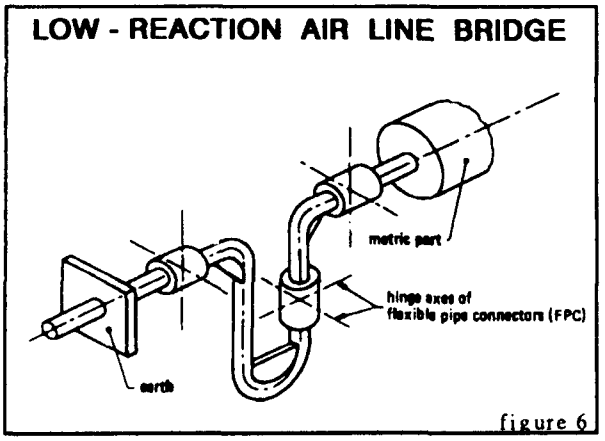

figure 6

To minimize the interferences between the model balance and the drive air pipes, a so-called air line bridge system is necessary. This consists of three cardanic joints in such a position, that the two degrees of freedom from each joint combine to a system with 6 degrees of freedom (Fig. 6).

Covered in each joint is a metal bellow to seal the piping system. This air line bridge system was modified such that the drive air pressure now is loading the outer side of the bellows instead of the inner and which stabilizes the bellows laterally. Figure 7 shows the A340 model from top with balance and airbridges.

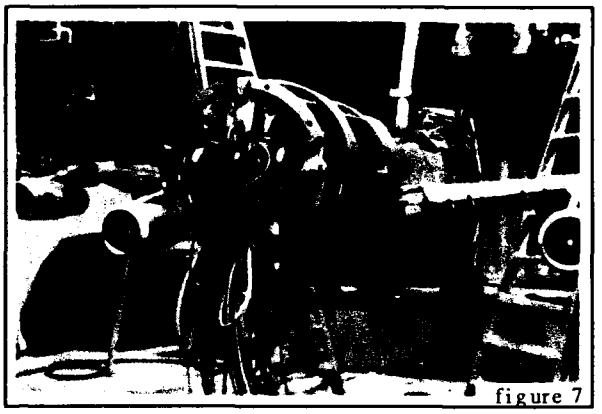
figure 7

2.2.3 Test procedure

The high accuracy needed for second segment climb jet interference drag measurements can only be obtained through a careful, step by step approach. It is not necessary to emphasize that, after each step, a throughout check of the system completed so far is necessary. The basic steps are :

- check of balance calibration;
- if not available, calibration of the balance for temperature gradients. The balance is equipped with 18 temperature sensors which measure the heat flux through the balance;
- calibration of the combination of balance and airline bridges, effect of temperature gradients in airline bridge is included;
- after mounting of balance and airline bridges in the model, check of parasitic forces due to TPS lubrication piping and electrical wiring;
- a test with cubic nozzles to determine the residual parasitic forces due to the airline bridges. Earlier this was only measured statically, but experience has shown that flow through the airline bridges alters the correction. The correction is found by measuring the balance forces and moments twice : once with the nozzles pointing in flow direction, and once with the nozzles turned over 180 degrees;
- a static pre-test with a bellmouth on each engine. The bellmouth measurement is repeated after the test is completed. The pre- and post-test results are used to access the validity of the calibration over the test period;
- repeat of polars and power polars (free stream velocity, angle of attack constant, rpm increasing);
- to reach thermal equilibrium in model and balance the simulators run for at least half an hour prior to the measurement run.

An essential element of the test procedure is a continuous control of all TPS-data. Malfunctioning of either total pressure probes or temperature probes in the TPS results in errors in thrust calculation. To this end, special software was developed following the Christmas tree struc-

ture. During the measurement, the global values like the overall thrust are compared with the values measured during the TPS calibration phase. When differences are noted, the next level such as the mean pressures and temperatures are examined. At the lowest level, each single rake total pressure profile and and temperature probes can be checked. To account for any difference in rpm in calibration and wind tunnel, the calibration values are all curved fitted as function of the rpm.

2.3 Recent test results

2.3.1 General

All improvements in testing techniques made since the first low-speed tests in DNW have led to a reduction of testing time as well as in data accuracy and repeatability such that today a high quality standard for industrial measurements has been achieved.

While results from tests on ground effects during landing were discussed earlier (Ref. 11) and the results of thrust reverser and reingestion tests are shown below, the next chapters concentrate on flow phenomena in context with the second segment climb phase.

2.3.2 Performance prediction for second segment climb

To predict the performances in the second segment climb phase (from short after take-off until the retraction of high lift devices), normally an increment for engine jet interference is added to the results on the models with conventional through flow nacelles. To get this increment, the procedure of Deutsche Airbus is to test a model with a TPS-nacelle as engine simulator. The TPS is then first set at maximum take-off power (MTO) and next at a condition similar to the through-flow nacelle (TFN). For this TFN-condition the TPS is running at a rpm, where the fan nozzle exit velocity is about equal to tunnel velocity, such representing the nozzle exit condition of a real TFN.

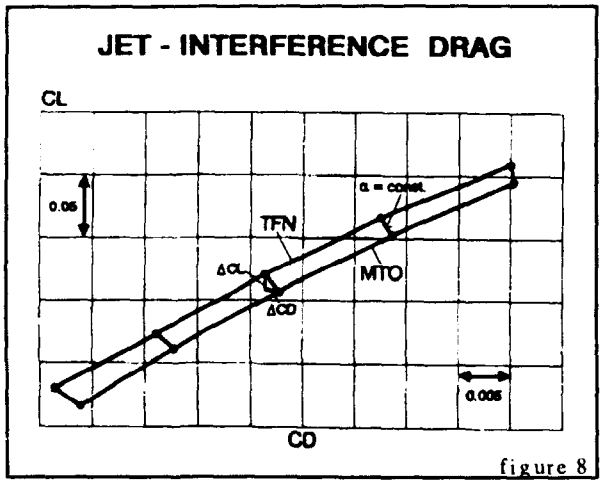

figure 8

The difference in drag between MTO- and TFN-setting is called jet-interference. Figure 8 shows a test result from the A340 model tests in DNW. As can be seen from this figure, the shift of the polar at MTO-power is not only due to a drag increase, but also due to a loss in lift at constant incidence. The lift loss is increasing with the increasing incidence. This phenomenon can be explained in such a way that the jet velocity of the engine located below the wing center-line counters the wing circulation and such leads to a decrease in lift plus increase in drag.

Another contribution to the jet-interference drag was found first during TPS-tests on an isolated TPS-powered nacelle in the wind tunnel of Deutsche Airbus at Bremen and later confirmed by tests on the "single engine strut" at DNW.

To simulate an engine on a wind tunnel model, the TPS is equipped with scaled down cowlings and pylon of the real engine. To make the jet-flow-field as similar as possible, all details like pylon-core cowl-fairing etc., are made as similar as possible.

The test in the Deutsche Airbus wind tunnel with such a simulator, mounted on a six components wind tunnel balance showed, that the overall thrust vector was not acting only in the direction of the engine center-line as assumed until now and also used in the flight-test evaluation, but deviated from this line. Further test with other configurations showed deviations in both directions, leading to a positive or a negative normal force increment.

This interesting result could not easily be verified by the engine manufacturer because all thrust stand balances are only "one-component balances" until today. Only one test on a real engine has been done in cooperation with Deutsche Airbus, DLR and Airbus Industrie on an A320 (see ref. 14). In this test a laser doppler anemometer was used to measure the flow-field directions behind the nozzle exits. As will be shown in paper no 20, the tendency of thrust vector deviation was in accordance with the wind tunnel results.

In the last years the thrust vector measurement on TPS engines have been made for different engine- and aircraft-types, by different Airbus Industrie's partners. Figure 9 shows some of the results, where the thrust vector "angle" is defined as the angle between overall thrust and engine center-line. It should be noticed here, that this effect must not be due to a pure deviation of the engine nozzle flow direction, but it can also cover effects due to differences in static pressure on the lower and upper regions of the core cowl (upper bifurcation blockage ?).

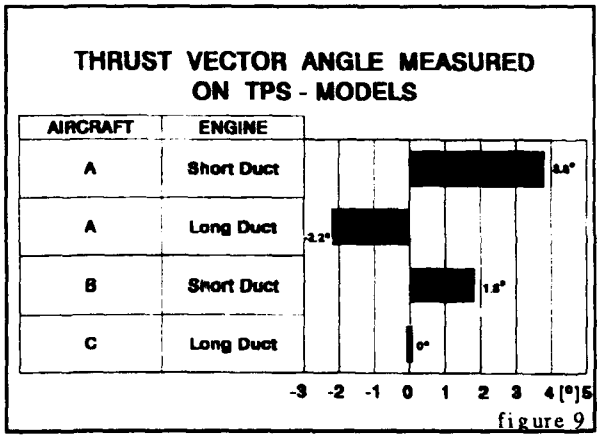

figure 9

For a better understanding of the consequences of these thrust vector effects, Figure 10 shows a schematic drawing of an engine installed on a wing and the corresponding angles and vectors.

Assuming stabilized flight conditions, engine axis parallel to horizontal fuselage datum (HFD) and thrust (F) acting along engine center-line, the main correlations between aerodynamic and thermodynamic forces are :

$$L = W - F_L$$
$$D = F_D$$

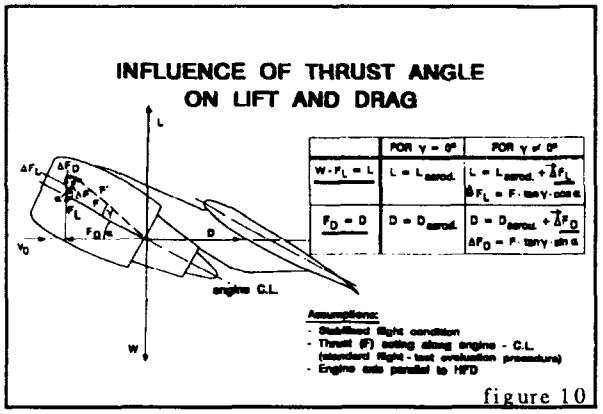

figure 10

Under these conditions, lift and drag are the pure aerodynamic forces L_{aerod} and D_{aerod}. If however the true or effective thrust vector is deviating by an angle γ from the engine center-line, it consists not only of the component F along the engine center-line which is delivered by the engine manufacturer as total thrust, but also of a component ΔF normal to this.

The consequence in this case is, that, if only vector F along the engine center-line is taken into account for analyzing wind tunnel and flight test results while the effective thrust vector is F', the contributions due to ΔF are included in the aerodynamic interference data for lift and drag. So, they are assumed to be aerodynamic forces while indeed they are propulsion ones. This can then lead to misinterpretation of test results while the overall performance calculation based on wind tunnel results is not affected as long as the wind tunnel data evaluation is in accordance with flight test analysis. An example for such a case is shown on Figure 11, where the incremental jet interference drag versus CL2 is plotted resulting from a wind tunnel test on an Airbus model with two different engine types and for different slat/flap settings during second segment climb. Without knowing the normal forces components of thrust, the differences in drag would be explained as aerodynamic phenomena. The tests of isolated TPS-powered nacelles however showed a deviation of the thrust vector from the engine center-line of +3.8° for one and -2.2° for the other engine type. With this information it is possible to split the overall engine-airframe interference into an aerodynamic and a propulsion component, which is very helpful for a better understanding of the underlying phenomena and finding possible areas of improvement.

The normal force component of thrust ΔF affects both the aerodynamic components lift and drag depending on incidence. As can be seen from Figure 10, at low incidence (cruise condition of aircraft) the main influence is on lift, while for higher incidence (second segment climb condition) the influence on lift is decreasing, and the drag component of ΔF is increasing.

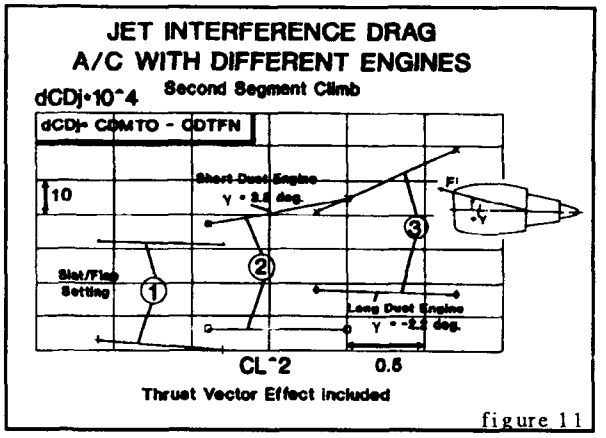

figure 11

Taking this into account, the results from Figure 11 can be reduced to the pure aerodynamic component of jet interference drag. The result is shown on Figure 12. This leads to the conclusion, that the pure aerodynamic jet effects are the same for both engine types while the differences in the direction of the thrust vector lead to the differences in the overall engine-airframe jet-interference.

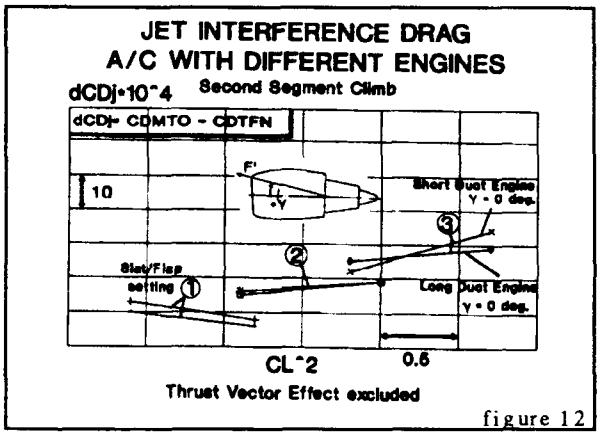

figure 12

2.3.3 Engine flow field investigations

For a better understanding of the flow phenomena leading to a deviation of the overall thrust vector from the engine center line, some tests with a wake-flow rake behind the TPS-powered nacelles have been done in the low-speed tunnels of Deutsche Airbus and DNW. The test setup for DNW is shown on Figure 13

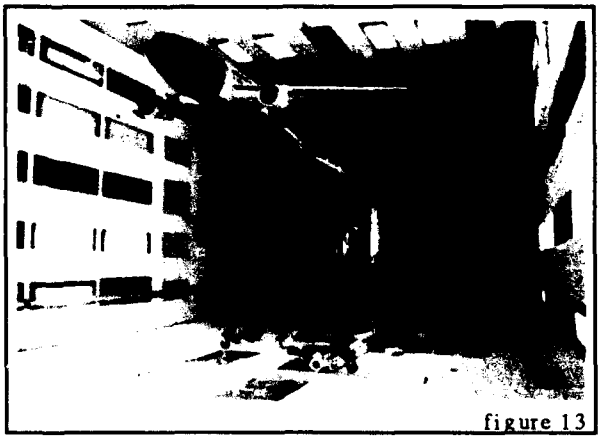

figure 13

The total pressures were measured at different stations behind the fan nozzle exit and summarized on Figure 14. What can be concluded from this figure is a strong unsymmetry in the flow-field close to the nacelle exit. This is an indication of a deviation of the nozzle flow direction from the engine center-line. Also measurements of static pressure distributions on the engine core cowls showed unsymmetries on the upper and lower regions leading to normal force components of overall thrust.

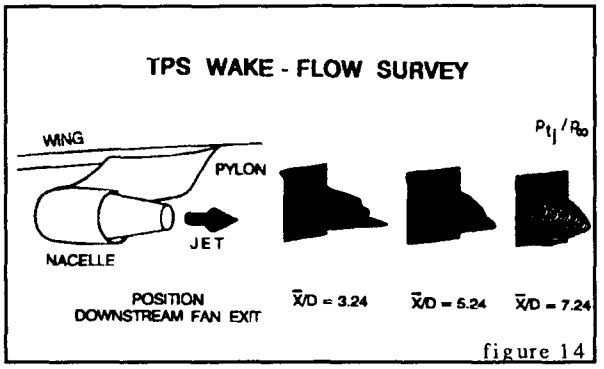

figure 14

2.3.4 Possibilities for performance improvement

Summarizing the results shown above, it can be concluded, that tests with TPS-powered nacelles in the wind tunnel indicate the existence of a normal force components of the thrust which have not been taken into account as such until now and thus are included in the overall engine-airframe jet interference effects. The next steps, necessary now, are :

- first a better understanding of the mechanisms leading to the thrust vector deviation
- second a verification of the tunnel results by tests on a full scale engine.

As already mentioned, for the latter case a first investigation was made on an Airbus at Toulouse by Deutsche Airbus, DLR and Airbus Industrie (see ref. 14).

Especially important however is now the assistance from the side of engine manufacturers for both necessary steps in order to verify the airframers data. Without this, all performances predictions will cover some uncertainties concerning these effects.

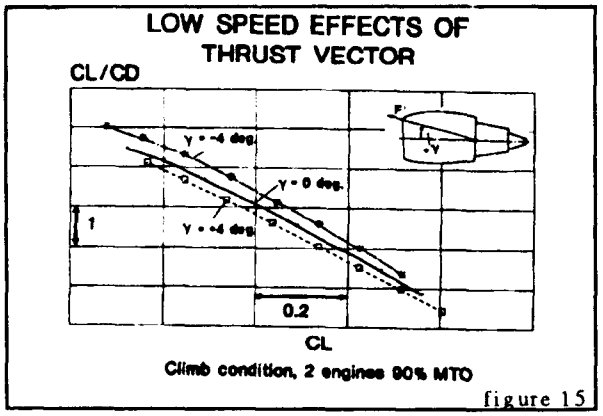

figure 15

Some first estimates have shown that, if the mechanisms of thrust vector deviation are understood and could be influenced, the overall performances of aircraft could be improved. A result for the low-speed regime for second segment climb with high incidences is shown on Figure 15. The variation of thrust vector angle of ± 4° leads to a variation in lift versus drag of +1% to 4% compared with an engine with a vector angle of zero degree. It should be noticed, that the higher lift versus drag is achieved for a negative thrust vector angle, i.e. an incremental force consisting of a lift- and drag-reducing component. Due to the high incidences, the negative effect of lift reduction is overcompensated by the positive effect of drag reduction.

Making a similar calculation for an aircraft at cruise condition, i.e. at low incidence, leads to a contradictory result, as shown on Figure 16. Under these conditions a positive thrust vector deviation angle is favorable due to the positive effect of the lift-component of thrust, while the drag-component at small angles is nearly zero. The possible increase in lift versus drag for an angle of 4° is also about 3% to 4% in the low-speed case.

The results shown here lead to the following conclusions and recommendations :

- it is necessary to understand and verify the phenomena with the help of engine manufacturers,
- negative angles of thrust vector deviation are favorable in the second segment climb, while,
- positive angles are desirable for cruise conditions.

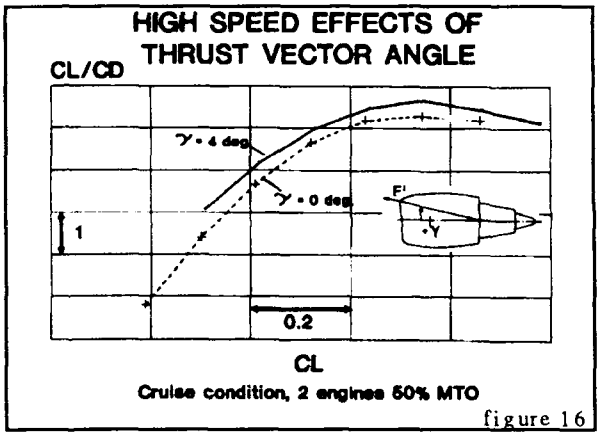

figure 16

So, an onboard mechanism to vary the direction of overall thrust vector could improve the performances of modern transport aircraft. If this mechanism is not feasible due to technical or financial reasons, the best compromise probably is to design the engine nozzles and pylons such, that the overall thrust vector acts along the engine center-line, unless situations where e.g. climb performance is insufficient (negative angle could help) or power reserves in low-speed performances are existing (positive angle improves cruise performances).

3. Installed Thrust Reverser Simulation

3.1 Test objectives

The fundamental objective of these installed reverser tests was to improve the aircraft landing performances prediction, as well as to reduce aircraft development cost. This main goal was effectively achieved through a number of clearly identified technical subjects such as :

- reverser static efficiency check-out
- reingestion speed limit
- plume effect on pilot probes
- local induced loads on slats

- reverser normal operation performances
- reverser inadvertent opening in flight

The associated financial benefit came from the reduction of the corresponding full scale development programme at Aerospatiale (reingestion for example) and the reduction of the full scale reverser-test at Hispano-Suiza.

3.2 Static tests

In association with the thrust reverser manufacturer Hispano-Suiza, Aerospatiale has conducted a six weeks static test campaign in the specially modified ONERA-Modane calibration tank S4b, using a turbine powered nacelle.

3.2.1 Static bench

The use of TPS for engine installation studies has driven ONERA to develop the necessary means for their calibration. As already said, the bookkeeping procedure of nacelle installation drag requires the assessment of the TPS thrust, wind off, but with the internal flow similar as under wind tunnel conditions (pressure). Two static benches have been build. The first one for TPS fan diameters below 6 inches and a second one for bigger TPS (fan below 16 inches), both described in reference 12. The principles are the same, only components size is different (balance, mass flow measurement,...). Figure 17 showss the larger TPS calibration facility arrangement.

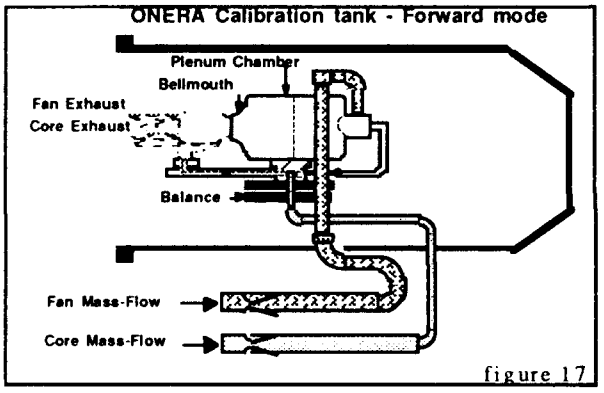

figure 17

The nacelle is connected to the balance interface strut, which also supplies the high pressure drive air (15 bars) to the turbine. As described in Chapter 1, this mass flow is then discharged through the turbine and exhausted by the nacelle core nozzle. The fan-mass flow is provided through a metric plenum chamber by the secondary piping connected to a 9 bars air supply. The nacelle is connected on this plenum chamber by a bellmouth.

The balance directly measures the jet thrust, while bellows disconnect the piping's metric and non-metric parts. The drive air mass flow crosses the balance in the middle, by use of a "Donahue" type of bellow (see ref. 13) minimizing "bottom effect". Two secondary bellows, on each balance side, provide air to the plenum chamber. Both mass flows are measured upstream the balance.

Balance calibration is done in situ, with all bellows connected. It showed (corrected for the tests) :

- low parasitic loads, pressure on (4 N on drive air bellow, 7 N on secondaries),
- weak pressure dependant thrust axis sensitivity variations (0,6 to 0,7% at 50 bars).

The facility is installed in a sealed vacuum tank (S4b). For transonic calibration (high fan nozzle discharge ratio), ambient static pressure is decreased by use of a ejector (ref. 12). For low speed tests (lower fan discharge ratio), Mach number effect is simulated only by plenum chamber "total pressure" increase.

The facility described hereabove is dedicated to classical forward thrust calibration, where plume does not impinge on the hardware. In reverse mode, the problem is different : the jet exhausted upstream creates parasitic loads on the metric parts, and disturbs the pressure field in the vicinity of reverser doors, that modify plume characteristics.

These two problems have been carefully studied in 1986, during the Airbus A320 program (see ref. 7 and 8). A pre-test has been performed with a blown nacelle fitted with reverser doors, in order to define a new optimized facility configuration (see fig. 18).

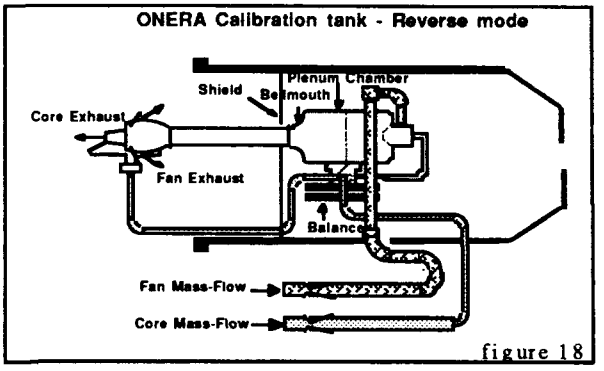

figure 18

First of all, the metric plenum chamber had to be shielded to avoid any impingement. This shield had to be sealed to avoid any pressure field disturbances in its vicinity, that could induce bouancy parasitic thrust. On the other hand, this shield, close to the reverser doors created a suction effect increasing exhausted mass flow up to 1,5%. As can be shown from the pressures recorded on the shield (figure 19), a nacelle 300 mm downstream displacement deleted this effect.

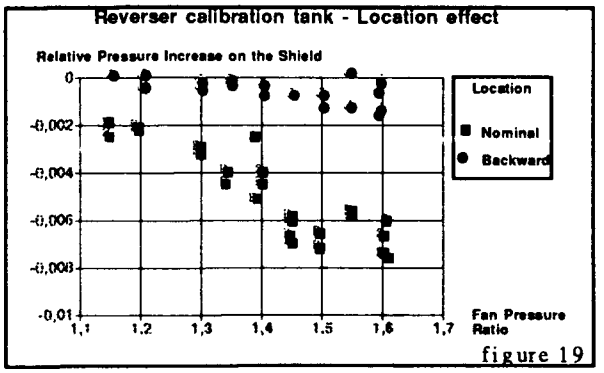

figure 19

These modifications leading to an homogeneous pressure field around the reverser, have forced to manufacture a new thin balance interface strut (including drive air supply line). Finally, the overall facility (model/plenum chamber/balance) has been moved backward, out of the vacuum tank, in order to avoid wall interactions.

Facility validation is achieved by use of two reference nozzles :

- Φ 130 mm reference nozzle, simulating the total mass flow (core+fan) crossing the balance. It can be feed, either by the turbine drive air-line or the secondary air-line, or even both. It is used to check loads and mass flow measurement repeatability campaign to campaign.
- DNW reference cubic nozzle, only feed by the drive air-line, and used to check repeatability measurement from S4b to the DNW.

3.2.2 Model hardware

The model used was a scaled down Airbus A340/CFM nacelle (1/10,6) powered with a turbine simulator (7,1" fan diameter) from Deutsche Airbus. The basic forward and reverse mode nacelles were manufactured by Aerospatiale and all plume tailoring components (leakages, kicker-plate and fan ramp fairing) by Hispano-Suiza. Full representation of all steps and gaps was even achieved. The reversed thrust nacelle was also able to simulate forward thrust by closing and sealing the four movable doors, just like on the real powerplant (see figure 20).

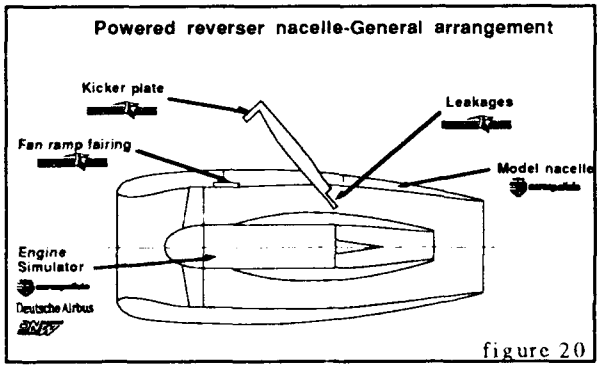

figure 20

The instrumentation used was based on the same definition as the Deutsche Airbus one (Fig 1) :
- one measurement ring downstream the last turbine stage, fitted with 4 total pressure rakes with 5 probes each, plus 6 PT100 for temperature data
- one measurement ring downstream the fan, fitted with 6 total pressure rakes with 5 probes each, plus 6 PT100 for temperature measurement.

3.2.3 Results

The goal of this static test campaign was two folds :
- forward and reverse TPS thrust calibration versus fan mass flow and fan pressure ratio
- reverser fan efficiency measurement.

The calibration laws used by Aerospatiale and ONERA have already been described in a previous paper (see reference 1). Their final expression is the following :

$$(1) \qquad \frac{WF\sqrt{TF}}{Po} = f\left(\frac{PTF}{Po}\right)$$

The law (1) gives fan mass flow in the tunnel.

$$(2) \qquad \frac{X}{PoS} = f\left(\frac{WF\sqrt{TF}}{Po} + \frac{WG\sqrt{TG}}{Po}\right)$$

The law (2) gives TPS thrust in the tunnel.

Concerning the second goal of static tests, the definition used for reverser fan efficiency is :

$$\eta = \frac{Xrev\text{-}Cis}{Fis}$$

An example of reverser efficiency is shown on figure 21. These data are coming from three different runs (1832/1833/1841) performed on the same model configuration. It is shown that on the overall measurement range, discrepancy is below ±0.5%.

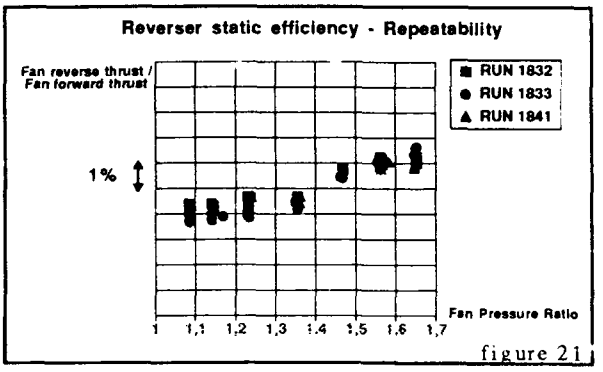

figure 21

As on a real engine, the first exercise is to match the reverser effective area to the TPS normal forward mode operating line. This is achieved by optimizing the reverser leakages. What is called "leakage" is the residual mass flow still exhausted by the forward fan nozzle in reverse mode. This flow is tailored by the gap height existing between the fully deployed reverser door trailing edge and the core cowl external line (see figure 22).

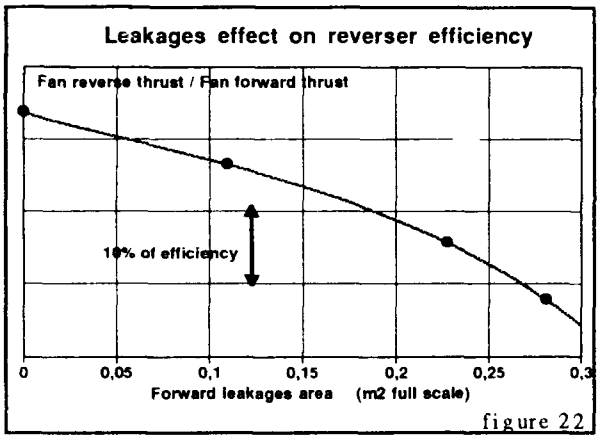

figure 22

The figure hereabove, showing results from the last test campaign, is a clear demonstration of reverser efficiency losses due to the "fan effective area match" exercise. Three different level of "leakages" have been tested, plus one reference configuration completely sealed, which means that 100% of the flow succeed through the inlet was exhausted through the reverser. This configuration is not realistic because a minimum level of forward fan flow is always required for core nozzle cooling at least.

Once the reverser effective area has been properly matched to the TPS operating line (as close as possible to the forward mode one), several reverser configurations have been tested (kicker plates and fan ramp fairings). This is shown in the following figure 23.

The main goal was to insure that the alternative configurations to be tested later in the DNW wind tunnel, in order to optimize the reingestion

limits (see § 3.3.2) were not unrealistic as far as efficiency was concerned. Efficiency and reingestion margins are generally heading in opposite directions because an efficient reverser exhaust plumes as parallel as possible to the engine axis, in order to get the lowest radial thrust component and keep most of it axial. But reingestion is caused by the suction of reversed plume which is easier when it is axial and consequently close to the inlet lips.

In this particular Airbus A340 case, the solution was a basic configuration on the outboard engine and an alternative on the inboard. The overall efficiency loss is then 5% (see figure 23 hereafter) on two engines compensated by a speed limit reduced by 10 kts (see § 3.3.2).

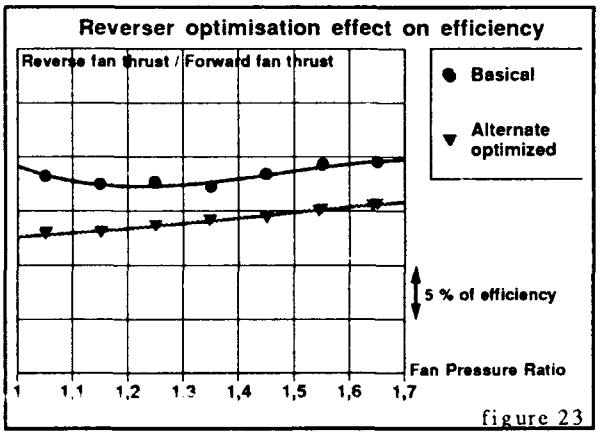

figure 23

3.3 Installed tests

Still in association with Hispano-Suiza, Aerospatiale has then conducted a six weeks test period in the DNW low speed tunnel, using the Airbus A340-300 complete airframe model available at Deutsche Airbus, as described in 2.2.2.

3.3.1 Hardware

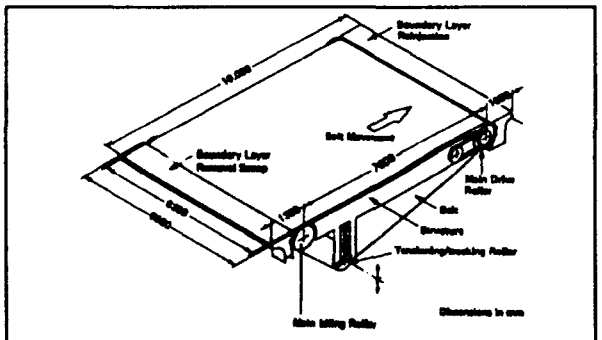
Moving Belt Ground Plane figure 24

The model was mounted in the 8x6 meters test section on the same dorsal sting as used by Deutsche Airbus. The only specific hardware added to it was the Moving Belt Ground Plane (MGBP) for ground effect simulation. A schematic drawing of the MBGP is shown in figure 24. The MBGP system replaces the test section standard floor element. When installed in the test section, the belt surface is 200 mm raised over the test section floor level. A boundary layer scoop at the leading edge of the MBGP removes the oncoming wind tunnel wall boundary layer. The removed mass flow is re-injected through a slot at the downstream end. An endless belt width of 5.2 m was used. To match the free stream velocity, the belt speed can be continuously varied from 5 m/s to 50 m/s. With the belt tension/tracking system the position and flatness of the belt is controlled.

The basic model hardware used for this second set of test is the same as described in the first part (complete powered Airbus A340 model fitted with three TPS units, at the scale 1/10,6). The main difference were the fan cowlings, manufactured by Aerospatiale and fitted with movable four pivoting doors reverser, as during the static tests phase.

Some additional instrumentation was also implemented on the model, i.e. :

- static pressure taps on high lift surfaces, horizontal tail, fuselage front section, pylon and reverser doors (247 more in total);
- 5 rakes of 3 thermocouples each on the two port engines inlets (see figure 25), specially dedicated to the reingestion tests.

3.3.2 Reingestion tests

The very first step for any consistent installed reverser test is to check the safety margins in the model (or aircraft) test envelop, by identifying the minimum speed limits, free of TPS (or engine) stall due to reversed flow reingestion. This input will also be of primary interest when the aircraft braking distances will be predicted through the airframer data bank. An highly efficient reverser is indeed of no use as long as it can't be used for more than a few seconds, due to its limitated speed range.

A good way to check if reingestion occurs, is to measure the air temperature in the engine or TPS inlet. The compressed air from the reversed flow is hotter than the ambient (30 to 60°C more) and can be easily detected. On the model, it is possible to implement a large number (15) of temperature probes in front of the fan, without any risk for its health (see figure 25). It is consequently possible to achieve a good value of the inlet temperature versus the engine power setting and the aircraft (or tunnel) speed. The reingestion development can then be quantified by the following parameter :

$$\tau = \frac{Tin - Tio}{TF - Tio}$$

This coefficient increases in principle from 0 (Tin is very close to Tio) to 1 (Tin is very close to TF). In practice, the TPS is in danger above 0.1

Another coefficient is then helpful to clearly identify the occurrence of reingestion phenomenon. It is possible, if the rakes position has been refined, to highlight the first reingestion spot, generally located at the bottom of the inlet inboard side. Then a "distortion parameter" can be defined as follows :

$$\tau' = \frac{Tmax - Tio}{TF - Tio}$$

An example of distortion coefficient result is shown in figure 25.

It shows the clear identification of reingestion initiation achieved with this process as well as the scale of phenomena studied with this TPS simulation. From a technical point of view, it has been finally possible to define an alternative reverser configuration, prior to the flight

test, and take it into account in the Hispano-Suiza production process.

The reingestion phenomenon quantified hereabove during the Airbus A340 tests, is typical for a four engine aircraft. The outboard inlet flow is spoiled by the reversed efflux exhausted by the inboard engine, located upstream the outboard, due to wing sweep. The easiest way to solve it is to change the inboard nacelle, outboard side, in order to modify the plume angle. As a reference, a self-reingestion example is also given (i.e. inboard engine shut down) to demonstrate that the reingestion is really not caused by any outboard engine plume sucked back by its own inlet (distortion curve stays flat).

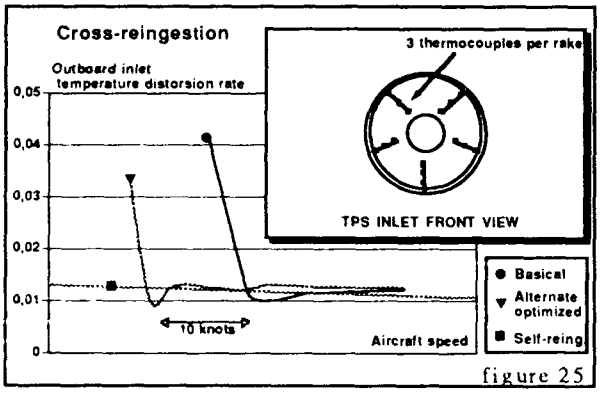

figure 25

These tests have been performed in landing configuration with all lift dumpers fully deployed, Airbus A340 model "on the ground" (50 mm above the moving belt), for three TPS power setting (max take-off, max reverse and idle) and tunnel speed continuously decreasing from 90 kts down to reingestion limit. The belt speed was constantly adjusted to the tunnel one, in order to simulate properly the aircraft speed relative to the runway and avoid any unrealistic plumes blockage effect under the wings. For safety reasons, the distortion rate in the inlets was constantly monitored, and TPS fan stall was detected with a microphone checking any variation in frequency.

During these tests, Hispano-Suiza has recorded the static pressures on reverser doors sides in order to check the loads on the doors hinges. These data are Hispano-Suiza proprietary and won't be shown here.

3.3.3 Reverser *normal operation tests*

The basic objective of such a test campaign is to identify the reverser effect on the basic aircraft aerodynamics, in order to supply the data bank with the most appropriate aero coefficients. These data are then used, in combination with the engine deck, to compute the overall braking forces acting on the aircraft during the landing phase. Landing distances can then be predicted for any kind of runway conditions (dry, icing,...).

The validity of this wind tunnel simulation has already been studied during the A320 program by Aerospatiale (see reference 7), through comparisons between wind tunnel and flight tests, on the predicted and measured braking distances. A simple comparison of these Airbus A320 tests and the Airbus A340 ones is shown in figure 26 hereafter, showing the reverser plume effect on airframe drag.

The reverser effect is quantified by the formula:

CDinteraction = CDreverse-CDforward

where all coefficients are corrected from TPS net thrust, and the difference is made at a given TPS power setting.
This is also valid for CL and Cm.

Two informations are provided in the figure :
- a comparison between Airbus A320 and A340 in landing high lift configurations,
- a comparison between two Airbus A340 high lift configurations and the clean one.

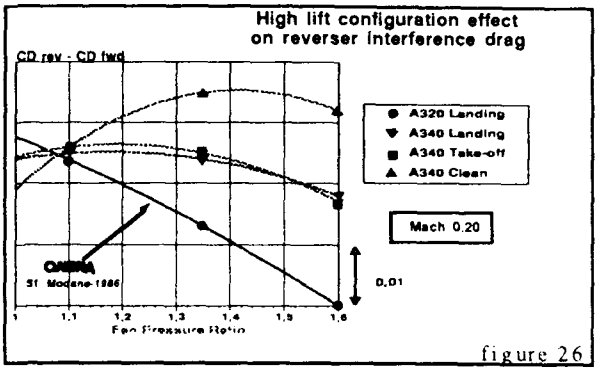

figure 26

The first remark is the good consistency of pure "reverser doors drag" represented by the lowest power setting tested (Fan pressure ratio 1.1) where no plume is exhausted. This demonstrates the quality of the results in spite of tunnels and model differences (A320 scale 1/7.6 in ONERA S1 in one hand, Airbus A340 scale 1/10.6 in DNW in the other).

The second remark is the improved situation of Airbus A340, relative to the A320, which keeps a higher drag level in spite of reverser plumes shielding, due to its large size, relative to its engines. The drag level directly increase the braking force.

The purely aerodynamic braking forces are produced by two devices : the reverser itself and the airbrakes. Their interaction has then to be taken into account. The easiest way is to divide the reverser plume effect on the airframe in two components : effect on the "clean" airframe (without lift dumper or airbrake) and the effect on airbrake efficiency (always negative). In the figure hereafter, an example of the drag interaction on the "clean airframe is given, as a function of aircraft speed and engine power setting.

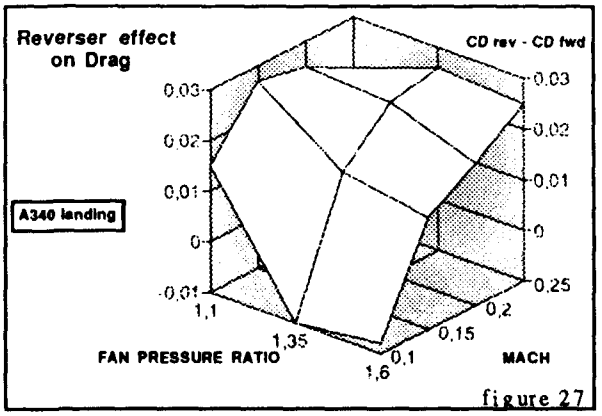

figure 27

In the figure 27 hereabove, the main remark is about the interaction drag decrease associated to the tunnel speed decrease and, more surprisingly to the TPS power setting increase. In fact, this phenomenon is the well known "shielding effect" produced by the reversed plume upstream the aircraft. The more the ratio plume speed-aircraft speed increases and the more this "shield" in extended in front of the airframe, which is more and more in a "static" environment is created. This "local speed" decrease in the neighborhood of the aircraft induces a drag decrease. In some extreme conditions, the drag can become smaller than the basic aircraft drag in forward thrust mode and could even be down to zero. This is the paradox of any reverser system which aerodynamic effect is opposite to the thrust effect.

Two coefficients have to be taken into account in the landing distances prediction process. The drag is directly combined with thrust, and the lift is introduced through the runway friction coefficient, which is depending on the weather conditions. Finally, the braking force formula, out of any direct action on wheels brakes is :

$$F = T + QoS[(CDa+CDr+CDab) + \mu(CLa+CLr+CLab)]$$

The integration of this formula as a function of time will then give directly the predicted aircraft landing distance.

These tests have been conducted on the Airbus A340 model, for three high lift configurations (landing, take-off and clean), three TPS power settings (max take-off, max reverse and idle), and different tunnel speeds from Mach 0.25 to Mach 0.10. The model was "on the ground", above the moving belt for propre ground effect simulation.

During these tests, static pressures have also been recorded in order to check the consequences on revered plumes impingements on slats (local loads) and on the fuselage (pilot instrumentation probes disturbances). On the Airbus A340, no direct impingement has been noticed, due to the engine location, on critical airframe component.

3.3.4 Reverser inadvertent opening in flight

The major improvement in the aircraft development program coming from this "installed reverser study" technics using wind tunnel simulation is not relevant of normal operation, but more of failure conditions. It allows to explore in detail the complex physical phenomena and the large number of parameters involved in such a critical event.

The flight test only provides limitated informations, while in the wind tunnel it is possible to go up to aircraft's most dangerous attitude and stay there to achieve a good knowledge about aerodynamics and handling qualities.

Since 1986, starting with the Airbus A320, Aerospatiale uses the wind tunnel simulation for this purpose. This technic has been validated at that time, and reported in the reference 7 document. The figure 28 shows for two coefficients (rolling and yawing moments) the effect recorded during the A310 flight test (1986) at one incidence only, compared to the wind tunnel results for A320/ CFM (ONERA S1 1986), A320/IAE (ONERA S1 1986), and to the Airbus A340 (DNW 1990) for inboard engine failure and outboard engine failure (incidence range from 0 to 8°).

The failure effect is quantified by the formula :

$$CDinteraction = CDfailure - CDforward$$

where all coefficients are corrected from TPS net thrust, and the difference is made at a given TPS power setting of the non failed engines and given incidence and sideslip angles.

This is also valid for all other coefficients.

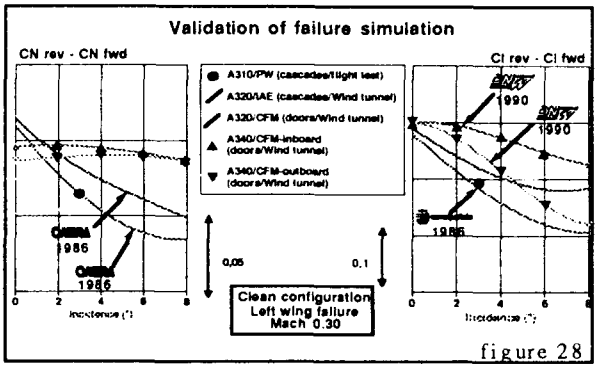

figure 28

First remark is the relatively small difference between a classical cascade type of reverser (Airbus A320/IAE or Airbus A310) and the four pivoting doors one for a twin engines aircraft (fig. 28).

Second remark is the good coincidence for all these configurations at the lowest incidences. Then the evolution at higher angle of attack is quite different for a twin or a four engines aircraft. It is smoother for the four engines, which is logical due to the relatively smaller size of the engine compared with wing span (fig. 28).

For this particular Airbus A340 test campaign, a very large number of parameters have been explored in order to answer properly the question put forward by the airworthiness authorities :

- 3 high lift configurations (landing, take-off and clean),
- 3 power settings (max climb, max reverse and idle),
- 7 incidence angles (0° to 12°)
- 4 sideslip angles (-4° to 8°)
- full inboard failure/outboard failure
- 3 types of outboard single door failure
- 1 type of inboard single door failure.

The basic failure case to be certified is the full four doors opening on either inboard or outboard engine. Some examples of forces (drag on figure 29) and moments (roll on figure 30) are shown hereafter, versus the explored flight envelope (i.e. incidence and sideslip), for the landing.

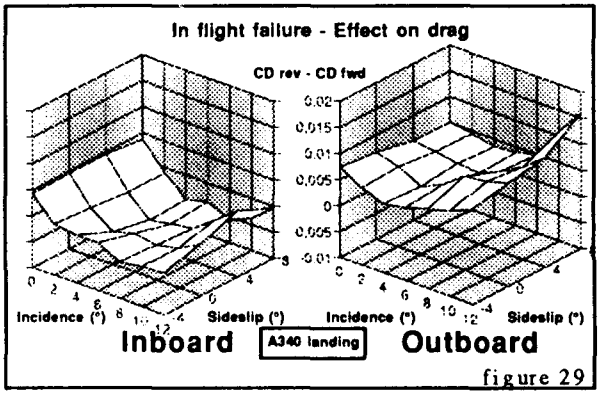

figure 29

On figure 29, the Airbus A340 does not appear to be very sensitive to sideslip effect, but the outboard failure seems more severe than the inboard one.

For the rolling moment shown on figure 30, the sensitivity to sideslip is slightly higher on the outboard engine, but the most important remark stays the relatively important effect of outboard failure. This leads to the foreseen conclusion that the outboard failure is more dangerous, mainly due to the longer lever-arm. Additionally, the local chord length at the outboard engine station is about equal to the Airbus A320 one. This leads to a situation comparable to this aircraft because the size of the reverse efflux is bigger relative to the local wing.

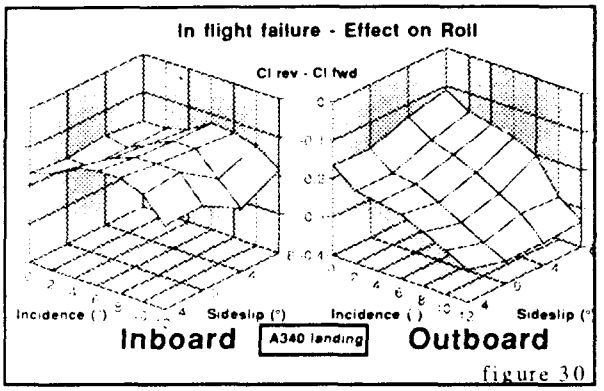

figure 30

A fundamental question is now to identify if one particular door is spoiling the wing flow and if yes, which one. This information is also helpful to answer some specific certification questions. As the outboard engine is the most important failure case, the major number of test configurations have been produced on that powerplant, and some of these results are shown hereafter (fig. 31 to 33).

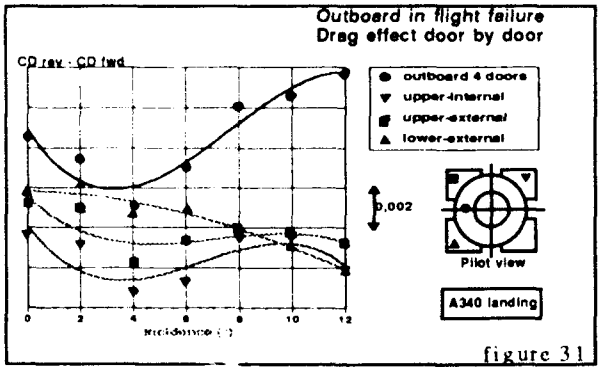

figure 31

The interesting doors are the two upper ones, which have a direct effect on the wing (even if there is no plume exhausted, and thus no physical shielding) and the lower external one due to the maximal lever-arm it creates.

In figure 31, the drag effect of 4 doors and the three single doors is compared. It appears clearly that the drag effect is never additive. All single doors produce a comparable effect, mainly at high incidence. On the other hand, the fully deployed reverser stays comparable to the single doors except for the high incidences, where its effect is much bigger.

It is interesting to have a look to the lift effect on the figure 32, in order to correlate it to the rolling moment induced. This lift effect (negative) is very small for the two external doors, which are far from the wing due to sweep. But the upper internal door, which is closer to the wing, produces almost the total effect by its own.

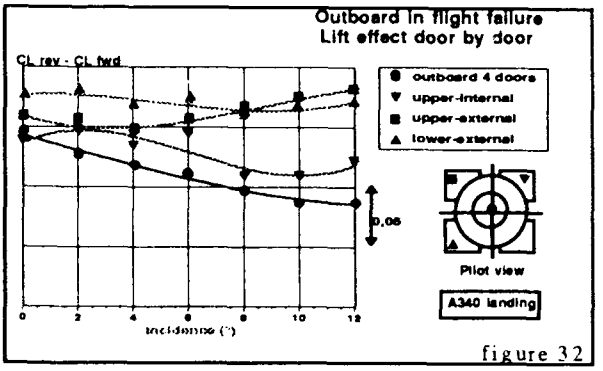

figure 32

In figure 33, the induced rolling moment is shown. The same tendency as for the lift effect is found, but the lever-arm increases the differences between the single doors and the fully deployed reverser. Even the upper internal door does not provide a critical moment by its own, in spite of its great influence on lift.

Anyway, in all explored cases, the full failure remains the critical one.

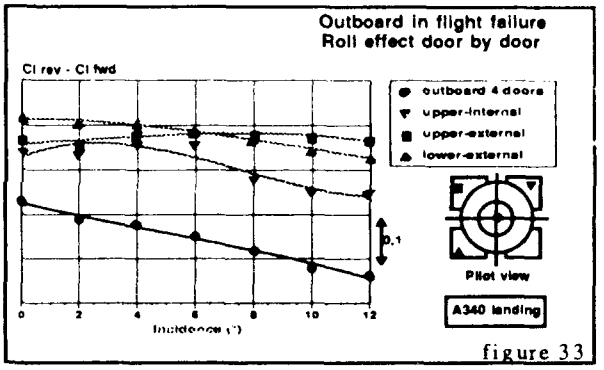

figure 33

Another interesting parameter is the engine (or TPS) power setting. But it has to be said that the potential main effect linked to any kind of power setting is not relevant of the aerodynamics (plume interference) but of the thermodynamics and thrust effects, which are not the purpose of the wind tunnel test as the following figures 34 and 35 show :

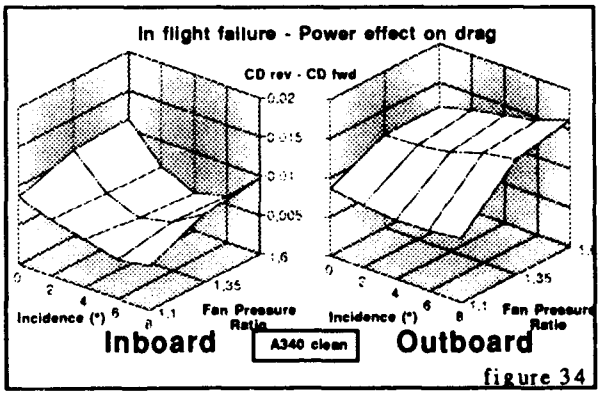

figure 34

The drag effect, as any force effect, is not primarily sensitive to the power setting on the in-

board side, which is consistent with the conclusions of the reverser normal operation study (§ 3.3.3). Once again, the outboard engine, due to the relatively short local wing chord is more sensitive and comparable to the A320 situation. It is also important to notice that, at higher aircraft speed and out of ground effect, the separation on the wing induced by the reverser plume impingement dominates the shield effect described in the paragraph 3.3.3, consequently increasing the aircraft drag instead of decreasing it. But, in any case, the power effect on the aerodynamic interference is about the same order of magnitude as the incidence effect is, which seems to be relatively small compared to the same power effect on pure thrust forces.

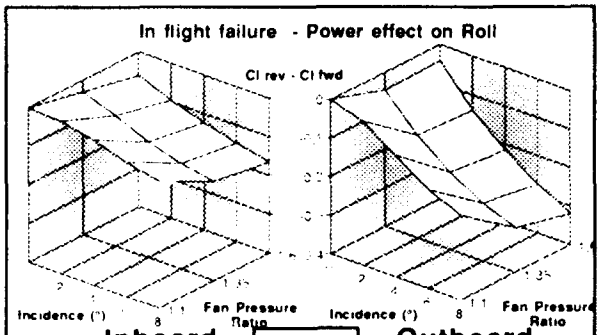

figure 35

The moments problem could be different, but, as shown on figure 35, it seems to be the same order of magnitude, if not smaller. The dominant effect is clearly the attitude, and mainly incidence effect, which is particularly demonstrated on the outboard engine.

Once all these aerodynamic informations have been collected, the certification process can still not start. Other inputs are necessary :

the reverse thrust from the engine deck
the Mach number effect from transonic test

The first component is provided by the engine manufacturer, as a pure thermodynamic input, without any nacelle aerodynamic data. All these aero data are already taken into account, together with the airframe data, through the installed tests.

The second input has been obtained in both Airbus A320 and A340 programs from transonic wind tunnel tests in the ONERA S1 Modane wind tunnel on a complete model fitted with "Through Flow Nacelles" simulating engine idle. One of them was equiped with four opened reverser doors. This test has been performed at several aircraft speed from the DNW Mach numbers (0.25 to 0.30) to the cruise Mach numbers (0.78 to 0.82).The Mach number effect is then computed using as a basis the data from the powered low speed model at idle power setting. Unsteady data are also recorded during this particular test.

Now the data set is complete and can be implemented in any development flight simulator. Pilots come to handle the aircraft during reverser failure sequence in any flight conditions, down to the landing. The handling qualities demonstration is then performed for the airworthiness authorities and future airlines pilots could even train this very particular type of failure.

But the certification process is not only a question of handling qualities. Prior to it, a statistical safety analysis is done and delivered to the authorities, and, as a final step a structural check-out is also completed, using the unsteady informations obtained from the transonic test.

4. Conclusion

The technical work, done in close cooperation between airframers (Deutsche Airbus and Aerospatiale) and the wind tunnels (DNW and ONERA) over the ten past years has led to a matured standard concerning low-speed testing techniques with engine simulation by TPS-powered nacelles.

Three types of concluding remarks have to be pointed out.

From a technical point of view, the goals for this series of A340 powered test was particularly ambitious, as well for the wind tunnel (moving belt), the model (three TPS) or the test itself (failure cases). But all of them have been successfully achieved, demonstrating in the same time the quality of the product under development at Airbus Industrie. More particularly, in context with the second segment climb investigations, effects of thrust vector deviation from the engine center-line have been detected, which were not known before. A verification of these results is necessary in cooperation with the engine industry.

From a financial point of view, in spite of what some people think about the high level of powered models and wind tunnels costs, the amount of aircraft full scale development and engine tests saved is still regarded by Aerospatiale and Deutsche Airbus as widely effective. Additionally, the future saving potential, related to the thrust vector improvement is still to be identified, but will anyway be very positive.

From a political point of view, finally,the European cooperation and unity has been once again enhanced through this fruitful German/French/Dutch aeronautical joint effort, via the industries and research centers directly involved, i.e. Deutsche Airbus, Aerospatiale, Hispano-Suiza, DNW, ONERA and NLR.

5. References

1 *"Essais en soufflerie de maquettes motorisées. Comparaison de deux méthodes de simulation de jets réacteurs"*
J.P. Bècle - R. Périn
AGARD-CP 331 - Toulouse, 1981

2 *"Experimental Investigations of Transport Aircraft Low speed Engine Interference Effects and Flight Correlation"*
B. Ewald - W. Burgsmüller
AGARD-CP 339, paper no6, Oct. 82

3 *"Low Speed Engine Simulation on Large Scale Transport Aircraft Model in the DNW"*
D. Eckert - J.C.A. van Disthuisen - B. Munniksmaa - W. Burgsmüller
ICAS-paper no 84-2.10.1, 1894

4 *"Benefit and Costs of Powered Simulation at Low Speeds"*
W. Burgsmüller - J. Szodruch
AIAA-paper no. 85-0381

5 *" Simulation und Messung von Triebwerkseinflussen an einem Zweistrahligen Grossmodell mit Hilfe von Modelltriebwerken"*
D. Eckert - W. Burgsmüller
DGLR-paper no. 85-92

6 *"Engine Simulation with Turbo-Powered Simulator"*
W. Burgsmüller-E. Akkermann-J.W Kooi
"Ten years of testing at DNW", Colloquium at DNW, 16, Oct. 1990

7 *"Efficacité des inverseurs"*
C. Castan
AAAF-paper - Poitiers, Oct. 1987

8 *"Détermination de l'effet de sol sur les caractéristiques de l'avion A320"*
A. Condaminas - J.P. Bècle
AGARD-CP 465 - Madrid, 1989

9 *"Engine Installation Design for Subsonic Transport Aircraft"*
J.J. Mirat - R. Périn - C. Castan
ICAS Paper no 90-2.7.4 Stockholm 90

10 *"Take off Drag Prediction for Airbus A300-600 and A310 Compared with Flight Test Results"*
B. Haftmann F.J. Debbeler - H. Gielen
J. of Aircraft, Vol. 25, no 10, Dec. 88

11 *"Results of Wind Tunnel Ground Effect Measurements on Airbus A320 Using Turbine Power Simulation and Moving Tunnel Floor Techniques"*
H. Flaig
AIAA-paper no. 90-1427

12 *"Nouveau banc d'étalonnage de nacelles équipées de turbines pour soufflantes (TPS), et essais d'éjecteurs"*
J.P. Bècle - J. Coste - J. Leynaert
AGARD-CP 348, Cesme 1983

13 *"Analysis of pipe system with special expansion feature"*
Donahue
ASME-paper no. 54 SA 70

14 *"The Jet Behaviour of an Actual High Bypass Engine as Determined by LDA - Measurement in Ground Tests"*
H. Hoheisel - K.A. Butefisch -
B. Lehmann - R. Henke - H.J. Roscher -
U. Seelhorst
AGARD-paper no. 20, Fort Worth 1991

AERODYNAMIC INTEGRATION OF THRUST REVERSERS ON THE FOKKER 100

J. van Hengst

Fokker Aircraft B.V.
Aerodynamics and Aeroelasticity Dept.
P.O. Box 7600
1117 ZJ Schiphol
Holland

SUMMARY

The Fokker 100 is a twin engined T-tailed aircraft developed as a short to medium haul passenger and cargo transport. The engines are located on the aft fuselage.
The development of thrust reversers on this type of aircraft was accomplished through different type of windtunnel model tests and full scale tests.

Model tests on an isolated exhaust configuration, scale 1:5, were conducted at Fluidyne in order to establish nozzle suppression and, thrust reverser efficiency and side plume effects.
Effects on directional and longitudinal stability characteristics were investigated by model tests on a complete model, scale 1:12, in the LST of NLR.
Reingestion tests were performed on the same complete model in the RR low speed facility at Hucknall.
Attached photographs show the model in the NLR and RR facilities.
This paper discusses the integration process, showing test results from windtunnel model tests as well as full scale boiler plate and flight tests.
A succesfull mean to control side plume effects on the directional stability and a configuration change to suppress induced reverse plume empennage buffet will also be discussed.

ABBREVIATIONS AND SYMBOLS

$\bar{c}$	mean aerodynamic chord
C_{n30}	Yawing moment about .30 $\bar{c}$
D	jet pipe diameter
EPR	Engine pressure ratio
FAR	Federal Airworthiness Regulations
FOD	Foreign object damage
H	end plate height
JAR	Joint Airworthiness Requirements
kCAS	Knots calibrated airspeed
kts	knots
LP	Low pressure compressor spool
LST	Low Speed Wind Tunnel
M_{MO}	maximum operating Mach number
NPR	Nozzle pressure ratio
S	T/R spacing to jet pipe
$\bar{T}$	Mean total temperature in the inlet at fan face
T_J	Jet total temperature
T_M	Maximum total temperature in inlet at fan face
T_O	Ambient total temperature
T/R	Thrust reverser
u/c	under carriage
V_{MO}	maximum operating speed
θ	clocking angle of reverser
β	sideslip angle
α	door sweep angle

1.0 INTRODUCTION

The use of thrust reversers is since long time an accepted means to augment the braking system on commercial transport aircraft. As a deceleration device that is independent of wheel brakes, thrust reversers increase the safety level in landings on wet or icy runways. Moreover thrust reversers can also be useful for ground manoeuvring and for counteracting residual thrust in high idle engine conditions during ground roll.
Installing a thrust reserver however also means an increase of the weight, cost and maintenance of the aircraft.
During the design work of the F28 Fellowship (in 1962) it appeared to be difficult to justify the installation of a thrust reverser. The Fellowship was designed as a short haul aircraft (reference 1) that can operate from short and/or undeveloped airfields (figure 1). For this the Fellowship features among other things a wing with low sweep and airfoil sections with relative large nose radii, a single slotted Fowler flap at take-off positions which changes to a double slotted at approach and landing flap settings. Large brake flaps were installed in the rear fuselage where they would not deteriorate the maximum lift of the wing nor influence the trim changes significantly. Analysis of landings on wet runways with one engine out and full reverse thrust on the life engine revealed that the F28 Fellowship is uncontrollable and will eventually slip from the runway.

The Fokker 100 (figure 2) is a new generation, high performance, twin engined aircraft developed as a short-to-medium haul commercial passenger and cargo transport. It is designed for a M_{MO} = .75 and a maximum cruise altitude of 35000 ft.
The range with 107 passengers plus cargo equals 1340 n.m.
The requirement to operate from short and/or undeveloped airfields was not taken into consideration in the Fokker 100 design.
Studies of landings as mentioned before indicated the need to install thrust reversers on the Fokker 100. This result was supported by the requirement for thrust reversers from (potential) customers.
The design work of the propulsion package of the Fokker 100 was carried out within a cooperative propulsion design programme with Gulfstream Aerospace Corporation. The goal of the programme was to save cost by achieving a common engine and nacelle suited for installation on the business jet Gulfstream GIV and the commercial transport Fokker 100. The combined design efforts of both airframe manufacturers are discussed in reference 2.
It should also be noted that in this cooperative propulsion programme, the engine manufacturer Rolls Royce and the nacelle and thrust reverser manufacturer Grumman Aerospace were participants.

2.0 NOZZLE/THRUST REVERSER DESIGN

A thrust reverser, T/R, for ground operation usage was considered in the design.
The design objectives of the thrust reverser were:

- with the T/R stowed:
  - no effect on engine performance
  - avoid extra drag penalties
  - aim for good jet noise attenuation.
- with the T/R deployed:
  - no effect on engine operating limits
  - a reverser efficiency of 35% or higher
  - satisfactory aircraft directional stability and controllability
  - no exhaust ingestion or FOD behaviour
  - a cancellation speed down to 50 kts.

A fixed-pivot target type reverser was selected. Through an extensive test programme at Fluidyne in Minneapolis on an approximate 1:5 Tay exhaust model (figure 3) and engine cycle studies of Rolls Royce, it appeared that the Tay engine favoured a flared convergent type nozzle (figure 4). More details of the selection process of the nozzle and the T/R configuration viz. the T/R spacing ratio and the door sweep angle are discussed in reference 2.

3.0 THRUST REVERSER/AIRFRAME INTEGRATION

The aerodynamic integration of a T/R to an aircraft was new in the design process of Fokker.
In order to reduce the design risks an extensive development programme (figure 5) was defined, utilizing different types of wind tunnel tests and full scale tests. The potential aerodynamic risk areas are:

- degradation of directional stability and controllability
- pitch-up behaviour
- re-ingestion
- impingement of aircraft components.

3.1 Stability and control test programme

3.1.1 Model

The low speed facility (LST) of NLR in the North East Polder was used to investigate the influence of thrust reversers on aircraft stability and controllability.
An existing F28 model scale 1:12 was partly modified to represent a Fokker 100 configuration as close as possible. The modifications concerned the fuselage length and the distances between nozzle exit and the empennage and between the nozzle exit and the wing/inner flap.
Axis-symmetrical blown nacelles of the same volume distribution as the full scale nacelles were fitted with elliptically faired inlet pieces, so the inlet flow was not simulated in these tests.
The exhaust configuration selected from the nozzle T/R Fluidyne programme with the T/R in the stowed and deployed position was represented viz. door angle 9 degrees, no door clocking, end plates on upper and lower door of 4 mm model scale and a spacing ratio of .76 (figure 6).

Measures were taken to enable clocking of the T/R doors during the tests.
The model (figure 7) was mounted on a sting above a groundboard. The sting, which was hollow, served as air supply line and was attached to an air distribution chamber.
Nacelle, thrust reverser and stubwing were also connected to this air distribution chamber (figure 8). Fuselage, wing and empennage were connected to a six-component internal balance which was fastened to the air distribution chamber. In this way the balance measured all the forces and moments on the model except those on the nacelle, thrust reverser and stubwing combination.
The thrust of either the cruise nozzle or the T/R was derived from static calibration tests. The calibration results and T/R base drag were transformed to the axis system of the 6 component balance.
The T/R base drag component was obtained from integrating the pressures on the back-side of the T/R door.
In addition pressures and temperatures were measured (figure 8) to monitor the propulsor performance, leakage through the labyrinth sealing and heat transfer to the balance.

3.1.2 Scope of test

The model was tested in the landing configuration i.e. flaps at 42 degrees, lift dumpers at 60 degrees, undercarriage extended and the horizontal stabilizer set at -8 degrees. Limited variations of stabilizer and flap settings were tested.
The model placed at a touch-down distance above the ground board at an angle of attack of 0 degrees was yawed from -10 degrees upto +30 degrees.
Nozzle pressure ratio was varied from 1.03 (idling) to 1.60 (take-off) and the tunnel speed ranged from 30 m/s (60 kts) to 6.0 m/s (120 kts).

Other model parameters investigated were rudder deflection, T/R door clocking, side plates, strakes and end plates on the reverser doors.
The flow was visualized by tufts and for interesting reverse thrust conditions the plume was visualized using liquid nitrogen and steam. The fog was illuminated by either two 1000 W spot lights or a light sheet from a 5 W ion laser (figure 9). The latter was useful to study the vortices in the reverse plume formed in front of the horizontal tail plane.

3.1.3 Test Results and Conclusions

From the flow visualization tests it was observed that the reversed jet from the thrust reverser was composed of two main jet plumes and four side jet plumes.

The way the top main jet plume turned off backwards and flowed over or beneath the horizontal tail was the result of the interaction between the reversed plume and the free stream momentum forces (figure 10).

For the bottom main jet plume the presence of the ground board moreover played an important role. It was observed that at a NPR = 1.10 and a forward speed of 50 m/s both main plumes turned off strongly and the top plume passed below the horizontal tail.
Keeping the NPR at 1.10 and reducing the forward speed to 40-30 m/s it was found that the horizontal tail was submerged in the top reversed plume. At 30 m/s the bottom reversed plume impinged on the ground board. At 20 m/s the top reversed plume passed well above the horizontal tail.

At zero speed both reversed plume were directed forward except for some flow diffusion of the bottom plume impinging the ground board.

Furthermore the top inboard side plumes towards the fuselage and vertical tail caused flow unsteadiness on the vertical tail and flow separation on the rudder.

The force measurements substantiated the directional stability and controllability degradations as observed during the tuft runs.
Nozzle pressure ratios (figure 11a) and forward speeds (figure 11b) could be traced at which the configuration became directional instable and beyond which side slip angle stability recovery occurred.

It became clear from these tests that restoration of the directional stability will also improve controllability.
Means to manage the plumes were explored such as end plate modifications, strakes on the door and door clocking to influence the main plumes, side plates, edge caps and also door clocking to counteract the side plumes and combinations of aforementioned gadgets (figure 12).

Positive (top outboard) door clocking angles exceeding 10 degrees were required to restore the directional stability of the model with the basic T/R configuration. The inherent disadvantage however was an unacceptable pitch-up moment and an increased risk of reingestion.

As the inboard side plume also contributed to the destabilizing behaviour by blanking off the vertical tail from dynamic pressure, the effect of side plates were tested (figure 13).
"Chinese fan" type side plates located on the inner quadrant of stang beam and door edge were considered. Shape of the edge member on the side plate and the radius of the side plate were varied.
It was found that only the side plates on the upper door quadrant improved the directional stability.

After a laborious process of trial and error two configurations were selected, a preferred and an alternative one. The alternative one was meant as a backup configuration in case the prefered one showed unacceptable reingestion characteristics in the next part of the integration programme (figure 5).

The prefered T/R configuration (figure 14) features on full scale dimensions:
- an end plate on the top door with a height of 48 mm.
- a "Chinese fan" type side plate on the inboard top T/R door. The radius of the fan equals 456 mm and originates from the T/R door pivot point. On the circular fan part a lip type edge member with a lip height of 48 mm.
- an end plate on the bottom door with a height of 72 mm.
- no clocking (θ = 0°) of the T/R doors.

The alternative T/R configuration holds the same top door end plate and side plate of the prefered T/R configuration. The differences with respect to the preferred T/R configuration were:
- no end plate on the bottom T/R door.
- 5 strakes of 300 mm length on bottom T/R door. The strakes were tapered from 48 mm to 72 mm and were arranged on the T/R door in such away that the bottom main plume was directed to flow outward (i.e. away from the fuselage plane of symmetry).
- 5° clocking (top door outward) of the T/R doors.

Although the alternative T/R configuration showed better yawing moment characteristics, the preferred T/R configuration (figure 15) was selected because of its simplicity. Furthermore T/R doors are thermally and aerodynamically highly loaded components and consequently the end plate on the T/R door improved its structurally integrity.
Deletion of the end plate and installing strakes on the bottom T/R door of the alternative configuration meant an unwanted structural complication and weight increase.

The investigation was completed with test runs on the preferred T/R configuration in order to collect aerodynamic and reverse thrust data for the engineering data base.
From these tests it was found that during a-symmetrical T/R operation (i.e. one side T/R deployed and operative and the other side T/R stowed and engine not operative) the directional stability and control was improved with respect to the symmetrical T/R operation cases.
Variations of pitching moment were small and no pitch-up tendency was measured.
At high NPR and low forward speed a small increase in lift was measured; this was most probably caused by induced circulation on the inner wing from the bottom main plume ground board interaction.

Other important conclusions were that:
- at a NPR of 1.42 and a forward speed of 120 kts the dynamic pressure sensor at the horizontal/vertical tail junction registrated a peak at 72 Hz (equals 6 Hz at full scale) in its spectral density plot. This indicates a top plume/tail interaction.
  forward speed resulted in an additional exhaust suppression due to T/R deployment. Also the basic nozzle characteristics were influenced by forward speed.
- speedbrakes on the rear fuselage did not contribute in restoring the directional stability.

3.2 Reingestion test programme

3.2.1 **Model**

The same F28 model used in the stability and control test programme was modified in the rear fuselage to incorporate high pressure air supply pipe and an intake flow suction pipe (figure 16). The nacelles were fitted with representative intakes having a full array of thermocouple instrumentation (figure 17). Furthermore the nacelles configured the preferred T/R configuration as discussed in the previous chapter and some end plate modifications were included for diagnostic tests (figure 18).

3.2.2 **Scope of test**

The model was tested in configurations representing 1) a landing (i.e. flaps 42° and liftdumpers 60°), 2) an aborted Take-off (i.e. flaps 20° and liftdumpers 60°) and 3) ground taxiing (i.e. flaps and liftdumpers retracted).
Three nozzle pressure ratios 1.2, 1.3 and 1.4 were tested and the tunnel speed was varied from 100 kts down to 30 kts. Heated air of approximately 110°C was used to simulate the engine exhaust flow.
Side slip angles explored were zero, -15° and -30°; (-) meant starboard engine out of wind. In the a-symmetrical T/R operation test case (port engine shut down) +30° and -30° slip angles were measured. Flow visualisation was carried out by supplying pre-mixed steam/hot air to the nacelles.

3.2.3 **Results and Conclusions**

The measured temperatures in the fan face were expressed in terms of a distortion $\left(\frac{T_M-\overline{T}}{T_J-T_O}\right)$ and a reingestion $\left(\frac{\overline{T}-T_O}{T_J-T_O}\right)$ parameter.

It was found that at a NPR = 1.4, reingestion started at about 90 kts with a peak temperature distortion at 80 kts. These speeds were reduced by 20 kts, i.e. reingestion at 70 kts and distortion at 60 kts, at a NPR = 1.2 (figure 19).

For SL/ISA conditions the measured maximum reingestion of .09 at NPR = 1.2 meant an increase of 8°C above ambient of the intake flow. The measured peak distortion of .07 at NPR = 1.2 meant an increase of 6°C in the bypass flow entering the intake. This latter was derived from the radial temperature distributions measured by the intake rake.

At a NPR of 1.42 and -15° side slip angle the starboard, out of wind engine, which would be expected to reingest first has a better reingestion characteristic than the port in to wind engine.
At -30° side slip angle the starboard out of wind engine reingested first as one would expect. This peculiar result could be explained by considering the aircraft geometry. At a side slip angle of -15° the inboard flap geometry provided a clear channel in front of the starboard intake for air to blow through and keep the starboard engine free from reingestion for an extended period. At a side slip angle of -30° this channel disappeared and the expected result occurred.
Ventilation of the bottom end plate resulted in a significant improvement in the distortion level. The reingestion characte-ristics did not change.
It was concluded to plan tests on the prototype to determine the engine tolerance to reingestion and distortion characteristics as measured in this programme. Furthermore the cancellation speed should also be measured during these prototype testing.

3.3 Boiler plate test programme

As part of the engine development and certification programme the engine manufacturer carried out tests on a complete engine.
The engine test set up comprised a so-called boiler plate T/R unit (figure 20 and 21).
Only the internal aerodynamic lines of this T/R unit

were representative for the actual T/R.
The door deployment mechanism was simplified.
From these tests it was found that the engine tolerated T/R operation in static condition and during transient behaviour.
Various temperatures on the T/R door and stang beam were measured for structural design optimization studies.

3.4 Engineering flight simulator studies

3.4.1 **Purpose of the study**

In order to demonstrate compliance with the JAR/FAR requirement, par. 25.933(a)(2), a flight test must be performed on the F28 Mk0100 prototype aircraft. During this flight test a T/R bucket must be deployed and stowed on one side at 180 kCAS and 200 kCAS. The restow capability up to 200 kCAS must be demonstrated and it must be shown that the flight can be continued safely including an approach and landing with one T/R deployed.

It was decided to carry out a comprehensive flight simulator test program in order to gather additional compliance material to support the above mentioned flight tests.
The flight simulator test program includes a variety of loading conditions and configurations throughout the complete flight envelope.

Furthermore an opportunity for the pilots was created to familiarize themselves with the T/R operation on the aircraft well before flight testing took place. Landings, aborted take-off's and taxiing and powerback under various runway conditions including a range of cross winds were explored.

3.4.2 **Method**

The study was performed on a fixed-base type simulator, having a representative cockpit lay-out, including preproduction aircraft compatible Efis-displays and instrumentation.
The control loading system was of analog type with hardware featuring hydrostatic bearings. Calculation of aerodynamic hinge moments of the control surfaces was digital, whereas the transfer functions of hydraulic and mechanical flight control systems were analog.
The T/R door deployment aerodynamic effects derived from the stability and control test programme were coupled with the standard simulation system through a separate software module.
Engine response on automatic throttle retardation to idle power after inadvertent T/R deployment validated during the boiler plate tests, were provided by Rolls Royce.
The test pilot was unaware of the time at which inadvertent bucket deployment was initiated and unaware at which engine, with exception of the tests compatible with the actual flight tests, i.e. L/H side.

3.4.3 **Results and Conclusions**

From the simulator flight tests it could be concluded that after sustaining an inadvertent T/R deployment in flight (cruise, dive, approach), it was possible to continue safe flight and landing without extreme pilot skills. Maximum roll angle encountered was 22.2 degrees and maximum sideslip was 4.4 degrees (with yawdamper off).

Critical conditions found were the inadvertent T/R deployment during take-off (with T/R deployment beyond V_1 and the a/c at MTOW) and the go-around (with MLW), in which marginal controllability and climb perfor-mance were found, even when the engine with the deployed T/R was shutdown.

When during the take-off with flaps selected 18 degrees an inadvertent deployment occurred beyond V_1, the remaining engine should be set at maximum thrust (max. HP rotation speed) in order to gain speed and altitude for recovery.
From the above the following recommendations were made by the pilots: After and inadver-tent T/R deployment during any phase of the flight it is recommended to shut down the engine with the failed T/R as soon as possible in order to achieve best climb and cruise performance.
Furthermore the flaps should be selected 25 degrees on the approach (as recommended after any engine failure) to enable a go-around with flaps 11 degrees.

3.5 Flight test programme

3.5.1 **Aircraft instrumentation**

The Fokker 100 flight test programme was carried out on two prototype aircraft, Q1 and Q2, equipped with the Fokker/NLR measuring and registration system (MRVS) (figure 22).
In addition a straingauged fan was installed in order to check the inlet compatibility during ground and flight testing by recording the alternating stresses. The equipment, straingauges and their positions were identical to that used on the boiler plate test programme.
During T/R evaluation and certification tests the straingauged fan was also installed.
These tests were performed mainly on prototype aircraft Q1. On this aircraft additional instrumentation was installed, such as

1) thermocouples on various locations on the fuselage, fuselage/wing fairing, stubwing and nacelle and T/R.
2) mini microphones on the fuselage surface adjacent to the T/R.
3) straingauges on the horizontal stabilizer pivot lugs, accellerometers in the horizontal stabilizer tip sections and on the T/R drive rod.

3.5.2 **Scope of tests**

Flight tests were performed to evaluate aircraft behaviour and handling during T/R operation and to show compliance among others with JAR/FAR requirements 25.125, 25.143, 25.933 and 25.1091.
Furthermore tests were required by the Authorities before clearance could be given for powerback operations (JAR/FAR 25.939).

3.5.3 **Results and Conclusions**

It was demonstrated that no exceptional skill was required to control the aircraft during a landing with T/R deployed (JAR/FAR 25.125).
It was observed that there was no strong change of longitudinal pitch due to T/R selection during the landing and that after touch down the nose could be lowered smoothly (JAR/FAR 25.143(b)(3)).

During the inflight T/R deployment (figure 23), it was demonstrated at 180 and 200 kCAS that the deployed T/R could be restowed. The restow time was less than 4 seconds.
Adequate controllability was demonstrated at 180 kCAS with 1.2 NPR reverse power on the LH engine and MCT on the RH engine.
A rudder deflection of 7.5 degrees was required to counteract the thrust asymmetry with only minimum trim changes of rudder, aileron and stabilizer (figure 24).

Satisfactory flight handling characteristics (flap extension and roll capability) are demonstrated throughout the manoeuvre.

In the landing with the flaps deflected 25 degrees, u/c down and a speed of 1.3 V_S, the LH engine was set at approach idle power and the thrust reverser at the RH engine was deployed. Full reverse power was selected on the RH engine only after touch down. No adverse handling characteristics were encountered during the landing (figure 25).
In these flight tests, continued safe flight and landing was demonstrated with thrust reverser deployed and the relevant engine at idle power (JAR/FAR 25.933).

It was also found that throughout the flight test the aircraft sustained regular but moderate buffeting when the thrust reverser was deployed.

From the straingauge readings collected during static ground runs with cross-winds, landing and take-off rolls, landing with use of reverse thrust, flight manoeuvres and powerback trials it was concluded that the vibrational behaviour of the fan was satisfactory for all service conditions that can be envisaged. No unusual modes of vibration or flutter were observed (JAR/FAR 25.939).
High fan peak stresses (figure 26) were recorded during static tail-wind testing and a powerback operation when the engine LP was operated at about 6000 rpm. For a satisfactory blade fatigue life this engine LP rotational speed should be avoided during service. The appropriate aircraft manuals include a caution.

During the T/R test trials, also high alternating loads were measured on the horizontal stabilizer when maximum reverse thrust was selected at speeds well above cancellation speed.
These loads had an impact on the fatigue life of the stabilizer support. The load levels must be reduced in order to maintain infinite life for the pivot lugs. This was accom-plished by reducing the day to day reverse NPR to about 1.2 and to install wedges on the T/R trailing edge.

These wedges create a gap between the deployed top and bottom T/R door (figure 27). The size of the gap was selected in such away that the loss in overall T/R efficiency was kept to a minimum i.e. the thrust bleed through the gap was compensated more or less by an increase of T/R efficiency due to the increase of doorsweep (figure 28).
The bleed flow through the gap suppresses the low frequency fluctuations in the wake behind the deployed T/R doors.

4.0 FINAL CONCLUSIONS

An extensive development programme was carried out in order to integrate and certify the thrust reverser successfully on the Fokker 100.

5.0 REFERENCES

1. Fokker F28 Fellowship, 50-65 seat short haul airliner, Aircraft Engineering June and July 1967.

2. H.F. Nawrocki, J. van Hengst and L. de Haij, Design and Testing a common engine and nacelle for the Fokker 100 and Gulfstream GIV Airplanes. AIAA-89-2486.

Figure 1 F28 Fellowship in operation in Pakistan

Figure 2 Fokker 100 in operation with USAir

Figure 3 Nozzle and thrust reverser model at Fluidyne

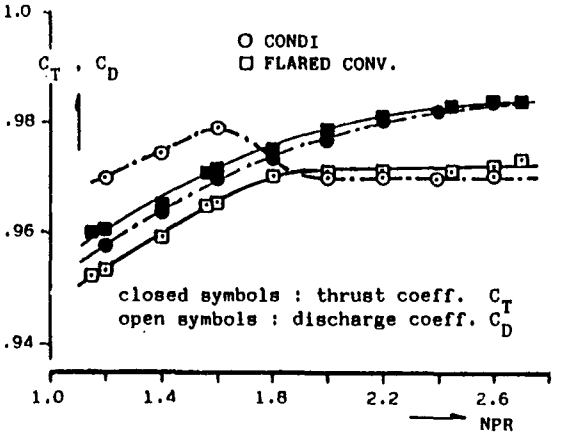

Figure 4 Fluidyne nozzle test data

• Nozzle & Thrust reverser test programme	Fluidyne, Minneapolis USA
• Stability & Control test programme	NLR, NOP Holland
• Reingestion test programme	Rolls Royce, Hucknall UK
• Boiler plate test programme	Rolls Royce, Hucknall UK
• Engineering Flight Simulator Studies	In-House
• Prototype flight test programme for evaluation and certification	In-House

Figure 5 Thrust reverser development programme

- Based on best compromize
  - Engine cycle
    - static
    - transient
  - Reverser efficiency of 37%
- Configuration selected
  - Spacing ratio = .76D
  - T/R door angle = 9°
  - Door end plate height (F.S.) = 2"

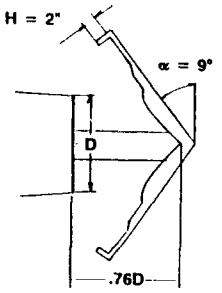

Figure 6 Selected T/R configuration

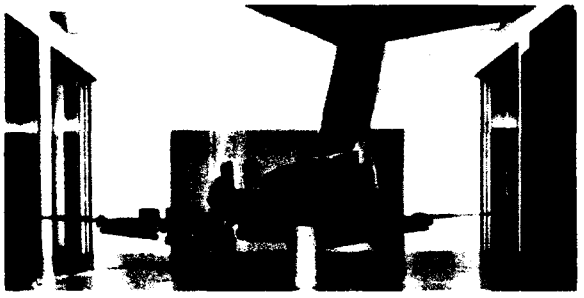

Figure 7 Model in low speed NLR windtunnel

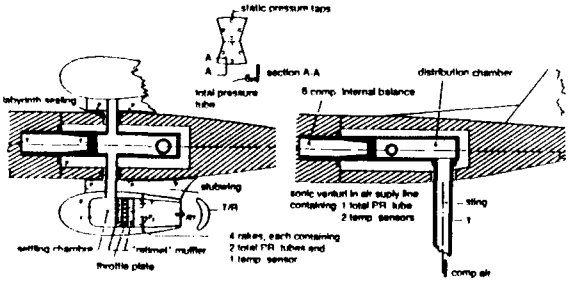

Figure 8 Details of nacelle and sting test set-up

Figure 9 Flow visualization technique in low speed windtunnel

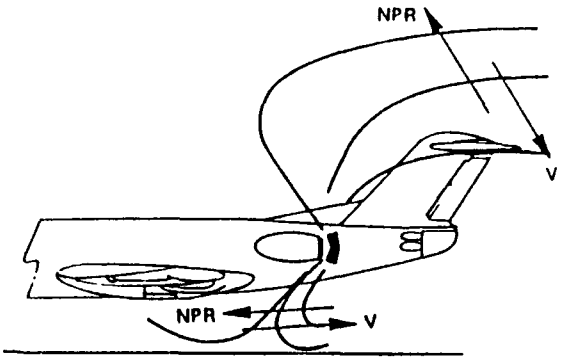

Figure 10 Effect of NPR and speed on reverse plume direction

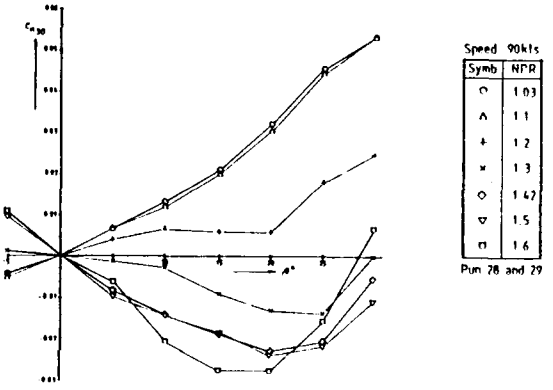

Figure 11a Effect of NPR on directional stability

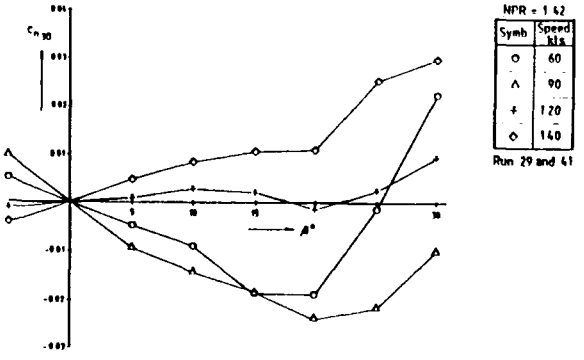

Figure 11b Effect of speed on directional stability

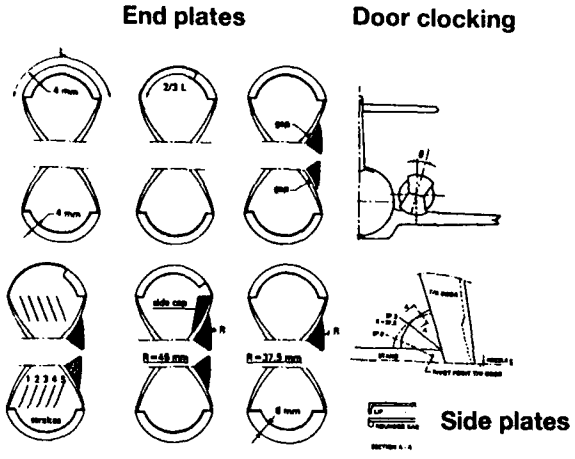

Figure 12 Plume control configurations

Figure 13 Side spill suppression by side plate inboard on upper LH side

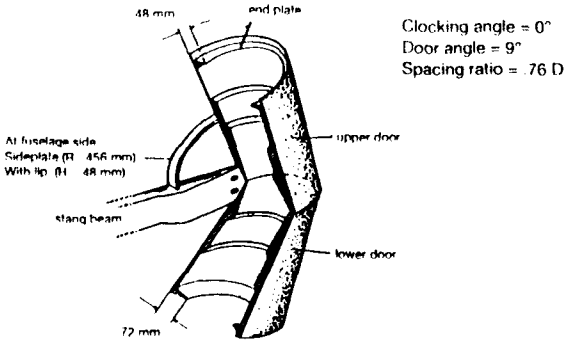

Figure 14 Selected T/R configuration

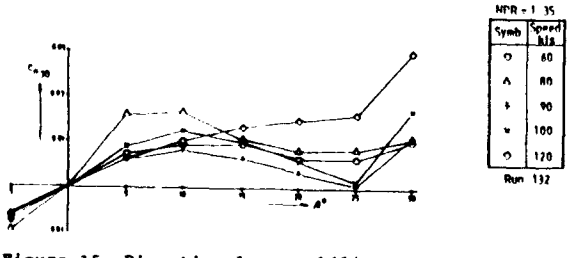

Figure 15 Directional stability of selected configuration

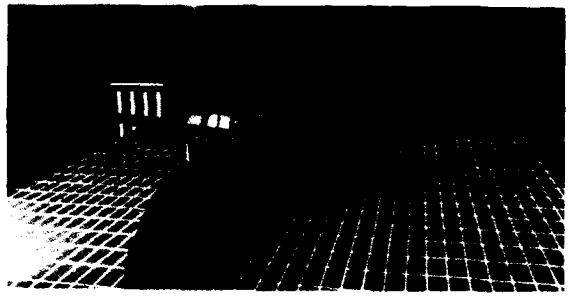

Figure 16 Model in Hucknall Test Facility

Figure 17 Details of blowing and suction facilities

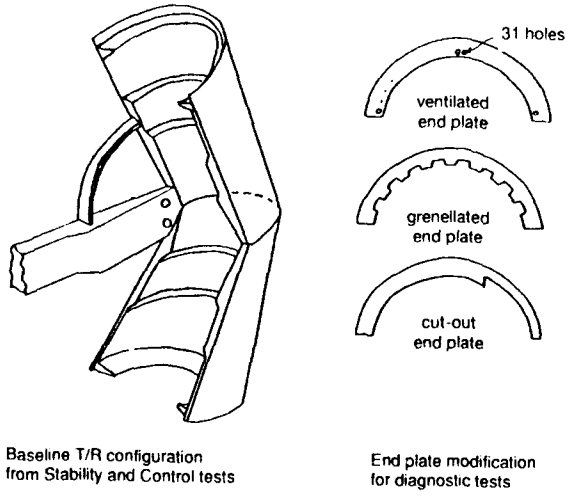

Figure 18 T/R configuration and end plate modifications

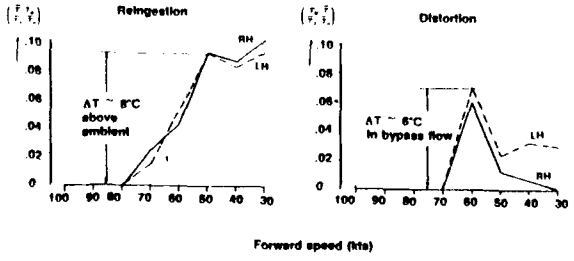

Figure 19 Reingestion and distortion at NPR 1.2 and 0° side slip

Figure 20 T/R door deployed during boiler plate test

Figure 22 Instrumentation on board Fokker 100 prototype

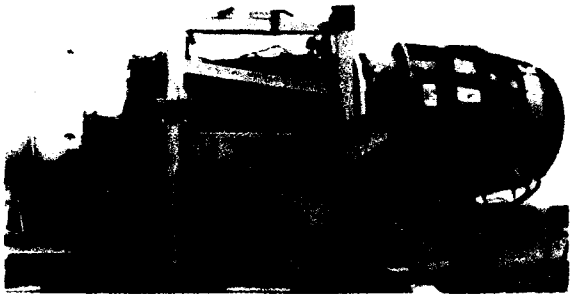

Figure 21 T/R door stowed during boiler plate test

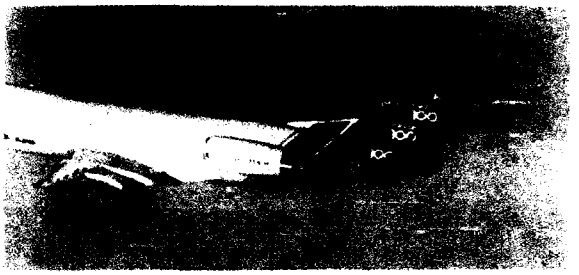

Figure 23 Inadvertent deployment during flight test

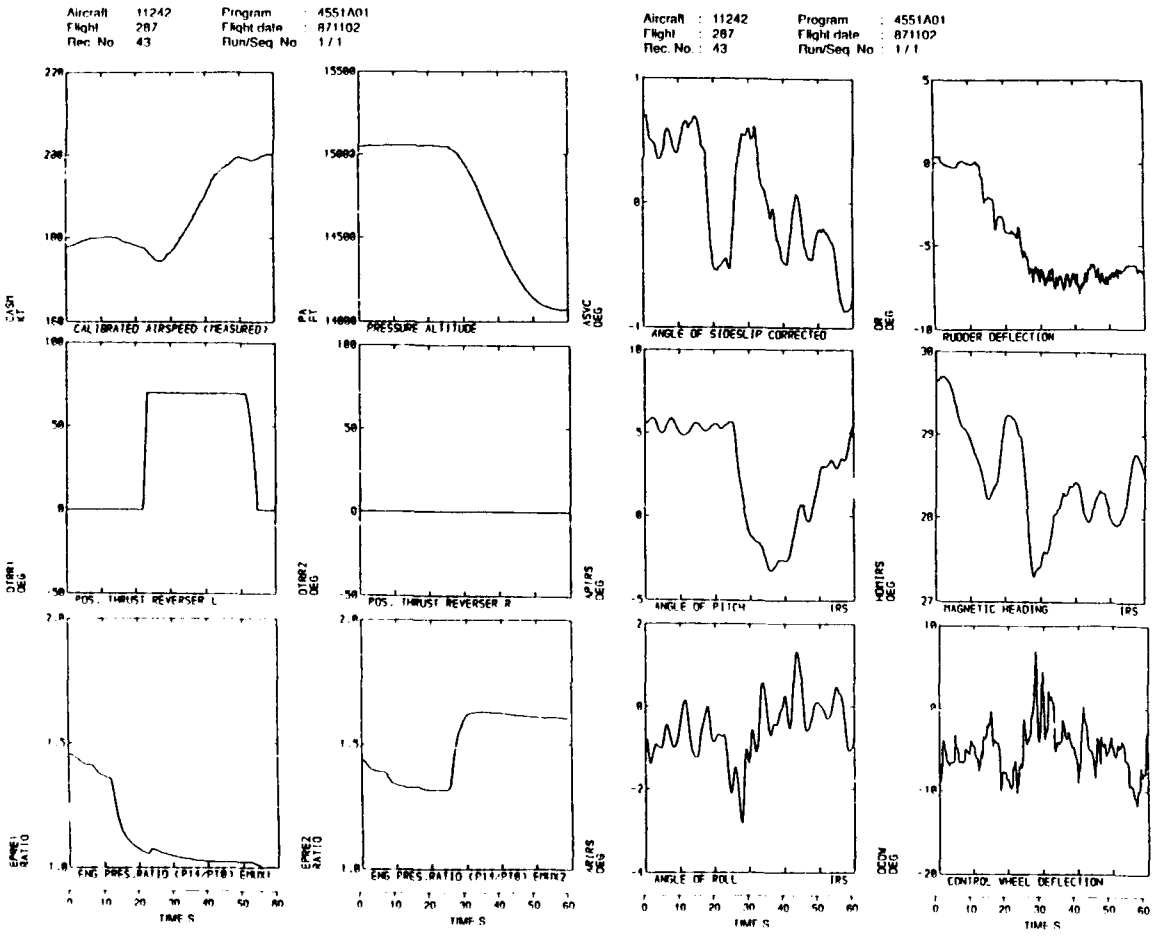

Figure 24 Flight test data during inadvertent T/R deployment

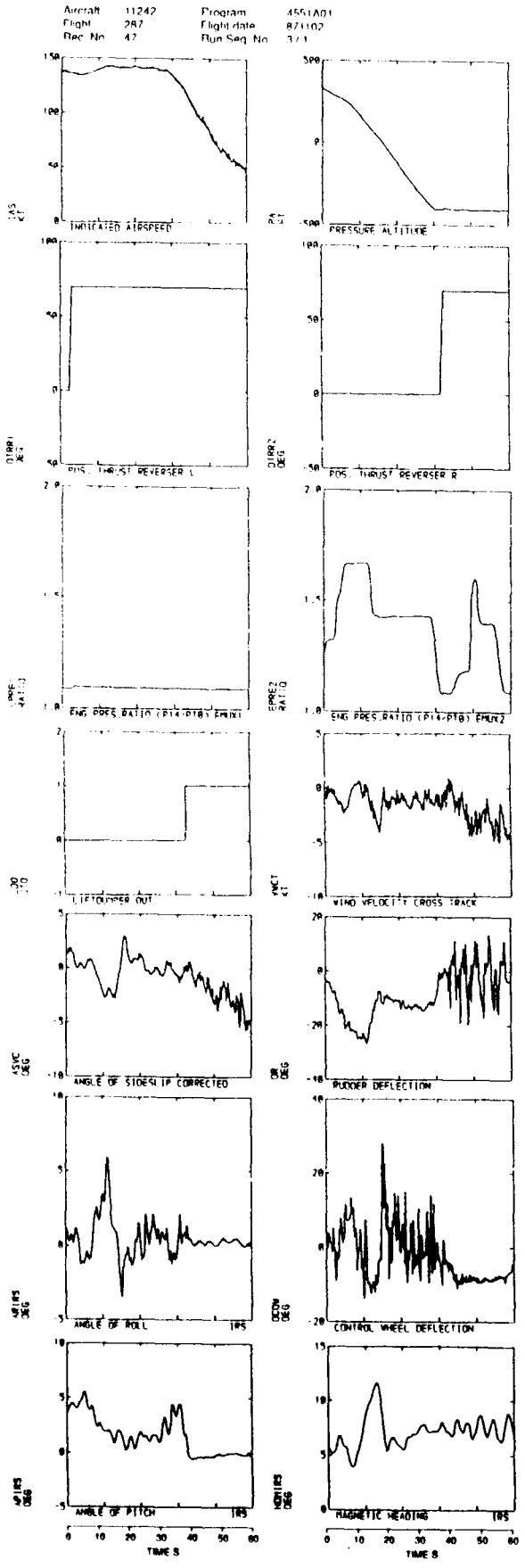

Figure 25 Flight test data during landing with inadvertent T/R deployment

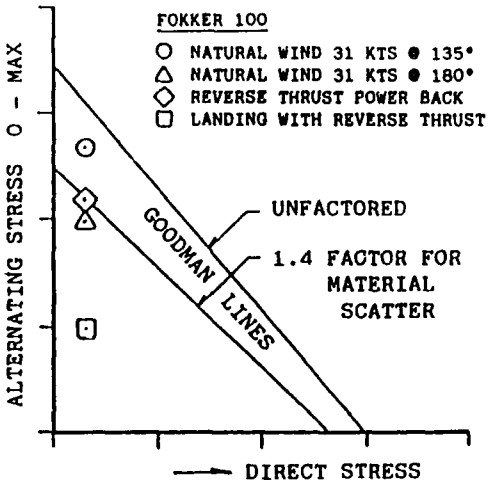

Figure 26 Fan blade test data

Figure 27 T/R door modification for tail buffet load suppression

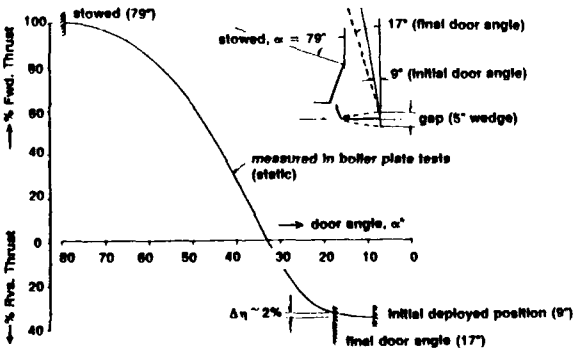

Figure 28 Effect of gap in T/R door apex on efficiency

OVERVIEW ON TEST CASES FOR COMPUTATION OF INTERNAL FLOWS IN TURBOMACHINES

by

Leonhard Fottner
Universität der Bundeswehr München
Institut für Strahlantriebe
Werner Heisenberg-Weg 39
8014 Neubiberg
Germany

ABSTRACT

Aero engine component design and development makes increasing use of computer codes for flow field calculations, such as two- or three-dimensional flow fields and flow fields with strong viscous effects. The accuracy of these calculation methods depends on the mathematical models and numerical schemes used to describe the physical reality. The proof of validity and the refinement of such methods depend on verification against relevant test cases, primarily experimental test cases. The AGARD Propulsion and Energetics Panel established Working Group 18 to specify relevant reference test cases to serve as validation bases for new methods, but also as check for existing production codes. The present paper gives an overview on the results of the Working Group and briefly describes the different test cases. These test cases refer to analytical and experimental test cases for steady flow in linear compressor and turbine cascades, single blade rows, single and multistage axial compressors and turbines and ducts. In addition, suggestions for future tests designed to reduce the limitations are discussed.

OBJECTIVES, ORGANISATION OF THE WORKING GROUP

Following the conclusions of AGARD Working Group 12 "Through Flow Calculations in Turbomachinery" (AGARD, 1976,1981), there is a lack of reliable and publicly available well-documented test cases for verification of different calculation methods applied for design and analysis of turbomachinery components.

Dr. J. Dunham, at this time member of the AGARD Propulsion and Energetics Panel initiated discussion of this topic within an ad hoc committee of the Panel in October 1982. After thorough discussion of different aspects on necessary types of test cases on the basis of a position paper prepared by Dr. J. Dunham and taking into account restrictions with respect to the types of problem areas to be considered, the AGARD Propulsion and Energetics Panel in 1983 requested the creation of Working Group 18 "Test Cases for Computation of Internal Flows in Aero Engine Components" to start in 1985 with a scheduled working period of 3 years.

The terms of reference were defined as follows:

Objectives

Aero engine design and development makes increasing use of computer codes for flow field calculations, such as two- or three-dimensional flow fields or flow fields with strong viscous effects. The accuracy of these computer codes depends on the mathematical models used to describe the physical reality. Therefore, they need to be verified against experimental test cases before they can be used with confidence for the design of engine components. Recent experiences with test cases show however that such verifications often suffer from poor knowledge about experimental boundary conditions, from limited measuring accuracy etc. Therefore a need for better test cases is generally recognized. A coordinated international search for and evaluation of suitable test cases would be appropriate. In order to limit the scope of the work, only steady flow phenomena in axial compressors and turbines including the ducts ahead of and between them shall be treated."

Scope of work

1. To define the types of test cases needed now and in the next five years, relating to axial compressors, axial turbines, and the ducts ahead of and between these components.
2. To assess what measurements are required for each type of test case, and with what accuracy.
3. To identify existing and define potential future test cases and document them, checking their suitability as far as possible.
4. To make recommmendations about future experiments needed to fill gaps in test cases.
5. To prepare an Advisory Report cataloguing the selected test cases and to provide a *separate* detailed set of documentation for each of them.

The activities started in 1985 under the chairmanship of Prof. Dr. L. Fottner with a four years working period (1985-1988). From the beginning of the work there was agreement to limit the activities to steady-average flow conditions and that certain analytical solutions (considered to be exact) should be considered as the equivalent of experimental test cases for some classes of computational codes. The above mentioned objectives with respect to experimental test cases were soon recognized to represent an enormous task due to the large number of candidate test cases and the need to define their limitations and degree of validity.

Group members and meetings

To assess, screen and identify the highest quality data available for the data base and to assemble these data into a final report specialists in theoretical and experimental turbomachinery flow research have been nominated by the delegates of the AGARD Propulsion and Energetics Panel. After collection of available material for candidate analytical and experimental test cases the members of the working group agreed on a list of 27 potential experimental test cases. For each of these test cases subreports were to be prepared, a proposal for the content of each subreport had been agreed on.

OVERVIEW ON TEST CASES

In agreement with the objectives described in the terms of reference the selection of test cases included:

- cascades for axial compressors and turbines
- compressors (single blade row, single and

multi-stage machines
- ducts (including diffusers)
- turbines (single blade row, single and multi-stage machines)

For practical purposes the following numbering system for the different test cases was adopted (for example: A/CA-1):
- A for analytical, E for experimental test case
- CA for cascade, CO for compressor, DU for duct, TU for turbine
- 1 number

Analytical test cases

All analytical test cases described in this chapter refer to two-dimensional inviscid flow calculations for cascades. Table 1 contains a brief description of the analytical test case type, types of data included in respective subreport, author and source of data of the test case and recommendations for types of codes to be verified. Information in addition to the subreport content can be requested by direct contact to the respective author or source of test case.

Experimental test cases

To select the highest quality data from all data submitted to the Working Group, some decisive criteria were used covering items related to
- type of model and model geometry
- completeness of publicly available information
- range of test conditions and testing techniques employed
- test facility, instrumentation used in gathering the test data
- types of measurements necessary for validation of calculation methods

Table 2 contains a brief description of the experimental test case type, types of data included in the respective subreport, author and source of the test case and recommendations for types of codes to be verified. Information in addition to the subreport content can be requested by direct contact to the respective author or source of test case.

The AGARD Advisory Report (AGARD-AR-275) is organized as follows:

Chapter I : Introduction and overview of test cases
Chapter II : Requirements for flow prediction code evaluation
Chapter III : Validity of experimental test cases
Chapter IV : Analytical test cases for cascades
Chapter V : Experimental test cases for cascades
Chapter VI : Experimental test cases for compressors
Chapter VII : Experimental test cases for ducts
Chapter VIII: Experimental test cases for turbines
Chapter IX : Conclusions and Recommendationes

The subreports on test cases are as complete as possible and are included in the main report. For some test cases additional data is given in microfiche form in an Appendix or can be requested by direct contact to the respective authors. Each test case is documented in similar format according to the following subdivision:
1. Description of test case, facility and instrumentation
2. information on geometrical details
3. experimental conditions and results
4. evaluation method and data uncertainty
5. recommendations for comparison with calculation methods
6. Nomenclature

It is suggested that authors of future publications of test cases should include complete information in their reports according to this subdivision.

CRITICAL COMMENTS ON TEST CASES

Most of the analytical test cases presented are rather academic and do not include some of the important features of real turbomachine blades. All the test cases are 2D and a case including Q3D effects such as change of radius and stream tube thickness is also desireable.

In order to validate a calculation method by an experimental test case it is necessary to model the experimental boundary conditions in the best possible way. Hence the experiments should be chosen to reproduce the analytical or numerical boundary conditions. Because of this requirement, it turns out that the greater the degree of simplification of the flow model the more difficult it is to provide a suitable experimental test case. For example, it is almost impossible to provide an experimental test case for a one-dimensional calculation, whilst in principle all experimental data is amenable to comparison with a 3D, vicous, unsteady calculation. Currently theoreticians cannot tackle the full complexities of real turbomachinery flows and often assume simplified flow physics and/or simplified geometry. Simplified geometries, like linear cascades, are also used by experimentalists, but the flow physics do not usually become as simple as in the theoretical model.

From the 8 experimental test cases for linear cascades only 3 can be considered to represent nearly 2D flow conditions. This puts into evidence the difficulties in achieving 2D flow conditions. This is in particular true for transonic compressor cascades especially for choked cascades with strong shocks. In regard of turbine cascades the situation is somewhat more favorable. Even in absence of active sidewall boundary-layer control the axial velocity density ratio is sufficiently close to one provided that the inlet sidewall boundary-layer is small compared to the blade height.

The compressor test cases consist of an isolated low speed rotor (E/CO-1), an isolated transonic fan rotor (E/CO-2), a subsonic stage (E/CO-3), a transonic stage (E/CO-4) and a low speed 2-stage machine with only the second stage documented in detail (E/CO-5). Various types of data are available for checking computational solutions. Radial traverse information is available at rotor exits for all cases (pitchwise and pitchwise-averaged results are also available for E/CO-1 and E/CO-5 respectively, in a rotating frame) Stator exit radial distributions are available for E/CO-3, E/CO-4 and E/CO-5; test case E/CO-3 also has stator exit area surveys. Blade surface pressures are available for the rotor of E/CO-1 and the final rotor and stator of E/CO-5. Laser velocimetry measurements of the rotor internal flow field between about 10% and 90% span are available for E/CO-2 and E/CO-4. The major omission from the range of compressor test cases is a good multistage machine.

The duct experimental test cases consist only of a low speed S-shape duct (E/DU-1) and an annular diffusor (E/DU-2). For the S-shape duct which was of square cross-section a water tunnel was used; Laser anemometry data on velocity (3 components), turbulence quantities and cross-correlations as well as pressure measurements are available for laminar and turbulent flow. The annular diffusor was operated at low speeds, too, however with a turbine stage at the diffusor inlet. Only velocity data deduced from pressure probe measurements as well as flow angle data in the diffusor inlet and exit planes are available. However, little information was available on circumferential variations at entry to and within the diffusor.

Of the 4 turbine experimental test cases 2 are for complete turbines and 2 are single blade rows (annular cascades). The former are primarily test cases for throughflow calculati-

TABLE 1 OVERVIEW ON ANALYTICAL TEST CASES FOR CASCADES

BL Boundary-layer correction, PMD Profile Mach number distribution,
SP Shock pattern, 2Di 2D-inviscid flow calculation method

Test Case	Description	data types	code types	source of data	author of rep.
A/CA-1	SANZ supercritical compressor cascade	PMD	2Di	Sanz	Denton, et al
A/CA-2	Supersonic staggered wedge cascade	SP	2Di	Denton	Denton, et al
A/CA-3	SANZ subcritical turbine cascade	PMD,BL	2Di	Sanz	Denton, et al
A/CA-4	SANZ supercritical turbine cascade	PMD,BL	2Di	Sanz	Denton, et al
A/CA-5	HOBSON cascade 1	PMD	2Di	Hobson	Denton,
A/CA-6	HOBSON cascade 2	PMD	2Di	Hobson	et al

ons whilst the latter are more suitable for fully 3D viscous or inviscid single blade row calculations. The E/TU-1 test case is a typical test case for 3D viscous calculations in spite of lack of blade boundary-layer data. The end-wall boundary-layer data are fully documented.

CONCLUSIONS AND RECOMMENDATIONS

This report presents an overview on an AGARD activity to provide an analytical and experimental data base intended as support in the development of new and the refinement of existing computer codes for internal flows in turbomachines (cascades, compressors, turbines and ducts ahead of and between them). The data are believed to belong to the "highest quality" analytical and experimental test cases available to-day. All analytical test cases described in this report refer to steady, 2-dimensional, inviscid flow calculations, the experimental test cases respectively being referred to steady 2-dimensional, quasi- and fully 3-dimensional flow calculations for viscous flows in axial turbomachinery components.

There are so few analytical test cases available that any addition to them would be most welcome. In particular a blunt leading edge with a detached shock would be a desireable test case as would be a wedge shaped trailing edge designed to model the trailing edge shock system on a transonic turbine blade. The absence of a 3D analytic test case is a serious omission. If such a case cannot be obtained analytically then "reference solutions" should be obtained from numerical methods with a very large number of grid points.

Fluid dynamic experiments are performed for two reasons: a) to increase the knowledge about the flow behaviour and by this to improve the design tools and b) to check fluid dynamic calculation procedures. In the first point the experiments serve to fill up the unknown and incalculable parts of the design procedures by deriving correlations for losses, deviations, blockages, etc. In these experiments differences are expected and the tests are normally directed to special aspects of the overall flow. In the second type of experiment, however, differences between measurement and calculation should not occur. If they do occur, it may be due to measurement inaccuracies, due to different boundary conditions or due to imperfections of the theoretical solution. Only in an iterative procedure between theory and experiment the actual reason can be detected. Thus, a close collaboration between theoreticians and experimentalists is necessary. It is important to draw the attention of the theoretician towards the problems which unavoidably impair the quality of experimental results. A meaningful validation of computational results requires knowledge of the experimental procedures and measuring problems. Before using an experimental test case it is recommendable to make sure that the dominating physical processes in the theoretical model to be validated coincide with those governing the experimental case. In many cases it is not so much the measuring inaccuracy which influence the validity of a test case but more the physical processes caused by the specific boundary conditions of the experiment. An assesment of the boundary conditions and flow field similarity for the computational and experimental results is necessary. In test cases where unsteady flow effects prevail the physics of many measuring techniques are impaired. Particular care is recommended in these cases, not only concerning the measurements themselves but also the procedures for averaging the results.

Turbine cascades can be considered for 2D code validation for the following flow conditions: (a) highly accelerating subsonic cascades, (b) choked cascades with fully established oblique trailing edge shocks. For compressor cascades quasi 2D conditions may be obtained for subsonic flows with appropriate side wall boundary-layer suction. All transonic cascade configurations and choked cascades with strong, normal shocks exhibit strong 3D flow features and require full 3D measurements for 3D viscous code validation. Future tests should provide: (1) clearly defined upstream flow conditions including turbulence flow properties, (2) detailed boundary-layer measurements including heat transfer and turbulence data and (3) information on trailing edge vortex formation to allow better modelling of wake mixing process. In order to check various aspects of computational methods for compressors, including prediction of stage matching, one could argue a need for three cases: a) a repeating stage low speed test case with highly detailed internal measurements; b) a high speed (but mainly subsonic) test case of four or more stages with interrow aerodynamic traversing measurements, backed up if possible by some Laser anemometry; c) a fan test case of two or more transonic stages with Laser measurements. More generally, the range of compressor cases may in future need to include more "advanced" configurations which could test the computational methods more severely, for example: very high duty or tip speed, sophisticated aerofoil or end bend designs, swept blades and propfans. Radial and mixed flow turbomachinery will also need to be catered for. In all types of turbomachinery, as the ability to study and model end wall flows improves, tip clearance effects will be of concern; test cases documented at more than one level of clearance may be needed to check codes fully. For stators, data on the effect of hub clearance will be needed, and the skewed end wall boundary-layers at stator inlet will need careful documentation. Concerning test measurements, the present lack of data on internal flows within stator rows need to be remedied. Within both rotors and stators, Laser anemometer measurements of all three velocity compo-

TABLE 2 OVERVIEW ON EXPERIMENTAL TEST CASES

BL Boundary-layer, CD circumferential distribution, CP Contour plots, LV Laser velocimetry, OP Overall performance, PMD Profile Mach number distribution, PPD Profile pressure distribution, PVD Profile velocity distribution, RD Radial distribution, SCH Schlieren, SF Secondary flow, WT Wake traverses,

2D 2-dimensional flow calculation, Q3D quasi-3-dimensional flow calculation, 3D 3-dimensional flow calculation, TF through-flow calculation

AGT Allison Gas Turbines, General Motors Corporation, DFVLR BS Deutsche Forschungs- und Versuchsanstalt für Luft- und Raumfahrt, Braunschweig, DFVLR CO Deutsche Forschungs- und Versuchsanstalt für Luft- und Raumfahrt, Köln, ECL Ecole Centrale de Lyon, IC Imperial College, ISU Iowa State University, MEL Marchwood Engineering Laboratories of Central Electricity Generating Board, NASA National Aeronautics and Space Administration, ONERA Office Nationale d'Etudes et de Recherches Aerospatiales, RAE Royal Aerospace Establishment, RR B Rolls Royce plc, Bristol, RR D Rolls Royce plc

Derby, UH Universität Hannover, UTRC United Technologies Research Center, VKI von Karman Institute for Fluid Dynamics, VUB Vrije Universiteit Brussel, WL Whittle Laboratory, Cambridge University

Test Case	Description	data types	code types	source of data	author of rep.
E/CA-1	Low subsonic compressor cascade NACA 65	PVD, BL, SF	3D	ECL	Leboeuf
E/CA-2	High subsonic compressor cascade DCA	PPD, WT, BL	Q3D	DFVLR BS, RR B	Hoheisel
E/CA-3	High subsonic compressor cascade 115	PPD,BL	2D	ONERA	Meauze
E/CA-4	Low supersonic compressor cascade MCA	PPD, WT	Q3D	DFVLR CO	Starken et al
E/CA-5	Transonic compressor cascade ARL SL 19	PPD, WT,	Q3D	DFVLR CO AGT,ONERA	Starken, et al
E/CA-6	Subsonic turbine cascade T 106	PPD, WT, BL	2D	DFVLR BS	Hoheisel
E/CA-7	Subsonic turbine cascade LA	SF	Q3D,3D	WL	Denton
E/CA-8	Transonic turbine cascade	PMD,WT, SCH	2D	VKI	Sieverding
E/CO-1	Single low speed compressor rotor	OP,RD,CD, PPD,WT,CP	TF,Q3D, 3D	UTRC	Serovy
E/CO-2	Single transonic fan rotor	OP,LV,RD, CP	TF,Q3D, 3D	NASA	Wood et al
E/CO-3	Single subsonic compressor stage	OP,RD,CD, WT	TF,Q3D, 3D	RR D	Ginder, et al
E/CO-4	Single transonic compressor stage	OP,RD,LV, CP	TF,Q3D, 3D	DFVLR CO	Dunker
E/CO-5	Low speed two-stage compressor	PPD,RD	TF,Q3D, 3D	UTRC	Serovy
E/DU-1	Low speed S-shape duct	LV,CP	3D	NASA, IC	Martlew
E/DU-2	Annular diffuser	RD,CD	TF	DFVLR CO	Quest
E/TU-1	Low speed annular turbine blade row	RD,CP	3D	VKI	Sieverding
E/TU-2	Transonic annular turbine blade row	PPD,CD,CP WT	3D	MEL	Ball, et al
E/TU-3	Single stage subsonic turbine	OP,RD,LV	TF	DFVLR CO	Förster, et al
E/TU-4	4-stage low speed turbine	OP,RD	TF	UH	Kötzing

nents would be valuable, and the end wall region certainly needs much closer attention. Data from high response instrumentation mounted in blade surfaces and casings would be a valuable addition. More comprehensive and better quality measurements are needed at rotor exit/stator inlet using Laser anemometry, high-frequency-response total pressure and temperature probes able to resolve the rotor-locked flow field, and instrumentation which gives true averaged flow conditions. Advances in measurement techniques will be needed to satisfy these requirements. Concerning the range of operating conditions, modelling of off-design operation will become more tractable as computational methods improve; the operating conditions of interest include part speed as well as "near surge" cases especially for transonic rotors and stages and for multistage machines. In the longer term unsteady flow effects, which were specifically excluded from the scope of WG 18, may need to be given closer attention. Measurements of unsteady properties, distinguishing between components which are phase locked to the rotor and those which are random, will be needed. Also correlations between unsteady velocity components which give rise to the apparent stresses needed for "average passage" and spanwise mixing computations may be needed.

The major omissions from the range of interesting duct test cases are a) annular diffusor with and without upstream moving blade rows; b) annular S-shape duct with and without upstream blade rows, both moving and stationary. All test cases should be for compressible flow. The measurements should comprise full velocity traverses by hot wire or Laser anemometry for inlet, exit and a number of intermediate planes, including turbulence measurements, wall pressure and wall shear stress measurements. Flow visualization would be very helpful for qualitative information on flow separation etc. Particularly, detailed flow measurements are needed when blade rows are present at the diffusor inlet. In the case of rotating blade rows at the diffusor inlet also measurements with correctly averaging instrumentation are recommended. In the long run also inclusion of unsteady flow conditions due to local separations would be necessary. On a short term basis priority should be given for a future test case of the annular diffusor listed under a) above. On a longer term also test cases on ducts containing splitters will become necessary.

For throughflow calculations a turbine test case with more details of the blade row loss distributions including tip leakage and with radial and circumferential traverses after the stators is needed. A multistage high speed turbine with geometry and loading typical of an aircraft gas turbine would be the most suitable for obtaining this data. Since the development of end-wall boundary-layers is greatly affected by radial pressure gradients and centripetal accelerations test cases with detailed boundary-layer measurements on both fixed and moving blade rows are needed for comparison with modern 3D viscous flow calculation methods. In the longer term, measurements of the unsteady flow in a multistage turbine, both stator and rotor will be necessary for comparison with unsteady flow calculations. These should include both Laser measurements of the unsteady mainstream flow and hot-wire or hot film measurements of the unsteady blade and end-wall boundary-layers.

In conclusion, it is clear that the magnitude of measurement errors and of departures from the ideal flow situation are often significant but difficult to estimate. The test cases presented should thus not be taken as absolute standards against which to judge theoretical predictions. However, experience has shown that they can be valuable in developing and verifying codes if used wisely, for example by including sensitvity checks for quantities where the experimental data are uncertain. Such theoretical checks will also assist experimentalists in understanding their test cases better and in improving them. It ist hoped that this report will stimulate fruitful interchange which will help narrow the gap between theory and experiment.

In spite of the limitations of the present data and the need for additional testing, it is believed that the data base presented here will largely meet the set objective. This is mainly due to the fact that for all of the configurations selected a fairly large amount of information on actual geometry and on test conditions as well as an estimation of the data accuracy is presented. This will enable the user to judge the merit of each individual data set and allow him to draw conclusions concerning the quality of and necessary refinement to his computer code.

It is recommmended that university institutes and research institutions like DFVLR, NASA, ONERA, RAE and VKI which have the needed facilities and the resources take the initiative for a cooperative work using their own resources to generate new test cases along the conclusions mentioned above.

ACKNOWLEDGEMENT

The research effort summarized here was unquestionable greater than was expected in 1985. Throughout, there was excellent cooperation and exchange of ideas within and among all of the participating organisations and individuals. As chairman of the AGARD Working Group I want to thank all organisations who have contributed by release of the material, all authors of subreports on different test cases and my collegues from WG 18 for their continuing effort during these 3 years. The working group was composed of the following members:

J.F. Chevalier, FR, A. Dadone, IT, J.D. Denton, UK, L. Fottner, GE, R.B. Ginder, UK, Ch. Hirsch, BE, F. Martelli, IT, D. Matlow, UK, G. Meauzé, FR, G. Oates, US (deceased), F. Psarudakis, IT, G.K. Serovy, US, C.H. Sieveding, BE, H. Starken, GE, A. Ucer, TU, G. Winterfeld, GE, J.R. Wood, US

REFERENCES

AGARD Propulsion and Energetics Panel Through-Flow Calculations in Axial Turbomachinery. AGARD-CP-195. 1976.

AGARD Propulsion and Energetics Panel Working Group 12. Through-Flow Calculations in Axial Turbomachines. AGARD-AR-175. 1981.

AGARD Propulsion and Energetics Panel Working Group 18. Test Cases for Computation of Internal Flows in Aero Engine Components. AGARD-AR-275. 1989.

THE PEP SYMPOSIUM ON "CFD TECHNIQUES FOR PROPULSION APPLICATIONS"

by

Ch. Hirsch

Dept. Fluid Mechanics, Vrije Universiteit Brussel

Pleinlaan 2, 1050 Brussels, Belgium

ABSTRACT

This paper is part of the PEP contribution to the 69th FDP meeting on "Aerodynamic Engine/Airframe Integration for High Performance Aircraft and Missiles". It presents an overview of the main outcomes of the last PEP meeting dealing with "CFD Techniques for Propulsion Applications". The emphasis was given to computational work on realistic 3D configurations, covering the four following topics: Full 3D Validations; Full 3D Numerical Techniques; Unsteady Flows and Multidimensional Reacting Flows. In addition, an invited paper from FDP on the state of the art of computational techniques for 3D Navier-Stokes equations and a Technical Evaluation of the meeting were presented. The most widely stressed conclusion was the urgent need for a large scale effort on validation of numerical accuracy and of physical models.

1. INTRODUCTION

The objectives of the 77th PEP Symposium on **"CFD for Propulsion Applications"**, held in San Antonio, Texas, US, from 27 to 31 of May 1991, were to assess the state of the art of 3D aerodynamic computations in propulsion related components and evaluate the present CFD capabilities for more complex flow systems, such as multistage, unsteady environments and reacting flows.

The main focus of the meeting was set towards the question of validation of numerical accuracy and of physical models, essentially turbulence and transition modelling as well as some aspects of chemical kinetics. Although some contributions were aimed at an evaluation of 3D numerical techniques, the algorithmic developments were not considered as a main topic, so more that an excellent review was offered by Dr D. Hänel, as a FDP contribution, and provided a reference on algorithmic properties to many presentations.

The development of a CFD-based analysis and design methodology for propulsion components still requires a great amount of evaluation work, and this requirement was largely emphasised by many contributions, as well as by the technical evaluator of the meeting, Dr. L. Povinelli from the NASA Lewis Research Center.

This paper will review the four topics of the PEP Symposium listed above, and attempt to provide a summary of the main achievements and of the problems raised, as reported by the authors. Unless otherwise stated, all contributions to the PEP meeting will be referred to by the paper number, as to be found in the final Proceedings, AGARD CP 510.

The first section will cover contributions dealing with numerical accuracies and the applications of different flow models to specific propulsion components. The second section will cover the important question of validation of the Reynolds averaged Navier–Stokes simulations, in particular turbulence and transition modelling. The third section covers some inputs to unsteady flow computations, while the fourth section will summarize the inputs to chemical reacting flows. Finally some concluding remarks will be presented.

2. NUMERICAL TECHNIQUES

Although Navier–Stokes computations are currently becoming the most widely applied approach to practical flow simulations, a certain number of difficulties have still to be overcome, in order to achieve fast and reliable computational results. The major techniques and problems of the present state of the art in CFD–technology have been reviewed by D. Hänel (Paper 1) in an outstanding review paper, as a contribution from FDP to the PEP Symposium.

D. Hänel discussed the current approaches of central and upwind space discretizations, the most widely applied implicit and explicit time integrations, including the important aspects of multigrid acceleration techniques, as applied to Euler and Navier–Stokes solvers. A most interesting section of this review deals with an analysis of the numerical errors in viscous solutions, as generated by various schemes. In particular, the numerical dissipation of standard flux splitting schemes has to be carefully monitored to avoid excessive drag predictions and too much dissipation in the viscous regions. This problem becomes particularly severe in unsteady flows, were time accuracy is strongly dependent on space accuracy. When the relevant space and time scales of the computed flow are large compared to the stepsizes, the computed solutions are reliable with most of the current methods, provided sufficient space resolution is applied.

However, with spontaneous, self-induced flow unsteadiness, such as the Von Karman street behind a cylinder at high Reynolds numbers, the separating vortices are created out of the very small vortices formed at the solid wall surface and subsequently growing in time. Since the numerical dissipation acts as a filter on the small scales, the time development of the flow will be very sensitive to mesh configurations and to the numerical scheme. This is illustrated by figure 1, taken from Hänel [1], which shows the influence of mesh configuration and numerical dissipation for a central scheme on the time evolution of the laminar vortex street around a circular cylinder. The figure shows the time history of the lift coefficient, for different grid stretchings. Particularly interesting is the non-zero average lift coefficient when a tangential stretching is introduced, fig. 1a, revealing a non-symmetrical development of the vortex street. This effect disappears on a circumferentially uniform mesh, but a very strong dependence of the value of the fourth order numerical dissipation is clearly seen. Similar dependences have been reported on other geometries and with other schemes. This creates a major difficulty for the computation of unsteady flows, particularly in 3D and in presence of geometrical complexities. At present, there is no known solution to these difficulties, unless use is made of excessive, and probably prohibitive, fine meshes. It has to be mentioned however, that these problems might be slightly less severe in turbulent flows because of the higher value of the physical dissipation generated by turbulence.

This review paper provided also some insight in the question of structured versus unstructured meshes, emphasizing the advantages of unstructured meshes for complex geometries and for adaptive meshes. The excellent presentation and the large list of references did contribute to the basic material offered by this contribution.

Presently, a variety of numerical methods are applied for turbomachinery blades, intakes, ducts, nozzles and other propulsion related configurations. Due to the flow complexity and the requirements for fast design methods, simplified approaches, based on approximations to the full Navier-Stokes solutions are often considered. Several of them were presented at the PEP meeting and are summarized in the following sections.

2.1. VISCID-INVISCID INTERACTIONS

A prediction and design tool for subsonic and transonic turbomachinery blade–to–blade flows has been presented by W. Calvert [3]. It is constructed by the combination of a 2D time marching Euler solver and an integral boundary method, covering laminar, transitional and turbulent regions. The main application area of this method is the performance prediction of axial compressor blade sections and of full compressor stages when coupled to an appropriate through-flow method in a Quasi-3D approximation.

Validation results were presented for four blade-to-blade test cases and three high speed compressor stages, documented in the PEP WG18 Report on test cases, AGARD AR275. Globally, very good agreement is observed for the blade sections, but the predictions are less accurate for blade rows and complete stages. This is due to the greater complexity of the loss mechanisms, such as end–wall effects, spanwise mixing connected to full 3D effects, flow separations at higher incidences. Clearly more accurate models are required for full stage performance predictions, but in simpler cases the viscid-inviscid model, developed by Calvert [3] provides excellent predictions.

Similar good predictions are obtained by Weiland, Hartmann and Menne [32] for rocket motor and free expansion nozzles with equilibrium real gases, by the coupling of 2D or axisymmetric Euler solvers with a boundary layer differential computation. The Euler solver is based on an upwind flux splitting formulation plus artificial dissipation to damp oscillations, instead of the more current approach based on limiters, and a Runge-Kutta time integration. A variety of examples are presented by the authors, including effects of turbine exhaust gas injections, however without comparisons to experimental data. Figure 2 shows calculated results for a plane and plug nozzle of a hypersonic aircraft, for a highly integrated cell–air breathing propulsion system. The computations for the plane nozzle at M=6.8 clearly show the shock waves due to the displacement of the external airflow and the contact discontinuity separating the combustion gases from the airflow. The plug nozzle has a more complicated flow structure, the shock and shear layers being more pronounced for the plane case computations. The addition of the external flow leads to a still more complicated flow field, including separated regions at the back of the plug. This configuration would clearly require some Navier–Stokes computations for validation.

2.2. INVISCID CODE APPLICATIONS

Several applications of full 3D inviscid computations have been presented, for curved ducts by Martini, Massardo and Satta [5], for blade rows by Haarmeyer and Stubert [16], for hypersonic intakes by Bissinger and Eberle [26], for blade rows and internal flows by Oktay, Akmandor and Ucer [27], for hypersonic nozzle flows by Weiland, Hartmann and Menne [32], Koschel, Rick and Bikker [33].

Martini, Massardo and Satta [5] calculate 3D inviscid rotational flows in ducts, comparing two numerical time–marching methods: an explicit Lax method with corrected viscosity and an implicit ADI approach based on the Beam and Warming scheme. Qualitative results are presented for the secondary flow in curved ducts on relative coarse meshes.

Haarmeyer and Stubert [16] describe efforts in mesh generation and visualisation algorithms, applied to 3D Euler solutions of turbine and compressor blades.

Bissinger and Eberle [26] describe an Euler code based on a new, characteristic based upwind, conservative scheme, with implicit time integration. The scheme can be extended in a standard way to Navier-Stokes, but only inviscid results are presented. Various scramjet and intake configurations are computed, showing excellent accuracy for these high speed flows with very thin viscous regions. An example is shown on figure 3, for a scramjet, indicating excellent shock capturing properties on a fine mesh of 405x155 grid points.

Oktay, Akmandor and Ucer [27] presented a cell-vertex Lax–Wendroff type scheme for the Euler equations, applied to subsonic and transonic internal flows.

Koschel, Rick and Bikker [33] presented a finite element, adaptive mesh technique for the 2D and 3D Euler equations, applying a Taylor-Galerkin method, with Flux Corrected Transport (FCT) as limiting procedure. This scheme is a Lax–Wendroff formulation on unstructured meshes, and is applied to hypersonic expansion nozzles. Figure 4 shows calculation results for a 3D plug nozzle with adaptive grid enrichment, leading to an improved resolution of the shock structure and jet boundary. This contribution was the only one presenting an unstructured adaptive solver.

Non–equilibrium inlet flows, are calculated by Marsilio and Pandolfi [42] with a special flux difference method, adapted to steady supersonic flows, with second order accuracy. Similarly Onofri [43] applies a λ-type scheme with an operator splitting between the gasdynamic and the chemical operators. A similar algorithm is applied by Walther [44] for non–equilibrium flow calculations in converging-diverging nozzles.

2.3. PRESSURE CORRECTION METHODS

Pressure correction methods, in a fully elliptic formulation, enabling the computation of streamwise backflows, have been presented by Moore and Moore [4], and applied to a turbine blade row with tip clearance. This code is based on an original upwind definition of control volumes, leading to a scheme with reduced cross-diffusion and hence, improved spatial accuracy. Additional validation tests of this code are reported by Cleak and al [8], and will be discussed in the next section on Validation.

Another code, based on a staggered mesh, SIMPLE-type, fully elliptic algorithm, is applied by Abou Haidar et al [34] for an interesting comparison of different turbulent models in S-bends. The code makes use of a quadratic, upwind discretization of the convection terms.

Fotea et al [35], on the other hand, rely on a parabolized Navier–Stokes approximation for their duct flow computations, while Katheder [36] applies a commercially available code, based on a elliptic, pressure correction method. A similar algorithm is applied by Bond at al [38] to the flow computation in a gas turbine combustion chamber. Rachner [37] applies a non-staggered grid formulation, coupled to a zonal approach, with a particular attention to the pressure–velocity decoupling problem. This paper contains a detailed investigation of the numerical accuracy of various boundary treatments at solid walls and at zonal interfaces. A very similar approach is followed by Coelho and Pereira [30].

All these codes are applied to incompressible flows, with the exception of Hah [10]. In this paper, the code is applied to a transonic compressor rotor, including tip clearance. Interesting shock-boundary layer interactions are identified and some comparisons of overall performance are presented, without detailed flow comparisons.

2.4. FULL NAVIER–STOKES CODES

All the contributions, not yet mentioned, were based on full Navier–Stokes, time marching, discretizations, covering central or upwind schemes, explicit or implicit time integrations, with various turbulence models.

In Vogel's [7] contribution, the code developed by W. Dawes at Cambridge is applied, coupled to a heat transfer calculation. This solver is based on a central, cell-centered space discretization with artificial dissipation and implicit time integration. The same N–S solver is used by Sehra et al [13] and by Horton et al [19], who present an interesting mesh sensitivity analysis.

The Jameson-type code based on central space discretizations, artificial dissipation and explicit, Runge-Kutta type time integrations is applied by Gerolymos [11], Sehra et al [13], Chima [21], Birtch and Kitchen [25].

Flux difference splitting, with implicit time integration based on a Beam and Warming approximate factorisation, is applied by Dorney and Davis [22] and by Dutoya et al [29], although these codes can differ strongly by their practical implementation.

The codes developed by Escande and Cambier [14] and Lemeur [23] are based on a Lax-Wendroff two step scheme with artificial dissipation. In the code of Hirsch et al [17] a unified formulation of central and upwind schemes is introduced, by a choice of different dissipation expressions, whereby all the schemes are written as central fluxes plus additional terms. Similarly, both explicit and implicit time integrations can be applied as different options for a multigrid smoother.

The incompressible codes of Combes [18] and Taylor et al [28] are based on finite elements. The former applying a fractional step method, separating the convection from the diffusion step. A different finite element formulation is developed by Habashi et al [31].

2.5. NUMERICAL ACCURACY OF FULL NAVIER–STOKES CODES

It it is clear, from numerous comparisons on a variety of applications, that results of similar accuracy can be obtained with different algorithms, for the same physical models. In particular, there are no indications that any of the central or upwind schemes, explicit or implicit methods, behave significantly better than any other. Hence, the main question is connected with the numeri-

cal accuracy on a given mesh and with the mesh dependence of the computed results.

Several of the contributions investigated these problems, in particular, mesh size and mesh aspect ratio dependence. The calculations of Horton, Harasgama and Chana [19] compare results on four different meshes of a nozzle guide vane with high exit angle, figure 5. A considerable mesh influence is observed at these relative coarse meshes; meshes 1 and 2 having 55625 nodes, while meshes 3 and 4 have 129591 mesh points. Figure 6 compares Mach number distributions in the trailing edge region for meshes 2 and 4, while figure 7 shows the mesh sensitivity of the computed total pressure losses. This is again illustrated by figure 8, were the total pressure contours at an exit plane are compared for the four meshes under consideration. These differences are larger than the variations resulting from different turbulence models. The high sensitivity of coarse meshes is also recognized by Birtch and Kitchen [25], where large differences between a H and a C–mesh are observed around the lip of a 3D intake.

In order to obtain mesh independent results, it is clearly required to define fine meshes, having also good regularity properties. This is further emphasized by the computations of Dorney and Davis [22], who investigated turbine blade heat transfer and performance, including a mesh sensitivity analysis. Since heat transfer coefficients are very sensitive quantities, a mesh independent solution required 900000 points for a full span blade row, with values of y^+ for the first mesh line close to the solid walls, below 1. This requires very efficient codes in order to be able to perform large scale computations on a routine basis.

3. CODE VALIDATIONS

The problem of validation of Reynolds averaged Navier-Stokes equations is essentially connected to turbulence models, transition, complex geometrical configurations, such as tip leakage flows in turbomachinery blade rows, combustion and real gas models. The process of validation itself has to be clearly defined. It is obvious that a surface pressure distribution is a weak validation criterium for Navier-Stokes computations; while wall stresses, drag, boundary layer velocity profiles, Reynolds stresses, temperature profiles, heat transfer coefficients are basically more severe tests for an accurate simulation at the level of Navier-Stokes simulations. These data are difficult and costly to obtain in experimental tests, but it is essential that a major effort in this direction be undertaken. The AGARD Panels, in particular FDP and PEP, have been and still are currently engaged in the tasks of compiling available data of good quality and providing them at large to the CFD community.

3.1. 'INDUSTRIAL'–TYPE VALIDATIONS

Moore and Moore [4] presented computations on a turbine cascade with tip leakage, comparing total pressure contours, secondary velocities, tip gap velocity fields, with experimental data. Although the mesh is rather coarse, 32760 points with 6 points in the tip gap, and the turbulence model based on a simple Prandtl mixing length, good predictions are obtained for global flow properties, such as pitch averaged flow angles, overall losses, vortex sizes. However, turbulence modelling appeared to have a strong influence on the mean exit flow angle, as did the position of transition. Although this coarse mesh calculation cannot provide sufficient accuracy for very fine comparisons of flow details, it is representative of a level of 'engineering' computations, close to design methodology, allowing to predict global trends and effects, such as the loss in efficiency due to unshrouded turbines.

This situation is very representative of a current trend in the turbomachinery design industry, where full 3D Navier-Stokes calculations are performed on complex configurations such as splittered rotors, full stages, with rather coarse meshes, of the order of 50000-100000. The clear objective being to identify trends and signs of variations of selected global quantities such as overall losses or pitch averaged flow properties, with modified design parameters, more than to simulate all the flow details. The paper by Sehra, Abolfadl and Zedan [13], was most representative of this situation. Computations on a transonic compressor, a high work turbine are reported with a mesh of 81685 points, identifying the most salient flow features and with reasonably good quantitative predictions of pitch averaged flow quantities.

Figure 9 shows computed flow fields for a splittered axial compressor rotor with 33915 points. At all sections a leading edge weak oblique shock can be seen, with a normal shock at the splitter level and shock induced separation at the tip section. This predicted lower work of the compressor tip sections were also observed experimentally. Other examples, such as exhaust mixer-nozzles (73500 points), inlet particle separators are also presented.

Another 'industrial' oriented application has been presented by Vogel [7], were combined flow and blade heat conduction computations with coolant injection, are applied to film cooled gas turbine blades.

The paper by Cleak, Gregory-Smith and Birch [8] fits also in this category and presents an analysis of the mesh and turbulence model effects on a turbine cascade with inlet boundary layer, performed with Moore's code. Approximate mesh independence is considered to occur for over 20000 mesh points, defined within 'engineering accuracy', although with 65000 points the midspan losses were reduced. However, very large effects were observed with varying turbulence models and point of transition.

Combes [18] applies a k-ε turbulence model with wall functions to the computation inside a centrifugal pump,

with 43000 nodes of an unstructured tetrahedral mesh. Comparisons with measured velocity fields show reasonably good agreement, but no systematic investigation of turbulence models is presented.

Birtch and Kitchen [25] present calculations of a 3D intake, typical of a modern high bypass ratio engine in an underwing, twin-jet installation. The calculations are performed with a Prandtl mixing length turbulence model and 47450 mesh points. The authors recognize that a higher grid resolution and more adequate turbulence models are necessary in order to capture accurately the details of this complex flow.

3.2. TURBULENCE VALIDATIONS

We are ranging, under this heading, the contributions aiming at a detailed validation of turbulence models, implying computations with a large number of points. The code presented by Escande and Cambier [14] is applied to a high pressure annular turbine cascade, with a mixing length turbulence model and 626727 mesh points. Unfortunately, no experimental data were available at the time of writing of this paper.

Chima [21] applies a Baldwin–Lomax algebraic model to a transonic compressor fan, with 362600 points. This fine mesh calculation allows the identification, through particle traces, of regions of separation at the leading edge and at the trailing edge, too small to have been seen in the experimental laser data. Figure 10a shows the rotor, parts of the mesh and the performance curves, while figures 10b and 10c show the computed particle traces at design and at near-stall conditions.

Dorney and Davis [22] have pushed the validation a step further by including heat transfer data on a turbine blade. Since this is a most severe criterium, 450000 points over the half-span are needed for mesh independency. A Baldwin–Lomax turbulence model is applied, with fixed positions of transition. The heat transfer data clearly indicate that the accuracy of the predictions is very strongly dependent on a reliable estimation of transition.

Taylor et al [28] calculate the flow and heat transfer in turbine blade cooling ducts, including muti-ribbed passages. Detailed flow patterns are obtained with a one equation turbulent model, but no comparisons with other models are presented. The flow in rotating cavities is also computed by Dutoya et al [29] with a two equation turbulence model, again without comparisons with data or other turbulence models.

Abou Haidar, Iacovides and Launder [34] compare different turbulence models for the flow in a circular sectioned S-duct. An algebraic Reynolds stress model is applied, with various near wall corrections such as one and two equation models, on a grid formed of 117800 mesh points. The main conclusion of the authors is that full second moment closure equations over the complete cross-section might be required for highly accurate simulations.

4. UNSTEADY FLOWS

Relatively few papers were presented in this difficult and computer intensive part of CFD. A general analysis of the conditions of consistency at the computational boundaries between stages of a multistage turbomachine has been presented by Adamczyk [9]. Gerolymos [11] presented an interesting development towards a coupled aeroelastic prediction capability for vibrating compressor cascades. The approach is based on a 3D Euler solver, based on central schemes plus artificial dissipation and a time accurate Runge-Kutta integration. The author concludes about the necessity to develop time accurate viscous solvers within the aeroelastic approach in order to be able to predict supersonic and, more importantly, subsonic stall flutter.

Lemeur [23] developed a very interesting investigation of the unsteady flow in rotor–stator interactions. A detailed analysis of the conservation and continuity conditions at the interface between domains in relative motion is given, which is shown to allow a reduced number of blade passages to be included in the computed flow domain. In particular it is shown that the time averaged unsteady flow data are well approximated by the steady-state values.

In Hadzikadis et al [24], the unsteady flow field is represented as a superposition of a scalar potential field and a vector potential. Preliminary results are presented for the subsonic flow in a duct.

5. REACTING FLOWS

Several papers were presented dealing with chemical reacting flows, combustion chambers, or introducing real gas effects. Rachner [37] applied his numerical investigations to a cold combustion chamber, while Bond, Le Vallois and Menzies [38] present a detailed computation of the vaporizer and primary zone flows in a modern gas turbine combustion chamber. The method applies a k-ε turbulence model and a pdf model for the fuel fraction. Computations with over 190000 points of the vaporizer and its fuel injectors are shown on figure 11a, together with the flow domain and some of the computed flow patterns and fuel concentration, fig.11b.

Scheurlen, Noll and Wittig [39] presented a discussion of the numerical problems connected to the application of Monte-Carlo simulations to the transport of a scalar pdf. Veynante et al [40] gave an interesting review and discussion of the potential applications of the flamelet model of turbulent combustion for propulsion applications. This topic is somewhat outside the general scope of the meeting, since it addresses mainly the question of physical models, and we refer therefore the interested reader to this excellent reference.

The papers by Marsilio and Pandolfi, [42], Onofri [43] and Walther [44] were essentially dealing with inviscid hypersonic flows with real gas effects and applied to inlets and nozzles.

6. CONCLUSIONS

The main emphasis of the PEP meeting on **"CFD for Propulsion Applications"** was clearly directed at 3D flow simulations, with some reduced input to unsteady and reacting flows.

The presented papers covered a variety of numerical approaches and physical flow models. The latter were ranging from viscid-inviscid interactions, to inviscid models, pressure correction and full time dependent Navier-Stokes solvers. A large number of numerical approaches are applied within the propulsion community.

An interesting aspect is the systematic use, within the turbomachinery industry, of coarse mesh computations of 3D turbulent Navier–Stokes flows, with the main objective of identifying general trends on global quantities such as losses.

More detailed validations unanimously indicate the great need for better turbulence and transition models.

Finally, some of the recommendations of the Technical Evaluator, Dr L. Povinelli, are worthwhile reporting, since they most certainly are of general validity.

i). More emphasis should be given to validation and to a strong interaction between experimentalists and CFD specialists.

ii). Efforts should be expanded on turbulence and transition modelling, including compressibility effects, higher order closures, pdf modelling, direct numerical simulations (DNS) of turbulence.

iii) Three-dimensional Navier–Stokes simulations are essential for propulsion system simulations, having already led to significant progress. Fine grids are needed, since coarse computations will normally not be sufficient.

iv) Future activities, such as Symposia, should be encouraged within the AGARD Panels, in the field of Validation for Propulsion CFD

REFERENCES

Proceedings, 77th Propulsion and Energetics Panel Symposium on **CFD Techniques for Propulsion Applications** . AGARD CP 510, 1991.

(The authors and reference numbers given in the Figure Captions refer to the corresponding papers in AGARD CP 510.)

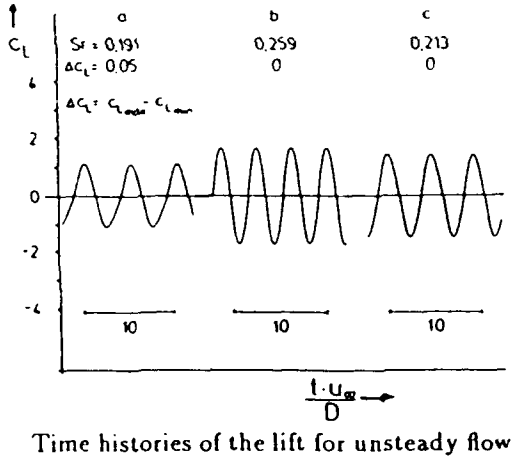

Time histories of the lift for unsteady flow around a circular cylinder, Re=3000, Ma=0.3, 177x113 grid points.
a) grid stretched in cirumferential direction, coefficient of fourth order damping $\epsilon^{(4)} = 1/256$
b) grid equidistant in cirumferential direction, coefficient of fourth order damping $\epsilon^{(4)} = 1/256$
c) grid equidistant in cirumferential direction, coefficient of fourth order damping $\epsilon^{(4)} = 1/32$

Figure 1. From Hänel [1]

Free - Expansion Nozzle (plane)
simulated freeflight $M_\infty = 6.8$

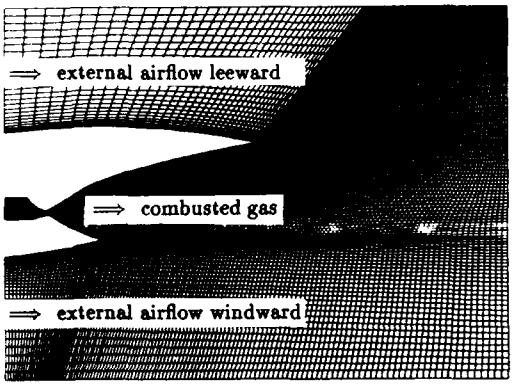

Three block grid

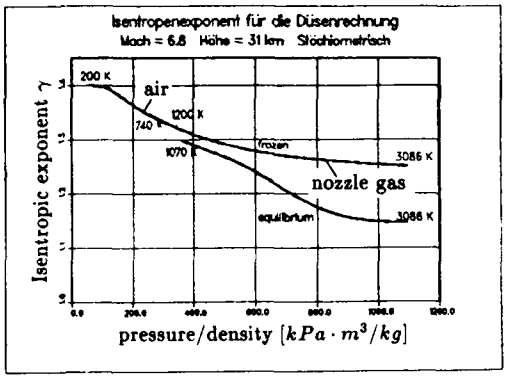

Isentropic exponent γ

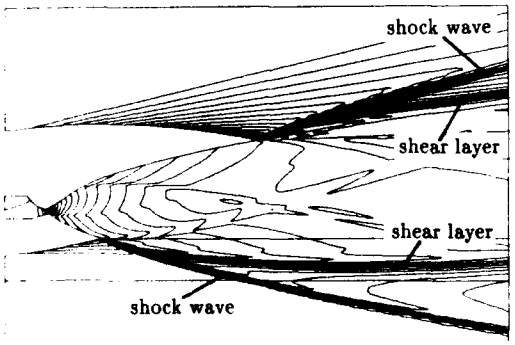

Euler solution, perfect gas $\gamma = 1.27$
Machnumber distribution, thrust = 290.5[KN/m]

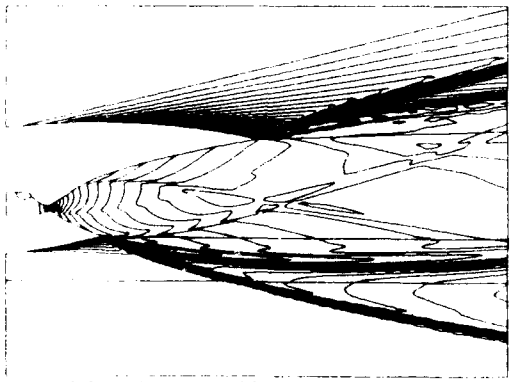

Euler solution equilibrium real gas
Machnumber distribution, thrust = 288.8 [KN/m]

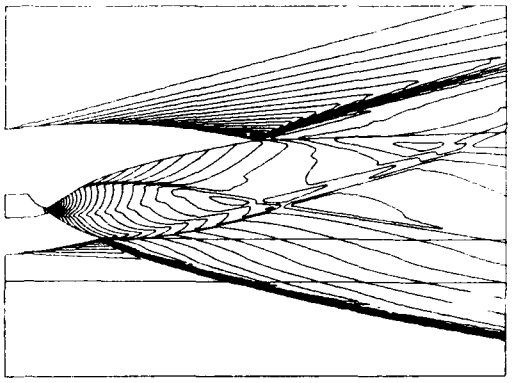

Euler solution equilibrium real gas (air)
pressure distribution

Free - Expansion Nozzle (plug)
perfect gas; simulated freeflight $M_\infty = 3.5$

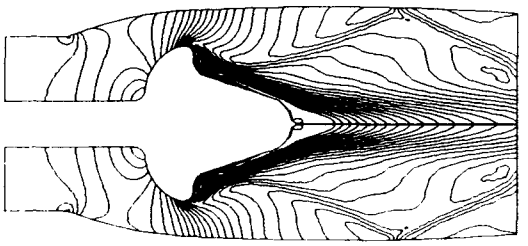

Euler solution (axisym.)
Machnumber distribution, no external air flow

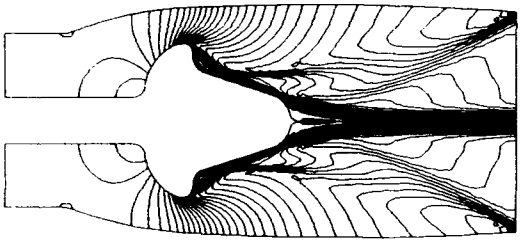

Euler solution (plane)
Machnumber distribution, no external air flow

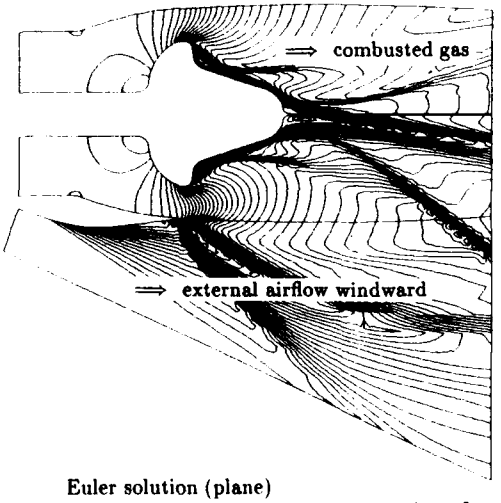

Euler solution (plane)
Machnumber distribution, with external air flow

Figure 2. Free-Expansion Nozzle, Euler Computations, from Weiland et al. [32]

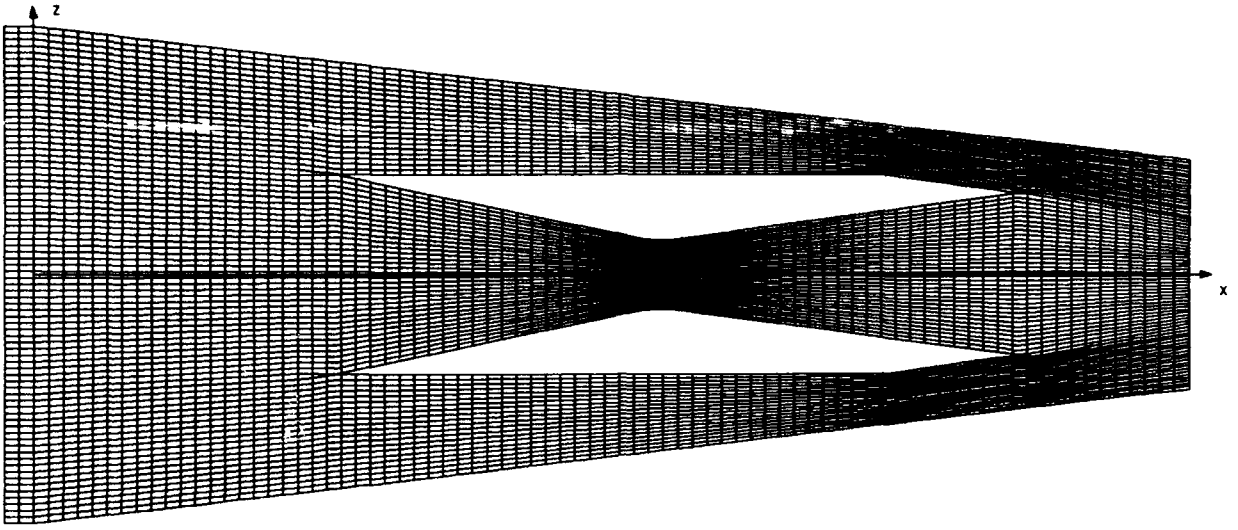

Grid for Scramjet (407x155 grid points)

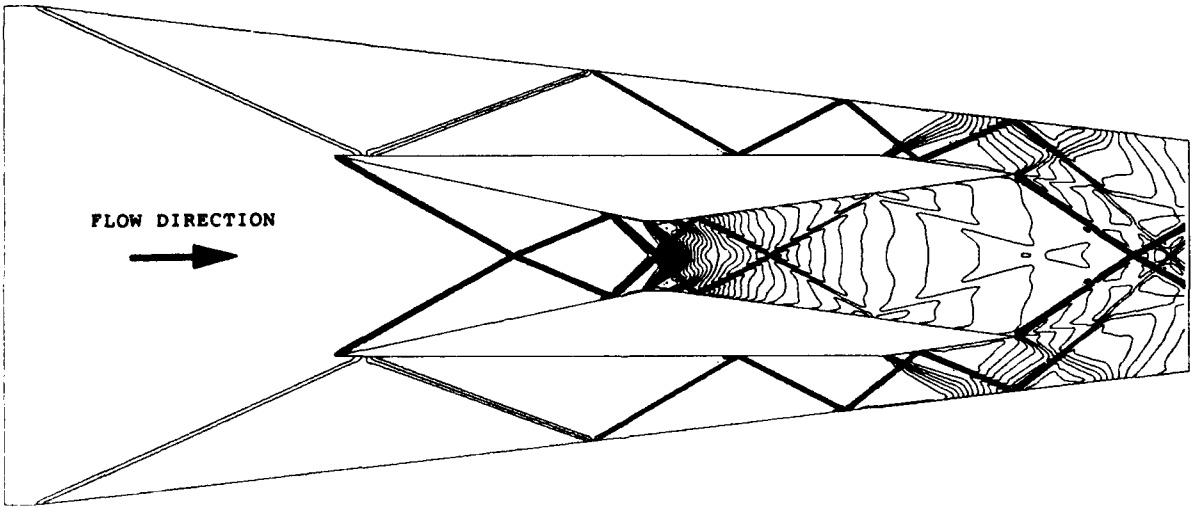

Lines of constant density - M = 3.0

Figure 3. Grid and density field for scramjet, calculated with the Euler code of Bissinger and Eberle [26]

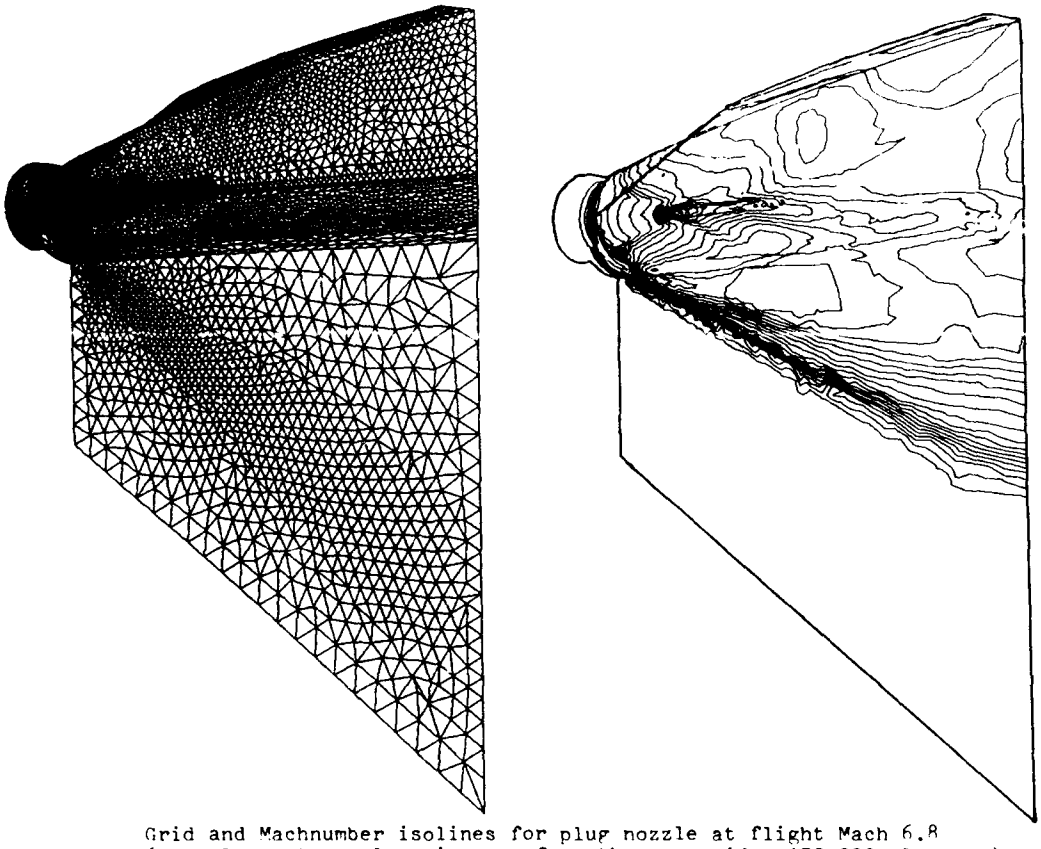

Grid and Machnumber isolines for plug nozzle at flight Mach 6.8
(x,y-plane at nozzle axis seen from the rear side, 150 000 elements)

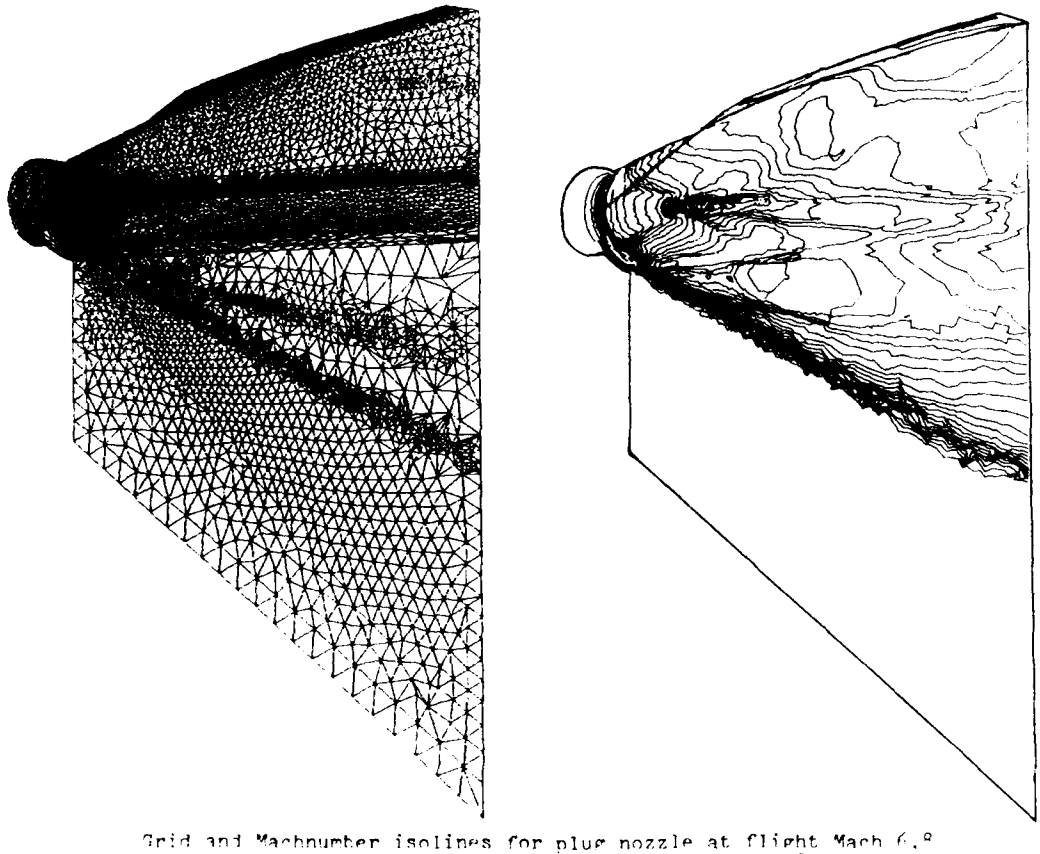

Grid and Machnumber isolines for plug nozzle at flight Mach 6.8
(x,y-plane at nozzle axis seen from the rear side, 380 000 elements)

Figure 4. Three-dimensional adaptive Euler computation on a plug nozzle, from Koschel et al. [33]

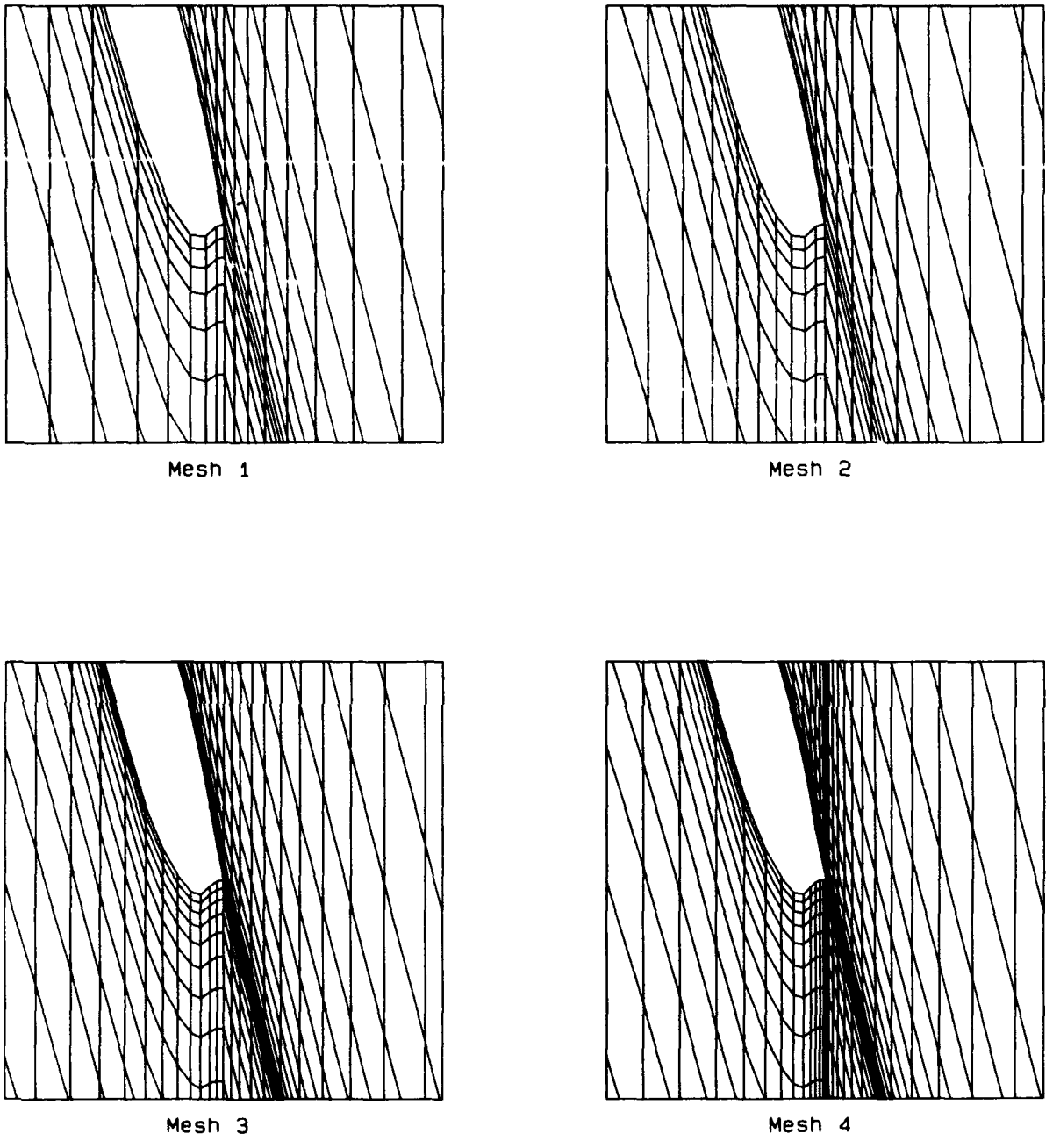

Figure 5. Details of mesh near trailing edge, from Horton et al. [19]

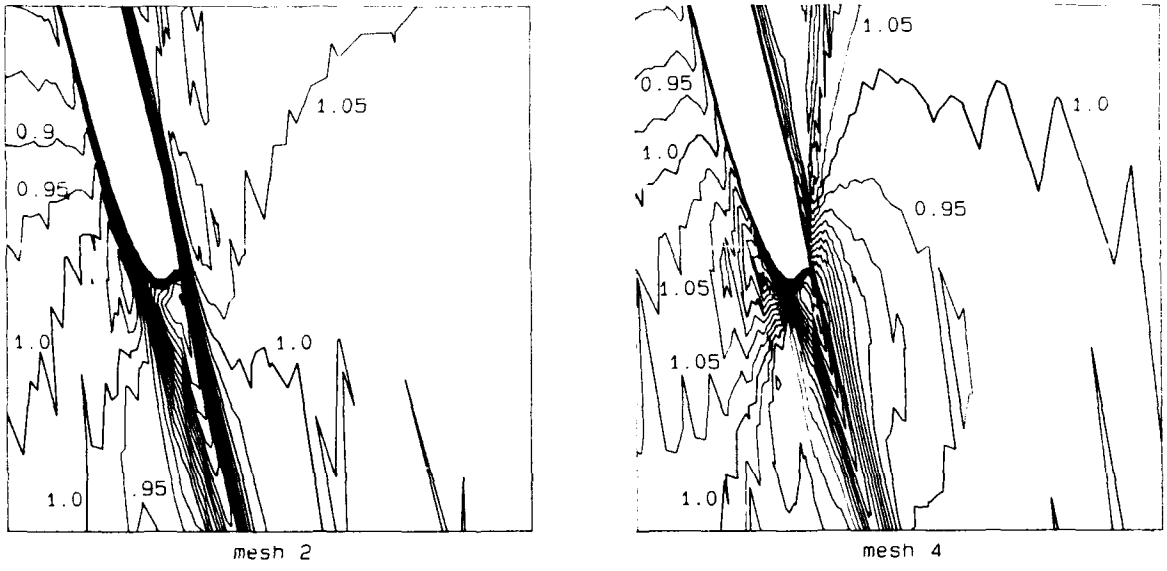

Figure 6. Contours of Mach number near trailing edge from Horton et el. [19]

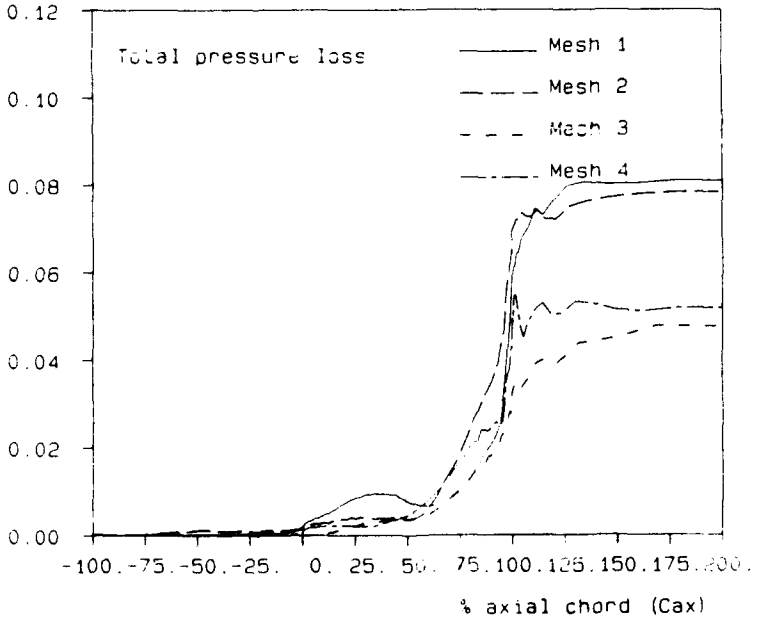

Figure 7. Development of total pressure loss with different meshes, from Horton et al. [19]

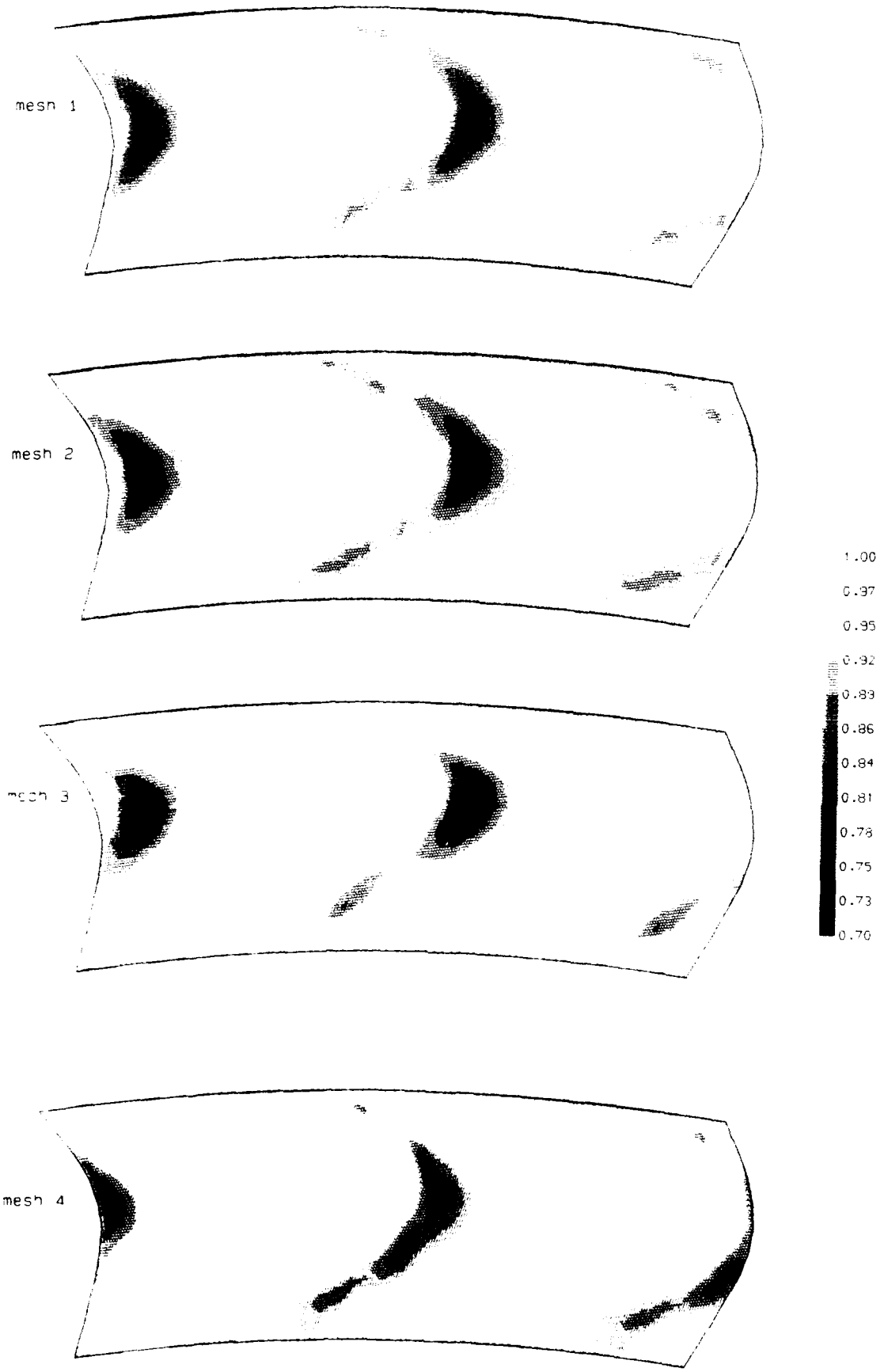

Figure 8. Contours of total pressure on a plane at 120% axial chord. Comparison of results with different meshes. from Horton et al. [19]

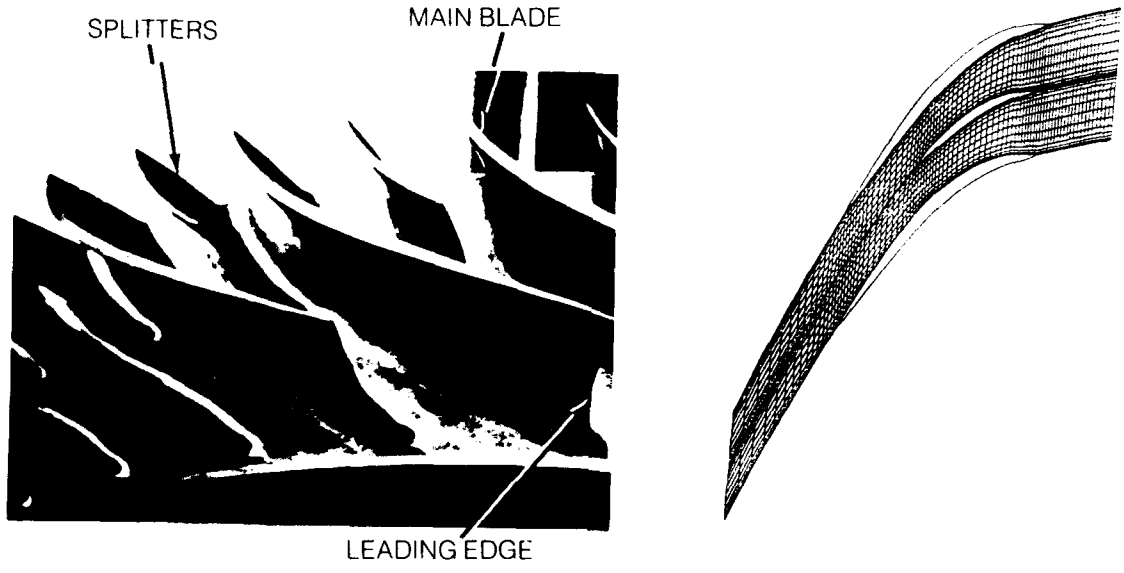

Wennerstrom's Splittered Rotor

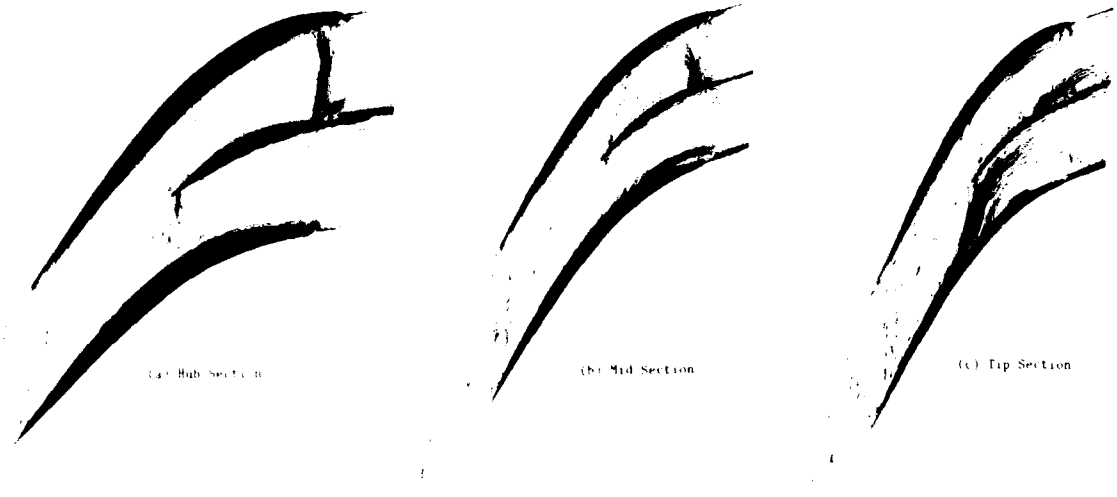

Mach Number Contours of Wennerstrom's Splittered Rotor Predicted by Dawes' Viscous Code

Figure 9. From Schra et al. [13]

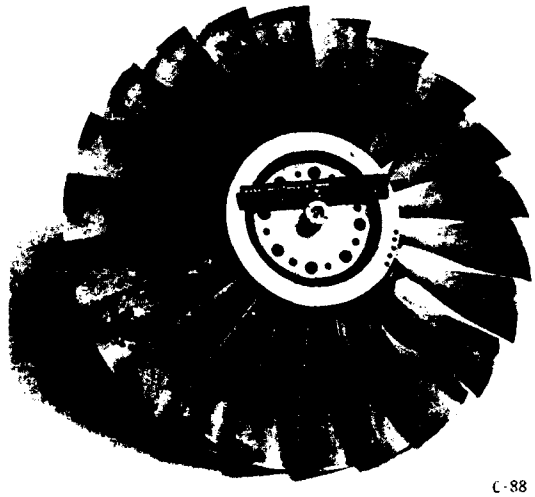

C-88 05331

Rotor 67 test hardware.

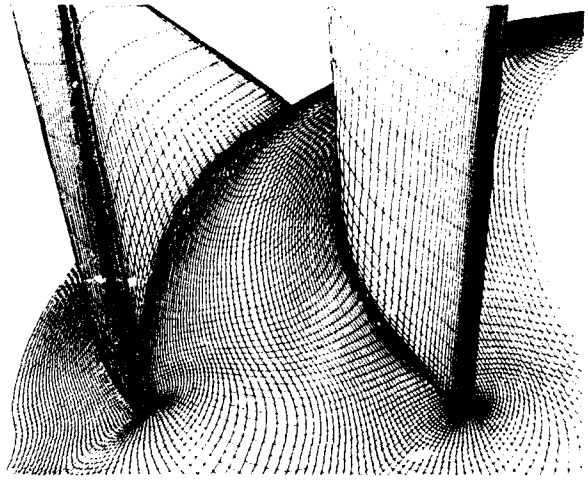

Grid leading edge enlargement.

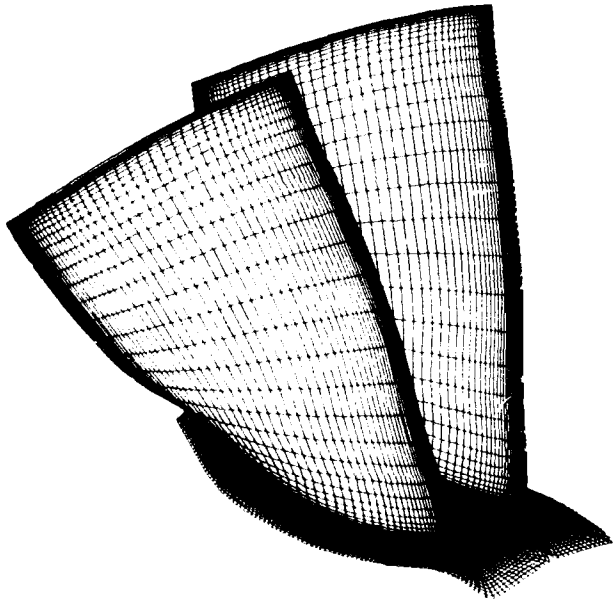

Computational grid.
185 C x 40 tangential x 49 spanwise points.

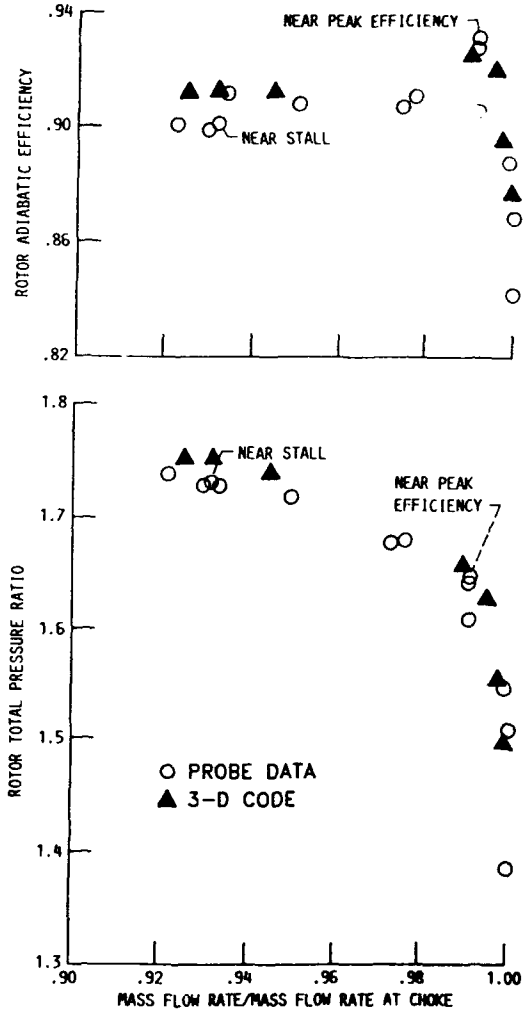

Comparison of computed and measured adiabatic efficiency and total pressure ratio characteristic at 100 percent speed. Points labelled "NEAR STALL" and "NEAR PEAK EFFICIENCY" are discussed in detail in the text.

Figure 10a. From Chima [21]

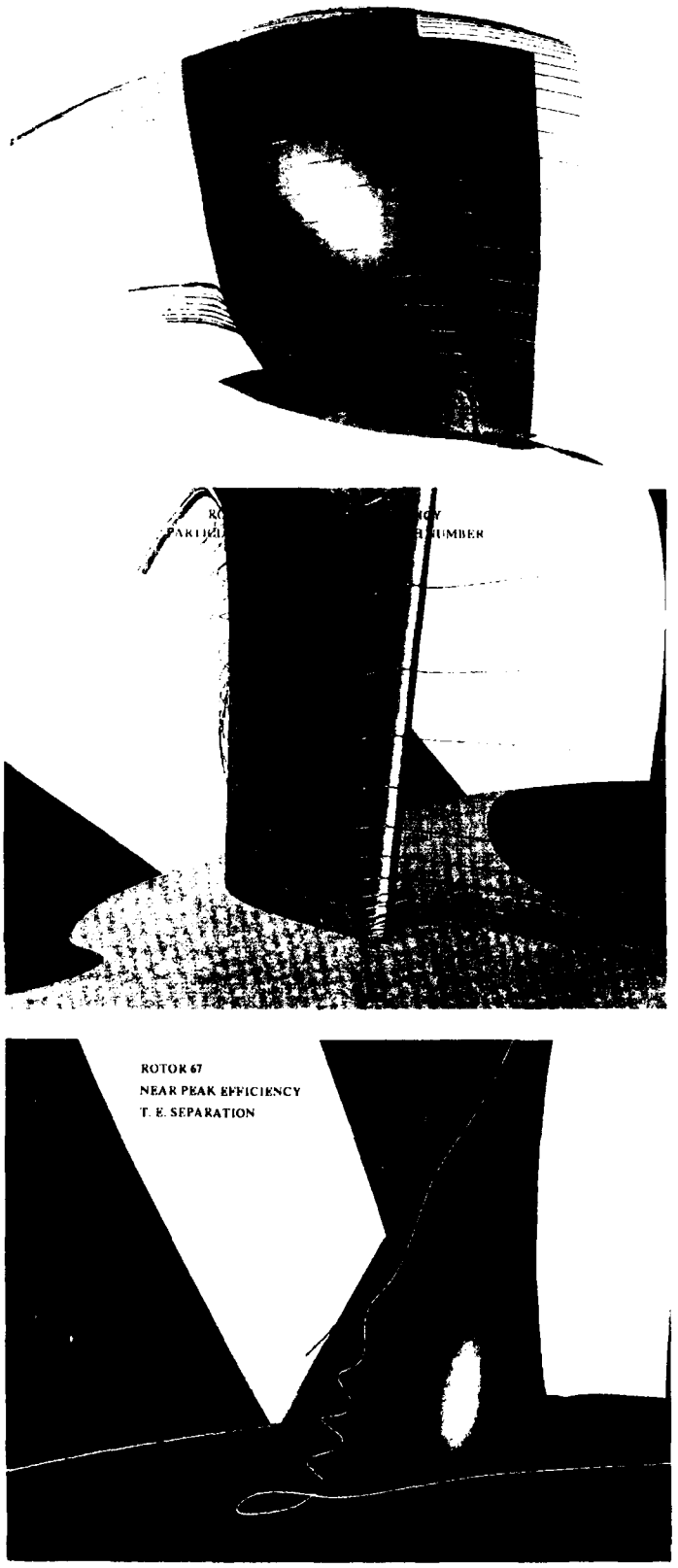

Computed particle traces, near peak efficiency.
Top: Suction surface overview.
Center: Leading edge enlargement looking downstream.
Bottom: Trailing edge enlargement looking upstream.

Figure 10b. From Chima [21]

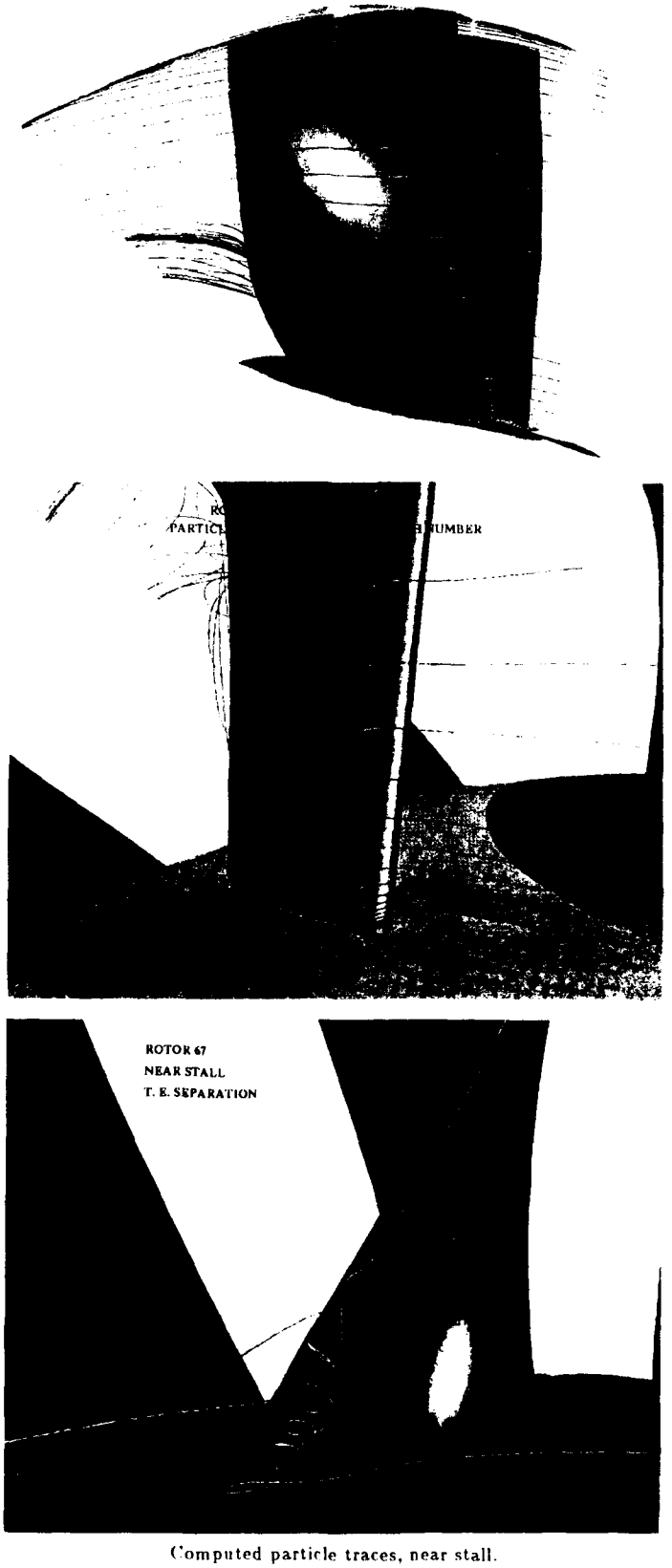

Computed particle traces, near stall.
Top: Suction surface overview.
Center: Leading edge enlargement looking downstream.
Bottom: Trailing edge enlargement looking upstream.

Figure 10c. From Chima [21]

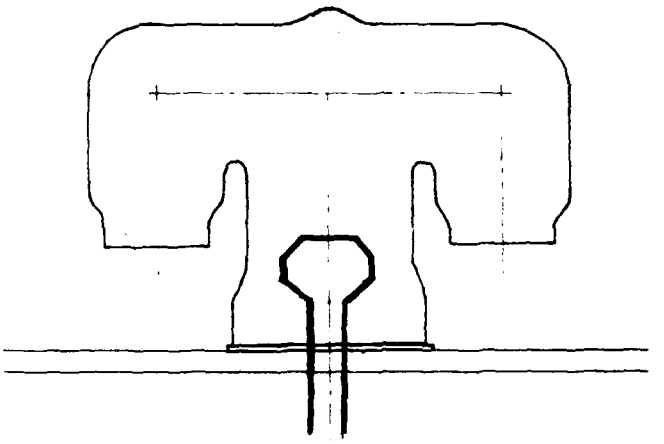

GEOMETRY OF T-VAPORISER WITH STANDARD FUEL INJECTOR

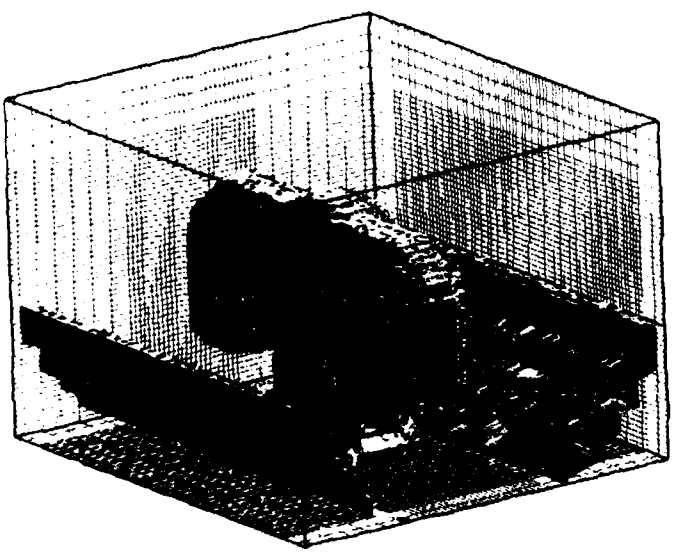

MODELLING OF VAPORISER, GRID AND GEOMETRY REPRESENTATION

Figure 11a. From Bond et al. [38]

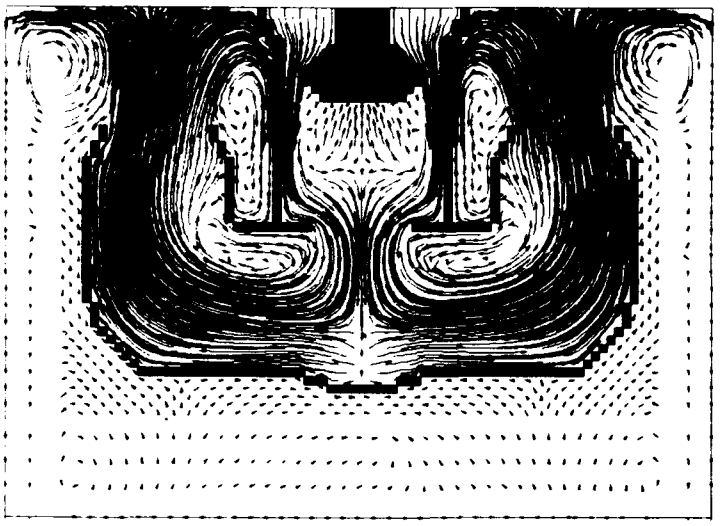

(a) Flow streaklines

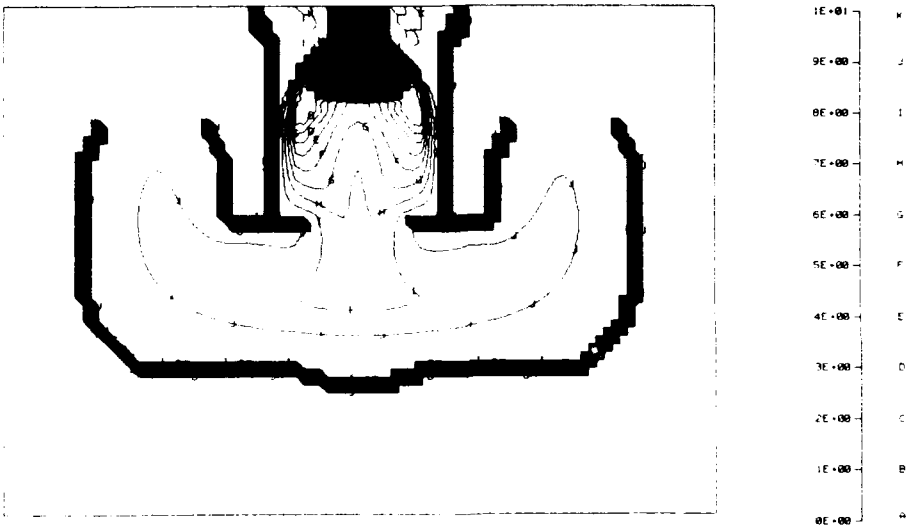

(b) Fuel concentrations on plane through injector centreline

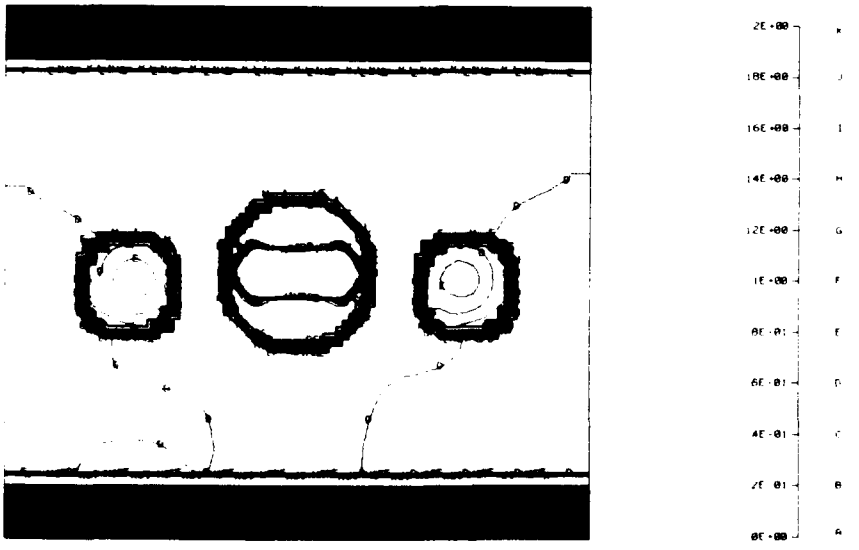

(c) Fuel concentrations on plane through vaporiser exits

Figure 11b. Datum solution, flowfield and fuel concentration, from Bond et al. [38]

THE INFLUENCE OF INTAKE SWIRL DISTORTION ON THE STEADY-STATE PERFORMANCE OF A LOW BYPASS, TWIN-SPOOL ENGINE

W. Meyer*, W. Pazur, and L. Fottner****

*MTU München GmbH, Postfach 500640, 8000 München 50, Germany

**Universität der Bundeswehr München, Werner-Heisenberg-Weg 39, 8014 Neubiberg, Germany

SUMMARY

Intakes of supersonic aircraft can produce intake swirl configurations in front of the engine which are important for intake/engine compatibility assessment throughout the flight envelope. The main objective of this investigation was to get more information about the influence of intake twin swirl on the steady-state engine behaviour. The twin swirl was simulated using a movable delta wing positioned between the bellmouth intake and the engine. By changing the angle of attack of the delta wing, the intensity of the intake swirl could be varied. Increasing the intensity of the twin swirl resulted in a deterioration of engine performance. The analysis of the test results showed that these effects on engine performance were mainly due to a modified characteristic of the low pressure compressor (LPC). Therefore, it was very important to investigate the changed LPC performance to be able to understand the effects of an intake swirl distortion on the engine performance.

Hence, an experimental method was set up to measure the performance map of the installed LPC by defined changing of the engine operating line. An analysis of experimentally determined compressor maps for varying intensities showed that the performance parameters of the LPC decrease. However, there is essentially no variation of the engine's working line due to an intake twin-swirl distortion.

Semi-empirical calculations which took account of this influence of the generated swirl on the performance of the LPC confirmed the loss of engine performance observed during the engine tests.

NOMENCLATURE

b_s	specific fuel consumption (SFC)
corr	corrected to INA conditions
C	calculated value
DC(θ)	circumferential total pressure distortion coefficient
FAR	fuel-air-ratio
F_s	thrust
$\dot{m}$	total mass flow
M	measured value
n	rotor speed
p	static pressure
p_t	total pressure
PLA	power lever angle
rel	relative to design point
SM	surge margin
SL	surge line
SC(θ)	swirl parameter (Ref 11,12)
SC*(θ)	swirl parameter
T_t	total temperature
WL	working line
v	absolute velocity
v_{ax}	axial component of velocity
v_r	radial component of velocity
v_u	circumferential component of velocity
α_0	angle of attack
$\alpha_M(\theta)$	mean swirl angle in circumferential direction
α	angular deviation in circumferential direction
β	angular deviation in radial direction
Δ	difference between undistorted and distorted conditions
η_{is}	isentropic efficiency
θ	circumferential position
Π	total pressure ratio
τ	local swirl angle
$\bar{\tau}$	mean swirl angle
2	entry of LPC
21	exit of LPC

1. INTRODUCTION

In the past, a distorted intake flow was considered to be a local non-unifom total temperature (Ref 1,2) and/or total pressure (Ref 3,4) distribution at the engine face or a non-uniform distribution with respect to time (Ref 5). In the scope of the design and development of jet engines with even higher power densities and in connection with a higher thrust/weight ratio without intake guide vanes (IGV), an additional distortion phenomenon in the form of intake swirl distortion was found (Ref 6,7).This phenomenon can have a significant influence on engine performance, stability, or acromechanics and thus has to be taken into account in the assesssment of intake/engine compatibility. This means that due to an intake swirl distortion, the quality of the flow field at the LPC entry may deteriorate to such an extent that the engine cannot tolerate it.

An intake swirl distortion is usually generated by an S-shaped intake duct in combination with extreme flight conditions such as high angles of attack or supersonic flight velocities which cause flow separation at the intake cowl or ramp. Investigations (Ref 6) have shown that essentially all supersonic intakes produce a swirl configuration which is considered to be a superposition of a twin swirl and a bulk swirl with varying intensity depending on intake configuration and flight conditions. Indeed, this fact is attributed to the similar geometry of supersonic aircraft intakes, because these intakes usually require S-shaped diffusers due to the offset of the engine relative to the intake.

As a basic principle for the design of advanced turbojet engines the compatibility of the quality of the flow provided by the intake and the tolerance of the engine has to be considered from the beginning of the development phase. For this reason, numerous investigations were performed in the past simulating non-uniform total temperature or pressure distributions in front of a turbojet engine. During the last few years, as more information was obtained on another distortion in the form of intake swirl (i.e. Ref 5), experimental work has been started to simulate first of all typical swirl patterns in front of the engine face with a defined intensity and to investigate the effects on the engine performance and, in particular, the deterioration of the performance and the stability of the compressors of turbojet engines in the presence of intake swirl. The evaluation of these tests showed that the sensitivity of jet engines without IGVs to intake swirl distortion may result in effects similar to those well-known from non-uniform total pressure or total temperature distribution. The consequence of these effects is a decrease in engine performance such as reduced thrust and increased specific fuel consumption and a deterioration of the compressor behaviour involving a loss in surge margin and induced fan blade vibrations. So far, however, no fundamental investigations were performed on this topic. Thus it became necessary to investigate the influence of intake swirl on a jet engine in detail.

The work reported herein shows the possibility of the simulation of an intake twin-swirl distortion using a movable swirl generator in front of a twin spool low bypass turbofan engine. Subsequently, the major effects of the generated intake swirl on the steady-state engine performance are presented. In order to be able to explain the deterioration in engine performance further investigations aimed at studying the influence of intake swirl on the performance of the installed LPC were performed. In this way a possibility was found to measure the performance map of an installed compressor.

In order to verify the decrease in engine performance resulting from a deterioration of the LPC performance semi-empirical performance calculations were carried out using measured LPC data with intake swirl.

2. SIMULATION OF TYPICAL INTAKE SWIRL DISTORTION

Investigations on the influence of intake swirl distortion on the performance and the stability of compressors and engines necessitate a device for the generation of typical aircraft intake swirl flow patterns. Detailed analyses of the intake flow patterns measured for distorted ground and flight conditions are required for definition of swirl patterns intended as a basis for the design of such a swirl simulator. This has been done in a preliminary study (Ref 8), where extensive model wind tunnel investigations with subscale swirl generators were performed. The results of this study show that engine tests should start with a movable swirl generator, consisting of a sharp-edged delta wing with trapezoidal cross-section and a leading-edge sweep angle of 60^{o}. This model delta wing selected has demonstrated its capability of simulating defined twin swirl patterns. In addition, it allows the intensity of the generated swirl to be varied by changing its angle of attack. Even at low angles of attack the flow separates at the sharp leading-edges of the wing and rolls up into two vortex sheets above its upper surface.

The results of the flow field measurements downstream of the model delta wing, which could be pitched up to an angle of attack of $\alpha_o = 23^{o}$, show that the flow deflection within the vortex cores increases continuously with increasing angle of attack (Ref 8). The local swirl angle τ used for the description of the cross flow is defined as the angular deviation of the local flow direction from the axial direction (Fig 1). Its sign is defined as positive when the circumferential component of the swirl angle is in the same sense as the LPC rotation. Fig 2 shows the cross flow pattern measured for an angle of attack of $\alpha_o = 15^{o}$. The counter-rotating double swirl can clearly be recognized as symmetrical about the y-axis. According to the theory of vortex formation over a slender delta wing (Ref 9,10) the flow deflection in circumferential direction increases within the vortex core towards the swirl axis up to about 30^{o} at the maximum angle of attack.

An investigation on the influence of a pure intake swirl distortion on engine performance requires a low-level total pressure non-uniformity across the engine face. Thus, the effect of the vortex formation on the total pressure distribution of the flow field behind the delta wing is very important for a qualitative assessment of the generated swirl distortion. Fig 3 presents the normalised total pressure contour map of the measured flow field downstream of the model delta wing for an angle of attack of $\alpha_o = 15^{o}$. According to the pertinent flow pattern in Fig 2 the total pressure distribution was found to be symmetrical with respect to the y-axis. The two total pressure minima in the center of the vortices can be attributed to the flow separation at the leading edges of the delta wing. This total pressure drop inside the vortex sheets increases up to about 6% at the maximum angle of attack.

For describing the circumferential total pressure distortion the DC(θ)-coefficient was used, which has proved to be very valuable for the assessment of intake/engine flow compatibility. The analysis of the measured flow field behind the model delta wing shows that the time-averaged DC(60)-value increases with increasing angle of attack up to a maximum of DC(60) = 0.11 for $\alpha_o = 23^{o}$.

3. ENGINE TEST SET-UP, DISCUSSION OF THE SWIRL PATTERNS

The main objective of this investigation was to obtain more in-

formation on the effects of intake twin swirl on the steady-state engine performance. These engine tests are the continuation of the model wind tunnel investigations with the subscale swirl generators described in Ref 8.

The tests were conducted at the engine test facility of the Jet Propulsion Institute at the Universität der Bundeswehr München. As a test object a Larzac 04 turbofan engine (Fig 4) was chosen which is the powerplant of the Alpha Jet aircraft. The Larzac 04 is a twin-spool low bypass turbofan engine in the 13kN takeoff thrust class. It has a two-stage LPC and a four-stage high pressure compressor (HPC), each spool being driven by a single-stage turbine. The combustor is of annular, straight-through design. Bypass stream and core stream emerge through separate fixed-area exhaust nozzles. To ensure stable engine operation during acceleration the Larzac 04 is equipped with a handling bleed which is open at HP spool speeds below 80% to maintain the matching of both spools. In this case compressor bleed air is extracted from bleed ports located at the HP compressor exit and discharged into the bypass duct.

Although no intake swirl distortion occurs during normal operation of this engine it is well suited for these investigations because of the absence of inlet guide vanes which normally have a flow straightening effect.

The main components of the engine test set-up are shown in Fig 5. Between the original bellmouth intake and the engine a swirl generator and a measuring device, which allows measurement of the flow field across the whole cross-section in the engine aerodynamic interface plane (AIP), are fitted. A delta wing (see Fig 6) geometrically similar to the subscale model, which was investigated in Ref 8, is used as a movable swirl generator. Its fastening inside the intake and the mechanism for variation of the angle of attack is shown in Fig 7. In the case of compressor instability the driving mechanism can be disengaged very quickly. The system is designed for an infinitely variable angle of attack up to a maximum of $\alpha_0 = 23^0$.

The measuring device in front of the engine consists of a rake, which is mounted as a diagonal strut in a separate, rotatable, sealed intake segment. This rotating rake, featuring eight 5-hole probes, can also be traversed in radial direction to cover the whole cross-section. To allow measurements of complex flow fields to be performed with this measuring configuration, each of the 5-hole probes had to be calibrated in the installed condition.

In addition to the rake, further instrumentation of the engine (Fig 8) is necessary to be able to analyse and assess overall engine performance and component behaviour with varying intake swirl distortion intensity. LPC and HPC delivery pressures and temperatures were measured using rakes at two different circumferential positions in each case. To measure the exhaust temperature after expansion in the turbine 9 harness thermocouples are located at the exit of the LP turbine.

The investigation comprised two parts:

- measurement of the flow patterns downstream of the delta wing with the rake,
- measurement of the effects of the intake distortion generated on the steady-state performance of the engine and the behaviour of the compressor system (rake removed).

The flow patterns measured downstream of the full-scale delta wing within the engine intake confirm the results of the subscale wind tunnel tests. In Fig 9 the cross-flow patterns in front of the LPC are shown for the maximum angle of attack of $\alpha_0 = 23^0$ and a reduced LP spool speed of $n_{LP}/\sqrt{T_{t2}} = 1060(\text{min}/\sqrt{K})^{-1}$. As in the model investigations a symmetrical flow field consisting of two counter-rotating swirls with similar cross flow intensities was found.

The total pressure distribution behind the full-scale delta wing, depending on the angle of attack, is very similar to the model test results of the feasibility study. The dependence of the circumferential total pressure distortion, in terms of DC(60)-values, on the angle of attack also shows a similar relationship and increases up to a maximum of 0.15 for $\alpha_0 = 23^0$. Although the maximum DC(60)-value of the engine tests is higher than the corresponding value of the model wind tunnel tests it may be assumed that the pressure distortion is still too small to have any influence on the engine behaviour.

Suitable parameters for describing the intensity of an arbitrary swirl distortion provided by the intake and the tolerance of the engine in numerical terms could not be found so far. An SC(θ)-parameter, equivalent to the DC(θ)-coefficient, is suggested in Ref 11,12 for the assessment of bulk swirl flow patterns. If this parameter is applied to such a complex swirl pattern generated by the delta wing the circumferential velocity components within a sector, containing one of the vortex cores of the double swirl, almost neutralize each other when the mean is taken; therefore, they are not taken into account by quantifying the swirl. As a result, the SC(θ)-parameter is not suitable for describing the intensity of a twin swirl.

The usefulness of a modified version of this parameter has been investigated in Ref 13. There, a SC*(θ)-coefficient, where the average value for the absolute values of the circumferential velocity components within a critical sector was used, shows a more significant dependence on the angle of attack, but does not give any additional information about the characteristic of the swirl patterns evaluated.

A mean swirl angle was used for describing the intensity of the whole cross flow pattern. This mean swirl angle $\bar{\tau}$ is the mass weighted average of all measured absolute values of the local swirl angles τ in the cross-section. The evaluation of the measured flow fields generated by the delta wing in the engine intake produces a growth of this mean swirl angle up to $\bar{\tau} = 13^0$ with increasing angle of attack. As shown in Fig 10 $\bar{\tau}$ is independent of the reduced LP spool speed up to an angle of attack of $\alpha_0 = 20^0$. Above $\alpha_0 = 20^0$ minor effects of the spool-speed on the intensity of the generated cross flow were found, resulting in a modest increase of $\bar{\tau}$ at lower speeds. This influence of LP spool speed on $\bar{\tau}$ can mainly be attributed to the fact that at high angles of attack the incident flow and the flow around the delta wing is changed significantly because of blockage and variation of streamline curvature, caused by the presence of lateral flow constraints.

A very similar relationship between LP spool speed, angle of

attack and intensity of the swirl was found in Ref 14. In this paper a swirl angle $\alpha_M(\theta)$ was defined by averaging the angular deviation in circumferential direction, i.e. neglecting the radial component of the generated flow deflection, within a critical sector. This swirl angle α_M, obtained for a sector of $\theta = 90^0$, was used for analytical calculations of the performance of a swirl distorted LPC using a theoretical distortion model, which considers four compressors working in parallel.

The difficulties in finding a suitable coefficient for the description of the intensity of the swirl including its direction of rotation in connection with the tolerance of the engine resulted in the decision to use the mean swirl angle $\bar{\tau}$ as a "swirl parameter".

4. INFLUENCE OF GENERATED INTAKE SWIRL ON ENGINE PERFORMANCE

The engine tests for the investigations about the effects of the simulated intake swirl on engine performance were carried out using the following test procedure: The specified reduced spool speeds were set at an angle of attack of $\alpha_0 = 0^0$. During the subsequent variation of the angle of attack the engine rating was held constant (i.e. the power lever angle (PLA) was not changed).

The decrease in reduced mass flow with increasing intensity of the generated twin swirl within the intake is shown in Fig 11. At low LP spool speeds (i.e. handling bleed open) the mass flow decreases with increasing mean swirl angle by up to 2%. After the handling bleed was closed, a more significant mass flow reduction was measured which reached a maximum of 5.5%.

The test procedure used for these engine tests (i.e. constant PLA during variation of swirl intensity) did not ensure constant LP and HP spool speeds. A check of the spool speeds at constant PLA showed a maximum decrease of LP spool speed of 0.2% at maximum swirl intensity for engine ratings with handling bleed open. For engine ratings with handling bleed closed, the LP spool speed decreased by about 0.8%. The HP spool speeds showed only minor variations, i.e. less than 0.1%, over the whole operating range which, therefore, were not considered in this investigation. The evaluation of the mass flow reduction caused by a lower LP spool speed showed that in the low speed region it was approximately in the same percentage range as the LP spool speed decrease. At higher spool speeds (i.e. handling bleed closed) a mass flow reduction of 0.75% was found for PLA = 50° and PLA = 100° and of 1.1% for PLA = 63°.

The mass flow reduction resulting from the increasing twin swirl intensity could be attributed to periodically changing instationary flow conditions relative to the first rotor of the LPC and thus to a resulting unsteady behaviour of this rotor.

The effects of intake swirl generated by the movable swirl generator on thrust are presented in Fig 12. The diagram shows the reduction of thrust, corrected to entry total pressure, with increasing mean swirl angle. Similar to Fig 11 a difference can be noted between engine running with open and with closed handling bleed. In the lower speed range a maximum thrust decrease of 3% was measured while at higher spool speeds the thrust decreased by up to 9% at maximum mean swirl angle, independent of the power setting.

An analysis of the measurements shows that a variation of the delta wing incidence, i.e. a change of the simulated intake twin swirl intensity, at constant PLA did not decisively affect the bypass ratio. As the fuel-air-ratio is held constant by the control system, a mass flow reduction can only lead to a decrease in thrust of approximately the same percentage. A comparison of Fig 11 and Fig 12 shows that especially at high spool speeds the percentage of the thrust decrease is often more than twice the mass flow reduction. The difference can only be due to a rematch of the cycle, giving lower component efficiencies and thus a reduction of the core and bypass nozzle exit velocities. The test results do not show any influence of the twin swirl intensity on HP compressor operating points and overall turbine expansion. As discussed in the next chapter in greater detail, the operating points of the LP compressor are shifted in the map to lower reduced mass flows, pressure ratios and isentropic efficiencies with increasing swirl intensity.

Fig 13 shows the effect of swirl intensity on the specific fuel consumption (SFC). As mentioned before, the engine control system regulates the fuel flow maintaining a constant fuel-air-ratio in the core flow at constant PLA and the bypass ratio does not change during variation of the swirl intensity. Thus the reduction of fuel flow is directly associated with the reduction of the total mass flow. Because of the high thrust drop, this results in the SFC increase shown.

5. LOW PRESSURE COMPRESSOR PERFORMANCE WITH INTAKE SWIRL DISTORTION

It was necessary for further investigations to find a method to measure the performance map of the installed LPC. The problem is, that the installed compressor can only follow the operating line of the engine. Nevertheless, there are some possibilities of a defined changing of the engine working line on the basis of different configurations of the Larzac 04 engine:

- a bleed from the HPC into the bypass duct. This bleed air leads to a throttling of the LPC over the whole operating range and is especially severe in the upper partial power setting and at maximum power.
- the bypass nozzle can be separated from the jet engine and tests can be run without the nozzle. This leads to a significant unthrottling of the LPC.
- running the engine with external air. This configuration is very similar to the standard configuration.
- the bypass nozzle area can be reduced by up to 28% of its nominal area by fixing area restrictors at the exit of the nozzle. This leads to a throttling of the LPC.

Thus it is possible to determine a surge point of the LPC by decreasing the bypass nozzle area by a certain amount and opening the bleed valves at the same time. This observed surge can only occur in the LPC because throttling of the LPC leads to a constant surge margin of the HPC.

However, due to the exhaust gas temperature which is limited by the engine control system, it is not possible to run all of the above mentioned engine configurations over the whole

operating range of the compressor. Fig 14 shows the measured performance map of the undistorted LPC which has been obtained in the way mentioned before.

Fig 15 shows the measured performance maps of the installed LPC for different intake twin-swirl intensities. The characteristics were obtained by changing the engine operating line as described before. In comparison with engine operation without swirl distortion, an increase in the intensity of the swirl distortion leads to a decrease in the reduced mass flow rate, the pressure ratio, and the isentropic efficiency. Furthermore, there is a decrease of the surge margin of the compressor.

Fig 16 shows the decrease of the reduced mass flow,

$$\Delta\dot{m}_{red} = \left[1 - \frac{\dot{m}_{red,distorted}}{\dot{m}_{red,undistorted}}\right] \cdot 100\% \qquad (5.1)$$

with $$\dot{m}_{red} = \frac{\dot{m}_2\sqrt{T_{t2}}}{p_{t2}}$$

and $$n_{red} = \frac{n}{\sqrt{T_{t2}}}$$

of the pressure ratio,

$$\Delta\Pi_{LP} = \left[1 - \frac{\Pi_{LP,distorted}}{\Pi_{LP,undistorted}}\right] \cdot 100\% \qquad (5.2)$$

and of the isentropic efficiency

$$\Delta\eta_{is} = \left[1 - \frac{\eta_{is,distorted}}{\eta_{is,undistorted}}\right] \cdot 100\% \qquad (5.3)$$

as a function of the mean swirl angle. The three graphs show two distinct regions. One of them refers to moderate swirl distortion, which leads to low losses. These are essentially independent on the power setting of the engine. The other region containing extensive swirl distortion shows a significant increase in the losses, which are additionally a function of the power setting of the engine. The reason for this phenomenon is the tolerance of the blading of the compressor for changed incidence at the 1st rotor of the LPC, caused by the generated intake swirl, up to a certain limit depending on the blading and the inlet Mach number. When increasing the intensity of the inlet swirl above this limit the losses of the main flow rise rapidly according to the cascade characteristic, which describes the variation of the loss factor with incidence and relative Mach number. The working line range of the cascade is considerably reduced with increasing Mach number, which leads to higher sensitivity to distorted incidence in the upper speed range

Fig 17 shows the losses in surge margin

$$\Delta SM = \left[1 - \frac{SM_{distorted}}{SM_{undistorted}}\right] \cdot 100\% \qquad (5.4)$$

$$SM = \frac{\Pi_{SL} - \Pi_{WL}}{\Pi_{WL} - 1}$$

as a function of the swirl intensity. These losses show a rising tendency even for moderate swirl distortion i.e. there is no tolerable limit of swirl intensity for the surge margin of the compressor. A possible explanation can be that a swirl distortion affects especially the tip region of the LPC which is often responsible for the location of the surge line.

A very important result of this investigation, also shown in Fig 15, is the fact that there is no variation of the standard working line of the engine in the LPC performance map due to an intake swirl distortion. This means that all of the steady-state operating points of the engine with intake swirl remain on the undistorted operating line. This fact can be verified by performance calculations (see chapter 6.)

As a result of the traversed total pressure and total temperature distributions in the exit area of the compressor at different measuring locations it is interesting to see if there is an uniform or non-uniform circumferential distribution of these parameters.

The pressure ratio of the LPC is shown in Fig 18 for two different measuring locations in circumferential direction at the compressor exit. As can be seen, the decrease of the pressure ratio is nearly equal at both measuring locations for the same mean swirl angle which leads to the conclusion that essentially no total pressure distortion exists at the exit of the LPC in circumferential direction.

In order to investigate the temperature rise in the compressor the total temperature ratio was plotted versus the reduced speed in Fig 19 for two circumferential positions. A comparison of the measured temperature ratios for the various mean swirl angles with the measurements with undistorted intake flow showed that at one location the temperature ratio increases with increasing intensity of the swirl distortion, whereas at the other location, it decreases with increasing intensity of the swirl distortion. This leads to the conclusion that a circumferential total temperature distortion exists at the exit of the LPC. This total temperature distortion becomes more and more severe with increasing intensity of the swirl distortion at the compressor intake.

This circumferential total temperature distortion is the result of a change of the velocity triangles at the compressor entry. The simulated twin swirl is in general a superposition of two bulk swirls, one co- and one counter-rotating to the rotation of the LPC with different swirl centers. Accordingly, there is a component of the absolute velocity in the direction of the circumferential velocity for the co-rotating and a component of the absolute velocity opposite to the circumferential velocity for the counter-rotating part of the twin swirl at the compressor entry in each case.

As a result there is a different increase in the total enthalpy for the co- and the counter-swirl causing a different increase in the total temperature. This leads to the aforementioned non-uniform distribution of the total temperature at the exit of LPC in circumferential direction.

During the experimental investigations only minor changes of the high-pressure compressor performance were noted. This fact will be confirmed by a performance calculation for the

engine with intake swirl using the characteristics of the distorted LPC in combination with the undistorted HPC performance map to compute the deterioration in engine performance due to intake swirl distortion.

6. SEMI-EMPIRICAL CALCULATIONS OF THE STEADY-STATE ENGINE PERFORMANCE WITH INTAKE SWIRL CONDITIONS

A very important objective was to verify the experimentally determined changes in engine performance with a performance calculation on the basis of changed LPC performance maps. Semi-empirical calculations were also carried out to make sure that inlet swirl distortion does not result in changes to the engine working line.

For this investigation an engine performance program for twin-spool turbofan engines was available, which was successfully used for Larzac 04 performance calculations at the Jet Propulsion Institute at the Universitat der Bundeswehr München. This program is of modular design and uses the characteristics of the individual engine components to calculate the overall performance. Matching of the operating points of the components is ensured by an iteration routine. The measured LPC characteristics for different twin swirl intensities were prepared for the performance synthesis program.

Since the experimental test results had not shown any influence of the simulated intake twin swirl on the performance of the HP compressor, HP and LP turbines, the effects on the engine performance were attributed to a changed LP compressor characteristic. The objective of these calculations was to check whether an LPC characteristic changed according to the measured results could cause a similar deterioration in engine performance.

In Fig 20 to Fig 22 the results of the calculations using measured LPC characteristics are compared with the measurements. The calculated and measured deterioration from clean-flow engine performance expressed in terms of a reduction of reduced mass flow and thrust and of an increase of SFC agree very well.

Fig 23 shows the steady-state working line of the Larzac 04 engine in the LPC performance map, not only on the basis of the performance calculation but also as measured in the experimental investigations for different intake swirl intensities. Experimental as well as analytical result is a single operating line for the engine without a change for the distorted case in comparison with the undistorted one, i.e. the analytical results confirm the experimental fact that there is no change of the operating line caused by this type of distortion.

7. CONCLUSIONS

Experimental investigations have shown that swirl distortion has to be considered as important parameter which affects engine performance and intake/engine compatibility. Typical supersonic intake flow patterns, with flow separation at the intake cowl or ramp and the S-shaped diffusers, always showed a combination of twin- and bulk-swirl. A delta-wing used as a movable swirl generator and integrated in a test rig in front of the Larzac 04 engine has proven its capability to produce a typical twin swirl, one of those two basic swirl types.

By changing the angle of attack of the delta wing, the intensity of the intake swirl could be varied. In this way, twin-swirl patterns could be generated up to a maximum mean swirl angle of about 13^{O}.

Further work was done to find a method to obtain experimentally an LPC performance map by defined changing of the engine operating line. Thus, it was possible to measure the performance map of the LPC with and without intake swirl distortion.

At a maximum mean swirl angle of 13^{O} the thrust decreased by 9% while the reduced mass flow rate dropped by 5.5%, the total pressure ratio by 4.5 %, and the isentropic efficiency by 6.5% at maximum power setting. At the same time the surge margin decreased by 25% and the SFC increased by 5%. In addition, a minor total temperature non-uniformity could be verified at the LPC exit area which arises from a variable total enthalpy increase along the circumference of the compressor due to inlet swirl distortion.

Additional semi-empirical calculations confirmed that the drop in engine performance resulted from changed LPC characteristics. In this way, the fact that there is no change of the operating line of the engine due to an intake distortion could also be established.

ACKNOWLEDGEMENT

The work reported *herein* was supported within research programmes of the German Bundesministerium der Verteidigung and of the Bundesamt für Wehrtechnik und Beschaffung. The permission to publish the results is greatly acknowledged.

REFERENCES

1. Kunkler,H., Tonskotter,H.,1979,"Zum Einfluß stationärer Temperatur- und Druckstörungen auf die Strömungsverhaltnisse in einem installierten, vielstufigen Strahltriebwerk-Verdichter", Z. Flugwiss. Weltraumforsch. 3, Heft 6, S. 360-378.

2. Mehalic,Ch.M., Lottig,R.A.,1974,"Steady-State Inlet Temperature Distortion Effects on the Stall Limits of a J85-GE-13 Turbojet Engine", NASA TM X-2290.

3. Lecht,M.,1983,"Beitrag zum Verhalten von Axialverdichterstufen bei stationarer Storung in der Zuströmung", DFVLR-FB83-39.

4. Hercock,R.G.,1982,"Effect of Inlet Flow Distortion on Engine Stability", AGARD-CP-324.

5. Williams,D.D.,1986,"Review of Current Knowledge on Engine Response to Distorted Inflow Conditions", AGARD-CP-400.

6. Aulehla,F.,1982,"Intake Swirl - a Major Disturbance Parameter in Engine/Intake Compatibility", ICAS/AIAA, ICAS-82-4.8.1.

7. Seddon,J., Goldsmith,E.L.,1985,"Intake Aerodynamics", William Collins Sons&Co. Ltd. London.

8. Genßler,H.P., Meyer,W., Fottner,L.,1986,"Development of Intake Swirl Generators for Turbo Jet Engine Testing", AGARD-CP-400.

9. Wedemeyer,E.H.,1978,"Stable and Unstable Vortex Separation", AGARD-CP-247.

10. Hummel,D.,1978,"On the Vortex Formation over a Slender Wing at Large Angles of Incidence", AGARD-CP-247.

Guo,R.W., Seddon J. 1983,"The Swirl in an S-Duct of Typical Air Intake Proportions", The Aeronautical Quarterly, May 1983.

12. Guo,R.W., Seddon,J.,1983,"Swirl Characteristics of an S-shaped Air Intake with Both Horizontal and Vertical Offset, The Aeronautical Quarterly, May 1983.

13. Meyer,W.,1988,"Theoretische und experimentelle Untersuchungen über den Einfluß von Eintrittsdrallstorungen auf das Betriebsverhalten von Turbostrahltriebwerken. Dissertation UniBw München, Institut für Strahlantriebe.

14. Pazur,W., Fottner,L.,1990,"The Influence of Inlet Swirl Distortions on the Performance of a Jet Propulsion Two-Stage Axial Compressor", ASME 90-GT-147.

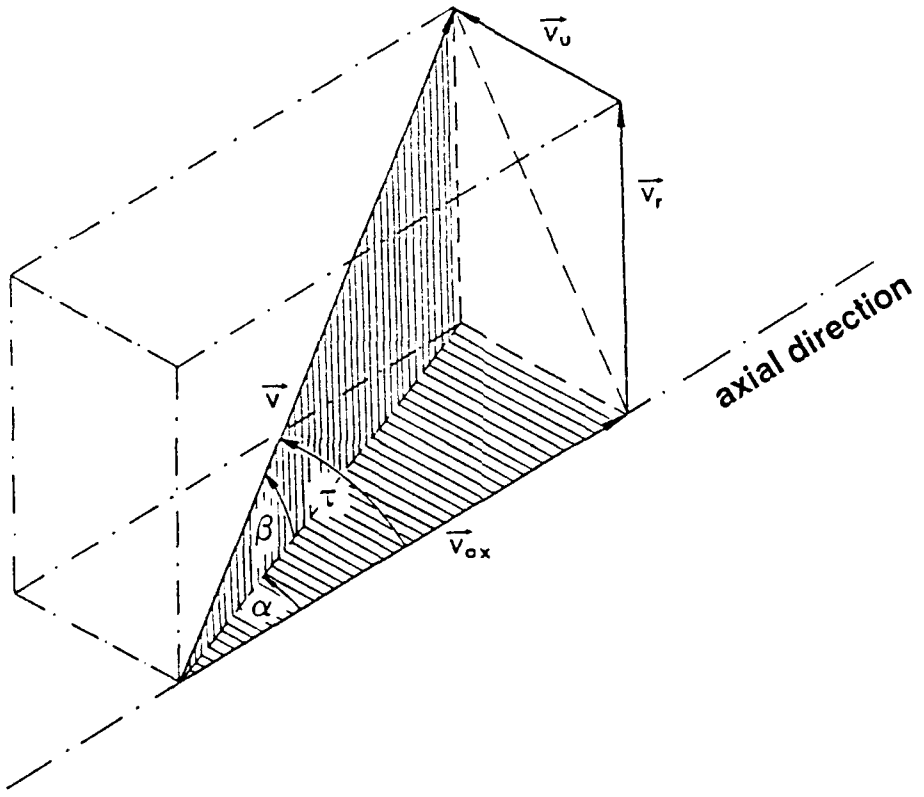

1. Definition of the local swirl angle τ

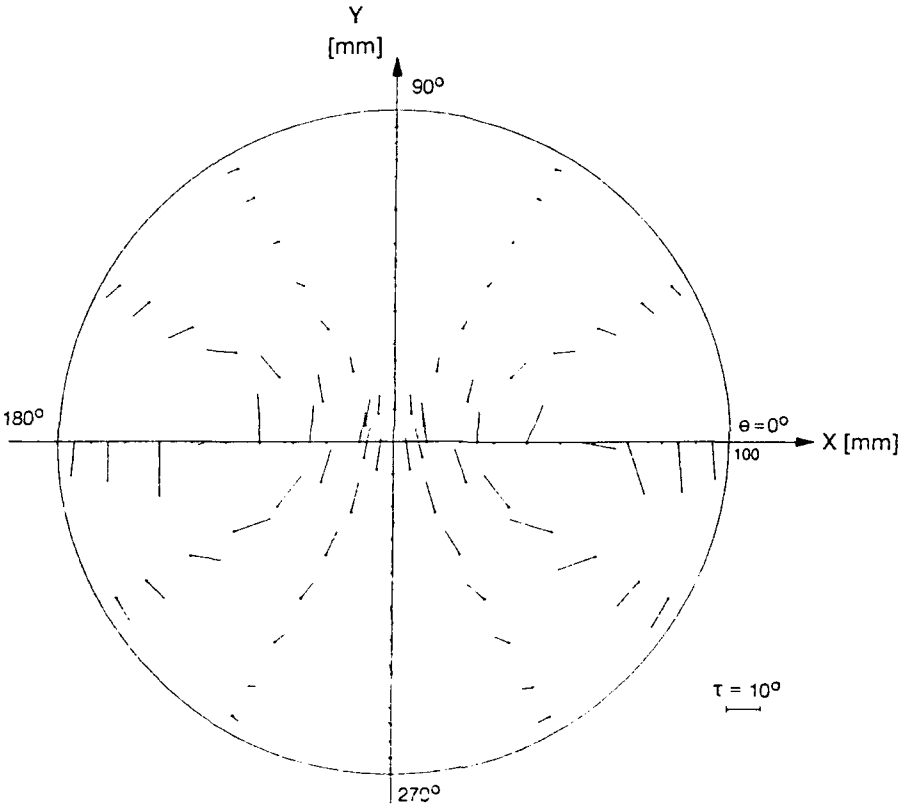

2. Cross flow pattern (model delta wing; $\alpha_0 = 15^0$)

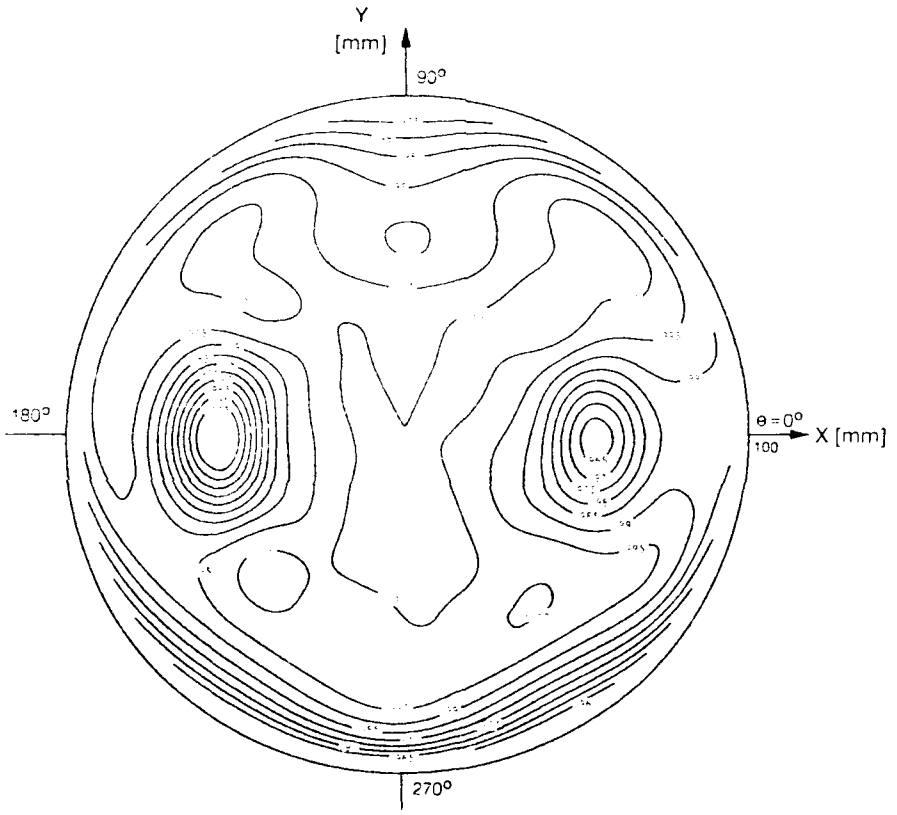

3. Normalised total pressure contours (model delta wing; $\alpha_0 = 15^0$)

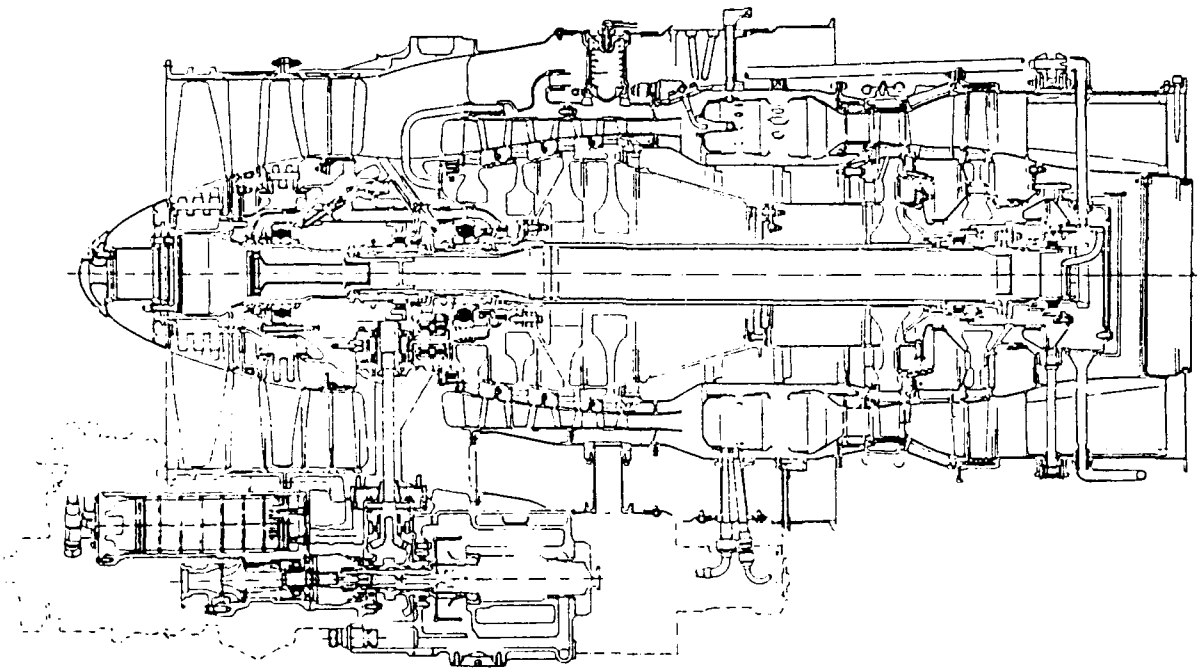

4. Larzac 04 turbofan engine

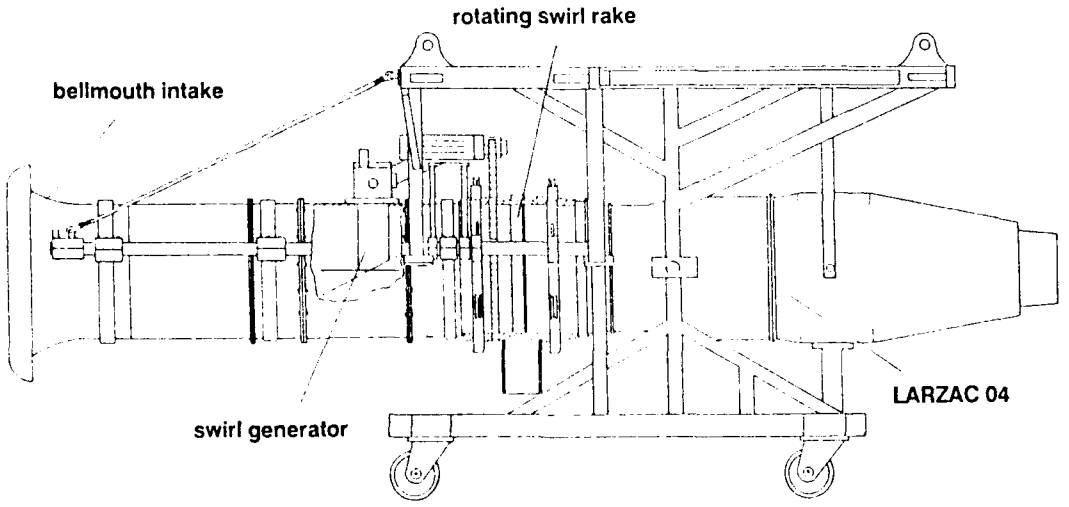

5. Test arrangement for the engine investigations with distorted inlet flow

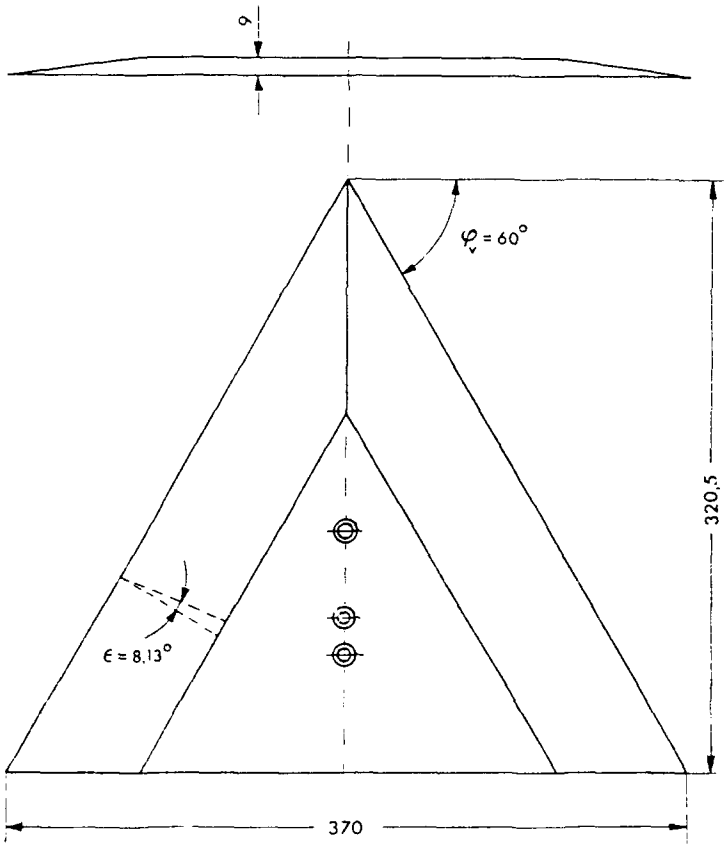

6. Geometry of the full-scale delta wing (movable swirl generator)

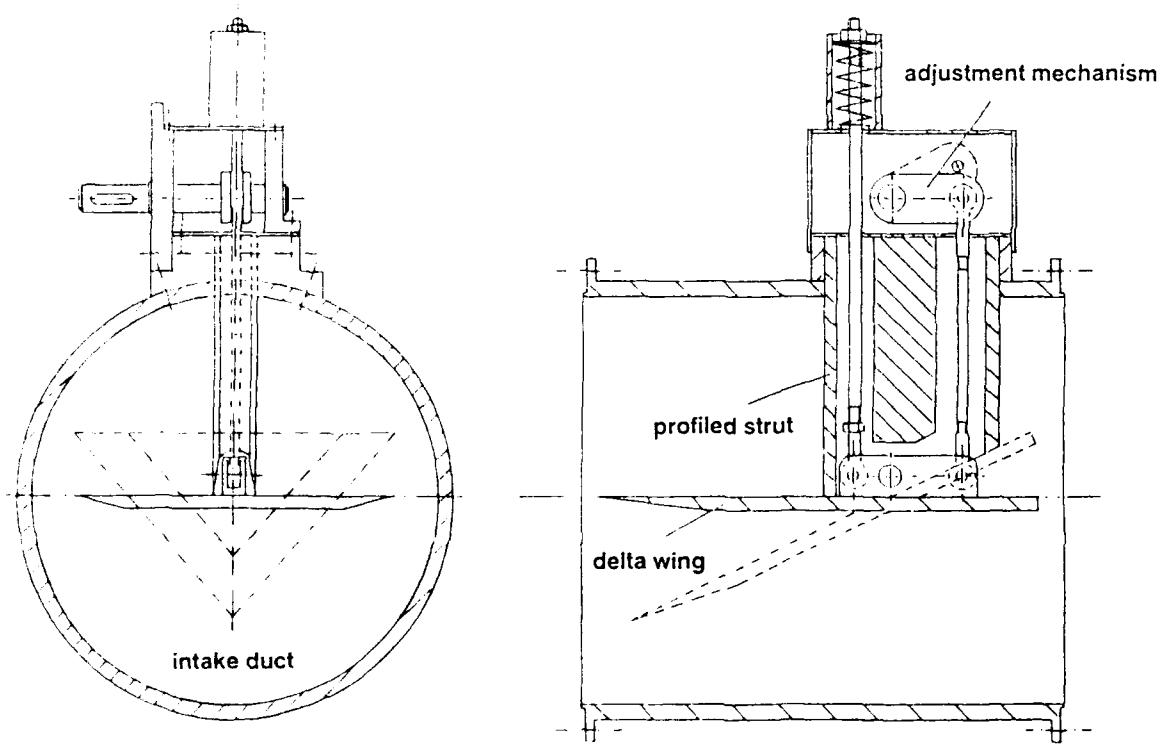

7. Movable swirl generator for full-scale investigations

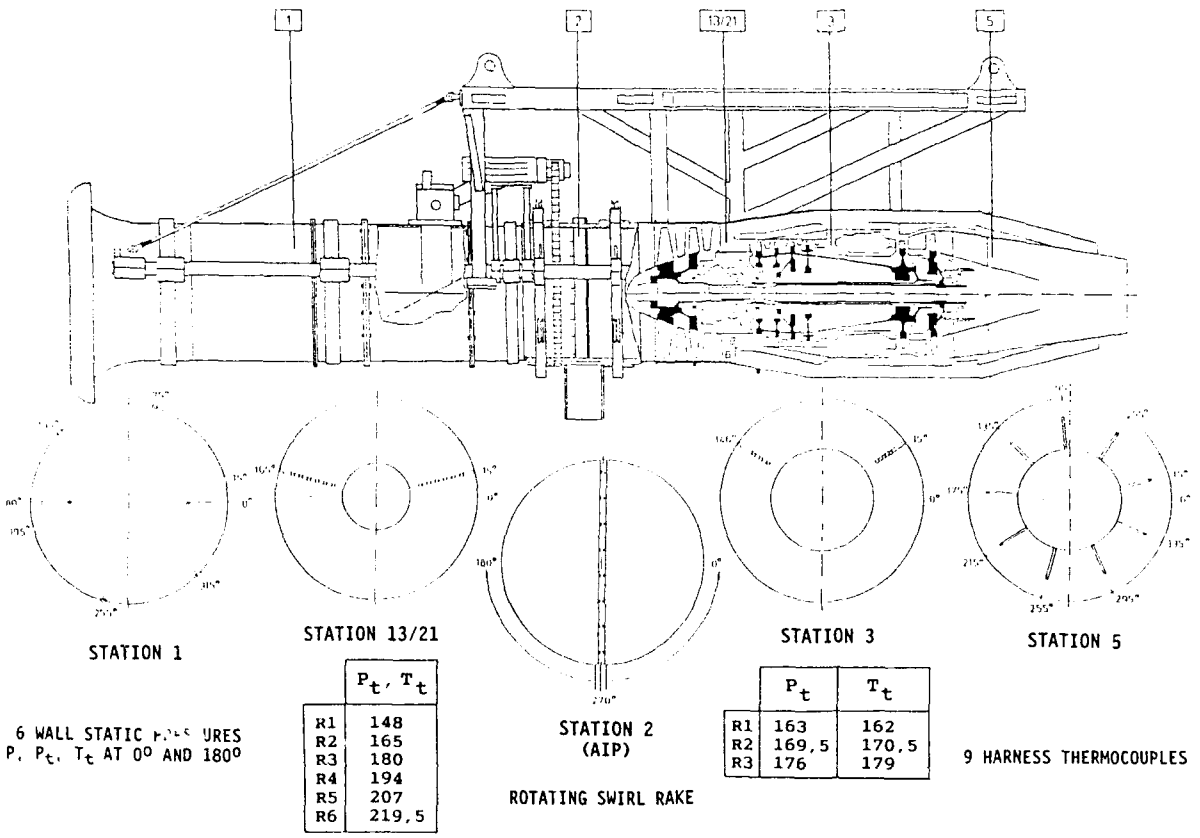

	P_t, T_t
R1	148
R2	165
R3	180
R4	194
R5	207
R6	219,5

	P_t	T_t
R1	163	162
R2	169,5	170,5
R3	176	179

8. Instrumentation of the Larzac 04 engine

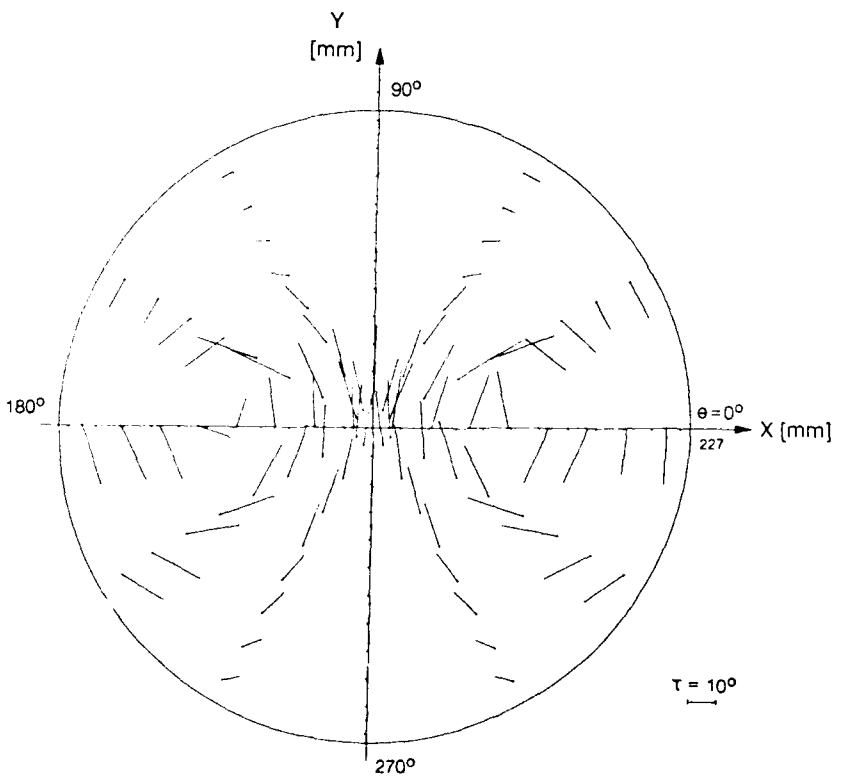

9. Cross flow pattern generated in the Larzac 04 intake
(α_0 = 23°; $n_{LPC}/\sqrt{T_{t2}}$ = 1060 (min $\sqrt{K}$)$^{-1}$)

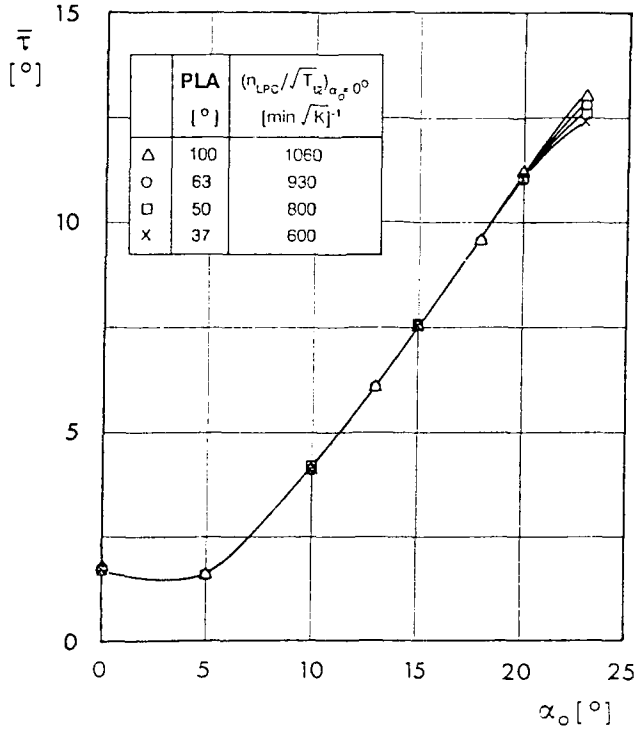

10. Mean swirl angle as a function of the angle of attack of the delta wing at different LP spool-speeds

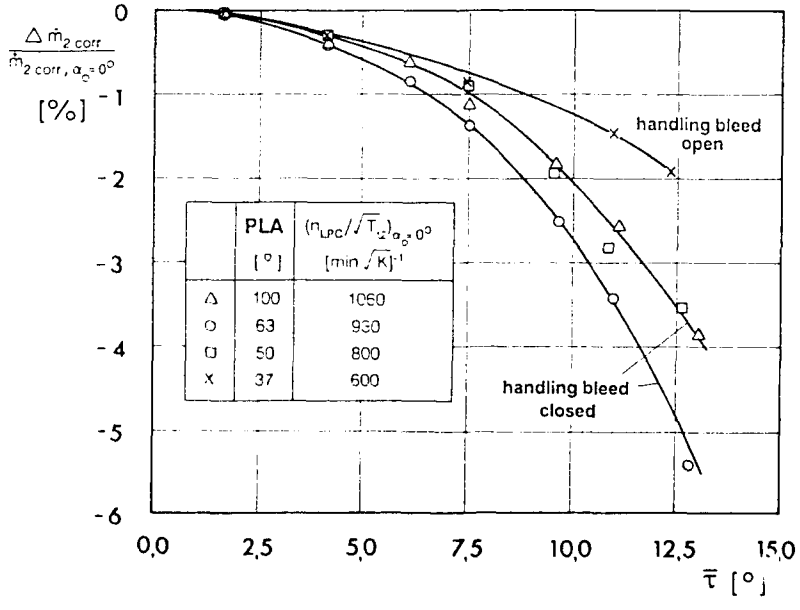

11. Reduction of corrected mass flow as a function of the mean swirl angle at different LP spool-speeds

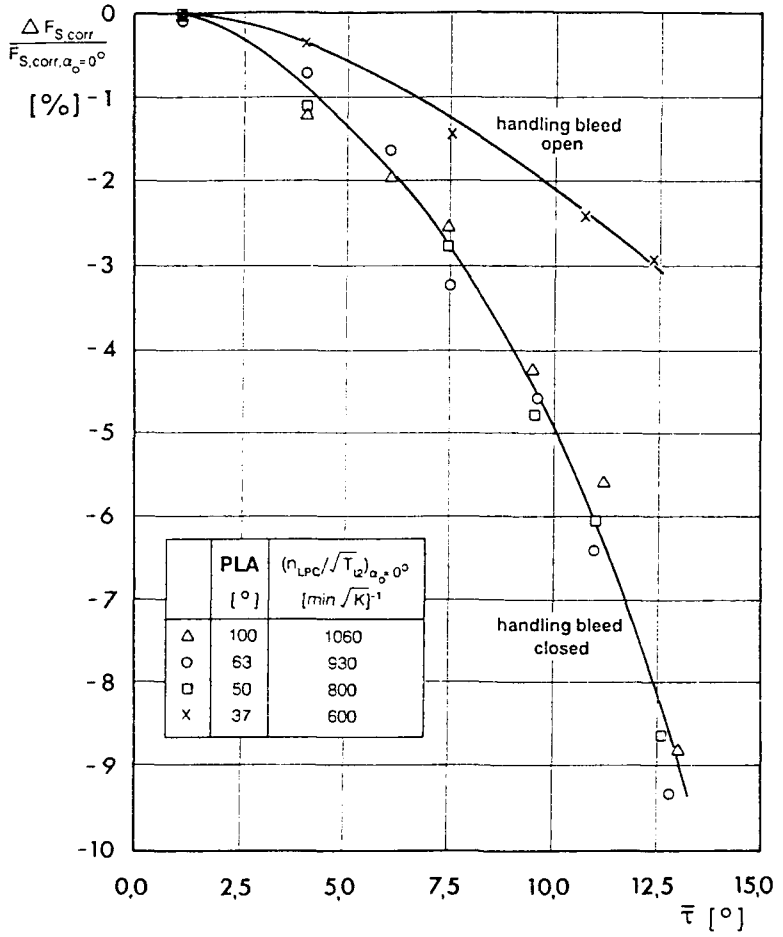

12. Reduction of thrust as a function of the mean swirl angle at different LP spool-speeds

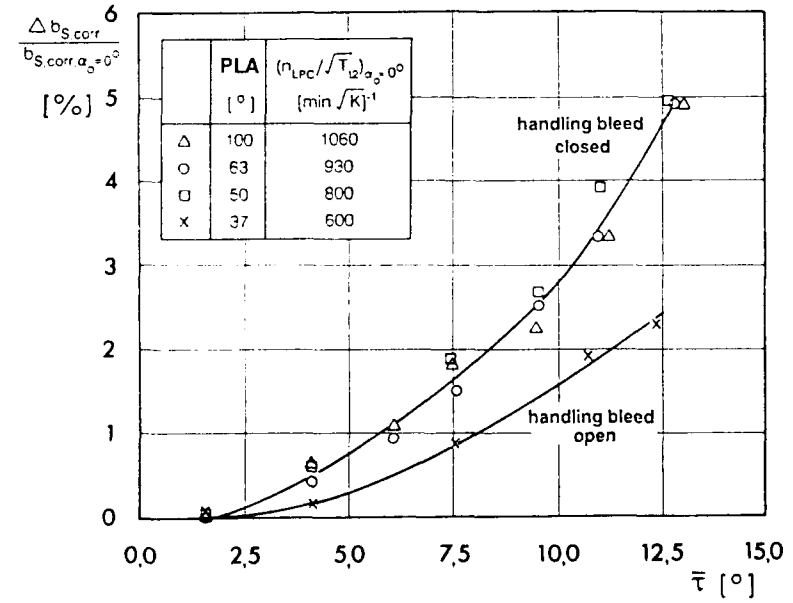

13. Increase of SFC as a function of the mean swirl angle at different LP spool-speeds

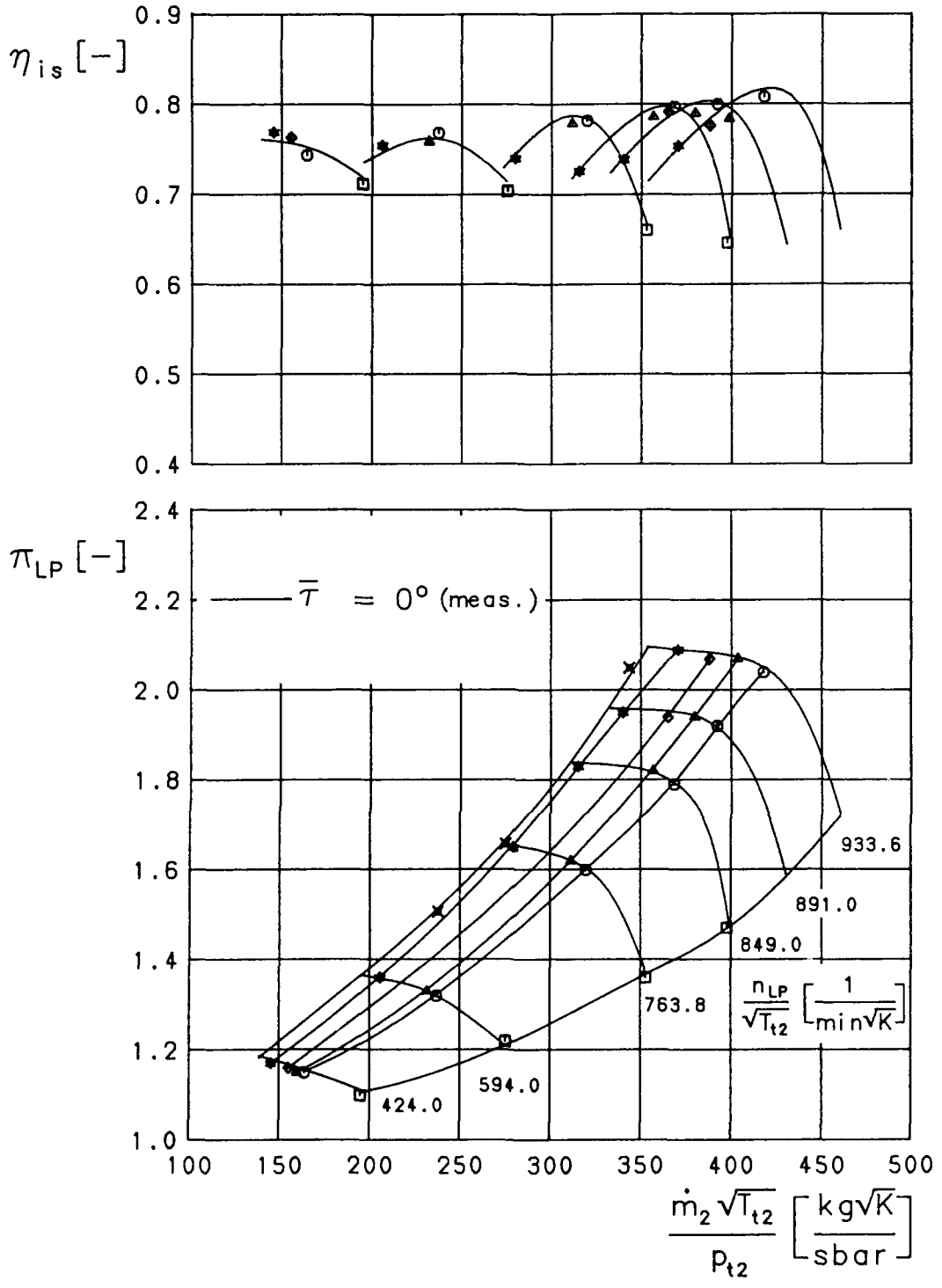

- without bypass nozzle
- with external air
- bleed valves open
- area decrease of the bypass nozzle (14%)
- area decrease of the bypass nozzle (28%)
- area decrease of the bypass nozzle and bleed valves open

14. Measured LPC characteristic with clean intake

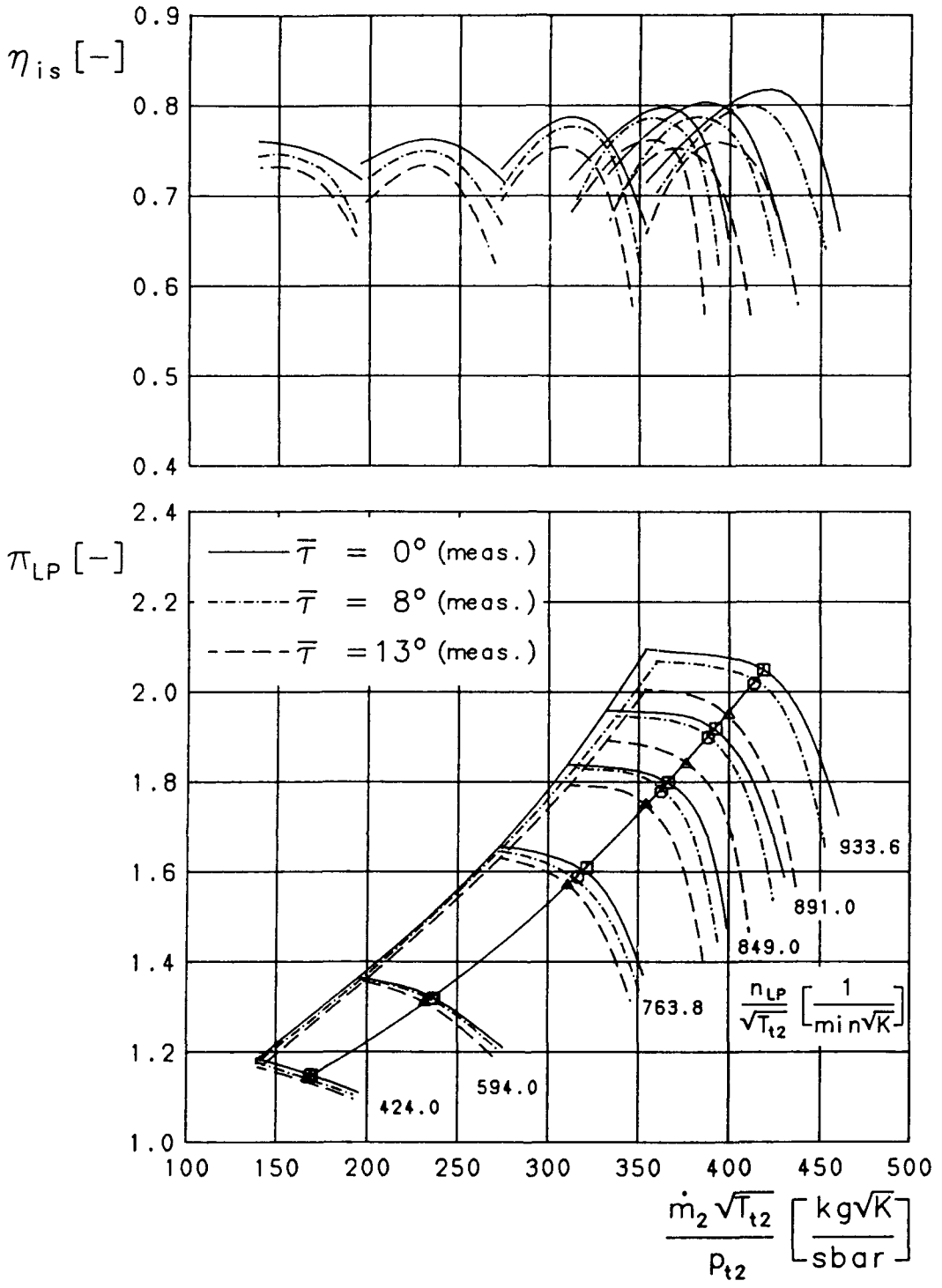

15. Measured LPC characteristic with intake swirl distortion

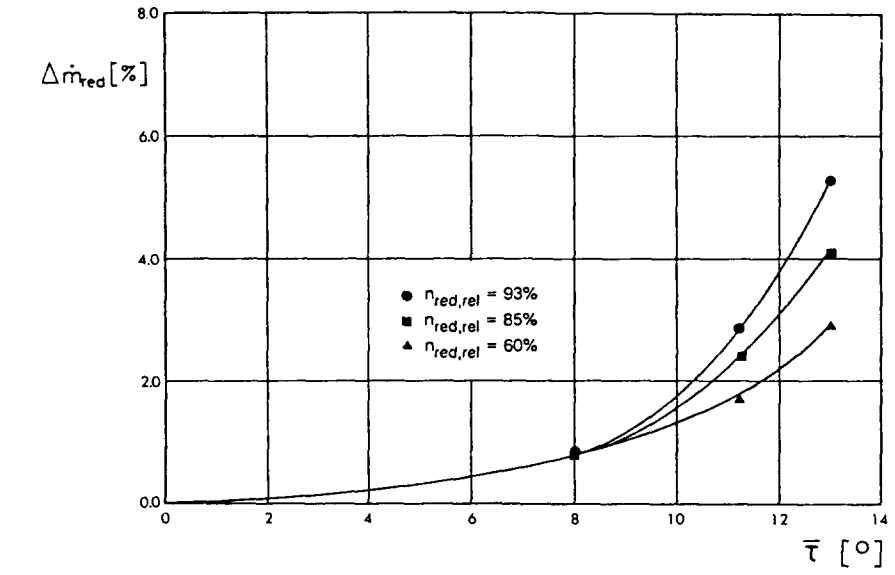

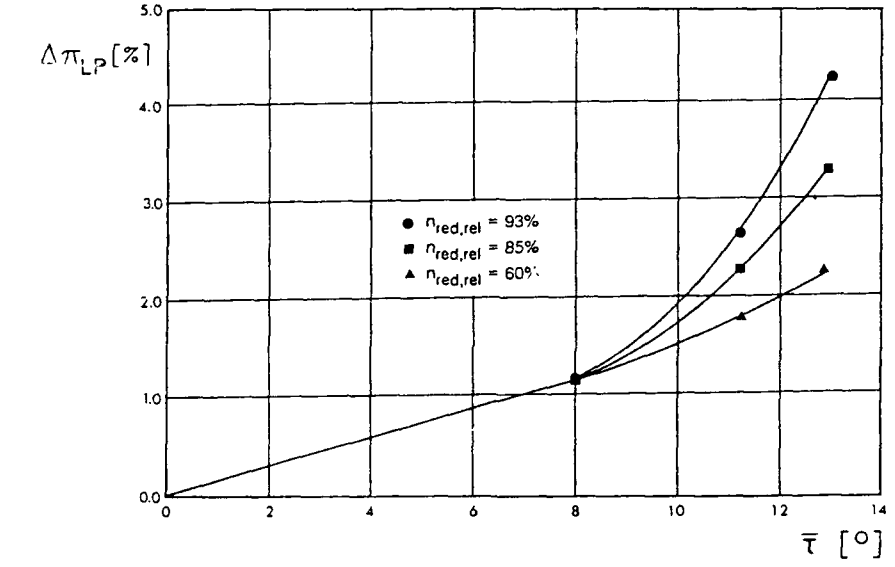

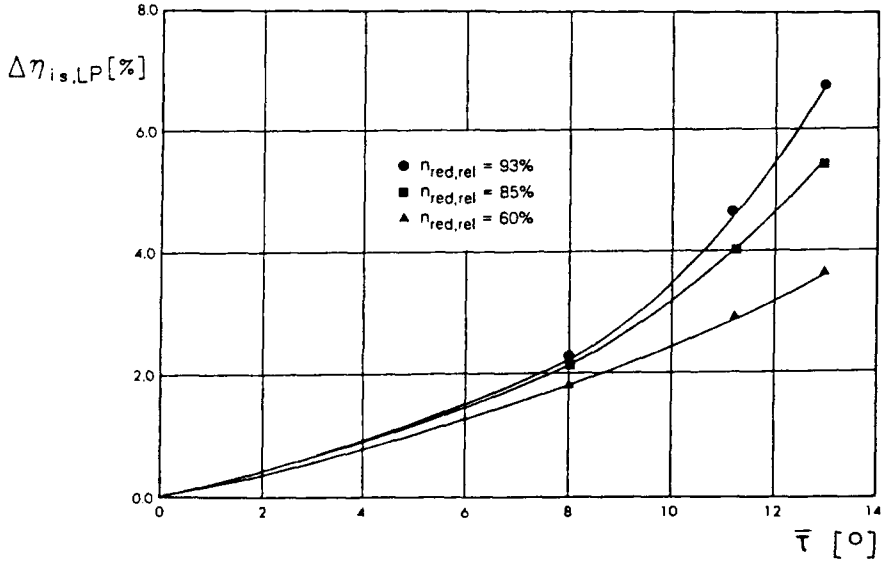

16. Reduction of LPC performance parameters due to intake swirl distortion

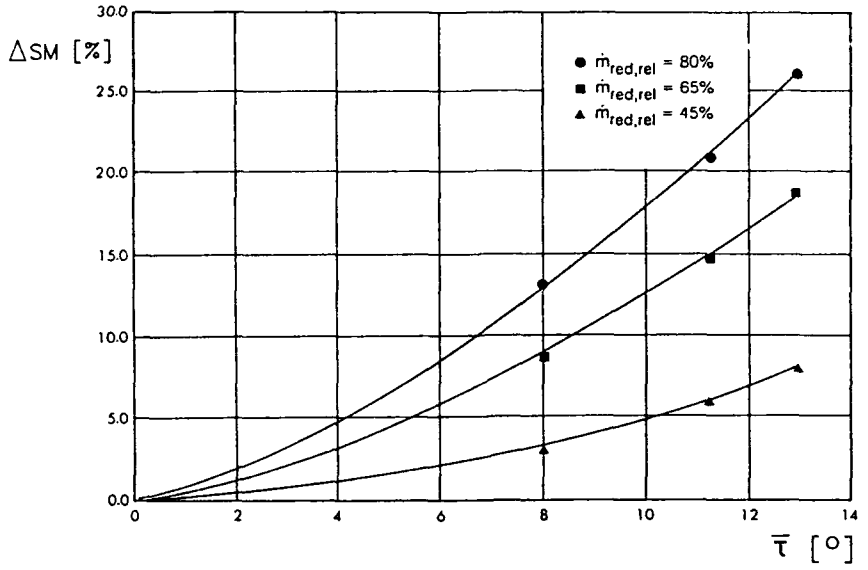

17. Reduction of LPC surge margin due to intake swirl distortion

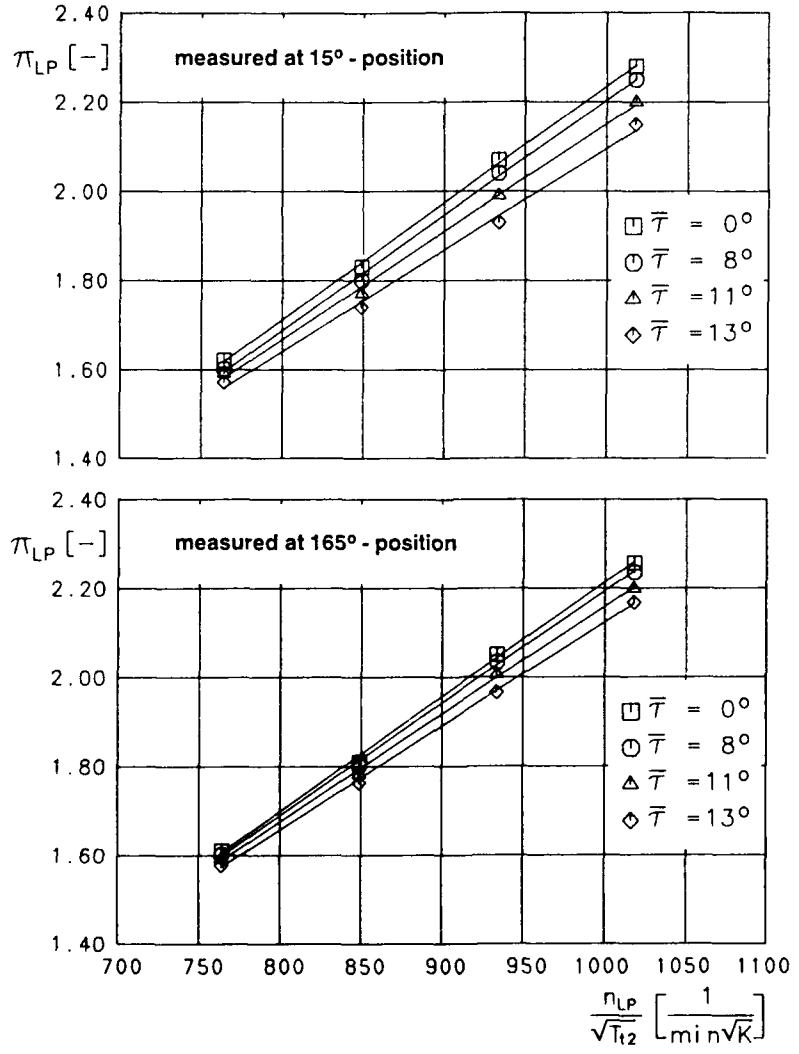

18. Pressure ratio measured at different circumferential LPC exit positions

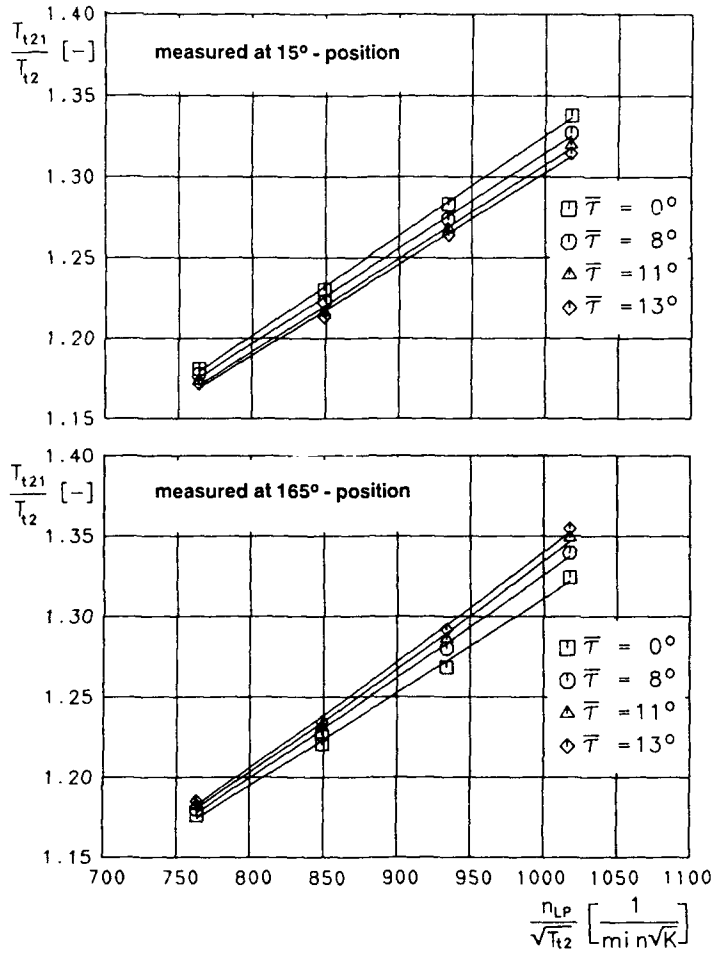

19. Total temperature ratio measured at different circumferential LPC exit positions

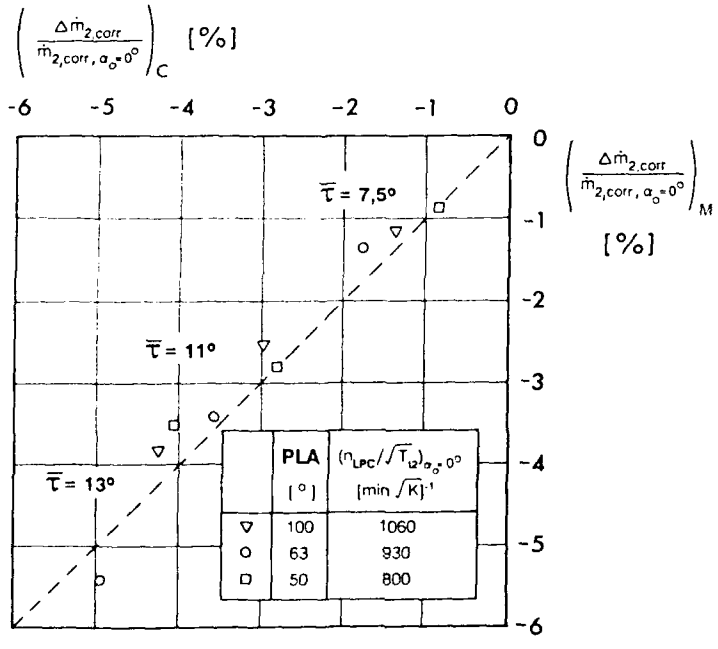

20. Comparison of calculated "C" and measured "M" total mass flow reduction

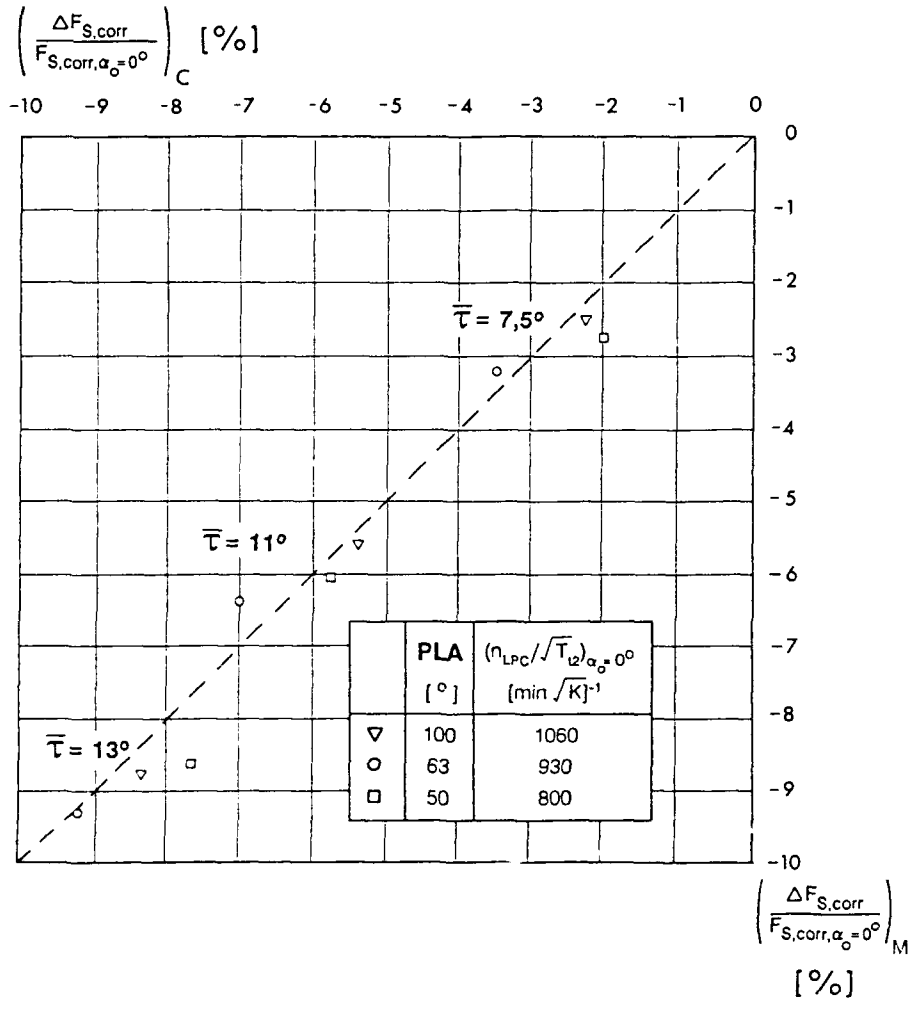

21. Comparison of calculated "C" and measured "M" thrust drop

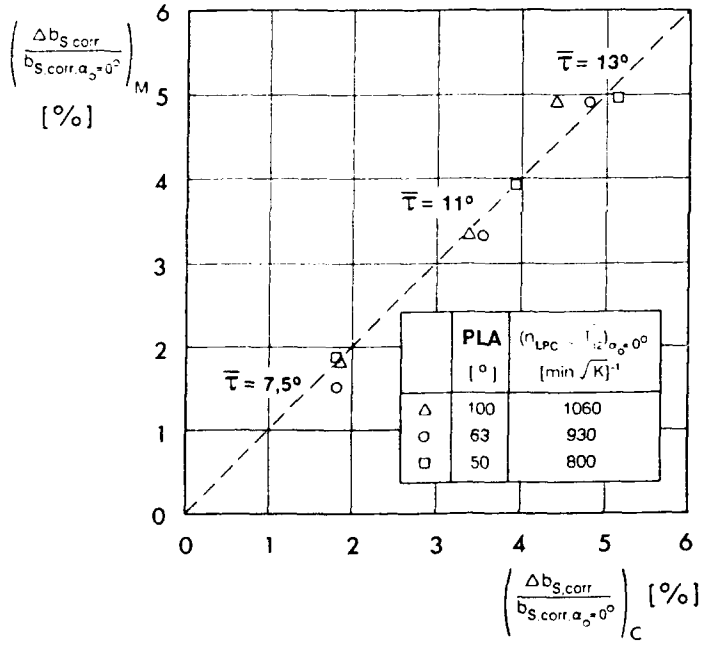

22. Comparison of calculated "C" and measured "M" SFC increase

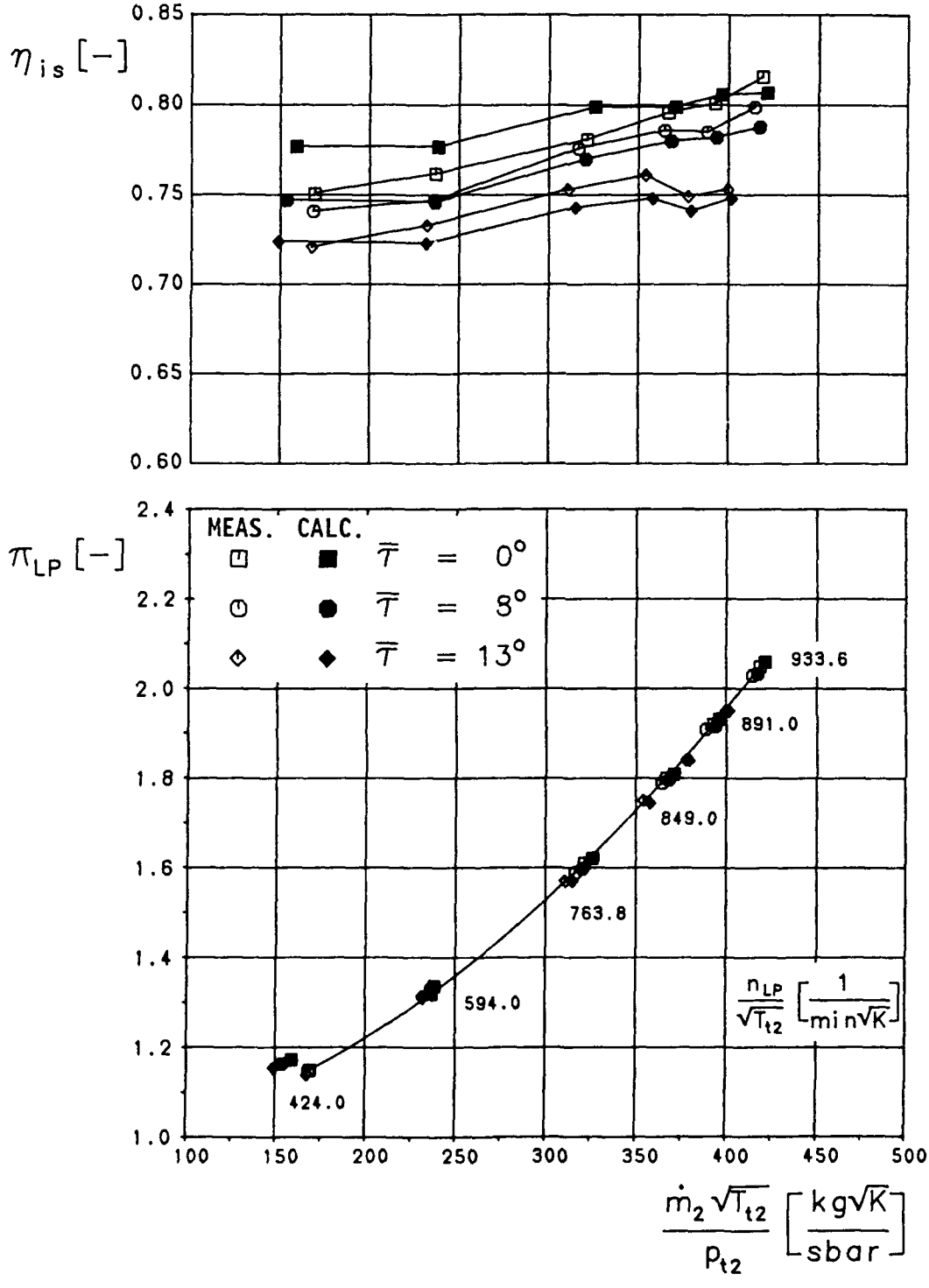

23. Measured and calculated operating line of the LPC due to intake swirl distortion

Analyse en Vol de la Compatibilité Entrée d'Air - Moteur

H. JOUBERT et J.L. EYRAUD
SNECMA Villaroche, 77550 Moissy-Cramayel, France

0 RESUME

La mise au point d'un ensemble avion de combat-moteur performant passe par une optimisation de la compatibilité entrée d'air-moteur. Cette optimisation nécessite des essais en vol spécifiques au cours desquels la perte de marge au pompage des compresseurs due à la distorsion est déterminée. La méthodologie générale d'analyse de la compatibilité entrée d'air-moteur est décrite depuis les premiers essais en soufflerie jusqu'aux essais en vol. Afin de déterminer la perte de marge au pompage due à la distorsion d'entrée d'air une instrumentation très complète a été installée sur l'avion Mirage 2000 (Dassault Aviation) équipé du moteur M53-P2 (SNECMA). La procédure d'essai ainsi que le traitement des signaux instationnaires sont décrits.

Les corrélations liant les coefficients de distorsion instationnaires à la perte de marge au pompage du compresseur Basse Pression sont présentées. Il est montré qu'une corrélation à un seul paramètre permet d'atteindre une précision de $\pm$ 2 %. En revanche l'utilisation d'une corrélation à deux paramètres (circonférentiel et radial) permet de réduire la précision à $\pm$ 1 %.

L'utilisation au banc moteur dans un caisson d'altitude de manches de simulation de distorsion instationnaire permet de reproduire de façon satisfaisante les phénomènes observés en vol et en particulier de mesurer des valeurs de sensibilité à la distorsion similaires aux valeurs obtenus en vol. Ce moyen permet donc d'améliorer l'optimisation du moteur tout en réduisant le nombre d'essais en vol.

1 INTRODUCTION

Les problèmes liés à la compatibilité entrée d'air-moteur jouent un rôle majeur dans la mise au point d'un ensemble avion-moteur performant.

De nombreuses études ont été consacrées à ce sujet tant d'un point de vue théorique qu'expérimental (Réf n°1). Cependant la plupart de ces études présentent des résultats obtenus au sol en soufflerie ou sur banc moteur. Peu de résultats obtenus en vol sont disponibles.

L'objectif de ce papier est de présenter les essais en vol conduits par la SNECMA et DASSAULT AVIATION sur l'avion Mirage 2000 équipé d'un moteur M53-P2.

Dans une première partie nous passerons en revue la méthodologie générale des études relatives à la compatibilité entrée d'air-moteur depuis les premiers essais en soufflerie jusqu'à la phase finale des essais en vol.

Nous décrirons ensuite les moyens et la méthodologie utilisée pour obtenir des pompages moteur à forte incidence. Les résultats des corrélations liant la perte de marge au pompage aux coefficients de distorsions seront présentés. Dans une dernière partie, les essais réalisés au sol dans un caisson d'altitude avec une simulation de la distorsion instationnaire seront comparés aux résultats acquis en vol.

2 METHODOLOGIE

Lors de la conception d'un nouveau moteur et d'un nouvel avion, il est indispensable d'analyser avec précision la marge au pompage des compresseurs pour les cas de vol les plus défavorables.

Sur un avion de combat adapté au vol supersonique, lors du point fixe ou de prises d'incidence rapide le contournement de l'écoulement autour des lèvres de l'entrée d'air provoque un décollement important de la couche limite.

Ces gros décollements sont convectés par la manche à air jusqu'au compresseur basse pression qui est alimenté par un écoulement présentant de fortes hétérogénéités de pression totale. La turbulence à grosses structures générée dans les décollements rend ces hétérogénéités de pression instationnaire assimilables à une sorte de bruit blanc sans fréquence dominante.

L'optimisation de l'ensemble moteur-cellule rend nécessaire une coopération très étroite entre l'avionneur et le motoriste de sorte que la prise en compte des distorsions d'alimentation soit réalisée dès le stade du projet.

Nous allons maintenant décrire les différentes phases d'études nécessaires pour parvenir à cet optimum.

ESSAIS AU SOL (fig n°1)

Phase 1 : Essais en soufflerie

Après qu'un projet de dessin d'entrée d'air ait été figé par l'avionneur, un premier essai est conduit en soufflerie afin de déterminer les niveaux de distorsions instationnaires alimentant le moteur pour les points les plus critiques du domaine de vol de l'avion.

La cartographie de pression totale dans le plan interface moteur-avion est mesurée à l'aide d'un peigne de 8 bras comportant 5 prises de pression, équipé de 40 capteurs à large bande passante (Kulites) (fig n°2).

Les signaux issus des capteurs rapides sont conditionnés, enregistrés et traités en temps réel avec la Chaîne d'Analyse et de Traitement Instationnaire (CATI) afin d'obtenir en temps réel les coefficients de distorsion instationnaire délivrés par l'entrée d'air.

Phase 2 : Conception des compresseurs

La connaissance de la cartographie de l'écoulement alimentant le moteur permet, dans cette seconde phase, de réaliser des estimations théoriques du comportement du moteur vis à vis des distorsions.

Ces calculs sont réalisés à l'aide de méthodes simplifiées telles que les compresseurs en parallèle (Ref n°1) ou de méthodes plus complexes telles que celles décrites dans la référence n°3.

Ces méthodes sont utilisées pour déterminer la perte de marge au pompage des compresseurs due à la distorsion ainsi que le comportement local de l'écoulement au niveau de chaque roue des compresseurs. Le projet de compresseur peut alors être optimisé en prenant en compte toutes les conditions de vol et en particulier les conditions d'alimentation rencontrées dans les phases de vol à grande incidence.

A l'issue de ces deux premières phases, un premier bilan de la compatibilité entrée d'air-moteur peut déjà être établi.

Phase 3 : Essais au banc

A l'issue des études théoriques et des essais en soufflerie, des manches de simulation caractéristiques de certains des cas de vol les plus critiques sont définies et fabriquées.

Afin de reproduire des phénomènes aérodynamiques similaires à ceux rencontrés sur l'entrée d'air d'un avion, un pavillon non axisymétrique équipé de becquets est installé à l'amont du moteur (fig n°3)(Réf n°5). Ce type de dispositif permet de reproduire assez fidèlement des conditions d'alimentation du compresseur proches de celles rencontrées en vol.

L'écoulement à l'amont du moteur est mesuré à l'aide d'une virole comportant 8 peignes à 5 prises de pression stationnaire et instationnaire (fig n°4).

De la même façon qu'en soufflerie les signaux issus des capteurs stationnaires et instationnaires sont conditionnés et analysés en temps réel à l'aide de la chaîne CATI (Réf n°4).

Dans un premier temps, les essais sont conduits au banc partiel compresseur de sorte qu'une importante instrumentation puisse être installée afin de mesurer finement l'écoulement au sein du compresseur. La mesure des pertes de marge au pompage permet d'établir des corrélations avec les coefficients de distorsion. Ces mesures sont comparées aux estimations théoriques effectuées dans la phase 2 et un raffinement du bilan de compatibilité entrée d'air-moteur peut alors être effectué.

En second lieu les manches de simulation sont installées devant un moteur au caisson d'altitude afin de s'approcher le plus fidèlement possible du fonctionnement du moteur installé dans l'avion. Ces essais, préliminaires aux essais en vol, permettent de reproduire au sol toutes les manoeuvres qui seront réalisées en vol telles que transitoire rapide et lent, allumage de la post-combustion.

Ils permettent de vérifier le bon comportement du moteur avant son premier avionnage et d'assurer la sécurité des premiers vols. De plus, au cours de ces essais, la marge au pompage résiduelle est également mesurée afin de vérifier sur le moteur complet les valeurs déterminées au banc partiel compresseur.

ESSAIS EN VOL (fig n°5)

Phase 1 : Caractérisation de la distorsion

L'objectif de ces essais est de mesurer en vol la distorsion alimentant le moteur. Le plan interface avion-moteur est équipé de la virole de mesures instationnaires utilisée pour les essais au sol au banc moteur (fig n°4).

Ces mesures permettent de calculer l'efficacité de l'entrée d'air ainsi que les coefficients de distorsion pour tous les points du domaine de vol. Ces valeurs peuvent alors être comparées aux résultats des essais en soufflerie. Elles sont également utilisées pour vérifier la bonne compatibilité de l'entrée d'air et du moteur.

Phase 2 : Mesure de la marge au pompage

La dernière phase de la mise au point de l'ensemble avion-moteur consiste à déterminer la perte de marge au pompage due aux distorsions. Le moteur est équipé de la même instrumentation que pour la phase n°1 mais le système de régulation du moteur est adapté afin de pouvoir modifier la ligne de fonctionnement des compresseurs pour pouvoir générer des pompages du moteur.

De la même façon qu'au cours des essais au sol au banc moteur, des corrélations perte de marge au pompage coefficients de distorsion sont établies.

Ce sont ces dernières corrélations qui sont utilisées pour ajuster l'optimisation de l'ensemble entrée d'air-moteur avant les essais en vol finaux préparatoires à la mise en service de l'avion.

Après cette brève description de l'ensemble des travaux à mener pour assurer la compatibilité entrée d'air-moteur, nous allons détailler la dernière phase des essais en vol. Nous comparerons les résultats obtenus en vol avec ceux issus du banc moteur au sol.

3 MATERIEL UTILISE

3.1 Essais en vol

Ces essais en vol ont été conduits sur un avion de combat Mirage 2000, conçu et fabriqué par DASSAULT AVIATION. Ce chasseur multirôle permet à la fois l'interception, l'attaque et la pénétration, il atteint une vitesse de Mach 2.2. Le moteur M53-P2 équipant cet avion a été conçu et est fabriqué par la SNECMA. Sa poussée au sol avec réchauffe est de 9500 daN, il est monocorps double flux. Le compresseur basse pression est composé de 3 étages sans roue directrice d'entrée.

Instrumentation

Pour réaliser les mesures de distorsion instationnaire, une virole de mesure a été conçue et fabriquée par la SNECMA (fig n°4). Celle-ci comporte 8 Peignes "sabre" à 5 prises de pression. Chaque prise est équipée d'un capteur stationnaire différentiel CZ1077 et d'un capteur instationnaire absolu ENDEVCO à large bande passante. Les capteurs stationnaires différentiels sont reliés à un capteur barométrique absolu SE40.

Cette technologie a été sélectionnée afin d'obtenir une précision satisfaisante malgré les fluctuations de température et les vibrations induites par l'environnement sévère d'un moteur avionné.

En outre, trois capteurs instationnaires de pression statique sont installés sur la paroi de la virole afin de détecter l'apparition du pompage moteur.

De plus, afin de mesurer le taux de compression du compresseur basse pression, des peignes de pression totale sont implantés dans le plan de sortie du compresseur.

Acquisition des mesures

Les mesures stationnaires sont amplifiées puis filtrées à l'aide d'un filtre passe-bas à 7 Hz. Les signaux sont ensuite numérisés à la cadence de 16 Hz puis sont transmis au sol via une télémesure (fig n°6). Les signaux issus des capteurs instationnaires sont filtrés à l'aide d'un filtre passe-haut à 0.25 Hz et d'un filtre passe-bas à 500 Hz. Ces mesures sont ensuite multiplexées et enregistrées sur un magnétophone analogique embarqué (fig n°7).

Traitement des signaux

Au sol, les signaux analogiques sont démultiplexés puis numérisés à la fréquence de 1250 Hz. Les pressions instationnaires sont filtrées numériquement à la fréquence de révolution du moteur. Les signaux instationnaires sont ajoutés aux signaux stationnaires afin d'obtenir un signal complet permettant le calcul de l'efficacité et des coefficients de distorsions instantanés.

3.2 Essais au caisson d'altitude

Instrumentation

Comme il a été décrit dans le chapitre précédent, une manche non axisymétrique générant des décollements est installée devant le moteur afin de reproduire un écoulement similaire à celui rencontré sur l'avion (fig n°3). La virole instationnaire utilisée lors des essais en vol est installée dans le plan interface manche-moteur afin de caractériser la distorsion instationnaire délivrée par la manche de simulation
(fig n°4).

Acquisition et traitement des mesures

Au sol les mesures stationnaires et instationnaires sont conditionnées, enregistrées et analysées en temps réel. Ceci est réalisé à l'aide d'une chaîne conçue et développée par la SNECMA.

Ce système est articulé sur deux pôles (fig n°8) :

- d'une part un système d'acquisition, de numérisation et de stockage sous forme d'un message numérique à haute densité du type P.C.M.

- d'autre part d'un calculateur vectoriel qui permet de traiter en temps réel les signaux instationnaires afin d'obtenir les coefficients de distorsion instantanés.

Cet équipement est implanté dans une remorque mobile indépendante de sorte qu'elle soit transportable sur tous les sites où les essais de distorsion sont réalisés (souffleries, bancs partiels, bancs moteurs...).

4 RESULTATS

4.1. Procédure

L'objectif des essais de pompage en vol est de provoquer un pompage du compresseur basse-pression pour des conditions de vol bien identifiées (altitude, Mach, incidence, dérapage, régime moteur). Pour atteindre cet objectif la manoeuvre suivante a été mise au point :

- **Avion à faible incidence**

Le moteur est réduit à faible régime. La section de tuyère du moteur est fermée à l'aide d'un système de régulation spécifique de sorte que le compresseur fonctionne à un taux de compression plus élevé. Le moteur est ensuite accéléré jusqu'au régime nominal, la vitesse de l'avion s'élève jusqu'à Mach 0.95.

- **Prise d'incidence**

Parvenu à Mach 0.95, le pilote met l'avion à cabrer, l'incidence augmente, le niveau de distorsion de pression totale dans la manche s'accroit et lorsqu'elle atteint la valeur correspondante à la limite de stabilité du compresseur le moteur se met à pomper.

- **Retour à faible incidence**

Le pilote met alors l'avion à piquer de sorte que l'incidence et la distorsion décroisse. Le régime moteur est réduit puis parvenu à faible incidence le pilote peut engager une nouvelle manoeuvre avec un nouveau réglage moteur (fig n°9).

4.2 Analyse

A l'issue du vol, des bandes magnétiques contenant les informations stationnaires et instationnaires sont crées pour être traitées en temps différé au sol.
Le traitement est effectué de la façon suivante :

- o Les coefficients de distorsion instantanées et les pressions statiques de paroi sont calculées pour chaque instant de discrétisation (1250 Hz) puis sont tracés en fonction du temps.
- o L'apparition du pompage du compresseur est repérée sur le tracé des pressions statiques en fonction du temps.
- o La troisième étape consiste à identifier le plus fort niveau de distorsion précédant le pompage et qui l'a provoqué. La cartographie de pression totale ainsi que les différents coefficients de distorsionsont alors calculés pour cet événement.
- o La quatrième étape de l'analyse consiste à déterminer le taux de compression et le débit du compresseur au moment du pompage afin de déterminer la perte de marge au pompage due à la distorsion. Celle-ci est définie de la façon suivante :

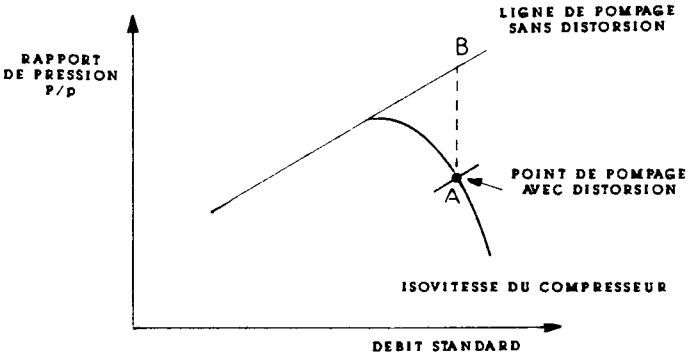

$$PRS = \frac{(P/P)_B - (P/P)_A}{(P/P)_B}$$

où $(P/P)_A$ est le rapport de pression de pompage avec distorsion.

$(P/P)_B$ est le rapport de pression de pompage sans distorsion pour le même débit. Cette valeur est issue des essais au sol avec une alimentation homogène.

- o La dernière phase de ce travail consiste, à l'aide de l'ensemble des informations recueillies pour tous les pompages, à rechercher des corrélations entre la perte de marge au pompage et les coefficients de distorsion.

Caractérisation de la distorsion

Afin de caractériser la cartographie de pression totale alimentant le moteur, un certain nombre de critères ont été proposés et sont utilisés par les motoristes et les avionneurs (Ref n°7).

Pour ces essais la SNECMA a utilisé plusieurs types de coefficient de distorsion, les meilleurs résultats ont été acquis avec les coefficients (KΘ - KRA2). Par conséquent seuls ces résultats seront présentés.

A partir d'une instrumentation comportant 5 couronnes de 8 prises réparties tous les 45° les coefficients KΘ et KRA2 se définissent de la façon suivante :

$$K\Theta = \frac{\sum_{j=1}^{5} K\Theta j \times \frac{1}{Rj}}{Q \sum_{j=1}^{5} \frac{1}{Rj}}$$

où
Rj est le rayon de la couronne

$$K\Theta j = \max_{n=1}^{4} \frac{(Ajn)}{n^2}$$

$$Ajn = \sqrt{(aj^2_n + bj^2_n)}$$

$$aj_n = \frac{1}{8} \sum_{i=1}^{8} Pij \cos(in\Delta\Theta)$$

$$bj_n = \frac{1}{8} \sum_{i=1}^{8} Pij \sin(in\Delta\Theta)$$

Q pression dynamique stationnaire dans le plan de mesure.

$$KRA2 = \frac{\sum_{J=1}^{5} (\bar{P} - \bar{Pj}) \frac{1}{Rj}}{2 \sum_{J=1}^{5} \frac{1}{Rj}}$$

où $\bar{P}$ est la pression moyenne de la carte

$\bar{Pj}$ est la pression moyenne sur la couronne j.

Le coefficient KΘ est basé sur un développement en série de Fourier de la pression totale de chaque couronne, il attribue un poids inversement proportionnel au rang de l'harmonique. De plus la distorsion circonférentielle est pondérée par l'inverse du rayon de sorte que les distorsions situées au moyeu du compresseur aient plus d'importance que les distorsions situées en tête.

Le coefficient KRA2 est un indicateur de la distorsion radiale. De la même façon que pour le coefficient KΘ la distorsion radiale de chaque couronne est pondérée par l'inverse du rayon.

Ces deux coefficients sont adimensionnés par la pression dynamique stationnaire dans le plan de mesure de sorte que ces coefficients soient peu sensibles aux variations de débit moteur.

Corrélations pompage - Distorsion

Au cours de cette campagne d'essai en vol réalisée sur le Mirage 2000/M53-P2, une dizaine de pompage du compresseur basse pression ont été exploités au régime nominal.

La première exploitation a été réalisée en considérant le seul coefficient KΘ. La précision obtenue est de ± 2 % sur la valeur absolue de la perte de marge au pompage (fig n°11).

Afin d'améliorer la précision de la prédiction une corrélation faisant intervenir à la fois la distorsion circonférentielle et la distorsion radiale à été recherchée. Celle ci se présente sous la forme d'une fonction bilinéaire de KΘ et de KRA2.

$$\Delta PRS = K_c \times K\Theta + K_r \times KRA2$$

La perte de marge au pompage calculée avec cette corrélation en utilisant les coefficients de distorsion initiateurs du pompage est représentée en fonction de la perte de marge effectivement mesurée (fig n°12).
Avec ce type de corrélation la précision est améliorée et atteint ± 1% en valeur absolue.

Comparaison avec les essais au sol

Afin de valider la méthodologie générale d'essais décrite au chapitre 2, la SNECMA a conçu et fabriqué une manche de simulation représentative de la distorsion délivrée par le Mirage 2000. La cartographie de pression totale fournie par la manche de simulation est comparée à une carte typique relevée dans l'entrée d'air du Mirage 2000. L'allure générale de l'écoulement est bien représentée avec deux zones à haute pression situées dans le haut de la manche et une zone à basse pression placée dans la partie inférieure. Les coefficients KΘ délivrés par ces deux manches sont également en bon accord puisque l'on mesure une valeur de 0.35 au sol pour un objectif mesuré en vol de 0.34 (fig n°13).

Cette manche a été installée dans un caisson d'altitude du Centre d'Essais des Propulseurs (Saclay, France) devant un moteur M53-P2. Des pompages du compresseur basse pression ont été provoqués au régime nominal par une fermeture de la tuyère. Ces essais ont été été analysés selon une procédure analogue à celle utilisée en vol.

La comparaison des résultats au sol avec les essais en vol a été faite d'une part avec la corrélation en KΘ uniquement et d'autre part en utilisant la corrélation à deux paramètres déterminée en vol. Les points obtenues au sol sont en bon accord avec les corrélations issues des essais en vol ce qui confirme la validité de la méthodologie utilisée.

5 CONCLUSIONS

La mise au point d'un ensemble avion de combat-moteur optimisé nécessite la réalisation de nombreuses études tant théoriques qu'expérimentales au sol ou en vol.
La dernière phase de cette optimisation est constituée par la réalisation d'essais en vol. Ceci a été conduit sur un Mirage 2000 équipé d'un M53-P2. Le plan interface entrée d'air-moteur a été équipé d'une virole de mesures instationnaires.
Les différents pompages provoqués du moteur ont été analysés à l'aide de cette instrumentation et ont permis de définir une corrélation perte de marge au pompage coefficients de distorsion précise à ± 1 %.

Les simulations de distorsion conduites au caisson d'altitude au sol ont permis de déterminer des sensibilités à la distorsion similaires au sol et en vol.

Ces résultats confirment la confiance que l'on peut apporter aux simulations réalisées au sol afin d'optimiser le moteur avant les vols de sorte que la durée des essais en vol puisse être réduite.

REFERENCES

1 AGARD Conference Proceding n° 400
"Engine Response to Distorted Inflow Conditions"
MUNICH (Germany) September 1986.

2 MAZZAWY, R.S. and G.A. BANKS
"Circumferential Distortion modeling of the TF30-P-3 Compression System"
NASA CR 135124 January 1977

3 JOUBERT H.
"Flowfield Calculation in Compressor Operating with Distorted Inlet Flow"
ASME Brussels (Belgium)
June 1990

4 EYRAUD J.L. and AUZOLLE F.
"Unsteady pressure data acquisition and processing in air inlet flow distortion surveys"
Royal Aeronautical Society Forum
Bath (U.K.) April 1989

5 B. DELAHAYE, G. LARUELLE
"Dispositif de simulation au banc compresseur d'une prise d'air à grande incidence"
AGARD / FDP n°14 May 1981

6 M. BOURASSEAU - M. RAPUC
Etude expérimentale d'une entrée d'air d'avion militaire en soufflerie. Comparaison avec le vol.

7 Inlet Total-pressure distortion considerations for gas-turbine Engines
AIR n° 1419 SAE May 1983

REMERCIEMENTS

Ces études ont été conduites à la Direction Technique de la SNECMA. Les auteurs remercient toutes les personnes ayant été associées à ce programme aussi bien à la SNECMA que chez Dassault Aviation qu'à la Délégation Générale pour l'Armement.
Ils remercient également la Direction de la SNECMA d'avoir autorisé cette publication.

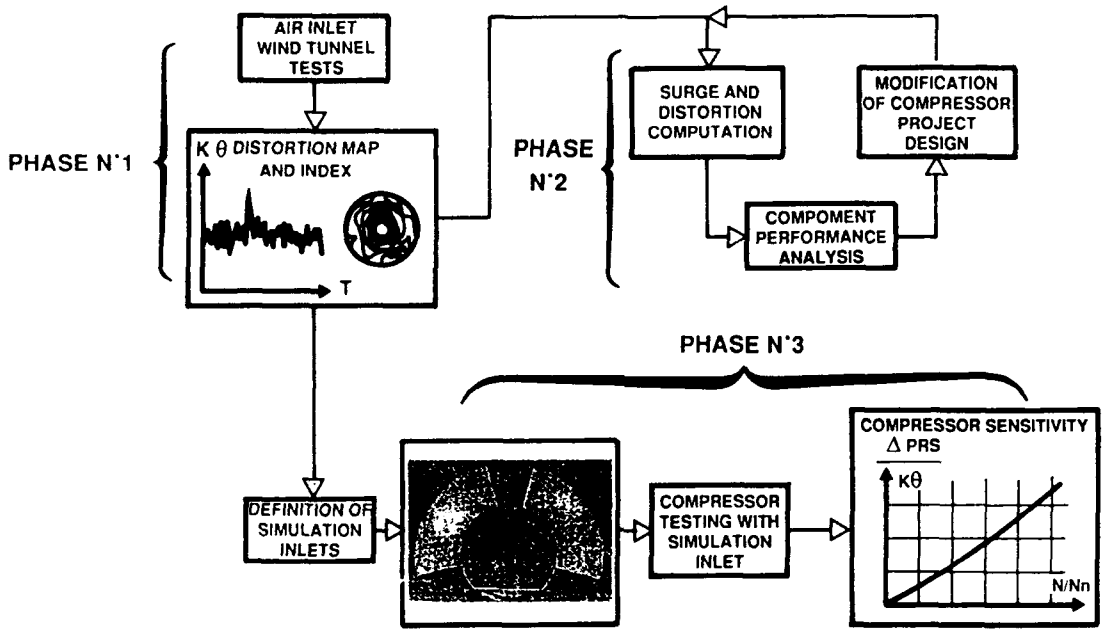

Figure 1 : Méthodologie - Essais au sol

Figure 2 : Essais en soufflerie - Peignes instationnaires

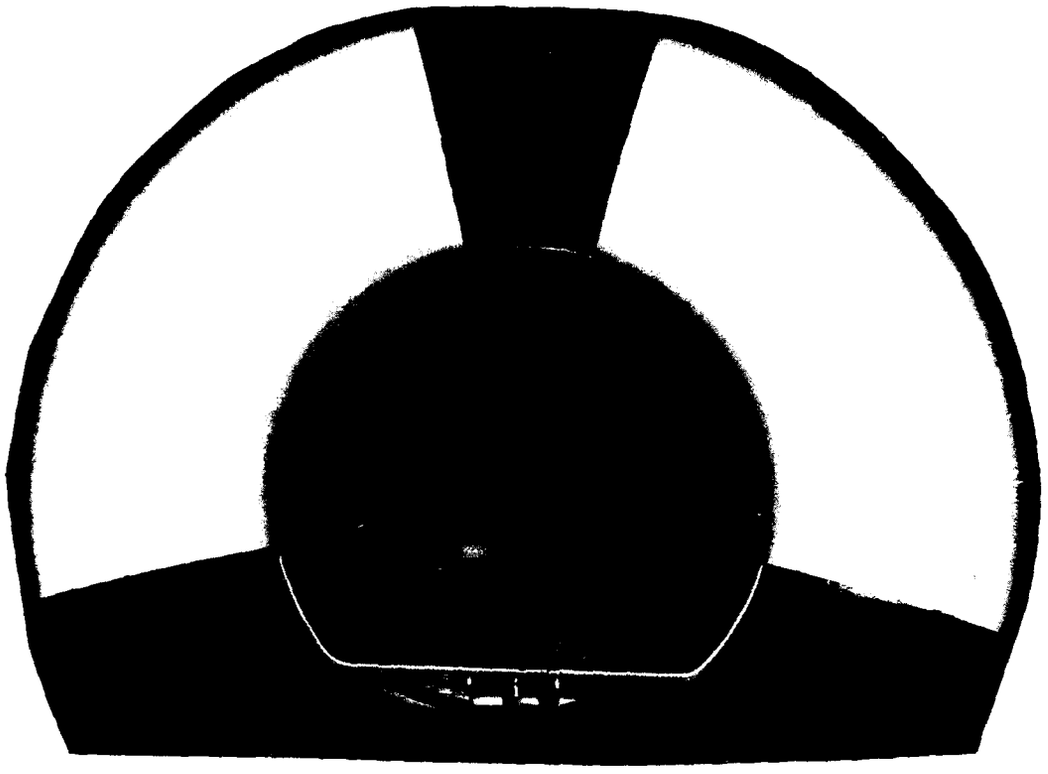

Figure 3 : Essais au sol - Manche de distorsion

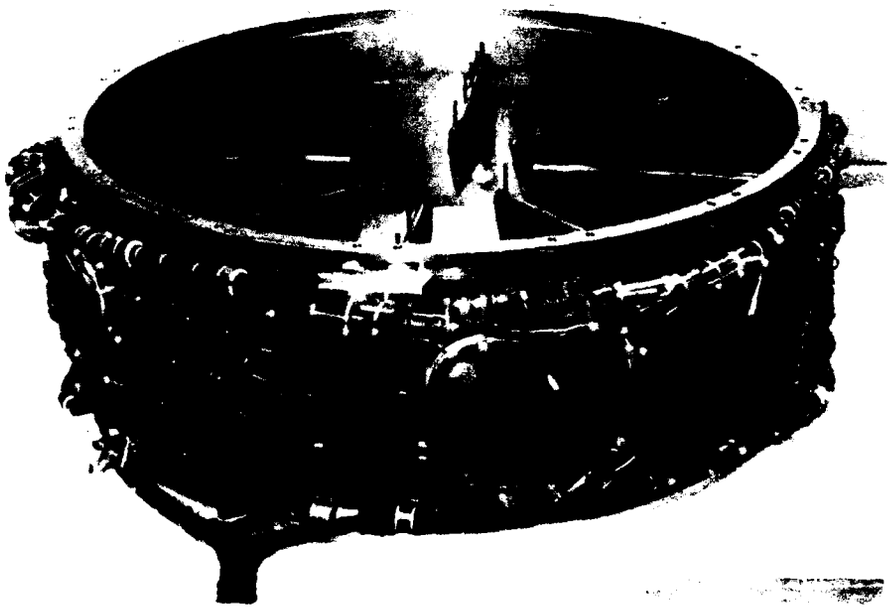

Figure 4 : Virole de mesure instationnaie

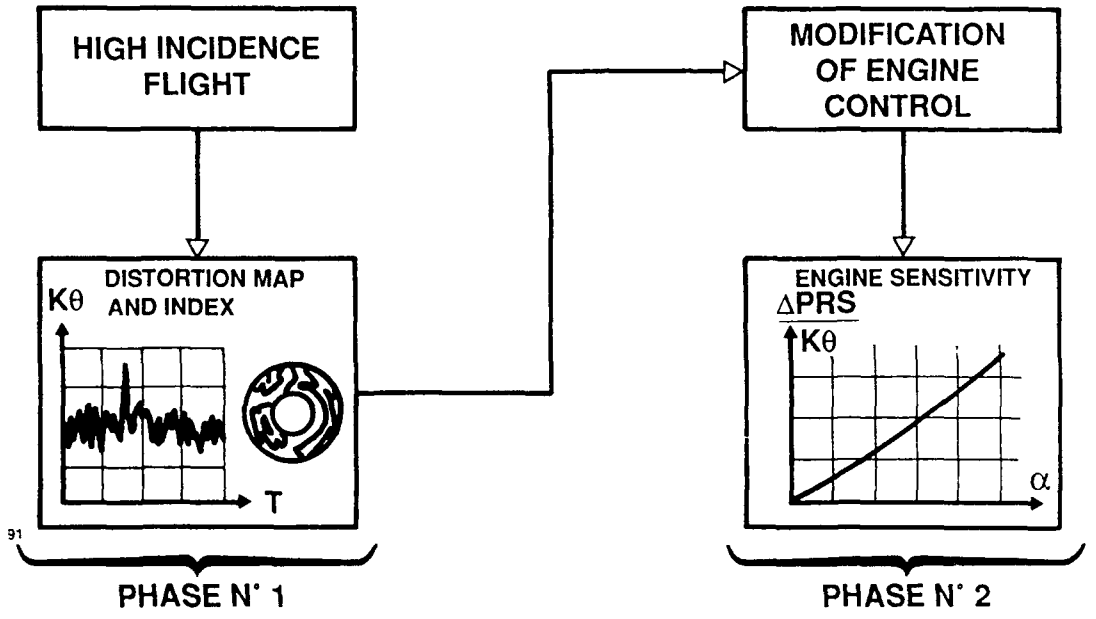

Figure 5 : Essais en vol - Méthodologie

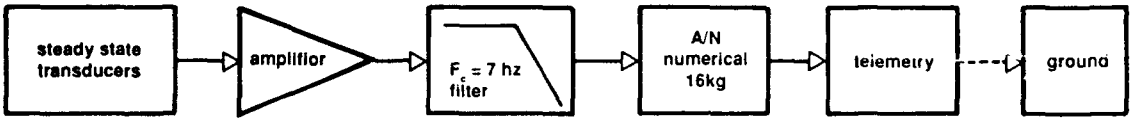

Figure 6 : Essais en vol - Schéma de la chaîne stationnaire

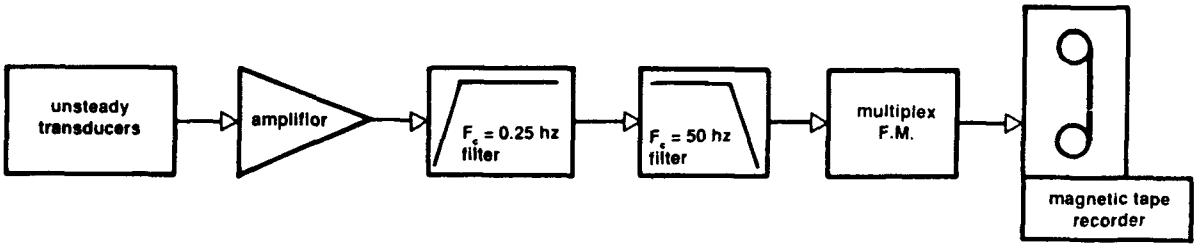

Figure 7 : Essais en vol - Schéma de la chaîne instationnaire

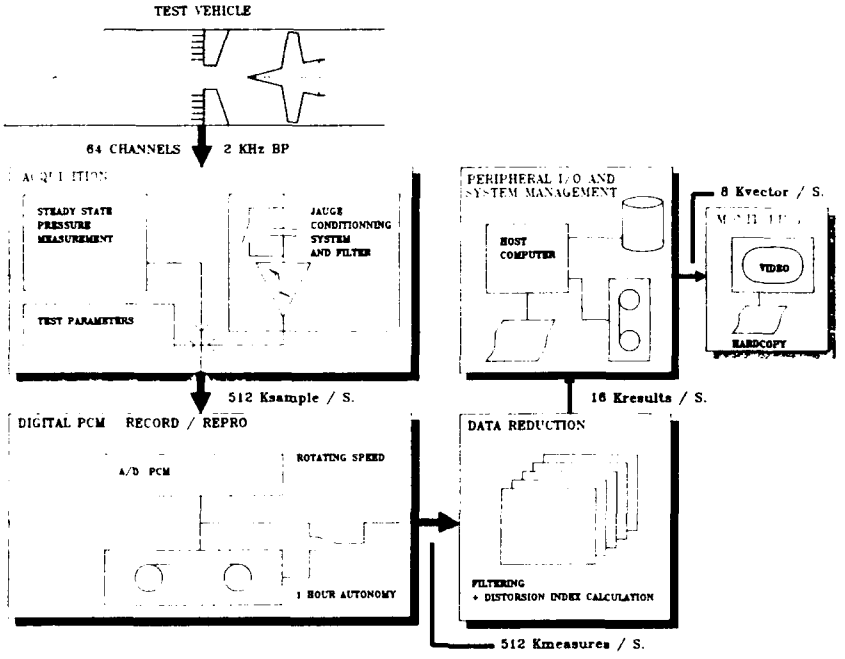

Figure 8 : Schéma de la chaîne CATI

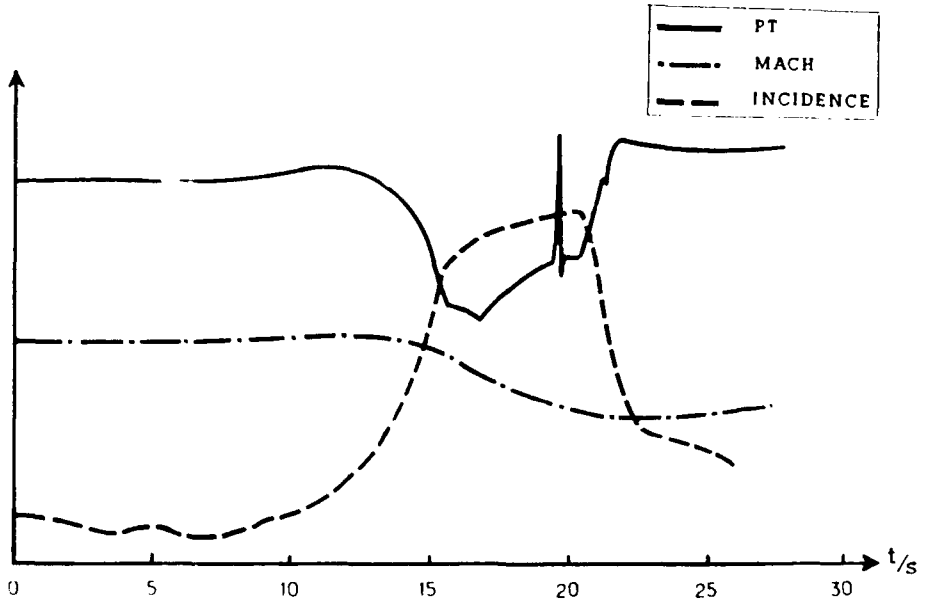

Figure 9 : Essais de pompage en vol

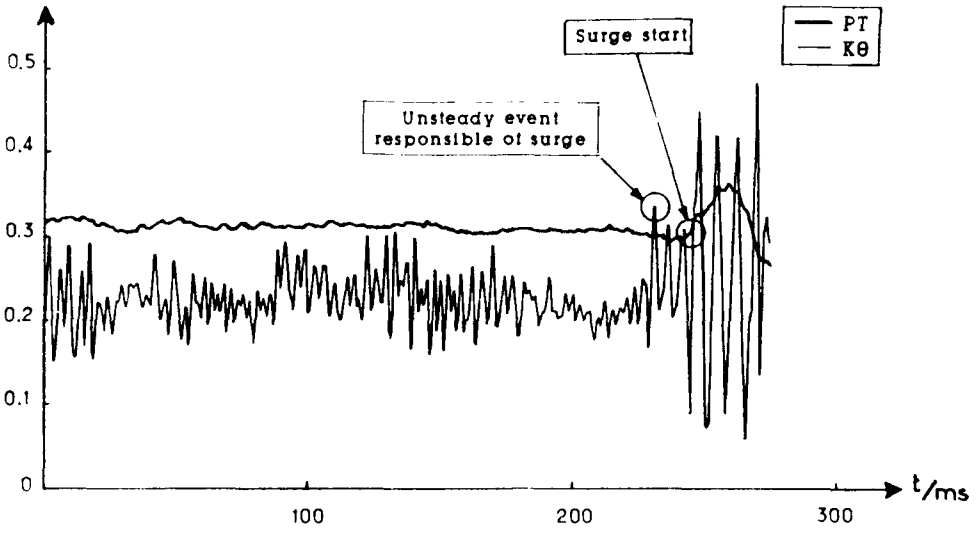

Figure 10 : Historique d'un pompage compresseur

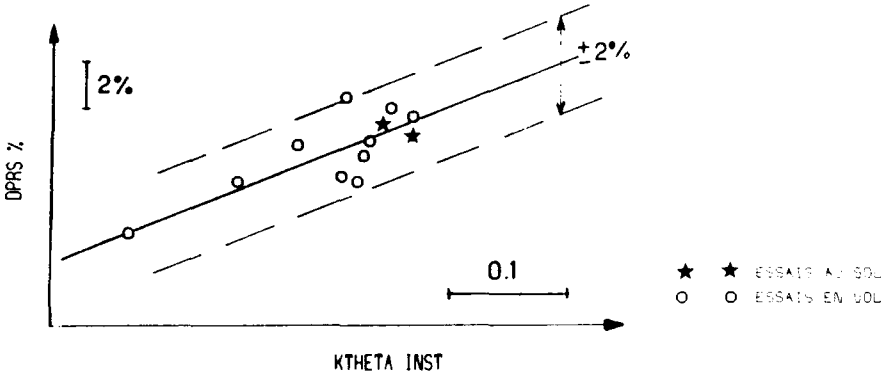

Figure 11 : Essais en vol - Corrélation ΔPRS/KΘ

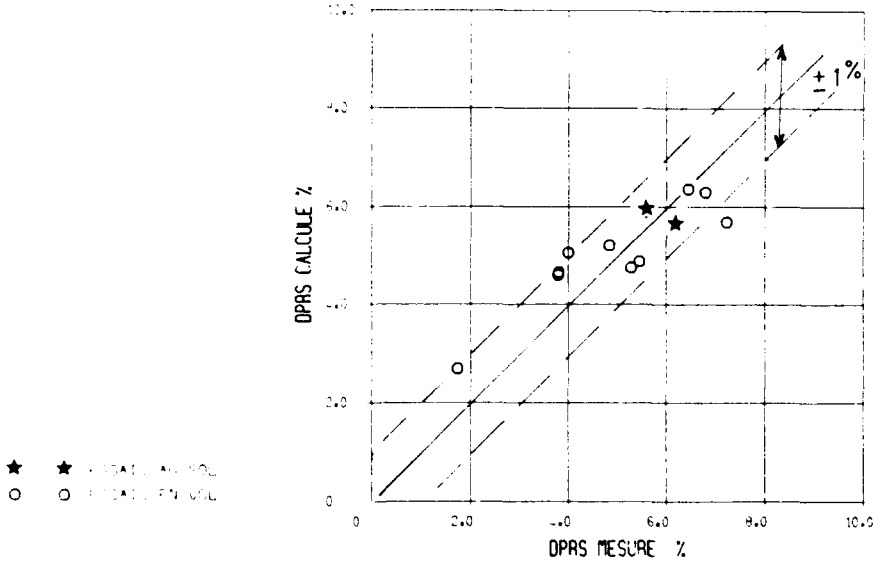

Figure 12 : Essais en vol - Corrélation ΔPRS/(KΘ-KRA2)

Mirage 2000

Carte instantanée (KΘ max)

KΘ = 0.34

Manche de simulation

Carte instantanée (KΘ max)

KΘ = 0.35

Figure 13 : Comparaison des cartes de distorsion au sol et en vol

ASTOVL MODEL ENGINE SIMULATORS FOR WIND TUNNEL RESEARCH

A E Harris
Aircraft Research Association Ltd
Manton Lane, Bedford, England
G L Wilde, V J Smith
TKD Ltd
A R G Mundell
DRA (Aerospace Division) Farnborough
D P Davidson
Rotadata Ltd

SUMMARY

Feasibility studies have been conducted into the use of military turbine powered simulators (MTPS) for wind tunnel research on typical Harrier/AV8B and ASTOVL aircraft.

The MTPS approach has shown significant promise for full simulation of inlet airflow ratio and nozzle thrust representations. The studies were made in two parts. In the first instance simulation of the basic Pegasus of the Harrier/AV8B was examined. A simulator at 1 to 7.5 model scale using compressed air drive has been shown to be feasible. The design develops 467 SHP and is well adapted for use in available high-speed and low-speed wind tunnels. In the low-speed facility a strut mounted arrangement coupled to the existing external force balance presents only minor difficulties; for the high-speed tunnel further work is required to develop/refine an internal balance/sting arrangement. Overboard bleed is used in an optimised manner to match cycle requirements to the need for minimum compressed air feed and bleed cross sectional area.

In subsequent studies cycles and layouts appropriate to the evolving ASTOVL powerplants have been examined. It is shown that MTPS designs can be developed to match a representative ASTOVL layout although compromises may be required to the support strut design to suit airfeed and bleed requirements.

This paper concludes with a recommendation for a staged evolution of ASTOVL model simulations which is geared to a realistic ASTOVL project timescale in a cost effective manner.

LIST OF SYMBOLS AND ABBREVIATIONS

ASTOVL	Advanced Short Take-Off, Vertical Landing
A_N	A_{NOZZLE} (sq ft)
BPS	Blown powerplant simulator
C_L, C_m	Lift, pitching moment coefficients
δC_L,δC_D,δC_m	Incremental lift, drag, pitching moment
CMAPS	Compact Multi-Mission Aircraft Powered Simulator
CTOL	Conventional Take-Off and Landing
D,ϕ	Diameter (in)
EPS	Ejector Powered Simulator
HGR	Hot Gas Reingestion
LP,HP	Low pressure, high pressure
M	Mach number
MFR	Mass Flow Ratio (intake capture ratio)
MTPS	Military Turbine Powered Simulator
MoU	Memorandum of Understanding
NCR	Duct to Nozzle Exit Contraction Ratio
NPR	Nozzle Pressure Ratio
P	Pressure (psia, bar)
PTP/PTO	Ratio of ejector drive pressure to upstream total pressure
RALS	Remote Augmented Lift System
S&C	Stability and Control
SHP	Shaft Horse Power
T	Temperature (°K)
W,W_I	Airflow, inlet airflow (lb/sec)
X/D	Ratio of inlet/nozzle spacing to fan/compressor diameter

1 INTRODUCTION

The current approach to ASTOVL wind tunnel model representations needs to be set against that arising for conventional take-off and landing (CTOL) combat aircraft.

The established approach to wind tunnel research for CTOL is to test a suite of models consisting of:

a) Complete forces and pressures model of the aircraft, with free flow through the air intake ducts and the best possible representation of the geometry of the intake and afterbody allowing for the presence of the support sting;

b) Specialised intake models to study the effects of changes in intake mass flow and intake geometry on the intake internal (recovery, distortions) and external (spillage drag) performance;

c) Specialised afterbody/nozzle models which can include representation of both true blowing nozzle geometry (at appropriate NPR) and with geometry matched to that tested in a) above with free flow NPR matching and with sting representations where appropriate.

The overall predicted full scale CTOL engine/airframe performance is derived from a lift/thrust/drag synthesis of the results from all three CTOL model representations. For CTOL aircraft layouts it has been reasonable to regard the various aerodynamic interferences associated with intake conditions, nozzle conditions and airframe conditions (MFR, NPR, C_L, C_M) to be relatively 'uncoupled'; however, for future ASTOVL designs this is not likely to be an acceptable assumption and the 'conventional' suite of models will not alone suffice.

For ASTOVL aircraft the full suite of low speed and high speed aerodynamic wind tunnel models should include the above 'conventional' suite as well as a 'simulator' based model that permits simultaneous representation of intake and exhaust streams with full airframe representation. Only in this manner will it be possible to make appropriately accurate representations of the complex engine/airframe interferences; thus, in turn, permitting development of suitable flight control systems and margins.

The model turbine powered simulator (TPS) approach has been recognised for some years. In Europe and the USA the TPS has been widely used in pursuit of conventional transport engine/airframe interference investigations (Refs 1,2) whilst the CMAPS (compact multi-mission aircraft powered simulator) has been developed in response to the need for military TPS representations (Refs 3,4). In general, for transport or combat aircraft types, less costly and less sophisticated simulations using compressed air ejector powered (EPS) and blown powered (BPS) models have been extensively used. However, for current and future STOVL projects exploitation of sophisticated TPS techniques has yet to emerge.

In this note we present the results of a set of STOVL MTPS feasibility studies starting with examination of Pegasus/Harrier AV8B representation and progressing to more advanced ASTOVL arrangements. Lewis (Ref 5) has provided a comprehensive guide to propulsion systems for ASTOVL and a suitable starting point for the current work.

2 ENGINE/AIRFRAME DESIGN TRENDS

The term 'close-coupled aerodynamics' has come into vogue as a means of distinguishing between those engine/airframe designs and operating conditions in which

a) the air intake and nozzle system flows create significant interferences with respect to each other and/or which, when combined, create interferences to airframe surfaces differing from the sum of the individual interferences; and those in which

b) air intake/airframe interference and nozzle flow/airframe interferences can be justifiably regarded as separate, independent effects which can be summed (δC_L, δC_M, δC_D) to yield the overall aerodynamic data.

Some clarification is necessary since it is clear that, in subsonic flow, in principle at least, all flow field elements are required for fully representative aerodynamic modelling; however, it is not practical to represent either intake flow or nozzle flows as well as the overall airframe without significant geometric compromises; some geometric additions (stings, struts) have generally proved inevitable for wind tunnel model simulations.

The advent of closely integrated propulsion/airframe systems as exemplified by the Pegasus/Harrier design led to a clear need for enhanced simulation capability and it is relevant to consider some simple parameters which can be used to characterise the layout.

Thus, aircraft designs in which

$X/D)_{\text{front nozzles}} \leq 3$, where X is length from the intake face to the front nozzle and D is the fan/compressor face diameter

will undoubtedly feature 'close-coupled' aerodynamics for many ASTOVL flight conditions; whereas for designs in which

$X/D)_{\text{front nozzles}} \geq 8$

the aerodynamics will frequently be considered to be 'uncoupled'; in the range

$3 \leq X/D \leq 8$

it is likely that 'coupled' aerodynamics will arise in a significant portion of the overall operating envelope of an ASTOVL aircraft.

'Close-coupled' aerodynamics will also arise if vectored or deflected jets are located close to the wing or control surfaces or when intake airflows result in significant interferences at control or lifting surface locations.

It is clear from the above and examination of the candidate ASTOVL powerplants (Ref 5), that most, if not all, practical ASTOVL designs will feature 'coupled' aerodynamics and that powered model simulations will be required in hover, low speed (and possibly high speed) ASTOVL wind tunnel studies. In Figures 1,2 the various significant aerodynamic interactions relevant to current and future STOVL aircraft are summarised. The need for full flow field model representations using simulators with 'live' inlet and exhaust flows (inlet ram drag, nozzle thrust levels) is clearly evident.

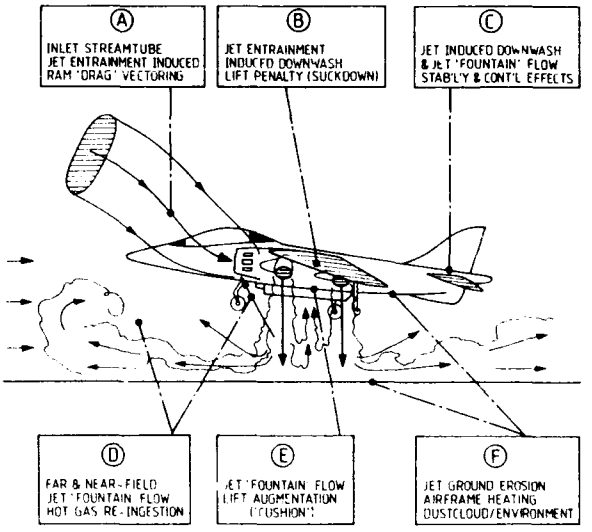

Fig 1 STOVL AERODYNAMIC INTERACTIONS NEAR M = 0

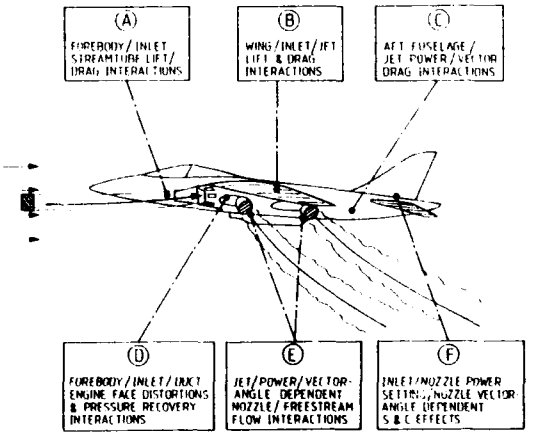

Fig 2 STOVL AERODYNAMIC INTERACTIONS FOR M ≫ 0

3 ENGINE CYCLE TRENDS AND SIMULATOR BACKGROUND

Fig 3 shows the operating characteristics of a range of mid-1980s and projected mid-1990s full scale military powerplants in terms of nozzle pressure ratio (NPR) and inlet air flow per unit nozzle area, W_I/A_N. This airflow parameter reflects the fact that, for a simulator to give adequate representation, it is widely accepted that the inlet MFR and nozzle NPR should be equal to, or close to, those of the full scale powerplant; also the inlet external geometry and the exposed nozzle geometry must be correctly scaled along with the aircraft airframe geometry. The plot of Fig 3 is based, in part, on Bailey (Ref 3), and partly on projected engines including those considered under the UK/USA ASTOVL MoU. This figure clearly demonstrates the trend towards higher nozzle pressure ratios for future military engines.

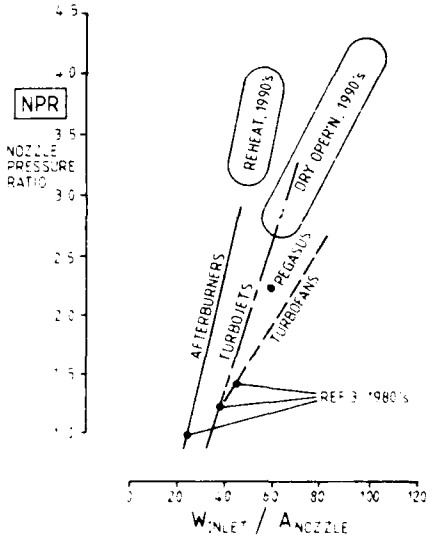

Fig 3 MILITARY POWERPLANT CHARACTERISTICS

It should be noted here, however, that the simulator package does not necessarily need to match the full scale engine lines; the requirement is to match the installation airflows at certain specific (inlet, nozzle) locations and to provide an accountable set of internal flow pressure, temperature, mass flow and thrust conditions. The simulator must, however, fit within the airframe lines, with due allowance for the model support strut/s or sting/s.

In Figure 4 the cycle characteristics of EPS and CMAPS simulators are compared to the full scale engine cycles It is clear that, compared with the CMAPS version of MTPS, the EPS is deficient in inlet mass flow for the cases where high specific thrusts, or high NPR, are involved. In References 3,4,6,7,8 extensive data is given for CMAPS performance whilst References 9 and 10 give the essential features of EPS for high speed wind tunnel models. Before leaving the comparisons of EPS and TPS it is important to note that a supersonic/subsonic dual mixing mode of operation can arise when very high single stage EPS performance is required. This dual mode operation results in a hysteresis loop of predictable but undesirable character in the mass augmentation ratio cycle of the EPS; Fig 5 is from Whitaker (Ref 10) who has provided a very clear description of this dual (hysteresis) cycle behaviour.

This brief comparison has pointed the way for further attention to be paid to achievement of fully representative W_I/A_N and

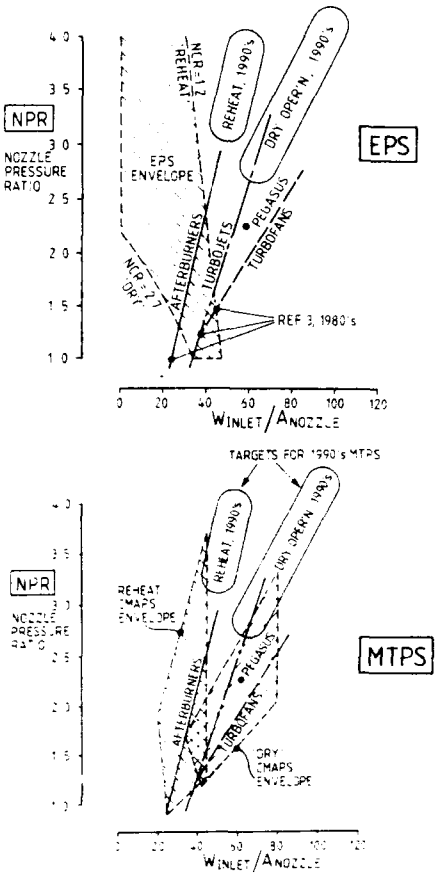

Fig 4 SIMULATOR & FULL SCALE CYCLE CHARACTERISTICS

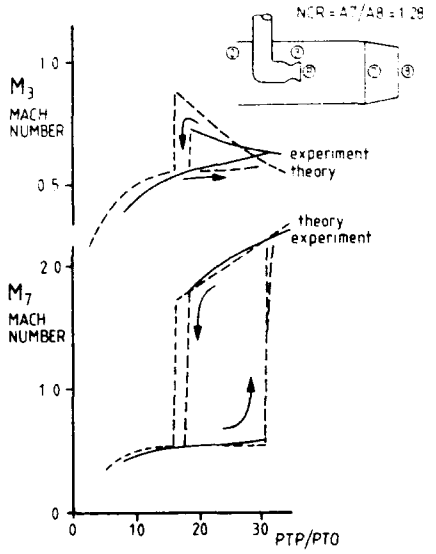

Fig 5 EPS CYCLE HYSTERESIS CHARACTERISTICS

NPR within an acceptable simulator package size. We can expect to find that the MTPS must be closely matched to, and developed for, the defined full scale ASTOVL powerplant/ airframe. In this context it has been found that carefully developed civil turbofan simulators can match essential fan and core operating pressure ratios with largely representative inlet airflows, whilst matching package size constraints.

It is also clear that, despite the strength of the civil TPS background, the development of a specific ASTOVL simulator is likely to absorb significant time and effort. Clearly, too, an inventory of simulator design expertise will reduce technical risks when firm future project requirements emerge. The direction chosen for the current study was to examine:

a) Pegasus/Harrier AV8B simulator design as a possible basis for a more extensive technique evolution exercise noting that the costly conventional model components exist at a suitable scale (1/7.5) and that a large model and full-scale data base exists covering all relevant flight phases; and

b) a particular ASTOVL variant based on a generic aircraft layout and specific full-scale engine cycle requirements allied to wind tunnel constraints in respect to size and compressed air supply.

4 PEGASUS SIMULATOR STUDY

It was first decided that a sea level standard take-off power specification would provide sufficient and representative simulation requirements recognising that high speed cycle data would be similar, Table 1. The 1 to 7.5 scale simulator design is compared to the scaled Pegasus engine in Figure 6. It should be noted that the aim was for fully scaled intake airflow, front and rear nozzle pressure ratios with cold flow simulation of the rear jets (if necessary). The wind tunnel conditions were also to be sea level standard day for intake airflow (1 bar pressure level, 288°K temperature).

	INTAKE		FRONT NOZZLE		REAR NOZZLE	
	F/S	MODEL	F/S	MODEL	F/S	MODEL
TOTAL AREA (sq in)	-	-	2×198	2×3·52	2×282	2×5 01
NOZZLE DIAMETER (in)	-	-	-	2 1	-	2 5
MASS FLOW (lb/sec)	453	8	257	4 6	196	TBD
TOTAL PRESSURE (PSIA)	14 7	14 7	33 92	33 92	28 36	28 36
TOTAL TEMP (°K)	288	288	398	398	960	TBD
NPR	-	-	2 31	2 31	1 93	1 93

TBD - To be determined during study

TABLE 1 SPECIFICATION DATA FOR PEGASUS SIMULATOR

In the course of the study (Ref 11) compressor and turbine cycle analyses were developed in parallel with schematic model Pegasus layouts. In all cases the compressed air drive gas was to be introduced either along a sting from aft or along a strut from nominally above the rear nozzles.

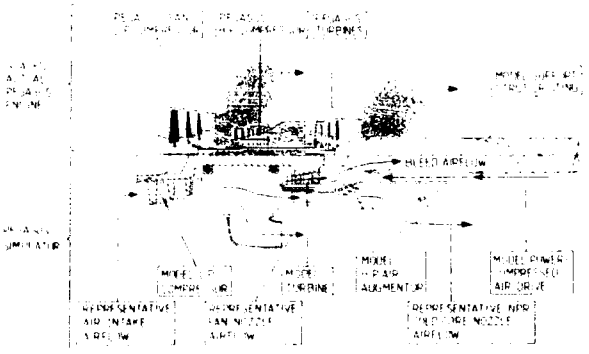

Fig 6 SCHEMATIC LAYOUT OF 1/7.5 SCALE PEGASUS SIMULATOR

Early cycle analyses demonstrated that it was necessary to use overboard bleed to achieve the best overall match to the required nozzle conditions. This approach was allied to a mixed flow process for rear nozzle simulation and in all reflects similar design decisions to those reached in the development of CMAPS, albeit to a quite different overall specification.

The cycle analysis data of Reference 11 has shown that the simulator cycle can be optimised to minimise both drive gas strut (or sting) sectional area and bleed flow area.

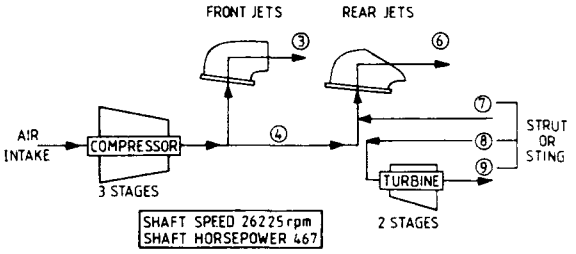

STATION	TEMP °K	PRESSURE PSIA	FLOW LB/SEC	AREA SQ INS	MACH NO
0	293	14 70	8·05	-	-
1	293	14 70	8 05	28 36	0 60
2	386 1	33 92	8 05	16 05	0 52
3	386 1	33 92	4 56	2×3 52	1 0
4	386 1	33 92	3 48	-	-
5	349 8	28 36	5 71	-	-
6	349 8	28 36	5 71	2×5 01	1 0
7	293	400	2 23	0 26	0 75
8	293	400	12 74	1 48	0 75
9	233	148 2	12 74	3 55	0 75

MODEL SCALE 1 to 7·5

Fig 7 CYCLE DATA FOR MTPS PEGASUS IN HARRIER/AV8B MODEL

Fig 7 shows the overall cycle selected with values of the key variables. It is notable that full intake airflow and nozzle pressure ratio (front and rear) simulation is achieved. The flow chart also indicates that the compressor flow feed to the rear nozzles is supplemented by mass addition from the compressed (drive) airfeed to compensate for the absence of heat addition (in the full scale gas generator). A two stage turbine of inlet hub/tip ratio 0.90 and exit hub/tip ratio of 0.775 has been designed to give the 467 SHP required. With an inlet tip relative Mach number of 0.95 and a hub/tip ratio of 0.513 the 3 stage compressor design is conventional to match the Pegasus fan cycle. In Fig 8 it is shown that, in order to use a comparatively conservative compressor design, a growth in the length above scale Pegasus Mk 103 was adopted; this growth implies a foreshortened air intake duct to mate to the revised compressor face location.

A three bearing shaft layout design was evolved in the Ref 11 study based on the needs for compressor and turbine component assemblies as well as provision of the complex internal flow manifolds, as shown in Fig 8.

In Figure 8 the airfeed is illustrated for a sting mounted assembly; an alternative strut mounted design has also been shown to be feasible. A suitable region between the front and rear nozzles has been recognised as a possible location for an annular 6-component force balance; however, appreciable additional study would be required before the characteristics of a bellows airfeed flexure system and annular force balance could be firmly defined.

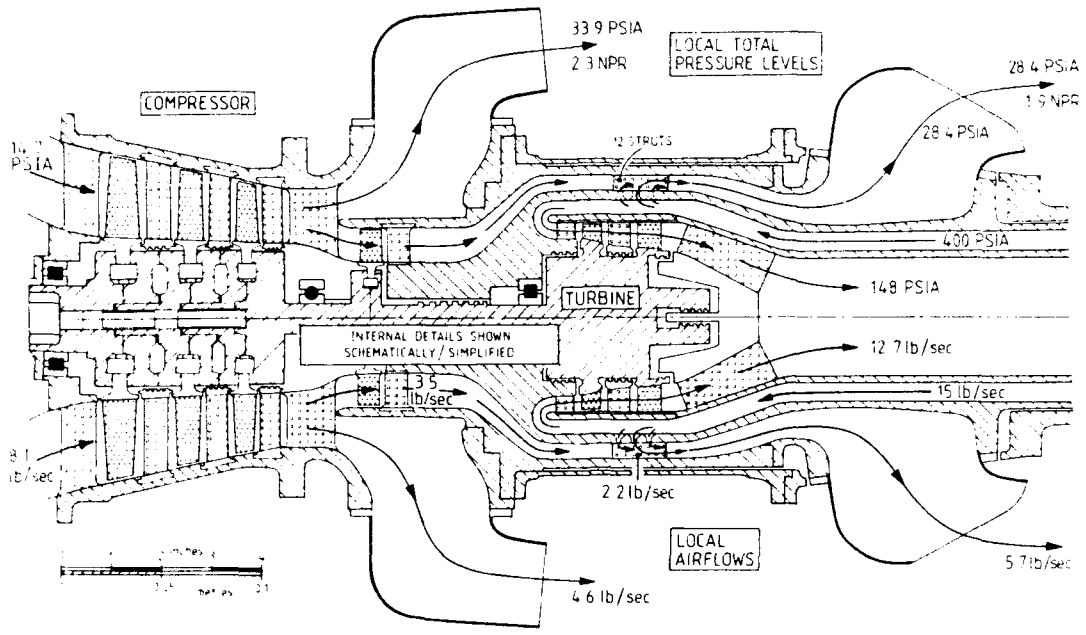

Fig 8 PEGASUS MODEL ENGINE SIMULATOR LAYOUT

Schematic designs of the aerofoil section strut for both model support and compressed airfeeds (feed and bleed) was also carried out in Reference 11; this work is generally relatively routine for an established force balance. In a comparable programme involving a strut supported twin TPS civil model a set of airfeed flexures and swivel joints has been engineered without serious difficulty.

The simulator flow paths have been designed to permit the use of rotating nozzles for vertical, vectored or horizontal thrust modes and with appropriate nozzle rakes placed at the plane of nozzle rotation.

From the above study it was concluded that a full representation of Pegasus in Harrier/AV8B is feasible, giving 100% intake airflow at a realistic model scale of 1 to 7.5 using a compressed-air driven MTPS design of 467 SHP, although the intake duct shape has had to be compromised slightly. Further studies have pointed the way to representation of advanced Pegasus variants. By adoption of less conservative compressor stage designs it is likely that an advanced Pegasus can be represented with only modest increases in scaled compressor length.

5 ASTOVL SIMULATOR STUDY

5.1 General Requirements

In a follow-up study (Ref 12) the specific aspects of MTPS design for simulation of a RALS (remote augmented lift system) engine variant in a generic ASTOVL layout were addressed. The study was aimed at identification of a simulator cycle suitable for a model to be tested in the pressurised 5 metre tunnel at RAE Farnborough.

The selected aircraft layout is shown schematically in Fig 9. Model scale was selected at 15% and the overall model dimensions were appropriately scaled in terms of fuselage sections, intake and nozzle locations. It was considered that this ASTOVL variant would be sufficiently representative for the purpose of a relatively detailed feasibility study whilst accepting that design variations would inevitably arise in a real project ASTOVL scenario.

The basic specification for the model/simulator stated that the design must provide:

a) scaled air intake geometry and airflow;
b) scaled nozzle geometry and flow area;
c) fully representative Nozzle Pressure Ratios (NPR);
d) a simulator to fit within the defined airframe geometry;
e) compressed airfeed requirements within defined facility pressure/temperature/flow capacities;
f) a minimised demand for strut/airfeed cross-sectional area;
g) for simulation at 2.5 bar wind tunnel (ambient) pressure level to maximise overall Reynolds number levels for improved aerodynamic simulation of aero-propulsion interactions.

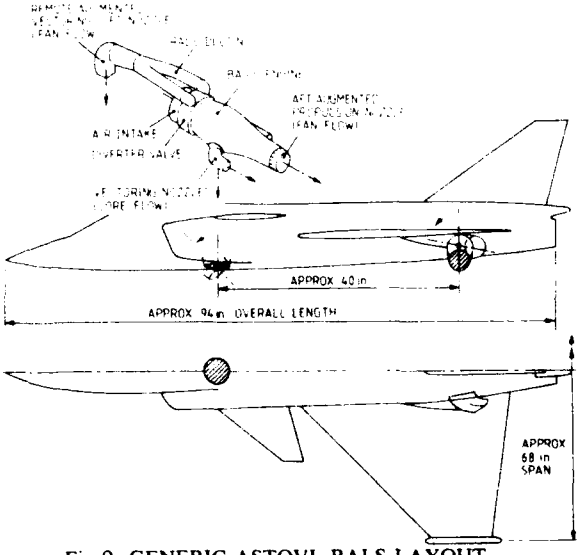

Fig 9 GENERIC ASTOVL RALS LAYOUT

These three latter specification requirements proved to be quite stringent and a moderation of the pressure level to 1.5 bar operation was also considered as the study progressed.

The 5 m wind tunnel facility operating envelopes for pressure, temperature and flow are given in Figure 10, whilst the outline engine simulation and model requirements are listed in Table 2. A front nozzle NPR of 5 and a maximum intake airflow of over 24 lb/sec is called for at the defined elevated tunnel ambient pressure level.

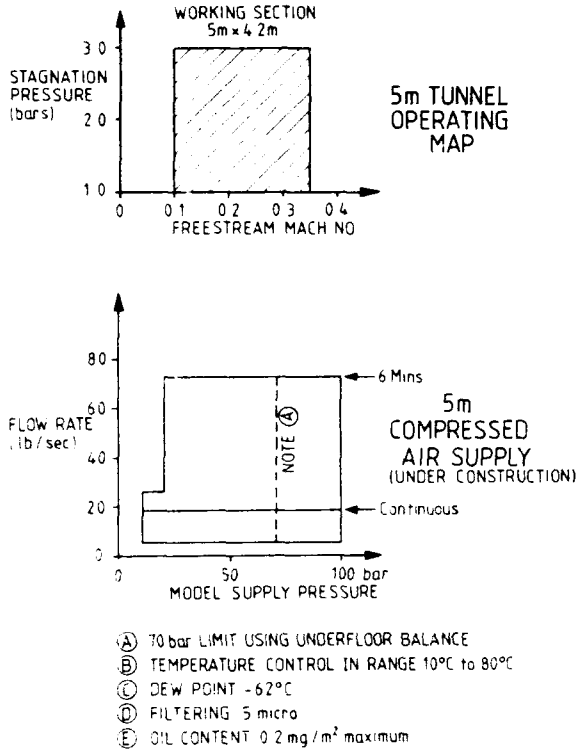

Fig 10 5 m TUNNEL FACILITY COMPRESSED AIR FLOW, PRESSURE & TEMPERATURE

5.2 Cycle Options

At the outset it was recognised that there were a large number of cycle layouts which may be suitable to satisfy the above requirements. An initial set of seven cycle options was selected but later two further options were added to total 9 in all. The cycle options included, for reference purposes, a non-simulator case which employed direct suction and blowing of intake and nozzles respectively. Figure 11 shows the flow schematics for the various options with a few leading particulars of the design solutions.

The following notes give the key findings for each of the simulator cycle options considered:

Cycle option 1 (non-simulator reference case) has been shown to require a total strut airfeed area of about 37 sq in, based on blow and suction duct Mach numbers of 0.3 and 0.65 respectively with a blow duct pressure of 1020 psia, the facility limit. As the intake air is not pressurised it requires a large duct area, and the best that could be achieved would be an arrangement of multiple tubes with two suction ducts at 4.6" diameter and one blowing duct at 2.2" diameter.

Front Nozzle Area	4 sq in
Rear Nozzle Area	11 sq in
Front Nozzle Pressure Ratio	5
Rear Nozzle Pressure Ratio	2.9
Tunnel & Intake Temperature	303.15 K
Tunnel & Intake Total Pressure	1.3 to 2.5 bar
Intake Mass Flow (proportional to pressure)	12.7 to 24.4 lb/sec
Model Pitch Range	$\pm 30^{o}$
Model Yaw Range	$\pm 15^{o}$

Facility Capabilities

The facility can provide air at a pressure of 1020 psia (70 bar).

Maximum Acceptable Strut Diameter 4.72 in (Max area = 17.5 sq in)

TABLE 2 SPECIFICATION DATA
ASTOVL MODEL SIMULATOR

The design of flow paths and flow conditioning hardware for option 1 is not a trivial task; a significant design/development effort would be required to evolve a sufficiently well conditioned set of flows to satisfy requirements for good nozzle flow uniformity; large pressure losses need to be installed to drop the airfeed pressure from 70 bar to the nozzle pressures shown in Figure 11.

Cycle option 2 A heated drive air supply, to 461°K permits a viable thermodynamic solution using a 3 stage compressor and a 2 stage turbine. A shaft horsepower of 2250 is derived at a shaft speed of 41,000 rpm; turbine expansion ratio is 6.55 with a compressor pressure ratio of 3.5. However, this option was not considered feasible because, at the large mass flows involved, the additional heating requirements would be excessive and would create formidable difficulties in bridging the air supply across the tunnel force balance.

Cycle option 3 Due to flow requirement limitations at the front nozzle combined with a strut feedline maximum pressure of 1020 psia, a thermodynamic solution was not feasible due to limitations of available shaft power.

Cycle option 4 Using a stepped compressor to process front nozzle and strut overboard bleed airflows, the shaft is driven by the rear nozzle compressed airfeed. The 1020 psia feed pressure limit results in a requirement to preheat the turbine drive air to achieve the required the shaft power of 3028 SHP at 41,000 rpm shaft speed. Unfortunately, the level of preheating was again excessive and thus this cycle offered no solution within the 5 m tunnel facility.

Cycle option 5 This was an attempt to avoid the need for the use of overboard bleed by a modification to option 4 that routed the remainder of the compressor flow to the rear nozzles. However, this reduced the available turbine drive flow so that the cycle was again no longer viable due to shaft power limitations.

Cycle option 6 This was a development of option 4 aimed at reducing the heating requirement by increasing the turbine drive flow, some of which had to be ducted overboard (bleed); this option resulted in an unacceptably large strut flow area requirement.

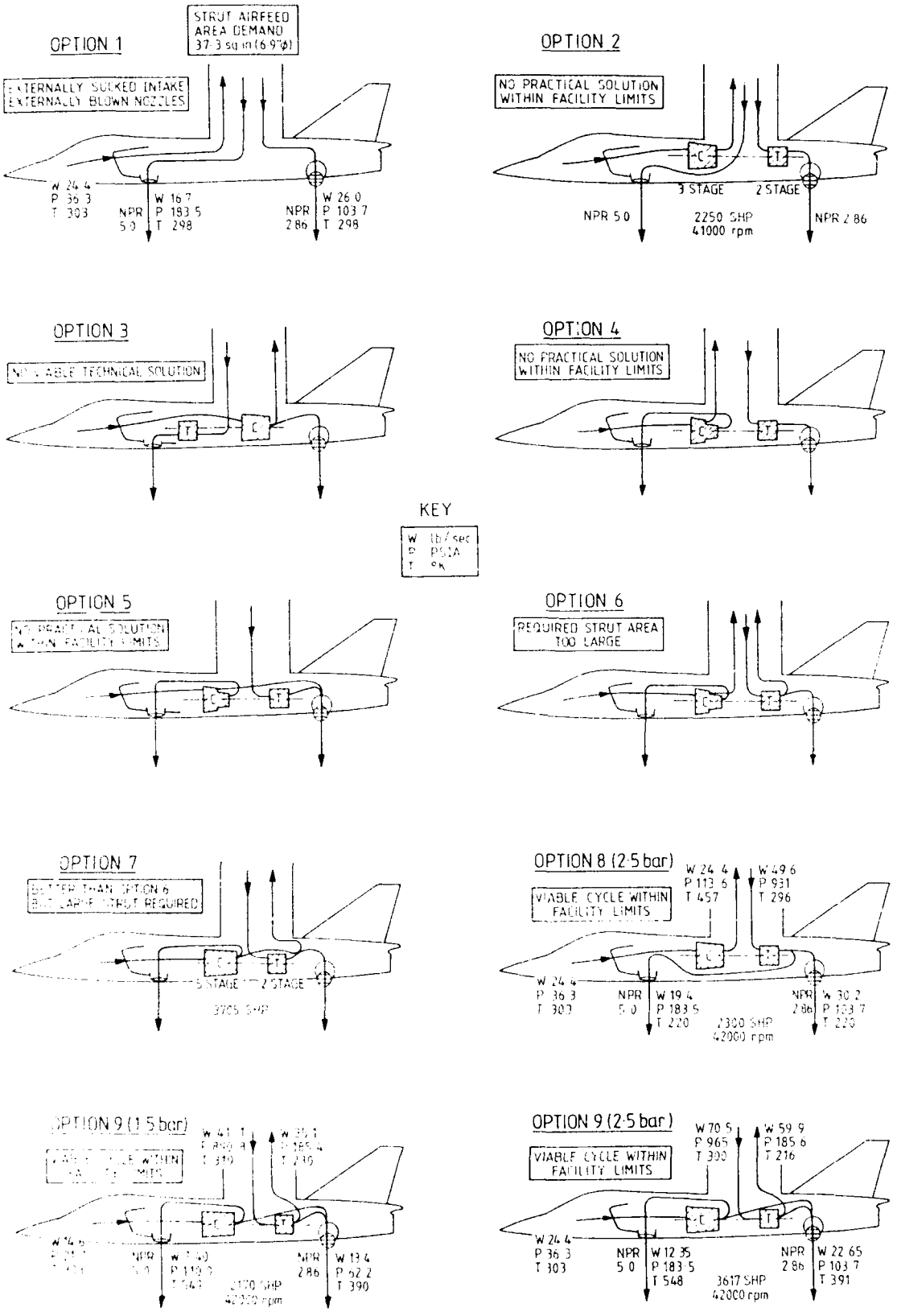

Fig 11 FLOW OPTION SCHEMATICS FOR ASTOVL MTPS

Cycle option 7 Option 7 is a development of option 5 with increased turbine drive air, some of which is routed back through the strut, ie uses overboard bleed. Note that in this cycle all the intake air was compressed to the full front nozzle pressure. An increased shaft power of 3705 SHP was required by this option; however, the strut area demand was again considered unfavourable.

Cycle option 8 In all the previous options, air from the turbine only exited from one set of nozzles; for options 6 and 7 the available turbine power was increased by using overboard bleed; in option 8 the turbine flow is increased by feeding the drive air to both nozzles. The intake air is compressed by a factor of just over three to reduce its volume prior to being ducted overboard. A viable cycle was thus established albeit with very cold flow from both front and rear nozzles (which could lead to icing problems). Strut area demands compared well with the baseline (option 1), being only 48% of the option 1 sectional area at a supply duct Mach number of 0.3 and an outflow Mach number of 0.65. At the design point the shaft power is 2300 SHP at 42000 rpm.

Cycle option 9 In order to avoid the cold nozzle flows of option 8, a layout was considered in which the total intake airflow exits via the compressor through the front and rear nozzles. The rear nozzle flow is supplemented using part of the turbine exit flow which is mixed with the ex-compressor flow. This cycle is close to that used for CMAPS although levels and details are quite different. Despite the fact that the strut is called upon to carry nearly 71 lb/sec into the model and 60 lb/sec out, the sectional area demand is still only 54% of the reference (option 1) case. For option 9 design point shaft power is high at 3617 SHP and shaft speed 42000 rpm.

In overall terms it can be observed that for 2.5 bar operation the preferred solutions, options 8 and 9, both demand about one half of the strut airfeed area of the reference non-simulator case.

5.3 Considerations of Reduced Tunnel Pressure Level

A set of cycle analyses for options 8 and 9 has been performed for operation of the 5 m tunnel at 1.5 bar ambient pressure level. Different effects arise due to the differing cycle designs when the drop from 2.5 to 1.5 bar is considered, a shown in Table 3.

	5 m Wind Tunnel Pressure Level			
	2.5 bar		1.5 bar	
PARAMETER	Option 8	Option 9	Option 8	Option 9
Intake Airflow (lb/sec)	24.4	24.4	14.6	14.6
Intake Total Pres. re (psia)	36.3	36.3	21.8	21.8
Front Nozzle Airflow (lb/sec)	19.4	12.35	11.7	7.4
Front Nozzle Total Pressure (psia)	183.5	183.5	110.0	110.0
Front Nozzle Temperature (°K)	220.0	548.0	216.0	549.0
Rear Nozzle Airflow (lb/sec)	30.2	22.65	18.3	13.4
Rear Nozzle Total Pressure (psia)	103.7	103.7	62.2	62.2
Rear Nozzle Temperature (°K)	220.0	391.0	216.0	390.0
Turbine Power (SHP)	2300.0	3617.0	1700.0	2170.0
Compressor Pressure Ratio	3.4	5.75	4.25	5.75
Turbine Drive Airflow (lb/sec)	49.6	70.5	30.0	41.1
Required Airfeed Area @ M = 0.3 (sq in)	4.7	6.5	2.8	4.2
Compressor Overboard Bleed Flow (lb/sec)	24.4	0	14.6	0
Turbine Overboard Bleed Flow (lb/sec)	0	59.9	0	35.1
Overboard Bleed Flow Area @ M = 0.65 (sq in)	13.2	13.6	10.8	8.2
Total Strut Area (sq in)	17.9	20.1	13.6	12.4

TABLE 3 COMPARISON OF 1.5 BAR AND 2.5 BAR DESIGNS

For cycle option 8 the reduced nozzle flows and pressures with unchanged supply maximum pressure allow an increase of turbine expansion ratio; this in turn permits an increased compressor pressure ratio and a substantial reduction in strut area demand. Retaining a turbine discharge at 225°K the power is reduced to 1700 SHP; strut airfeed area demand reduces to 36% of the Option 1 reference value.

For cycle option 9 the retention of high pressures in the strut feed and bleed ducts whilst requiring reduced turbine workload again results in a substantial reduction in the strut area demand; at 12.4 sq inches this is the lowest requirement of all the layouts considered. Equivalent airfeed demand diameters and areas are:

Option 1 (reference) 6.9" dia, 37.39 sq in (100%)
Option 9 4.0" dia, 12.56 sq in (33%).

This was the option finally selected for a detailed design exercise.

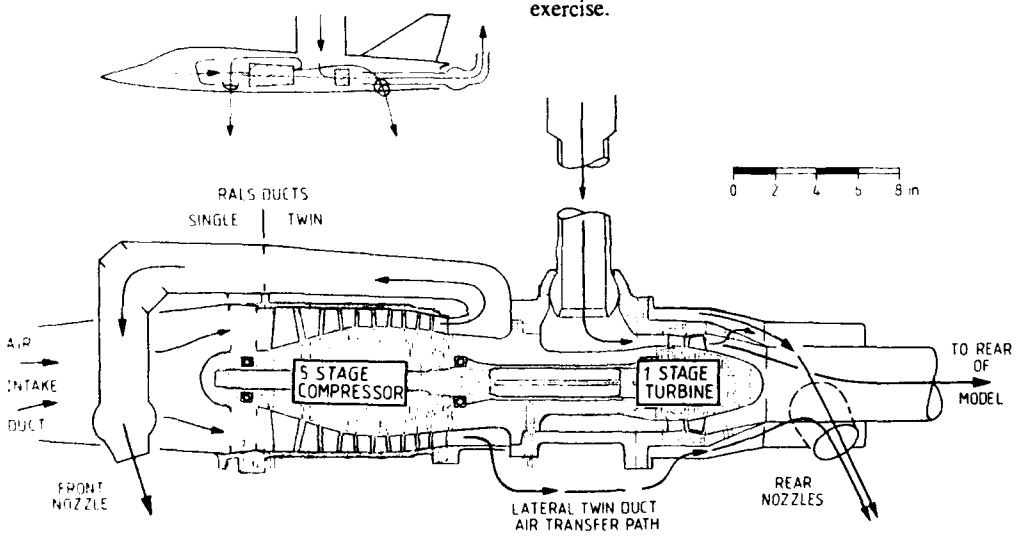

Fig 12 MILITARY TURBINE-POWERED SIMULATOR (MTPS) FOR 5 m TUNNEL ASTOVL MODEL

The resulting simulator is shown in Fig 12. The compressor and turbine design particulars have been evaluated and performance risks have been assessed by comparing the stage and overall design duty to published data on existing small compressors and turbines. The analysis has shown that sufficiently conservative design assumptions have been made for both the compressor and turbine.

The compressor design compares reasonably closely with a number of known helicopter compressor front ends; a review comparing the option 9 compressor with the Pratt & Whitney ERDA industrial compressor has supported the concept with regard to all leading design parameters including that of the assumed polytropic efficiency (assumed 85% versus 91% ERDA measured).

The turbine design has been compared with that defined by Okapu (Ref 13); again the duty compares closely and it has been shown that the assumed efficiency level is conservative (85.6% assumed versus 89.5% measured by Okapu).

5.4 Overview of ASTOVL Simulator Designs

The discussions above have clearly demonstrated that a feasible MTPS simulator is a realistic option; fitting the defined simulator (option 9) within the generic ASTOVL airframe model lines has also been shown to be feasible. On the other hand, it is recognised that more detailed design work will be necessary to facilitate suitable strut or sting mounting of the complete model and MTPS. Some design efforts have been expended but not all problems of strut or sting interference have yet been resolved; some compromises are clearly necessary when compared with unpowered models. Also further sting interference reference testing would inevitably be necessary for enlarged, possible non-standard strut or sting designs.

Further advances in cycle design could arise if more advanced turbomachinery designs were to be considered as opposed to the relatively conservative approach used here; against this higher technical risks would inevitably arise. On balance, a relatively conservative approach should be accepted for MTPS design; costly model hardware with high risk would not be viable.

6 DEVELOPMENT OF POWERED SIMULATION CAPABILITY

In Figure 13 a plan of attack is outlined in which a parallel activity involving blown (BPS) and simulator (MTPS) approaches are followed to facilitate powered ASTOVL wind tunnel tests. The programme of work outlined gives suitably interactive design stages to minimise overall model hardware costs.

The scheme has been developed in response to the recognised need to start with BPS model studies whilst the MTPS development continues; also, use of a common set of basic model hardware, airframe and expensive components (flaps, wings etc), is envisaged.

Consideration should also be given to the use of MTPS for zero and near-zero speed model experiments (ie ground interference, ski-jump, STOL, HGR tests), as the overall cost-effectiveness and design decisions require that a minimised set of models and rigs become integrated overall.

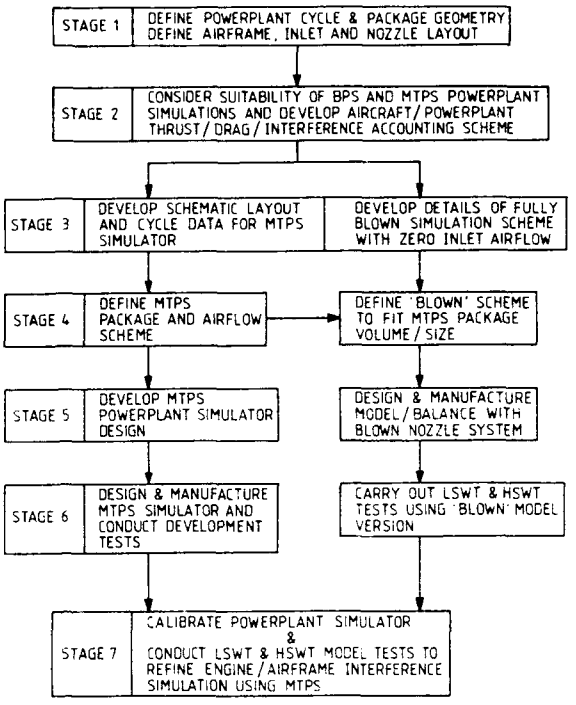

Fig 13 SCHEME FOR DEVELOPMENT & UTILISATION OF ASTOVL POWERPLANT SIMULATOR

7 CONCLUDING REMARKS ON MTPS

7.1 A technically feasible simulator has been defined for representation of a basic Pegasus in Harrier/AV8B; the design includes use of overboard bleed and is rated at 467 SHP. Full representation of intake airflow and front and rear nozzle pressure ratios has been achieved in the design study as specified. The design has been evolved to be adaptable to either strut mounting for low speed tunnel or sting mounting for low or high speed tunnel service.

7.2 A technically feasible ASTOVL simulator to represent a RALS derivative powerplant has been defined. Two optional designs (options 8 and 9) have been shown to be viable for operation at elevated tunnel pressure (1.5 or 2.5 bar) for high Reynolds number aerodynamic interference studies. Comparisons with existing turbomachinery hardware designs have shown performance assumptions to be conservative.

7.3 Both Pegasus/Harrier AV8B and the ASTOVL model simulator designs require further design effort to establish viable sting and/or strut definition. Some compromises with regard to range of test programme sideslip or sting/strut interference may well prove to be necessary to embody fully representative powerplant models for engine/airframe integration studies.

7.4 Further work is also warranted with regard to definition of instrumentation for the MTPS designs for calibration and tunnel thrust/drag accounting.

7.5 Whilst it is recognised that the MTPS designs outlined above will prove costly to develop, the alternative routes will undoubtedly prove to be similarly costly and at least equally risky.

7.6 A scheme has been defined to facilitate a well versed, staged development programme for MTPS in an ASTOVL or Harrier/AV8B model suite.

8 ACKNOWLEDGEMENTS

Design work on the Pegasus and ASTOVL simulators by TKD Ltd, ARA Ltd and Rotadata Ltd has been supported by Procurement Executive Ministry of Defence. The support of BAe and Rolls-Royce plc in provision of necessary design information and of P A Farr in preparation of this paper is gratefully acknowledged.

All views expressed are those of the authors and do not necessarily represent those of TKD, ARA, MOD(PE) or Rotadata Ltd.

This paper is dedicated to the memory of Valentine J Smith, our respected co-author, who sadly died just prior to publication of this paper.

REFERENCES

1 Harris A E, Paliwal K C, "Civil turbofan propulsion system integration studies using powered testing techniques at ARA, Bedford", AIAA 84-0593, May 1984

2 Decher R, Tegeler D, "High accuracy force accounting procedures for turbo-powered simulator testing", AIAA 75-1324, October 1975

3 Bailey R O, Harper M, Janetta T, "Evaluation of turbo-propulsion simulators as a testing technique for fighter aircraft", AIAA 79-1149, June 1979

4 Wagenknecht C D, Hoff G E, "Performance calibration results for a compact multimission aircraft propulsion simulator", AIAA 82-0254, January 1982

5 Lewis W J, "Propulsion systems for supersonic V/STOL aircraft", ASME 89-GT-309,

6 Smith S C, "Determining compressor inlet airflow in the compact multimission aircraft propulsion simulators in wind tunnel applications", AIAA-83-1231, June 1983

7 Wagenknecht C D, Dusa D J, Norbut T J, "Performance capability for a compact multi-mission aircraft propulsion simulator", AIAA-83-1358, June 1983

8 Bailey R O, Smith S C, Gustie J B, "Propulsion simulation test technique for V/STOL configurations", SAE 83-1427, October 1983

9 Whitaker A R, "Initial development of techniques for the use of ejector powered simulators in high speed combat aircraft models", BAe Warton Report AXR 98, March 1983

10 Whitaker A R, Cassie A M, " High pressure ratio engine simulator requirements and ejector performance in sub- and supersonic modes", BAe Warton Report HSWT TN32, October 1985

11 Wilde G L, Smith V J, "Model vectored thrust engine simulator for aircraft wind tunnel research. Phase 1 feasibility study", MOD-contracted TKD report.

12 Wooler A, Timmis P, "A feasibility study into an ASTOVL simulator for the Royal Aerospace Establishment, Bedford", MOD-contracted Rotadata report.

13 Okapu U, "Some results from tests on a high work axial gas generator turbine", ASME 1974.

MASS FLOW EFFECTS ON THE LOW SPEED CHARACTERISTICS OF AN ADVANCED COMBAT AIRCRAFT.

E. Barbantini, A. Ferretti, A. Gatti

ALENIA AERONAUTICA
Defence Aircraft Division

Torino, Italy

ABSTRACT.

In this paper the experimental results obtained on a low speed six components wind tunnel model representative of a delta-canard configuration and featuring an ejector based internal flow augmentation system are described in order to outline at what extent the near field distortions induced by the air intake operating conditions can modify the aircraft aerodynamic stability characteristics and foreplane control effectiveness.

1. INTRODUCTION.

Aim of the model whose results are herein described is to assess, by using experimental measurements, how the near field changes related to the air intake operating conditions can affect stability and control characteristics of a far-coupled/delta winged canard configuration.
It is worth to outline how these effects are conceptually different from the so called "Internal Mass Flow Correction" usually applied to wind tunnel data, the last referring to the internal momentum variation and accountless of any "external" change in the airplane near field.

Rationale behind the usual approach is that on conventional combat aircraft configurations seldom a combination of high angle of attack (AoA) and high Mass Flow Ratio (MFR) at the air intake is found.
At take off as a consequence of the low speed and high engine setting the MFR is well beyond the unity but the AoA doesn't exceed 10°-12° at lift off.
In the other flight conditions, even for very high "G" manoeuverings, maximum incidence can be achieved still mantaining MFRs as small as 0.7-0.8.
On an agile combat aircraft this is not totally true anymore, conditions of high MFR and high AoA becaming possible during a close in combat.

Furthermore one of the requirements usually involved into the design of a fighter aircraft concerns the capability of reaching supersonic speeds.
This usually leads to low aspect ratio / highly swept delta wings on which the flow field, even for median values of the Angle of Attack, is deeply influenced by several vortical structures whose shedding, growing and burnsting is basically ruled by the local flow conditions existing where the vortex sheds.

The configuration, which the tests refer to, features an air intake located just forward the wing apex and very close to the foreplane (fig. 1); this suggests the consideration that the air intake operating conditions, by altering the local incidence patterns and the pressure/velocity gradients, can affect the aerodynamic behaviour of the foreplane,of the wing and the related interferences therefore modifying basic stability and control characteristics.

2. MODEL DESCRIPTION.

The model involved in this test phase was a 1/14 (7.14 %) low speed wind tunnel model fitted with a 6 components balance, pressure taps on the wings (fig. 1A) and on the ventral surface of the forebody along the symmetry plane .

3. EXPERIMENTAL TECHNIQUE AND DATA CORRECTION PROCEDURE.

Suction necessary to obtain model inlet MFR beyond the natural value has been provided by using two ejector units fed with compressed air (controlled by a fast acting, electronic controlled, regulation valve system) up to 4.5 absolute atm. thus allowing a model inlet MFR of 2.3 with a tunnel dynamic pressure of 50 Kg/m^2; lesser values of the MFR were obtained using combinations of lower feeding pressures and higher wind tunnel dynamic pressures; consequently Reynolds Number ranges between 1. and 1.5 millions.
The inner part of both the ejectors has been designed in order to be non-metric, thus avoiding any effect related to the momentum variation due to the flow feeding the ejectors.
The measurement of all the additional forces and moments generated by the enhanced internal flow and acting on the internal surfaces of the model duct has been accomplished by using a special rig (fig. 2).
Basically this rig consists of an external non metric aerodynamic shroud able to house the model fuselage exept for the forebody.

This part is complete of its internal duct, ejector units, the same strain gauge balance used for the tests and fitted with additional pressure taps .

In order to get a better understanding about this additional rig the effects of the mass flow augmentation system should be thought as splitted betweeen:

- **effects on the external aerodynamics** (i.e. alterations of the flow field), whose determination is the aim of the tests;

- **effects on the internal duct** whose determination is essential in order avoid spurious contributions to the previous ones.

Having the effects on the internal duct to be measured at the same inlet and nozzle pressure conditions measured on the complete model it was decided to reproduce them by installing the model fuselage (except for the forebody) complete of internal duct and ejector units in the wind tunnel and shielding it with a properly shaped external (and non-metric) shroud in order to avoid any aerodynamic interference on the fuselage skin thus allowing to measure the net internal contribution.

Static and total pressures are measured in the duct throat section so that the Mass Flow Ratio can be computed using the following formulae:

$$\frac{p}{p_t} = \left(1 + \frac{\gamma - 1}{2} \cdot M^2\right)^{-\frac{\gamma}{(\gamma-1)}}$$

$$MFR = \frac{A_\infty}{A_0} = \frac{M_0}{M_\infty} \cdot \left(\frac{1 + \left[\frac{(\gamma-1)}{2}\right] M_0^2}{1 + \left[\frac{(\gamma-1)}{2}\right] M_\infty^2} \right)^{-\frac{(\gamma+1)}{2(\gamma-1)}}$$

By testing the additional rig for several different values of feeding and freestram dynamic pressure (fig. 3) it was possible to get a working map of the rig which gives the variations of the MFR caused by different settings of the forementioned parameters.
From the rig balance outputs (figs. 4 to 9) is possible to note that:

- the coefficients of forces and moments acting on the duct are in a first approximation related only to the operating conditions of the duct, that is to say to its MFR.

- The effects induced by the Mass Flow augmentation system (with the exception of the axial force) are generally small when compared to the relevant values typical of an aircraft.

During the tests a very good agreement for every coupling of feeding and freestream dynamic pressure was found between the MFR values of the air intake when installed on the complete model and on the additional rig even if a slight difference in MFR should have expected between the two configurations due to the presumably different flow field at the intake in the two arrangements.
Experimentally this difference was proven to be so little to enable the use of the data obtained by the auxiliary rig directly to correct the relevant model data without the need of any interpolation.

In other words the so called "corrected results" shown in the following paragraphs have been obtained as a difference between the complete model balance outputs and the auxiliary rig ones.

4. MASS FLOW RATIO EFFECT ON STABILITY AND CONTROL CHARACTERISTICS.

4.1 LONGITUDINALS

When looking at the corrected data the shift in the Lift Coefficient linear stroke (fig. 10) is almost neglegible, beyond 30° a more evident effects is present the CL increasing with MFR.

About pitching moment (figs. 11-12) a similar shift towards negative values has to be outlined together with a sharp change in the slope $Cm\alpha$ beyond α = 25°.
The reasons for both the shifts appear to be a coupled effect of a changed local incidence at the foreplane and of a changed pressure distribution on the ventral surface of the forebody (fig. 13) as it seems to be accounted for when looking at the foreplane-off configuration where the shift in Cm is still negative but smaller (fig. 14) and by the pressure distribution on the ventral surface of the fuselage confirming the existence of a global downloading for high MFR's; anyway the order of magnitude of the correspondent pitch shift could be defined as equivalent to a flaperon deflection lesser than 2°.
At higher incidence (α > 25°) a different behaviour can be noticed, low MFR curves being very similar whereas a sharp change occurs for MFR > 1.3 as a consequence of a retarded foreplane stall.
This is confirmed by the wing pressure distribution for the two extreme MFR.

4.2 LATERALS AND DIRECTIONALS

As far as laterals are concerned (figs. 15-18), increasing the mass flow gives a progressive reduction of the unstable $Cl\beta$ peak (fig. 16) reaching a fully stable behaviour at the higher values of MFR without any influence by the relevant change in Reynolds Number (fig. 15).
A possible explanation comes from the pressure distribution (fig. 16 A) of the wing for the two extreme MFR which shows a significative increase of the load on the windward wing whereas for zero sideslip the pressure distribution is unaffected by the variation in MFR.

About $Cn\beta$ (fig. 17), its trend is similar with a significative reduction of the unstable peak, it is worth to outline that , in the incidence range up α = 25° the reduction in directional stability, when related to the relevant increment in side force (fig. 18), states that the additional side force is located at the intake station.

5. FOREPLANE EFFECTIVENESS.

Three different foreplane deflections have been tested both for natural mass flow (0.7) and 2.0 in order to assess the effect of intake operating conditions on foreplane effectiveness. The relevant results are shown in fig. 19 in terms of Cm with respect to the foreplane zero deflection.
As it's possible to see from the variation in pitching moment the foreplane effectiveness is pratically unaffected for α lesser than 25° for the whole set of deflections tested; upon this value the trend is different when going from $\delta foreplane$ +10 to -20°, the foreplane effectiveness increment with MFR growing along with negative deflections confirming as the MFR acts substantially reducing the local incidence with a consequent foreplane stall delay.

6. CONCLUSIONS.

The effects of air intake operating conditions on external aerodynamics have been assessed as significative at high incidence.
For α < 25° nothing but a slight shift in Cl and Cm has to be pointed out, the variations in $Cl\alpha$ and $Cm\alpha$ being practically neglegible; otherwise for α > 25° strong depedence of lift, pitching moment, $Cn\beta$ and , above all, $Cl\beta$ is shown together with an increase of foreplane effectiveness, especially for negative deflections.

REFERENCES.

- Bowers,D.L."Aerodynamic Effect Induced by a Vectored High Aspect Ratio Nonaxisymmetric Exhaust Nozzle.", J. Aircraft, VOL 16, NO 8, Aug 1979, pp 512-520.

- Seddon,J.,and Goldsmith,E.L."Intake Aerodymnamics.",William Collins ,1985

- Knott,P.G."V/STOL Aerodynamic Testing Techniques at British Aircraft Corporation.",J. Aircraft, VOL 15, NO 6, June 1978, pp. 339-344.

- Roskam,J."Airplane Flight Dynamics and Automatic Flight Controls.",Roskam Aviation and Eng. Corp., 1979.

- Von Der Decken,J.,and Joos,R."Measurements Techniques for Jet Interference Effects.", AGARD CP 174 Paper No 28, Oct 1975.

- Whitaker,R.,Matthews,A.W.,Knott,P.G. ,Anger,R.,and Steward,D.J."Air Driven Ejector Units for Engine Simulation in Wind Tunnel Models", AGARD CP 174, Paper No 27, Oct 1975.

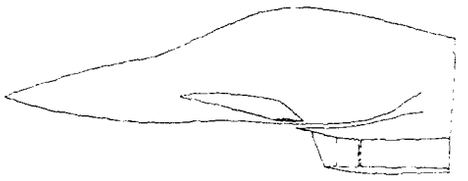

Fig. 1 FOREBODY CONFIGURATION

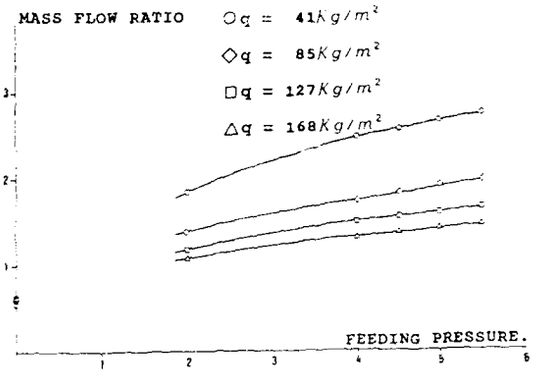

Fig. 3 MASS FLOW AUGMENTATION SISTEM WORKING MAP.

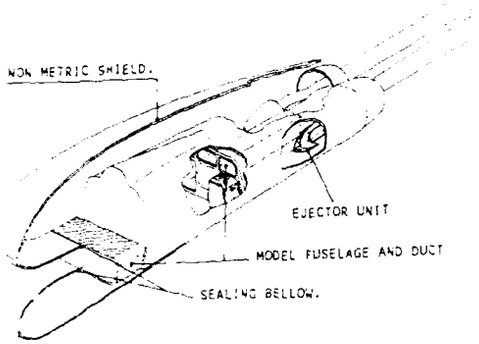

Fig. 2 AUXILIARY RIG.

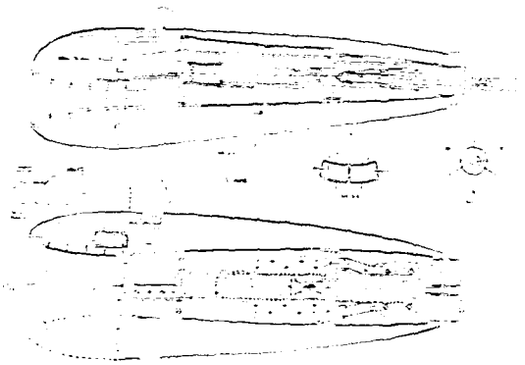

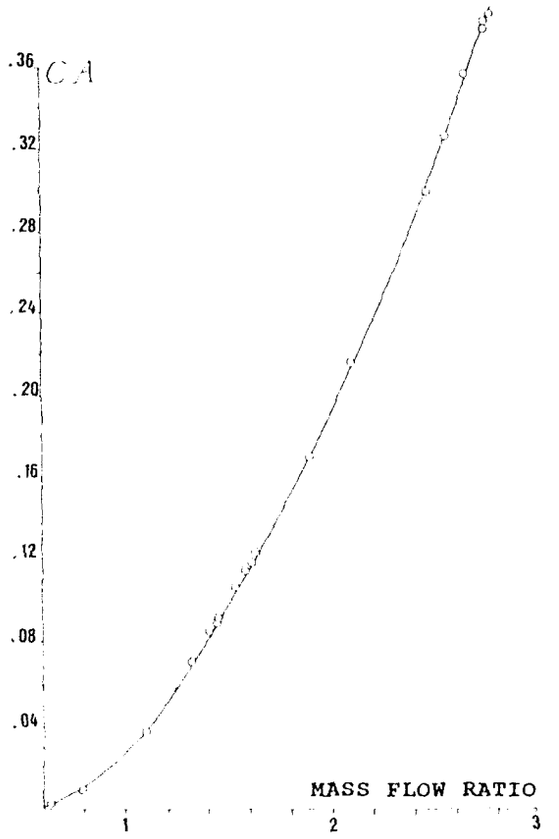

Fig. 4 MASS FLOW AUGMENTATION SISTEM EFFECT ON AXIAL FORCE.

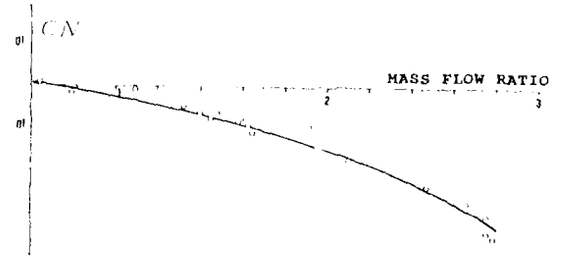

Fig. 5 MASS FLOW AUGMENTATION SISTEM EFFECT ON NORMAL FORCE.

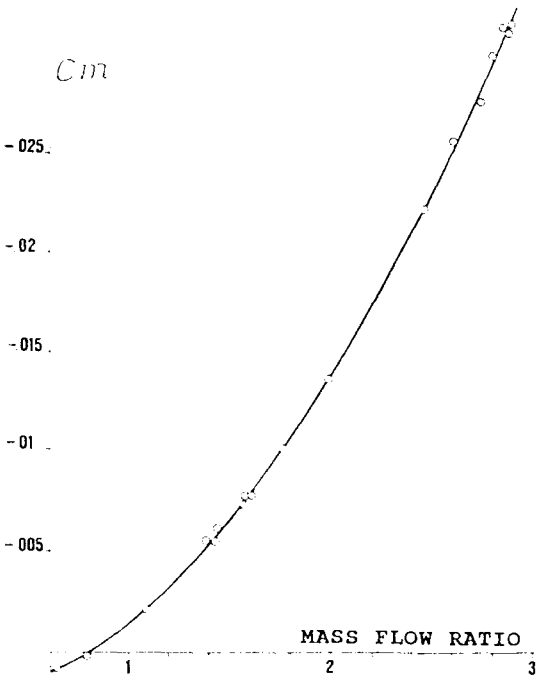

Fig. 6 MASS FLOW AUGMENTATION SISTEM EFFECT ON PITCHING MOMENT.

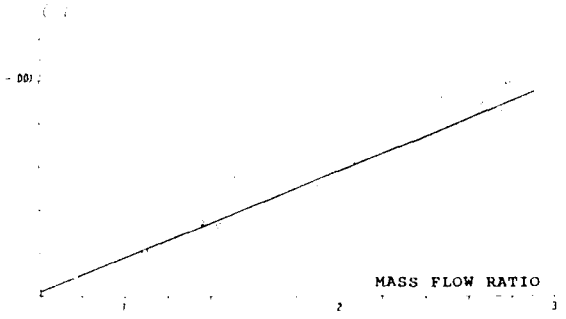

Fig. 7 MASS FLOW AUGMENTATION SISTEM EFFECT ON ROLLING MOMENT.

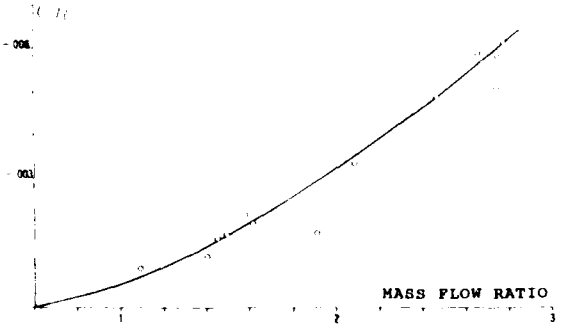

Fig. 8 MASS FLOW AUGMENTATION SISTEM EFFECT ON YAWING MOMENT.

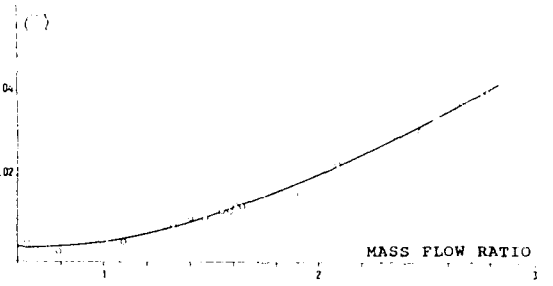

Fig. 9 MASS FLOW AUGMENTATION SISTEM EFFECT ON SIDE FORCE.

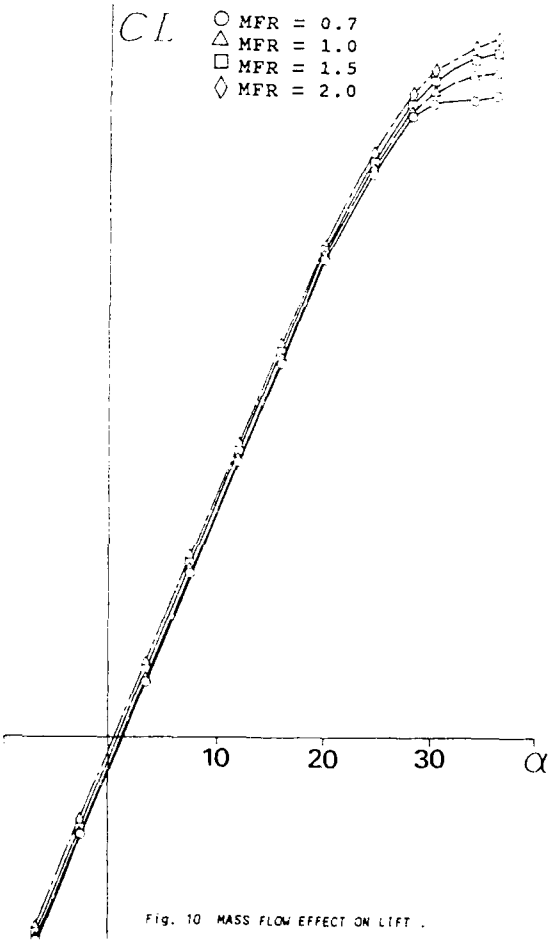

Fig. 10 MASS FLOW EFFECT ON LIFT .

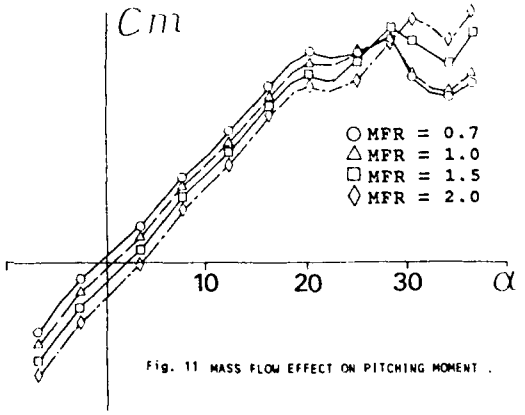

Fig. 11 MASS FLOW EFFECT ON PITCHING MOMENT .

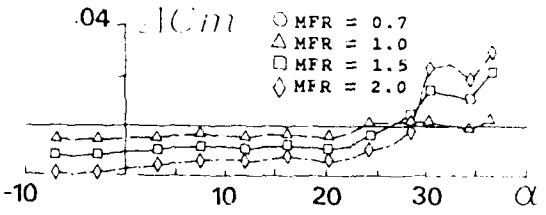

Fig. 12 MASS FLOW EFFECT ON PITCHING MOMENT W.R.T NATURAL MFR.

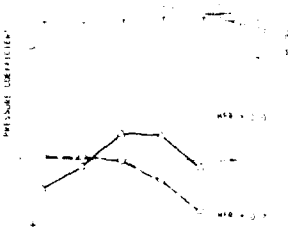

Fig. 13 MFR EFFECT ON PRESSURE DISTRIBUTION ALONG SYMMETRY PLANE

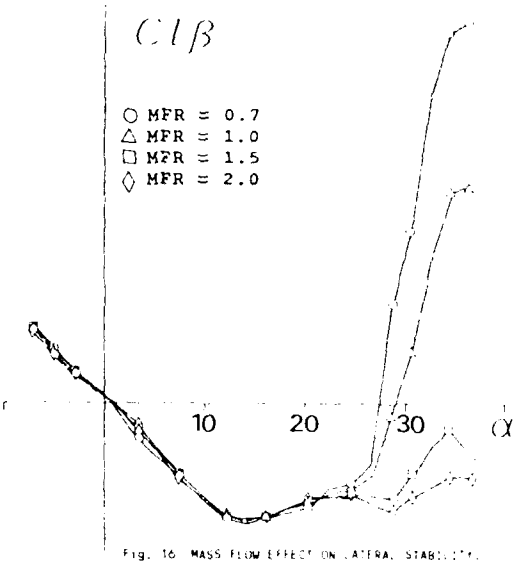

Fig. 16 MASS FLOW EFFECT ON LATERAL STABILITY.

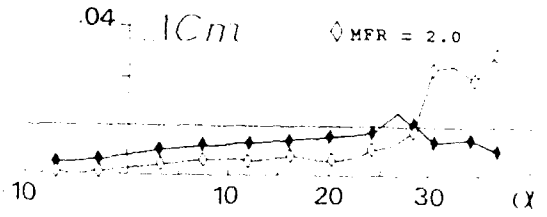

Fig. 14 MASS FLOW EFFECT ON PITCHING MOMENT OF FOREPLANE OFF CONFIGURATION.

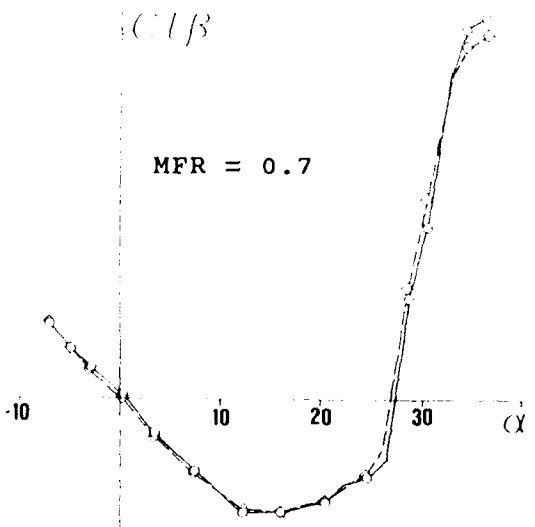

Fig. 15 REYNOLDS EFFECT ON LATERAL STABILITY.

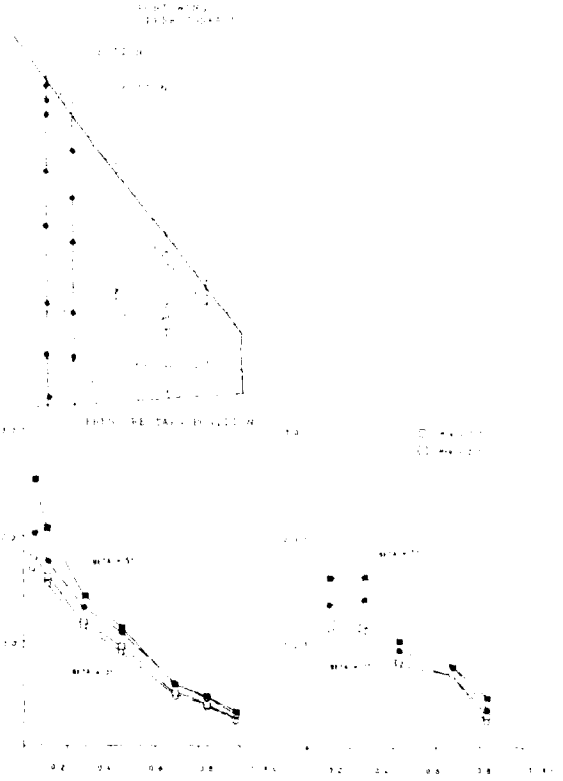

Fig. 16A MFR EFFECT ON PRESSURE DISTRIBUTION WITH AND WITHOUT SIDESLIP.

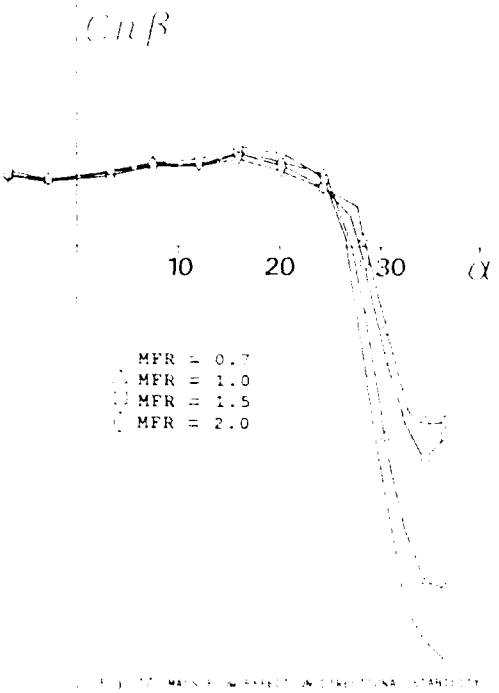

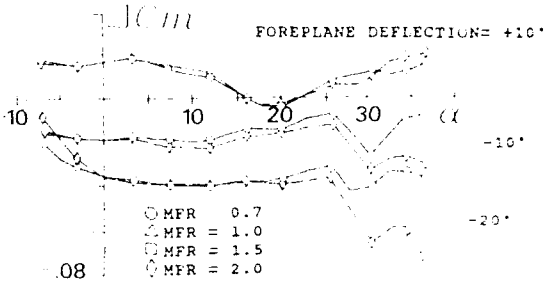

Fig. 19 MASS FLOW EFFECT ON FOREPLANE EFFECTIVENESS.

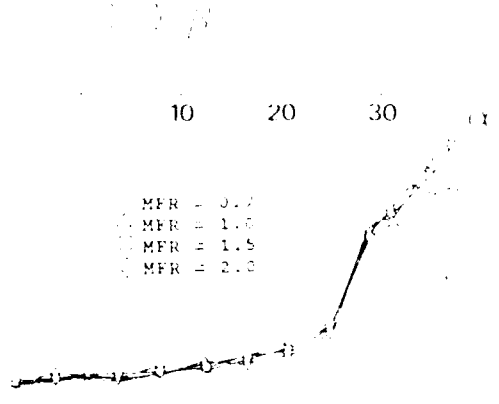

A Novel High-Performance System for Recording and Analysing Instantaneous Total Pressure Distortion in Air Intakes

K.W. Lotter and R.-D. Scherbaum
Messerschmitt-Bölkow-Blohm GmbH
Military Aircraft Division
P.O. Box 80 11 60
8000 München 80
Germany

SUMMARY

Instantaneous intake total pressure distortion parameters are generally used to assess aerodynamic intake/engine compatibility. Different distortion parameters are applied by the various engine manufacturers.

Distortion boundaries are specified which are not to be exceeded in the intake during the whole flight regime. The quantification of those parameters is generally made in intake wind-tunnel model tests. In these tests the instantaneous total pressure is measured in the Aerodynamic Interface Plane AIP (a short distance upstream of the engine compressor face) by high-response pressure transducers, typically installed on an eight-arm rake with five probes on each arm.

In the past, after having undergone the relevant signal conditioning process, the signals from the transducers were combined to the above-mentioned distortion parameters by the use of an analog computer. Later on, this was supplemented by limited digital analysis of the high-frequency signals. Because of the large amount of data, the digital analysis was only applied over a predetermined short time period.

The evolution of high-performance digital data storage facilities combined with highspeed analog-digital conversion now allows a major step forward to longtime digital recording and analysis during intake distortion tests.

The novel system that has been installed at MBB and successfully applied during various intake wind-tunnel test campaigns is described in this paper. Dynamic signals from up to 144 high-response differential transducers can be recorded. Individual control lines are used for sensing, power supply and in-situ calibration. A specially configured computer system is used to control the signal frequency band, the number of sign' channels, the control lines and the sample rate. The computer is also used to control the storage of the digitised data on an advanced high density tape recording system that allows continuous recording of up to 1 hour on a cassette tape. The data rate for tape storage is as high as 107 Mbits/s.

Parallel to this storage process it is possible to calculate, in an on-line real-time mode, the desired instantaneous distortion parameters using an analog computer. For recording times of up to 5 seconds for each data point, digital on-line analysis is also possible. The data can be displayed on a screen and are also plotted during the test, thus allowing the test engineer to react quickly and alter or adapt the test programme.

Typical results from tests with different intake models in various wind-tunnel facilities are presented. The effect of digitisation rate and recording time on the error of the calculated instantaneous distortion parameters is shown.

LIST OF SYMBOLS

A/D, ADC	analog-digital converter
AIP	Aerodynamic Interface Plane
bpi	bits per inch
CPU	central processor unit
CSS	channel sample selector
DACP	data acquisition control processor
D/A, DAC	digital-analog converter
$DC60_{SS}$	steady-state distortion parameter
$DC60_{TA}$	time-average instantaneous distortion parameter
$DC60_{TV}$	time-variant instantaneous distortion parameter
DCRSi	digital cassette recorder system
DLR	Deutsche Forschungs- und Versuchsanstalt für Luft- und Raumfahrt
DVM	digital voltmeter
FM	frequency modulation
H	steady-state total pressure, referred to tunnel total pressure
H_{60}	steady-state total pressure averaged over 60° sector and referred to wind-tunnel total pressure
H_I	instantaneous total pressure, referred to wind-tunnel total pressure
$H_{I\ 60}$	instantaneous total pressure averaged over 60° sector and referred to wind-tunnel total pressure
H_{mean}	average total pressure, referred to wind-tunnel total pressure
KH	instantaneous total pressure, referred to wind-tunnel total pressure
KP	instantaneous static pressure, referred to wind-tunnel total pressure
MC	MassComp
MUX	multiplexer
O/B	outboard
P	static pressure, referred to wind-tunnel total pressure
Q_{AIP}	dynamic pressure in AIP, referred to wind-tunnel total pressure
R	duct radius
RAE	Royal Aerospace Establishment
RC	remote control
RMS	root mean square
SID	Side-wash angle, i.e. swirl angle
S/H	sample-and-hold
T_{RMS}	total pressure turbulence factor (root mean square)
UP	upwash angle, i.e. radial angle

1. INTRODUCTION

The stability characteristics of high-performance turbofan engines are adversely affected by distorted intake flow. Intake/engine aerodynamic compatibility, therefore, continues to be a major issue during design and development of a new aircraft. A great deal of progress has been made during the last two decades on the technical aspects of the intake/engine compatibility problem. A consensus has been reached on the elements needed to formulate empirical total pressure distortion parameters or descriptors at the intake/engine Aerodynamic Interface Plane (AIP), see Fig. 1. A methodology for the treatment of time-variant, spatial total pressure distortion has been consolidated into general practical engineering guidelines (Refs. 1 and 2). Other forms of intake flow distortion, such as swirl have also been identified and treated (Ref. 3).

Wind-tunnel tests with scaled intake models are generally used to measure flow distortions in the AIP and to assess intake/engine compatibility based on relevant compatibility parameters to be mutually agreed between aircraft and engine manufacturer.

Early work aimed at improving engine stability correlations was based on the use of spatially-averaged root mean square (RMS) total pressure turbulence levels. While correlations improved, these were far from satisfactory. Developments have subsequently shown that the major stability features of turbulence-induced distortion can be described as an extension of steady-state distortion concepts to a time-scale of the order of one rotor revolution, typically 5 milliseconds, i.e. 200 Hz. This has meant that sophisticated data acquisition and processing techniques utilising high-response instrumentation and analog/digital computation have been developed to handle the enormous quantities of data involved.

Ten to fifteen years ago, pure analog data processing was applied. Later on, peak detectors and digital handling of peak distortion levels were incorporated.

Although a digital computer requires more time to perform complex problems, an analog computer requires more computational elements or hardware. For complex operations, an analog computer will be less flexible for computational and input changes, such as inlet rake configurations, especially if it has been hardwired. Another drawback of the analog computer is its reduced accuracy. Thus, analog computation was later applied for data sorting and data screening only while digital computation was used on selected segments identified by the less accurate analog analysis.

With the evolution of high-performance digital computers and the resulting possibility of storing huge quantities of data, purely digital data handling during instantaneous intake distortion measurement and analysis became possible.

In this paper, a novel all-digital processing system with improved accuracy and flexibility is described. This Digital Signal Processing (DSP) System has been established at MBB, Military Aircraft Division. It was successfully applied in a number of intake wind-tunnel tests during the European Fighter Aircraft (EFA) development phase.

2. INTAKE/ENGINE AERODYNAMIC COMPATIBILITY ASSESSMENT

2.1 The Aerodynamic Interface Plane

The inlet/engine Aerodynamic Interface Plane (AIP) is the instrumentation station used to define total pressure recovery and distortion interfaces between the inlet and the engine (Fig. 1). This plane, typically located a short distance upstream of the engine compressor face plane has to be mutually agreed between airframe and engine manufacturer and should be maintained for all investigations from wind-tunnel test through rig test to flight test to facilitate comparison of the results from the different data sources.

2.2 Distortion description

A major compatibility goal is the development of sufficiently general numerical descriptors or indices, which would enable all major aspects of distortion shape, intensity, etc. affecting the engine surge pressure ratio to be correlated with minimum scatter. The evolution of distortion descriptors and their components from those reviewed in AGARD LS 72 (Ref. 4) has stemmed from an engineering consensus derived from a thorough co-operative effort involving a great deal of experience in application. While no universal parameter has emerged or is thought possible for the general distortion case, agreement has been reached on the elements of a general parameter defined from pressure-probe measurements in the intake. Four basic elements have been recommended:

Circumferential Intensity, Extent and Multiple-Per-Rev Elements, defined at constant radius (per ring), and a Radial Intensity Element (Ref. 5).

A typical plot of instantaneous total pressure pattern from an intake model test is shown in Fig. 2. The aircraft manufacturer still has to cope with different distortion descriptors, depending on which of the four major engine manufacturers in Europe and the USA is involved in the aircraft development.

Each engine manufacturer has established empirical correlations (Fig. 2) between a relevant distortion parameter and the loss in compressor surge pressure ratio.

In Fig. 3, three different circumferential total pressure distortion parameters derived from a typical measurement during an intake model test are shown:

time-variant ($DC60_{TV}$), time-average ($DC60_{TA}$) and steady-state ($DC60_{SS}$) distortion.

The time-variant parameter, although widely used for compatibility assessment, does not reflect planar wave or "in-phase" pressure disturbances. These disturbances are covered by the time-average paramter $DC60_{TA}$.

Another essential parameter, especially for engines without inlet guide vanes is intake swirl (Ref. 3). A typical flow pattern with the appertaining swirl angles at 87% of the duct radius is shown in Fig. 4.

2.3 Instrumentation in the Aerodynamic Interface Plane

For precise definition of distortion it is desirable to have as many total pressure measurements as possible. However, practical considerations, such as duct blockage, rake-induced turbulence, transducer costs, and limitations on the number of high-frequency transducers that can be measured by the data acquisition system, restrict the number of measurements.

As desribed in Refs. 1 and 2, a rake configuration with 40 probes, located area-weighted on 8 equally spaced rake arms has been recommended as an acceptable compromise.

The AIP rakes routinely used at MBB are shown in Fig. 5. At top left of the illustration the rake for instantaneous pressure measurement is shown. It comprises 8 equally spaced arms with 5 high-response transducers each (filled symbols). As only the AC component of these transducers is used, steady-state probes (open symbols) are placed adjacent to the high-response differential transducers. For a more accurate measurement of intake internal performance (pressure recovery), 8 additional rake arms with 5 steady-state pitot probes are placed between the high-response rake arms, the support strut of these rakes being axially staggered to reduce flow blockage. The installation of the high-response transducers is shown in the lower half of the illustration. The probe head is internally chamfered (15°) to cope with flow misalignment and the transducer is shielded by a screen against particle damage.

4 high-response wall pressures and 16 steady-state wall pressures are measured along the duct circumference in the AIP.

At top right of the illustration the rake for measurement of flow angularity is shown. It comprises 8 arms with 3 five-hole probes and 4 pitot probes each. Again, 4 high-response wall pressure taps and 16 steady-state wall pressure taps are installed, the same as on the instantaneous pressure rake. The swirl rake can be remotely rotated by 22.5° to increase the number of measurement points in the AIP.

2.4 Essential intake flow parameters to be measured

During intake testing, measurement of a considerable number of steady-state and instantaneous pressures is involved (see Fig. 5). In addition to these rake measurements pressure pick-ups are located at the forward intake, in the intake diffuser, at the exit mass flow rakes etc. resulting in some 900 to 1000 steady-state pressure pickups and some 80 to 100 high-response transducers. These measurements, especially those for instantaneous content, result in a huge amount of data to be processed and converted to engineering parameters (Fig. 6). The essential intake flow parameters to be assessed for intake/engine compatibility, internal performance and intake structural integrity are:

- Steady-state and instantaneous distortion (type of parameter depending on engine manufacturer involved)
- Total pressure turbulence factor T_{RMS}
- Intake swirl
- Pressure recovery
- Steady-state and dynamic loads

In sophisticated intake wind-tunnel models such as those required during the development phase of an aircraft for the purposes of intake/engine compatibility demonstration and flight clearance, all the above-mentioned parameters are measured simultaneously, which makes good sense with a view to reducing costs and aircraft development time.

This requires processing of a huge amount of data that is involved in digital handling of high-frequency signals.

3. DESCRIPTION AND FEATURES OF THE DIGITAL SIGNAL PROCESSING SYSTEM

The need for short times between the individual test phases and the high costs of operating large high-speed wind tunnels demand that the large amount of data is quickly processed and displayed already during the test campaign to allow test program alterations and optimisations at an early stage. For this purpose a novel Digital Signal Processing (DSP) System has been established which will be described in the following.

3.1 System arrangement

The elements of the DSP system are shown schematically in Fig. 7. The system not only takes over the pneumatic and electric signals from the wind tunnel for transfer to various front ends of the digital data processor to convert them into engineering units for final display on screens and storage on disc and cassette tape but also fully automatically controls the whole test sequence, the sensor calibrations and the signal conditioning. In addition to the full digital data processing and signal storage, analog computing and analog data output is still maintained to facilitate monitoring of the digitisation process and to direct the digital analysis.

An example of a system arrangement as used during air intake wind-tunnel testing is given in Fig. 8. It is capable of simultaneously handling up to 144 high-frequency transducer signals. The system was made possible by the evolution of an advanced digital cassette tape recorder (Ampex DCRSi, see centre of Fig. 8) with a data flow rate of up to 107 Mbits/s and one hour continuous operation resulting in a storage capability of 47.3 GBytes. Simultaneous data flow of the high-response transducers is possible through five different system routes, after signal conditioning and both low-pass and high-pass filtering have been performed:

a) through a sample-and-hold unit and a digital multiplexer (12 bit word) directly to the digital processor incorporating 3x 1 Msamples/s units for immediate analysis and storage

b) through a sample-and-hold unit (12 bit word) with a digitisation rate of up to 200 ksamples/s for each channel to the Channel Sample Selector (CSS) and directly to the digital cassette recorder DCRSi for later detailed analysis by the digital processor

c) to the 40 channel Analog Computer which can be inserted behind the filters or, as shown in Fig. 8, after the Channel Sample Selector

d) to two synchronized 24 channel FM recorders serving as a back-up system for selected analog signals

e) to the RMS Converter for total pressure turbulence evaluation.

All sub-units are linked to the digital processor by suitable interface units, the processor also controlling the complete data flow procedure. The display units and data storage capabilties are shown on the right-hand side of Fig. 8.

The lower end of Fig. 8 shows the data flow from all the steady-state pressure scanner units (i.e. 960 individual pressure taps) through an optical interface to the digital processor. The individual sub-systems of the complete arrangement are described in more detail in the following chapters.

The essential feature of the DSP system is the high data flow rate for both the DCRSi cassette recorder and the special digital processor configuration incorporating an A/D converter system, a vector processor and a floating point processor. This configuration allows on-line data recording and analysis and thus a considerable reduction in wind-tunnel running time and cost.

3.2 Detailed description

3.2.1 Signal conditioning unit

The signal conditioning unit is shown in Fig. 9. It essentially comprises three sub-units, i.e.

- power supply
- signal gain and zero setting unit and
- transducer calibration unit.

To supply the transducers with stable power, a transformer with rectifier is applied. In order to reduce the number of power lines to the wind-tunnel model, common power lines with sense lines are provided. Seven controlled systems with a sensed voltage range from 5 V to 16 V and a performance of 300 mA for each system are installed.

An auto-calibration module was designed for retro-fit to the Preston wide-band floating differential amplifiers. The retro-fit unit incorporates

a) an automatic zero-setting by generating a DC offset correction voltage which is fed into the buffer amplifier and

b) a gain setting unit to provide a unified sensitivity range for all transducers.

The transducer calibration unit represents an automated system which generates the reference and calibration pressure levels for the pressure controller, the PSI (electronic multi-pressure scanner) system and the differential transducers. An electric switch is incorporated behind all steady-state and high-response pressure transducers to allow change-over from test mode to calibration mode. During the calibration mode, all transducers are supplied with defined reference pressures for in-situ calibration before and after the test segments. Pressure supply is accomplished by two individual HYCO pump systems.

3.2.2 Filters

To avoid antialiasing effects and to tailor the frequency range to the test requirements the high-frequency signals can be filtered via 48 dB Bessel low-pass filters. Programmable cut-off frequency ranges are incorporated ranging

from 10 Hz to 2550 Hz in steps of 10 Hz or
from 100 Hz to 25500 Hz in steps of 100 Hz

For the intake tests performed also high-pass filtering with 12 dB Bessel filters and a cut-off frequency of 0.25 Hz was applied to eliminate the DC component of the transducer signal.

3.2.3 Channel Sample Selector

The Channel Sample Selector (CSS) has been specially developed for the DSP system (Fig. 10). This unit enables up to 128 channels to be digitised (12 bit word resolution) and serially transferred with sample-and-hold units at a rate as high as 100 Mbits/s to the Digital Cassette Recorder (DCRSi). For data transfer, preselection of the sample rate in 9 different steps, ranging from 3 to 200 ksamples/s for each channel (Fig. 11) is possible, the choice being dependent on the required signal resolution and the number of channels to be recorded. For the 40 signals from the AIP distortion rake D/A conversion for 40 analog outputs is possible. This is to allow an immediate check that the essential signals have been correctly stored and to enable the analog computer to make distortion descriptor calculations, as already mentioned in Fig. 8. The signals digitally stored on the DCRSi can later on be used for any type of a more detailed analysis. The whole data flow is then again controlled by the MC 6700 central processor. However, manual control of the CSS is also possible. By this means test execution and data storage on the DCRSi is possible without using the MC 6700 data processor at the wind-tunnel site. This is preferable when only small test campaigns are to be executed.

3.2.4 Digital Cassette Recorder (DCRSi)

The Digital Cassette Recording System (DCRSi), see Fig. 12, with solid state memory emulation is a one-inch transverse rotary digital recorder with a cassette capacity of 47.3 GBytes. It is capable of recording and reproducing digital data at any user rate ranging from zero up to 107 Mbits/s. The recording time is one hour at 107 Mbits/s, equivalent to 8 hours at 13.735 Mbits/s or 107 hours at 1 Mbit/s. A sophisticated error correction system is incorporated which reduces the bit error rate to $1 \cdot 10^{-7}$.

3.2.5 FM video tape recorder

Two 24-channel RACAL recorders (Fig. 13) with a synchronisation unit and using standard 1/2 inch VHS video cassette tapes can be used as back-up system. The recording time is 7.5 minutes at 30 in/s tape speed (tape E240). The frequency range for each data channel is up to 100 kHz at 30 in/s tape speed. Remote control with RS232 is applied.

3.2.6 Analog computer with peak detector

The analog computer (Fig. 14) with peak detector is programmed to calculate, in the on-line real-time mode, the time-variant and time-average distortion parameters ($DC60_{TV}$ and $DC60_{TA}$) and to detect the peak value during the test. Its integration into the DSP system is possible in the way shown in Fig. 8, when monitoring of the digitisation process and directing of the digital analysis is desired.

Fig. 14 shows the arrangement when only analog computation is envisaged. The 40 high-frequency and already filtered analog signals from the AIP rake are then directly transferred to the analog computer. The required steady-state data from the AIP rake as well as the wind-tunnel flow parame-

te 3 are supplied via the MC6700 processor by the use of the multiprogrammer with D/A conversion.

Within the analog computer a peak detector is installed. Peak distortion values are then converted to digital data and transferred to the MC6700 processor for final plotting and storage.

The peak detector scheme is shown in Fig. 15. The distortion parameters, produced by analog computation pass two peak detectors which overlap each other by 50 ms. The peak value detected by either of these detectors is then selected by the digital processor. Overlapping is provided to prevent signals from being lost during the peak detector switching process.

3.2.7 RMS Converter

Total pressure turbulence data from the AIP and other locations represents further essential information in the assessment of intake/engine compatibility.

The 80 channel RMS converter (Fig. 16) has been specially configured to simultaneously calculate 80 RMS values during the test. This highspeed processor provides on-line evaluation of the 80 channels during the test without the need for the prolonged testing time required in the case of consecutive RMS calculation.

The RMS converter uses operational circuitry to convert AC signals to DC data. Sample and hold units store the data and a multiplexing system transfers the data to the MC6700 processor.

3.2.8 Masscomp processor MC6700

The MC6700 configuration is depicted in Fig. 17. It allows on-line real-time continuous simultaneous high-speed data acquisition and control of the whole DSP system.

Three MC 68030 central processor units with floating point processor, lightning, vector processor and three bus systems, (memory bus, multibus, Std$^+$ bus) are incorporated. Three terminals with individual processors and a high-resolution graphic system with on-line data display are available. A 2 GByte disc and a 2 GByte streamer are installed. Data transfer at a rate of 5.4 MBytes/s to a 43 GByte video tape is possible. The operating system is enhanced real-time UNIX with FORTRAN 77 and C compilers. The data rate that can be processed by the MC6700 system and sample-and-hold unit is of course dependent on the number of data channels (Fig. 18). A maximum sample rate of 500 ksamples/s is possible for up to 3 channels, when using 3 DACPs with sample-and-hold. For 96 channels (3x32 channels) the data rate is still as high as 30.3 ksamples/s per channel.

4. SYSTEM APPLICATION

The DSP System in its present configuration has been successfully applied in 3 test phases with a 1:10 scale intake model and in 4 test phases with a 1:7 scale intake development model of the European Fighter Aircraft (EFA). Fig. 19 shows the 1:7 scale model in the 8ft supersonic wind tunnel of RAE Bedford, United Kingdom. The AIP rake for measurement of instantaneous distortion is depicted in Fig. 20. The model incorporates 877 steady-state and 68 high-response pressure taps and an internal six-component straingauge balance. The inboard arrangement of the model with its comprehensive instrumentation can be seen in Fig. 21, which shows the model, shells removed, in the low-speed wind tunnel of DLR Braunschweig, Germany.

The DSP System was used not only for the recording and evaluation of all signals, especially for the instantaneous distortion analysis, but also for control of the test sequence and the movable model parts such as foreplane, rotatable AIP swirl rake and the two cone plugs used to throttle the intake mass flow.

5. DATA PRESENTATION

For quick decisions during the test phase, immediate data reduction and data presentation is possible by means of the DSP System. A wide range of data plot forms has been provided within the system's software. Any of these plots can be provided for the test engineer upon special request.

Some typical examples of data plots are presented in Figures 22 to 25. In Fig. 22 the presentation of instantaneous distortion is shown. The left-hand diagram shows the instantaneous total pressure versus time in the AIP (upper curve) and in the 60° AIP sector having minimum average pressure. These data are used, together with the relevant steady-state data, to calculate the $DC60_{TA}$ distortion index (right-hand diagram). Also shown is a plot of the reduced variate of $DC60_{TAmax}$ which allows a prediction of the maximum instantaneous distortion level for extended observation times.

Typical AIP total pressure contour plots with indication of those 60° sectors having minimum pressure are shown in Fig. 23 for turbulence, instantaneous and steady-state total pressure.

The essential intake parameters required for assessment of internal performance and intake/engine compatibility are presented in Fig. 24. Here, pressure recovery, distortion, mean swirl and turbulence factor are plotted versus intake mass flow ratio.

Plots of flow angularity in the AIP, derived from measurements made with the 5-hole probes, can be produced in various forms. A typical example is shown in Fig. 25.

6. EFFECT OF RECORDING TIME AND DIGITISATION RATE ON DISTORTION INDEX

An available database, with a frequency content of up to 2 kHz, recorded at a digitisation rate of 80 ksamples/s for an observation period of 30 seconds per test point, allows an investigation to be made into the loss in accuracy when a reduced digitisation rate and shorter time periods are applied.

In Fig. 26 the effect of recording length on $DC60_{TA}$ is shown for test data from a supersonic test and a static test with high and low digitisation rate. A data recording length of 30 seconds was used as the reference against which the shorter recording lengths were compared. It can be seen that a rapid reduction in error is achieved when the recording length is increased from a few seconds to about 10 seconds. While the error in the distortion index for short recording times is high (15% and above), the error for 10 seconds recording time is only between 1% and 6% relative to the 30 seconds reference.

The loss in accuracy of the distortion index due to a reduced digitisation rate is shown in Fig. 27 for the two distortion indices $DC60_{TV}$ and $DC60_{TA}$. With a digitisation rate of 5 ksamples/s for the individual signals the error relative to 80 ksamples/s is of the order of 3%. A digitisation rate of 20 ksamples/s reduces the error to 1% or less for the distortion indices considered. This suggests that a digitisation rate that is 5 times higher than the highest recorded frequency, (i.e. 5 x 2000 Hz) is sufficient.

Figures 26 and 27 suggest that a sufficiently long recording time improves the accuracy of the distortion index more than increasing the digitisation rate. Further investigations of the effect of recording times up to 2 minutes are presently being performed.

7. CONCLUSION

Measurement and analysis of intake flow distortion is a major issue in intake/engine compatibility assessment. A system has been described which allows all-digital data recording and distortion analysis for complex intake wind-tunnel models delivering a large quantity of high-frequency signals and steady-state data.

Although the system operates to a great extent in the automatic mode and with built-in failure detection systems, it should be mentioned that considerable care is required in editing and processing the data.

Automatic data processing is not really automatic. Great attention must be given to every detail of the data chain from the sensing probe to the output of the final result. This can only be achieved by skilled and experienced personnel.

8. ACKNOWLEDGEMENT

The authors gratefully acknowledge the work done by Messrs. W. Heil and R. Küttner from the wind-tunnel data reduction group and by Mr. A. Schmidt from the model instrumentation group during concept design and structuring of the DSP System. Without their ideas and contributions the realization and successful operation of that system would not have been possible.

9. REFERENCES

|1| Society of Automotive Engineers
Aerospace Recommended Practice, ARP 1420
Gas Turbine Engine Inlet Flow Distortion Guidelines, March 1978

|2| Society of Automotive Engineers
Aerospace Information Report, AIR 1419
Inlet Total-Pressure-Distortion Considerations for Gas Turbine Engines, Mai 1983

|3| F. Aulehla
Intake Swirl, a Major Disturbance Parameter in Engine/Intake Compatibility
ICAS-82-4.8.1

|4| R.G. Hercock and D.D. Williams
Aerodynamic Response
AGARD LS 72, Nov. 1974

|5| D.D. Williams
Review of current knowledge on engine response to distorted inflow conditions
AGARD CP-400, paper 1, Sept. 1986

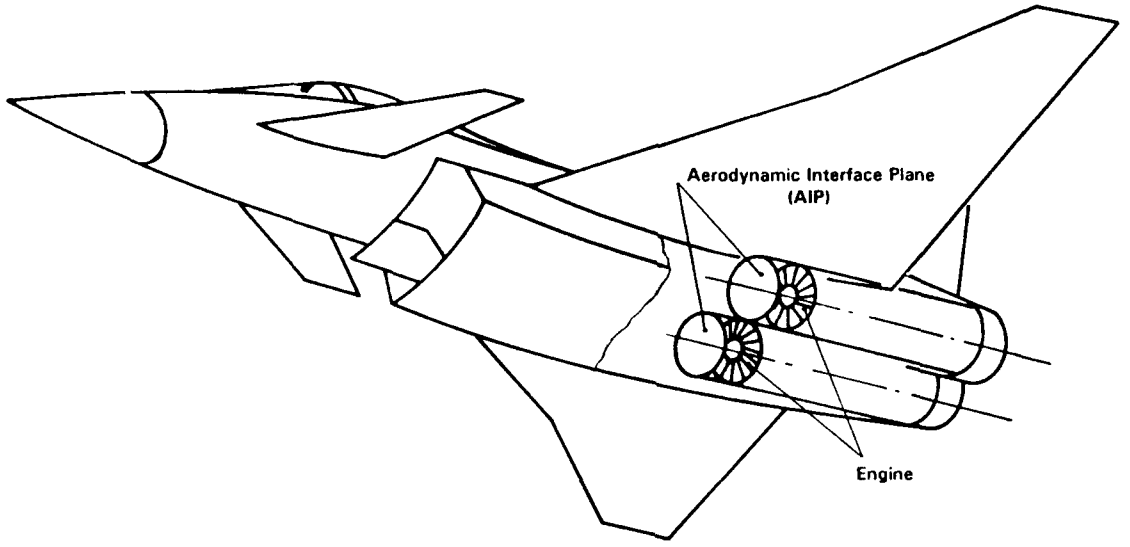

Fig. 1 The Aerodynamic Interface Plane

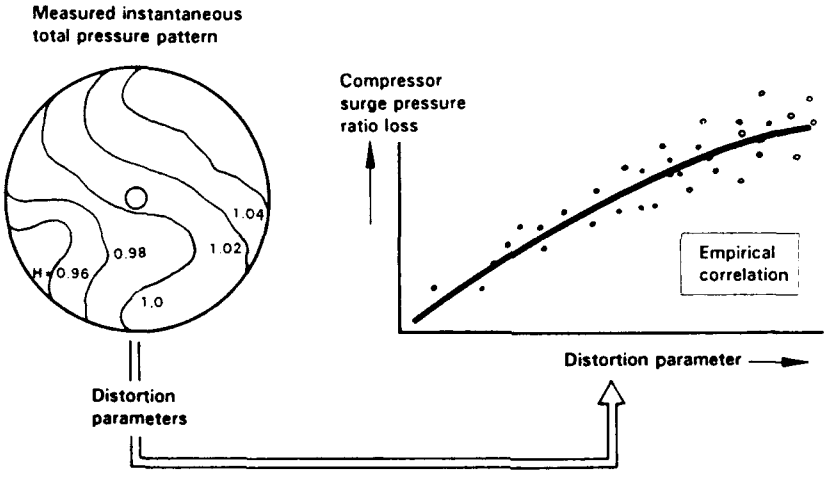

Fig. 2 Correlation of Distortion Parameter with Compressor Surge Pressure Ratio Loss

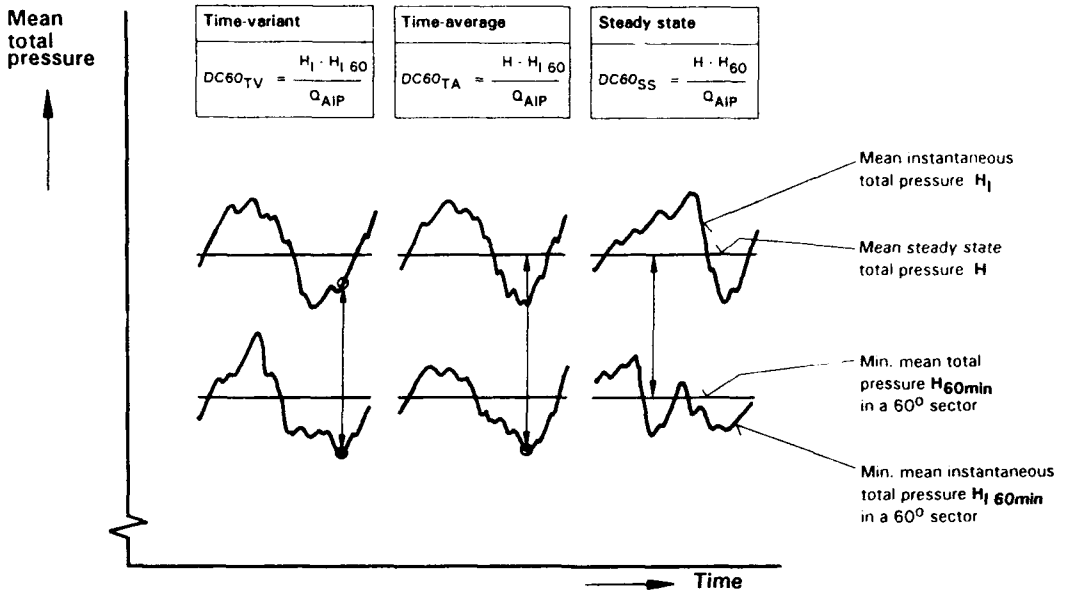

Fig. 3 Circumferential Total Pressure Distortion Descriptors

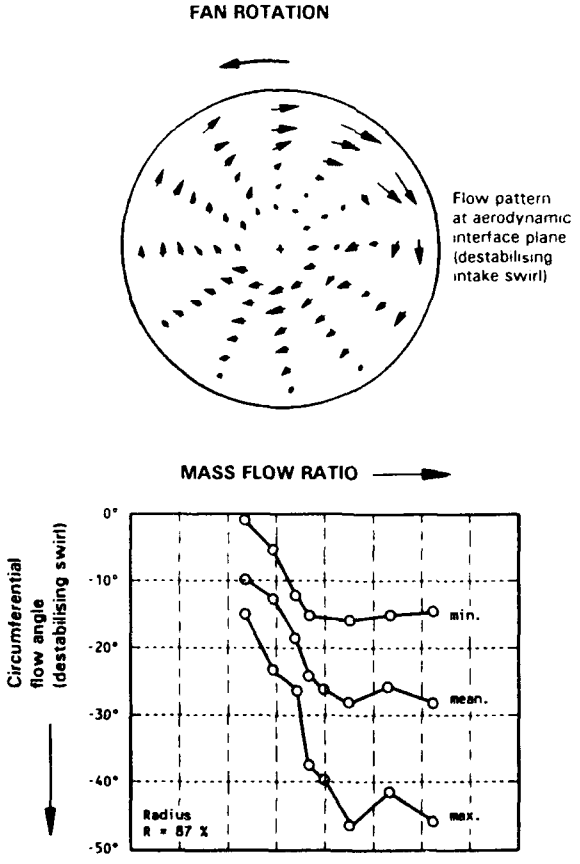

Fig. 4 Intake Swirl Pattern at AIP

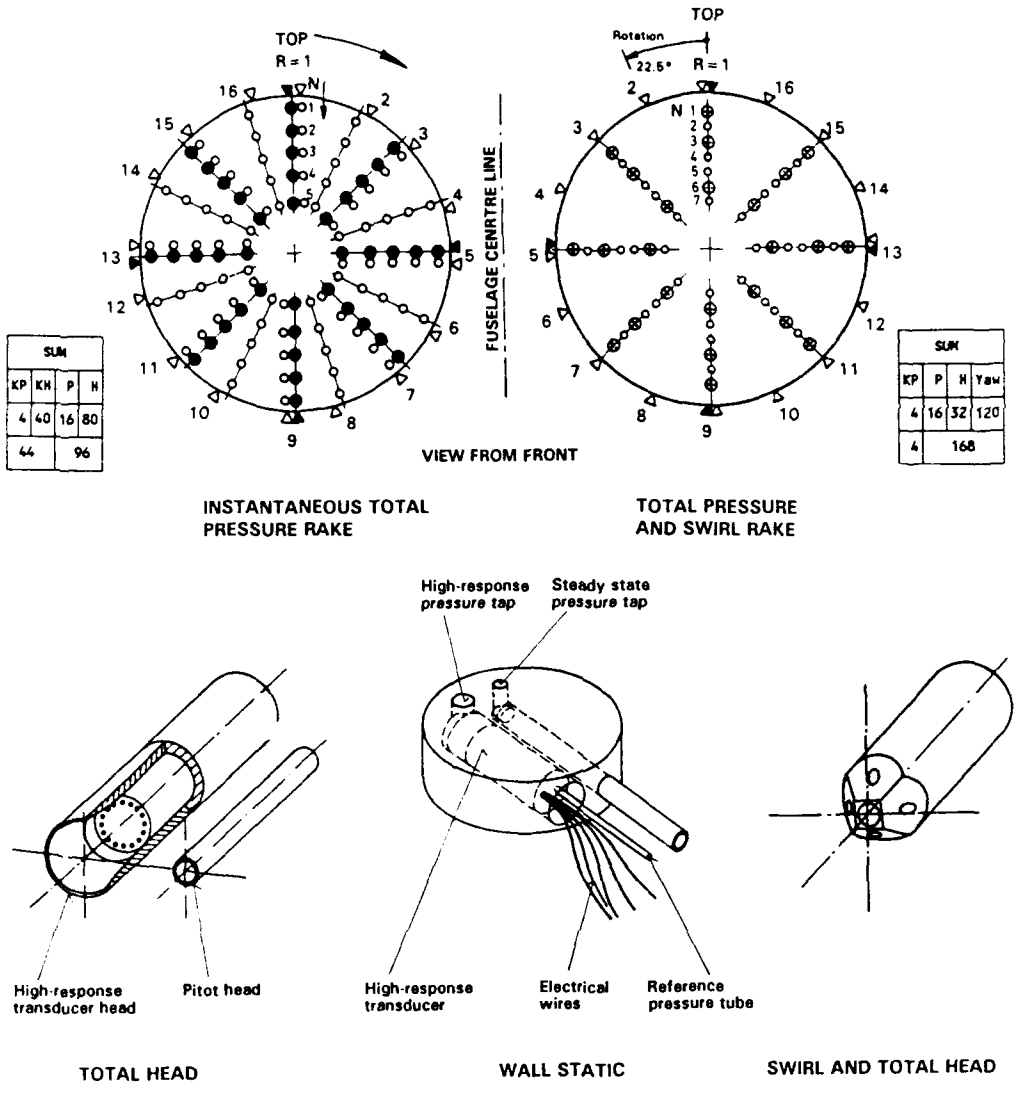

Fig. 5 Rake Arrangement and Pressure Probe Design

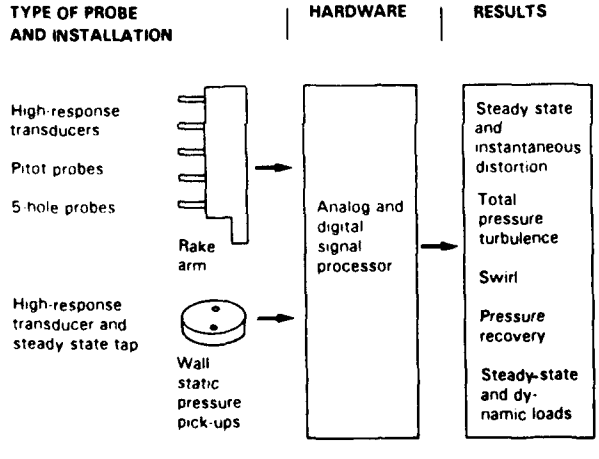

Fig. 6

Probes and Data Reduction System for Assessment of Intake Parameters

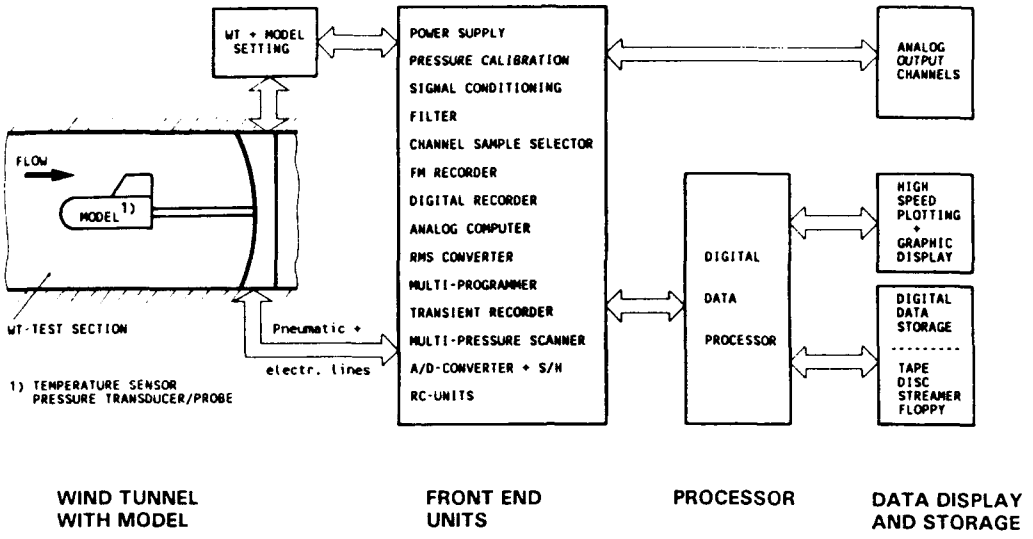

Fig. 7 Elements of Digital Signal Processing System

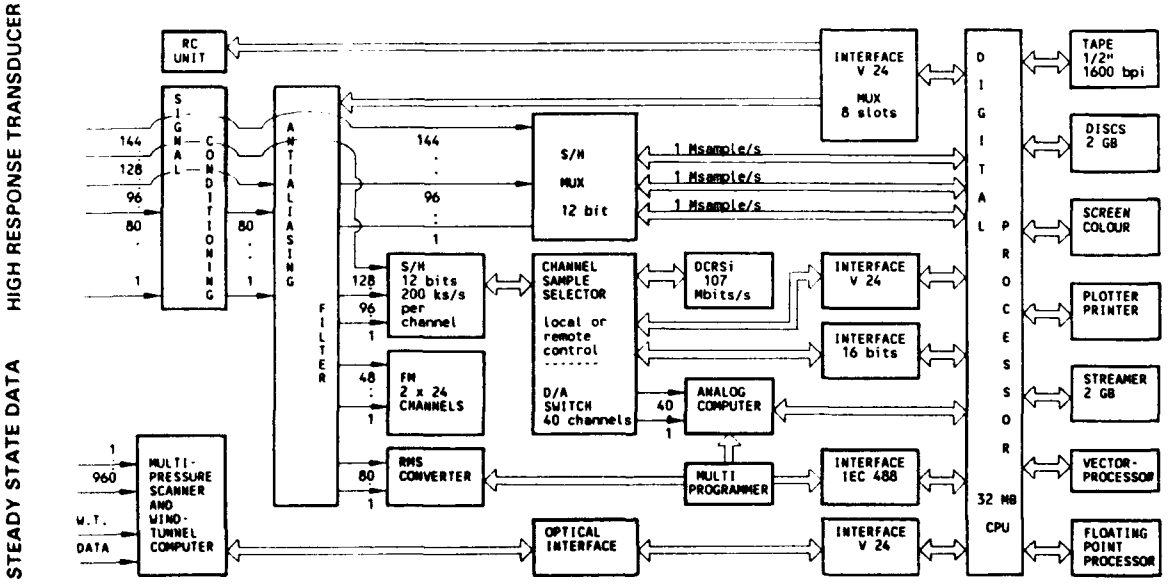

Fig. 8 Digital Signal Processing System

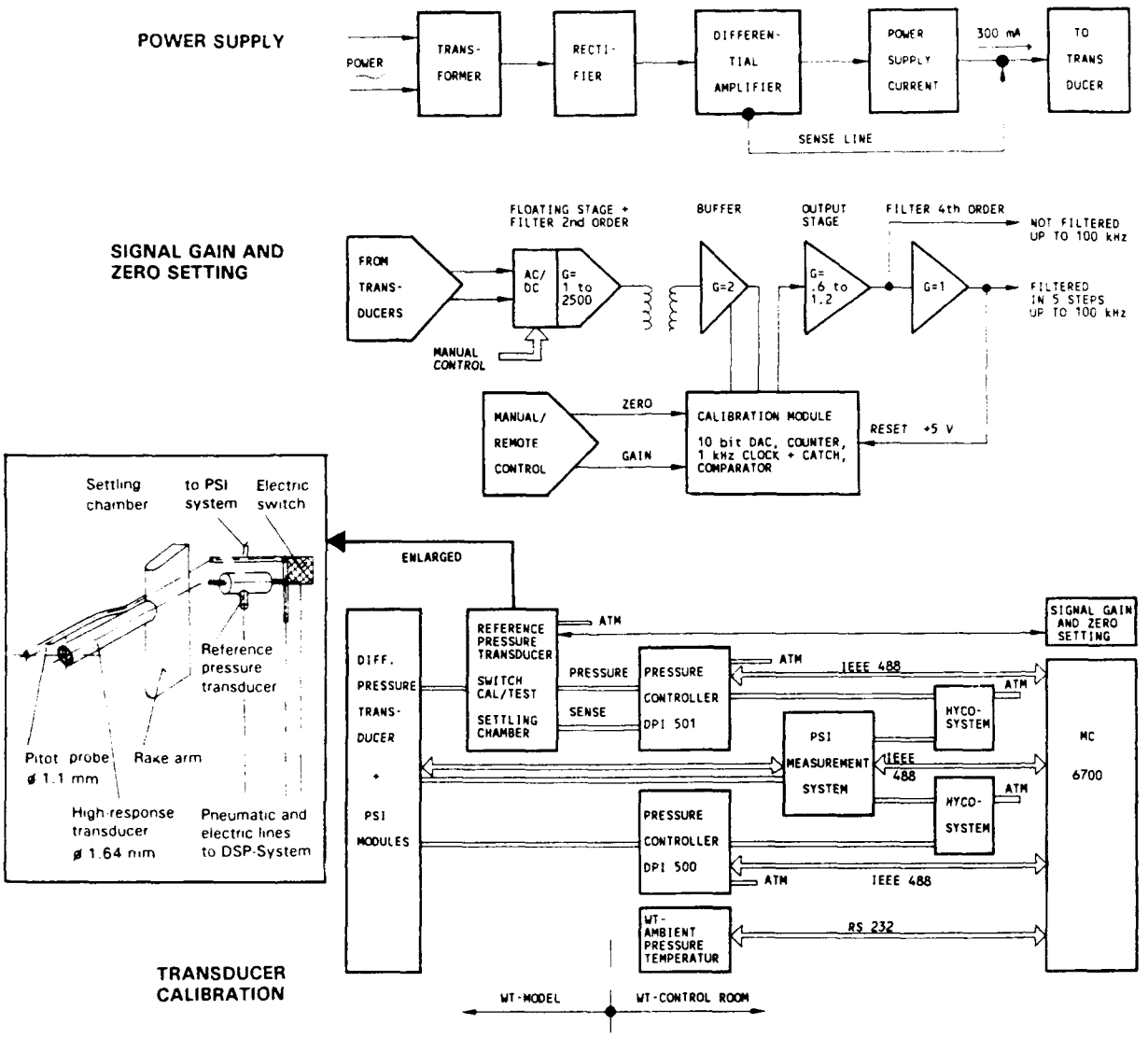

Fig. 9 Signal Conditioning

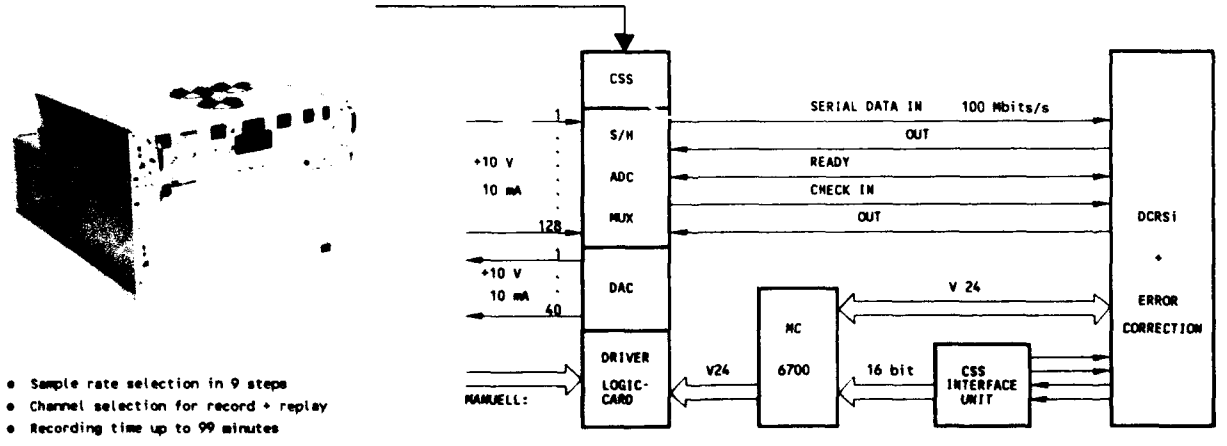

Fig. 10 Channel Sample Selector

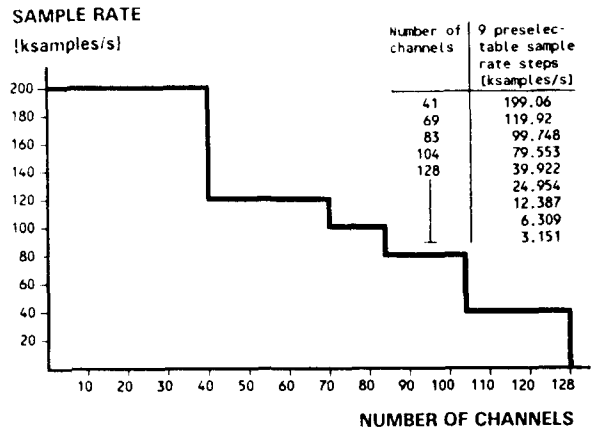

Fig. 11 Maximum Sample Rate Depending on Number of Channels - Channel Sample Selector

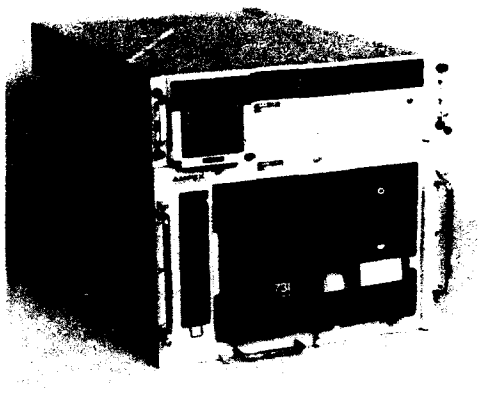

Fig. 12 Digital Cassette Recorder (DCRSi)

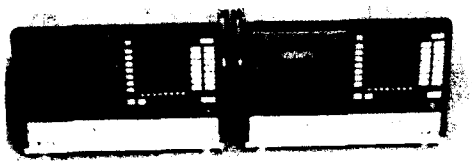

Fig. 13 FM Video Tape Recorder

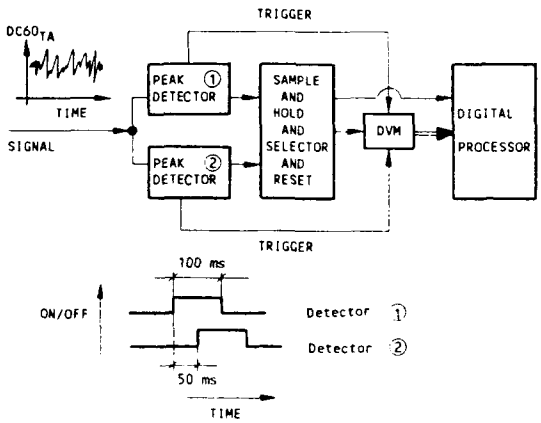

Fig. 15 Switch Sequence of Peak Detector

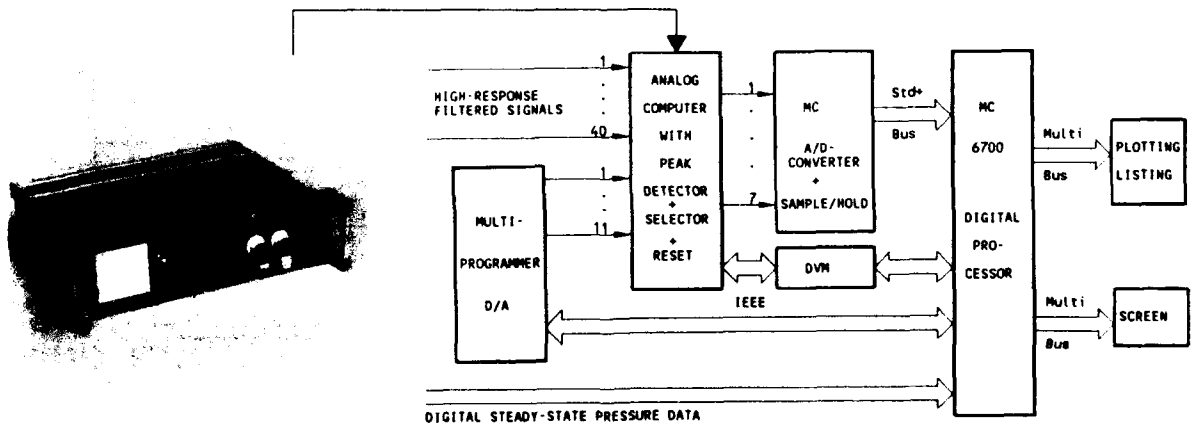

Fig. 14 Integration of Analog Computer into DSP-System

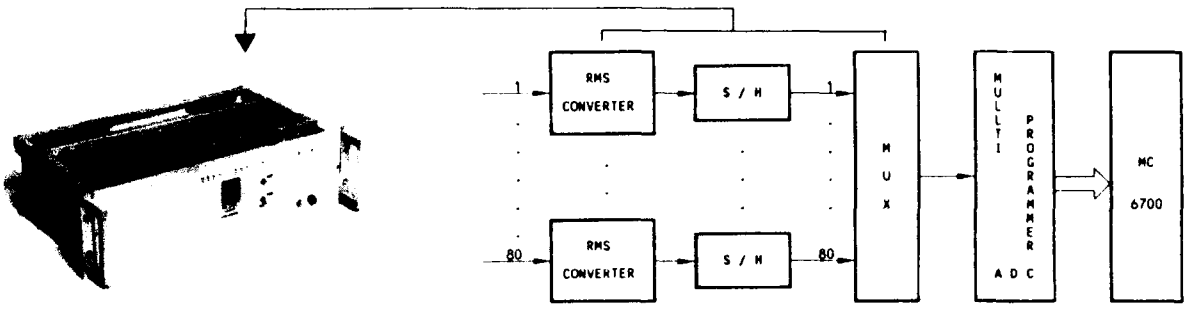

Fig. 16 RMS Converter

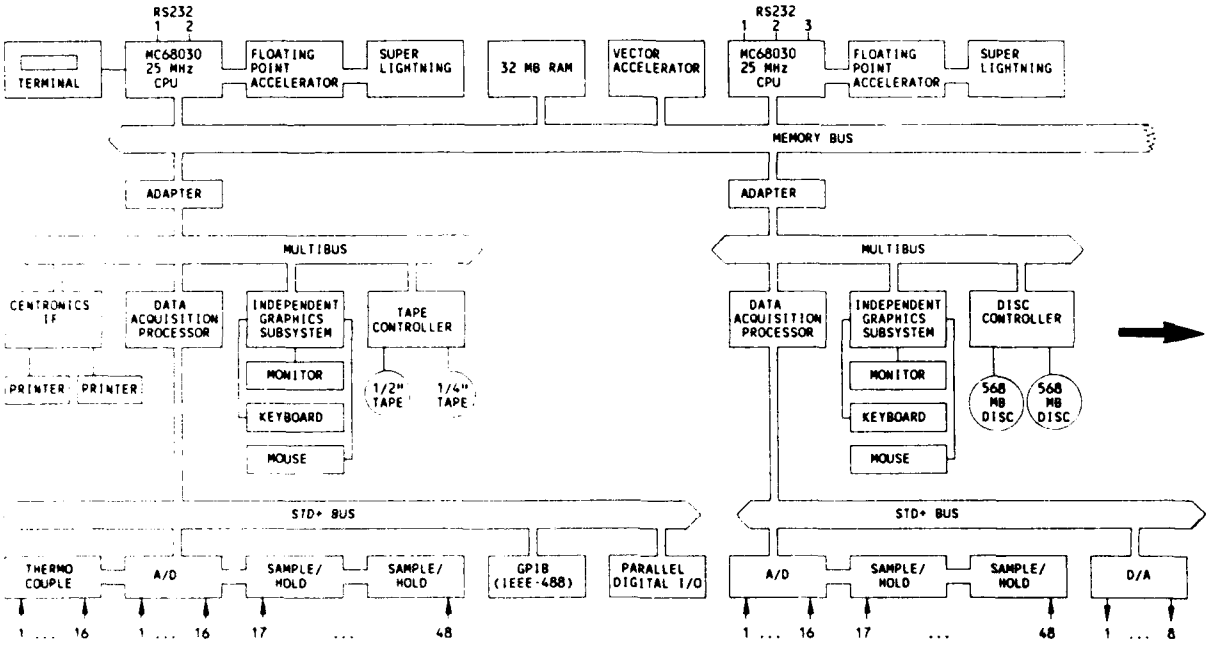

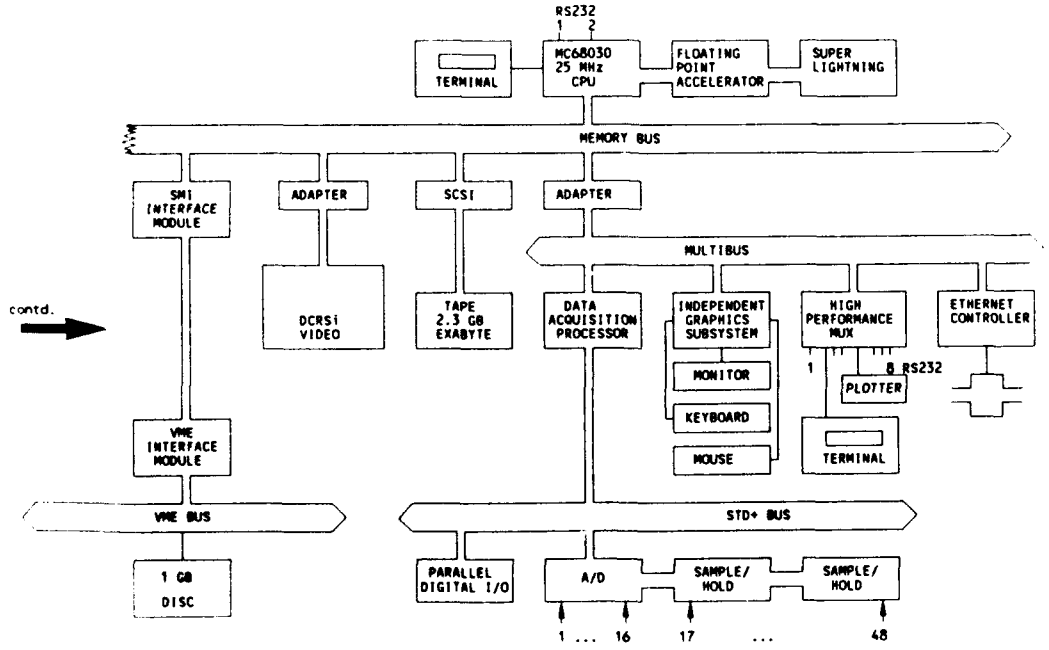

Fig. 17 Flow Chart MC 6700

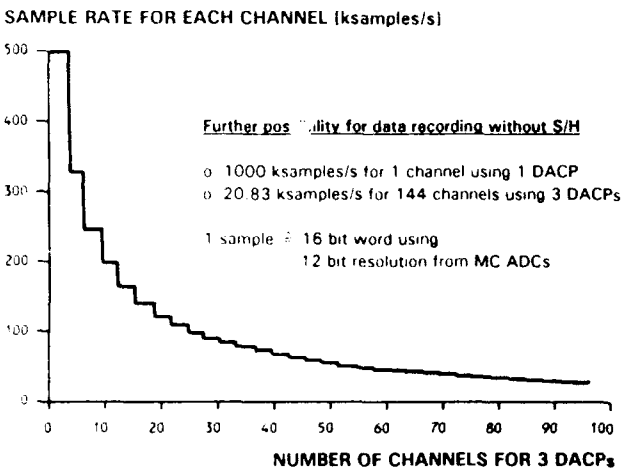

Fig. 18 Maximum Sample Rate for MC 6700 Depending on Number of Channels (S/H installed with 3 DACPs)

Fig. 19 EFA Intake Model in RAE 8 ft. Supersonic Tunnel

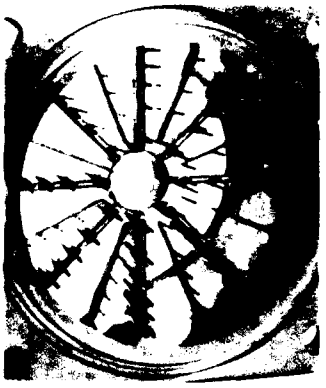

Fig. 20 Total Pressure AIP Rake for Instantaneous Distortion Measurement

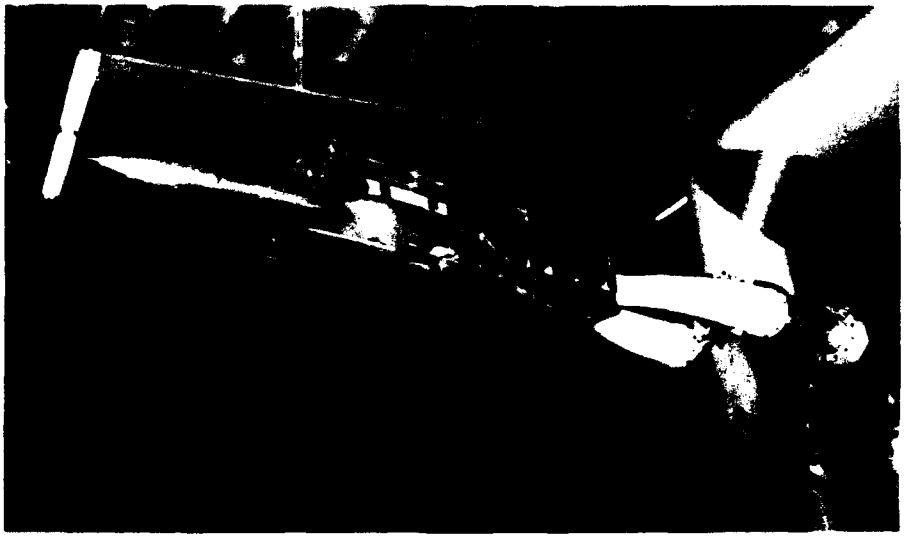

Fig. 21 EFA Intake Model in Low Speed Tunnel of DLR Braunschweig (shells removed)

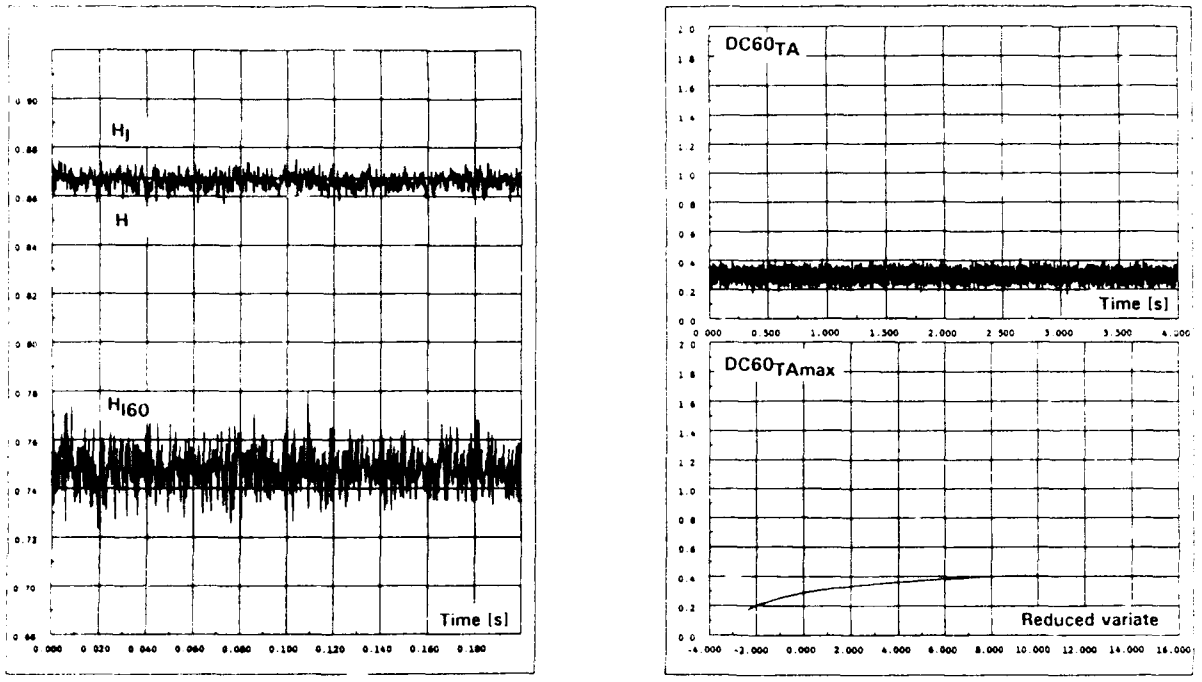

DISTORTION COMPONENTS

DISTORTION COEFFICIENTS

Fig. 22 Presentation of Instantaneous Distortion

TOTAL PRESSURE TURBULENCE

INSTANTANEOUS TOTAL PRESSURE

STEADY-STATE TOTAL PRESSURE

Fig. 23 Typical AIP Total Pressure Contour Plots for Turbulence, Instantaneous and Steady-State Data

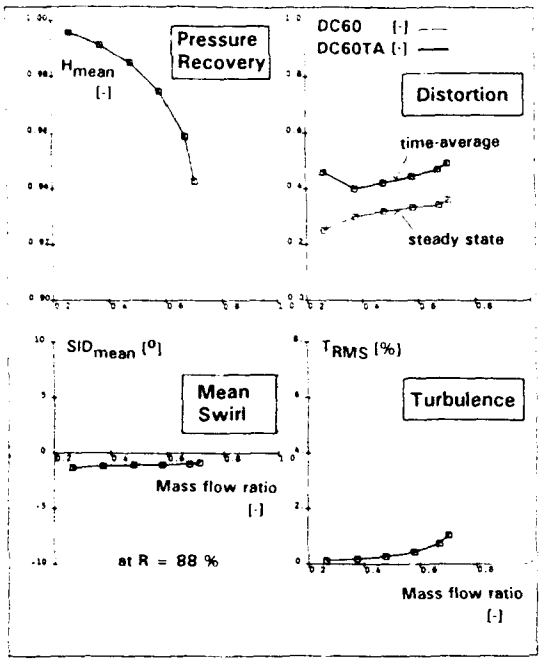

Fig. 24 Typical Plot of Essential Intake Flow Parameters

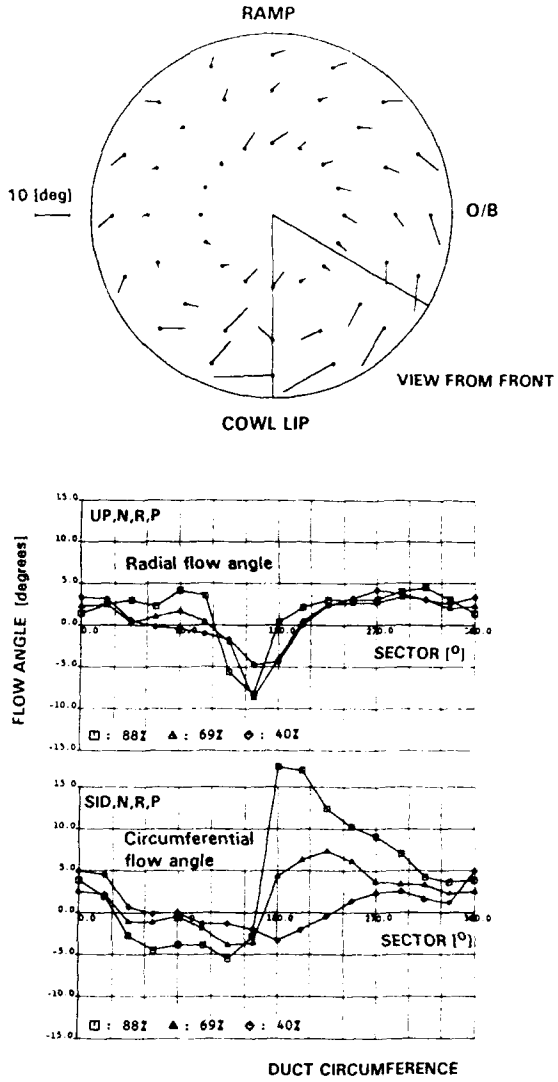

Fig. 25 Typical Plot of Flow Angularity

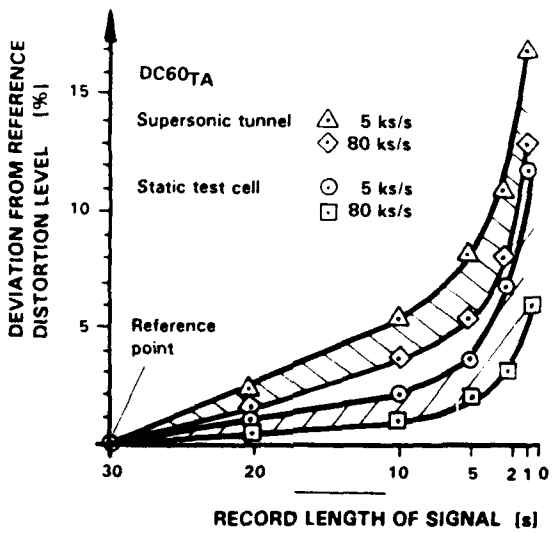

Fig. 26 Effect of Record Length on Distortion Level Deviation

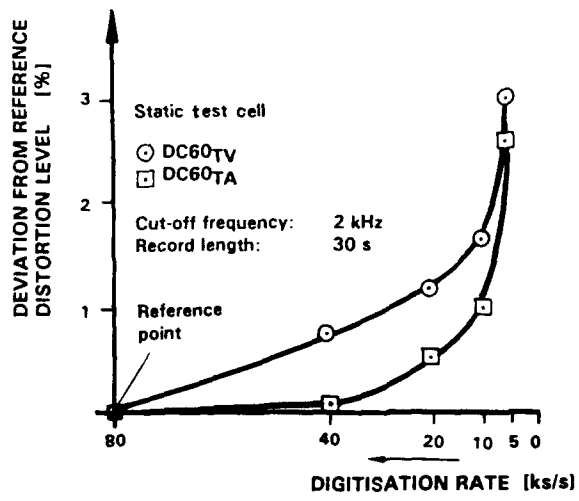

Fig. 27 Effect of Digitisation Rate on Distortion Level Deviation

WATER TUNNEL STUDIES OF INLET/AIRFRAME INTERFERENCE PHENOMENA

R.Maggio
Aermacchi S.p.A.
Aerodynamics Dept.
Via Sanvito, 80
21100 - Varese
(Italy)

SUMMARY

This paper presents some experimental studies of inlet/airframe interference, conducted at the Aermacchi's Water Tunnel facility about aircraft configurations under consideration for an Advanced Trainer Project.
The chin inlet and the bifurcated inlet configurations have been considered, and the following phenomena have been investigated.

Inlet/Forebody Interference at low incidence: the forebody effect on the shape of the streamtube approaching the chin inlet has been visualized, in order to evaluate changes of the local lip incidence respect to the isolated inlet configuration, and to evaluate performance penalties and lip shape modifications.

Inlet/Ground Interference at Take Off conditions: the typical inlet ground vortex has been visualized, and its existence conditions investigated; a comparison between the chin inlet and the bifurcated one has been made in this respect.

Inlet/Airframe Interference: in this section various typical interference phenomena between the inlet and other airframe components have been studied; components considered are the wing, wing strakes, fuselage, etc., and high incidence/yaw performances of the two inlet configurations have been studied as well.

All the above mentioned studies are based on flow visualizations in water tunnel, merged with theoretical studies, semiempirical and handbook methods.

NOTATION

A = inlet cross sectional area	cm^2
C = wing chord	cm
h = inlet cross sectional height	cm
H = inlet centerline height above the ground	cm
MFR = inlet Mass Flow Ratio = V_i/V_o	-
P = total pressure	Pa
Q = flow rate through the inlet	cm^3/s
V = water speed	cm/s
X_{BD} = abscissa of vortex breakdown	cm
α = aircraft angle of attack	deg
β = aircraft angle of sideslip	deg
λ = inlet contraction ratio = A_i/A_t	-

SUBSCRIPTS

o = undisturbed flow conditions
i = inlet capture section
t = inlet throath section
m = inlet maximum external section
r = wing root section

1. INTRODUCTION

Since the 1913 Aermacchi has been involved in the trainer aircraft design and manufacture.
Nowadays, the modern military aircraft flight envelope extension in the high incidence range, requires a parallel evolution of the trainer aircraft configurations as well, so Aermacchi too is studying new geometries for such aircraft.
A useful tool extensively used at Aermacchi for preliminary configuration studies is the water tunnel, by means of which the first validation just after the preliminary design can be made.
Water tunnel investigations are considered an essential step in a new project, because of their low costs/benefits ratio; in fact tests can be made easily and fastly, the tunnel power is negligible, it's management economic, and the model's manufacture cost is very low compared to the wind tunnel models one. In spite of these low costs many interesting phenomena can be observed, qualitatively at least, and some possible design modifications can be defined before undertaking further expensive activities, such as wind tunnel testing or sophisticated computational fluid dynamics analysis.

Experiments in Water Tunnel are limited by the low Reynolds number ($1 \div 4 \times 10^4$) and low water speed; that means that it isn't possible to study phenomena depending of such parameters, like to boundary layer transition, turbulent flow separations, etc.
Flow visualizations of fully developed

vortical flows and streamlines are instead very helpful to understand various phenomena, such as interferences among various aircraft components.

2. EXPERIMENTAL FACILITIES, MODELS AND TEST TECHNIQUES

Aermacchi's Water Tunnel is a closed loop facility at continuous flow, with horizontal test section whose dimensions are: height = 90 cm, width = 60 cm, length = 180 cm.
The maximum water speed is about 30 cm/s, and an auxiliary pump can suck up to 1200 cm^3/s through the inlet and internal ducts.
Flow visualizations are made by dye injection through holes on model surface or rakes, while hydrogen bubbles and laser sheet techniques are also available but have not been used for the present investigation.
Water speed and angles of pitch and yaw of the model can be continuously varied by means of a remote control device, and their values can be read on digital displays.
The auxiliary pump suction can also be continuously varied, and the flow measurement is made by a rotameter kind of flowmeter. A water tunnel layout is shown in fig. 1.

Two complete models 1:20 scale have been used for testing both the chin inlet and the side mounted one (fig. 2).
A third partial model 1:15 scale, consisting of a forefuselage configuration, has also been used for inlet/forebody interference studies about a chin inlet; in this case the inlet could even be tested separately from the fuselage.
All the three models have a distribution of holes on their surfaces for dye injection.

Concerning the test techniques it must be pointed out that they are always based on flow visualizations of streamlines, vortices and various phenomena.
Parametric studies can be made by varying aircraft attitude, inlet Mass Flow Ratio, geometric configurations, etc.

3. INLET/FOREBODY INTERFERENCE AT LOW INCIDENCE

The preliminary design of air inlets can generally be made considering as first approximation isolated inlets at zero incidence, because many handbook methods and experimental data are available for this simple case.
Later on the appropriate modifications are defined in order to consider the airframe interference and the angle of attack.
In this paragraph some aspects of inlet/forebody interference studies at zero incidence are shown, concerning their effect on lip design. The forebody effect on the shape of the streamtube approaching the inlet has been investigated, because the presence of the forebody will generally change this shape compared to the isolated inlet condition, and the local incidence on lips will be modified too. A method to evaluate this effect is thus presented.

The preliminary lip design can be made by using standard profiles, such as Elliptical or NACA1, whose thickness/lenght ratio is defined in order to satisfy specific design requirements. Two classical requirements for the inlet lips are the absence of flow separations: on the internal lip, at high engine demand and low speed (Take Off conditions), and on the external one at high speed (Cruise conditions).
Flow separations depends on lip thickness and MFR, because this defines the local incidence on lips, and many methods are available to calculate the critical value of MFR for separations, as a function of lip shape.
Fig. 3 shows the procedure in common use at Aermacchi, based on critical MFR from references 1 and 2.
Starting from the low speed (Take Off) and high speed (Cruise) design mach numbers, the corresponding design points L, M are firstly evaluated on the MFR–Mach curves; such curves have been previously evaluated, based on the inlet throat area and engine demand at the mentioned conditions.
The geometrical parameters L, h_i/h_m, which give the thinnest lips with no flow separations at the design points, can then be evaluated on the critical MFR curves for both internal and external lips.
Finally lip thickness can be deduced from L, h_i/h_m, in addition to other parameters having been previously fixed. It should be pointed out that the choice of the design points, and the validation of the selected geometry, are made by considering the compatibility with further performance requirements such as Drag Rise, Wave and Profile Drag, and configuration constraints.

At this point it is perfectly understandable that if the forebody displaces the streamtube, as shown in fig. 4, we have a local incidence on *lower lip* corresponding to a higher value of MFR on the isolated inlet.
A new, "equivalent" value of MFR, can be defined as better representative of the actual working conditions of the inlet lip. To make that, at first the streamtube approaching the inlet has been visualized, both in the isolated inlet and inlet + forebody configuration in a range of working conditions (MFR up to 8.0), by using a rake of dye ports. This was useful to have a first idea of the forebody effect on the streamtube shape, as shown in the example of fig. 5.

Afterwards, with a single dye port, the lower lip stagnation streamline which defines the streamtube shape was visualized in the same range previously considered, and its height under an inlet reference line was measured at each test condition.
The results are summarized in fig. 6, where it can be seen that the forebody locally displaces, enlarges the streamtube of about 10 + 15% of inlet height; that means an increase of local incidence on the inlet lower lip.

Fig. 6 can be explained in this way: if we have a complete configuration, we must associate to it higher "equivalent" values of MFR in order to consider it as an isolated inlet for apply the available handbook methods; the corresponding increased values can be read on the figure at the same height Z/h_i.
Note that in this case we are not interested about the upper lip, because it will be replaced by a compression ramp, but the same procedure could be also applied to it.
It is now possible to evaluate some performance penalties depending on MFR, such as the lip pressure recovery shown in fig. 7.
We are also allowed to correct the dimensioning procedure of fig. 3, taking in account the above mentioned considerations as shown in fig. 8.
We note that now, at the two design Mach numbers, the new operating points L, M become L_1, M_1, and without any modification the flow working conditions become A_1, B_1; that means that the external lip working point falls into the no separations region, while the internal one works with flow separation at its design point.
To restore the required design conditions, new values of L and h_i/h_m could be evaluated from points A_2, B_2; in this case we obtain that the inlet capture area should be increased by about 1.3% (thicker external lip) while the external lip could be designed about 1.0% thinner. Fig. 9 shows the modified profile of the lower lip nose region.
It is important to note that modifications related to a change in lip incidence will be always opposite in sign, therefore they require enlarged inlet area and thinner external lip, thus leaving the maximum lip thickness roughly untouched.
It should be pointed out now that such a modifications are the simplest to define at this stage, and can be chosen as a first step in the project development; further analysis could validate them and eventually define more sophisticated modifications of the inlet cross sectional shape, lip profiles, etc.
At the end of this paragraph we want to emphasize that the method presented here is a semiempirical method, based on flow visualizations and some rough measurement; thus it is affected by natural approximations, but it's very simple, rapid and perfectly acceptable as a preliminary tool, as a first approach to interference studies.

4. INLET/GROUND INTERFERENCE AT TAKE OFF CONDITIONS

The object of this paragraph is a special kind of interference between the inlets and the ground, the well known Inlet Vortex (fig. 10) which may appear during the first phases of the take off run, at low speed and high engine demand (high MFR).
It is an undesirable phenomenon, because it produces large flow angularities and total pressure gradients, mostly in the core region, that means large flow distorsion to the engine face and related thrust penalties.
It is also able to suck debris and small stones from the ground, and cause severe F.O.D. (Foreign Object Damage) to the compressor.
A basic mechanism of Inlet Vortex formation is the amplification of an existing ambient vorticity that happens when the vortex lines are stretched and sucked by the inlet. Vortex lines can be ingested from the ground boundary layer which forms when a headwind or crosswind exists. In a theoretical situation, two vortex lines with an equal and apposite circulation should appear (fig. 10), but in practice only one vortex is generally observed; the perfect understanding of that is still under study.
The following parameters characterize the phenomenon:

- the inlet Mass Flow Ratio
- the inlet height above the ground
- the wind speed and direction
- the magnitude of ambient vorticity.

The existence of a stagnation point, on the ground under the inlet, is also mandatory for the phenomenon to appear.

The basic mechanism of formation of the Inlet Vortex was the object of many works by different authors (ref. 3 + 7), but most of them are referred to isolated inlet of circular shape, and have produced the fundamental knowledge of the phenomenon.
In the present work two different inlets, chin inlet and bifurcated one, in a complete aircraft configuration have been investigated in order to apply the basic knowledge on two real configurations and to have a comparison between them.
Therefore the Inlet Vortex was visualized in the water tunnel during a simulated Take Off condition with headwind, and its existence domain was thus evaluated. Starting from a static point the inlet flow was at first switched on to its maximum value, and the vortex appeared; then the water speed was slowly increased till the vortex disappeared.

Figures 11 through 14 show some images taken during the experiment, like the vortex evolution due to speed increases (Fig. 11, $H/h_i = 3.$).
The vortex firstly appears at V = 2 + 3 cm/s (MFR = 50. + 60., Fig. 11-1) which was found to be a minimun value to produce an appreciable ambient vorticity.
A small speed increase gives more energy to the vortex, because it produce an increase of the ambient vorticity as well (Fig. 11-2, V = 4 cm/s); after further increases the vortex gets quite unstable (Fig. 11-3, V = 6 cm/s) and finally is blown away (Fig. 11-4, V = 8 cm/s).
The water speed corresponding to this situation was measured for various heights above ground, and the graph of fig. 15 was put down; it represents the vortex existence domain for the two inlet configurations under study. The more interesting result is that the bifurcated inlet vortex is blown away at a slower speed (higher MFR), respect to the chin inlet one, which means that it exists in a shorter range of headwind speed.
In practice the inlet vortex of the bifurcated inlet configuration is weaker, and even by sight it was observed that it has a slower rotational speed and is quite spread respective to the chin inlet vortex.
This wasn't a foreseen result, and points out that other geometrical parameters have an influence on the vortex, more than those known from the literature; possible effects can arise from the inlet size, shape, width and position respective the fuselage.
Thus the phenomenon deserves further investigation in the future.

Further interesting results were observed, concerning the different behaviour of the two configurations.
The two bifurcated inlet vortices are always counter-rotating and quite stable on the inlet lower lip, while very different is the situation for the chin inlet.
In this case the vortex frequently moves along the lip, and sometimes a second counter-rotating vortex appears (fig. 12).
Such a difference probably exists because the bifurcated inlets ingest the forebody boundary layer vortex lines, which have an opposite circulation on the two sides where the inlets are located; the capture sections have then a shape with large curvature at the bottom, which maybe fixes the vortex there.
The chin inlet has instead a quite flat shape at the bottom and, in theoretical conditions, is a perfectly symmetric configuration; thus any small external disturbance, such as flow disuniformities, may influence the phenomenon.
Tests have been done even with 30 degrees of sideslip angle, which is the maximum value actually allowed by tests set up, but no difference was observed nor measured respective to the zero sideslip condition.
It would be interesting to test in the future, with dedicated models and/or sting, the 90 degrees of sideslip condition, which should produce the worst situation (maximum asimmetry) corresponding to the stationary aircraft in cross wind.
Concerning the Reynolds number effect, depending on flow viscosity, speed and ground plane length, even in the past it was considered of second order by many authors, and thus neglected because it doesn't influence the phenomenon by the qualitative point of view.
As a final remark, it is noted that tests have demonstrated a high degree of repeatibility, though the vortex shows large instability before being blown away.

5. INLET/AIRFRAME INTERFERENCE

In this section the results of interference studies between the inlet and other airframe components are presented.
More interest has been given to the inlet/wing-strakes interference, in terms of MFR effect on the wing vortex breakdown.
The strake vortex has been visualized, as fig. 16 shows, and the chordwise position of its breakdown has been measured for various α and MFR. The most interesting result obtained is that the bifurcated inlet has a strong and beneficial effect on the wing vortex breakdown, which is delaied about 50% of the wing root chord as the MFR is increased from 0 to 2. (see fig. 17 + 20).
The chin inlet flow also gives more energy to the vortex, which is quite spread and slow for MFR = 0. + 1, but faster for MFR = 1 + 2 (fig. 21); in this case however, the position of vortex breakdown doesn't move.
Such effect of the mass flow through the inlet is probably due to the acceleration that the inlet gives to the flow just ahead of it; since the wing strakes are located near the inlet, the local higher speed produce higher vorticity around them.
The bifurcated inlet produce then a stronger effect because is nearer to the strake respect to the chin one.

These results are very important, at this preliminary stage of the project, not only for the wing and wing-strakes design, but mostly for the planning of experimental activities in wind tunnel.
Before to plan such tests in fact, is very useful to know the MFR effect on wing aerodynamics, in order to decide for a flow-through, faired or choked inlet model.

The shielding properties of the airframe at high incidence for both configurations have also been investigated.
As fig. 22 shows, the bifurcated inlet suffers a fuselage upwash, while the chin one has a beneficial downwash and thus is much better in this respect.
Opposite is the behaviour at negative attitude: no problem arises from the bifurcated inlet, while the chin one seems to be quite in shadow under the forebody, as the sketch of fig. 23 shows.

Another interesting phenomenon observed during the activity is that the side mounted inlet configuration shows bad flow conditions at high incidence and yaw, because of large flow angularities and vorticity on the bottom fuselage, around the inlet (fig. 24); some geometry modification could therefore be defined.

6. CONCLUSIONS

Various phenomena have been observed during this experimental activity, and many useful suggestions have been deduced for the next phases of the project.
Only some aspects of inlet/airframe interference were studied, and these allowed us to plan a more accurate wind tunnel testing, and to define some geometrical modification to the aircraft baseline.
A very simple method has been found to evaluate the forebody effect on lip design of a chin inlet, in terms of performance penalties and geometrical changes to cancel them; it was found that, for the configuration studied, the forebody reduces the lip recovery factor about 0.5% at low speed, respect to the isolated inlet configuration.
A 1.3% increase in capture area would be necessary to cancel such a penalty, while a 1.0% reduction of external lip thickness could be defined without any disadvantage, because of the reduced local incidence on it; the maximum inlet gross size would be in this way roughly unchanged.

Concerning the Inlet Vortex it was found that the bifurcated inlet is less sensitive to the phenomenon, which means that the vortex is weaker and disappears sooner respect to the chin inlet.
In this configuration it was also observed that the vortex is quite unstable, it moves along the lower lip and a second counter-rotating vortex sometimes appears.

A very large interference was observed between the inlet and the wing-strake, mainly for the bifurcated configuration; in this case in fact, the wing vortex breakdown is delayed about 50% of the wing root chord, when increasing the MFR from 0 to 2.
Further interference phenomena have been observed between the inlet and fuselage, concerning the shielding properties and the general behaviour at high incidence and yaw.
Data have always been repeatable, and their approximation is perfectly acceptable in a preliminary testing like this.
Therefore tests have been very useful as a preliminary configuration analysis, and very efficient because the high quality and quantity of results obtained, compared to their low costs and short times.

7. REFERENCES

1. J.Seddon, E.L.Goldsmith: Intake Aerodynamics
2. ESDU Aerodynamics Vol. A7: Internal Flow Systems
3. F.De Siervi, H.C.Vignier, E.M.Greitzer, C.S.Tan: Mechanism of Inlet-Vortex formation
4. J.L.Colehour, B.W.Farguhar: Inlet Vortex
5. S.O.Ridder, I.Samuelsson: An Experimental Study of Strenght and Existence Domain of Ground to Air Inlet Vortices by Ground Board Static Pressure Measurements
   ICAS-82-4.8.2
6. D.L.Motycka, W.A.Walter, G.L.Muller: An Analytical and Experimental Study of Inlet Ground Vortices
   AIAA Paper No. 73-1313
7. W.Liu, E.M.Greitzer, C.S.Tan: Surface Static Pressures in an Inlet Vortex Flow Field - ASME 84-6T-201
8. N.T.Frink, J.E.Lamar: Water-Tunnel and Analytical Investigation of the Effect of Strake Design Variables on Strake Vortex Breakdown Characteristics - NASA TP 1676

ACKNOWLEDGMENTS

Many thanks to Ing. M.Giachi, who at first experimented the Inlet Vortex in the Aermacchi's Water Tunnel two years ago, obtaining the first encouraging results.
This works have been done under the supervision of Ing. L.Visintini, and by the cooperation of the tunnel technicians Mr. Orlandi, Mr. Mattiuzzo and Mr. Chiesa.

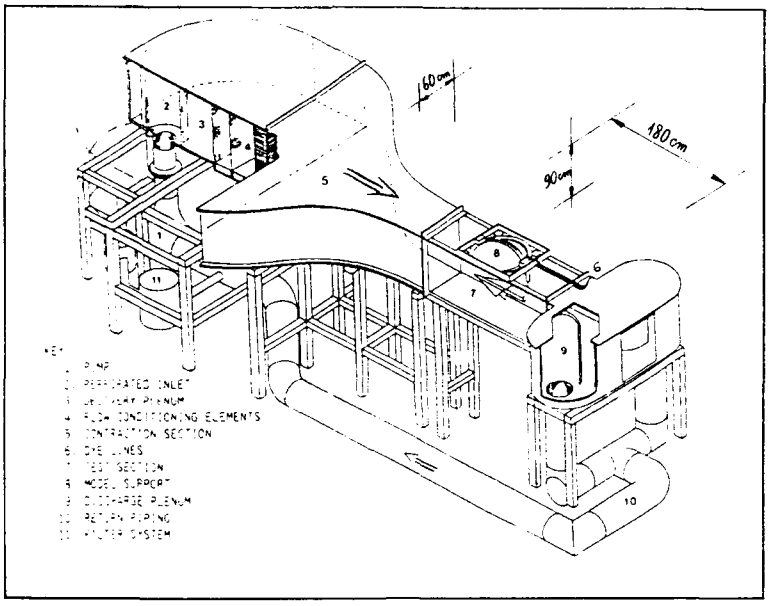

FIG. 1 AERMACCHI WATER TUNNEL FACILITY

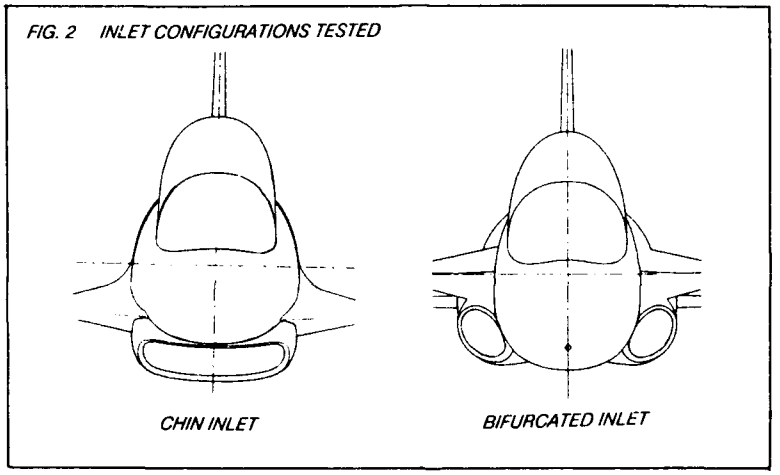

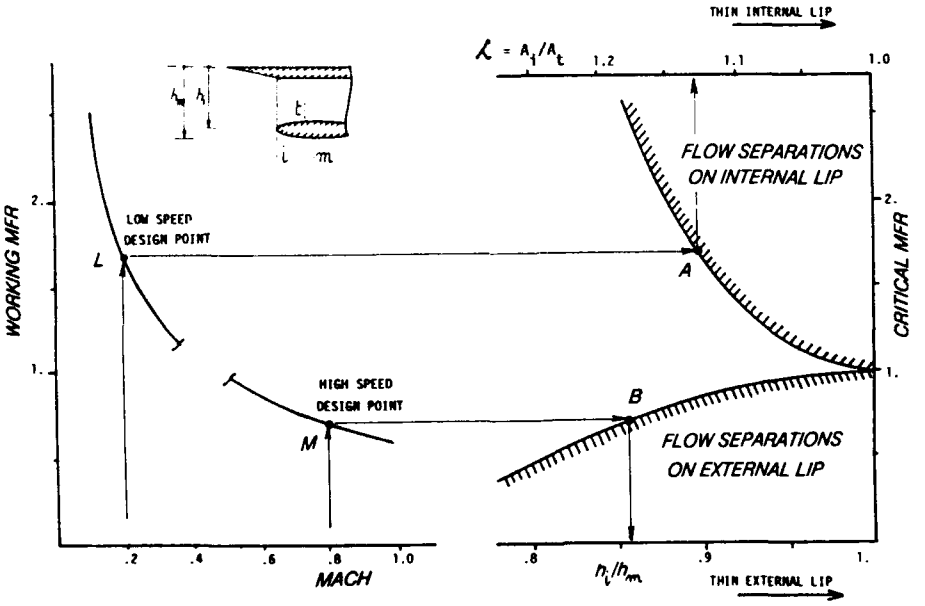

FIG. 3 PRELIMINARY LIP SIZING PROCEDURE

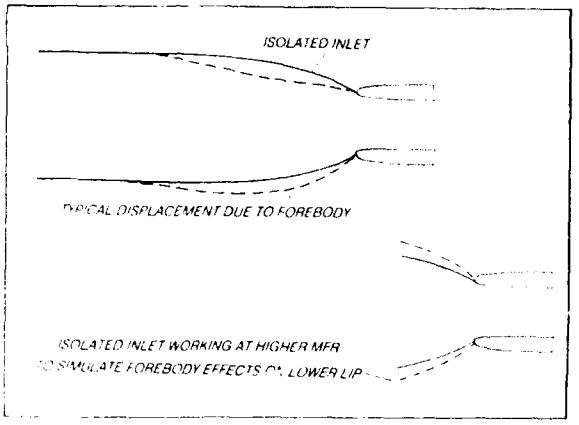

FIG. 4 TYPICAL FOREBODY EFFECT ON THE STREAMTUBE APPROACHING THE INLET

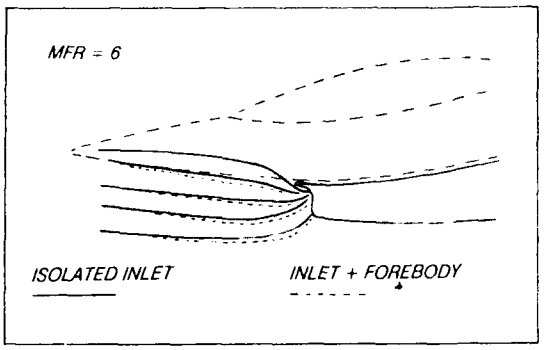

FIG. 5 STREAMTUBE DISPLACEMENT DUE TO FOREBODY

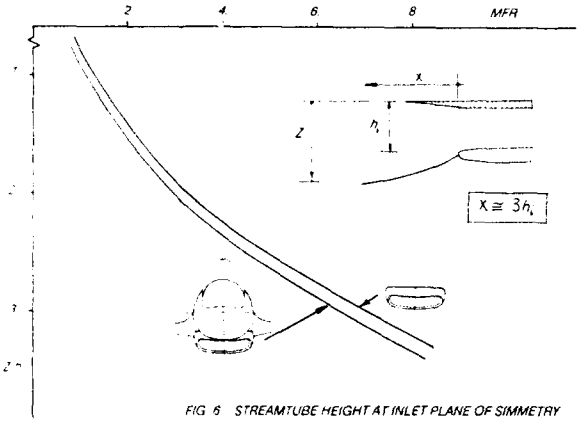

FIG. 6 STREAMTUBE HEIGHT AT INLET PLANE OF SIMMETRY

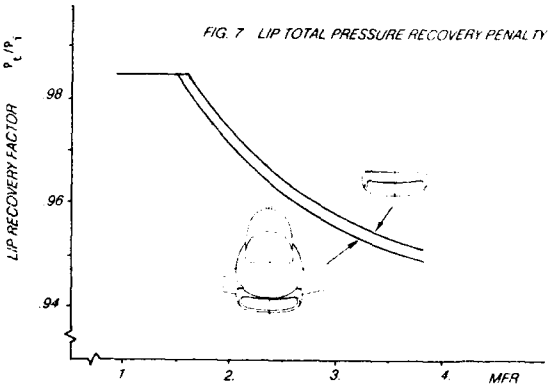

FIG. 7 LIP TOTAL PRESSURE RECOVERY PENALTY

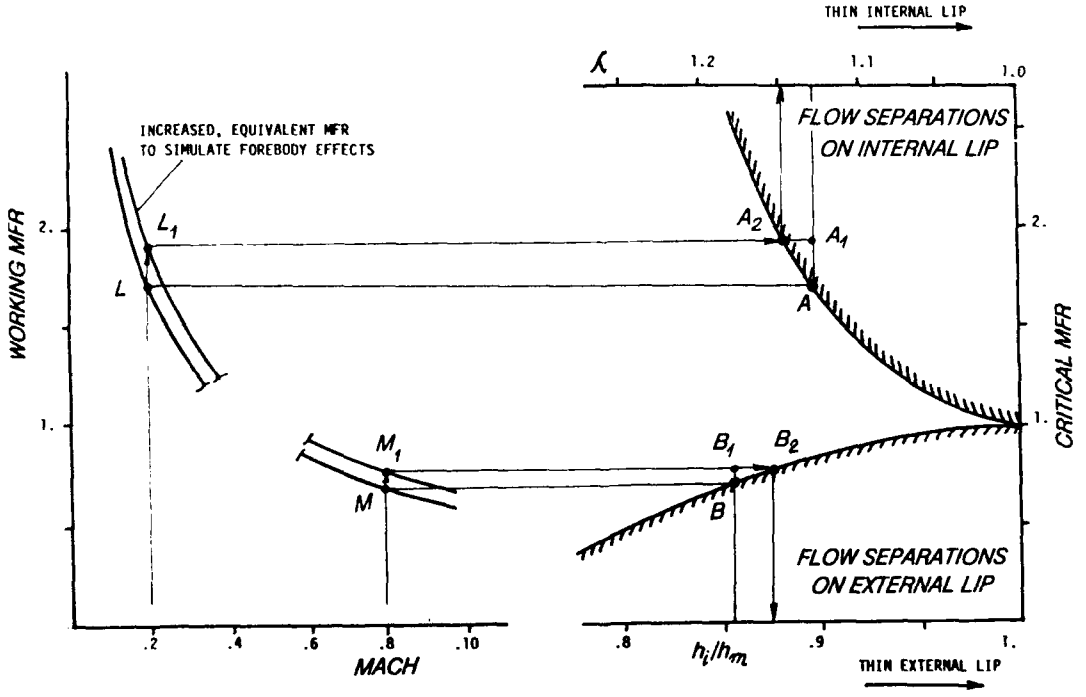

FIG. 8 PRELIMINARY LIP SIZING PROCEDURE - FOREBODY CORRECTIONS

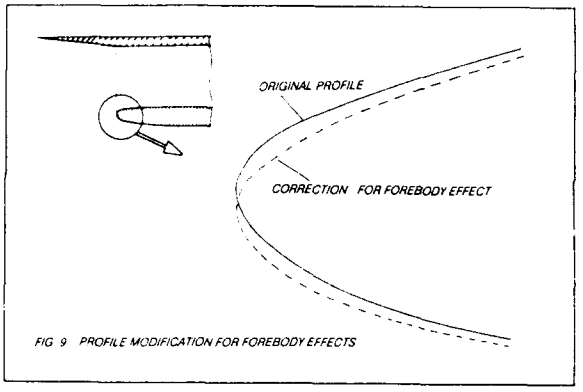

FIG. 9 PROFILE MODIFICATION FOR FOREBODY EFFECTS

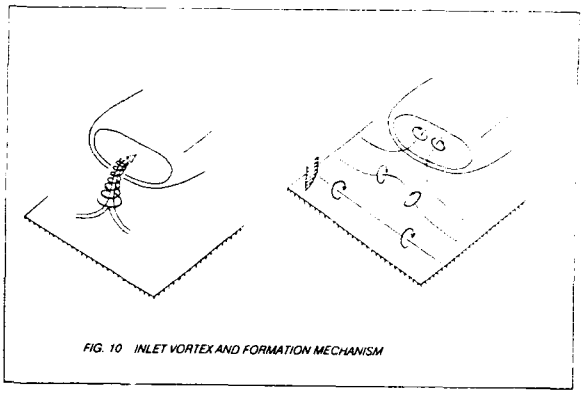

FIG. 10 INLET VORTEX AND FORMATION MECHANISM

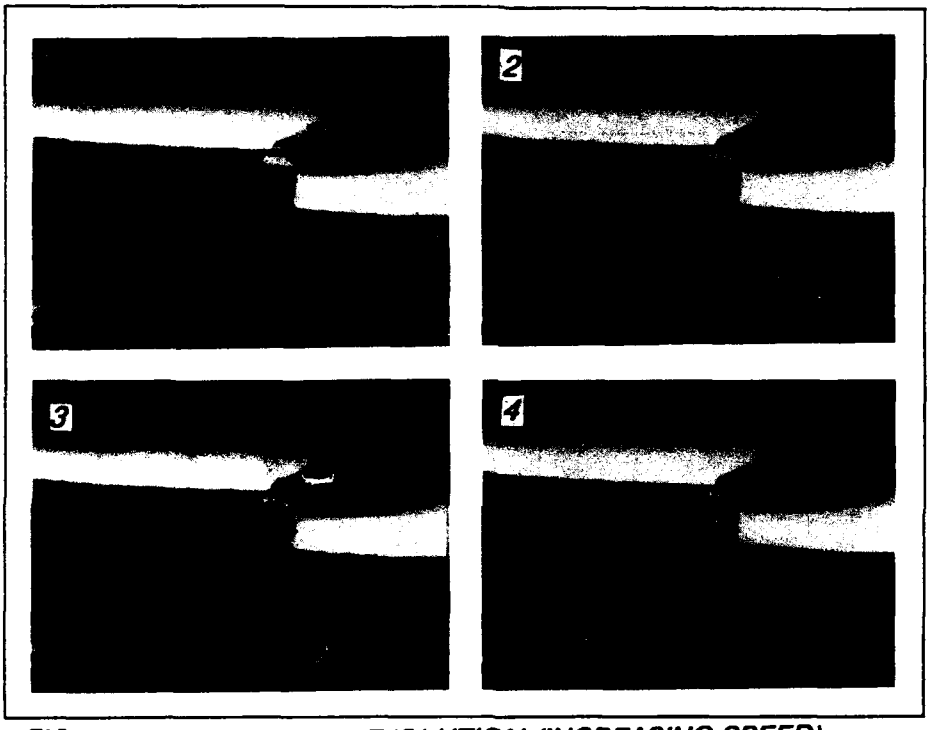

FIG. 11 INLET VORTEX EVOLUTION (INCREASING SPEED)

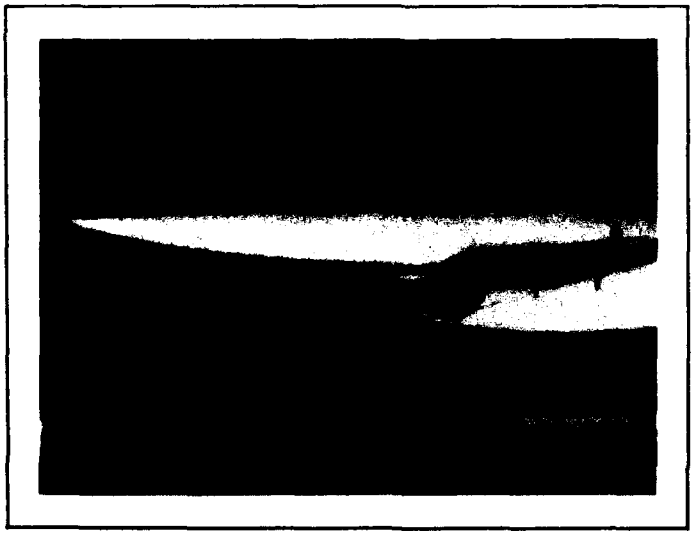

FIG. 12 TWO COUNTER-ROTATING VORTICES

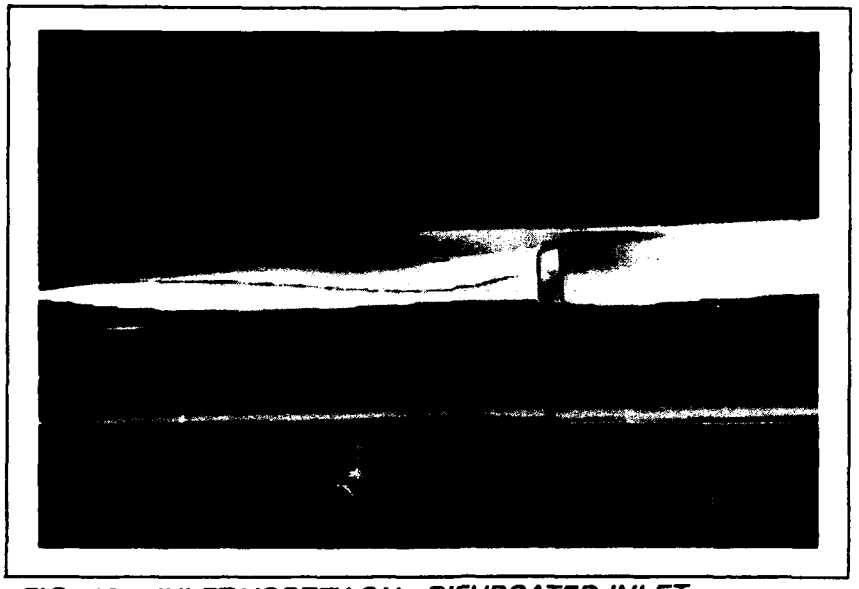

FIG. 13 INLET VORTEX ON BIFURCATED INLET

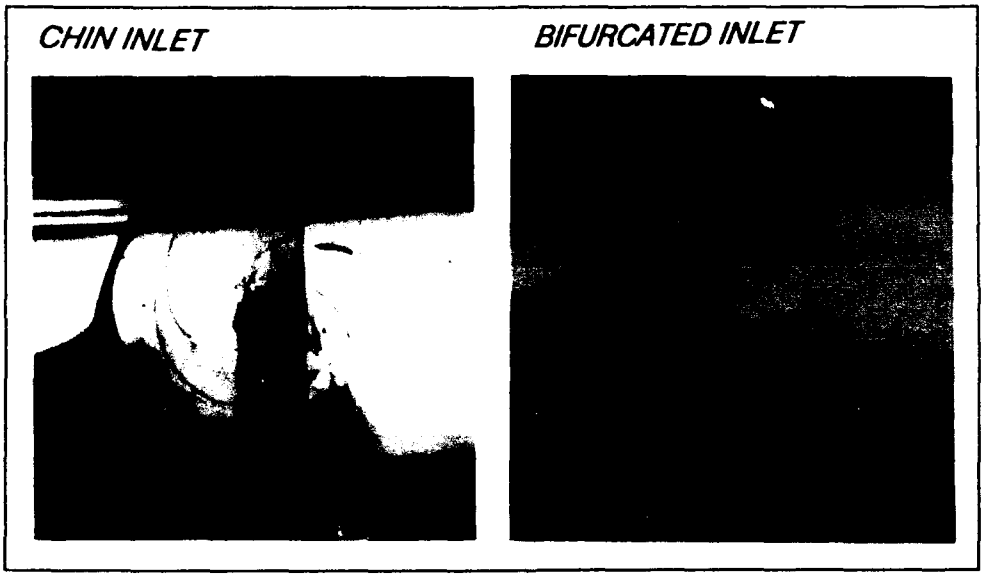

FIG. 14 INLET VORTEX (BOTTOM VIEW)

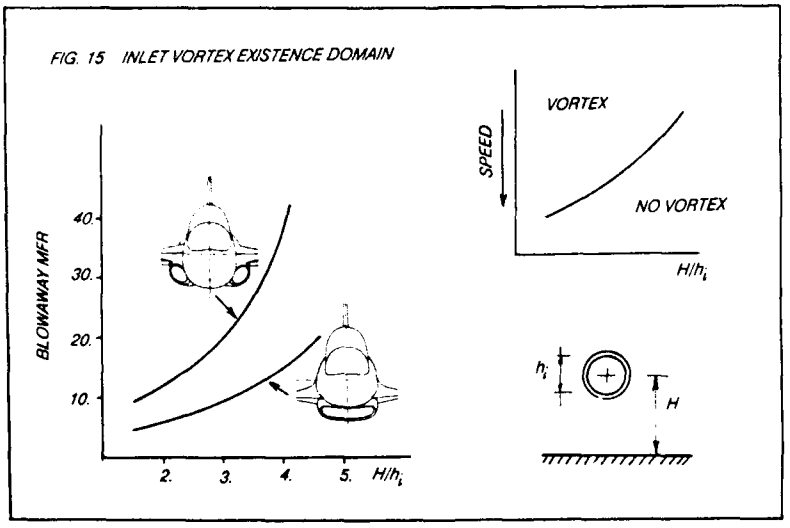

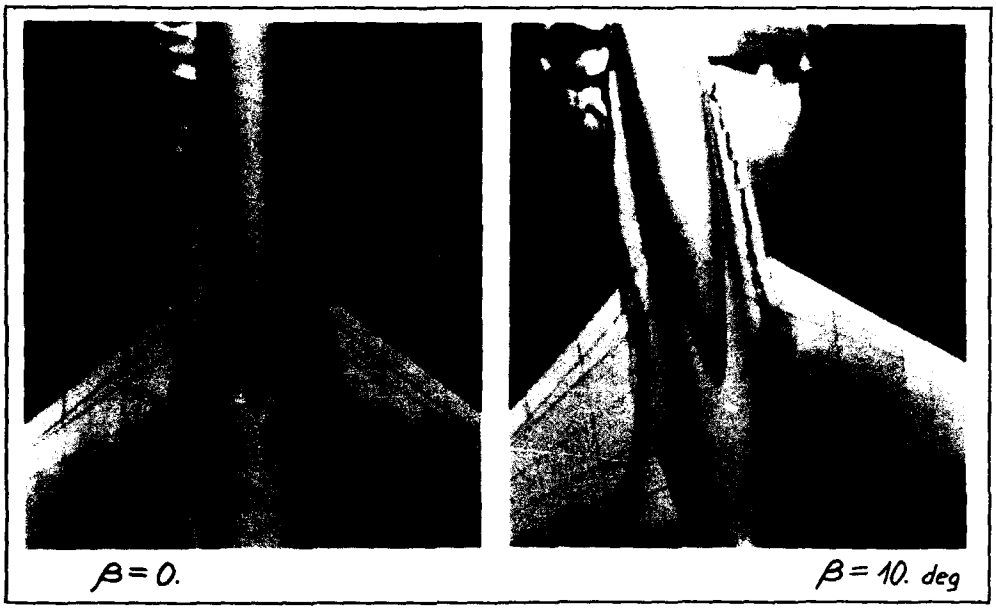

FIG. 16 WING STRAKE VORTICES

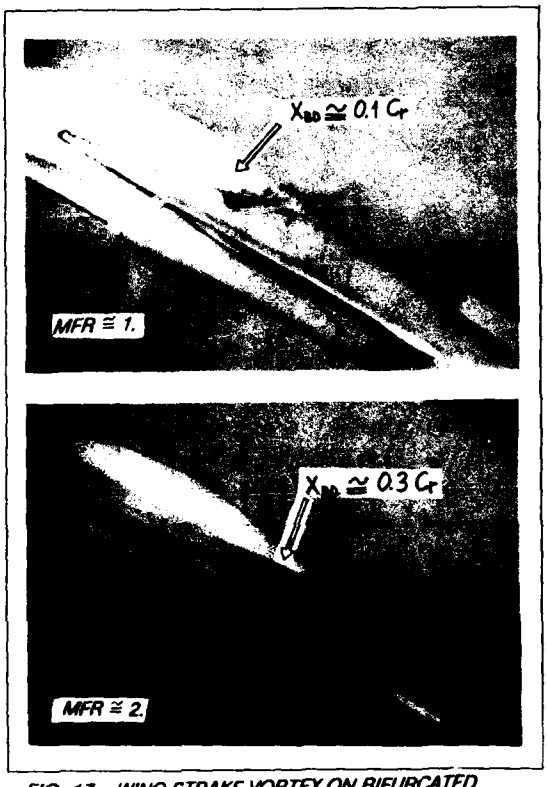

FIG. 17 WING STRAKE VORTEX ON BIFURCATED INLET CONFIGURATION ($\alpha \simeq 30$ deg)

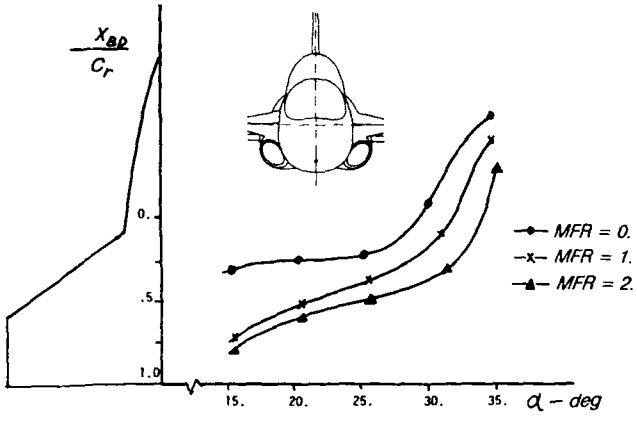

FIG. 18 VORTEX BREAKDOWN POSITION VS INCIDENCE MFR EFFECT ON BIFURCATED INLET

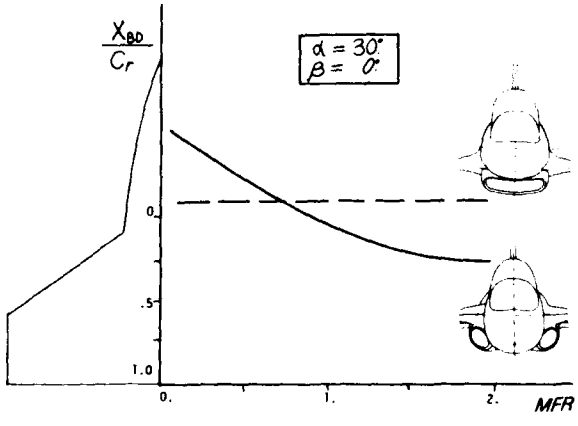

FIG. 19 VORTEX BREAKDOWN POSITION VS MFR BIFURCATED - CHIN INLET COMPARISON

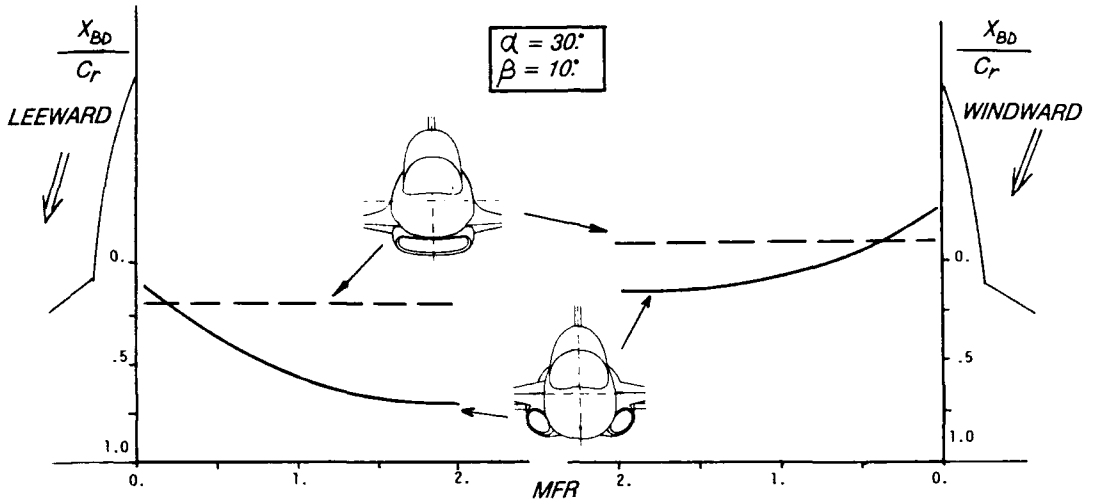

FIG. 20 VORTEX BREAKDOWN POSITION VS MFR
BIFURCATED - CHIN INLET COMPARISON AT YAW

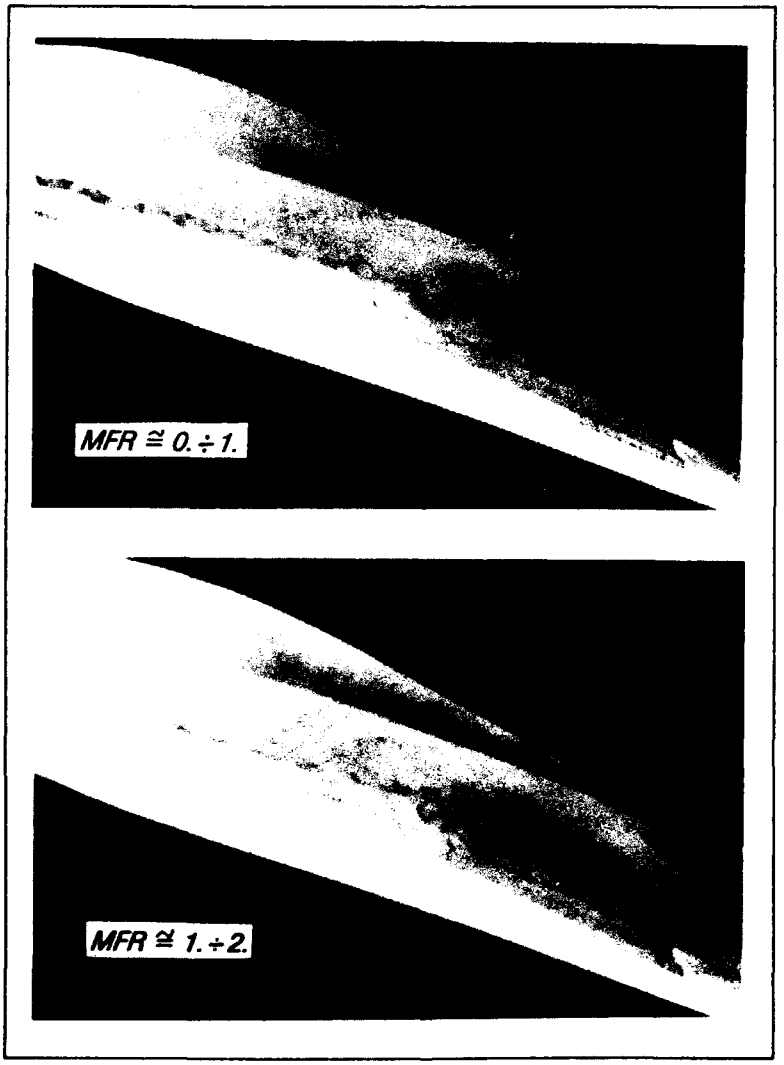

FIG. 21 WING STRAKE VORTEX ON CHIN INLET CONFIGURATION

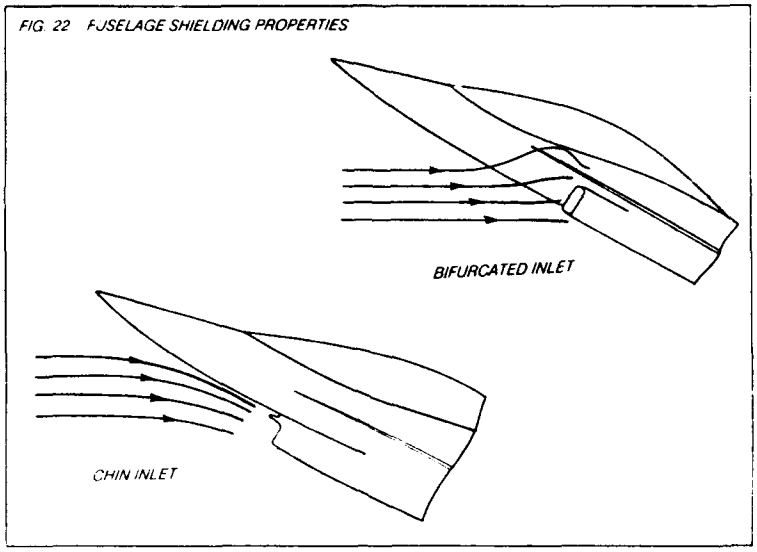

FIG. 22 FUSELAGE SHIELDING PROPERTIES

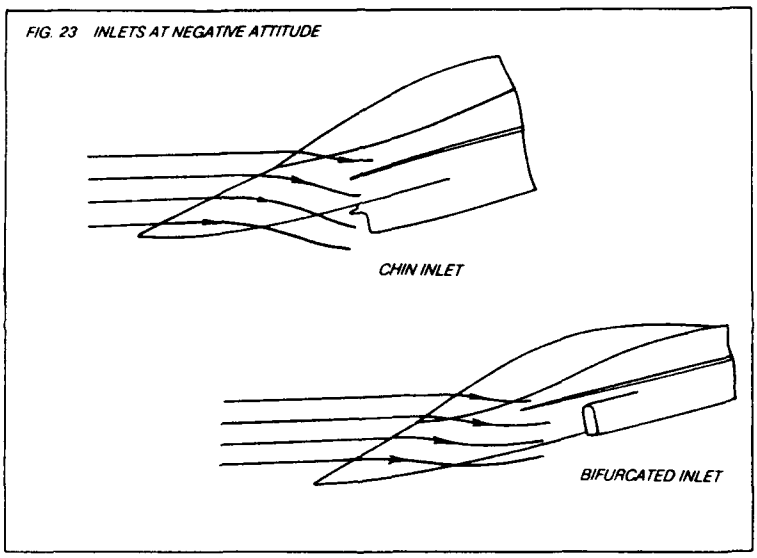

FIG. 23 INLETS AT NEGATIVE ATTITUDE

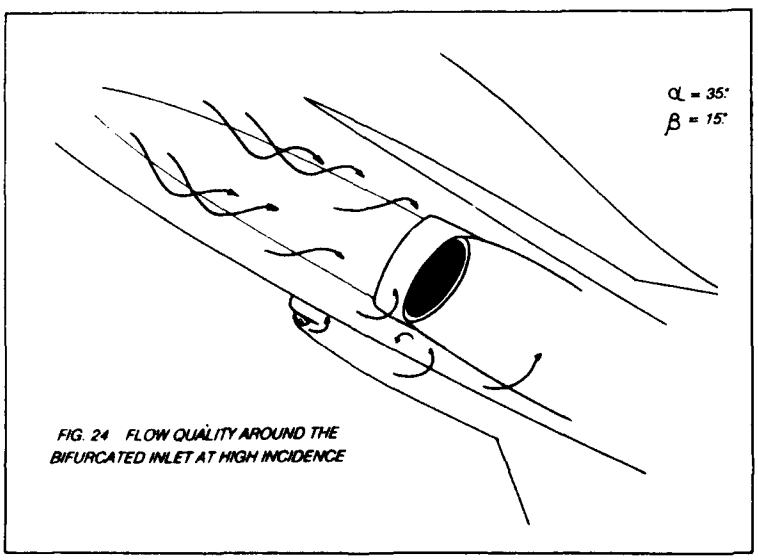

FIG. 24 FLOW QUALITY AROUND THE BIFURCATED INLET AT HIGH INCIDENCE

EXPERIMENTAL STUDIES OF THE FLOWFIELDS AND THEIR EFFECTS DUE TO A PAIR OF LIFT JETS DISCHARGING IN THE GROUND EFFECT REGION

by

L.J. Hope and **E.C.P. Ransom**
School of Mech., Aero., Prod. Engineering
Kingston Polytechnic
Canbury Park Road
Kingston upon Thames
KT2 6LA
United Kingdom

SUMMARY

A small rig has been designed and made to study fountain flows formed by subsonic jets impinging onto a ground plane.

A series of tests was carried out to investigate three dimensional flow patterns and pressure distributions in the fountain flows. A programme of tests was then devised to establish fountain flow pressures and normal forces on rectangular blocking trays of various designs. Most tests were carried out at ambient temperature but some tests were carried out with pre-heated compressed air.

The effect of the distance between the jets and the trays from the ground plane was examined and recorded. Moving ground board tests were also carried out.

LIST OF SYMBOLS

D	emergent jets' diameter.
F_f	fountain flow aerodynamic net force on a blocking tray.
F_j	thrust of the pair of emergent jets.
H	distance between the nozzles' plane and the ground board plane.
h	distance between the nozzles' plane and the surface of a blocking tray.
l	tray lip (strake, dam) height.
M	Mach number.
p	pressure (gauge).
p_{jet}	emergent jets' total pressure (gauge).
w	width of blocking tray.
x,y,z	Cartesian co-ordinate system, see fig. 5.

1. BACKGROUND

Upwash or 'fountain flow' occurs between two or more adjacent substantially vertical matched jets when they impact with a horizontal plane. The effect of such an upwash can be a significant change in the magnitude and distribution of the aerodynamic forces on the underside of the airframe of a short take-off vertical landing (STOVL) aircraft when it is hovering near the ground. Since the flowfield is essentially three-dimensional and strongly influenced by turbulence it is complex in nature and gives rise to a range of design and performance problems including hot gas reingestation by the gas turbine(s), jet-lift interference, localised airframe forces and overall control changes.

The purpose of the research was to provide further information on fountain flow and its effects, This entailed flow visualisation , pressure measurements in the main volume of the fountain flow with no blocking tray present (ie unconfined fountain flow) and impingement pressures and upthrust forces on a representative model of the underside of the fuselage of a STOVL aircraft. The study was undertaken because there appeared to be little pertinent information in the public domain on this important aspect of aerospace science.

2. INTRODUCTION

The experimental arrangement employed was simple and inexpensive. The jets were of diameter about 1/25th scale of the British Aerospace Harrier but in all other respects the rig was not configuration specific. Experimental studies of the free fountain flow created by the pair of round jets were carried out in order to establish the total pressure distribution in the main fountain volume. This was followed by flow visualisation tests. A programme of tests was then undertaken to investigate the magnitude and distribution of normal force on a blocking tray (in effect a simulated fuselage undersurface) mounted between the pair of jets. The test facility is shown diagrammatically in fig.1 and the main geometric parameters are displayed in fig.2.

The test rig was designed to incorporate existing components where possible so as to reduce cost and delay. Thus it was designed to be mounted on top of a pressure vessel previously employed for jet entrainment research by Barnes and Ransom[1]. The vessel provided a stable platform for the two-jet rig and also incorporates an array of electric heaters which enabled the compressed air to be delivered to the plenum chamber at almost 200°C at M =0.20. The plenum chamber has an internal baffle designed to avoid direct flow from the inlet to the jet nozzles and at the same time to give satisfactory contraction ratios. The chamber was sized to be large enough to ensure that the flow velocity inside it would be very small compared with the velocity through the jet nozzles. The nozzles were mounted directly onto the top plate of the plenum chamber and discharged vertically upwards as shown in fig.2. The distance between the axes of the nozzles was jigged to be five jet diameters. Their design, shown in fig.3, was based on a configuration developed by Hawker Siddeley Aviation of Kingston in the 1960s. Particular care was taken in the manufacture of the nozzle bores so that they were closely matched. The removable top plate of the plenum chamber incorporated a pressure port and a thermocouple. Linear traverses were set up as shown in fig.4 with the vertical 'y' traverse set parallel to the nozzles' axes, with the 'x' traverse set parallel to the line joining the centrelines of the nozzles and in the nozzles' exit plane. The 'z' axis completed the right-handed Cartesian co-ordinate system. The initial use of the traverses was to determine the velocity profiles of the emergent jets. It was also intended to be used to survey total pressures in the main volume of the fountain . Finally it would be used to move the ground board up or down either in steps or at a chosen rate. Each traverse was driven by a stepper motor controlled by software written to a microcomputer.

Having designed and made the rig a number of commissioning tests were conducted to investigate its performance and to check that the jets were in fact closely matched. A high frequency audible vibration of the jets was overcome by trial-and-error using baffles of various designs mounted over the intake to the plenum chamber.The optimisation procedure eventually ensured that the flow from each nozzle was substantially the same as shown in figs.6 & 7. The tuning process was considered to be worthwhile because of the need to obtain fountain flows which would be closely parallel to the jets. The initial tests were to be conducted at jet Mach numbers in the range 0.2 to 0.3, for ground board distances,H, from 2 to 8 jet diameters, for various nozzles' plane to tray plane distances,h, with rectangular blocking trays of various lengths, L and lip heights, l. See fig.2.

3. THE EXPERIMENTS

The programme comprised the following sets of tests:-

3.1 Pitot pressure surveys of the main volume of the fountain flow.

3.2. Flow visualisation.

3.3. Trayforce and pressure measurements.

3.1 PITOT SURVEYS

The pitot probe was aligned vertically and the traverse restricted to cover that part of the three dimensional field where positive pressures were reckoned to occur.

Pressure sampling surveys were carried out in vertical 'xy' planes for a number of stations along the z axis. The emergent jets' velocity was held at Mach 0.2, ie about 70 m/s depending upon ambient atmospheric conditions. For these surveys the ground board distances, H, were chosen to be 4D, 6D and 8D. Since the flowfield was expected to be most vigorous in the datum xy plane an intensive survey was carried out there. At a number of locations the pressure appeared to be negative, ie slightly below ambient, such values were regarded as suspect because the flow may have been far out of line with the pitot head at such points. Typical total gauge pressure profiles are displayed in figs. 8 & 9 but they should be treated with caution as at some locations the airflow will not have been within the required 20° cone angle[2]. It is perhaps worth noting that it had been intended to present a survey at H = 3D but it was realised that the jet flow might not have been fully developed before impact with the ground board[3].

It is evident from the pressure profiles mentioned above that the fountain flows are relatively narrow and do not extend very far in the fore-and-aft directions. When the non-dimensional total pressures, p/p_{jet} were plotted against distance from the ground plane, H-y, the data points collapsed towards a single curve suggest-

ing that the strength of a fountain flow is heavily dependent upon the radial wall jets produced by the impingement of the main jets onto the ground board. Supporting evidence for the crucial importance of the wall jets is presented in a report by Barry Gilbert[4].

3.2 FLOW VISUALISATION

Attempts were made to examine the strongest part of the fountain flows - that lying more or less in the datum plane - by means of a hypodermic wand from which oil vapour from a special heater was issuing in a steady stream. With H/D set at 4 and with an emergent jet velocity of 6 m/s the wand was held close to each x-axis side of each jet in turn and four photographs taken on the same frame of black and white film. See fig.10. The fountain shows up quite well but is rather diffuse in appearance because the camera records a total view in the z direction.

A dyed-water in clear water set-up was employed contemporaneously by Ing[5] to obtain qualitative insights into the development of two-jet fountain flow over a short time span. The results may be considered to be most useful in displaying the nature of fountain flow and its limited penetration normally from the ground plane as indicated by the pitot surveys described above. Figs.11 & 12 show the development of the flow for various values of H/D.

3.3 TRAY FORCE AND PRESSURE MEASUREMENTS

3.3.1 Tray forces:

A large number of tests were carried out to determine trayforces for various H/D, tray height h, tray length L and for several lip heights etc. All of the trays were of a standard width to just fit between the nozzles and were of lengths from 4D to 10D. Sets of trays were made with lip heights from 0.2D to 0.8D and a few trays were made with no lips or with lips on 3 or 4 edges. For a tray of L/D = 8 the magnitude of the fountain upwash force was found to vary from zero near an H/D ratio of 10 to a distinct peak of almost 20% of the jets' lift force at an H/D of about 2.5. As the ground board was moved closer to the tray the fountain seemed to change abruptly culminating in a suckdown force of between 10% and 20% of the jets' lift force. The abrupt change in the fountain force was later explored by means of tray pressure surveys as described below. Only very small forces were found to occur for unlipped trays and it was observed that increase of lip height only added slightly to the trayforce. Lipping the forward or aft edges of trays to form 'dams' seemed only to be worthwhile if strakes were present too.The prime effect of the strakes was deduced to be to roll up the fountain flow into a pair of quite strong and stable fore-and-aft vortices which were clearly seen to be present by means of a miniature wool-tuft wand. The vortex pair extended well beyond the tray in the fore-and-aft directions and so, for an aircraft, would be expected to be instrumental in promoting hot gas reingestation for configurations with engine intakes on either side of the fuselage.

A measurement difficulty was posed by the low magnitudes of the model trayforces. A simple calculation established that the jets' force at the most often used Mach number of 0.3 was about 4N (0.9 lbf) so it was considered to be necessary to discriminate fluctuating forces of about 0.04N (0.14 ozf). This was achieved by making an operational amplifier designed to in effect multiply the strain gauged load cell's signals by x1000. With such an amplification, signal interference from the stepper motors was found to be a major problem as the interference was both 'airborne' and cable borne. This elusive interference was eventually reduced to an acceptably small level and force discrimination was found to be better than 0.02N.

Time-averaged trayforces were first recorded manually over a time interval of a few seconds, also the highest and the lowest values in each time interval were logged. The range of fluctuation was typically +7% to -7% at H/D = 4 but only +2% to -2% at H/D = 2. Later the experimental system was substantially redesigned so that time-averaged data could be collected and processed automatically under microcomputer control. Typical plots of non-dimensional trayforce versus H/D and versus L/D are shown in figs. 13 & 14. Fig.13 is of especial interest because the data was mainly collected with the ground board moving towards the tray at from 5 to 60 mm/s and as can be seen the descent velocity made no discernable difference to the trayforce; a few data points were collected with the ground board in fixed positions - these are arrowed on the curve drawn through the main data. In order to attempt to relate the ground board range of descent velocities to full scale conditions it is noted that a descent rate of 45 mm/s was considered by Ing[6] to represent an aircraft descent rate of under 3 m/s. The

implication of fig.13 for a STOVL aircraft coming in to land vertically is that there will be a sudden suckdown following a peak of fountain flow buoyancy. An attitude control change might well occur if the aircraft approached the ground with even slight asymmetry - such asymmetry would be almost inevitable for a single-engined aircraft due to residual swirl from the engine compressor/turbine system.

Tests with pre-heated compressed air: At lower values of H/D a reduction in trayforce occurred when the jets' temperature was held at 180°C as compared with around 23°C for the previous tests. Some results are displayed on fig. 21 for several H/D for two tray heights, h. An earlier report by Karemaa et al[6] contained experimental evidence which is different in character. If the current results are correct then it would appear that it is sufficient only to conduct cold jet tests when investigating near-ground fountain flowfields because the trayforces are likely to be somewhat on the high side and it is clearly easier to set up the rig and do the tests.

3.3.2 Tray pressures.

A tray of length L = 40D was designed and made[7] with a set of pressure tappings across its width. This tray is shown in fig.15. The tray, which was longer than the diameter of the ground board, could be moved in the axial (z) direction; it could also be moved vertically so that h/D could range from +1 to -1. The lips were removable so that tests could be made with different lip heights, l.

Data was collected with the jets' Mach number held at 0.3 for a range of H/D, h/D, l/D and for z/D from zero to just under 5. The plotted results, of which figs. 16 - 18 are typical, are characteristically of a 'W' shape. A maximum peak value occurs near the datum position (ie where z = 0) for lower values of H/D. For z/D = 3 or more the peak was less pronounced and for H/D = 6 a peak was scarcely discernible beyond z/D = 3.

A short tray (L/D = 8) with pressure tappings was later designed and made. A large number of tests were carried out at M = 0.3 for various combinations of the geometric parameters H, h, l. Fig. 19 displays typical distributions of pressure across the tray for H/D = 2 & 3. Fig. 20 displays distributions of trayforce over the length of the tray for the same two H/Ds. Calculations confirmed that there is good correlation between tray forces determined from the pressure distributions and from direct measurements of force on a similar tray.

Comparisons with theoretical analyses:

Two limited attempts[9,10] at computational fluid dynamics (CFD) solutions to the model trayforce and its associated pressure distribution were made. The first analysis predicted a squarish strong axial vortex pair and a trayforce which was of the same order, but not closely the same as, the directly measured tray force. The second analysis resulted in much the same squarish vortex pair and a tray pressure distribution similar to those found from the model tests.

4. DISCUSSION

4.1. Data reliability.

Much care was taken to ensure that the relative positions of all parts of the rig were accurately defined, this was considered to be particularly important in view of the small scale of the rig.

All the experimentally obtained data were corrected for variations in ambient atmospheric pressure and temperature. Mach number effects were allowed for in the data processing computer-based calculations even though the jets' flow velocities were chosen to be low. The reason for allowing for compressibilty was the intention of working at a Mach number approaching 1.0 for subsequent tests.

There was found to be excellent correlation between the earlier trayforce tests, in which data was collected manually, and later tests conducted under computer control.

A high level of repeatability was achieved for the tray pressure tests and the fact that the trayforce found by integrating pressure correlated well with direct trayforce measurements for the same sets of values of H/D, L/D, h/D, l/D and M confirmed the reliabilty of the test data.

4.2 Relevance of the test results.

The application of the model test data collected and presented in this paper to full scale aircraft conditions is known to depend on Reynolds' number (R_e) and Mach number. Even approximate equality of R_e is clearly impossible as the corresponding jet velocity for the model would

have to be of the order of 25 times that of the prototype - totally unrealistic. It has to be accepted therefore, that the viscosity-dependent characteristics of the fountain flowfield will be different in the model tests to what would be expected to occur for a prototype. The extent to which this may matter is conjectual but intuitively felt not to be very significant. It could be checked by CFD studies. The effect of Mach number was much more readily accommodated as it simply demanded that the jets' velocity should be the same for the model and the prototype; for the range of low Mach numbers used in the model tests compressibility was of minor importance.

It may be fairly concluded that the results of the model tests provide a useful insight into the salient characteristics of two-jet fountain flow fields and that such tests may provide an inexpensive means of verifying computational fluid dynamics (CFD) analyses.

5. RECOMMENDATIONS

5.1 Instrumentation

As indicated in Section 1,Introduction, the tests were inexpensive to set up and conduct. The method of measuring tray-force by means of a load-cell designed to measure a vertical force vector irrespective of its line of action proved to be satisfactory although it would have been useful to have had a load cell constructed specifically to measure the small forces encountered; high primary signals would then have been obtainable which would have been less affected by electrical interference from outside sources such as stepper motors.

The miniature pitot head used to explore the unconfined fountain flow field could with advantage, be replaced by a laser-Doppler system which is totally non-intrusive. Alternatively, or additionally hot-wire anemometry could be used. In either case velocity vector surveys could then be conducted directly.

For flow visualisation it would be useful to employ the laser sheet illumination technique to obtain views of the flow field in xy 'slices' at various axial (z) stations and various yz slices at various transverse stations (x).

5.2 Concluding remarks

A thorough examination of the fountain flow field due to two parallel subsonic jets has been completed and the main characteristics of such fields determined. The usefulness of small-scale testing has been demonstrated so it is hoped that it will be further employed and exploited. It is likely that systems using under-expanded arrays of three or more jets will attract STOVL aircraft designers in the future so there is clearly much scope for developing model experimentation along the lines, for instance, of that pursued by Smith et al[11].

6.ACKNOWLEDGEMENTS

A major part of the experimental research described in this paper was funded by Logico Systems Ltd under a British Aerospace (Military Aircraft) Ltd. contract. The advice, encouragement and contribution to the analysis of data by the Director of the former company, Dr Dan Ing, is gratefully acknowledged.

Grateful thanks are also due to the Head of the School of Mechanical, Aerospace and Manufacturing Engineering, Professor Brian Dawson and members of the staff of the Faculty of Technology at Kingston Polytechnic.

References

1. Ransom, E C P & Barnes, J H.

The calculation of jet interference pressure distribution using integral and numerical methods based on actual measurements of entrainment. Kingston Polytechnic, UK. 1982.

2. Pope, A & Harper, J J.

Wind tunnel testing, chapter 3. Wiley, USA, 1966.

3. Rajaratnam, N.

Turbulent jets. Elsevier, Holland. 1976.

4. Gilbert,Barry.

Turbulence measurements in a radial upwash. AIAA journal, vol. 27, pp 44-51. Jan. 1989.

5. Ing, D N.

Preliminary flow visualisation tests with water on the early stages of jet fountain development. Logico

Systems Ltd. UK. 1987.

6.Ing D N, Hope L J & Ransom E C P.

Static and transient measurements of force, pressure and temperature distribution of a twin-jet impingement fountain flow. Logico Systems Ltd. UK. 1989.

7.Dixon G M
Twin jet impingement investigation for STOVL flight. Undergraduate Project.Kingston Polytechnic. UK. 1990.

8.Karemaa A, Smith C W, Weber H A & Garner J E.

The aerodynamic and thermodynamic characteristics of fountains and some far-field temperature distributions. General Dynamics Convair Division. USA. August 1978.

9. Vasquez-Malebran S & Ing D N.

Navier-Stokes simulations of a twin-jet ground impingement. Logico Systems Ltd. UK. 1988.

10.Williams A.

Computer-based airflow modelling. Undergraduate project. Kingston Polytechnic. UK. 1990.

11.Smith A G, Ing D N & Bailey P J.

The experimental and computational study of jet impingement flowfields with reference to VSTOL aircraft performance.

International Powered Lift Conference Royal Aeronautical Society. UK. August 1990.

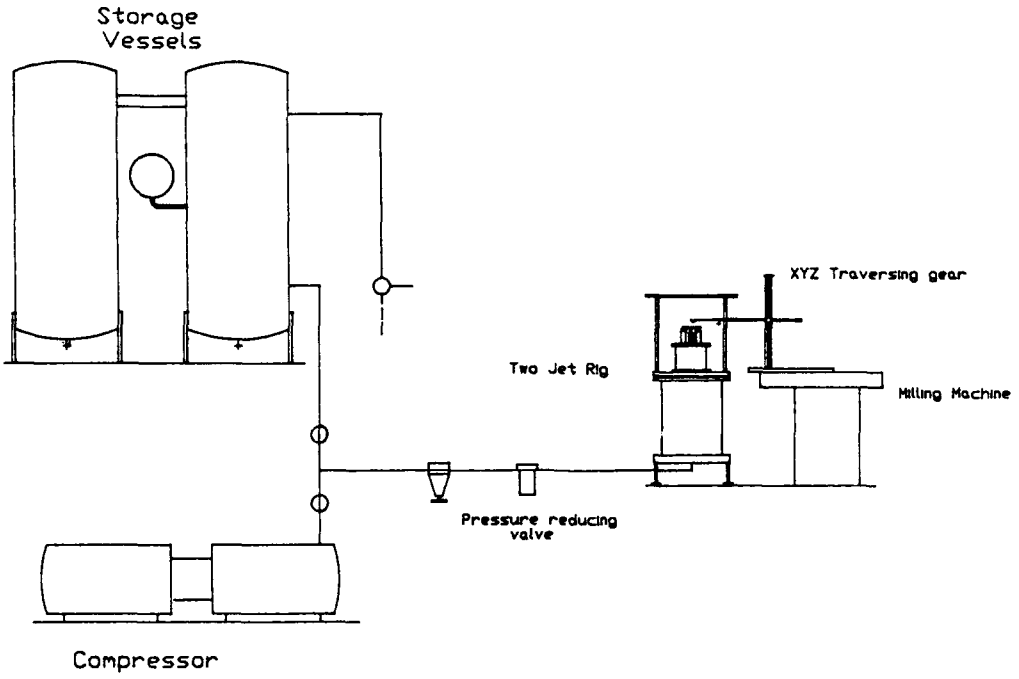

Fig.1 Schematic view of two-jet test facility

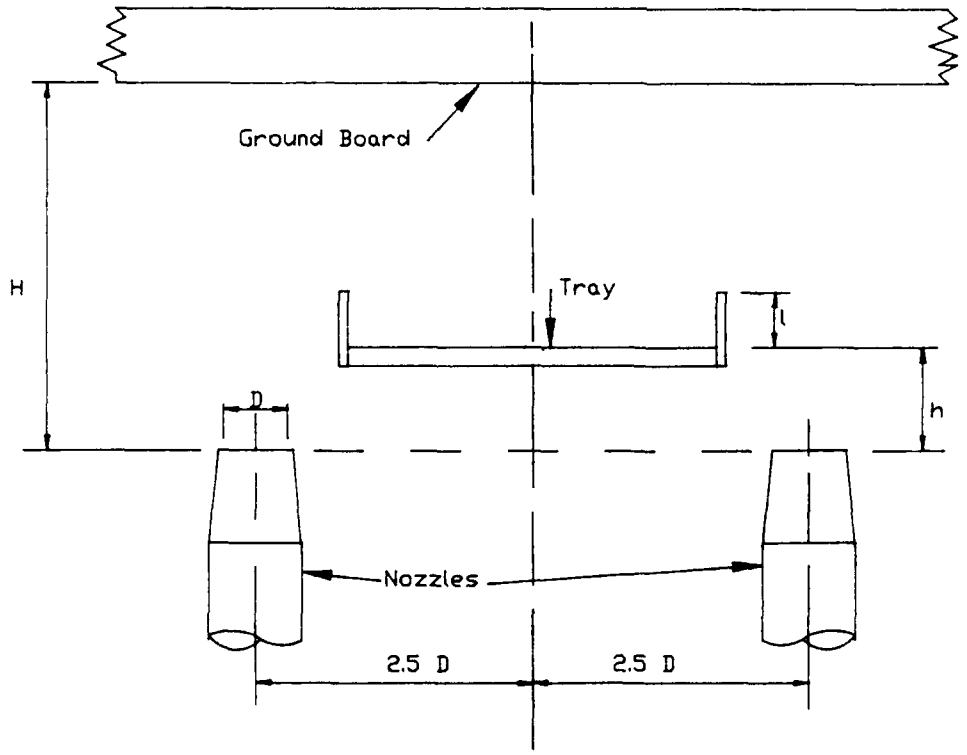

Fig.2 Arrangement of nozzles, tray and ground board

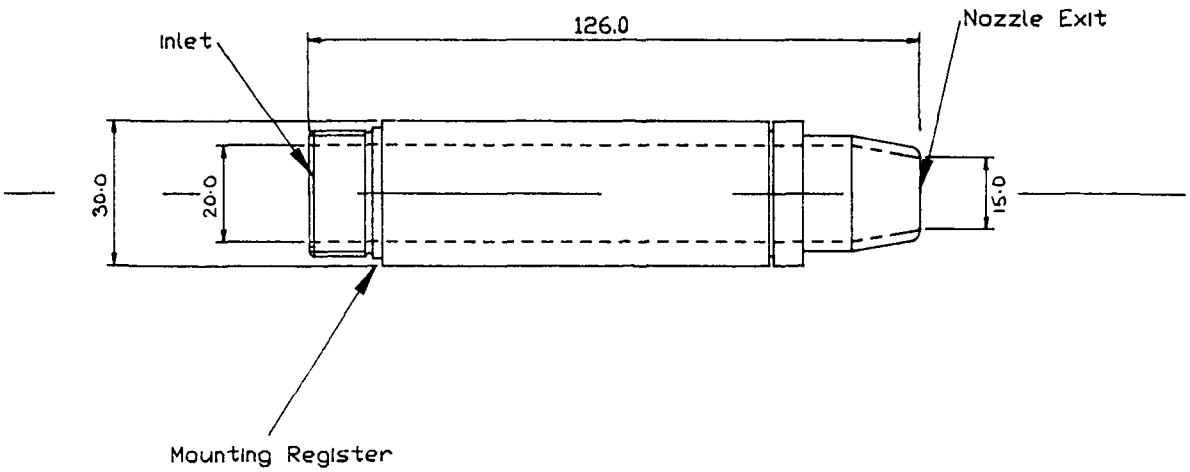
Inlet
126.0
Nozzle Exit
30.0
20.0
15.0
Mounting Register

Fig.3

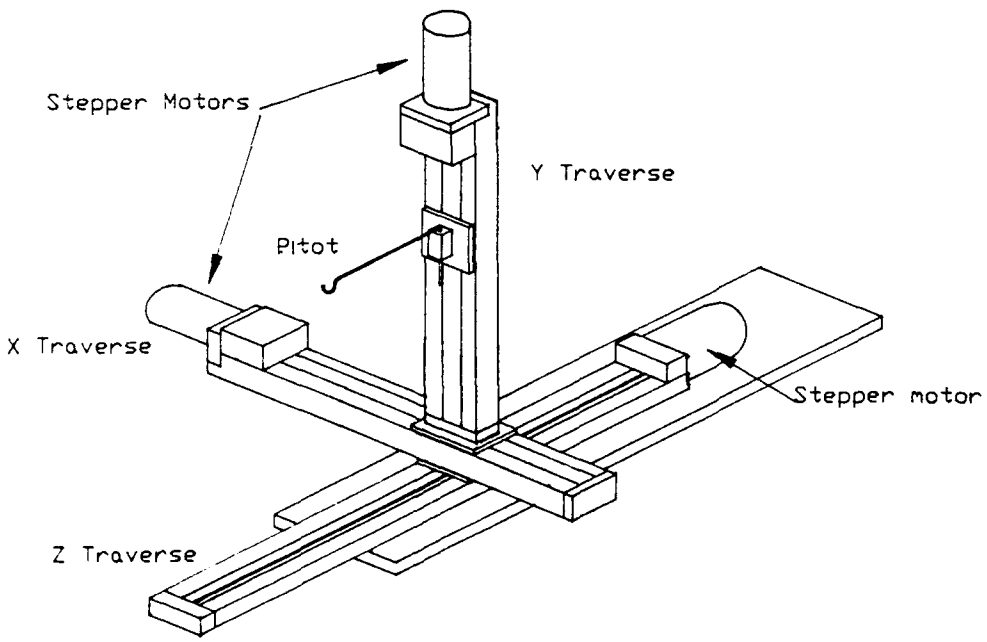
Stepper Motors
Y Traverse
Pitot
X Traverse
Stepper motor
Z Traverse

Fig.4

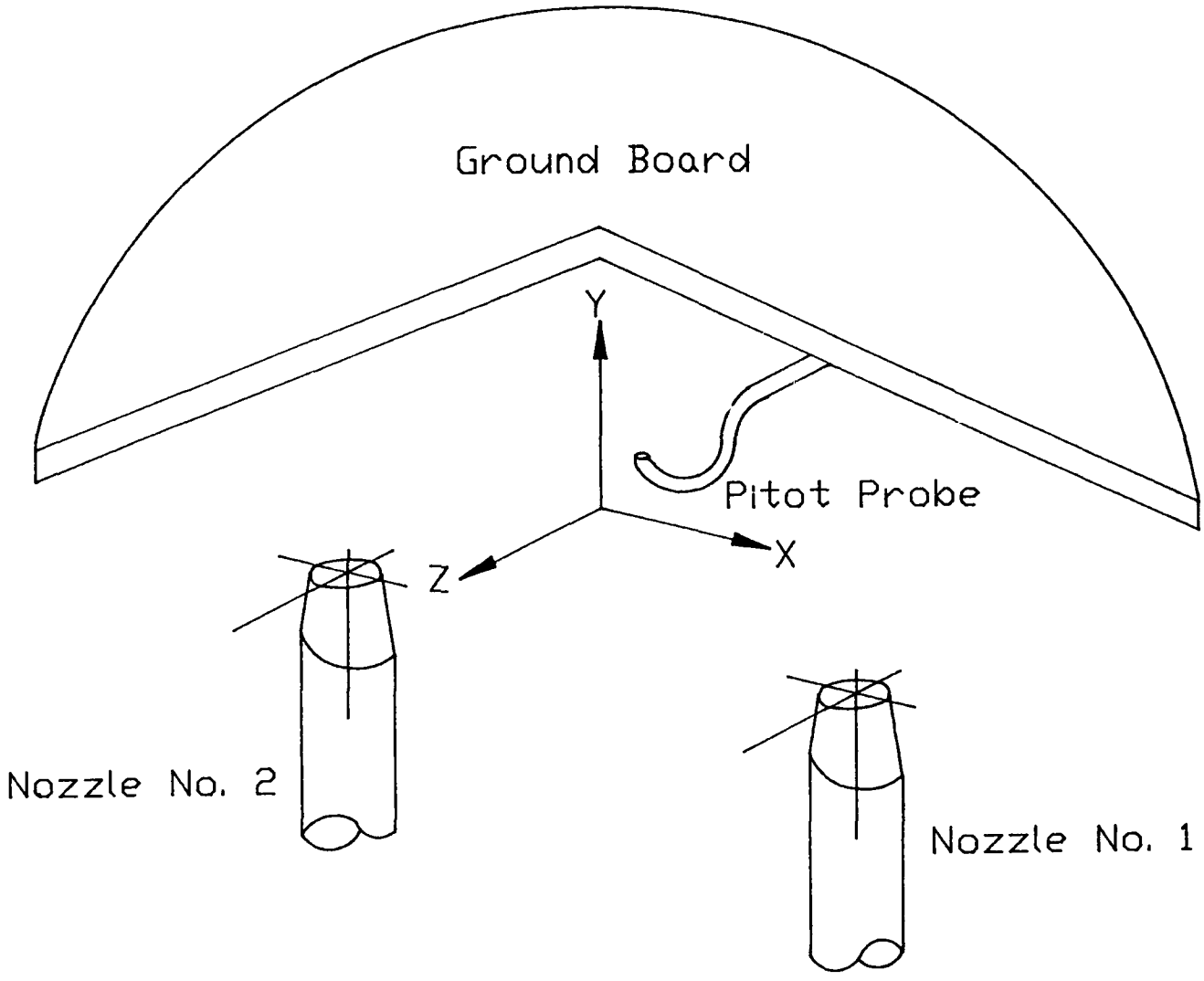

Fig.5

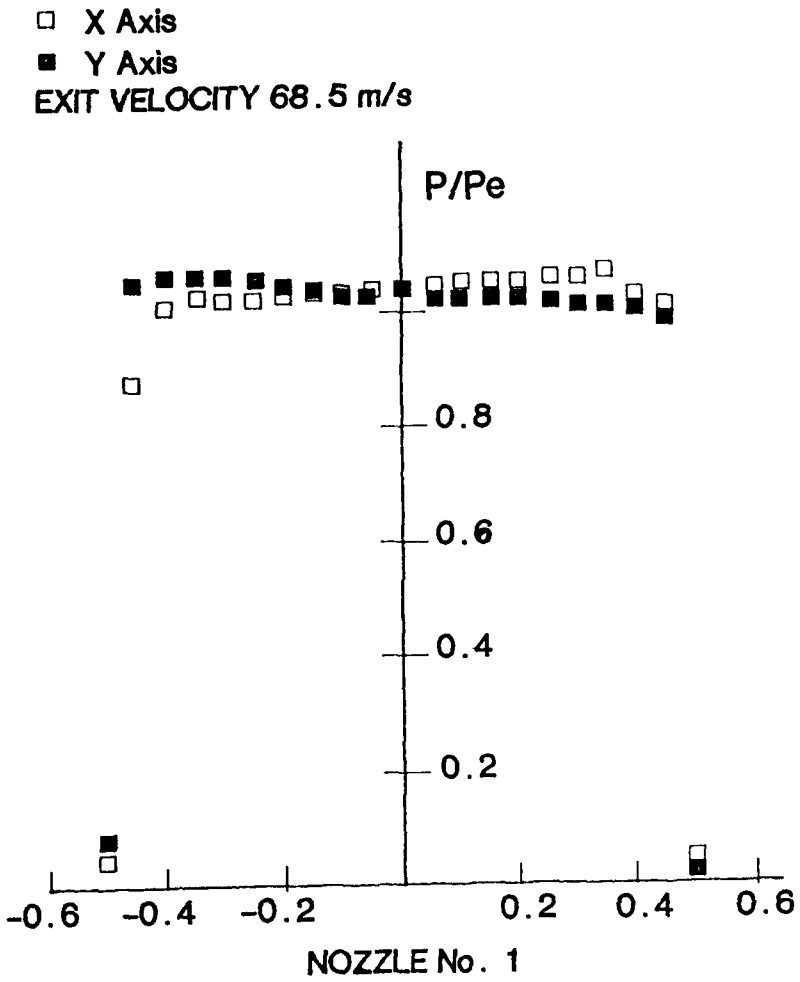
X Axis
Y Axis
EXIT VELOCITY 68.5 m/s
P/Pe
0.8
0.6
0.4
0.2
-0.6
-0.4
-0.2
0.2
0.4
0.6
NOZZLE No. 1

Fig.6

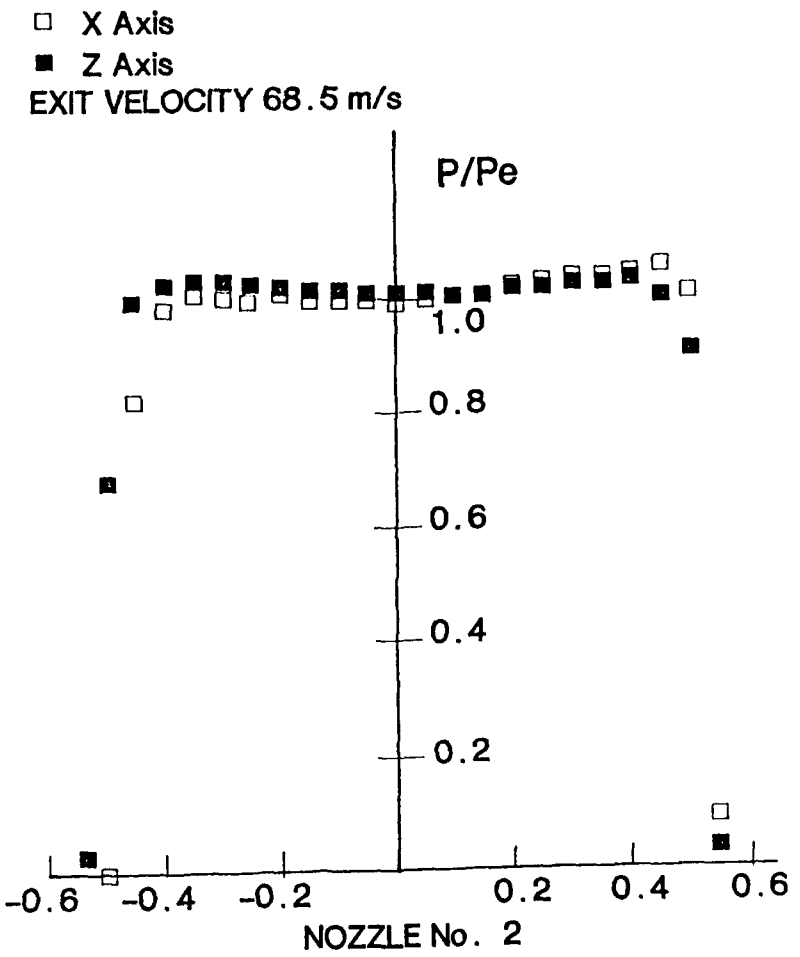
X Axis
Z Axis
EXIT VELOCITY 68.5 m/s
P/Pe
1.0
0.8
0.6
0.4
0.2
-0.6
-0.4
-0.2
0.2
0.4
0.6
NOZZLE No. 2

Fig.7

Total Pressure Profiles

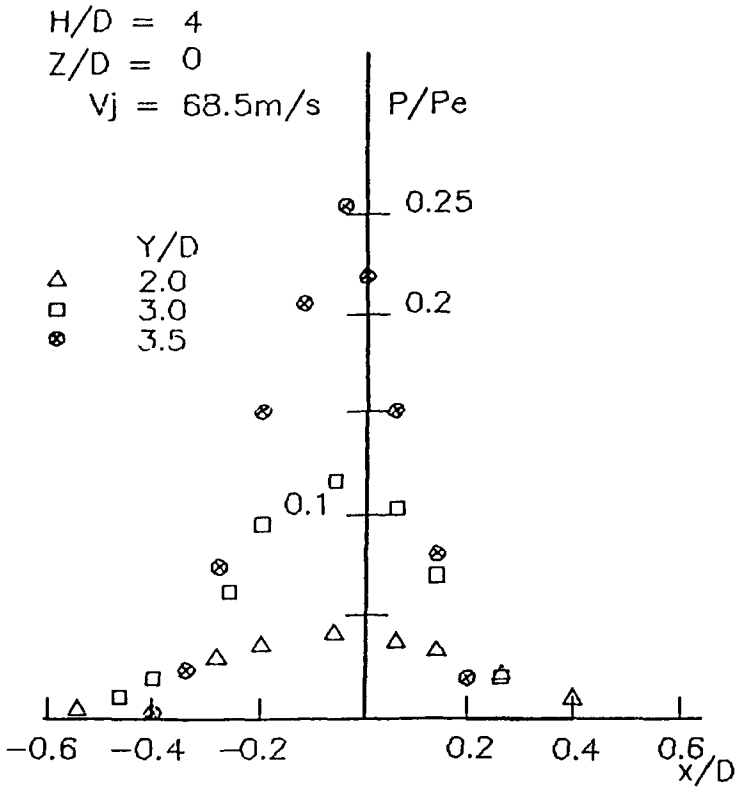

Fig.8

Total Pressure Profiles

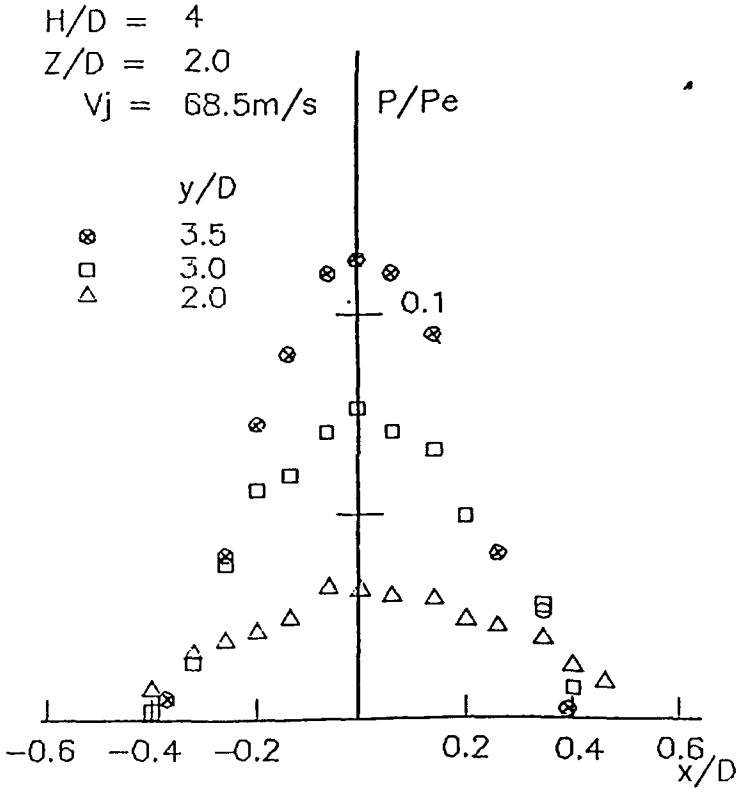

Fig.9

(a) SMOKE VAPOUR $H/D=4$, $V_j \sim 6m/s$

(b) OIL FILM ON GROUND BOARD

Fig.10 Flow visualisation of two-jet fountain

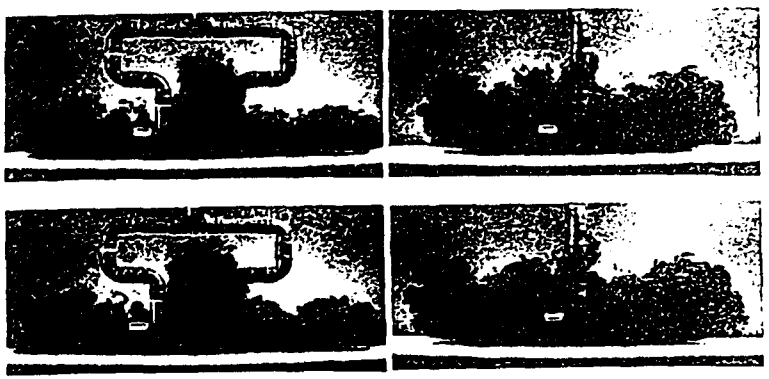

Front Side

H/D = 1.9

Front Side

H/D = 4.7

Fig.11

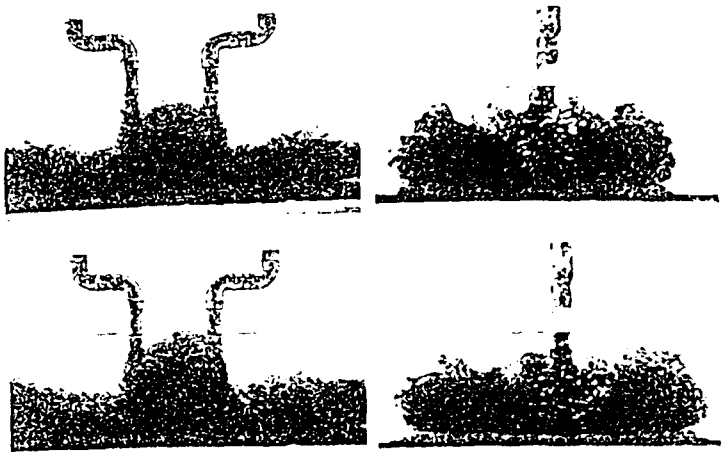

Front Side

H/D = 6.6

Front Side

H/D = 7.9

Fig.12

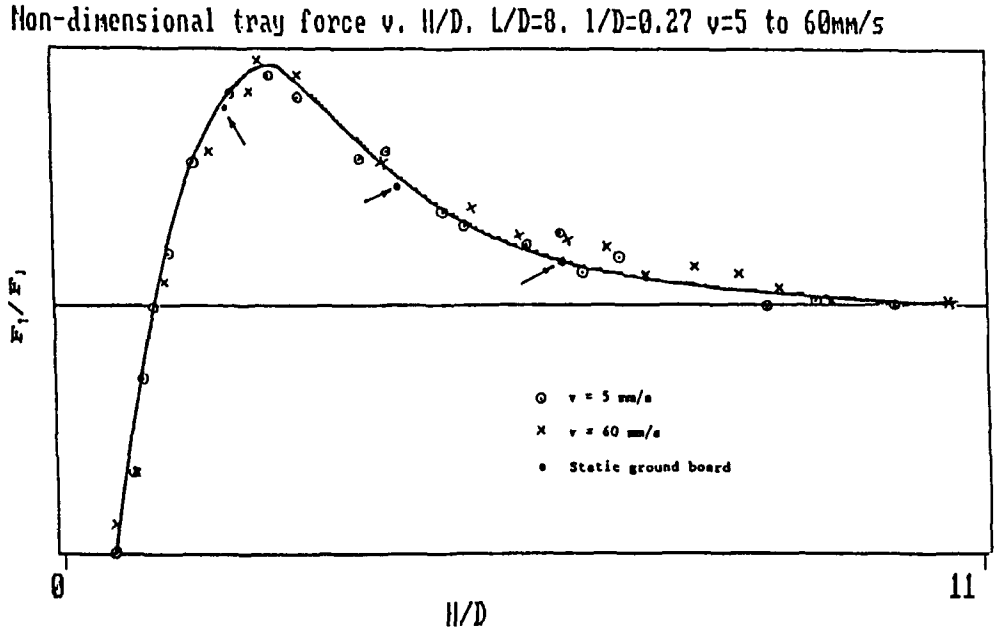
Non-dimensional tray force v. H/D. L/D=8. l/D=0.27 v=5 to 60mm/s
F_t / F_1
v = 5 mm/s
v = 60 mm/s
Static ground board
0
11
H/D

Fig.13

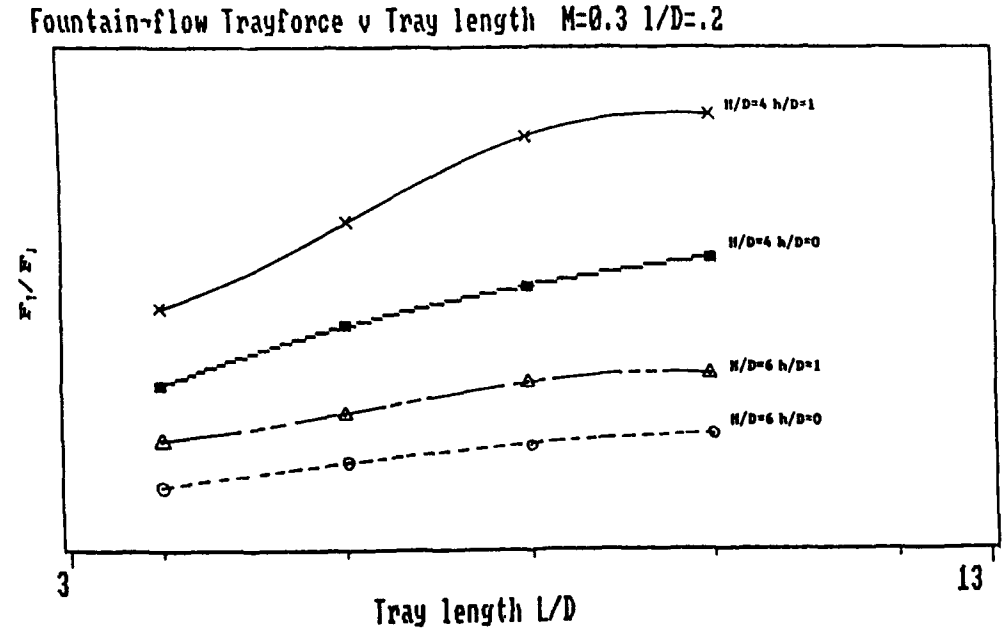
Fountain-flow Trayforce v Tray length M=0.3 l/D=.2
F_t / F_1
H/D=4 h/D=1
H/D=4 h/D=0
H/D=6 h/D=1
H/D=6 h/D=0
3
13
Tray length L/D

Fig.14

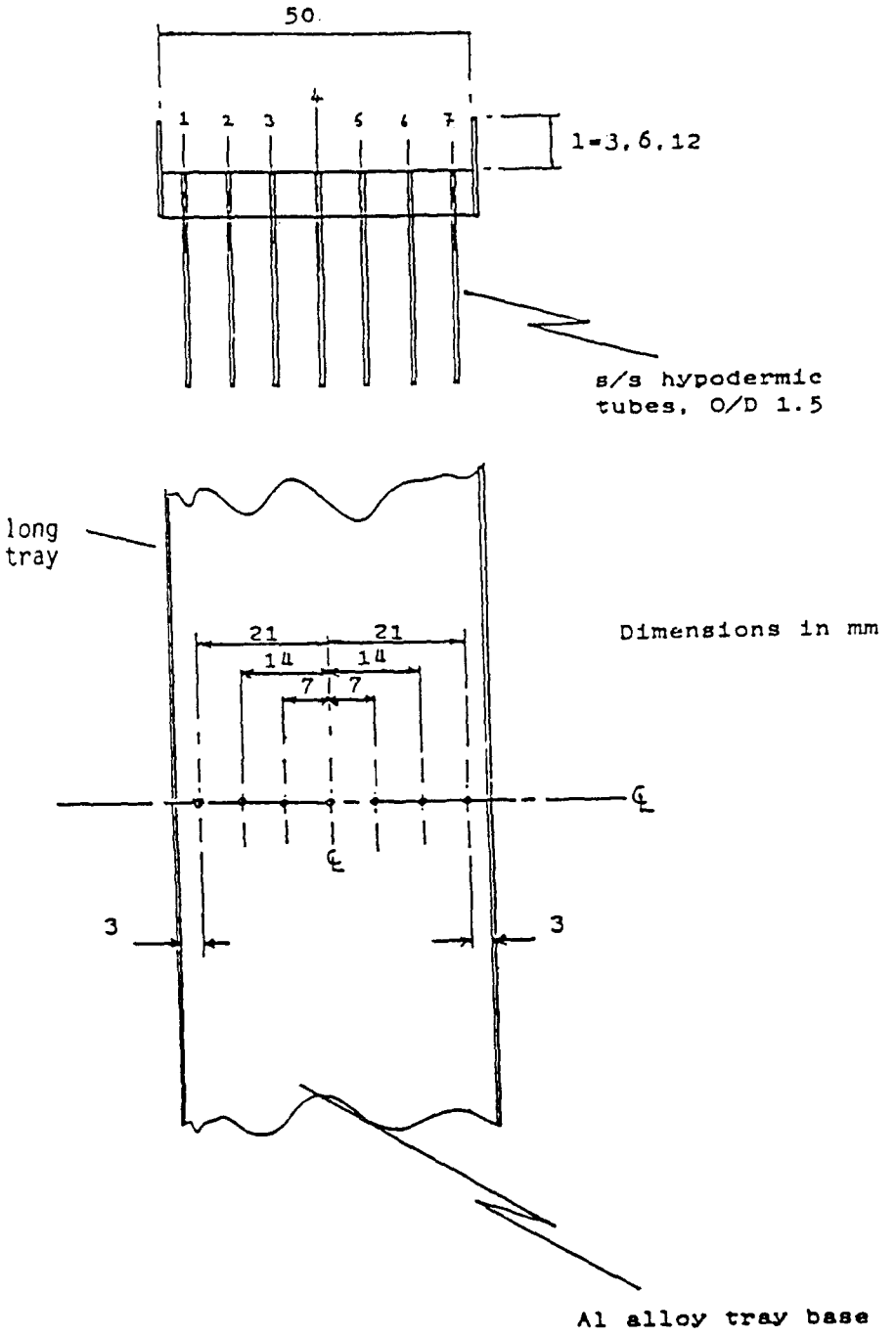
50
1 2 3 4 5 6 7
l=3, 6, 12
s/s hypodermic tubes, O/D 1.5
long tray
21
21
14
14
7
7
℄
℄
3
3
Dimensions in mm
Al alloy tray base

Fig.15

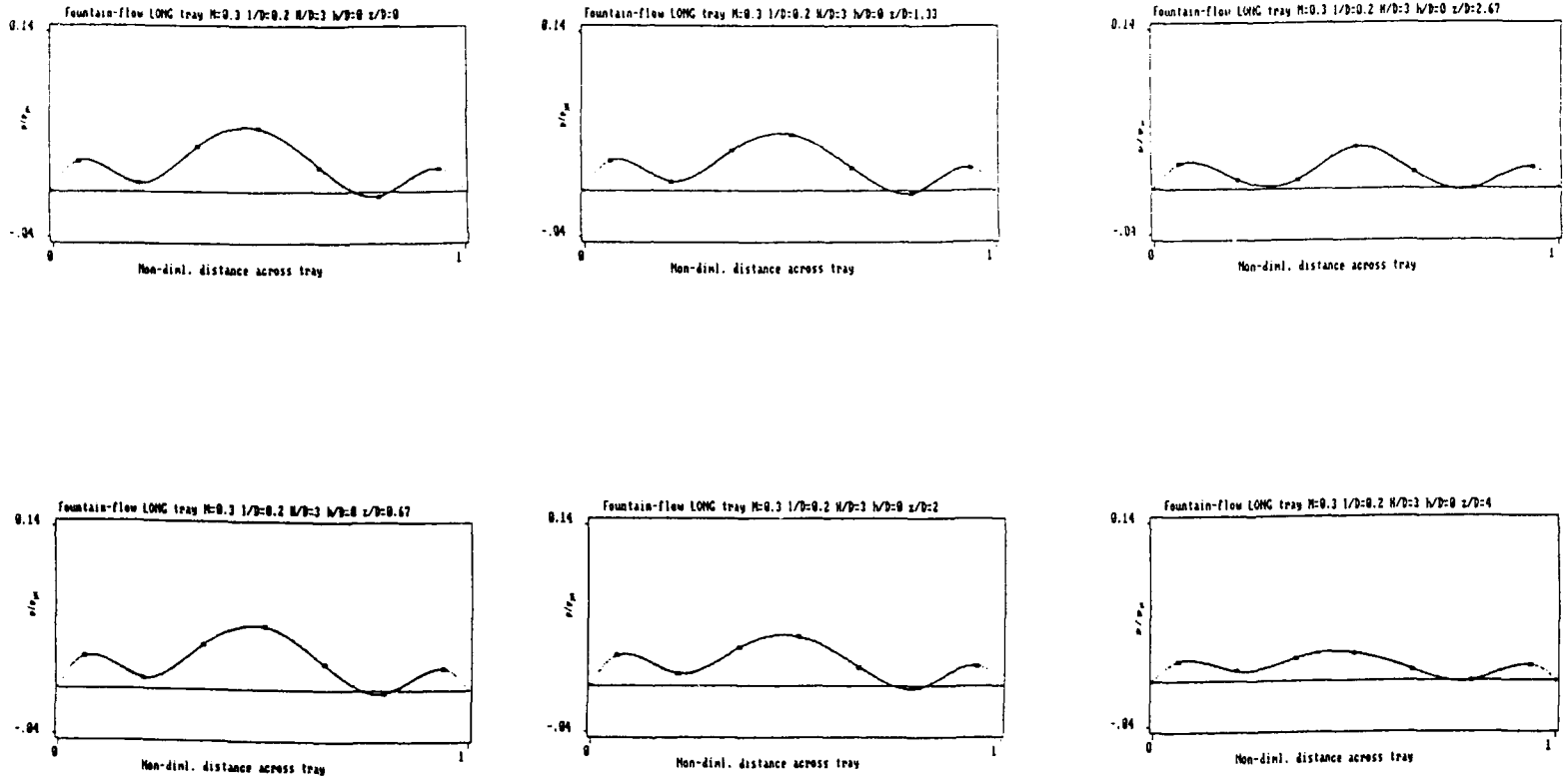
Fountain-flow LONG tray M:0.3 l/D:0.2 H/D:3 h/D:0 z/D:0
0.14
-.04
0
1
Non-dim. distance across tray
Fountain-flow LONG tray M:0.3 l/D:0.2 H/D:3 h/D:0 z/D:1.33
0.14
-.04
0
1
Non-dim. distance across tray
Fountain-flow LONG tray M:0.3 l/D:0.2 H/D:3 h/D:0 z/D:2.67
0.14
-.04
0
1
Non-dim. distance across tray
Fountain-flow LONG tray M:0.3 l/D:0.2 H/D:3 h/D:0 z/D:0.67
0.14
-.04
0
1
Non-dim. distance across tray
Fountain-flow LONG tray M:0.3 l/D:0.2 H/D:3 h/D:0 z/D:2
0.14
-.04
0
1
Non-dim. distance across tray
Fountain-flow LONG tray M:0.3 l/D:0.2 H/D:3 h/D:0 z/D:4
0.14
-.04
0
1
Non-dim. distance across tray

Fig.16

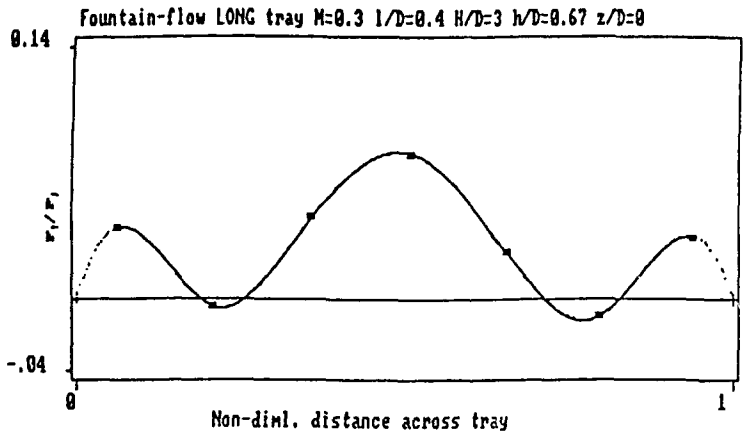
Fountain-flow LONG tray M=0.3 l/D=0.4 H/D=3 h/D=0.67 z/D=0
0.14
-.04
0
1
Non-diml. distance across tray

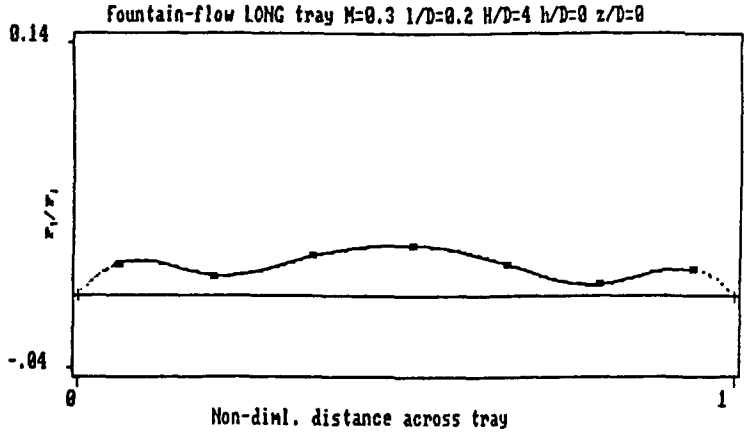
Fountain-flow LONG tray M=0.3 l/D=0.2 H/D=4 h/D=0 z/D=0
0.14
-.04
0
1
Non-diml. distance across tray

Fig.17

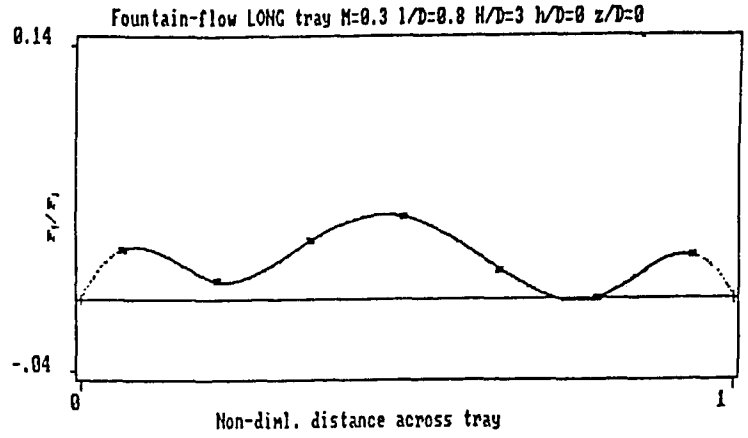
Fountain-flow LONG tray M=0.3 l/D=0.8 H/D=3 h/D=0 z/D=0
0.14
-.04
0
1
Non-diml. distance across tray

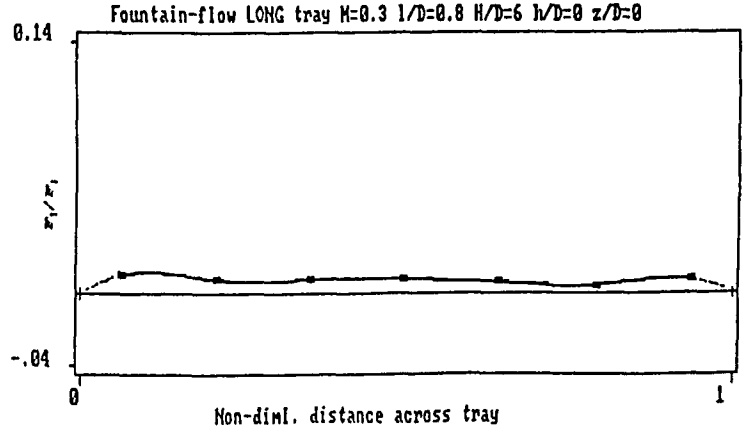
Fountain-flow LONG tray M=0.3 l/D=0.8 H/D=6 h/D=0 z/D=0
0.14
-.04
0
1
Non-diml. distance across tray

Fig.18

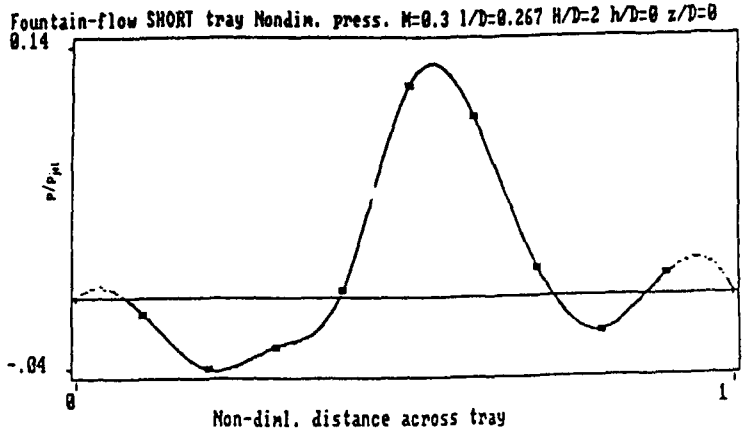
Fountain-flow SHORT tray Nondim. press. M=0.3 l/D=0.267 H/D=2 h/D=0 z/D=0
0.14
p/p_jet
-.04
0
1
Non-diml. distance across tray

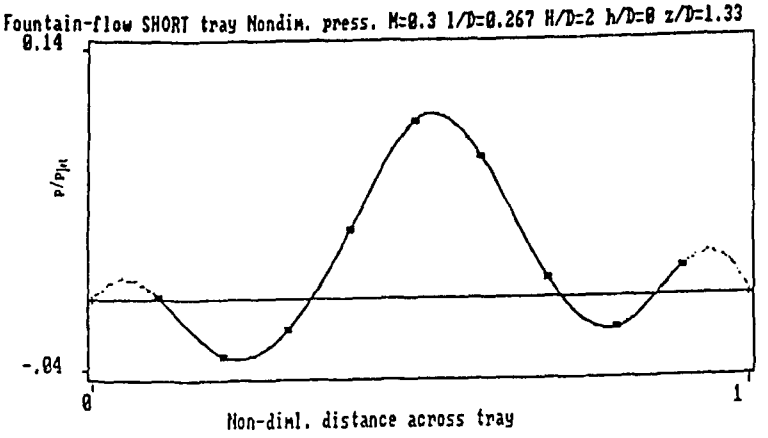
Fountain-flow SHORT tray Nondim. press. M=0.3 l/D=0.267 H/D=2 h/D=0 z/D=1.33
0.14
p/p_jet
-.04
0
1
Non-diml. distance across tray

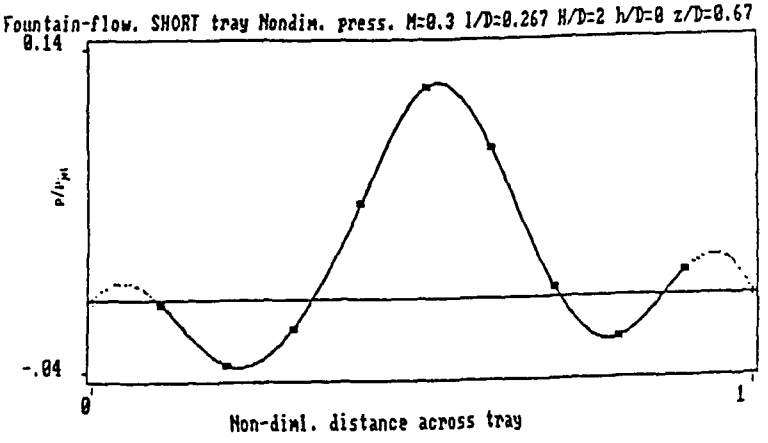
Fountain-flow. SHORT tray Nondim. press. M=0.3 l/D=0.267 H/D=2 h/D=0 z/D=0.67
0.14
p/p_jet
-.04
0
1
Non-diml. distance across tray

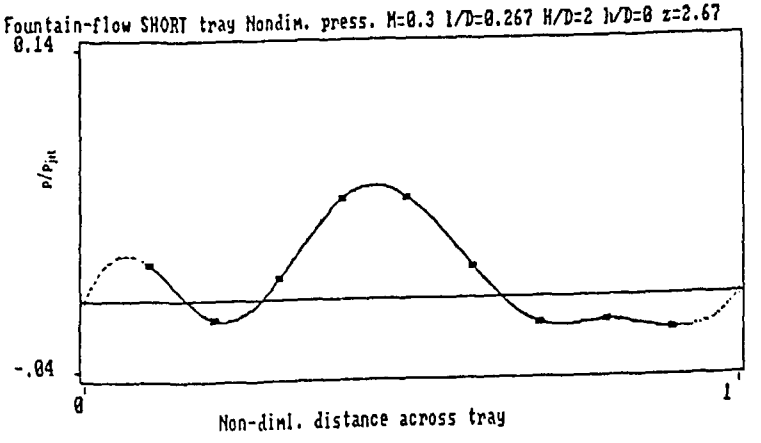
Fountain-flow SHORT tray Nondim. press. M=0.3 l/D=0.267 H/D=2 h/D=0 z=2.67
0.14
p/p_jet
-.04
0
1
Non-diml. distance across tray

Fig.19

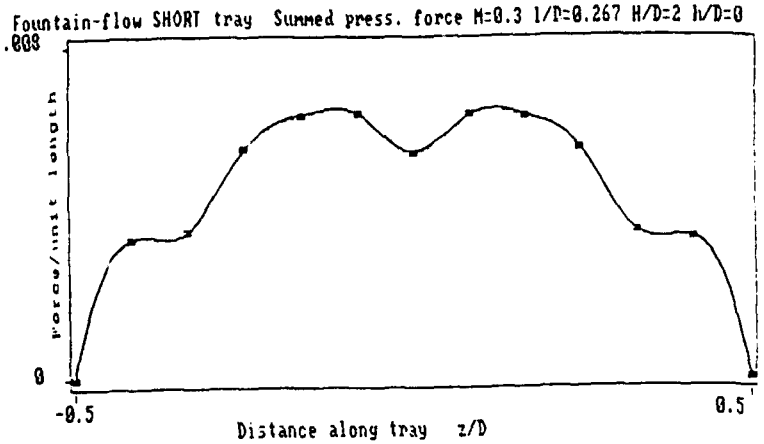
Fountain-flow SHORT tray Summed press. force M=0.3 l/D=0.267 H/D=2 h/D=0
.008
Force/unit length
0
-0.5
0.5
Distance along tray z/D

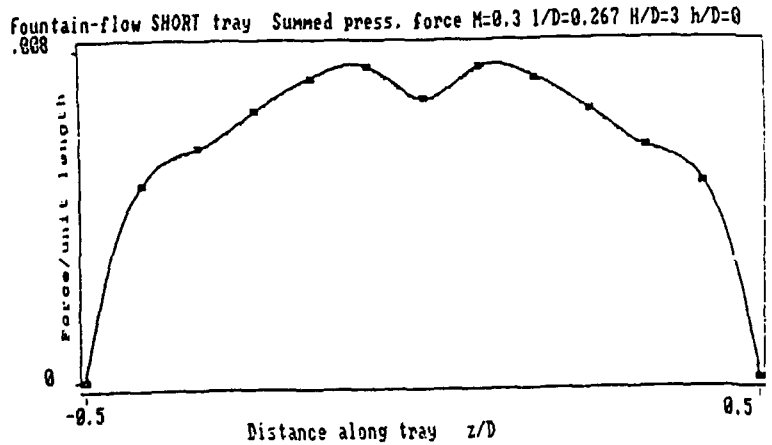
Fountain-flow SHORT tray Summed press. force M=0.3 l/D=0.267 H/D=3 h/D=0
.008
Force/unit length
0
-0.5
0.5
Distance along tray z/D

Fig.20

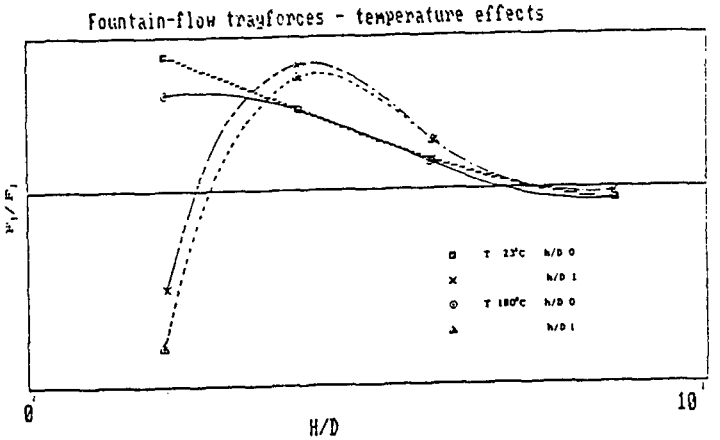
Fountain-flow trayforces - temperature effects
0
10
H/D

Fig.21

THE JET BEHAVIOUR OF AN ACTUAL HIGH-BYPASS ENGINE AS DETERMINED BY LDA-MEASUREMENTS IN GROUND TESTS

by

H. Hoheisel*, K.A. Bütefisch, B. Lehmann*****
R. Henke****, H.J. Roscher* and U. Seelhorst****

* Deutsche Forschungsanstalt für Luft- und Raumfahrt (DLR)
Institut für Entwurfsaerodynamik, Braunschweig, Germany
** DLR, Institut für Experimentelle Strömungsmechanik
Göttingen, Germany
*** DLR, Abteilung Turbulenzforschung, Berlin, Germany
**** Deutsche Airbus GmbH, Flughafen, 2800 Bremen,
Germany

SUMMARY

The present contribution describes the measurements of a three-component LDA within the jet of a bypass engine CFM56-5 installed on an A320, in the form of ground tests. The aerodynamic data obtained at the fan exit and in two sections at the turbine nozzle exit near cruise condition allow an insight into the complete jet behaviour. The velocity components in the specified position for all three coordinate directions are discussed allowing the evaluation of the radial velocity distribution and the swirl components. In addition, the important parameters of the turbulence intensity and the direction of the thrust vector are considered.

LIST OF SYMBOLS

A	Area
Ma	Mach number
N1	Fan speed (RPM)
p_t	Total pressure
p	Static pressure
R	Radial distance from the surface (see figure 10)
u,v,w	Velocity components
u',v',w'	Components of velocity fluctuations
u_∞	Free stream velocity
VTA	Swirl component
x,y,z	Coordinates (see figure 10)
φ	Angle in circumferential direction
ϑ	Flow direction between x and z (see figure 10)
ϵ	Jet spread angle
A,B,C,D	Different sections behind fan exit (see figure 3)
LDA	Laser Doppler Anemometer
j	Jet
-	Above symbols = average value
max	Maximum

1. INTRODUCTION

For the development of computation procedures as well as for the actual design of transport aircrafts there exists a real need for knowledge concerning the mechanism of the aerodynamic interference between the engine flow and the wing-body. In particular the development of present fan engines with bypass ratios of around 5 follows a trend to new engine concepts with extreme high bypass ratios. This development leads to larger dimensions of the engines so that the problems of aerodynamic integration is of special importance. The real physical conditions of the jets under the influence of the airframe aerodynamics must be taken into account [1, 2, 3]. Also in wind tunnel testing the real conditions of the engine flow has to be completely simulated [4]. The best simulation technique consists in the application of so-called Turbine-Powered Simulators (TPS-technique) which allow at least the fan flow to be realistically simulated [5]. Therefore, for the computation procedures as well as for performing experiments there exists a strong interest to know the real conditions in the jet flow field of actual high bypass fan engines.

As very few data have been published on engine jet flow, e.g. [6] an agreement between the DLR (Institute for Design Aerodynamics Braunschweig and the Institute for Experimental Fluid Mechanics Göttingen) and the firms Deutsche Airbus/ Airbus Industrie respectively was met to obtain such data for an actual aircraft. The relevant experimental data are to be acquired by means of a 3-D LDA system developed by the DLR-Göttingen [7]. These LDA-measurements took place on a CFM56-engine at Toulouse two years ago on a flight test aircraft A320 with relevant test equipment, in form of "ground tests".

The present contribution describes the measurements performed with a three-component LDA within the jet. The jet data obtained at the fan exit and at the turbine nozzle exit allow an insight into the jet behaviour without external flow for about 80% engine speed. The velocity components in the specified positions for all three coordinate directions are discussed, allowing the evaluation of the overall quantities like swirl, flow direction, thrust vector and turbulence level.

2. EXPERIMENTAL SET-UP

2.1. Aircraft set-up and test programme

The complete set-up of the used aircraft A320 on the Engine-Test-Place at Toulouse is shown in figure 1. The LDA-measurements were carried out on the left engine. The figure 2 shows the position of all devices relative to the airplane. The engine runs were controlled by the flight engineer from the cockpit. All engine data like RPM corrected to standard atmospheric condition, ambient temperature and pressure, direction and velocity of wind were recorded by the data acquisition system of the aircraft.

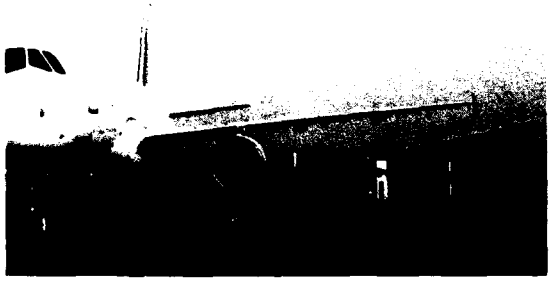

Figure 1. Aircraft set-up

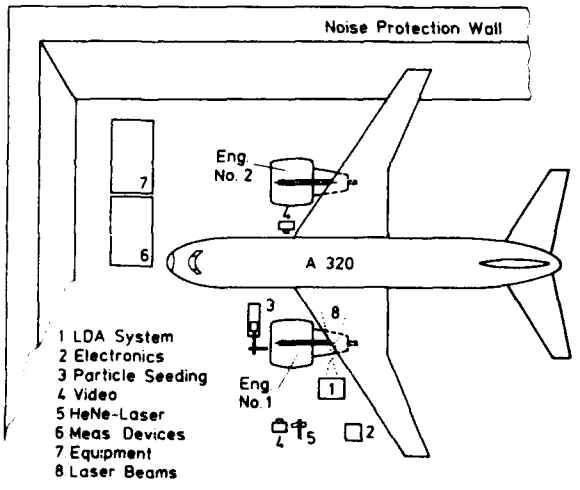

Figure 2. Position of the devices relative to the aircraft

Main purpose of the tests is to get information regarding

- jet velocity profiles including the three components, turbulence level and swirl behaviour and
- possibly the direction of the total thrust vector.

The determination of the radially sampled velocity profiles was carried out in three sections A, B and C at φ = 200° as shown in figure 3. The position φ = 200° in sector 7 was chosen in order to avoid scatter of the laser light from walls of the aircraft. In a section B2 - parallel to the ground - the symmetry behaviour of the fan flow was to be estimated.

To get information on the complete jet flow field behind the engine and to get information possibly on the total thrust-direction, measurements in six sections D1 to D6 were carried out along vertical lines behind the hot jet nozzle (see figure 3).

All measurements were carried out at N1 = 80% RPM of maximum speed, with the exception of section A, where measurements at N1 = 60%, 70%, 80% and 85% were carried out. For all measurements only the left engine of the aircraft was in operation. Before starting the laser measurements preliminary tests on the following items were necessary:

- Tests for the seeding on the flow.
- Determination of engine center line.
- Tests for determination of the engine position running with power.

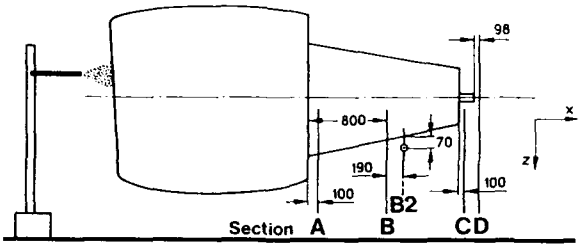

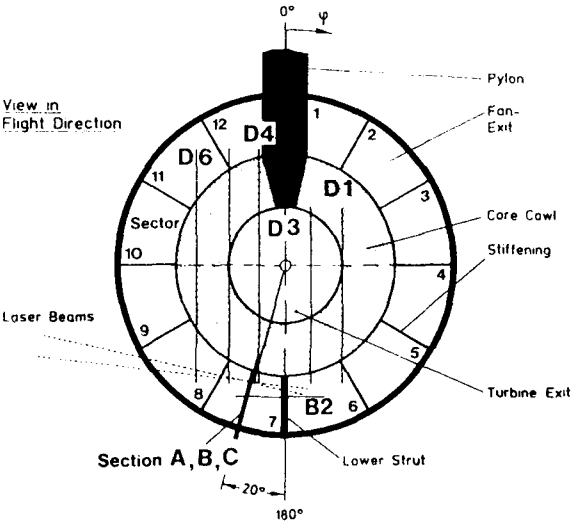

Notation

A 1 03
- 03 — Test-No.
- 1 — Radial for sections A, B, C and transverse section (Y) for D
- A — Section in X-direction

Figure 3. Test section on the engine

2.2 Laser-Doppler-Anemometer

The three-component Laser-Doppler-Anemometer used for this investigation has been developed at the Institute of Experimental Fluid Mechanics Göttingen. It works on a

back-scatter off-axis using a 4 Watt argon-ion laser and has a focal length of 2.3 m. Details are described in [7]. The LDA system was mounted on a traversing system with an x-axis range of 0.5 m and y- and z-axis ranges of 1.0 m respectively. Figure 4 shows the schematic set-up of the 3D-LDA system. The installed LDA by the side of the engine can be seen on figure 5. For comparison of the level of the velocities measured with the LDA system a Prandtl- and temperature probe respectively was mounted in the fan exit plane and can also be seen in figure 5. The LDA-system was remotely controlled, because the distance between the LDA and the recording devices was about 50 m (see figure 2) and nobody was permitted to stay close to the engine during a run. Additionally a video camera was mounted in order to monitor the position of the measuring volume during the runs. When the LDA was moved the seeding probe had to be also readjusted, again remotely controlled.

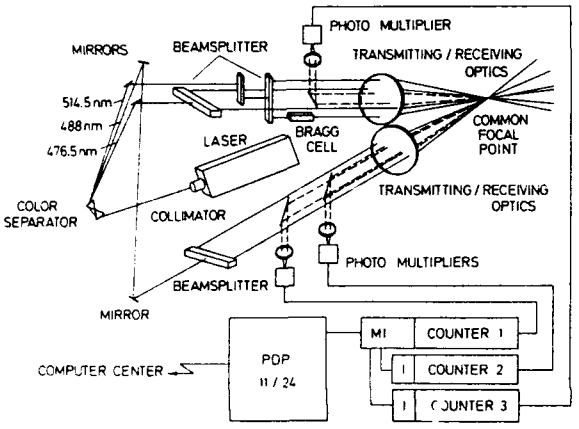

Figure 4. Optical arrangement of the three-component LDA-system

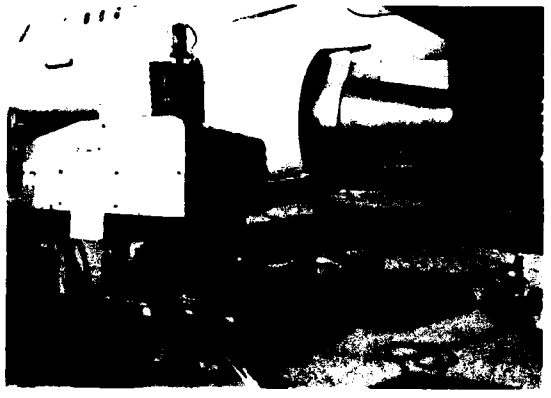

Figure 5. LDA set-up

Using the highly complex three-component LDA-system a main task of a suitable Doppler-signal analyser is to acquire the signals and to analyze their different frequencies as fast as possible. The related individual velocity events are accumulated in data stores in order to compute the local mean flow-field data. Two fundamentally different techniques were applied to analyze these frequencies received from the three-component optical Doppler arrangement. The first technique used is the so-called counter technique [7]. This technique is very fast but needs very good signal-to-noise ratios which cannot be expected in all measurement position of interest. The second technique used, digitizes the Doppler signal and computes its frequency spectrum by means of a fast-Fourier transformation [18]. All the results presented here are optimized by using the data of the two techniques.

The most important problem in using the Laser-Doppler-Anemometry for investigation of engine-jet flow is to provide for enough seeding particles. There was only some experience available how to seed the flow of a real aircraft engine from earlier tests on a Rolls-Royce M45 H engine [8]. In the case of the present CFM56-5 engine some engine runs were necessary to get particles at the correct measuring volume (see figure 6). In the fan flow so-called "disco-fog" was used. In order to increase the low data rate within the shear layer, an additional seeding device was installed outside the jet (see position 2a in figure 7). The seeding of the turbine jet flow was not possible, because the use of titan dioxide (T_iO_2) was not allowed. Obviously, due to the high efficiency of the combustion there were only very few soot particles. For this reason, the collection of 1000 individuell samples

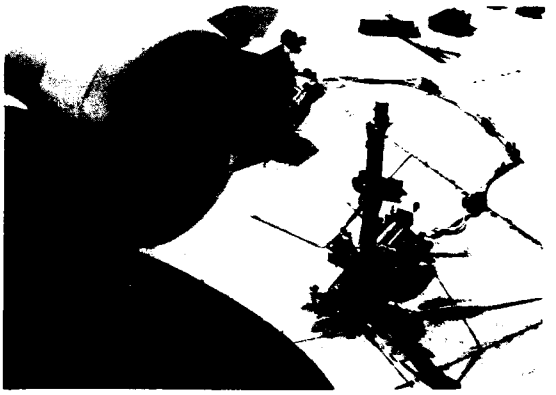

Figure 6. Seeding equipment in front of the engine

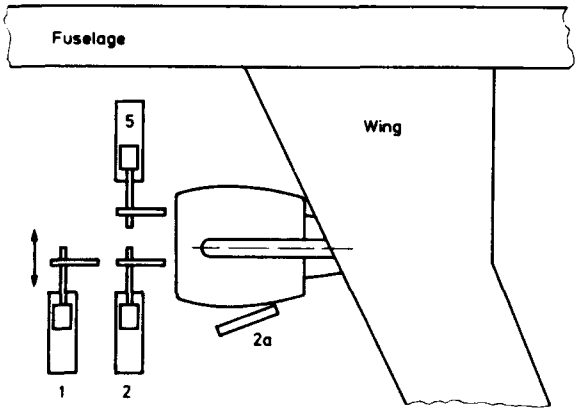

Figure 7. Seeding positions from top

at one measuring station within the hot turbine exit flow took up to 5 minutes acquisition time and hence the number of data points in section C and D was deminished. More details of these special problems are described in [9].

3. DETECTION OF THE ENGINE AXIS AND THE POSITION OF THE ENGINE

In order to align the optical axes of the LDA correctly in reference to the engine, the detection of the engine axis was demanded. This was done without engine thrust (no operation) as shown in figure 8. A small mirror was fixed on the engine's inlet cone nearly rectangular aligned to its axis. In front of and about 5 m away from the inlet a small laser beam was directed into the center of the mirror. When the engine cone together with the mirror was manually rotated the reflection of the laser beam was observed on a screen near the laser. If this reflex moved concentrically around the original beam which was achieved by shifting the laser, the beam direction indicated the wanted axis. Then a perpendicular line was drawn from the light beam to the ground and extended to the outlet region below the engine. Different measurements of distance of the laser beam to the ground permitted to measure the angle of attack of the engine. This resulted in about 1.2 degree measured against the horizontal direction for the switched off engine.

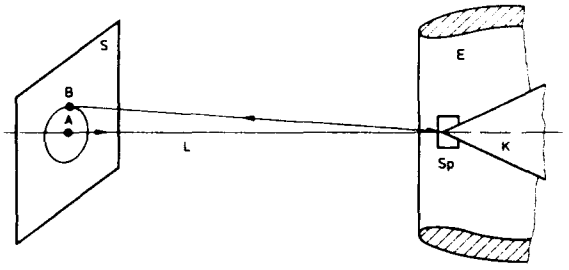

Figure 8. Arrangement to detect the axis of the engine

A special instrumentation was also developed to determine simultaneously to the velocits measurements the real position of the engine being in operation on ground. This instrumentation was able to record the movement on the axis x, z. From these measurements the overall movement in x-direction was obtained, for N1 = 80% this being about 80 mm. The maximum amplitude of engine vibration was found for the axial component 0.98 mm and for the vertical component 0.95 mm. Also when one engine was switched on and kept running rotation of the aircraft about a vertical axis took place which amounted approximately to 0.4°. More details of this expensed instrumentation and some results are described in [9].

Additional static pressure measurements below the engine were carried out using small PVC hoses on the ground. The pressure was measured by means of simple U-tubes filled with water. Directly below the engine no pressure differences against the ambient pressure were observed, only 2980 mm away from the engine's end, a static pressure was measured being about 40 mm of water over the ambient pressure when the engine was running at 80% speed. From this additional observation the conclusion was drawn, that below and around the engine only very low flow velocities do exist. That means also that entrainment effects of the engine's jet to the surrounding were negligable.

4. RESULTS

Before discussing the results in detail, it is necessary to remark, that the flow behind the fan and turbine exit on a real engine is not comparable with an ideal nozzle flow. Looking into the details of the CFM56-5-engine (see figure 9) the following statements can be made:

- The fan flow is influenced by the thrust reverser in particular in the sectors 9, 10 (see figure 3). The laser measurements were carried out in sector 7. This part of the fan nozzle showed only small disturbances on the inner surface and no reflection of the laser beam could be expected.
- From turbine nozzle geometry only a very small acceleration of the flow is possible, because of the area ratio $A_{Turbine-Exit}/A_{Nozzle} = 1.14$. At the inner part of this nozzle a decelerated flow may exist.

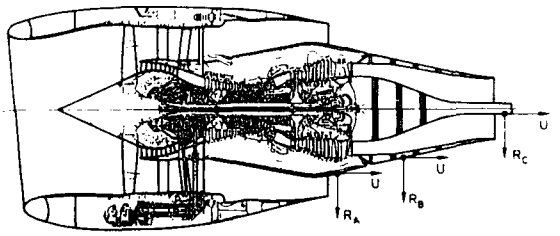

Figure 9. CFM56 - 5 engine

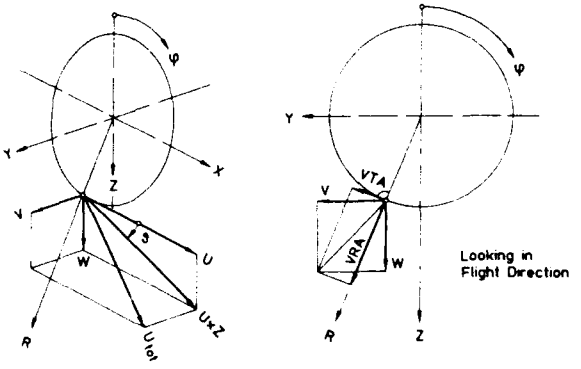

Figure 10. Definitions of velocities and directions

The results of the present investigations will be discussed in form of the velocity components u, v, w as measured in the x-y-z coordinate system (see figure 10). These components can be transformed into a orthogonal coordinate system e.g. to get the tangential component v_{TA}. In addition to the mean velocity values of the measured velocity components the turbulence levels will be discussed and the angle ϑ giving the local mean flow direction in the x-z plane.

4.1 Velocity profiles

Figure 11a gives a first impression of the axial velocity profiles at fan exit plane A for four different engine speed of 60, 70, 80 and 85 % N1. These velocity profiles look very uniform at the different speeds. Near the inner wall a normal boundary layer profile is present, the shape of this distribution looks quite well. In the outer part, the profiles are influenced by the boundary of the jet and the ambient atmosphere. In this section A, total and static pressure were also measured with a Prandtl probe. These measurements were carried out at a fixed radial position. In the case of the probe measurements the velocity is obtained from the energy equation for compressible flow using

$$u = a \cdot Ma \qquad (1)$$

with the velocity of sound expressed in terms of the static temperature by

$$a = \sqrt{\kappa \cdot R \cdot T} \qquad (2)$$

and the Mach number

$$Ma = \sqrt{\frac{2}{\kappa-1}\left[\left(\frac{p_t}{p}\right)^{\frac{\kappa-1}{\kappa}} - 1\right]}. \qquad (3)$$

The temperature was also measured at the same position as the pressure probes using a standard thermocouple. As seen in the diagram of figure 11a, the velocities measured with the probe and the LDA are in very good agreement. Because of the low turbulence level in the present flow, no consideration of fluctuating values are necessary as was shown in [10]. From the Prandtl-probe measurements a static pressure lower than ambient pressure by about 10 mbar was observed.

To control the level of the fan exit velocity an averaged velocity was taken by the flight engineer and estimated from the engine performance data. These values $\tilde{u}_{AS}$ are marked in figure 11a, showing smaller values than the maximum velocity measured by the LDA-system and also by the Prandtl-probe as was expected.

With respect to the limited test time running the engine it was decided to continue the measurements only with the constant speed of N1 = 80 %. This dicision was also

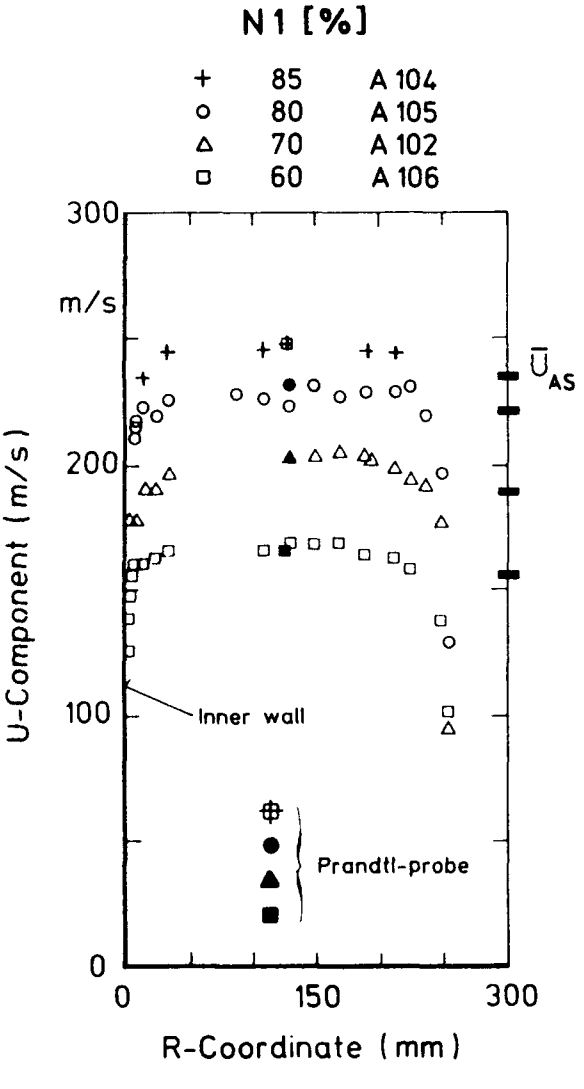

Figure 11a. Axial velocity distribution in section A at different fan speed

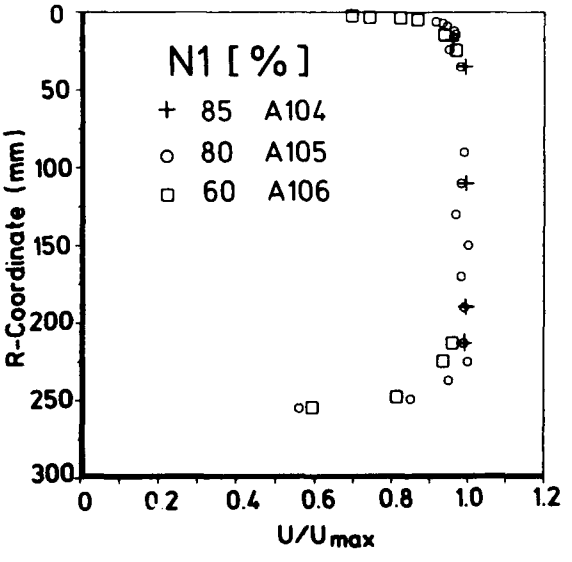

Figure 11b. Axial velocity distribution dimensionless in section A

supported by the nearly constant shape of the velocity profiles at different engine speed (see figure 11b). The development of the three components u, v, w in the sections A, B and C are plotted in the figures 12 to 14. The axial velocity component u within the fan flow shows at the inner wall a normal boundary layer velocity development without separated flow. The outer jet flow of the fan shows very clearly the tendency towards a smaller gradient at the jet boundary region as the jet develops. In section C a clear distinction of the velocity distributions of the turbine flow and fan flow is indicated by the strong jump at R ≈ 280 mm. A surprising feature is the non uniform turbine velocity distribution which can be explained by the inner shape of the turbine nozzle. Summarizing, the turbine flow quality is worse compared to the good flow quality behind the fan.

The velocity component v in particular responsible for the swirl behaviour of the total flow shows in section A (fan exit) and B (downstream of fan exit) positive values so that a small swirl can be stated. This swirl in the fan flow decays with the distance from the fan exit which can be seen from the results in section C (see figure 14). Also in this section at the turbine exit the v-component indicates a swirl on the outer part of the turbine nozzle. The w-components in the three sections of the fan flow correspond directly to the slope of the cowling at the inner part and follow the wall direciton with the very clear tendency of a decaying gradient from section A (fan exit) to section C (turbine exit) in the fan flow velocity distribution.

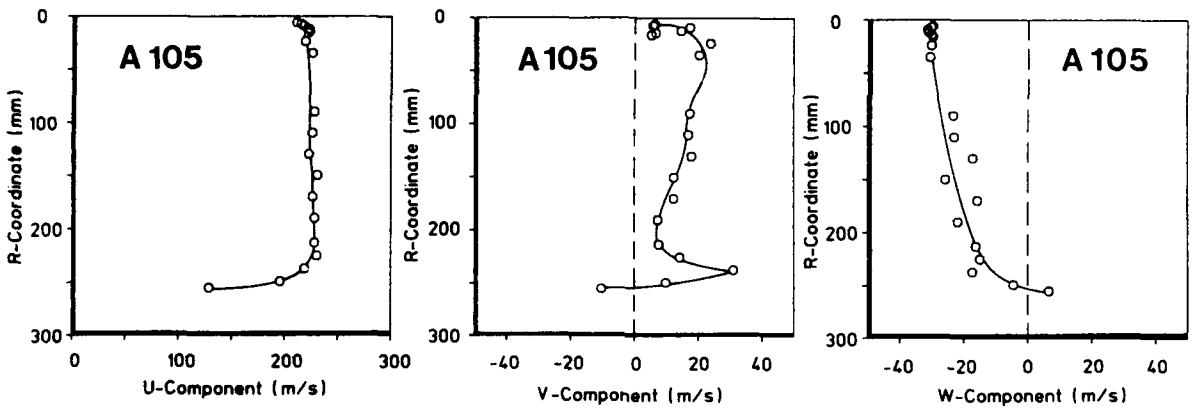

Figure 12. Velocity components u, v, w in section A

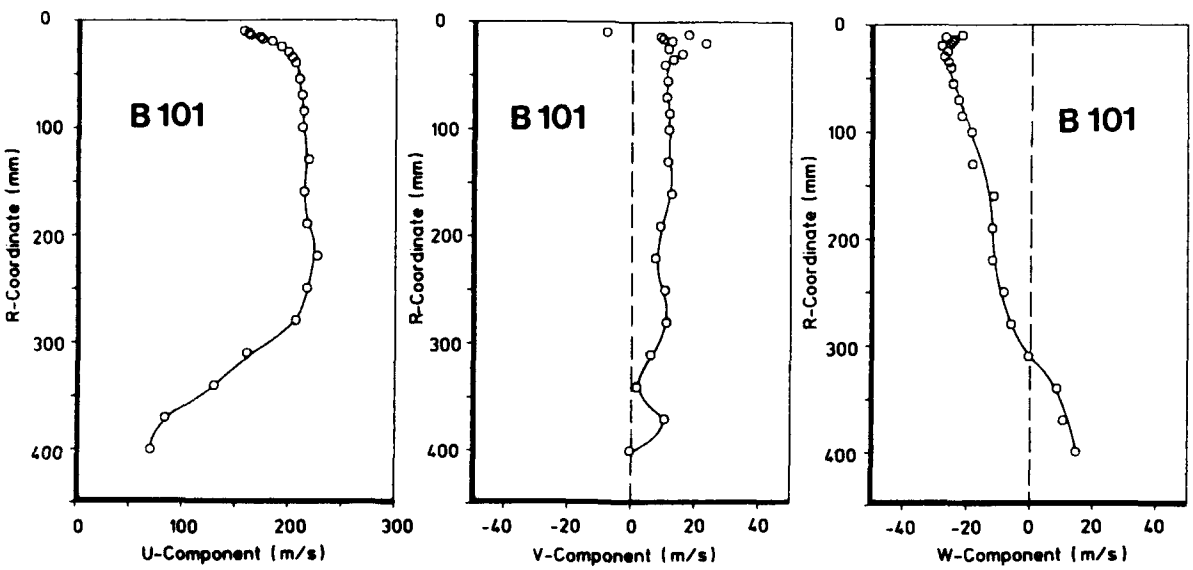

Figure 13. Velocity components u, v, w in section B

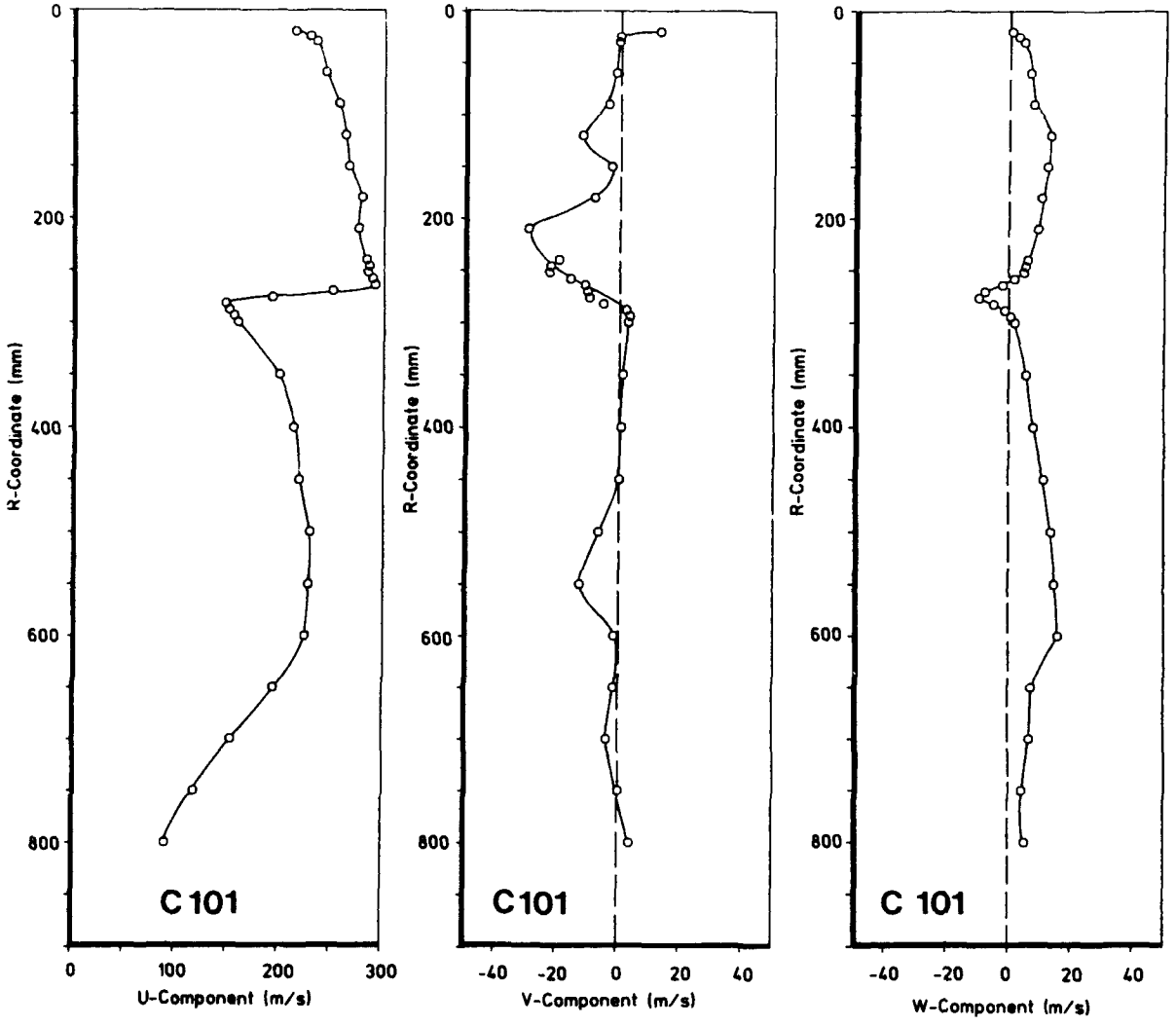

Figure 14. Velocity components u, v, w in section C

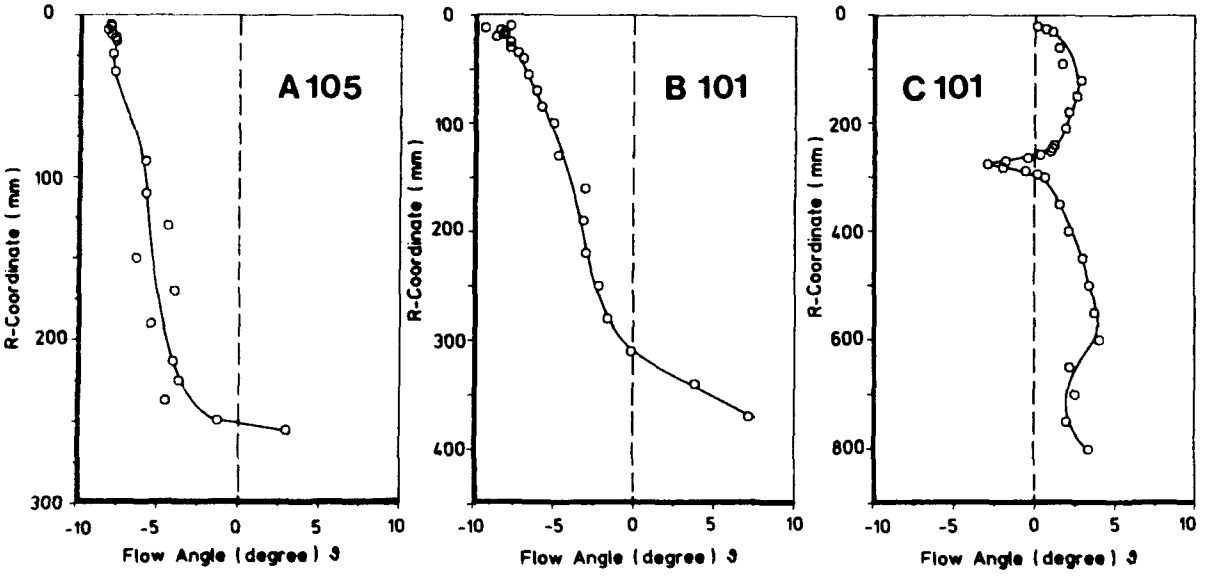

Figure 15. Angle of flow direction in section A, B, C

The w-component and the axial component u were used to estimate the flow direction. The development of the flow direction is shown in figure 15 for the three sections. In the sections A and B the flow direction at the inner part is nearly parallel to the core cowling and changes along the radius R from negative to positive direction (section B). It should be also noted that the radial gradient of the flow direction changes from section A to B with the very clear tendency of stronger gradient downwards of the fan exit plane (section B). A change of the jet flow direction cannot be excluded. In section C only a positive flow direction is observed, with the exception of the shearflow between turbine and fan flow.

Summerizing the jet behaviour of the fan flow, figure 16 shows the dimensionless velocity distribution for the three sections using the half velocity radius with R ($u_{max}/2$) being the radial distance where the velocity is 0.5 u_{max}. In the present case two types of jet exist, at the inner part a wall-jet and at the outer part a free-jet. The results on figure 16 demonstrate for the inner part a wall boundary layer behaviour. On the other hand the outer jet velocity profiles of section A represent the jet exit and the profiles for section B and C illustrate the spreading of the shear layer with increasing distance from the fan nozzle exit. Similar behaviour was observed in an axi-symmetric jet [11].

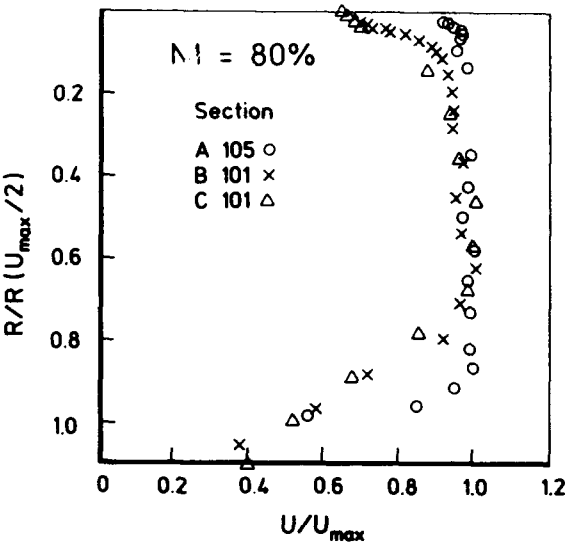

Figure 16. Axial velocity distribution dimensionless for section A, B, C

4.2 Turbulence profiles

The distribution of the fluctuating velocity in R-direction is plotted in figure 17 as turbulence intensity

$$\sqrt{\overline{u'^2}}/u$$

for the three sections A, B and C where u is the average velocity in all cases. A very small influence of fan speed was observed in section A [12], so only results for the constant speed of N1 = 80 % will be presented. The turbulence intensity profiles obtained at section A has a level of 5 % to 6 % in the main flow. Such values are well known from axial flow compressors [13]. In the inner part (wall of the core cowling) the turbulence increases due to the shear flow in the boundary layer and in the outer part it is influenced by the shear flow of the fan boundary layer. In section B the turbulence intensity level increases but on the inner and outer part it is influenced for different reasons. At the inner part the

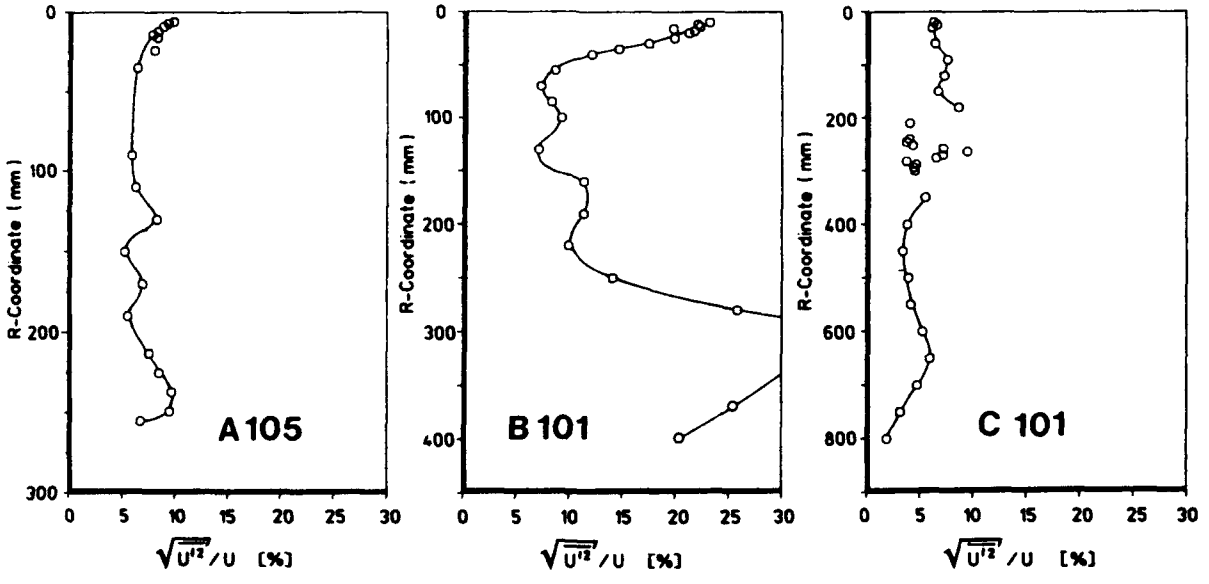

Figure 17. Turbulence intensities in section A, B, C

strong increase of fluctuation is mainly generated by bleed air coming out upstream of section B (see figure 9). On the outer part the increased turbulence intensity is caused by the mixing region at the jet boundary.

The turbulence intensity in section C (fan- and turbine flow) has in the fan flow the same level as seen in section A but is also influenced by the jet mixing process. In the turbine flow (R = 0 to 280 mm) the turbulence intensity level has nearly the same level compared with the fan exit but strong variations between z = 200 and 300 mm which may possibly be caused by local separation within the turbine nozzle.

The turbulence intensities of the other velocity components v' and w' were also obtained during these measurements and are of the same order [12], so that nearly an isotropic turbulence behaviour is present.

4.3 Symmetry condition

Measurements were carried out in section B2 (see figure 3) parallel to the ground to get an information on the symmetry quality of the total jet flow. Figure 18 shows the axial velocity component u and the swirl componment VTA. Between left and right side of the engine center line no deviation of these velocities can be observed. Also from the other component v and w - not presented here - no remarkable deviation could be stated. This confirms the findings made before that only a very small swirl in a range of 3° to 4° does exist.

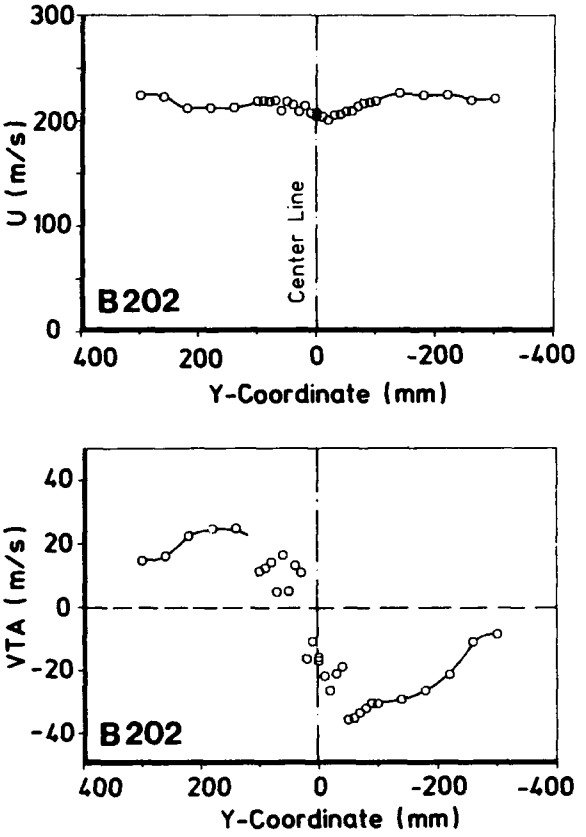

Figure 18. Axial- and circumferential velocity distribution in section B2 parallel to the ground

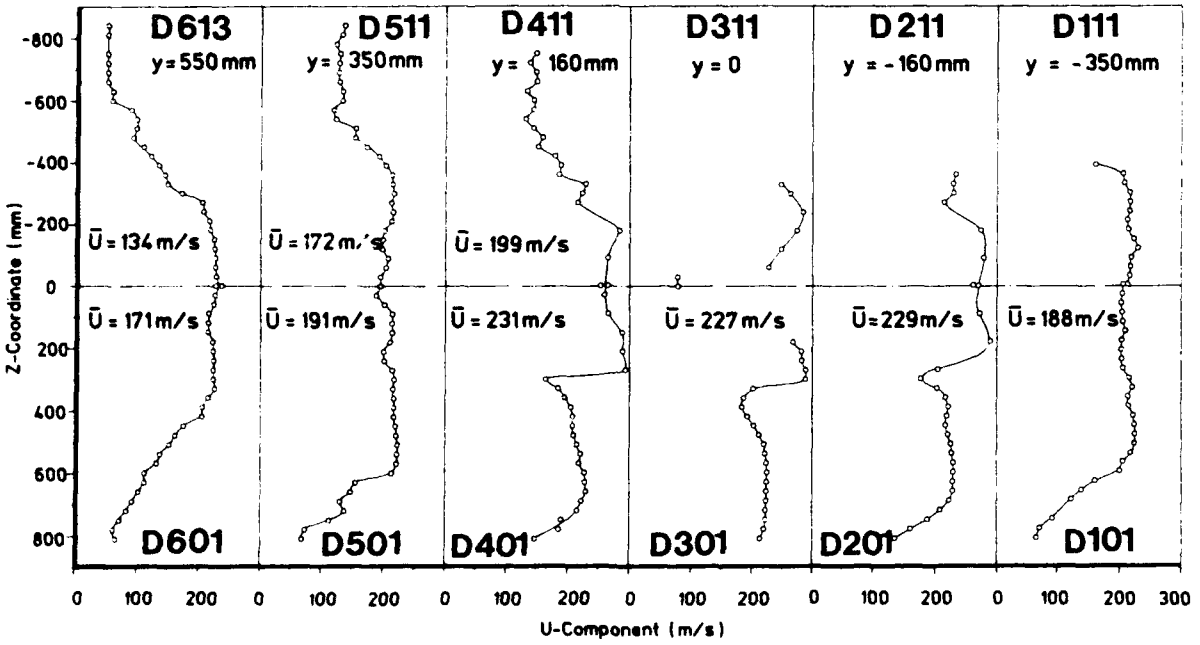

Figure 19. Axial velocity distribution in Section D

4.4 Total flow field

To get the important information on the total flow field behind the engine measurements in a section D were carried out. With the very large dimensions of the jet in this area a great number of different positions of the LDA-equipment would have been necessary. Because of the limited test time available, only a limited area could be covered. Especially in the sections D1 and D2 (see figure 3) masked the pylon no data were available. All measured axial velocity components u in section D are plotted in figure 19. Comparing the symmetry conditions between the y-directions (y = ± 160 - D2/D4 - and y = ± 350 mm - D1/D5 - respectively) good agreement can be noted concerning the velocity level in the inner part (turbine) and the outer part (fan). This result is in agreement with the result found in section B2. Comparing the symmetry conditions in the z-direction (looking into flight direction, values y = 160, 350 and 550) no symmetry of the flow conditions can be observed. It can be assumed that a different mass flow distribution exists in the upper and the lower part of the engine jet flow. To get quantities of the velocity differences, average values for each section were estimated to

$$\bar{u} = \frac{1}{z_o - z_n} \int_{z=0}^{z=n} u(z)\, dz \,. \qquad (4)$$

The results of these data are summarized in the following table for the lower part:

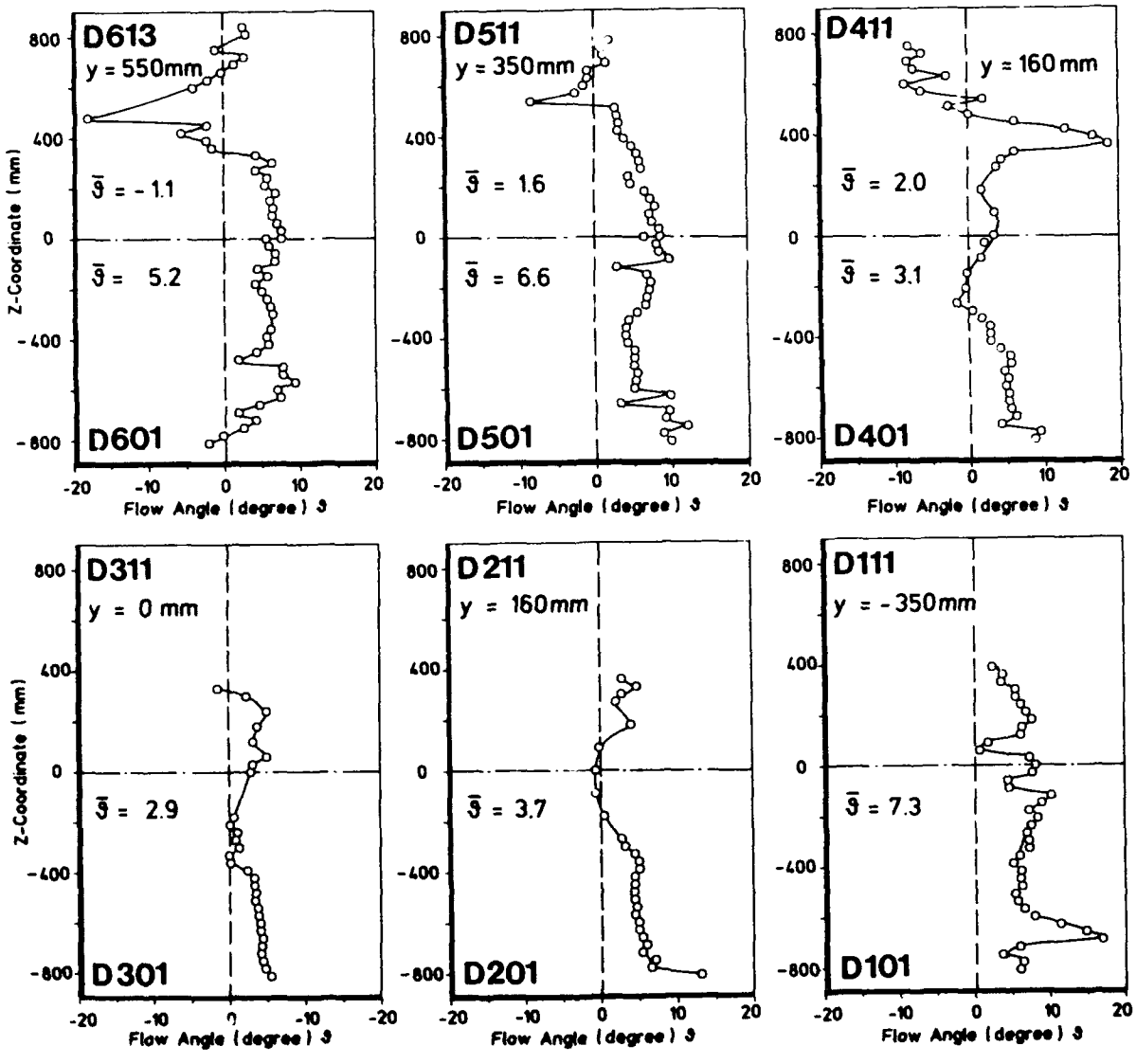

Figure 20. Angle of flow direction in section D

engine side	left	right
section $\bar{u}$ [m/s]	D 401 231	D 201 229
section $\bar{u}$ [m/s]	D 501 191	D 101 188

The velocity differences between left and right are smaller than 1.5%, the symmetry conditions are good as stated above. The average values for the upper and lower part of the engine are summarized in the following table (left side, looking into flight direction):

above	section $\bar{u}$ [m/s]	D 613 134	D 511 172	D 411 199
below	section $\bar{u}$ [m/s]	D 601 171	D 501 191	D 401 231

Very large velocity differences up to 28% can be stated between upper and lower part of the jet flow, so that also different mass flow distribution exists in the upper and the lower part of the engine jet flow, if comparable densities of the flow is assumed.

Now, looking at the results of the flow direction given from the u-w-velocity components shown in figure 20 (vanishing v-components in this section, see figure 14) leads to the same conclusion as stated before: Good symmetry conditions between left and right side of the jet flow, which can be derived from the average angle estimated to

$$\bar{\vartheta} = \frac{1}{z_o - z_n} \int_{z=0}^{z=n} \vartheta(z)\,dz \,. \qquad (5)$$

The average values between left and right section D 101/ D 501 and D 201/D 401 respectively show maximum differences of 0.8° and 0.6° only. Comparing the flow direction between upper and lower part of the jet flow no symmetry condition can be stated and at lower part higher positive flow angles are observed. In the upper part average angles between 1° and 2° and in the lower part average angles between 3° and 6.5° respectively exist. In comparison with the development of the flow direction measured in section A and B it can be stated, that the mean direction of the complete jet shows a deviation from the engine axis in +ϑ-direction, meaning downwards as demonstrated in figure 21. This result is in agreement with TPS-windtunnel measurements carried out by Deutsche Airbus using different types of models with short fan nozzles, comparable to the present CFM56-nozzle [19].

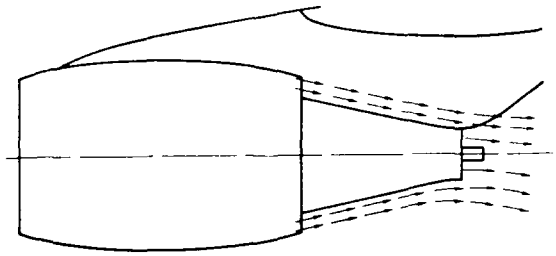

Figure 21. Total flow field of the engine jet (schematic)

4.5 Thrust deflection

To find an explanation for this jet behaviour as detected by the present laser-measurements, the photograph in figure 22 showing the installed engine on the pylon. The following statements can be made:

1. It can be assumed that the large velocity differences between upper and lower part of the jet flow are generated by high total pressure losses in the upper part where the pylon is installed. In addition losses will be also generated from the fairings (pylon/cowling) and the thrust reverser respectively which is mainly located in the sectors 3, 4, 9 and 10 (see figure 3).

2. These higher total pressure losses in the upper part of the jet flow are responsible for the lower velocities. The fan jet nozzle is working with lower pressure ratio p_{tj}/p_∞, while in the lower part the jet it is working with a higher fan nozzle pressure ratio.

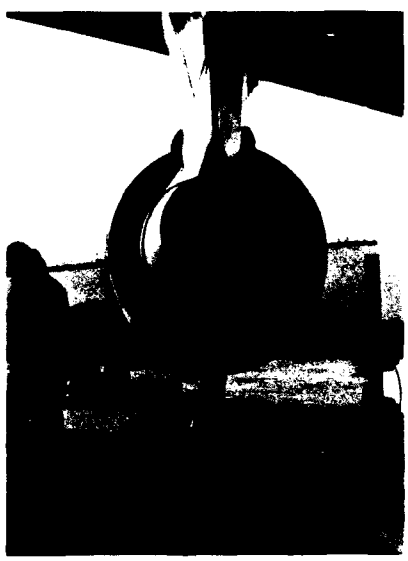

Figure 22. View to pylon

From basic investigations on the jet flow of afterbody configuration the following is well known, see [14] and [15]:

- Independent of the free stream Mach number increasing jet pressure ratio (increasing jet Mach number) p_{tj}/p_∞ leads to larger spreading of the jet, demonstrated in the sketch of figure 23. The maximum velocity at the jet center line decreases further downstream.

- The free stream Mach number influences the level of the jet spreading angle ϵ, higher free stream Mach number Ma_∞ leads to smaller values of ϵ.

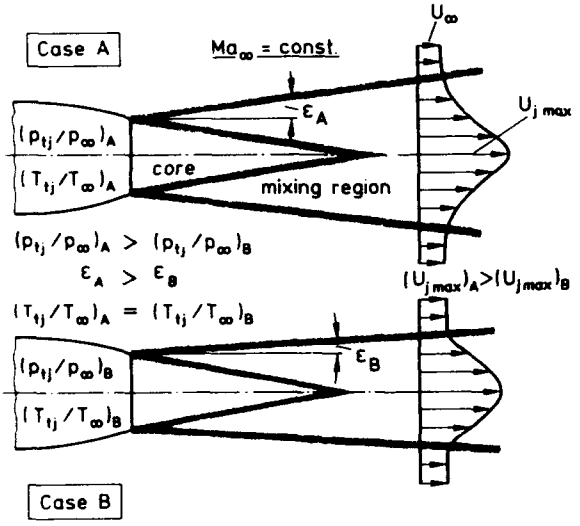

Figure 23. Jet behaviour (schematic)

Transfering this knowledge to the present engine jet flow problem leads to the conclusion:

- In the upper part of the jet flow smaller spreading exists compared to the jet flow of the lower part. This behaviour causes the mean flow direction of the complete engine jet to be directed downwards by about $\bar{\vartheta} = 3.5°$.

To support this result, a theoretical investigation was carried out for the CFM56-configuration, calculating the complete behaviour of the exit jet such that viscous flow effects can be considered [16]. Using the STC-GENMIX-code which consists of a Stream-Tube-Curvature methode coupled with a boundary layer method with the extension described in [17]. In figure 24 the calculated isotaches are obtained. This result consists of two separated axi-symmetric calculations for two flow conditions, in the upper part for a fan pressure ratio of NPR2 = 1.41 and in the lower part for a fan pressure ratio NPR2 = 1.70. In both cases the turbine pressure ratio was kept constant to NPR1 = 1.41. In this calculation the jet boundary is defined where the free stream velocity and the jet velocity is the same. From these results it can be seen that in the lower part larger jet spreading exists compared to the smaller spreading in the upper part.

As a consequence of the observed jet vector deflection the following conclusion can be assumed: An engine with short cowling generates non-symmetrical velocity distribution in the core flow exit plane, in particular induced by the pylon. In contrast a long cowling with the pylon not installed directly in the fan jet should lead to more axi-symmetric flow condition, than having no thrust vector deflection.

5. Conclusions

Measurements with a three component LDA-system have been performed successfully on an aircraft A320 with installed CFM56 engines. These measurements were carried out as ground tests providing data for the jet behaviour. The fan flow and in particular the three-dimensional flow field in different sections behind the engine have been regarded. These investigations were carried out mainly at N1 = 80 % fan speed, which is not far away from cruise condition. The present data leads to the following statements:

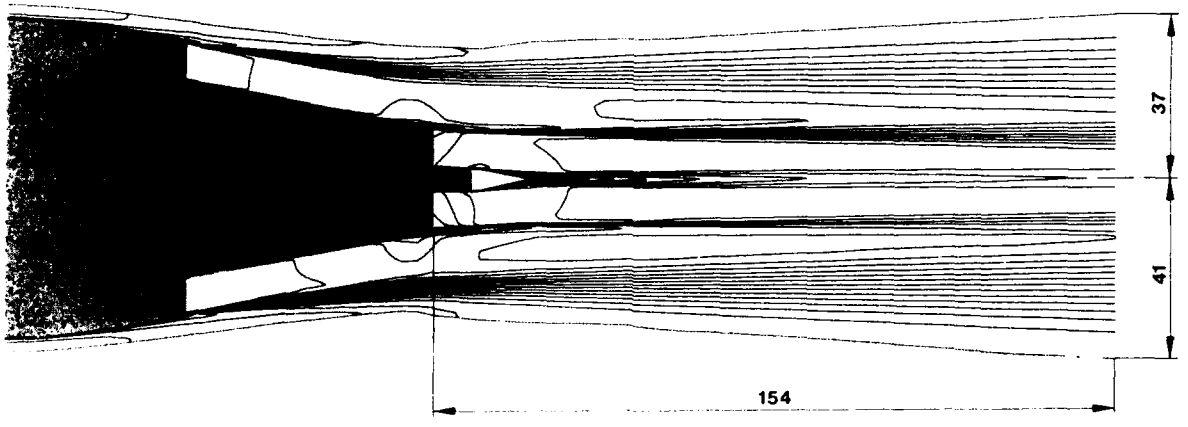

Figure 24. Calculated viscous jet, isotachs, Ma=0.4, NPR1 = 1.41 hot core-jet, NPR2 = 1.41/1.70

- The jet of the fan flow is of good quality which regard to a flat velocity profil. The flow at the turbine nozzle exit shows a non-uniform velocity distribution.

- A small local swirl of approximatly 3° was observed within the fan exit jet flow.

- Turbulence intensities are of normal values of 5% to 6%. Nearly isotropic turbulence behaviour is present, within the central part of the jet.

- The upper part of the engine jet is working with a smaller jet pressure ratio which leads to smaller jet spreading compared with the lower part. A theoretical investigation confirms this observed jet behaviour.

- The direction of the total jet shows a deviation from the engine axis of $\vartheta \approx 3.5°$ and is directed downwards. This jet deflection can be explained by the reduced overall velocity in the upper part of the engine.

Acknowledgement

The authors wish to thank Airbus Industrie for providing the aircraft and for permission to publish these results. The help of Aerospatiale staff during the tests and the assistande of H. Grauer-Carstensen, D. Palleck, K.H. Sauerland, J. Helbig, B. Simon and A. Korus during the measurements and the data evaluation is appreciated very much.

References

1. Murthy, S.N.B., Paynter, G.C.,
Numerical Methods of Engine-Airframe Integration. Progress in Astronautics and Aeronautics, Volume 102 (1986).

2. Rossow, C.C., Ronzheimer, A.,
Investigation of Interference Phenomena of Wing-Mounted High-Bypass-Ratio Engines by the Solution of the Euler-Equation.
Contribution to 9th Fluid Dynamic Panel Meeting of AGARD on Aerodynamic Engine/Airframe Integration for High Performance Aircraft and Missiles, Fort Worth, Texas, USA, Oct. 1991.

3. Hoheisel, H.,
Zelle-Triebwerks-Integration - Aufgabe zukünftiger Verkehrsflugzeugentwicklungen. DLR-Nachrichten, Heft 61, Nov. 1990, S. 34-39.

4. Hoheisel, H., Kiock, R., Rossow, C.C., Ronzheimer, A., Baumert, W., Capdevila, H.
Aspects of Theoretical and Experimental Investigations on Airframe/Engine Integration Problems. 17th ICAS Congress Stockholm, Sept. 1990, Paper No. 2.7.3, Vol. II, pp. 1277-1289.

5. Eckert, D., van Ditshuizen, J.C.A., Munniksma, B., Burgsmüller, W.,
Low Speed Twin Engine Simulation on a Large Scale Transport Aircraft Model in the DNW, 14th ICAS Congress, Sept. 1984, Paper-No. ICAS-84-2-10.4.

6. Smart, A.E., Moore, C.J.,
Aero-engine Applications of Laser Anemometry, AIAA J., Vol. 14, No. 3, March 1976.

7. Bütefisch, K.A., Sauerland, K.-H.,
A Three Component Dual Beam Laser-Doppler-Anemometer to be Operated in Large Wind Tunnels, 11th *ICIASF Record*, Stanford University (1985), p. 48.

8. Pallek, D., Sauerland, K.-H,
Bütefisch, K.A., Roscher, H.-J.,
Hoheisel, H.,
3-D LDA-Measurements in the Jet of a Bypass-Engine, 4th Intern. Symposium on Applications of Laser Anemometry to Fluid Mechanics, July 1988, Lisbon, Portugal.

9. Seelhorst, U., Bütefisch, K.A., Grauer-Carstensen, H., Sauerland, K.-H., Pallek, D., Hoheisel, H.,
Time-Dependent 3-Component Laser-Doppler-Anemometer and Simultaneous Position Measurements in the Flow of an Aircraft Engine. Contribution to the 4th International Conference on Laser Anemometry, August 1991, Cleveland, Ohio.

10. Hoheisel, H., Hoeger, M., Meyer, P., Koerber, G.,
A comparison of Laser-Doppler Anemometry and Probe Measurements within the Boundary Layer of an Airfoil at Subsonic Flow.
Laser Anemometry in Fluid Mechanics, Publ. by Ladoan-Instituto Superior Tecnico, Lisboa, Portugal (1984).

11. Schäfer, H.J.,
Measurements of mean-flow and turbulence characteristics in a turbojet exhaust using a laser velocimeter. ISL-Report CO 226/88 (1988).

12. Hoheisel, H., Bütefisch, K.A., Henke, R., Lehmann, B.,
Laser Measurements on the Ground in the Jet of the CFM56 Engine installed on the Airbus 320. DLR-IB 129-90/31 (1990).

13. Schlichting, H., Das, A.,
On the Influence of Turbulence Level on the Aerodynamic Losses of Axial Turbomachines. In: L.S. Dzung, Flow Research on Blading, Proc. of the Symp. Baden, Switzerland (1969), Elsevier Publ. Comp. (1970).

14. Zacharias, A.
Experimentelle und theoretische Untersuchungen über die Wechselwirkung zwischen Triebwerksstrahl und dem umgebenden Strömungsfeld. Dissertation TU Braunschweig, Dez. 1980.

15. De Wolf, W.B., Munniksma, B.,
Comparison of Hot and Cold Subsonic Jets in an External Flow with Reference to Jet Engine Simulation. NLR TR 80042 U (1980).

16. Korus, A.,
Viscous Effects on Jet Flows. Meeting of CFD-Methods for Airframe-Engine-Integration Problems. DLR-IB 129-91/3 (1991).

17. Radespiel, R.,
Ein Berechnungsverfahren für den Triebwerksstrahl und deren aerodynamische Wechselwirkung mit einem Heckkörper, Dissertation TU Braunschweig, DFVLR-FB 86-29 (1986).

18. Lehmann, B.
Laser-Doppler-Messungen in einem turbulenten Freistrahl, DFVLR-FB 86-55 (1986)

19. Burgsmüller, W., Castan, C.,
Kooi, J.W., Bècle, J.P.
Recent Developments in Low-Speed TPS-Testing for Engine Integration Drag and Installed Thrust Reverser Simulation. Contribution to 9th Fluid Dynamic Panel Meeting of AGARD on Aerodynamic Engine/Airframe Integration, Fort Worth, Texas, USA, Oct. 1991

SOME ASPECTS OF INTAKE DESIGN, PERFORMANCE & INTEGRATION WITH THE AIRFRAME

E L Goldsmith
Aircraft Research Association Ltd
Manton Lane, Bedford MK41 7PF, England

SUMMARY

A selection of topics has been made from the 'state of the art review' in the Fluid Dynamics Panel Working Group 13 Report on Intakes for High Speed Vehicles. The first topic is a brief account of results from a programme of research on internal and external flow in pitot intakes conducted in the UK over the period 1978-88. The main topic is that of intake airframe integration and is illustrated by examples from systematic work done in the USA and Europe on agile strike fighters and multi-intake missiles.

NOTATION

A	cross sectional area
C_D	drag coefficient [$=D/q_o A_{ref}$]
CR	intake lip contraction ratio ($=A_c/A_t$)
D,d	diameter
KA_2 & DC_{60}	specific distortion indexes
K/K_{limit}	proportion of maximum allowable engine face distortion
$L_{,\ell}$	length
M	Mach number
P	total pressure
PR	pressure recovery ($= P/P_o = \eta$)
$\Delta P/P_o$ =	($1 - P/P_o$) at subsonic speeds; Shock P.R. - P/Po at supersonic speeds.
q	dynamic pressure
R,r	radius
α	angle of incidence
ß	angle of sideslip/yaw
δ_a	compression surface angle
ϕ	roll angle

Suffices

c	capture plane
d	design
f	engine face
L	local
o	free stream
t	throat
b	body

1 INTRODUCTION

The Report of the AGARD Fluid Dynamic Panel Working Group 13 ' Intakes for High Speed Vehicles' includes a 'State of the Art Review' as is customary in such documents. This paper presents a personal selection of the topics in that review.

Most light agile fighters of recent years have featured pitot intakes and therefore before moving on to the main theme of intake-airframe integration a brief review is made of some isolated pitot intake research conducted in the U.K. over the Mach number range 0-2.0 and incidence range O-40°.

The general subject of intake - airframe integration is introduced using a restricted aspect of this theme that is mainly relevant to the aerodynamics of long range supersonic cruise vehicles. This leads to a very brief mention of intakes for the next generation of supersonic transport aircraft.

However the more general aspects of intake-airframe integrations became more apparent when considering the problems of layout of strike-fighter aircraft. These are illustrated by combinations of fuselage and pitot intakes at subsonic and supersonic speeds and very brief illustrations of results for compression surface intakes and fuselages at supersonic speeds only. This leads on naturally to the combination of compression surface intakes and long bodies that occur on many guided missile configurations.

2 PITOT INTAKE PERFORMANCE (Refs 1 & 2)

For the Mach number range from zero to 2.0, the general pressure recovery characteristics of a pitot intake are well known Fig.1(a). Losses in total pressure originate from three sources, from skin friction on the duct walls, from the intake lip and from the normal shock. If the ingested streamtube is smaller than the capture area then losses up to an incidence of about 10° are basically skin friction losses that for a given duct and Reynolds number are a function of throat Mach number only Fig.1(b). At low forward speeds when the streamtube is liable to be larger than the capture area, particularly at high throat Mach number then separation can occur around the whole periphery of the cowl lip which results in mixing losses downstream in the subsonic diffuser (Fig.1(c)). Above an incidence of about 10° the boundary layer on the inside of the windward lip will thicken rapidly and then depending on lip thickness, will separate which again gives rise to mixing losses.

Thus at subsonic speeds the loss can be considered as the sum of a basic duct skin friction loss and a lip separation loss Fig 1(d). For a given Reynolds number and geometry the former is a function of throat Mach number only and the latter is a function of capture ratio A_o/A_c and throat Mach number. Note that free stream Mach is not a parameter except in so far that it controls the relationship between capture ratio and throat Mach number. Total loss at subsonic speeds (skin friction + lip loss) is shown as a function of throat Mach number and inverse capture ratio A_c/A_o so that the static case at A_o/A_c of infinity can be plotted (Fig.1(c) and (d). However at supersonic speeds M_o is a relevant parameter in its own right because at incidence it controls the strength of the shock and boundary layer interaction on the inside of the windward lip as flow ratio is increased towards full flow (Fig.2). The ratio M_o/M_t rather than A_c/A_o is found to be more relevant as a correlating parameter to cover the full range of M_o from zero to two. When shock loss and basic skin duct skin friction loss have been deducted, lip loss can be presented for a given incidence for the full Mach number and mass flow range as shown in Fig.2 (ref.1). At low subsonic speeds a further compression of loss data can be achieved by plotting loss $\Delta P/q_t$ versus M_o/M_t for all incidences to give the carpet plot shown in Fig.3. A reasonable collapse of measured results using these parameters can also be obtained at high subsonic speeds but only for configurations with well rounded lips.

Presenting a lip loss allows intake losses to be evaluated for other diffuser geometries with different basic duct skin friction characteristics. However this is only applicable if initial duct diffusion rates are similar. If the subsonic diffuser shapes result in a much higher rate of diffusion then obviously mixing losses will change as shown in the example (Fig 4, ref.1) and the simple addition of a changed skin friction loss with an unchanged lip loss will not be valid.

For a given diffuser shape the two intake geometric features which most affect lip loss at incidence are contraction ratio and intake plane rake (Fig.5, ref.1). Increase in contraction ratio decreases lip loss at all values of throat Mach number and A_c/A_o. However the effect of intake plane rake or stagger is to increase lip loss at values of $A_c/A_o < 1.0$ compared to zero stagger but markedly decrease loss at $A_c/A_o > 1.0$.

The nature of the external flow around pitot intakes, the variation of pre-entry (or additive) drag and associated changes in cowl thrust with flow ratio are well known. In potential flow these two quantities are equal and opposite and they can be measured by any of the means shown (Fig.6(a)). For a thick lipped cowl the division between internal and external flow can be determined by accurately locating the stagnation point by pressure plotting Fig.6(b) and this will retreat from the highlight position to the underside of the lip as flow ratio is reduced (Fig. 6(c)). When $A_{stagnation}/A_{capture}$ has been determined (ref.2) cowl thrust can be evaluated by a summing of the external flow pressures on the cowl. Pre-entry force can also be determined by pressure measurements on the internal surfaces of the cowl from the stagnation point back to the internal survey pressure station combined with the evaluation of mass flow and momentum of the internal flow at this station (Fig.6(a), ref.2).

Cowl thrust is well predicted by potential flow methods at subsonic speeds and by Euler methods at supersonic speeds until a flow ratio is reached at which the flow over the cowl external surface separates at the lip (Fig.7). The departure of measured and calculated curves clearly indicate the onset of lip separation (Ref.2).

Pre-entry drag can also be evaluated by potential flow or Euler methods and agrees well with measured values (Fig.8, ref.2). If the intake lip is sharp then the classic one dimensional momentum evaluation of pre-entry drag is sufficiently accurate for most purposes. However for a blunt lip, it is important that the right combination of pre-entry and cowl forces is used. The one dimensional pre-entry force to the stagnation point can be combined with cowl thrust from the stagnation point or alternatively the two forces taken to the highlight point can be combined (Fig.9, ref.2). However an inconsistent mix i.e. the cowl thrust from the stagnation point plus the pre-entry force to the highlight point must not be used.

3 AIRFRAME-INTAKE INTEGRATION

Airframe-intake integration is liable to have different emphases depending on the context. For supersonic cruise vehicles the phrase engine-airframe integration is probably better. Integration is concerned with adding the intake, engine and exhaust nozzle to the basic wing and body with as little as possible deterioration to the value of lift to drag ratio of the wing and body at cruise Fig.10(a). This theme becomes increasingly important as cruise Mach number increases and body and wing tend to merge so that the completely integrated body/wing/propulsion unit becomes a desirable objective. Practically the whole of the undersurface of the vehicle becomes either part of the intake compression surface or the nozzle expansion surface as has been illustrated many times in conceptual studies of hypersonic cruise vehicles with combinations of turbojet, ramjet and scramjet powerplants (Fig 10(b),ref.3).

However returning to the probably much lower supersonic cruise Mach number of a successor to Concorde there will be three features of the engine installation that will distinguish the Avion de Transport Supersonique due Futur from its predecessor (Fig.10(c)). The first is the blending of the wing undersurface with four separate nacelles because the twin nacelles of Concorde will almost certainly never again feature on a commercial aircraft because of potential problems with engine containment. The second is that for noise reduction reasons a very efficient high and uniform secondary flow ejector nozzle will be needed. To achieve this the secondary flow will need to be ingested circumferentially into the nozzle just aft of the wing trailing edge. As a result intakes will be further back from the wing leading edge than they are on Concorde and weight considerations will dictate that individual subsonic diffusers will be even shorter than were achieved on Concorde. If double sided compression surfaces perpendicular to the wing surface are employed the result will be a halving of subsonic diffuser length. The third feature will be the very difficult choice of the actual form of the intake compression. As design Mach number climbs inexorably upwards, the aerodynamic performance advantages of a combined external-internal compression system become very apparent. Combined compression aims to halt the external compression process at the point where flow deflection away from the free stream direction is relatively small and then to complete the supersonic compression by orienting the flow via shock waves or isentropic compression fans from the undersurface of the cowl internally back towards the free stream direction. The advantages are great as shown by the performance of combined compression designs when compared to the Concorde intake (Fig.11). At design Mach numbers of 2.5-3.0, critical flow pressure recoveries and bleed flow are often very comparable to those of Concorde at its design Mach number of 2.0. In addition cowl drags at around 0.01 or less are much lower than Concorde's 0.099 (refs.4,5,6,7,8 & 9). The difficulties of

achieving these performance figures at engine matched flow conditions however are great. The intake has to be 'started' i.e. the internal shock waves have to be established as the aircraft accelerates from low supersonic speeds and this requires geometry variation. The internal shocks then have to be maintained under all conditions of engine variation and possible malfunction and variation of unexpected flight atmospheric conditions and aircraft attitude. As a consequence the critical flow pressure recovery values measured experimentally often cannot be utilised in practice as a significant degree of supercritical operation has to be adopted to ensure that the intake remains started at all times. To further guard against intake 'unstart' very quick acting spill valves have to be installed just downstream of the throat.

The result can be the complication of the 1972 Boeing Supersonic Transport intake (Fig.12, ref.10). The bleed system is now vital to the 'starting' and maintenance of the internal compression as well as functioning to reduce losses other than shock loss. The system becomes mechanically complex because every bleed region needs to have its own collection plenum duct and exit and these need to maintain their independence and ability to function as intake geometry changes. So far such a design has never had to satisfy the full rigours of civil aircraft certification procedures.

If a successor to Concorde has a design Mach number that is not very much higher, then it will be a fine judgement as to whether or not a half way house between the external compression intake of Concorde and a combined compression intake can be developed. This with advantage, might be self starting at its design Mach number and then it should be possible to design it to be mechanically much simpler than the 1972 Boeing design. Achieving the right balance will be a worthwhile goal. It could markedly contribute to maintaining perhaps one of the greatest attributes of Concorde design judgement and engineering that to date in operation not a single life has been lost throughout its entire flight history.

For supersonic cruise aircraft with intakes sited under a large wing and well away from the fuselage, intake integration is essentially a matter of placing the intake clear of the wing boundary layer on either a short strut or a diverter. The problems of non-uniform flow entering the intake are mainly confined to ensuring satisfactory performance under the small sideslip angles that are encountered for this type of aircraft. The effect of increase in incidence is only to reduce local Mach number at the intake entry plane below the free stream value and this is wholly beneficial to intake performance.

Strike-fighter aircraft almost invariably have their one or two engines in the fuselage and the air intakes can be situated on the top, the bottom or the sides of the body. With increasing emphasis on high agility at subsonic speeds all of these positions and particularly the side fuselage position can result in intake approach flow that is highly non-uniform in both flow direction and Mach number. Typically a design Mach number range from zero to 2.0-2.5, a range of incidence (without the added complication of post stall manoeuvre capability) from -10° to +40°. a sideslip variation of ±10° or more and a range of engine airflows from maximum to idling may be required. Under these conditions separated flow and complex shock and boundary layer interactions in the region of the intake entry plane will be present over an appreciable part of the flight envelope.

Even at zero incidence the low speed and high speed patterns can result in separated flow into the intake emanating either from the cowl lip or the pre-entry flow (Fig.13(a)(b) and (d). These patterns can be accenuated by incidence and sideslip and by operation at supersonic speeds. (Fig.13(c)(d) and (e). Vortex generation from the body or from wing or strake and body junctions can also grossly affect intake performance as illustrated (Fig.13f and g). The only really favourable position is the underbody position where like the underwing supersonic cruise configuration the installation effect is in the main wholly favourable (Fig.13(h)). Although all these effects are reasonably easy to see in principle, the quantification of the effects leads to a vast proliferation of geometric variables that defied even such a large experimental programme such as the Tailor-Mate exercise that was carried out in the 1970s in the USA (ref.11) Fig.14.

Some general principles can be applied to improve the incidence performance of unshielded side intakes (Fig.15(a) and comparative test results illustrate the magnitude of the effects at subsonic speeds. The effect of simple design features such as lip thickening and camber (Fig.15(b)) are small (ref.12). More complex variable geometry in the form of hinged cowl lip, slats and leading edge blowing Fig.15(c) lead to much greater efficiency gains (ref.13).

Some of the effects of shielding the intake by positioning under a wing and strake (Fig.16(a)) and under a fuselage illustrate the fundamental difficulties associated with the former position (ref.14) and the undoubted advantages of the latter (Fig.16(b), ref.15).

At supersonic speeds the favourable effect of the lambda shock formation in front of a pitot intake placed on a fuselage boundary layer diverter is well known. By assuming that the duct skin friction loss at supersonic speeds for a given throat Mach number is the same as at subsonic speeds the favourable effect can be quantified (Fig.17, ref.16). This is a function of free stream Mach number and of flow ratio as these two quantities define the proportion of the entering streamtube that is affected by the two shock formation corresponding to the 10° separation angle associated with the lambda shock. Thus at a free stream Mach number of 1.4 the lambda shock formation covers the whole of the entering streamtube at all flow ratios. At $M_o = 1.6$ the lambda shock formation only affects part of the entering streamtube when flow spillage is small but the shock formation progressively increases in size as spillage increases with resultant increase in shock recovery. Finally as flow spillage reaches high values the separated flow region is no longer confined to the diverter passage and the favourable increment is progressively lessened by the ingestion of some of the separated flow into the intake.

The favourable effect of intake stagger which is a form of local shielding has already been mentioned. At high subsonic speed the full effect on a fuselage side intake is obtained with 50° of stagger although there is still some favourable effect at 20° (Fig.18(a), ref 12). The deletion of the swept endwalls leads to a large deterioration in the favourable effect for the 50° stagger. At supersonic speeds the deleterious effect of shock boundary interaction on the endwalls results in a progressive lessening of the favourable lambda shock effect with increase in stagger angle (Fig.18(c), ref.16).

At a Mach number of 2.0 it is not easy to assign mean values for the flow field Mach number, total pressure and flow direction in front of a compression surface intake as incidence is varied (Fig.19, ref.17). However despite this difficulty reasonably good agreement can be obtained between measured characteristics of the intake in isolation adjusted for the effect

of the measured flow field and the characteristics of the intake measured in situ (Fig.20, ref.17).

At higher Mach number and particularly higher incidence values the situation can become complex and variation is very much a function of the detailed shapes of both fuselage and intake as referred to earlier. All body shapes result in reductions in pressure recovery compared to the performance of the isolated rectangular intake at incidences above about 5° (Fig.21,ref 18). However it is above an incidence of 10° where the squared forebody has a particularly deleterious effect on intake efficiency and the inlet plane total pressure contours at $\alpha = 15°$ provide the explanation.

4 MISSILES WITH MULTI-INTAKES

This last topic concerns the performance of four intakes situated at the rear of a long missile body. The argument for using single or twin intakes which remain on the underside of the body using a bank-to-turn mode for manoeuvre rather than the use of four equally spaced intakes around the periphery that uses skid-to-turn for manoeuvre are well known (Fig.22). Propulsion companies that have produced ramjets such as Rolls-Royce and Marquardt have been tireless in promoting the bank-to-turn philosophy which for good intake performance probably cannot be matched by any other configuration. However the Royal Aerospace Establishment in conjunction with British Aerospace at Filton in the U.K. and ONERA in France have worked on the other line of attack. This is to acknowledge the inherently inferior performance of the multi-intake skid-to-turn missile and then to try to improve the performance of such an arrangement.

For any four intake configuration there are two main reasons why multi- intake performance should be inferior to the performance of the same design in the form of a single nose intake. The first is the loss in total pressure sustained by the four separate intake flows as they negotiate a sharp S bend and then mix in a common ramjet or ram rocket combustion zone (Fig.23, ref.19). The loss can be minimised by adopting a low angle of entry for the four flows as they mix and by diffusing the individual flows (ideally before the first bend) to a low Mach number before mixing.

The second source of inevitable loss is related to the condition of coexistence of the four flows. The condition of equality of static pressure in the mixing region is probably the major influence in this process and results in the worst performing intake dictating that the inherently more advantageously placed intakes must operate in an inefficient supercritical mode to achieve this equality of static pressure (Fig.24(a) and (b), ref.19). As the diagram shows it is the two 'side' intakes which are subject to body upwash that are more inefficient than the shielded top and bottom intakes which for small to moderate incidence 'see' the effect of incidence as only a change of local Mach number.

The form and orientation of the individual intakes are key factors affecting this situation. The illustration in Fig.25 shows possible orientations of wedge and conical compression surfaces with respect to the body surface. The single sided wedge compression surface with the shock waves orientated away from the body surface is the classical configuration as exemplified by the Concorde and Phantom aircraft and the ALVRJ missile (Fig.25(a)). The double side wedge compression surface with shock waves that have a glancing interaction with the body boundary layer has been used consistently by North American/Rockwell from the F107 aircraft of 1958 to the present day B1b aircraft (Fig.25(b). The inverse of the classic configuration with the single sided compression surface placed so that the shock waves impinge on the body surface results in the scoop intake which was used on the LASRM missile (Fig.25(c)). This has two desirable features for a supersonic intake; the compression process ends with the airflow at intake entry orientated in towards the body centreline (i.e. there is no turning back of the airflow towards the free stream direction in the region of the final terminal normal shock and there is no cowl wave drag. However this configuration has two design problems; the compression shock system may not 'start' unless restrictions are placed certainly on the height to width ratio and possibly also on the amount of supersonic compression and the form of the end walls enclosing the compression surface. The 'starting' can also be markedly influenced by the form and quantity of flow associated with the boundary layer bleed where the shock waves impinge on the body boundary layer. This interaction region varies in position and intensity with change in free stream Mach number, missile attitude and intake flow spillage and this compounds the difficulty of bleed design.

Laruelle of ONERA decided to forego some of the theoretical advantages of the scoop intake when he adopted an inverted position for the conventional form of intake (Fig.25(d). His primary aim was to place the compression surface in the side intake position so as to reduce the influence of body upwash as it falls away from the peak value at the body surface (Fig.26(a), ref.20).

The resulting performance is particularly successful in increasing the region where the four intake flows remain stable as the missile rolls at angles of incidence up to 15° Fig.26(b), ref.21). It also increases pressure recovery by as much as 0.1-0.15 at a free stream Mach number of 2.0 (Fig.26(c)).

The second way of improving performance of the four intake configuration is to use strakes on the missile body in front of the intakes. Four strakes can be placed half way between the intakes or in line with the centreline of the intakes. The position of the vortices shed from the body at incidence in the crucial roll angle range 22.5°-45° without and with strakes in these two positions show the evident superiority of the in line strakes in minimising the injestion of body vortices (Fig.27(a)). At an incidence of 8° the superiority of performance in terms of pressure recovery (at a matched flow condition) η_{OP} for the position of the strakes in between intakes is evident (Fig.27(b)). However at an incidence of 12° when the body vortices are more fully developed there are large advantages for the in-line strake position over all other configurations (Fig.27(c)). The influence of diverter size for the no strake configuration is also seen to be significant.

Strake span, strake length and longitudinal position on the body are all relevant parameters in optimising the favourable effect of in-line strakes on the performance of four inverted rectangular intakes (Fig.28(a)). Compression surface endwall shape also has some influence but the effect of endwall geometry changes are usually not large (Fig.28(b)).

A final summary of strake effects illustrates the broad areas of advantage and disadvantage for all configurations of intakes as incidence is varied from 0° to 15° (Fig.29).

5 CONCLUSIONS

In a review paper specific conclusions are probably inappropriate. The broad principles of intake-airframe integration (shielding of the intake from incidence and sideslip angles, the influence of the relative proportions of intake, engine and exhaust nozzle at high cruise Mach numbers etc) are well known. The utility of this kind of paper is to draw attention to the detailed reports that contain the quantified results that are associated with these principles.

REFERENCES

1. Goldsmith, E.L. "The internal performance at incidence of pitot intakes with circular cross section and elliptic lip shapes". ARA Report 76 Jan. 1990.

2. Goldsmith, E.L. "Forces and pressure distributions at subsonic and supersonic speeds on circular section pitot intakes". ARA Report 75. Jan.1990.

3. "Propelling the Aerospace Plane" Mechanical Engineering. June 1986.

4. Rettie, I.H., & Lewis, W.G.E. "Design and Development of an air Intake for a Supersonic Transport Aircraft". Journal of Aircraft 5. No.6 (1968).

5. Cubbison, R.W., Meleason, E.T., Johnson, D.F. "Effect of porous bleed in a high performance axisymmetric mixed compression intake at Mach 2.50". NASA TM X 1692 (L968).

6. Wasserbauer, J.F., Shaw, R.J., Neumann, H.E., "Design of a very low bleed Mach 2.5 mixed compression inlet with 45% internal contraction". NASA TM X3135 (March 1975)

7. Koncseck, J.L., and Syberg, J., "Transonic and supersonic test of a Mach 2.65 mixed compression axisymmetric intake", NASA CR-1977 (March 1972).

8. Obery, L.J. and Stitt, L.E., "Performance of external-internal compression intakes with abrupt internal turning at Mach numbers 2.0 to 3.5", NACA RME57 H07a (1957).

9. Stitt, L.E. and Salmi, R.J., Performance of a Mach 3.0 external-internal compression axisymmetric intake at Mach numbers from 2.0 to 3.5". NACA TM X-145 (1960).

10. Tjonneland, E., "The design, development and testing of a supersonic transport intake system AGARD CP No.91 (Sept.1971).

11. Antonatos, P.P, "Inlet/Airframe Interference and Integration. Airframe and Engine Integration AGARD LS53 May 1972.

12. Goldsmith, E.L. and McGregor, I., "The effect of intake geometry changes on the internal performance of a rectangular pitot intake on the side of a fuselage" Part I: Subsonic and transonic speeds. RAE Technical Report 88070. Nov. 1988.

13. Latham, E., Gawienouski, J., Merriweather, F., "Investigation of inlet concepts for manoeuvre improvements at transonic speeds". NASA TMX 73.215.

14. Goldsmith, E.L., and McGregor, I., The effect of shielding on the performance of rectangular pitot intake at subsonic and supersonic speeds". RAE Technical Report 88018. March 1988.

15. Welte, D., "Pitot-Seiteneinlauf BF 10/30-2673/84 Zwischenbericht Zu BMVg-Auftrag-Nr T/RF42/DOO18/D1418.

16. Goldsmith, E.L., McGregor, I., "The effect of intake geometry changes on the internal performance of a rectangular pitot intake on the side of a fuselage", Part II "Supersonic speeds" RAE Technical Report 88071. Nov.1988.

17. Brown, C.S., and Goldsmith, E.L., "Measurement of the internal performance of a rectangular air intake mounted on a fuselage at Mach numbers from 1.6 to 2.0". Part IV RAE Technical Report 72136. June 1972.

18. Surber, L.E., "Inlet Airframe integration,VK1 Intake" Aerodynamics Lecture Course Feb 1988.

19. Goldsmith, E.L., "Some aspects of engine and airframe integration for ramjet and ramrocket powered missiles. AGARD Lecture Series 136 (Sept. 1984).

20. Richards, C.J., "Supersonic air intakes for missiles Royal Aeronautical Society Symposium on Weapon Aerodynamics". Dec. 1988.

21. Jell, C.S., "Air intake aerodynamics AGARD R-754 Special Course on Missile Aerodynamics" March 1987.

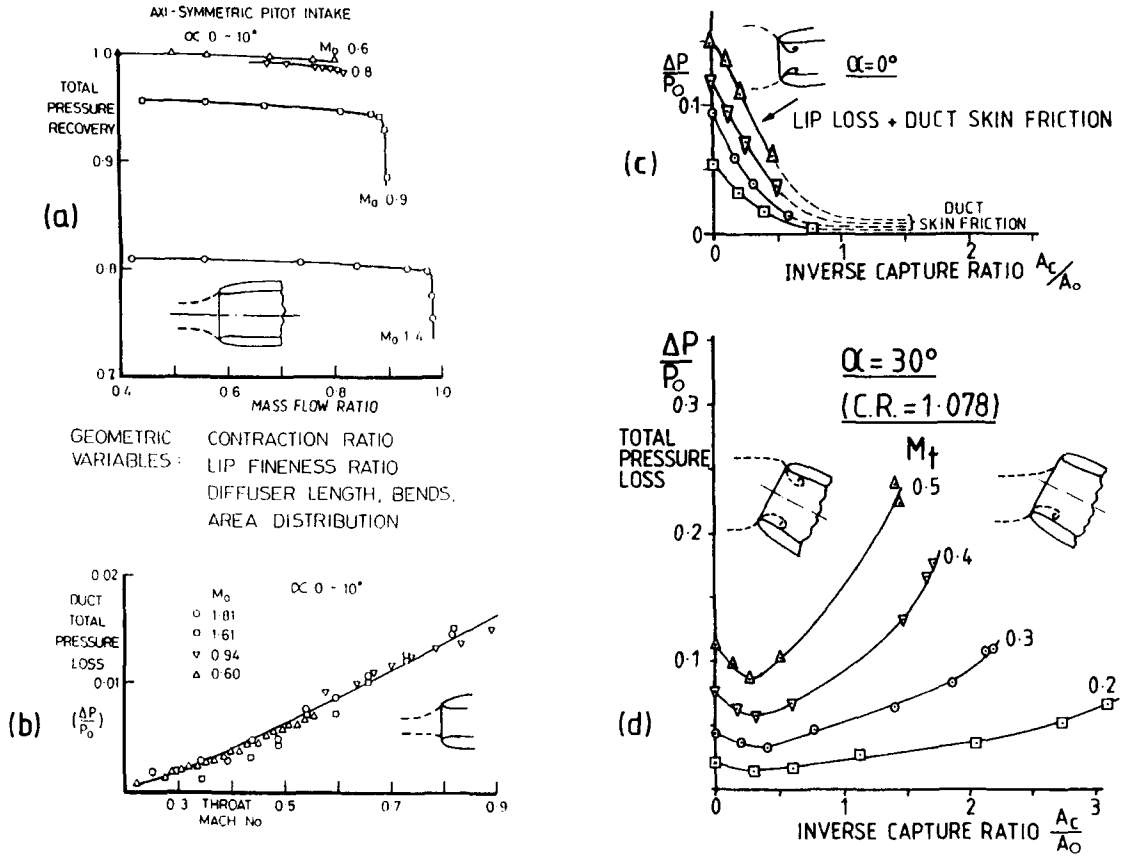

FIG 1 LOSSES IN PITOT INTAKES AT SUBSONIC SPEEDS

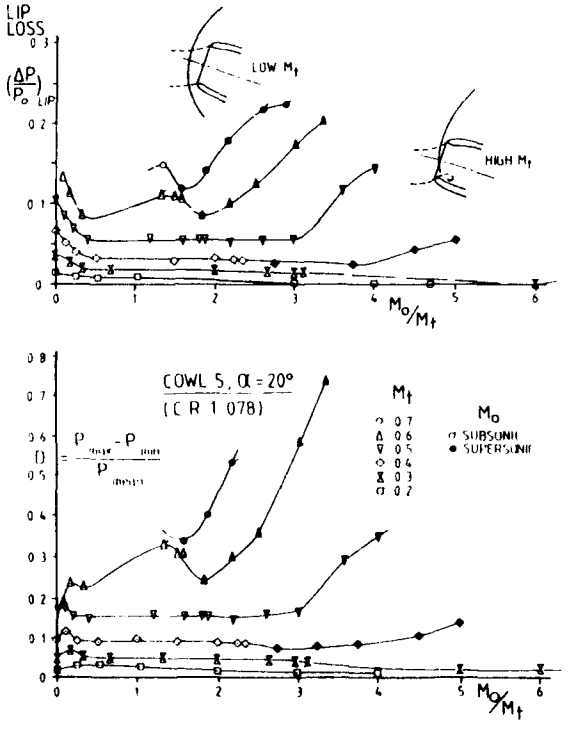

FIG 2 CORRELATION OF MEASURED VALUES
$M_o = 0 - 2{\cdot}0$

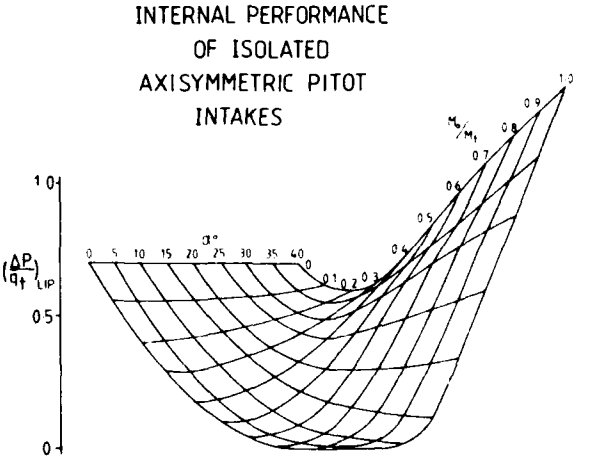

FIG 3 CORRELATION OF MEASURED VALUES
$M_o = 0 - 0{\cdot}2$

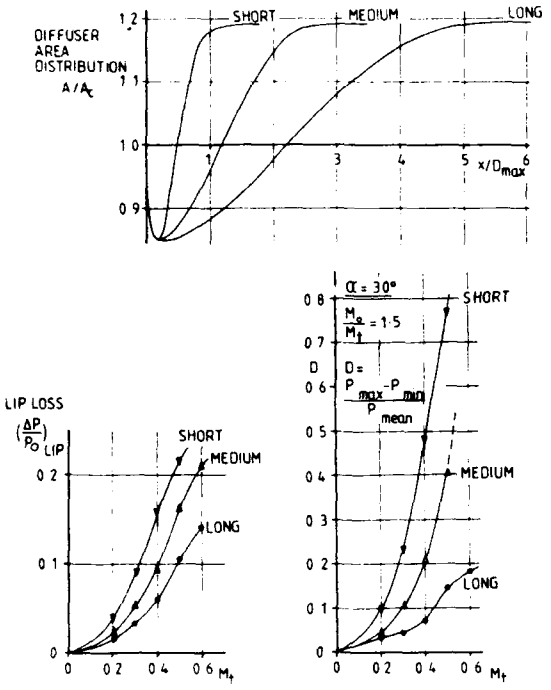

FIG 4 THE EFFECT OF RATE OF DIFFUSION ON LIP LOSS

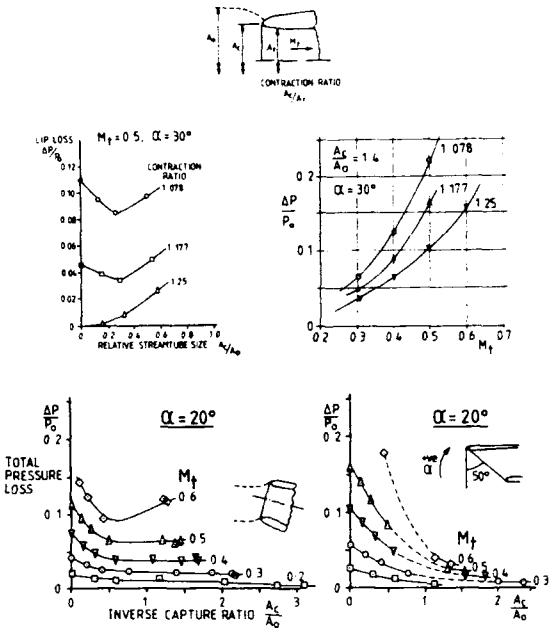

FIG 5 EFFECT OF LIP CONTRACTION RATIO & OF LIP STAGGER ON TOTAL PRESSURE LOSS AT SUBSONIC SPEEDS

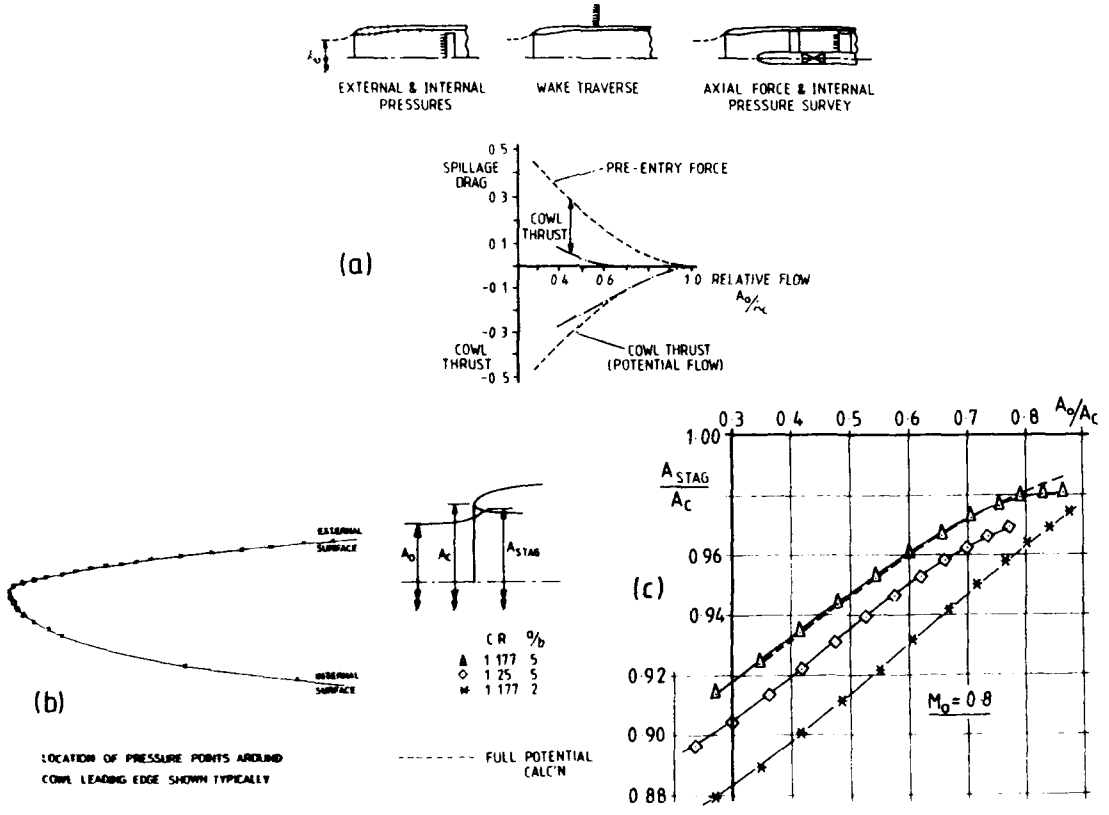

FIG 6 PITOT INTAKE EXTERNAL DRAG

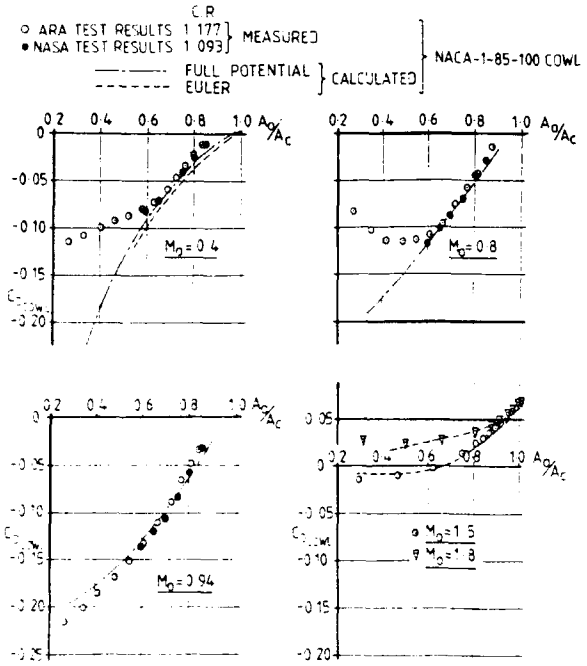

FIG 7 COMPARISON OF MEASURED & CALCULATED AXISYMMETRIC COWL PRESSURE FORCE AT SUB & SUPERSONIC SPEEDS

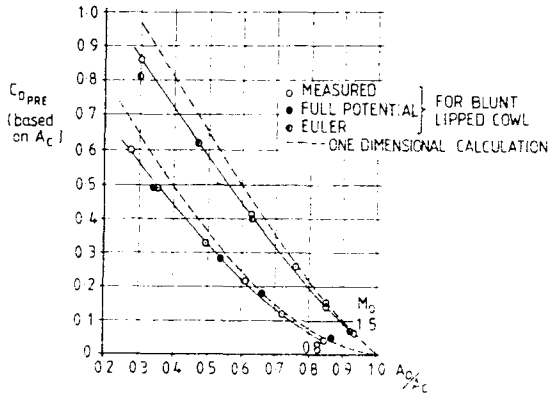

FIG 8 COMPARISON OF MEASURED & CALCULATED PRE-ENTRY DRAG FOR AXISYMMETRIC PITOT INTAKES AT SUBSONIC & SUPERSONIC SPEEDS

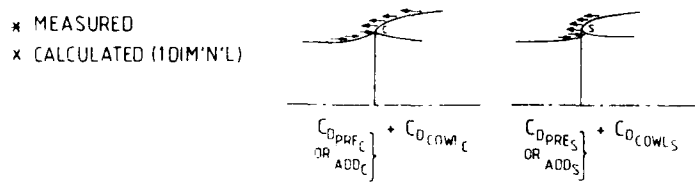

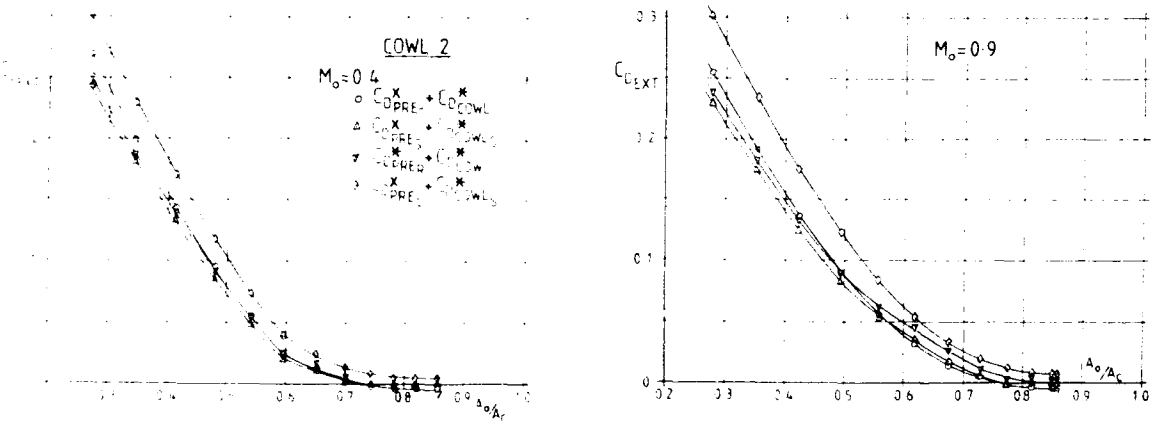

FIG 9 VARIATION OF $C_{D_{EXT}}$ WITH FLOW RATIO FROM DIFFERING COMBINATIONS OF $C_{D_{PRE}}$ + $C_{D_{COWL}}$

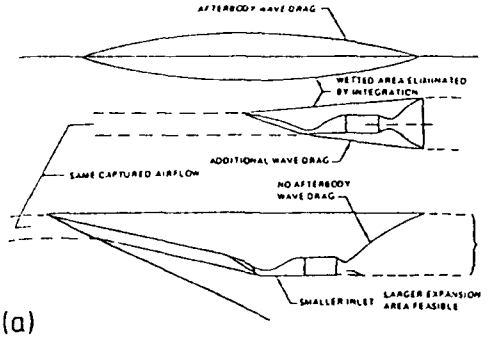

(a)

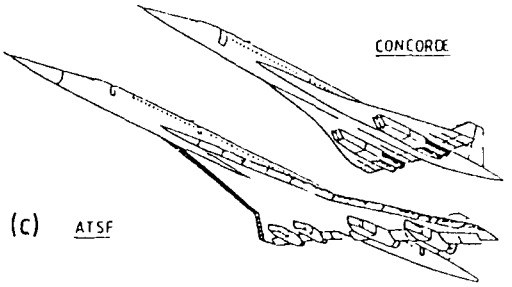

(c) ATSF

POTENTIAL PERFORMANCE BENEFITS DUE TO INTEGRATION

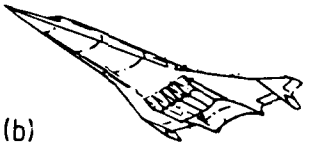

(b)

FIG 10 INTAKE - AIRFRAME INTEGRATION FOR SUPERSONIC CRUISE VEHICLES

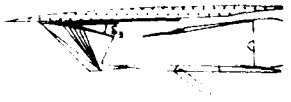

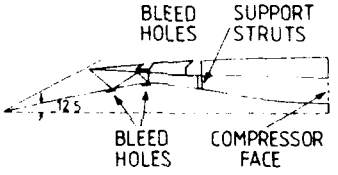

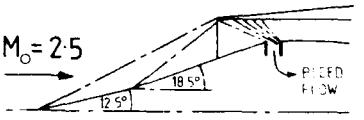

M_d	2·0	2·5	2·5
COMPRESSION	ALL EXT (δ_1 7° δ_2 9·5° δ_3 15·25°)	40% EXT 60% INT	55% EXT 45% INT
PRESSURE RECOVERY %	93·7 94·6	89·9 92	90·6
BLEED FLOW %	3·5 6·0	4·7 10	2
COWL DRAG (on A_C)	0·099		
REF	4	5	6

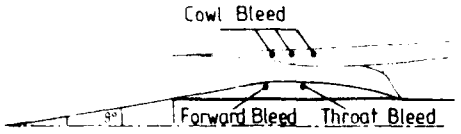

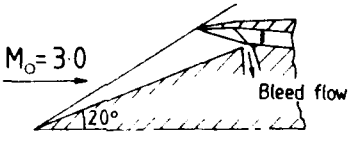

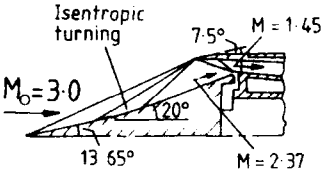

M_d	2·65	3·0	3·0
COMPRESSION	COMBINED	COMBINED	COMBINED
PRESSURE RECOVERY %	93·7	78	83 87
BLEED FLOW %	8·1	2	4·5 12
COWL DRAG (on A_C)		0·011	0·013
REF	7	8	9

FIG 11 INTAKES FOR SUPERSONIC CRUISE FLIGHT

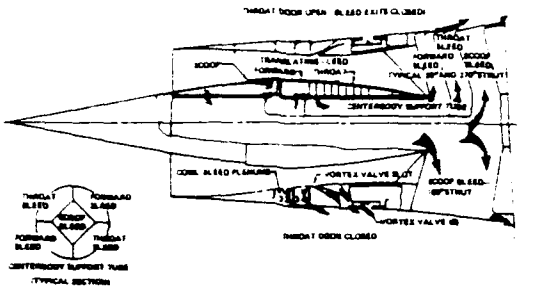

CRUISE CONFIGURATION

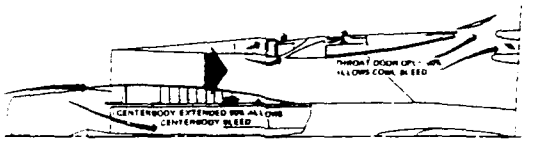

BUZZ SUPRESSION $1{\cdot}2 \leq M_o \leq 2{\cdot}9$

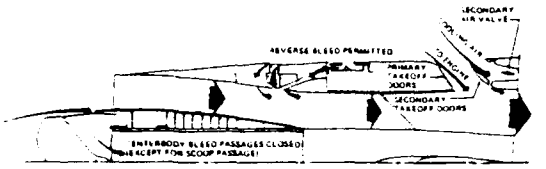

TAKE OFF AND LANDING $0 \leq M_o \leq 0\ 5$

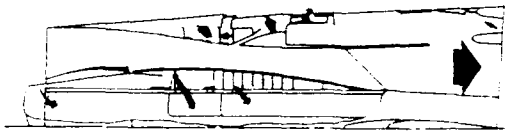

INTAKE 'STARTED' $1\ 6 \leq M_o \leq 2\ 9$

FIG 12 BOEING SST INTAKE 1972

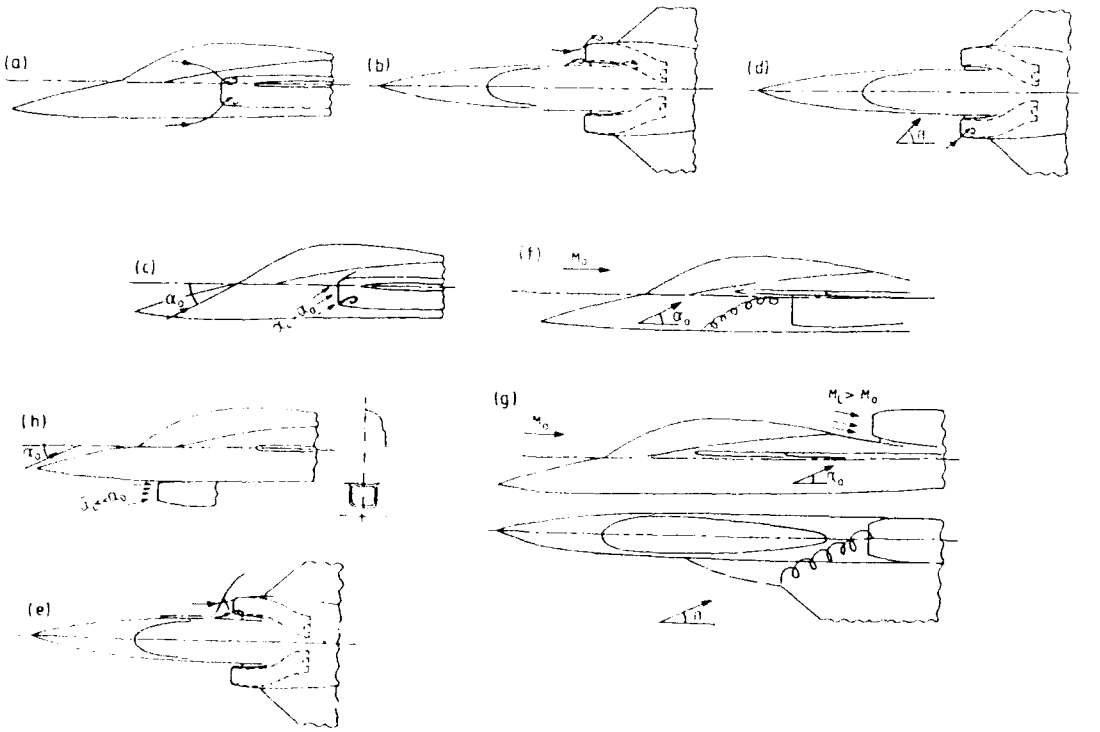

FIG 13 FLOW PATTERNS FOR BODY MOUNTED INTAKES

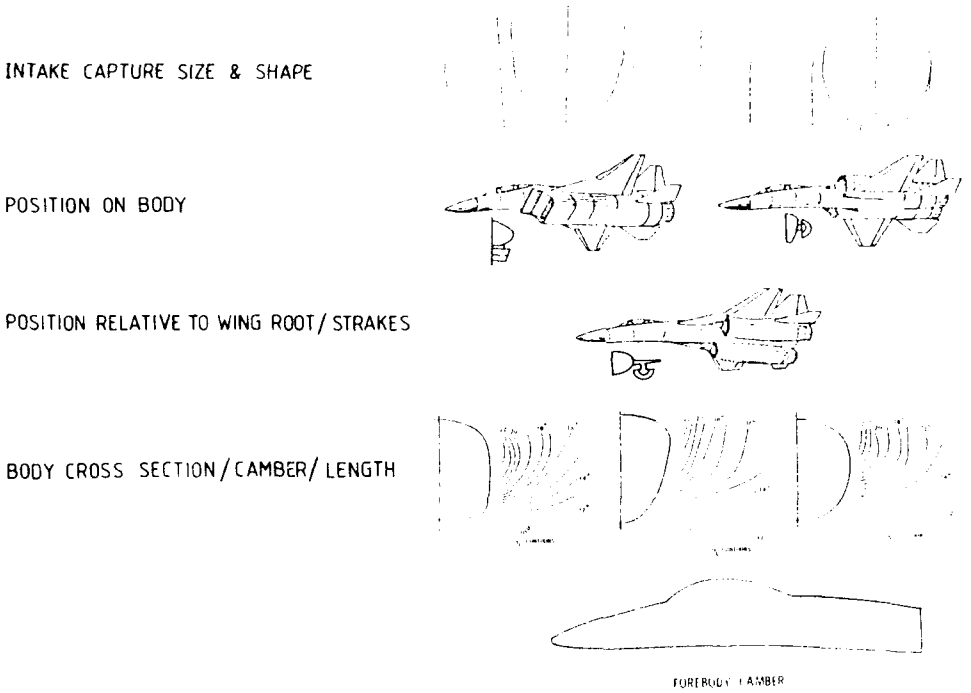

FIG 14 THE FLOW INGESTED INTO A BODY MOUNTED INTAKE — THE MAIN INFLUENCES ON QUALITY & QUANTITY

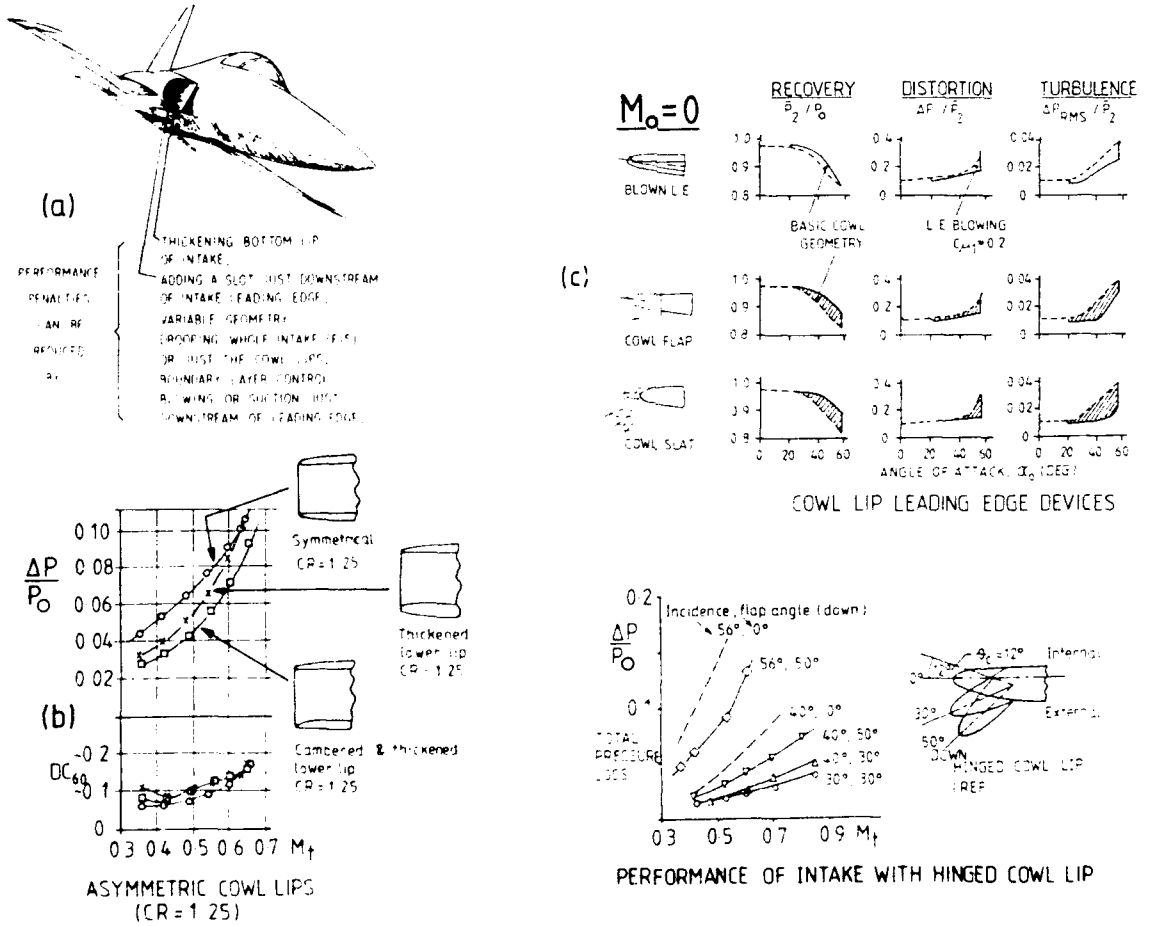

FIG 15 THE UNSHIELDED INTAKE AT SUBSONIC SPEEDS

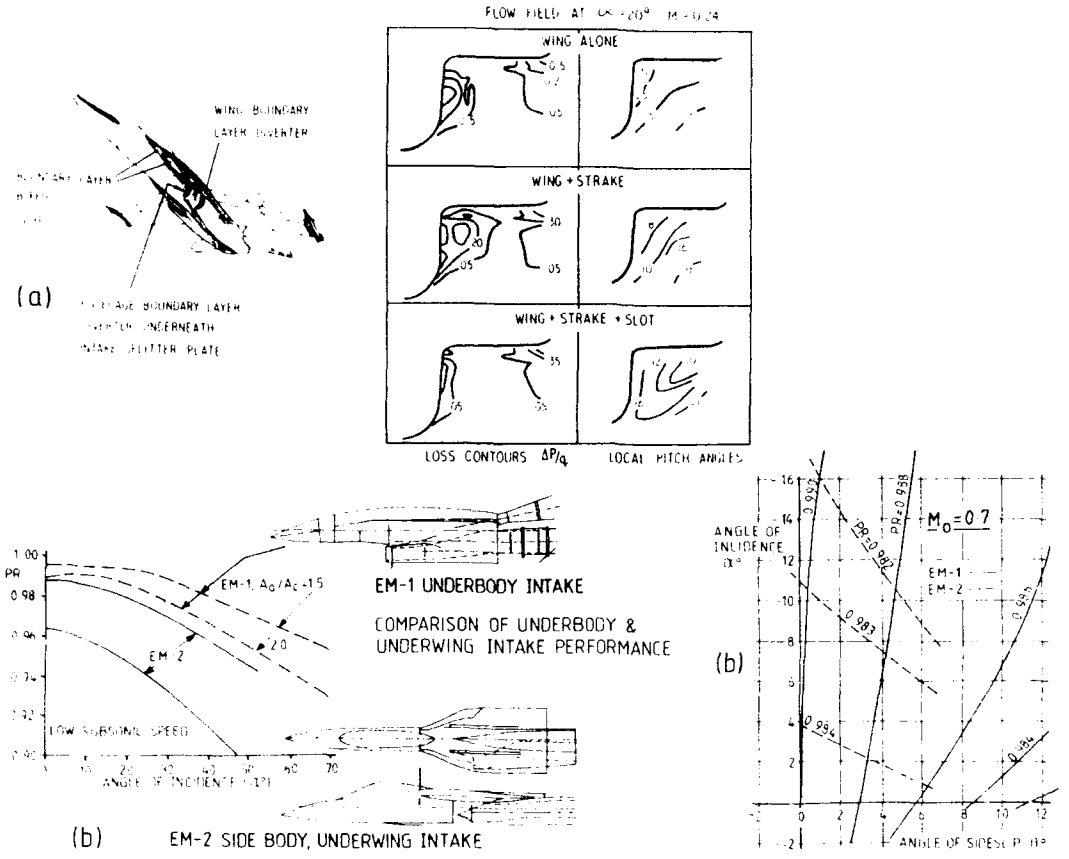

FIG 16 THE SHIELDED PITOT INTAKE AT SUPERSONIC SPEEDS

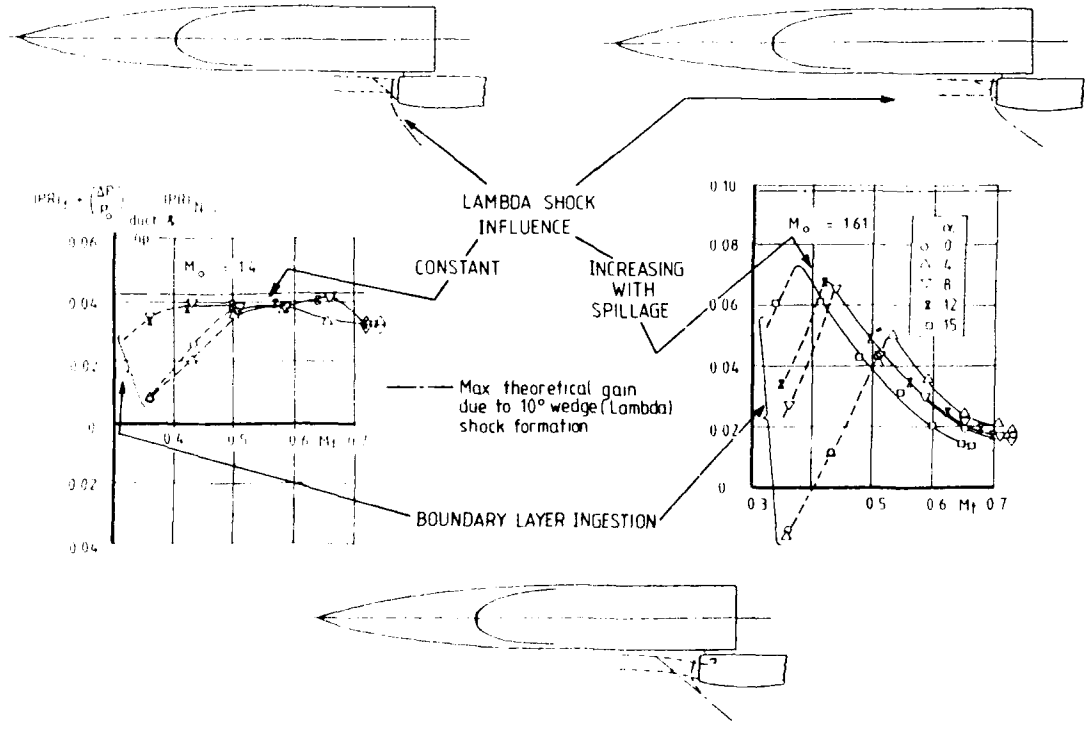

FIG 17 NORMAL SHOCK INTERACTION EFFECTS FOR PITOT INTAKE ON A DIVERTER

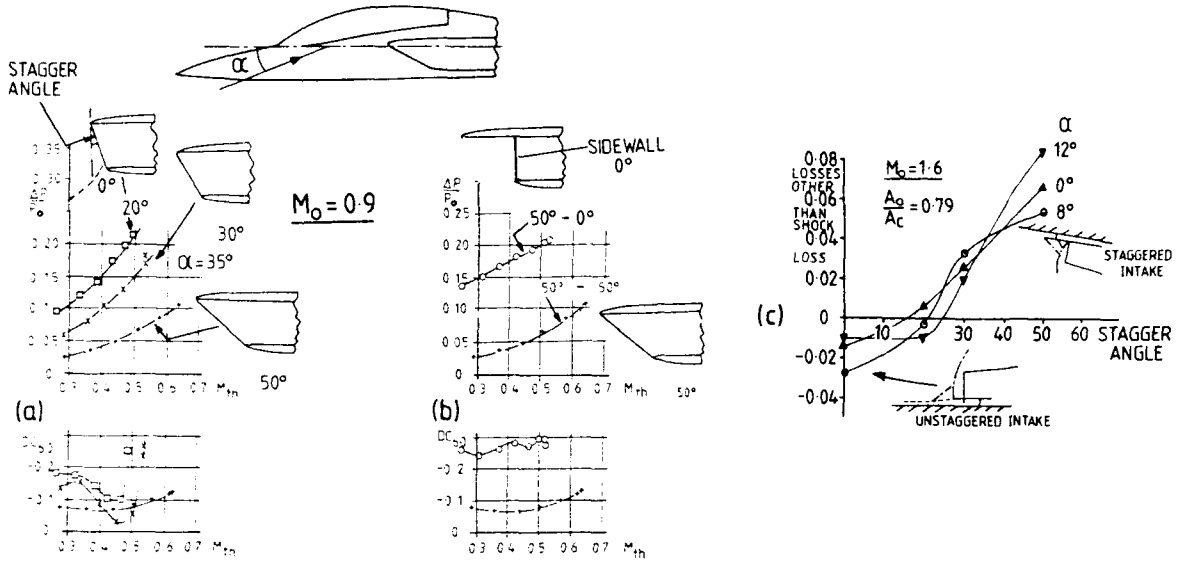

FIG 18 EFFECT OF INTAKE STAGGER AT SUBSONIC & SUPERSONIC SPEEDS

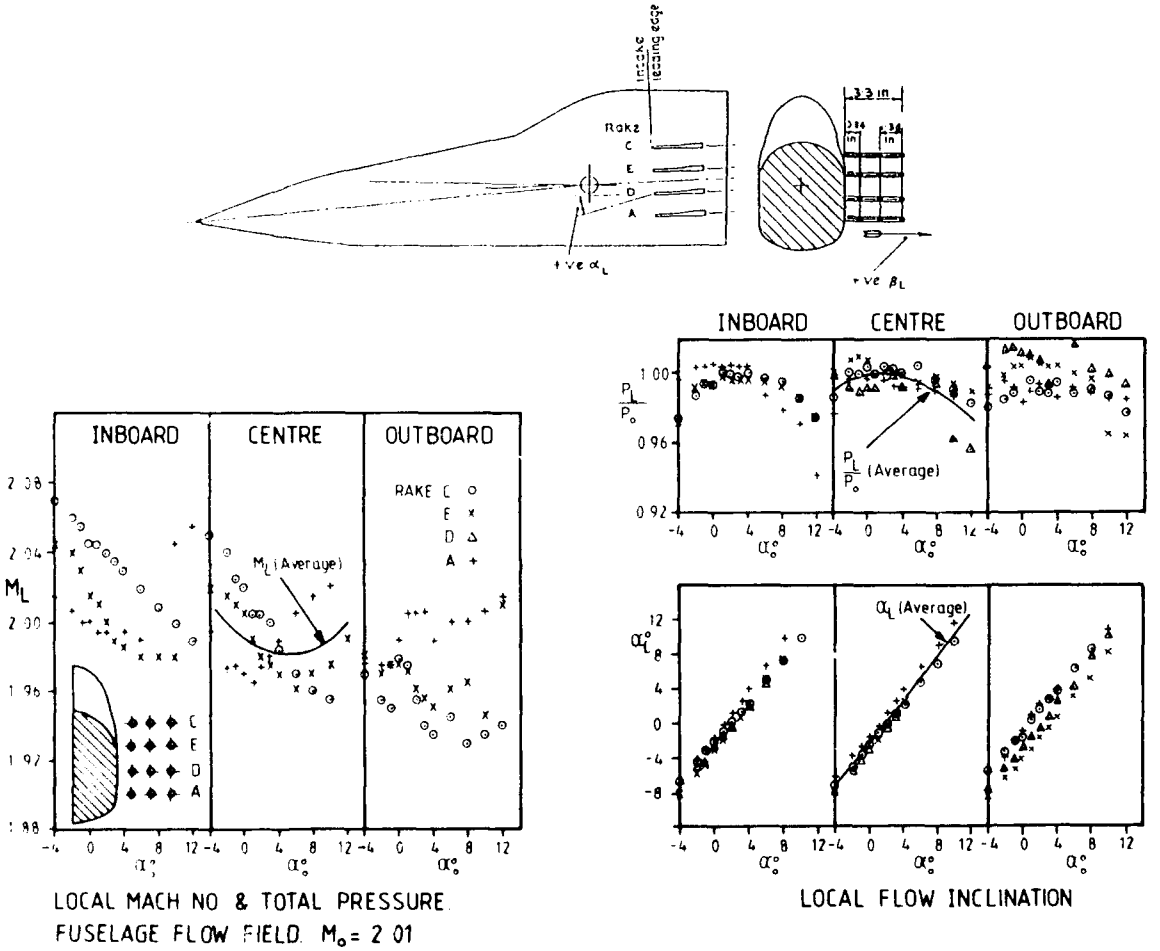

LOCAL MACH NO & TOTAL PRESSURE
FUSELAGE FLOW FIELD $M_o = 2.01$

LOCAL FLOW INCLINATION

FIG 19 FUSELAGE FLOW FIELD AT INTAKE POSITION AT $M_o = 2.01$

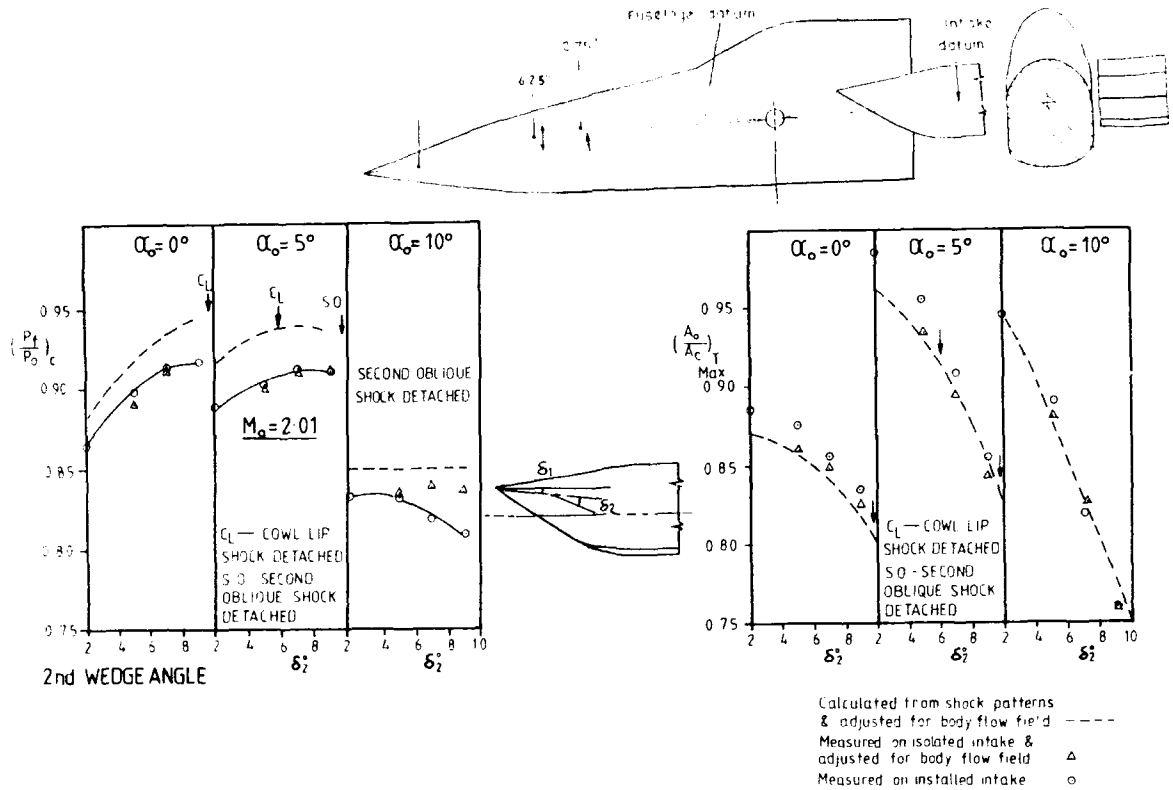

a) PRESSURE RECOVERY AT CRITICAL FLOW CONDITIONS

b) MAXIMUM TOTAL MASS FLOW $M_o = 2·01$

FIG 20 CORRELATION OF ISOLATED & INSTALLED INTAKE PERFORMANCE

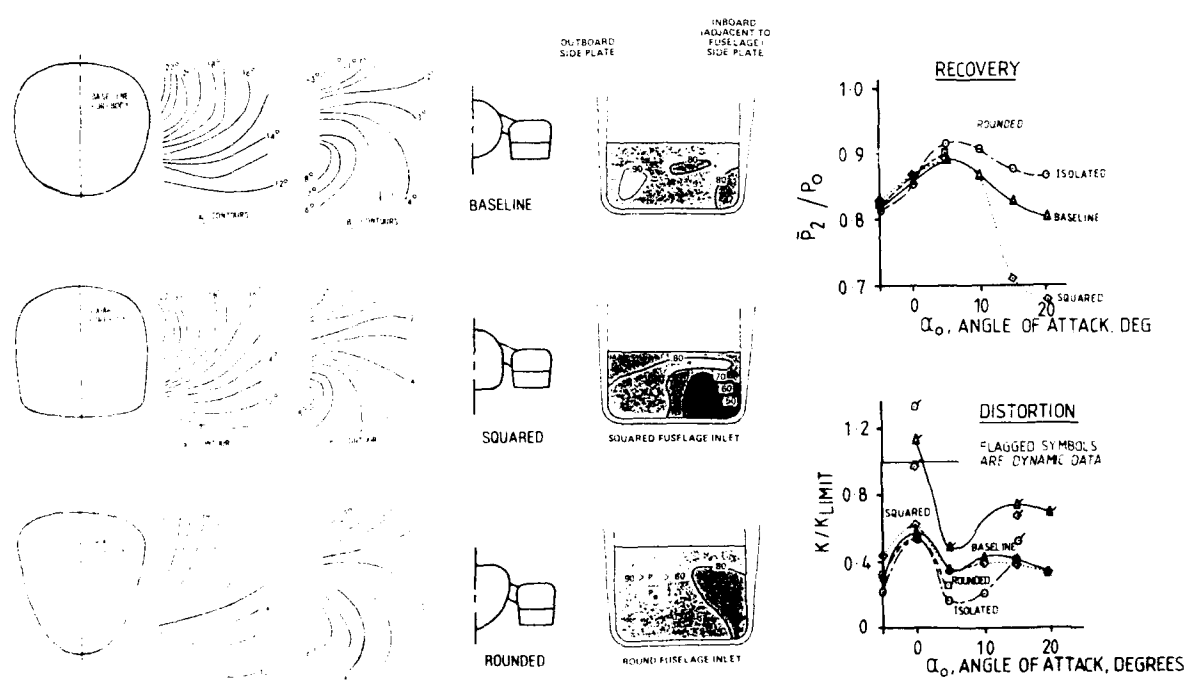

FIG 21 SIDE-MOUNTED 2-D INLET — EFFECT OF FOREBODY SHAPE ON PERFORMANCE $M_o = 2·2$, $\alpha_o = 15°$

PROBLEMS

(1) INGESTION OF BODY VORTEX INTO ONE OR MORE INTAKES

(2) UNEQUAL FLOW INTO INTAKES

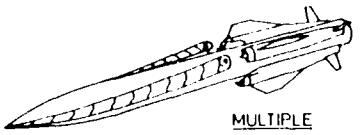

MULTIPLE

FOUR INTAKES

CARTESIAN OR SKID - TO - TURN CONTROL

OTTOMAT - SUBSONIC

LOW ALTITUDE ANTI - SURFACE RAMJET MISSILE - LASRM
ADVANCED LOW VOLUME RAMJET - ALVRJ
ANTI - SURFACE SHIP MISSILE - ANS
FUTURE MISSILE SYSTEM
SA 6
} SUPERSONIC

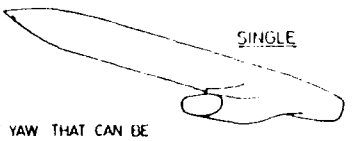

SINGLE

PROBLEMS

(1) AMOUNT OF YAW THAT CAN BE TOLERATED IF SOME SKID - TO - TURN IS REQUIRED

(2) STATIC & DYNAMIC ENGINE FACE FLOW DISTORTION TO AVOID ENGINE SURGE (TURBOJETS)

(3) ULTRA SHORT S DUCT AERODYNAMICS

SINGLE INTAKE

TWIST - STEER OR BANK - TO - TURN CONTROL

HARPOON
TOMAHAWK
SEA EAGLE
} SUBSONIC

ADVANCED STRATEGIC AIR - LAUNCHED MISSILE - ASALM
} SUPERSONIC

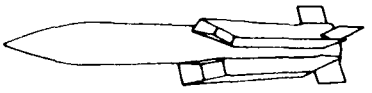

TWO INTAKES

ADVANCED LONG RANGE AIR - TO - AIR MISSILE - ALRAAM

AIR - SOL MOYENNE PORTÉE - ASMP

FIG 22 MISSILE INTAKE CONFIGURATIONS

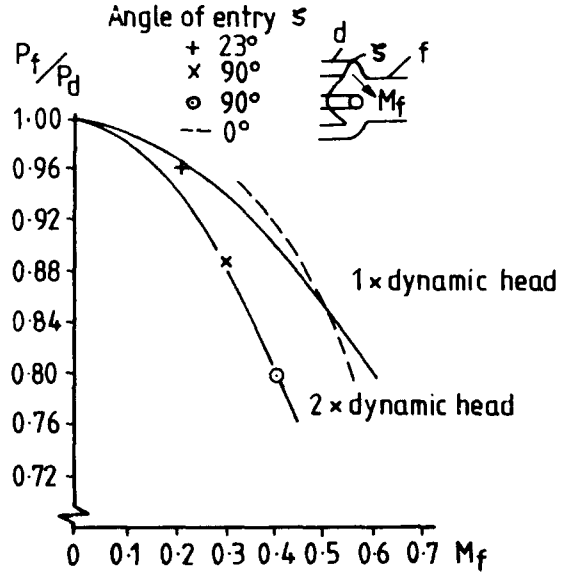

FIG 23. PRESSURE RECOVERY PENALTY DUE TO MIXING OF 4 FLOWS AT ZERO INCIDENCE

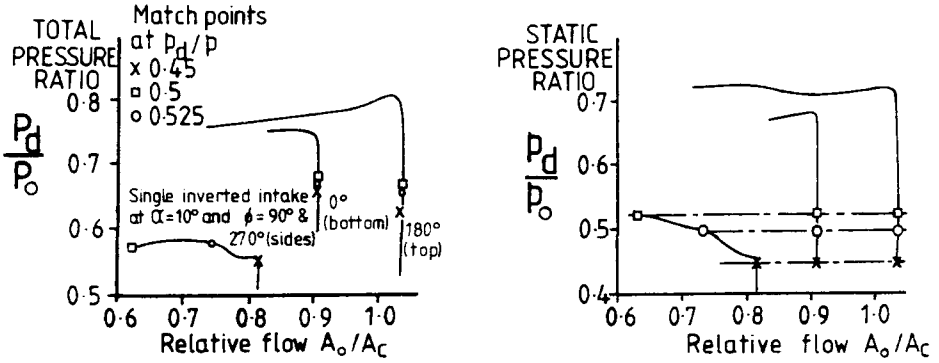

(a) MATCHING OF CHARACTERISTICS FOR SINGLE INVERTED RECTANGULAR INTAKE POSITIONED AT TOP, BOTTOM & SIDES OF A BODY AT $M_o = 2{\cdot}3$

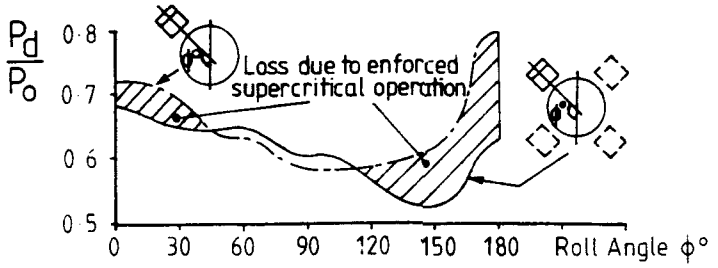

(b) VARIATION OF PRESSURE RECOVERY WITH ROLL ANGLE FOR ONE INTAKE ALONE & ONE INTAKE IN PRESENCE OF THREE OTHERS AT $\alpha = 10°$, $M_o = 2{\cdot}3$

FIG 24 REASONS FOR REDUCED PERFORMANCE OF MULTI-INTAKE CONFIGURATIONS

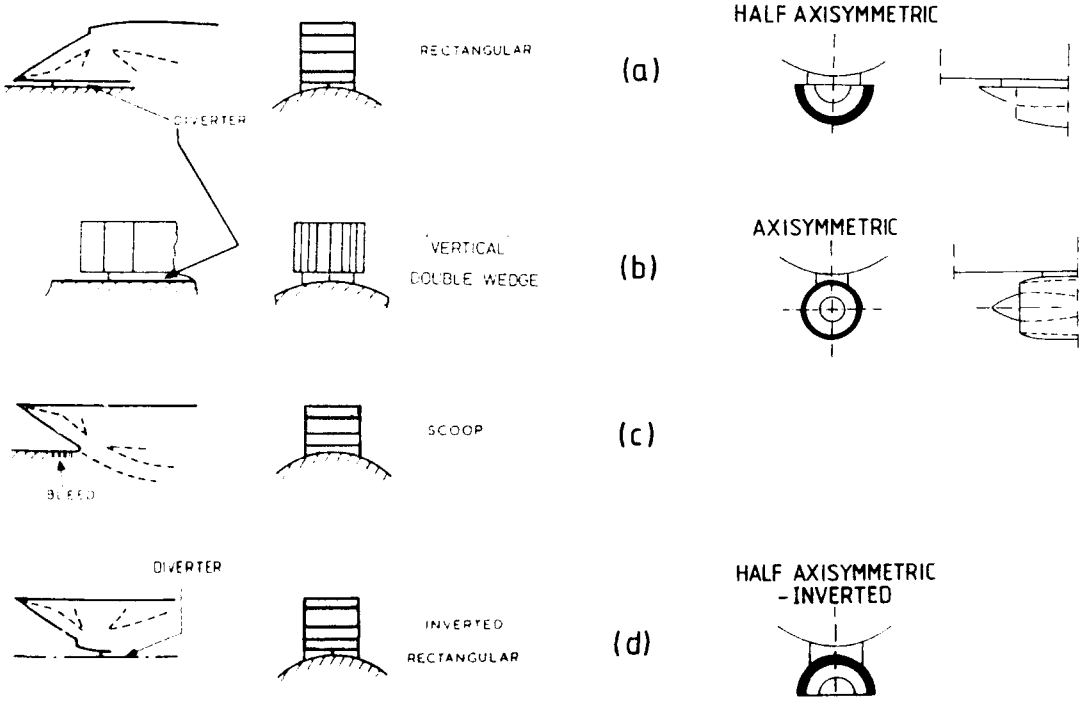

FIG 25 INTAKE TYPE & ORIENTATION

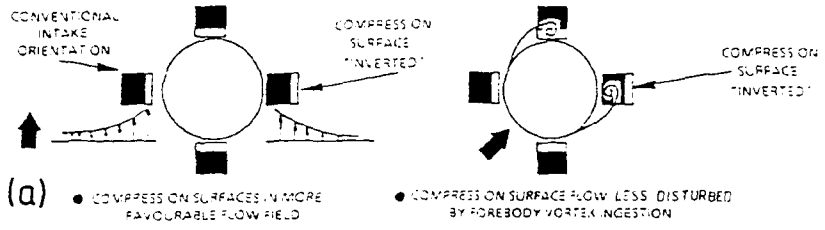

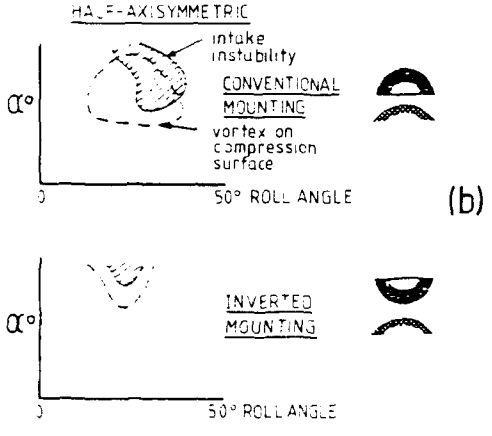

EFFECT OF HALF AXI-SYMMETRIC INTAKE INVERSION

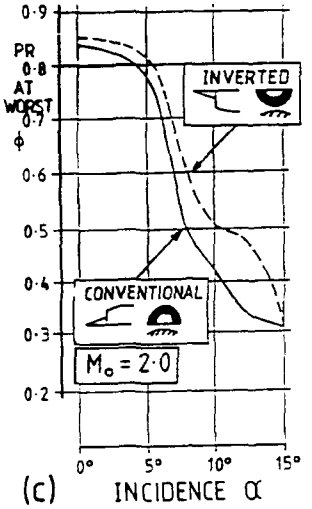

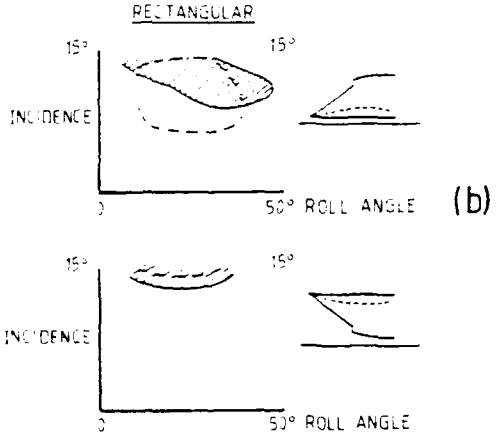

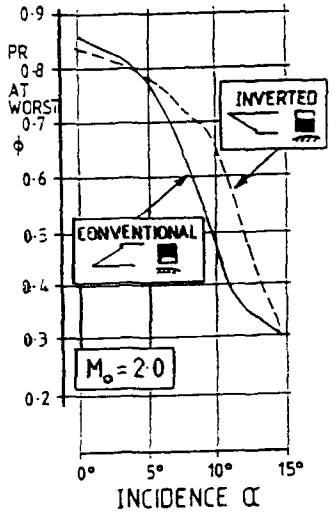

EFFECT OF RECTANGULAR INTAKE INVERSION

FIG 26 THE ADVANTAGES OF INTAKE INVERSION

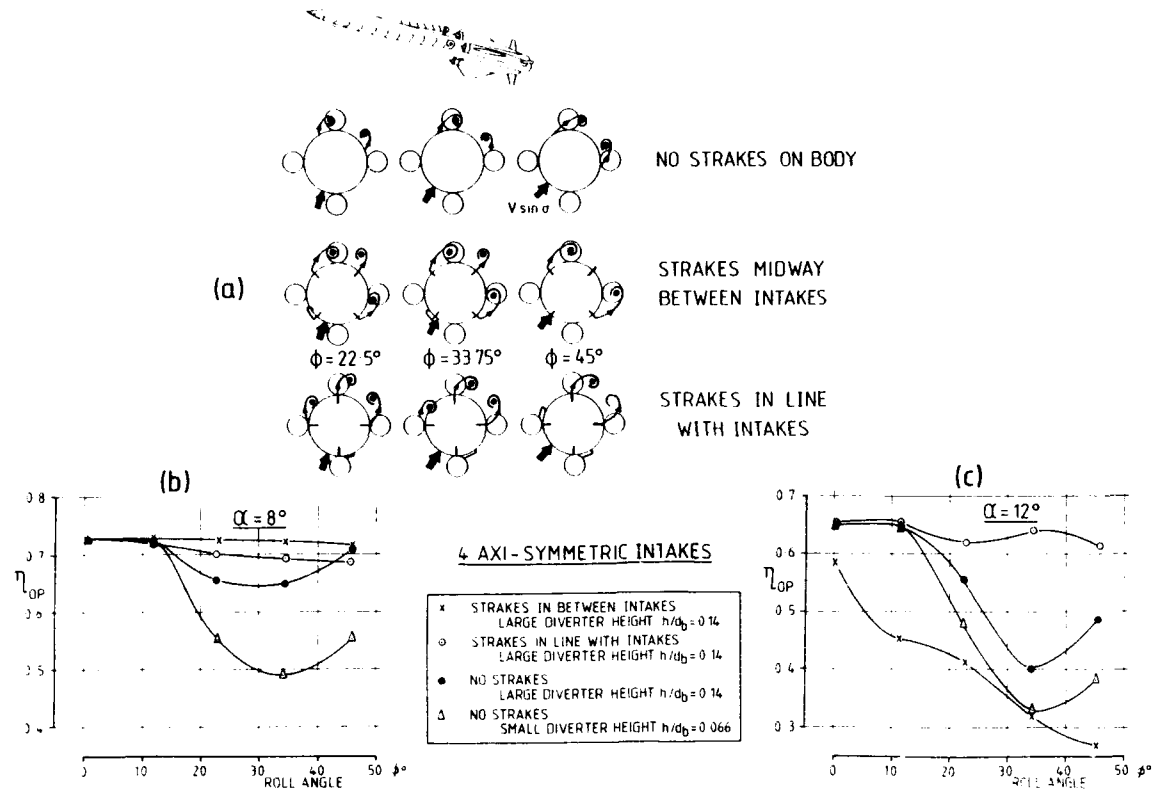

FIG 27 INGESTION OF BODY VORTEX INTO ONE OR MORE INTAKES AS BODY ROLLS.

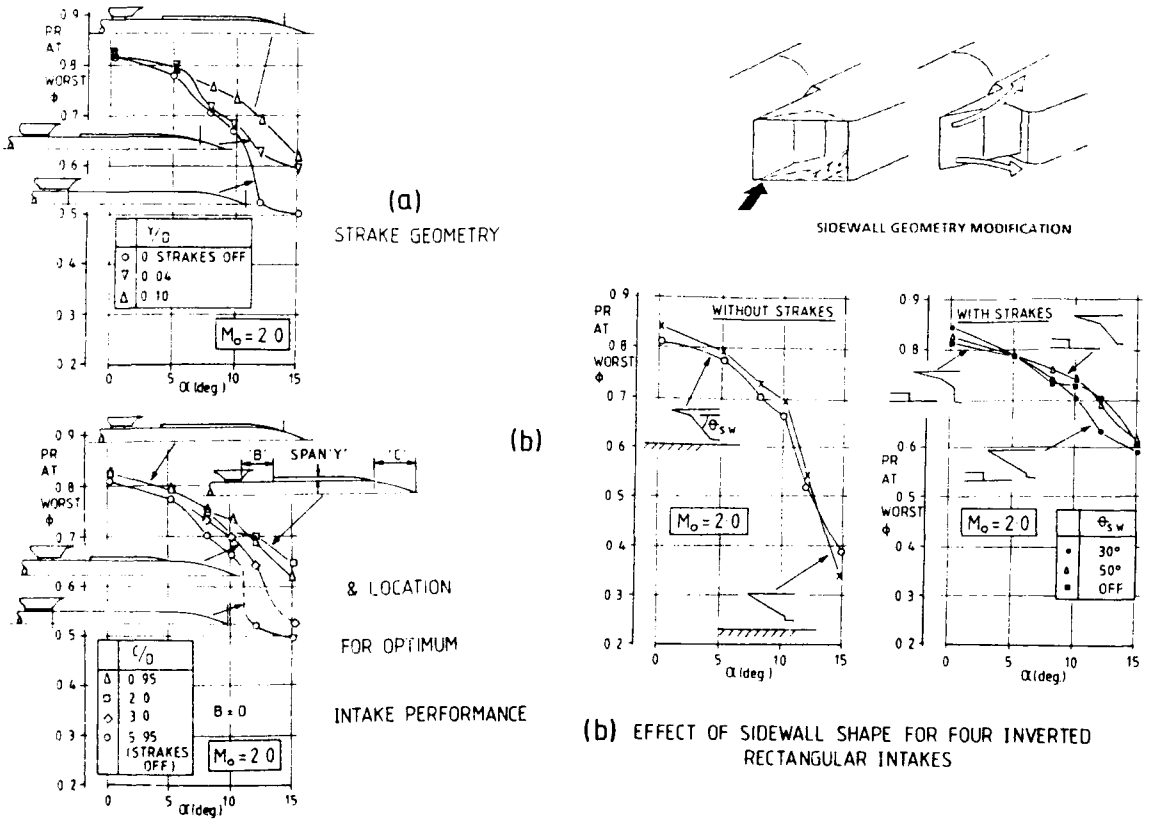

(b) EFFECT OF SIDEWALL SHAPE FOR FOUR INVERTED RECTANGULAR INTAKES

FIG 28 EFFECT OF STRAKE & SIDEWALL VARIATIONS

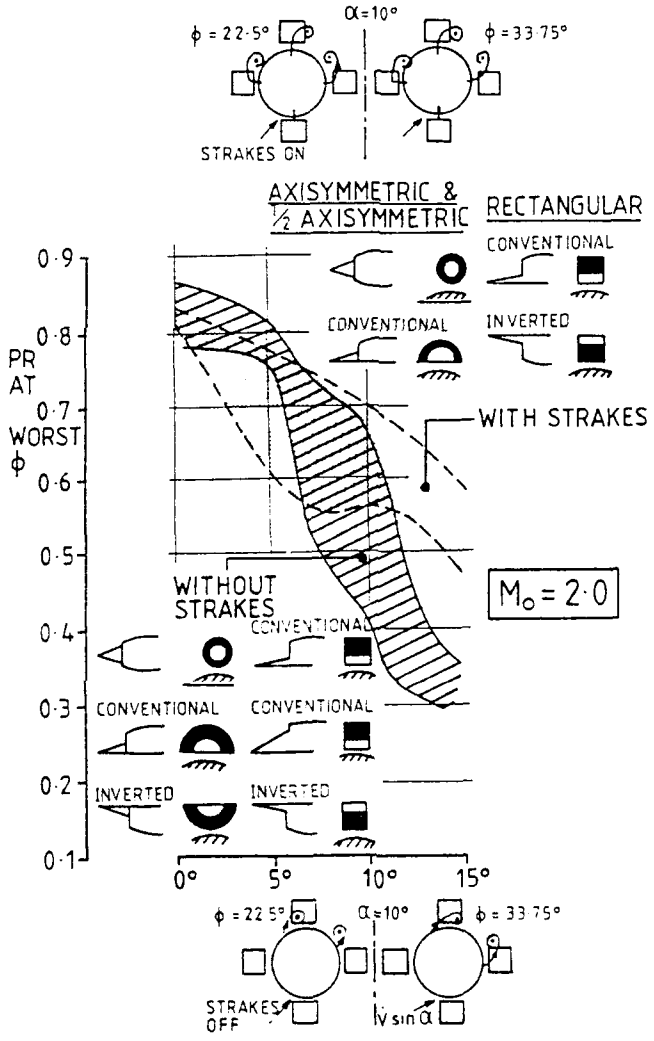

FIG 29 SUMMARY OF EFFECT OF FOREBODY STRAKES ON PRESSURE RECOVERY OF VARIOUS INTAKES IN CONVENTIONAL AND INVERTED POSITIONS

AGARD WG13 "Aerodynamics of High Speed Air Intakes": Assessment of CFD results

By

N.C. Bissinger
Messerschmitt Bölkow Blohm GmbH
P.O. Box 801160
D-8000 Munich 80, Germany

T.J. Benson
NASA Lewis Research Center
Cleveland, Ohio 44135, USA

R.G. Bradley, Jr.
General Dynamics
Fort Worth, Texas 76101, USA

Abstract

This paper presents a brief review of the work accomplished by the numerical subgroup of AGARD Working Group 13 on "Aerodynamics of High Speed Air Intakes". This work comprised the selection of test cases for which experimental data were available. The test cases were chosen to range in complexity from normal-shock/boundary-layer interaction to full forebody-inlet combinations. Computations for these test cases were solicited from a large number of organizations and individual researchers within the NATO countries. The computation methods reached from Euler solvers (with and without boundary layer corrections) to full Reynolds averaged Navier-Stokes codes. The group compared these results with the test data available for each test case.
A short overview of the CFD methods employed, a description of the test cases selected and some of the comparisons between CFD solutions and test data are presented. The conclusions and recommendations drawn from this assessment are given.

1. Introduction

The design of high speed air intakes for aircraft has been significantly affected by the recent development of computational fluid dynamics (CFD) methods for analysis. CFD provides the designer with flow field solutions for air intake geometries that are more detailed and provide more information than wind tunnel test data. In general these solutions do not replace wind tunnel test but rather compliment the experimental methods to provide greater insight and understanding to the detailed flow interactions that greatly affect the performance of air intakes. As a result, the resulting designs can be expected to exhibit superior performance characteristics.

Since CFD provides such a powerful design tool, the Working Group 13 elected to perform an evaluation of the current state-of-the-art in CFD analysis. The approach for this evaluation was to select a number of test cases for which rather detailed experimental data were available and to solicit investigators from all of the NATO countries to provide solutions to the selected test cases. From these solutions and their comparisons with experimental data as well as with other solutions, the Working Group tried to attain a global overview of the efficiency, effectiveness and accuracy of CFD as a design tool. The comparisons were not intended to serve as a validation of CFD, but rather, give an indication of the viability of CFD for design application.

2. Test Cases and Calculation Methods

Eight test cases were selected by the group for evaluation. These test cases are summarized briefly in Table I. The actual geometries of some test set-ups will be presented in chapter 3. Test case 1 consisted of three different flows comprising shock/boundary layer interactions that result in no separation, just starting separation and strong separation. Although test case 2 is geometrically simple it should still give hints into the accuracy of CFD codes which are designed for full intake modeling. Both test case 1 and 2 represent flow details/phenomena that are typical for internal compression intakes. The intake ducts of test cases 3 and 4 are typical for many current military aircraft. Depending on mass flow and/or curvature these ducts can exhibit boundary layer separation. For both test cases two mass flows (with and without separation) were specified. The intake of test case 5 was a straight pitot type intake for which three mass flows were defined. The highest mass flow lead to nearly chocking of the intake. So the influence of the flow at the entrance of the intake onto the duct flow was to be investigated in this test case. For the two-dimensional intake of test case 6 only the supersonic compression was to be calculated. Because the free stream total temperature is much too low real-gas models need not to be applied. However, free stream Mach number is high enough to assess the ability of the codes to perform hypersonic flow calculations. Also, comparisons between two-dimensional and three-dimensional modeling of the flow can be made. The

intake of test case 7 is axi-symmetric with 40% external and 60% internal compression. The flow was to be calculated as far as into the subsonic diffusor downstream of the terminal shock including effects of wall bleed. For test case 8 the Tailor-Mate series of experiments was chosen. For a transonic and a supersonic flight Mach number the flow around a forebody/intake configuration was to be calculated. Detailed information on the test cases can be found in the reference (AGARD-AR-270) to be published soon.

Table II gives an overview of the computer codes used in this study. The left column gives the name of the code. The second column identifies the user of the code by affiliation, the third gives the type of code, and the fourth the particular test cases against which this code was applied.

The PARC3D code (Sverdrup) is a derivative of the NASA Ames developed ARC codes, which employs a Beam-Warming approximate factorization scheme to solve the NS equations by marching the time dependent equations to steady state and usually employs a Baldwin-Lomax algebraic turbulence model. The code used a diagonalized form of the implicit matrices for efficient execution times and a Jameson-style artificial dissipation scheme to stabilize the scheme near shock waves. For subsonic outflow boundaries, a static pressure is specified and density and velocity are extrapolated in the basic code. The HAWK3D code is a specially modified version of the PARC3D code which was used by General Dynamics. This code employs a two-equation k-kl turbulence model not available in the basic PARC3D code. The FALCON code was also used by General Dynamics to study test case 6. This code is a finite volume solver which uses Roe's flux difference splitting to solve the 2D or 3D NS equations. The code contains a multi-blocking capability and a Baldwin-Lomax algebraic turbulence model. For this supersonic test case, flow quantities were extrapolated at the downstream boundary.
The PEPSI-S code was used to solve several of the supersonic test cases. This code solves the PNS equations using a Briley-McDonald LBI scheme to make a single sweep in the predominately supersonic flow direction. The code has a variety of turbulence models available, the algebraic McDonald-Camarata was used for case 2, a version modified for compressibility was used for case 6, and a one equation turbulent kinetic energy model was used for case 7. A variety of boundary conditions are also available to this code, including distributed mass removal for the bleed regions of test case 7. Because this code is used only for supersonic flows, and is a single sweep code, the downstream computational boundary is the last solution plane and is not specified by a boundary condition. The NS2D code was adapted for air intakes (and used here for test case 6) from the code used by ONERA for test case 2. This code solves the Reynolds averaged NS equations by a centered explicit finite difference scheme with a multigrid convergence accelerator. The discretization is performed using a two-step Lax-Wendroff type scheme. The code employs an algebraic turbulence model. The FLU3M code was used to analyze test case 6 and 8. This code was developed by ONERA and Aerospatiale for multiblock grids with an emphasis on supersonic and hypersonic flows. The code solves the Euler equations by an implicit upwind TVD finite volume scheme of van Leer's MUSCL type. Its implicit part consists of an ADI like inversion in cross-section planes coupled with a Gauss-Seidel relaxation in the third direction. The ARA Euler multiblock method is based on the scheme originally proposed by Jameson et al. It is a finite volume scheme with explicitly added artificial dissipation. The multi-stage-time-stepping scheme uses total enthalpy acceleration and a variable time step supported by residual smoothing. For test case 5, viscous effects were included by performing boundary layer calculations using results from the Euler calculations. Ikarus (Dornier) is a three-dimensional Navier-Stokes code derived from ENSFL2D which is a two-dimensional/axisymmetric code for the solution of the Euler and Navier-Stokes equations. Both codes are based on the finite volume spatial discretization and the Runge-Kutta type time integration presented by Jameson et al. The solution method is characterized by explicit artificial viscosity, local time stepping, implicit residual smoothing, multilevel grid technique accompanied by multigrid strategy within each grid level. The viscous terms in the Navier-Stokes equations are simulated in full and their thin layer approximation. The Baldwin-Lomax turbulence model (with modifications) is used. RANSAC (BAe) is a three dimensional, cell centered, finite volume, implicit, pressure correction method for the solution of the Reynolds averaged Navier-Stokes equations. A non-staggered grid pressure correction algorithm due to Rhie is employed, in which the addition of explicit fourth order dissipation terms damp out pressure instabilities in the momentum equations. For the momentum equations, the scheme enforces central differencing for very slow flows and upwind differencing for fast flows. The linearization of the transport equation for all the cells creates a coefficient matrix that is septadiagonal. The matrix inversion is performed by an over-relaxation black/red iterative matrix inversion technique which takes two sweeps through the mesh on each iteration. For turbulent closure the standard k-e model is used. NSFLEX is a finite volume Navier-Stokes code for subsonic, transonic and hypersonic flows developed at MBB. Its basis is the Euler method EUFLEX for the conservative Euler equations. The fluxes at the cell faces are determined by a linear Riemann problem using a nominally third order accurate characteristic flux extrapolation scheme of MUSCL type. At strong shocks the method switches to a modified flux vector splitting method. The switching between the two methods is accomplished by an improved flux limiter of the van Albada type. The resulting unfactored difference equations are solved in their implicit and time depending form by a point

Gauss-Seidel method. The viscous fluxes are approximated by central differences. The turbulence model is that of Baldwin-Lomax. The code has a block and real gas capability.

3. Analysis

Comparisons have been made between the results of calculations and measurements and will be reported on in the Reference. In the following an overview about these efforts will be given for some of the test cases.

3.1 Test case 1 - Transonic Normal Shock/ Turbulent Boundary Layer Interactions

The experiments for this test case have been performed in a "two-dimensional" tunnel the main features of which are given in Fig 3.1.1. For the formation of the shock interchangeable bumps are mounted on the upper and lower wall of the rectangular test section. The position of the shock on these bumps is determined by the adjustable second throat downstream of the test section. Flow variables at three different nominal Mach numbers at the shock had been measured by a two-color laser velocimeter. The flows depicted small to large separation respectively at the foot of the shock inside the boundary layer. The boundary layer is considered turbulent without any information from experiment about transition. The tunnel wall is assumed to be adiabatic. The dimensions of the second throat are not given. Therefore, with the total pressure and total temperature known from experiment the calculations had to be repeated with different exit pressures until the shock location of the calculation agreed with that of the experiment.

CFD TECHNIQUES

This test case was attempted by two different research groups as noted in Tables I and II. Both used Navier-Stokes methods designated NS1 and NS2. Details of the analyses can be found in the Reference.

SELECTED RESULTS

Comparisons between calculation results and measured data are given here for the test case without (test case 1.1) and with a small separation (test case 1.2) only.

For test case 1.1 Figs. 3.1.2 and 3.1.3 show a comparison of the computed and experimental static wall pressure distributions. As can be seen the shock standing at the downstream end of the tunnel wall insert spans the whole tunnel width with the same X-station at the lower and upper tunnel wall. The static pressure distribution ahead of the shock compares well between both solutions NS1 and NS2 and experiment. Whereas in the solution NS1 the foot of the shock is nearly exactly at the same X-station as in the experiment in solution NS2 the shock foot is slightly ahead of the experimental one. This is somewhat surprising because solution NS2 shows a lower static pressure at the exit of the test section (at $X/h_t=3.5$) than solution NS1. From this pressure difference one would expect quite the opposite in shock location between NS1 and NS2. The pressure behind the shock (between $X/h_t=1.6$ to 2.1) is overpredicted by both calculation methods.

A selection of scaled mean velocity profiles at five X-stations is shown in Figs. 3.1.4 to 3.1.6. At the station just in front of the shock ($X/h_t=1.4$) solution NS1 underpredicts the velocities whereas NS2 near the wall underpredicts and above that layer slightly overpredicts the velocities. This situation changes inside the shock (Fig. 3.1.5) in that now both solutions underpredict the velocities by a noticeable amount. That solution NS1 even produced negative velocities can be seen in Fig. 3.1.5. A separation of this small size could not be recognized in the measured data. Solution NS2 agrees better with the "free-stream" velocity which is underpredicted by NS1 (Fig. 3.1.6). This is in agreement with the static pressure difference at the exit of the test section. However, the boundary layer profile is fuller in solution NS1 and closer to experiment near the wall than in solution NS2 (Fig. 3.1.6).

Shear stress data have been supplied for solution NS1 only. They are plotted in Figs. 3.1.7 to 3.1.9 for the same X-stations as the velocity profiles. Near the wall the Reynolds stress in the calculations is generally smaller than in experiment. The calculation delivers a maximum whose magnitude is lower in the upstream part, becomes higher inside the shock and reduces to values again that are smaller than that of the experiment. The distance of the maximum from the wall is larger in solution NS1 than in the experiment around the downstream side of the shock. Upstream and downstream of this area there is a good agreement in this variable. Fig. 3.1.9 seems to indicate some small scatter in the measurements closest to the wall.

For test case 1.2 Figs. 3.1.10 and 3.1.11 show a comparison of the computed and experimental static wall pressure distributions along the lower and upper wall, respectively. As can be seen the shock standing at the downstream end of the tunnel wall insert spans the whole tunnel width with the same X-station at the lower and upper tunnel wall. The static pressure distribution ahead of the shock compares well between both solutions NS1 and NS2 and experiment. The foot of the shock in solution NS2 is slightly ahead of the experimental one. This shock location difference is to be expected from the difference of the static pressures between the two solutions at the exit of the test section where the pressure of NS1 is higher than that of NS2. The pressure behind the shock indicates the beginning of a plateau which is to be expected in a flow just starting to separate. The pressure in this area is overpredicted by both calculation methods. NS1 exhibits a distinctive and longer plateau whereas NS2 seems to possess a shorter plateau than

the experiment. After the separation region the pressure in NS1 is smaller than that of the experiment. Its positive slope indicates a steadily decelerated flow down to the intake exit. The pressure of solution NS2 behind the shock is larger than that of experiment but it is leveling off similar to the experiment.

Scaled mean velocity profiles are shown in Figs. 3.1.12 to 3.1.14. At the station in front of the shock (see Fig. 3.1.12 - X/h_t=1.6) solution NS1 underpredicts the velocities even showing negative velocities, i.e. separation, near the wall.Solution NS2 near the wall does not produce negative velocities and overpredicts the velocities above the "wall layer". The measurements are not close enough to the wall to recognize separation. This situation changes closer and inside the shock (Fig. 3.1.13) in that now both solutions underpredict the velocities by a noticeable amount. The separation bubble in solucion NS1 is steadily growing. Separation is indicated in solution NS2 at X/h_t=1.95. Negative velocities are reported from experiment at X/h_t=2.0 only. The differences between calculations and experiment become smaller further downstream (Fig. 3.1.14). Solution NS2 agrees better with the "free-stream" velocity which is underpredicted by NS1 (Fig. 3.1.14). The boundary layer profile is fuller in solution NS2 and somewhat closer to experiment near the wall than in solution NS1 which still shows negative velocities (Fig. 3.1.14).

Shear stress data have been supplied for solution NS1 only. Representative plots are given in Figs. 3.1.15 to 3.1.17. Compared with test case 1.1 there are larger discrepancies between calculation results and experiment.

CONCLUSIONS

Both methods applied used the Baldwin/Lomax turbulence model. It is known that this model is not very good for flows with separation. This general statement can be made for the flows analysed in this test case too. Unfortunately, from the fact that no calculation results with an alternate turbulence model have been presented, it can not be deduced that no better model exists. Definitely it is very badly needed.

On the other hand there are questions also for the experimental people. CFD needs detailed data on the boundaries of the computational domain, in this case at the entrance and exit of the test section. These data have not been collected for the flows considered. It would be worthwhile to repeat those tests and gather all the data needed for a more detailed comparison than was possible here. The question of the accuracy of the test data should also be raised. Raising this question does not mean that the data presented here are in doubt. But in a future effort, i.e. future comparison, the dependency of the measured data on, for example, particle size or laser power should be investigated. It should also be determined how close to the wall the measuring technique selected does deliver correct data.

3.2 Test case 2 -
Glancing Shock/Boundary Layer Interaction

In this experiment a ten degree wedge is mounted on a flat plate which extends upstream of the wedge leading edge (see Fig. 3.2.1). A supersonic freestream flow sweeps along the plate and strikes the wedge. The shock wave generated by the wedge interacts with the boundary layer formed on the plate to produce a highly three-dimensional supersonic flow field. From this flow field three principal types of data were taken. Surface static pressures were measured along the plate across the shock wave at a variety of distances from the wedge leading edge. Additionally, a traversing nulling pitot probe was used to determine both pitot pressure and flow yaw angle at selected locations through the interaction. The yaw angle was measured in a plane parallel to the flat plate.

CFD TECHNIQUES

This test case was attempted by five different research groups as noted in Tables I and II. The analysis techniques included five Reynolds-averaged Navier-Stokes (designated NS1 to NS4) and one Parabolized Navier-Stokes (designated PNS) methods. Details of the various analyses can be found in the Reference.

SELECTED RESULTS

The static pressure distribution on the plate is shown in Fig. 3.2.2 as a function of distance from the wedge at a specified distance from the wedge leading edge. The pressure is seen to increase from a free stream value of one (on the right of the figure) to a value of nearly two at the wedge surface. The pressure increase is not abrupt, as one would expect across a shock wave, but is seen to be a gradual, distributed increase to the wedge. The initial increase in the pressure occurs upstream of the shock wave. In the vicinity of the shock the pressure reaches a plateau value. Considering the CFD results, we see that, in general, both NS and PNS calculations have qualitatively modeled this pressure variation. The NS1 solution has correctly predicted the upstream influence, the location and strength of the plateau, and the increase into the wedge. The NS2 solution does an excellent job in the plateau and near wedge region, but slightly overpredicts the upstream influence of the interaction. The PNS solution has correctly predicted the upstream influence while overpredicting the pressure levels downstream of the shock. The NS3 solution, while slightly underpredicting the upstream influence, has accentuated the plateau region near the shock wave. The NS4 solution has greatly underpredicted the upstream influence and has missed the pressure plateau.

Fig 3.2.3 shows a pitot profile normal to the plate at a location that is far downstream of the inviscid shock location

and represent an outflow condition from the interaction between shock and boundary layer. This profile is somewhat similar to a turbulent boundary layer profile, except near the wall, at the left. The near-horizontal portion of this curve resembles boundary layer profiles in the vicinity of flow separation. Considering the CFD results, we see that the NS1, NS2 and NS4 analyses have predicted this feature, with the NS4 analysis overpredicting the pressure level and the NS1 analysis smoothing the feature somewhat. The NS1, NS2, NS4 and PNS analyses have maintained the turbulent boundary layer shape through the interaction and, in general, give good prediction of the profile shape. The NS1 analysis overpredicts the pitot pressures near the free stream. The NS2 analysis is slightly overpredicting the boundary layer thickness while correctly modeling the near wall region. The NS3 analysis has produced a laminar-type boundary layer profile and has returned little of the complex profile seen in the experiment.

A comparison of the CFD and experimental yaw angles is given in Fig. 3.2.4. The yaw angle is measured in a plane parallel to the flat plate. The particular profile of Fig. 3.2.4 was taken at the same location as the pitot profile in Fig. 3.2.3. The figure shows the computed yaw angle along the vertical, versus distance above the flat plate along the horizontal. In the external flow, the yaw angle is seen to be nearly nine degrees, corresponding to the wedge angle and the inviscid turning of the flow by the shock wave. Near the wall, however, the flow is seen to turn nearly twenty-two degrees, with the break in the curve occurring near the edge of the boundary layer from Fig. 3.2.3. If we now consider the comparison of the CFD results, we see that all analyses properly model the external flow and predict increased turning near the plate. While the NS1, NS2, NS4 and PNS analyses nearly predict the wall flow turning angle, the NS3 analysis slightly underpredicts the flow turning. The NS3 analysis seems to predict the beginning of the flow turning too near to the wall.

CFD analysis provides a powerful qualitative representation of the test case flow field and thus leads to better understanding of the three dimensional nature of the flow. This is demonstrated in Fig. 3.2.5, which shows computed particle traces through the interaction. In this figure particles are released near the wedge leading edge and near the center of the flow field. In both cases, the lower portion of the traces are seen to be swept more sharply to the right than the upper portions. The lowest traces, which would correspond to surface oil flow patterns, are seen to coalesce into a single line; a feature which is also seen experimentally. The upper traces on the wedge are pulled down onto the plate surface far downstream from the wedge leading edge, while the upper traces at the right flow up and over the low energy flow on the surface.

CONCLUSIONS

In general, the CFD analyses used in this study, which have been designed and built for full intake calculations, have done a good job of modeling this fundamental three dimensional interaction. It appears that the salient physical features of the interaction can be modeled with CFD. There are some interesting differences between the various computational results, particularly concerning the three similar NS calculations. Since the basic algorithms used here are the same, the differences can be attributed to differences in turbulence models, the way the problem was modeled and possible enhancements to the computer codes. In this case, one group chose to model this interaction with a plane of symmetry, thus doubling the grid resolution onto the plate, while another allowed the flow to slip along the wedge, thus increasing the resolution of the shock wave. These types of choices, which are often made in CFD analysis, are examples of user involvement in the flow solution. The current state of CFD analysis still requires user involvement in obtaining flow solutions. The same code run on the same computer by different users can often give different answers.

3.3 Test case 3 -
Subsonic/Transonic Circular Intake

This intake is a side-mounted circular intake with a horizontal symmetry plane and an S-bend diffusor (see Fig. 3.3.1). Although the "flight Mach number" was rather small (M_0 = 0.21) the solicitors were asked to calculate the complete flow from free-stream into the intake instead of just the duct flow. With this approach the problem of differing entrance conditions at the duct entrance within different calculations could be eliminated. The flow for a high and a low mass flow was to be calculated. The flow approached the intake with no angle of attack and no sideslip. The test data available from the experiments included static pressures, total pressures and some circumferential flow angles in the engine face plane. The total pressures within the boundary layer were scanned by total pressure probes at four circumferential stations just in front of the engine face plane. Along the duct walls four rows of static pressure taps were located.

CFD TECHNIQUES

This test case was attempted by two different research groups as noted in Tables I and II. The analysis techniques included two Reynolds-averaged Navier-Stokes (designated NS1 and NS2) and one Euler (designated EU) method. Details of the various analyses can be found in the Reference.

SELECTED RESULTS

A description and interpretation of the flow of this test case using the experimental static wall pressures along the duct is somewhat difficult. As can be

seen in Fig. 3.3.2 the static wall pressure in the high mass flow test case 3.1 drops from the stagnation point on the intake lip to supersonic values (p/p_{t_0} less than approx. 0.52). There is no explanation for the pressure increase between the second and third data point from the left. It seems that the flow downstream of the pressure minimum goes subsonic again through a lambda shock system which could have been triggered by a separation bubble at the throat. There is the indication of a small pressure plateau at about X/D_{max} ~ 0.3 which supports this supposition. At least the second leg of this shock system is hard to recognize in the pressure plots due to the relatively large distance between the pressure taps. The level of the wall pressure behind the shock system is already influenced by the first bend following the constant area duct piece. In addition the starboard pressure shows a pressure drop that indicates the acceleration of the flow necessary to counteract the centrifugal forces inside the bend (X/D_{max} ~ 0.8). On the starboard side the flow becomes supersonic again with a shock at about X/D_{max}=1.0. In front of this shock the pressure depicts a somewhat erratic behaviour (the numerical people would talk of "wiggles"). This same behaviour has been observed in test case 4. The pressures reveal a steadily decelerating flow with a sudden reduction in the deceleration magnitude at X/D_{max} ~ 1.4. This could be an indication for a further separation bubble the extent of which cannot be derived from these wall pressure plots. The further development of the pressure downstream in the duct is typical for an S-bend with constant area which shows a deceleration in the first bend and an acceleration in the second bend, i.e. some sort of a sinusoidal pressure distribution.

The wall pressures from the inviscid solution EU can be expected to be higher than those measured. This is due to the fact that the Euler calculations have been performed for the mass flows given in the experiments. Due to the missing displacement effect of the boundary layers, i.e. larger effective duct areas, the velocities must be lower and therefore the pressures must be higher than in the experiment. Fig. 3.3.2 shows this very clearly. There is only a small supersonic pocket on the cowl followed by a shock in front of the throat of the intake. Behind the shock the flow is subsonic. The pressure drop at the beginning of the first bend, i.e. the acceleration of the flow, is obviously not large enough for the flow to go supersonic again. There is no indication of a local shock.

The Navier-Stokes solution NS1 modelled the flow in the S-bend only. The guess of the starting values for the calculations gave a static wall pressure that is very close to that of the Euler solution EU. This guess misses all the losses due to the shocks on the cowl and therefore must lead to a totally different flow inside the duct. This could be the reason for the differences in static wall pressures in Fig. 3.3.2 between the experiment and solution NS1.

The pressure distribution on the cowl in the Navier-Stokes calculation NS2 shows a very good agreement with experiment although it does not reproduce all details. Instead of going through the second branch of a lambda shock the flow in this solution stays supersonic in the constant area duct in front of the S-bend (Fig. 3.3.2). It even accelerates behind the first shock on the lip which could point to a shorter separation bubble. The supersonic area ends with a local and relatively strong recompression or shock after the start of the S-bend diffusor. The pressure distribution in the S-bend comes close to that of the experiment.

Comparing Fig. 3.3.2 with Fig. 3.3.3 one can recognize that the differences between the Navier-Stokes solutions and the measurements are most likely due to problems in the modeling of boundary layers and their interaction with shocks. The low mass flow of test case 3.2 in Fig. 3.3.3 does not lead to supersonic flow nor to local shocks on the intake lip. Here the agreement between NS2 (and even EU) and the measurements are very good. There is only some indication of a separation in the S-bend starting at about X/D_{max} = 1.7. In this area the Euler solution deviates from the measured data whereas the Navier-Stokes solutions come pretty close to the experimental data.

Without showing evidence here it was also found that the agreement between calculations and experiment was much better in the total pressures in the boundary layers and the static wall pressure on the circumference at the engine face for the low mass flow case 3.2 than for the high mass flow case 3.1.

The difference of the possible extent of the separation inside the S-bend between the high and low mass flow test case can be recognized when comparing Fig. 3.3.4 and 3.3.5. From the lines of constant total pressures in the engine face (Figs. 3.3.6 and 3.3.7) it could be concluded that for both mass flows the radial extent of the separation bubble is slightly underpredicted.

CONCLUSIONS

It is very difficult to come to a reasonable conclusion from the comparison between experiment and calculations if the experimental data are so sparse as in this test case. However, from the difficulties experienced when interpreting the flow from measured data it became clear that there is a very large potential in CFD for flow diagnostics which are possible due to the increased amount of information on the flow. This information can be used for placing instrumentation in intake models and/or optimizing intake shapes for better performance.
Because intake flows with strong secondary flows are very sensitive to the onset flow it is very important for the calculations that the boundary conditions are specified as exact as possible. Detailed information

on freestream flow conditions and duct exit flow conditions are needed. Only with correct transition and turbulence models will the results of CFD become good enough quantitatively to be used in actual project work.
It still seems to be an art to produce very good results for complex intake flows. Only the engineer with good aerodynamic background can decide where in CFD grids for example need refinements to improve results.

3.4 Test case 6 - 2D Hypersonic Intake

The hypersonic intake to be calculated for Test Case 6, designated P8, is shown in Fig. 3.4.1. The intake is a Mach 7.4 rectangular mixed-compression design. Only the supersonic flow was to be calculated. On design the nominal 6.5 degree wedge produces an oblique shock which passes just outside the cowl lip and delivers a Mach 6.0 flow at the entrance to the intake. Another shock is generated by the cowl lip and this shock traverses the internal flow passage and is reflected from the ramp surface back onto the cowl. The interior of the cowl is contoured to provide additional distributed compression. In the vicinity of the shock reflection, the flow field was surveyed with a traversing pitot pressure probe to obtain pressure profiles throughout the intake. Static pressures were measured along the ramp and cowl surfaces and some temperature profiles were obtained with the pitot pressure profiles. While the high throat width to height ratio of this intake makes it possible to model the centerline flow two dimensionally, some comparison of 2D versus 3D modeling of the flow can also be assessed. The three dimensional effects are present in this intake due to the glancing shock/sidewall boundary layer, internally, and the outflow along the ramp surface, externally. In addition, while the free stream Mach number is sufficiently high to assess hypersonic flow calculations, the free stream total temperature is much too low to assess real-gas chemistry models. Boundary layer transition has been specified on the wedge and on the cowl, so some assessment of transition and turbulence models can be made.

CFD TECHNIQUES

This test case was attempted by six different research groups, using seven different codes, as noted in Table II. The analysis techniques included both two and three dimensional Reynold-Averaged turbulent Navier-Stokes (NS), laminar Navier-Stokes (LNS), Parabolized Navier-Stokes (PNS), and two dimensional Euler (EU). Details of the various analyses can be found in the Reference.

SELECTED RESULTS

Static Pressure Distributions

The static pressure distributions on the ramp and cowl of the intake downstream of the cowl are plotted in Figs. 3.4.2 and 3.4.3. Considering the distribution on the ramp from the experimental data (Fig. 3.4.2), and moving from left to right, one sees that the pressure increases sharply at the location where the shock generated by the cowl strikes and reflects from the ramp surface, near X/XREF=6.2. The internal portion of the cowl has been contoured to produce a distributed compression near the shoulder of the intake. Because of this contouring and the interaction of the shock with a thick boundary layer, the pressure rise is spread from near X/XREF=6.2 to X/XREF=6.4. Near X/XREF=6.4 the flow turns over the shoulder of the intake and the pressure increases much more slowly with distance. Also, the measured data exhibit some scatter for X/XREF>6.4. Considering the CFD analyses, there appears to be a great deal of scatter about the experimental results. In general, the three dimensional computations more closely match the experimental results than the two dimensional calculations which would imply that three dimensional effects are quite important in this speed regime in spite of the high aspect ratio of the intake. Some calculations predicted the shock impingement correctly like DNS3, MNS2, PNS2, PNS3, and SNS2. Others predicted the pressure rise through the shock reflection like DNS3, MNS2, PNS3. Some of the deviations could be attributed to the effects of the representation of boundary layers. For example, solution EU underpredicted the pressure rise, probably because it does not account for the additional compression effects of the cowl boundary layer displacement. The slight underprediction of the pressure rise and the downstream shock location in solution LNS3 are both effects consistent with underpedicting the boundary layer thickness. At the impingement point of the cowl shock the SNS2 code predicts a small separation bubble, which accounts for the rise in pressure upstream of the impingement point. The experiment gives no indication of such a separation. That possible three dimensional effects are present in this shock reflection can be seen when comparing solution GNS2 with GNS3. Both analysis are nearly identical up through the early parts of the shock reflection. They split following the shock impingement.

Considering the experimental pressure distribution on the cowl, Fig. 3.4.3, and again moving from left to right, the pressure slowly increases due to the internal contouring of the cowl. Near X/XREF=6.6, the pressure decreases due to the expansion from the ramp shoulder striking the cowl and then sharply increases as the cowl shock strikes this surface after being reflected from the ramp. Considering the CFD analyses, we again see substantial scatter from the experimental results and, in general, the three dimensional computations compare better with the experiment than the two dimensional computations. Upstream of the shock the static pressures of all calculations are equal or higher than those of the experiment. The pressure rise through the shock can be larger or smaller than the experimental one. Only very few calculations reproduce the correct shock sharpness. The spike near X/XREF=6.6 in the SNS2 solution is the result of an

additional shock set up by the computed separation on the ramp.

Pitot Pressure Profiles

In Figs. 3.4.5 and 3.4.6 comparisons of the CFD and experimentally determined pitot profiles through the intake at a location just ahead and just downstream of the snock impingement point (Fig. 3.4.4) are shown. Considering the experimental data of Fig. 3.4.5, the lower part of the figure shows the thick boundary layer which has grown on the ramp surface; the thickness is indicated by the location where the curve turns vertical, at Y/XREF=.075. Continuing up the curve, the sharp turn to the right is indicative of the cowl shock location while the gradual rise to the right and up is caused by the distributed compression on the inside of the cowl. Near the top of the curve, it turns sharply back to the left which indicates the thickness of the boundary layer on the cowl. Noting the shapes of the boundary layer profiles, we see that the cowl profile is thin and curved which usually indicates a laminar profile. On the ramp, the profile is thick with a nearly linear section which usually indicates a turbulent boundary layer. Considering the CFD results, we again see substantial scatter between the analyses, although all of the CFD results fall to the right of the experimental results in the core flow. All of the analyses predict a similar, though different from experimental, value of pitot pressure upstream of the cowl shock. This is the nearly vertical portion of the profile. This shock is smeared out by all calculations. They also deliver different turbulent boundary layer heights on the ramp. The pitot profile of the SNS2 solution is even becoming vertical on the ramp which is indicative of nearly separated flow. The PNS3 analysis has a similar type profile. The boundary layer thickness on the cowl is more or less overpredicted by all calculations. The vertical scatter at the upper left hand portion of the curve can be due to incorrect modeling of the intake geometry or to graphical errors in the post-processing of the computed results.

The next location to consider is at a station just downstream of the reflection of the cowl shock from the ramp surface (Fig. 3.4.6). Considering the experimental data, the lower portion of the figure shows that the ramp boundary layer has been compressed by the reflecting shock wave and is thinner than at the previous station. The reflected shock is just emerging from the boundary layer near Y/XREF=.025 as shown by the break in the curve. The effect of the distributed cowl compression is seen in the sloping section of the curve from Y/XREF=.05 to .125, while the cowl boundary layer is seen at the top. Considering the CFD results, we see again a great deal of scatter in the results with three dimensional calculations closer to the data than two dimensional calculations for the same code. In the center part, from Y/XREF=.04 to Y/XREF=.11, the calculated data are to right of the measured ones. There are two solutions, SNS2 and PNS3, that are predicting profiles near the ramp which indicate a flow separation which is not seen in the experimental results. The LNS3 analysis again underpredicts the boundary layer thickness and the shock reflection because the analysis is laminar. The other computations do a reasonable job of predicting the shape of the boundary layer profile near the ramp although the boundary layer thickness does not agree always. All of the codes pick up the emerging reflected shock wave, though each of the codes model this feature differently. Except LNS3, all other analyses predict the break in the curve farther away from the ramp than the experiment. This would correspond to predicting the shock above its true location relative to the ramp. Most of the codes correctly predict the slope of the distributed compression region, but all of the analysis fall to the right of the experimental data. The large bulge in the SNS2 analysis is caused by the shock generated by the previously discussed separation on the ramp. The cowl boundary layer profile is fairly well modeled by all the codes, although some variations in the height of the profiles at the extreme left part of the curve can be seen again.

Moving now to Fig. 3.4.7, at X/XREF=6.65, a comparison is made near the end of the measuring stations. At this location, the reflected cowl shock is just striking the cowl boundary layer, as shown in the break in the experimental data near Y/XREF=.10. The lower portion of the curve shows that the ramp boundary layer has been compressed to a thickness which is about one third of that ahead of the interaction (Fig. 3.4.5) of the cowl shock with the ramp. The distributed compression is still evident by the sloping central portion of the experimental data. Considering the CFD results, again a great amount of scatter between the various computations can be seen. The laminar solution underpredicts the ramp boundary layer thickness as expected. Two calculations indicate a separation on the ramp which is not seen in either the experiment or the other analyses. All of the other codes overpredict the boundary layer pitot profile on the ramp, yet do a reasonable job of predicting the boundary layer thickness. All of the ananlyses are overpredicting the distributed compression in the central portion of the duct. There is quite a bit of scatter in the predicted cowl boundary layer profiles and the reflected shock wave. As seen in the previous figure, each of the codes was predicting the shock wave in a slightly different location and with a different strength.(Whether this is due to the codes used or the grid density cannot be determined here.) As the shock hits the cowl, these variations are magnified in the profiles. In this type of intake, small variations at the beginning of an analysis can become larger variations as one proceeds downstream.

Total Temperature Profiles

Considering the experimental data in Fig. 3.4.8, we see that thermal boundary layers

are generated on the ramp and cowl and that the central inviscid portion of the flow field has maintained a constant total temperature. This temperature ratio is less than one because it was not corrected due to uncertainties in other measurements. The corrected value should be one. With only two exceptions all of the analyses have done an excellent job modeling this flow field. However, some of the analyses produce values smaller than one downstream of the shock reflection point on the ramp (see Reference). The parabolized Navier-Stokes analysis has major problems to reproduce the total temperatures of the experiment. As expected, the thermal boundary layer thickness in the laminar calculation is too small. At the end of the duct all analyses indicate underpredicted thermal boundary layer thicknesses (see Reference).

CFD Flow Field

While the experimental data is too sparse to quantify three dimensional effects, full three dimensional CFD results can give some indication of the extent of these effects. Fig. 3.4.9 shows pitot pressure contours through the intake from the GNS3 analysis. Only half of the duct is plotted with a plane of symmetry along the left edge of each plot. Clearly the boundary layers on the ramp and cowl can be recognized. The horizontal lines away from the walls are indicative of the cowl shock. Because of shock/boundary layer interactions, such as the ones studied in test case 2, low pressure regions develop in the corners of the intake. The effect of this corner phenomenon is seen to extend nearly a quarter of the distance across duct from the sidewall.

CONCLUSIONS

From the complete comparison of CFD and experimental results given in the Reference one can draw several interesting conclusions. First, there was a wide variation in the CFD results. In general, three dimensional calculations seem to agree better with the experimental results than do two dimensional calculations. Second, nearly all of the codes were able to match the experimental temperature profiles. However, because the wind tunnel enthalpy was too small no conclusions can be drawn about the codes ability to correctly model flight conditions. Third, there is some evidence that in each of the analyses the intake geometry was modeled in slightly different ways. For hypersonic flows, even small differences in geometry can produce significant differences in flow properties. It would appear that additional work is required in the area of geometric specification and flow solver grid generation. Fourth, none of the CFD analyses were able to predict the pitot pressure downstream of the ramp shock, but upstream of the cowl shock although many CFD analyses tend to agree with one another. One is therefore lead to suspect that the wind tunnel conditions specified in the test reports were in some way different from the conditions that were actually present in the tunnel. And fifth, for this class of intakes, it would appear that even small variations in the flow field upstream lead to large variations between codes downstream.

4. Conclusions/Recommendations from the Complete Assessment

From the complete assessment of all test case the numerical subgroup of AGARD Working Group 13 formulated the following statements:

In this study, experimental test cases have been proposed for calculation to assess the current ability of CFD to model inlet flow fields. The proposed test cases covered the speed regime from subsonic to hypersonic, and considered flow configurations from simple, benchmark experiments to full intake/airframe combinations. Computational techniques from 2D Euler to 3D Navier-Stokes have been employed. Having considered the computation of each of the test cases individually, the following general conclusions and recommendations can be drawn.

PARTICIPATION

The members of the AGARD Working Group 13 wish to thank and commend all of the contributors to this study. A great deal of donated time and effort was spent in the analysis and computation of these test cases. Of the eight proposed test cases, the greatest number of calculations was performed on test case 6, the 2D hypersonic intake. This probably reflects the increased interest in this speed regime and the important role that CFD could play in an area where experimental testing is most difficult. The test case with the fewest number of calculations was the D-shaped intake with offset diffusing duct, followed closely by the offset duct case and the intake/airframe case. It is ironic, and alarming, that the most calculations were performed on a configuration which has never flown, while the fewest calculations were done for configurations which exist on most aircraft.

RESULTS

From a comparison of CFD calculations and experimental results for eight test cases the following conclusions have been drawn. Not surprisingly, CFD has better modeled the simple benchmark experiments than the full intake/airframe configurations. This, of course, can be attributed to better definition of the problem, both computationally and experimentally. In general and as expected, the full Navier-Stokes solvers have done a better job than the simpler Euler and Parabolized Navier-Stokes solvers, but with a greater computational expense. There is some evidence in these test cases that better, faster grid generation codes should be developed for intake applications. When comparing experimental and computational results, there are two chief sources of disagreement; the experiment and the computation. In some of the test cases

discussed here, it is clear that the experimental results were either incorrect or not completely described so that they could be calculated. In all fairness, most of the test cases chosen were completed before the rise in interest in CFD and the lack of detailed information for CFD comparison is understandable. However, in the future, all experimental programs should be conducted in a way which can benefit and be the benefit of CFD analysis. As pointed out in most of the test cases, CFD can provide additional information concerning the flow fields in intakes which one can not obtain in experiments. The codes must, however, be checked at some points to insure accurate calculations.

Between different calculations performed for the same test case one usually has seen variations in the results. These variations can be attributed to different computational techniques, different representations of the physics problem (i.e. different grids, different convergence levels, different boundary conditions), and ultimately different CFD users with different levels of experience. CFD is not yet, nor will it ever be, a mathematical genie in a bottle capable of returning accurate flow fields to any novice who rubs the lamp. CFD requires a lot of experience and physical insight to obtain meaningful results. When used in conjunction with an experiment, it can lead to a better understanding of complex physical flows.

OUTLOOK

It was the aim of the numerical subgroup of AGARD Working Group 13 to give an overview of today's numerical method's capablity for calculating intake flows of high speed aircraft. The conclusions to be drawn are limited and can be given in general terms only. A more careful study is recommended in which the accuracy of CFD and its dependency on parameters like grids and turbulence models can be investigated. For this study, it is recommended that the number of test cases should be limited to a few cases where experimental data are plentiful and the accuracy of the measurements is well documented. The complexity of the problems should be restricted so that computers available in all Nato countries will be capable of modeling the flow. AGARD seems to be a good forum to initiate and bring together sufficient researchers and institutions necessary to provide a comprehensive study for a successful completion of such an exercise.

5. Reference

AGARD-AR-270,
"Aerodynamics of High Speed Air Intakes"
published September 1991.

TEST CASE	FLOW TYPE	NUMBER OF CALCULATIONS
1	Transonic Normal Shock/Turbulent Boundary Layer Interactions	2
2	Glancing Shock/Boundary Layer Interaction	5
3	Subsonic/Transonic Circular Intake	3
4	Subsonic/Transonic Semi-circular Intake	1
5	Supersonic Circular Pitot Intake	2
6	2D Hypersonic Intake	10
7	Axisym. Mixed Compression Intake	2
8	Intake/Airframe Integration	2

TABLE I TEST CASES FOR CFD CALCULATIONS

CODE	USER	TYPE	TEST CASE
PARC3D	SVERDRUP-AEDC SVERDRUP-CLEVE.	NS	1 2 6 8 2 7
HAWK3D	GENERAL DYNAMICS	NS	2
FALCON	GENERAL DYNAMICS	NS	6
PEPSI-S	NASA-LEWIS	PNS	2 6 7
NS2D	ONERA AEROSPATIALE	NS	2 6
FLU3M	AEROSPATIALE	EU	6 8
	ARA	EU EUBL	3 4 5
ENSFL2D	DORNIER	NS	5
IKARUS	DORNIER	NS	3 6
RANSAC	BAE	NS	3
NSFLEX	MBB	NS	1 6

TABLE II CODES USED IN CFD ASSESSMENT

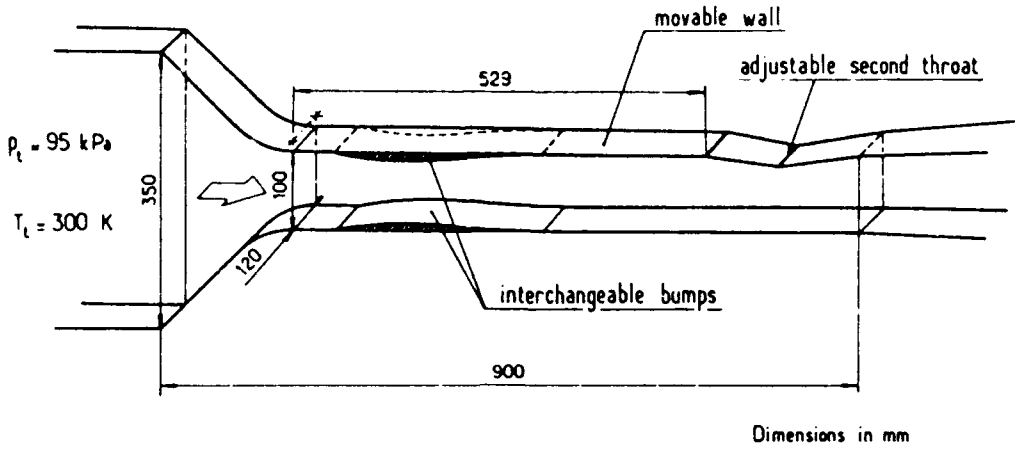

FIG. 3.1.1 EXPERIMENTAL ARRANGEMENT FOR TEST CASE 1

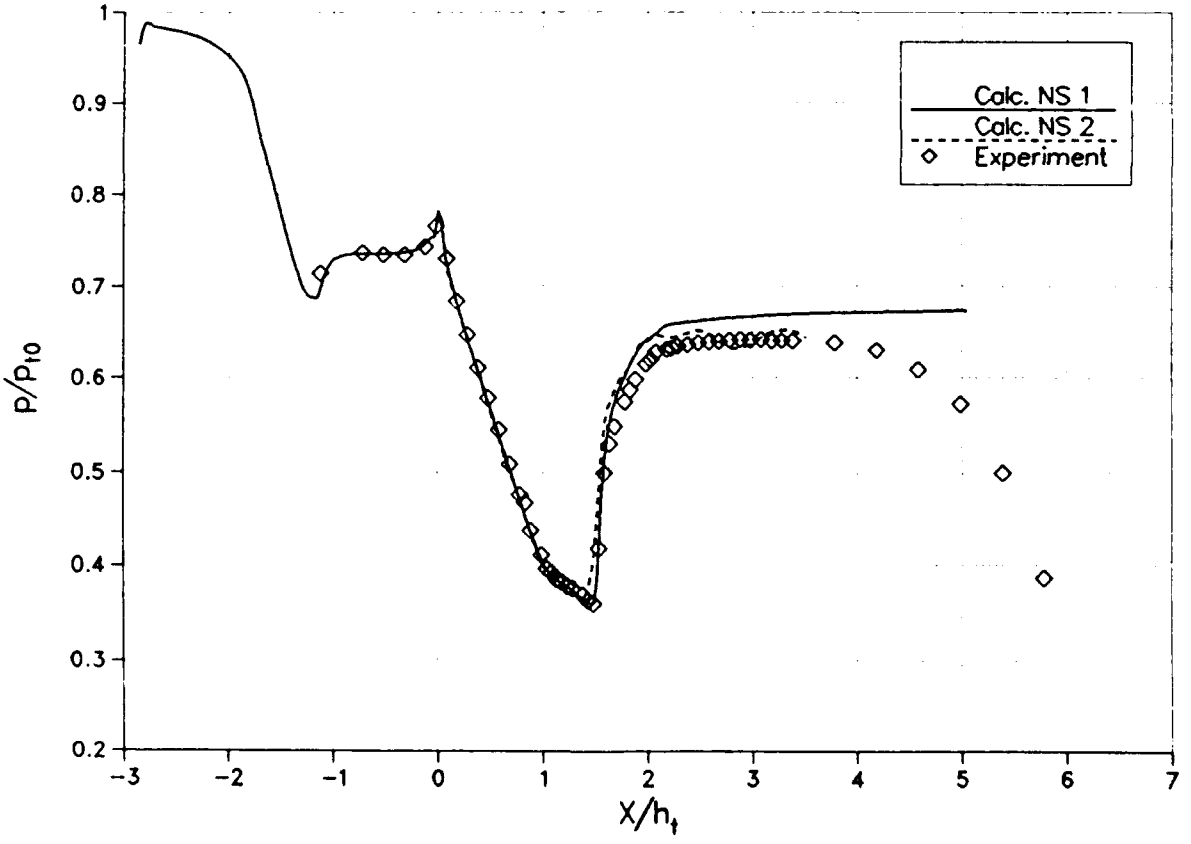

FIG. 3.1.2 TEST CASE 1.1: STATIC WALL PRESSURE ON LOWER TUNNEL WALL

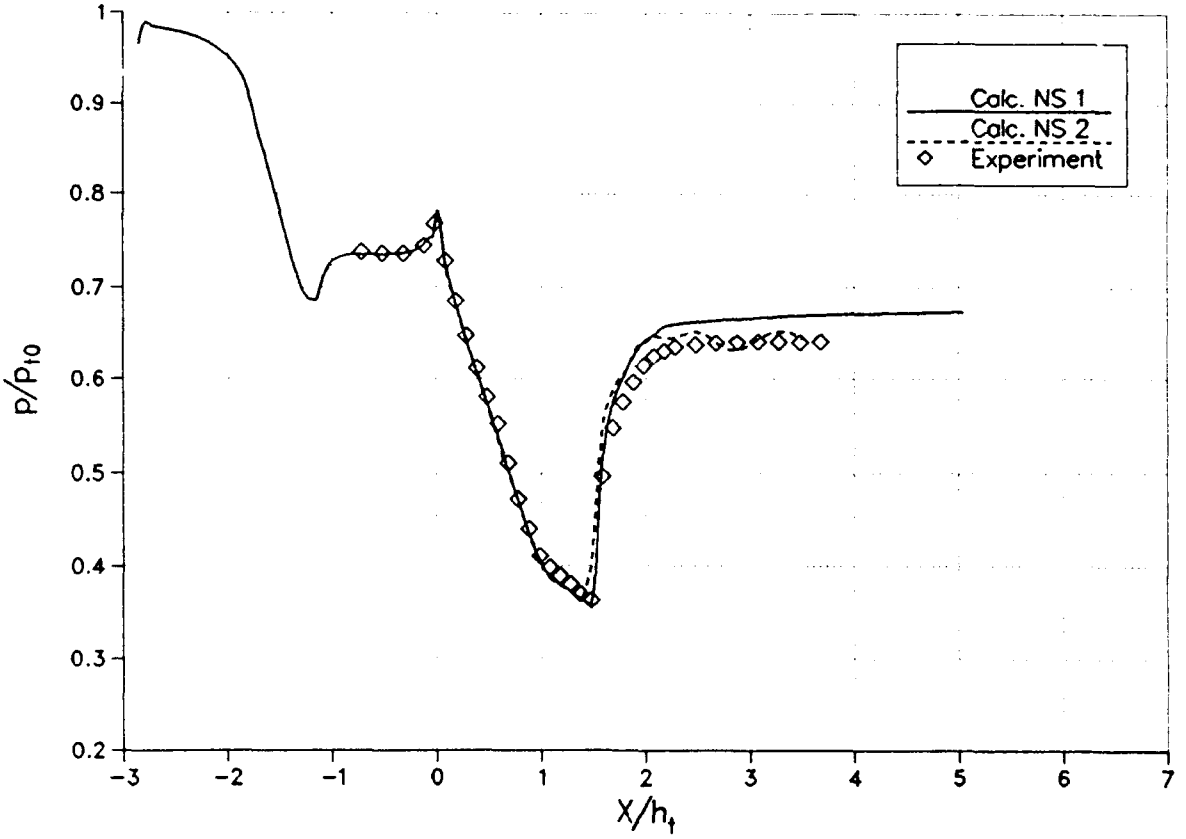

FIG. 3.1.3 TEST CASE 1.1: STATIC WALL PRESSURE ON UPPER TUNNEL WALL

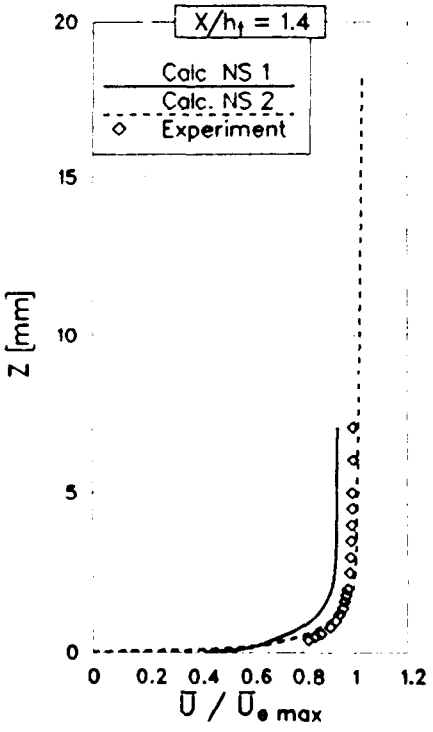

FIG. 3.1.4
MEAN VELOCITY PROFILES
TEST CASE 1.1

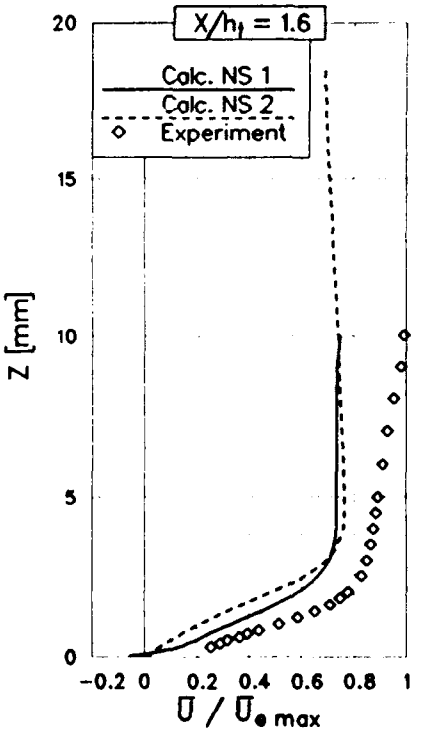

FIG. 3.1.5
MEAN VELOCITY PROFILES
TEST CASE 1.1

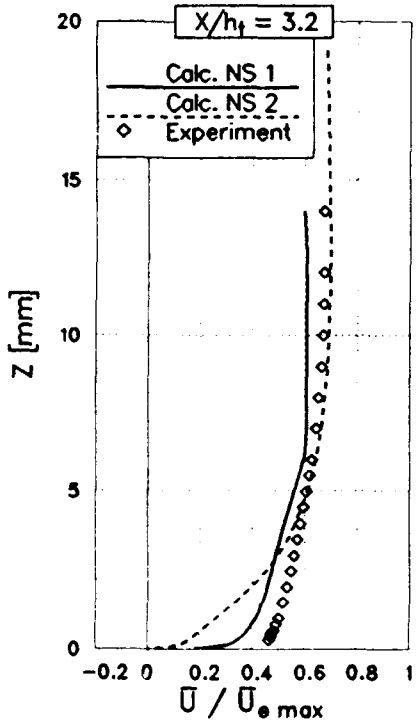

FIG. 3.1.6
MEAN VELOCITY PROFILES
TEST CASE 1.1

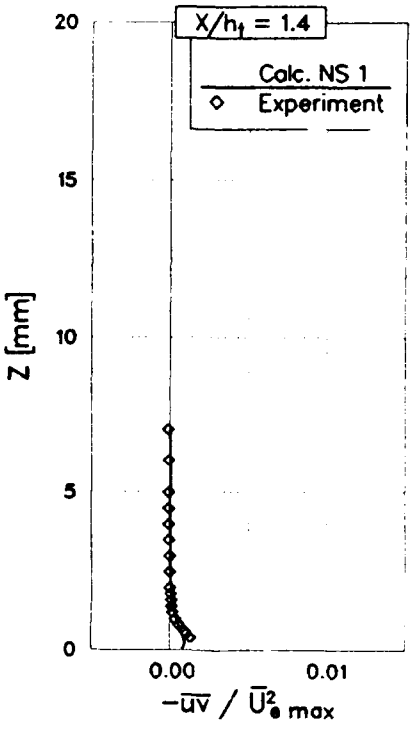

FIG. 3.1.7
SHEAR STRESS PROFILES
TEST CASE 1.1

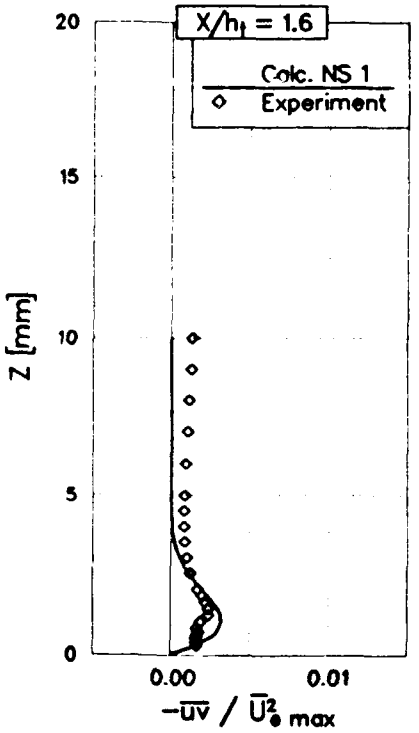

FIG. 3.1.8
SHEAR STRESS PROFILES
TEST CASE 1.1

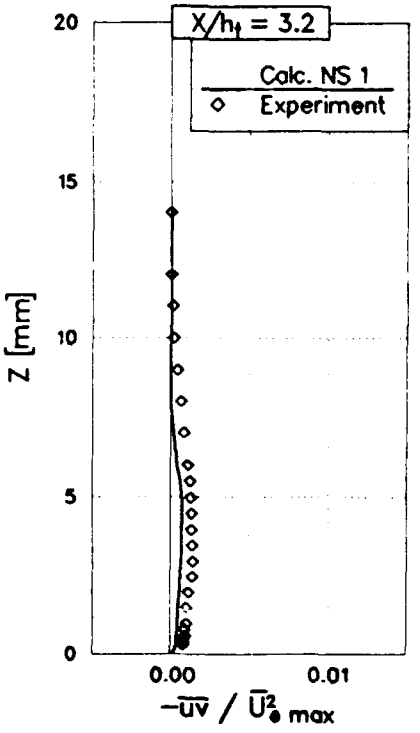

FIG. 3.1.9
SHEAR STRESS PROFILES
TEST CASE 1.1

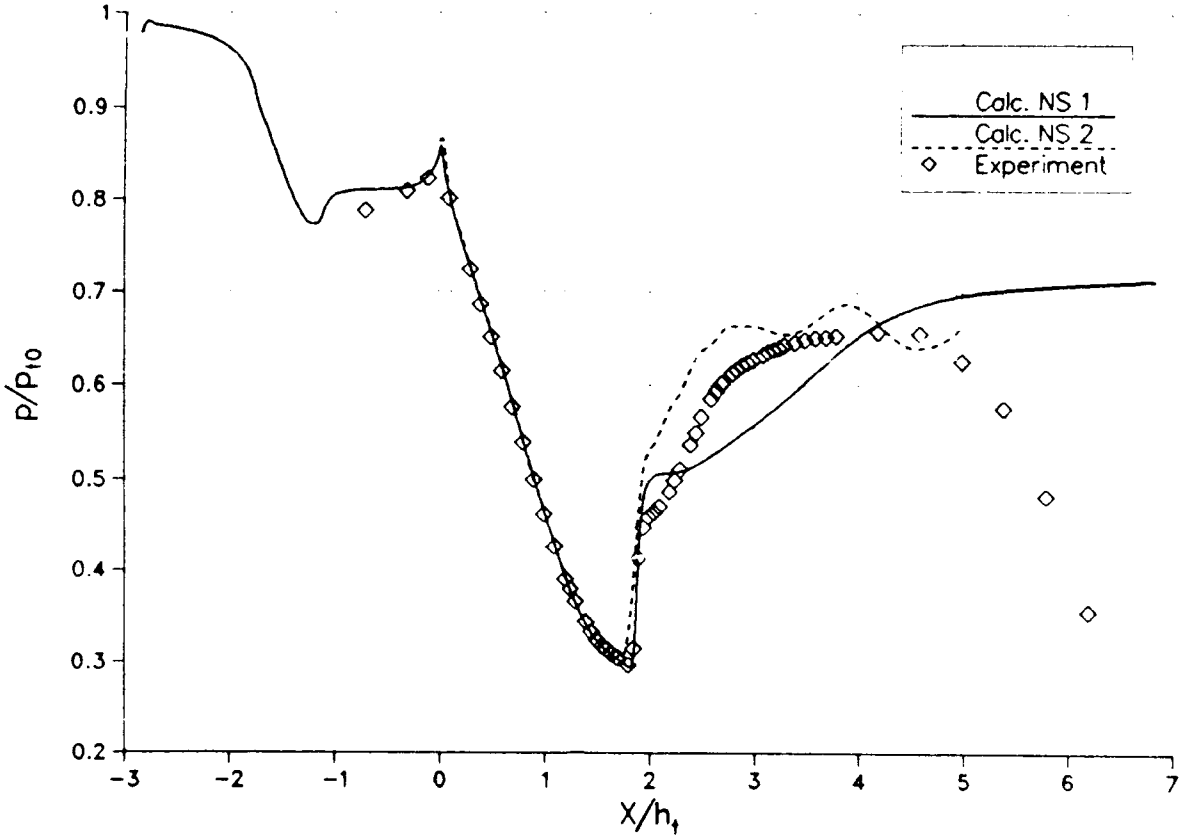

FIG. 3.1.10 TEST CASE 1.2: STATIC WALL PRESSURE ON LOWER TUNNEL WALL

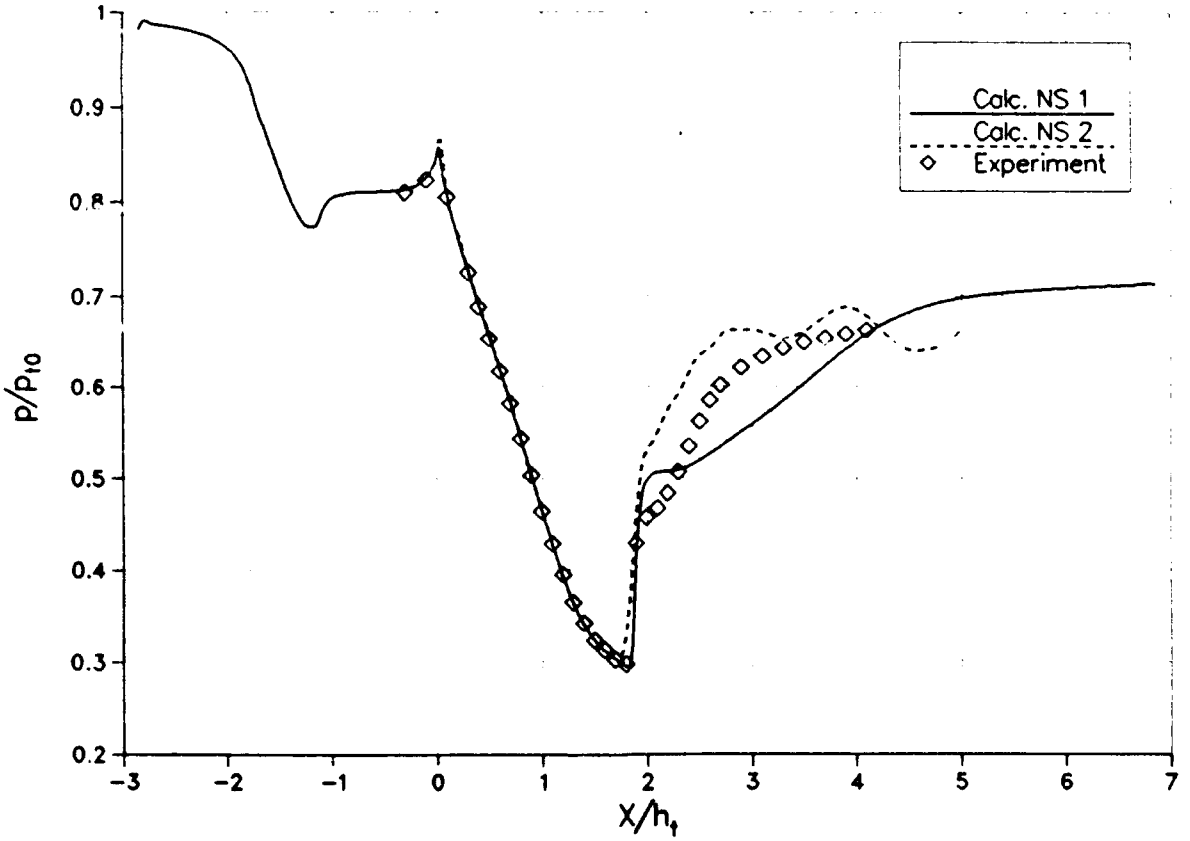

FIG. 3.1.11 TEST CASE 1.2: STATIC WALL PRESSURE ON UPPER TUNNEL WALL

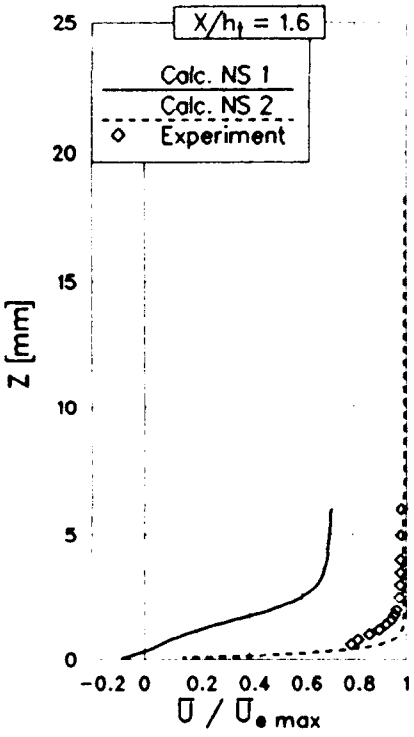

FIG. 3.1.12
MEAN VELOCITY PROFILES
TEST CASE 1.2

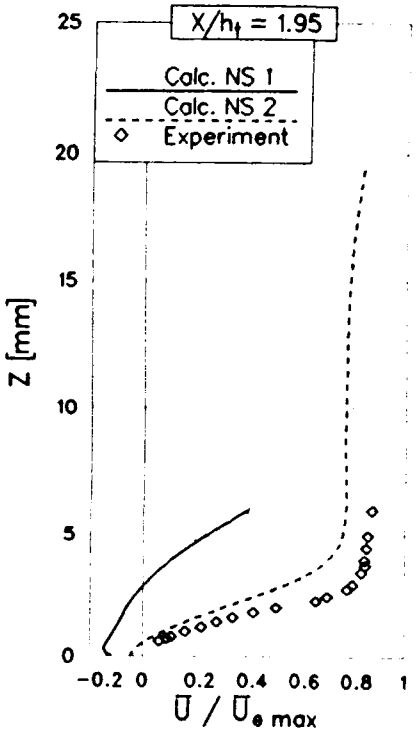

FIG. 3.1.13
MEAN VELOCITY PROFILES
TEST CASE 1.2

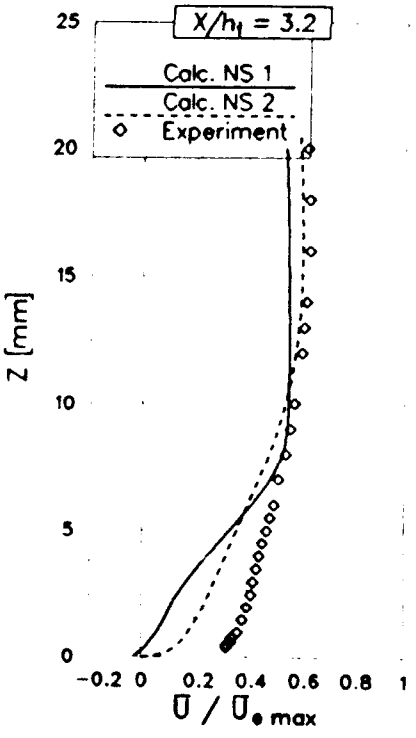

FIG. 3.1.14
MEAN VELOCITY PROFILES
TEST CASE 1.2

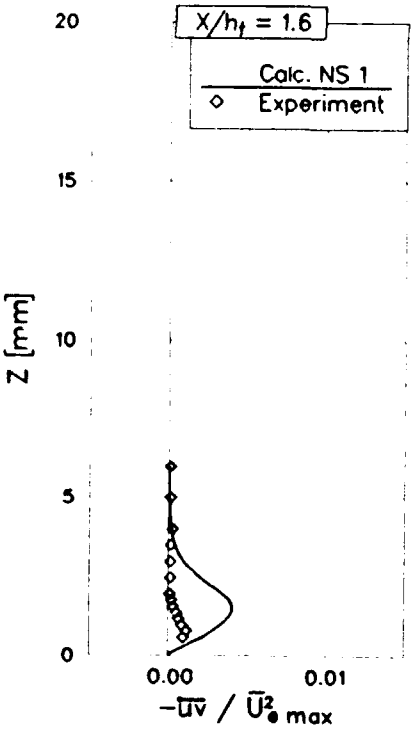

FIG. 3.1.15
SHEAR STRESS PROFILES
TEST CASE 1.2

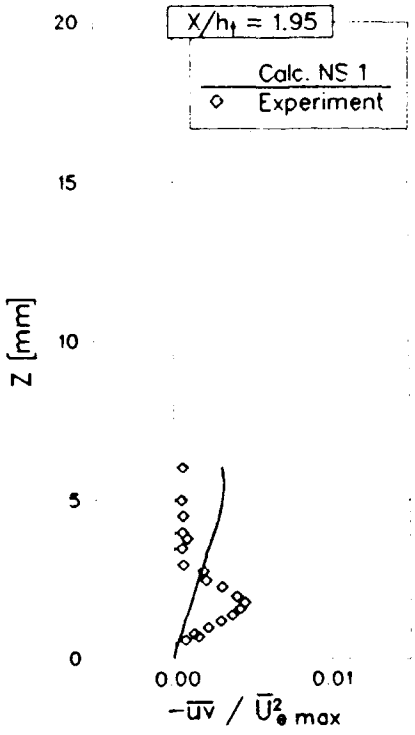

FIG. 3.1.16
SHEAR STRESS PROFILES
TEST CASE 1.2

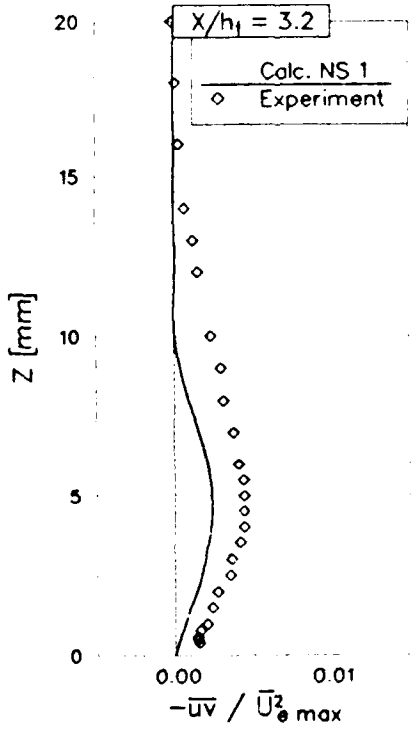

FIG. 3.1.17
SHEAR STRESS PROFILES
TEST CASE 1.2

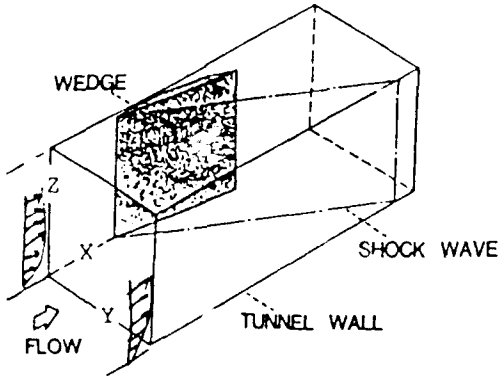

FIG 3.2.1 SCHEMATIC DRAWING OF GLANCING SHOCK/BOUNDARY LAYER INTERACTION TEST GEOMETRY.

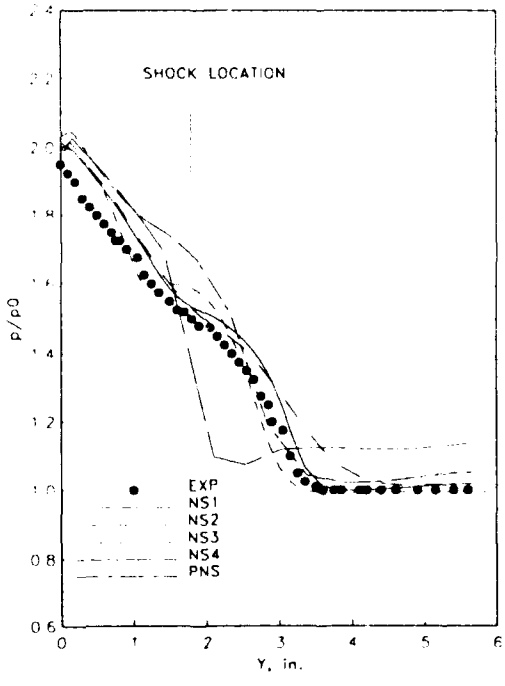

FIG 3.2.2 COMPARISON OF CFD AND EXPERIMENTAL WALL STATIC PRESSURE DISTRIBUTION AT X=5.1 INCHES.

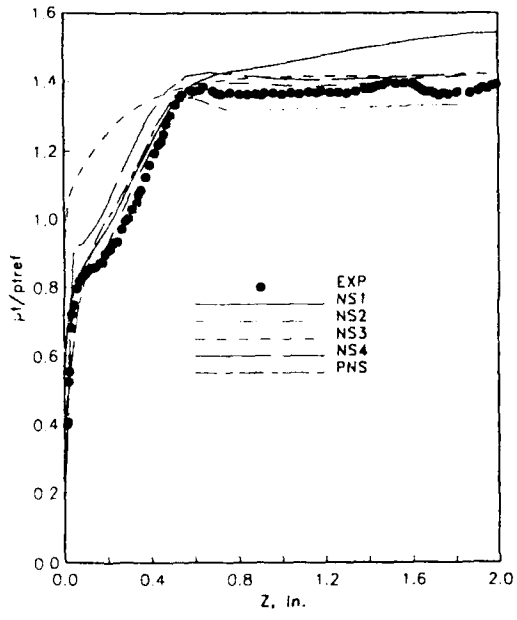

FIG **3.2.3** COMPARISON OF CFD AND EXPERIMENTAL PITOT PRESSURE DISTRIBUTION AT X=7.1 AND Y=0.75 INCHES.

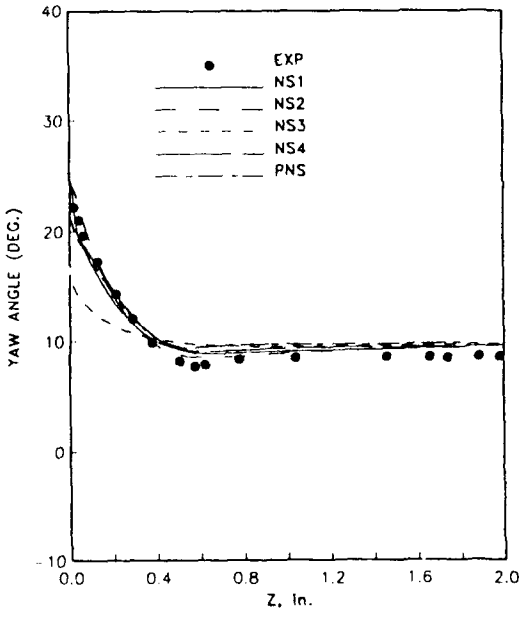

FIG **3.2.4** COMPARISON OF CFD AND EXPERIMENTAL YAW ANGLE DISTRIBUTION AT X=7.1 AND Y=0.75 INCHES.

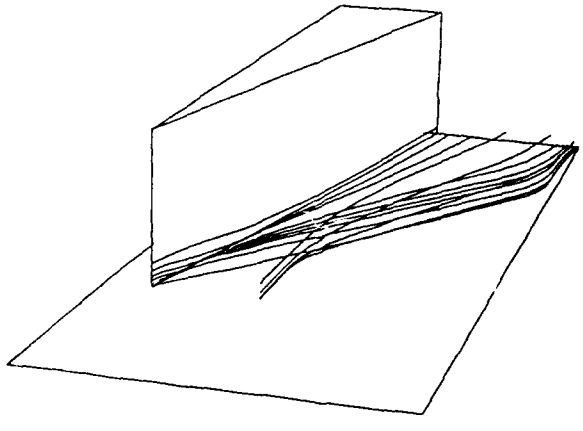

Figure **3.2.5** PARTICLE TRACES FROM CFD ANALYSIS OF GLANCING SHOCK BOUNDARY LAYER INTERACTION.

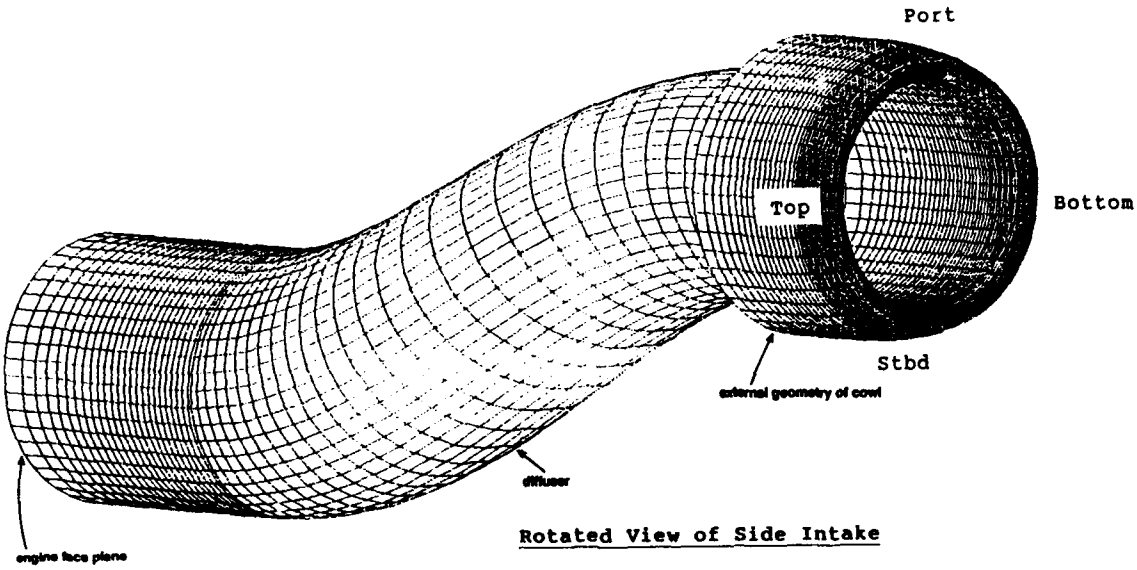

FIG. 3.3.1 VIEW OF GEOMETRY FOR TEST CASE 3 -
Surface grid from ARA Euler calculations

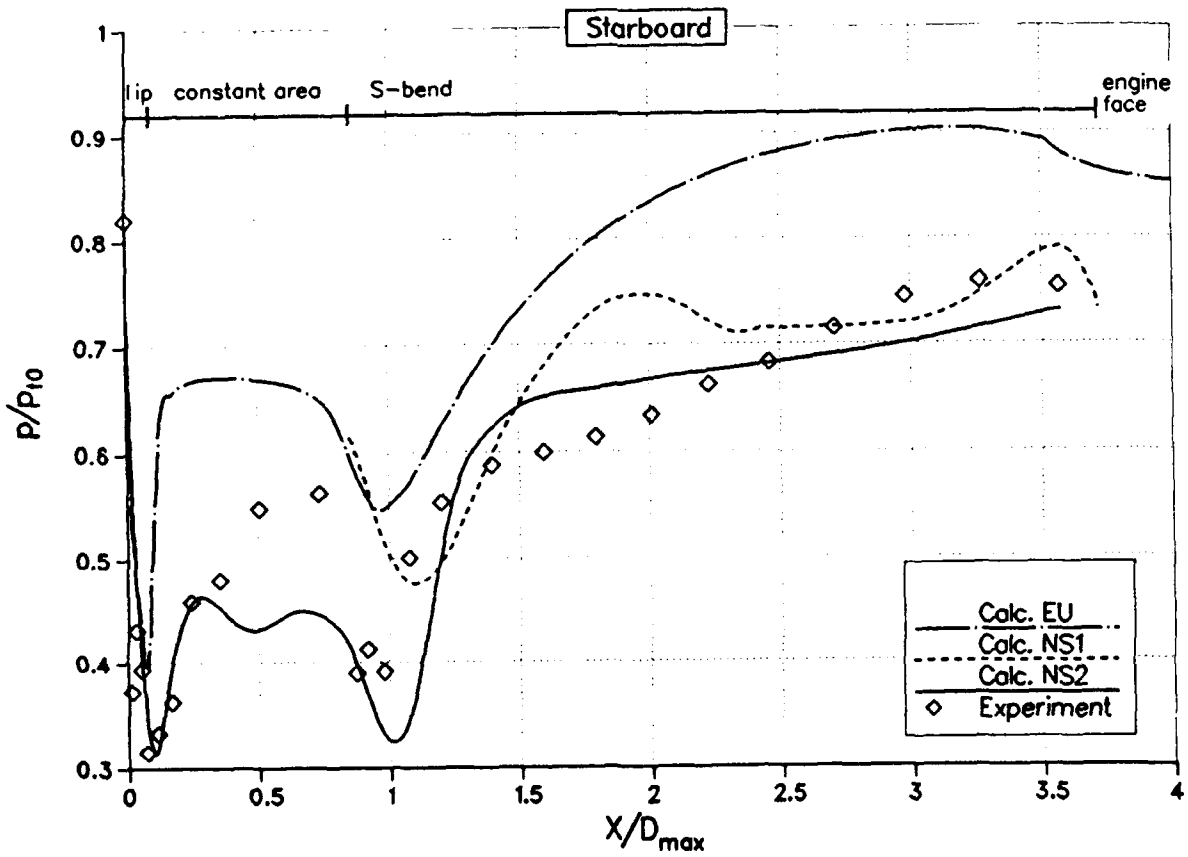

FIG. 3.3.2 TEST CASE 3.1: STATIC WALL PRESSURE ALONG DUCT - STBD

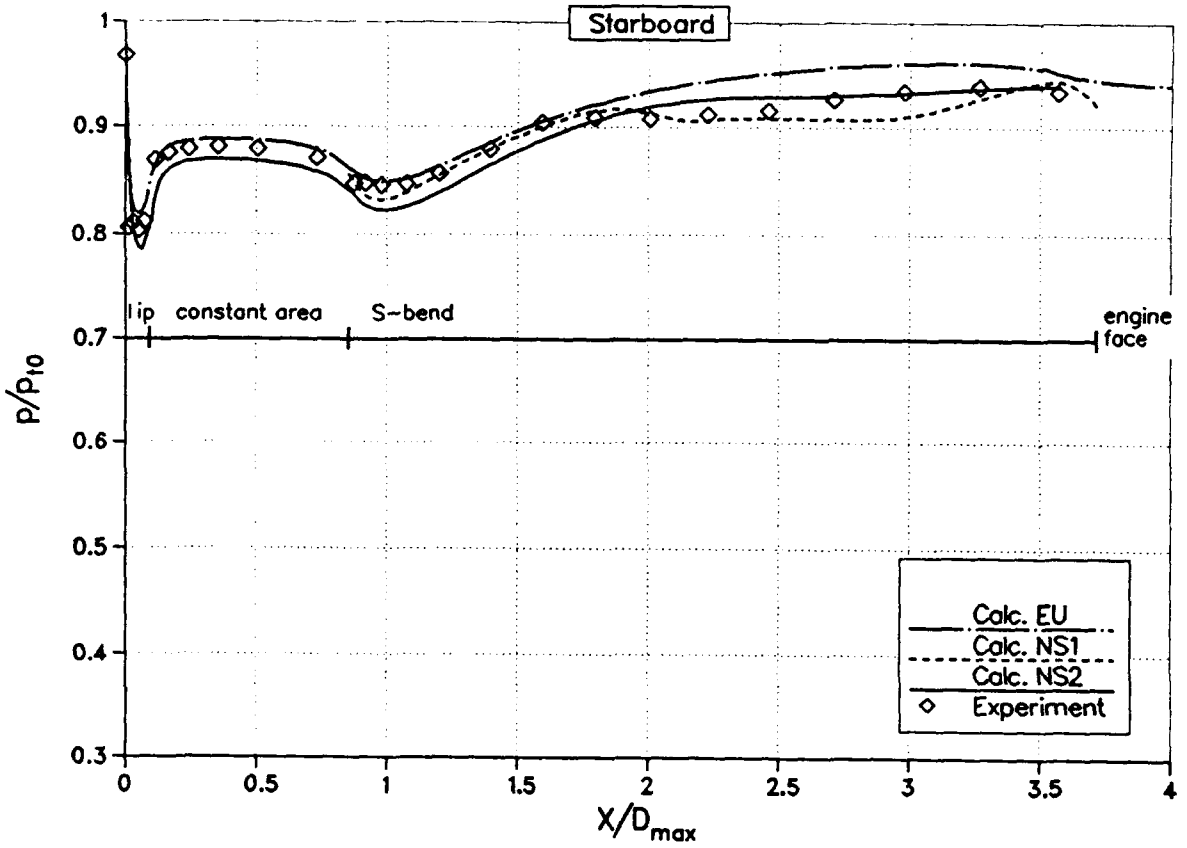

FIG. 3.3.3 TEST CASE 3.2: STATIC WALL PRESSURE ALONG DUCT - STBD

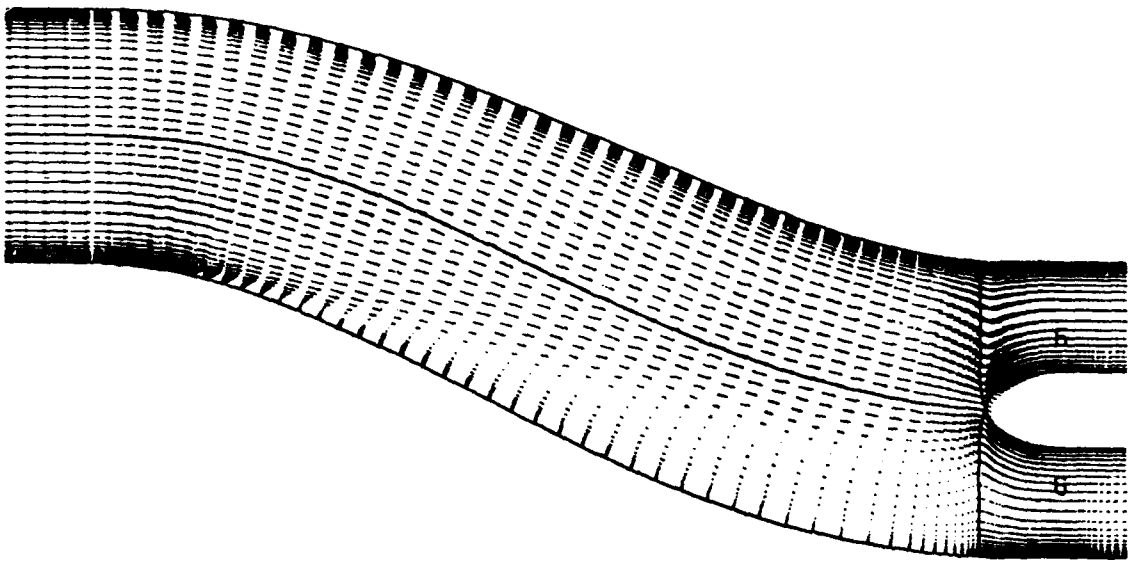

FIG. 3.3.4 TEST CASE 3.1: VELOCITY VECTORS IN THE SYMMETRY PLANE FROM SOLUTION NS2

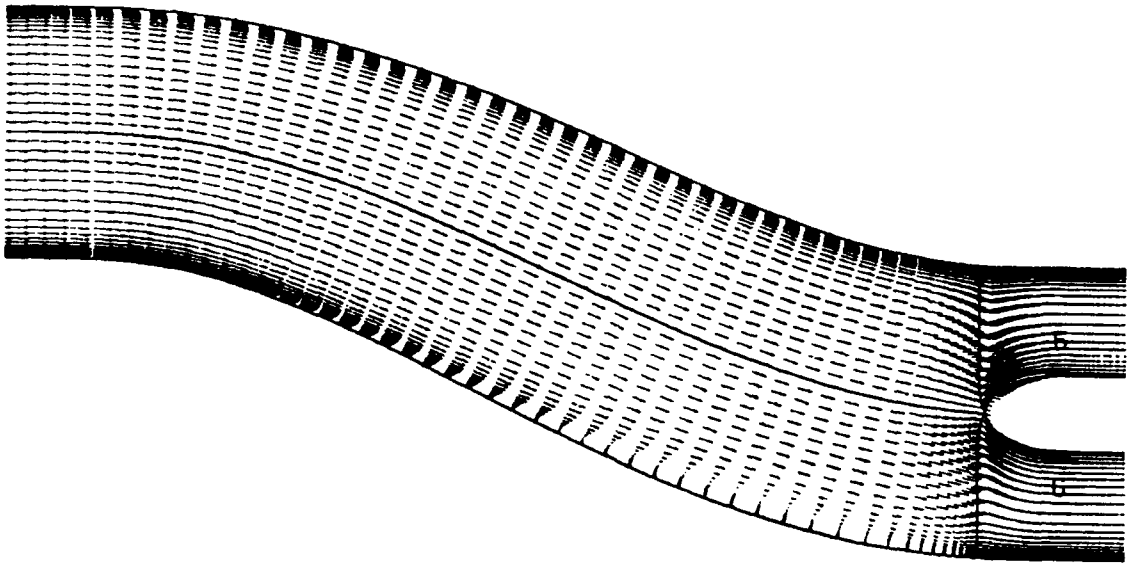

FIG. 3.3.5 TEST CASE 3.2: VELOCITY VECTORS IN THE SYMMETRY PLANE FROM SOLUTION NS2

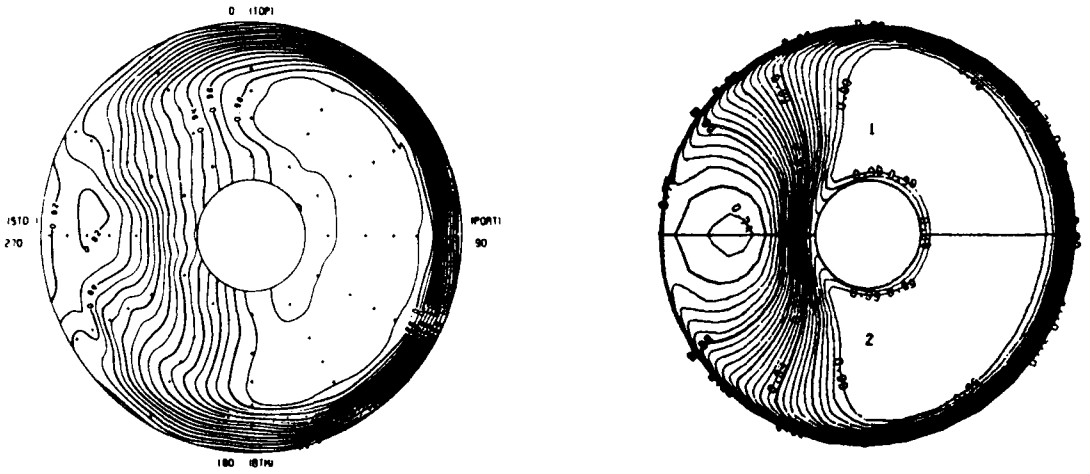

EXPERIMENT SOLUTION NS2

FIG. 3.3.6 TEST CASE 3.1: ENGINE FACE TOTAL PRESSURE DISTRIBUTION

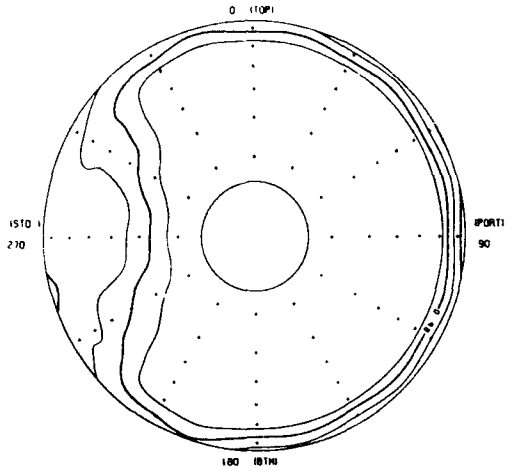

EXPERIMENT

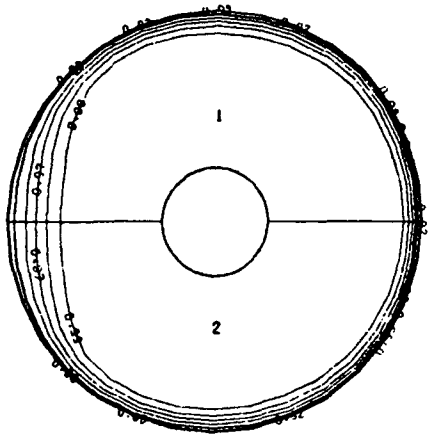

SOLUTION NS2

FIG. 3.3.7 TEST CASE 3.2: ENGINE FACE TOTAL PRESSURE DISTRIBUTION

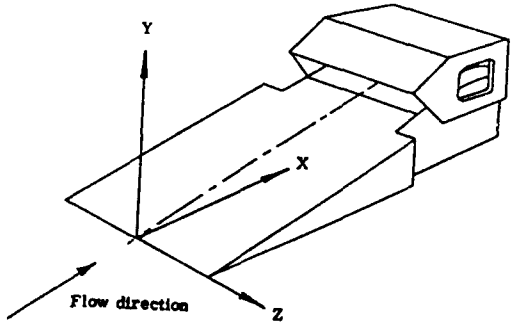

FIG **3.4.1** SCHEMATIC DRAWING OF P8 INTAKE FROM REF 3.6.1.

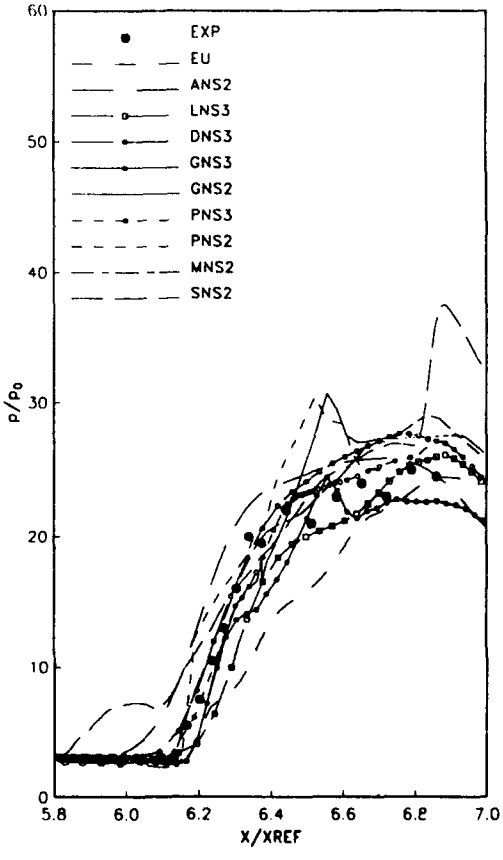

FIG **3.4.2** COMPARISON OF CFD AND EXPERIMENTAL RAMP STATIC PRESSURE DISTRIBUTION.

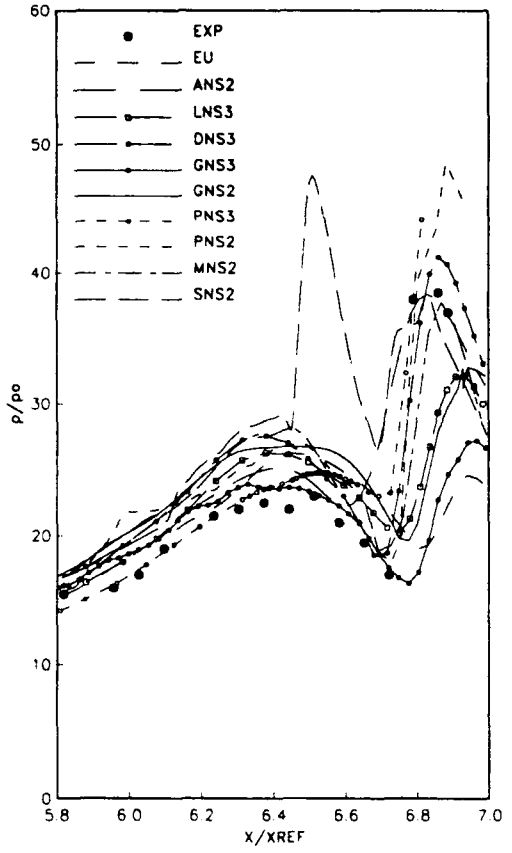

FIG **3.4.3** COMPARISON OF CFD AND EXPERIMENTAL COWL STATIC PRESSURE DISTRIBUTION.

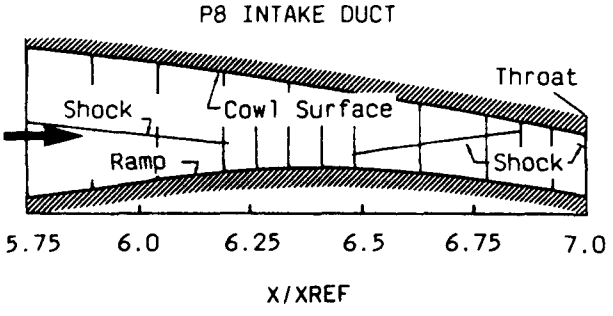

FIG **3.4.4** EXPERIMENTAL RAKE LOCATION WITHIN THE P8 INTAKE.

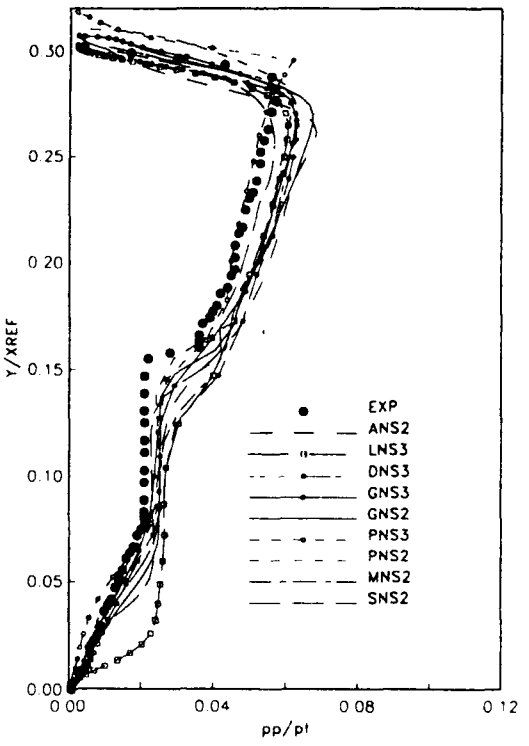

FIG **3.4.5** COMPARISON OF CFD AND EXPERIMENTAL PITOT PRESSURE DISTRIBUTION AT X=5.78.

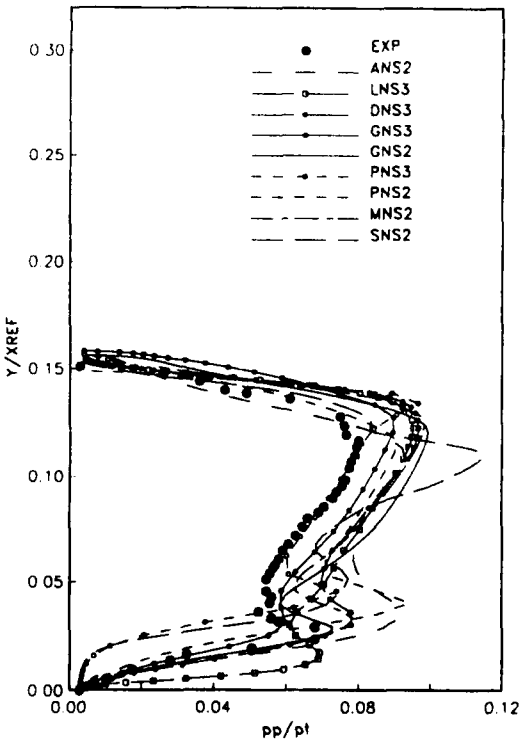

FIG **3.4.6** COMPARISON OF CFD AND EXPERIMENTAL PITOT PRESSURE DISTRIBUTION AT X=6.37.

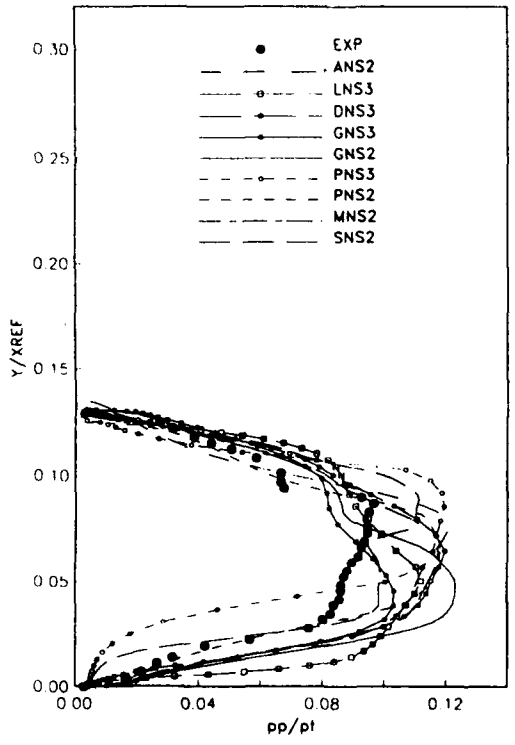

FIG 3.4.7 COMPARISON OF CFD AND EXPERIMENTAL PITOT PRESSURE DISTRIBUTION AT X=6.65.

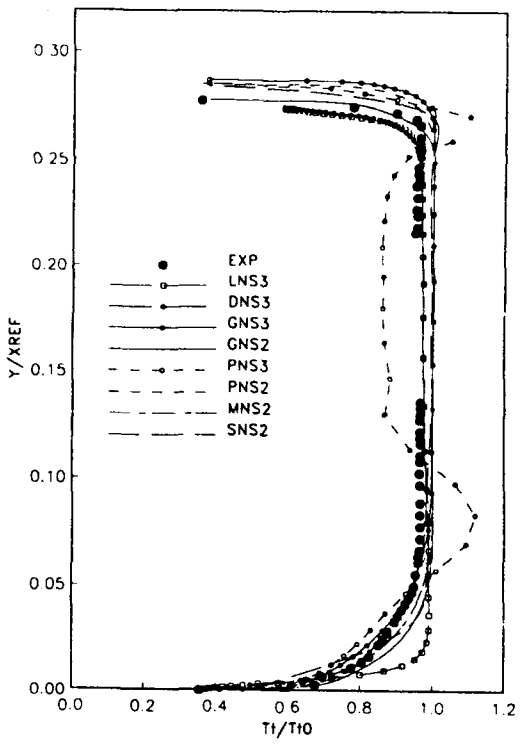

FIG 3.4.8 COMPARISON OF CFD AND EXPERIMENTAL TOTAL TEMPERATURE DISTRIBUTION AT X=5.78.

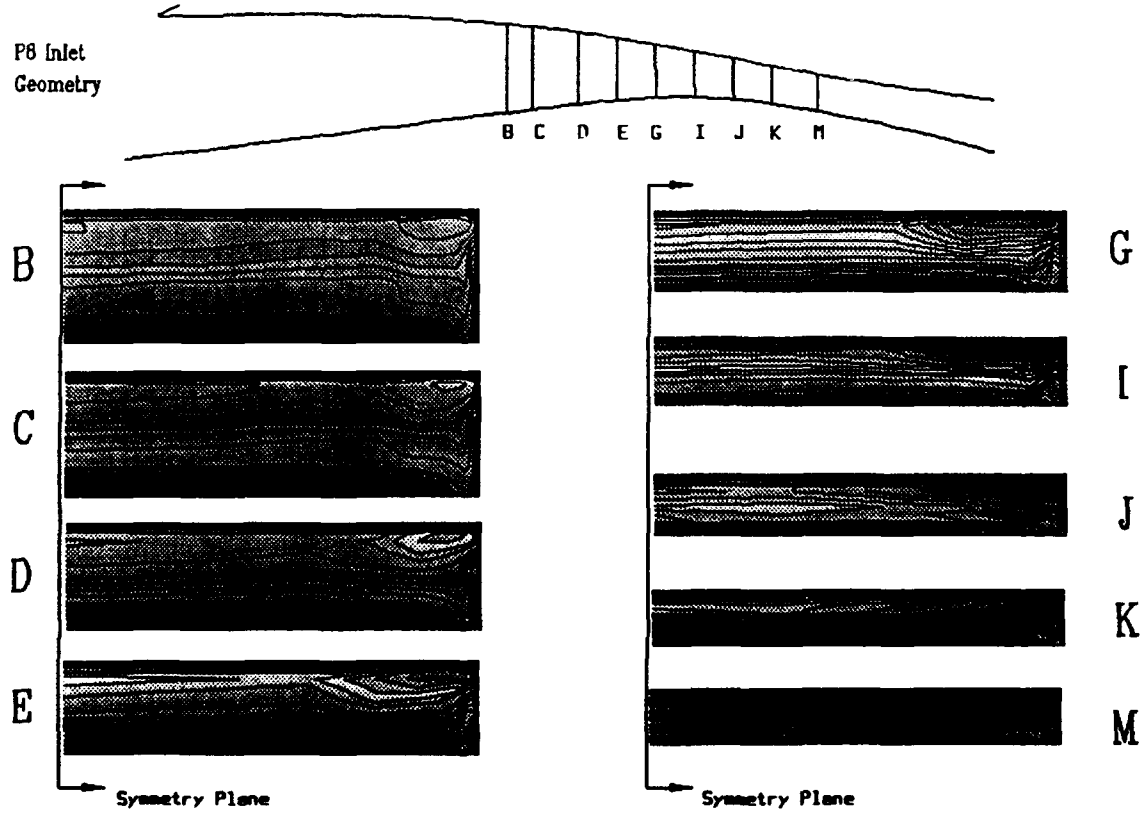

FIG 3.4.9 PITOT PRESSURE CONTOURS THROUGH THE P8 INTAKE.(GNS3)

Comparative Performance Tests of a Pitot-Inlet in Several European Wind-Tunnels at Subsonic and Supersonic Speeds.

by

P.-A. Mackrodt, DLR Göttingen; F. L. Goldsmith, ARA Bedford
I. McGregor, RAE Bedford; J. Leynaert, ONERA Paris
F. Garçon, ONERA Modane; L. Brill, MBB München

Abstract

A common design of inlet model (*RAE Model 7421 Cowl 2*) but built to slightly different scales (convenient to the specific wind tunnel) was investigated in the RAE 8 ft x 8 ft tunnel, the ONERA S2MA-tunnel (1,75 m x 1,77 m), and in the transonic 1 m x 1 m wind tunnel TWG of DLR. The measurements were carried out at subsonic and supersonic Mach numbers, at several Reynolds numbers and angles of attack.

The paper presents - aside of a short description of the wind tunnels and the models - details of the instrumentation and the formulae used to calculate the steady-state and the instantaneous distortion parameters. A brief description of the data acquisition and reduction systems is also given. Results of the three tests are presented in the usual format, and from the comparison of the results the differences are analyzed and the main origins of the discrepancies discussed and explained. Finally some recommendations are given for reducing those discrepancies in further tests.

1. Nomenclature

1.1 Notation

A	cross sectional area
a	speed of sound
C_c	discharge coefficient
D	diameter
DC_{60}	engine face distortion coefficient of 60° sector; $DC_{60} = \frac{\bar{p}_{t,cf} - p_{t,cf,min\,60}}{\bar{q}_{cf}}$
M	Mach number; $M = \frac{U}{a}$
p	static pressure
PR	pressure recovery; $PR = \frac{\bar{p}_{t,cf}}{p_0}$
$\bar{q}_{cf}$	incompressible dynamic pressure at engine face; $\bar{q}_{cf} = \bar{p}_{t,cf}\left[1 - \left(1 + \frac{1}{5}M_{cf}^2\right)^{-3.5}\right]$
R	radius
Re	Reynolds number; $Re = \frac{U \cdot D}{\nu}$
U	flow speed
α	angle of incidence
γ	ratio of specific heat
ν	kinematic viscosity

1.2 Subscripts

0	free stream
c	capture (highlight) plane
cf	compressor (engine) face
t	stagnation
T	throat

2. Introduction

During discussions in the AGARD Working Group *Inlets of High-Speed Vehicles* the (old) question arose, whether tests with a geometrically identical model in different wind tunnels would lead to the same results or not. The answer to this question is certainly more interesting for inlets - especially regarding the importance of unsteady distortion parameters - than for other kinds of model because of the complexity and diversity of the instrumentation as well as the data acquisition and reduction systems. It was therefore agreed to investigate a certain model in as many wind tunnels as possible. In a first test phase each organisation would build their own model to a convenient scale, fit it with their own instrumentation, do the tests using their standard techniques and equipment, and evaluate the results with their own computer codes. The main goal of the tests was to find out the dispersion of the results at common test conditions, and to identify the origins of any significant differences.

In the course of the experiments three models of a simple subsonic pitot inlet with circular cross section and a blunt lip (*RAE Model 7421, Cowl 2*; see section 3.1) built to slightly different scales were investigated in wind tunnels at RAE, ONERA, and DLR. The measurements included steady state values of the usual inlet parameters such as pressure recovery, PR, engine face flow distortion, DC_{60}, and mass flow ratio, A_0/A_c, as well as dynamic distortion. The tests concentrated on Mach number $M_0 = 0.8$ and angles of attack $0° < \alpha < 25°$ in all three wind tunnels.

However, variations of Mach number (up to $M_0 = 1.8$) and Reynolds number, Re, were also carried out in two of the three tunnels.

3. Models and equipment

3.1 The RAE model

The common model geometry was that of *RAE Model 742L Cowl 2* which had already been investigated by RAE and ARA in 1983 and 1984 [1], [2] over the Mach number range $0.2 \leq M_0 \leq 2.0$ at incidences between $\alpha = 0°$ and $\alpha = 40°$. Details of the geometry of the lip, the external cowl, and the diffuser as well as the main dimensions of the RAE model are shown in **Figure 1**. The highlight diameter is $D_0 = 81.5\,mm$ and the diameter of the engine face $D_{ef} = 88.9\,mm$. The engine face instrumentation for these tests consisted of 40 Kulite ±5 psi high response differential pressure transducers of 2.36 mm diameter which were fitted with Boeing screens and a 3 mm extension to ensure that the true total pressure was measured. The reference pressure was about the average total pressure in the duct. The 40 Kulite transducers were arranged five per arm in an eight arm rake. There was no bullet in the centre of the rake because the arms were inserted and supported by the duct wall (see **Figure 2**). Downstream of the rake the duct diameter decreased slightly and static pressures measured in this reduced section were used in conjunction with the rake total pressures and a duct calibration factor to obtain values for the mass flow ratio at subsonic speeds. At supersonic speeds the choked exit area (modified by an experimentally determined discharge coefficient) was used together with the rake total pressures to obtain mass flow. To control the mass flow ratio, A_e/A_c, the exit area was varied by means of a sliding cone throttle.

The form of the engine face instrumentation used by RAE (Figure 2) and ONERA (see section 3.2) was similar. The only total pressure probes used for both steady and unsteady measurements were the 40 above mentioned Kulite transducers. Compared to the MBB rake (see section 3.3) which was equipped with 80 normal pitot tubes *in addition* to the 40 Kulites, the choice of only 40 probes results in less blockage. Moreover, preliminary experiments at the RAE also indicated a superior accuracy for steady state values, which are obtained by time averaging the DC coupled individual Kulite recordings, over the use of adjacent pitot probes linked to one or two transducers via a Scanivalve system. **Table 1** gives results from this preliminary investigation (made on

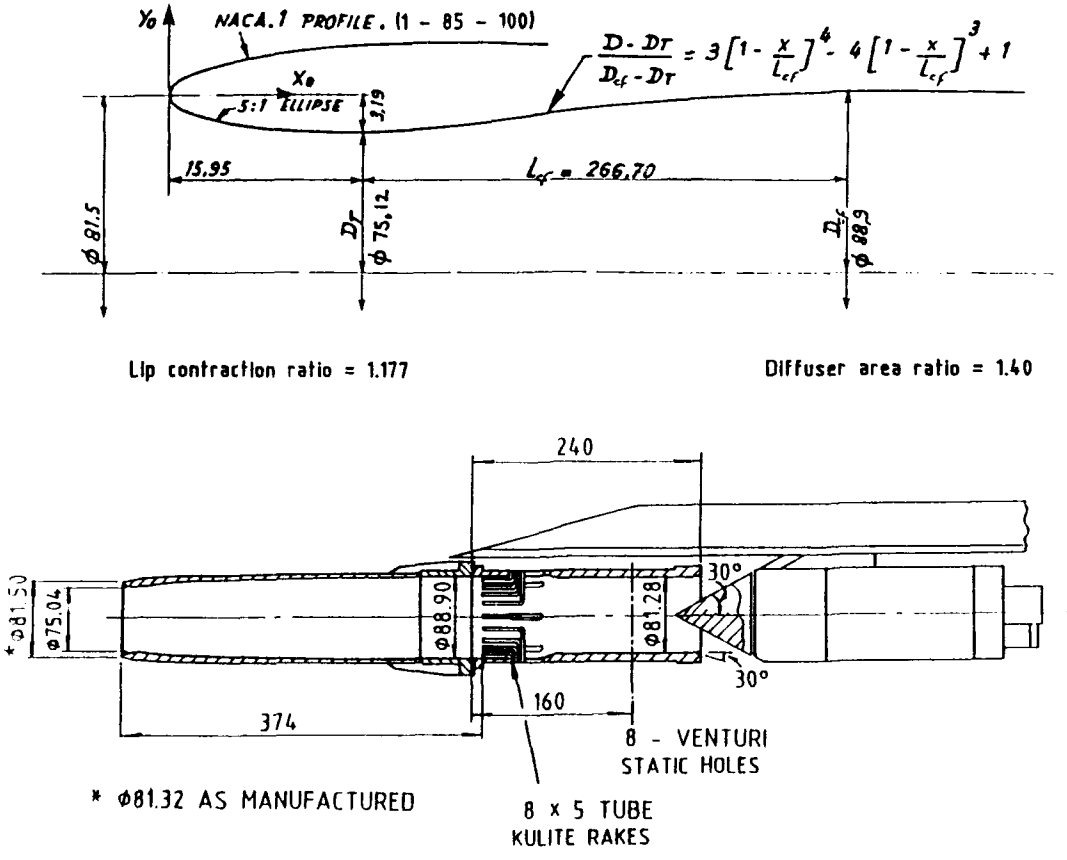

Figure 1: The RAE model 742L Cowl 2.

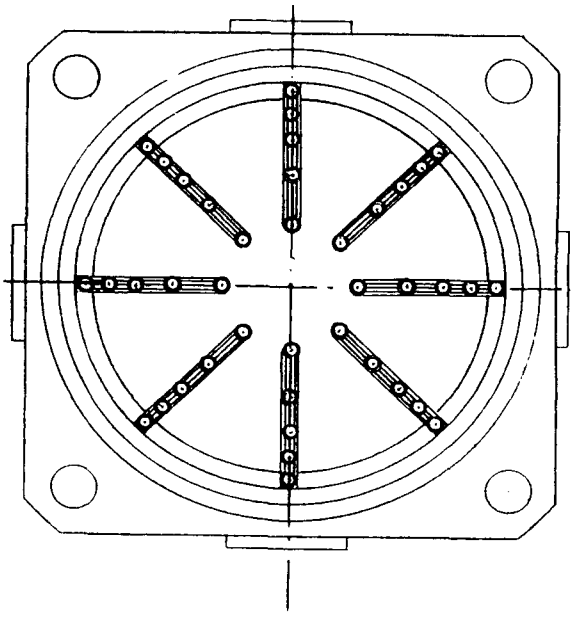

Radial positions of centres of Kulites

No.	R/R_{cf}
1	0.316
2	0.548
3	0.707
4	0.837
5	0.949

R_{cf} = 44.45

Figure 2: The RAE engine face rake.

a different inlet model) for two conditions where considerable dynamic activity was present.

3.2 The ONERA model

The ONERA model (**Figure 3**) was built to a slightly larger scale than the RAE model: the highlight diameter was D_c = 86.3 *mm* and the engine face diameter D_{cf} = 94.18 *mm*. The engine face instrumentation was identical to that applied by RAE (see section 3.1): 40 Kulite ±5 psi transducers of 2.36 mm diameter arranged five per arm in an eight arm rake (**Figure 4**). The Kulites were protected by ONERA screens and an 8.5 mm extension ahead. There was a bullet in the duct but this was positioned downstream of the rake (see Figure 3). The duct diameter increased slightly here to account for the blockage effect of the bullet. To vary the mass flow ratio, A_c/A_t, a butterfly valve was installed downstream of the engine face. It was followed by two grids to smooth the flow and reduce distortions. The flow was exhausted back to the free stream via a convergent-divergent nozzle which was used to determine the mass flow. When the nozzle was choked, mass flow measurement was based on the theoretical discharge coefficient for the sonic throat. At low Mach number, M_∞, or low mass flow, A_c/A_t, Venturi formulae were used with corrections derived from measurements in the choked flow conditions.

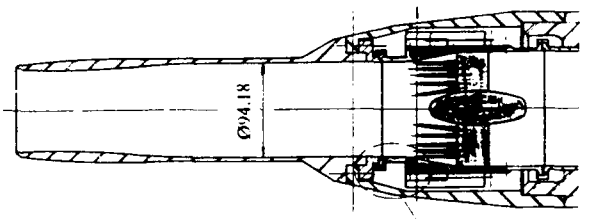

Figure 3: The ONERA model

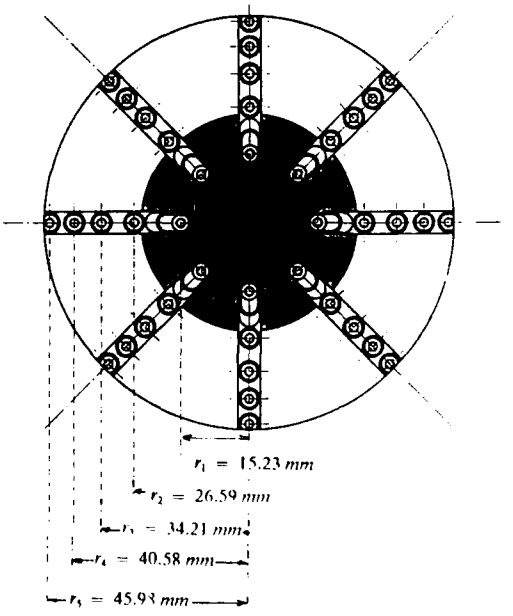

Figure 4: The ONERA engine face rake.

3.3 The DLR model

The DLR model was the largest of the three otherwise similar models investigated. The highlight diameter was D_c = 97.86 *mm* and the engine face diameter accordingly D_{cf} = 107.36 *mm* (see **Figure 5**). The engine face rake provided by MBB for the DLR model was also equipped with 40 Kulite high response pressure transducers arranged five per arm in eight arms (**Figure 6**) in the same angular positions as those in the RAE and ONERA rakes. The diameter of the Kulites was 1.64 mm, they were protected by Boeing screens and had a range of ±15 psi. But, different from the other two rakes, the Kulites were used only for the dynamic measurements whereas steady state measurements were made with the aid of 80 pitot tubes of 1.1 mm diameter placed in 16 arms; 8 immediately adjacent to the Kulites and eight interdigitated midway between them (Figure 6). The pitot tubes were connected to individual PSI transducers [3].

M_∞ = 0.8 α = 40° Repeat	Pitot tubes + scanis.	Kulites (Time average)
1	0.377	0.384
2	0.366	0.387
3	0.368	0.393
4	0.396	0.393
5	0.367	0.389
M_∞ = 1.8 α = 5° Repeat	Pitot tubes + scanis.	Kulites (Time average)
1	0.240	0.261
2	0.255	0.259
3	0.261	0.263
4	0.239	0.262
5	0.226	0.265
6	0.269	0.260

Table 1. Repeatability of DC90 measurements.

There was no bullet in the rake but a thin-walled ring of a diameter slightly less than that of the innermost probe joins the eight Kulite/pitot arms as shown in Figure 6. The duct diameter increased just downstream to more than compensate for the blockage of the 16 arm rake. Further downstream the duct remains unobstructed as far as the exit, the area of which was varied using the common conical plug arrangement to control the mass flow rate, A_1/A_2. To determine the mass flow rate the same method was applied as used by RAE (see section 3.1).

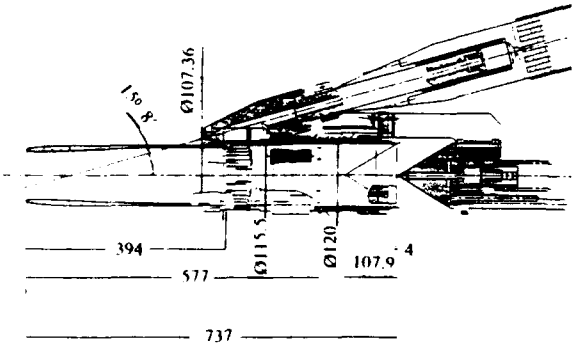

Figure 5: The DLR model

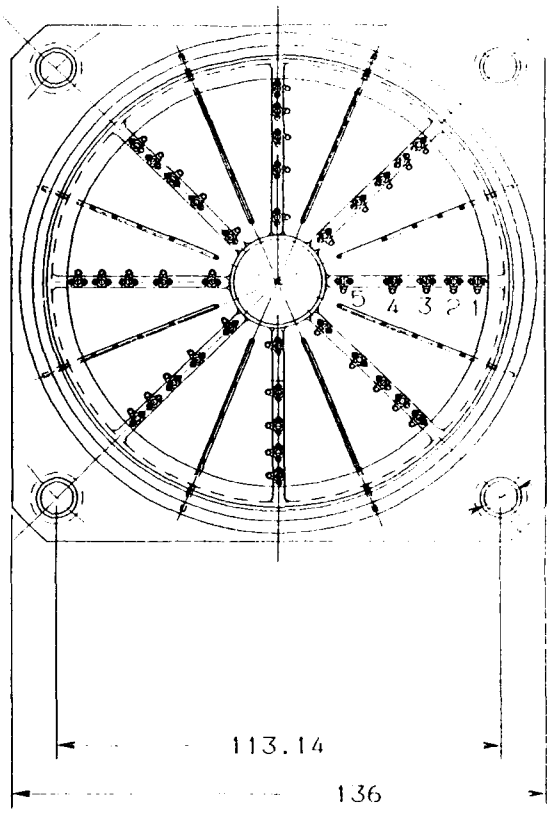

Figure 6: The MBB engine face rake.

4. Test facilities and test programmes

4.1 Tests at RAE Bedford

4.1.1 The 8 ft x 8 ft wind tunnel of RAE Bedford

The RAE Bedford subsonic/supersonic tunnel is a closed-circuit, continuous flow wind tunnel with a working section 2.4 m square (**Figure 7**). There is no ventilated wall transonic test section, and so the maximum usable subsonic Mach number is limited to about $M_\infty = 0.85$. The top and bottom walls of the tunnel are adjustable, and at supersonic speeds, continuous variation of Mach number between $M_\infty = 1.3$ and $M_\infty = 2.5$ is possible. Maximum stagnation pressure varies between $p_0 = 4$ bars at $M_\infty \leq 0.6$ and $p_0 = 1.2$ bars at $M_\infty = 2.5$.

A more detailed description of the tunnel, and the method used to correct working section Mach number for blockage effects at subsonic speeds, is given by D. Isaacs [4].

4.1.2 Test programme in the RAE wind tunnel

The tests at RAE concentrated on angle of incidence effects at two Mach numbers. Experiments were carried out at $M_\infty = 0.8$ and 1.8 at five angles of attack each. The Reynolds number, based on highlight diameter, $D_c = 81.5\,mm$, was kept at $Re_c = 1.25 \times 10^6$. Repeatability checks were done at $M_\infty = 0.8$ at $\alpha = 15°$ and at $M_\infty = 1.8$ at $\alpha = 10°$. The model was equipped with a transition strip 2 mm wide located 12 mm downstream of the high-

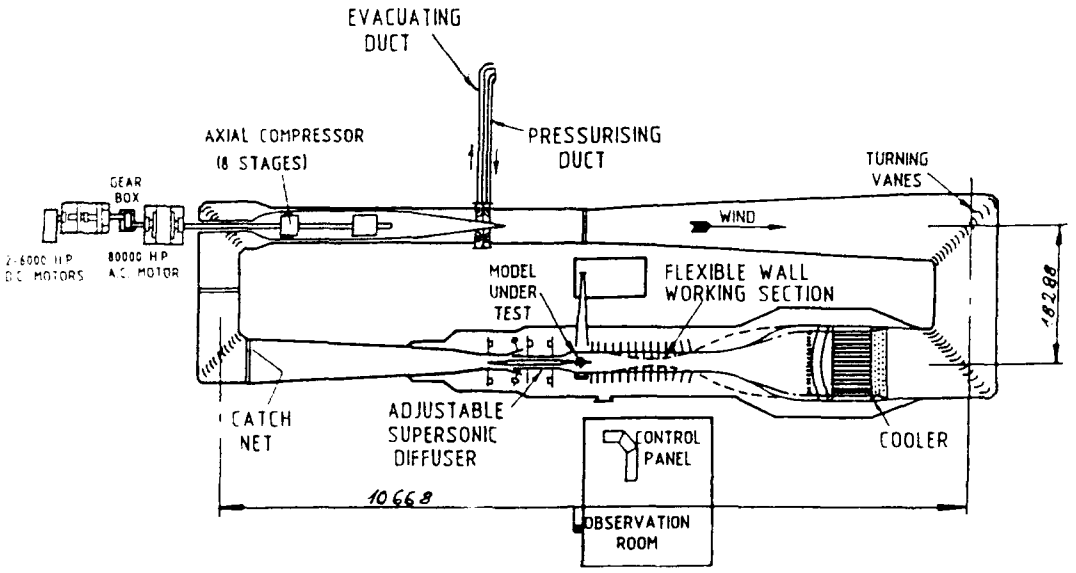

Figure 7: The 8 ft x 8 ft windtunnel of RAE Bedford

light position. Details of the test programme are given in **Table 2**. **Figure 8** shows the installation of the model in the RAE wind tunnel.

4.2 Tests at ONERA Modane

4.2.1 The S2MA 1.75 m x 1.77 m wind tunnel of ONERA Modane

The ONERA S2MA wind tunnel is a closed-circuit continuous flow transonic and supersonic wind tunnel (**Figure 9**). Two interchangeable rectangular test sections are installed in a sealed enclosure. The transonic test section (1.75 m x 1.77 m) has perforated

M_∞	α	Re_c
0.80	0^0	1.25×10^6
	1^0	
	1.5^0	
	2^0	
	2.5^0	
1.80	0^0	1.25×10^6
	$.5^0$	
	1^0	
	1.5^0	
	2^0	

Table 2. Test programme of RAE Bedford

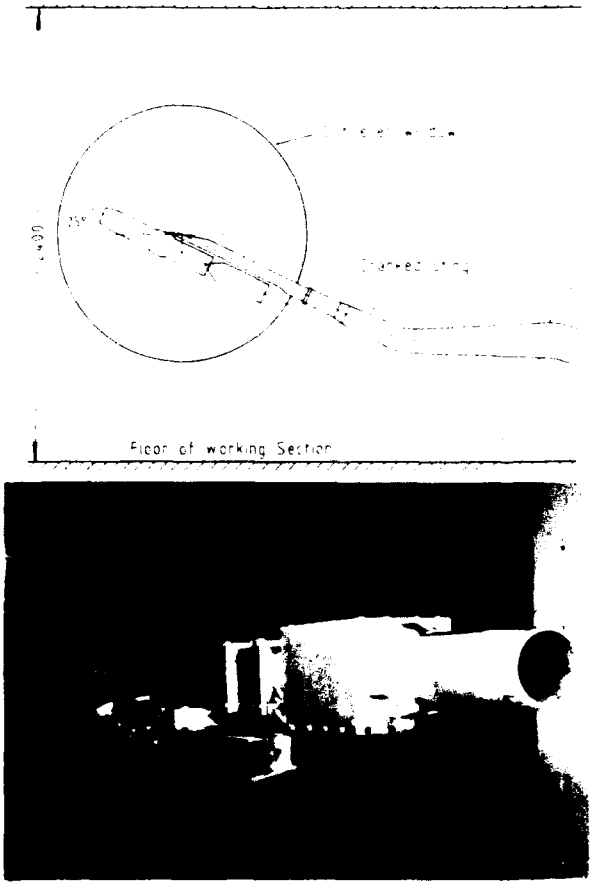

Figure 8: Installation of the RAE model in the 8 ft x 8 ft windtunnel

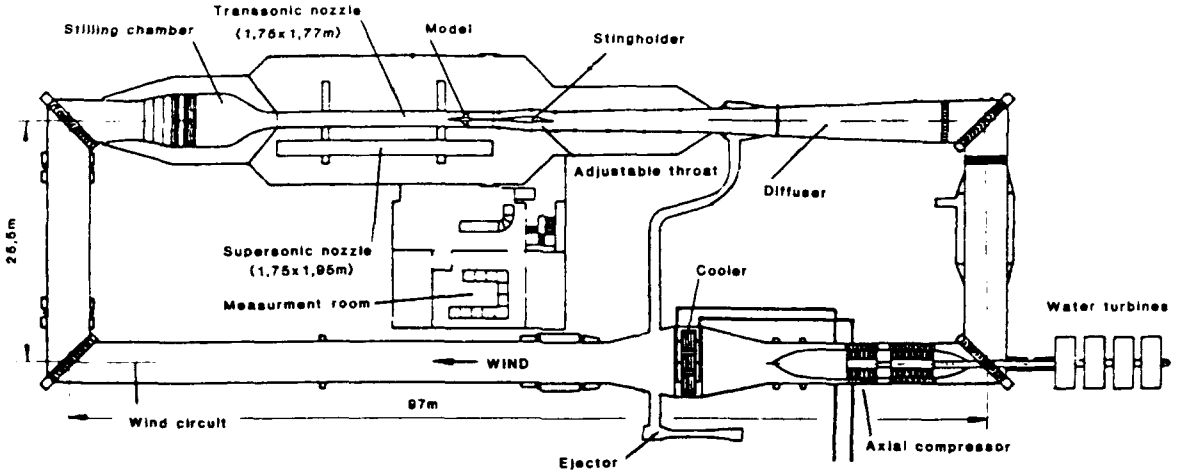

Figure 9: The S2MA transonic/supersonic windtunnel of ONERA Modane.

horizontal walls and is used for tests between M = 0.1 and M = 1.3. The supersonic test section (1.75 m x 1.93 m) is used for tests at Mach numbers $1.5 < M < 3.1$. By variation of the stagnation pressure, p_t, between 0.15 and 2.5 bar Reynolds numbers $1.8 \cdot 10^6 < Re < 39 \cdot 10^6$ are achievable.

A more detailed description of the tunnel is given by J. Lacarrère & L. Charpin [5].

4.2.2 Test programme of ONERA.

The measurements at ONERA were carried out at M = 0.8 at the same angles of incidence and the same Reynolds number (based on the highlight diameter, D = 86.3 mm) as at RAE. Additional tests were done at further four Mach numbers $0.75 < M_\infty < 0.95$ and at Re = $1.9 \cdot 10^6$. The model was equipped with a transition strip 3 mm wide located 6.5 mm downstream of the highlight position. Details of the test programme are given in **Table 3**. The installation of the ONERA model in the S2MA wind tunnel is depicted in **Figure 10**.

M_∞	α	Re
0.80	0°	$1.25 \cdot 10^6$
	5°	
	10°	
	15°	
	20°	
	25°	
0.80	15°	$1.90 \cdot 10^6$
	20°	
0.75	15°	$1.25 \cdot 10^6$
0.80		
0.85		
0.90		
0.95		

Table 3. Test programme of ONERA Modane

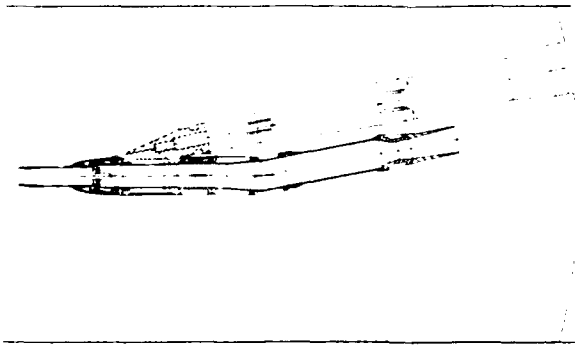

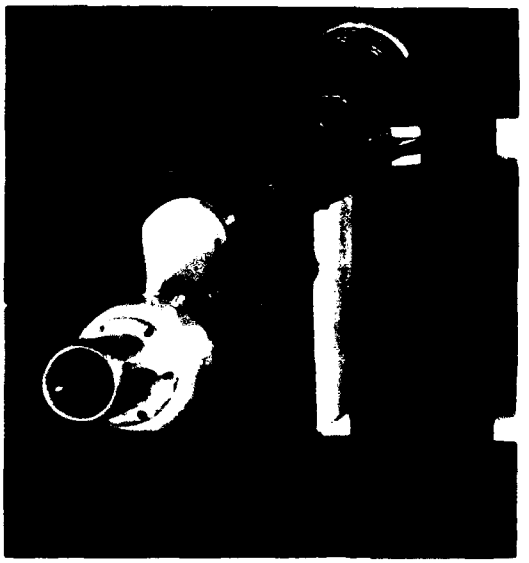

Figure 10: Installation of the ONERA model in the S2MA windtunnel

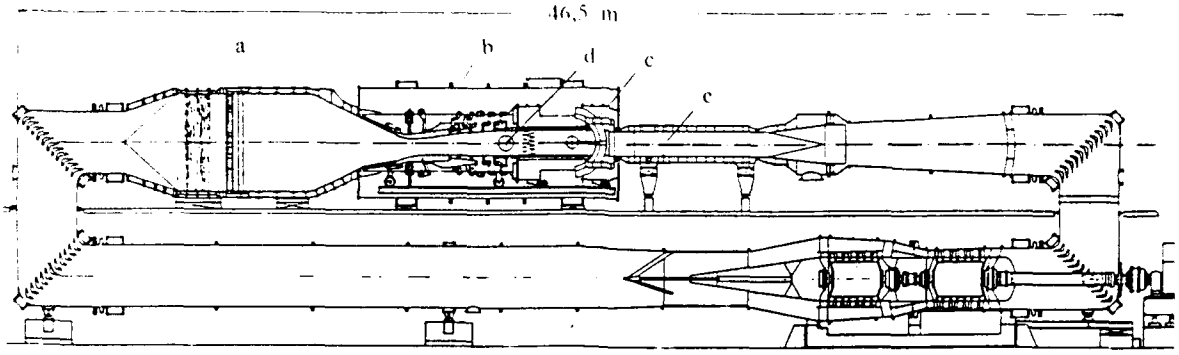

Figure 11: The transonic windtunnel of the DLR Göttingen (TWG).

4.3 Tests at DLR Göttingen

4.3.1 The 1 m x 1 m transonic wind tunnel of DLR Göttingen

The Transonic Wind Tunnel of the DLR Göttingen (TWG) is also a closed circuit, continuous flow (Göttingen) type wind tunnel with a cross sectional area, A, of 1 m x 1 m (**Figure 11**). The horizontal walls of the transonic test section (d in Figure 11) are slotted. The slots are adjustable in width and shape to achieve minimum wall interferences by adjusting the slots according to the kind of model investigated. In the subsonic range ($0.5 \leq M \leq 0.9$) the Mach numbers are controlled by an adjustable second throat diffuser (e). To achieve transonic velocities ($0.9 \leq M \leq 1.2$) and for boundary-layer suction an auxiliary compressor is provided. For measurements at supersonic speeds ($1.3 \leq M_\infty \leq 2.0$) the model is mounted in the supersonic test section (c) and the Mach numbers are controlled by an adjustable Laval nozzle (b). By variation of the stagnation pressure, p_0, between 0.3 and 1.6 bar the Reynolds number is adjustable between $Re_\infty = 0.4 \times 10^7\, m^{-1}$ and $Re_\infty = 1.2 \times 10^7\, m^{-1}$.

More detailed descriptions of the tunnel are given by H. Ludwieg et al [6], T. Hottner & W. Lorenz-Meyer [7], and W. Lorenz-Meyer [8].

M_∞	α	Re_c
0.75	5° 15°	0.8×10^6
0.90	5° 15°	0.8×10^6
0.80	0° 5° 10° 15° 20°	0.8×10^6
1.80	0° 5° 10° 15° 20°	0.8×10^6
0.80	5° 15°	0.2×10^6
0.80	5° 15°	1.9×10^6

Table 4. Test programme of DLR

4.3.2 Test programme of DLR

As at RAE the DLR MBB tests were carried out at $M_\infty = 0.8$ and 1.8 at five angles of attack each. Additional measurements were made at $M_\infty = 0.75$ and 0.90. The Reynolds number, based on highlight diameter, $D_c = 97.9\,mm$, was kept at $Re = 0.8 \times 10^6$. To cover the effect of the Reynolds number further experiments were done at $M_\infty = 0.8$ at $\alpha = 5°$ and 15° at the two Reynolds numbers $Re_c = 0.2 \times 10^6$ and 1.9×10^6. The model was equipped with a transition strip 3 mm wide located 10 mm downstream of the highlight position. Details of the test programme are given in **Table 4**. **Figure 12** shows the installation of the DLR model in the transonic wind tunnel Göttingen (TWG).

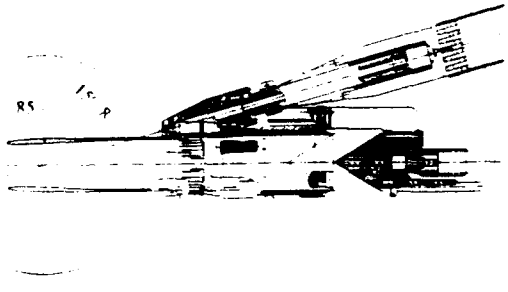

Figure 12: Installation of the DLR model in the TWG.

5. Data acquisition and reduction systems

5.1 The RAE-system

The dynamic data signals of the 40 Kulites were digitised and stored in real time on 67 Mbyte exchangeable discs. The maximum digitisation rate of the system was 300 k, 10-bit words per second. Sample and hold amplifiers were used to ensure that all pressures were measured at the same instant in time. Signal conditioning was achieved using 48 high stability variable gain DC amplifiers (which can be AC coupled if required) together with 48 low pass Butterworth filters (48 dB per octave roll-off). The cut-off frequency was variable from 10 Hz to 2.5 kHz and was set to 1.7 kHz, which is equivalent to 200 Hz full scale for an assumed model scale of 1/8.5. The sampling rate was three times the cut off frequency i.e. 5.1 k samples/s on the evidence of **Figure 13** [9]. The record length was 4.016 seconds.

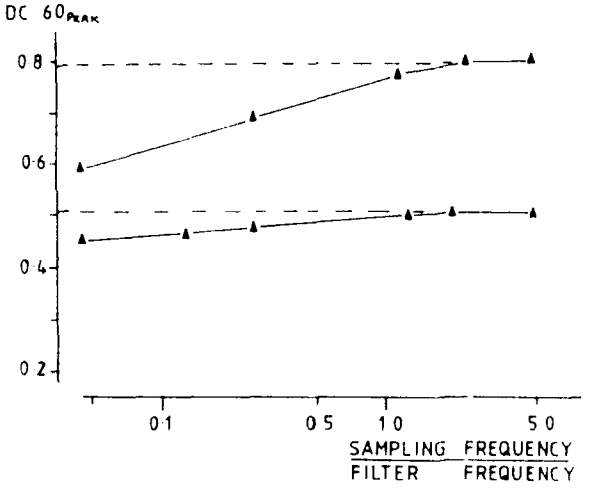

Figure 13: Effect of sampling frequency [9]

5.2 The ONERA-system

The records were obtained in real time by succesive acquisitions (every second) of batches of 256 pressure maps at the maximum frequency of 20 kHz, 12-bit words. The filter cut off frequency was set to 1.6 kHz and the sampling rate was five times the cut off frequency, i.e. 8 k samples/s. The record length was 3.84 s. For a few points the cut-off frequency was doubled to 3.2 kHz and then the sampling rate became 16 k samples/s.

5.3 The MBB-system used for the tests at DLR

The dynamic signals were digitised and stored in real time on 47 Gbyte tapes. The maximum digitisation rate was 200 k, 12-bit words per second *for each channel*. For data storage purposes the sampling rate was 80 k samples/s each channel, using a resolution of 12 bit for one word. The record length was then extended to 30 seconds. For the on-line presentation MBB used a reduced sampling rate of 20 k samples s/channel, 12-bit words resolution, with a record length of only four seconds. These data were stored on 2 Gbyte discs. The 40 channels were simultaneously recorded by using a sample and hold system. The signal conditioning used DC AC low pass Bessel filters (8 pole, 48 dB per octave roll off) and the cut off frequency could be varied from 10 Hz to 2.55 kHz in steps of 10 Hz or from 100 Hz to 25.5 kHz in steps of 100 Hz, respectively. During the tests the cut-off frequency was set to 1.42 kHz for all characteristics except one, when it was set to 2.8 kHz. Furtheron a lot of samples was taken with a record length of two minutes, but these are not yet evaluated.

6. Presentation and discussion of the results

6.1 Data reduction and presentation

The steady state intake characteristic data are presented in the usual format i.e. pressure recovery, $PR = \bar{p}_{t,ef}/p_{t,\infty}$, and DC_{60} versus relative mass flow, A_0/A_c. Unsteady DC_{60} can be presented as maximum values recorded DC_{60IX} or, using the Jacocks statistical method [10], as the maximum values *2 min* DC_{60} that would predicted after two minutes operation at full scale.

DC_{60IX} is defined as

$$DC_{60IX} = \frac{\bar{p}_{t,ef} - \bar{p}_{t,ef,min,60}}{\bar{q}_{ef}}$$

where now $\bar{p}_{t,ef,min,60}$ is the *instantaneous* value of the minimum total pressure averaged over any sector of 60° at the engine face; and $\bar{p}_{t,ef}$ is the mean steady state total pressure there [1]:

$$\bar{p}_{t,ef} = \frac{1}{N} \sum_{i=0}^{N} p_{t,ef,i}$$

($N = 40$ for RAE and ONERA, $N = 80$ for DLR)

Using the Rolls Royce recommendation, $\bar{q}_{ef}$ is the mean steady dynamic pressure as obtained from a mass flow derived Mach number at the engine face.

The Jackocks statistical method is summarized as follows:

1. Peak DC_{60} values are calculated for each of the K blocks of data available in the three to four seconds of recording time. K is normally in the range of 15 to 25.
2. Peak DC_{60} values are arranged in ascending order of value and assigned an index m, where $m = 1, 2, \ldots K$.
3. The reduced variate

$$y = -\ln \ln \frac{K+1}{m}$$

is calculated.

[1] Strictly, $\bar{p}_{t,ef}$ is the *area weighted* mean steady state total pressure, so the equation for $\bar{p}_{t,ef}$ should include an area weighting factor (w_i, say). RAE generally use rakes where the tubes are arranged to govern annuli of equal area (as recommended in [13]), so $w_i = 1$. Allocating weighting factors for other tube arrangements is, to some extend, arbitrary, and this is an additional argument for standardizing engine face instrumentation.

4. Peak DC_{60} values are plotted versus y and a least squares fit straight line through the points is calculated.

5. Extrapolation of this straight line allows estimation for a longer time period (e.g. 14 s RAE model scale, 14.83 s ONERA model scale, equivalent to 2 minutes full scale).

Whereas RAE and ONERA provided $DC_{60/X}$ as well as *2 min* DC_{60} values DLR/MBB concentrated on $DC_{60/X}$ and resigned to calculate *2 min* DC_{60}[11] . However, it could be interesting to evaluate at a later time the stored samples of DLR/MBB with a record length of 30 seconds and of two minutes and to compare these results with the *2 min* DC_{60} values obtained with the Jacocks method by RAE and ONERA.

6.2 Analysis of the results

6.2.1 Effect of incidence variation

Pressure recovery versus mass flow characteristics at M_o = 0.8 (**Figure 14**) show close agreement at all incidences except at $\alpha = 20°$. If the maximum mass flow rate is considered on the supercritical leg of the characteristics close to the critical point, then there may be seen a tendency for the ONERA values to be slightly in excess of the RAE and DLR values at $\alpha = 0°$ and 10°. At $\alpha = 0°$, the theoretical choking

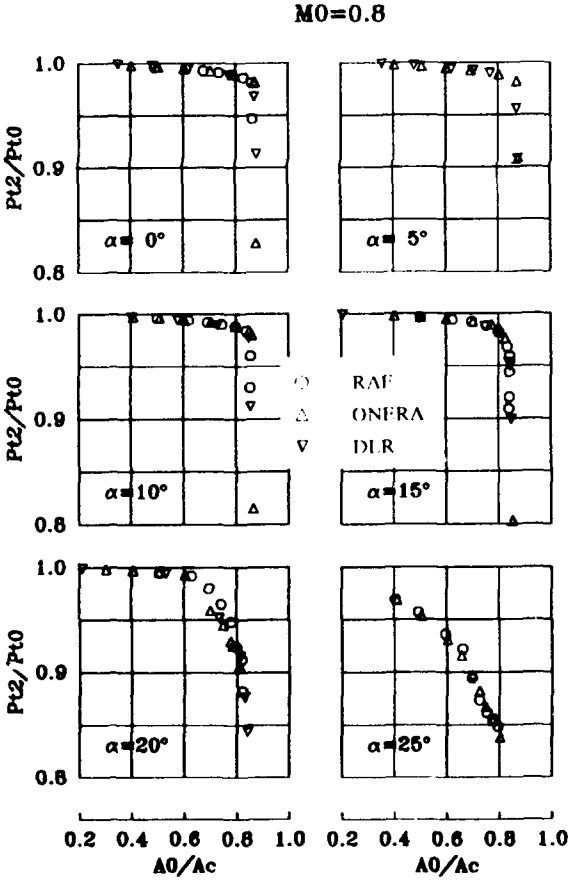

Figure 14: Comparison of pressure recovery at M_o = 0.8.
Effect of incidence variation

mass flow ratio is 0.882, which indicates throat discharge coefficients of C_d = 0.992 for the ONERA results, C_d = 0.978 for RAE and C_d = 0.987 for DLR. Pressure recoveries measured by ONERA and DLR at $\alpha = 20°$ are in close agreement over the full mass flow range whereas RAE values are 1 to 2 % higher in the mass flow range 0.6 to 0.8. At $\alpha = 25°$ results are available only from RAE and ONERA. Pressure recovery values again differ by about 1 % over the mass flow ratio range 0.6 to 0.8 but there is no consistent one way trend.

For the supersonic Mach number M_o = 1.8 results are available only from RAE and DLR. In general,

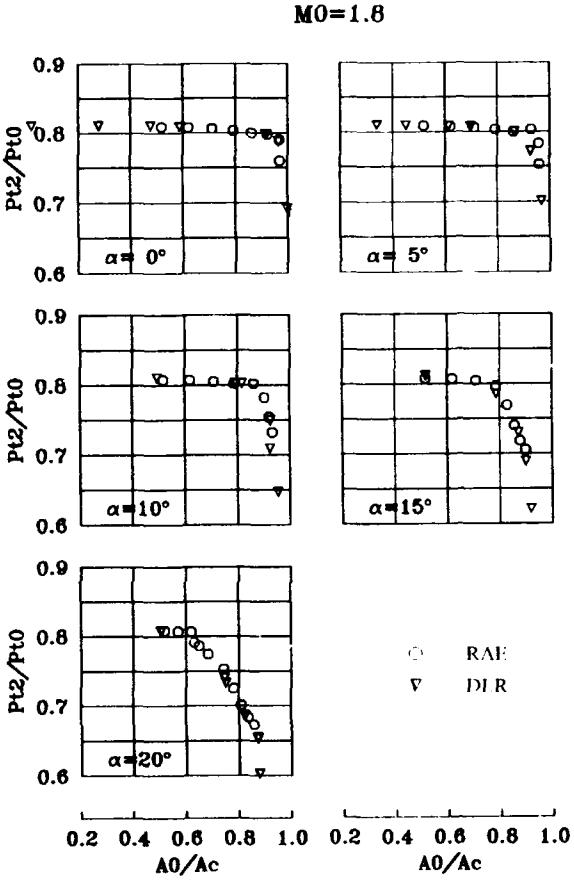

Figure 15: Comparison of pressure recovery at M_o = 1.8.
Effect of incidence variation

pressure recovery versus mass flow characteristics (**Figure 15**) are very similar at $\alpha = 0°$ and 5°. At low mass flow at $\alpha = 0°$ pressure recovery is very close to the normal shock value of 0.813 at M_o = 1.8. Maximum theoretical choking flow at these conditions is 0.994 which compares with the measured value of 0.977 for both sets of results. This gives a throat discharge coefficient of C_d = 0.983, which is the mean of the values 0.978 and 0.987 found at M_o = 0.8. At $\alpha = 10°$ to 20°, there is a tendency for DLR values of pressure recovery at flow ratios above 0.8 to be slightly higher than RAE values: this is also true for maximum flow ratios. This latter difference may be exaggerated by a lack of truly supercritical values for the RAE results at these incidences.

A possible explanation for the deterioration in pressure recovery at $\alpha = 20°$ and $M_o = 0.8$ may be obtained from the internal cowl lower lip surface Mach number plots from [2]. **Figure 16** shows the collapse of the lip suction that occurs on changing mass flow ratio from 0.559 to 0.604 indicating the advent of lip separation. The steady increase in separation bubble Mach number as A_o/A_c varies from 0.652 to 0.796 then gives rise to rapidly increasing mixing losses and results in the observed deterioration in engine face pressure recovery. At $\alpha = 25°$, the flow is separated from the lower lip of the cowl over the complete range of measured mass flow [2].

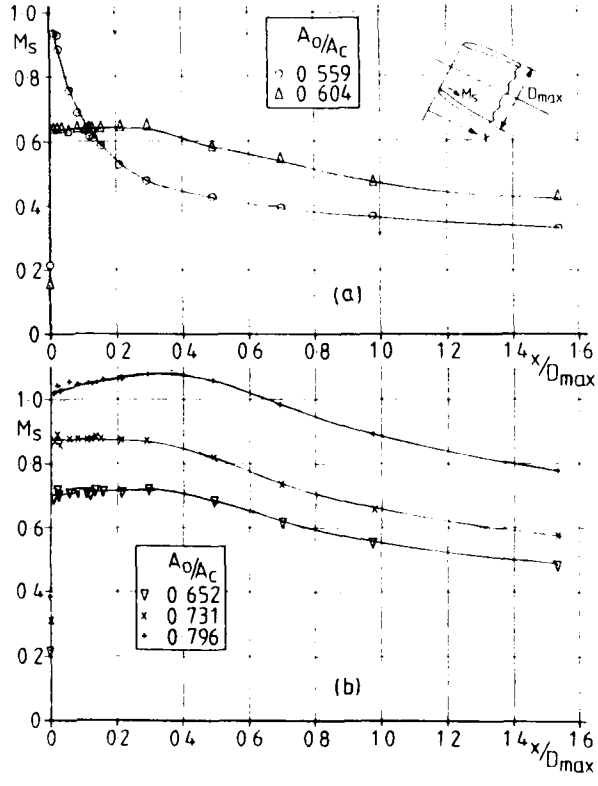

Figure 16: Internal lower lip Mach number distributions at $M_o = 0.8$ and $\alpha = 20°$ [2].

Steady state DC_{60} values at $M_o = 0.8$ (**Figure 17**) show a greater variation between the three sets of results. In particular at $\alpha = 0°$, theoretically DC_{60} should be zero as any distortion of the engine face flow in an axisymmetric intake and duct should be purely radial. All results approximate to this at flow ratios above 0.6 but RAE and DLR values tend to increase (though remaining small) below $A_o/A_c = 0.6$. DLR values show the same tendency at $\alpha = 5°$ to 15° but increase to fairly high values at mass flow rates below 0.6 whereas RAE and ONERA values remain below $DC_{60} = 0.05$ over the full measured flow range. At $\alpha = 20°$, DC_{60} climbs rapidly above $A_o/A_c = 0.6$ remarkably consistently from all three tunnels. At $\alpha = 25°$ from $A_o/A_c = 0.7$ upwards values from RAE are considerably higher than ONERA values. At $M_o = 1.8$ (**Figure 18**) DC_{60} values from DLR show the same tendency as at $M_o = 0.8$ of being slightly higher than RAE values at mass flow rates below the critical point. The

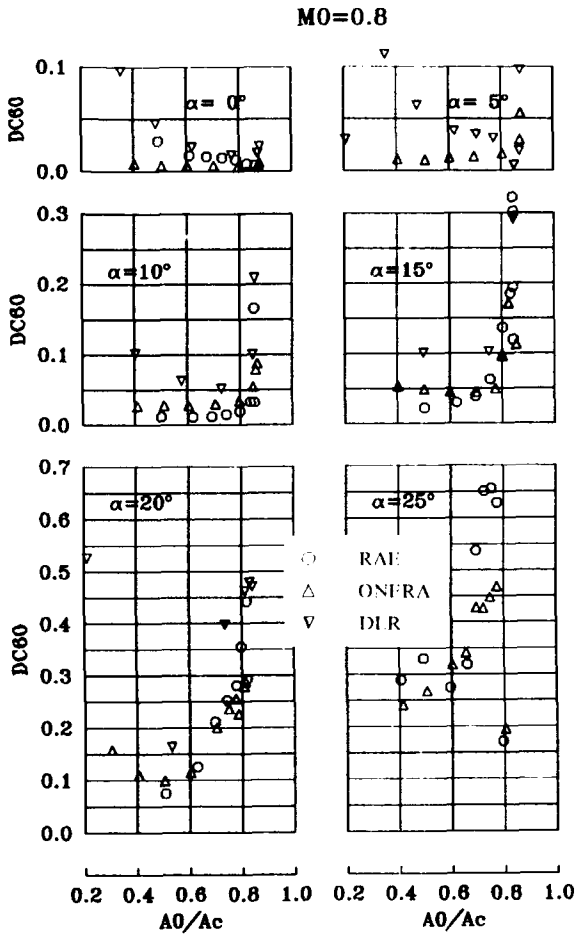

Figure 17: Comparison of steady state DC_{60} at $M_o = 0.8$
Effect of incidence variation

reason for the especially high values of DC_{60} measured by DLR at the lowest mass flow rate of $A_o/A_c = 0.2$ at $M_o = 0.8$ remains undetected because neither RAE nor ONERA have comparable results. However, it may be noted that the dynamic pressure $\bar{q}_{cf}$ is extremely low at this mass flow ratio, which has the effect of greatly magnifying any (even very small) errors in the pressure measurements, or in the procedure for calculating the lowest 60° sector mean pressure.

Values for DC_{60IX} from all three tunnels are in reasonably close agreement up to $\alpha = 15°$ over the full flow range at subsonic (**Figure 19**) as well as at supersonic speed (**Figure 20**). In this case, some increase in DC_{60IX} with reducing mass flow might be expected, as tunnel turbulence will provide a significant component of the flow unsteadiness measured at the engine face. At $M_o = 0.8$ a little more scatter between the three sets of results occurs at $\alpha = 20°$. At $\alpha = 25°$ ONERA values are considerably lower than RAE values but both sets are, numerically, very high. At the supersonic Mach number $M_o = 1.8$ high peak values of DC_{60IX} can be observed at $\alpha = 5°$ to 20°. These are probably the results of coincidence of lip separation and shock-boundary layer interaction in the region of the lip. The DLR results show that the DC_{60IX} values can drop considerably

when the internal supersonic flow pattern has become properly established and the terminal shock has moved downstream of the lip.

6.2.2 Effect of variation of free stream Mach number

Comparisons at $M_o = 0.75$ and 0.90 are limited to ONERA and DLR results (**Figure 21**). Values of pressure recovery at $M_o = 0.75$ are not in such close agreement as at $M_o = 0.8$, with ONERA values being 0.5 to 1 % higher than those from DLR. DC_{60} values show the same (but opposite) trend throughout the flow range. At $M_o = 0.9$ one value of the DLR pressure recovery versus mass flow characteristic (at $A_o/A_c = 0.57$) is much lower than the corresponding ONERA value. This is not accompanied by a correspondingly large increase in DC_{60} at this condition which indicates that the pressure recovery value is in error. Again, as at $M_o = 0.8$, DC_{60IX} values between the two tunnels are remarkably consistent.

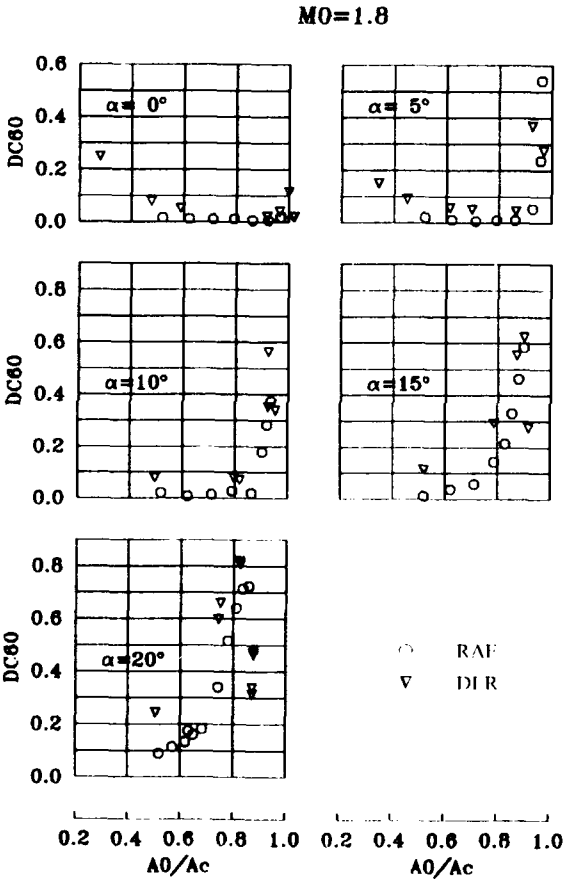

Figure 18: Comparison of steady state DC_{60} at $M_o = 1.8$
Effect of incidence variation

6.2.3 Effect of Reynolds number variation

Variation between $Re_c = 1.25 \times 10^6$ and 1.91×10^6 for all three (PR, DC_{60} and DC_{60IX}) ONERA results are negligible, as might be expected for this small Reynolds number change (**Figure 22**). DLR results are similar for the two higher Reynolds numbers. However, the values at the low Reynolds number of 0.2×10^6 illustrate the large adverse effects of going below the well known "rule of thumb" of intake testing that the Reynolds number based on intake diameter should if possible exceed 1×10^6.

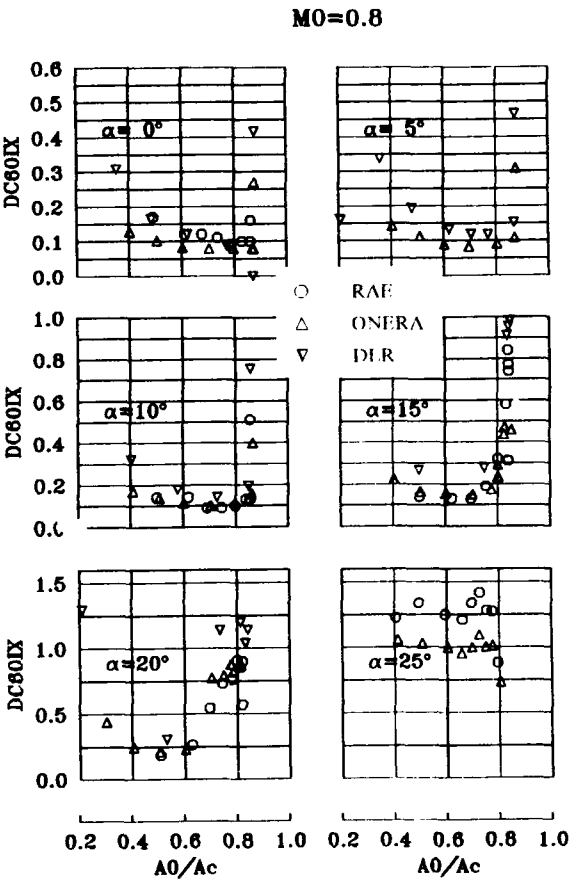

Figure 19: Comparison of DC_{60IX} at $M_o = 0.8$

6.3 Discussion of results

Considering the differences in the models, instrumentation, basic flow calibrations, data acquisition systems and analysis techniques, the results from the three tunnels show a gratifying measure of agreement. In general, the differences are of little practical significance, but three possible contributory factors may be mentioned.

1. Although the three models were of nominally identical geometry, normal manufacturing tolerances could lead to very slight differences in shape - particularly in the critical area of the cowl lip. This could have some effect on flow separation at incidence and possibly explain the small differences in pressure recovery at high mass flow ratios at $\alpha = 20°$.

2. The internal transition trips of the three models were different in width and location. The trip of the RAE model was at the largest distance from the highlight, and had the smallest extension, which could result in a thinner boundary layer and possibly lower losses. On the other hand, the trips on the RAE and the DLR model were too far downstream to influence flow separation from the lip. However, the sensitivity of the results to the form of transition trip is largely

speculative. It would be valuable if tests could be done on the same model with and without a transition band present, as this would indicate whether such a trip serves any useful purpose or not.

3. The definition of the distortion parameter DC_{60} is seemingly quite precise, but the calculated value is very sensitive to the method used to calculate the minimum 60° sector mean pressure [12]. RAE and ONERA both used the Lagrangeian interpolation procedure recommended by Rolls Royce, but this is only defined for an eight or 12 arm rake. The MBB rake used by DLR has 16 arms and so a different procedure had to be used. It is quite likely that, even with an identical pressure distribution, this would produce a somewhat different DC_{60} value than the RAE/ONERA method.

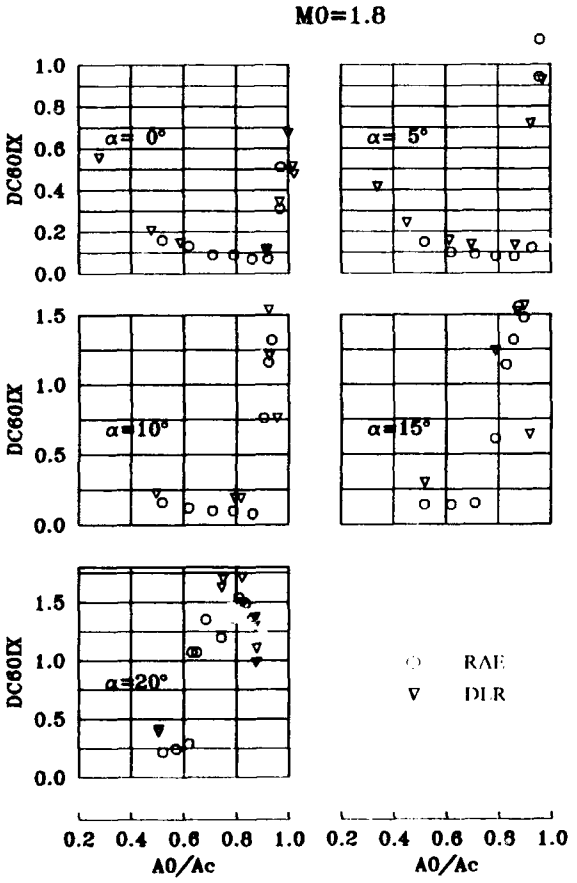

Figure 20: Comparison of DC_{60IX} at $M_o = 1.8$

With regard to the conduct of the tests themselves, three other factors may be mentioned that would have facilitated comparison of the results:

1. The tests by ONERA and DLR at different Reynolds numbers were very useful and indicated that there is little effect in the range $0.8 \times 10^6 \leq Re_c \leq 1.9 \times 10^6$. However it would have eliminated one cause of uncertainty if all the basic tests could have been done at the same Re_c.

2. It would have been helpful if more points had been taken on each characteristic, particularly in regions where pressure recovery or DC_{60} were changing rapidly with mass flow.

3. Overall confidence level in the ONERA and DLR results would be increased if a number of repeats had been taken at one or more points. Of course, such repeats cannot reveal any systematic errors, but they do give a good indication of random errors that may occur in the steady-state quantities. For example, RAE took 14 sets of measurements at one point on a characteristic (during tests with another model) at $M_o = 1.8$, $\alpha = 10°$, $A_o/A_c = 0.904$. It was found that all pressure recovery and mass flow values were within a 0.001 band and all DC_{60} values were in a 0.006 band. Eleven repeats at $M_o = 0.8$, $\alpha = 15°$, $A_o/A_c = 0.832$ showed identical error bands.

The question of the accuracy of the unsteady measurements is much more complex, since the pressure fluctuations are essentially random in character. That the flow is "stationary" in a statistical sense (i.e. samples taken at different times will have the same mean values) is borne out by the very low dispersion of the steady-state values found in the RAE repeat tests (these values being obtained by time-averaging

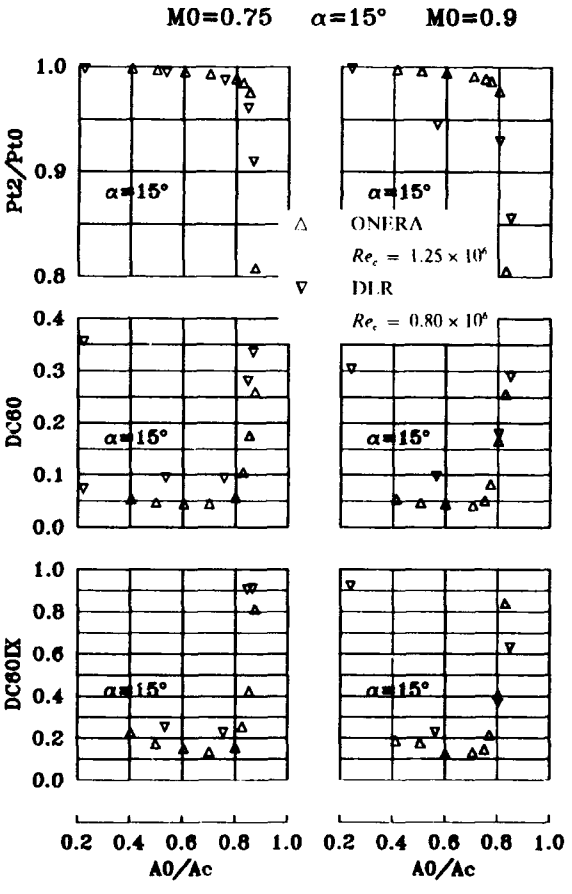

Figure 21: Effect of variation of free stream Mach number.

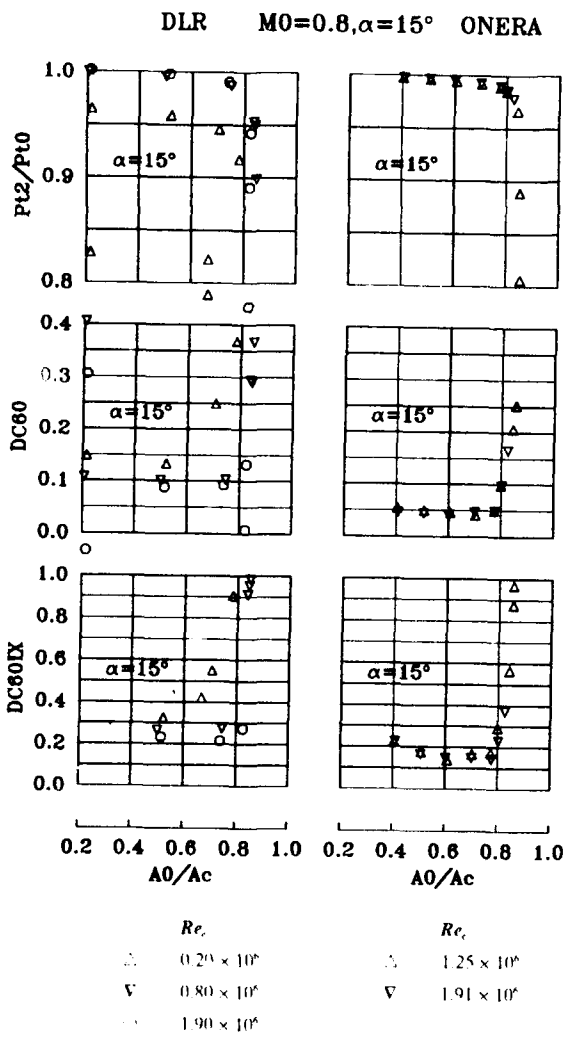

Figure 22: Effect of variation of Reynolds number.

the Kulite recordings). However, the repeat tests showed large variations in DC_{60IX}, particularly at $M_\infty = 1.8$, where turbulence level was high due to extensive flow separation from the cowl lip. The magnitude of this random variation is such that it is likely to mask any systematic differences in the methods of acquiring and processing the unsteady data. The only way of investigating such differences is to take a number of (unfiltered) analogue tape recordings of the Kulite signals and analyze them on the various systems. This would be an useful exercise, which could also be used to study the effect of different scanning frequencies on the same set of data - something not possible with a digital recording. Obviously, minimising the scan rate is a most effective way of reducing the massive data storage/computing problem inherent in dynamic distortion work.

The three models were built to different scales to accomodate existing engine face instrumentation, in the interests of economy. Apart from the problem discussed above of calculating DC_{60} using the standard Rolls Royce method with the MBB rake, there do not appear to be any differences in the results that can be ascribed solely to differences in rake geometry. However, to eliminate any uncertainty on this score, engine face instrumentation really needs to be standardised. The guidelines laid down in Reference [13] provide an excellent basis for this.

The geometry of the models also differed downstream of the engine face, but this is not considered to be an important factor provided the flow does not separate for any reason (such as overexpansion) and cause pressure disturbances to be propagated upstream to the engine face. More important for subsonic testing is the shape of the duct exit, as it has been found that this can generate high frequency pressure waves of considerable amplitude at pressure ratios just below the choking value [14]. These waves can affect DC_{60IX}, but spectral analysis of the Kulite records is necessary to detect their presence.

Two different methods of controlling and measuring the intake flow were used - a translating cone by RAE and DLR and a butterfly valve/convergent-divergent nozzle by ONERA. Both are well established techniques and capable of measuring mass flow to an adequate accuracy provided they are suitably calibrated. Judging from the generally good agreement in maximum mass flow ratio this has obviously been done. However, the accurate measurement of mass flow in intake testing is notoriously difficult and, at subsonic speeds in particular, an accuracy of better than 0.5 % is very unlikely to be achieved.

7. Conclusions

Measurements of pressure recovery, mass flow, steady state DC_{60}, and instantaneous distortions DC_{60IX} have been made on a common design of an axisymmetric pitot intake in three European wind tunnels. Although the models differed slightly in size, and considerably in the instrumentation and the techniques of data acquisition and reduction, the results in most cases are very similar. Numerically, DC_{60} and DC_{60IX} tend to show the most marked differences, but even here, the variation with mass flow generally follows a similar pattern.

In a comparative test such as this, one set of results cannot be said to be "better" than another. Apart from the experimental errors inherent in any intake test, each dataset must be regarded as valid for the particular model and instrumentation used. It could be argued that *any* differences in the models and instrumentation are, to some unquantifiable extent, responsible for the differences found in the results, but this is not a very helpful approach. Certainly, a greater standardisation of the engine face instrumentation is desirable, but apart from that, the most significant causes for differences in the steady-state parameters are considered to be

- slight differences in lip shape,
- differences in the location and extent of the transition trip,

and

- the method of calculating DC_{60}.

Assessment of the dynamic distortion measurements is bedevilled by the fact that DC_{60IX} is essentially a random variable. Consequently repeat measurements at nominally identical conditions when the turbulence level is high can, and do, show considerable differences. This random variation may be greater than any systematic differences due to the model, instrumentation, and the data acqusition/analysis systems.

8. References

[1] E.L. Goldsmith: *Forces and pressure distributions at subsonic and supersonic speeds on circular section pitot intakes.* ARA Report 75 (Jan. 1990).

[2] E.L. Goldsmith: *The internal performance at incidence of pitot intakes with circular cross section and elliptic lip shapes.* ARA Report 76 (Jan. 1990).

[3] D.B. Juanarena: *A multiport sensor and measurement system for aerospace pressure measurements.* 25th Annual ISA Arospace Symp., May 1979.

[4] D. Isaacs: *Calibration of the 8 ft x 8 ft wind tunnel at subsonic speeds.* RAE TR 67038 (1967).

[5] J. Laverré, F. Charpin: *La soufflerie S2MA du Centre d'essais aerodynamiques de Modane-Avrieux.* ONERA N.T. 1983.5 (1983).

[6] H. Ludwieg, W. Lorenz-Meyer, W. Schneider: *Der Transsonische Windkanal der Aerodynamischen Versuchsanstalt Göttingen.* Jahrbuch 1966 der WGLR, S. 145-155.

[7] T. Hottner, W. Lorenz-Meyer: *Der Transsonische Windkanal der Aerodynamischen Versuchsanstalt Göttingen (zweite Aushaustufe).* Jahrbuch 1968 der DGLR, S. 235-244.

[8] W. Lorenz-Meyer: *Der Transsonische Windkanal 1m x 1m der DFVLR-AVA.* Nr.4 in "Beiträge zur experimentellen Strömungsmechanik", Festschrift z. 65. Geburtstag von H.Ludwieg, DFVLR-AVA IB 251-77 A 37 (1977).

[9] D. E. Colbourne and J. E. Flitcroft,: *Prediction and measurement of time variant three dimensional flows in military aircraft intakes.* Aerodynamics of Power Plant Installation. AGARD CP 301, May 1981.

[10] J. L. Jacocks,: *Statistical analysis of distortion factors.* AIAA paper 72-1100 (1972).

[11] K. W. Lotter, R. D. Scherbaum: *A Novel High Performance System for Recording and Analyzing Time-Variant Total Pressure Distortion in Air Intakes.* AGARD 69th FDP Meeting and Symposium on "Aerodynamic Engine/Airframe Integration for High Performance Aircraft and Missiles", Fort Worth, Texas, USA, 7-10 October 1991.

[12] I. McGregor, R. Clark: *A note on the calculation of the Rolls Royce flow distortion parameter DC(Θ).* RAE TM Aero. 2086 (1986)

[13] *Gas turbine engine inlet flow distortion guidelines.* SAE ARP 1420 (March 1978).

[14] I. McGregor, J. Gibb, M. Cameron: *Flow induced pressure fluctuations in model air intake flow metering devices.* RAE Report 1990, unpublished.

ETUDES AERODYNAMIQUES DE PRISES D'AIR SUPERSONIQUES

(AERODYNAMIC STUDIES OF SUPERSONIC AIR INTAKES)

par
P. GARNERO et R.G. LACAU
---
aerospatiale - Division Engins Tactiques
91370 Verrières-Le-Buisson - FRANCE

RESUME

aerospatiale Division Engins Tactiques utilise les statoréacteurs sur ses missiles depuis plus de trente ans et étudie l'adaptation de ce type de propulsion à des avions à très grande vitesse ainsi qu'à des lanceurs spatiaux aérobies. Nous sommes ainsi amenés à étudier des véhicules conçus pour des vitesses de vol de plus en plus élevées et à optimiser plus rapidement et à moindre coût nos configurations de missiles aérobies. Nous avons donc complété notre méthodologie de conception des prises d'air supersoniques en mettant en œuvre des codes de simulation numérique pour nos travaux en aérodynamique externe et interne.
Ces moyens de calcul composés de codes Euler, Navier-Stokes et d'outils de maillage sont des aides à la conception complémentaires aux essais en soufflerie.

ABSTRACT

aerospatiale Tactical Missile Division has been using ramjets on its missiles for more than thirty years and studies the adaptation of this kind of propulsion to very high speed aircraft and airbreathing launchers.
So we have to study vehicles designed for higher and higher speeds and to optimize more rapidly and at lower cost our airbreathing missiles configurations. Then completed our supersonic air intake design methodology by using CFD for our work in external and internal aerodynamics.
These CFD tools involving Euler and Navier-Stokes codes, and mesh generators are complementary to wind tunnel tests.

1-INTRODUCTION

aerospatiale Division Engins Tactiques utilise la propulsion par statoréacteurs depuis plus de trente ans [Réf.1]. De part la nécessité d'étudier des véhicules conçus pour des vitesses de vol de plus en plus élevées (missiles et lanceurs à statoréacteurs,...), **aerospatiale** a complété sa méthodologie de conception des prises d'air en mettant en œuvre des codes de simulation numérique pour ses travaux en aérodynamique externe et interne. En effet, l'utilisation exclusive de moyens expérimentaux ne suffit plus, en terme de temps et de coût, pour définir et optimiser des prises d'air.

Dans la première partie de cet article, nous rappelons les différents concepts de prises d'air utilisés sur les missiles aérobies à statoréacteur ainsi que les contraintes générales de conception aérodynamique que l'on doit avoir à l'esprit avant d'entreprendre l'étude d'une prise d'air intégrée.

Dans la seconde partie, nous présentons les méthodes de calcul utilisées pour déterminer finement les caractéristiques de l'écoulement capté par les prises d'air de véhicules à statoréacteurs et l'évolution de cet écoulement dans la prise d'air.

Enfin nous présentons les résultats obtenus lors de notre contribution au "Working Group 13" de l'AGARD sur une configuration de prise d'air hypersonique et sur le calcul complet d'une prise d'air supersonique montée sur un fuselage.

2-CONSIDERATIONS GENERALES SUR LA CONCEPTION AERODYNAMIQUE DES VEHICULES AEROBIES

Le développement d'une prise d'air montée sur un véhicule repose sur des calculs en aérodynamique externe et interne, des essais en soufflerie et des essais en vol (Réf.[1]).
La figure 1 présente cette méthodologie sous forme de schéma fonctionnel.

Avant d'entreprendre la conception et l'optimisation d'une prise d'air intégrée sur un véhicule avec des outils de calcul, il est indispensable de connaître les grandes lignes des configurations à étudier, les contraintes induites sur la prise d'air par l'aérodynamique externe du véhicule et les phénomènes physiques auxquels nous serons confrontés.

Nous présentons ci-après, une revue critique des différentes configurations de prises d'air que l'on peut utiliser.

2.1-Forme et aérodynamique des missiles aérobies (Réf. [2] et [3])

2.1.1 -Configurations à section de fuselage circulaire.

Le nombre, la forme et la position des prises d'air doivent être choisis en prenant en compte les aspects suivants :
-performance interne: poussée, ISI (Impulsion Spécifique);
-aérodynamique externe: traînée, finesse;
-contraintes opérationnelles: encombrement (emport sous avion), discrétions électromagnétique (SER) et infrarouge (SIR);
- Pilotage/Guidage: "tous azimuts" ou "type avion".
Plusieurs types de configurations sont présentés sur la figure 2.

*Prise d'air unique
- Prise d'air frontale :
Cette prise d'air permet des efficacités élevées, mais est difficilement intégrable. Elle n'est plus utilisée;
- Prise d'air annulaire
L'intégration de ce type de prise d'air est meilleur que celui de la précédente mais les performances sont mauvaises en incidence;
- Prise d'air nasale ("en menton")
Cette prise d'air est bien adaptée au pilotage "type avion" et est utilisée pour les missions longue portée. Elle utilise l'intrados du missile comme une surface de compression supersonique;

- Prise d'air ventrale
Cette configuration est une excellente solution. La compacité est bonne, les fonctions détection, charge militaire et propulsion sont séparées et les performances sont élevées;
- Prise d'air dorsale
Cette configuration a des limites en incidence. Cependant, elle possède les meilleures caractéristiques au niveau de la SER (la prise d'air est masquée vis à vis des radars terrestres);

*Deux prises d'air latérales (Exemple: Missile ASMP Air Sol Moyenne Portée)
Une configuration de missile avec deux prises d'air latérales est bien adaptée au pilotage "type avion". Les prises d'air sont diamétralement opposées ou inclinées vers l'intrados. Le premier cas est le meilleur au point de vue de l'alimentation de la chambre de combustion et de l'augmentation de portance due aux manches à air. Le second cas permet des performances plus élevées des prises d'air;

*Trois prises d'air latérales
Elle peuvent être toutes identiques (adapté au pilotage "tous azimuts") ou composées de deux prises identiques et d'une prise différente à l'intrados (adapté au pilotage "type avion");

*Quatre prises d'air latérales (Exemple: Missile ANS Anti Navire Supersonique)
Une configuration de missile munie de quatre prises d'air latérales est bien adaptée au pilotage "tous azimuts" (le meilleur pour une manœuvrabilité élevée). Cependant, pour les fortes incidences les prises d'air d'extrados atteignent leur limite opérationnelle et la finesse de ce type de configuration n'est pas optimale (deux prises d'air sont suffisantes pour assurer la portance, les deux autres augmentent la traînée).

Pour toutes ces configurations, la forme des prises d'air peut être axisymétrique, semi-axisymétrique, rectangulaire (classique ou inversée) - Cf figure 3.

En ce qui concerne la position longitudinale sur le fuselage, elle résulte d'un compromis entre l'écoulement autour du fuselage, la longueur du diffuseur, le centre de poussée et le système de fixation sur le missile. Cependant la force normale est peu modifiée.

2.1.2 Configurations à section de fuselage non circulaire

Certaines formes typiques de missiles aérobies hypersoniques sont présentées sur la figure 4.

Les objectifs de ces configurations sont :
-une intégration optimale des prises d'air vis-à-vis de l'écoulement sur l'avant-corps,
-une traînée minimale,
-une finesse élevée,
-une SER et SIR faibles,
-une bonne intégration sous le lanceur.

Différentes formes sont possibles : "waverider", missile à section elliptique, triangulaire ou carrée,...
La figure 4 présente deux exemples :
- les "waveriders" qui sont conçus pour minimiser la traînée et maximiser la portance.
- la forme lenticulaire qui est conçue pour une finesse importante à section droite donnée et pour une portance importante en incidence (le bord d'attaque pointu génère une portance tourbillonnaire).

2.1.3 -Les problèmes de l'aérodynamique externe des missiles

Du point de vue de l'aérodynamique externe, les missiles aérobies peuvent être classés en deux familles :
-configurations avec des prises d'air nasales, "en menton" ou annulaires;
-configurations avec des prises d'air latérales. Seules ces prises d'air ont une influence sur la portance, la stabilité et la traînée du fuselage.

La contrainte de traînée minimale doit toujours être présente dans la conception d'une prise d'air. En effet, la traînée des prises d'air peut être très importante, et peut, par exemple, s'élever à 38% de la traînée totale dans le cas d'un missile supersonique à quatre prises d'air axisymétriques volant à Mach 2 au niveau du sol.
Pour optimiser la traînée, nous devrons donc étudier avec précision le bilan traînée-poussée.

Pour ce qui concerne l'écoulement capté par les prises d'air, il est indispensable d'avoir une bonne connaissance du champ aérodynamique autour de l'avant-corps.

En effet, pour obtenir des performances importantes, un écoulement à faible vitesse est souhaité, tandis que l'on cherche à éviter les écoulements à faible énergie (couche limite, tourbillons). L'écoulement capté par les prises d'air doit être aussi homogène que possible et de niveau de pression totale compatible avec le bon fonctionnement du moteur.

Un problème délicat concerne les tourbillons d'ogive qui apparaissent sur l'extrados des missiles pour les incidences supérieures à 5° environ (cf. figure 5). Ces tourbillons créent des pertes très importantes de pression totale dans les prises d'air. Il est à noter que l'adjonction d'arêtes longitudinales en amont des prises d'air modifie le développement naturel de la couche limite autour du fuselage et peut permettre de déplacer les tourbillons en dehors des prises d'air. (cf. figure 5 et Réf. [4])

2.1.4 -Les problèmes de l'aérodynamique interne des missiles

Les principales caractéristiques aérodynamiques à déterminer sont :
-coefficients de débit du diffuseur et du piège à couche limite interne, efficacité, traînée additive de sous-adaptation et traînée de carène, pour un vaste domaine de nombre de Mach, d'incidence et d'altitude,
-les répartitions de pression et de température sur les parois des prises d'air pour concevoir les structures.

Elles dépendent de phénomènes physiques complexes tels que:
-couche limite,
-interactions choc/choc et choc/couche limite,
-turbulence,
-écoulement de coin,
-écoulement dans les pièges à couche limite.

Compte tenu de cette complexité, l'étude d'une prise d'air est généralement décomposée en deux étapes.
Dans un premier temps, on l'étudie isolément en prenant comme données les valeurs moyennes de l'écoulement

externe que capte la prise d'air (nombre de Mach local, pression totale locale, incidence locale, dérapage local,...). Mais cette méthode simplifiée n'est pas parfaite et, dans la phase de développement du projet, une étude avec le champ aérodynamique réel capté par les prises d'air est indispensable.

2.2 - Problèmes aérodynamiques des prises d'air d'avions et de lanceurs spatiaux

aerospatiale a également été amenée à étudier l'application de la propulsion par statoréacteur à des avions à très grande vitesse (AGV) et des lanceurs spatiaux (STS2000).

Comme pour les missiles, l'intégration des moteurs sur les véhicules crée une très forte interaction entre cellule et système propulsif (cf. Etudes NASP(USA) et STS 2000).

Sans rentrer dans le détail de la conception de ce type de prises d'air, on peut noter que:
-pour les avions de transport civil, l'optimisation de la configuration est faite pour le vol de croisière à faible incidence. La prise d'air sera donc très soignée au niveau efficacité utilisable et traînée. Pour exemple, on peut donner une équivalence des pertes de charge utile en fonction des pertes de rendement des prises d'air pour un avion civil supersonique (Mach 2): 1% d'efficacité en moins induit 2,5% de charge utile en moins.
-pour les lanceurs spatiaux, c'est la capacité d'accélération des moteurs que l'on veut exploiter. Alors les prises d'air vont fonctionner sur une grande plage de nombre de Mach. Elles devront donc souvent être à géométrie variable et optimisées pour tout le domaine de vol.

3 -LES METHODES DE CALCUL

3.1 -Aérodynamique externe

Comme nous l'avons souligné plus haut, si nous voulons concevoir des prises d'air intégrées à un véhicule, nous devons connaître l'écoulement capté, en particulier les valeurs locales de la pression totale, du nombre de Mach, de l'incidence, du dérapage ainsi que la hauteur de la couche limite sur le fuselage. Toutes ces caractéristiques peuvent être obtenues par des calculs tridimensionnels autour de l'avant-corps.

Les outils numériques que nous utilisons sont basés sur des méthodes Euler, avec couplage couche limite éventuel, et P.N.S. (Parabolized Navier-Stokes).

Cependant, dans les applications présentées ici, la faible incidence et le nombre de Reynolds élevé justifient, dans une première approximation, l'utilisation des équations d'Euler. Aussi, dans la présente communication, nous nous limiterons à une description rapide et à quelques applications du code FLU3C.
Ce code, développé en coopération étroite entre l'ONERA et **aerospatiale** (Réf. [5]) résout les équations d'Euler tridimensionnelles sous forme conservative. On utilise un schéma de type volumes finis, explicite en temps et le calcul décentré des flux, suivant l'approche de Van Leer, assure à la méthode une grande robustesse. La précision d'ordre deux en temps et en espace est assurée par l'utilisation d'un schéma prédicteur-correcteur de type MUSCL. Pour les calculs supersoniques, une technique d'accélération de convergence de type marche en espace permet un gain important en temps de calcul.

Pour générer le maillage, nous utilisons un mailleur elliptique plan résolvant les équations de Poisson. Les fonctions de contrôle sont déterminées automatiquement, selon le schéma mis au point par Steger et Sorenson (Réf. [6]), par spécification de l'espacement et de l'orientation des mailles au voisinage des frontières. Ce type de mailleur est bien adapté à la technique de marche en espace.

Pour montrer les capacités de ce code, nous présentons quelques applications industrielles sur un missile aérobie, un lanceur et un avion à très grande vitesse pour lesquels nous étudions la motorisation par statoréacteurs.

-Le missile anti-navire supersonique ANS à statoréacteur
L'ANS est un projet de missile aérobie étudié conjointement avec MBB pour succéder à la famille de missiles anti-navires EXOCET.
La figure 6 présente la répartition du coefficient de pression sur la surface du missile. Le calcul a été réalisé pour un nombre de Mach de vol de 2, et une incidence de 4 degrés. Cet exemple montre la capacité de FLU3C à calculer des géométries aérobies très complexes.

-Le système de transport spatial futur STS 2000
Le STS2000 est un ensemble de projets **aerospatiale** de lanceurs spatiaux aérobies réutilisables mono-étage, bi-étage ou mono-étage à statoréacteurs largables. C'est cette dernière configuration munie de quatre statoréacteurs que nous présentons. Les statoréacteurs sont équipés de quatre prises d'air rectangulaires à compression mixte simulées par une prise d'air équivalente fonctionnant de Mach 2 à Mach 6 avant largage.
La figure 7 présente le maillage et la répartition du coefficient de pression sur la surface du lanceur.
Le calcul Euler a été réalisé pour un nombre de Mach de vol de 5 et une incidence de 4 degrés.
Pour ce type de configuration, les calculs Euler sont principalement utilisés pour déterminer les caractéristiques de l'écoulement dans la section de captation de la prise d'air, les coefficients globaux de portance et de moment, ainsi que la répartition de vitesse sur la surface du lanceur pour effectuer un calcul d'épaisseur de couche limite au droit de la prise d'air.
La figure 8 montre l'écoulement dans un plan transverse passant par l'apex de la première rampe de la prise d'air. Les lignes iso - (pression totale locale /pression totale amont) et iso-Mach sont représentées. Ceci nous permet de connaître finement l'écoulement capté par la prise d'air et d'optimiser l'avant-corps en conséquence.

-L'avion à Grande Vitesse (A.G.V.)
L'AGV est un projet **aerospatiale** d'avion de transport commercial hypersonique (Mach 5 en croisière). Il utilise un mode de propulsion par turbo-réacteurs jusqu'à un nombre de Mach de 3 et ensuite il est propulsé par des statoréacteurs jusqu'à la vitesse de croisière, à Mach 5.
La figure 9 présente la répartition du coefficient de pression sur le corps de l'avion pour un nombre de Mach de vol de 4,5.

3.2 - Aérodynamique interne

Les outils que nous utilisons actuellement sont basées sur:
a) des méthodes analytiques et une base de données expérimentales,
b) des méthodes numériques.

a) - Méthodes analytiques et base de données expérimentales

Le but est d'obtenir aussi rapidement que possible et à faible coût, une estimation suffisamment précise des performances d'une prise d'air prédéfinie géométriquement, afin d'évaluer la poussée du moteur.

Un programme bidimensionnel plan, fondé sur des calculs analytiques de chocs, fournit l'efficacité de compression critique (η_{O2} critique) et le coefficient de débit total (ε_T) entrant dans une prise d'air supersonique de section rectangulaire. Le code de calcul prend en compte le fonctionnement critique de la prise d'air avec le choc droit terminal accroché à la lèvre de carène. Ce point critique est défini ici par la position, sur la courbe caractéristique de la prise d'air, pour laquelle l'efficacité de compression et le coefficient de débit total entrant sont maximaux.

La figure 10 illustre cette méthode pour une prise d'air supersonique à compression externe. Le calcul fournit les caractéristiques de l'écoulement sur les rampes de compression externe d'une prise d'air supersonique et nous permet de déterminer l'efficacité de compression maximale et le coefficient de débit total.

Cette approche est complétée par l'utilisation d'une base de données expérimentales résultant des différents essais en soufflerie.

b) - Méthodes numériques

Les outils numériques utilisés pour les calculs d'aérodynamique interne sont de type Euler ou Navier-Stokes, et la discrétisation des équations est faite sur des maillages structurés.

-Code Euler FLU3M

Actuellement, pour la conception en aérodynamique interne, nous effectuons principalement des calculs Euler 2D et 3D. Bien que les équations d'Euler ne prennent pas en compte les phénomènes visqueux, importants en aérodynamique interne, de tels calculs permettent d'analyser l'écoulement dans toute la prise d'air, même avec un piège à couche limite interne, et d'estimer le coefficient de débit, l'efficacité de compression et les pressions sur les parois.

Pour traiter des géométries très complexes et pour raffiner le maillage dans certaines zones critiques, il est nécessaire d'adopter une stratégie multidomaine. Ce choix simplifie considérablement la construction du maillage et permet de s'affranchir de certaines difficultés propres aux maillages structurés. Cette stratégie multidomaine est utilisée dans le code FLU3M développé par l'ONERA en collaboration avec **aerospatiale** (Réf. [7] et [8]).

FLU3M est un code qui résout les équations d'Euler tridimensionnelles par une méthode instationnaire. Le schéma numérique utilisé repose, comme dans FLU3C (Cf. 3.1), sur une discrétisation décentrée de type volumes finis. Pour le calcul des flux de convection-pression, différentes approches sont disponibles: VAN LEER, ROE, OSHER, et la précision du second ordre en espace est obtenue au moyen de l'approche MUSCL. Dans sa version implicite, le code utilise une technique de factorisation de type ADI plan par plan, couplée à une méthode de relaxation GAUSS-SEIDEL dans la troisième direction. Le traitement des conditions aux limites est réalisé soit par relations de compatibilité, soit par calcul des flux. FLU3M peut également être utilisé pour des calculs axisymétriques et bidimensionnels plans.

Configurations calculées avec FLU3M

La figure 11 présente les lignes iso-nombre de Mach dans une prise d'air supersonique, à compression mixte (M3), calculée isolément. Elle est le résultat d'un calcul bidimensionnel plan par un algorithme explicite. La décomposition topologique en quatre domaines permet de traiter les rampes de compression, la carène, le piège à couche limite interne et le diffuseur. Le nombre de Mach amont est de 2,89 et l'incidence de 0 degré.
On observe les chocs de compression externe, les chocs de carène et le choc droit terminal près de l'entrée du piège à couche limite interne qui limite l'écoulement supersonique.

Lors des essais en soufflerie, le fonctionnement du moteur est simulé par un obturateur placé en fin de diffuseur. Dans le calcul, deux solutions sont envisageables:
-soit imposer une contre-pression P2 (c'est le cas pour la figure 11),
-soit ajouter en fin de diffuseur une géométrie avec col adapté et divergent qui effectue un blocage en débit imposant à l'amont une pression statique.

La figure 12 montre une comparaison entre le calcul Euler de la figure 11 et une visualisation strioscopique obtenue en soufflerie pour cette configuration de prise d'air isolée. La comparaison montre une bonne corrélation calcul/essais en particulier pour la position des chocs dans cette configuration complexe.

La figure 13 présente une comparaison calcul/essais de la pression statique sur les parois inférieure et supérieure du diffuseur pour cette même prise d'air. Le calcul a été réalisé avec ou sans piège à couche limite interne.
L'effet du piège est de déplacer le choc droit terminal vers l'amont et sa prise en compte est nécessaire pour obtenir une bonne corrélation avec les résultats expérimentaux (confirmation des résultats de la figure 12). On constate donc que l'écoulement dans la prise d'air peut être correctement représenté dans le cadre d'une stratégie "Euler". L'écoulement réel dans le piège reste cependant dominé par les effets visqueux et c'est principalement la perte de débit due au piège et la pression statique dans la zone d'eau morte tourbillonnaire à l'entrée du piège qui est ici simulée par le calcul.

Ce type de calcul permet de simuler différents régimes de fonctionnement de la prise d'air (du régime supercritique au régime subcritique) par augmentation de la contre-pression P2 en fin de diffuseur. On peut ainsi déterminer la courbe caractéristique (efficacité en fonction du débit en fin de diffuseur) dont une comparaison calcul/essais est présentée sur la figure 14. Les calculs au voisinage du point critique de fonctionnement nécessitent cependant certaines précautions (instabilité du choc droit).

Deux autres applications sont données à titre d'exemples et traitées plus brièvement.

La figure 15 présente la répartition de nombre de Mach sous forme de dégradés de couleur et de lignes iso-valeur pour un calcul 2D d'une prise d'air supersonique générique isolée. Pour cette configuration, une tuyère avec col dans le piège à couche limite interne simule le fonctionnement réel du piège dans les essais en soufflerie. Le nombre de Mach à l'amont est de 2,6 et l'incidence de zéro degré. Le calcul représente un cas de fonctionnement supercritique de la prise d'air.

La figure 16 présente les lignes iso-nombre de Mach et des lignes de courant dans une prise d'air axisymétrique d'un

projet d'avion supersonique. Le piège à couche limite interne est pris en compte dans le calcul. Le calcul axisymétrique de la prise d'air isolée a été effectué pour un nombre de Mach de 2 et une incidence de zéro degré pour un fonctionnement critique de la prise d'air (le choc droit terminal est accroché à la lèvre de carène).

-Code Navier-Stokes NS2D

Pour certains calculs d'aérodynamique interne, nous utilisons le code Navier-Stokes moyenné bidimensionnel NS2D développé par l'ONERA (Réf. (9)). La méthode de résolution pseudo-instationnaire utilisée met en œuvre un schéma explicite en temps, centré en espace, de type volumes finis, combiné à une technique d'accélération de convergence multigrille. Deux modèles de turbulence algébriques sont disponibles: le modèle de Baldwin-Lomax (Réf.(10)), et le modèle de Michel (Réf.(11)).
Ce type de simulation reste coûteux et n'est encore utilisé que de manière ponctuelle.

Une comparaison entre un calcul bidimensionnel (Euler) FLU3M et un calcul NS2D pour la prise d'air M3 est présentée sur la figure 17.
Pour ces calculs, un col fixe a été imposé dans le piège à couche limite interne tandis que dans le diffuseur un col de section variable permet de parcourir la courbe caractéristique.
Le calcul NS2D représente les effets visqueux tels que le décollement résultant de l'interaction du choc terminal et de la couche limite. On s'aperçoit sur la figure 17 que le calcul Navier-Stokes fournit un choc terminal situé légèrement en amont de celui obtenu par le calcul Euler (la couche limite réduit la section de passage dans le diffuseur). Ce résultat permet une meilleure corrélation avec les essais pour ce fonctionnement supercritique.

La figure 18 présente une visualisation d'un calcul NS2D sur la prise d'air M3 au niveau de l'orifice du piège à couche limite interne. On observe bien la captation de la couche limite, le tourbillon engendré dans le piège (Réf.[12]) et le décollement de couche limite dans le diffuseur induit par l'interaction du choc droit terminal sur la couche limite de paroi.

3.3 - Cas tests réalisés pour l'AGARD FDP Working Group 13

Notre participation au WG13 de l'AGARD nous a permis de tester nos outils de calcul concernant l'étude de prises d'air supersoniques et hypersoniques.
Deux cas ont été étudiés:
-le cas test 6 portant sur la prise d'air hypersonique NASA P8
-le cas test 8 portant sur le calcul de la prise d'air Tailor Mate A-1 montée sur fuselage.

-Cas test 6: prise d'air NASA P8

La figure 19 présente la configuration d'une prise d'air générique de superstatoréacteur (prise d'air NASA P8) étudiée en vue de la motorisation d'un véhicule hypersonique évoluant à un nombre de Mach de 12.
La figure 20 montre les résultats obtenus par un calcul Euler bidimensionnel plan sur la prise d'air NASA P8. Les répartitions de nombre de Mach et de pression statique fournissent des renseignements intéressants pour la compréhension de l'écoulement. Les profils de pression sur le corps central et la surface interne de la carène ont été tracés en fonction de l'abscisse. Les résultats sont assez proches des essais sauf au niveau du pic de pression induit sur la surface de la carène par la reflexion du choc interne sur le corps central. Ce pic de pression n'est pas bien positionné par le calcul du fait de la non prise en compte des interactions choc/couche limite.
La figure 21 présente les résultats obtenus dans ce même cas à l'aide du code NS2D. La visualisation du profil de vitesse tangentielle sur une normale à la rampe de compression permet de contrôler l'évolution de la couche limite. La visualisation du profil de nombre de Mach dans la section du bord d'attaque de carène permet de s'apercevoir de la très bonne corrélation calcul/essais jusqu'à la paroi. Les profils de pression statique sur le corps central et sur la paroi interne de la carène ont été tracés en fonction de l'abscisse. Une très bonne corrélation calcul/essais a été obtenue même après les interactions choc/couche limite.

-Cas test 8: prise d'air Tailor Mate A-1 sur fuselage

La configuration étudiée est présentée sur la figure 22. Il s'agit d'un avion de type F15 muni d'une prise d'air de section rectangulaire Tailor Mate A-1.
Les essais réalisés par GENERAL DYNAMICS (Fort Worth Division) fournissent les paramètres aérodynamiques dans le plan de captation des prises d'air ainsi que les pressions dans le conduit interne de la prise d'air.
Pour traiter cette configuration, nous avons utilisé notre code Euler tridimensionnel FLU3M couplé à la procédure de maillage multidomaine exposée sur la figure 23.
Avant de générer un maillage, il faut déterminer les limites géométriques conformes avec la surface de l'objet. Ainsi, les surfaces doivent être définies et une série de points surfaciques représentatifs de ces surfaces doivent être retenus comme conditions aux limites pour le mailleur. Afin de définir géométriquement les surfaces et de définir des points représentatifs pour le mailleur, un système de CAO est utilisé. La procédure de maillage adoptée est construite autour de l'outil de décomposition topologique MULCAD et du mailleur transfini PADAMM (Réf. [13]).
Les figures 24 et 25 présentent la décomposition topologique, sur une demi-configuration formée de 11 domaines.
Cette méthode permet de traiter tous les détails géométriques: fuselage avec cockpit, piège à couche limite externe, conduit interne de la prise d'air et piège à couche limite interne. Un maillage structuré en H est généré dans chaque domaine pour un nombre de points, sur l'ensemble des 11 domaines, de 882000.
Le figure26 présente une partie du maillage sur le corps de l'avion et dans le plan de symétrie de la configuration ainsi que la visualisation de lignes isobares dans le plan de symétrie et sur la surface de l'avion. On observe bien le choc conique de tête, le choc devant le cockpit, la détente en arrière du cockpit, le choc induit par le piège à couche limite externe et les chocs internes dans la prise d'air.
La figure 27 présente le maillage surfacique de la configuration symétrisée ainsi que la répartition pariétale de nombre de Mach pour un nombre de Mach de vol de 2,2 et une incidence de zéro degré. On observe la compression dans la prise d'air où le choc droit terminal fait passer l'écoulement du régime supersonique au régime subsonique. Le point de fonctionnement critique de la prise d'air est simulé en imposant une contre-pression en fin de diffuseur et en fin de piège à couche limite interne.
La figure 28 présente une comparaison calcul /essais au niveau de la répartition de nombre de Mach dans la section transverse de captation de la prise d'air. Les calculs fournissent une répartition assez proche de celle des essais même si le phénomène d'accroissement du nombre de Mach dans les zones proches du fuselage n'est pas bien simulé. Les différences calcul/essais obtenues restent cependant de l'ordre de 2%.

4 - CONCLUSION

En mettant en œuvre des outils numériques adaptés à l'étude de ses prises d'air supersoniques , **aerospatiale** Division Engins Tactiques se donne des moyens d'aide à la conception, complémentaires aux expérimentations en soufflerie.
Cette méthodologie permet d'optimiser plus rapidement et à moindre coût les configurations nouvelles de missiles aérobies.
De plus, ces outils permettent d'étudier les futurs véhicules hypersoniques propulsés par statoréacteurs ou superstatoréacteurs pour lesquels l'utilisation des moyens expérimentaux devient très coûteuse voire impossible.

REMERCIEMENTS

Nous remercions C. Stylemans pour sa participation à la réalisation des calculs présentés dans cet article.

REFERENCES

[1] Garnero, P.; Chevalier, A.; Lacau, R.G.:
"Ramjet Applications at **aerospatiale**"
The third joint Europe/U.S. short course in hypersonics - Aachen October 1990 .

[2] Lacau, R. G: "A Survey of Missile Aerodynamics " Missile Aerodynamics - Conference in Honor of Dr. Jack Nielsen - Monterey, California, November 1988.

[3] Laruelle, G.: " Missiles intakes"
Lecture Series Programme Intake Aerodynamics, VKI, Bruxelles- February 1988.

[4] Laruelle, G.: " Internal Aerodynamics of Air Breathing Missiles"
10 th ISABE - Nottingham - September 1991.

[5] Borrel, M.; Montagné, J.L.; Diet, J.; Guillen,P; Lordon, J. : "Méthode de calcul d'écoulements supersoniques autour de missiles tactiques à l'aide d'un schéma décentré"
La Recherche Aérospatiale - Mars-Avril 1988.

[6] Sorenson, R.L.: "A computer program to generate two-dimensional grids about airfoil and other shapes by the use of Poisson's equations".
NASA Ames Research Center, NASA TM-81198.

[7] Guillen, P.; Borrel, M.; Dormieux, M.: "Numerical simulation of perfect fluid flows around complex 3D configurations by a multidomain solver using the MUSCL approach "
Conference GAMNI/SMIA-IMA sur les Méthodes de Calcul en Mécanique des Fluides Appliquées à l'Aéronautique Antibes, Mai 1989.

[8] Guillen, P. ; Dormieux, M. :"Design of a 3D Multidomain Euler Code" Supercomputing in Fluid Flow - Boston October 1989.

[9] Cambier, L.; Veuillot, J.P. & Vuillot, A.M.:
"Développement récents sur les méthodes de calcul d'écoulements internes par résolution des équations d'Euler ou de Navier-Stokes"-ONERA - Revue française de Mécanique n°1988-4.

[10] Baldwin, B.S.; Lomax , H.: "Thin Layer Approximation and Algebric Model for Separated Flows" AIAA Paper 78-257.

[11] Michel, R. ; Quenard, C.; Durand, R.: "Application d'un schéma de longueur de mélange à l'étude des couches limites turbulentes"-ONERA, Note Technique No. 154, 1969

[12] Leynaert, J.: "Aspects aérodynamiques des problèmes de prises d'air et de sorties de réacteurs pour un avion de transport supersonique"
Association Technique Maritime et Aéronautique, session 1964.

[13] De la Viuda, J.; Diet, J.; Ranoux, G.: "Patch-Independent Structured Multiblock Grids for CFD Computations"
The Third International Conference on Numerical Grid Generation in Computational Fluid Dynamics. Barcelona, Spain 3-7 June 1991.

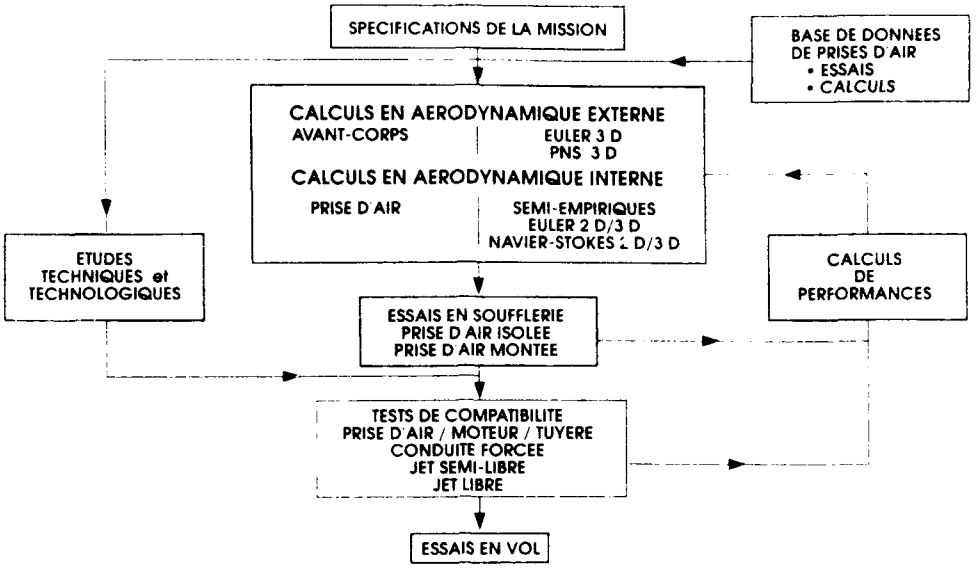

METHODOLOGIE DE DEVELOPPEMENT D'UNE PRISE D'AIR SUPERSONIQUE INTEGREE

Figure 1

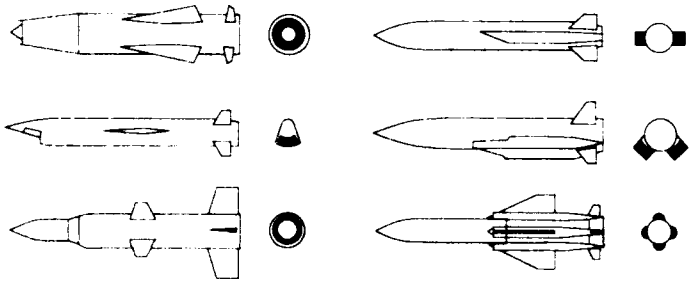

(REF JELL)

DIFFERENTES POSITIONS DE PRISES D'AIR DE MISSILES A STATOREACTEUR

Figure 2

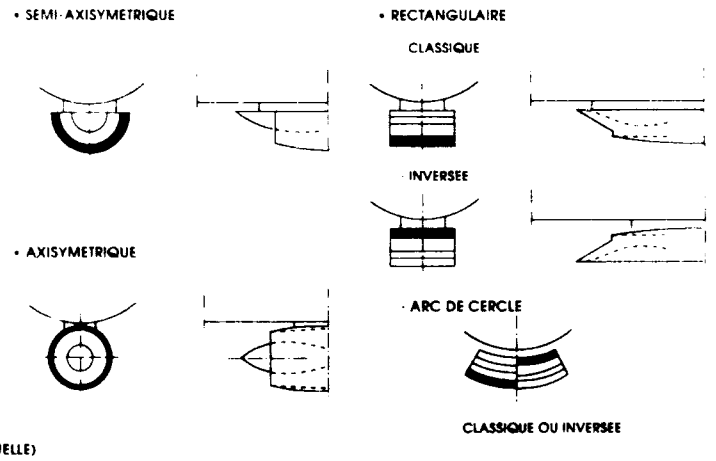

(REF LARUELLE)

PRISES D'AIR VENTRALES

Figure 3

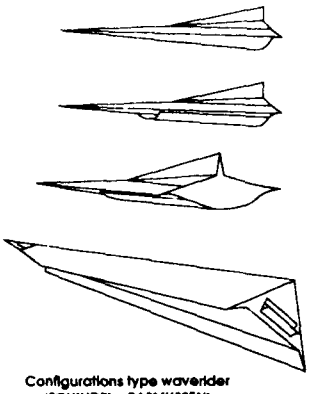

Configurations type waverider
(SCHINDEL - RASMUSSEN)

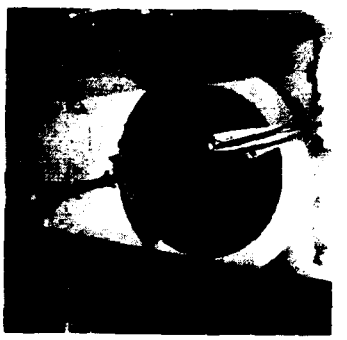

Configuration lenticulaire
(ONERA)

CONFIGURATIONS DE VEHICULES A SECTION DROITE NON CIRCULAIRE

Figure 4

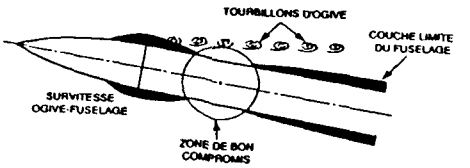

POSITIONNEMENT LONGITUDINAL

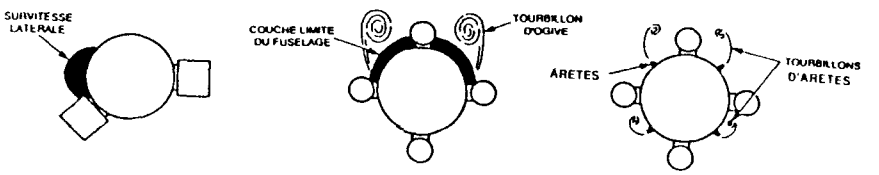

POSITIONNEMENT AZIMUTAL

POSITIONNEMENT DES PRISES D'AIR SUR FUSELAGE

(REF. LABUELLE)

Figure 5

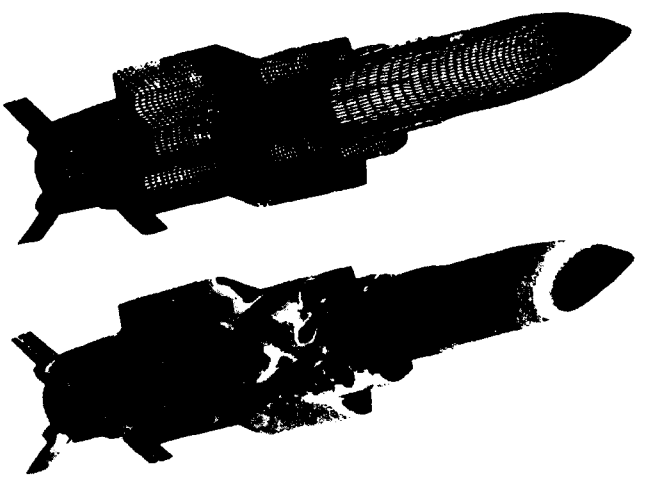

MAILLAGE ET REPARTITION DE PRESSION SUR LE
MISSILE ANTI-NAVIRE ANS A STATOREACTEUR
$M_\infty = 2$

Figure 6

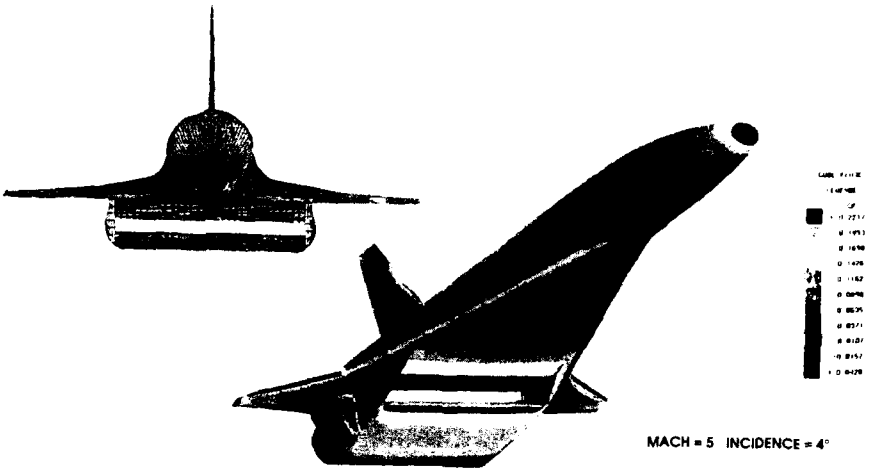

MACH = 5 INCIDENCE = 4°

STS 2000
SYSTEME DE TRANSPORT SPATIAL AEROBIE
CALCUL AERODYNAMIQUE

Figure 7

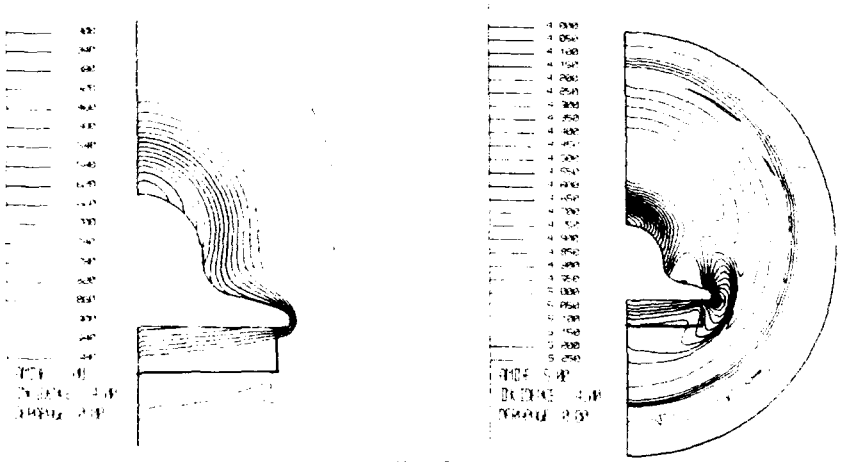

ISO Pt/Pto Δ = 0,04

M∞ = 5
α = 4°

ISOMACH Δ = 0,05

STS 2000 : VISUALISATION DE L'ECOULEMENT AU NIVEAU DE LA SECTION DE CAPTATION DES PRISES D'AIR
CALCUL EULER 3D

Figure 8

CONFIGURATION DE L'AGV

REPARTITION DE COEFFICIENT DE PRESSION
SUR LA SURFACE DU VEHICULE
M∞ = 4,5

CALCUL EULER 3D DE L'AVION A GRANDE VITESSE (AGV)

Figure 9

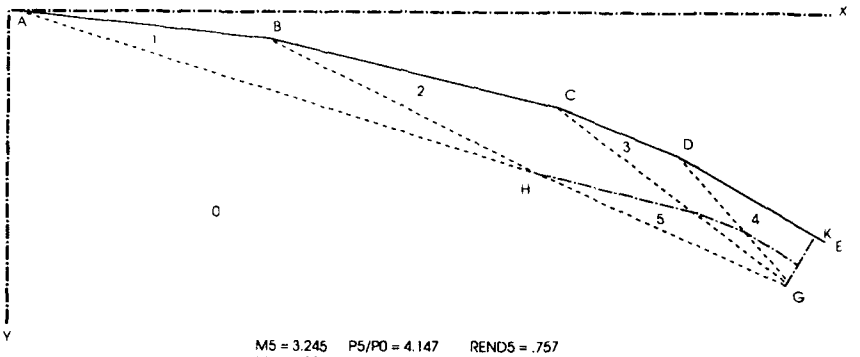

M5 = 3.245 P5/P0 = 4.147 REND5 = .757
M4 = 2.524 P4/P0 = 14.381 REND4 = .882
M3 = 2.908 P3/P0 = 8.132 REND3 = .898
M2 = 3.362 P2/P0 = 4.268 REND2 = .923
M1 = 3.836 P1/P0 = 2.254 REND1 = .948
RENDCOMPEXT = .821 RENDTOT = .404
M0 = 4.500 EPS = 1.080 CAAD = 0.000 CNAD = 0.000
ENTREE D'AIR - COMPRESSION EXTERNE - ALPHA = 1.6

CALCUL ANALYTIQUE 2D D'UNE PRISE D'AIR A COMPRESSION EXTERNE

Figure 10

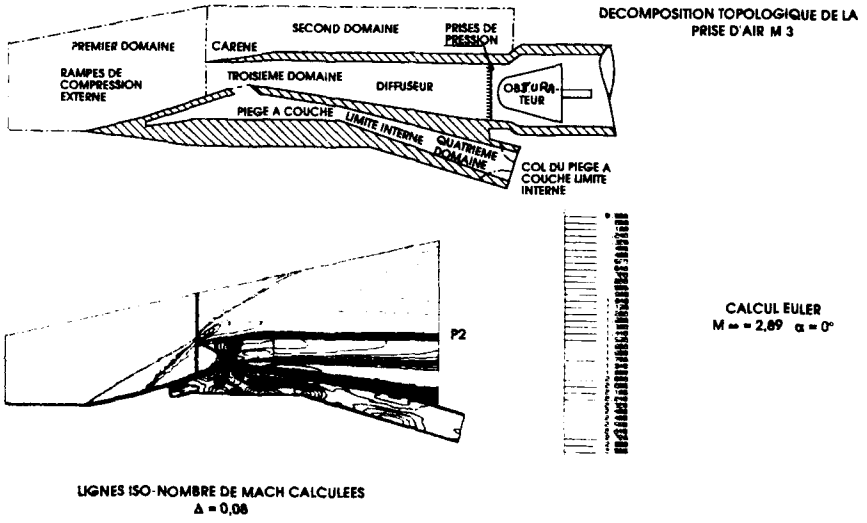

APPROCHE MULTIDOMAINE POUR LE CALCUL D'UNE PRISE D'AIR SUPERSONIQUE

Figure 11

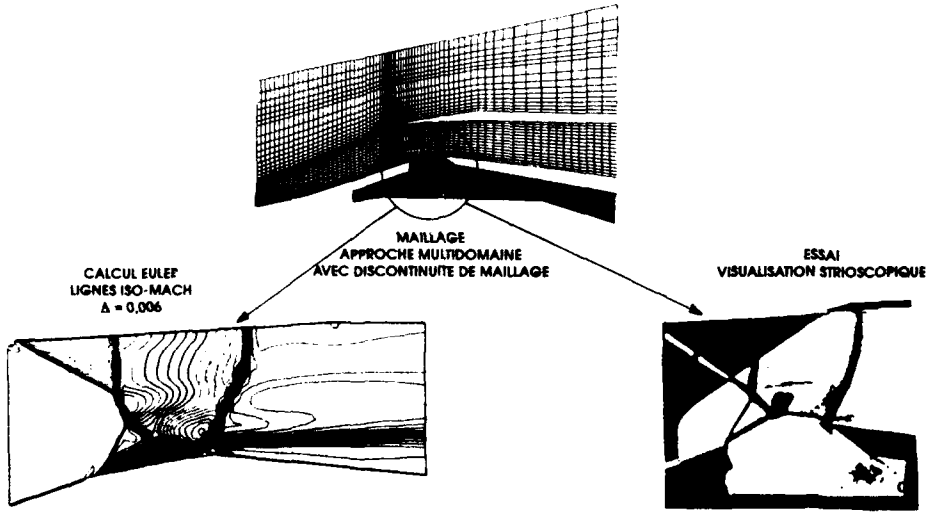

PRISE D'AIR SUPERSONIQUE M3 - ECOULEMENT INTERNE
COMPARAISON ENTRE CALCUL EULER ET ESSAI

Figure 12

SURFACE SUPERIEURE DU DIFFUSEUR

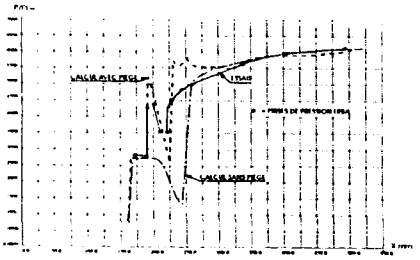

P/Pi ∞ EN FONCTION DE X - CALCUL SANS PIEGE ET AVEC PIEGE

SURFACE INFERIEURE DU DIFFUSEUR

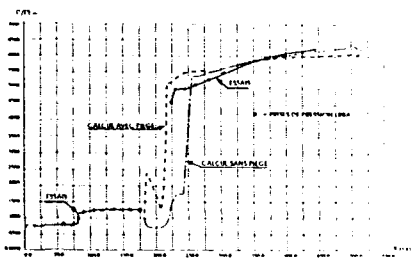

P/Pi ∞ EN FONCTION DE X - CALCUL SANS PIEGE ET AVEC PIEGE

PRISE D'AIR SUPERSONIQUE M3
COMPARAISON ENTRE CALCUL EULER ET ESSAI

Figure 13

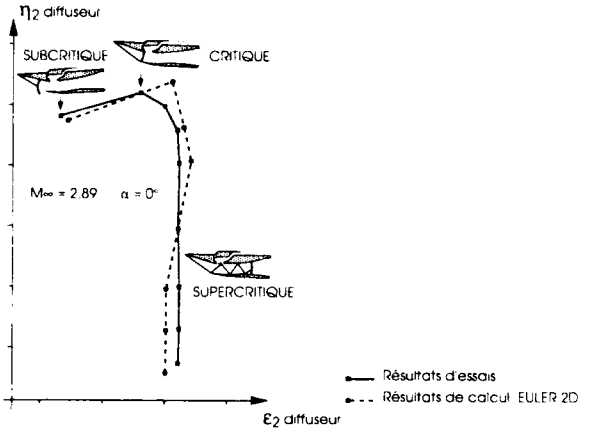

COMPARAISON ENTRE LES COURBES CARACTERISTIQUES EXPERIMENTALE ET CALCULEE POUR LA PRISE D'AIR M3 ISOLEE

Figure 14

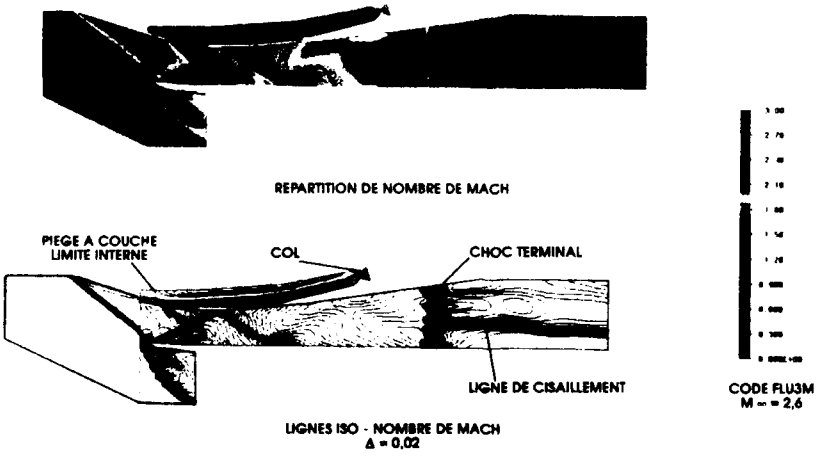

CALCUL EULER 2D D'UNE PRISE D'AIR SUPERSONIQUE DE STATOREACTEUR

Figure 15

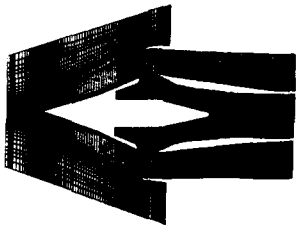

MAILLAGE MULTIDOMAINE

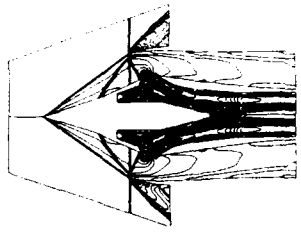

LIGNES ISO - MACH
$M_\infty = 2$ - $\Delta = 0.05$

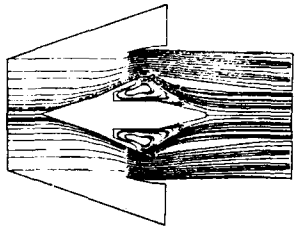

LIGNES DE COURANT

CALCUL EULER D'UNE PRISE D'AIR AXISYMETRIQUE
D'AVION SUPERSONIQUE AVEC PIEGE A COUCHE LIMITE INTERNE

Figure 16

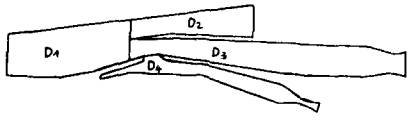

TOPOLOGIE DU MAILLAGE EULER

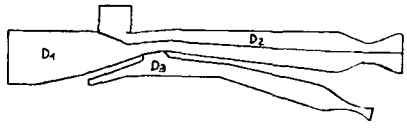

TOPOLOGIE DU MAILLAGE NAVIER-STOKES

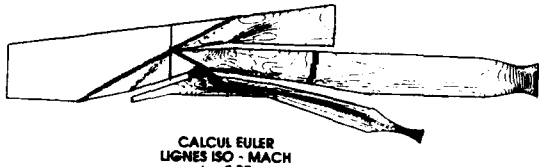

CALCUL EULER
LIGNES ISO - MACH
$\Delta = 0.07$

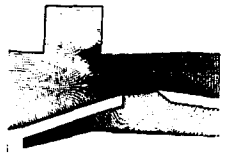

MAILLAGE NAVIER STOKES
PRES DE L'ENTREE DU PIEGE A
COUCHE LIMITE INTERNE

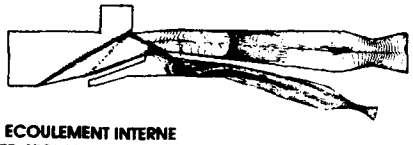

CALCUL NAVIER-STOKES
LIGNES ISO-MACH
$\Delta = 0.07$

PRISE D'AIR SUPERSONIQUE M3 - ECOULEMENT INTERNE
CALCULS EULER ET NAVIER-STOKES 2D
APPROCHE MULTIDOMAINE

Figure 17

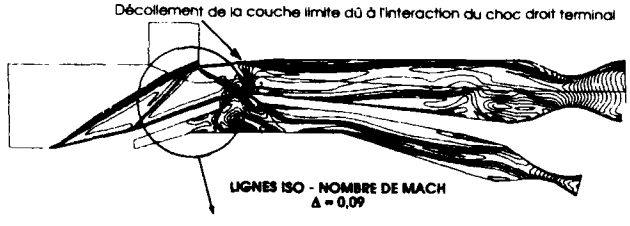

LIGNES ISO - NOMBRE DE MACH
$\Delta = 0,09$

PROFILS DE VITESSE AU
NIVEAU DE L'ENTREE
DU PIEGE A COUCHE
LIMITE INTERNE

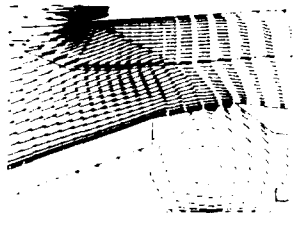

CALCUL NAVIER-STOKES MOYENNE BIDIMENSIONNEL
PRISE D'AIR SUPERSONIQUE M3 AVEC COLS EN FIN DE DIFFUSEUR ET EN FIN DE PIEGE A COUCHE LIMITE

Figure 18

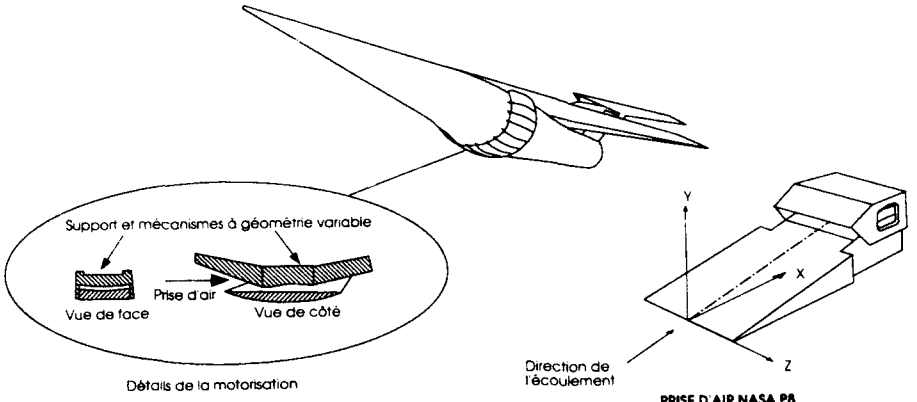

AGARD FDP WG13 - CAS TEST 6
PRISE D'AIR TYPE SUPERSTATOREACTEUR

Figure 19

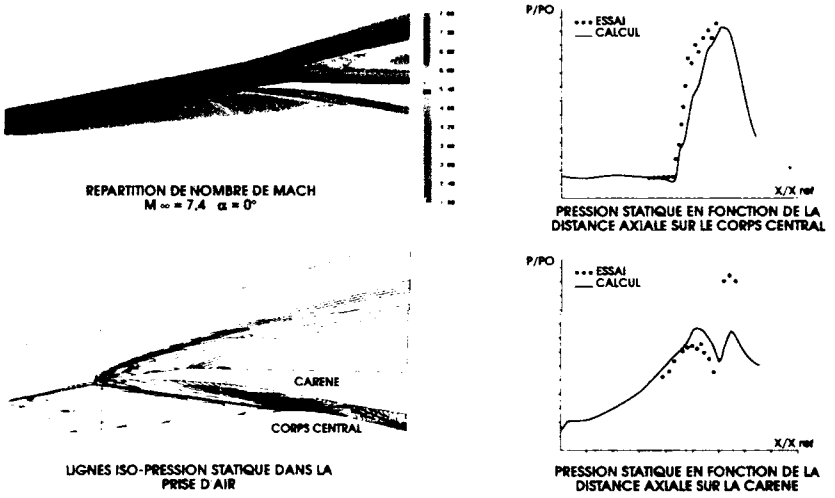

CALCUL EULER 2D DE LA PRISE D'AIR NASA P8

Figure 20

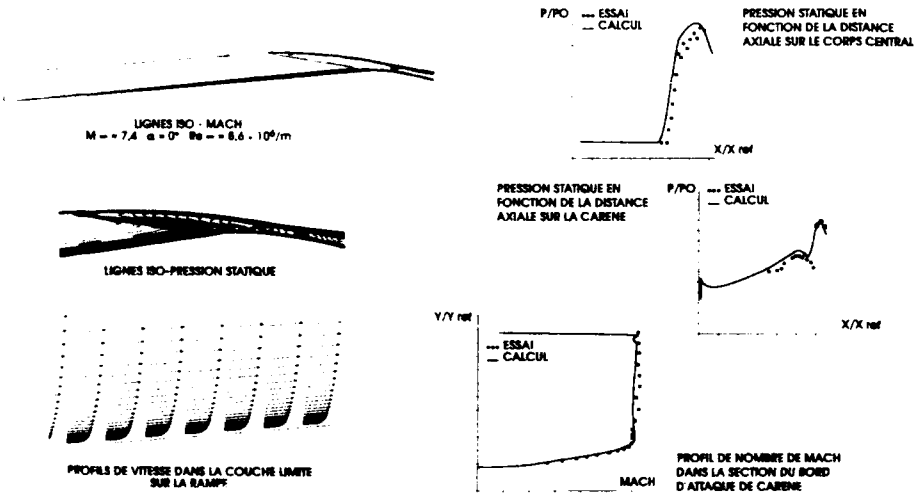

CALCUL NAVIER-STOKES MOYENNE 2D DE LA PRISE D'AIR NASA P8

Figure 21

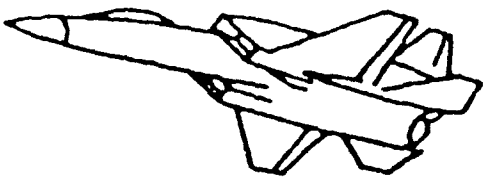

$M_0=2,2$ $\alpha=0°$ $\beta=0°$

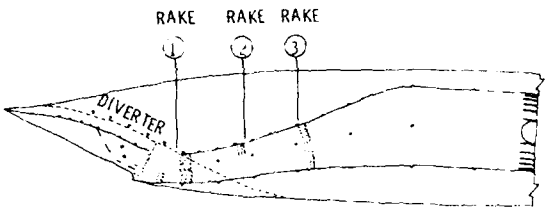

AGARD FDP WG13 - CAS TEST 8
PRISE D'AIR TAILOR MATE A-1 SUR FUSELAGE

Figure 22

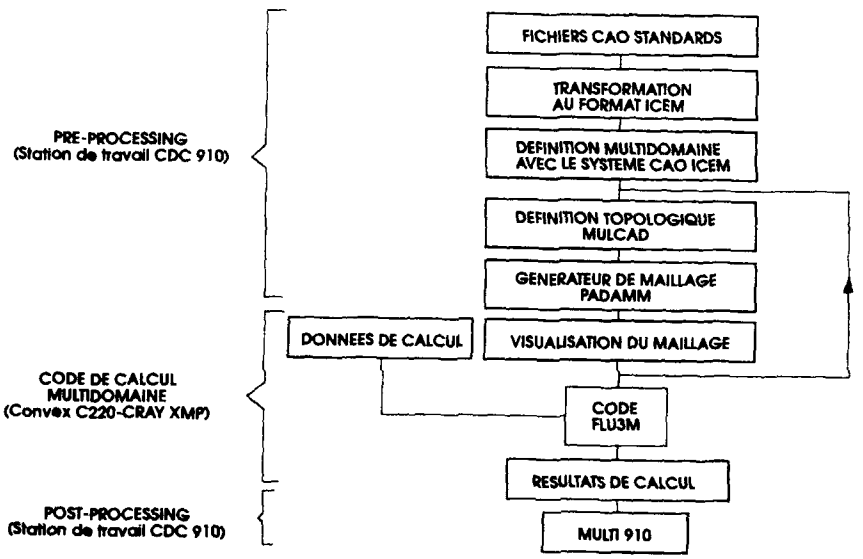

LA PROCEDURE MULTIDOMAINE

Figure 23

PRISE D'AIR TAILOR MATE A-1 AVEC FUSELAGE
AGARD FDP WG 13
CAS TEST N° 8

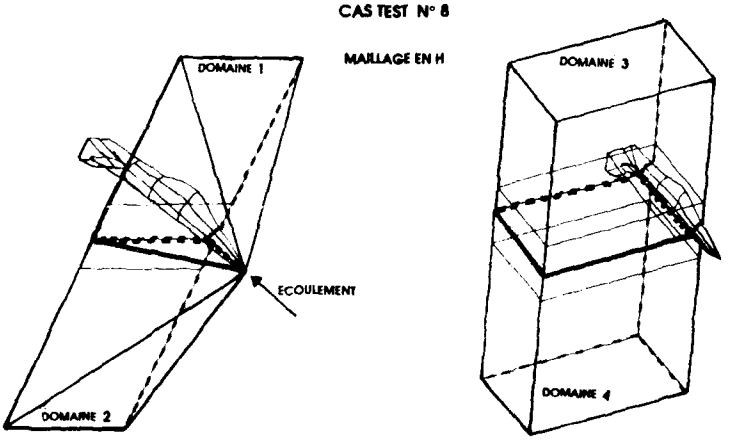

DECOMPOSITION TOPOLOGIQUE POUR UN MAILLAGE MULTIDOMAINES STRUCTURES

Figure 24

PRISE D'AIR TAILOR MATE A-1 AVEC FUSELAGE
AGARD FDP WG 13
CAS TEST N° 8

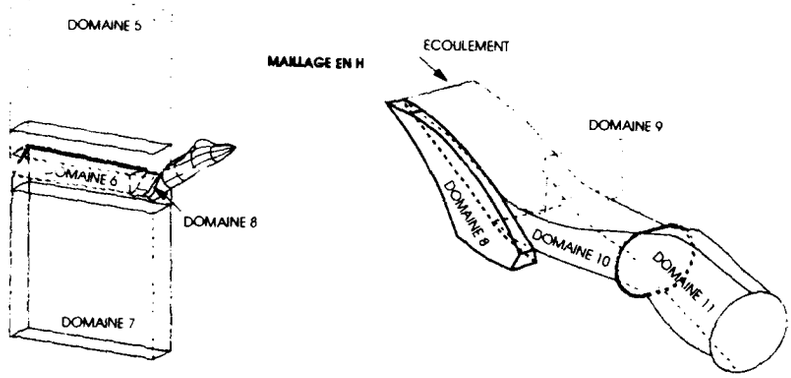

DECOMPOSITION TOPOLOGIQUE POUR UN MAILLAGE MULTIDOMAINES STRUCTURES

Figure 25

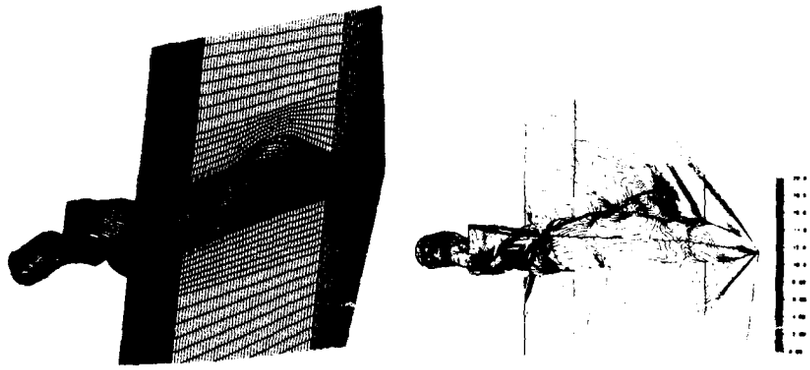

MAILLAGE DE LA CONFIGURATION COMPLETE

LIGNES ISO - (P/P_∞) DANS LA PLAN DE SYMETRIE
ET SUR LA SURFACE DE L AVION
Δ = 0,05

AGARD FDP WG13 - CAS TEST 8
PRISE D'AIR TAILOR MATE A-1 SUR FUSELAGE
CALCUL EULER AVEC FLU3M

Figure 26

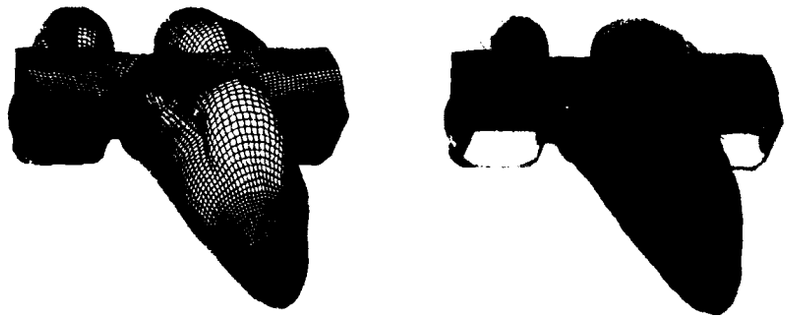

MAILLAGE DE LA CONFIGURATION COMPLETE

REPARTITION DE NOMBRE DE MACH SUR LA SURFACE DE
L'AVION

AGARD FDP WG13 - CAS TEST 8
PRISE D'AIR TAILOR MATE A-1 SUR FUSELAGE
CALCUL EULER AVEC FLU3M

Figure 27

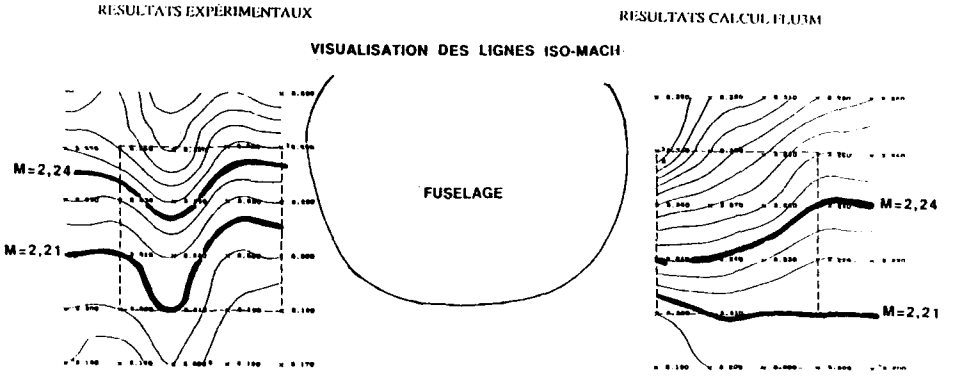

AGARD FDP WG13 - CAS TEST 8
PRISE D'AIR TAILOR MATE A-1 SUR FUSELAGE

COMPARAISON DU CALCUL EULER FLU3M AVEC LES ESSAIS
DANS LA SECTION DE CAPTATION DE LA PRISE D'AIR

Figure 28

APPLICATION OF SUBSONIC FIRST-ORDER PANEL METHODS FOR PREDICTION OF INLET & NOZZLE AERODYNAMIC INTERACTIONS WITH AIRFRAME

Dr. R.K.Nangia & Mr. M.E.Palmer

Consulting Engineers
NANGIA ASSOCIATES
Bristol, BS8 1 QX, UK.

SUMMARY

Modern aircraft require intake and nozzle flows to be closely integrated with the airframe and various layouts are possible. In some cases, the intake/nozzle is integral with the fuselage providing a relatively "compact" layout. This contrasts with configurations in which the nacelles are displaced from the fuselage but are near lifting surfaces.

Engine intake flow conditions may range from very high Mass Flow Ratio (MFR) at take-off, to very low MFR on approach and may include zero MFR during in-flight shut-downs. The effect of the intake flows on adjacent components will vary with intake MFR, aircraft attitude and Mach number. Designers need to know the magnitude of these effects to ensure that they can be contained to satisfactory levels within the available control parameters.

Currently, several types of CFD methods are being developed world-wide, ranging from surface panel to field flow types. The "compact" type layouts have always presented a challenge for all these methods. Estimation of aerodynamic forces is closely linked to the design geometry and panelling of the intake and neighbouring surfaces. Compared with the Panel type methods, the Field Flow methods require the generation of meshes which involve lengthy analysis and are computer intensive. It is therefore considered prudent, to use the more economic Panel methods as far as possible, in the early design phase.

In this paper, a first-order panel method has been used to analyse the MFR effects on several configurations. These range from simple "generic" type to complex, Canard-Delta configurations and include various intake and nozzle arrangements. Mach number and asymmetric effects have been studied in particular cases.

Several useful working techniques have been established. These include rationalising the geometry (complexity and smoothness) and lifting surface intersections. Special techniques were developed to integrate a nacelle for simulation of a compact Canard-Delta configuration.

The panel method results have been encouraging. For the Canard-Delta configuration, good agreement between panel method and Euler results and experiment has been obtained. Analysis of the results has given a better understanding of the possible effects of intake and nozzle flows on neighbouring surfaces. This has led to greater confidence in undertaking more complex configurations in the future.

Areas of further work and future developments have been outlined. These include assessment of viscous effects, comparison of thick and thin nacelle modelling, further effects of wake relaxation and alternative boundary conditions for the first-order panel method.

© *R. K. Nangia & M. E. Palmer*

1. INTRODUCTION

The intake and nozzle flows are required to be closely integrated within the modern aircraft configurations and many variations are possible (Fig.1 a-l). In some cases the intake/nozzle is integral with the fuselage providing a relatively "compact" layout (b, c, e, f, k, l). In others, the nacelles may be displaced from the fuselage but near the lifting surface (d, g, i, j). Pylon-wing layouts (h) represent another possibility often used on high aspect ratio wings.

Engine intake flows affect the flow fields on adjacent components. The effects will vary with intake Mass Flow Ratio (MFR), α, β and Mach number. Designers need to know the magnitude of these effects to ensure that they can be contained to satisfactory levels within the available control parameters. It is known that gradual changes in intake MFR, due to thrust demand requirements (high MFR at take-off, low MFR on approach), as well as more drastic situations such as engine surges, engine shut-downs (zero MFR) due to damage, etc. will have noticeable effects on the motion of the aircraft. The severity of these effects must be accounted for when stability and control requirements are defined.

From the point of view of calculation methods, it is the "compact" type layouts that pose the difficulties. In such, the sensitivity to α and β depends strongly on the design geometry and panelling, not only of the intake itself but also on the neighbouring surfaces.

Currently, several CFD methods are being developed, for example, field flow methods (Navier Stokes (NS) and Euler) and first- and second-order Surface singlarity, Panel methods. First-order methods, together with their application to nacelle flows/airframe interactions are discussed in Refs.1 to 6. The method of Ref.2 models through flow nacelles but as yet does not model MFR effects. Second-order methods, together with their application to nacelle flows/airframe interactions are discussed in Refs.7 to 12. As yet, the NS methods have not reached full aircraft capability. They require very fine field meshes and hence intensive computational resources. The Euler methods are gradually evolving but they still require very appreciable cpu time. The generation of the field meshes required for both NS and Euler methods can take lengthy analysis. Second order Panel methods require, of the order of, 10% of the cpu and storage use needed for the Euler methods. The first-order panel methods computational needs are likely to be 1% of the Euler.

It is therefore considered prudent, to use and validate the more economic first-order Panel methods in the early stages of design and development. Such panel methods have been applied in wing-pylon-nacelle arrangements and have given a good understanding of the aerodynamic - propulsion interactions. Experience suggests that the panel methods can be used with greater confidence than Euler methods at the lower Mach numbers, $M < 0.4$.

2. BRIEF DETAILS OF METHOD AND TYPES OF CONFIGURATION

2.1. Basic Theoretical Method

A first-order subcritical flow panel method (SPARV) has been used to obtain Mass Flow Ratio effects and aerodynamic loads on a variety of configurations. This method has been continually developed at BAe Brough since late 1970's. In common with other panel methods, the geometry of a configuration is defined as a series of planar panels.

Thick, lifting components are represented by two surfaces (upper and lower). Each panel, on each surface has a doublet (or ring vorticity) and source intensity associated with it. By placing the doublets and sources on the panels at the surface the use of a mean surface within the component is avoided. Thin lifting components, which do not require a source distribution, are modelled by doublets only.

The method uses the direct, normal velocity (Neumann) boundary condition, in which the normal velocity at each panel control point is required to be zero. In the literature, several other first-order panel methods are discussed and some of these use the indirect, potential (Dirichlet) boundary condition, which in general, is found to be more "robust" (Ref.Morino). In addition, the indirect type of boundary condition and modelling may be more suitable for lifting fuselage and powered nacelle work. The indirect boundary condition is usually a feature of second-generation first- and second-order Panel methods (Refs.5 to 12).

In Fig.2, the essential features and differences between first and second-order methods are outlined. In first-order methods, planar panels are formed by straight lines between points on the surface of the configuration. The sources and doublets associated with each panel may be of constant or linearly varying intensity. In second-order methods the curvature of the true surface is taken into account (parabolic or higher order) and also the source and doublet intensities vary non-linearly across the panel. The second-order methods are therefore cpu intensive.

In all panel methods, the experience is that geometry definition needs to be reasonably smooth and continuous. For example, the sharp edge formed at the hinge line of a deflected flap would either be smoothed or the panelling density gradually increased either side of the hinge-line. Sudden changes in surface curvature or panel size should be avoided.

There are some additional features that have to be borne in mind when using panel methods on configurations with a mix of lifting and non-lifting components, in particular where the effects of MFR are to be assessed.

It should be mentioned that the SPARV programme offers a 'viscous option' which incorporates the displacement effects of the viscous boundary layer into the basic inviscid theory. In the present work, viscous effects have not yet been included and this subject remains open for the future.

2.2. Lifting Surface Carry-Over at Body Junctions

Depending on a given configuration, a fuselage may be either "non-lifting" or "lifting". Non-lifting body panels carry sources only. To ensure continuity of the wing lift distribution across a non-lifting body, the wing geometry is "carried-over" to the centreline.

However, when part or all of the fuselage is represented as a lifting component the necessity for this type of enforced carry-over is avoided since the lifting fuselage continues the lift distribution to the centre-line. Various methods of joining thick lifting surfaces with thin lifting bodies are shown in Fig.3. It was found that conventional constant x/c type distribution over the wing led to an irregular panel distribution on the body, Fig.3(a). This tended to give erroneous peak pressures on the body. Therefore, a more regular body panel distribution shown in Fig.3(c) might be preferred but this could lead to inaccuracy in wing pressures. The 'C' type grid illustrated in Fig.3(b) is often used as the best compromise.

2.3. Lifting Surface Trailing Wakes

Lifting surface trailing wakes are treated as individual line vortices stemming from the Trailing Edge (TE), which may be relaxed to take up new geometries under the influence of local flow fields or set at a suitable angle (unrelaxed wake). To allow the vortices to relax, each one is subdivided into a number of segments, Fig.4. The segmentation (number and distribution) must be appropriate for each configuration and requires careful consideration, especially where two or more line vortices are close together. This may occur, for example, at a wing tip under high lift conditions. Care has to be exercised to ensure that neither rigid nor relaxed trailing wakes pass through or too close to the centroids of other panels. A particular aspect of this problem is shown in Fig.4. Here, the trailing vortex geometry in the 'near field', adjacent to the body needs to be pre-defined to ensure that it follows the body profile. Alternatively, the geometry of the lifting body may be modified locally, to ensure that it follows the path of the unrelaxed inboard trailing vortex.

2.4. Non-Lifting or Lifting Fuselage Modelling and "Leakage"

In general, the off-surface effects of lifting components extend over greater distances than those of non-lifting components. This feature distinguishes between lifting (source and doublet) and non-lifting (source only) fuselages and it can have a significant effect on the modelling of MFR.

The boundary condition of zero normal velocity at the control point of each panel is to be satisfied, as illustrated in Fig.5. Away from the control point, there is usually a small variation in normal velocity, Fig.5(a). In most cases, these effects are small and self-cancelling. On more compact geometries, there arises the possibility of significant non-cancelling variations, as sketched in Fig.5(b). This implies "leakage" which may have its own repercussions associated with slow convergence or reduced MFR effects. These will be discussed with reference to the Canard-Delta configuration in Section 4 and are also noted in Refs.3 and 4.

2.5 Mass Flow Ratio Modelling

The Mass Flow Ratio (MFR) of the engine nacelle may be varied by adjusting the normal velocities on a distribution of source panels inside the nacelle, Fig.6. The source panels lie in a plane normal to the longitudinal axis of the nacelle and this plane is referred to as a Mass Flow Ratio Control Face (MFRCF). The MFRCF area (A_C) and the Intake highlight area (A_H) are illustrated in Fig.6 for a thick nacelle. The areas are used to calculate the required velocities at the MFRCF for a given MFR.

These velocities then affect the flow elsewhere on the configuration leading to changes in pressures, load distribution and total loads (See also Refs.1 and 3).

We now describe applications involving MFR effects. We begin with straightforward "generic" configurations, and then gradually evolve into complex combinations of thick wings, part lifting fuselages and nacelles.

3. GENERIC BODY WITH EITHER CHIN INTAKE OR NOZZLE

The "generic" configuration, Fig.7 comprised a simple body (non-lifting) with an integrated nacelle (thin lifting) and either a Canard, adjacent to a chin intake, (Case 1) or a Tailplane behind a nozzle (Case 2). The panelling density was kept intentionally moderate for this essentially preliminary analysis.

Case 1 (Canard + Chin Intake) is reminiscent of the layout in Fig.1(c). Three MFR (1.0, 0.6 and 0.2), simulating reduced intake flow conditions, were modelled at M=0.2, α=0° and 4°, to give an indication of the effects of intake flow on canard pressure distribution and loading. The results, Fig.7, show that the canard lower surface is affected to a greater extent than the upper surface and that these effects are more noticeable towards the trailing edge.

Case 2 (Tailplane + Nozzle), Fig.1 (k). Again three MFR were modelled but this time representing increasing engine thrust (MFR=1.0, 1.2 and 2.0) at M=0.2, α=8°. The results, Fig.7, suggest that tailplane upper and lower surfaces might be equally affected by MFR changes, the effects being concentrated towards the leading edge, indicating possible changes in tailplane pivot torques.

In view of the strong effects on the lifting surfaces, it is possible that significant pitching moment changes will arise.

4. HIGH-WING CONFIGURATION WITH SIDE MOUNTED INTAKE

We needed to understand the differences between the modelling of intakes with thin or thick lifting components. A suitable configuration appeared to be an almost circular nacelle, representing side mounted intakes, with thin lifting wings and canard. No other components were included.

A possible method of modelling the side mounted intakes as a lifting nacelle is shown in Fig.8. Calculations were carried out on thick, and thin, lifting nacelles together with the wing and canard. The MFRCF was located at the intake lip. It was noted that the nacelle internal cross section distribution could affect the solution process, a near constant cross section along the nacelle gave improved convergence rate. The contributions to C_N (Normal force coefficient) due to MFR reduction, for the individual components, with the nacelle modelled either as a thick or thin lifting component, are shown in Fig.9. It was determined that thick lifting nacelle representation gave larger (possibly more representative) C_N increments with reducing MFR than thin lifting nacelles. The effects of MFR on the chordwise pressure distributions at root, mid semi-span and tip of the canard, for the thick nacelle configuration are shown in Fig.10. The effects of MFR decrease across the canard span. As was shown in the case of the "Generic" configuration, the effects are more noticeable towards the trailing edge of the canard lower surface.

The effects of MFR on a thin lifting Canard, located at various positions forward of the intake lip, were also investigated. Canard C_N variation with MFR and position is shown in Fig.11. As might be expected, close-coupled Canards, positions 1 and 4, incurred greater C_N increments due to MFR than far-coupled Canards, positions 2 and 3. Indeed, for Canards at the same height, the close coupled Canard C_N was approximately twice that of the far-coupled Canard.

5. CANARD - DELTA CONFIGURATION WITH CHIN INTAKE

The Canard-Delta configuration sketched in Fig.12 is typical of current fighter designs which feature a degree of longitudinal instability. The designer will need accurate pitching moment predictions and the effects of MFR on canard lift and pitching moment must be accounted for when stability and control requirements are defined.

5.1. Panelling of the Canard - Delta Configuration

The geometry needs to be smooth and continuous and from this point of view certain small simplifications to the geometry of specific aircraft are inherently required to ensure that the solution with a first-order method is stable. Because we are primarily interested in effects on neighbouring lifting surfaces, some detail such as boundary layer diverters and secondary air intakes may be blended out or omitted. Gaps or sharp corners due to control surface deflection would have to be closed or blended.

As illustrated in Fig.12, the Canard and Wing are modelled as thick lifting surfaces. The fuselage is modelled using both lifting and non-lifting components. The forward and upper fuselage components are non-lifting. The intake/nacelle is modelled as a thin lifting surface to enable MFR effects to be realised. The intersection between the lifting and non-lifting components can be visualised in the figure. Also shown are the locations of the Control Face (MFRCF) and a "Blocking Face". The "Blocking Face" inhibits internal flow between the nacelle and forward fuselage. It must be mentioned that for this particular configuration, the "Blocking Face" did not have any significant effect on the canard or nacelle pressures.

5.2. Effects of MFRCF Location

As may be expected, it is important to select an appropriate location for the MFRCF. If this is located too far along the nacelle the effects of leakage, section 2.4, will be increased. If it is too far forward, unrealistic intake flows might result. The effects of MFRCF location, at M=0.7, are shown in Fig.13 (Total and Canard C_N against MFR) and Fig.14 (spanwise distributions of C_N for the Canard and Wing). With the MFRCF at location 'C' the effects of MFR are not detected at the canard. Locations 'A' and 'B' gave similar canard loads but noticeably different total loads. Location 'B' was selected as being the most representative.

5.3. Effects of MFR on Chordwise, Spanwise and Total Loads

At M=0.7, α=8°, the effects of MFR on the wing spanwise loads are quite minor whereas the canard distributions are significantly affected, Fig.14 (Location 'B'). These trends are confirmed by the total loads in Fig.15 where MFR change has little effect on C_N but a noticeable effect on C_m due mainly to the effects on the Canard. Results from experiment are for MFR=0.6.

Fig.15 also illustrates the effects of modelling the fuselage (from some earlier work) as a non-lifting body. This type of modelling did not adequately simulate the effects of the lower MFR (0.6 and 0.2) and the C_m - α and C_N - α trends are similar to those of the thin lifting nacelle / fuselage at MFR = 0.95.

The effects, from theory, of reducing MFR from 0.95 to 0.6 and from 0.95 to 0.2, on the Canard spanwise loads at α=0° and 8°, are shown in Fig.16. Also shown are results from experiment for MFR reduction 0.6 to 0.2. It is noted that the nacelle has been modelled as a thin lifting surface and consequently the full effects of MFR reduction are not achieved (see Section 4). It would be expected that modelling the nacelle as a thick lifting surface will significantly improve these results. Chordwise surface pressure distributions (C_P-x/c) are presented as 3-D spanwise plots in Fig.17. Panel method results for lifting and non-lifting fuselages are compared with results from the Euler method and experiment. The panel method results are very encouraging and compare well with both Euler method and experiment. The relative costs of grid generation, computation and analysis for the two theoretical methods should be borne in mind and compared with the costs of wind tunnel experiment.

5.4. Mach Number Effects

The variation of MFR effects with Mach number has also been assessed for the Canard-Delta wing configuration. Total C_N and C_m variation with MFR are shown in Fig.18, M=0.2 and 0.7, α=0° and 8°. This shows similar results for M=0.2 and 0.7 at α=8° with a linear increase in pitch-up as MFR is reduced. At α=0° the trends are similar but at lower C_m values. The C_N levels are almost invariant with MFR and show a small Mach number effect at the higher incidence.

It is worth emphasising that, in general, it is difficult to obtain solutions to Euler calculations at low Mach numbers, whereas the potential flow panel method is able to provide valid answers up to high subsonic Mach numbers.

5.5. Relaxed Canard Wakes

Canard relaxed wake geometry is shown in Fig.19 for MFR=0.95 and 0.2 at M=0.7, α = 8°. It can be seen that the reduction in MFR has significantly changed the relaxed wake geometry. The Canard root vortices have moved down in z with increasing x and the tip vortices are more tightly rolled-up. However, these changes to the canard wake did not significantly alter the wing loading.

5.6. Fuselage Surface Pressures

It is necessary to have an understanding of the effects of MFR on the fuselage surface pressures for a variety of reasons. These might include topics such as structural loading, skin stressing and the location of pitot probes, aerials, etc. The panel method has assisted with analysis of fuselage side pressures and the effects of MFR. In Fig.20, it can be seen that MFR effects on the fuselage of this particular configuration are confined to the area beneath and aft of the Canard, up to the intake lip.

6. DELTA WING WITH EMBEDDED NACELLE

Wing embedded nacelles are being studied in design of modern aircraft. This has led to a preliminary study of the effect of MFR on total, spanwise and chordwise loads on the geometry shown in Fig.21. This represents a nacelle with its intake beneath the lower surface of the wing and a nozzle above and at the trailing edge of the wing.

6.1. Longitudinal Characteristics

The effects of MFR (0.95, 0.6 and 0.2) on total forces (C_L and C_m) and spanwise distributions are shown in Fig.22. Also included are results for the plain wing (no nacelle). The addition of the nacelle, in free flow condition (MFR = 0.95) results in a loss of C_L and a notable increase in C_m. As MFR is decreased, on the wing-nacelle configuration, C_L is slightly increased and C_m is significantly decreased. The C_L and C_m trends with decreasing MFR are in general, consistent at each incidence. Spanwise distributions of C_{NL} are given at α = 0° and 4° for each of the three MFR. It can be seen that at α = 0°, as MFR is decreased, the effects on C_{NL} are confined mainly to the nacelle location, with a small increase in C_{NL} inboard of the nacelle. At α = 4°, the effects are similar but the increase in C_{NL} due to MFR inboard of the nacelle is reduced and a reduction in C_{NL} occurs outboard of the nacelle.

Chordwise pressure distributions at three spanwise stations, for the three MFR, at α = 4°, M=0.7, are given in Fig.23. Considering C_P - x/c for the nacelle centreline, at MFR = 0.95, as would be expected, the presence of the nacelle has modified the upper surface pressures locally. The magnitude of the effect reduces either side of the nacelle. As MFR is decreased, the circulation around the wing is altered and the pressures are affected. Small discontinuities are due to thin surface modelling and moderate panel density selected for this preliminary analysis. The lower surface pressures show the trends expected. As MFR is decreased, pressures forward of the MFRCF increase, from a peak suction at the freeflow condition. Either side of the nacelle, C_P - x/c trends with MFR are similar but the effects are more significant on the outboard station. This supports the general form of the spanwise loads. Further work is required to obtain improved distributions and MFR trends using a thick wing with fully integrated thick lifting nacelle.

6.2. Lateral and Asymmetric Characteristics

Asymmetric effects of MFR variation (effectively right engine shut down, left engine free-flow) have also been studied on this configuration. Fig.24 shows the variation of C_N, C_m and C_D with MFR at α=4°, ß=0°, -1° and -5°, M=0.7. Fig.25 shows the variation of C_Y, C_l and C_n with MFR at α=4°, ß=0°, -1° and -5°, M=0.7. Lateral derivatives, $dC_Y/dß$, $dC_l/dß$ and $dC_n/dß$, obtained over the range $-1° < ß < 0°$, at α=4°, M=0.7, are also shown in Fig.25.

Taking typical values of the lateral derivatives of roll from a similar configuration, the likely aileron deflection required to overcome the asymmetric loads predicted would be of the order of 2° to 3°.

This relatively brief study has enabled an appreciation some of the important aerodynamic features and emphasised the strong MFR effects. Further work with a more representative and realistic configuration can be attempted with confidence.

7. NON-LIFTING BODY WITH CHIN INTAKE

Fig.26 shows a simple non-lifting body of trapezoidal cross- section. A rectangular nacelle leads from a chin mounted intake to a nozzle, exhausting at the rear of the body. The nacelle was modelled as a thin lifting component.

The effects of MFR reduction on C_m and C_N are shown in Fig.27. Reducing MFR by approximately 40% at α=4° causes a slight nose up pitching moment. Reducing MFR by 80% increases this pitch up ten fold. The changes in C_N at these conditions are of the same order for both magnitudes of MFR reduction. The effects of MFR on the body surface pressures are shown in Fig.26. The effects appear to be maximum on the centre-line, decreasing with increasing y, and are confined to the intake face location.

8. POSSIBLE FUTURE DEVELOPMENTS

Although several useful results have been obtained with the present method, further work can be foreseen in following areas, for example:-

- More realistic modelling of detailed geometry in close proximity to the intake may be required. These detailed geometries include, ramps or hoods in front of the intake face acting as boundary layer diverters. This will of course imply increased panel density.

- Assessment of the likely effects of viscous boundary layers on components near the intakes. A knowledge of these effects and indications of possible flow separation, is important from both airframe and powerplant considerations. The present method with its viscous option can be used to estimate some of these effects. However complex internal geometries cannot be analysed.

- When relaxing lifting surface trailing wakes, it was noted that the wake segmentation is very much dependent upon the configuration under analysis. The overall length of the relaxed wake, its proximity to other wakes and bodies, the number of line vortex segments and their distribution within the length of the vortex must all be carefully considered. This approach needs to be developed for the variety of configurations considered in this paper in order to establish a few major guide-lines.

- Relaxation of the nacelle trailing wake may be necessary in the case of nozzle/tailplane configurations. An assessment of the likely effects with the potential flow can be made although it must be appreciated that heat transfer effects may not be negligible.

- The preliminary investigation into the modelling of side mounted intakes as thick lifting bodies has been encouraging and a similar approach needs to be developed for chin mounted intakes.

  Similarly, thickness should be added to both the wing and nacelle of the delta wing with embedded nacelle configuration and the effects of MFR re-analysed.

- Although we have been able to use the direct, normal velocity (Neumann type) boundary condition with some success this may not be the best choice for intake/nacelle type problems. Methods using the first-order indirect, potential, Dirichlet type boundary condition need to be explored with compact and complex configurations. These may possibly be more robust and easier to use on duct flows.

9. CONCLUDING REMARKS

The effects of MFR have been studied on a series of varied configurations with different intake and nozzle types, with emphasis on the effects on adjacent surfaces. In particular cases, the effects of Mach number and in others the effects of asymmetry have also been studied. The configurations include a "generic" body with chin intake or nozzle and canard or tailplane, side mounted intake with high wings, Canard-Delta configuration with chin intake, delta wing with embedded nacelle and a non-lifting body with chin intake.

These studies have been achieved within the limitations of the first-order panel method using the direct velocity boundary condition.

Several useful working techniques have been established, for example:-

- Nacelle modelling as a thick or thin lifting body is largely determined by the complexity of the configuration and selection needs to be made early in the analysis.

- The method required smooth, continuous geometry, particularly for thin lifting nacelles.

- It may be expedient to omit the more detailed items of the geometry, especially when overall effects are of interest.

- The intersection of lifting surfaces required careful consideration with regard to the trailing wake vortices.

The major part of the analysis has been concerned with a Canard-Delta configuration. The panel method results showed good agreement with those from Euler calculations and experiment and in particular, incremental MFR effects. This analysis has given a better understanding of the possible effects of intake and nozzle flows on neighbouring surfaces. This has led to greater confidence in undertaking more complex configurations in the future.

In relative terms, the panel method costs can be an order (or two) less than those of the Euler results. The panel method requires the generation of panel geometry only on the surface of the configuration considered, whereas the field grid methods need not only the surface panel geometry but also the field grid around the configuration. Consequently the running costs of the field grid methods are much higher, not only due to the geometry generation but also the subsequent running and analysis costs.

The first-order panel method has shown the potential of predicting intake/nozzle effects on neighbouring surfaces and therefore offering significant savings in computer resources over the field flow methods. Applicability is to both Civil and Combat aircraft.

Avenues for further work and future developments have been proposed. This includes exploration with panel methods using indirect or Dirichlet conditions.

ACKNOWLEDGEMENTS

The authors have pleasure in acknowledging helpful and valuable technical discussions with Mr.D.E.Shaw, Mr.T.J.Pemberton and Mr.W.R.Marchbank. We acknowledge the general advice of BAe (Brough) on the use of the SPARV panel programme.

Lastly it should be mentioned that any opinions expressed are those of the authors.

REFERENCES

1. PETRIE, J.A.H., "A Surface Source and Vorticity Panel Method (SPARV)", Aero Quart., Vol.29, pp. 251-269, Nov. 1978. See also User Manual for SPARV (Updated Regularly).

2. HUNT, B. & SEMPLE, W.G., "The Panel Method for Subsonic Flows: A survey of Mathematical Formulations and an outline of the new BAe Scheme", AGARD, VKI LS 1978-4, 1978.

3. BOPPE, C.W., "Elements of Computational Engine / Airframe Integration", AIAA Paper 84-0117, 1984.

4. MORINO, L., "Computational Methods in Potential Aerodynamics", Springer-Verlag, 1985.

5. CLARK, D.R., MASKEW, B.R. & DVORAK, F.A., "The Application of Second-Generation Low-Order Panel Method (VSAERO) to Powerplant Installation Studies", AIAA Paper 84-0122, 1984.

6. NATHMAN, J.K. & FRANK, J.N., "Application of VSAERO to Internal Flows", AIAA Paper 87-2415, 1987.

7. FORNASIER, L,."HISSS - A Higher-order Subsonic/Supersonic Singularity Method For Calculating Linearized Potential Flow", AIAA Paper 84-1646, 1984.

8. HEISS, S. & FORNASIER, L., "Analysis of a Fighter Type Aircraft Configuration with the HISSS Panel Method at Subsonic and Supersonic Speeds", Z.Flugwiss, Weltrsumforsch. 12(1988) pp.224-32.

9. CARMICHAEL, R.L. & ERICKSON, L.L., "PANAIR - A Higher order Panel Method for Predicting Subsonic and Supersonic Linear Potential Flows about Arbitrary Configurations", AIAA Paper 81-1255, 1981.

10. TINOCO, E.N. & RUBBERT, P.E., "Panel Methods: PANAIR", Computational Methods in Potential Aerodynamics", Springer Verlag, 1985.

11. CHEN, A.W., & TINOCO, E.N., "PANAIR Applications to Aero-Propulsion Integration", AIAA Jo. of Air., Vol.21, No.3, pp.161-7, March 1984.

12. CHEN, A.W., CURTIN, M.M., CARLSON, R.B. & TINOCO, E.N., "TRANAIR Applications to Engine/ Airframe Integration", AIAA Jo. of Air., Vol.27, No.8, pp.716-21, August 1990.

LIST OF SYMBOLS

A Aspect Ratio
c Local Chord
c_{aero} = c, Aerodynamic wing chord
c_{ref} = c, Standard mean chord
C_A = Axial force/(q S), Axial Force Coefficient
C_D = Drag force/(q S), Drag Coefficient
C_L = Lift force/(q S), Lift Coefficient
C_m = Pitching moment/(q S c_{ref}), Pitching Moment (Body Axis)
ΔC_m Increment in Pitching Moment Coefficient
C_N = Normal force/(q S_{ref}), Normal Force Coefficient
C_{NL} Local Normal Force Coefficient
LE Leading Edge
l Length (Bodies)
M Mach No.
MFR Mass Flow Ratio, a_0/a_c, See Fig.6
MFRCF Mass Flow Ratio Control Face
q = 0.5 V^2, Dynamic Pressure
s Wing semispan
S Wing Area = S_{ref}
t Aerofoil thickness
TE Trailing Edge
V Velocity
x,y,z Orthogonal Wing axes, x along bodyaxis

α Angle of Attack, measured at the fuselage axis
β Angle of Sideslip
λ Taper Ratio
Λ LE Sweep Angle
η = y/s, Non-dimensional spanwise Distance
ρ Air Density

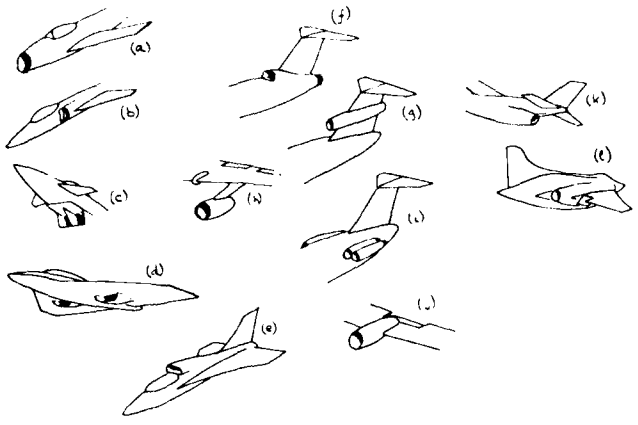

FIG. 1 INTAKE / NOZZLE CONFIGURATIONS & INTERACTIONS WITH NEIGHBOURING SURFACES

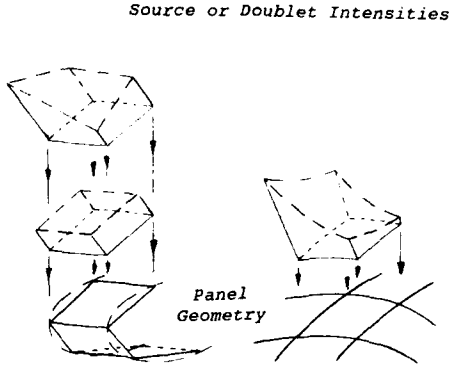

FIG. 2 FEATURES, FIRST- & SECOND- ORDER PANEL METHODS

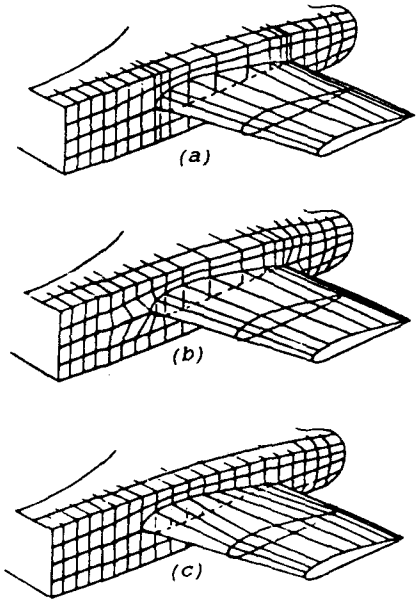

FIG. 3 JOINING THICK LIFTING WING WITH LIFTING FUSELAGE

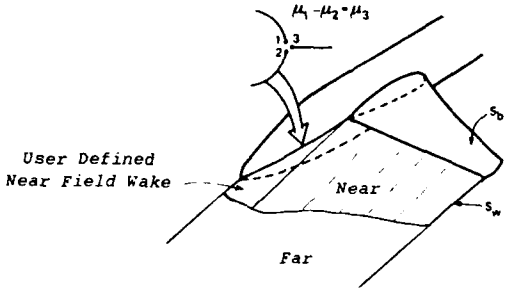

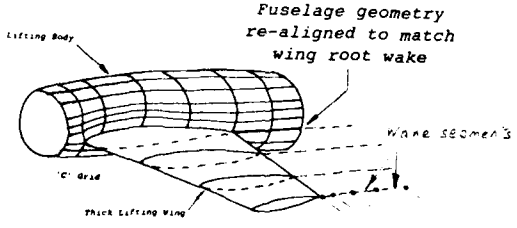

FIG. 4 TRAILING EDGE VORTICITY AND LIFTING BODY MATCHING

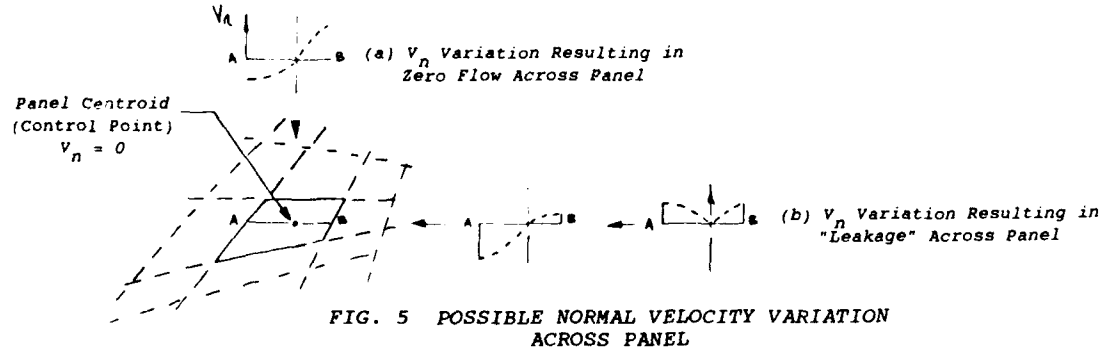

FIG. 5 POSSIBLE NORMAL VELOCITY VARIATION ACROSS PANEL

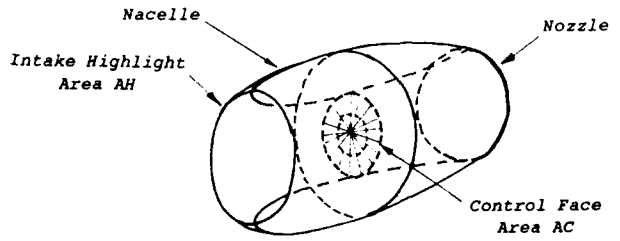

FIG.6 THICK NACELLE WITH CONTROL FACE

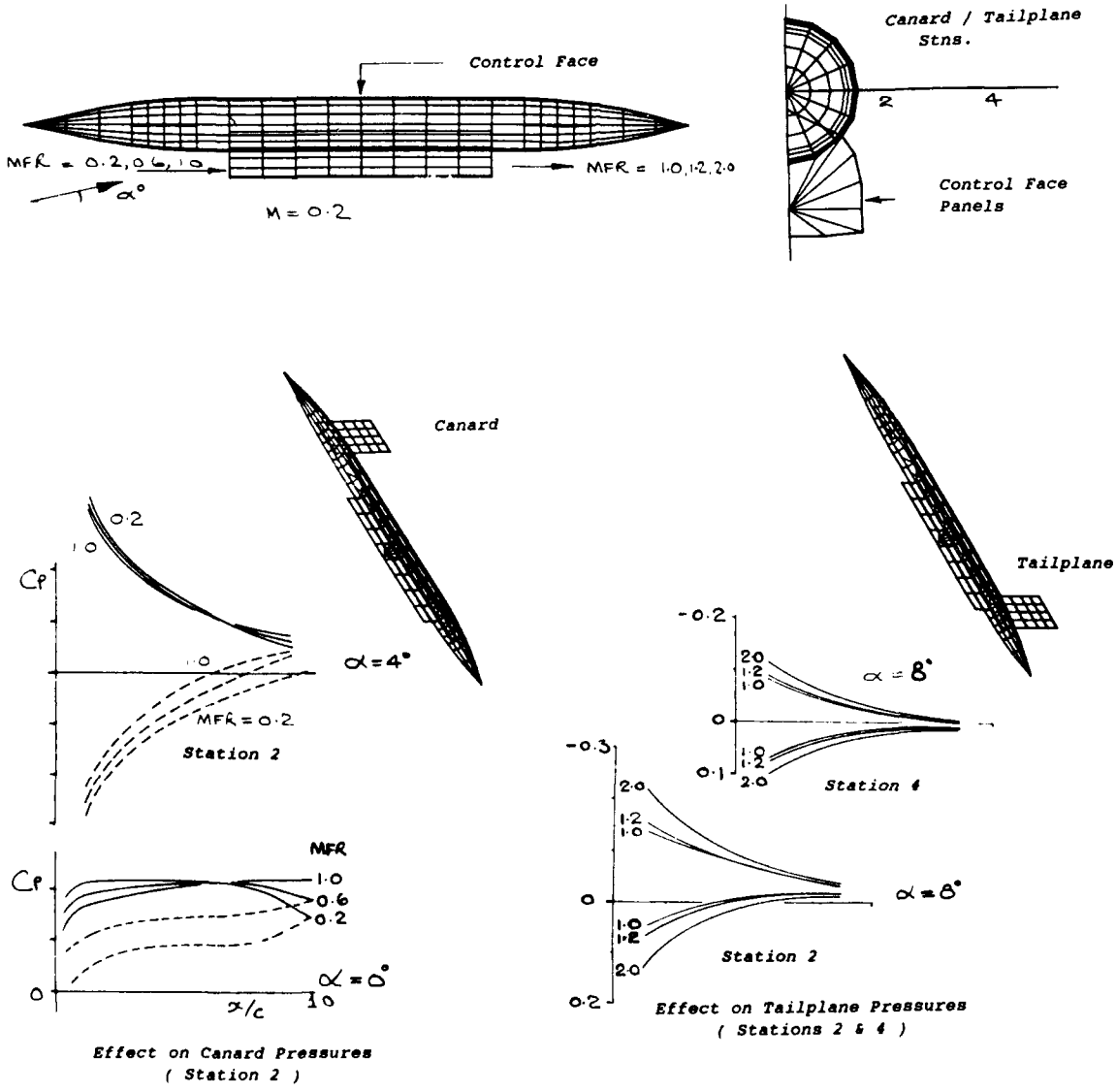

FIG. 7 "GENERIC" COMPACT CONFIGURATION, INLET OR NOZZLE, EFFECTS ON NEIGHBOURING SURFACES

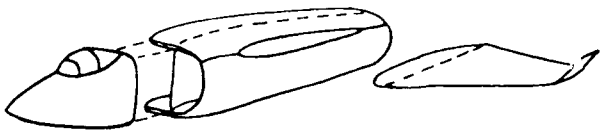

Generic Configuration (Thick Nacelle, Thick Wing)

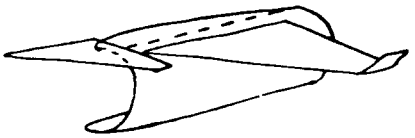

Simple Multi-Surface Configuration
(Thick Nacelle, Thin Wing and Canard)

Well Defined Throat | Near Constant Cross Section

Thick Nacelle

FIG. 8 MODELLING SIDE MOUNTED INTAKES, THICK OR THIN LIFTING NACELLES, THIN LIFTING CANARD AND WING

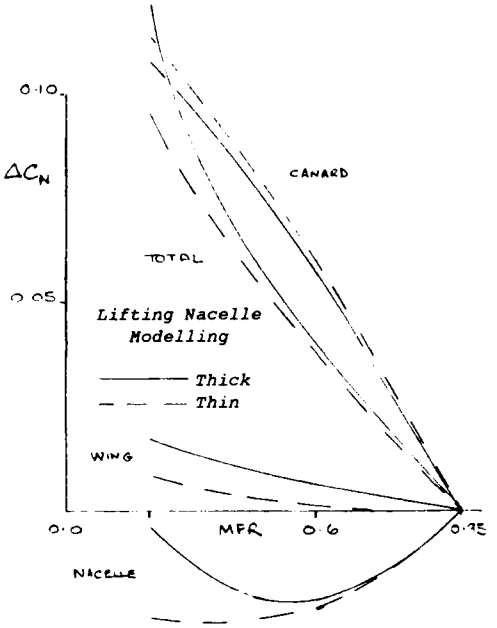

FIG. 9 EFFECT OF MFR AND NACELLE MODELLING ON C_N (TOTAL AND BY COMPONENT), THIN CANARD & WING

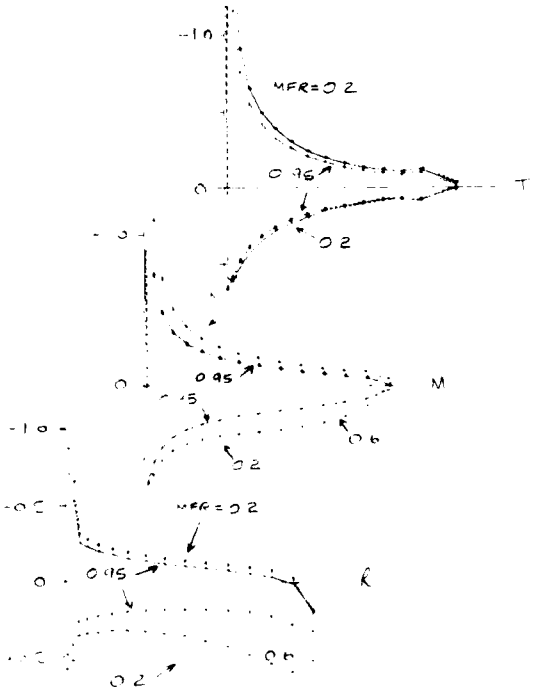

FIG. 10 EFFECT OF MFR ON CANARD CHORDWISE PRESSURES
(THICK NACELLE, THIN CANARD & WING)

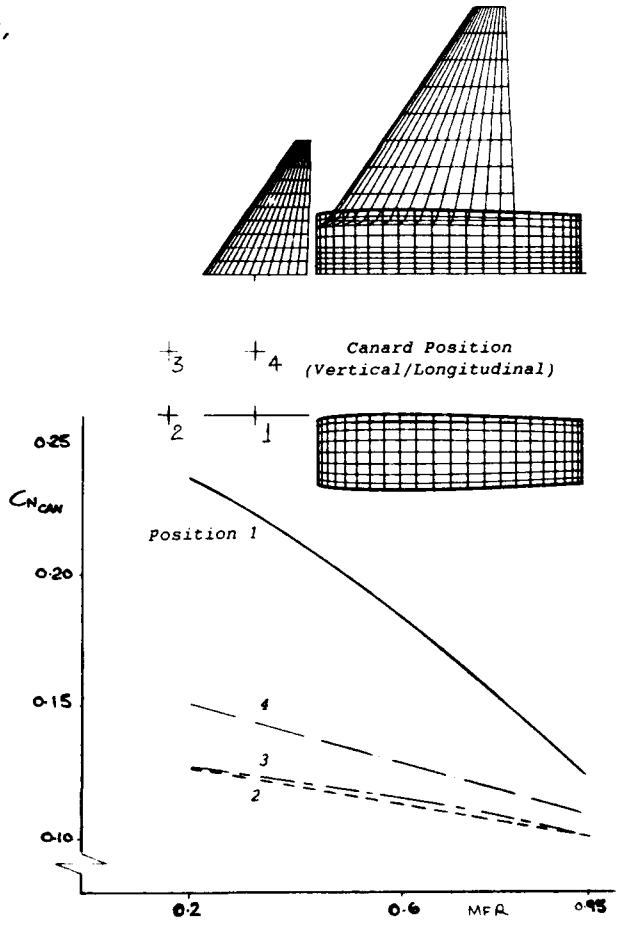

FIG. 11 EFFECT OF CANARD LOCATION ON CANARD C_N, SIDE MOUNTED THICK LIFTING NACELLE, THIN CANARD & WING

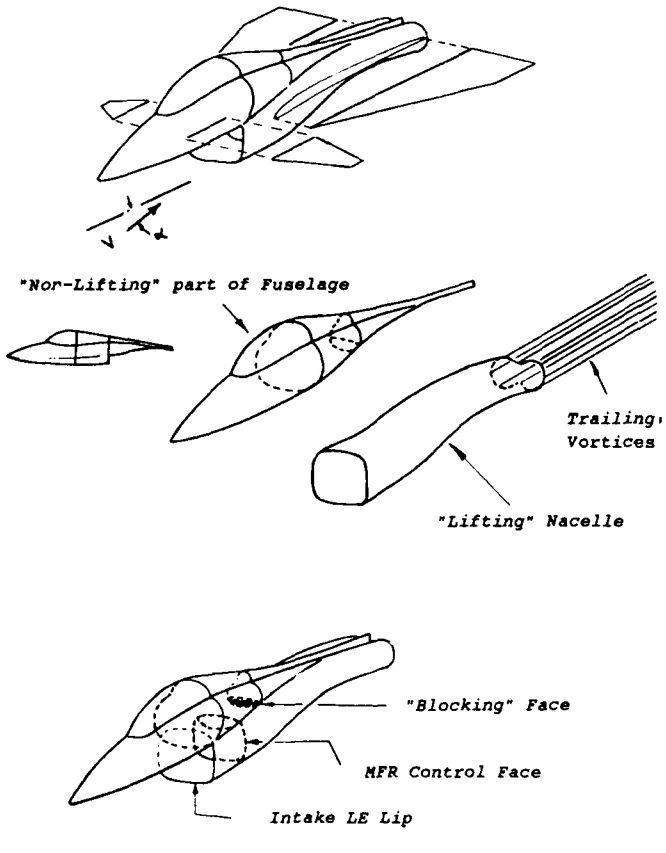

FIG. 12 CANARD - DELTA CONFIGURATION SUBDIVIDED INTO COMPONENT PARTS

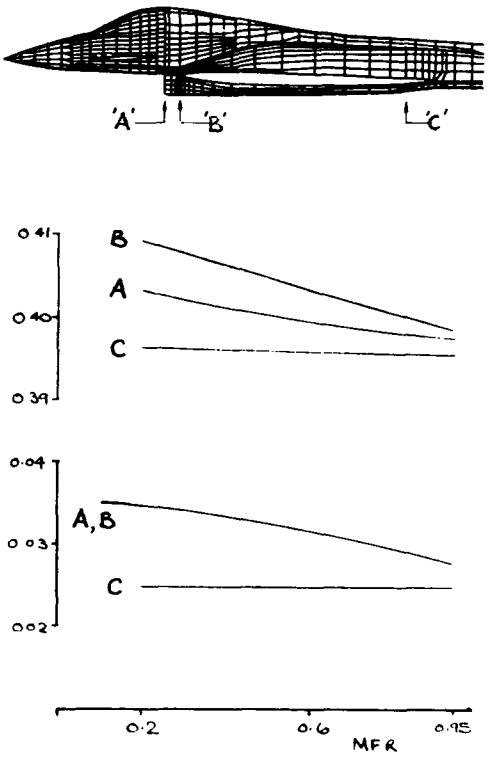

FIG. 13 EFFECT OF CONTROL FACE LOCATION ON TOTAL & CANARD C_N, (CANARD - DELTA)

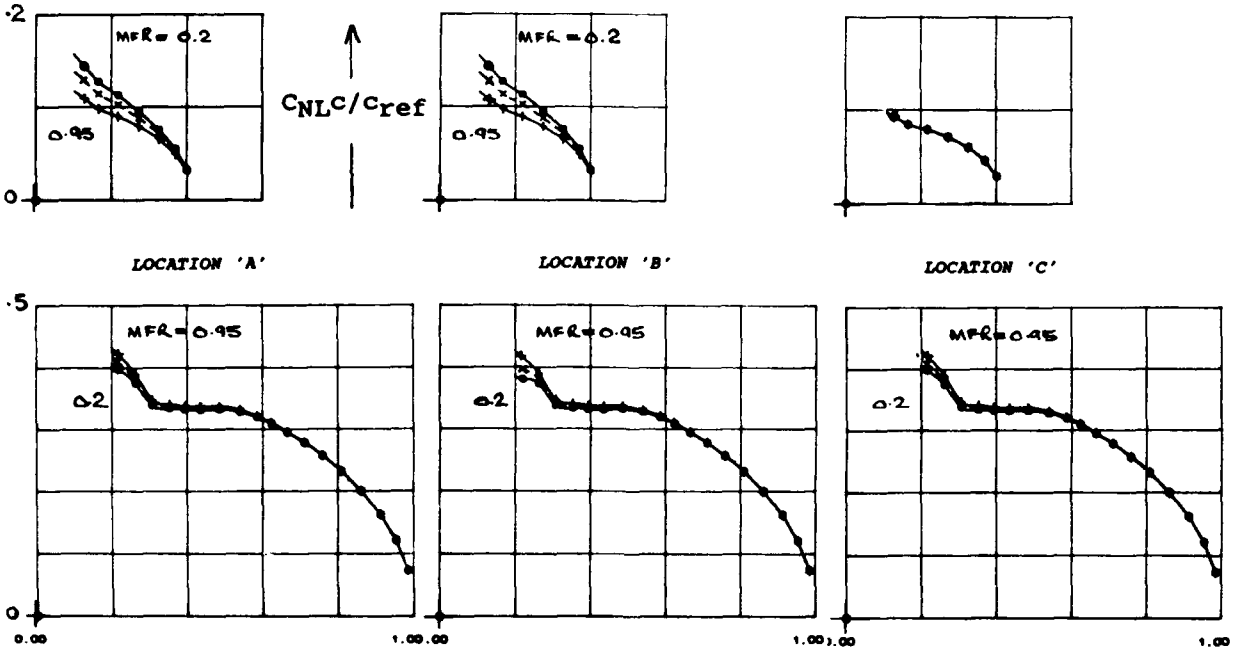

FIG. 14 EFFECT OF CONTROL FACE LOCATION ON CANARD & WING SPANWISE LOADS, (CANARD - DELTA)

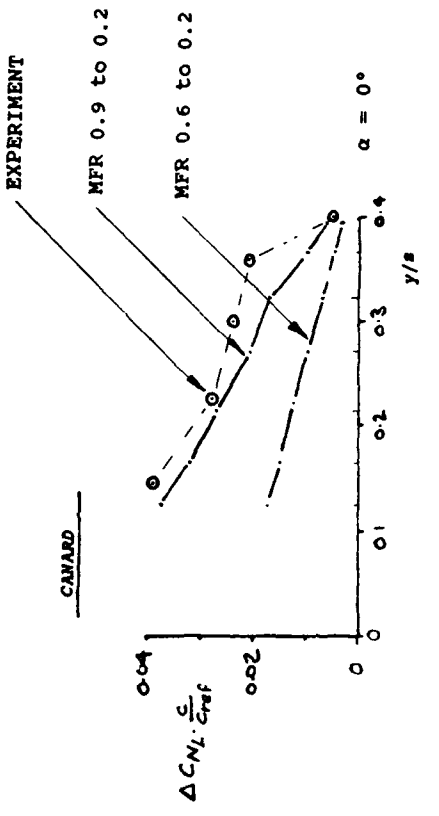

FIG. 16 EFFECT OF MFR ON CANARD SPANWISE LOADS, (CANARD - DELTA)

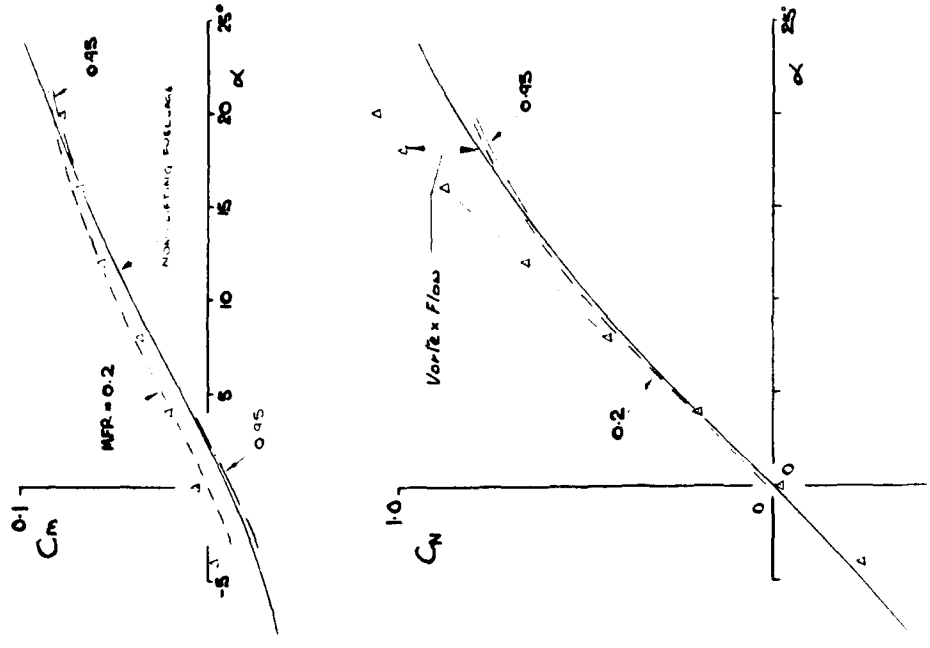

FIG. 15 EFFECT OF MFR AND FUSELAGE MODELLING ON C_m & C_N, (CANARD - DELTA)

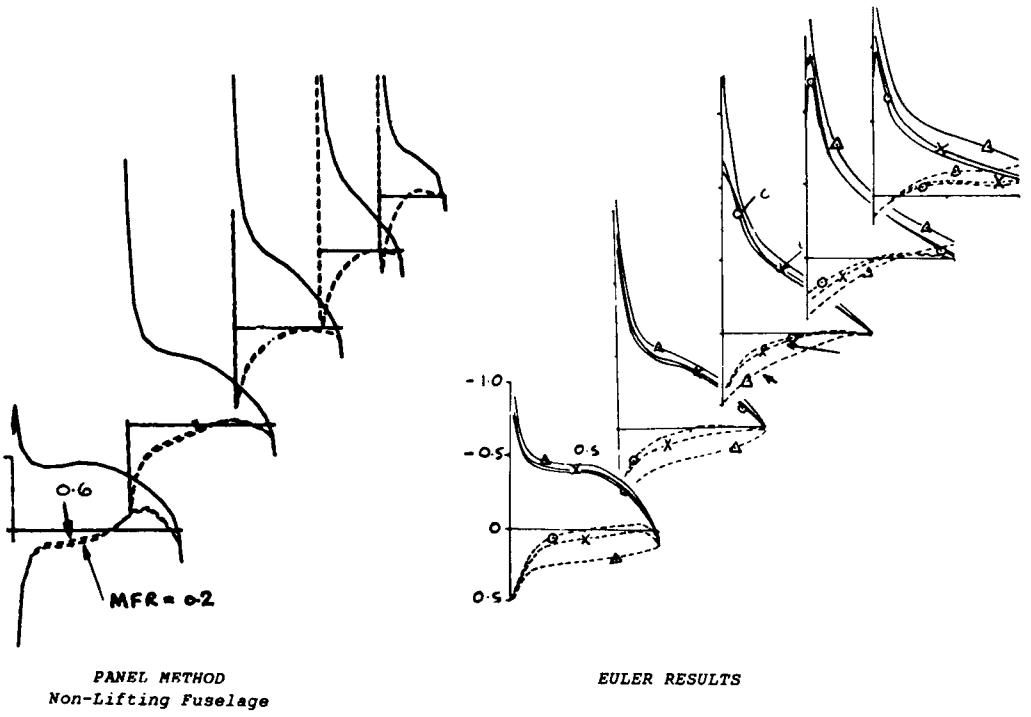

PANEL METHOD
Non-Lifting Fuselage

EULER RESULTS

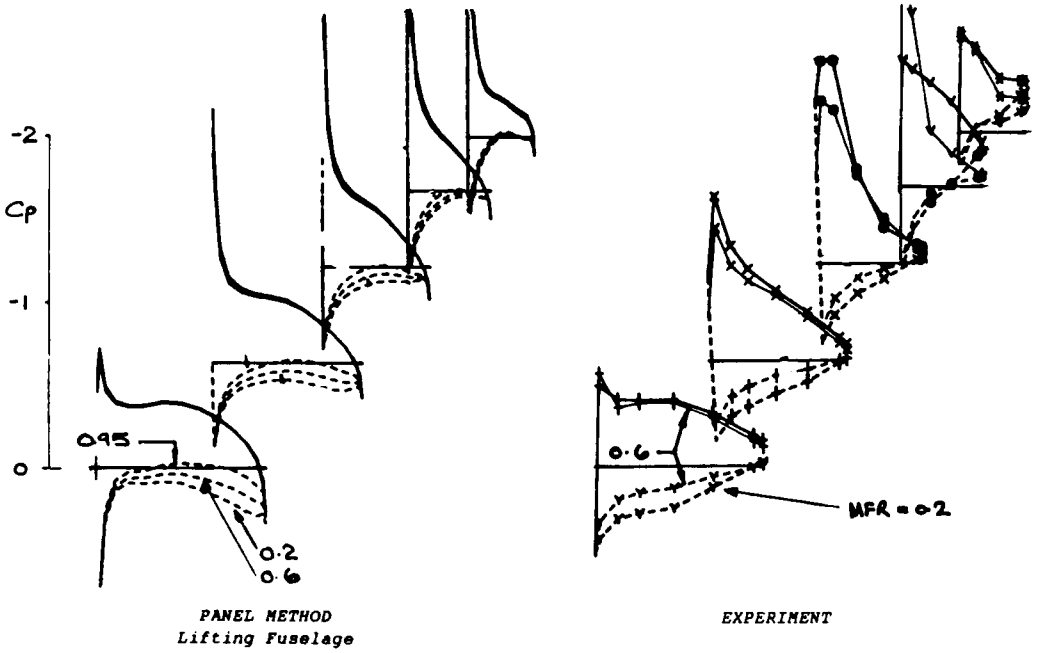

PANEL METHOD
Lifting Fuselage

EXPERIMENT

FIG. 17 CP - X DISTBNS. ALONG CANARD SPAN, PANEL METHOD, EULER & EXPERIMENT, EFFECT OF MFR, $\alpha = 8°$, $M = 0.7$ (CANARD - DELTA)

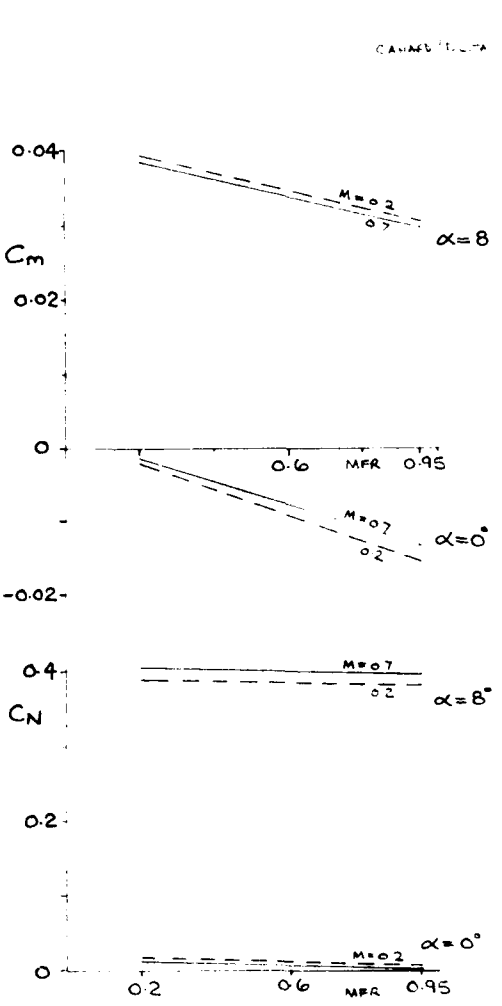

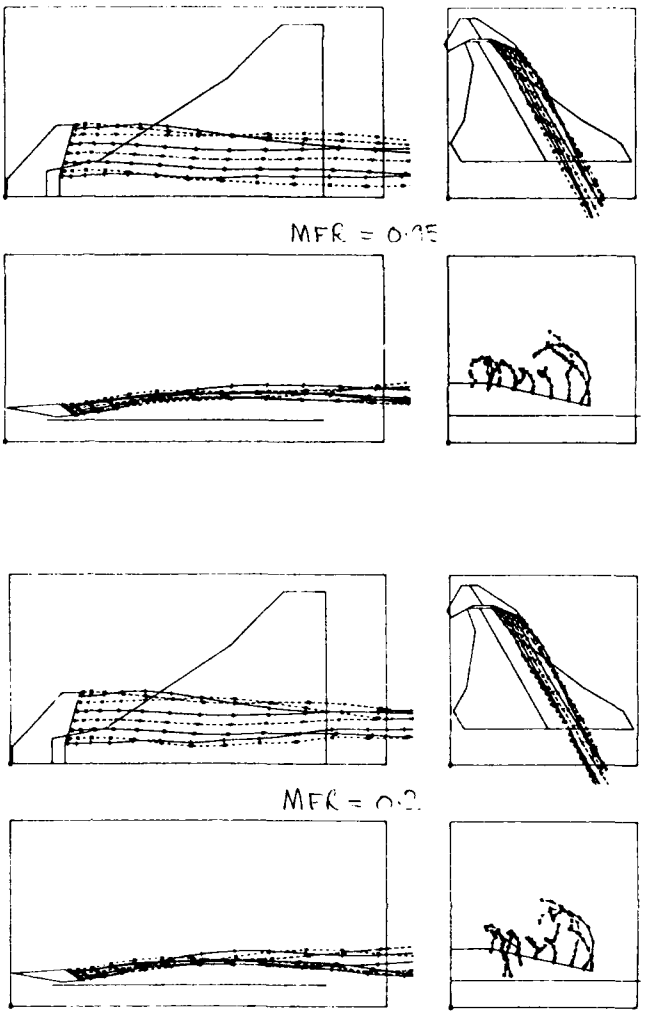

FIG. 18 EFFECT OF MFR AND MACH NUMBER C_m & C_N, (CANARD - DELTA)

FIG. 19 EFFECT OF MFR ON CANARD WAKE, α = 8°, M = 0.7, (CANARD - DELTA)

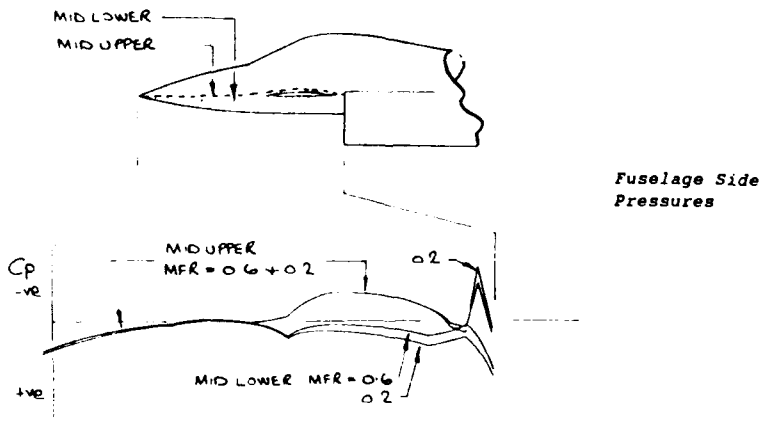

Fuselage Side Pressures

FIG. 20 EFFECT OF MFR ON FUSELAGE PRESSURES, α = 8°, M = 0.7 (CANARD - DELTA)

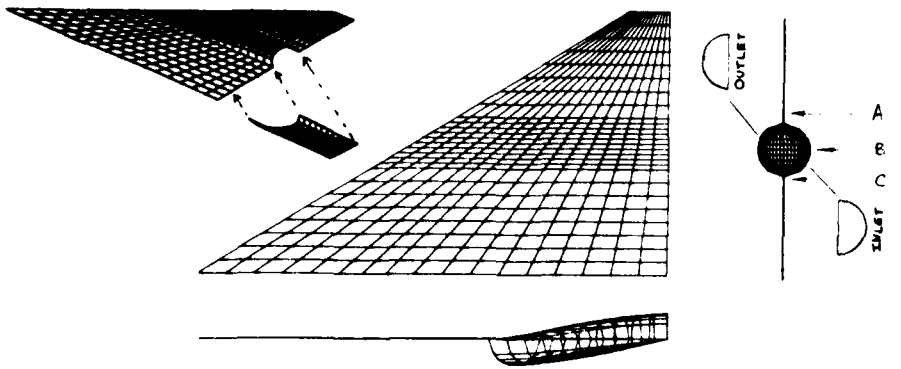

FIG. 21 DELTA WING WITH EMBEDDED NACELLE

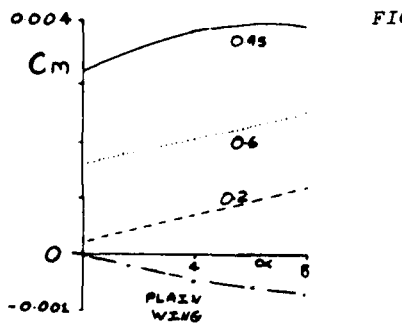

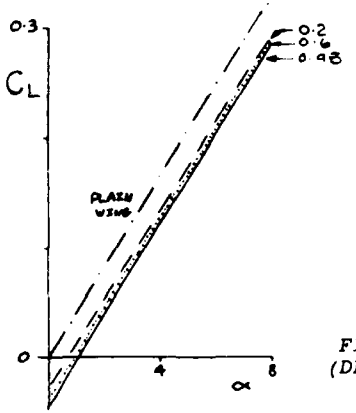

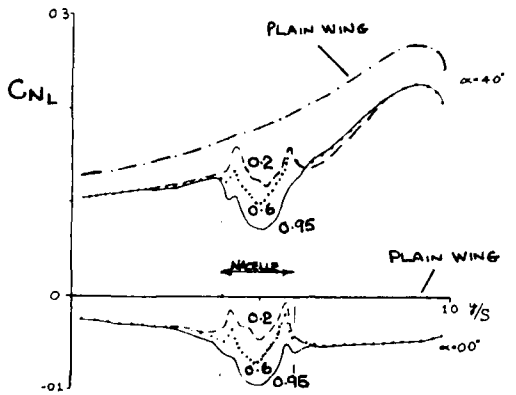

FIG. 22 EFFECT OF MFR ON TOTAL LOADS (DELTA WING, EMBEDDED NACELLE), M = 0.7

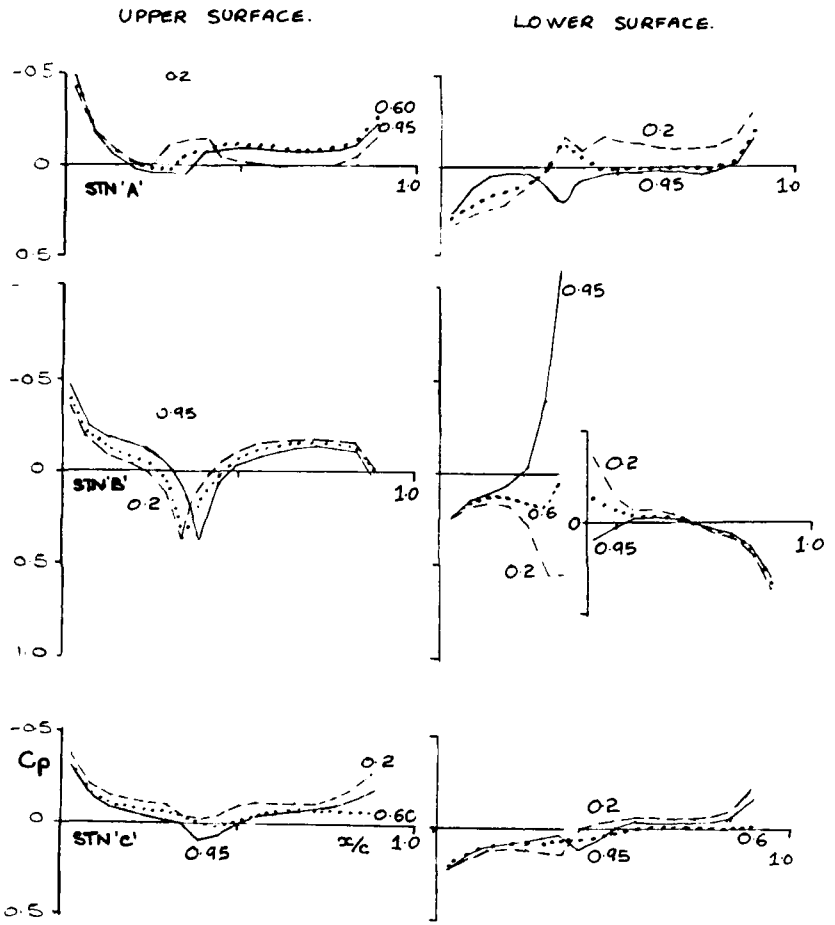

FIG. 23 EFFECT OF MFR ON WING CHORDWISE PRESSURES (DELTA WING, EMBEDDED NACELLE), α=4°, M=0.7

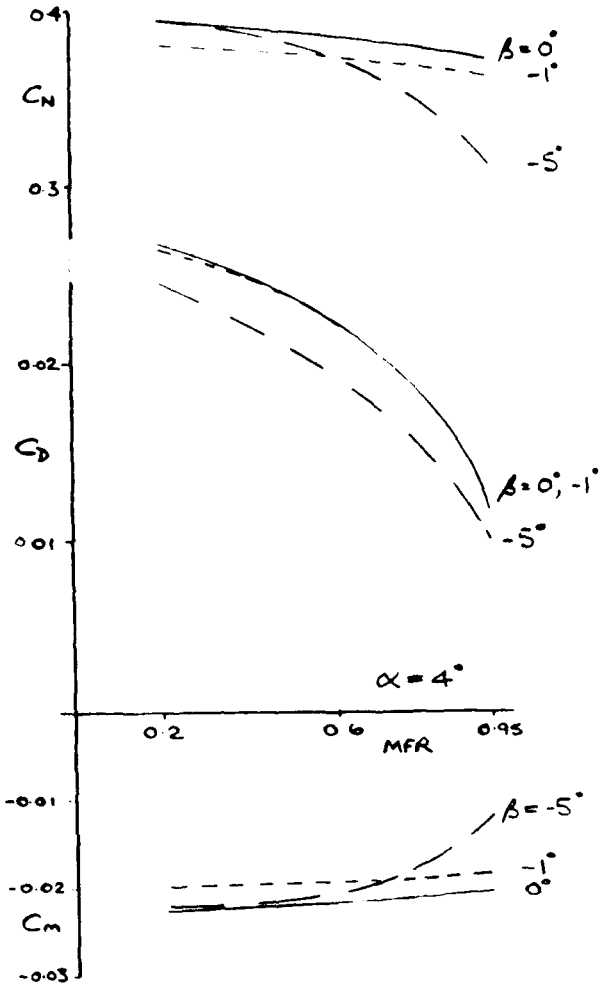

FIG. 24 EFFECT OF MFR ON C_N, C_D AND C_m, $\alpha = 4°$, $M = 0.7$

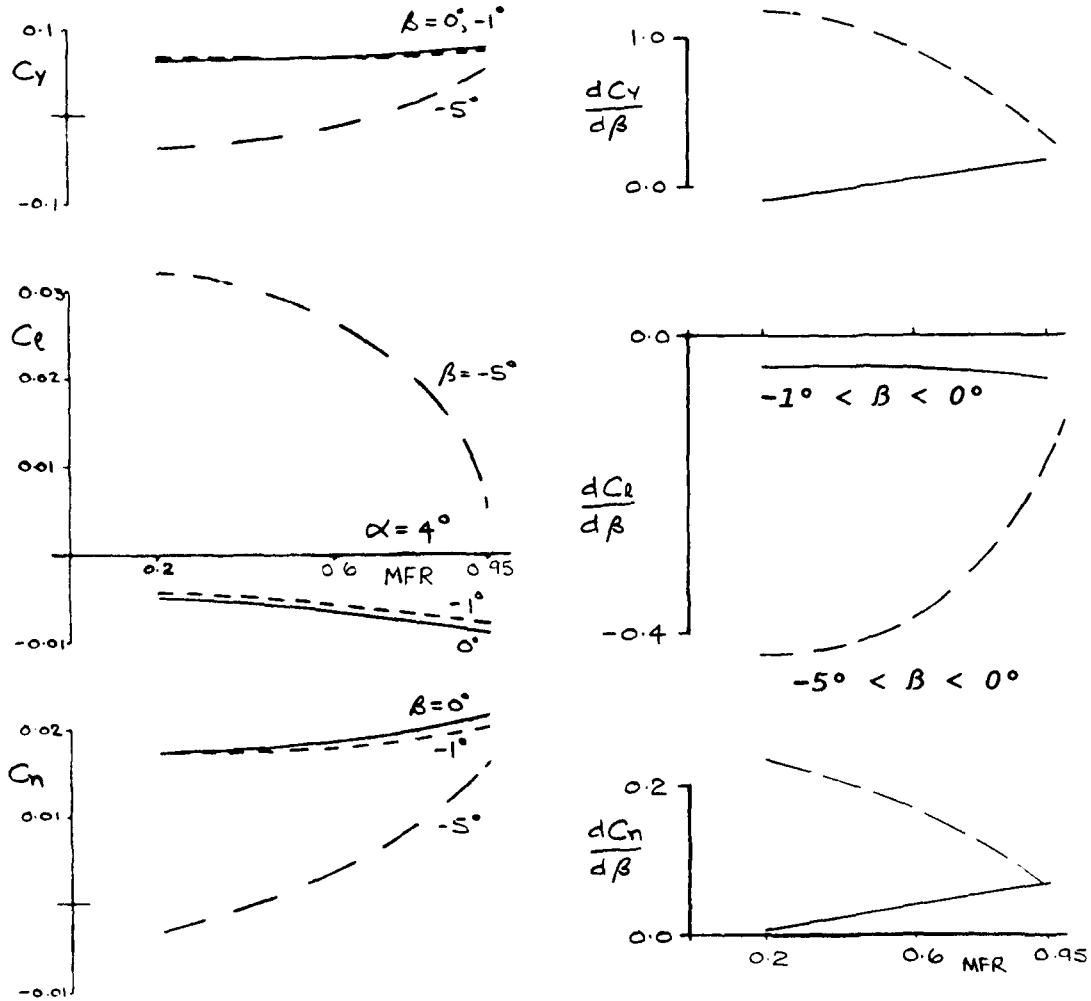

FIG. 25 EFFECT OF MFR ON C_Y, C_l, C_n, $dC_Y/d\beta$, $dC_l/d\beta$ AND $dC_n/d\beta$

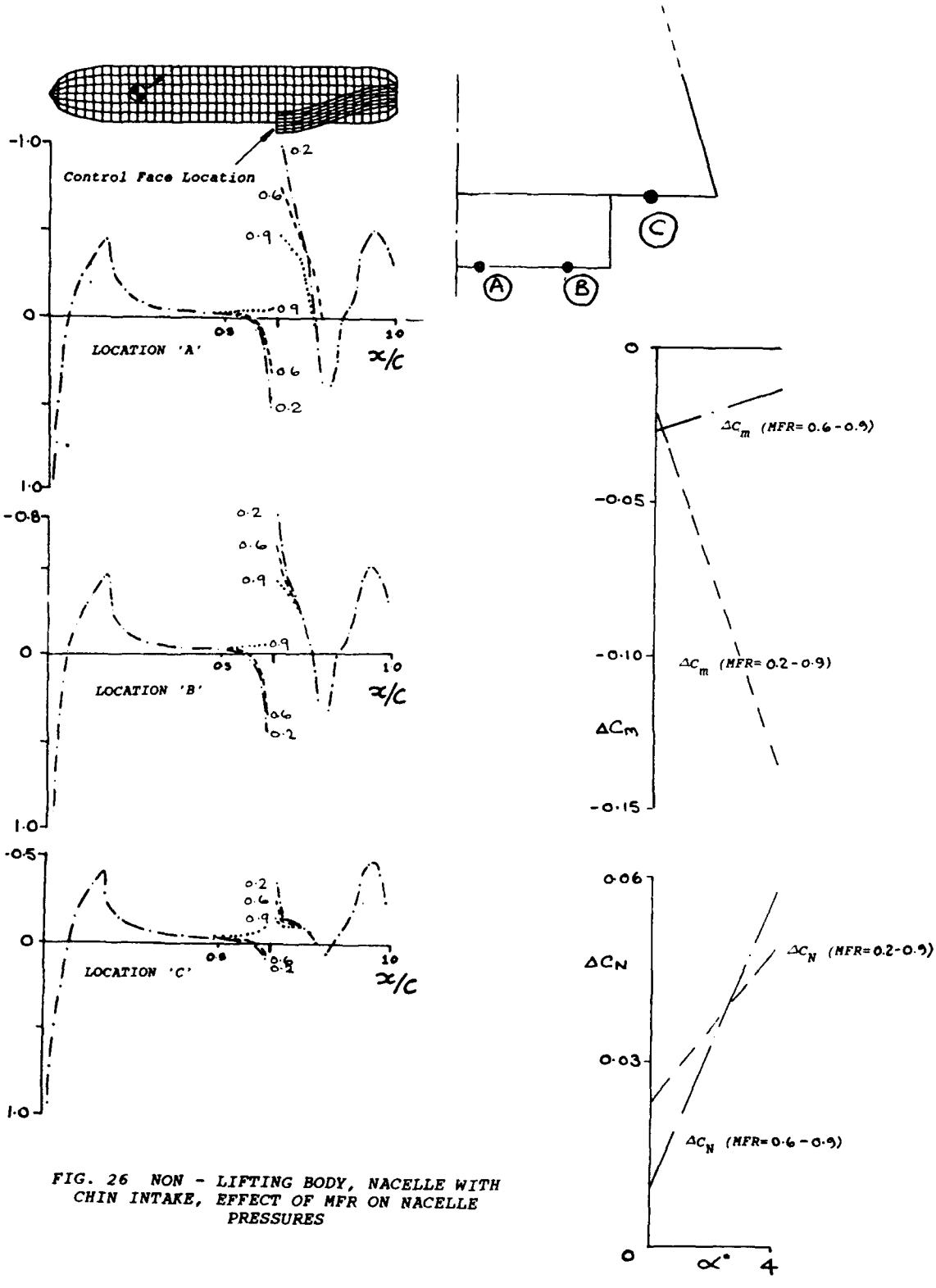

FIG. 26 NON - LIFTING BODY, NACELLE WITH CHIN INTAKE, EFFECT OF MFR ON NACELLE PRESSURES

FIG. 27 NON - LIFTING BODY, NACELLE WITH CHIN INTAKE, EFFECT OF MFR REDUCTION ON C_m AND C_N

Survey on Techniques Used in Aerodynamic Nozzle/Airframe Integration

Douglas L. Bowers
James A. Laughrey
Wright Laboratories
Wright Patterson AFB, OH 45433
USA

1. Summary

Building on a survey conducted in 1984 of the state-of-the-art of experimental and computational tools used to evaluate aerodynamic nozzle/airframe integration, this paper critically re-assesses these techniques in 1991. For experimental techniques, there have not been significant developments in the intervening seven years and these mature techniques still serve the design engineer well. On the computational side, Euler techniques applied to nozzle problems where there are not strong viscous interactions are now being applied as design tools. Computation of the viscous regions, especially the nozzle boattail, with Navier-Stokes algorithms is still lacking.

2. Introduction

The interest in AGARD in advanced nozzles and specifically the computational and experimental tools used to design and test new concepts has been evident over the past years in the two working groups started in 1974 and 1982. AGARD Working Group 04 "Improved Nozzle Testing Techniques in Transonic Flow" (reference 1) utilized a series of three reference aftbody boattails to investigate the influence of test facilities and model support systems on the resultant data. A number of installation techniques in a variety of tunnel types produced different results when comparing nozzle boattail pressure distributions. AGARD Working Group 08, "Aerodynamics of Aircraft Afterbody" (references 2,3), was formed in 1982 to critically review the state-of-the-art (SOA) in computational and experimental tools for aftbody/nozzle aerodynamics, nozzle integration and jet/airframe interference. The scope of the SOA assessment for the working group included looking at the range of applicability and accuracy of inviscid and viscous computational codes with respect to aftbody drag prediction. For experimental techniques, the working group reviewed progress since 1975 with respect to measurement, primarily in the wind tunnel, of drag and thrust. Progress was also evaluated for aftbody nozzle testing techniques to detect nozzle external/internal flow instabilities and unsteadiness, boundary layer separation effects and buffeting. The report included a section on wind tunnel correction methods and recommended future experimental investigations. One of the concluding remarks for the effort is indicative of the foresight demonstrated in this project....

"In the ten years since the publication of AGARDograph 208, much progress has been made on both experimental and numerical methods. ...Because of the tremendous progress which can be expected from the use of Vector-Computers within the next years, ... the report may be considered to be only a 'snapshot' from 'Status 1984.' ...the present WG08 report should be revised in time, considering especially the progress of computational methods for three-dimensional viscous flow. Experimental techniques have reached a very high level of reliability if proper correction procedures are applied and error analysis is performed as recommended."

"It can be definitely stated that numerical analysis will not replace the wind tunnel test, but as an outcome of the Working Group, it may be stated that numerical analysis will play a more and more important role as a supplement to the experiment in the future."

The WG 08 final report is a good point of departure for this 1991 snapshot of the state-of-the-art in exhaust nozzle integration. The objective of this paper is to proceed, as the concluding remarks suggested, and provide a seven year update to the "Status 1984" provided by WG 08. As we shall see, while many of the areas identified for future work have been addressed in the intervening years, many are still wanting. Further, in the interim time period, exhaust nozzles have evolved into even more complex shapes making both the CFD and experimental analysis tasks both more necessary and more difficult. These comments are primarily from a U.S. perspective. A more comprehensive treatment of advancements will be produced by a new AGARD Working Group 17, "Aerodynamics of 3-D Aftbodies," which has been approved but not yet initiated.

3. "Exhaust Nozzles Aren't Always Round Anymore!"

Since the 1984 report, exhaust nozzle geometry is rapidly changing away from the traditional axisymmetric as the expectations of the exhaust nozzle has expanded. Figure 1 from reference 4 shows the increasing role of the

1950	1985	1990
Engine Control Valve	Engine Control Valve Thrust Efficiency Minimize Drag	Engine Control Valve Thrust Efficiency Minimize Drag Thrust Reversing Thrust Vectoring Pitch Thrust Vectoring Yaw Thrust Vectoring Roll Signature Reduction Acoustics
Reference 4		

Figure 1 Evolution of Exhaust System Design Requirements

exhaust nozzle from that of its use as a simple engine control valve in the 1950s. Advanced nozzles for supersonic aircraft are now projected to be highly three dimensional with variable geometry features such as independent area control and thrust vectoring in at least two planes and perhaps thrust reversing. V/STOL aircraft beyond the Harrier may have ventral nozzles and fully articulating main thrust nozzles further complicating the aircraft/nozzle integration. The utility and viability of these nozzle concepts have been assured by a number of flight programs. The F-15 STOL and Maneuver Technology Demonstrator (SMTD) program aircraft has landed in 1500 feet and shown further benefits for inflight vectoring and reversing (reference 5). These will be discussed in a subsequent paper in this conference. The X-31 demonstrator aircraft promises to explore and quantify aircraft agility enhancement by means of thrust vectoring up to 70 degrees angle-of-attack (reference 6). Further, thrust vectoring is part of the new technology set on the USAF F-22, Advanced Tactical Fighter. In the future, the design of advanced nozzles will include consideration of balanced performance including the traditional thrust and drag plus low observables, weight, cost, reliability and maintainability. As shown in Figures 2 and 3, the advanced nozzle may be highly blended into the aircraft aftend necessitating consideration of the entire aircraft flowfield in the component analysis. From reference 7, Mace and Doane of McDonnell Douglas state.....

"The integration of the nozzle with the MRF (Multirole Fighter) airframe will be a balance between supportability, performance, signature and cost. ... Like the inlet system, the exhaust nozzle will be light weight and have a simple geometry. Thrust vectoring could be beneficial for high angle-of-attack maneuverability. The exit shape will be three-dimensional and highly blended aerodynamically and structurally integrated with the surrounding airframe."

Utility of advanced exhaust nozzles for air-to-ground fighter aircraft is amplified in references 8, 9 and 10. These benefits include increased air-to-ground effectiveness and survivability for low angle weapons delivery, dive bombing, standoff weapons launch, target acquisition, self defense, threat evasion, IR break lock, spin departure prevention/recovery and redundant

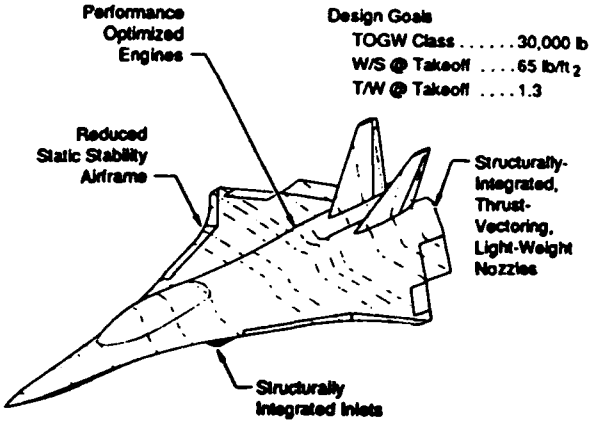

Figure 2 Conceptual Multi-Role Fighter, Reference 7

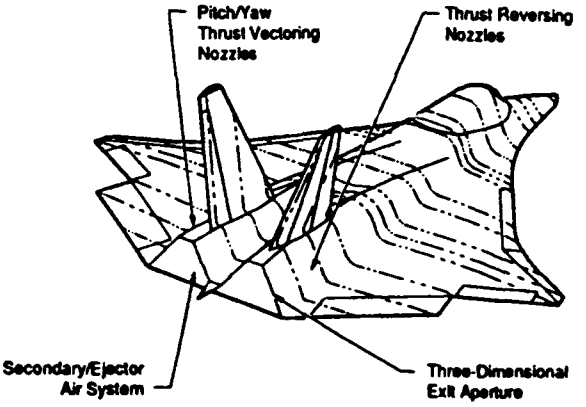

Figure 3 Conceptual Multirole Fighter Nozzle, Reference 7

controls. Aircraft agility metrics are now being defined which will dictate exhaust nozzle usage in the future. While this paper will concentrate on supersonic fighter aircraft, the problems and challenges are no less for high speed vehicles which cruise at Mach 4-6 or accelerate through the true hypersonic speed regimes of the NASP and Saenger. The highly blended aftbody/nozzles with chemically reacting jets associated with high speed flight further complicate the integration challenge beyond those issues already mentioned.

4. Working Group 08 Experimental Testing Technique Assessment

The experimental subgroup of WG 08 looked at jet simulation including the effect of temperature, turbine and ejector powered simulators, testing techniques such

as force balances, pressure area integration and model support effects, and flow visualization. Other topics included the simulation of aftbody flow instabilities and error analysis in aftbody testing. The conclusions as a result of this study were as follows...

-- "The choice of wind tunnel testing techniques for aircraft aftbodies must include consideration of many factors with the test objective, available facilities and model hardware the most important."

-- "Force balances.. must be used with great care to minimize and account for all tares and corrections, and an assessment should be made of the predicted levels of accuracy and repeatability versus levels required to meet the test objectives."

-- "Wind tunnel model support must be chosen with great care..."

-- "The key to utilization of both computations and experiments is understanding the flow physics involved in the aftbody area."

-- "Special advanced and more complex testing techniques... should be emphasized for future... development."

-- "... during aftbody buffeting is a very delicate (problem), requiring proper model/aircraft instrumentation together with careful analysis of the test results..." (reference 2)

5. Updating the State-Of-The-Art of Experimental Testing Techniques....

The test facilities most used in the aerodynamic development of exhaust nozzles are the static test facility and the large scale wind tunnel. State-of-the-art static test facilities are found in the U.S. at NASA Langley Research Center, General Dynamics/Fort Worth, The Boeing Company in Seattle and at FluiDyne Engineering in Minnesota. Typical test arrangements for the test model and the force balance are shown in figures 4 and 5. These facilities produce high quality data at nominal cost compared to large scale nozzle tests. Instrumentation traditionally includes a calibrated venturi for massflow measurement, pressure and temperature measurements (static and total) in the nozzle flow and along the sidewalls and divergent sections and a six component strain gage balance.

Reference 16

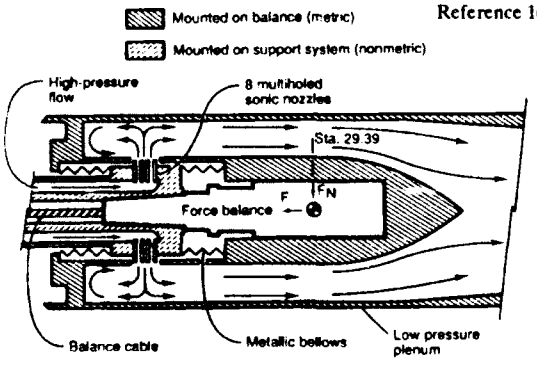

Figure 4 Schematic Cross Section of Flow Transfer System

Reference 12

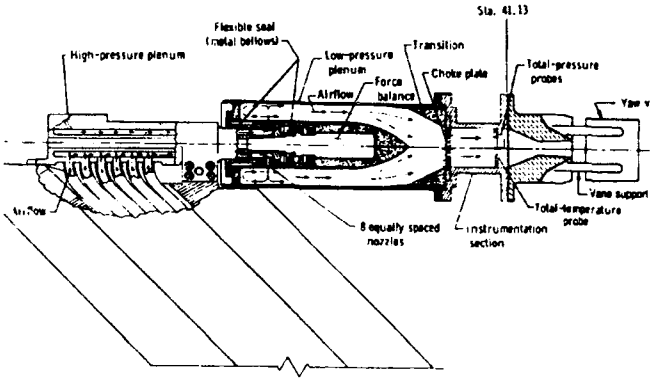

Figure 5 Static Test Model Arrangement, Reference 12

Upgrades projected to these facilities include providing larger amounts of airflow at higher temperatures and nozzle pressure ratios to account for new, larger massflow, higher temperature advanced engines. An overview of many multiaxis thrust vectoring nozzle static tests can be found in reference 11. Other references concerning exhaust nozzle cold flow static testing worthy of note are 12, 13 and 14, and for a STOVL ventral nozzle test, reference 15, all for the NASA Langley facility. Due to the excessive cost to fabricate large scale wind tunnels, those facilities that were in existence in 1984 are for the most part still in use today. Large scale wind tunnels in the U.S. suitable for using 10-12 percent scale jet effects wind tunnels models are primarily the NASA Langley 16 Foot and the Arnold Engineering Development Centers 16T (transonic) and 16S supersonic facilities. In general, they still provide high quality data as before. A research test program in the 16 Foot tunnel is discussed in reference 16. This test investigated isolated rectangular nozzles with respect to aftend closure and corner treatment, see figures 6, 7 and 8. Over the range of Mach 0.4 to 1.25, at 0 angle-of-attack, a six component balance force balance and 110 surface static pressure orifices provided parametric data which would be useful for designers to develop optimum aftbody integrations.

Acknowledging that exhaust nozzle integration and nozzle components have become more complicated over the last seven years (and promise to become more

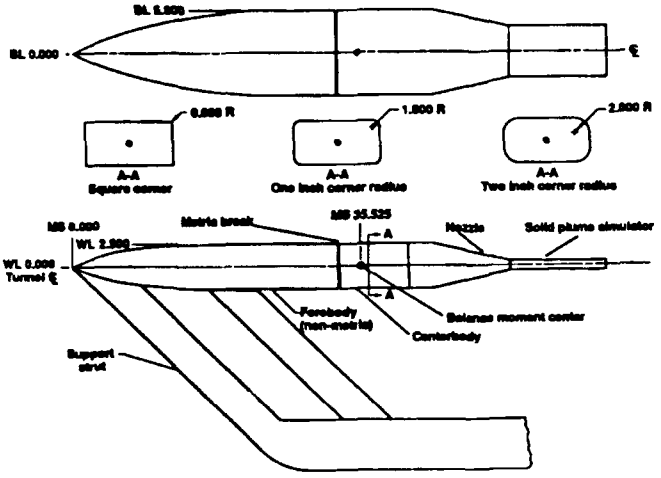

Figure 6 Wind Tunnel Model, Reference 16

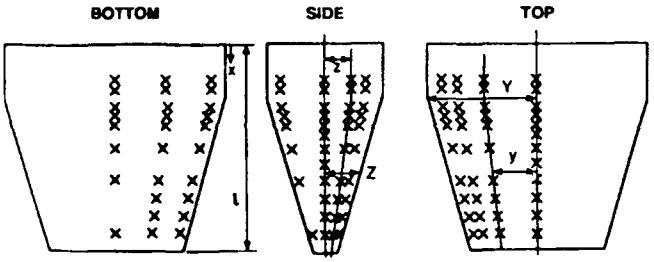

Figure 7 Typical Nozzle Pressure Tap Locations, Ref 16

so), the assessment of experimental testing facilities and techniques reported by Working Group 08 should be reexamined. As a reminder, the concluding remarks indicated that...

"Experimental techniques have reached a very high level of reliability if proper corrections are applied and error analysis is performed as recommended."

Over the last seven years there has been very little visible progress in experimental techniques. No advancements in the area of jet temperature simulation and turbine or ejector powered simulators for fighter aircraft are apparent. "Cold" or tempered high pressure air is still the medium of choice to simulate the exhaust plume. Upgrades in computer equipment and sometimes new support systems capable of higher degrees of freedom are the primary changes. Force balances have also

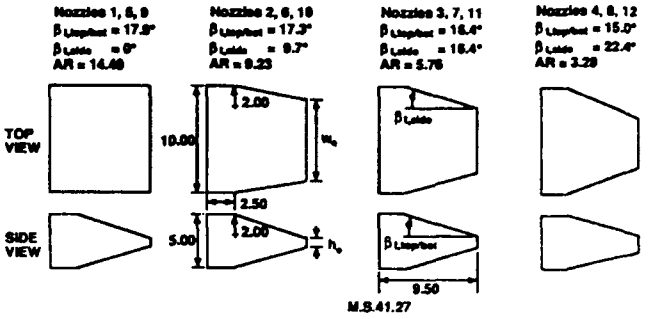

Figure 8 Schematic of Nozzle Geometry, Reference 16

changed very little with the same class of force balances available as options now as before. With new configurations becoming more blended, the trend is toward more total body measurement of forces. Improvements are evident in flowfield and body flow visualization with laser light sheets and other techniques adding quantitative as well as qualitative data to that previously available. These include pressure sensitive paint which may give full body forces from a very accurate pressure area integration. New methods of rapid pressure sensing and recording using electronically scanned pressure modules have increased the speed at which many surface pressures are recorded. Numerical analysis has not replaced the wind tunnel for analysis of complex three dimensional shapes. However, as forecast by the report, numerical analysis including online computations is slowly being incorporated into test preparation, being used to design the test hardware and to partially direct the path of the wind tunnel run schedule increasing testing efficiency. In summary, while there have been no real breakthroughs in experimental testing techniques, there will continue to be a need for high quality experimental data. The challenge for the next six years is to keep the facilities in excellent condition as the funds to upgrade and maintain them are reduced. The next great breakthroughs will come in conjunction with the new workstations and advanced computational methods directing the test onsite. The 1984 assessment is still valid today. The most important question is: due to decreased funding, will the state-of-the-art be as good tomorrow as it is today?

6. Working Group 08 CFD Assessment

The WG 08 test cases used for the CFD comparisons were limited to axisymmetric configurations at zero degrees angle-of-attack. The thirteen test cases included external pressure distributions, and some boundary layer and flowfield measurements. Eighteen contributors submitted solutions to one or more test cases. At that time, the solutions consisted of a few full Navier-Stokes methods, many mixed or patched methods with inviscid solvers and a viscous

displacement, and a few Euler solvers. The problem of turbulence models for Navier-Stokes solvers and artificial viscosity in the numerical scheme of Euler solvers was identified. For subsonic cases, some of the coupled inviscid-plus-boundary layer approaches predicted the surface pressure distributions, the boundary layer separation point and the drag coefficients very well. The Navier Stokes solutions were found in good agreement with the experimental surface pressure distributions up to the point of flow separation. Quoting the final report...

"Today's Navier Stokes calculations generally cost 5 to 20 times as much as an inviscid/viscous interaction calculation on the same super computer... The rapid increases in hardware technology and improvements in numerical techniques... may soon make Navier Stokes codes inexpensive enough for production calculations."

The conclusions and recommendations of the CFD subgroup were as follows:

-- "Computational research should... improve two-dimensional modeling of the separation region for inviscid/viscous interactions methods."

-- "Navier Stokes code development should continue with concentration on grid generation, solution algorithms, turbulence modeling and user friendliness."

-- "Detailed studies of the effect of turbulence modeling should be undertaken."

-- "Three-D methods should be developed."

-- "Zonal approaches plus full 3-D Navier Stokes solutions should be pursued."

-- "Careful 'test case' experiments should be undertaken to provide flow field details for the development of turbulence models."

-- "Results indicate the potential of Navier Stokes analysis to predict many features of the flow correctly."

-- "The rapid growth and improvements of computers and in theoretical methods should in the future provide significantly better methods for predicting the effects of engine installation on the airplane aerodynamics."

7. Updating the State-Of-The-Art of Computational Techniques

Progress in CFD since the WG 08 assessment has come a "long way." Though the capability is not yet available, improvements in computer memory, speed, and graphics have rapidly moved forward the moment in time when a design engineer can computationally design the nozzle aftbody integration. Codes of choice which are applicable to select design areas are Euler algorithms or Euler versions of Navier-Stokes solvers and simplified and full Navier Stokes codes. In areas where there are not strong viscous interactions and flow separation, the Euler codes, as we shall see, do very well calculating internal nozzle pressures and subsequent effective thrust vector angles and forces. The Navier Stokes codes, used by necessity in highly viscous areas such as the nozzle boattail, are still hampered by inadequate turbulence models, grid generation, and computer memory and speed constraints. Further, there has been great progress in calibrating these types of codes for particular problems, in increasing the productivity of the grid generation task and in improving user friendliness of the codes as design tools. The final area of discussion will center on the emerging power and speed of inexpensive desktop computer workstations.

The expeditious use of Euler codes for the internal performance of exhaust nozzles as a supplement to the traditional static test has evolved as a useful tool for the designer. Where viscous effects are not prevalent, these codes have been shown to predict thrust coefficient to within one percent, effective thrust vector angle to within one degree and internal surface pressures well within the experimental accuracy. Further, the advent of unstructured grids, especially for shapes that can be analyzed as two-dimensional has greatly decreased the clock time, measured in hours, to complete a calculation. The paper of Bergman and Treiber (reference 17) in 1988 set the stage for the further development of 2D and 3D Euler calculations for this type flow solution. Their conclusion was that 3D Euler is suitable for external flow for integrated nozzle aftbody configurations where flow separation and boundary layer effects are minimal. This implies that the codes will reliably predict and integrate the surface pressures for design loads and aftbody pressure drag. Cheatham, in references 18 and 19, applied both structured and unstructured grid Euler codes to both 2D and 3D nozzle test cases and showed excellent agreement with the experimental data. A thrust vectored axisymmetric nozzle, the two-dimensional thrust vectoring F-15 SMTD nozzle, an advanced exhaust nozzle with an innovative internal vectoring scheme and additional geometric and flow parametrics for each of these nozzles were calculated and results compared favorably with the static test data, figures 9, 10, and 11. The real power for the designer in the use of Euler codes will lie in the development and refinement of a user friendly system

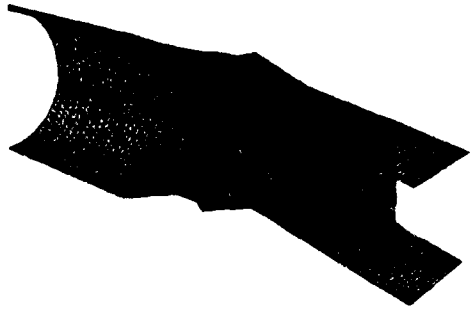

Figure 9 F-15 S/MTD 3D Internal Grid, Reference 18

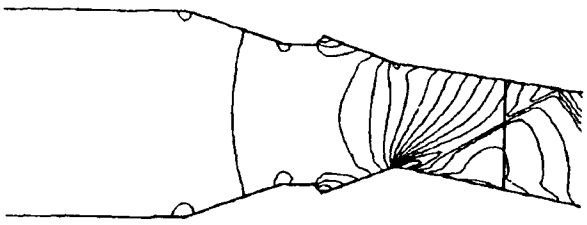

Figure 10 F-15 S/MTD Mach Number Contours, Reference 18

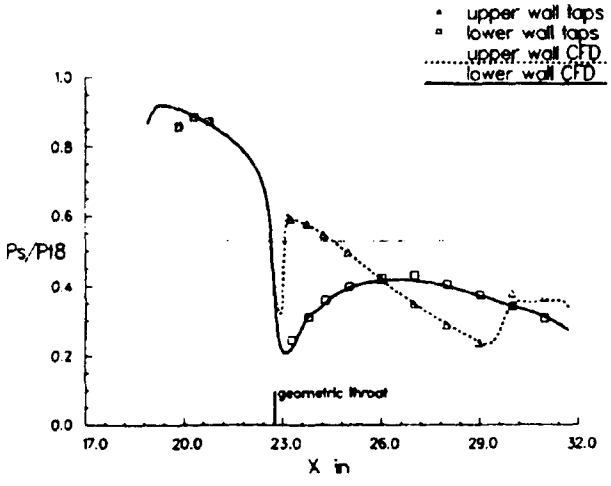

Figure 11 F-15 S/MTD Flap Pressure Comparisons, Ref 18

coupled with an adaptive unstructured grid. Rowe from General Electric and Syed from Pratt and Whitney, references 20 and 21 respectively, describe systems which use 2D unstructured self-adaptive grid Euler solvers with a boundary layer analysis added to predict thrust coefficient, discharge coefficient, and effective thrust vector angle. Equally important is the philosophy surrounding the user friendliness of these codes.

"... in order for CFD tools to be effectively used in a design environment, various tasks... need to be integrated and automated....It should also be supported on a user friendly easy to use platform so that it can be used by a designer who is not expected to be a CFD expert" (reference 20).

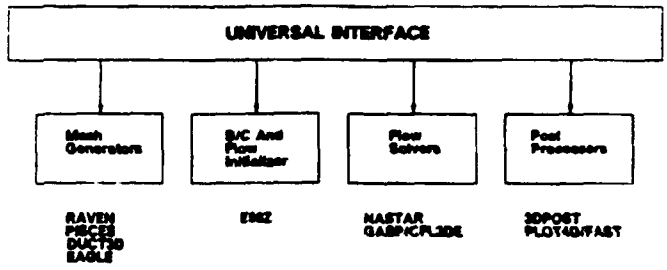

Figure 12 CFD Based Analysis System, Reference 21

All of the interfaces between programs, see figure 12, are automatically written with compatible files for the post processor and all output options are menu driven. For 3D cases, there is still a need for....

"CFD methods that are accurate, economical and have reasonable short turn around times, i.e. from when the geometry is available to the time when the results are generated to make a design decision... Fast and user friendly methods of generating computational meshes are needed to reduce overall analysis time for complex configurations" (reference 21).

Note that in reference 22, a Propulsion Energetics Panel paper, Koschel demonstrated an adaptive 3D unstructured grid for hypersonic nozzles. For complex shapes, this approach may offer the breakthrough in time and ease-of-use that will satisfy many of the constraints to the use of CFD that exist for the designer today. Euler codes now offer a very good tool to supplement and complement the traditional static tests used to screen nozzle candidates based on internal performance. If no strong viscous regions are present in the case being calculated, these tools are now available for the designer.

For those highly viscous dominated areas of propulsion flows, like the external nozzle boattail, the only methods with a reasonable chance of calculating the flowfield are the simplified or full Navier-Stokes codes. Codes which are known for their widespread use that have had some success for exhaust nozzle flows are the PARC code, a derivative of the NASA Ames ARC code, and PAB3D, whose development was sponsored by NASA Langley.

Versions of the PARC code reside in various places in industry and government with each code having capabilities unique to itself. Garrard (reference 23) and Cooper (reference 24) discuss the application and calibration of this code for various propulsion installations and wind tunnel design. The code is described as "well tested, user friendly... with generalized boundary conditions allowing complex geometries to be readily treated using a single simple grid." This Reynolds averaged compressible

Navier-Stokes solver was used for the design of a thrust reverser exhaust gas management system, and a freejet engine/inlet compatibility 2DCD nozzle. Parameters such as the centerline Mach number, jet spreading rate and velocity profiles were useful for the freejet nozzle design. This code has options for 2D or 3D, inviscid, viscous, laminar or turbulent and steady state or transient. While Garrard suggests that PARC should be used with caution for diffusers, backward facing steps and areas where there is flow separation and reattachment, it is useful for flows in 2DCD nozzles if the modified algebraic turbulence model is used.

Another Navier-Stokes code of prominence is the PAB3D code developed in conjunction with NASA Langley. This thin layer Navier-Stokes solver incorporates a multi-block multi-zone approach which simplifies grid generation. Each block can use a different numerical approach and topology. Four turbulence models are available in the code. The grid is adaptable based on geometry or pressure distribution for defining shock location or velocity distribution for the shear layer. References 25 through 28 all describe different aspects and applications of the code. A true afterbody nozzle calculation for an aftbody at a freestream Mach number of 0.94 is presented in figure 13. The different turbulence models used is this study, Baldwin Lomax and the Goldberg model, produced different aftbody flowfields with neither predicting the experimental boattail pressure data in the separated flow region downstream of a standing shock, figure 14. Future upgrades indicated as desirable for this program include a better turbulence model, a time dependent adaptive grid, and finite rate chemistry.

All of these codes would benefit from comprehensive experimental data with detailed measurements to validate the code and the turbulence models. The two papers which follow this one in the symposium address the important matter of calibrating CFD codes for particular applications. Both of these papers, references 29 and 30, see calibration as a way to gain confidence in the solver's ability to provide useful design information. Reed and Karman of General Dynamics looked at both qualitative and quantitative figures of merit including internal flow of a thrust vectoring nozzle, the development of an exhaust plume from a rectangular nozzle and the flow over the aftbody of a high aspect ratio nozzle. As will be shown, good agreement with the experimental data is evident. The conclusions of the authors will be left to their own presentations.

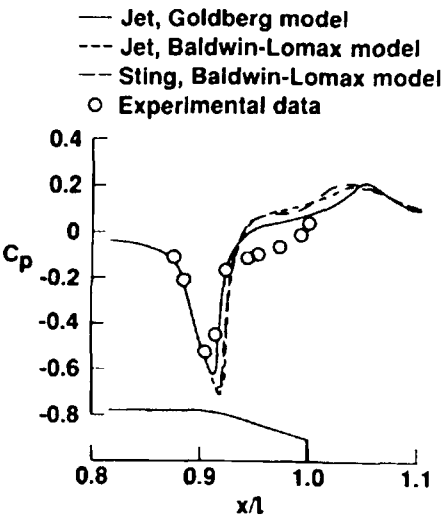

Figure 13 Effect of Turbulence Modeling, Reference 25

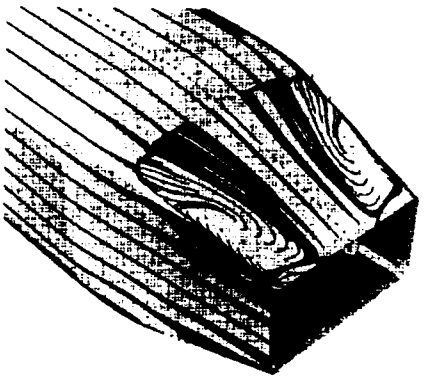

Figure 14A Afterbody Particle Traces, Baldwin-Lomax, Ref 25

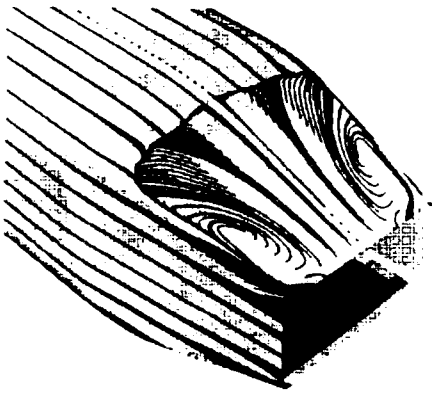

Figure 14B Afterbody Particle Traces, Goldberg, Ref 25

The issue of the correct or suitable turbulence model remains a problem for exhaust nozzle flows as well as other viscous dominated problems with flow separation and reattachment. Lowrie, reference 31, looked at a multi-zone k-e turbulence model for complex configurations. For his test case, an ejector nozzle, the k-e model matched the experimental data better than the Baldwin Lomax model though more data such as velocity profiles were desired to better define the differences. Many of the prior references also looked at different turbulence models for their code of interest. For most of the comparisons, the different models gave different results and it is apparent that no one model is appropriate at this time for all cases.

The comments expressed earlier with regard to user friendliness and Euler methods and especially with unstructured grids are reemphasized here for all CFD algorithms, Euler or Navier-Stokes. For a CFD method to be suitable for a design tool, the interface software and the user friendly considerations must be written into the codes so that input to a design decision can be made in a reasonable time and with reasonable effort and limited CFD knowledge. Rout in reference 32 describes a 2D/3D finite volume method for vectored nozzles which is highly interactive with automated advanced graphics based on a code with an intelligent data base system. The surface and volume grid generation is semi-automatic. The steps include defining the surface and inputing the grid density on the edges. The code then defines the surface and volume grid and satisfies the connectivity. Use of color graphics aids in analysis of the results. A propulsion design engineer who requires the use of higher power CFD codes for his decisions shouldn't have to examine each block and edge of the grid, define the surface and volume grids, address orthogonality and ensure that the connectivity is satisfied. With the movement to highly 3D complex shapes, the considerations of user friendliness must be incorporated into these grid generators. The code developers that answer these considerations will be assured of further use of their products.

The next great breakthrough in the use of CFD as a design tool may come with the increasing use of powerful "inexpensive" work stations. This may be the increase in computer speed and memory that the authors of WG 08 were projecting. From a series of articles from Aviation Week and Space Technology, August 19th, 1991, references 33-35, the increase in computing power of these desktop computers has increased dramatically.

"While the entire division of a major aerospace firm might have been lucky to command computing capability on the order of 10 million instructions per second (MIPS) just 10 years ago, an individual engineer can now have 10-75 MIPS of processing power sitting on his desktop" (reference 33).

Work stations with 100 MIPS are projected by next year and 1000 MIPS machines are discussed by the middle 90's. Further, the cost of these machines is dropping as competition increases and new products are introduced. Work stations that can compute over 70 MIPS are available for less than $20,000. These work stations will avoid the slowdown of computing experienced when mainframes are saturated and allow engineers to work together as a team by sharing data bases to enable true concurrent engineering. The full impact of these devices will be great but will not be known until the next seven year update is accomplished.

Many of the recommendations made seven years ago by the computational fluid dynamics subgroup for exhaust nozzle flow calculations are still valid today. Computational research should continue to improve modeling of flow separation. While detailed studies of the effect of turbulence modeling have been undertaken, an inadequate turbulence model is still the most stated reason for the inability of Navier-Stokes codes to predict flow separation. Three dimensional and zonal methods have been developed and this promising work must continue. There is still a need for the Navier-Stokes code development called for by WG 08 in grid generation, better solution algorithms and user friendliness. Finally, the coming of new faster workstations that are reasonably priced may result in "significantly better methods for predicting the effects of engine installation on the airplane aerodynamics" (reference 2). As suggested before, this paper is only a snapshot at the end of 1991 and should also be revisited after 5-10 years to reevaluate the state-of-the-art in CFD for exhaust nozzle aftbody applications.

8. Jet Noise... An Especially Troublesome Problem...

As difficult as the viscous nozzle boattail flow is to calculate for Navier-Stokes codes, the problem of calculating unsteady jet flow and the interaction with the adjacent freestream flow and the resulting noise, figure 15, is an order of magnitude more difficult and may not be possible at this time. Unfortunately, the interest and the need to address this problem has become more acute with considerations of sonic fatigue which plagues close spaced twin jet fighter aircraft and community noise associated with supersonic transport aircraft. This time dependent problem is not yielding in spite of a...

"significant increase in research efforts to investigate the role of unsteady jet flow in the production and propagation of aerodynamic noise with the objective of controlling such flow in a manner that significant noise reduction (occurs)" (Scott, reference 33).

The phenomenon is believed to be the interaction of the shock waves in the jet with other unsteady flow features such as the shear layer. A pioneer in this area, Jack Seiner of the NASA Langley Research Center, states that...

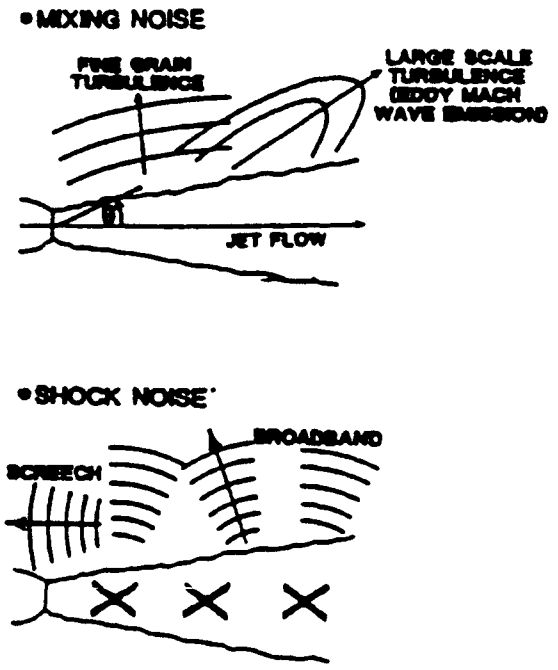

Figure 15 Noise Sources in Supersonic Jets, Reference 33

"...satisfactory solution of the aeroacoustics problem will depend highly on our understanding of the important flow disturbances that produce intense near field pressures. Understanding how these noise mechanisms are related to the plume dynamic structure must be achieved to provide a successful outcome" (reference 34).

The schemes which ensure that a numerical algorithm converges contribute to the inability of the method to compute this time dependent phenomenon by "quenching" the very turbulence that is responsible for the interaction (Sinha, reference 35). Sinha goes on to state that...

"A tentative conclusion drawn from our studies to date is that present capabilities to accurately simulate the detailed mean flow structure of imperfectly expanded jets, as requisite for evaluation of HSCT noise suppression concepts and acoustics application in general, is quite rudimentary. Turbulence modeling at a practical level is identified as the primary area of uncertainty..."

Scott indicates that more work is needed on the appropriate boundary conditions, avoidance of the damping of numerical oscillations affecting the acoustic oscillations being calculated, and the effect of the order of accuracy and the nature of the truncation errors with acoustic applications. Some calculations have been completed. Berman (reference 36) solved the incompressible Navier-Stokes equations with time dependent turbulent flow fluctuations but was not satisfied with the results. Further, he suggests a time averaged approach as a method to reduce the time required for the computations. The time averaged approach, however, loses important information when special applications are evaluated for noise prediction.

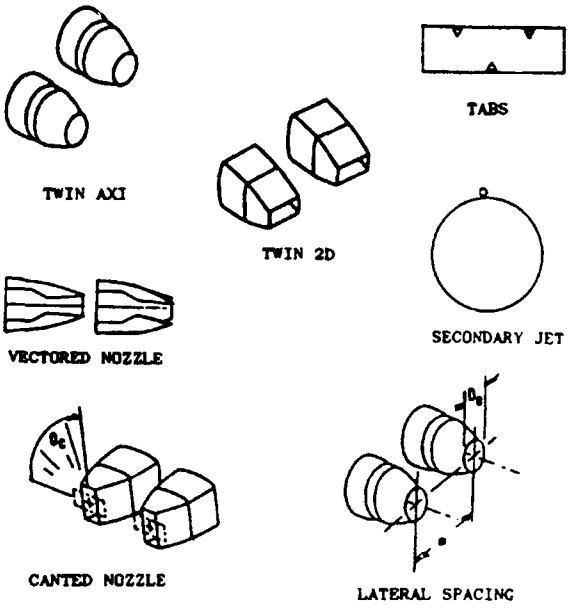

Figure 16 Parametric Nozzle Configurations, Reference 37

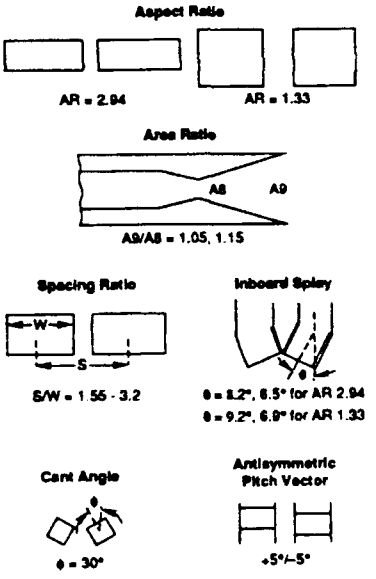

Figure 17 Summary of Twin Nozzle Orientations, Reference 38

An alternative to the computation is still the experiment. Walker (reference 37), Zilz (reference 38) and Seiner have parametrically characterized the noise produced for close spaced twin jets with the intent of providing design guidelines to avoid sonic fatigue problems in the aftbody area. For each of the parametrics shown in

figures 16 and 17, the overall sound pressure level was recorded in subscale tests. Seiner has also conducted full scale flight tests with the F-15 to record the dynamic pressure levels in the boattail region between the engines (reference 39).

The state-of-the-art for computing or measuring the noise generated by an unsteady jet exhaust plume is poor. To determine and satisfy the noise requirements for new high speed transports and to avoid sonic fatigue on advanced materials used in fighter aircraft, further work is needed in turbulence modeling and in systematic experiments that identify the physical mechanisms involved in the problem. Progress in this area will be slow depending on the development of turbulence modeling, experimental techniques and computer resources.

9. Conclusions and Recommendations

Both the experimental and computational techniques used for aerodynamic analysis of nozzle/aftbodies have changed since the 1984 WG 08 review.

For experimental techniques, the improvements have been small. New diagnostic techniques and electronically scanned pressure modules now provide additional qualitative data and more accurate pressure data, respectively. The next improvements will come with online computations using high power workstations, aiding test data analysis and overall test efficiency.

For nonviscous dominated nozzle flows, the Euler codes, especially with 2D and 3D adaptive unstructured grids, are being used as design tools, especially for internal nozzle performance. These codes can supplement the traditional static test, predicting thrust coefficient, internal pressures and thrust vector angle. For viscous flows, the use of Navier-Stokes codes have progressed from 1984, yet still suffer from many of the same problems as before. While computer power continues to improve due to larger and faster mainframes and new high power work stations, the scourge of CFD is still inadequate turbulence models. Special experimental test cases must be obtained as needed. Grid generation is still user-intensive in many organizations and must become user-friendly. Program interfaces must also be automated.

Jet noise, a highly viscous time dependent problem, still defies solution. This is the next great challenge for the nozzle designer who can use both the experiment and CFD to predict jet noise levels.

Based on this review of the state-of-the-art for techniques to analyze the aerodynamics of the nozzle/aftbody, these recommendations can be made:

1)The experimental facilities as we now know them, must be maintained and upgraded as necessary.

2)The use of Euler codes should be expanded for inviscid flows especially if 3D unstructured grids and solvers can be developed for complex shapes.

3)Turbulence models adequate for the nozzle aftbody must still be developed.

4)Calibration and validation of all CFD tools against good available data or generated data should be continued.

5)The user-friendliness of grid generation and code-to-code interfaces must be improved to increase efficiency and reduce clock time.

6)The difficult problem of jet noise must be addressed as tools and methods develop.

Finally, as with the 1984 report, this look at the state-of-the-art for nozzle aftbody aerodynamic analysis should be revisited now to include the European perspective and in the future as new developments become available.

10. References

1. Ferri, A., "Improved Nozzle Testing Techniques in Transonic Flow," AGARD-AG-208, Sept 1974.

2. "Report of the Working Group on Aerodynamics of Aircraft Afterbody," AGARD-AR-226, June 1986.

3. Bowers, D., Laughrey, J., "A Summary of an AGARD Assessment of Testing Techniques for Aircraft Afterbody Flows," AIAA-85-1465, July 1985.

4. Dusa, D.J., Speir, D.W., Rowe, R.K., "Advanced Technology Exhaust Nozzle Development," AIAA-83-1286, June 1983, Seattle, WA.

5. Laughrey, J.A., Moorhouse, D.J., "Propulsion Integration Results of the STOL and Maneuver Technology Demonstrator," AGARD-CP-498, October 1991, Fort Worth, TX.

6. Dornheim, M., "X-31 Flight Tests to Explore Combat Agility to 70 Degrees AOA," Aviation Week & Space Technology, March 11, 1991.

7. Mace, J., Doane, P., "Integrated Air Vehicle/Propulsion Technology for a Multi-Role Fighter - a McAir Perspective," AIAA 90-2278, July 1990, Orlando, FL.

8. Mace, J.L., et al, "Advanced Thrust Vectoring Nozzles for Supercruise Fighter Aircraft," AIAA 89-2816, July 1989, Monterey, CA.

9. Herrick, P.W., "Air-to-Ground Attack Fighter Improvements through Multi-Function Nozzles," SAE 901002, April 1990, Dayton, OH.

10. Dorn, M., "Aircraft Agility: The Science and the Opportunities," AIAA 89-2015, August 1989, Seattle, WA.

11. Berrier, B.L., "Results from NASA Langley Experimental Studies of Multiaxis Thrust Vectoring Nozzles," SAE 881481, October 1988, Anaheim, CA.

12. Foley, R.J., Pendergraft, O.C., Jr., "Static Thrust-Vectoring Performance of Nonaxisymmetric Convergent - Divergent Nozzles with Post-Exit Yaw Vanes," NASA TP-3085, May 1991.

13. Wing, D.J., Asbury, S.C., "Static Performance of a Multiaxis Thrust-Vectoring Cruciform Nozzle," AIAA 91-2137, June 1991, Sacramento, CA.

14. Taylor, J.G., "A Static Investigation of a Simultaneous Pitch and Yaw Thrust Vectoring 2-D C-D Nozzle," AIAA-88-2998, July 1988, Boston, MA.

15. Meyer, B.E., Re, R.S., Yetter, J.A., "Scale Model Test Results of Several STOVL Ventral Nozzle Concepts," AIAA-91-2134, June 1991, Sacramento, CA.

16. Bangert, L.S., Carson, G.T., Jr., "A Parametric Experimental Study of Isolated Rectangular Nozzles," AIAA-91-2136, June 1991, Sacramento, CA.

17. Bergman, B.K., Treiber, D.A., "The Application of Euler and Navier-Stokes Methodology to 2-D and 3-D Nozzle-Afterbody Flowfields," AIAA 88-0274.

18. Cheatham, P.L., Walker, S.H., Gridley, M.C., "Computation of Vectoring Nozzle Performance," AIAA 90-2752, July 1990, Orlando, FL.

19. Cheatham, P.L., Gridley, M.C., Walker, S.H., "Numerical Evaluation of a Two Dimensional Pitch and Yaw Vectoring Nozzle Using an Inviscid Flow Solver," SAE 91-GT-160, June 1991.

20. Rowe, R.K., et al, "Flowfield Performance Prediction of a 2D-CD Vectored Nozzle Using Self Adaptive Solution Method," AIAA 91-2367, June 1991, Sacramento, CA.

21. Syed, S.A., et al, "Application of CFD to Pitch/Yaw Thrust Vectoring Spherical Convergent Flap Nozzles," AIAA 90-2023, July 1990, Orlando, FL.

22. Koschel, W., et al, "Application of Finite Element Method to Hypersonic Nozzle Flow Computations," AGARD Propulsion Energetics Panel, Paper 33, May 1991, San Antonio, TX.

23. Garrard, G., et al, "Calibration of Parc for Propulsion Flows " AIAA 91-2152. June 1991, Sacramento, CA.

24. Cooper, G., Sirbaugh, J., "The PARC Distinction: A Practical Flow Simulator," AIAA 90-2002, July 1990, Orlando, FL.

25. Compton, W., Abdol-Hamid, K., "Navier Stokes Simulation of Transonic Afterbody Flows with Jet Exhaust," AIAA 90-3057, August 1990, Portland, OR.

26. Carlson, J.R., Abdol-Hamid, K.S., "Prediction of Internal Performance for Two-Dimensional Convergent - Divergent Nozzles," AIAA 91-2369, June 1991, Sacramento, CA.

27. Abdol-Hamid, K.S., "Application of a Multiblock/Multizone Code (PAB3D) for the Three-Dimensional Navier-Stokes Equations,"AIAA 91-2155, June 1991, Sacramento, CA.

28. Pao, S.P., Abdol-Hamid, K.S., "Application of a New Adaptive Grid for Aerodynamic Analysis of Shock Containing Single Jets," AIAA 90-2025, July 1990, Orlando, FL.

29. Reed, C.L., Muyshondt, A., "CFD Calibration for Three-Dimensional Nozzle/Afterbody Configurations," AGARD CP-498, October 1991, Fort Worth, TX.

30. Karman, S.L., Spragle, G.S., "Calibration of 2D Unstructured Grid Methods on Propulsive Flowfields," AGARD CP-498, October 1991, Fort Worth, TX.

31. Lowrie, B.W., "A Multi-Zone - Turbulence Model for Complex Configurations," AIAA 90-2001, July 1990, Orlando, FL.

32. Rout, R.K., et al, "Three-Dimensional Transonic and Supersonic Flow Prediction in Axi-Vectored Nozzles Using a Finite Volume Methods," AIAA-90-2026, July 1990, Orlando, FL.

33. Scott, J.N., "Numerical Analysis of Noise Generation in Unsteady Jet Flow," AIAA 91-2254, June 1991, Sacramento, CA.

34. Seiner, J.M., "Advances in High Speed Jet Aeroacoustics," AIAA 84-2275, October 1984, Williamsburg, VA.

35. Sinha, N., et al, "Prediction of Jet Mean Flow Structure in Support of HSCT Noise Suppression Concepts," AIAA 91-2253, June 1991, Sacramento, CA.

36. Berman, C., et al, "Three-Dimensional Jet Noise Computations," AIAA 91-2256, June 1991, Sacramento, CA.

37. Walker, S.H., "Twin Jet Screech Suppression Concepts Tested for 4.7% Axisymmetric and Two-Dimensional Nozzle Configurations," AIAA 90-2150, July 1990, Orlando, FL.

38. Zilz, D.E., Wlezien, R.W., "The Sensitivity of Near-Field Acoustics to the Orientation of Twin Two-Dimensional Supersonic Nozzles," AIAA 90-2149, July 1990, Orlando, FL.

39. Seiner, J.M., "Model and Full Scale Study of Twin Supersonic Plume Resonance," AIAA 87-0244, January 1987, Reno, Nevada.

Calibration of 2D Unstructured Grid Methods on Propulsive Flowfields

Steve L. Karman Jr.
Gregory S. Spragle
General Dynamics Fort Worth Division
Box 748, MZ 2877
Fort Worth, Texas 76101, USA

SUMMARY

A computational fluid dynamics (CFD) method is presented for the analysis of complex two-dimensional (2D) geometries using unstructured grid techniques. The grid generation procedure uses a split tree technique for subdividing the domain and generating internal mesh points. A Delaunay triangulation method is employed to triangulate the points, then iteratively refines the mesh based on cell aspect ratios and area variation to improve the quality of the initial mesh. The full Navier-Stokes equations are solved using an upwind flux difference splitting scheme for the inviscid flux and a central differencing scheme for the viscous flux. A two equation turbulence model is included for analyzing turbulent flows. A Jacobi iteration procedure is used to solve the linear set of implicit equations at each time step. Two 2D propulsive flowfields are analyzed and compared with experimental data. The grids are adapted to the flowfield by refinement based on the flowfield gradients. Improved resolution of the pertinent flowfield features were a result of the grid adaption employed.

LIST OF SYMBOLS

E	Total energy per unit volume
F	Inviscid flux vector
G	Viscous flux vector
$h_{x,y}$	x, y components of heat flux
l	Turbulent length scale
L_w	Wall proximity function
$\hat{n}_{x,y}$	x, y components of unit normal
$\hat{n}_t$	Normal velocity of moving face
NPR	Nozzle pressure ratio
p	Static pressure
$\frac{p_s}{p_p}$	Secondary to primary nozzle static pressure ratio
Q	Conservative variables
q^2	Turbulent kinetic energy
Re	Reynolds number based on U_∞
S	Source term vector
t	Time
T	Temperature
u, v	Cartesian velocity components
U	Contravarient velocity
x, y	Cartesian coordinates
γ	Ratio of specific heat
ρ	Density
κ	Thermal conductivity
μ	Kinematic viscosity
τ	Viscous stress tensor
Ω	Area of cell
σ	Length of side of cell

INTRODUCTION

Complex geometries and flow structures associated with propulsive flowfields can create challenges for the grid generation phase of an analysis. The geometries often demand elaborate grid topologies when the traditional boundary conforming structured grids are used. Not only is the grid generation more difficult, but the number of grid points required to resolve the geometry is often excessive. In addition, the gradients in the final numerical solution cannot be anticipated with much accuracy during the generation of the grid. As a result, the grid density can be too coarse in some regions and too fine in other regions. Unstructured grid methods provide a tremendous flexibility in the distribution of grid points to resolve complex geometries and flow physics. Highly complex geometries can be easily discretized with a minimal number of grid points. The data structures associated with unstructured grid methods also make refinement of the grid easier during the solution phase of the analysis. New grid points can be introduced into the mesh based on error indicators derived from the gradient information of the flowfield. With the proper selection of the error indicator, improved accuracy can be achieved. This paper will describe the use of unstructured grid methods in the analysis of two-dimensional propulsive flowfields. Two example cases will be analyzed and compared with experimental data and solutions from structured grid methods.

Copyright ©1991 by General Dynamics Corporation
All rights reserved
Published by AGARD with permission

GRID GENERATION

The generation of the initial mesh begins with the description of the boundaries and the distribution of grid points on the boundaries. Typically, the boundary shapes are prescribed using a series of simple geometric shapes such a lines and arc segments or by a discrete set of points. Grid points are then distributed on the boundaries with sufficient resolution to define the shape and with a smooth variation in grid point spacing along the boundary to minimize truncation errors in the solution method. This initial boundary distribution is important since it will be used by the flow solver in splining the boundary as grid refinements are performed.

After the boundary nodes are defined, interior nodes are produced using a split tree node generation procedure[1]. The domain is recursively subdivided into quadrilaterals based on the boundary node spacing and the proximity of the quadrilateral to the boundaries. Figure 1 shows the split tree subdivisions for the multiple slot ejector case described later. The actual nodes are introduced at the centroids of the quadrilaterals. Denser node distributions are evident near boundaries with smaller spacings.

The nodes are then triangulated using Bowyer's scheme[2]. In this scheme, a super-structure with a known triangulation is generated which surrounds the outer boundary of the domain. The nodes are introduced into the existing mesh one at a time. The triangles in the region of the new node which violate the Delaunay criteria are broken and the nodes are retriangulated. The process continues until all of the nodes are introduced. The triangles outside of the boundaries are then discarded. Figure 2 shows the triangulation of the split tree generated nodes for the multiple slot ejector.

The split tree node generation scheme produces nodes which, when triangulated, can result in cells with excessively high cell aspect ratio or large cell area variations. An iterative refinement node generation procedures[3] is used to introduce additional points into the mesh using the Bowyer's scheme. This procedure introduces new nodes at the center of the circumscribing circles of the violating cells based on user prescribed tolerance for minimum cell area and aspect ratios. The reduction in the high aspect ratio cells and large area cells is evident in figure 3.

The final step in the generation of the initial mesh is smoothing of the grid using a Laplacian smoothing scheme. The nodes are repositioned in a Jacobi iteration procedure where the new grid point location is computed as the average of the present value of the contiguous nodes, based on the connectivity established in the triangulation process. The resulting mesh, shown in figure 4, is a smooth grid with low aspect ratio cells.

GOVERNING EQUATIONS

The governing equations are the two-dimensional Navier-Stokes equations. A two equation turbulence model is included for computing turbulent flows[4]. The equations, shown below as one system of equations, are loosely coupled and actually solved as two independent systems in an implicit sense. The equations are given by

$$\frac{d}{dt}\int\int_{\Omega} Q d\Omega + \oint_{\sigma}(\vec{F}+\vec{G})\cdot\hat{n}d\sigma = \int\int_{\Omega} S d\Omega \quad (1)$$

where Q is the vector of conservative variables, F is the inviscid flux vector, G is the viscous flux vector, and S is the vector of source terms.

$$Q = \begin{bmatrix} \rho \\ \rho u \\ \rho v \\ E \\ \rho q^2 \\ \rho q^2 l \end{bmatrix}$$

$$\vec{F}\cdot\hat{n} = \hat{F} = \begin{bmatrix} \rho U \\ \rho u U + (p + \frac{\rho q^2}{3})\hat{n}_x \\ \rho v U + (p + \frac{\rho q^2}{3})\hat{n}_y \\ (E + p + \frac{\rho q^2}{3})U - (p + \frac{\rho q^2}{3})\hat{n}_t \\ \rho q^2 U \\ \rho q^2 l U \end{bmatrix}$$

$$\vec{G}\cdot\hat{n} = \hat{G} = \frac{-1}{Re}\begin{bmatrix} 0 \\ \tau_{xj}\hat{n}_j \\ \tau_{yj}\hat{n}_j \\ \hat{n}_j(\tau_{xj}u + \tau_{yj}v + h_j) \\ -\rho q l S_q (q^2)_j \hat{n}_j \\ -\rho q l S_q (q^2 l)_j \hat{n}_j \end{bmatrix}$$

$$S = \begin{bmatrix} 0 \\ 0 \\ 0 \\ -(P_s - \epsilon) \\ 2(P_s - \epsilon) \\ l E_1 P_s - \frac{\rho q^3}{B_1}\{1 + [E_3 + S_q B_1 l_j^2]\frac{l^2}{(KL_w)^2}\} \end{bmatrix}$$

The subscript j indicates a summation over x and y. The viscous stress terms and heat flux terms are given by

$$\tau_{xx} = \frac{2\mu}{3}(2u_x - v_y), \tau_{xy} = \mu(u_y + v_x),$$

$$\tau_{yy} = \frac{2\mu}{3}(2v_y - u_x), h_x = \kappa\frac{\partial t}{\partial x}, h_y = \kappa\frac{\partial t}{\partial y}$$

The pressure is computed using the ideal gas law

$$p = (\gamma - 1)[E - \frac{\rho}{2}(u^2 + v^2)]$$

and the contravarient velocity is given by

$$U = u\hat{n}_x + v\hat{n}_y + \hat{n}_t$$

The turbulence production and dissipation terms are

$$P_s = \left(\frac{\mu_{Turb}+\mu_{Lam}}{\mathrm{Re}}\right)^2 \frac{B_1^{\frac{1}{3}} q}{\rho q^2 l}\{2(u_x^2+v_y^2)+ (u_y+v_x)^2 - \frac{2}{3}(u_x+v_y)^2\} - \frac{1}{3}\rho q^2(u_x+v_y)$$

$$\epsilon = \frac{\rho q^3}{B_1 l}$$

The equations contain several empirical constants which were determined from simple shear flows, boundary layer flows and the decay of isotropic turbulence.

$B_1 = 19.25$, $S_q = 0.2$, $E_1 = 1.7$, $E_3 = 0.7$, K = 0.41

The turbulent viscosity is obtained from

$$\mu_{Tur} = \left(\frac{\chi^3 + f(6.9)^3}{\chi^3 + (6.9)^3}\right)\frac{\mathrm{Re}\rho q l}{B_1^{\frac{1}{3}}}$$

with

$$\chi = \frac{\mathrm{Re}\rho q l}{\mu_{Lam} B_1^{\frac{1}{3}}}$$

$$f = e^{-30(\frac{l}{\kappa L_w})^4}$$

The wall proximity function, L_w, is used to account for the dissipative effect of the wall on the turbulent length scale. For unstructured grids, this function will simply be closest distance to any wall.

FLOW SOLVER

The flow solver, known as JAGUAR2D, uses an implicit, finite-volume upwind scheme to solve the governing equation[5][6]. Cell-centered values of the conservative variables are computed by solving the discrete form of the integral equations over the triangular shaped cells. The inviscid portion of the flux on each face is computed using a flux difference splitting scheme. Higher order accuracy is obtained using extrapolated values of the primitive variables $\rho, u, v, p, \rho q^2$ and l. The extrapolation uses values of the primitive variables at the cell centers and averaged values at the nodes to obtain face values. A limiter is used to prevent overshoots in the extrapolations. The viscous portion of the flux is computed using central differences. The derivatives of velocity, temperature and the turbulent quantities are computed using local curvilinear transformations at the face using cell center values and nodal values.

The implicit scheme uses a Jacobi iteration procedure to solve the linearized equations. The residual, the sum of the fluxes around each cell, is computed once for each global timestep. The linearized implicit equation is then solved in an iterative manner where the off-diagonal terms are transferred to the right hand side of the equation. Information for the neighboring cells from the previous sub-iteration is used, thereby allowing the scheme to fully vectorize. Typically 10 to 20 subiterations are used with CFL numbers ranging from 1 to 200, depending on the problem being analyzed.

GRID ADAPTION

The grid is adapted to the flowfield by refining the grid in regions where large flowfield gradients exist. Grid adaption is generally performed periodically, allowing the solution to develop sufficiently between each adaption. The adaption function is generally a function such as pressure or Mach number. Refinement consists of bisecting any one or all three sides of the cell and assigning the values of the conservative variables of the parent cell to the new cells. Thus, mass, momentum and energy are conserved during the refinement. The adaption function is used as an error indicator in the refinement process. Nodal values of the adaption function are computed by averaging the surrounding cell center values. The normalized values of the difference in the adaption function between the nodes multiplied by the distance between the nodes are used to determine which edges are the be refined. Edges where the normalized difference is greater than a prescribed tolerance is marked for refinement.

Grid points can also be deleted from the grid based on the flowfield adaption gradients across the cell. In regions where the flowfield is not varying greatly and the grid spacing is too fine, grid points are deleted and the local region is reconnected with a Delauney connection scheme.

The grid is also smoothed between each refinement. The smoothing employed attempts to minimize, for each interior node, the sum of the aspect ratios of the surrounding cells[7]. A global iteration scheme updates the node locations computed using subiterations performed at each node. Each coordinate of the node is incrementally changed and the new sum of the aspect ratios is computed. If the new sum is greater than the old sum the direction of the point movement for the coordinate is reversed. The process is repeated for the other coordinate. The number of global iterations required to reach a stationary grid is generally less the ten.

APPLICATIONS

Two propulsive flowfields were analyzed with the unstructured CFD method described above. Both contain very complex flowfields and one involves a very complex geometry. The versatility awarded by using unstructured grids is demonstrated in these calibration cases..

Hypersonic Inlet

The first calibration case is a hypersonic inlet commonly referred to as the P8 inlet[8]. The geometry and initial grid are shown in figure 5. The ramp and center body are simulated in the bottom boundary of the grid, while the cowl and upper wall of the inlet are shown in the last third of the upper boundary. The initial mesh contained 2469 nodes and 4210 cells. Freestream conditions were : Mach 7.4 flow, Reynolds number of 8.86E06 per meter and temperature of 67.86 K. A no-slip isothermal wall boundary condition was imposed on the ramp, center body and cowl portions of the boundary with a wall temperature of 303.06 K. A no gradient outflow boundary condition was imposed on the rearward facing portion of the boundary above the cowl and the right end of the grid. Freestream conditions were maintained on the diagonal inflow boundary. A symmetry boundary condition was used for the small horizontal portion of the boundary ahead of the start of the ramp.

The grid was refined based on the gradients in Mach number in order to resolve the boundary layer and the shock reflections ocurring in the inlet. An adaption function based on the gradients in the velocity magnitude resulted in insufficient refinement in the shock regions because of the very large gradients present in the boundary layer. Pressure, alternately, would not refine the boundary layer at all. The Mach number tended to be the single best function to use for an adaption criteria for this analysis. The final grid, containing 39,864 points and 76,200 cells, is shown in figure 6. The details of the flowfield structure are apparent in the grid. Higher grid densities are evident in the boundary layer, the initial oblique shock wave and the internal portion of the inlet.

Mach and pitot pressure ratio contour lines are shown in figure 7. The ramp shock and cowl shock ar captured very crisply and the reflection pattern in the inlet is plainly visible. Very few grid points were wasted in the region between the ramp surface boundary layer and ramp shock and ahead of the ramp shock where the flowfield gradients are small.

Normalized surface pressures for the cowl and ramp are displayed in figure 8. The second CFD solution shown in the plot are the results from a structured grid flow solver, known as FALCON2D, which uses a very similar numerical scheme[9]. The present solution has the advantage of being able to refine the grid as the solution develops to resolve the pressure rise on the cowl surface. The cause of the oscillations in the unstructured solution is unknown, but could be the result of the rapid variation in cell areas that can occur in unstructured grids with the grid smoothing employed.

Rake data is compared against CFD results in figures 9 and 10. The unstructured solution is comparing as well as or better than the structured grid solution. The agreement at the top and bottom of the profiles appears to be slightly better for the present solution. One possible explanation is the refinement performed on the unstructured grid results in a finer grid density in the flow direction. As a result, the gradients in the flow direction near the walls are better resolved.

Multiple Slot Ejector

The second calibration case is a multiple-slot ejector nozzle tested by General Electric Aircraft Engines (GEAE) at FluiDyne Engineering Corporation[10]. The geometry and initial grid were shown in figure 4. This configuration contains four ejector nozzles feeding into one primary nozzle. The nozzle pressure ratio (NPR) was 14.0 with a secondary to primary static pressure ratio ($\frac{p_s}{p_p}$) of 0.30. No-slip adiabatic wall boundary conditions were imposed on the ejector bodies and internal walls of the nozzle. The top and left inflow boundaries used a characteristic inflow boundary condition with the appropriate reference conditions. A no-gradient outflow condition was imposed on the right boundary.

The grid was refined based on the gradients in Mach number. The final grid, containing 37,323 points and 71,067 cells, is shown in figure 11. The details of the shock reflections in the nozzle are visible in the changing grid density in the core portion of the nozzle. A tremendous amount of refinement was also performed in the mixing region of the nozzle. The Mach contour lines shown in figure 12 reveal the large gradients present in the solution. The reflection pattern in the contours also shows the reason for the grid refinement in the core region of the nozzle. This type of resolution would be difficult to anticipate with a stationary structured grid.

Particle traces at each ejector plane are shown in figure 13. The mixing of the multiple shear layers is evident in the plots. A small recirculation region ocurrs just aft of the first slot. This was also predicted in the structured grid solution computed by McFarlan, McMurry and Scaggs[11]. Their results and the current results are compared with test data in figures 14 through 16. There is good agreement between the two CFD solutions and the experimental data. The pressure comparison matches the limited experimental data very well. The weight flow ratios increases for each successive slot, as expected. The present solution predicts lower values of the weight flow ratios for the first two slots. This may be the result of inadequate refinement because of small Mach number gradients. The resulting computed thrust coefficients match data slightly better than the HAWK2D solution.

CONCLUSIONS

A CFD method using unstructured grid techniques has been applied to two propulsive flowfields. Grid

refinement was employed to adapt the grid to the gradients in the flowfield as the solution developed. Improved resolution of important flowfield features was a result. The comparisons made with experimental data showed agreement can be as good as results from structured grid analyses.

The selection of the error indicator is very important to the resulting refined grid. The most commonly used error indicator is based on the gradients in the velocity magnitude[12]. For high speed flows such as found in the first calibration case, the adaption concentrated more on resolving the velocity gradients in the boundary layer and tended to neglect the shocks and strong pressure gradients in the inlet. An error indicator based on the gradients of a combination of functions provides a topic for further investigation. The combination must be carefully selected, however. One possible choice for a combined function may be enthalpy and stagnation pressure. The enthalpy would produce adaption in the boundary layer and the stagnation pressure would produce adaption in the interior of the inlet and the shocks

ACKNOWLEDGEMENTS

The authors would like to acknowledge NASA for providing computer resources on the National Aerodynamic Simulation System.

REFERENCES

[1] S.R. Kennon. "A Vectorized Delaunay Triangulation Scheme for Non-Convex Domains With Automatic Nodal Point Generation". Technical Report AIAA-88-0314, American Institute of Aeronautics and Astronautics, 1988.

[2] A. Bowyer. "Computing Dirichlet Tessellations". *The Computer Journal*, 24(2):162-166, 1981.

[3] D.G. Holmes and D.D Snyder. "The Generation of Unstructured Triangular Meshes Using Delaunay Triangulation". In S. Sengupta, J. Hauser, P.R. Eiseman, and J.F. Thompson, editors, *Numerical Grid Generation in Computational Fluid Mechanics '88*, pages 643-652. Pineridge Press Limited, 1988.

[4] B.R. Smith. "The k-kl Turbulence Model and Wall Layer Model for Compressible Flows". Technical Report AIAA-90-1483, American Institute of Aeronautics and Astronautics, 1990.

[5] S.L. Karman Jr. and G. S. Spragle. "Development of an Unstructured CFD Method". Technical Report AIAA-91-0019, American Institute of Aeronautics and Astronautics, 1991.

[6] S.L. Karman Jr. *"Development of a 3D Unstructured CFD Method"*. PhD thesis, University of Texas at Arlington, May 1991.

[7] D.A. Anderson. " Smoothing of unstructured grids.". Unpublished presently, 1991. Personal consultation.

[8] A.V. Gnos, E.C. Watson, W.R. Seebaugh, R.J. Sanator, and J.P. DeCarlo. "Investigation of Flow Fields Within Large-Scale Hypersonic Inlet Models". NASA Tech. Note NASA TN D-7150, NASA, April 1973.

[9] M.C. Bissinger, T.J. Benson, and R.G. Bradley. "Aerodynamics of High Speed Air Intakes, Assessment of CFD Results - Review on AGARD FDP WG13". In *AGARD Conference Proceedings, Aerodynamic Engine/Airframe Integration for High Performance Aircraft and Missiles*, 1991.

[10] J.F. Federspiel and A.P. Kuchar. "Performance Evaluation of a Two-Dimensional Convergent-Divergent Ejector Exhaust System". Technical Report AIAA-88-2999, American Institute of Aeronautics and Astronautics, 1988.

[11] J.D. McFarlan, C.B. McMurry, and W.F. Scaggs. "Computational Investigation of Two-Dimensional Ejector Nozzle Flow Fields". Technical Report AIAA-90-2148, American Institute of Aeronautics and Astronautics, 1990.

[12] G.P. Warren, W.K. Anderson, J.L. Thomas, and S.L. Krist. "Grid Convergence for Adaptive Methods". Technical Report AIAA-91-1592, American Institute of Aeronautics and Astronautics, 1991.

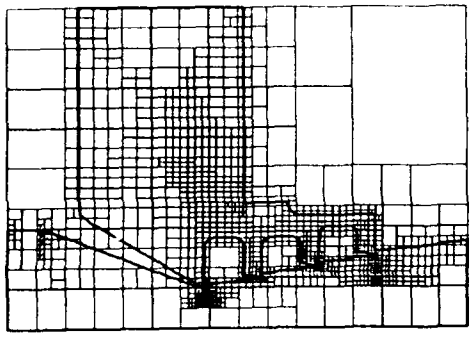

Figure 1: Split tree subdivision of multiple slot ejector case.

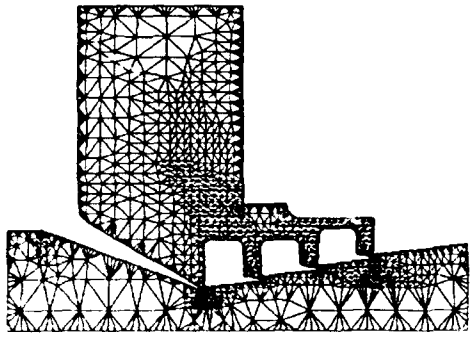

Figure 2: Delaunay triangulated mesh of split tree nodes.

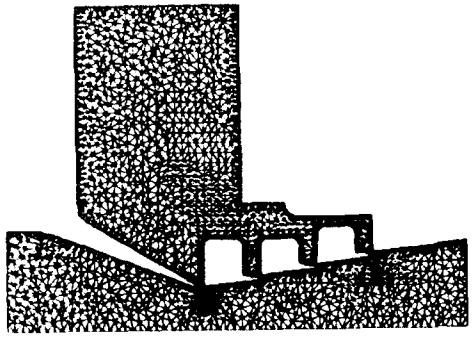

Figure 3: Refined mesh based on cell area and cell aspect ratio.

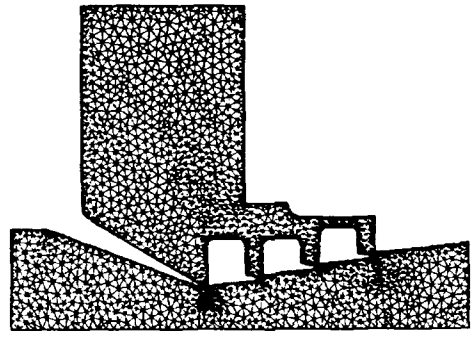

Figure 4: Laplacian smoothed mesh.

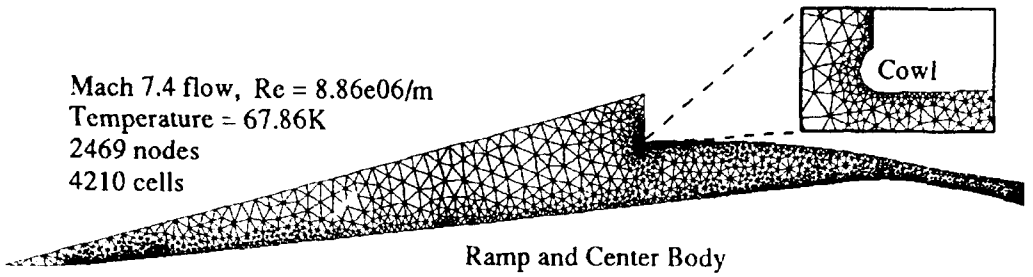

Figure 5: Initial mesh for P8 calibration case.

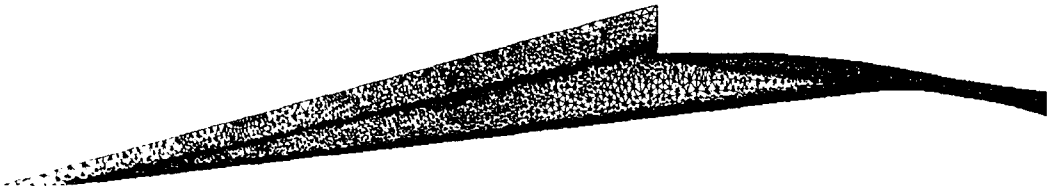

Figure 6: Final mesh for P8 calibration case.

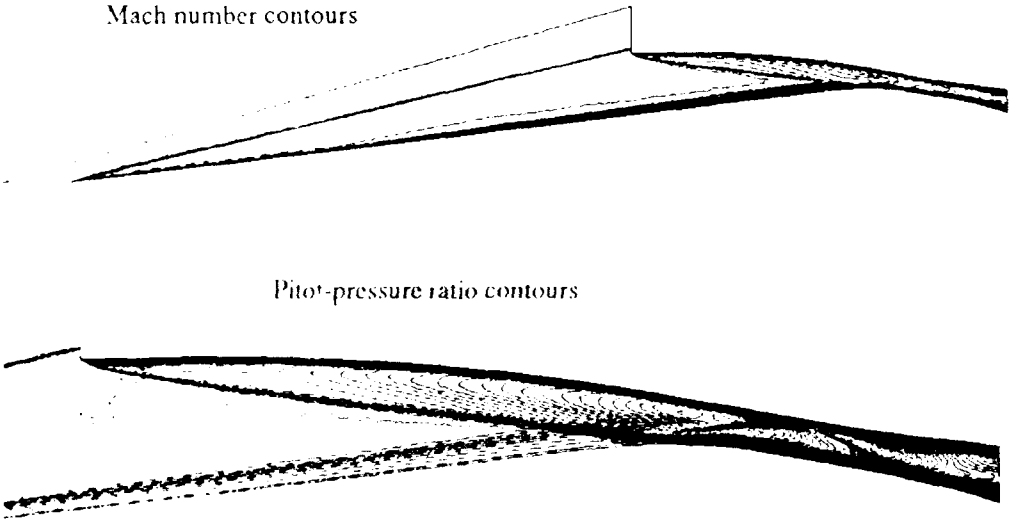

Figure 7: Contour lines of Mach and pitot pressure ratio for P8 calibration case.

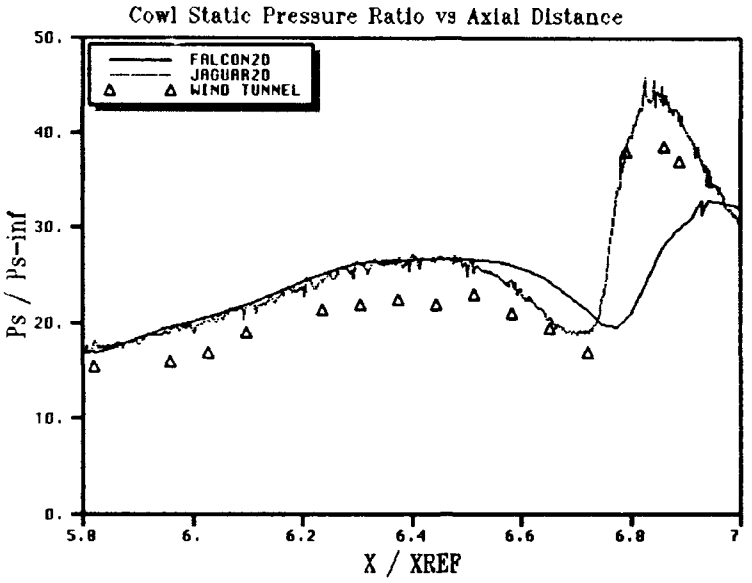

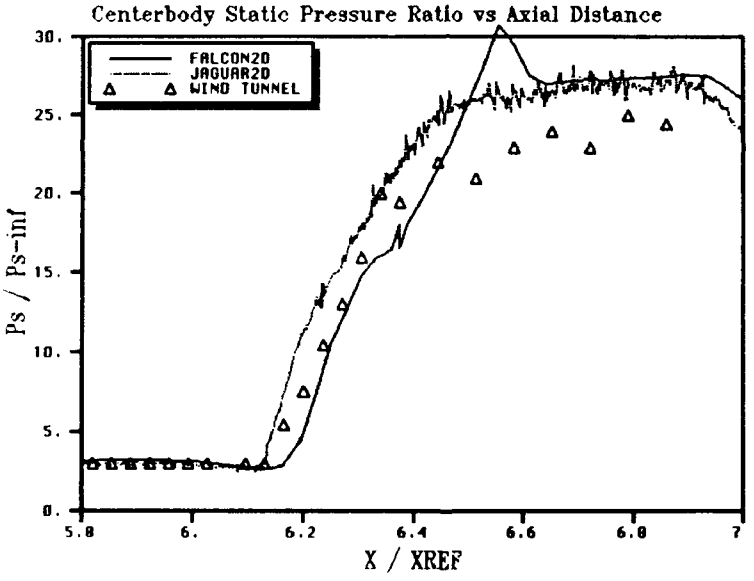

Figure 8: Normalized pressure comparison for P8 calibration case.

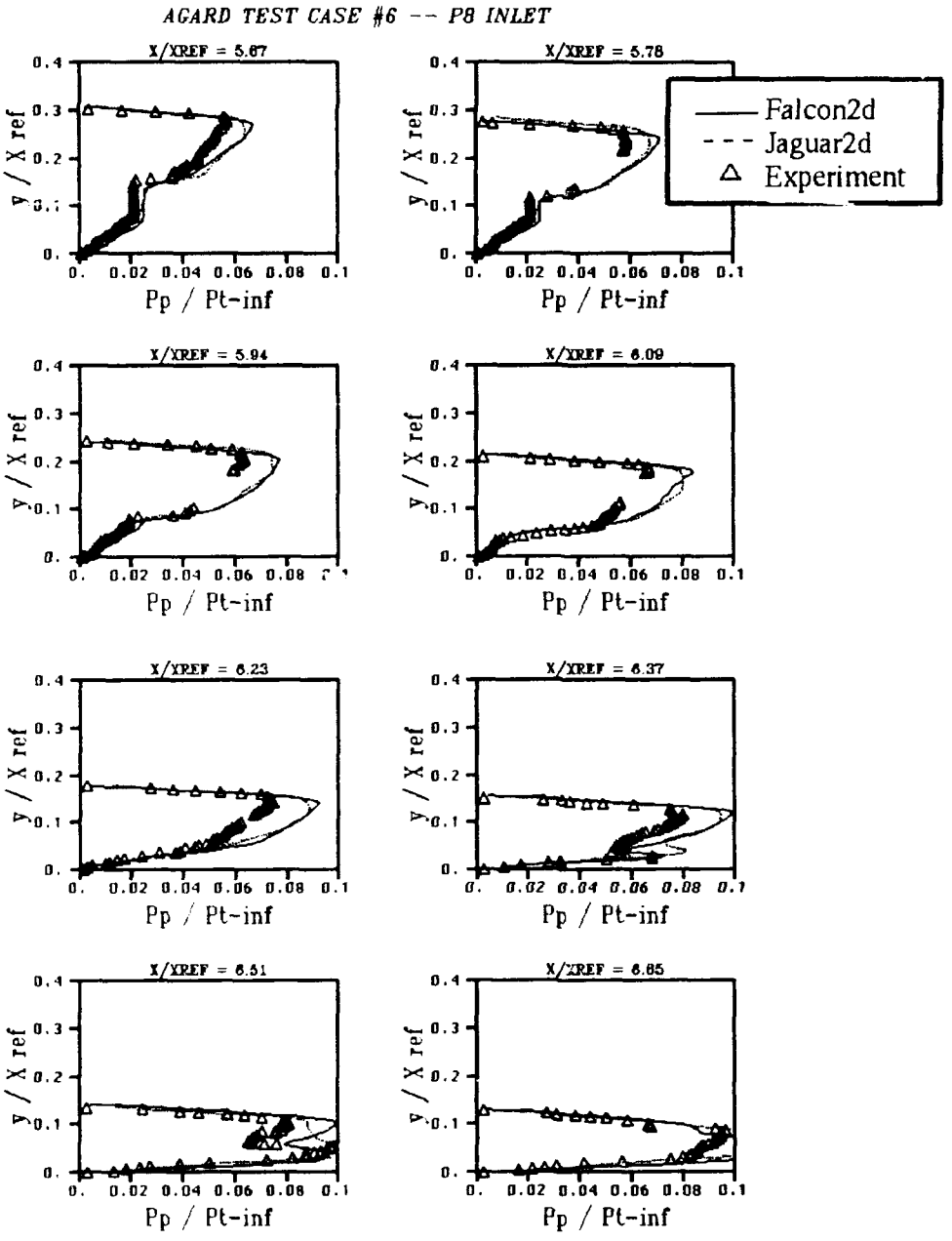

Figure 9: Pitot-pressure ratio comparison for P8 calibration case.

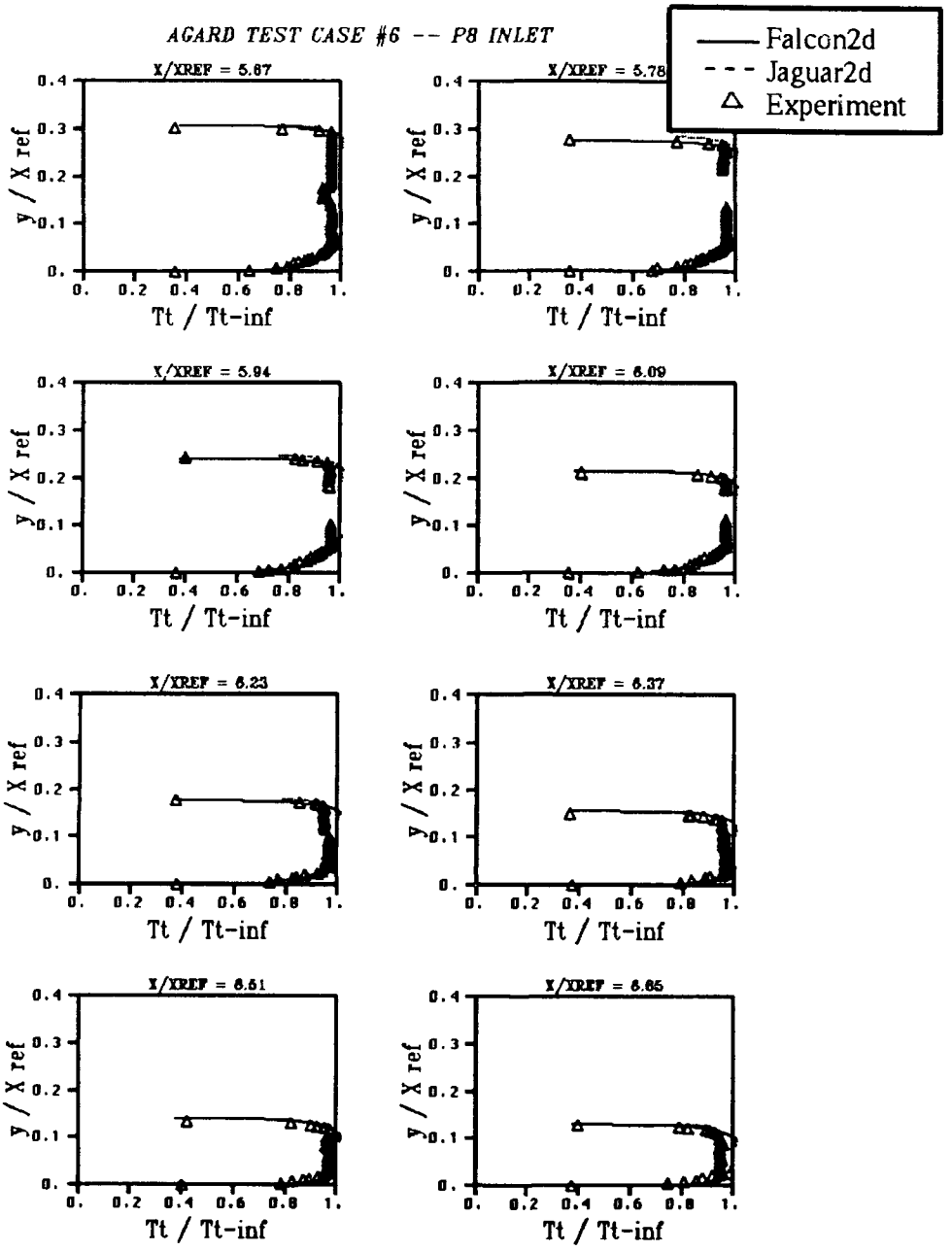

Figure 10: Stagnation-temperature ratio comparison for P8 calibration case.

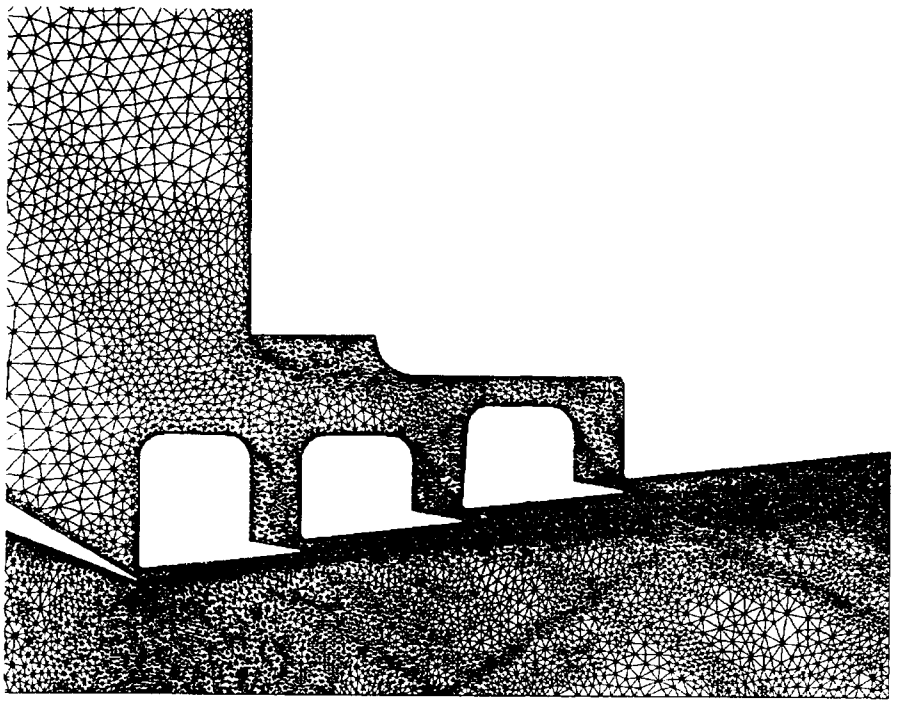

Figure 11: Final mesh for ejector calibration case.

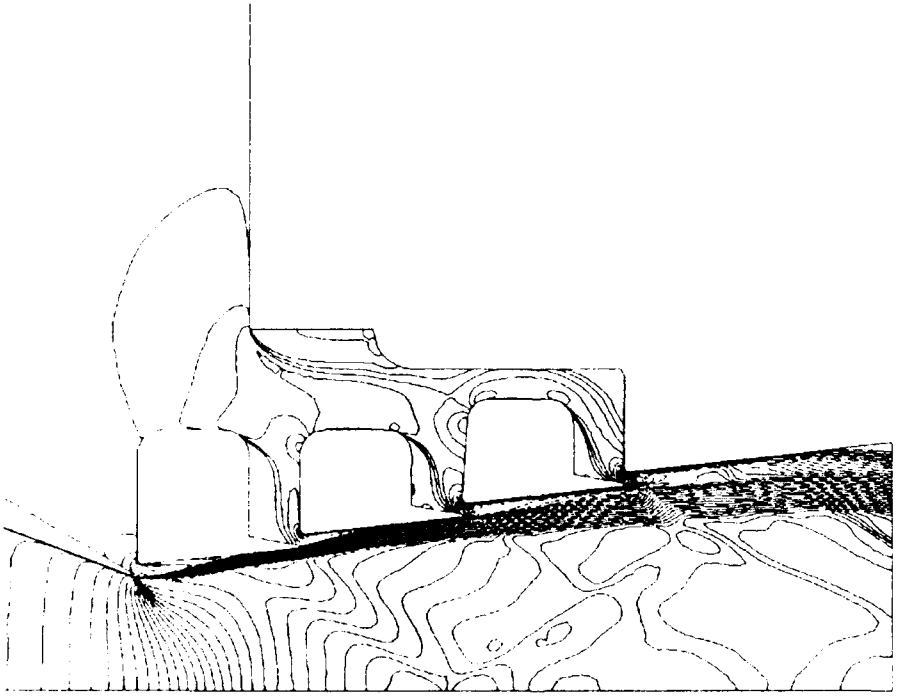

Figure 12: Mach Contour lines for ejector calibration case

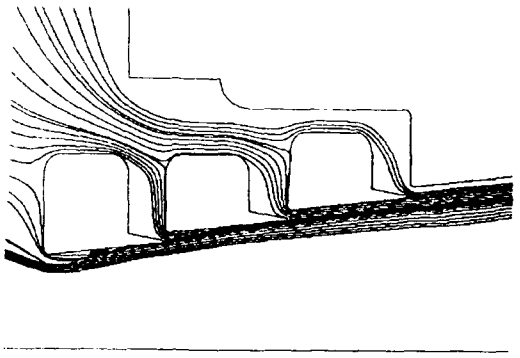

Figure 13: Particle traces at the secondary ejector nozzles.

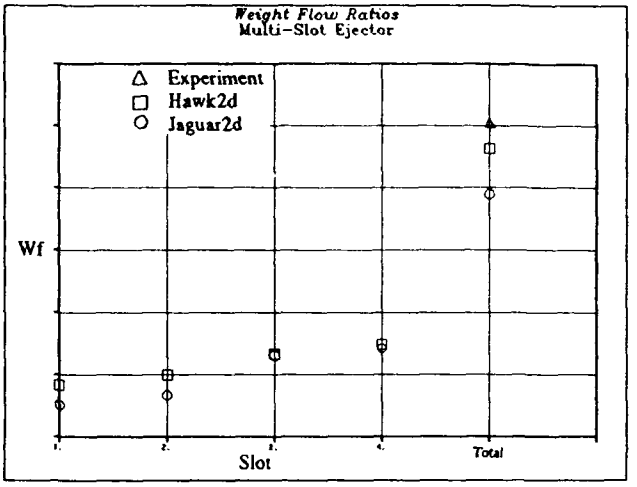

Figure 15: Secondary-to-primary weight flow ratio comparison for ejector calibration case.

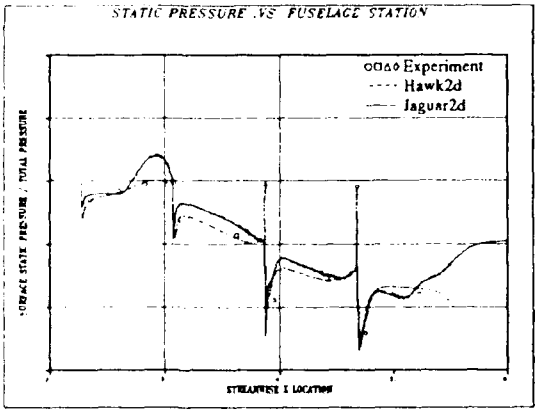

Figure 14: Pressure distribution comparison for ejector calibration case.

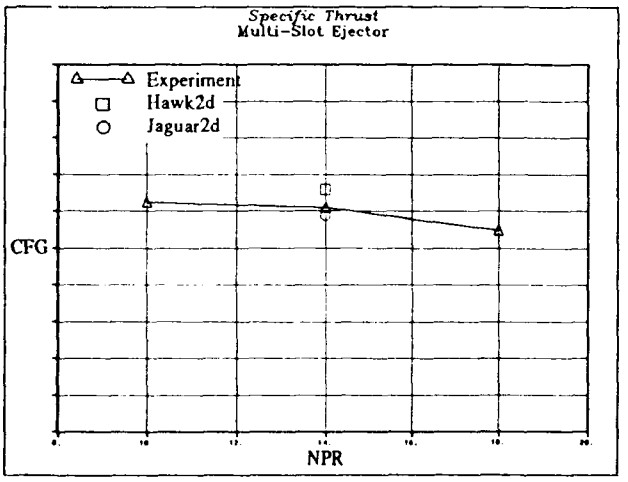

Figure 16: Thrust coefficient comparison for ejector calibration case.

CFD Calibration for Three-Dimensional Nozzle/Afterbody Configurations

Christopher L. Reed
Arnold Muyshondt
General Dynamics Fort Worth Division
Box 748, MZ 2877
Fort Worth, Texas 76101, USA

SUMMARY

The current trend in fighter aircraft design is toward highly integrated propulsive exhaust systems. In order to achieve this level of integration, extensive testing and analysis is required. Modern computational fluid dynamics(CFD) techniques have become popular in performing a part of the required analyses. Because of the complexity of most nozzle/afterbody type flow fields, Navier-Stokes codes are generally the preferred CFD methods. To gain confidence in these solvers ability to provide useful design information, a number of calibration analyses must be conducted for which extensive test data are available for comparison. This paper describes three such analyses which have been used to calibrate two Navier-Stokes codes. The first case deals with the internal flow through a vectored nozzle. The second case looks at the development of an exhaust plume issuing from a rectangular nozzle. The third case considers the flow over an afterbody with a high-aspect-ratio rectangular nozzle. In all cases, both qualitative and quantitative comparisons are made between the test data and the CFD data. Good comparisons are obtained and additional confidence is gained in these CFD codes ability to provide useful engineering data.

LIST OF SYMBOLS

C_{fg}	Thrust coefficient
k	Turbulent kinetic energy
l	Length scale of turbulence
M	Mach number
p	Static pressure
P_t	Total or stagnation pressure
Re	Reynolds number
t	Temperature
u, v, w	Cartesian velocity components
x, y, z	Cartesian coordinates
y^+	Nondimensional Law of the Wall length
ρ	Density
∞	Freestream conditions

Copyright ©1991 by General Dynamics Corporation
All rights reserved.
Published by AGARD with permission

INTRODUCTION

Current advances in military aircraft design require a highly integrated configuration. This is especially true for the nozzle/afterbody region of a fighter type aircraft where numerous flow interactions take place which greatly affect the performance of the aircraft. Traditionally, propulsive nozzles were designed and built by engine manufacturers and the aircraft was designed to fair back into the axisymmetric nozzle. Currently, airframe and engine manufacturers are working closely to optimize highly integrated designs. Axisymmetric nozzles are giving way to a variety of nonaxisymmetric forms such as rectangular or diamond shaped. Since the flow path through a turbine engine is basically axisymmetric (because of rotating machinery), shapes other than axisymmetric require transition sections and flow turning greater than that required in axisymmetric nozzles. Externally, many nonaxisymmetric nozzle/afterbody configurations are geometrically simpler than axisymmetric configurations particularly for twin-engine designs. However, a detailed understanding of the flow field is needed to avoid flow separation and increased drag. Development of these new designs requires extensive testing and analysis. Computational fluid dynamics (CFD) techniques have played an increasingly important role in the design and optimization of nozzle/afterbody configurations. This paper presents three test cases in which three-dimensional nozzle/afterbody configurations are analyzed using CFD techniques and the results compared with experimentally obtained data.

DESCRIPTION OF THE CFD CODES

Two different computational fluid dynamics codes were used in the analyses. The following sections describe the theory and features of these codes. Also included is a section describing the pre- and post-processing programs used to set-up the analyses and analyze the results.

HAWK Code Description

The HAWK CFD analysis code is a derivative of the PARC code[1] which is in turn a derivative of the ARC code[2]. HAWK is a finite-difference code which solves the complete Navier-Stokes equations in conservation law form. These equations are solved at discrete grid points on a curvilinear set of coordinates. The Navier-Stokes equations are solved using the implicit Beam and Warming approximate factorization algorithm[3]. In three-dimensions, the Beam and Warming algorithm approximately factors the equations into three parts (representing the three coordinate directions). For efficient steady-state calculations, the block pentadiagonal equation is diagonalized to form a set of scalar pentadiagonal equations which are easily solved. Since this code makes use of central differences, artificial dissipation is added both implicitly and explicitly. This dissipation is the switched fourth-order and second-order form of Jameson[4] except that it is implemented separately in each coordinate direction. This directional implementati .1 reduces the need for artificial viscosity in the boundary layer where natural viscosity provides sufficient smoothing for numerical stability.

Unlike the ARC and PARC codes, the HAWK code makes use of the *k-kl* two-equation turbulence model[5] and wall function boundary condition[6]. The *k kl* turbulence model adds two additional transport equations which are solved to obtain the turbulent kinetic energy and the turbulent length scale. These equations are solved using the same solution algorithm as the mean flow equations. The *k-kl* equations are coupled to the mean flow equations through a modification to the pressure term in the momentum and energy equations and through the calculation of a turbulent viscosity which is added to the molecular viscosity.

A wall function boundary condition is applied along no-slip walls where a very fine grid spacing is usually required in order to resolve a turbulent boundary layer. Generally, to adequately resolve a turbulent boundary layer requires that the first grid point off of a no-slip wall be located in the viscous sublayer where $y^+ \leq 5$. The wall function boundary condition actually patches in to the solution a boundary layer profile based on the solution of an ordinary differential equation. With this approach, the first grid point off of the wall can be located in the logarithmic region of the boundary layer where the y^+ is from 50 to 200. The overall reduction in the number of grid points and the increase in size of the minimum grid spacing lead to faster convergence of the solution without a significant reduction in accuracy.

The HAWK code includes a number of other boundary condition types which allow the user to have a great deal of versatility in specifying the boundary conditions. These additional boundary condition types include slip wall, adiabatic no-slip wall, isothermal no-slip wall, symmetry, specified total pressure- total temperature, characteristic inflow/outflow, specified mass flux, specified static pressure(subsonic outflow), and extrapolation. The specific boundary conditions used in each of the calibration cases will be discussed below.

FALCON Code Description

The FALCON CFD analysis code has been developed at the General Dynamics Fort Worth Division. Although it is similar in features and capability to the HAWK code, it has some distinct features which make it attractive. FALCON solves the complete Navier-Stokes equations using a finite-volume approach. The finite-volume approach means that the flow field is discretized by dividing it into a number of rectangular-parallelepiped regions over which the integral form of the Navier-Stokes equations are solved. Since the conservation equations are solved in an integral form on each cell, the method is naturally conservative (unlike finite-difference methods). The discretized equations are solved using the diagonally inverted LU implicit scheme of Yokota and Caughey[7]. In this method, the block-banded implicit delta operator is factored into two block triangular operators which are based on one-sided implicit spatial differences. The solution of the LU factorization is simplified by diagonally inverting its 5X5 matrix systems. This diagonalizing procedure transforms the lower and upper sweeps into uncoupled systems of scalar equations that retain both the stability and time accuracy of the original LU factorization. Unlike the diagonalized Beam-Warming scheme used in HAWK, time conservation is not altered by the decoupling process.

Since FALCON is a central difference code, artificial dissipation is added explicitly. This dissipation is the switched fourth-order and second-order form of Jameson[4] implemented separately in each direction. The FALCON code also makes use of the *k-kl* two-equation turbulence model[5] and wall function boundary conditions[6]. The *k-kl* equations are solved in the same manner as the mean flow equations. The turbulence model is coupled to the mean flow equations by a turbulent viscosity which is added to the molecular viscosity. Optionally, it can be coupled by a modification to the pressure term in the momentum and energy equations.

The same type of wall function boundary condition described for HAWK is implemented in the FALCON code, allowing the first grid point off of a no-slip wall to be located at a much greater distance from the wall. This increase in the minimum grid spacing off of a no-slip wall translates into a reduction in the overall number of grid points and leads to faster convergence of the solution.

As with the HAWK code, the FALCON code contains a number of built-in boundary condition types which the user can use to specify a particular analy-

sis. These boundary condition types include slip wall, adiabatic no-slip wall, isothermal no-slip wall, symmetry, specified total pressure- total temperature, characteristic inflow/outflow, and extrapolation. The specific boundary conditions used in each of the calibration cases will be discussed below.

Grid Generation

The GRIDGEN series of codes[8] were used to develop the grid system for each analysis. This series of grid generation codes were developed at the General Dynamics Fort Worth Division under contract to the United States Air Force. They were developed to provide efficient, user friendly, and robust grid generation tools that would allow for routine application of multiple-block computational fluid dynamics flow solvers to complex aircraft systems. The GRIDGEN system consists of four main programs: GRIDBLOCK, GRIDGEN2D, GRIDGEN3D, and GRIDVUE3D. The GRIDBLOCK program is a highly interactive graphical program which allows the user to define the grid topology, block structure, grid size, basic geometry, and boundary conditions. The GRIDGEN2D program is used to develop all of the surface grids using algebraic and elliptical grid generation techniques. GRIDGEN2D is also graphically oriented and highly interactive. After the surface grids are developed, the GRIDGEN3D program is used to generate the three-dimensional volume grids. The volume grid generation process is the only part of the procedure that is not interactive. The GRIDVUE3D program is used to view the volume grid once it is generated. Additional information about the grid generation system is available in reference [8].

Post Processing

Integrated quantities and local flow data shown in this paper were computed by the flow solver program or other specialty programs written specifically for these analyses. A large part of the graphics used in this article was produced using the PLOT3D program[9] developed at the NASA Ames Research Center. This program reads a grid file containing the physical grid point locations (x, y, z) and a solution file containing the conservative variables (ρ, ρu, ρv, ρw, ρe). The user can then specify the subset (or subsets) to view, as well as, geometrical features (walls) which should be plotted. A number of different functions can then be computed and displayed. The functions include any of the conservative variables, as well as, Mach number, temperature, pressure, stagnation temperature, stagnation pressure, velocity, velocity vectors, particle traces, the grid, and much more.

CALIBRATION CASES

Three test cases have recently been used in the calibration of the previously discussed three-dimensional Navier-Stokes codes. Each of these test cases is a nozzle/afterbody type flow. Two of the analyses were carried out using the HAWK code and one was carried out using the FALCON code. The following sections describe these calibration cases including the physical experiments, the numerical analyses, and comparisons between the test data and the analytical results.

SCF Internal Nozzle Flow

The Spherical Convergent Flap (SCF) nozzle was tested under the Exhaust Nozzles for Aerocontrol program sponsored by the Air Force Wright Aeronautical Laboratories and conducted by the McDonnell Aircraft Company with participation from General Electric Aircraft Engines and Pratt & Whitney Aircraft. The nozzle was tested statically on the NASA Langley six-component strain-gage balance thrust stand. The SCF test model and approximate instrumentation locations are shown in Figure 1. Geometric parameters tested included throat aspect ratio (1.27, 2.08, and 2.5), area ratio (1.46 and 1.63), yaw angle (0, 7, 15, 20, and 25 deg.), and pitch angle (0, 20, and 25 deg). The nozzle stagnation temperature was kept at 530°R and the stagnation pressure ranged up to thirteen atmospheres, allowing for nozzle total pressure to free-stream static pressure ratios of thirteen. The model was outfitted with eight static pressure taps along the sidewall and transition section on both the right and left sides. Both sidewalls were instrumented with eight static pressure taps along the centerline. The upper and lower flaps of this model had pressure taps along the centerline with two additional taps on either side [10][11].

The configuration selected for the CFD analysis had a throat aspect ratio of 1.27, an area ratio of 1.46, and was tested at 25 degrees pitch and 0 degrees yaw vector angle. A two block, H-topology surface grid was generated using GRIDGEN2D[8]. The internal domain of each block was generated with GRIDGEN3D[8]. Taking advantage of symmetry, it was only necessary to model one half of the test geometry. The grid spacing at the solid walls was such that $50 < y^+ < 200$. Both blocks had dimensions of 46 X 40 X 60 for a total of 220,800 grid points. Point-to-point matching was observed at the block interface.

The flow field was analyzed using the HAWK solver. All solid walls were modeled using a no-slip adiabatic wall function boundary condition. The nozzle inflow plane was modeled with a constant total pressure, subsonic inflow boundary condition such that $P_t/p_\infty = 5.9$ to match the test point. The exit plane of the grid was modeled using a supersonic extrapolation boundary condition, and the symmetry plane was modeled with a symmetry boundary condition.

The HAWK code was run in the viscous mode including the two-equation turbulence model on a CRAY

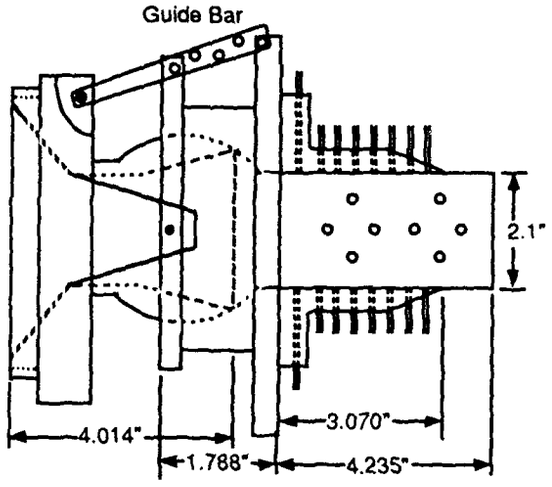

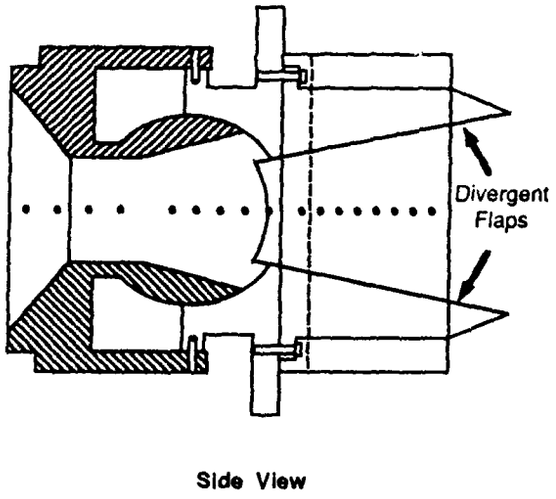

Figure 1: SCF Model and Instrumentation.

Table 1: SCF performance characteristics.

	C_{fg}	C_{fg_x}	C_{fg_y}	Thrust Angle
CFD	0.9703	0.8959	0.3719	22.55°
Test	0.9803	0.8989	0.3910	23.51°
% Δ	1.02	0.34	4.88	4.08

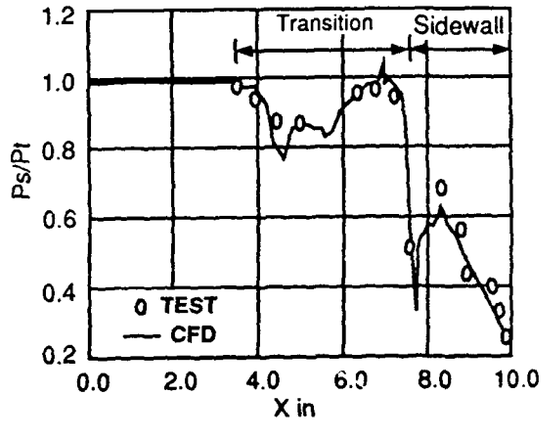

Figure 2: SCF static pressure along the transition section and sidewall.

XMP. The solution was stopped af'er 1800 iterations at which time the L^2 residual had dropped over three orders of magnitude. While solving, mass flow and thrust coefficient at the nozzle exit plane were also tracked. At the time the solution was stopped, both mass flow and thrust coefficient had changed less than 0.01 percent during the previous 500 iterations.

Figures 2, 3 and 4 show comparisons of the static pressures along the transition section, convergent section, sidewall, and upper and lower divergent flaps. Good agreement is seen for most of the comparisons except for a slight discrepancy in the predicted underexpansion and recompression on the lower flap. This discrepancy is likely due to an under prediction by the solver of the separated flow region on the lower flap and a lack of grid resolution in the area. Table 1 shows a comparison of measured and calculated thrust coefficients and angles. Excellent agreement is observed between the measured and the calculated axial thrust coefficient. The discrepancy in normal thrust coefficient, and consequently total thrust and thrust angle is again attributed to the underprediction of the separated flow region and the lack of grid resolution in this area. Figure 5 shows Mach contours along the symmetry plane for the CFD solution. Separation is evident along the lower flap.

NASA Langley Afterbody Plume

An investigation was conducted at the NASA Langley 16-Foot Transonic Tunnel to characterize the flow

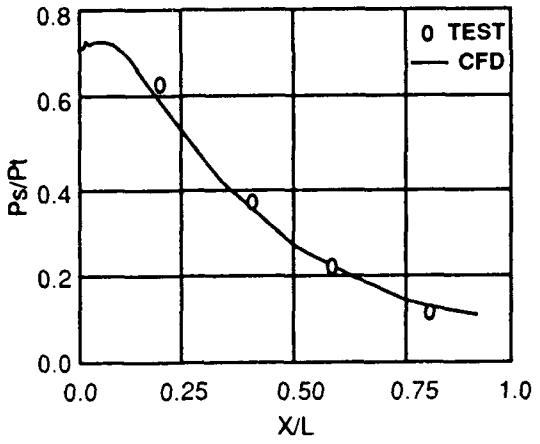

Figure 3: SCF static pressures along the upper divergent flap.

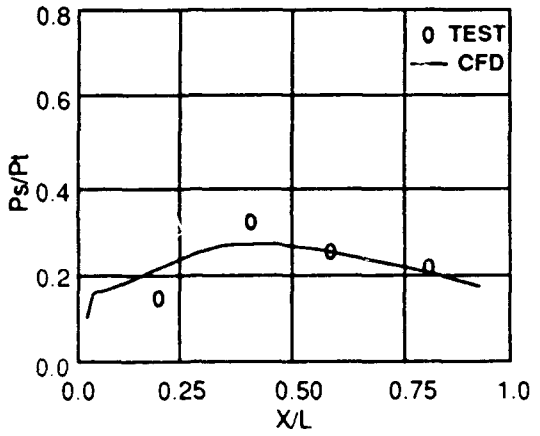

Figure 4: SCF static pressures along the lower divergent flap.

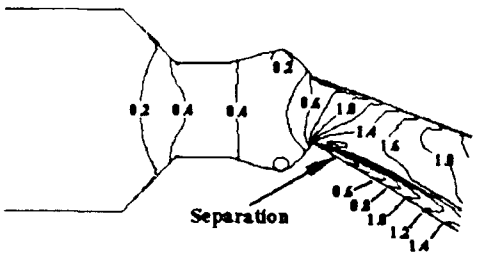

Figure 5: SCF centerline Mach contours for CFD solution.

field in and around the jet plume of a nonaxisymmetric nozzle configuration [12]. The nozzle tested had an aspect ratio of 1.9 and an area ratio of 1.25. Pitot-pressure measurements were made at five locations downstream of the nozzle exit to a maximum downstream distance of five nozzle heights (0.0, 2.6, 5.2, 7.8, and 10.4 in.). The nozzle was operated at a nozzle total pressure to free-stream static pressure ratio of 4.0. Measurements were taken at free-stream Mach numbers of 0.0, 0.6, and 1.2. The jet total temperature was held at approximately 530°R for all tests. The test model is shown in figure 6.

The flow field behind the nozzle was characterized with a seven probe rake with the probes spaced 0.5 inches apart. At each longitudinal station, pitot pressure measurements were taken every 0.1 inches from the jet centerline to approximately 6.5 inches outward. A total of 11 roll angles were obtained to give a sweep from 0 to 90.0 degrees at each longitudinal station.

The Mach 1.2 case was chosen for analysis due to the vortex-like flow known to exist near the corners on the afterbody closure section and nozzle exit. A five block surface H-grid was generated using GRIDGEN2D[8] and GRIDGEN3D[8] was used to generate the internal domain for each block . Taking advantage of symmetry, it was only necessary to model one fourth of the test geometry. The support strut was considered to have a minimal effect on the jet plume; therefore, it was neglected for this analysis. Proper modeling of the test geometry required the block dimensions to be 45 X 65 X 37, 45 X 65 X 30, 36 X 30 X 30, 46 X 30 X 37, and 46 X 65 X 30 for a total of 369,135 grid points. Point-to-point matching was observed between block interfaces, and the grid spacing at the solid walls was such that $50 < y^+ < 200$. The grid terminated at approximately 13 nozzle heights downstream of the nozzle exit and the far-field was at 4 heights at the beginning of the forebody, and 20 heights at the end of the grid. In order to conserve grid points the grid was started at the tip of the forebody.

The five block system was analyzed using the HAWK solver. All solid walls were modeled using a no-slip adiabatic wall function boundary condition. The nozzle inflow plane was modeled with a constant total pressure, subsonic inflow boundary condition such that $P_t/p_\infty = 4.0$. The exit plane of the grid was modeled using a supersonic extrapolation boundary condition, while the far-field was modeled using a characteristic far-field boundary condition. The symmetry planes were modeled with a symmetry boundary condition, and the forebody inflow plane was fixed at free-stream conditions.

The HAWK code in the viscous mode, including the two-equation turbulence model, was run on a CRAY YMP. Solution time was 45 seconds per iteration. The solution was stopped after 4600 iterations at

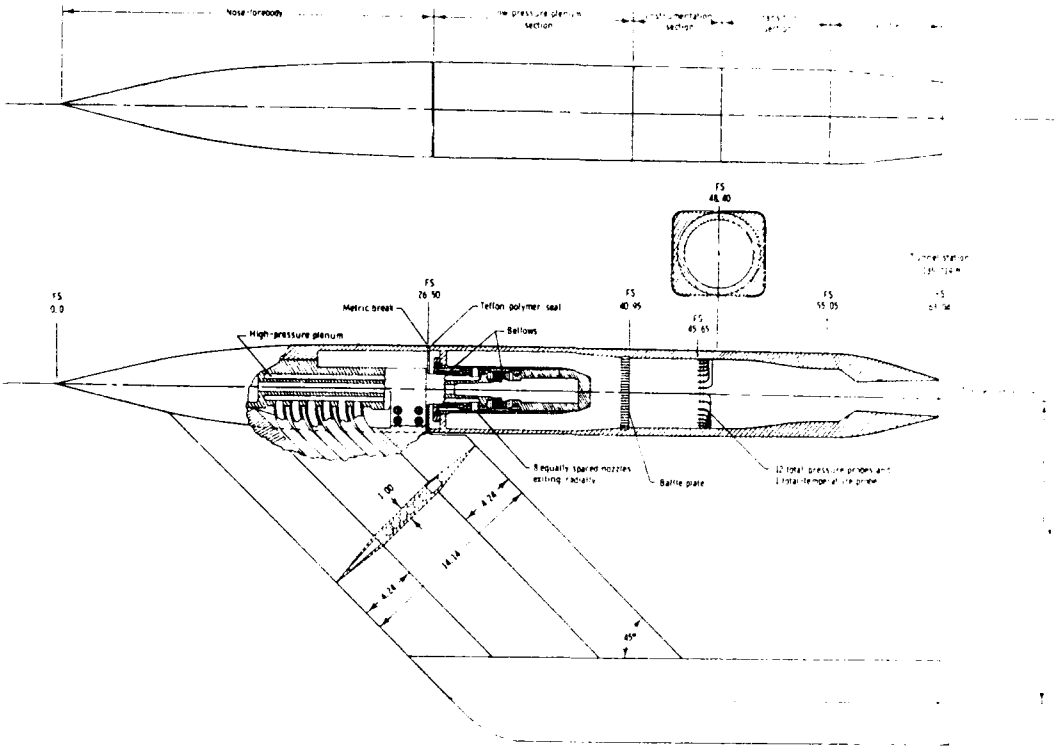

Figure 6: Afterbody Model Test Geometry

which time the L^2 residual for all blocks had dropped over three orders of magnitude. Total pressure contours for the test data and CFD at x=5.2 and x=7.8 inches behind the nozzle exit are compared in figures 7 and 8.

Vortex flow can be seen on both CFD and test data. These plots were generated by interpolating the CFD values for the same locations as the test data. For both occasions the CFD data shows good agreement with the test. In addition, the CFD is compared to individual rake locations in figures 9 and 10.

Traditionally, CFD results are compared to model surface data, such as wall pressures, and very seldom to mid flow field quantities. This problem offered the unique opportunity to validate the flow solver with properties in the middle of the flow field. The HAWK flow solver showed good agreement with the test data; however, the mixing layer between the nozzle and the external flow was underpredicted.

Conformal Nozzle with 3 Tails

An experimental investigation was conducted in the NASA Langley 16-foot transonic wind tunnel to determine the effects of nozzle aspect ratio, empennage surfaces and vectoring on twin engine aircraft afterbody aerodynamics[13][14]. Three nonaxisymmetric conformal nozzles and one twin axisymmetric nozzle were tested with various tail configurations and vector angles. The tests were conducted through a range of Mach numbers, angles-of-attack, and nozzle pressure ratios (P_t/p_∞).

The nozzle model was mounted on NASA's twin-engine fighter model with a wing-tip-mounted support system (Figure 11). The model included a nonmetric portion which consisted of the twin support booms, the forebody and the wing/centerbody. The metric portion of the model aft of FS 44.75 consisted of the internal propulsion system, afterbody, tails and nozzle. This whole assembly was supported by the main force balance which was in turn grounded to the nonmetric wing-centerbody section. A second force balance was attached to the main force balance and was used to measure the forces on the afterbody from FS 48.25 to FS 66.25 and the forces on the tails. In addition to balance data, thirty-six surface static pressure taps were used to investigate the external flow field properties. Flow rates through the propulsion system were measured by venturis.

To calibrate the FALCON code, the high aspect ratio nozzle with 1 vertical tail and two horizontal tails was chosen. A sketch of the nozzle geometry is shown in figure 12. The high aspect ratio nozzle analyzed had more closure on the top and bottom surfaces than on the sides and had an aspect ratio at the exit of 5.378. The design pressure ratio of this nozzle was 5.6 which simulated a dry-power operating mode. For this test case, a Mach number of 1.2 and a P_t/p_∞ of 5.6 were selected. The nozzle vector angle was chosen to be 0.0 degrees and the angle-of-attack was also chosen to be 0.0 degrees. The tunnel conditions were $M_\infty = 1.2$, $p_\infty = 6.131$ psi, and $t_\infty = 458.452°$R. The Reynolds number was 4.17 million per ft. The internal part of

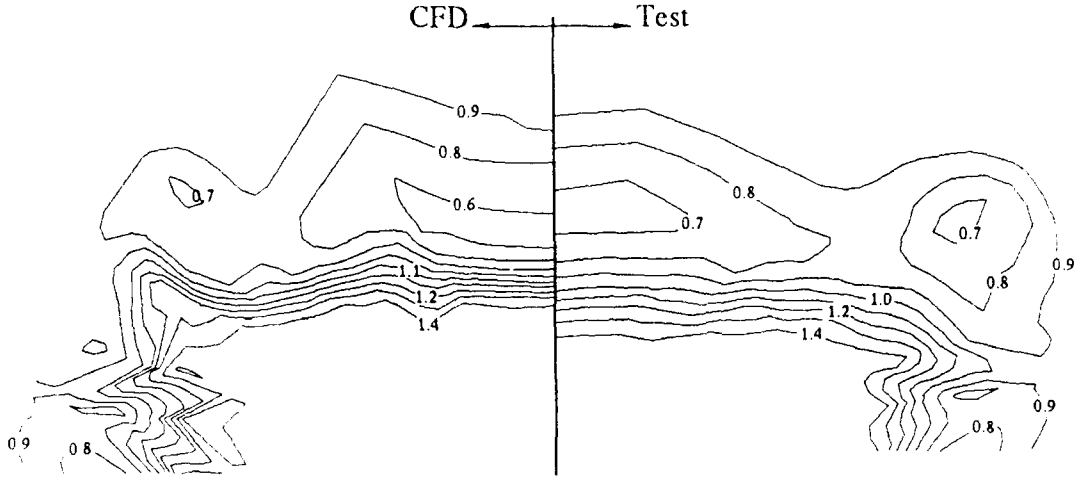

Figure 7: Total Pressure Contours at x=5.2

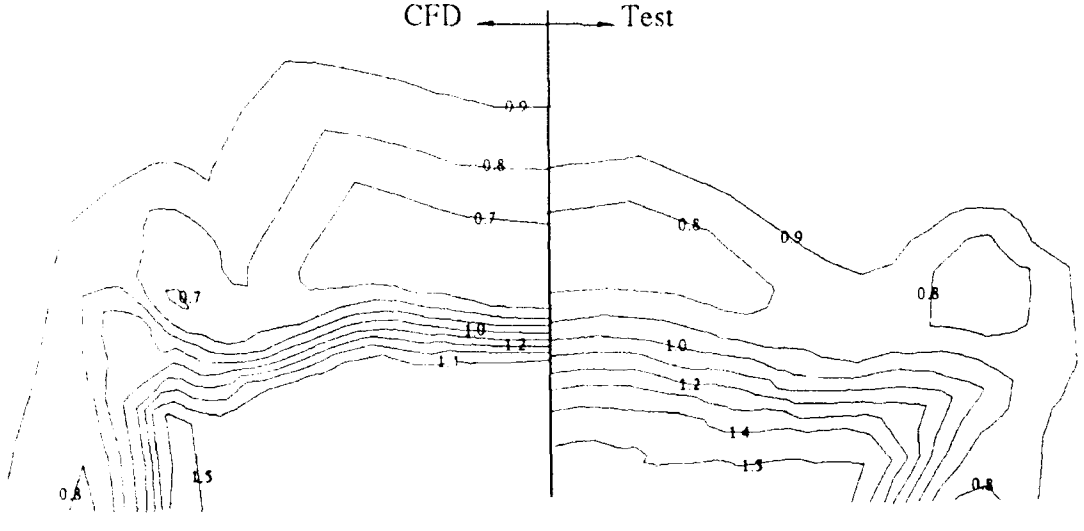

Figure 8: Total Pressure Contours at x=7.8

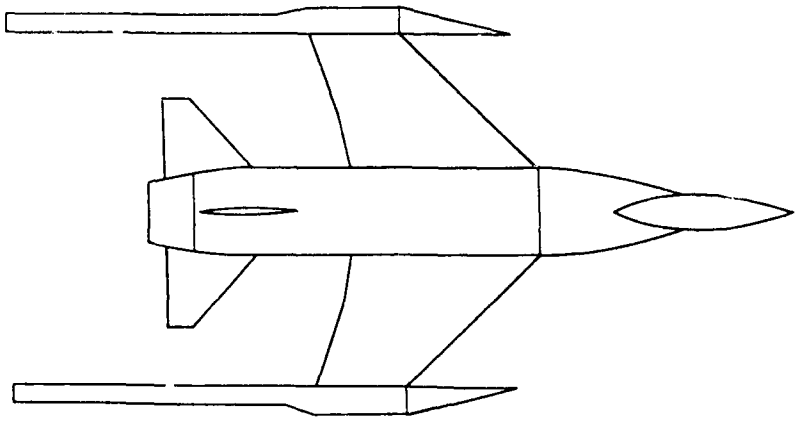

Figure 11: NASA twin-engine fighter model and support system.

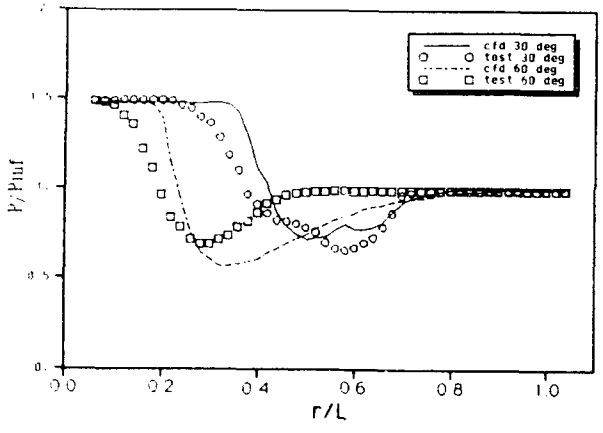

Figure 9: Total Pressure at x=5.2, 30 and 60 deg. Roll

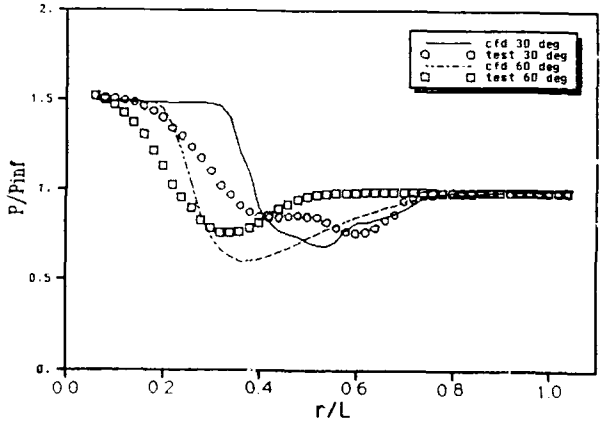

Figure 10: Total Pressure at x=7.8, 30 and 60 deg. Roll

the flow path started at FS 65.0. At that location the internal flow field was assumed to have a uniform total pressure and total temperature.

The GRIDGEN codes (described earlier) were used to develop the grid for this configuration. A nine block H-topology grid system was generated with each block having point-to-point matching with its neighbor blocks. Before executing the FALCON code, the blocks were combined into a single large block since the code allows boundary conditions to be set anywhere inside of or on the boundary of a block. Running the solution as a single block also increases the computational efficiency and allows the solution to converge faster. The combined single block grid was 71 X 69 X 97 for a total of 475,203 grid points. Advantage was taken of the symmetry plane such that only the right half of the configuration was solved. The grid began at FS 48.9 (just aft of the wing) and did not include the aircraft forebody or wing-centerbody section. The nozzle ends at FS 71.7 and the grid concludes at FS 110.0 so that there are approximately 10 nozzle widths downstream of the nozzle exit. Above, below and on the side of the configuration, the grid extended out approximately 13 nozzle widths. Before generating the grid, the minimum grid spacing required off of a no-slip wall

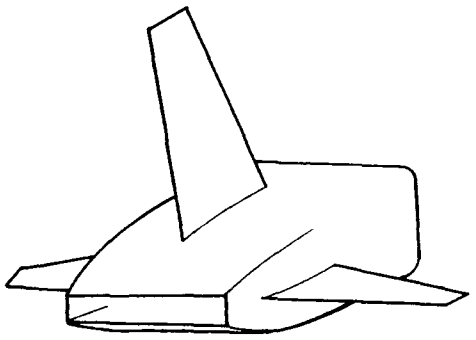

Figure 12: High aspect ratio conformal nozzle design.

(using wall functions) was estimated using simple flat plate theory. In order to have the y^+ of the first grid point at approximately 50, a minimum grid spacing of 0.005 inches was chosen.

The boundary conditions were set from the standard FALCON boundary conditions. A symmetry boundary condition was set all along the plane of symmetry Solid walls were modeled using the no-slip wall function boundary condition described earlier. The external inflow, outflow and farfield were set to a characteristic inflow/outflow boundary condition. Subsonic inflow on the internal part of the nozzle was set using a characteristic based boundary condition which holds both total pressure and total temperature constant. At startup, the flow field was initialized to freestream everywhere except at boundaries where the correct boundary condition was set.

The solution to this analysis was obtained by running the FALCON code, including all viscous terms and making use of the 2-equation k-kl turbulence model. The solution was executed to 4000 iterations at which point the L^2 residual of the mean flow equations had dropped 3 orders of magnitude and the L^2 residual of the turbulence equations had dropped 2.5 orders of magnitude from their initial values. In addition to monitoring the residuals, the nozzle mass flow and external pressures were monitored during the last half of the run to insure convergence.

The analysis results indicate that not modeling the forebody and centerbody-wing section had a significant impact on the results. Figure 13 shows a comparison between test and CFD data along the top of the model at an angle of 11.8 degrees from the vertical. This plot indicates that the pressure drop due to the forebody and wing section is significant in the forward region. Figures 14, 15 and 16 show comparisons between test and CFD around the nozzle at fuselage stations FS 62.1, 67.1 and 71.1, respectively. In each of these plots, the data starts at the top centerline and goes around the nozzle clockwise to end at the bottom centerline. Again, the pressure distribution plots indicate a discrepancy due to not modeling the

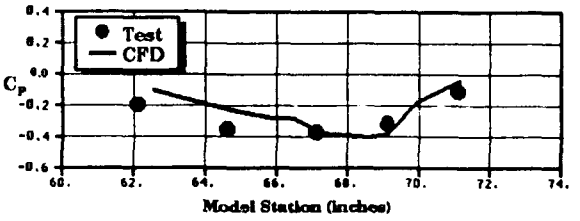

Figure 13: Conformal nozzle axial pressure distribution comparison at 11.8 degrees from vertical.

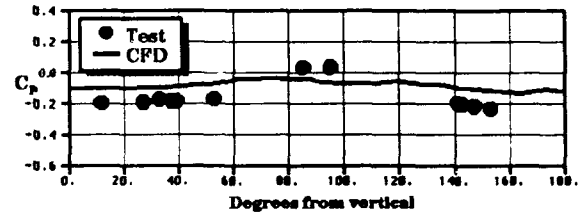

Figure 14: Conformal nozzle circumferential pressure distribution comparison at FS 62.1.

forebody and wing. Figure 17 shows pressure contours on the nozzle and tail surfaces. This plot indicates that extensive pressure instrumentation would be required to adequately define the pressure variations on this nozzle configuration. Figure 18 shows how particles released into the flow at the beginning of the domain would traverse the flow field obtained by CFD. Because of the nonuniform closure between top and sides, extensive spillage from the side onto the top is seen. In addition, separation and vortical flow are apparent.

Overall, the conformal nozzle analysis should be considered a success. However, it is obvious that in order to more closely match the test data, the forebody and wing-centerbody section should be modeled.

CONCLUSIONS

Computational fluid dynamics techniques can be used to complement and enhance experimental techniques in the design of advanced aircraft exhaust systems. CFD provides details of the flow field which are difficult if not impossible to obtain experimentally. CFD techniques can also be used in pre-test

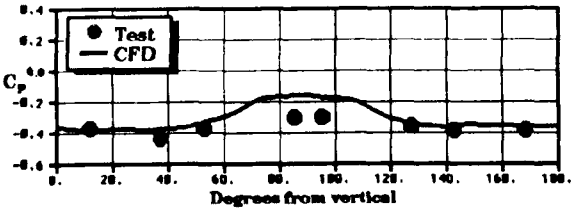

Figure 15: Conformal nozzle circumferential pressure distribution comparison at FS 67.1.

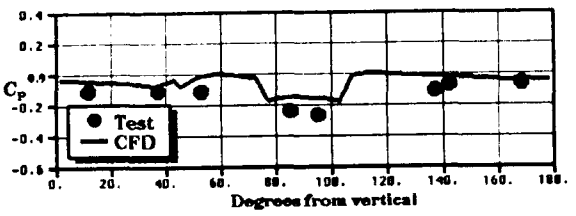

Figure 16: Conformal nozzle circumferential pressure distribution comparison at FS 71.1.

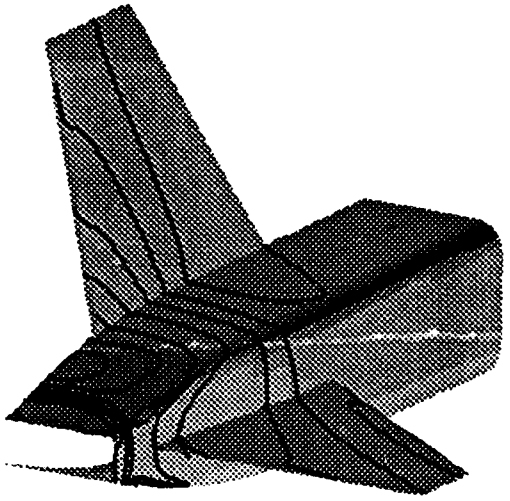

Figure 17: Conformal nozzle surface pressure contours.

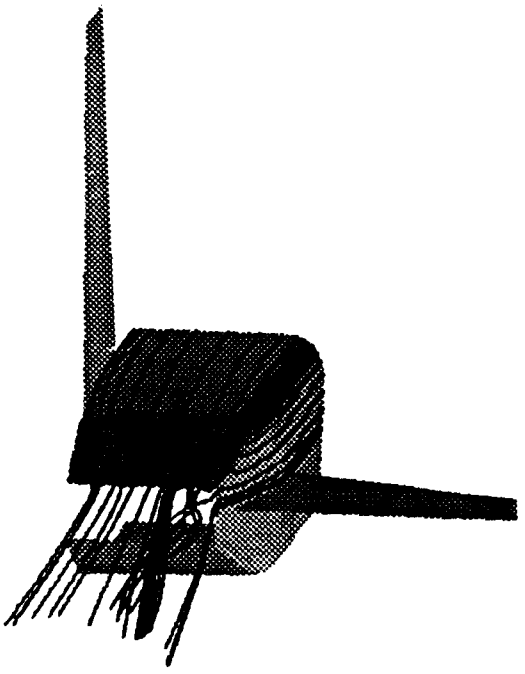

Figure 18: Conformal nozzle particle traces.

analyses to screen concepts and aid in determining proper instrumentation locations.
Simplified geometries are useful for preliminary prediction of general flow trends and concept evaluation. However, in order to obtain precise performance data or match actual test results, detailed geometries and accurate flow conditions should be used. Adequate grid resolution is also necessary to capture many detailed flow features.

ACKNOWLEDGEMENTS

The authors would like to acknowledge NASA for providing computer resources on the National Aerodynamic Simulation System.

REFERENCES

[1] G. K. Cooper. "The PARC Code: Theory and Usage". Technical Report AEDC-TR-87-24, Arnold Engineering Development Center, 1987.

[2] T. H. Pulliam. "Euler and Thin Layer Navier-Stokes Codes: ARC2D, ARC3D". In *Notes for Computational Fluid Dynamics User's Workshop*, Tullahoma, Tennessee, March 1984. UTSI Publication E02-4005-023-84.

[3] R. Beam and R. F. Warming. "An Implicit Finite-Difference Algorithm for Hyperbolic Systems in Conservation-Law Form". *Journal of Computational Physics*, 22(1):87–110, September 1976.

[4] A. Jameson, W. Schmidt, and E. Turkel. "Numerical Solutions of the Euler Equations by Finite Volume Methods Using Runge-Kutta Time-Stepping Schemes". Technical Report AIAA-81-1259, American Institute of Aeronautics and Astronautics, 1981.

[5] B. R. Smith. "The k-kl Turbulence Model and Wall Layer Model for Compressible Flows". Technical Report AIAA-90-1483, American Institute of Aeronautics and Astronautics, 1990.

[6] B. R. Smith. "A Wall Layer Model for use in Reynolds Stress Closure Turbulence Modeling". In *The Proceedings of the First National Fluid Dynamics Congress*, pages 858–865, Cincinnati, Ohio, July 1988. Paper Number 88-3579-CP.

[7] J. W. Yokota, D. A. Caughey, and R. V. Chima. "A Diagonally Inverted LU Implicit Multigrid Scheme". In *The Proceedings of the First National Fluid Dynamics Congress*, pages 104–111, Cincinnati, Ohio, July 1988. Paper Number 88-3565-CP.

[8] J. P. Steinbrenner, J. R. Chawner, and C. L. Fouts. "The GRIDGEN 3-D Multiple Block

Grid Generation System". Technical Report WRDC-TR-90-3022, Wright Research and Development Center, July 1990.

[9] P. P. Walatka and P. G. Buning. *"PLOT3D User's Manual"*. NASA Ames Research Center, Moffett Field, California, 1988. Rough Draft.

[10] J. Mace et. al. "Advanced Thrust Vectoring Nozzles for Supercruise Aircraft". Technical Report AIAA-89-2816, American Institute of Aeronautics and Astronautics, 1989.

[11] S. A. Syed, J. J. Erhart, and E. W. King. "Application of CFD to Pitch/Yaw Thrust Vectoring Spherical Convergent Flap Nozzles". Technical Report AIAA-90-2023, American Institute of Aeronautics and Astronautics, 1990.

[12] L. E. Putnam and C. E. Mercer. "Pitot Probe Measurements in Flow Fields Behind a Rectangular Nozzle With Exhaust Jet for Free-Stream Mach Numbers of 0.0, 0.6, and 1.20". Technical Report NASA TM-88990, NASA Langley Research Center, 1986.

[13] B. L. Glass and J. D. McFarlan. "Effects of Nozzle Shape, Empennage Arrangement, and Vectoring on the Propulsion Induced Aerodynamic Characteristics of Conformal Nozzles". Technical Report MR-P-443, General Dynamics Fort Worth Division, 1986.

[14] L. S. Bangert, L. D. Leavitt, and D. E. Reubush. "Effects of Afterbody Boattail Design and Empennage Arrangement on Aeropropulsive Characteristics of a Twin-Engine Fighter Model at Transonic Speeds". Technical Report NASA TP-2704, NASA Langley Research Center, 1987.

Investigation of the Flowfield around an Isolated Bypass Engine with Fan and Core Jet

R.Rudnik, A. Ronzheimer, C.-C.Rossow, H. Hoheisel

DLR Institut für Entwurfsaerodynamik
Flughafen, D-3300 Braunschweig, Germany

SUMMARY

A finite-volume scheme for the discetisation of the three-dimensional Euler equations is extended for the purpose of calculating the flowfield around an isolated bypass engine with fan- and core-jet. Flow calculations for a typical high bypass engine are performed for take-off and cruise conditions under consideration of realistic operational jet parameters. Several variations of the jet pressure and temperature ratio show that the jet flowfield is dominated by the pressure ratio as far as inviscid flow is concerned.
A comparison of the numerical results to experimental investigations which are carried with a turbine powered simulator for low speeds exhibit good agreement. The influence of numerical parameters on the solution in the region of the jet flow is analysed by varying the coefficients of the artificial dissipation.

1. INTRODUCTION

The development of modern jet engines for transport aircraft tends to an increasing bypass ratio to improve the propulsion efficiency. This leads to Very-High Bypass (VHB) and Ultra-High Bypass (UHB) engine concepts characterized by large secondary mass flows and fan diameters. Taking into account that the wetted surface of the nacelle can amount to 30 % of the wing surface, a carefull design of the isolated engine gains increasing importance. Furthermore the investigation of the flowfield around the engine represents a substantial aspect with regard to the integration of the airframe and the propulsion system. In this context numerical methods have proved to be an appropriate tool for analyzing complex aerodynamic interference phenomena [1,2]. The numerical scheme presented in this study is used to calculate the flowfield around isolated bypass engines. Besides of the simulation of the fan inflow and the surrounding flow, especially the fan and core-jet is considered. The simulation is based on the three-dimensional Euler-equations.

2. NUMERICAL ALGORITHM

2.1 Solution Scheme

To investigate the flowfield around isolated bypass engines the Finite Volume Code CEVCATS [3,4], which was developed at the DLR Institute for Design Aerodynamics, is adjusted to the requirements of the problem under consideration. The numerical scheme discretizes the governing equations for inviscid, compressible flows, which can be written in integral form using a cartesian coordinate system as:

$$\iiint_V \frac{\partial}{\partial t} \vec{W} dV = \iint_{\partial V} \bar{\bar{F}} \cdot \vec{n}\, dS \qquad (1)$$

$\vec{n}$ is the outward facing normal vector on the closed boundary ∂V of the arbitrary control volume V. The control volume is regarded to be constant in space and time. W denotes the vector of the unknown flow variables and $\bar{\bar{F}}$ the flux density tensor:

$$\vec{W} = \begin{bmatrix} \rho \\ \rho u \\ \rho v \\ \rho w \\ \rho E \end{bmatrix}, \quad \bar{\bar{F}} = \begin{bmatrix} \rho \vec{q} \\ \rho u \vec{q} + p \vec{i}_x \\ \rho v \vec{q} + p \vec{i}_y \\ \rho w \vec{q} + p \vec{i}_z \\ \rho H \vec{q} \end{bmatrix}.$$

$\vec{q}$ represents the velocity vector. With respect to the unit vectors and the velocity components of the cartesian coordinate system $\vec{q}$ is defined as:

$$\vec{q} = u\vec{i}_x + v\vec{i}_y + w\vec{i}_z \qquad (2)$$

ρ, E, and H are the density, total energy, and total enthalpy, respectively. Assuming a perfect gas the pressure is thus determined by the relation:

$$p = (\kappa - 1)\,\rho \left[E - \frac{u^2 + v^2 + w^2}{2}\right] \qquad (3)$$

Equation (1) describes the balance between the rate of change of W and the convective flux over the surface ∂V of the control volume. The discretisation of equation (1) is done separately in space and time following the method of lines [5]. The spatial discretisation is accomplished using a cell vertex scheme that assgins the flow variables to the vertices i,j,k of the control volume. Using central differences the approximation of the surface and volume integrals leads to an ordinary differential equation:

$$\left(\frac{d}{dt}\vec{W}\right)_{i,j,k} = -\frac{1}{V_{i,j,k}} \left(\vec{Q}_{i,j,k} - \vec{D}_{i,j,k}\right) \qquad (4)$$

$Q_{i,j,k}$ denotes the numerically calculated convective flux and $D_{i,j,k}$ is a dissipative operator, which is neccesary to damp high frequency oscillations that occur because of the use of central differencing. Following Jameson et. al. [5] the dissipative operator consists of a blending of second and fourth differences of the flow variables. The integration in time of equation (5) is performed using a five stage Runge-Kutta time stepping scheme. The convergence to the steady state solution is accelerated by implicit residual smoothing and local time stepping. Enthalpy damping is used in cases where the total temperature of the flowfield is constant, that means when the total temperature of the jet is prescribed to be equal to the freestream total temperature.

2.2 Boundary Conditions

At solid walls the tangent flow condition is enforced by setting the flux normal to the surface to zero. The farfield boundary condition is imposed following the concept of Riemann Invariants introduced by Jameson et. al. [5], assuming one-dimensional subsonic flow normal to the farfield boundary. If supersonic jet flows occur this farfield condition is replaced by 0. order extrapolation of the flow variables at the outflow farfield boundary.

The treatment of the engine inflow and outflow boundaries is sketched in **Figure 1**. The fan inflow is simulated by the specification of non-dimensional inlet mass flow expressed by the ratio of the inlet streamtube at infinity A_∞ and the fan face area A_F:

$$\varepsilon_F = \frac{A_\infty}{A_F} = \frac{\dot{m}_{ref}}{A_F \cdot Ma_\infty \cdot \sqrt{\kappa \cdot p_\infty \cdot \rho_\infty}} \quad (5)$$

The undisturbed flow state at the fan face is then calculated using one-dimensional isentropic relations. The jet flow is characterized by the ratio of the jet total pressure to the freestream static pressure $p_{t,j} / p_\infty$ and the ratio of total temperature between the jet and the ambient flow $T_{t,j} / T_{t,\infty}$. The assumption of the flow direction to be parallel to the engine axis reveals two additional boundary conditions. Following the theory of Kreiss [6] the last boundary condition has to be specified by extrapolating one quantity from the flowfield. Instead of taking the magnitude of velocity according to Chen et. al. [7], the static pressure is extrapolated from the interior of the computational domain. This procedure has shown to improve the stability during the transient phase of the solution, especially when a flow with high enthalpy difference has to be calculated. The remaining quantities at the exhaust planes are computed using isentropic relations. By specifying the jet-pressure and the total temperature ratio at the fan and core exhaust planes together with a freestream mach number, the mass flow adjusts itself during the solution. Fan and core jet are treated independently.

2.3 Grid Generation

The grid generation method used in this study is based on the grid generation procedure for three-dimesional nacelles without core engine described in [8]. A multi block approach is used for the generation of body-fitted, structured grids consisting of hexahedral cells. The physical domain is divided into 4 blocks. In the longitudinal section a H-type topology is used whereas the cross section exhibits an O-topology. Using the symmetry of the engine only a half model is considered. The grid generation process starts with the geometry definition in the longitudinal section. The point distribution on the engine surfaces and the block edges is attained by solving a one-dimensional Poisson equation. By subdividing the block edges into segments the local grid density can be controlled to achieve a good resolution of regions with high gradients of the flow variables as near the leading edge of the nacelle and at the jet boundaries. A smooth two dimensional grid in the longitudinal section is generated by solving an elliptical system of equations with source term control. Finally the three dimensional grid results from a combination of rotation and interpolation of the previously generated grids in the longitudinal sections. This procedure enables the computation of non-axisymmetric nacelles with droop inlet or changing nacelle profiles in the circumferential direction.

In this study a **T**urbine **P**owered **S**imulator (TPS)-engine is investigated, namely the TPS 441 with a geometry similar to the GE CF 6-50 engine. The model has a nacelle diameter of 170 mm and an overall length of 466 mm. The choice of this model enables the comparison with experimental results carried out with the TPS 441 in the low speed range as well as the use of published data of the CF 6-50 engine for the specification of the jet parameters. The three dimensional grid, shown in **Figure 2** in a perspective view and in **Figure 3** in the longitudinal section consists of about 125.000 grid points.

3. RESULTS

The discussion of the numerical results is split into three parts. At first the influence of the jet parameters on the engine flowfield is analysed. After this the computed Mach number distribution is compared to experimental results in the low speed range. Finally the influence of numerical parameters on the solution is investigated be varying the coefficients of the artificial dissipation.

3.1.1 Influence of the Jet Parameters

The investigation of the influence of several jet conditions is performed for typical cruise conditions [9]. The freestream Mach number is chosen to $Ma_\infty = 0.75$, the angle of attack to 0°. The mass flow amounts to 254 kg/ sec. Assuming a flow without incidence allows an axisymmetric computation. **Figure 4** shows lines of constant Mach numbers for a calculation without jet influence. To achieve this condition the jet pressure ratio is calculated using the Bernoulli equation for isentropic, compressible flows, assuming that the total pressure in the jet is equal to the total pressure in the ambient flow. This leads to a relation for the so called isentropic jet pressure ratio:

$$\frac{p_{t,j}}{p_\infty} = \left[1 + \frac{\kappa - 1}{2} \cdot Ma_\infty^2\right]^{\frac{\kappa}{\kappa - 1}} \qquad (6)$$

The total temperature in the jet exhaust plane is set equal to the total freestream temperarure. The inlet flow is determined by the streamtube area ratio of $\varepsilon_f = 0.93$, which leads to a position of the stagnation points at the leading edge of the nacelle. In the outer flow gradients of the Mach number appear up to about 25 % of the chord length including a small supersonic region. Behind this the flowfield is comparatively homogeneous due to the approximately cylindrical contour. Differences between the jet flows and the surrounding flow dissapear shortly behind the nozzle exits. In **Figure 5** a computation with powered jets is presented. On the upper half of the figure a cold jet is calculated, on the lower half an increase of the total temperature is simulated by prescribing the total temperature ratio of the core jet to $T_{t,j}/\ T_{t,\infty} = 3.05$ and of the fan jet to $T_{t,j}/\ T_{t,\infty} = 1.19$, respectively. The freestream conditions and the inlet mass flow are held constant. The nacelle flowfield is not influenced by the jet. Because the jet pressure ratios have overcritical values of about $p_{t,j}/p_\infty \cong 2.5$ the accelerated jet flow in the nozzle reaches the speed of sound at the nozzle exit plane. Behind the exit plane the jet flow is supersonic, characterized by a pattern of compression and expansion areas. A better resolution of the oblique shock wave pattern can be achieved by an adequate grid refinement [10]. Following the theory for compressible, inviscid flows, a discontinuity of the velocity is expected at the boundary of a jet with high total pressure and the surrounding flow. Due to the numerical dissipation an artificial shear layer develops at the jet boundary that is slightly spread downstream characterized by the high density of Iso-Machlines, leaving from the trailing edge. The shape of the fan jet, which can be detected by these Iso-machlines follows the contour of the core cowl. Behind the engine the contour of the jet plume is nearly cylindrical. Although this shear layer indicates a certain analogy to the real viscid flow, it has to be considered as purely numerical, because it is exclusively caused by the numerical dissipation of the solution algorithm. The developement and shape of the artificial shear layer is influenced by the grid density as well as by the numerical disspation [10]. A comparison of the mach number distribution of the cold jet on the upper half of **Figure 5** and the hot jet on the lower half of **Figure 5** reveals only weak differences in the core jet flowfield, although the total temperature and thereby the energy is increased by a factor of three. The reason for this becomes clear if one regards the velocity and the density behaviour of the cold and the hot jet. The evaluation of the velocity at a short distance behind the nozzle exits, **Figure 6**, reveals that the rise of energy in the hot jet has lead to an increased velocity. On the other hand the density has considerably decreased due to the high static temperature, depicted in **Figure 7**. This leads to the conclusion that the influence of a hot jet on the flowfield is rather weak with regard to Mach number or pressure coefficients. re concerned, because the increase of velocity is compensated by the decrease of the density. The comparison of the C_p-distribution for the isentropic cold jet, the powered cold jet and the powered hot jet on the nacelle contour, **Figure 8** and on the core cowl, **Figure 9**, prove this thesis. **Figure 8** shows that the maximum pressure value in the fan nozzle reaches a value of about $C_p \cong 3{,}0$ for the powered jet, caused by the high total pressre of the jet. The C_p-distribution on the outer nacelle surface is characterized by the suction peak in the inlet region and the weak overcritical region at 20 % chord length. The outer flowfield and the inlet flow is not influenced by the different jet conditions. The distribution on the core cowl, **Figure 9**, shows the acceleration in the fan nozzle with the pressure minimum at 50 % chord length near the nozzle exit. The differences between the powered cold jet and the powered hot jet are very small. The distribution of the isentropic jet exhibits a much smaller acceleration in the fan nozzle as well as a lower pressure level in the core jet.

3.1.2 Comparison to experimental results

The experimental results, referred to in this investigation, were carried out at a Mach number of $Ma_\infty = 0{,}176$ with a TPS 441 model engine in a low speed wind tunnel [11]. The inlet mass flow amounts to 2,11 kg/sec, the angle of attack is chosen to $\alpha = 0.0°$. The jet conditions of the simulator are specified in **Figure 10**. The low total temperature level in the core jet results from the expansion of the high pressure drive air. The experimental results, marked by circles, are calulated using the local static pressure on the surface with reference to the axial and radial averaged total pressure measured in a nozzle reference plane. **Figure 10** shows the distribution of the local Mach number on the nacelle contour

and on the core cowl. The distribution of the nacelle is characterized by a relatively uniform local Mach number on the outer contour, the stagnation point near the leading edge and the high acceleration around the intake lip. The jet flow in the fan nozzle is accelerated with a maximum at the nozzle exit, but remains subsonic. Behind the exit the Mach number drops slightly to the trailing edge of the core cowl. The numerical solution shows good agreement to the measured Mach number distribution. This results reveal that the flowfield around the nacelle is decisively determined by the massflow and the connected total pressure level of the jet flow. Viscous effects, that lead to a change of the flow direction at the trailing edge of airfoils, have only a secondary influence on the flowfield of a powered nacelle. This is the reason for the good agreement of the experimental results and the simulation based on inviscid theory.

3.1.3 Influence of numerical dissipation

The variation of the constant $k^{(4)}$ of the artificial dissipation serves as an example for the investigation of the influence of numerical parameters on the solution [10]. The constant appears in the term for the coefficient of the fourth difference $\varepsilon^{(4)}$. For the derivation of the numerical dissipation operator used in this study see [4,5]. The variation of the artificial dissipation constant is performed for cruise conditions with a powered cold jet. **Figure 11** shows lines of constant Mach number in the region of the jet flowfield. Above the engine axis the constant $k^{(4)}$ is set to 1/128, corresponding to weak dissipation, whereas below the axis a value of $k^{(4)} = 1/32$ is prescribed. This leads to a stronger influence of the numerical dissipation. If a lower dissipation constant is used the resolution of small gradients in the flowfield is higher and the spreading of the artificial shear layer normal to the main flow direction is smaller, especially behind the nacelle trailing edge. The corresponding pressure distributions on the core cowl are presented in **Figure 12**. Here the main differences appear at about 90 % chord length where the high dissipation constant causes a smoothing of pressure decrease. The variation of the constant of the artificial dissipation shows that the overall influence on the quality of the numerical solution are small.

4. CONCLUSION

An analysis of the flowfield around a powered high-bypass ratio engine with fan and core jet is performed using a finite volume scheme for the solution of the threedimensional Euler-equations. The solution of the Euler-equations enables the simulation of the jet flowfield with regard to realistic jet pressure and total temperature ratio. The investigation shows that the jet flowfield is decisively determined by the jet pressure ratio as far as Mach number and pressure distributions are concerned. A comparison to experimental results using a TPS-model engine in the low speed range reveals good agreement to the calculated solution. The numerical dissipation of the solution algorithm causes an artificial shear layer between the jet and the outer flow which has to be considered as pureley numerical. The constant of the artificial dissipation is varied by a factor of four without any significant influence on the solution. Entrainment and jet spreading effects are not taken into account by the theory of inviscid flows and are subject of future work.

5. References

[1] Hoheisel, H., Kiock, R., Rossow, C.-C., Ronzheimer, A., Baumert, W., Capdevila, H. *Aspects of Theoretical and Experimental Investigations on Airframe/Engine Integration Problems.* ICAS-90-2.7.3, 1990.

[2] C.-C. Rossow, A. Ronzheimer *Investigation of Interference Phenomena of Modern Wing-Mounted High-Bypass-Ratio Engines by the Solution of the Euler-Equations* AGARD Fluid Dynamic Panel Symposium, 7-10 Oct 1991

[3] C.-C. Rossow *Berechnung von Strömungsfeldern durch Lösung der Euler-Gleichungen mit einer erweiterten Finite-Volumen Diskretisierungsmethode* DLR FB 89/38, 1989.

[4] R. Radespiel *Calculation of the Flow around high Bypass Ratio Nacelles Using An Euler-Code* DFVLR IB 129-87/16 1987.

[5] Jameson, A., Schmidt, W., Turkel, E. *Numerical Solution of the Euler Equations by Finite Volume Methods Using Runge-Kutta Time Stepping Schemes.* AIAA 81-1259, 1981.

[6] H. O. Kreiss *Initial Boundary Value Problems for Hyperbolic Systems* Communications of Pure and Applied Mathematics, Vol 23, P. 277-298, 1970.

[7] H.C. Chen, N.J. Nu, P.E. Rubbert, A. Jameson *Flow Simulations for General Nacelle Configurations Using Euler Equations* AIAA 83-0539, 1983.

[8] A. Ronzheimer *Erweiterung eines Euler-Verfahrens zur Strömungsberechnung um dreidimesionale Gondeln mit hohen Bypass-Verhältnissen* DFVLR-IB 129-89/42, 1989

[9] R. John, W. Burgsmüller *Kennfeldrechnung für die CF6-50 C2-Großausführung* MBB-Mitteilung vom 11.09.1986

[10] R. Rudnik *Erweiterung eines dreidimensionalen Euler-Verfahrens zur Berechnung des Strömungsfeldes um Nebenstromtriebwerke mit Fan- und Kernstrahl* DLR-FB 91/13, 1991.

[11] R. Kiock, W. Stäger *Druckverteilungsmessung an einem Modelltriebwerk bei inkompressibler Strömung* DFVLR-IB 129-87/39, 1987.

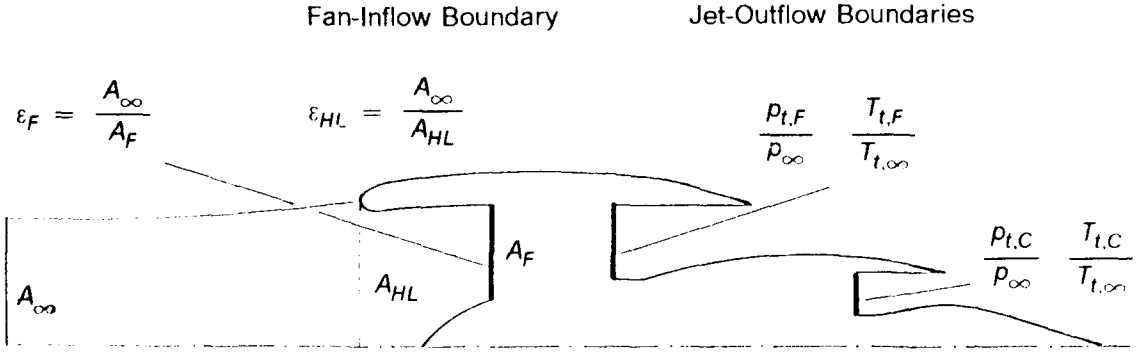

Figure 1. Simulation of engine operation condition

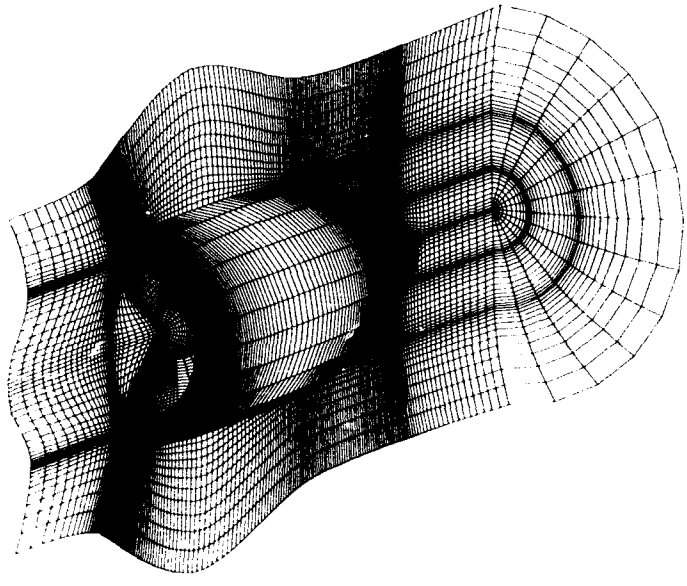

Figure 2. 3D grid around bypass engine

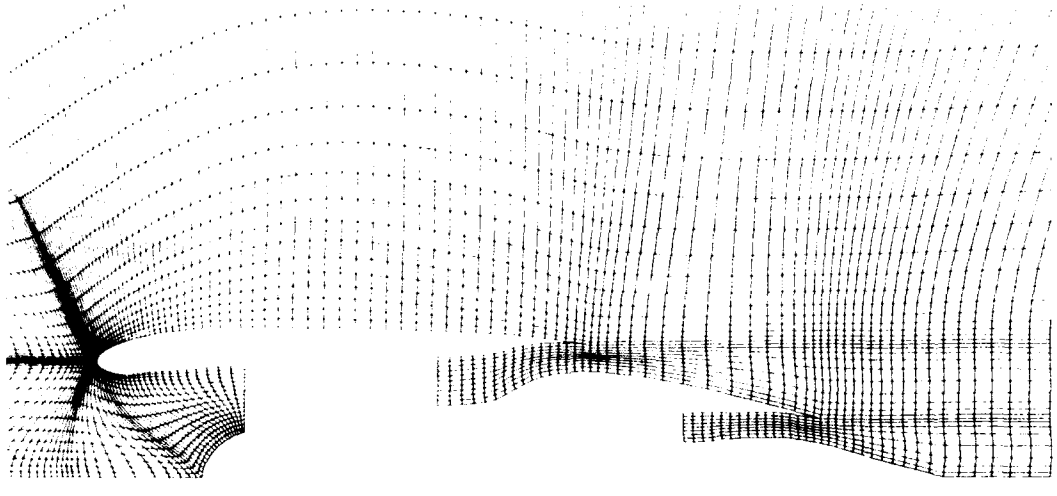

Figure 3. Longitudinal section of the grid

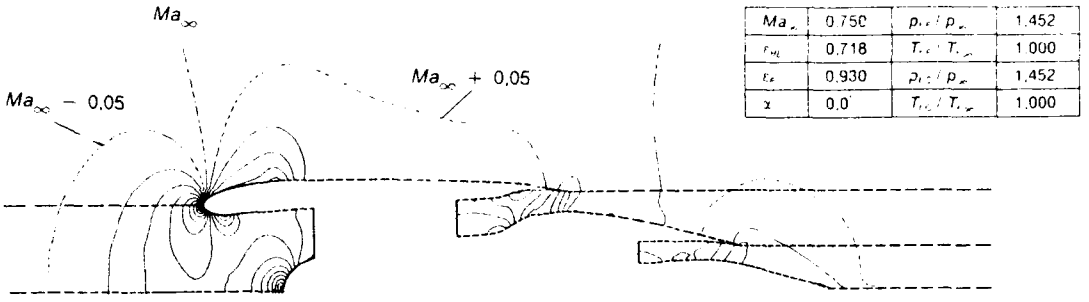

Ma_∞	0,750	$p_{t\infty} / p_\infty$	1,452
η_{HL}	0,718	$T_{t\infty} / T_\infty$	1,000
ε_F	0,930	p_{tC} / p_∞	1,452
χ	0,0°	T_{tC} / T_∞	1,000

Figure 4. Iso Machlines for cruise conditions, unpowered jet

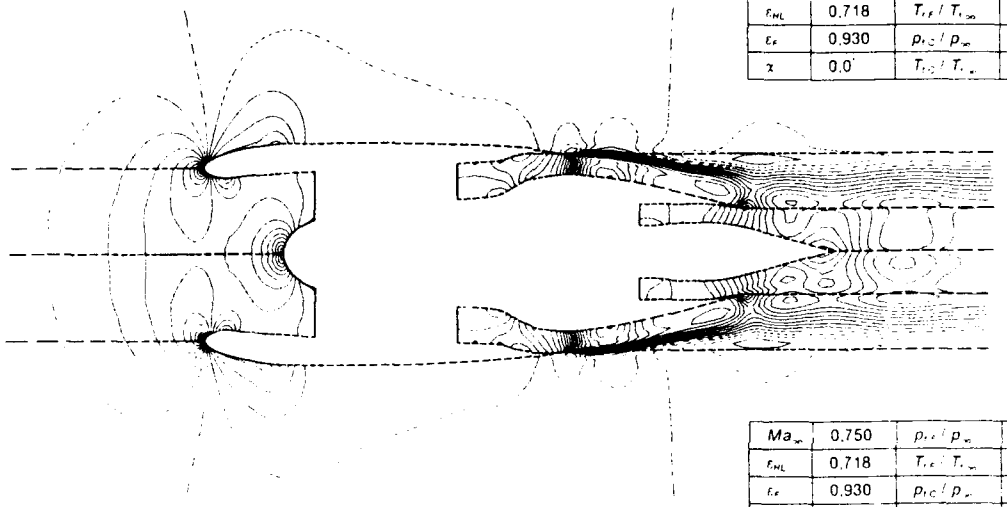

Ma_∞	0,750	$p_{t\infty} / p_\infty$	2,517
η_{HL}	0,718	$T_{t\infty} / T_{t\infty}$	1,000
ε_F	0,930	p_{tC} / p_∞	2,510
χ	0,0°	T_{tC} / T_∞	1,000

Ma_∞	0,750	$p_{t\infty} / p_\infty$	2,517
η_{HL}	0,718	$T_{t\infty} / T_\infty$	1,212
ε_F	0,930	p_{tC} / p_∞	2,510
χ	0,0°	T_{tC} / T_∞	3,005

Figure 5. Iso Machlines for cruise conditions, powered jet

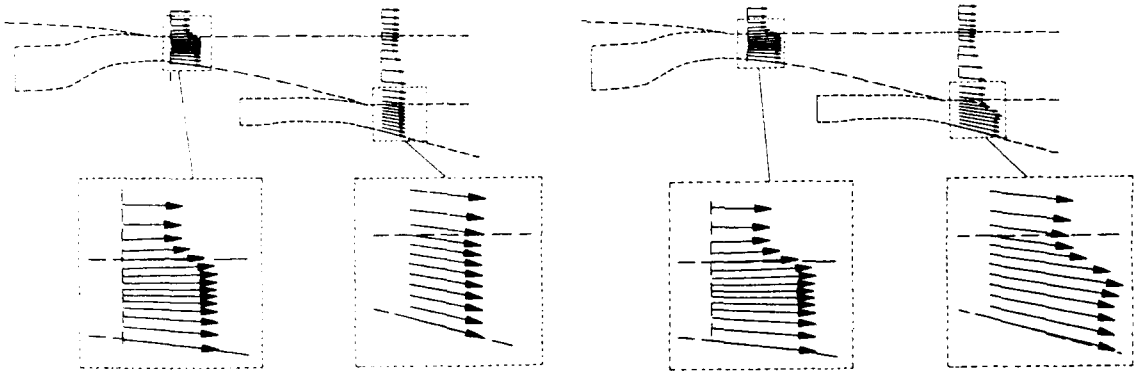

cold jet

hot jet

Figure 6. Velocity distribution in the jet flowfield

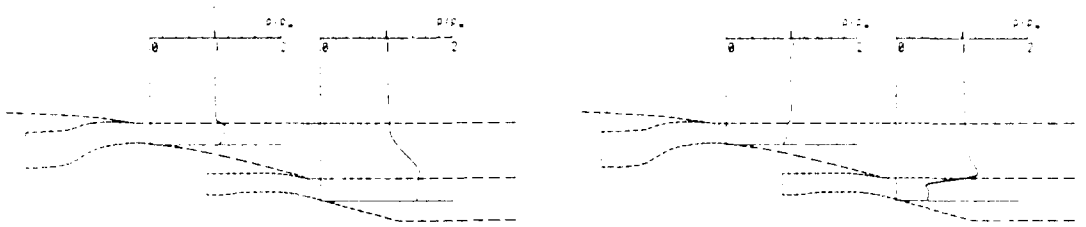

cold jet hot jet

Figure 7. Density distribution in the jet flowfield

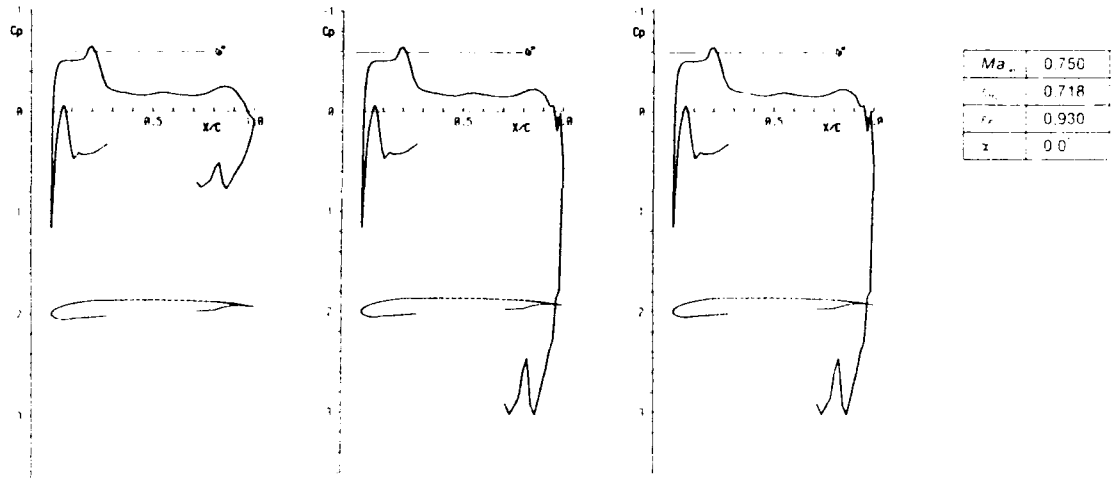

free stream total pressure
free stream total temperature

realistic jet pressure ratio
free stream total temperature

realistic jet pressure ratio
realistic total temperature

Figure 8. Comparison of C_p distribution on nacelle contour

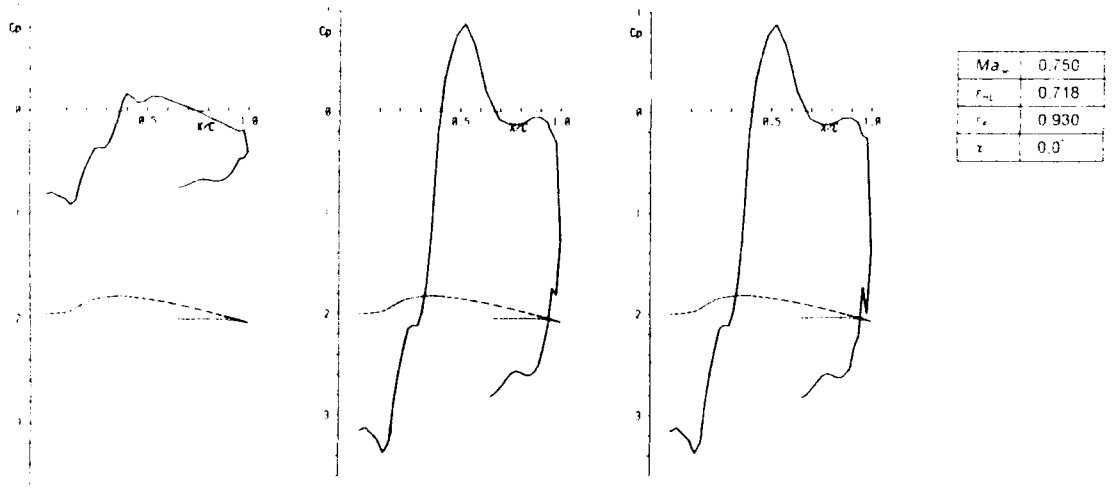

free stream total pressure
free stream total temperature

realistic jet pressure ratio
free stream total temperature

realistic jet pressure ratio
realistic total temperature

Figure 9. Comparison of C_p distribution on core cowl contour

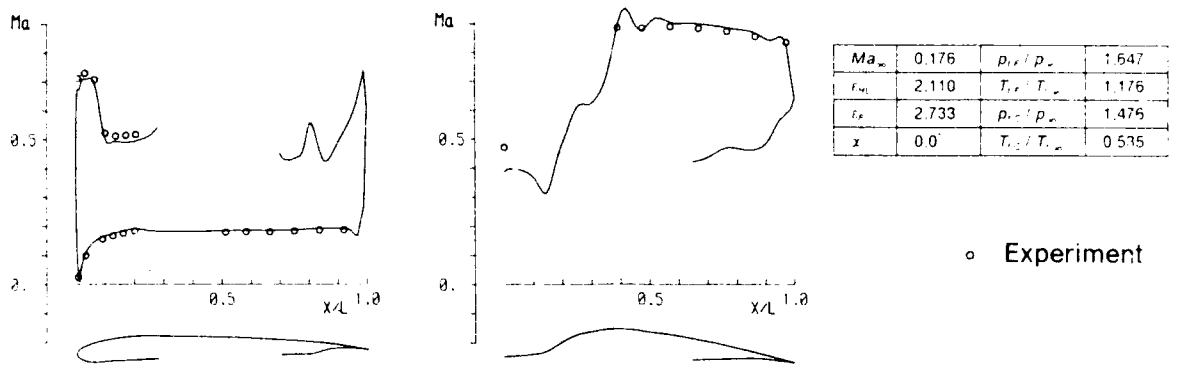

Ma_∞	0.176	$p_{t,\infty} / p_\infty$	1.647
r_{HL}	2.110	$T_{t,\infty} / T_\infty$	1.176
r_e	2.733	$p_{t,2} / p_\infty$	1.476
α	0.0°	$T_{t,2} / T_\infty$	0.535

Figure 10. Comparison to experimental results at TPS-Simulator
Local Mach number on nacelle and core cowl contour

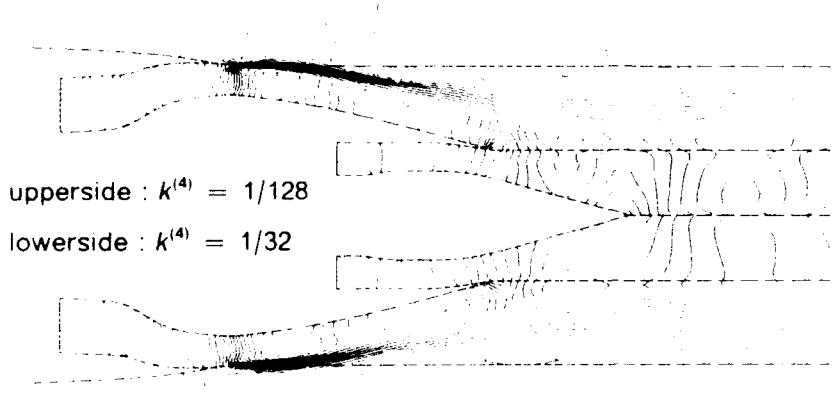

Ma_∞	0.750
r_{HL}	0.718
r_e	0.930
α	0.0°

$p_{t,\infty} / p_\infty$	2.517
$T_{t,\infty} / T_\infty$	1.000
$p_{t,2} / p_\infty$	2.510
$T_{t,2} / T_\infty$	1.000

Figure 11. Iso Machlines for cruise conditions, powered jet;
Variation of $k^{(4)}$ constant of the artificial disspation

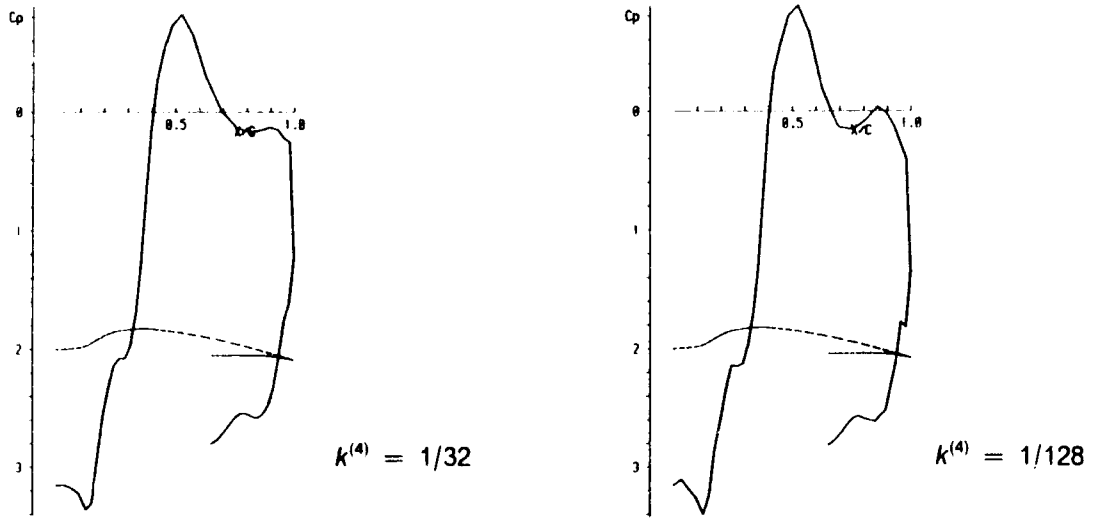

Figure 12. C_p distribution, powered jet; Variation of
$k^{(4)}$ constant of the artificial disspation

PROPULSION INTEGRATION RESULTS OF THE STOL AND MANEUVER TECHNOLOGY DEMONSTRATOR

J. A. Laughrey
D. J. Moorhouse
U.S. Air Force Wright Laboratory
Wright-Patterson AFB, Ohio 45433-6553
United States

SUMMARY

The STOL and Maneuver Technology Demonstrator program has achieved its original goals established to demonstrate the benefits of thrust vectoring and reversing on a fighter aircraft. It has been shown that thrust vectoring will enhance up-and-away aircraft maneuverability at low speeds and can be used to improve tracking and capture tasks plus contribute significantly to improve takeoff performance and rough or damaged runway operations. Thrust reversing has been shown to permit quicker changes in energy states that could provide an advantage in tactical arena and can greatly reduce landing distances. It was also demonstrated that an integrated flight and propulsion control system that incorporates the appropriate control laws can significantly simplify pilot workload during all vectoring and reversing operations, including the approach, landing and stopping tasks. Results of this program are being used to transition these proven technologies into future fighter systems.

LIST OF SYMBOLS

AEDC	- Arnold Engineering Development Center
AFB	- Air Force Base
AFTI	- Advanced Fighter Technology Integration
AOA	- angle of attack
BIT	- built-in-test
CD	- convergent/divergent
CL	- lift coefficient
CM	- pitching moment coefficient
DEEC	- digital electronic engine control
DFBW	- digital fly-by-wire
FPCS	- flight path control set
FT	- Feet
GH	- ground handling
h/b	- height/wing span ratio
HIDEC	- Highly Integrated Digital Electronic Control
HIL	- Hardware-in-the-Loop
HQDT	- Handling Qualities During Tracking
IFPC	- integrated flight and propulsion controls
KCAS	- calibrated airspeed (knots)
LaRC	- Langley Research Center
LeRC	- Lewis Research Center
LSWT	- low speed wind tunnel
MIL	- military
NASA	- National Aeronautics and Space Administration
NC	- nozzle controller
NPR	- nozzle pressure ratio
Nx	- axial acceleration
OFP	- operational flight program
PVI	- pilot/vehicle interface
RPM	- revolutions per minute
SDF	- six degrees of freedom
SLAND	- short landing flight control mode
S/MTD	- STOL/Maneuver Technology Demonstrator
STOL	- short takeoff and landing
STOL-GH	- ground handling control mode
STOL-TOA	- takeoff and approach control mode
TRP	- Temperature Rise Parameter
2D	- two dimensional
4T	- four foot transonic
16T	- sixteen foot transonic

1.0 BACKGROUND

As discussed in reference 1, the increasing threat of runway denial caused the Air Force Systems Command to direct the Air Force Research Laboratories to pursue those emerging technologies that could diminish this threat. The STOL and Maneuver Technology Demonstrator (S/MTD) program is a result of that direction. The prime objective of the program was to flight demonstrate and validate maturing technologies that will add short takeoff and landing (STOL) capability to a supersonic fighter without degrading up and away performance. The significant technologies (Figure 1) related to the S/MTD program were 1) Two-Dimensional Thrust Vectoring/Reversing Exhaust Nozzles, 2) Integrated Flight and Propulsion Controls, 3) Pilot/Vehicle Interface, 4) Landing Gear, and 5) Close Coupled Canards.

The two technology drivers in the evolution of the STOL and Maneuver Technology Demonstrator have been the continuing development of two-dimensional vectoring and reversing exhaust nozzles and integrated flight and propulsion controls (IFPC). Further improvements in the pilot/vehicle interface (PVI) and landing gear were utilized to fully demonstrate these driving technologies. Of course, the principal technology being developed and refined was one of integration.

1.1 Two-Dimensional Nozzles

From an indepth review of the development of non-asymmetric or two-dimensional nozzles (2)* up through 1979, it was concluded that two-dimensional nozzles, with a capability to vector and reverse the thrust, had the potential for a high payoff to improve fighter maneuverability along with a significant reduction in landing

* Numbers in parentheses designate references at end of paper.

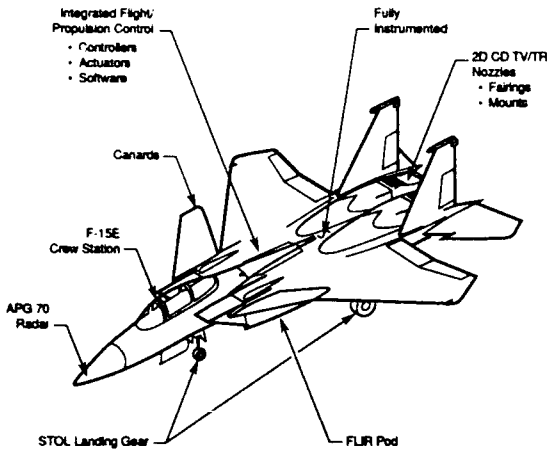

Figure 1. S/MTD Configuration

ground roll. During this same time period, results of several nozzle integration systems studies (3) stressed the need for a "timely" flight research program that would build confidence in two-dimensional nozzle technology so that it might be transitioned into use on operational fighter aircraft. Consideration of using thrust reversing for ground roll and inflight deceleration had been under consideration for several years (4,5,6). In general, most of these early studies were indicating that reversing and vectoring could be incorporated into a two-dimensional nozzle with less of a weight increase than if built into an axisymmetric nozzle. There was also the benefit of a possible reduction of drag because of a more favorable integration of the two-dimensional design into a twin-engine fighter aircraft (2). Some of the significant concerns of technical areas that needed further development were 1) reduction in weight, 2) improved cooling techniques, 3) improving structural integrity, 4) development of high temperature materials, and 5) enhancement of aircraft stability and control during vectoring and reversing.

The genesis of the two-dimensional nozzle being developed for the S/MTD occurred in an analytical and experimental program sponsored by the Air Force (7,8,9). The unvectored static performance of the two-dimensional nozzle was shown (8) to be equivalent to a comparable axisymmetric nozzle from tests using scaled models. A comparison at installed unvectored conditions (9) indicated the two-dimensional nozzle could have the same level of performance; however, the magnitude could change depending on how the nozzle was integrated into a twin-engine airframe. For example, the geometry of the interfairing between the nozzles can significantly change the installed drag levels. During a follow-on program to the above (10,11), it was shown that for a supersonic strike or air combat fighter, reversing for STOL capability and vectoring for trim benefits could be achieved for essentially no penalty in takeoff gross weight if a two-dimensional nozzle was used. The trend of using multifunction

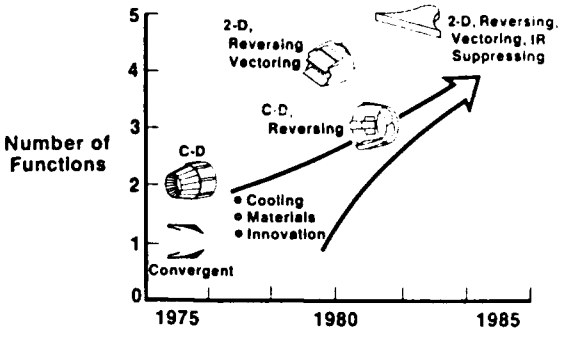

Figure 2. Trend in Nozzle Technology (Ref. 12)

nozzles (Figure 2) is discussed in Reference 12.

A full scale demonstration sea level test of a non-flight weight two-dimensional nozzle was successfully completed in 1982 (13). The results of this test were used to further evaluate the suitability of the two-dimensional nozzle concept and its potential for further development, to provide a more comprehensive data base, and to have a test vehicle with which to evaluate advanced two-dimensional nozzle components and cooling schemes. This same "boiler-plate" nozzle was then tested in the engine altitude test cells at the NASA Lewis Research Center (1985) and at the USAF's Arnold Engineering Development Center (1986). The tests were conducted in the forward thrust, vectoring and reverse modes at appropriate engine power settings.

1.2 Integrated Flight and Propulsion Controls

For a vehicle such as the S/MTD, the control system must be capable of coordinating the forces generated by the aerodynamic surfaces and the propulsion system so that acceptable flying qualities are produced. In a review of V/STOL and STOL flight experiences (14), there is a compilation of the different vehicles that have been flown since 1953 along with their key features and control problems. Practically all of the STOL flight experience had been with transport configurations. The review emphasized that STOL vehicles require a fully integrated control system because of the strong coupling between the airframe and propulsion systems and concluded that classical control design techniques will have to be supplemented with modern multivariable control techniques. As noted in Reference 15, the "first era of control system development ended in the 1960's." Up to this point, aircraft dynamics were dominated by the forces being produced by the aerodynamic control surfaces. With the advent of propulsive forces being used to control the aircraft flight path, the need for a more fully integrated control system became a requirement. The development of fly-by-wire and digital electronic control systems over the past few years is giving the flight control designer the flexibility to meet these more stringent requirements. Examples of flight vehicles using digital fly-by-wire (DFBW) controls are AFTI/F-16,

X-29, F-16, F/A-18, F-20, Digitac F-8, Space Shuttle and, of course, the STOL/MTD.

Another recent development that is very critical for the complete integration of the airframe propulsion control systems has been the increasing use of integrated engine controls that are being used for such things as optimization of engine performance or to continuously monitor engine stall margin (16, 17, 18, 19, 20). Over the past several years, the USAF, NASA and Navy (21) have sponsored many research and development programs in the area of integrating the propulsion system with the flight controls. Several of the programs have involved flight tests at the NASA Dryden Flight Research Facility (16, 17, 18, 19). An indication of the relationship between the development of control technology to various technical disciplines is shown in Figure 3. The S/MTD involved all of these disciplines except weapons.

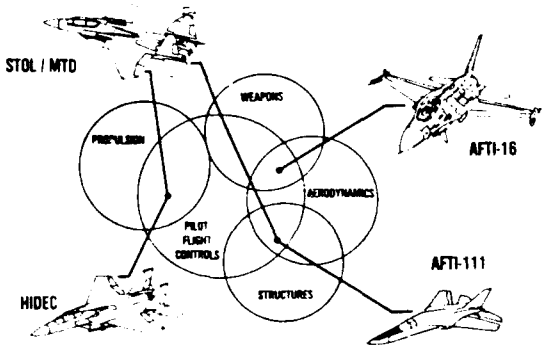

Figure 3. Control Technology Development

1.3 Landing Gear

The ability to land in a crosswind on damaged runways that may be wet and icy requires landing gear that can traverse not so ideal repaired surfaces and that have braking and steering functions that keep the aircraft aligned with the runway. This directional control is particularly critical when using a high degree of reverse thrust. The S/MTD solution to these problems was to have gear that would take a partial flare and negotiate a typical profile repair and to integrate the braking and steering functions into the IFPC.

1.4 Canard

An extensive review of wind tunnel tests with a canard on a F-15 is given in reference 22. As is stated, the addition of the independently variable close coupled canards allowed the S/MTD to more fully investigate the potential of the two-dimensional thrust vectoring/reversing nozzle. The coupling of thrust vectoring and canard leads to relaxed static margin and reduced trim drag (10, 11, 23). The S/MTD is using modified F-18 horizontal stabilators for canards. They are used to increase maximum lift and to control longitudinal stability plus generate side force subsonically and roll supersonically.

2.0 S/MTD AIRCRAFT SYSTEM

Modifications to the F-15B being used for the S/MTD included the aircraft control system which involved the removal of the mechanical controls and installation of a digital fly-by-wire system that incorporates the aerodynamic surfaces with their new actuators, the engine with its own digital control, a new digital nozzle controller and the main gear brakes along with nose gear steering. The nozzle controller takes the vectoring and reversing signals from the flight controller and nozzle area requests from the Digital Electronic Engine Controller (DEEC) to command the nozzle actuators to their appropriate position. An electromechanical throttle servo is used as an interface between the flight controller and the engine fuel control. The nozzle controller also generates a thrust calculation which is used by the flight controller to schedule vector requests.

2.1 Flight Control Modes

There are five main control modes (Figure 4) designed to meet the demonstrator requirements for the different phases of flight and ground operation. The STOL mode consists of three subset modes, which includes the "STOL-LAND" mode that is used just prior to touchdown to minimize dispersion by having airspeed control through throttle position. The engine RPM is kept at MIL-Power and thrust is varied by changing the angle of the rotating vanes. STOL-TOA allows for the use of vectoring on takeoff and normal power settings on approach. At touchdown, all the modes go automatically to STOL-GH, the speed hold is disengaged and the throttles are used for direct control of the vanes to attain the maximum thrust reversing allowed for deceleration.

MODE		CAPABILITY
1 CONVENTIONAL	FLAPS UP	ALL EFFECTORS EXCEPT VECTORING / REVERSING
	FLAPS DOWN	ALL EFFECTORS EXCEPT VECTORING / REVERSING
2 CRUISE	FLAPS UP	OPTIMUM FLIGHT PATH CONTROL
3 COMBAT	FLAPS UP	OPTIMUM ATTITUDE CONTROL
4 STOL LAND	FLAPS DOWN	MAXIMUM PERFORMANCE APPROACH
TOA	FLAPS DOWN	MAXIMUM PERFORMANCE TAKEOFF AND NORMAL APPROACH
GH	FLAPS DOWN	MINIMUM STOPPING DISTANCE AND GROUND HANDLING
5 SPIN RECOVERY	FLAPS UP	FULL SURFACE DEFLECTIONS WITH NO FEEDBACKS

Figure 4. IFPC Control Modes

The other control modes give the S/MTD the operational capabilities that allow for an inflight assessment of performance improvements that can be attributed to the technologies being demonstrated. The cruise and combat modes allow optimization of all the control effectors to improve maneuvering and to reduce trim drag. Thrust reversing is still available up to aircraft structural limitations. Although the demonstration program has not included high angle of attack, a spin recovery mode is provided which gives the pilot full-authority control capability. The various control modes are selected by use of the appropriate switches located on the

throttle or the control panel.

2.2 Nozzle Operating Modes

The nozzle has three main operating modes (Figure 5) of conventional, primary jet only vectoring and vectoring or reversing with the rotating vanes. In the conventional mode, the expansion area ratio can be controlled with the convergent and divergent flap actuators to allow flexibility in the thrust level and to maximize thrust minus drag. In this mode the thrust is through the engine centerline. In the vectoring mode, the nozzle can be scheduled to its required area ratio up to full afterburner while vectoring in pitch up to a maximum of + or - 20 degrees. The actual vector angle required and allowed is dependent on flight condition and thrust level with a limit of 6,000lb normal force. To operate the nozzle on the vanes, the convergent flap is closed or partially closed and the exhaust flow is directed through the vanes on the upper and lower surface of the nozzle. The vanes can be varied from 35 degrees to 135 degrees from the aft centerline. During vane operation the afterburner is inhibited.

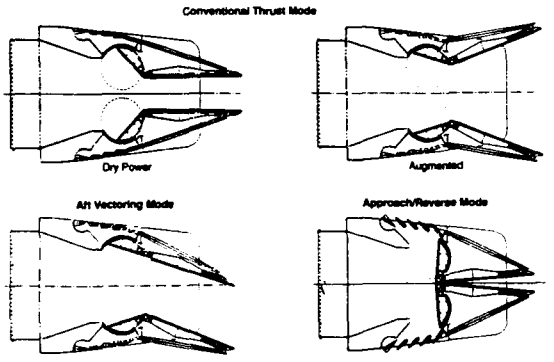

Figure 5. Nozzle Operating Modes

2.3 S/MTD Throttle Operation

All pilot commands were integrated into natural stick, pedal and throttle movements and no new controls were added for vane operation. A standard F-15 throttle quadrant was modified (Figure 6) so that above idle the throttle is no different than the normal F-15 throttle (24). In the CRUISE and COMBAT modes, pulling the throttles slowly back from afterburner to normal idle produces a conventional response with the engine spooling down to the flight idle speed. As the throttle is pulled aft of the spoiled idle detent the convergent flaps start to close and the vanes are deployed up to 135 degrees with continued backward movement of the throttle. Further aft movement with the vanes at 135 degrees will spool up the engine to 100% RPM to the maximum reverse thrust.

Vane operation as implemented in the SLAND mode is the key to the short landing capability. In SLAND the normal throttle function of controlling RPM is changed to a speed command function. Selecting SLAND spools up the engine, closes the convergent flaps and deploys the vanes. The throttle angle is interpreted as a speed command and feedback holds the speed constant by varying the vane angle to increase or decrease thrust (24). This allows the pilot to point the aircraft at the touchdown point thereby reducing his workload and giving improved touchdown precision (reduced dispersion) which is critical to stopping on very short runways. The transition to full reverse takes less than 0.5 seconds after touchdown.

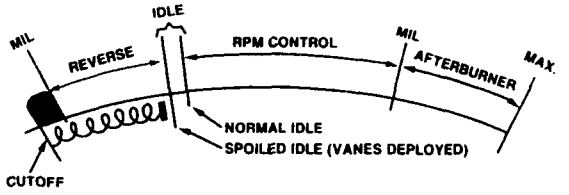

a. Normal Operation

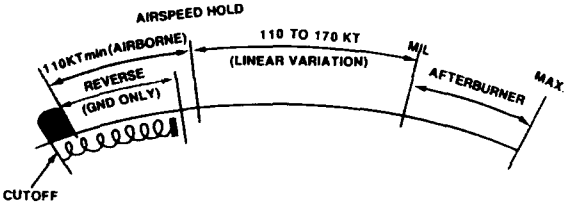

b. SLAND Operation

Figure 6. Throttle Geometry

3.0 GROUND TESTS AND SIMULATIONS

The S/MTD program had some very intensive test and analysis activities to prove that all systems were ready for first flight and beyond. Included in the major activities prior to flight test were several wind tunnel tests, manned flight simulations, propulsion and system component, sea level and altitude tests, laboratory structural tests, avionic systems tests and other subsystems tests. Many of the tests were developmental in nature to assist in the evaluation of the performance and operational characteristics of the new concepts and technologies to be flight tested. Additional tests were conducted to show the airworthiness of a particular component, subsystem or complete system. In some cases, airworthiness was shown by analysis or similarity to a previously flight rated component. During flight tests, loads were measured on the canards, wings, stabilators, vertical tails. engine ducts and mounts, control system and inlet actuators, and landing gear.

Following is a summary of the more critical test activities along with representative results and how these results were used to assure a successful flight test.

3.1 Wind Tunnel Tests

The performance plus the stability and control characteristics of the S/MTD were generated from existing F-15 flight data incremented with wind tunnel data giving

the effects of the canards, the two-dimensional thrust vectoring and reversing nozzle and the combined use of the flaperon/drooped ailerons. The nine wind tunnel test efforts to acquire the incremental and other data are listed in Figure 7. The data from the first five tests were used in the development of the flight control laws and in the prediction of flight performance. Information from the other tests was used to estimate component loads, establish flutter boundaries, evaluate the degree of reverser flow into the inlet during landing, and to evaluate the aerodynamic data base in a dynamic environment.

TYPE TEST	FACILITY (MODEL SCALE)	PURPOSE
HIGH SPEED AERO	AEDC 16T/4T (4.7%)	PERFORMANCE, STABILITY & CONTROL
LOW SPEED HIGH AOA	NASA LaRC. 30 X 60 (13%)	STABILITY & CONTROL
LOW SPEED HIGH LIFT	MCAIR/LSWT (13%)	HIGH LIFT STABILITY & CONTROL, GROUND EFFECTS
LOW SPEED JET EFFECTS	MCAIR/LSWT (7.5%)	JET EFFECTS STABILITY & CONTROL, GROUND EFFECTS, TAIL LOADS
HIGH SPEED JET EFFECTS	AEDC 16T (8.33%)	JET EFFECTS STABILITY & CONTROL, DRAG INCREMENTS, TAIL LOADS
HIGH SPEED LOADS	AEDC 16T/4T (4.7%)	COMPONENT LOADS
LOW SPEED FLUTTER	MCAIR LSWT (13%)	FLUTTER BOUNDARIES
INLET REINGESTION	NASA LaRC 9 X 15 (7.5%)	INLET INGESTION OF REVERSER FLOW, SURFACE HEATING
TETHERED FREE FLIGHT	NASA LaRC 30 X 60 (13%)	EVALUATION AERODYNAMIC DATA BASE IN DYNAMIC ENVIRONMENT

Figure 7. S/MTD Wind Tunnel Tests

Some of the more interesting data was acquired during the low speed jet effects test (25) and the inlet reingestion test (26). The low speed jet effects tests were conducted to determine the jet induced effects on aircraft control during the STOL approach and landing phase with the test objective being to expand the aerodynamic data base for control law development and flight simulation. The more significant results indicate an observable change in lift and pitching moment as the aircraft transitions through ground effects on approach. As is shown in Figure 8 and 9, the greater lift loss and nose-up pitching moment changes were observed at landing gear height on touchdown. These data were combined with other data, including that from the low speed high lift and low speed high angle-of-attach tests, to derive the appropriate control laws that gave more than adequate control of the aircraft during landing approach and roll out. The was accomplished using a combination of the aerodynamic controls and the rotating vanes of the 2-D nozzles. Reference 25 gives more detail on how these changes varied with aircraft speed, angle-of attack, sideslip angle, and nozzle pressure ratio. Also discussed are changes in directional stability and rudder effectiveness which were strongly influenced by the exit angle of flow through the upper rotating vanes.

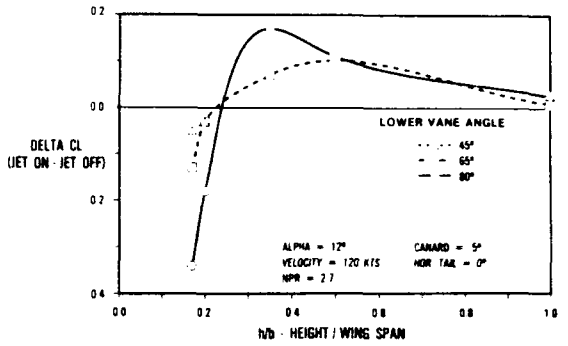

Figure 8. Lift Change in Ground Effects (Ref. 25)

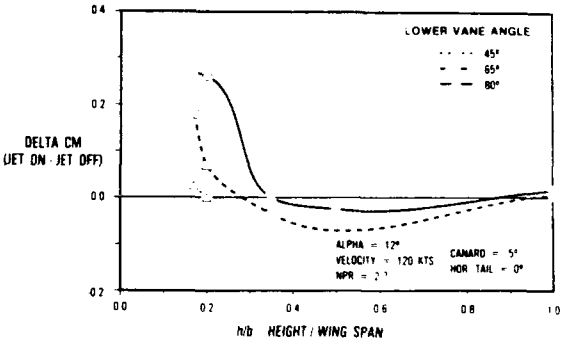

Figure 9. Pitching Moment Change in Ground Effects (Ref. 25)

The low speed jet effects data discussed above was obtained in the traditional method of placing the model at several stationary positions above a fixed ground plane. The NASA Langley Research Center (27) developed a testing technique of measuring time-dependent ground effects by utilizing a moving model over an inclined ground plane that simulates rate-of-descent. The reported results indicated rate-of-descent can be important in determining actual ground effects and that the traditional test methods, particularly when an exhaust plume may be impinging the ground, may predict a greater lift loss than will occur during actual flight. The flight tests of the S/MTD clarified the importance of simulating these dynamic effects.

The same model used in the low speed jet effects was modified to have heated air (500°F) simulating the exhaust gases and used in the inlet reingestion tests (26) to evaluate the level of exhaust flow ingestion in the inlet during landing. Results (Figure 10) from the tests indicate the difficulty of maintaining zero ingestion during roll out. The temperature rise parameter (TRP) can be related to a percentage increase in temperature at the engine face, whereas the reverser mass flow ratio is an indicator of ground roll velocity. An increase in mass flux ratio correlates with a decrease in ground speed. As can be seen, maintaining the desired no flow ingestion (TRP=0) is very much dependent on aircraft speed and the angle of the lower rotating vanes. It is obvious from these reingestion results and those of the low speed jet effects test that the

schedule for moving the rotating vanes, especially the lower ones, during approach and landing is dependent on many factors. The current schedule is a function of pitch attitude and airspeed.

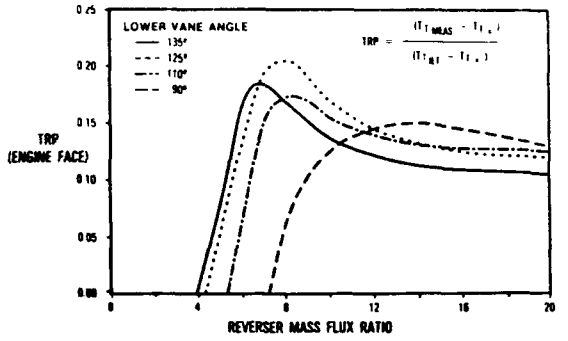

Figure 10. Engine Face Temperature Variation (Ref. 26)

3.2 Simulations

As previously discussed, the data base obtained from the wind tunnel tests plus existing F-15 flight data were used to develop the control laws for the different control modes (Figure 11). Several simulations were conducted to prove the acceptability of the control laws and to check that the different control modes would perform as expected. The objectives of these simulations included control law development, evaluation of flying qualities, verification of hardware/software interfaces, refinement of the pilot/vehicle interface and pilot training. Both fixed base and moving base simulators were used. The manned simulations tasks included up and away flight in the conventional, cruise and combat modes plus takeoff, approach and landing in the STOL mode. Included in these simulations, when required, were the aerodynamic ground effects on approach and landing, landing gear brake usage and nose wheel steering and differential use of the engines for asymmetric thrust forces and moments.

Discussed in two different reports is an evaluation and the simulation results of precise flight path control plus pitch attitude during fine tracking (28) and the development and simulation results of the coupled longitudinal and airspeed control laws for the STOL landing task (29). As pointed out by Bland et al (28), the S/MTD program emphasizes an optimization of the cruise and combat modes which in turn has highlighted the different flying qualities required for these modes. During an initial evaluation of the control laws developed for these modes on both the fixed and moving base simulators, Level 1 flying qualities were attained for the general maneuvering task; however, the fine tracking task received an unsatisfactory Level 2 at all flight conditions. An improvement in the aircraft tracking characteristics was reached with the development of a technique that increases the apparent lift due to angle of attack term in the pitch rate response. Further simulation results indicated a considerable improvement in pitch control and the attainment of Level 1 flying qualities for the precision tracking task.

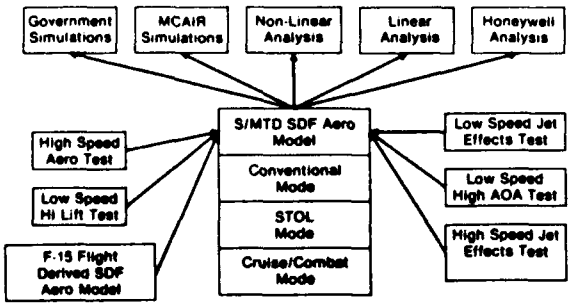

Figure 11. Data Base for Control Law Development

The STOL mode landing task has required the development of decoupled longitudinal and airspeed control laws (29). Precise airspeed control on approach is obtained by varying the thrust, using the movable rotating vanes. Pitch control is the result of a combined use of the stabilator, canard, trailing edge flaps and asymmetrical movement of the top and bottom rotating vanes.

Results of the piloted simulations of the approach and landing tasks indicate acceptable flying qualities, even with an increased pilot workload due to simulated moderate turbulence and crosswinds up to 30 knots. A significant improvement over current fighter capabilities noted by the simulation pilots was the airspeed control feature. Moomaw and Lowry (29) conclude that the multivariable design and analysis methods were successfully applied in the development of the control law modes that integrate the propulsion controls into the IFPC system. These are the STOL, CRUISE and COMBAT mode longitudional axes. The resulting design gives the required performance without being too complex for implementation.

3.3 Propulsion Systems Tests

Shown in Figure 12 are the major propulsion component and systems tests conducted to develop and substantiate the flightworthiness of the S/MTD engine/nozzle system. One of the more critical tests to be conducted early in the S/MTD program was the evaluation of the nozzle internal aerodynamics. Prior to this test, there was a very limited data base on the internal flow characteristics of two-dimensional exhaust nozzles. The data (e.g., discharge coefficients) from this test were used to establish the schedule for the convergent and divergent flaps, the arc valve and the rotating vanes (Figure 13) so that the correct effective exhaust area is maintained to ensure stall-free engine operation. Other useful information from the tests included internal static pressures that were used to verify the loads predicted for the nozzle structure and actuation system.

Several component tests were conducted to support the development and to verify the design of the flightweight two-dimensional

nozzle. These included structural tests of the titanium honeycomb beams, pressure loss tests of the nozzle cooling system and tests to evaluate creep forming of titanium honeycomb. Tests to support the development and flightworthiness of the nozzle control system included evaluations of both the hardware and software of the nozzle controller, along with appropriate tests of the nozzle's hydraulic actuators.

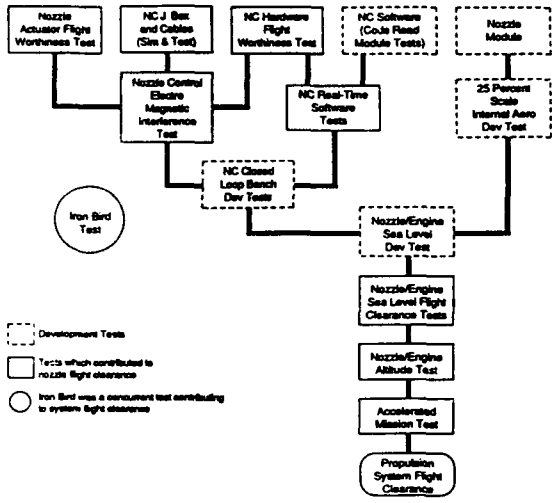

Figure 12. S/MTD Propulsion System Tests

Further evaluation of the two-dimensional nozzle and its control system was accomplished during the full scale engine/nozzle system tests. These development and flightworthiness tests were conducted in both a sea level engine test stand and an engine altitude simulation facility. The more critical test objectives were:

- Verification of the structural design
- Evaluation of performance and operability
- Optimization of the nozzle control system
- Evaluation of the cooling air distribution
- Verification of the throttle operation
- Demonstration of engine stability
- Demonstration of hardware durability

Following sea level acceptance tests for the two flight test engine/nozzles, there was an integrated test of the aircraft and engine systems conducted prior to the first flight with the two-dimensional nozzles.

The testing of engines that utilize reversing and vectoring created some new demanding requirements on jet engine test facilities. The capability to reverse and vector in the altitude facility required a complete new test scheme to capture the flow and direct it out through the exhausters. Accurate measurement of forces other than in the axial direction also required a complete redesign and new fabrication of the force measurement systems.

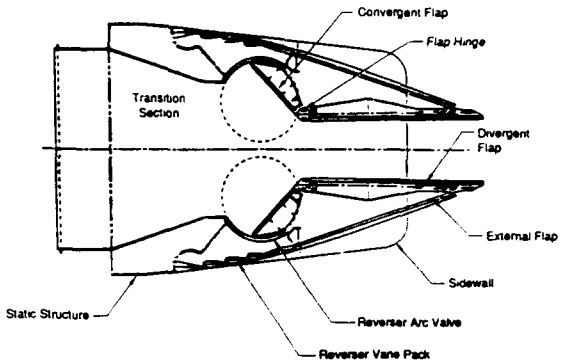

Figure 13. Nozzle Functional Features

3.4 "Iron Bird" Simulations

A control system loads and response characteristics simulator (i.e., "Iron Bird") was used to determine the structural and dynamic characteristics and limitations of the complete control system. All elements of the full scale S/MTD control system were used, including the exhaust nozzle and engine controls, to validate the totally integrated control functions. the five test phases conducted on the "Iron Bird" were an integration and interface test, a hydraulic test, an open loop test, a closed loop test and an actuator built-in-test (BIT) evaluation. Some of the more important objectives of this series of tests were to:

- Verify power for IFPC system components
- Verify cockpit and FPCS interfaces
- Verify functional operation of hydraulic systems
- Verify operation of IFPC/ hydraulic interfaces
- Verify Throttle Servo Operation
- Demonstrate emergency operation of the hydraulic system
- Verify IFPC system stability
- Determine the magnitude of uncommanded motion in the control systems
- Determine overall system frequency responses from sensors to actuators
- Determine control mode, power and signal failure transients

3.5 Hardware-in-the-Loop (HIL) Simulation

Another test series to verify the integration of flight hardware of the digital control systems and the Operational Flight Program (OFP), and also provide pilot familiarization and training was conducted on a Hardware-in-the-Loop (HIL) Simulation. The tests utilized a fixed base simulator along with the IFPC test benches, the FPCS test console and the nozzle controller (NC) test interface unit. The flight hardware items used were the central computer, the Flight Path Control Set (FPCS), the Nozzle Controllers and the Multi-Purpose Display Processor that was installed in the aircraft cockpit.

Some of the specific simulation objectives were to:

- Verify hardware/software interfaces
- Provide confirmation of the control laws
- Verify the adequacy of failure accommodation
- Provide verification of the OFP
- Provide pilot training
- Verify cockpit controller and display information
- Establish emergency flight procedures

4.0 FLIGHT TESTS

An initial series of flights using only the conventional mode control laws were flown with axisymmetric nozzles installed to obtain a functional check of the aircraft subsystems, including the calibration of airspeed and angle-of-attack instrumentation, to provide information for the flutter clearance of the canard surfaces and to verify no canard induced aircraft flutter mechanisms. Following installation of the two-dimensional (2D) nozzles, there were flights to clear a limited flight envelope to allow a ferry flight from the contractor's facility to the Air Force Flight Test Center. The 2D nozzle flights were begun with a vector only capability and then completed with the capability to vector and reverse.

4.1 2D Flight Test Results

The first flight with the 2D engines was successfully flown on 10 May 1989. Following successful accomplishment of engine operability checks, testing proceeded toward verification of flutter margins established during the axisymmetric testing. Due to the close similarity of external aircraft configurations between the axisymmetric and 2D, only the critical flutter test conditions (0.7, 0.8, 0.9, and 0.95M/5K feet) were tested. Results from these tests did not significantly differ from results obtained during the axisymmetric flutter evaluation, clearing the 2D configuration throughout the previously cleared flight envelope.

Further flight test focused on expanding the subsonic enhanced mode envelope for up and away flight (CRUISE and COMBAT modes). Handling Qualities During Tracking (HQDT) tests were accomplished in both modes using a 3g cooperative target with excellent results.

CONVENTIONAL and COMBAT mode pilot ratings are all Level 1 for tracking, while the CRUISE mode (designed for flight path control) is actually better than the expected level 2 ratings; see Reference 30 for further discussion of pilot comments and preferences. More important from a designer's viewpoint, pilot comments in support of the small differences shown were exactly the same as in the ground-based piloted simulations.

Thrust reversing was functionally verified first in taxi tests building up in speed and the amount of reverse commanded. In-

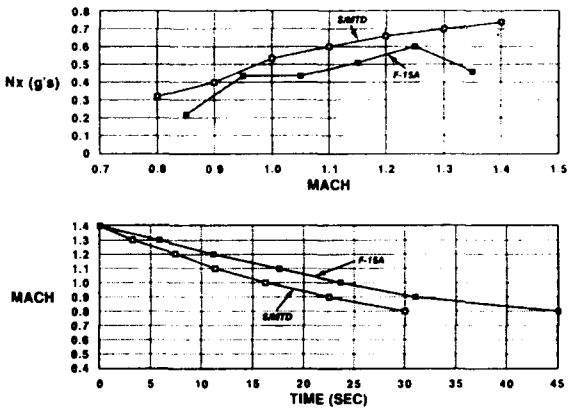

Figure 14. S/MTD Deceleration

flight reverser operability was verified by reversing on one engine initially at Mach 0.8 at 30,000 and 40,000 ft. After that initial verification, reversing has only been commanded on both engines. The reversing envelope was expanded to M1.6, with parameter identification maneuvers and data analysis at M0.9 and 1.2. Figure 14 shows the deceleration capability of S/MTD configuration compared with a production F-15 chase plane with speed brake deployed and flight idle thrust setting. It is also worth noting that this does not represent the maximum reverse thrust of the S/MTD nozzles. The forward vane angle (reverse thrust) has to be software limited at supersonic speeds to maintain vertical tail bending moments within strength limits. More reverse thrust could be available by strengthening the vertical tails, or by avoiding the interference in the design of a new configuration.

Buildup flights were also performed to evaluate the SLAND mode handling qualities, and also to demonstrate a maximum performance landing. Touchdown dispersion in the SLAND mode has been consistent with the design goal of a "box" 60 ft long by 20 ft wide. Data were accumulated for comparison of all three flaps-down modes.

Thrust reversing is also the major factor in achieving the short landing distance. The final approach is made with the engine at 100% RPM, the nozzle exhaust closed and the efflux controlled by the reverser vane deflection. Nozzle design requirements specified that the vanes be able to go from the nominal approach position to full reverse in less than 1 second. At touchdown, the pilot can select reverse thrust which commands the top vanes to their full forward deflection and the lower vanes to an angle determined by two schedules. An angle-of-attack schedule ensures rotation to a three-point attitude (31) and an airspeed schedule prevents hot gas reingestion. In addition, the pilot can select an Autobrake function which gives maximum anti-skid braking after touchdown. Measured landing distance of less than 1500 ft is half the dry runway capability of an F-15, and the wet runway landing distance was demonstrated to be less than 1/3 of the F-15 value.

The capability of thrust vectoring to enhance takeoff rotation was also demonstrated. It is possible to maintain a precise two-point attitude at steady taxi speeds as low as 40kts. Figure 15 shows the takeoff distances that can be achieved using different rotation speeds - rotating too soon incurs a loss of acceleration due to the additional drag and longer distances. The optimum takeoff distance is approximately 25% less than a production F-15 at similar conditions. The benefits of vectoring have also been quantified up and away at low speeds. Envelope expansion was done to 30° angle of attack. Pitch captures and nose-down recovery maneuvers from 30° AOA were flown back-to-back in CONVENTIONAL and COMBAT modes to evaluate the effectiveness of thrust vectoring. Figure 16 illustrates the additional pitch rate capability available in a recovery from high angle attack, and also the quicker onset. The figure also shows that the control laws have not been optimized for maximum effectiveness - the responses converge to the same steady state pitch rate. The S/MTD program was initiated as a full-envelope demonstration without any high-angle-of-attack emphasis. A simple linear gradient of pitch rate command vs deflection was used, and would obviously be changed in application.

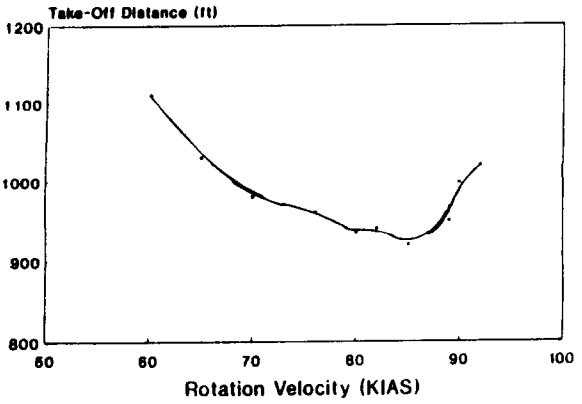

Figure 15. Takeoff Distance with Thrust Vectoring

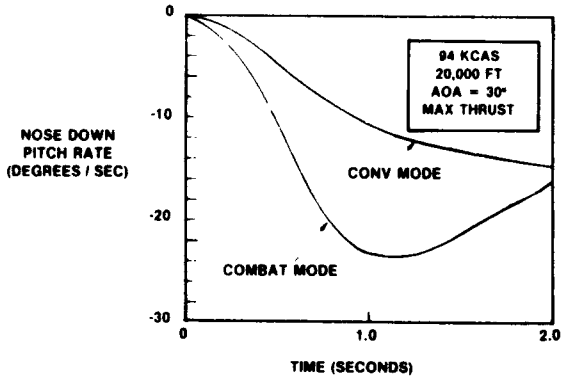

Figure 16. Pitch Response with Thrust Vectoring

5.0 LESSONS LEARNED

The development of the STOL & Maneuver Technology Demonstrator has spanned ten years from formulation of the design requirements through the final flight test. In that time the team has documented many lessons (references 32-36 address specific topics in more detail). Since we are using judgement with hindsight, these lessons learned range from someone else's lesson re-learned, through interpretation of specifications to a speculation as to why things worked or did not work.

5.1 Management

An old lesson was revalidated on this program, i.e. all the contractor project personnel were located in the same building. Some things that seemed to be new at the time are now more widely accepted. One example is the treatment of integration as a technology by itself. In order to guarantee the "Integrated" in the IFPC system, a Control System Integration Board (CSIB) was formed at the start of the contract. The CISB was co-chaired by the government Chief Engineer and McAir's controls Integration Manager, with membership by representatives of all technical functions and subcontractors. The agenda was to review all the various components that were being integrated into the IFPC system. Attendees represented McAir different functional areas, all the major subcontractors and different Government agencies. The Interface Control Sheets are defined in one-on-one meetings between Contractor and the various suppliers. In any complex system there are likely to be indirect effects of one component on some other, apparently unrelated component or function. the rationale behind the CSIB was to address integration questions as early as possible, and also to involve all the Subcontractors and Subsystem Managers in the discussions, so as to uncover any possible indirect effects. Government participation was also an integral part of the meeting, and frequently provided timely interpretation of Statement of Work requirements. Other engineering representatives gained a familiarity with the system that they would later be responsible for clearing for flight. Similarly, the AF Flight Test Center personnel became knowledgeable on the system they would be testing, as well as ensuring that the test requirements were understood during the design process.

Faced with managing a complex integration process, a formal Integration Board is a necessity not a luxury, with all Subsystem Managers, Suppliers and appropriate Government representatives as attendees. The Board should be responsible for tracking the design, development and test of each component, and the implementation and verification of each interface. Deliberations should be required to bring into view any problem or area of concern, so that all Board attendees can assess possible interactions with their area of responsibility, or where appropriate, potential solutions to "system" problems which may involve components other than those which encountered the anomaly.

Stress should be placed on including all components and interfaces in the discussions, since a system problem can be generated by a component which is performing well within the performance boundaries specified for it as a unit. The meetings should be detailed technical working meetings (not committee meetings) with the agenda and frequency driven by addressing current and future integration questions. Conversely any suggestion of unwilling participation or "too busy to attend" should raise a red flag to the managers responsible for the integration process.

5.2 2D Nozzle

When the S/MTD program was formulated, there were questions about the utility of a 2-D thrust reversing and vectoring nozzle. It is now clear that such a multi-function nozzle can be integrated into a supersonic fighter with performance benefits. Pitch thrust vectoring has also been flown on the YF-22, and thrust reversing can be considered a viable design option. A lesson learned on a detail design level is that it is critical to forecast the correct flight usage for the ground testing. A composite flight test usage was defined for use in an Accelerated Mission Test (AMT) to provide flight clearance for the nozzles. During the AMT, a serious wear condition occurred when the nozzle made a transition from vane operation to conventional thrust while at a high power setting. Such transitions had to be minimized during the flight test program. Conversely, a transition from afterburner to vane operation was not included in the AMT. This caused a minor nozzle failure when it was done in flight, and is no longer allowed in the flight test program. As an aside, this nozzle failure validated the failure accommodation and reconfiguration logic of the IFPC system. The failed nozzle reconfigured to a fail-safe mode (full open); the other nozzle reconfigured to the conventional thrust mode and the aircraft made a routine landing.

Many of the lessons learned on this nozzle are applicable to the first-generation, one-of-a-kind article. A Propulsion System Integration Board similar to the Control System Integration Board helped to keep all participants aware of problems and progress during the design, fabrication and ground testing of the propulsion system.

5.3 IFPC System

The Statement of Work required integration of all possible control effectors, so the use of multivariable control theory was strongly encouraged. In the actual design process, McAir used classical design techniques and Honeywell used a Linear Quadratic Gaussian (LQG) technique. Reference 32 contains lessons learned, the primary one being that a combined design approach is more efficient than either one individually. The final implementation is LQG for the enhanced mode longitudinal axes, and classical for the conventional mode longitudinal axes and all lateral/ directional axes. To some extent this follows the definition of requirements as complex or conventional. The combined design approach, however, provides a more rational method of trading off performance for acceptable system complexity.

Reference 34 is a documentation of the special interpretation or other criteria that were required to produce Level 1 flying qualities for all flight phases. The desire for optimum air-to-air tracking characteristics required careful interpretation of the available pitch axis criteria, but required a new criterion for the lateral/directional axes. New criteria were also proposed for achieving precise touchdown capability, although further research is needed to define the inter-relationship of the pitch and speed axis requirements and also the tradeoff of required control bandwidth vs touchdown precision.

The S/MTD landing performance was to be achieved in crosswinds up to 30kts with wind shear and turbulence as defined in the military flying qualities specification. A significant amount of piloted simulation was devoted to this problem. All the simulations and the early flight tests indicated Level 1 flying qualities. It was a surprise, therefore, when a CONVENTIONAL mode landing in gusty conditions showed indications of stabilator rate limiting. There was no apparent effect on flying qualities, but a stabilator gain reduction was implemented to eliminate any potential problems. The condition could only be repeated in flight using a flaps-down target tracking test maneuver to increase pilot gain. Reference 33 documents a piloted simulation evaluation of the problem, continuous turbulence could not replicate the rate limiting. The lesson learned from this experience is a proposed model combining discrete gusts with continuous turbulence that provides a realistic system excitation for control law design. Finally, control system hardware and software lessons learned are contained in Reference 35.

5.4 Pilot Vehicle Interface

A very simple lesson was learned in this area. The mission avionics that are on a tactical fighter facilitates the on-board generation of all required guidance to land on a designated touchdown point. In normal peacetime operation this will enhance overall situational awareness, providing a subjective increment in safety. It can backup the ILS and enhance landings in marginal weather conditions. In combat operations, it removes the dependence on ground-based radiation and provides significant flexibility in the landing strips that can be used.

6.0 CONCLUSIONS

An overall "lesson learned" is that the S/MTD program has generated flight test data to validate four specific technologies:

- 2-D thrust vectoring and reversing nozzle

- Integrated Flight/ Propulsion Control
- Advanced Pilot/Vehicle Interface including Autonomous Landing Guidance
- Rough field/high sink rate landing gear

These technologies have been integrated into an F-15B to provide mission benefits across the complete flight envelope from on-board guidance to a bad weather short landing, through significantly enhanced maneuvering benefits to supersonic performance. These technologies are either transitioning on to other aircraft, or can be considered viable design options for future aircraft.

7.0 ACKNOWLEDGEMENTS

Much of the content of this paper can be directly attributable to the dedicated efforts of S/MTD program personnel at McDonnell Aircraft Company and Pratt and Whitney, plus their subcontractors. We are deeply appreciative of their input. We also want to thank Pat Rotterman, who had to endure the many changes in this paper.

8. REFERENCES

1. Selegan, D., "STOL Fighter Technology Program," ASME Paper 83-GT-243, April 1983.

2. Capone, F.J., "The Nonaxisymmetric Nozzle - It is For Real," AIAA Paper 79-1810, August 1979.

3. Richey, G.K., Berrier, B.L. and Palcza, J.L., "Two-Dimensional Nozzle/Airframe Integration Technology - An Overview," AIAA Paper 77-839, July 1977.

4. Linderman, D.L. and Mount, S.J., "Development of an In-Flight Thrust Reverser for Tactical/Attack Tactical/Attack Aircraft," AIAA Paper 70-699, June 1970.

5. Weiss, D.C. and McGuigan, W.M., "Inflight Thrust Control for Fighter Aircraft," AIAA Paper 70-513, March 1970.

6. Capone, F.J., Re, R.J. and Bare, E.A., "Thrust Reversing Effects on Twin-Engine Aircraft Having Nonaxisymmetric Nozzles," AIAA Paper 81-2639, December 1981.

7. Hiley, P.E., Wallace, H.W. and Booz, D.E., "Non-Axisymmetric Nozzles Installed in Advanced Fighter Aircraft," J. Aircraft, Vol. 13, No. 12, pp. 1000-1006, December 1976.

8. Willard, C.M. et al, "Static Performance of Vectoring/Reversing Non-Axisymmetric Nozzles," AIAA Paper 77-840, July 1977.

9. Hiley, P.E., Kitzmiller, D.E. and Willard, C.M., "Installed Performance of Vectoring/Reversing Non-Axisymmetric Nozzles," AIAA Paper 78-1022, July 1978.

10. Hiley, P.E., and Bowers, D. L., "Advanced Nozzle Integration for Supersonic Strike Fighter Application," AIAA Paper 81-1441, July 1981.

11. Wallace, H.W. and Bowers, D.L., "Advanced Nozzle Integration for Air Combat Fighter Application," AIAA Paper 82-1135, June 1982.

12. Richey, G.K., Surber, L.E., and Berrier, B.L., "Airframe-Propulsion Integration for Fighter Aircraft," AIAA Paper 83-0084, January 1983.

13. "New Nozzle Design Aimed at F-15, F-16 Aircraft," Aviation Week and Space Technology, pp. 70-73, September 13, 1982.

14. Moorhouse, D., "STOL Flying Qualities and the Impact of Control Integration," Proceedings of NAECON 83, Dayton, OH, May 1983.

15. Moorhouse, D., and Selegan, D., "The STOL and Maneuver Technology Program Integrated Control System Development," Proceedings of AGARD, Active Control Systems Conference, Paper 26, Toronto, Canada, October 1984.

16. Burcham, F.W., Jr. and Batterton, P.G., "Flight Experience with a Digital Integrated Propulsion Control System on an F-111E Airplane," AIAA Paper 76-653, June 1976.

17. Burcham, F.W., Jr., Meyers, L.P. and Walsh, K.R., "Flight Evaluation Results for a Digital Electronic Engine Control in an F-15 Airplane," NASA TM 84918, October 1983.

18. Burcham, F. W., Jr., Haering, E. A., Jr., "Highly Integrated Digital Engine Control System on an F-15 Airplane," NASA TM86040, June 1984.

19. Myers, S.P. and Burcham, F.W., Jr., "Propulsion Control Experience Used in the Highly Integrated Digital Electronic Control (HIDEC) Program," NASA TM 85914, October 1984.

20. Shaw, P.D. et al, "Development and Evaluation of an Integrated Flight and Propulsion Control System," AIAA Paper 85-1423, July 1985.

21. Linebrink, K. L. and Vizzini, R. W., "Full Authority Digital Electronic Control (FADEC)-Augmented Fighter Engine Demonstration," SAE Paper 82-1371, October 1982.

22. Mello, J.P. and Kotansky, D. R., "Aero/Propulsion Technology for STOL and Maneuver," AIAA Paper 85-4013, October 1985.

23. Bowers, D.L. and Laughrey, J.A., "Integration of Advanced Exhaust Nozzles," AGARD-CP-301, Paper No. 11, May 1981.

24. Lewis, G.V., "F-15 S/MTD Thrust Vectoring/Reversing Flight Test Results," SAE Aerotech 90, Long Beach, CA, October 1990.

25. Blake, W.B., "F-15 SMTD Low Speed Jet Effects Wind Tunnel Test Results," Proceedings of NASA Ames Research Center Workshop on Ground Effects, April 1987.

26. Blake, W. B., and Laughrey, J. A., "F-15 SMTD Hot Gas Ingestion Wind Tunnel Test Results," AIAA Paper 87-1922, July 1987.

27. Kemmerly, G.T., Paulson, J.W., Jr. and Compton, M.,"Exploratory Evaluation of a Moving-Model Technique for Measurement of Dynamic Ground Effects," AIAA Paper 87-2289, August 1987.

28. Bland, M., Citurs, K., Shirk, F., and Moorhouse, D., "Alternative Design Guidelines for Pitch Tracking," AIAA Paper 87-2289, August 1987.

29. Moomaw, R. and Lowry, D., "Application of Multivariable Control to the STOL and Maneuver Technology Demonstrator," AIAA Paper 87-2403, August 1987.

30. Moorhouse, D.J., et. al., "Handling Qualities of the STOL & Maneuver Technology Demonstrator from Specification to Flight Test", AGARD Symposium on Flying Qualities, AGARD CP 508, October 1990.

31. Moorhouse, D.J., Laughrey, J.A. and Thomas, R.W., "Aerodynamic and Propulsive Control Development of the STOL and Maneuver Technology Demonstrator", AGARD CP 465, October 1989.

32. Moorhouse, D.J., and Kisslinger,R.L. "Lessons Learned in the Development of a Multivariable Control System", Proceedings of NAECON 89, Dayton, OH., May 1989.

33. Leggett, D.B., Moorhouse, D.J., and Zeh,J.M., "Simulating Turbulence and Gusts for Flying Qualities Evaluation", AIAA Paper 90-2845, August 1990.

34. Moorhouse, D.J., "Lessons Learned from the S/MTD Program for the Flying Qualities Specification", AIAA Paper 90-2849, August 1990.

35. Clough, B.T., "Integrated Flight Control - Lessons Learned", AIAA Paper 90-3307, September 1990.

36. Kisslinger, R.L., and D.J. Moorhouse, "Lessons Learned in Control System Integration & Management from the S/MTD Program", SAE Paper 901849, SAE Aerotech 1990, October 1990.

Hypersonic Propulsion System Force Accounting

K. Numbers
Aerospace Engineer
WL/FIMM
Wright Laboratory,
Wright-Patterson Air Force Base, Ohio 45433-6553
USA

1. SUMMARY

A generic matrix of propulsion force accounting procedures has been developed from a survey of the U.S. aerospace community. The matrix includes definitions for propulsion system and control volume boundary specification. Aerodynamic reference conditions are also discussed relative to off-design performance. The advantages and disadvantages of each of the force accounting procedures are discussed as they apply to some typical hypersonic force accounting problems.

2. LIST OF SYMBOLS

A	flow area
A0	freestream flow area
AC	inlet capture area
API	aero-propulsion interface
ARC	aero-reference condition
EAI	engine-airframe interface
F	stream thrust
$\Im$	surface pressure and shear integral
F_{ADD}	additive drag
F_{NP}	net propulsive force
ΔL	incremental propulsive lift
ΔM	incremental propulsive moment
M	Mach number
$\dot{m}$	massflow
P	pressure
S	vehicle or streamtube surface area
V	velocity
α	angle of attack
δ	ramp or cowl angle
ρ	density
τ	shear stress
Π	engine throttle setting

Subscripts

RAM	freestream stream thrust station
R1	first ramp stream thrust station
COWL	inlet cowl plane stream thrust station
E. FACE	engine face stream thrust station
THROAT	nozzle throat stream thrust station
G	nozzle exit stream thrust station

3. INTRODUCTION

The traditional approach to an air vehicle configuration study requires an assessment of the installed propulsion system performance. This assessment is accomplished by or supported by the propulsion integration specialist through various analysis techniques. The resulting thrust and propulsion related drag estimates are then combined with the airframe lift and drag (estimated by the aerodynamicist) through a force accounting procedure to yield the vehicle net forces and moments and ultimately the vehicle mission performance. For highly integrated hypersonic vehicles, the definition of an appropriate force accounting procedure can depend on a number of factors. Propulsion integration schemes, engine cycles, vehicle development maturity, analysis methodology/accuracy, and personal preference all influence the selection of the force accounting procedure. Knowledge of existing procedures and the specific applications to which they are best suited will help the propulsion and aerodynamics disciplines avoid common pitfalls.

4. DISCUSSION

Force accounting is the procedure by which the air vehicle components and the forces that act on them are defined and categorized as either aerodynamic or propulsion related. Each discipline (aerodynamics or propulsion) is then responsible for determining the forces and moments on components which are assigned to them. However, identifying the propulsion system of a highly integrated hypersonic vehicle is not a trivial matter. Consider first the unintegrated Mach 5 cruise aircraft shown in Figure 1a. The inlet, engine, and nozzle which are contained in the propulsion nacelles are distinctly separate from the basic airframe. Since the aerodynamic and propulsion components have little influence on each other, the aerodynamicist and propulsion analyst can conduct independent assessments easily. Conversely, an integrated Mach 5 cruise vehicle is shown in Figure 1b. Here, the various vehicle components are *designed* to have mutually beneficial interaction. For example, the vehicle forebody provides a significant amount of compression of the propulsion streamtube. It also has a large planform area which generates lifting forces and

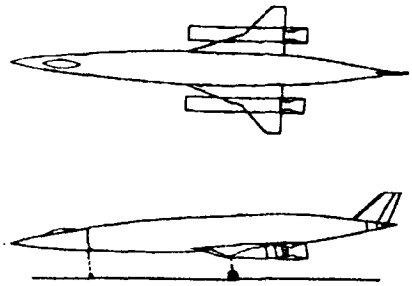

Figure 1a. Pod Mounted Mach 5 Cruise Vehicle

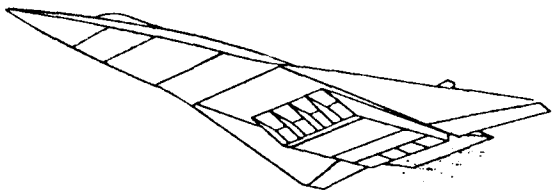

Figure 1b. Integrated Mach 5 Cruise Vehicle

pitching moments. The aft expansion surface is designed for optimum thrust, but it generates important contributions to lift and pitching moments as well. Thus the forebody and aft expansion surface are key components in both the airframe aerodynamics and the propulsion cycle, and their proper integration is necessary to the success of the vehicle design. Consequently, the aerodynamic or propulsion components are somewhat ambiguously defined. This hampers the ability of the aerodynamic and propulsion disciplines to conduct independent assessments.

The result of the ambiguous hypersonic propulsion system definition is the usage of many dissimilar force accounting procedures in the hypersonic propulsion community. This lack of force accounting standardization presents several problems.

First, evaluation of competing configurations becomes difficult if not impossible when unique procedures are used for each configuration. Key propulsion performance parameters for hypersonic flight, such as specific impulse and excess thrust, may not be directly comparable due to differing definitions of thrust and propulsion related drag. Moreover, the detailed analysis information required to normalize these performance parameters to a common definition is usually not reported.

Second, continuity is lost between preliminary propulsion system analyses and scale test results during the vehicle development process. The type of information required for the selected force accounting procedure may not be obtainable during the test. Also, the measured quantities from the test may provide some but not all of the force components determined in the preliminary analysis. For example, a detailed inlet drag breakdown of several components (bleed, bypass, additive, etc.) is difficult to obtain from wind tunnel force balance measurements. Typically, the balance only measures the total drag level. This limits the extent to which the accuracy of the preliminary analysis methods can be verified by the test results.

Third, insight into the effects of vehicle performance from component design parameters may be sacrificed. Each discipline naturally wants to use a procedure which yields the most visibility into their respective performance sensitivities. Unfortunately, the various force accounting procedures are able to highlight only certain performance effects. A procedure which allows the propulsion analyst to determine the sensitivity of forebody compression and aft surface expansion on thrust may not allow the aerodynamicist to optimize the lift to drag ratio.

It is evident that a single best force accounting procedure has not yet been devised. In fact, the results of past standardization efforts have not been universally adopted by the aerospace industry. An alternative approach described herein is to gather all proposed force accounting procedures into a generic force accounting matrix. The matrix would accommodate a majority of hypersonic airbreathing vehicles at all Mach numbers because the procedures are drawn from many existing applications. With this approach, the propulsion integration engineer is afforded the flexibility to select the procedure which is best suited to the situation. The problems discussed above can be minimized because transformation to other procedures is easily accomplished.

5. HYPERSONIC FORCE ACCOUNTING INTERFACES

As indicated by the previous discussion, propulsion force accounting involves the definition and separation of propulsion and aerodynamic force generating surfaces on the vehicle. Also, a control volume specification is necessary to determine engine forces. This is because a direct integration of pressure and shear stress on complicated internal engine components is normally not practical even with state of the art computational fluid dynamics.[4] To circumvent this problem, the conservation of momentum equation is employed to deduce the engine forces as the change in momentum between appropriately selected control volume boundaries.

Thus two force accounting interfaces must be specified: one for the separation of propulsion and aerodynamic surfaces and another for the engine control volume boundaries. These interfaces form the basis of the generic force accounting matrix and are described in detail below.

5.1 Aero-Propulsion Interface (API)

The separation of aerodynamic and propulsion surfaces will be called the aero-propulsion interface (API). It is the main division of primary responsibility between the aerodynamics and propulsion disciplines. This does not imply division of responsibility between the airframe company and the engine company, because the engine may be considered only a part of the propulsion system. An example of an API is shown in Figure 2, where the propulsion analyst is responsible for determining the forces and moments on the ramps, internal surfaces, and aft expansion surface.

The two-dimensional vehicle representation is a drastic simplification, and a real configuration will require a complex three-dimensional specification of the API. Also the interface boundaries may change with Mach number, angle of attack, and engine airflow. These details will be borne out later.

5.2 Engine-Airframe Interface (EAI)

The control volume approach utilized to deduce engine forces brings about another interface, called the engine-airframe interface (EAI). The control volume boundaries define this interface and are usually specified as propulsion streamtube stations (ie. freestream, nozzle exit, etc.) where the fluid stream thrust is known. An example of the EAI is also shown in Figure 2, again with the two-dimensional simplification. The example shows that the engine forces are the difference in stream thrust between the engine face and the nozzle throat.

EAI can be considered the portion of the propulsion system forces which are supplied by the engine company. That is, the engine company provides cycle decks, tabular data, or thrust stand data in the form of net engine forces between the EAI boundaries. It should be clear that the API defines the entire propulsion system, and the EAI defines that portion of the propulsion system which is provided by the engine company. The airframer propulsion analyst must analyze the remainder of the propulsion system.

5.3 Aero-Reference Conditions (ARC's)

In certain situations, operation of the propulsion system can have an influence on the flowfield about aerodynamic surfaces. These influences result from engine airflow throttling and propulsion system variable geometry, which can change forebody/inlet compression shock strengths and nozzle plume expansion characteristics. Exterior cowl surface pressures are predominantly affected, especially if variable cowl flaps are employed. Also, the forebody flow is influenced by engine throttling at subsonic freestream conditions. Other minor affects are possible as well, such as exhaust flow influence on trimming surfaces in the tail region.

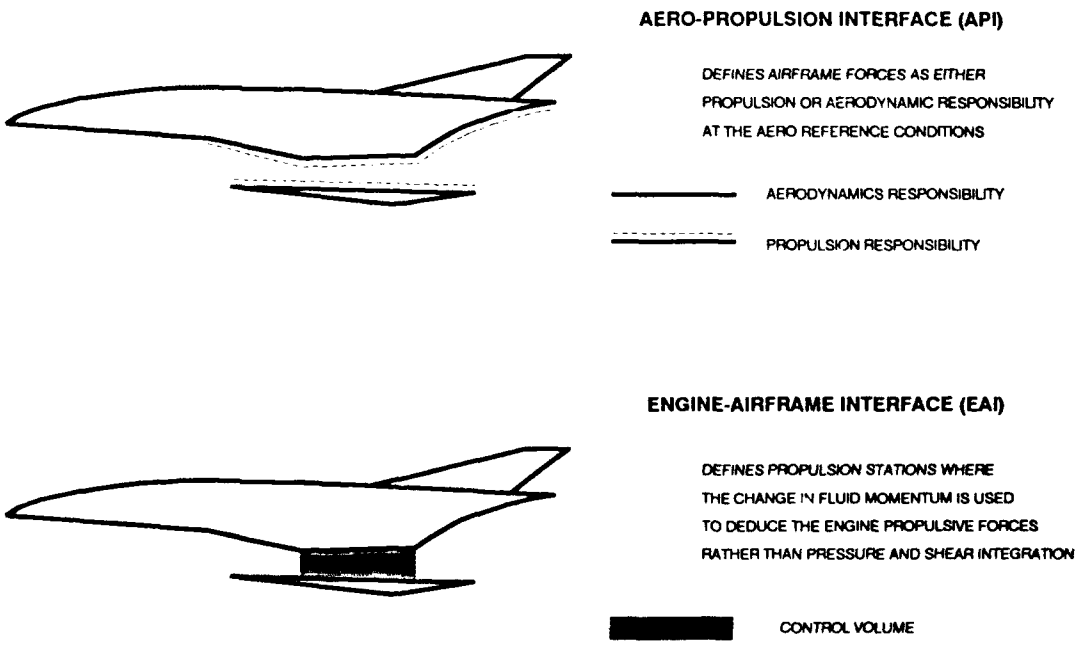

Figure 2. Definition of Force Accounting Interfaces

Because the aerodynamicist is not responsible for determining propulsive influences, aero-reference conditions (ARC's) are specified such that the aerodynamic forces are completely divorced from propulsion effects relative to force accounting.

The ARC's are specified as engine airflow and propulsion system variable geometry position at each freestream condition. The change in forces felt on aerodynamic surfaces due to propulsion system operation at other than the ARC's are charged to propulsion as off-reference force corrections. Therefore, the off-reference force corrections are *defined* to be zero at the reference conditions. Figure 3 is an example of typical ARC's and illustrates the off-reference force corrections applied to the exterior cowl. In the example, all variable geometry has a reference position, the inlet flow is started (critical inlet flow), and the nozzle pressure ratio is set by the unrestricted passage of the inlet flow in the duct aft of the inlet throat (flow through nozzle pressure ratio). The off-reference corrections may be a function of Mach number, angle-of-attack, inlet airflow, nozzle pressure ratio, and variable geometry settings.

Specification of the ARC's are important for CFD and wind tunnel testing. Aerodynamic analysis of numerical or test models at the aero-reference conditions saves considerable computer or wind tunnel expenses because the variation of aerodynamic forces and moments as a function of propulsion operation is eliminated. Thus the aerodynamicist does not need to simulate propulsion operation. The propulsion analyst is responsible for reproducing the aero-reference conditions in the propulsion models to determine the zeros for the off-reference corrections. The ARC's do not have to represent any realistic propulsion operating condition, as the objective is to specify conditions which are easily and accurately reproduced.

5.4 Putting The Pieces Together

Finally, the net propulsive force F_{NP} (parallel to the vehicle velocity vector), the incremental propulsive lift ΔL (normal to the vehicle velocity vector), and the incremental pitching moment ΔM, are the component sums of the forces generated on the primary propulsion surfaces as defined by the API, plus any corrections due to propulsion system operation at off-reference conditions. All other forces on the vehicle are charged to aerodynamics. The EAI governs who (the airframer or the engine company) provides specific components of F_{NP}, ΔL, and ΔM.

Using these definitions for force accounting interfaces, a generalized matrix of all proposed force accounting procedures was developed using inputs from the aerospace community. To accomplish this, a survey was conducted as discussed below.

6. FORCE ACCOUNTING SURVEY RESULTS

The industry survey was conducted to obtain details of those procedures which are currently being used in the U.S. The survey included information about current hypersonic vehicle configurations being analyzed, engine cycles, type of propulsion integration, and the force accounting details. Responses were received from five major airframe companies. Also, over 500 literature sources were reviewed for additional information.

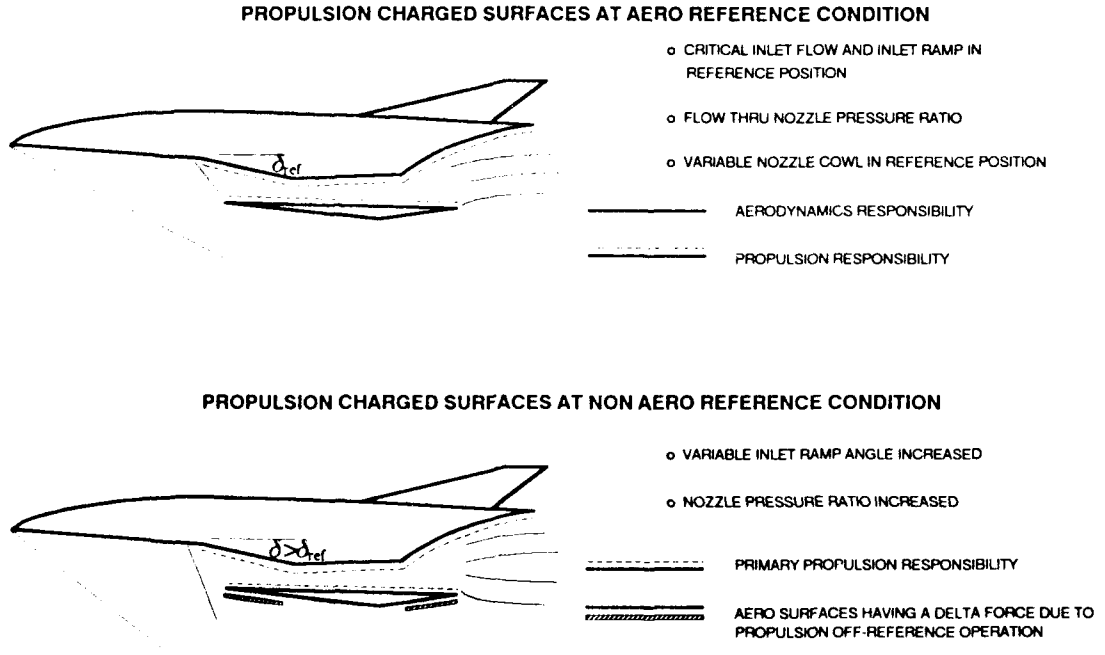

Figure 3. Typical Aero-Reference Conditions

Figure 4 shows the API's that are in the survey database. A description of the propulsion charged surfaces and comments about particular advantages or disadvantages are included.

In the first API, ideally all surfaces wetted by the propulsive streamtube are charged to propulsion. In some responses to the survey, the actual forebody and aftbody wetted surface areas were determined, which requires streamline tracing of the propulsive streamtube. In this case, the API designation may change with freestream condition if the propulsive streamtube changes shape. In other responses to the survey, the forebody and aftbody "propulsion areas" were pre-assigned prior to analysis. In this case, surfaces not washed by the propulsion streamtube may be charged to propulsion anyway (or vice versa). Off-reference corrections for this API are minimal.

The second API in the database starts propulsion accounting at the first inlet compression ramp (which may be arbitrarily specified) and extends to the aftbody; the forebody is not counted as part of the propulsion system. If the first inlet ramp is not fully enclosed by sideplates, this API will also require streamline tracing along the ramp surface. Unfortunately, the propulsion analysis is initiated in a complex flowfield which must be obtained from aerodynamics.

The third API begins propulsion accounting at the inlet cowl plane, or inlet aperture, and extends to the aftbody. This means the interface is well defined and remains constant with respect to freestream conditions. In general, the inlet aperture will not be planar but a three-dimensional locus of points. Again, the propulsion analysis starts in a complex flowfield. Also, since aerodynamics accounts for the first ramp, more off-reference corrections are required when the ramp is variable.

The fourth API is similar to the third except that aerodynamics accounts for the internal surfaces up to the inlet throat. This may require many off-reference corrections when the ARC's are specified, especially if variable geometry is involved. Only one occurrence of the fifth API is in the survey database, which limits the propulsion system to the internal surfaces between the engine face and nozzle throat. The major disadvantage of this API is that the off-reference corrections are probably excessive. Because aerodynamics accounts for the aft expansion surface, a correction is required at every throttle setting, resulting in a "powered" drag polar.

Propulsion Definition	Description	Pro	Con
	• All Surfaces Wetted by Propulsion Flow	• Prop Analysis Starts in Uniform Flow • Minimum Corrections at Off-Reference Conditions • Prop Includes Aft Thrust Surface	• Aero Excludes Major Lifting Surfaces • Interface is a Function of M, α, Π
	• Wetted Surfaces Aft of First Compression Ramp	• Aero Includes Forebody Lifting Surface • Minimum Corrections at Off-Reference Conditions • Prop Includes Aft Thrust Surface	• Aero Excludes Nozzle Lift & Trim • Prop Analysis Starts in Complex Flow • Interface is a Function of M, α, Π
	• Wetted Surfaces Aft of Inlet Cowl Lip	• Aero Includes Forebody & Inlet Lifting Surfaces • Boundary is Well Defined • Prop Includes Aft Thrust Surface	• Aero Excludes Nozzle Lift & Trim • Prop Analysis Starts in Complex Flow • Aero May Include Ramp Variable Geometry
	• Wetted Surfaces Aft of Engine Face	• Aero Includes Forebody & Inlet Lifting Surfaces • Boundary is Well Defined • Prop Includes Aft Thrust Surface	• Aero Excludes Nozzle Lift & Trim • Prop Analysis Starts in Complex Flow • Extensive Corrections at Off-Reference Conditions
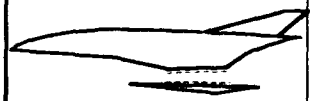	• Wetted Surfaces Between Engine Face and Nozzle Throat	• Aero Includes Major Lifting Surfaces • Boundary is Well Defined	• Aero Excludes Nozzle Lift & Trim • Prop Analysis Starts in Complex Flow • Extensive Corrections at Off-Reference Conditions

Figure 4. Survey Database Aero-Propulsion Interfaces

Figure 5 illustrates the EAI's that are in the survey database. Three upstream boundaries and three downstream boundaries have been considered in various combinations. The upstream boundaries include: freestream, inlet cowl plane, and engine face. The downstream boundaries include: nozzle throat, nozzle cowl plane, and nozzle exit. The advantages and disadvantages are similar to those in the API figure, except that the argument is between the airframer and engine company. The downstream boundary had only one occurrence in the survey database, and the survey respondent indicated that it was not the preferred method.

The term "engine face" is relative to turbomachinery based engine cycles and has no significance for open duct engines. In this case, the combustor entrance will be the "engine face". Likewise, the term "nozzle throat" does not have significance for scramjets, in which case the combustor exit will be the "nozzle throat". This terminology allows the EAI to be generalized to any engine type.

The ARC's included in the survey database are shown in Figure 6. In general, variable geometry (ramp and cowl flap angles specifically) has been specified at reference positions as a function of the freestream conditions. However, the reference flow conditions for the inlet and nozzle were not consistently addressed in the survey responses. In many cases, off-reference corrections due to nozzle flow were admittedly neglected. This indicates that either these corrections were assumed to be of negligible magnitude or they could not be accurately determined.

7. FORCE ACCOUNTING MATRIX DEVELOPMENT

The survey and literature search provided current force accounting procedures which when generalized are potentially applicable to the majority of hypersonic configurations. To this end, a force accounting matrix was developed which includes the API's and EAI's discussed above, as shown in Figure 7. Some exceptions were taken, however. The nozzle throat API and the nozzle cowl EAI were not included in the matrix because of their single occurrence in the survey database. These exclusions are supported by negative comments from the survey respondents. If a future growth in usage of these interface types arises, they can certainly be incorporated into the matrix. Also, a first inlet ramp upstream EAI boundary was added to cover several occurrences in the literature search. The matrix is organized as four API families with four options for the upstream stream thrust boundary and two options for the downstream stream thrust boundary. The matrix is therefore generalized to all combinations of API's and EAI's. Aerodynamic reference conditions were not generalized because they were found to be too specific to the vehicle configuration.

Control Volume Definition	Description	Pro	Con
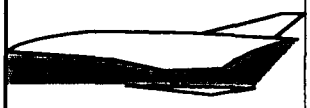	• Upstream: Freestream • Downstream Nozzle Exit	• Interface Starts in Uniform Flow • Simplest for Airframer	• Streamline Tracing Required • Engine Company Needs Inlet Performance Details • Airframer Cannot Optimize Aft Expansion
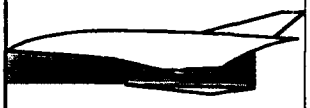	• Upstream: Freestream • Downstream Nozzle Cowl Lip	• Interface Starts in Uniform Flow • Nozzle Boundary is Well Defined • Airframer Can Optimize Part of Aft Expansion	• Streamline Tracing Required • Engine Company Needs Inlet Performance Details
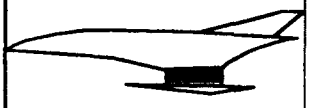	• Upstream: Engine Face • Downstream Nozzle Nozzle	• No Streamline Tracing • Boundary is Well Defined • Airframer Can Optimize Part of Aft Expansion	• Interface Boundaries in Complex Flow
	• Upstream: Inlet Cowl Lip • Downstream Nozzle Throat	• No Streamline Tracing • Boundary is Well Defined • Airframer Can Optimize Part of Aft Expansion	• Interface Boundaries in Complex Flow • Engine Company Needs Inlet Performance Details

Figure 5. Survey Database Engine-Airframe Interfaces

Reference Conditions	Description	Pro	Con
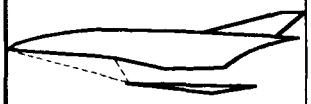	• Shock on Lip (A0/AC = 1.0)	• Aero Drag Independent of Shock Angle	• Off-Reference Correction at All Off-Design Conditions
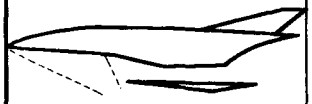	• Full Inlet Capture with Reference Ramp Angle (A0/AC = Critical)	• Off-Reference Corrections at Subcritical Operation Only • Closely Simulates Aero Force and Moment Model	• Aero Force Calculations More Complex • Specification of Reference Ramp Angle
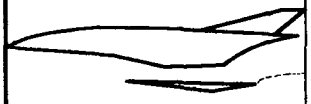	• Flow Thru Nozzle Pressure Ratio with Reference Nozzle Geometry	• Easily Produced Test Condtion in Aero Force and Moment Model	• Aero Force Calculations More Complex
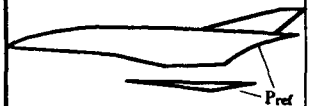	• Reference Nozzle Base Pressure ($P_{base} = P_{ref}$)	• Aero Force Independent of Nozzle Flow	• Nozzle Forces Must Be Removed From Aero Force and Moment Model
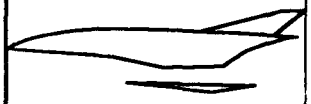	• Assume Aero Forces Independent of Propulsion Flow	• Simplest for Aero Force Calculations	• Influence of Propulsion Operation Neglected

Note: All variable geometry set at reference position.

Figure 6. Survey Database Aero-Reference Conditions

Force Accounting Family	Aero-Propulsion Interface	Options: Engine-Airframe Interface	
		Entrance	Exit
A	• Freestream to Nozzle Exit	1) Freestream 2) First Inlet Ramp 3) Inlet Cowl 4) Engine Face	1) Nozzle Exit 2) Nozzle Throat
B	• First Inlet Ramp to Nozle Exit	1) Freestream 2) First Inlet Ramp 3) Inlet Cowl 4) Engine Face	1) Nozzle Exit 2) Nozzle Throat
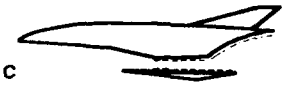 C	• Engine Face to Nozzle Exit	1) Freestream 2) First Inlet Ramp 3) Inlet Cowl 4) Engine Face	1) Nozzle Exit 2) Nozzle Throat
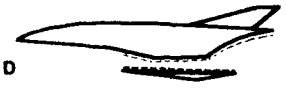 D	• Inlet Cowl to Nozzle Exit	1) Freestream 2) First Inlet Ramp 3) Inlet Cowl 4) Engine Face	1) Nozzle Exit 2) Nozzle Throat

Figure 7. Generic Force Accounting Matrix

Algebraic expressions for the net propulsive force can be found in Annex A for those who are interested in the force accounting matrix details. Expressions for incremental lift and pitching moment are not included because they do not add any new information. Deriving these expressions is simply a matter of resolving the force components along the desired axis. For example, the nozzle exit stream thrust F_G is a vector with components parallel and normal to the vehicle velocity. When net propulsive force is derived, it is assumed that the parallel component is used, etc.

8. THREE-DIMENSIONAL CONSIDERATIONS

The addition of the third dimension (width) to the API and EAI can make these interfaces very difficult to work with for some configurations. In two dimensions, propulsive wetted areas are assumed to remain unchanged with operating conditions. For three-dimensional flow however, the wetted areas may change on vehicles which have unconstrained external compressions and expansions. For instance, Figure 8 shows the forebody of a typical scramjet vehicle at two different freestream conditions: design angle of attack, and some higher angle of attack. The wetted area (shaded) is different for these two conditions because the propulsion streamtube has changed shape. Furthermore, the nozzle wetted area on the aftbody may change with the plume expansion characteristics. Therefore, the API specification will be a function of the operating conditions if it includes the forebody and aftbody. The actual wetted area must be determined by tracing streamlines in a computational fluid dynamics solution or some type of flow visualization technique during wind tunnel testing.

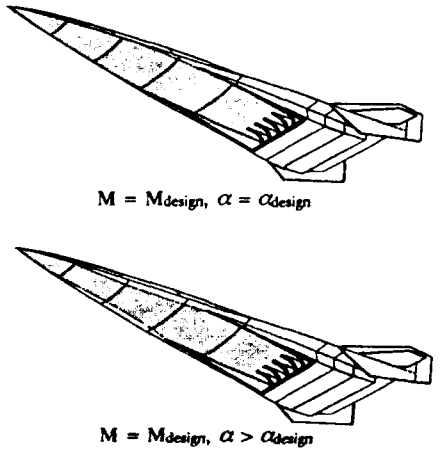

Figure 8. Forebody Streamtube Wetted Areas

To avoid streamline tracing, many propulsion analysts assign a constant wetted area which is close to the design situation so that the API specification does not change. Then at off-design conditions, either some of the propulsive flow spills onto the adjacent aerodynamic surfaces, or some of the assigned propulsion surface is not washed by propulsive flow. In the first case, off-reference corrections are required. In the second case, part of the propulsion surface forces may not be accounted.

For the EAI, the two-dimensional simplification results in planar control volume boundaries for which flow momentum integration is straight forward. In three dimensions, the boundaries may not be planar, as is the case of the swept sidewall compression inlet (Figure 9). The propulsion analyst must ensure that the momentum term includes flow crossing all parts of the boundary, including the spilled flow through the lower part of the aperture, and that the boundary does not involve unaccounted streamtube forces.

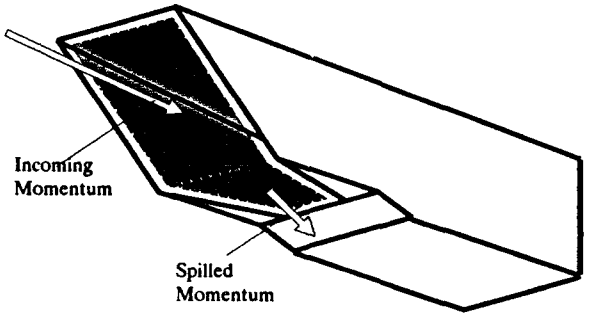

Figure 9. 3-D Cowl Plane Example

9. APPLICATIONS

The selection of an API/EAI combination from the matrix depends mainly upon three factors: 1) system configuration, 2) analysis data characteristics, and 3) analysis objectives. System configuration and analysis objectives have more bearing on the API, while data characteristics usually determine the most suitable EAI. One of the main arguments in terms of API selection is whether lifting surfaces should be included in the propulsion accounting. The other problem is the difficulty in obtaining the desired force components with existing analysis methods or test techniques. As usual, data accuracy and cost of analysis are conflicting. This section will illustrate through some common hypersonic propulsion analysis examples the use of the force accounting matrix.

9.1 Example 1 - Pod Mounted Turboramjet Mach 5 Cruiser (Figure 1a)

In this type of configuration, the effect of the weak forebody shock on the inlet approach flow is usually corrected for local Mach number, total pressure, and angle-of-attack. The effect of the forebody shock on the shape of the inlet streamtube is neglected, however. The most logical choice of API for this configuration is Family B, which has propulsion accounting from the inlet ramps to the nozzle internal surfaces (assuming the nozzle is not the single expansion ramp type). Family A would involve forebody force terms which are essentially zero since the propulsion flow does not wet the forebody. Use of Family C or D would require aerodynamics to determine forces on the internal inlet surfaces which are clearly propulsion related. Also, the number of off-reference corrections required by propulsion for Family C or D does not really reduce the propulsion analyst's amount of responsibility.

The type of engine data used during the analysis will determine the EAI. For typical uninstalled engine data, net engine thrust is quoted as the difference in nozzle gross thrust and freestream ram drag. Therefore, the freestream upstream boundary and the nozzle exit downstream boundary result in the least complications. Additive drag from the ramps must be determined but this may be easier and more accurate than integrating pressure and shear on the ramps and sideplates. Because the inlet flow is two-dimensional (or axisymmetric), the shock structure and additive drag is easy to predict using oblique (or conical) shock theory. If CFD is used, the integration of pressure and shear can be done, but the accuracy of the shear stress estimate along the ramps and sideplates must be considered. It is well documented that such calculations depend heavily on turbulence modelling. In its favor, the additive drag integral does not involve shear stress. For testing purposes, it is probable that ramp and sideplate forces cannot even be measured directly by force balance because of model size or complexity. Integration of ramps and sideplate pressures from static taps still requires a shear stress estimate. Thus an inlet massflow measurement (which automatically yields the freestream ram drag) and an additive drag estimate are a good alternative. Using the nozzle downstream boundary assumes that the engine data includes all the effects of internal nozzle performance. If the nozzle is a plug or single expansion ramp type, it may be desirable to use the nozzle throat downstream boundary and let the airframer determine the integrated nozzle forces.

9.2 Example 2 - Highly Integrated Turboramjet Mach 5 Cruiser (Figure 1b)

The propulsion system is more obscure in this case, so the analysis objectives and the data characteristics will drive the API selection.

Assume first that the analysis is to determine sensitivity of aerodynamic parameters on mission performance, in which the propulsion analyst plays a support role. That is, the propulsion analyst is to provide some typical turbojet and ramjet thrust data. API Family A is not a good choice in this case because the exclusion of the forebody lift form aerodynamics may yield strange (even negative) lift data. Also, the propulsion analyst may not be willing to sign up to the task of determining the forebody wetted area. Family C or D are better choices because most of the major lift producing components are accounted by aerodynamics. It will be easier for the propulsion analyst to provide the required data because the interface is not a function of the freestream conditions.

On the other hand, assume that the emphasis of the study is to determine propulsion parameter sensitivities. The propulsion analyst will want to know the effect of forebody precompression on the propulsion cycle, so API Family A is the natural choice.

If the vehicle is under system development where the aerodynamics and propulsion disciplines must work closely together, API Family B would be a good compromise between the to disciplines.

Engine data format is again the key to the EAI selection. If the propulsion analyst has the freedom to select any EAI, then it is desirable to keep the control volume boundaries within the propulsion system defined by the API. Otherwise, additional terms need to be evaluated to prevent double bookkeeping (refer to Appendix A). If the engine data format is mandated for some reason, then the decision is already made and the propulsion analyst has to deal with the consequences. For example, suppose the engine data uses the freestream upstream boundary and nozzle exit downstream boundary but the selected API is Family B. Some assumption about inlet and nozzle performance was made for the engine data which may not be compatible with the configuration being analyzed, and the propulsion analyst must determine forebody forces and subtract them from the engine data to prevent double bookkeeping.

Recall that accuracy of stream thrust estimates is critical to the accuracy of the deduced engine forces using the control volume approach. If the propulsion analysis calls for a flowfield averaging procedure (ie., going from a 2-D or 3-D inlet flow to a 1-D engine deck), the propulsion analyst will need to consider how the EAI boundaries will impact the accuracy of the stream thrust averaging. A boundary which has minimal flow distortions is desirable in this case.

9.3 Example 3 - Competing Configuration Audit

This example is meant to show how and why the procedure transformations are done. Assume that a government agency is down selecting between two contractor configurations. Configuration 1 uses API Family B, and Configuration 2 uses API Family C. The net propulsive force and associated performance parameters need to be compared, but Configuration 2 will always have higher net propulsive force because the ramp drag is not included.

The agency elects to perform a separate analysis using 2-D Parabolized Navier-Stokes (PNS) codes and a 1-D cycle deck. The PNS solutions provide the surface pressure and shear integrals on all propulsive surfaces except the scramjet, for which the cycle deck determines the change in stream thrust between the engine face and nozzle throat. Thus the direct comparison of Configuration 1 and 2 is done with API Family A and the engine face to nozzle throat EAI. To compare the agency analysis with each contractor, the forebody surface pressure and shear integral is removed from Configuration 1 to get API Family B, and the forebody and ramp surface pressure and shear is removed from Configuration 2 to get API Family C. Thus the agency has a valid comparison between each configuration, and also an assessment of the individual contractors' analysis accuracy.

10. CONCLUSIONS

The level of propulsion system integration required for hypersonic flight vehicles usually results in somewhat arbitrary definition of the propulsion system for vehicle force analysis purposes. The large number of force accounting procedures which are currently being used by the industry attests to this. At first, a single standard force accounting procedure appears to be an attractive solution, but it is not likely that such a procedure will be universally accepted by all involved. As shown by the preceding examples, a single standard procedure may not be advisable because of the inherent disadvantages in certain situations. A generic force accounting matrix which allows flexibility and guidance to select the appropriate procedure in original research and development efforts will help avoid these disadvantages. The ability to make simple transformations helps those organizations involved in configuration evaluation efforts to arrive at accurate and meaningful configuration comparisons.

11. ACKNOWLEDGEMENTS

The majority of information presented in this paper was provided under Air Force Contract F33615-87-C-3006, "Hypersonic Aircraft Propulsion Installation", by McDonnell Douglas, St. Louis, Missouri.

12. REFERENCES

1. Saleman, V., and Andrews, M., "Propulsion System Integration for Mach 4 to 6 Vehicles," AIAA Paper, 24th Joint Propulsion Conference, Boston, MA., 1988.

2. Hathaway, R.W., and Mack, J.T., "Propulsion System Characteristics and Force Accounting Options," Technical Operating Report 1, Air Force Contract F33613-87-C-3006.

3. Hathaway, R.W., and Mack, J.T., "Force Accounting Equations," Technical Operating Report 2, Air Force Contract F33615-87-C-3006.

4. Sullins, G.A., and Billig, F.S., "Force Accounting for Airframe Integrated Engines," AIAA-87-1965, 23rd Joint Propulsion Conference, Seattle, Washington, 1987.

5. Lehrach, R.P.C., "Thrust/Drag Accounting for Aerospace Plane Vehicles", AIAA-87-1966, 23rd Joint Propulsion Conference, Seattle, Washington, 1987.

6. Numbers, K.E., "Hypersonic Propulsion System Force Accounting", AIAA-91-0228, 29th Aerospace Sciences Meeting, Reno, Nevada, 1991.

7. Thrust and Drag: Its Prediction and Verification, Eugene E. Covert, Editor, Progress in Astronautics and Aeronautics, Volume 98, 1985.

13. ANNEX A

The special notation for the force accounting expressions is as follows.

The pressure and shear force integrated over a vehicle surface is given by Equation (1). The so called stream thrust integrated across a control volume boundary is given by Equation (2). The "$\Im$" and "F" terms are both identified by appropriate subscripts to indicate their location on the vehicle or within the propulsive streamtube.

$$\Im = \int_S (P - P_\infty)\, dS + \tau\, dS \qquad (1)$$

$$F = \int_A \{\rho \vec{V} \cdot \vec{V} + (P - P_\infty)\}\, dA \qquad (2)$$

The additive drag of the inlet propulsive streamtube is given by Equation (3). The concept of additive drag and its relation to propulsion surface forces is illustrated in Figure A1. Additive drag occurs when the EAI control volume encompasses the forebody or ramp surfaces and the shocks do not focus on the inlet cowl lip. The extra pressure force on the lower streamline must be subtracted because it does not actually act on the vehicle. Additive drag is bookkept in the force accounting expressions for the forebody and the ramps.

$$F_{ADD} = \int_{streamtube} (P - P_\infty)\, dS \qquad (3)$$

The off-reference correction on an aerodynamic surface are expressed as

$$\Delta\Im = \Im_{OPERATING} - \Im_{REFERENCE} \qquad (4)$$

where $\Im_{REFERENCE}$ is evaluated at the ARC's and $\Im_{OPERATING}$ is evaluated at the actual analysis conditions.

Other terms involving airflow allowances taken from or added to the main propulsive streamtube (inlet boundary layer bleed or blowing, environmental control system, leakage, engine cooling, etc.) are usually determined using the control volume approach. Since all possible situations cannot be anticipated here, a single term, $F_{ALLOWANCE}$, is added to each expression as a place holder. In an actual application, the individual forces associated with these allowances will need to be bookkept.

The net propulsive force equations for each API family are shown in Figures A2 through A5. The following trends can be observed: 1) as the EAI boundaries move closer to the engine, the additive drag terms are replaced by surface pressure and shear integrals, 2) when the EAI boundaries encompass surfaces which are charged to aerodynamics, then a double bookkeeping correction must be applied to remove the aerodynamic forces from the net propulsion force, and 3) as more of the vehicle is charged to aerodynamics, the more off-reference corrections are required.

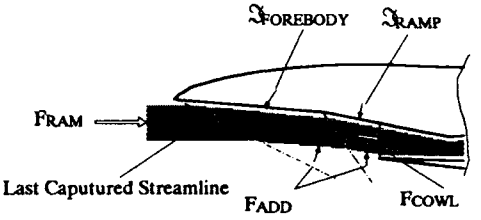

$$F_{COWL} - F_{RAM} = F_{ADD} - \Im_{FOREBODY} - \Im_{RAMP}$$

$$\Im_{FOREBODY} + \Im_{RAMP} = F_{RAM} - F_{COWL} + F_{ADD}$$

$\therefore$ surface force = Δstreamthrust + additive drag

Figure A1. Additive Drag Schematic

TABLE OF F_{NP} FORCE EQUATIONS FOR FAMILY A
FREESTREAM TO NOZZLE EXIT

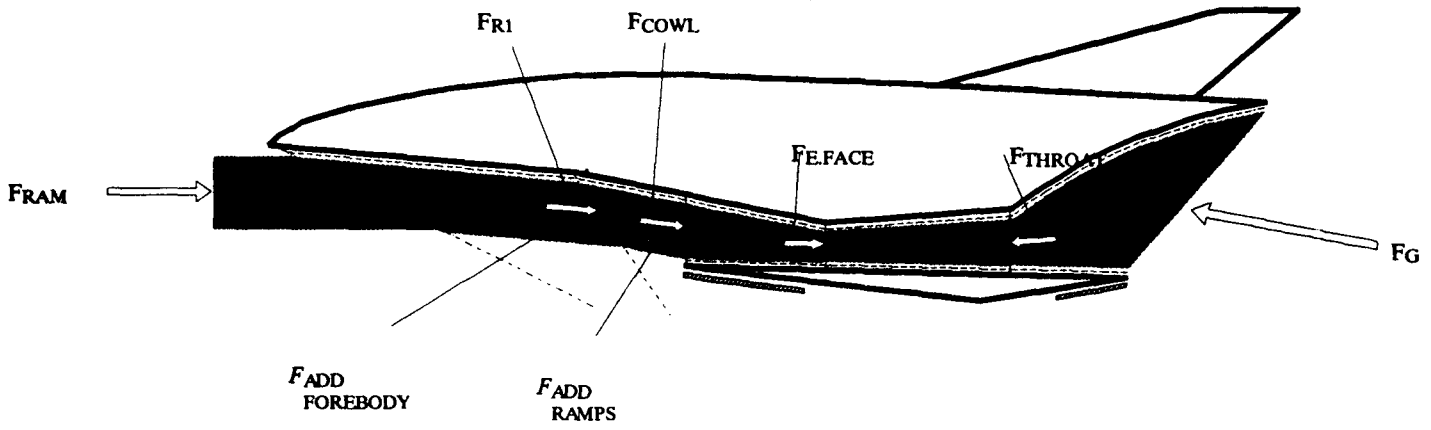

Momentum Interface Upstream/ Downstream	Option		Engine Co. Contribution	Inlet/Nozzle Surface Pressure and Shear	Additive Drag	Off-Reference Aero Corrections: All Speeds	Off-Reference Aero Corrections: Subsonic	Double Bookkeeping Correction
Freestream/ Nozzle Exit	1,1	F_{NP} =	$F_G - F_{RAM}$		$-F_{ADD\ FOREBODY} - \sum_{1}^{N} F_{ADD\ RAMPS}$	$-\Delta\mathfrak{I}_{INLET\ COWL} + \Delta\mathfrak{I}_{NOZZLE\ COWL}$		
Freestream/ Nozzle Throat	1,2	F_{NP} =	$F_{THROAT} - F_{RAM}$	$+\mathfrak{I}_{NOZZLE}$	$-F_{ADD\ FOREBODY} - \sum_{1}^{N} F_{ADD\ RAMPS}$	$-\Delta\mathfrak{I}_{INLET\ COWL} + \Delta\mathfrak{I}_{NOZZLE\ COWL}$		
First Ramp/ Nozzle Exit	2,1	F_{NP} =	$F_G - F_{R1}$	$-\mathfrak{I}_{FOREBODY}$	$-\sum_{1}^{N} F_{ADD\ RAMPS}$	$-\Delta\mathfrak{I}_{INLET\ COWL} + \Delta\mathfrak{I}_{NOZZLE\ COWL}$		
First Ramp/ Nozzle Throat	2,2	F_{NP} =	$F_{THROAT} - F_{R1}$	$-\mathfrak{I}_{FOREBODY} + \mathfrak{I}_{NOZZLE}$	$-\sum_{1}^{N} F_{ADD\ RAMPS}$	$-\Delta\mathfrak{I}_{INLET\ COWL} + \Delta\mathfrak{I}_{NOZZLE\ CQWL}$		
Inlet Cowl/ Nozzle Exit	3,1	F_{NP} =	$F_G - F_{COWL}$	$-\mathfrak{I}_{FOREBODY} - \sum_{1}^{N} \mathfrak{I}_{RAMPS}$		$-\Delta\mathfrak{I}_{INLET\ COWL} + \Delta\mathfrak{I}_{NOZZLE\ COWL}$		
Inlet Cowl/ Nozzle Throat	3,2	F_{NP} =	$F_{THROAT} - F_{COWL}$	$-\mathfrak{I}_{FOREBODY} - \sum_{1}^{N} \mathfrak{I}_{RAMPS} + \mathfrak{I}_{NOZZLE}$		$-\Delta\mathfrak{I}_{INLET\ COWL} + \Delta\mathfrak{I}_{NOZZLE\ COWL}$		
Engine Face/ Nozzle Exit	4,1	F_{NP} =	$F_G - F_{E.FACE}$	$-\mathfrak{I}_{FOREBODY} - \mathfrak{I}_{INLET} - \sum_{1}^{N} \mathfrak{I}_{RAMPS}$		$-\Delta\mathfrak{I}_{INLET\ COWL} + \Delta\mathfrak{I}_{NOZZLE\ COWL}$		
Engine Face/ Nozzle Throat	4,2	F_{NP} =	$F_{THROAT} - F_{E.FACE}$	$-\mathfrak{I}_{FOREBODY} - \mathfrak{I}_{INLET} - \sum_{1}^{N} \mathfrak{I}_{RAMPS} + \mathfrak{I}_{NOZZLE}$		$-\Delta\mathfrak{I}_{INLET\ COWL} + \Delta\mathfrak{I}_{NOZZLE\ COWL}$		

Figure A2. API Family A Net Propulsive Force Equations

TABLE OF F_{NP} FORCE EQUATIONS FOR FAMILY B
FIRST INLET RAMP TO NOZZLE EXIT

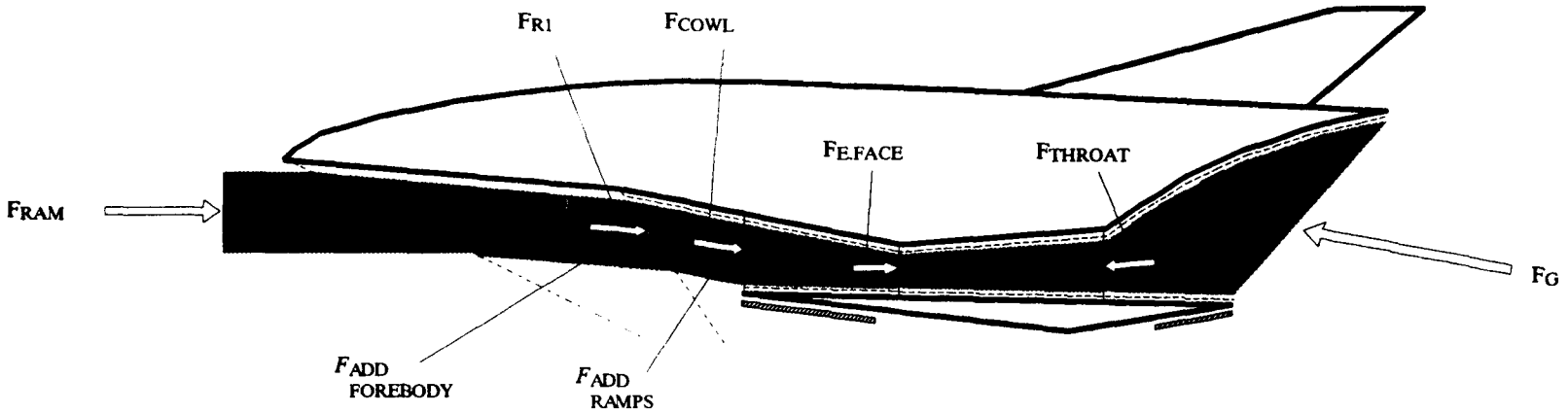

Momentum Interface Upstream/ Downstream	Option		Engine Co. Contribution	Inlet/Nozzle Surface Pressure and Shear	Additive Drag	Off-Reference Aero Corrections		Double Bookkeeping Correction
						All Speeds	Subsonic	
Freestream/ Nozzle Exit	1,1	F_{NP} =	$F_G - F_{RAM}$		$-F_{ADD\ FOREBODY} - \sum_1^N F_{ADD\ RAMPS}$	$-\Delta\mathfrak{I}_{INLET\ COWL} + \Delta\mathfrak{I}_{NOZZLE\ COWL}$	$-\Delta\mathfrak{I}_{FOREBODY}$	$+\mathfrak{I}_{FOREBODY}$
Freestream/ Nozzle Throat	1,2	F_{NP} =	$F_{THROAT} - F_{RAM}$	$+\mathfrak{I}_{NOZZLE}$	$-F_{ADD\ FOREBODY} - \sum_1^N F_{ADD\ RAMPS}$	$-\Delta\mathfrak{I}_{INLET\ COWL} + \Delta\mathfrak{I}_{NOZZLE\ COWL}$	$-\Delta\mathfrak{I}_{FOREBODY}$	$+\mathfrak{I}_{FOREBODY}$
First Ramp/ Nozzle Exit	2,1	F_{NP} =	$F_G - F_{R1}$		$-\sum_1^N F_{ADD\ RAMPS}$	$-\Delta\mathfrak{I}_{INLET\ COWL} + \Delta\mathfrak{I}_{NOZZLE\ COWL}$	$-\Delta\mathfrak{I}_{FOREBODY}$	
First Ramp/ Nozzle Throat	2,2	F_{NP} =	$F_{THROAT} - F_{R1}$	$+\mathfrak{I}_{NOZZLE}$	$-\sum_1^N F_{ADD\ RAMPS}$	$-\Delta\mathfrak{I}_{INLET\ COWL} + \Delta\mathfrak{I}_{NOZZLE\ COWL}$	$-\Delta\mathfrak{I}_{FOREBODY}$	
Inlet Cowl/ Nozzle Exit	3,1	F_{NP} =	$F_G - F_{COWL}$	$-\sum_1^N \mathfrak{I}_{RAMPS}$		$-\Delta\mathfrak{I}_{INLET\ COWL} + \Delta\mathfrak{I}_{NOZZLE\ COWL}$	$-\Delta\mathfrak{I}_{FOREBODY}$	
Inlet Cowl/ Nozzle Throat	3,2	F_{NP} =	$F_{THROAT} - F_{COWL}$	$-\sum_1^N \mathfrak{I}_{RAMPS} + \mathfrak{I}_{NOZZLE}$		$-\Delta\mathfrak{I}_{INLET\ COWL} + \Delta\mathfrak{I}_{NOZZLE\ COWL}$	$-\Delta\mathfrak{I}_{FOREBODY}$	
Engine Face/ Nozzle Exit	4,1	F_{NP} =	$F_G - F_{E.FACE}$	$-\mathfrak{I}_{INLET} - \sum_1^N \mathfrak{I}_{RAMPS}$		$-\Delta\mathfrak{I}_{INLET\ COWL} + \Delta\mathfrak{I}_{NOZZLE\ COWL}$	$-\Delta\mathfrak{I}_{FOREBODY}$	
Engine Face/ Nozzle Throat	4,2	F_{NP} =	$F_{THROAT} - F_{E.FACE}$	$-\mathfrak{I}_{INLET} - \sum_1^N \mathfrak{I}_{RAMPS} + \mathfrak{I}_{NOZZLE}$		$-\Delta\mathfrak{I}_{INLET\ COWL} + \Delta\mathfrak{I}_{NOZZLE\ COWL}$	$-\Delta\mathfrak{I}_{FOREBODY}$	

Figure A3. API Family B Net Propulsive Force Equations

TABLE OF F_{NP} FORCE EQUATIONS FOR FAMILY C
ENGINE FACE TO NOZZLE EXIT

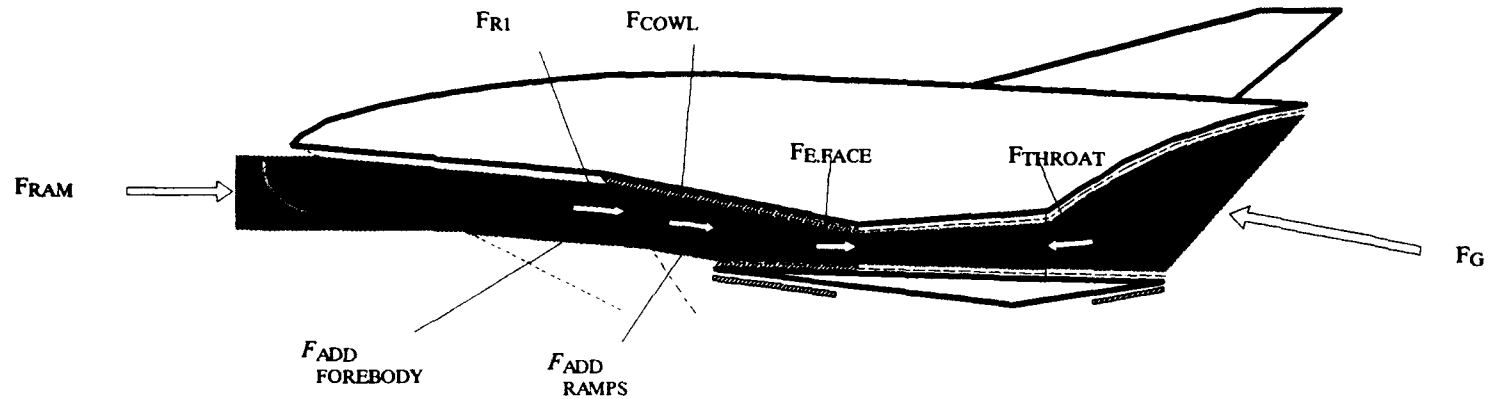

Momentum Interface Upstream/ Downstream	Option		Engine Co. Contribution	Inlet/Nozzle Surface Pressure and Shear	Additive Drag	Off-Reference Aero Corrections: All Speeds	Off-Reference Aero Corrections: Subsonic	Double Bookkeeping Correction
Freestream/ Nozzle Exit	1,1	F_{NP} =	$F_G - F_{RAM}$		$-F_{ADD\ FOREBODY} - \sum_{1}^{N} F_{ADD\ RAMPS}$	$-\Delta\mathfrak{I}_{INLET\ COWL} + \Delta\mathfrak{I}_{NOZZLE\ COWL} - \Delta\mathfrak{I}_{VAR.RAMP\ \&INLET}$*	$-\Delta\mathfrak{I}_{FOREBODY} - \Delta\mathfrak{I}_{FIXED\ RAMPS}$	$+\mathfrak{I}_{FOREBODY} + \sum_{1}^{N} \mathfrak{I}_{RAMPS} + \mathfrak{I}_{INLET}$
Freestream/ Nozzle Throat	1,2	F_{NP} =	$F_{THROAT} - F_{RAM}$	$+\mathfrak{I}_{NOZZLE}$	$-F_{ADD\ FOREBODY} - \sum_{1}^{N} F_{ADD\ RAMPS}$	$-\Delta\mathfrak{I}_{INLET\ COWL} + \Delta\mathfrak{I}_{NOZZLE\ COWL} - \Delta\mathfrak{I}_{VAR.RAMP\ \&INLET}$*	$-\Delta\mathfrak{I}_{FOREBODY} - \Delta\mathfrak{I}_{FIXED\ RAMPS}$	$+\mathfrak{I}_{FOREBODY} + \sum_{1}^{N} \mathfrak{I}_{RAMPS} + \mathfrak{I}_{INLET}$
First Ramp/ Nozzle Exit	2,1	F_{NP} =	$F_G - F_{R1}$		$-\sum_{1}^{N} F_{ADD\ RAMPS}$	$-\Delta\mathfrak{I}_{INLET\ COWL} + \Delta\mathfrak{I}_{NOZZLE\ COWL} - \Delta\mathfrak{I}_{VAR.RAMP\ \&INLET}$*	$-\Delta\mathfrak{I}_{FOREBODY} - \Delta\mathfrak{I}_{FIXED\ RAMPS}$	$+\sum_{1}^{N} \mathfrak{I}_{RAMPS} + \mathfrak{I}_{INLET}$
First Ramp/ Nozzle Throat	2,2	F_{NP} =	$F_{THROAT} - F_{R1}$	$+\mathfrak{I}_{NOZZLE}$	$-\sum_{1}^{N} F_{ADD\ RAMPS}$	$-\Delta\mathfrak{I}_{INLET\ COWL} + \Delta\mathfrak{I}_{NOZZLE\ COWL} - \Delta\mathfrak{I}_{VAR.RAMP\ \&INLET}$*	$-\Delta\mathfrak{I}_{FOREBODY} - \Delta\mathfrak{I}_{FIXED\ RAMPS}$	$+\sum_{1}^{N} \mathfrak{I}_{RAMPS} + \mathfrak{I}_{INLET}$
Inlet Cowl/ Nozzle Exit	3,1	F_{NP} =	$F_G - F_{COWL}$			$-\Delta\mathfrak{I}_{INLET\ COWL} + \Delta\mathfrak{I}_{NOZZLE\ COWL} - \Delta\mathfrak{I}_{VAR.RAMP\ \&INLET}$*	$-\Delta\mathfrak{I}_{FOREBODY} - \Delta\mathfrak{I}_{FIXED\ RAMPS}$	$+\mathfrak{I}_{INLET}$
Inlet Cowl/ Nozzle Throat	3,2	F_{NP} =	$F_{THROAT} - F_{COWL}$	$+\mathfrak{I}_{NOZZLE}$		$-\Delta\mathfrak{I}_{INLET\ COWL} + \Delta\mathfrak{I}_{NOZZLE\ COWL} - \Delta\mathfrak{I}_{VAR.RAMP\ \&INLET}$*	$-\Delta\mathfrak{I}_{FOREBODY} - \Delta\mathfrak{I}_{FIXED\ RAMPS}$	$+\mathfrak{I}_{INLET}$
Engine Face/ Nozzle Exit	4,1	F_{NP} =	$F_G - F_{E.FACE}$			$-\Delta\mathfrak{I}_{INLET\ COWL} + \Delta\mathfrak{I}_{NOZZLE\ COWL} - \Delta\mathfrak{I}_{VAR.RAMP\ \&INLET}$*	$-\Delta\mathfrak{I}_{FOREBODY} - \Delta\mathfrak{I}_{FIXED\ RAMPS}$	
Engine Face/ Nozzle Throat	4,2	F_{NP} =	$F_{THROAT} - F_{E.FACE}$	$+\mathfrak{I}_{NOZZLE}$		$-\Delta\mathfrak{I}_{INLET\ COWL} + \Delta\mathfrak{I}_{NOZZLE\ COWL} - \Delta\mathfrak{I}_{VAR.RAMP\ \&INLET}$*	$-\Delta\mathfrak{I}_{FOREBODY} - \Delta\mathfrak{I}_{FIXED\ RAMPS}$	

* Includes both external variable ramp and internal inlet corrections.

Figure A4. API Family C Net Propulsive Force Equations

TABLE OF F_{NP} FORCE EQUATIONS FOR FAMILY D
INLET COWL TO NOZZLE EXIT

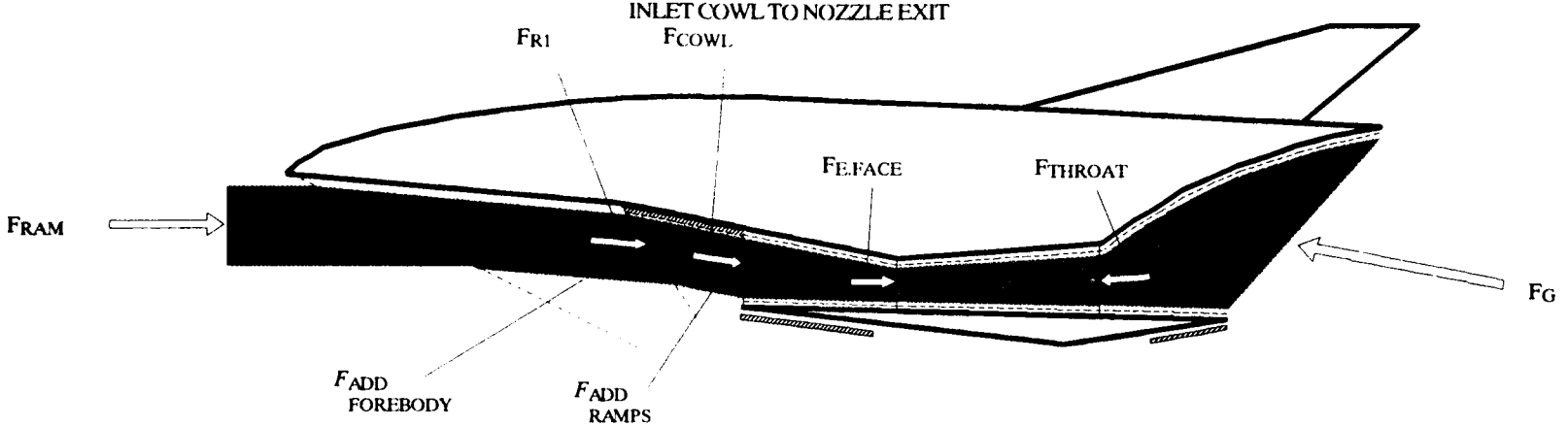

Momentum Interface Upstream/ Downstream	Option		Engine Co. Contribution	Inlet/Nozzle Surface Pressure and Shear	Additive Drag	Off-Reference Aero Corrections All Speeds	Off-Reference Aero Corrections Subsonic	Double Bookkeeping Correction
Freestream/ Nozzle Exit	1,1	F_{NP} =	$F_G - F_{RAM}$		$-F_{ADD\ FOREBODY} - \sum_{1}^{N} F_{ADD\ RAMPS}$	$-\Delta\mathfrak{I}_{INLET\ COWL} + \Delta\mathfrak{I}_{NOZZLE\ COWL} - \Delta\mathfrak{I}_{VAR.\ RAMPS}$*	$-\Delta\mathfrak{I}_{FOREBODY} - \Delta\mathfrak{I}_{FIXED\ RAMPS}$	$+\mathfrak{I}_{FOREBODY} + \sum_{1}^{N} \mathfrak{I}_{RAMPS}$
Freestream/ Nozzle Throat	1,2	F_{NP} =	$F_{THROAT} - F_{RAM}$	$+\mathfrak{I}_{NOZZLE}$	$-F_{ADD\ FOREBODY} - \sum_{1}^{N} F_{ADD\ RAMPS}$	$-\Delta\mathfrak{I}_{INLET\ COWL} + \Delta\mathfrak{I}_{NOZZLE\ COWL} - \Delta\mathfrak{I}_{VAR.\ RAMPS}$*	$-\Delta\mathfrak{I}_{FOREBODY} - \Delta\mathfrak{I}_{FIXED\ RAMPS}$	$+\mathfrak{I}_{FOREBODY} + \sum_{1}^{N} \mathfrak{I}_{RAMPS}$
First Ramp/ Nozzle Exit	2,1	F_{NP} =	$F_G - F_{R1}$		$-\sum_{1}^{N} F_{ADD\ RAMPS}$	$-\Delta\mathfrak{I}_{INLET\ COWL} + \Delta\mathfrak{I}_{NOZZLE\ COWL} - \Delta\mathfrak{I}_{VAR.\ RAMPS}$*	$-\Delta\mathfrak{I}_{FOREBODY} - \Delta\mathfrak{I}_{FIXED\ RAMPS}$	$+\sum_{1}^{N} \mathfrak{I}_{RAMPS}$
First Ramp/ Nozzle Throat	2,2	F_{NP} =	$F_{THROAT} - F_{R1}$	$+\mathfrak{I}_{NOZZLE}$	$-\sum_{1}^{N} F_{ADD\ RAMPS}$	$-\Delta\mathfrak{I}_{INLET\ COWL} + \Delta\mathfrak{I}_{NOZZLE\ COWL} - \Delta\mathfrak{I}_{VAR.\ RAMPS}$*	$-\Delta\mathfrak{I}_{FOREBODY} - \Delta\mathfrak{I}_{FIXED\ RAMPS}$	$+\sum_{1}^{N} \mathfrak{I}_{RAMPS}$
Inlet Cowl/ Nozzle Exit	3,1	F_{NP} =	$F_G - F_{COWL}$			$-\Delta\mathfrak{I}_{INLET\ COWL} + \Delta\mathfrak{I}_{NOZZLE\ COWL} - \Delta\mathfrak{I}_{VAR.\ RAMPS}$*	$-\Delta\mathfrak{I}_{FOREBODY} - \Delta\mathfrak{I}_{FIXED\ RAMPS}$	
Inlet Cowl/ Nozzle Throat	3,2	F_{NP} =	$F_{THROAT} - F_{COWL}$	$+\mathfrak{I}_{NOZZLE}$		$-\Delta\mathfrak{I}_{INLET\ COWL} + \Delta\mathfrak{I}_{NOZZLE\ COWL} - \Delta\mathfrak{I}_{VAR.\ RAMPS}$*	$-\Delta\mathfrak{I}_{FOREBODY} - \Delta\mathfrak{I}_{FIXED\ RAMPS}$	
Engine Face/ Nozzle Exit	4,1	F_{NP} =	$F_G - F_{E.FACE}$	$-\mathfrak{I}_{INLET}$		$-\Delta\mathfrak{I}_{INLET\ COWL} + \Delta\mathfrak{I}_{NOZZLE\ COWL} - \Delta\mathfrak{I}_{VAR.\ RAMPS}$*	$-\Delta\mathfrak{I}_{FOREBODY} - \Delta\mathfrak{I}_{FIXED\ RAMPS}$	
Engine Face/ Nozzle Throat	4,2	F_{NP} =	$F_{THROAT} - F_{E.FACE}$	$-\mathfrak{I}_{INLET} + \mathfrak{I}_{NOZZLE}$		$-\Delta\mathfrak{I}_{INLET\ COWL} + \Delta\mathfrak{I}_{NOZZLE\ COWL} - \Delta\mathfrak{I}_{VAR.\ RAMPS}$*	$-\Delta\mathfrak{I}_{FOREBODY} - \Delta\mathfrak{I}_{FIXED\ RAMPS}$	

* Includes only external portion of variable ramp corrections.

Figure A5. API Family D Net Propulsive Force Equations

Integration of Turbo - Ramjet Engines for Hypersonic Aircraft

O. Herrmann

Manager Propulsion Integration
Deutsche Aerospace
Messerschmitt-Bölkow-Blohm GmbH
P. O. Box 801160
D-8000 München 80

Summary:

The integration of turbo-ramjet engines for hypersonic transport vehicles operating in the Mach 0 to 6+ regime represents one of the most important development tasks. This paper presents a survey over the variety of interacting problem areas and faculties, which have to be integrated to lead to an optimized propulsion/airframe system.

The influence of the forebody flowfield on airframe and propulsion system is adressed. The precompression increases the net thrust at high speeds considerably and reduces inlet/engine airflow mismatch. On the other hand relevant forebody design may change aerodynamic and structural characteristics to the worse.

The severe demands to the nozzle, leading to the selection of the single ramp type with a large nozzle exit area are discussed. During transonic flight the nozzle runs far off-design, producing high forces in the downward direction resulting in strong nose up moments. Some methods to improve this situation by the use of bypass and boundary layer flows are proposed. Calculations of nozzle/aftbody flows show extreme variations in gross-thrust vector angle and position, leading to a considerable influence on aircraft trim and stability. These effects are compared to the moment characteristics of the airframe itself.

Both examples show the demand for intense collaboration between engine and airframe engineers to design an optimized vehicle.

1. Introduction

A successful propulsion system integration is often designated as one of the keys to hypersonic aircraft. Integrating airbreathing propulsion systems into vehicles like the lower stage of the Sänger leads to a manifold scope of tasks which due to forebody-precompression, unsymmetrical variable intakes and thrust-nozzles exceed the usual engine installation of subsonic aircraft by far and which demands an intense harmonization between engine and airframe companies / 1 /. Within this paper some of the items, shown in figure 1-1 , as forebody flow and precompression, fuselage nozzle extension being in context with base drag reduction and thrust vector definition and control are adressed.

Combined-cycle turbo ramjet propulsion systems for application in hypersonic air vehicles have to be operated efficiently from take-off up to the maximum required flight Mach number, which may exceed Mach 6, and - what should not be overlooked - again during deceleration, slowing down to landing.

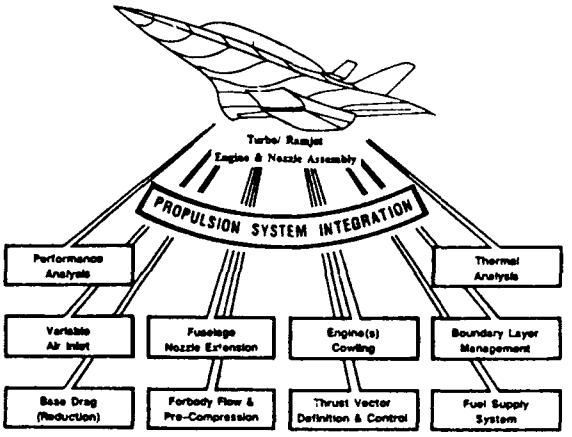

Fig. 1-1 Propulsion Integration Tasks

Whereas aircraft with maximum Mach number below 4 tend to be optimized with podded propulsion systems (SST), for the higher Mach numbers, as discussed here, highly integrated propulsion/airframe-systems are considered to be advantageous. As pointed out in fig. 1-2, the forebody of the aircraft is used to compress the airflow in front of the intake and thus - increasing the mass flow density - raises or even multiplies the thrust of the propulsion system at hypersonic speeds. So the bottom side of the forebody may be treated as a part of the airframe as well as a part of the propulsion system.

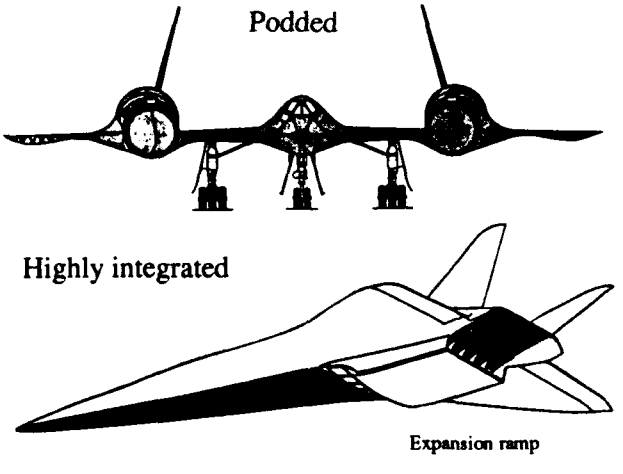

Fig. 1-2 Propulsion Integration Concepts

High Mach operation and fuel efficient acceleration to this final Mach number requires ultimate exhaust system performance due to the high sensitivity factor between gross thrust and net-thrust-minus-drag. To minimize underexpansion losses large nozzle exit areas are indispensable, which may be materialized as an integral part of the airplane to reduce the weight of the exhaust system. For instance the lower side of the airframe-afterbody may build the single expansion ramp for the exhaust gases (fig. 1-2). On the other hand these large nozzles have to be operated far off-design at low flight Mach numbers, leading to undesired internal and/or external losses due to overexpansion, unfavorable afterbody angles and flow-detachment at base areas.

Both, the forebody and nozzle/aftbody are picked out as examples to illustrate the variety of interacting problem areas and faculties, which have to be integrated to lead to an optimized propulsion/airframe system.

2. First Example: Forebody-Development.

Looking at highly integrated propulsion systems with intakes located below the fuselage (belly type), there are many different mechanisms, how the bottom side of the fuselage influences the intake flow while the intake itself influences the flow around the engine cowl, parts of the fuselage and wings or fins. These interactions between airframe and propulsion system generally are designated as propulsion integration tasks.

This first example deals exclusively with forebody effects *on* airframe and propulsion system.

The busy figure 2-1 indicates some of the influence paths of the forebody bottom side shaping, starting with the tip of the aircraft and ending in our case at the first ramp of the intake. The influences to the fuselage are aero-thermodynamic and structural ones.

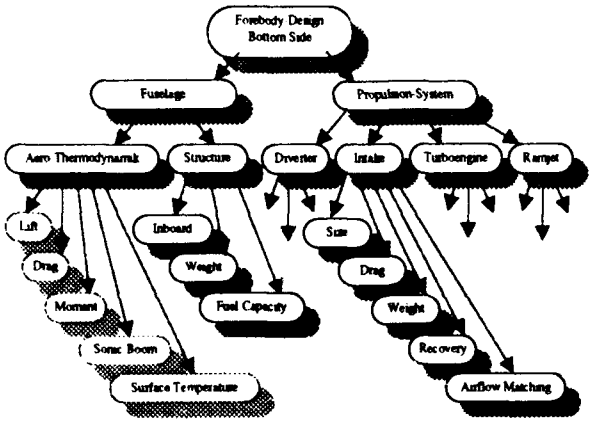

Fig. 2-1 Influence Paths of Forebody Design

Changing the design of the forebody alters lift-, drag- and moment coefficients and derivatives, surface temperatures (values and distribution) and sonic boom generation. Structural aspects are weight, inboard configuration and fuel capacity.
The propulsion system is influenced with very complex connections by the flow field generated by the fore-body. It is of effect on thrust, fuel consumption and weight of turbo and ramjet engines via intake and boundary layer diverter system.

In addition recovery, drag, size and weight of the intake and boundary layer diverter system itself are strongly influenced by the entering flow field. Some of these propulsion related features are explained in the following.

At supersonic and even more at hypersonic speeds the shock system at the forebody compresses the flow in front of the intake. This effect designated as *precompression* causes an increased air flow density and so increased captured mass flow. The ratio of mass flow densities is often expressed by the area of the entering stream tube in freestream devided by the area at the intake entry plain (A_∞ / A_0).

Fig. 2-2 shows these area ratios /2/ as created by a flat plate with incidence (left hand side) and of a typical Sänger-like forebody bottom side, calculated with Euler-methods at MBB /3/. The precompression ratio is strongly increased by freestream Mach number and aircraft incidence.

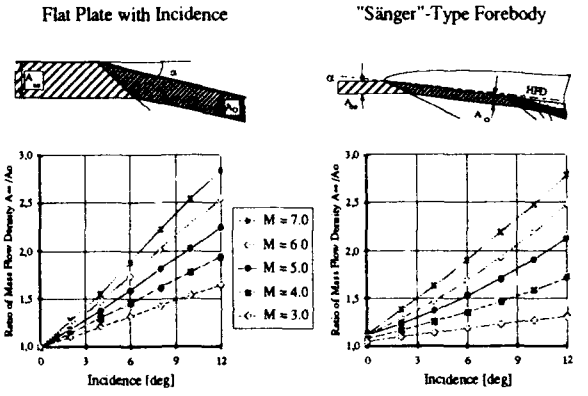

Fig. 2-2 Precompression of Forebody Bottom Side

One of the aims of forebody design is to produce an evenly precompressed flow field at the intake capture plain. Fig. 2-3 presents the results of an Euler-calculation (method Dr. Weiland, MBB) with isolines of Mach number and mass flow density factors (A_∞ / A_0) with the contour of the capture area sketched /3/.

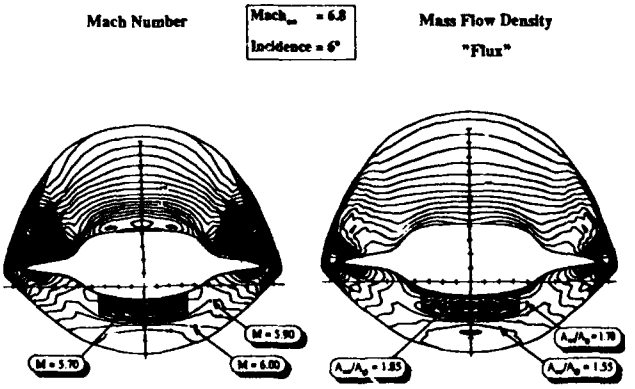

Fig. 2-3 Mach Number and Mass Flow Density at Intake Entry Plane

The effect of precompression on net thrust is shown in fig. 2-4 for a *constant* intake capture area. It is obvious, that during ramjet operation at high speeds, where the massflow is not limited by the ramjet burner or nozzle throat area, the thrust increases proportionally to the airflow (compare fig. 2-3). So this effect is very valuable to increase the accelerating force (thrust-minus-drag) at ultimate speeds, attainable with subsonically burning ramjets.

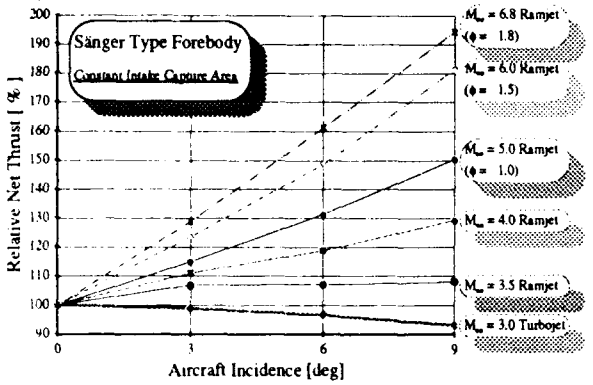

Fig. 2-4 Precompression Effect on Net Thrust of Turbo-Ramjet Engines

During turbo operation, precompression may help to reduce the inlet/engine airflow mismatch, since precompression is very low during transonic and low supersonic speeds, when the engine can only swallow a part of the intake flow, but is remarkably increased at maximum turbo engine flight Mach numbers, where the engine needs all the intake flow capacity /5/. So enhanced precompression will improve ramjet and turbo engine performance, but on the other hand may change aerodynamic, longitudinal moment characteristic, structural constraints a.s.o. to the worse.

Taking all the various effects into account, the determination of a suitable rate of precompression at relevant aircraft incidence during the ascent trajectory is one of the important trade-offs to be carried out iteratively by the design team during the aircraft development.

3. Second Example: Nozzle/Aftbody Integration

As a further example for the mutual influences of airframe and propulsion systems, some aspects of nozzle/-aftbody integration and the complex interaction of the propulsion group with different airframe faculties as aircraft aerodynamics and weights, flight performance and mechanics is addressed.

References /4/ to /11/ demonstrate the extreme scope of demands to exhaust systems of hypersonic turbo ramjet engines as to nozzle pressure ratios, ranging from about 2 to more than 500 and resulting nozzle throat and exit areas, both variing from 1 to 6 between minimum and maximum required size.

Fig. 3-1 illustrates the basic nozzle types, which were taken into consideration for the turbo-ramjet engines in our hypersonic aircraft studies.

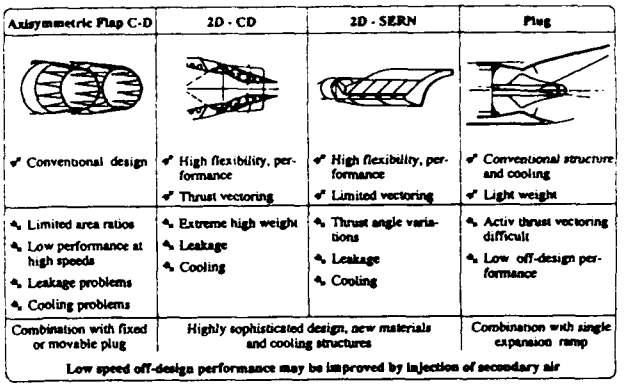

Fig. 3.1 Basic Nozzle Types Taken into Consideration

a) Axisymmetric flap C-D nozzle

From a practical standpoint, the minimum to maximum variation of nozzle throat or exit areas is limited to approximately 3.6, which is due to limits on flap and seal arrangements /8/. This limitation would lead to low performance at high flight Mach numbers, so preventing the use of this type for the hypersonic application.
A combination of axisymmetic flaps with a fixed or even movable plug leads to designs with better flexibility in area variation /5/. Cooling and leakage of flaps and seals in the high pressure region of the nozzle is characterized as critical.

b) Two-dimensional convergent-divergent (four flap) nozzle (2D-CD)

This nozzle type is analysed in detail in /7/ and /9/. It combines a good flexibility in area ratios, leading to high overall performance with the possibility of active thrust vectoring. Yet, the weight of the exhaust system, which may be twice as heavy as the engine itself is unacceptable, particularly at the rear section of the aircraft.

c) Two dimensional single expansion ramp nozzle (2D-SERN)

The variation of the throat area can be performed by relatively small flaps either only at one side (top or bottom) or at both sides. This nozzle shows a certain self-adaptibility at off-design conditions, so reducing the need to vary the exit area. Thus, the divergent part of the expansion system is partly shaped by the (fixed geometry) aircraft fuselage itself. Nearly the same high performance shown by the 2D-CD nozzle may be attained with only part of its weight.
For both, the 2D-CD and the 2D-SERN problems with mechanical integritv, leakage and cooling are expected, which implies highly sophisticated designs, combined with new materials and structures.

d) Plug nozzle (axisymmetric and in combination with SERN)

This type of nozzle may be built with proven structures and cooling provisions (rocket technology) and allows a light weight exhaust system. Since the exit area of the axisymetric design is constant, very poor performance at off-design points is shown, which may be slightly improved by combining the plug nozzle with a single

expansion ramp. Anyway, this would lead to unacceptable thrust losses during subsonic and low supersonic flight. As shown in the context, the performance of all nozzle types can be improved for the low speed areas by introducing ejector flows. This means may be especially effective to improve the plug nozzle performance.

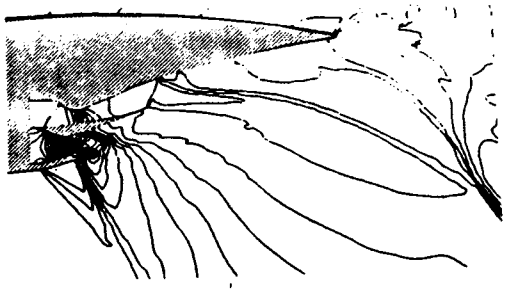

2-Flow-Configuration, Pressures at Ma_∞=1.2

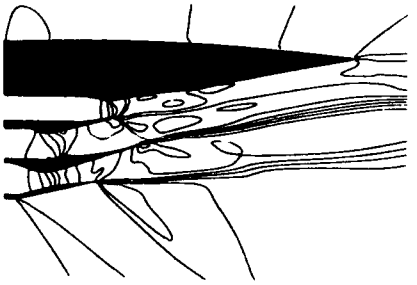

3-Flow-Configuration, Mach-No.s at Ma_∞=1.2

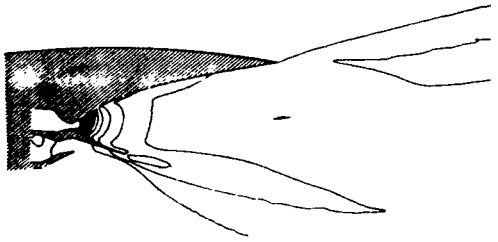

Ramjet Operation, Pressures at Ma_∞=6.8

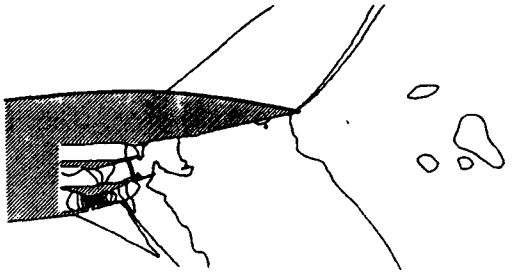

3-Flow-Configuration, Pressures at Ma_∞=1.2

Fig. 3-2 Previous Nozzle/Aftbody CFD-Calculations for Over-and-Under Configurations

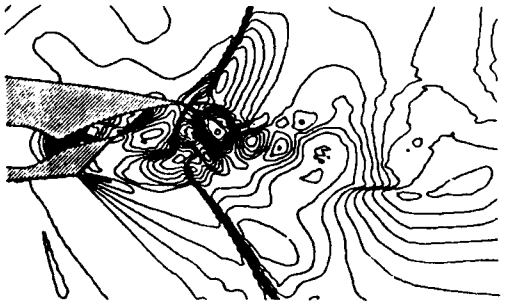

MTU-Configuration, Pressures at Ma_∞=1.2

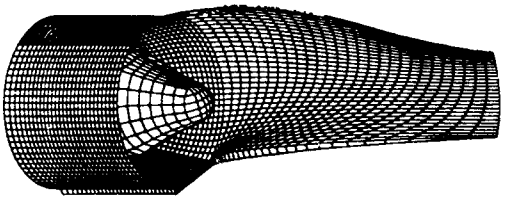

Plug-Configuration, 3-D Grid Lines

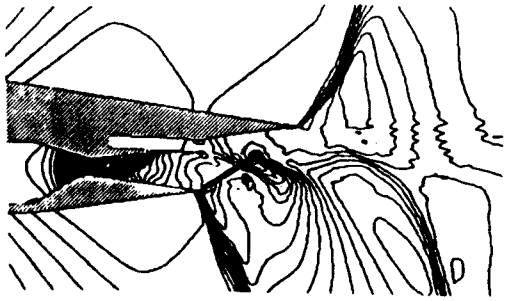

Alternate Configuration, Pressures at Ma_∞=1.2

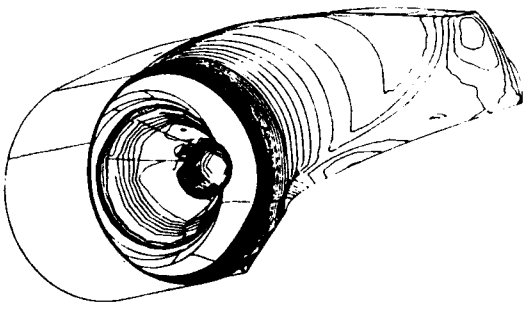

Plug-Configuration, Pressures at Ma_∞=5.6

Fig. 3-3 MBB-EUFLEX-Calculations for Current Coaxial-Tandem Configurations

In the present studies we concentrate on two basic nozzle types, the

* 2D-SERN

and * Plug-SERN,

both improved by injection of the forebody boundary layer flow into the nozzle (ejector) during turbo engine operation. Figures 3-2 and 3-3 illustrate a choice of CFD-calculations (Euler) for some designs of hypersonic nozzle/aftbody systems, investigated at MBB, MTU and LFA (Lehrstuhl für Flugantriebe, Technische Universität München) /12-15/.

During previous investigations we found that the nozzle/aftbody performance could be strongly improved during transonic flight by heating of the forebody boundary layer flow before injection or even more by simultaneous operation of turbo and ramjet engines, feasible with wrap-around or under-and-over configurations. Those systems may - in addition - be a potential solution to the inlet-engine airflow mismatch /8/.
Fig. 3-2 indicates that such 2- or 3-flow nozzles represent very complex configurations. Optimization of design and control, to prevent flow instabilities and to allow maximum thrust-minus-drag and advantageous thrust angle would be a challenge.

Fig. 3-3 shows current configurations being under consideration for the present coaxial tandem arrangement. In general, the 2-D-SERN and Plug-SERN nozzle produce the same two problems, pointed out in figure 3-4:

First, the absolute size of the nozzle exit area required for the high flight Mach numbers to avoid underexpansion losses, and secondly the extreme variability needed for the adaptation to (far) off-design conditions at subsonic and low supersonic flight regimes to avoid detrimental overexpansion losses and flow-detachment effects.

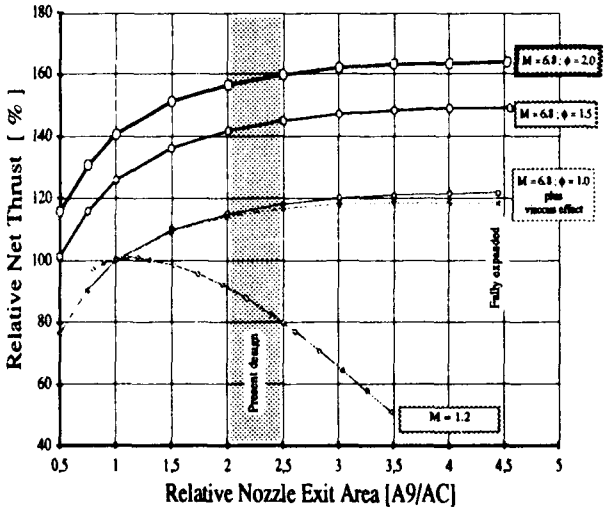

Fig. 3-4 Effect of Nozzle Exit Area on Net Thrust

Here the relative net thrust versus nozzle exit area for a transonic (Ma = 1.2) and a hypersonic flight Mach number (Ma = 6.8) is plotted. The data were approximated for a 2-D-SERN system /11/.

For the high speed case, where different fuel/air ratios are shown (Φ = 1 is stochiometric) the thrust is improved for increased nozzle exit areas (A_9), but levels off for A_9/A_C of about 3 (A_C = intake capture area), when viscous effects are taken into account. This number again is dependent on the level of forebody precompression, which is achieved for the relevant high speed case (compare chapter 3).

The low speed case shows just the opposite trend, despite injection of the total forebody boundary layer flow, diverted in front of the intake. Configurations and performance of 2D-SERN-ejector nozzles are demonstrated in various references /5,8,11/.

Since the low speed (transonic) case is as well thrust-minus-drag critical as the hypersonic case, the optimization of the effective nozzle exit area represents one of the important trade-offs. Considering the effects of nozzle exit area not only on the internal performance but also to external drag, thrust vector direction and longitudinal moments, nozzle weight and cooling requirements, this task becomes even more difficult. The fact, that the effects proved quite different for various nozzle/aftbody and airframe configurations makes the results of studies only partly transferable.

A further integration aspect is caused by the unsymmetry of the SERN configurations. The gross thrust vector is neither in line with the engine nor with the nozzle axis, but will vary with configuration and nozzle running condition. For a given configuration the position and angle of the gross-thrust vector was found to be dependent on

* nozzle pressure ratio (primary and secondary flow)
* nozzle mass flows (")
* temperature and fuel/air-ratios (")
* flight Mach number
* aircraft incidence

Fig. 3-5 shows the angle σ between gross thrust vector and horizontal fuselage datum (HFD) for three types of SERN-exhaust systems as functions of flight Mach number. All three nozzles have similar exit areas and lengths. The single flow nozzle, a nozzle without injection of secondary air flow shows extreme downward directed forces in the subsonic and lower supersonic flight regime. These are created by the low pressures at the expansion ramp due to strong overexpansion of the jet. The presented data were calculated under the assumption, that flow detachment of the surrounding airflow does not occur. It was shown, that the situation may be improved for single flow nozzles, taking detachments created by base areas into account.

Blowing additional air volume into the far too large nozzle exit at transonic flight speeds raises the pressures at the single ramp and so reduces the downward force respective angle σ.

Simultaneously the gross thrust coefficient is improved significantly. Optimum thrust coefficients and angles were found for the "three flow" configuration with

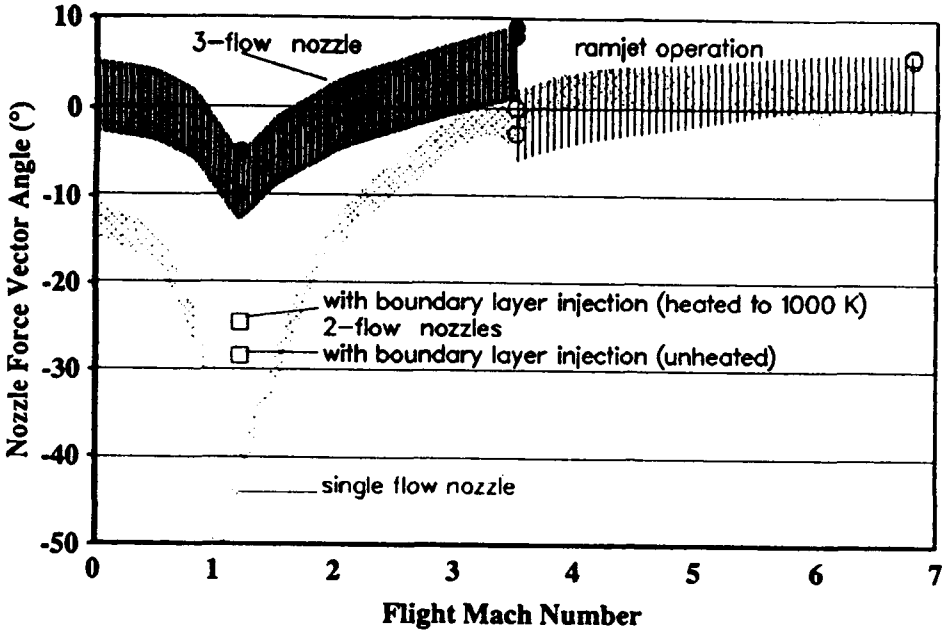

Fig. 3-5 First Results of Euler-Calculations for 2-D-SERN Nozzles: Nozzle Force Vector Angle σ rel. to HFD

simultaneously operated turbo and ramjet engines and ejection of the forebody boundary layer. At hypersonic speed, single flow nozzles with movable flaps at the bottom side as currently proposed for Sänger offer high performance and advantageous small thrust vector angles.

At both, the unsymmetrical intake located away from the centerline and the unsymmetrical exhaust system very large forces work, being in the magnitude of the aircraft weight (at hypersonic speeds). These forces create significant pitching moments to the aircraft system.
Fig. 3-6 illustrates the pitching moment contribution of a relevant propulsion system for the ascent trajectory in aerodynamic measures.

During turbo engine operation in the regime Mach 0 to 2.9 the propulsion created moments of this special configuration are nearly independent on aircraft incidence and show extreme nose up moments at transonic and low supersonic speeds. The propulsion moments contribution is in the same size as the moment coefficients of the airframe itself. Other nozzle configurations without flow detachment showed a stabilizing effect. Increasing the incidence reduced the downward force at the expansion ramp, so reducing the nose up moment of the propulsion system.

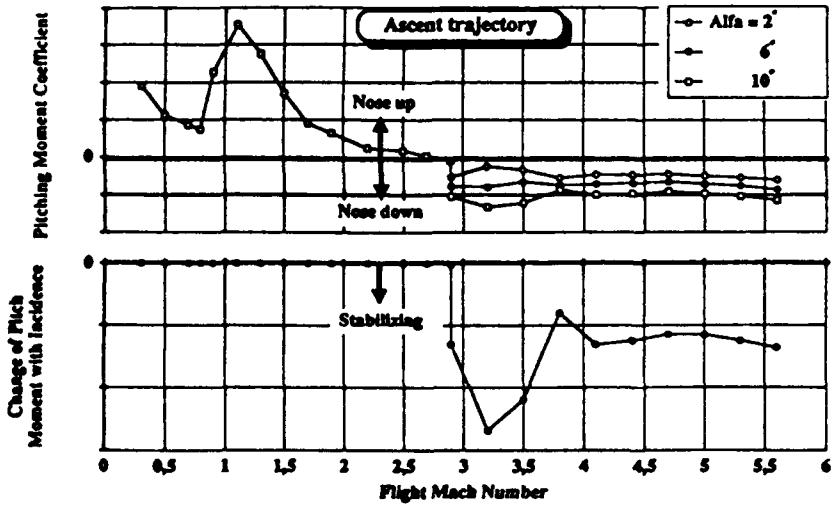

Fig. 3-6 Propulsion Effects on Aircraft Trim and Stability

In the ramjet regime (above Mach 2.9) the propulsion created moments act nose-down. This effect is mainly caused by the high momentum forces of the intake flow, with the intake located below the center of gravity. Since intake forces grow with aircraft incidence (compare chapter 2) as a result of forebody-precompression, the nose down moment of the propulsion system increases.

Another part of the nose down moment is created by the overpressure at the expansion ramp. This again raises with growing incidence, since higher precompression leads to higher mass-flow, nozzle throat area and pressure ratio. These stabilizing effects of the propulsion system are shown in the bottom part of figure 3-6.

It is obvious, that these moments and derivatives have to be taken into account during the design of the airframe configuration, when trim, stability and controlability of the total aircraft system is optimized.

4. Conclusions:

Hypersonic turbo-ramjet propulsion integration studies show:

- The design of the airframe forebody and aftbody has a great effect on the propulsion system performance.
- The design of propulsion system components, as intake and nozzle types, secondary airflow handling and engine characteristics effects not only aircraft performance, but also trim, stability and control characteristics.
- The design of the forebody/intake and of the exhaust nozzle/aftbody systems should be an integral part of the airframe design process.
- The selection of "propulsion" elements, as the adressed fore- and aftbody system cannot be based on component performance alone, but on how well they integrate with the total airplane system /8/.

An overall optimized aircraft system will only beobtained, if airframe and propulsion system are continuously harmonized during design and development. This aim of propulsion integration may be attainable on the premises that aircraft and propulsion engineers join to perform the outstanding trade-offs and to solve the problems together.

Important means in this process are:

- a well defined and appropriate bookkeeping system /16/
- continously arranged meetings and discussions to
- adapt and correct work planning structures and to
- understand the connections of propulsion and airframe system.

5. Acknowledgements

The author would like to gratefully acknowledge the assistance of his colleagues B. Zellner, Dr. A. Eberle, Th. Berens and D.M. Schmitz (DASA-MBB München) and of A. Bauer, R. Heninger and Prof. Dr. H. Rick, Technische Universität München).

6. References:

1. Kuczera, H.; Kleinau, W.: Konzeptuntersuchung und Systemdefinition SÄNGER-Raumtransportsystem. March 1991. Not published.
2. Künkler, H.: Der Einfluß der Luftvorkühlung vor der Verdichtung bei luftatmenden Antrieben eines Raumfahrzeugträgers Dissertation RWTH Aachen, 10.Nov. 1973
3. Schmitz, D.: Hyperschall Technologieprogramm: Berechnung der Vorverdichtung am Sänger-Vorkörper. MBB internal technical note. Not published.
4. Göing, M.;Heyse, J.: 2-D Supersonic Nozzle Design AGARD-CP-479, Hypersonic Combined Cycle Propulsion, Madrid, Spain, 1990
5. Schwab,R.R.: Airbreathing Propulsion Integration. Space Course Aachen, 1991
6. Dusa, D.J.: High Mach Propulsion System Installation and Exhaust System Design Considerations. AIAA-87-2941. St. Louis, Missouri, 1987
7. Dusa, D.J.: Exhaust Nozzle System Design Considerations for Turboramjet Propulsion Systems. ISABE 89-7077, Athens, Greece
8. Dusa, D.J.: Turboramjet Exhaust Nozzle Systems. Tenth International Symposium On Air Breathing Engines, September 1-6, 1991, Nottingham, England
9. Kuchar, A.P.; Wolf, J.P.: Preliminary Assessment of Exhaust Systems for High Mach (4 to 6) Fighter Aircraft. AIAA-89-2356, Monterey, California, 1989
10. Bauer, A.; Rick, H.; Schiebold, H.: Zur Auslegung von Expansionsrampen für Hyperschallflugzeuge mit Hilfe von Charakteristikenverfahren. Interner Bericht LFA- T.U.München, LFA-Ba/Ri/Schi-10.90, 1990
11. Herrmann, O.; Rick, H.: Propulsion Aspects of Hypersonic Turbo-Ramjet-Engines with Special Emphasis on Nozzle/Aftbody Integration. ASME-Paper 91-GT-395. Orlando, Florida, June 3-6, 1991
12. Eberle, A.: MBB-EUFLEX-Nachrechnung einer Rampendüse, 1989. MBB internal technical note. Not published.
13. Heninger, R.: Beeinflussung von Schubvektoren und Beiwerten durch Bypass-Luft in Hyperschall-Kombinationstriebwerken Diplomarbeit, Mai 1991
14. Berens, Th.: Berechnung des Strömungsfeldes einer Rechteckdüse mit Expansionsrampe für Hyperschallflugzeuge bei Ma_∞=1.2 (mit Einblasung der Vorderrumpfgrenzschicht) und Ma_∞=5.6. MBB internal technical note. Not published.
15. Eberle, A.; Schmatz, M.A.; Bissinger, N.C.: Generalized Fluxvectors for Hypersonic Shock-Capturing. AIAA-Paper 90-0390, 1990
16. Lehrach, R.P.C.: Thrust/Drag Accounting for Aerospace Plane Vehicles, AIAA-87-1966, San Diego, 1987

PRISES D'AIR A SECTION DE CAPTATION VARIABLE APPLICATION AUX LANCEURS AEROBIES

par

F. Falempin et **Ph. Duveau**
Office National d'Etudes et de Recherches Aérospatiales (ONERA)
BP 72
92322 Châtillon
France

RESUME

La faisabilité de la propulsion aérobie des lanceurs spatiaux futurs dépend largement de la possibilité de définir des prises d'air réalisant au mieux le compromis entre des performances internes permettant une alimentation convenable du moteur et une masse et une traînée faibles.

Le compromis peut être sensiblement amélioré par l'emploi de concepts de prises d'air à section de captation variable.

Les concepts sont définis et leur application aux lanceurs spatiaux est analysée sous les aspects performances internes, masse et traînée.

NOTATIONS

Aj	surface à la section j
CAo	coefficient de force axiale
F	poussée
Is	impulsion spécifique
L	longueur de la prise d'air
m	débit d'air
M	nombre de Mach
Pdyn	pression dynamique
Pij	pression génératrice de la section j
Sref	surface de référence
$\eta o2$	efficacité
α	incidence
θ	ouverture de la prise d'air

INTRODUCTION

Depuis plusieurs années, les projets de lanceurs spatiaux utilisant des moteurs aérobies sur une partie de leur trajectoire de montée se multiplient à travers le monde.

Les avionneurs français Aerospatiale et AMD/BA, associés aux motoristes SNECMA et SEP ainsi qu'à l'ONERA, évaluent également l'intérêt de tels lanceurs grâce à l'étude comparée de plusieurs avant-projets (Fig. 1), mono ou bi-étages, mus par divers types de moteurs combinant la propulsion aérobie et la propulsion fusée.

L'intérêt de la propulsion aérobie pour les lanceurs n'est pas encore confirmé en raison des incertitudes qui persistent sur les estimations de performances de chacun des constituants du véhicule.

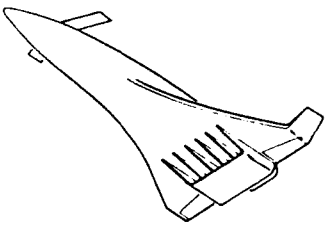

Fig 1 *STS 2000*

Il est cependant permis d'espérer que les fortes impulsions spécifiques des moteurs aérobies compenseront largement la nette augmentation de masse du système propulsif et permettront la réalisation de lanceurs récupérables à fort taux de charge utile.

Pour ce faire, il est essentiel de disposer de prises d'air réalisant au mieux le compromis entre d'une part, des performances internes suffisantes pour alimenter convenablement le moteur, et d'autre part un devis de masse et une traînée externe limités permettant d'obtenir un bon niveau de poussée installée ramenée à la masse du système propulsif dans tout le domaine de Mach envisagé pour la propulsion aérobie.

GENERALITES

Quel que soit le moteur aérobie à combustion subsonique considéré, le rapport optimal de la section du tube de courant capté à l'infini amont à la section du col sonique d'éjection (fig.2) croît fortement avec le Mach de vol comme le montre l'exemple du statoréacteur présenté sur la figure 3.

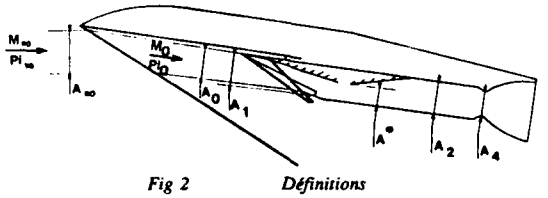

Fig 2 *Définitions*

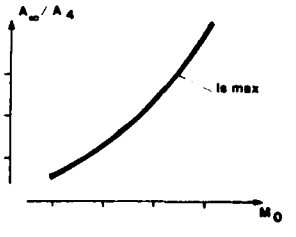

Fig 3 *Réglage optimal d'un statoréacteur*

L'amplitude des variations de ce rapport est telle qu'il est peu envisageable de ne faire varier que l'un des deux paramètres intervenant.

En effet, réaliser de telles variations de la section sonique d'éjection du moteur conduirait à des difficultés technologiques presque insurmontables.

Notons, à ce propos, que la moindre perte de rendement de la tuyère compromettrait très fortement la performance globale et ce d'autant plus gravement que le Mach est élevé.

Par ailleurs, la section du tube de courant capté à l'infini amont restant constante, le niveau de poussée diminuerait sensiblement avec le Mach limitant ainsi le domaine d'emploi de la propulsion aérobie, et par là-même, son intérêt pour les lanceurs.

A l'inverse, ne faire varier que la section du tube de courant capté conduirait à des niveaux de poussée très intéressants à Mach élevé, mais nécesiterait l'utilisation de prises d'air aux dimensions extrêmement importantes, qui augmenteraient de manière rédhibitoire le devis de masse du système propulsif.

Ces deux solutions extrêmes illustrent bien la nécessité et en même temps la difficulté de réaliser un bon compromis dans le cadre d'un problème général très complexe.

En effet, il s'agit de minimiser la masse de carburant nécessaire à la mise en orbite d'une charge utile donnée en jouant sur un nombre considérable de paramètres.

C'est ainsi qu'il faut choisir le type de moteur combiné, c'est à dire déterminer les moteurs de base qui le constituent, les régler et fixer les nombres de Mach de transition entre les différents modes de fonctionnement.

Il faut également définir des prises d'air dont la conception fixera dans tout le domaine de vol, la qualité de l'écoulement alimentant les moteurs en terme de débit, de niveau de pression et de distorsion, mais déterminera aussi une grande partie du devis de masse et de la traînée externe du système propulsif.

Il faut enfin déterminer une trajectoire tirant le meilleur parti du système propulsif mais aussi de l'aérodynamique globale de l'avion qui peut varier considérablement en fonction des contraintes structurales, thermiques ou de sécurité qu'on se fixe ou encore en fonction des contraintes opérationnelles et du nombre d'étages auquel on se limite.

Etant donné le grand nombre de paramètres et leur caractère éminemment interactif, il est impensable, à l'heure actuelle, de tirer des conclusions définitives sur tel ou tel aspect du problème, en particulier dans le domaine des prises d'air.

Nous nous limiterons donc ici à une présentation de l'avancement des travaux entrepris à l'ONERA pour tenter de définir une famille de prises d'air adaptées à la propulsion aérobie des lanceurs spatiaux.

LES BESOINS DU MOTEUR

De très nombreuses combinaisons sont envisageables pour le moteur. Le turbofusée à post combustion, le turbofusée-stato et le statoréacteur à éjecteur ont fait l'objet d'une étude approfondie (Fig. 4). Considérons à titre d'exemple le cas du turbofusée-stato.

Pour limiter les contraintes thermiques et structurales, une montée à pression dynamique de 0,6 bar a été choisie comme traiectoire de référence.

Le moteur considéré est dimensionné pour délivrer une poussée de 400 kN en mode fusée, au delà du domaine de la propulsion aérobie.

En tirant le meilleur parti d'une loi d'efficacité de la prise d'air, considérée comme la performance maximale réalisable dans

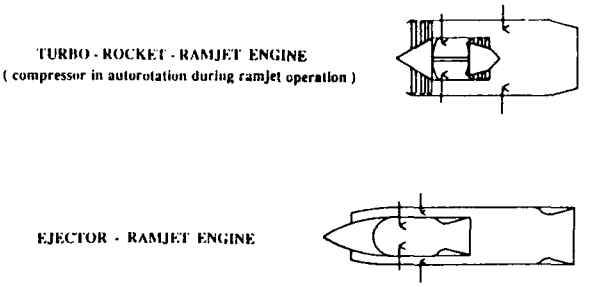

Fig 4 *Moteurs considérés*

tout le domaine de Mach, les performances théoriques obtenues son très intéressantes tant en ce qui concerne l'impulsion spécifique (3 à 6 fois plus importante que celle de la fusée) que le niveau de poussée (1 à 1,5 fois celle de la fusée) (Fig. 5). Ces performances ne sont obtenues que si une variation importante de la section du tube de courant capté à l'infini amont est réalisée (Fig. 6).

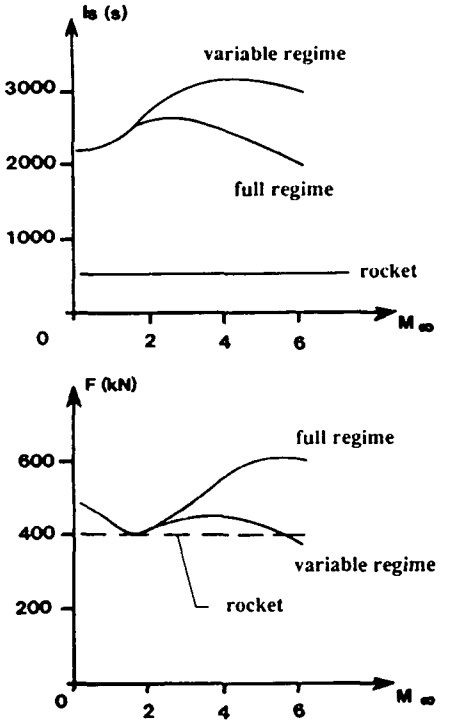

Fig 5 *Performances du moteur*

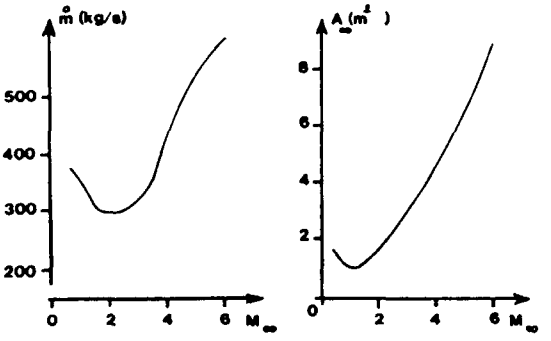

Fig 6 *Besoins du moteur*

L'intégration de la prise d'air au fuselage permet de tirer parti de l'effet très favorable du fuselage en incidence.

C'est ainsi qu'apparaissent les performances intrinsèques requises pour la prise d'air, caractérisées par la très grande variation de la section du tube de courant capté et par un niveau particulièrement élevé de l'efficacité dans tout le domaine de Mach *en raison du fonctionnement* en autorotation du compresseur aux Mach élevés (Fig. 7).

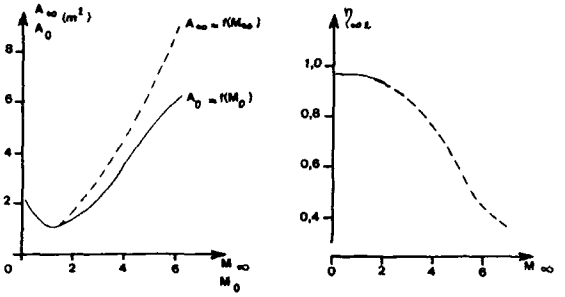

Fig 7 *Performances requises pour la prise d'air*

CHOIX D'UN TYPE DE PRISE D'AIR

Si les performances théoriques des moteurs considérés sont très intéressantes, encore faut-il que leur installation sous l'avion ne pénalise pas trop le bilan propulsif global.

C'est pourquoi, il convient d'apprécier les performances de la prise d'air en termes de débit et d'efficacité mais aussi de masse et de traînée.

Ainsi, nous avons opté pour une prise d'air bidimensionnelle en considérant qu'une prise d'air circulaire installée obligatoirement en nacelle et présentant une surface frontale de carène beaucoup plus importante, conduit à une traînée plus grande. Par ailleurs, moyennant certaines dispositions constructives, il est possible d'améliorer la tenue mécanique d'une prise d'air bidimensionnelle en se ramenant à un problème circulaire limitant, de ce fait, sa masse.

De la même manière, nous avons opté pour la géométrie variable en analysant les performances envisageables avec une prise d'air à géométrie fixe.

En effet, si on considère une prise d'air à géométrie fixe adaptée à grand Mach, on est confronté, à faible Mach, au problème d'une traînée additive très importante. De plus, le manque de débit en transsonique empêche de compenser cette traînée par une poussée élevée (Fig. 8).

A l'inverse, pour une prise d'air adaptée à bas Mach, le débit capté à grand Mach est trop faible pour obtenir un niveau de poussée satisfaisant (Fig. 9).

La difficulté de passer le transsonique dans un cas, ou l'obligation de passer très tôt en mode fusée dans l'autre, risque de réduire sensiblement l'intérêt de la propulsion aérobie.

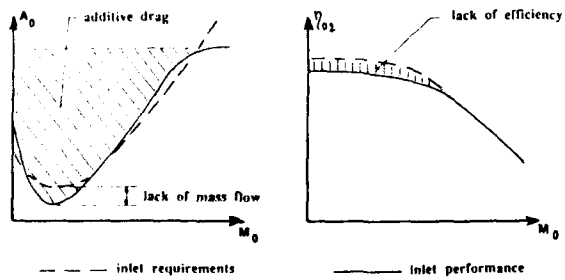

Fig 8 *Prise d'air à géométrie fixe : Mach d'adaptation élevé*

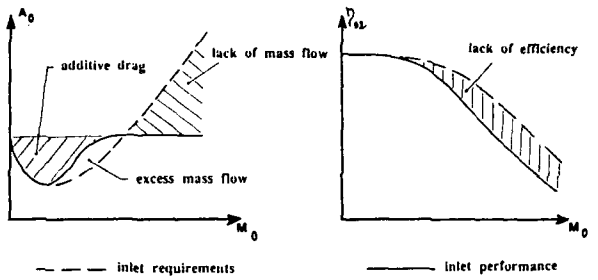

Fig 9 *Prise d'air à géométrie fixe : Mach d'adaptation faible*

CONCEPTS DE PRISE D'AIR A GEOMETRIE VARIABLE

Classiquement, une prise d'air à géométrie variable est dotée de rampes de compression et de diffuseur mobiles.

La compression est répartie sur les rampes (compression externe par les déviations Ψ ek) et sur la carène (compression interne par la déviation Ψ i) (Fig. 10).

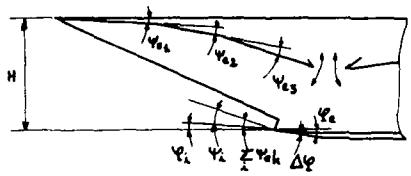

Fig 10 *Concept classique de prise d'air à géométrie variable*

Pour obtenir l'adaptation permanente de la prise d'air dans tout le domaine de vol, on augmente les déviations Ψ ek au fur et à mesure que le nombre de Mach augmente ; le diffuseur suit cette évolution.

Cela permet d'adapter la prise d'air en débit (les chocs issus des rampes focalisent juste un peu en amont du bord d'attaque de la carène) et en efficacité (la section minimale de la prise d'air diminue quand le nombre de Mach augmente).

Cependant, la très large gamme de nombres de Mach supersoniques à couvrir conduit à de grandes variations des angles Ψek et, par là-même, à une variation importante de la déviation Ψi.

Or, une forte contraction interne pose des problèmes d'amorçage et limite l'efficacité de la prise d'air notamment en régime de suradaptation par les forts gradients de pression qu'elle implique sur la carène.

Toute la difficulté de conception d'une prise d'air de ce type devant fonctionner jusqu'à Mach 5 et plus, réside donc dans le compromis entre une déviation totale pas trop faible à bas Mach pour garantir une bonne efficacité, et une compression interne pas trop intense à grand Mach pour réduire les problèmes de carène. Cette dernière condition limite la déviation totale à grand Mach si l'on fixe une valeur maximale pour l'angle extérieur de la carène Ψe de manière à éviter l'apparition de chocs détachés à bas Mach. En effet, on peut écrire :

$$\Psi_i = \Sigma \Psi_{ek} - \Psi_i$$

et $$\Psi_e = \Sigma \Psi_{ek} - \Psi_i + \Delta\Psi$$

d'où il vient : $$\Sigma \Psi_{ek} = \Psi_e + \Psi_i - \Delta\Psi$$

et donc déviation totale $$\Psi_T = 2\Psi_i + \Psi_e - \Delta\Psi$$

Si Ψ_i est limitée pour réduire les problèmes de carène et Ψ_e est limité pour éviter les chocs détachés sur la carène à bas Mach, la déviation totale ne peut augmenter que si l'angle du bord d'attaque de la carène $\Delta\Psi$ diminue ce qui n'est guère envisageable en deçà de 7° environ.

La figure 11 montre les gains que peut apporter la géométrie variable :

- aux faibles nombres de Mach, l'adaptation de la géométrie permet de capter un débit plus important qu'avec une géométrie fixe et donc de disposer éventuellement d'une poussée plus importante, si le moteur en est capable, pour contrer la traînée additive qui reste très importante ;

- aux Mach élevés, l'adaptation de la géométrie permet une augmentation de l'efficacité par rapport à une adaptation fixe à bas Mach, ce qui autorise une section d'entrée de prise d'air plus grande et donc une poussée plus importante.

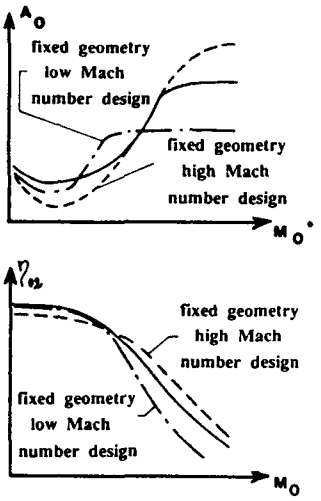

Fig 11 *Performances d'une prise d'air à géométrie variable classique*

Ces améliorations sont relativement limitées puisqu'il est toujours nécessaire de réaliser un compromis entre une traînée pas trop importante à bas Mach et une poussée pas trop faible à grand Mach.

Pour mieux répondre aux besoins du moteur, nous avons envisagé d'autres concepts de prise d'air à géométrie variable pour lesquelles la section d'entrée augmente avec le Mach d'adaptation.

La première solution envisagée consiste à basculer l'ensemble rampe de compression-carène autour d'un axe situé dans le piège interne comme le montre la figure 12.

Cette solution offre l'avantage du point de vue des performances internes de maintenir une compression interne relativement limitée dans tout le domaine de Mach.

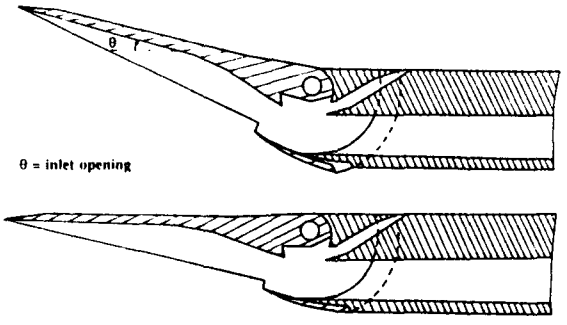

Fig 12 *Concept n°1*

Cependant, l'inclinaison progressive de la paroi externe de la carène peut générer une traînée importante, ce qui limite l'ouverture de la prise d'air et donc le domaine de Mach dans lequel elle peut être adaptée.

Par ailleurs, l'intégration de ce type de prise d'air n'est pas facilement envisageable sur un véhicule multimoteur. Elle a, en revanche, été expérimentée avec succès dans le cas des missiles dans la plage de Mach allant de 2 à 5.

La deuxième solution envisagée consiste à placer face à face des rampes mobiles comme si on avait mis en regard l'une de l'autre deux prises d'air du type précédent dont on aurait supprimé les carènes (Fig. 13).

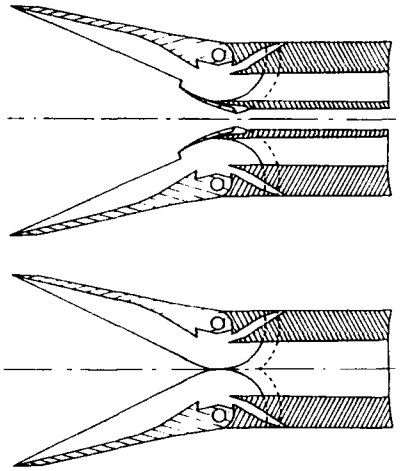

Fig 13 *Du concept n°1 au concept n°2*

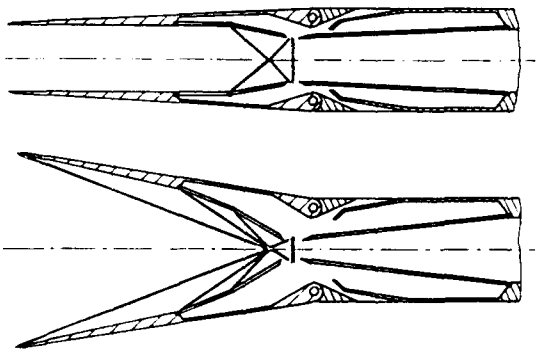

Fig 14 *Concept n°2*

Cette disposition fait que la déviation sur l'axe de la prise d'air est plus importante qu'auparavant sans que cela crée de problème d'interaction choc-couche limite sur une paroi (la carène) qui, en l'occurence, n'existe pas (Fig. 14).

Une interaction forte persiste toutefois sur les flancs comme dans le cas d'une prise d'air classique fonctionnant en régime de suradaptation.

On peut noter le gain important de traînée réalisé avec ce type de prise d'air, puisqu'une grande partie de la traînée d'onde d'une prise d'air classique est due à la carène qui est d'autant plus inclinée que le nombre de Mach d'adaptation est élevé.

Cependant, à Mach très élevé, la déviation totale répartie à parts égales entre les rampes de compression et le plan de symétrie de la prise d'air, conduira à un choc très intense sur ce dernier qui limitera l'efficacité de la prise d'air.

Pour résoudre ce problème, une troisième solution a été élaborée (Fig. 15). Elle consiste à réaliser la compression à l'aide

de deux rampes planes consécutives, séparées par un piège à couche limite, dont les dimensions et les positions angulaires entraînent l'existence de deux réflexions de choc sur le plan de symétrie.

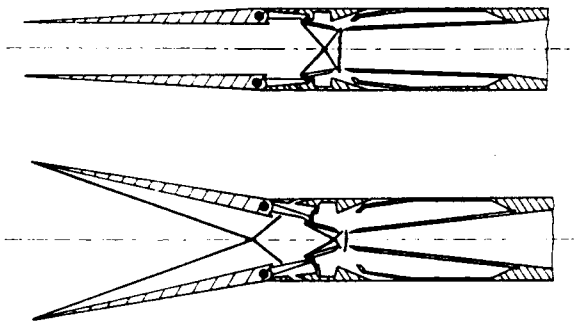

Fig 15 Concept n°3

Cette répartition de la compression sur le plan de symétrie permet d'obtenir une meilleure efficacité pour l'écoulement sain et de réduire les problèmes d'interaction choc-couche limite sur les flancs.

En revanche, cette solution présente l'inconvénient d'allonger assez sensiblement la prise d'air par rapport à la solution précédente (Fig. 16).

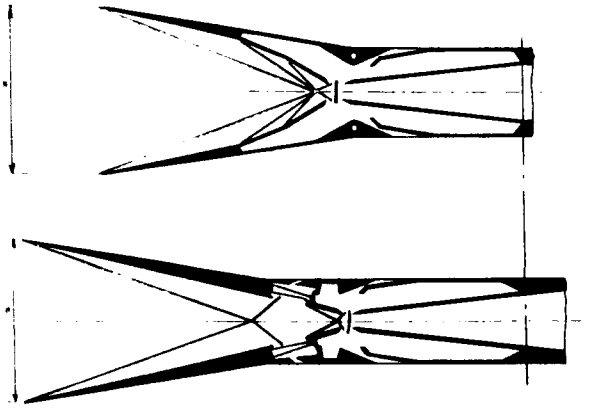

Fig 16 Comparaison des longueurs - concepts 2 et 3

Une bonne partie de la compression est obtenue par compression interne. Il est donc possible que des problèmes d'amorçage apparaissent. Cependant, la section minimale A* est constituée par des rampes mobiles et peut donc, si nécessaire, augmenter sensiblement pour permettre l'amorçage.

Etant donné le sens d'ouverture de ces deux concepts de prise d'air, leur intégration sous fuselage ne peut se faire qu'en plaçant verticalement les rampes de compression (Fig. 17).

Cette installation pose plusieurs problèmes importants. Tout d'abord, l'implantation des différents fuseaux moteur constituera des canaux qui risquent de créer une forte traînée en transsonique par blocage de l'écoulement et, dans une moindre mesure, en supersonique par les fortes dépressions sur la paroi externe des rampes de compression.

Par ailleurs, une prise d'air placée sur l'axe du véhicule bénéficiera d'une incidence locale favorable sur ces deux rampes de compression. En revanche, une prise d'air placée latéralement devra compenser, par des braquages différentiels des rampes, l'existence d'une incidence locale négative sur la rampe la plus proche du plan de symétrie du véhicule.

Enfin, et surtout, cette installation conduit en général à définir des sections d'entrée très applaties, donc des rampes de faible hauteur, ce qui a pour conséquence, d'une part d'augmenter sensiblement leur longueur, donc le devis de masse et l'importance des problèmes de tenue mécanique à résoudre, et d'autre part d'accroître considérablement les problèmes d'interaction choc-couche limite sur les flancs qui concernent une part très importante du tube de courant capté correspondant à une réduction très sensible des performances de l'entrée d'air notamment en terme de débit capté et sont très difficiles à régler en particulier du côté du fuselage en raison de l'importante couche limite développée sur ce dernier.

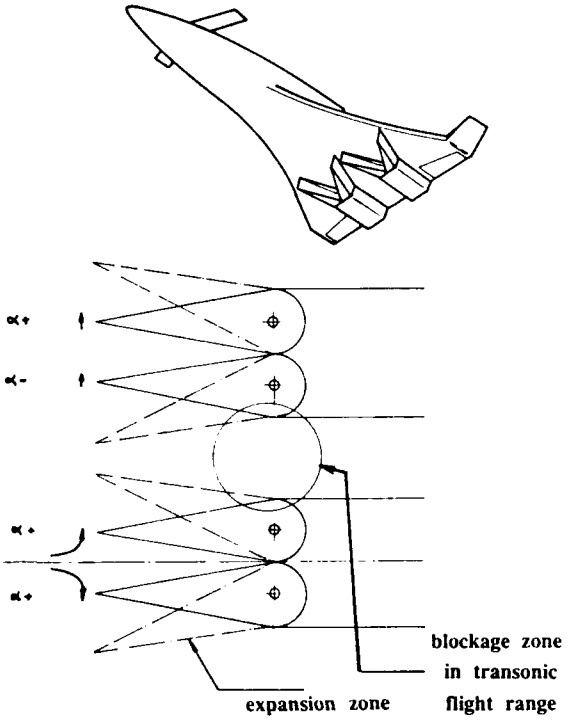

Fig 17 Intégration d'une prise d'air de concept n°3

Une validation expérimentale réalisée sur une version moins sophistiquée que celle du lanceur spatial pour laquelle seules les rampes amont sont motorisées, a montré qu'il est possible de réduire ces problèmes d'interactions choc-couche limite en utilisant des rampes biaises (compression moins importante du côté du fuselage) multidièdres (répartition de la compression et donc du gradient de pression sur les flancs) et des pièges à couche limite supplémentaires sur les parois inférieure et supérieure à l'entrée des rampes aval.

Cependant, si ces dispositions permettent d'améliorer le fonctionnement de la prise d'air, le coefficient de débit ne s'en trouve pas spécialement augmenté en raison de l'importance des débits à piéger, ce qui constitue un problème majeur étant donné le rapport de plus en plus faible de la poussée à la traînée de captation au fur et à mesure que le Mach augmente.

Pour remédier à ces inconvénients, un quatrième concept a été défini (Fig. 18). Il reprend le principe de fonctionnement du concept n°3 mais a été aménagé pour permettre une ouverture verticale de la prise d'air installée sous le fuselage du véhicule.

Cette disposition, qui correspond à une articulation supplémentaire du diffuseur, présente de nombreux avantages.

En premier lieu, elle conduit, pour une même géométrie de section de captation, à une prise d'air beaucoup plus courte donc de masse plus limitée et pour laquelle les problèmes de tenue mécanique des rampes sont beaucoup moins marqués (Fig. 19).

Elle permet également de limiter la part du tube de courant capté soumise aux interactions onde de choc-couche limite sur les flancs. Ces interactions étant d'ailleurs fortement réduites en raison de l'absence de couche limite prédéveloppée sur le fuselage (Fig. 20).

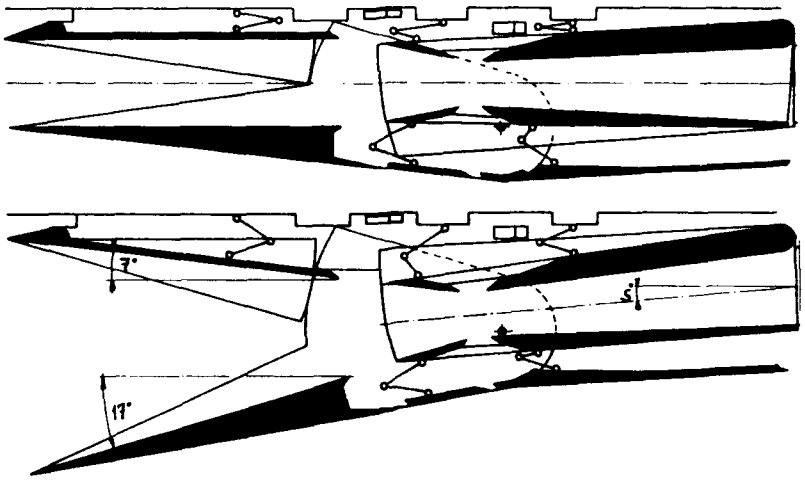

Fig 18 *Concept n°4*

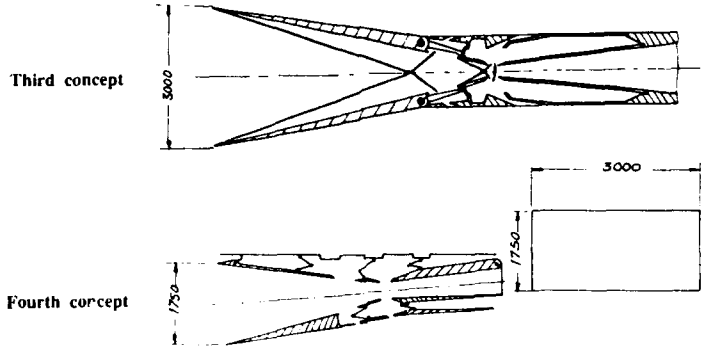

Fig 19 *Comparaison des longueurs - concepts 3 et 4*

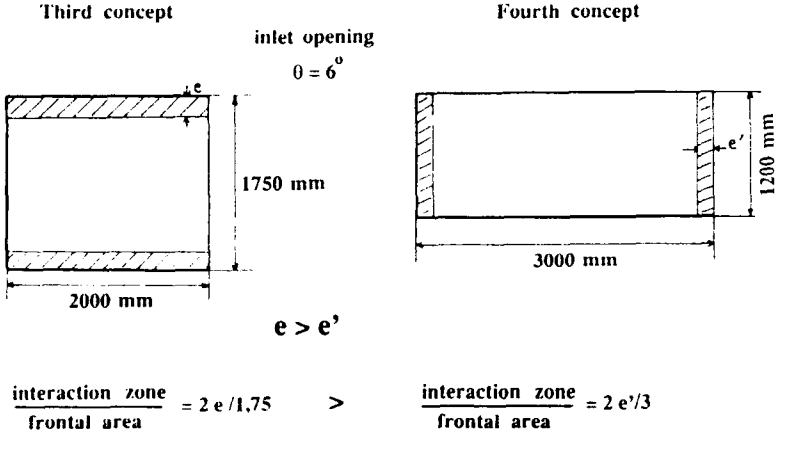

Fig 20 *Interactions choc-couche limite des flancs*

Notons qu'il est même possible, pour des véhicules n'utilisant qu'une prise d'air, d'envisager de supprimer les flancs jusqu'à la section minimale et ainsi annuler tout problème d'interaction.

L'inclinaison de l'axe de la prise d'air, au fur et à mesure de son ouverture, correspond à l'augmentation progressive de l'incidence locale moyenne quand le Mach, donc l'altitude, donc l'incidence de vol croissent.

Si la prise d'air est située sur le plan de symétrie du véhicule, le dérapage local sera favorable sur les deux flancs. Si la prise d'air est placée latéralement, le dérapage local défavorable sera du type de celui rencontré sur une prise d'air bidimensionnelle classique dont les effets sur les performances sont limités.

Enfin, ce concept de prise d'air autorise une implantation des fuseaux moteurs l'un contre l'autre ce qui doit conduire à une réduction du devis de masse (parois latérales des prises d'air et des fuseaux moteur en équipression) et à une meilleure homogénéité de l'alimentation des différents moteurs : concentration de la captation vers le plan de symétrie du véhicule.

APPLICATION AUX LANCEURS

Pour juger plus complètement de l'intérêt des solutions proposées, des prises d'air à géométrie variable ont été définies à partir du concept classique à section d'entrée fixe (prise d'air n°1)

d'une part et des concepts 2, 3 et 4 à section d'entrée variable d'autre part (respectivement prises d'air n°2, 3 et 4).

Les figures 21, 22 et 23 donnent une vue d'ensemble des prises d'air ainsi définies et un ordre de grandeur de leur masse.

Il est à noter que les dimensions pourraient être fortement réduites dans le cas de l'utilisation d'un statoréacteur à éjecteur de section bidimensionnelle.

Les figures 24 et 25 permettent de comparer les performances estimées des prises d'air 1 et 4 et de juger de leur adaptation aux besoins du turbofusée-stato considéré précédemment.

En ce qui concerne la prise d'air n°1, la section d'entrée a été fixée à 3 m², valeur qui apparait comme celle réalisant au mieux le compromis entre le niveau de poussée à grand Mach et la limitation de la traînée additive à bas Mach.

On constate que la prise d'air n°4 permet une meilleure adéquation des performances avec les besoins du moteur, tant en débit qu'en efficacité tout en réduisant très sensiblement la masse et la traînée jusqu'à Mach 3.

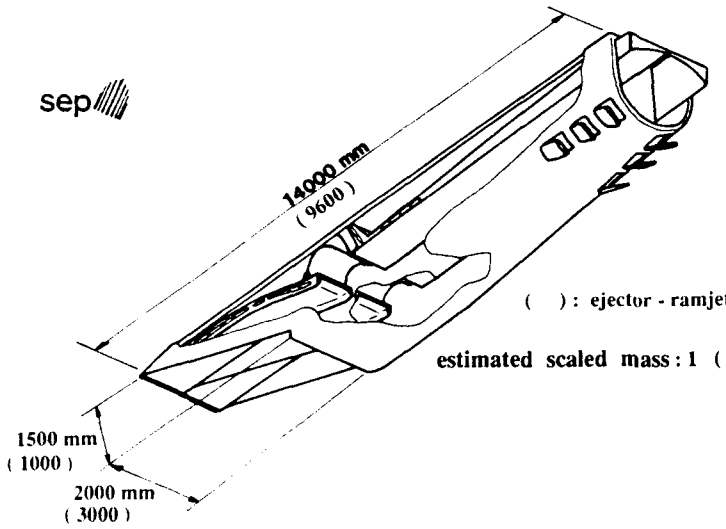

Fig 21 *Prise d'air n°1*

( ) : ejector - ramjet engine

estimated scaled mass : 1 (0,7)

( ) : ejector - ramjet engine

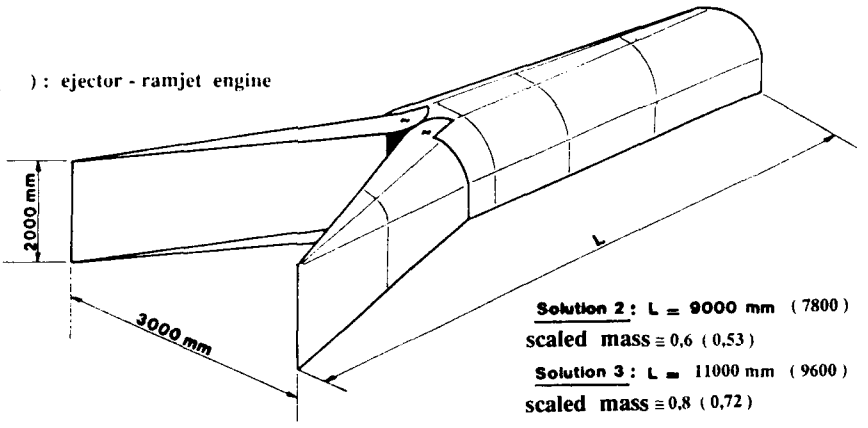

Fig 22 *Prises d'air n°2 et 3*

Solution 2 : L = 9000 mm (7800)

scaled mass ≡ 0,6 (0,53)

Solution 3 : L = 11000 mm (9600)

scaled mass ≡ 0,8 (0,72)

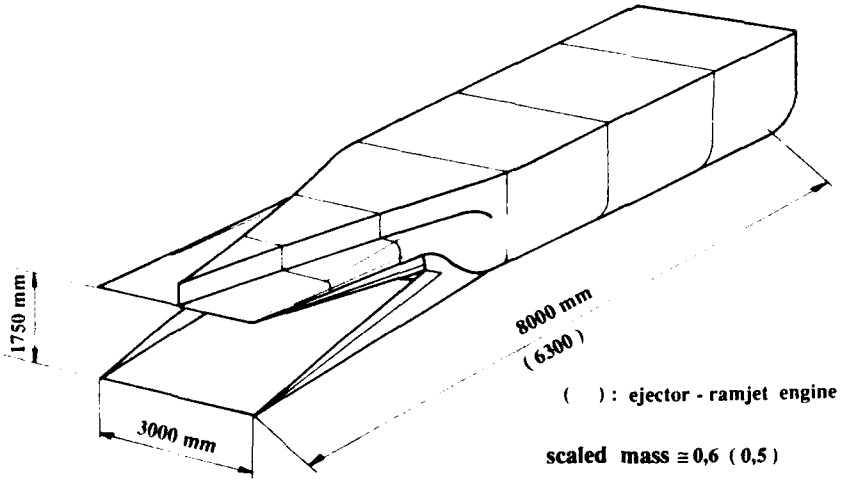

Fig 23 *Prise d'air n°4*

( ) : ejector - ramjet engine

scaled mass ≡ 0,6 (0,5)

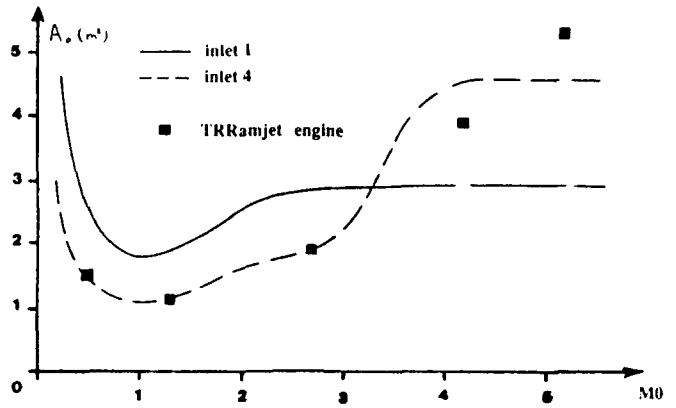

Fig 24 Débit moteur

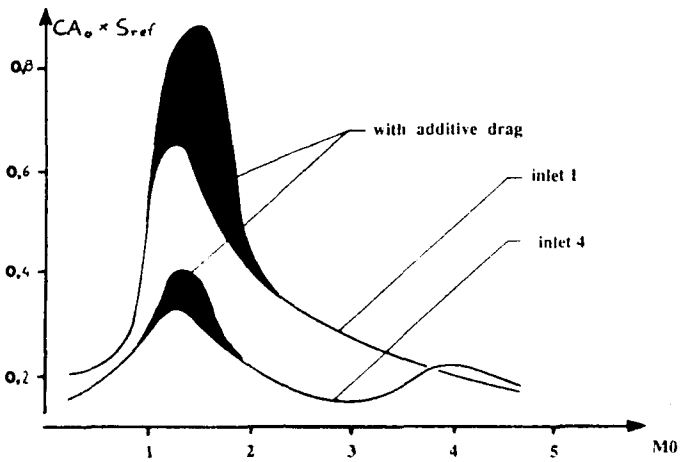

Fig 25 Estimation de la traînée

CONCLUSION

La faisabilité d'une propulsion aérobie des lanceurs futurs dépend largement de la mise au point de prises d'air réalisant le meilleur compromis entre les performances internes, la masse et la traînée. Une remise en question complète de la conception des prises d'air peut conduire à une amélioration très sensible de ce compromis.

En particulier, le recours à des concepts incluant la variation de la section d'entrée paraît très intéressant pour limiter la traînée en transsonique et permettre ainsi, pendant cette phase de vol, une propulsion purement aérobie sans en réduire le domaine d'emploi à grand Mach.

Bien sûr, l'étude des concepts envisagés à ce jour est trop peu avancée pour assurer la mise au point rapide d'une prise d'air répondant parfaitement au problème de l'alimentation d'un moteur donné. Cependant, la focalisation des travaux sur la définition d'une prise d'air adaptée au statoréacteur à éjecteur, qui supporte une efficacité plus limitée à haut Mach, devrait permettre d'obtenir assez rapidement des résultats satisfaisants et d'envisager l'adaptation du concept retenu à la combinaison statoréacteur à éjecteur superstato qui constitue l'une des voies de recherche les plus prometteuses pour la propulsion des lanceurs futurs.

Round Table Discussion

P.W. Sacher, MBB, Munchen, GE

Ladies and Gentlemen, it is now time to come to our concluding session, what we call the Round Table Discussion. I have asked the Session Chairmen from this week to support me in answering your questions during the discussions. They will help me to try an evaluation of the outcome of this meeting.

First of all, I would like to apologize for the absence of Wolfgang Schmidt from Germany who had to go back and he asked me to present to you the notes he has taken during the sessions. I hope to do my best in delivering his remarks. I know that it is impossible to replace Wolfgang Schmidt in any way, but I will try. My second apology is because of the poor quality of this hand written viewgraph.

After this presentation of about 20 to 25 minutes on the major findings or preliminary evaluations and remarks from Wolfgang Schmidt, I have asked the Session Chairmen to sit in front and to make some additional remarks if something is missing or in error. I will try to stimulate the discussion. I hope I have written down somewhat provocative statements and this may help you to start in an open discussion. I may need some help from the Session Chairmen if I cannot answer all your questions. Then, of course, we will have the concluding remarks on this meeting, made by our Panel Chairman, Jim McCroskey.

Just to start, I would remind you that the main objectives for this meeting have been to review of the state of the art in aerodynamic engine/airframe integration concerning the techniques reached in the present time and to report on progress achieved in engineering project work in past years. You all know that our last meeting on this subject was in 1982 in Toulouse, so at least 8 or 9 years have gone by. Our feeling was, that there must now be enough material to be presented at this meeting. We had intended to bring people together like experimentalists and theoreticians. I think that this has been the case during the week. And we had extensive reviews in some distinct AGARD activities like working groups or symposia. All of this has taken place.

The first question to raise is, "Were the meeting's objectives met by the contributions?". I will try to answer this question after reviewing the statements by Wolfgang Schmidt. In addition, we have to ask ourselves, "Does it seem timely?", and, "Are future activities needed?"

There is some logic in the program which divided the whole matter into sessions. We tried to start with the subject we considered to be at the simplest level: wing/pylon/nacelle interference where the integration level is low. This is of course related to civil transport projects. Due to increasing complexity in geometry and speed, the following sessions dealt with forebody inlet problems, afterbody/nozzle integration problems (which are clearly of great importance for any kind of military aircraft or in the missile business, perhaps also for the future SST or HST), and the highest level in the final sessions dealt with tip-to-tail propulsion airframe simulation for space transport of any kind (there is no difference between two stage or single stage to all those projects). They are all characterized by the highest degree of propulsion/airframe integration you can imagine.

Now I will go session by session and I have prepared two charts for each. One of them lays out some general observations and the other one is, of course, the conclusion which could be made only in a preliminary way. Of course, we have to write this TER in a much better and more professional way, reading carefully all the papers presented here. This will be included in the final Symposium Proceedings.

Civil Transport Aircraft are dominated by economic requirements. That is quite evident. The airframe/engine integration is very important for second segment climb and for cruise. That is the dominating feature. We have seen the high importance for any application of thrust reverser in flight, on the ground, and in interference with the aircraft. First of all, Wolfgang Schmidt said that we have had well-balanced sessions, experimental papers 1, 2, 4, 8, and 10 and the rest was theory. There is a strong feeling in Europe that TPS is a standard testing technique for turbofan and turboprop simulation. It was observed that TPS seems to be the facility owned equipment and this has, of course, some economical reason. To continue, in US industry, nacelles powered by pressurized air have been reported and less use of TPS for unclear reasons. That is one of the provocations for the discussions. Remember this statement. The theoretical analysis is made to a large extent by solving Euler equations. There is still ongoing work using panel methods and full potential approach.

Now to the conclusions on Session 1. There are well established test techniques using the TPS, at least in Europe. CFD is still rather limited to the cruise application. We have seen no Navier Stokes solutions. CFD is limited, not only due to cost, but also to a large degree to manpower cost for mesh generation or some have used the word, "user friendliness". Most efforts seem to deal with just adding pylon, nacelle, and engine to a designed wing. This was at least the impression from some of these presentations. The design of pylon and nacelle has been done for a given wing, in other words. So wing design in the presence of a propulsion system was missing. At least we have not seen any contribution of optimizing the wing shape in the presence of the propulsion system. We had no contributions to design optimization and no contributions to overall design concept principles, nor have we seen alternative designs.

Session 2 was the Engine Integration Session, an invited session, and the contributions came from the Propulsion and Energetics Panel. We had two types of contributions; survey papers and a detailed analysis of inlet flow distortion on the engine performance. PEP-WG 18 compiled an extensive experimental data base, a huge effect on test cases; but the feeling is, that a follow-on activity is needed, and the question is whether the experimental information is suitable or not to a CFD application. This is specifically important when you are just collecting or compiling tests which have not been originally designed for the purpose of CFD validation. If you just take tests which have been done, of course, for the purpose of project work, it may be, that there is not sufficient data available which fits in the

individual computational code requirements. CFD techniques are still in development, and used, in PEP-activities in very similar, if not in an identical way, to those used in FDP-work. That is quite clear. We have, of course, common problems and common limitations. The distortion handling needs some kind of strategy and the big question Wolfgang Schmidt raised is that the communication between the airframe and engine manufacturer is mandatory. In other words, if we provide some kind of distortion to the engine manufacturer, what is the response from the engine manufacturer to this data?

In conclusion, the experiments need a new quality to satisfy accuracy and detail requirements to be datum solutions for the CFD code validations. CFD validation is extremely difficult if there is nothing to validate against. The reaction might be not validation, but calibration of computer codes, as currently under way. This is another really provocative statement here, and I would like to have your opinions about that. Air-intake distortions require an extensive experimental effort. In this respect we have seen very limited CFD work, if any. The session indicated that many common areas of interest in PEP and FDP exist and consequently we need perhaps a better or improved communication and more joint efforts.

Observations for Session 3 concerning the Experimental Techniques: Wind tunnel, water tunnel, ground and flight testing is heavily used. TPS begins also to be used for military aircraft design. Significant interest and important tool developments for the advanced STOVL and Stealth projects are currently being undertaken in industry. Extensive data reduction or data acquisition systems, on more mobile basis are now available and the latest Doppler anemometry techniques are now being used for full-scale flow analysis allowing for the validation of experimental tools, like TPS, but also CFD work. Increased efforts were reported on the airframe side to understand flow fields due to integration effects and the question is, does there exist any kind of parallel effort on the engine manufacturer's side.

Conclusions for Session 3: TPS is starting to move into the military aircraft business. In Europe, TPS is owned by the test facility and requires a reasonable return of investment, therefore it is used in many programs, not specifically invested and designed for one project. How can we simulate hot gas with TPS? This is a remaining question. Something might be wrong considering that we have a real problem normally with the afterburner. We have no US contribution on the specific subject of TPS, and perhaps the question comes up: is the ASTF at AEDC the U.S. solution for dealing with that problem because TPS is not available for hot jet impingement. Another question is what can the engine manufacturers do with details obtained, concerning the interface between airframe and the engine and what is the response to the airframe manufacturer.

Now to Session 4. A huge variety of geometrical arrangements of intakes in different aircraft designs and missiles has been presented. There was no tendency to find optimum inlet positions in general because this is dependent on the mission profile of each individual vehicle design. A specific intake design might be an answer to high angle-of-attack requirements, it might be an individual response to speed requirements, and of course, it is different for aircraft types and missiles. What was missing to my feeling was the general philosophy of how to get the individual optimum inlet position for a selected configuration.

The results of the FDP Working Group 13 have been quite impressive. It is a compilation of a huge amount of data. One of the results is that requirement for CFD code validation is to perform a specifically designed experiment. The excuse of CFD people is somewhat in the direction, "garbage in = garbage out". If you don't have better experiments, the results are not good enough or unsatisfactory. CFD results differ even for the same class of physics. That should not happen, but it is the case. The mesh generation or mesh refinement technique of the flowfield seem to give some indication of what is going wrong if you are using the same physical equations, the same class of approximation in different codes.

Another observation is the need for highly experienced, trained-on-the-job engineers because these are not really "black box" codes. Results from internal test flow cases are even more confusing than for external flow. This could be observed. Experimental pitot type inlet test cases showed significant deviations for the DC 60 in three different wind tunnels. This means that the experimental situation comparing the results obtained using different wind tunnels is the same as for CFD.

The FDP-Working Group 13 effort was, last but not least, not really completed. At least, at the time requested there were missing contributions from different institutions. Some were specifically mentioned, but there were others. A remarkable effort was dedicated to the high-speed commercial transport, SST, in between mach 2 and 5. CFD tools applied to external 3-D and internal flow simulations have been demonstrated.

In conclusion, the report of the FDP Working Group 13 can be, in the future, considered as a state-of-the-art notebook for designers, a guide for CFD and testing techniques. As already stated, a new quality of experiment is needed. More approaches like Paper 24 are needed to set up a design concept philosophy for airframe/engine integration. The CFD community should not only share success - that is a remarkable statement - but also bad luck or bad results. Then we can learn from each other.

Some major observations from Session 5 follow. It was said that there has been no major breakthrough since publication of the FDP Working Group 08 in 1986. I like the statement from Mr. Bowers who said, "Will the state-of-the-art tomorrow be as good as today?" There are CFD requirements for test cases which are still as valid today as they were when written down 5 years ago. But progress in the use of Reynolds averaged Navier Stokes solvers using certain formulations of different turbulent models (maybe still unsatisfactory) has been reported. However, there are still some restrictions on the complexities of geometry. I have indicated on the left lower side some kind of magic triangle between the experimental test cases, the code validation on the right side and consequently the user environment friendliness on the left. Everything has to be done in an interactive way and has to be improved continuously in the future.

The last session, Session 6, is quite short. AGARD FDP Working Group 17 will start in 1992 and I think they will address specifically the subject of this session. Unfortunately, we had only a few papers submitted. This is in spite of the fact that it deals with the highest degree of engine/airframe integration. This is not yet a routine procedure today, and therefore, it can be explained by the fact that it is highly identified with the program or the project status of the engine/airframe integration represented by projects like NASP, HOTEL, SÄNGER, etc.; there are many others. This leads to the conclusion that this is at least company confidential or in some way classified. We should have expected some kind of a response in that direction. My idea is that we would have been well-advised to defer this subject to a future meeting when these projects are more clear and more open to be released to the public.

Overall conclusions: the successful airframe/engine integration relies to a large degree on the extensive wind tunnel testing using engine simulation tools. That is at least the European point of view. TPS is the most useful thing that we have for testing. Optimization of civil and military configurations need the complementary support from CFD. I like the word complementary; it has to be done in addition to the experiment, it cannot replace in any way, as many have already stated, the experiments. Due to the geometric complexity and need for viscous flow representation during engine/airframe integration, there are still considerable limitations for successful use of CFD. That has to be clearly stated. CFD is even more important for internal flow problems than it has been shown for external flow problems. It is not easier to do it for internal flows. The future trend goes to even higher integrated designs. That comes up perhaps more or less with the requirement for a tip-to-tail or front-end simulation of the whole configuration. The aircraft airframe cannot be considered in an isolated way as it has been treated in the past, at least for civil aircraft projects. But also for high speed civil projects, the degree of integration of engine and the airframe is going to higher and higher complexity.

I should now try to refer again to my second picture, and comment on whether the meeting objective was met by the contributions. I think, with some exceptions, we can say, "Yes". The next is, "Was the choice of this subject timely?". I think it was, because the response to our meeting was positive. We got a lot of contributions, positive reactions from different countries and if we continue our efforts with the new FDP Working Group WG17, dealing again with the afterbody, then we will have the next meeting on the same subject, let's say, within the next 10 years. "Are future activities needed?". Definitely. A joint effort is needed with other panels. I mean it is quite obvious that we have to coordinate and to collaborate with the PEP even more than we have done in the past.

Some general remarks on the meeting. I just mentioned that the overall aims might have been reached. But the second point is even more important. I feel that it was a success to integrate people working in different disciplines like working in experiment or in theory; we have brought together engineers from civil and military industrial work; we have experts for internal and external flow physics here on the floor; and we have brought together people from different AGARD panels, like FDP or PEP or FMP. We have had some active and stimulating discussions from the floor. I appreciate that very much. Remarkably, all these papers have been available in a written form which is not always the case. We had excellent professional presentations during this week. I want to congratulate all the session chairmen for keeping the program on time. That was first Symposium I observed when all the sessions were exactly on time, and this was certainly due to the discipline our session chairmen put on our speakers. We had optimum local arrangements and an outstanding hospitality provided by the hosting organization and I want to reserve this special observation to the effort of Dick Bradley.

Now I want to give the session chairmen the privilege to react on the statements which have been made by Wolfgang Schmidt and have been written down by myself. Sometimes I have included personal remarks in addition. Who would like to start first, Session 1?

Ir. A. Elsenaar, NLR, Amsterdam,NE

There is one remark that I would like to make. It is about the complementary nature between CFD and experiment in the design process for civil transport aircraft. It is not only important to get the final value of drag, which you can only derive from wind tunnel experiments, but also to get a good understanding of the flow. I think that we have seen some nice examples of that. Tony Harris started off his show with some surface flow visualizations and stressed the importance of doing that. We have seen LDV measurements to show how the flow around the nacelle behaves and we learned about the importance of the axis of the thrust vector as raised by several authors. We have seen advanced flow viz techniques for thrust reversers. It is really important to see what we are doing. In the same category I would think the Euler solutions give very important information in the design to show pressure distributions on the wing/nacelle combinations with such a detail that it is almost impossible to measure it in this way. It is a good example that all these tools, more probably now than in the past, help us to understand the nature of the flow and the detail of the flow. That is really what is important to improve design processes.

Prof. L. Fottner, Universitat der Bundeswehr, Munchen, Neubiberg, GE

I fully agree with the conclusions of Wolfgang Schmidt but I want to make some additional remarks. I found that it has been clearly demonstrated that the subject of this meeting was an interdisciplinary effort which overlaps the terms of references of both the Panels, PEP and FDP. But as Mr. Hermann asks in the first question on his paper, we found that the engine community, members of engine companies, were not well represented here. There were only some persons coming from the engine companies. Possibly there is one explanation and that is in connection with the information on AGARD activities. We found also in our panel, that information on AGARD activities in some NATO countries is not sufficient, and following my presentation on the Working Group 18 Report, I found some questions from people asking where they could get the report. This information should be better distributed. One additional remark is that I found that there are three groups which should cooperate much more intensively. The first is the suppliers of codes. Second are the industrial application people and the third one is the experimentalists. I would suggest that these three groups should not operate or should not work in their rooms very isolated, but should work together. This means also the validation of codes. We found, and this was a very important result of our working group, that the test cases, especially the experimental test cases, were not well-documented. It is very, very necessary to find and to perform new well documented test cases.

Therefore, working group activities like you mentioned, and like we will also do in our panel, are very, very necessary.

Dr. Leynaert, ONERA, Chatillon, FR
I will just mention a particular point coming back to a discussion of yesterday on the unsteady distortion measurement in the air intake. When we say that the unsteady distortion coefficient is 0.3, we have to add that during 10 minutes of flight at the given flight conditions, the probability to have a lower distortion than 0.3 is 99%, for example. Because it is a random process, we have to give these indications, or we are not sure of what we say. So to find that figure, 99%, we have to make a statistical analysis of the distortion. That is still to be done. There is a first attempt in that way in the WG13 AGARD Report, but that kind of work must be developed and generalized.

Dr. R. G. Bradley, Jr., General Dynamics, Fort Worth, Texas, US
I have some comments. Generally, I agree with Dr. Schmidt, but I must take issue with one statement. I really don't agree that the internal CFD is more confused than external. As a matter of fact, we have much greater success with internal than we do with external computations. When I started the session, I noted that Dr. Schmidt and I worked together on the Working Group 13. I was interested in what his review would reveal, whether he approved of that work or not. He seems to approve.

I would like to make another comment on CFD. There seems to be a continuing discussion of experiment and CFD. Validation seems to be having a difficult time; calibration is misunderstood, by everyone, including myself. There are some things that I think we must really understand, major problems that are fundamental, like transition. We continually compare with data, flight and experiment, and we often have no idea where transition occurs. We have no mechanism for computing transition, so we are very much in the dark. The grid effects can be overwhelming, perhaps more important than the turbulence modelling. There is just so much room for work. There must be some way to understand the band of error in experiment before we can ever really compare it successfully with CFD.

Then the other thing is the unsteady effect. Anytime you compute a flow with a shockwave-induced separation, chances are that the flow is not only separated but it is very unsteady. Steady computation with some kind of averaged data for a moving shock is just very difficult to reconcile with experiment. So, there is still a lot of work to be done there. I believe it is a real challenge.

A nose-to-tail solution for an airplane is not going to be really of value until we can recognize and reconcile the scale of the flow over an entire vehicle. A great problem we have is gridding and stepping schemes that can capture the scale, whether it is a turbulent boundary layer or a shock wave away from the configuration. The real measure of success is when we can successfully and confidently calculate the drag of a complex vehicle. I offer that as the real challenge; compute the drag accurately with CFD and then I will be convinced.

Mr. D. Bowers, Wright-Patterson AFB, Ohio, US
All of Dr. Bradley's comments concerning the Inlet Session apply to the Exhaust Nozzle Session as well. There have been some successful efforts for code calibration as evidenced by the papers of Reed and Karman in this session. There is a further need for calibration of CFD codes, but the primary missing ingredient is high quality, specially directed, high detail experimental data. The queston is, "who will do it?". The experimentalists don't necessarily want to do it, because that is higher detail than is typically taken. The computationalists don't have the resources many times to do it. The question is who will be responsible for providing this high quality experimental data? Certainly, it must be a collaboration of both the experimentalists, the very best we have, and the computationalists, who are providing the direction for the data needed. Perhaps a group like AGARD, through its working groups, can dictate the requirements for this experimental data and be a facilitator to get the data available to the community.

In the past, we have been able to do very well without CFD as evidenced by the F15 STOL demonstrator, but that is not a very high level of integration. The configurations we are looking at for advanced aircraft are. So we must address this problem now or we will have the same discussion later.

Mr. J.M. Muylaert, ESTEC, Noordwijk, NE
In the session this morning we had only 3 papers. In that respect it might be a little bit disappointing. On the other hand, we all clearly understand the reasons of classification. Let's hope that in the future we will have more research work, openly discussed. Maybe a proposal to improve this exchange of information is to define for the forebody compression as well as for the afterbody expansion, some kind of generic forms. This would allow the community to do detailed studies on critical phenomena, for example the matching of the forebody shape to the engine inlet, forebody boundary layer transition and its effect on inlet efficiency. What about the entropy layers when only Euler codes or Euler coupled with boundary layer are taken into account. In the same way, for the afterbody, I think it would be of interest to have a generic form and study the secondary injection, especially at transonic speed, as we have seen in the paper from MBB where the problems of local separation were addressed. Because one has the highest level of engine integration for the space transportation systems, not only isolated phenomenon on generic forms but also the overall system should be studied. Trimming the plane is partially done by thrust vector control.

Mr. Sacher
Well, that brings us to the open discussion.

Prof. Dr. C. Ciray, METU, Ankara, TU
I was trying to take notes and trying to formulate my view while Mr. Bowers came up with a few sentences to express exactly what I had in mind. It appears that detailed experimental flow measurements are needed. One practice which has been used up to now is to use some building block experiments. I am asking whether it is not possible to formulate some new building block experiments which will be used in

connection with this airframe integration or exhaust jet flows. I think that our AGARD Panel can try to formulate some activities needed to direct or to collect this kind of information. I think that this new set of information is needed if we want to make further progress in this field and give the opportunity to CFD people or turbulence modellers to create more effective means of calculation.

Mr. Elsenaar
Just one quick remark. Being an experimentalist I got a bit tired of the CFD community always complaining about not having sufficient experimental material. I think that this is not justified. I fully agree with Dick Bradley that as long as CFD is not capable yet of calculating drag, they still have a very long way to go. They do not need experiments to assess that problem.

Dr. Bradley
The fact that CFD cannot calculate drag does not take the responsibility from experimentalists to define error bands and understanding for their data.

Mr. J.W. Kooi, DNW, Emmeloord, NE
Working at a wind tunnel, I saw two remarks which touched us. One was that the TPS equipment is thought to be bought by the wind tunnel owner. This equipment costs quite a lot of money and that brings me to the second remark made, "can we continue to have our experimental facilities at the same standard today and in the future?". I think that the only way to go in the right direction is that instead of having quite a lot of competition between the wind tunnels, to attract work, rather cooperation is needed, so that this very expensive equipment can either be shared by the facilities or that some centers of excellence, you could say, are created with and specially suited for a particular type of work. In fact such a cooperation is already starting a little bit in Europe; we (DNW) are working on the A340 project as you have seen, together with ONERA. I hope that this cooperation will also reach over the ocean.

Mr. Sacher
Does somebody want to respond? We agree basically.

Mr. Bowers
I would say that in the future, that is the only way we will be able to maintain and conduct our business because there will not be the funds available to keep many centers with equal capability. I agree with you entirely.

Mr. A.E. Harris, ARA, Bedford, UK
One picture I didn't show was the compulsory CFD solution in color. I want you all to see this. The reason for saying this is that on here we have listed M local and I get ever so bored looking at c_p. I don't know what c_p means. I have to know M infinity and then I have to know what c_{pcrit} is and so on. Could the CFD community please lean towards M local distributions where we can all understand what we are looking at when we are looking at comparisons of CFD and experiment. We really want to know how much we are missing the mach number by, not how much the c_p is. There has been some discussion even about delta c_p. Good Lord, what does that mean? I don't know. I have got a serious point to make though, and that is when you talk about reference experiments, a lot of times people are putting large models in small tunnels. If you are going to run CFD on this comparison, I feel that you better be putting the tunnel in as well all the time, or at least qualifying the experiment to be sure there are not major model-tunnel constraints running into the picture. So that is kind of an appeal about reference experiments and at what quality level they are produced. Obviously the other thing you have all said about transition fixing and is it fixed and how well it is fixed, and so on. That is my contribution. The rest was rubbish.

Mr. Sacher
I am looking for somebody from the CFD community who can explain what c_p is.

Mr. Bowers
c_p and delta c_p are the usual parameters that wind tunnel data are reduced to.

Mr. Harris
The reply is that at the ARA we produce it in all sorts of forms, including c_p and M local and all the other things. A purist will stand up now and say that you don't know what M local is because you may have some head loss. I say just call it infinity total head for the sake of us looking at it at least, or qualify it and say it is true M local by some other head loss means.

Mr. B. Haines, ARA, (Ret'd), Bedford, UK

I do not want to prolong the discussion on this point, but local Mach number rather than pressure coefficient may not be the end of the story; for a sweptback wing, the Mach-number component normal to the isobars is often what one needs. Turning to a much nore significant point, I was somewhat disappointed with a lot of the CFD presentations, particularly on the first day in that they merely showed results which I instantly recognised as being similar to experimental data obtained many years ago. This was because both sets of results were for relatively simple configurations with flow that could not be described as acceptable. This was disappointing because one might have hoped for examples where the CFD methods had been used to refine the configurations to improve the flow. This is the prize that is now within our grasp; hopefully at the next conference, we will have such examples; only then will we be able to say that we are fully exploiting the CFD tools that are now available.

Mr. Sacher
Who wants to continue?

Prof. Ir. J.W. Slooff, NLR, Amsterdam, NE
If you have a problem in getting more responses, Peter, I will help you at the risk of making a fool of myself because I was able to attend only about half or so of all the presentations. I would like to offer a few comments and questions that popped up with me during the presentations that I was able to attend. Like on one of your viewgraphs, I noted that perhaps the main experimental technique that we seem to be lacking right now is a combination of TPS and hot-core simulation. It is not clear to me whether we really need that or not. If we need it, it is probably more so in the military applications, I suspect, than in the civil. If we need it, the question of course, is can we realize it technically. Maybe somebody from the audience can respond to that. Another thing that I noticed, but as I said I was present here only about half of the time, and I may have missed something, is that I have not really seen any new concepts in propulsion/airframe integration. Finally, it also struck me that I heard very little about the problem of thrust/drag bookkeeping. That might mean two things; either it is no problem at all anymore, which might be the case on the experimental side, although I suspect that there could still be some problems there; or it might not yet have been recognized or encountered as a problem. The latter, I suspect, is the case in CFD. Most CFDers fly their planes around without propulsion simulation at all. Many times even without tailplanes or even without fuselages and they can't even predict the drag correctly for those simple configurations. I don't think the problem of thrust/drag bookkeeping in CFD has even been tackled yet. There is a very long way to go there. A final remark concerns the field of validation type of experiments. This does not apply specifically to propulsion/airframe integration, it is more a point of CFD validation in general. Usually we have here the situation that if we have data for a given configuration that have been accepted by whatever person or institution as being a valid validation set of material, it has been obtained only in one wind tunnel. It would be very interesting, if not perhaps mandatory, to have experimental validation data, not from one facility only, but from several facilities. Perhaps even from several models. There are many factors involved that could lead to different results. In the few cases that there have been multiple tunnel entries, it was usually either only in Europe or only in the US. I don't know of any example, except one or two exceptions perhaps, where there has been testing on one similar model or configuration on both sides of the Atlantic. I think that it would really be a good thing if we could organize a validation type experiment that would go across the Atlantic and be taken both in US and European tunnels on the same model or at least the same configuration.

Mr. Sacher
Thank you very much. I think that there were at least four major remarks on different subjects which we have to discuss separately. The last one seems to be the most distinct proposal. We have had identical models, two-D sections and even three-D wings in different European wind tunnels already. We could now discuss all the discrepancies we have seen on this report. It was amazing and in many cases could not be explained where these differences are coming from. But anyway, it is true that these very extensively tested models have not been transferred to any wind tunnels overseas. We had it just in the four or five major European centers, the ONERA, NLR, UK, German tunnels. It was also including FFA at least for 2-D sections. We had those identical models in all European wind tunnels. In most cases, differences have occurred and in many cases they were not understood. Your proposal is now to define perhaps a new experiment for CFD validation, a new desiged wing or section which should be shared, not only in European facilities, but also overseas. I think it is perhaps up to AGARD to recommend such an action, or we can undertake it in our test committee. I think there is at least one very capable member to undertake it; Bram Elsenaar from NLR. I should mention that he has taken an active part in all these test cases and all these experimental transfer from wings and 2-D wing sections.

Mr. Elsenaar
That is not completely true, Peter. I agree that it should be encouraged. One thing that is quite clear, I think, is that validation experiments should be done in different wind tunnels. It is the only way to get rid of the bias error. There is a very good example of that in Europe; in the GARTEUR "thick wing" exercise where the experiment is completely doubled in different wind tunnels, and you can learn a lot from doing that. There are configurations that have been exchanged between the United States and Europe: CAST 7, CAST 10, the International Vortex Flow Experiment. But I agree it should be done more. One further remark. In the GARTEUR F4 comparisons that were done in the European wind tunnels, the experiments were reasonably close together, whereas the CFD calculations, showed very large differences. I think in 3-D situations where the wall interference effects are generally small you get reasonably good agreement between different wind tunnels in general. For 2-D models the situation is different. There you see very large differences. That is due to the fact that the model is large compared to the wind tunnel, and the wall interference is really a problem there.

Mr. E.N. Tinoco, Boeing, Seattle, Washington, US
One thing I have not heard addressed in the testing for validation or really for anything else, is knowledge of the geometry. Typically, what we are given is the geometry as to how the model should have been built. That is not necessarily what was built. Even if we measure after it was built, that was not necessarily the shape while it was tested. The wind tunnel models have significant aeroelastic effects, and we need to account for those in the process of making the flow measurement. The codes are getting to the point where we can pick up these differences. On a transport model, wing twist of one degree is not unusual. That has to be known, it has to be taken into account. We need to develop better techniques for doing this as we measure the forces on the model.

Mr. C.C. Rossow, DLR, Braunschweig, GE
I think CFD has taken some beating here. I want to defend it in some ways. You refer to the GARTEUR study and I think that this study was quite a long time ago. Now you have to keep in mind that CFD is, let us say, about 10 years old, it started in the 1980's really dealing with complex configurations. The GARTEUR Working Group was done with very early CFD codes, and I think we are now at the stage where we understand the mathematical properties of these codes a lot better than we did at that time. Let me refer only to the Euler part which was done for this GARTEUR studies. There I think that one can say that if you take the codes now, the scatter will be a lot smaller. I only wanted to defend the CFD community that way.

Mr. D. Nelson, Boeing, Seattle, Washington, US
I want to make just a general comment, I believe it is expanding on what Mr. Haines meantioned. Throughout the Conference I saw primarily CFD as an analysis tool. I think CFD has perhaps reached the level of maturity now that it can be used as design tool. We have used it to identify problems and now we have to use it to solve problems. That, maybe combined with optimizing routines, we can come up with more optimum configurations. That, too, lends itself to testing validation, that we can go in and validate that we have improved the design.

Mr. Sacher
Thank you for this comment, I think that it is very, very true that CFD is not only the pure simulation of analysis comparable to the experiment. It has much more flexibility. Concerning its use as a design tool, it is a unique tool. At least, during this Conference this topic was missing. So perhaps the picture of CFD is not quite right here. We have got out just looking at this presentation following this meeting.

Let me make two comments on the statement of Joop Slooff who said that drag accounting was missing or not treated well enough and before there were some complaints of the CFD people not being able to predict drag. First of all, I should remind you that drag is not one thing. Drag has several components which can be computed quite well by CFD, much better than from the experiment. If you look at the task of incremental value of, let us say, induced drag, or additional drag due to quick changes on the geometry, wave drag predictions, pressure drag. These may be computed as well or even better than from the experiments which cannot resolve these detailed information on the flowfield we need for a really optimum design. But it is certainly true that in any kind of viscous drag or even separated flow, we failed up till now in predicting drag for a reasonable 3-D or a complex configuration. My hope is that it may improve in the future. People are working very hard to do that job. I think that during this week we have not got the problem of drag accounting, because we are not dealing with the highest degree of engine/airframe integration. Somebody was mentioning that these pictures we have seen of even the military applications was not the highest degree of engine/airframe integration. That is certainly true for these cases where we have a single engine, small aircraft, even military. There is no problem directly related from the afterbody jet interactior problem, but if you look to a more complex design, like multi-engine configuration, and if you go to hypersonic aircraft, not to speak from a space transport system, you will very early come up with the conclusion that this is the highest degree of complexity that you can reach. Drag accounting system is a real tricky thing, how to deal, how to separate the airframe components from the engine components, how to deal with interference effects in between. I learned from the NASP program that at least 7 or 8 different kinds of drag accounting systems have been proposed at an early stage for this complex matter. So the reason why I did not talk too much about this is perhaps the reason why we don't have too many contributions out of this project.

Mr. W. Burgsmuller, Deutsche Airbus, Bremen, GE
Just a comment or remark to Herr Slooff and his first point concerning the hot primary flow. I think at least for the transport aircraft or the turbofan side, it can be stated that this is not absolutely necessary. Some experiments have been made with the hot primary flow and the differences were very, very small. There is a bit more flow spreading, but it starts far downstream behind the wing, and that is the only difference we found. It should not be forgotten that although the primary flow is very cold, the momentum ratio between primary and fan for TPS is not absolutely wrong; it is nearly correct.

Mr. Harris
I would just like to follow Wolfgang to say that on the one hand, in Paper 15 I think that you will find a paragraph in there that says that somebody has been looking at the potential for adding a burning simulator; I know that it sounds horrific, but it really isn't that bad, you know, you do it on real things. The other comment is that in fact there has been some hot simulation on the shuttle, I believe, by Northrup where they did very short burn times in the wind tunnel, I mean extremely short, but long enough to capture the data but not burn the model. Maybe this might be a way to contemplate hot simulations on even quite expensive pieces of gear where you risk only the nozzles and you really do have quite fine systems of fuel control and light on.

Mr. Bowers
The question of hot simulation of the jet with the TPS leads to another comment I would like to make. I should tell you up front that my background is as an experimentalist, so I am not prejudice to one side or the other. I believe in the future, if not now, we will have an additional figure of merit to drag and performance, thrust and weight, and that will be cost. To me, the cost of adding a hot flow capability to a TPS is not worth it, it is not of value. We must use both the experimental tools to their most efficient way and the CFD tools in their most efficient way to reduce the cost in an era of dwindling resources. I believe that that comes back to the comment on cooperative wind tunnel centers of excellence. We should recognize that we are dealing with another figure of merit other than thrust, weight, performance.

Mr. Sacher
I agree completely, at least concerning any civil applications or military applications like fighter aircraft or missiles, but if you go to further integrated space transport systems with non-axisymmetric nozzle types, where real gas effects and jet impingement play a significant role. There you have to go to thrust deflection and to thrust vectoring. Then perhaps you will have to do it, otherwise you will come up with a completely wrong solution for the afterbody of your configurations. This already was indicated, of course, from a very intensive use of CFD.

Mr. Muylaert
Let me just magnify a little bit the statement of Peter for hypersonic application because this is an area where the uncertainty is large; we really need high enthalpy data from sophisticated non-intrusive measurement techniques to be able to verify our modelization. Non-equilibrium Navier Stokes codes with different chemical reactions, are required here and need to be validated.

Mr. Sacher
Do we have any other comments from the floor?

Mr. Harris
I would just like to point to the fact that really the words TPS are getting locked onto here and I am talking really model-powered simulation, not TPS-powered simulation. The point being that there are other ways and therefore, whether you go hot or not might depend on your perception of what you mean by doing that.

Mr. K.W. Lotter, MBB, Munchen, GE
I would like to comment on the subject of inlet-engine compatibility. I recognized in the conclusions you have made some criticism concerning the contacts between airframe and engine manufacturers. I think this is not quite correct. I think there is a lot of contacts between them and there are, during a development of a new aircraft, frequent inlet-engine compatibility meetings being held. However, the problem is whether the correct parameters are addressed and looked at. If we look back decades, there were fighter aircraft intake-engine compatibility problems related to excessive dynamic distortion. Then a huge "Tailor-mate" program was initiated and a lot of dynamic distortion measurements were made by the aircraft industry. I think that today we are in a position where we can precisely measure dynamic distortion. Nevertheless, during the Tornado flight test program we had draw-backs because a new effect came in: we had measured all the dynamic distortions but not the intake duct swirl which harms engines having no inlet guide vanes. There are often easy means to cure a problem. We have done that, for example, with the simple invention of a fence that completely eliminated these swirls. The engine manufacturer has clearly to define what harms the engine and this is the problem. The investigations which Dr. Meyer from the University of Neubiberg reported on are the reaction on the intensive discussions between industry and research institutes or between aircraft and engine companies, and I would like to encourage the engine manufacturers to do more work in that direction: that means, simulation of relevant disturbances in front of an engine.

Mr. Sacher
Thank you for this comment. It was exactly what we meant by our conclusion that better communication and more joined efforts are needed between Engine manufacturer and airframer. And to start, the engine manufacturer should specify acceptable levels for distortion or swirl, or what could be tolerated by the engine. This is not the case up till now and a more critical question is if we are providing our data of distortion what the engine manufacturer is doing with this data.

Mr. J. Bousquet, Aerospatiale, Toulouse, FR
I would like to make three remarks. The first one: you stated that in general TPS is owned by the test facility. In fact it is not the case in France. I don't know the situation for other countries, but in France the TPS's are owned by the manufacturer directly. I wonder if it is not the case in Germany also. The second remark is that you stated that it is necessary to have collaborative work between engine manufacturers and aircraft manufacturers. In fact, as far as I know, in the Airbus industry area there is a big tradition of collaboration between the engine manufacturers and aircraft manufacturers. In fact, we collaborate very soon in a project with engine manufacturers like Pratt and Whitney, General Electric, Snecma and Rolls Royce. The third remark is that you stated that it seems that in the U.S. the manufacturers do not use very much the TPS technique and you wonder why this is so. I would like to have a comment about this question. It seems that there are two schools; the European school with TPS and the US school without TPS. It is very funny to discuss why it is like that.

Mr. Sacher
It is my question too. Is it true, what we have stated, that TPS is more or less dominating in Europe and at least referring to the complete TPS dual jet core simulation, or is it the case that this work is going on in the States, but hasn't been reported here at the meeting. I would like to have a statement from the U.S. Is ASTF the solution for this? What about Boeing?

Mr. Tinoco
We have done some TPS testing, but we do most of it with blown nacelles or domed over nacelles with high pressure air exhaust. We have found it to be adequate for our needs, but that is not to say that there are not some TPS's around that occasionally get used. It is very expensive testing, very difficult to get all the proper calibrations and the question is whether it is worth it for the type of problems we encounter.

Mr. Sacher
I get some indication that we are reaching our limit, so unless there is some really urgent need to articulate another comment, I would propose that we close our discussion. First I would like to thank the audience for participating in this discussion. Secondly, I would like to thank the Session Chairmen for helping me in organizing this final session. Thirdly I would like to invite Jim McCroskey to make his concluding remarks on this meeting. Thank you.

Dr. W.J. McCroskey, US Army Aeroflightmechanics, Moffett Field, California US
Thank you, Peter. As we do not charge registration fees for these AGARD meetings, there is another penalty that you have to pay. That is to listen to the Chairman make pithy and erudite remarks from time to time. So I will start with the standard phrase. Now it is time to bring our 69th Meeting of the Fluid Dynamics Panel to a close. Whatever your backgrounds or interests, I hope you found this Symposium both informative and stimulating and I hope that you enjoyed the Fort Worth atmosphere this week as much as I have. This Symposium was intended to bring out the aerodynamic issues of airframe/engine integration, the ones that effect the performance of both the flight vehicle and the engine. It included both civil transport and military aircraft and we have heard about both experimental and computational techniques and also external and internal flows. I somewhat regret that we still argue about wind tunnels vs CFD, and now we heard a little bit of argument about who is the more confused, internal or external specialists. Going back to the CFD/wind tunnel issue, a certain amount of healthy skepticism is good, but I hope we can keep these comments and criticisms on a constructive level.

Now in this meeting we were also fortunate to have had two valuable contributions from the Propulsion and Energetics Panel of AGARD. We thank you very much Dr. Fottner for your contribution, and also to Professor Hirsch who has left already. We anticipate even greater PEP and FDP collaboration and cooperation in the future. As Chairman I was pleased and gratified to see a wide range of backgrounds and interests represented here. That is something that we always hope for in planning AGARD activities, and particularly meetings of this type. On this point, I sincerely hope not to embarrass them, but I am also delighted to see a two generational team here, the Ransom's from the U.K. I think that is a good trend.

Now, back to the future. I would like to speak a bit about our coming attractions. This is the 1992 program of the Fluid Dynamics Panel. We will conduct a Symposium on Theoretical and Experimental Methods in Hypersonic Flows in Italy in May, and a Symposium on High Lift System Aerodynamics in Canada about this time next year. We also will offer two special courses put on collaboratively with the von Karman Institute; one on Skin Friction Drag Reduction to be held at VKI in March and one on Unstructured Grid Methods for Advection Dominated Flows at the VKI in May and at NASA, Ames in September. Please contact me or the AGARD office or your countrymen on the Panel for further details.

A general word about AGARD, it is unique, but nevertheless, like many organizations in this day and age, it is under pressure to justify its existence. So, I am going to make a blatant plea that if you found this Symposium useful, or any of the other AGARD functions that I have just advertised, please acknowledge us to your colleagues and management. If you have suggestions for improvement, and I am sure that there are ways that we could, the Panel Members would like to hear from you, and we will strive to improve.

Assuming that you did find something to cheer about, I would like, on your behalf, to thank the Program Committee - and especially the Chairman, Singer and Concert Master, Pieter Sacher - we appreciate your efforts very much, not the least of which was to take over the duties of Technical Evaluator.

Once again, I wish to thank our warm and efficient Texas hosts, Dick and Lois Bradley, Dolores Hensley, Shivaun Wilson and Mr. English of General Dynamics, and the US National Authorities for AGARD.

Successful meetings rely heavily on the Staff of AGARD - our Panel Executive, Winston Goodrich; our Panel Secretary, Anne-Marie Revault; and the Technicians who have operated the projection and audio equipment so efficiently during the week, John Baron and Mike Morgan.

Last, but by no means least, our interpreters have worked very hard all week integrating our supersonic conversations into coherent French, English, and Texan; Ms. Kaplan, Ms. Kieffer, Ms. Sweeteye, and Ms. Zandrowicz.

And finally, Thanks Very Much to you, Ladies and Gentlemen. Have a pleasant and safe trip home. We hope to see you at future AGARD functions.

REPORT DOCUMENTATION PAGE

1. Recipient's Reference	2. Originator's Reference	3. Further Reference	4. Security Classification of Document
	AGARD-CP-498	ISBN 92-835-0672-3	UNCLASSIFIED

5. Originator Advisory Group for Aerospace Research and Development
North Atlantic Treaty Organization
7 rue Ancelle, 92200 Neuilly sur Seine, France

6. Title AERODYNAMIC ENGINE/AIRFRAME INTEGRATION FOR HIGH PERFORMANCE AIRCRAFT AND MISSILES

7. Presented at the Fluid Dynamics Panel Symposium held at
Fort Worth, Texas, United States, 7th—10th October 1991.

8. Author(s)/Editor(s)	9. Date
Various	September 1992
10. Author's/Editor's Address	**11. Pages**
Various	460

12. Distribution Statement This document is distributed in accordance with AGARD policies and regulations, which are outlined on the back covers of all AGARD publications.

13. Keywords/Descriptors

Jet aircraft	Rocket engines
Missiles	Aerodynamics
Airframes	Aerodynamic configurations
Aircraft engines	Integrated systems

14. Abstract

The 32 papers presented at the AGARD Fluid Dynamics Panel (FDP) Symposium on "Aerodynamic Engine/Airframe Integration for High Performance Aircraft and Missiles" that was held 7th—11th October 1991 in Fort Worth, Texas, United States are contained in this report. In addition to these papers, the Technical Evaluation Report aimed at assessing the relevance and success of the symposium in meeting the technical needs of the aerospace community and the transcript of the Round Table Discussion held at the end of the meeting are included in this document.

The objective of the symposium was to review the state-of-the-art in aerodynamic engine/airframe integration techniques and to report on the progress which has been achieved during engineering project work in recent years. Because the treatment of this subject requires an interdisciplinary approach, both experimentalists and theoreticians were invited to contribute to the meeting. Six sessions were organized to cover the essential sub-disciplines requiring aerodynamic engine/airframe integration during the concept-assessment and design phases for new aerospace vehicles.

symposium in meeting the technical needs of the aerospace community and the transcript of the Round Table Discussion held at the end of the meeting are included in this document.

The objective of the symposium was to review the state-of-the-art in aerodynamic engine/airframe integration techniques and to report on the progress which has been achieved during engineering project work in recent years. Because the treatment of this subject requires an interdisciplinary approach, both experimentalists and theoreticians were invited to contribute to the meeting. Six sessions were organized to cover the essential sub-disciplines requiring aerodynamic engine/airframe integration during the concept-assessment and design phases for new aerospace vehicles.

ISBN 92-835-0672-3

symposium in meeting the technical needs of the aerospace community and the transcript of the Round Table Discussion held at the end of the meeting are included in this document.

The objective of the symposium was to review the state-of-the-art in aerodynamic engine/airframe integration techniques and to report on the progress which has been achieved during engineering project work in recent years. Because the treatment of this subject requires an interdisciplinary approach, both experimentalists and theoreticians were invited to contribute to the meeting. Six sessions were organized to cover the essential sub-disciplines requiring aerodynamic engine/airframe integration during the concept-assessment and design phases for new aerospace vehicles.

ISBN 92-835-0672-3

symposium in meeting the technical needs of the aerospace community and the transcript of the Round Table Discussion held at the end of the meeting are included in this document.

The objective of the symposium was to review the state-of-the-art in aerodynamic engine/airframe integration techniques and to report on the progress which has been achieved during engineering project work in recent years. Because the treatment of this subject requires an interdisciplinary approach, both experimentalists and theoreticians were invited to contribute to the meeting. Six sessions were organized to cover the essential sub-disciplines requiring aerodynamic engine/airframe integration during the concept-assessment and design phases for new aerospace vehicles.

ISBN 92-835-0672-3

symposium in meeting the technical needs of the aerospace community and the transcript of the Round Table Discussion held at the end of the meeting are included in this document.

The objective of the symposium was to review the state-of-the-art in aerodynamic engine/airframe integration techniques and to report on the progress which has been achieved during engineering project work in recent years. Because the treatment of this subject requires an interdisciplinary approach, both experimentalists and theoreticians were invited to contribute to the meeting. Six sessions were organized to cover the essential sub-disciplines requiring aerodynamic engine/airframe integration during the concept-assessment and design phases for new aerospace vehicles.

ISBN 92-835-0672-3

AGARD Conference Proceedings 498
Advisory Group for Aerospace Research and Development, NATO
AERODYNAMIC ENGINE/AIRFRAME INTEGRATION FOR HIGH PERFORMANCE AIRCRAFT AND MISSILES
Published September 1992
460 pages

The 32 papers presented at the AGARD Fluid Dynamics Panel (FDP) Symposium on "Aerodynamic Engine/Airframe Integration for High Performance Aircraft and Missiles" that was held 7th–11th October 1991 in Fort Worth, Texas, United States are contained in this report. In addition to these papers, the Technical Evaluation Report aimed at assessing the relevance and success of the

P.T.O.

AGARD-CP-498

Jet aircraft
Missiles
Airframes
Aircraft engines
Rocket engines
Aerodynamics
Aerodynamic configurations
Integrated systems

AGARD Conference Proceedings 498
Advisory Group for Aerospace Research and Development, NATO
AERODYNAMIC ENGINE/AIRFRAME INTEGRATION FOR HIGH PERFORMANCE AIRCRAFT AND MISSILES
Published September 1992
460 pages

The 32 papers presented at the AGARD Fluid Dynamics Panel (FDP) Symposium on "Aerodynamic Engine/Airframe Integration for High Performance Aircraft and Missiles" that was held 7th–11th October 1991 in Fort Worth, Texas, United States are contained in this report. In addition to these papers, the Technical Evaluation Report aimed at assessing the relevance and success of the

P.T.O.

AGARD-CP-498

Jet aircraft
Missiles
Airframes
Aircraft engines
Rocket engines
Aerodynamics
Aerodynamic configurations
Integrated systems

AGARD Conference Proceedings 498
Advisory Group for Aerospace Research and Development, NATO
AERODYNAMIC ENGINE/AIRFRAME INTEGRATION FOR HIGH PERFORMANCE AIRCRAFT AND MISSILES
Published September 1992
460 pages

The 32 papers presented at the AGARD Fluid Dynamics Panel (FDP) Symposium on "Aerodynamic Engine/Airframe Integration for High Performance Aircraft and Missiles" that was held 7th–11th October 1991 in Fort Worth, Texas, United States are contained in this report. In addition to these papers, the Technical Evaluation Report aimed at assessing the relevance and success of the

P.T.O.

AGARD-CP-498

Jet aircraft
Missiles
Airframes
Aircraft engines
Rocket engines
Aerodynamics
Aerodynamic configurations
Integrated systems

AGARD Conference Proceedings 498
Advisory Group for Aerospace Research and Development, NATO
AERODYNAMIC ENGINE/AIRFRAME INTEGRATION FOR HIGH PERFORMANCE AIRCRAFT AND MISSILES
Published September 1992
460 pages

The 32 papers presented at the AGARD Fluid Dynamics Panel (FDP) Symposium on "Aerodynamic Engine/Airframe Integration for High Performance Aircraft and Missiles" that was held 7th–11th October 1991 in Fort Worth, Texas, United States are contained in this report. In addition to these papers, the Technical Evaluation Report aimed at assessing the relevance and success of the

P.T.O.

AGARD-CP-498

Jet aircraft
Missiles
Airframes
Aircraft engines
Rocket engines
Aerodynamics
Aerodynamic configurations
Integrated systems

NATO OTAN
7 RUE ANCELLE · 92200 NEUILLY-SUR-SEINE
FRANCE
Télephone (1)47.38.57.00 · Télex 610 176
Télécopie (1)47.38.57.99

DIFFUSION DES PUBLICATIONS
AGARD NON CLASSIFIEES

L'AGARD ne détient pas de stocks de ses publications, dans un but de distribution générale à l'adresse ci-dessus. La diffusion initiale des publications de l'AGARD est effectuée auprès des pays membres de cette organisation par l'intermédiaire des Centres Nationaux de Distribution suivants. A l'exception des Etats-Unis, ces centres disposent parfois d'exemplaires additionnels; dans les cas contraire, on peut se procurer ces exemplaires sous forme de microfiches ou de microcopies auprès des Agences de Vente dont la liste suite.

CENTRES DE DIFFUSION NATIONAUX

ALLEMAGNE
Fachinformationszentrum,
Karlsruhe
D-7514 Eggenstein-Leopoldshafen 2

BELGIQUE
Coordonnateur AGARD-VSL
Etat-Major de la Force Aérienne
Quartier Reine Elisabeth
Rue d'Evere, 1140 Bruxelles

CANADA
Directeur du Service des Renseignements Scientifiques
Ministère de la Défense Nationale
Ottawa, Ontario K1A 0K2

DANEMARK
Danish Defence Research Board
Ved Idraetsparken 4
2100 Copenhagen Ø

ESPAGNE
INTA (AGARD Publications)
Pintor Rosales 34
28008 Madrid

ETATS-UNIS
National Aeronautics and Space Administration
Langley Research Center
M/S 180
Hampton, Virginia 23665

FRANCE
O.N.E.R.A. (Direction)
29, Avenue de la Division Leclerc
92322 Châtillon Cedex

GRECE
Hellenic Air Force
Air War College
Scientific and Technical Library
Dekelia Air Force Base
Dekelia, Athens TGA 1010

ISLANDE
Director of Aviation
c/o Flugrad
Reykjavik

ITALIE
Aeronautica Militare
Ufficio del Delegato Nazionale all'AGARD
Aeroporto Pratica di Mare
00040 Pomezia (Roma)

LUXEMBOURG
Voir Belgique

NORVEGE
Norwegian Defence Research Establishment
Attn: Biblioteket
P.O. Box 25
N-2007 Kjeller

PAYS-BAS
Netherlands Delegation to AGARD
National Aerospace Laboratory NLR
Kluyverweg 1
2629 HS Delft

PORTUGAL
Portuguese National Coordinator to AGARD
Gabinete de Estudos e Programas
CLAFA
Base de Alfragide
Alfragide
2700 Amadora

ROYAUME UNI
Defence Research Information Centre
Kentigern House
65 Brown Street
Glasgow G2 8EX

TURQUIE
Milli Savunma Başkanlığı (MSB)
ARGE Daire Başkanlığı (ARGE)
Ankara

LE CENTRE NATIONAL DE DISTRIBUTION DES ETATS-UNIS (NASA) NE DETIENT PAS DE STOCKS DES PUBLICATIONS AGARD ET LES DEMANDES D'EXEMPLAIRES DOIVENT ETRE ADRESSEES DIRECTEMENT AU SERVICE NATIONAL TECHNIQUE DE L'INFORMATION (NTIS) DONT L'ADRESSE SUIT.

AGENCES DE VENTE

National Technical Information Service
(NTIS)
5285 Port Royal Road
Springfield, Virginia 22161
Etats-Unis

ESA/Information Retrieval Service
European Space Agency
10, rue Mario Nikis
75015 Paris
France

The British Library
Document Supply Division
Boston Spa, Wetherby
West Yorkshire LS23 7BQ
Royaume Uni

Les demandes de microfiches ou de photocopies de documents AGARD (y compris les demandes faites auprès du NTIS) doivent comporter la dénomination AGARD, ainsi que le numéro de série de l'AGARD (par exemple AGARD-AG-315). Des informations analogues, telles que le titre et la date de publication sont souhaitables. Veuiller noter qu'il y a lieu de spécifier AGARD-R-*nnn* et AGARD-AR-*nnn* lors de la commande de rapports AGARD et des rapports consultatifs AGARD respectivement. Des références bibliographiques complètes ainsi que des résumes des publications AGARD figurent dans les journaux suivants:

Scientifique and Technical Aerospace Reports (STAR)
publié par la NASA Scientific and Technical
Information Division
NASA Headquarters (NTT)
Washington D.C. 20546
Etats-Unis

Government Reports Announcements and Index (GRA&I)
publié par le National Technical Information Service
Springfield
Virginia 22161
Etats-Unis
(accessible également en mode interactif dans la base de données bibliographiques en ligne du NTIS, et sur CD-ROM)

Imprimé par Specialised Printing Services Limited
40 Chigwell Lane, Loughton, Essex IG10 3TZ

NATO OTAN

7 RUE ANCELLE · 92200 NEUILLY-SUR-SEINE

FRANCE

Telephone (1)47.38.57.00 · Telex 610 176
Telefax (1)47.38.57.99

DISTRIBUTION OF UNCLASSIFIED AGARD PUBLICATIONS

AGARD does NOT hold stocks of AGARD publications at the above address for general distribution. Initial distribution of AGARD publications is made to AGARD Member Nations through the following National Distribution Centres. Further copies are sometimes available from these Centres (except in the United States), but if not may be purchased in Microfiche or Photocopy form from the Sales Agencies listed below.

NATIONAL DISTRIBUTION CENTRES

BELGIUM
Coordonnateur AGARD – VSL
Etat-Major de la Force Aérienne
Quartier Reine Elisabeth
Rue d'Evere, 1140 Bruxelles

CANADA
Director Scientific Information Services
Dept of National Defence
Ottawa, Ontario K1A 0K2

DENMARK
Danish Defence Research Board
Ved Idraetsparken 4
2100 Copenhagen Ø

FRANCE
O.N.E.R.A. (Direction)
29 Avenue de la Division Leclerc
92322 Châtillon Cedex

GERMANY
Fachinformationszentrum
Karlsruhe
D-7514 Eggenstein-Leopoldshafen 2

GREECE
Hellenic Air Force
Air War College
Scientific and Technical Library
Dekelia Air Force Base
Dekelia, Athens TGA 1010

ICELAND
Director of Aviation
c/o Flugrad
Reykjavik

ITALY
Aeronautica Militare
Ufficio del Delegato Nazionale all'AGARD
Aeroporto Pratica di Mare
00040 Pomezia (Roma)

LUXEMBOURG
See Belgium

NETHERLANDS
Netherlands Delegation to AGARD
National Aerospace Laboratory, NLR
Kluyverweg 1
2629 HS Delft

NORWAY
Norwegian Defence Research Establishment
Attn: Biblioteket
P.O. Box 25
N-2007 Kjeller

PORTUGAL
Portuguese National Coordinator to AGARD
Gabinete de Estudos e Programas
CLAFA
Base de Alfragide
Alfragide
2700 Amadora

SPAIN
INTA (AGARD Publications)
Pintor Rosales 34
28008 Madrid

TURKEY
Milli Savunma Başkanlığı (MSB)
ARGE Daire Başkanlığı (ARGE)
Ankara

UNITED KINGDOM
Defence Research Information Centre
Kentigern House
65 Brown Street
Glasgow G2 8EX

UNITED STATES
National Aeronautics and Space Administration (NASA)
Langley Research Center
M/S 180
Hampton, Virginia 23665

THE UNITED STATES NATIONAL DISTRIBUTION CENTRE (NASA) DOES NOT HOLD STOCKS OF AGARD PUBLICATIONS, AND APPLICATIONS FOR COPIES SHOULD BE MADE DIRECT TO THE NATIONAL TECHNICAL INFORMATION SERVICE (NTIS) AT THE ADDRESS BELOW.

SALES AGENCIES

National Technical
Information Service (NTIS)
5285 Port Royal Road
Springfield, Virginia 22161
United States

ESA/Information Retrieval Service
European Space Agency
10, rue Mario Nikis
75015 Paris
France

The British Library
Document Supply Centre
Boston Spa, Wetherby
West Yorkshire LS23 7BQ
United Kingdom

Requests for microfiches or photocopies of AGARD documents (including requests to NTIS) should include the word 'AGARD' and the AGARD serial number (for example AGARD-AG-315). Collateral information such as title and publication date is desirable. Note that AGARD Reports and Advisory Reports should be specified as AGARD-R-nnn and AGARD-AR-nnn, respectively. Full bibliographical references and abstracts of AGARD publications are given in the following journals:

Scientific and Technical Aerospace Reports (STAR)
published by NASA Scientific and Technical
Information Division
NASA Headquarters (NTT)
Washington D.C. 20546
United States

Government Reports Announcements and Index (GRA&I)
published by the National Technical Information Service
Springfield
Virginia 22161
United States

(also available online in the NTIS Bibliographic Database or on CD-ROM)

Printed by Specialised Printing Services Limited
40 Chigwell Lane, Loughton, Essex IG10 3TZ

ISBN 92-835-0672-3